



Final proceedings



An international conference on heat pipe science and technology organized with the financial support of Thales, ATHERM, Euro Heat Pipe and Calyos as well as the institutional and financial support of Région Rhône-Alpes



Rhône-Alpes Région

Proceedings of the 16th International to Heat Pipe Conference

- 2012 -

Editor

Prof. Jocelyn BONJOUR
CETHIL, INSA de Lyon, France

National Organizing Committee

Dr. Alain ALEXANDRE, International Committee on IHPC
Prof. Yves BERTIN, Institut PPrime, Poitiers
Dr. Stéphane LAUNAY, IUSTI, Marseille
Dr. Marc MISCEVIC, LAPLACE, Toulouse
Dr. Marc PRAT, IMFT, Toulouse
Prof. Frédéric LEFÈVRE, CETHIL, Lyon
Dr. Valérie SARTRE, CETHIL, Lyon
Dr. Stéphane LIPS, CETHIL, Lyon
Mrs. Florence CANALE, CETHIL, Lyon
Mr. Claude SARNO, THALES AVIONICS, Valence

The Committee expresses its gratitude to the PhD students at CETHIL:

Mr. Nathanaël RIVIÈRE,
Mr. Benjamin SIEDEL,
Mr. Manoj RAO,
as well as to INSAVALOR
for their support.



Correspondence Address

Prof. Jocelyn BONJOUR
CETHIL - Bât. Sadi Carnot - INSA de Lyon
20 av. Albert Einstein
69621 VILLEURBANNE Cedex - FRANCE
Email: jocelyn.bonjour@insa-lyon.fr
Tel: +33 4 72 43 64 27

Committee on International Heat Pipe Conferences

Honorary Chairman

Prof. M. Groll, Stuttgart, Germany (founding member)

Chairman

Prof. Yu. Maydanik, Ekaterinburg, Russia

Members

Dr. A. Alexandre	Poitiers, France
Prof. J. H. Boo	Seoul, Korea
Prof. C. A. Busse	Leggiuno, Italy (founding member)
Prof. P. D. Dunn	London, UK (founding member)
Prof. F. Kaminaga	Ibaraki, Japan
Prof. S. Khandekar	Kanpur, India
Prof. T. Z. Ma	Beijing, China
Prof. M. Mantelli	Florianópolis, Brazil
Prof. J. Ochterbeck	Clemson, SC, USA
Prof. P. Stephan	Darmstadt, Germany
Mr. W. Supper	Noordwijk, The Netherlands
Prof. L.L. Vasiliev	Minsk, Belarus
Prof. H. Zhang	Nanjing, China

Table of Content

Keynote lectures

20 YEARS OF PROGRESS IN THE USE OF GAS-CONTROLLED HEAT PIPES FOR THERMODYNAMIC MEASUREMENTS <i>A. Merlone, C. Musacchio, P. Marcarino, C. Bassani, J. van Geel, X. Yan, F. Sparasci, E. Georgin</i>	13
ENHANCEMENT OF VAPOR CONDENSATION IN HEAT PIPES <i>Oleg Kabov, Igor Marchuk, Andrey Glushchuk, Yuriy Lyulin</i>	27
TOWARDS QUANTITATIVE VALIDATION OF A CLOSED LOOP PULSATING HEAT PIPE NUMERICAL MODEL <i>Mauro Mamei, Marco Marengo, Sameer Khandekar</i>	41
APPLICATION OF PHASE CHANGE SYSTEMS IN AVIONICS <i>Claude Sarno</i>	47

Communications

HORIZONTAL CLOSED-LOOP PULSATING HEAT PIPE WITH MULTIPLE HEAT SOURCES <i>Niti Kammuang-lue, Phrut Sakulchangsattajai, Pradit Terdtoon</i>	57
THERMALLY INDUCED TWO-PHASE OSCILLATING FLOW IN A CAPILLARY TUBE: THEORETICAL AND EXPERIMENTAL INVESTIGATIONS <i>Manoj Rao, Frédéric Lefèvre, Jocelyn Bonjour, Sameer Khandekar</i>	63
INTERMEDIATE TEMPERATURE HEAT PIPE LIFE TESTS <i>William G. Anderson, Sanjida Tamanna, Calin Tarau, John R. Hartenstine, David Ellis</i>	69
AN EXPERIMENTAL STUDY OF LOCAL NUSSELT NUMBER FOR GAS-LIQUID TAYLOR BUBBLE FLOW IN A MINI-CHANNEL <i>Abhik Majumder, Balkrishna Mehta, Sameer Khandekar</i>	75
AUTOMATED FILLING AND SEALING OF EMBEDDED HEAT PIPES <i>Wessel W. Wits, Johannes van Es, Gert Jan te Riele</i>	81
MULTILAYER SINTERED POROUS MEDIA MINI HEAT PIPE <i>J.P.M. Florez, G.G.V. Nuernberg, K.V. Paiva, S.T.R. Velasquez, M.B.H. Mantelli</i>	87

ATV ACTIVE THERMAL CONTROL WITH VARIABLE CONDUCTANCE HEAT PIPES: DESIGN DESCRIPTION AND IN FLIGHT RESULTS <i>Patrick Oger, Frank Bouckaert</i>	93
AUTONOMOUS HEAT PIPE THERMAL CONTROL SYSTEMS FOR CCD COOLING OF SPACE SCIENTIFIC EQUIPMENT <i>Baturkin V.</i>	99
VARIABLE CONDUCTIVE HEAT PIPES FOR SPACE RADIATORS <i>K.A. Goncharov, A.N. Golikov, V. Antonov, A. Rukovishnikov, N. Tarnovsky</i>	105
VISUAL AND INSTRUMENTAL INVESTIGATIONS OF A COPPER-WATER LOOP HEAT PIPE <i>E. Bartuli, S. Vershinin, Yu. Maydanik</i>	111
A CAPILLARY AND GRAVITY PUMPED TWO-PHASE-TWO-LOOP-SYSTEM FOR COOLING OF ELECTRONIC DEVICES <i>Peter Stephan, Boris Schilder</i>	117
EFFECTS OF ACCELERATION FORCES ON THE THERMAL PERFORMANCES ON FLAT HEAT PIPES WITH DIFFERENT CAPILLARY STRUCTURES <i>M. C. Zaghdoudi, C. Tantolin, C. Sarno</i>	123
HORIZONTAL VAPORDYNAMIC THERMOSYPHONS, FUNDAMENTALS AND PRACTICAL APPLICATIONS <i>L. L. Vasiliev, L. L. Vasiliev Jr.</i>	129
EXPERIMENTAL INVESTIGATION OF FLAT HEAT PIPES TO REMOVE HIGH HEAT FLUXES <i>Valerij Derevyanko, Denis Nesterov, Sergey Suntsov</i>	135
LOOP HEAT PIPE THERMAL MODEL <i>C. Figus, T. Coquard, A. Lecossais</i>	141
SIMULATION OF THE OPERATING CHARACTERISTICS OF A CASCADED LHP WITH THERMAL CONNECTOR FOR ON BOARD ELECTRONIC COOLING <i>Nathanaël Rivière, Valérie Sartre, Jocelyn Bonjour</i>	147
THEORETICAL AND EXPERIMENTAL STUDY OF CPL AND LHP WITH CERAMIC WICKS <i>Paulo Henrique Dias dos Santos, Amir A. M. Oliveira, Edson Bazzo</i>	153
A THEORETICAL ANALYSIS OF THE TRANSIENT BEHAVIOR OF A CPL FOR TERRESTRIAL APPLICATION <i>A. Kaled, S. Dutour, V. Platel, L. Lachassagne, V. Ayel</i>	159
A THEORETICAL INVESTIGATION OF PHASE DISTRIBUTION IN THE EVAPORATOR CAVITY OF A LOOP HEAT PIPE <i>H. T. Phan, S. Dutour, V. Platel, A. Larue de Tournemine</i>	165

THE INFLUENCE OF GROOVE SHAPE ON LOOP HEAT PIPES' PERFORMANCE <i>Masakazu Kuroi, Hosei Nagan</i>	171
ON THE LOWERING OF THE OPERATING TEMPERATURE OF A COPPER-WATER LOOP HEAT PIPE <i>S. Yushakova, M. Chernysheva, Yu. Maydanik, S. Vershinin</i>	177
PERFORMANCE OF AN AMMONIA LOOP HEAT PIPE OPERATING AT TEMPERATURES UP TO 125° C <i>P. Prado, D. Mishkinis, A. Kulakov, A. Radkov, A. Torres, T. Tjiptahardja, A.S. Merino</i>	183
HIGH HEAT TRANSPORT CAPILLARY EVAPORATOR DEVELOPMENT FOR LOOP HEAT PIPES <i>Randeep Singh, Masataka Mochizuki, Kazuhiko Goto, Thang Nguyen, Tien Nguyen, Koichi Mashiko, Yuji Saito, Vijit Wuttijumnong</i>	189
A HIGH POWER DENSITY AND LOW WATER CONTENT HEAT PIPE NATURAL CONVECTION HEAT EXCHANGER FOR DOMESTIC HEATING APPLICATION <i>K. Kerrigan, G. E. O'Donnell, H. Jouhara, A. J. Robinson</i>	195
COMPARATIVE ANALYSIS OF TWO-PHASE THERMOSYPHONS SOLAR COLLECTORS <i>D. Del Col, A. Padovan, S. Filippeschi</i>	201
COMPLETELY PASSIVE HEAT PIPE BASED EMERGENCY CORE COOLING SYSTEM FOR NUCLEAR POWER REACTOR <i>Masataka Mochizuki, Randeep Singh, Thang Nguyen, Tien Nguyen, Koichi Mashiko, Yuji Saito, Vijit Wuttijumnong</i>	207
WETTING AND FILM BEHAVIOR OF PROPANE INSIDE GEOTHERMAL HEAT PIPES <i>Thomas Storch, Tom Weickert, Thomas Grab, Ulrich Gross, Manja Kasper</i>	213
THERMOSYPHONS FOR HIGH POWER LED LIGHTING PRODUCTS <i>Valery M. Kiseev, Victor G. Cherkashin</i>	219
A STUDY ON THERMAL CONDUCTANCE IN A LOOPED PARALLEL THERMOSYPHON <i>Fumito Kaminaga, Kunihito Matsumura, Ryo Horie, Akira Takahashi</i>	225
RELATIVE THERMAL PERFORMANCE OF SUPER-CRITICAL CO ₂ , H ₂ O, N ₂ AND He CHARGED CLOSED-LOOP THERMOSYPHON-TYPE HEAT PIPES <i>R. T. Dobson</i>	231
ANALYSIS RESULTS OF A TEN YEAR SODIM HEAT PIPE LIFE TEST <i>John H. Rosenfeld, James L. Sanzi</i>	237
AUGMENTING CAPILLARY SUCTION BY ELECTROWETTING FOR COOLING APPLICATIONS <i>Soubhik Kumar Bhaumik, Sunando DasGupta, Suman Chakraborty</i>	243
INCREASING THE CPL POWER AT STARTUP BY USING A CHECK VALVE <i>V. Dupont, S. Van Oost, L. Barremaecker</i>	249

DEVELOPMENT AND EXPERIMENTAL INVESTIGATION OF A HEAT-TRANSFER SYSTEM ON THE BASIS OF A LOOP AND A PULSATING HEAT PIPE <i>V. G. Pastukhov, Yu. Maydanik</i>	255
EXPERIMENTAL STUDY ON THE EFFECTS OF THE VAPOUR PRESSURE LOSSES ON A CAPILLARY PUMPED LOOP FOR TERRESTRIAL APPLICATION <i>Vincent Aysel, Laurent Lachassagne, Yves Bertin, Cyril Romestant</i>	261
DEPENDENCE OF LIQUID RESERVOIR ORIENTATION ON BEHAVIOR OF TEMPERATURE CONTROLLABLE OSCILLATING HEAT PIPE <i>Hiroyuki Ogawa, Naoko Iwata, Yoshiro Miyazaki</i>	267
MODELING TRANSIENT ACCELERATION EFFECTS ON HEAT PIPE PERFORMANCE <i>J. Ambrose</i>	271
VARIABLE CONDUCTANCE HEAT PIPES FOR VARIABLE THERMAL LINKS <i>William G. Anderson, John R. Hartenstine, Christopher J. Peters</i>	277
THEORETICAL AND EXPERIMENTAL STUDY OF THE THERMAL RESISTANCES IN THE UNIT, INCLUDING TWO AXIAL HEAT PIPES JOINED TO EACH OTHER <i>K. Goncharov, Yu. Panin,, V. Antonov, A. Kochetkov</i>	283
GROOVED HEAT PIPE EVAPORATORS WITH POROUS COATING <i>L. L. Vasiliev, L. P. Grakovich, M. I. Rabetsky, L. L. Vasiliev Jr.</i>	289
EVAPORATION FROM MICRO-POROUS SURFACES IN A MECHANICALLY PUMPED TWO-PHASE LOOP <i>M. Winter, P. Stephan</i>	295
A HIGH THERMAL DISSIPATION PERFORMANCE POLYETHYLENE TEREPHTHALATE HEAT PIPE <i>Guan-Wei Wu, Wen-Pin Shih, Sih-Li Chen</i>	301
SIMULATION OF HEAT TRANSFER IN LIQUID PLUGS MOVING INSIDE DRY CAPILLARY TUBES <i>Ashish Kumar Bajpai, Sameer Khandekar</i>	307
INDUSTRIAL MANUFACTURING OF LOOP HEAT PIPE POROUS MEDIA <i>Thomas Albertin, Jean-François Savard, Valérie Sartre</i>	313
COOLING SYSTEM FOR HERMETIC COMPRESSOR BASED ON THE PULSATING LOOP THERMOSYPHON <i>V. A. Aliakhnovich, L. L. Vasiliev</i>	319
SINTERED ALUMINUM HEAT PIPE (SAHP) <i>M. Ameli, B. Agnew, B. Ng, R. McGlen, C. J. Sutcliffe, J. Singh</i>	323
PRESSURE CONTROLLED HEAT PIPE APPLICATIONS <i>William G. Anderson, John R. Hartenstine, David B. Sarraf, Calin Tarau, Kara L. Walker</i>	329

EXPERIMENTAL PERFORMANCE COMPARISON OF AXIALLY GROOVED HEAT PIPES CHARGED WITH ACETONE AND AMMONIA <i>Jorge Bertoldo Junior, Valeri V. Vlassov, Pedro Antônio Cândido, Gino Genaro, Valery M. Kiseev</i>	335
EXPERIMENTAL STUDY OF PULSATING HEAT PIPES TESTED IN LOOPED AND UNLOOPED CONFIGURATIONS <i>Jean-François Bonnenfant, Vincent Ayel, Yves Bertin, Cyril Romestant</i>	341
INVESTIGATION ON OPERATIONAL CHARACTERISTICS OF THE MINIATURE LOOP HEAT PIPES WITH FLAT EVAPORATORS BASED ON DIVERSE VAPOR REMOVAL CHANNELS <i>Jeehoon Choi, Yunkeun Lee, Byungho Sung, Chulju Kim</i>	347
ON THE USE OF HEAT PIPE PRINCIPLE FOR THE EXPLOITATION OF MEDIUM - LOW TEMPERATURE GEOTHERMAL RESOURCES <i>Alessandro Franco, Maurizio Vaccaro</i>	353
CRYOGENIC THERMAL LINK WITH TWO PHASE COLD RESERVOIRS <i>P. Gully, F. Bonnet</i>	359
PERFORMANCE OF A GRAVITY-DRIVEN AND CAPILLARY-SIZED THERMOSYPHON LOOP WORKING WITH AMMONIA <i>Mathieu Habert, Bruno Agostini</i>	365
STUDY ON HEAT TRANSFER CHARACTERISTICS OF LOOP HEAT PIPE FOR SOLAR COLLECTOR <i>Shigeki Hirasawa, Shota Sato, Tsuyoshi Kawanami</i>	371
THERMAL PERFORMANCE OF HEAT PIPE-HEAT SOURCE USED FOR TEMPERATURE STABILIZATION IN EXTENDED TEMPERATURE RANGE <i>N. Koneva, L. Domorod</i>	377
RESEARCH OF FACTORS INFLUENCING HEAT TRANSFER CHARACTERISTICS OF MINIATURE HEAT PIPES <i>V.Yu. Kravets, Ia.V. Nekrashevych</i>	383
EFFECT OF COMPENSATION CHAMBER COOLING ON THE OPERATION OF A FLAT EVAPORATOR LOOP HEAT PIPE <i>Tae Hee Kim, Wukchul Joung, Sung pil Ma, Chun Bae Choi, Jinho Lee</i>	389
DEVELOPMENT OF A FLAT ALUMINIUM PANEL WITH MINICHANNELS AS LHP CONDENSER <i>Leonid Vassiliev, Maria Liakh</i>	395
A CLOSED LOOP THERMOSYPHON WITH CONVENTIONAL OR MINICHANNEL BASED CONDENSER AND EVAPORATOR <i>Henryk Bielinski, Jarostaw Mikielewicz, Dariusz Mikielewicz</i>	401
A TWO-PHASE LOOP THERMOSYPHON WITH NAPHTHALENE AS WORKING FLUID <i>F.H. Milanez, M.B.H. Mantelli</i>	407
COOLING DEVICE USING THE NATURAL CONVECTION, PHASE CHANGE OF SUBSTANCE AND CAPILLARY EFFECT PHENOMENON <i>Patrik Nemeč, Alexander Čaja, Milan Malcho</i>	413

ACTIVE CONTROL OF THE SET POINT OF A 2-WAY PRESSURE REGULATING VALVE IN A LHP <i>F. Romera, D. Mishkinis, A. Kulakov, A. Torres</i>	419
HYDRODYNAMICS OF A CONFINED MENISCUS IN A CAPILLARY TUBE <i>Gyana Ranjan Rana, Tushar Sahu, Sameer Khandekar, P. K. Panigrahi</i>	425
APPLICATION OF MINI HEAT PIPES FOR THERMAL MANAGEMENT OF OPTO- ELECTRONIC INSTRUMENTS <i>Sandeep Kumar Singh, Sameer Khandekar, Pankaj Srivastava, J. K. Bajpai</i>	431
THERMAL ANALYSIS OF A DIFFUSION MODEL APPLIED FOR A GAS-LOADED VAPOR CHAMBER CONDENSER <i>E.G. Tavares, K.W. Milanez, F.H. Milanese, M.B.H. Mantelli</i>	437
VISUALIZATION OF THE CONDENSATION CHARACTERISTICS IN MESH-WICKED HEAT PIPES <i>S.-C. Wong, H.-H. Tseng, S.-H. Chen</i>	443
EXPERIMENTAL INVESTIGATION OF TWO-PHASE CLOSED THERMOSYPHON WITH INTERNAL HELICAL MICROFIN <i>Xinyu Wang, Gongming Xin, Yifei Wang, Lin Cheng</i>	449
LOOP THERMOSYPHON FOR THE THERMAL MANAGEMENT OF AN AIRCRAFT ELECTRONIC BOX <i>C. Sarno, C. Tantolin, R. Hodot, Yu. Maydanik, S. Vershinin</i>	455
POSSIBILITY OF USING BIPHASIC PULSATING PUMP OF HEAT ACTION IN HEATING AND COOLING SYSTEMS <i>V.Y. Sasin, N. M. Savchenkova, I.V. Parehina, D.O. Murotyan</i>	461
DEVELOPMENT OF THE ALPHABUS EXTENDED DEPLOYABLE RADIATOR <i>C. Berend, A. Lecossais, E. Dehombreux, T. Tjijtahardja</i>	465
Li-ION BATTERY THERMAL MANAGEMENT SYSTEM WITH LOOP THERMOSYPHON OF ELECTRIC VEHICLE <i>Ju-Chan Jang, Seok-Ho Rhi, Kye-Bock Lee, Ki-Woo Lee, Young-Soo Lee, Wook-Hyun Lee</i>	471
Index of Authors	477

The communications and keynote lectures published in this document are under the sole responsibility of their Authors. They were printed directly from the files provided by the Authors.

20 YEARS OF PROGRESS IN THE USE OF GAS-CONTROLLED HEAT PIPES FOR THERMODYNAMIC MEASUREMENTS

A. Merlone¹

¹Istituto Nazionale di ricerca Metrologica (INRiM),
Strada delle Cacce, 91 10135 Torino, Italy
+39 011 3919734, a.merlone@inrim.it

C. Musacchio¹, P. Marcarino², C. Bassani³, J. van Geel⁴, X. Yan⁵, F. Sparasci⁶, E. Georjin⁷

²Retired from Istituto di Metrologia G. Colonnetti (IMGC), Torino, Italy

³Retired from Euratom Joint Research Center (JRC), Ispra, Italy

⁴VSL, Dutch Metrology Institute, Delft, the Netherlands

⁵National Institute of Metrology (NIM), Beijing, China

⁶Laboratoire Commun de Métrologie LNE-Cnam, Paris, France
LNE-CETIAT, Villeurbanne, France

ABSTRACT

Gas-Controlled Heat Pipes (GCHPs) have been studied, manufactured and used since more than twenty years for thermodynamics studies and applications in thermal metrology. Several different models of GCHPs have been made in different materials, filled with different working fluids and optimized for different temperature / pressure ranges. This wide scientific and technical applications cover different aspects such as vapour/pressure curves studies for pure elements and substances, innovative temperature standards, temperature sensors, calibration facilities, accurate pressure controllers. Since the first models of GCHP made by Joint research center (JRC) – Euratom in Ispra, substantial improvements have been achieved: new working fluids and new capillary structures adopted; gas-vapour interface positions tested and optimized; purity of the elements evaluated; dedicated new furnaces assembled with new power-control systems and cooling lines. Their capabilities have been constantly improved during the years, in terms of temperature stability and uniformity, heat and pressure control. A dedicated pressure controller has been studied, developed and tested, based on the thermodynamic relationship linking temperature and pressure in a fluid in liquid vapour phase transition, allowing a very accurate temperature and pressure control. GCHPs filled with different working fluids, thus operating at different temperature ranges, have been connected to the same pressure line in the so called “Temperature Amplifier” configuration. The relevance of the scientific activities involving the GCHPs and their application has been constantly demonstrated through a numerous series of publications in international reviews and conferences.

KEY WORDS: Gas-controlled Heat Pipe, Thermodynamics, Metrology

1.INTRODUCTION.

THE GAS-CONTROLLED HEAT PIPE

The Gas-Controlled Heat-Pipe is a special kind of Heat-Pipe equipped with a gas controlled line that enables a direct control of the inner pressure. An inert gas is used to control the vapour pressure of the working fluid. The gas needs to have a different density from that of the vapour of the working fluid, in order to origin a interface between the two. This interface is established at a variable point along the vertical axis of the pipe,

depending on some factors such as the heating power, the refrigerating capabilities, the pressure level, the kind of working fluid and controlling gas used. The inner chamber of the Heat-Pipe is in nearly isothermal conditions, since a stream of vapour, flowing from the heated section to the cooled one, continuously rinses it. Basically it is possible to recognize in a Gas Controlled Heat-Pipe two interfaces: one between the vapour and the liquid of the working fluid and another between the vapour and the gas. This second interface is placed in this upper part of the Heat-Pipe, closer to

the cooled zone. Therefore the controlling gas is almost at room temperature. This makes the gas control processes easier, and no peculiar attention on its temperature is required. The temperature of the interface between vapour and liquid is thermodynamically related to the pressure inside the Heat Pipe volume. This pressure can be controlled by the gas through the chimney. Therefore, the temperature inside the Heat-Pipe can be controlled and maintained at a desired value, by controlling the gas pressure.

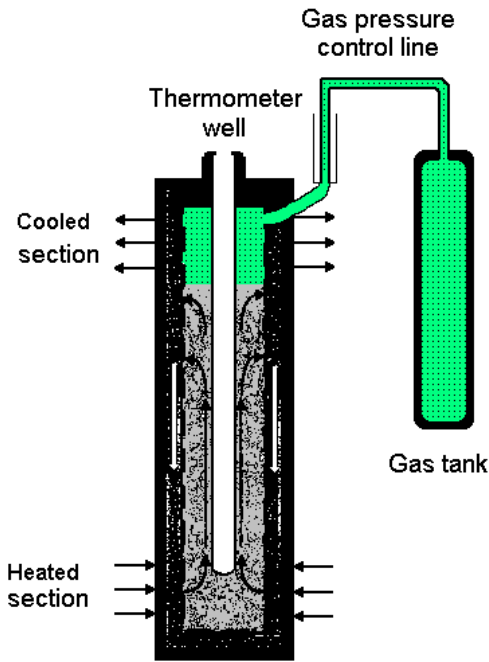


Figure 1. A schematic description of a Gas Controlled Heat-Pipe

Gas Controlled Heat-Pipes used in thermometry are specially developed for the purpose. They are equipped with a lateral chimney used both as the cooling zone and to connect the gas control line. Inside the cylindrical chamber one or more thermometer wells are placed. The liquid working fluid returns to the heated zone also along knurls machined around the external walls of thermometer wells, in order to keep the measuring zone wet. This ensures a liquid vapour interface all around the thermometer well. Accurate measurements of the liquid vapour phase transition temperature are then obtained by means of Standard Platinum Resistance Thermometers (SPRTs) inserted in the wells. In some case a mesh is also added to force the uniformity of liquid layer, in order to origin a complete phase transition interface.

The capabilities of the gas controlling system are directly responsible of the temperature stability inside the Heat-Pipe and of the wideness of the achievable range.

These furnaces offer unique possibilities with regards to the homogeneity, stability and reproducibility of the temperature, and the ease and speed of transition from one temperature level to another.

2. THE VERY BEGINNING. *Fourty years ago*

In 1972, it was decided to build at the Euratom Joint Research Centre of Ispra an improved Couette absolute viscometer.

For housing this instrument a thermostat with unusual properties was needed: large volume of 15 l, high temperature homogeneity (0.01 °C), operating temperature up to 140 °C and rapid transition from one temperature to another. These specifications were difficult to meet with the usual thermostats of the aquarium type. In particular the transition from one stabilized temperature to another is far from easy with this systems: each time a new isothermal zone has to be found in which to place the viscometer, and these zones become increasingly small with rises in temperature. Therefore the application of the gas controlled heat pipe was considered, on which a fair amount of experience was available at Ispra from work on thermionic space power supplies.

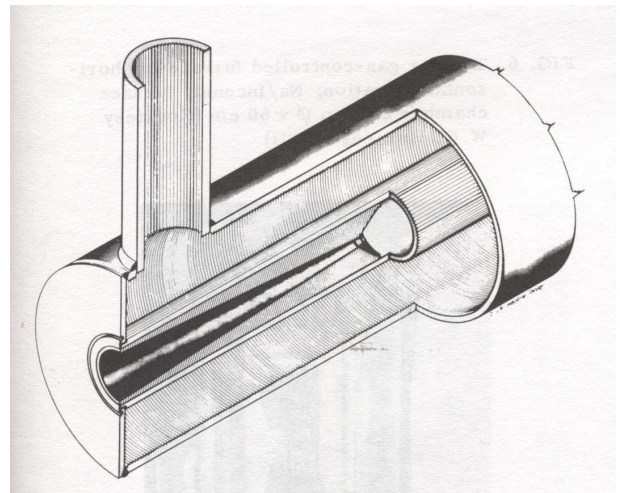


Figure 2a Grooved capillary structure in a tubular gas controlled heat pipe. An early years published scheme of a GCHP.

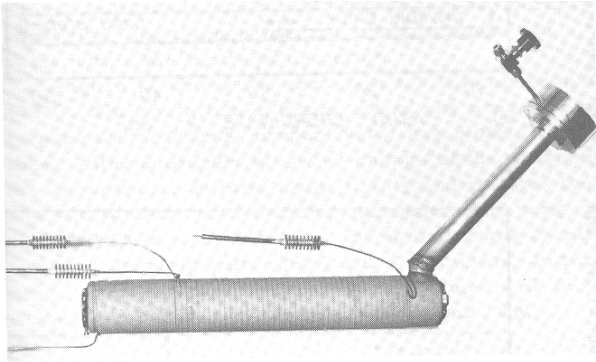


Figure 2b GCHP furnace for operation between horizontal and vertical position (Na / Inconel chamber, 50 cm length, 1.7 cm diameter)

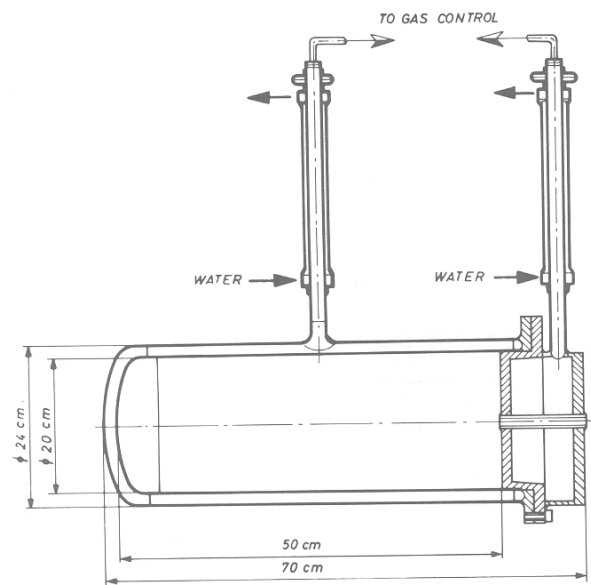


Figure 2c. Gas controlled furnace with heat pipes in the form of a one-sided closed tube and a lid (H₂O or Freon 11 / Stainless steel)

This was the beginning of development of gas controlled heat pipe furnaces. The new technology made it easy to meet the requirement for the viscometer (Bassani, 1976). This encouraging initial result then stimulated the extension of the work to higher temperatures where other areas of application of the furnaces were seen, e.g. in connection with the effort of improving the International Practical Temperature Scale of 1968 between 630 °C and 1064 °C. Cesium and sodium served as working fluid.

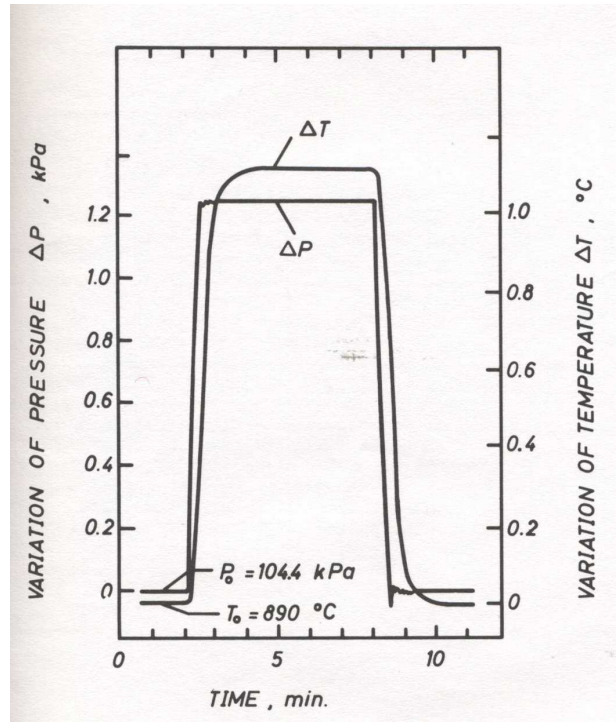


Fig 3a First evaluations of the transient behavior of a high temperature gas-controlled furnace (1980)

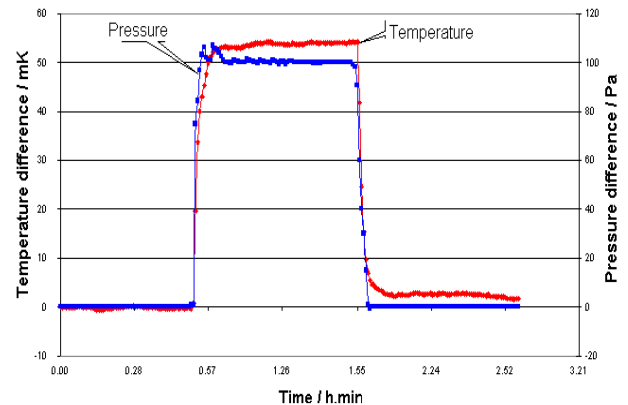


Fig 3b Same tests are still performed in those days, to evaluate the response capability and the correct startup (2010).

The investigated temperature ranges were 372 °C to 671 °C and 626 °C to 1068 °C respectively. For all the investigated temperature range up to 1000 °C the temperature variations were, in general, below the limits of detection of the measuring probe and remained within 10 mK over a length of some 25 cm. (Bassani, 1981).

During the 1982 6th Temperature Conference, a fruitful meeting between the scientists of JRC and those from the Italian Institute of Metrology (at that time the Istituto di Metrologia Gustavo Colonnetti - IMGC), made it possible to start to

adopt this technology for thermal metrology (Marcarino, 1992), where accurate, stable and reproducible temperature are the key aspect of any investigation.

3. INRiM, the world reference Institute for the GCHP technology.

Since the 1982 meeting, a cooperation between JRC Ispra and IMGC (now Istituto Nazionale di Ricerca Metrologica - INRiM) grew with relevant results, leading to development of new GCHPs, new machining and filling techniques, vapour pressure accurate investigations, dissemination of the use of such devices to other Institutions worldwide. When, in the end of the 90s JRC closed the GCHP production, the knowledge was transferred to INRiM where new GCHPs have been studied and manufactured. A dedicated laboratory has then been opened in the thermodynamics division and trained personnel is constantly operating such devices. (Merlone, 2004)

The devices are operated as thermometer calibration facilities (Marcarino, 1999; Marcarino 2002; Marcarino 2001), in support of research on the International Temperature Scale ITS-90 (Marcarino 2001; Marcarino 1992; Marcarino 2002) and for accurate thermodynamic studies. (Merlone 2002; Marcarino, 2002; Marcarino, 2003; Merlone 2003).

New Gas-Controlled Heat Pipes (GCHPs) have been manufactured at INRiM for primary resistance thermometry purposes, and are now commercially available (Merlone, 2004; Merlone 2008). The design of the new heat pipes is an improvement of the design of the heat pipes manufactured some years ago at JRC and takes into account all recent studies carried out at INRiM on this kind of devices. Inconel heat pipes are now available for being filled with potassium or sodium as working fluids for high temperature measurements. Stainless steel heat pipes have also been manufactured, to be filled with low-temperature working fluids, such as mercury. Six-well and three-well pipes are available, both for higher or lower temperature, on request. A new pressure control system was developed too (Giunta 2008): it's been designed purposely for the control of the pressure inside the heat pipes, by acting on the pressure of the controlling gas. This controller can use a Platinum Resistance Thermometer (PRT) as sensor, through its reading by an automatic F18

bridge processed by a computer passed on to the controller. The GCHPs are equipped with dedicated new furnaces, new power-control systems and cooling lines. Two or more GCHPs can be connected to the same pressure controlled line in order to realise the "Temperature Amplifier" or to obtain continuous temperature ranges for thermometer calibration, from 200 °C to 1000 °C. The new heat pipes are here presented together with an overview of all the dedicated equipment designed and manufactured.

Several contracts with other Institutes and calibration laboratories for providing or improving such devices, dedicated controllers and special software made it possible to enforce this central role of INRiM. Today INRiM is known as a world wide reference institute for this kind of technology.

In 2005, among the other activities, a new gas-controlled heat pipe operating with mercury as the working fluid has been designed, manufactured, and completely characterized (Merlone, 2008). This heat pipe is made in stainless steel and provided with three thermometer wells. A dedicated furnace has been constructed and specific software algorithms (Merlone, 2001; Giunta, 2008) have been implemented for the temperature and pressure control. Results in terms of temperature stability, uniformity, and time response demonstrated the capabilities of this gas controlled heat pipe to be a useful device for research and applications in contact thermometry.

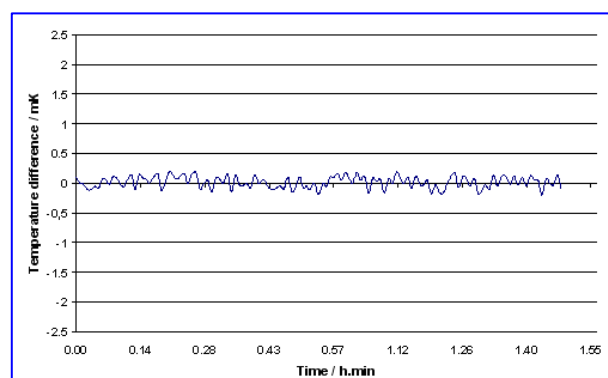


Figure 4. Temperature stability at the level of few tenths of millikelvin at 370 °C achieved inside the new stainless steel mercury filled GCHP.

This device was then used for multiple purposes. It became the low temperature reference for the new "Temperature Amplifier" (see below); a second one is used as calibration facility for thermometers calibration by comparison between 220 °C and

450 °C. A third model was used for the most accurate determination of the mercury liquid-vapour curve ever made (Merlone, 2001).

4. THE “TEMPERATURE AMPLIFIER”

In 1996 a sodium Gas Controlled Heat Pipe with six thermometer wells was used for accurate comparison of high temperature standard platinum resistance thermometers (HTSPRTs), for the study of the ITS 90 non uniqueness in the range between the aluminum and the silver freezing points (Marcarino, 1996). For this use, the temperature inside the Heat Pipe was directly controlled by means of a High Temperature Standard Platinum Resistance Thermometer (HTSPRT). The drift of the HTPRT at high temperature strongly limited the temperature long-term stability.

In order to improve the long-term stability and reproducibility, a novel approach was then studied. It consisted in connecting to the same pressure line of the sodium Heat-Pipe a dyphenil Heat-Pipe operating between 165 °C and 290 °C. By controlling the helium pressure at about 30 kPa, a temperature of 206 °C in the dyphenil Heat Pipe was "amplified" to about 762 °C in the sodium Heat-Pipe connected to the same helium line. The temperature stability was within $\pm 0,15$ mK in the dyphenil Heat Pipe and within $\pm 0,3$ mK in the sodium Heat-Pipe. Despite the encouraging results, no perfect operating conditions were achieved because a temperature non uniformity larger than 1 mK/cm was measured at all temperatures along the thermometer well of the dyphenil Heat-Pipe. This temperature gradient was attributed to a non isothermal liquid vapour interface surrounding the thermometer well, because of poorly adequate thermal properties of dyphenil.

To overcome those problems a new system has been setup, involving the use of the sodium Heat-Pipe, together with a mercury filled Heat-Pipe, both devices connected to the same pressure controlled line.

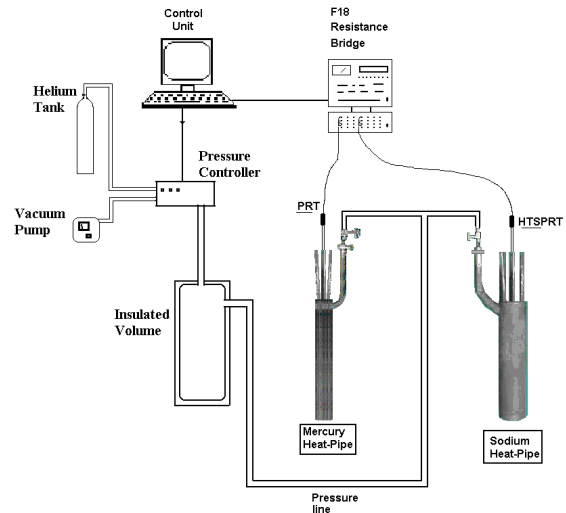


Figure 5. A schematic view of the experimental apparatus for the temperature amplifier with the two GCHPs connected at the same pressure line.

In the course of this study on the behavior of coupled Gas-Controlled Heat Pipes (GCHPs), for the first time perfect agreement has been obtained between measurements on the immersion characteristics in a mercury GCHP and the Clausius-Clapeyron profile. This result opened the perspective of using coupled GCHPs to thermodynamically relate two different temperature ranges, with the possibility of redefining one temperature range in terms of another. Indeed, by controlling the helium pressure by means of a SPRT inserted in the thermometer well of the mercury GCHP, any temperature in the range between 240 °C and 400 °C can be "amplified" in a sodium heat-pipe connected to the same helium line, to one, unique and very reproducible temperature in the range between 660 °C and 962 °C.

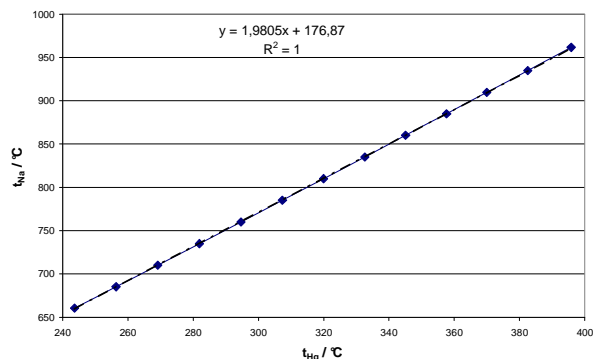


Figure 6. The experimental results on the first prototype of Temperature Amplifier and the $t_{Na}(t_{Hg})$ amplification relation.

This device, called “Temperature Amplifier” allows a temperature reproducibility between 660 °C and 961 °C that surpasses that of the High Temperature Standard Platinum Resistance Thermometer (HTSPRTs) used for the ITS-90.

The technique opens the prospect of realizing the ITS in a different way: any accurate reproducible temperature range may be used to generate another temperature range, the relationship between the two ranges being thermodynamically related by the two pure substances used for the vapor-liquid transitions (Marcarino 2003). This method and original approach is now the subject of research cooperation and joint research projects as reported below.

5. PRESSURE CONTROL

The thermodynamic relationship linking temperature and pressure in a fluid in liquid vapour phase transition, allows an innovative methods for aery accurate temperature and pressure control. As seen, the GCHP is a special kind of heat pipe equipped with a gas line that enables direct control of the inner pressure.

From the Clausius-Clapeyron equation and from the ideal gas law:

$$\frac{dT_i}{T_i} = \frac{RT_i}{ML} \frac{dP_v}{P_v} \quad (1)$$

where R is the universal gas constant, T_i the liquid vapour interface temperature, M the molar mass of the vapour, L the latent heat of vaporization, and P_v the vapour pressure. According to the Pictet Trouton rule, , where T_b is the boiling point of the working fluid; the factor RT/ML can then be approximated as $0.1T/T_b$. Since the GCHPs are generally operated in the pressure region between about 5 kPa and 500 kPa, which corresponds to a temperature variation within $\pm 20\%$ of the boiling point, the Eq. (2) may be approximated as:

$$\frac{\Delta T}{T} \cong 0.1 \frac{\Delta P_m}{P_m} \quad (2)$$

Thus, a pressure variation results in a corresponding temperature variation.

This physical principle, together with the modern available instrumentation and computer real time capabilities allow a new concept in pressure control: the use of the SPRT as a pressure sensor.

As seen, the accurate measurement of the liquid vapour phase transition temperature is obtained by means of SPRTs inserted in the thermowells. The resistance of the SPRTs is obtained by means of a specific resistance bridge, that allows sensibility in the order of 10^{-8} and ten digits resolution.

In this case, the set point is no longer a pressure value, but a temperature, by means of a resistance set point. Once the set point has been defined, the computer, via a resistance bridge, interrogates a SPRT located inside the thermometer well of one GCHP. The software compares the resistance value to the set-point value and configures the electro-valves appropriately to control the pressure. The smallest pressure variation achieved with the controller is less than 1 ppm, and the temperature stability can therefore be kept around this relative value.

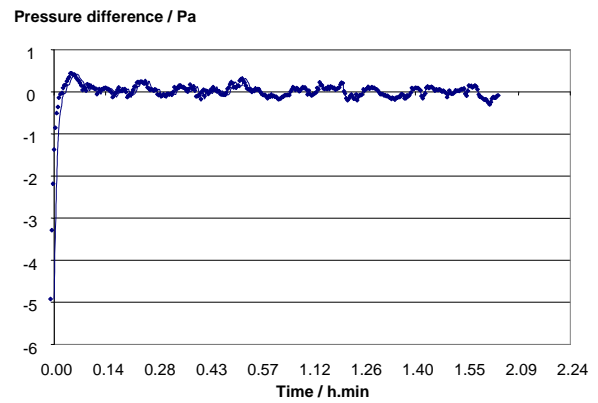


Figure 7. Temperature set point reaching and maintaining using a PRT. Pressure translated values showing stability within few tenths of a pascal at 120 kPa.

The quantity under control is the temperature T of the liquid vapour transition of the working fluid inside the GCHP, measured by means of a SPRT that translates the temperature values into resistance values. A simple way to realize control at a desired temperature set point as a resistance value R_{sp} is to compare it with the measured value $R(T)$ and supply a pressure difference to compensates the difference (proportional control). A new dedicated pressure controller, based on volumes ratios and computer driven electrovalves has been studied and developed at INRiM in cooperation with University of Cassino, obtaining capabilities in term of pressure stability and sensibility by now not achievable by any commercially available pressure controller (Giunta, 2008). Four pressure controllers have been assembled since February 2007. Since the

first prototype, now used for the Temperature Amplifier, other models have been assembled both for research and calibration purposes. One has been delivered to the LNE-INM/CNAM in St. Denis, France, for the pressure control automation of the GCHPs operating there. A second version will be used with a GCHP that operates with mercury, installed in the “calibration by comparison” Laboratory of INRiM where it will be used for the calibration of industrial PRTs and thermocouples. A further controller has been assembled and will be used by the Quality Centre of the “Politecnico di Torino”, where the device will be used for the control of a mercury-filled GCHP that will be devoted to the calibration of contact thermometers in the field between 240 °C and 400 °C. Another controller, equipped with a different pressure gauge operating up to 130 kPa, will be independent from the GCHP application and will be sent to the University in Cassino, Italy, for the calibration of pressure gauges; it will be used to control the pressure in a calibration line and will not use an SPRT or a resistance bridge. The electronics is now being implemented in order to make the system totally independent from any computer remote control.

6. A WORLD WIDE EXPERIENCE

GCHPs have been used by several Institutes of metrology and accreditation laboratories for studies on thermodynamics, thermal metrology and for calibration. Here the most involved NMIs report their experience. Due to obvious text limitation, this group is not complete and does not include calibration laboratories and other universities using the same devices for other researches.

6.1 LNE-Cnam, France

Since the 90's, LNE-Cnam and INRiM started a cooperation on the development of GCHPs used as temperature amplifiers for accurate calibrations of high-temperature SPRTs and thermocouples. The principle is based on the idea that several heat pipes are connected together and to one pressure controller. Each GCHPs are filled with different working fluids so that at a given pressure level, the temperature in each of them is different because the saturation curve (saturation pressure = $f(\text{saturation temperature})$) is different. Thus the pressure management of the system allowed to shift the temperature in each GCHP, the

temperature range in each GCHP depends only on the substance. To achieve the temperature amplifier, one of the GCHP works at relatively low temperature range (typically between 40 °C and +150 °C) and inside which the reference SPRT is kept, while the other GCHPs work at relatively high temperature range (typically between 400 °C and +900 °C) and inside which the high-temperature SPRTs or thermocouples are kept. By this way it is possible to carry out a calibration by comparison without exposing the reference SPRT at a high temperature which may lead to drift or damage.

LNE-Cnam carried out studies on a temperature amplifier composed by a heat pipe filled with dodecane (Do), which temperature was amplified by either sodium-filled (Na) or potassium-filled (K) heat pipes. Fig. 8 shows a picture of the temperature amplifier system at LNE-Cnam. The results were widely published and discussed (Renaot, 2003; Merlone 2003). Uncertainty budgets for the temperatures realized by each heat pipe were determined and are summarized in Table 1.

Recently, the LNE-Cnam developed a new heat pipe filled with pure water, suitable to be installed in the temperature amplifier system shown in Figure 8. The water heat pipe is made of copper, the external enclosure has a 88 mm base diameter is 600 mm high, and is equipped with four 9 mm diameter wells for thermometers. This is the typical design of LNE-Cnam heat pipes.

The water heat pipe was connected to the gas line of the temperature amplifier, where an improved pressure controller made at INRiM (Giunta, 2008) was used to ensure the regulation of the pressure with optimal stability and reproducibility. The system was used to “amplify” the temperature generated by the water heat pipe, working between 80 °C and 120 °C, with a sodium heat pipe whose corresponding temperatures ranged between 799 °C and 970 °C. Pressures were between 40 kPa to 200 kPa.

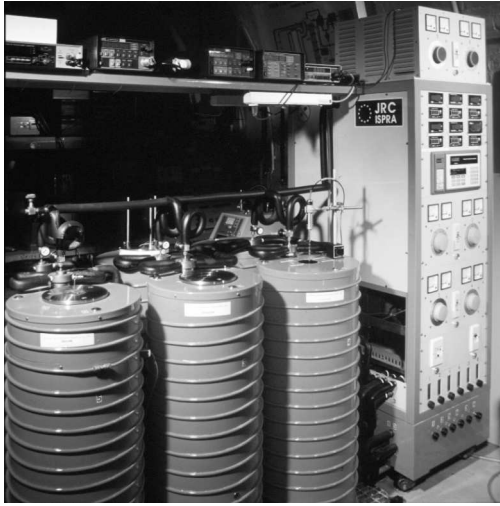


Figure 8 Temperature amplifier at LNE-Cnam, composed of six heat pipes filled with dodecane, water, sodium, potassium and cesium on a common gas line, connected to a pressure control system. Recently, the pressure control system has been replaced by an improved controller developed at INRIM.

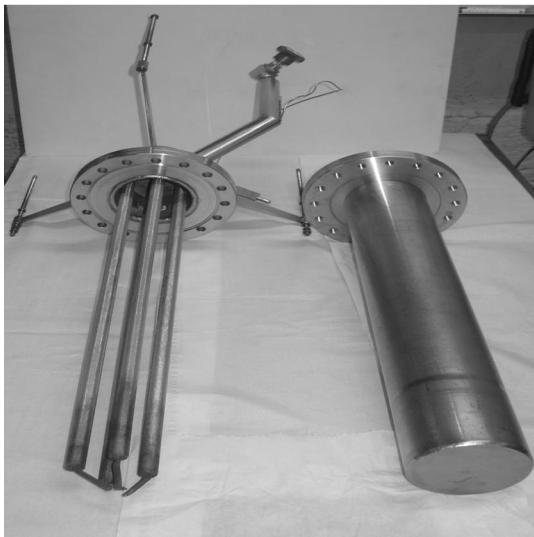


Figure 9. Typical design of a GCHP developed at LNE-Cnam

Table 1: uncertainties on temperatures realized with dodecane, potassium and sodium heat pipes at LNE-Cnam

Uncertainty component	Do 190 °C – 250 °C	K 600 °C – 840 °C	Na 799 °C – 965 °C
Pressure measurements	1.9 mK to 4.4 mK	7 mK to 3 mK	8 mK to 4 mK
Calibration and reproducibility of (HT)SPRT	2 mK	1.7 mK to 4 mK	4 mK to 7 mK
Temperature stability and uniformity of working volume	7.3 mK	8 mK	9 mK
Combined standard uncertainty	8 mK	10 mK to 11 mK	12 mK to 12.7 mK

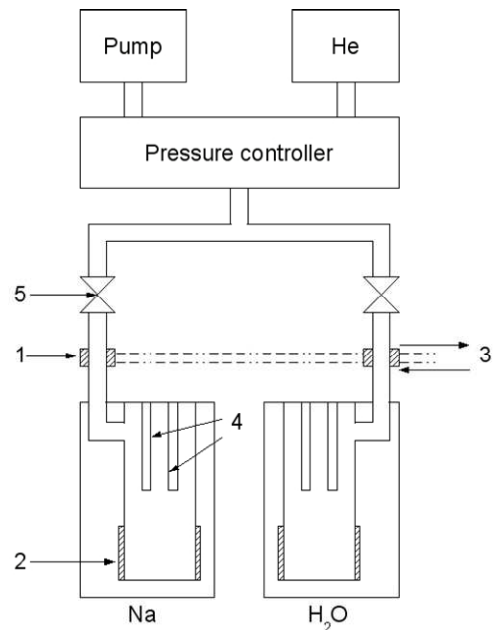


Figure 10. Scheme of the temperature amplifier with water and sodium heat pipes. 1 water cooled section, 2 heating resistor, 3 water, 4 thermometer wells, 5 valve

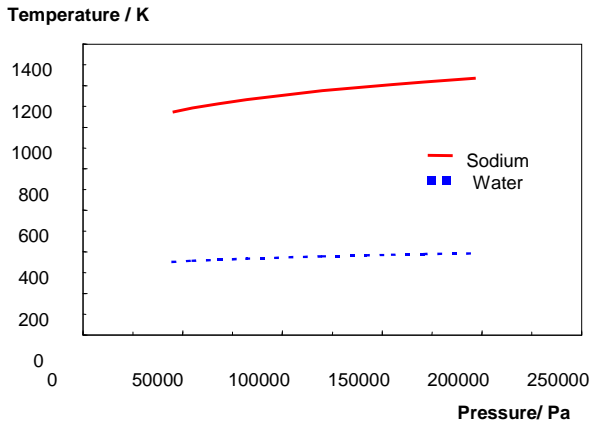


Figure 11. Relationships $T=f(p)$ for water and sodium, where T indicates the temperature and p is the pressure, and f is obtained by means of a least squares fit made on the basis of a solution of the Clausius-Clapeyron equation, assuming a linear variation of the latent heat of vaporization with temperature. When a temperature T_{H_2O} is set on the water heat pipe, the generated pressure p is transmitted through the gas line to the sodium heat pipe, setting its temperature to T_{Na} .

The system was characterized by using the pressure controller provided by INRIM. Pressures were applied on the gas line by the pressure controller and the corresponding generated temperatures were measured with calibrated thermometers on both heat pipes. In this first configuration, the feedback signal for the pressure control was generated by a pressure sensor included in the controller. Hence, the stability of the pressure in the line was mainly related to the sensitivity of the pressure sensor. The work was carried out in close cooperation with INRIM and the temperature amplification relationship between water and sodium temperatures was determined as follows:

$$T_{Na, amplified} = A \cdot \left[\frac{T_{H_2O}}{T_0} - 1 \right]^2 + B \cdot \left[\frac{T_{H_2O}}{T_0} - 1 \right] + C$$

where :

$$A = (16.46 \pm 0.16) 10^{-4} \text{ } ^\circ\text{C}^{-1}$$

$$B = 396.604 \pm 0.015$$

$$C = 883.082 \pm 0.004 \text{ } ^\circ\text{C}$$

$$T_0 = 100 \text{ } ^\circ\text{C}$$

Additional measurements were then carried out to validate the determined temperature amplification relationship. In this second configuration, the feedback signal for the pressure controller was the temperature measurement carried out with the low

temperature thermometer in the water heat pipe. This increased the stability of the pressure control, because the sensitivity of a SPRT is higher than that of the pressure sensor installed in the controller. In consequence, temperatures generated in the high temperature heat pipe showed an improved stability as well. As for the determination of the temperature amplification relationship, calibrated thermometers were used again in both the heat pipes. In this way, it was possible to calculate the difference between $T_{Na, amplified}$ and $T_{Na, ITS 90}$, i.e. the temperature measured in the sodium heat pipe as resulting from the thermometer calibration. The difference $T_{Na, ITS 90} - T_{Na, amplified}$ was less than 35 mK at all the measured temperatures, and the associated uncertainties were less than 50 mK, as shown in Table 2.

Table 2: Differences and associated uncertainties between the calibration temperatures and the temperatures determined with the temperature amplification relationship

Temperature in Na heat pipe $^\circ\text{C}$	$T_{Na, ITS-90} - T_{Na, amplified}$ $^\circ\text{C}$	Expanded uncertainty $U(T_{Na, ITS-90} - T_{Na, amplified})$ $^\circ\text{C}$
799	-0.029	0.034
818	+0.022	0.034
840	-0.006	0.034
902	-0.005	0.035
922	+0.005	0.035
944	-0.033	0.035

6.2 National Institute of Metrology (NIM), China.

In August 2006 a scientific cooperation agreement between the Italian National Research Institute of Metrology (INRiM) and the National Chinese Institute of Metrology (NIM) was signed (Merlone, 2008). Under this cooperation, INRiM manufactured, filled, characterized and delivered to NIM two gas-controlled heat pipes, one filled

with mercury and one with sodium to be connected together in the Temperature Amplifier configuration. During the period from 2009 to 2011, a further gas-controlled sodium heat pipe system was successfully developed at NIM. Also, investigations into the thermal characteristics of the NIM gas controlled sodium heat pipe were carried out. The temperature stability over 5 hours was better than ± 0.25 mK while controlling the pressure at 111250 Pa. The temperature uniformity within 14 cm from the bottom of the thermometer well was within 0.3 mK. While keeping the pressure stable at the same value, 17 temperature determinations were performed over 14 days, obtaining a temperature reproducibility of 1.27 mK. Additionally, the NIM gas controlled sodium heat pipe was compared with the sodium heat pipe produced by INRiM.



Figure 12 Photo of the NIM Sodium Heat Pipe

The temperature in the INRiM sodium heat pipe operating at 111250 Pa was determined, obtaining a difference of 21 mK with respect to the NIM GCHP. This difference was attributed to sodium impurities, pressure controller capabilities and reproducibility, and instabilities of high temperature standard platinum resistance thermometers (HTSPRTs). Further investigations will be carried out extending the pressure/temperature range and connecting both GCHPs to the same pressure line.

6.3 VSL, Netherlands

VSL use 2 GCHP as a temperature amplifier. While the high temperature is the “usual” sodium-filled GCHP, for the low range VSL adopted the biphenyl as working fluid, instead of mercury, to overcome safety regulations on the use of Hg. The helium pressure is regulated by means of a commercially available pressure controller. This allows any temperature in the range 158 – 290 °C to be “amplified” in a sodium heat-pipe connected to the same helium line, to one, unique and very reproducible temperature in the range between 660 °C and 982 °C.

The biphenyl and sodium heat-pipe at VSL have been characterised for temperature stability, uniformity along the wells, and response times over the whole operating range.

The heat-pipe setup consists of 2 temperature-controlled furnaces in which the heat-pipes are placed. The temperature of the furnace is controlled by a Eurotherm controllers.

The sodium heat pipe contains six stainless steel thermometer wells containing a Carborundum insert. The Carborundum inner tubes protect the (S)PRTs from contamination originating from the stainless steel thermometer wells. The biphenyl heat-pipe contains six stainless steel thermometer wells (no inserts) and is filled with 330 g of biphenyl. The power required to maintain the liquid/vapour phase transition inside the GCHP is provided by a one-zone furnace with side heaters but without bottom heating.

The pressure control system for the GCHPs is equipped with a commercially available PPC2+ pressure controller from DH Instruments provided with a high-pressure line to increase the pressure, and with a low-pressure line to decrease the pressure. The high-pressure line of the controller is connected through a pressure regulator to a pressurised helium cylinder, while the low-pressure line is connected to a vacuum pump. The controlled-pressure line is connected to the GCHP through a 25 L buffer volume that is thermally insulated. This buffer attenuates any pressure fluctuations that may be due to perturbations.

Temperature stability within a few millikelvins is achieved at intermediate temperatures, where the system exhibits the best performance.

Two separate cooling lines are in place. The first line provides the necessary cooling to the chimney of the GCHP, in order to keep it working properly; it represents the fundamental cooling that causes

the vapour to condense back to the liquid state and return to the bottom of the GCHP. The second water-cooling line is used to cool the furnace. The amount of water flowing in both cooling lines is separately controlled, in order to guarantee the best heating/cooling ratios and thus achieve the best operating capabilities of the heat pipe.

Using the commercial pressure controller, it is possible to obtain a reasonable stability at any pressure value in the range studied. The PPC2+ controller has a specified stability of $\pm 0.003\%$ of reading which is equivalent to 1 mK at 100 kPa (254 °C) for biphenyl. The measured temperature stability was found to be within 10 mK with a standard deviation of 2 mK

The gradients in the uniform zone between 5 and 20 cm from the bottom were found to be always smaller than 2 mK/cm down to less than 1 mK/cm in some thermo wells.

7 A EUROPEAN JOINT RESEARCH PROJECT up to 2014.

Together with the possible new definition of the kelvin, the unit of temperature, the International Temperature Scale will be object of improvement and studies. This new scale will have to be open to new ways for the “mise en pratique” of the unit, and to new definitions in specific fields of interest. At the present, since no temperature points are defined between the fixed points of aluminium and silver, corresponding to the wide interval between 660 °C and 962 °C, studies are carried out for the proposal of a new standard in this field.

In February 2004 a Euromet project has been discussed and proposed in agreement between nine European National Institutes of Metrology (Merlone, 2008). The project is aimed to the investigation of the use of the Temperature Amplifier as a new temperature standard in the field of platinum resistance thermometry, between the fixed points of Al and Ag. From the proposal date, several systems and devices have been studied, developed, manufactured, assembled at INRiM. New Gas Controlled Heat Pipes have been manufactured taking into account the experience on this devices acquired in the past years. An innovative pressure controller has been studied and built for the purposes; the relative electronic components have all been developed and made by INRiM. Dedicated furnaces have been designed and assembled, together with all the proper cooling lines. Control and acquisition software has been

developed at INRiM too. Some of those components have been tested and characterized both at the Italian and French Institutes of Metrology LNE-INM/CNAM. In 2011, on the basis of this cooperation, a proposal was submitted under the “SI-Broader Sope” call of the European Metrology Research Project of Euramet, the association of European National Institutes of Metrology. The proposal was successfully evaluated and became a work package of the SIB10 NOTED Joint Research Project on novel techniques for traceable temperature dissemination. The work will start in June 2012 and has two main deliverables planned for 2014: the study of the wideness of the non uniqueness of HT-SPRTs and thermocouples and a proposal for a new reference function and device for temperatures between the Al and Ag fixed points.

REFERENCES

Bassani, C., Busse; C.A. (1976) *A pressure controlled precision thermostat*. 2nd International Heat Pipe Conference, ESTEC, Noordwijk, report ESA SP-112 preprint, Vol. 1 (1976) p. 537-44

Busse, C.A., Bassani, C.(1982) *A new generation of precision furnaces*. Temperature: Its Measurement and Control in Science and Industry, Schooley J. F. ed., New York, American Institute of Physics, Vol. 5 p. 1265-1273

Bassani C., F. Geiger, G. Sciamanna (1981) *Progress on gas-controlled heat pipe precision furnaces for temperatures up to 1100°C*, Advances in heat pipe technology, Proceedings of the IV International Heat Pipe Conference, D.A. Reay ed., Pergamon Press, London (1981) p. 37-46

Giunta, S., Merlone, A., Marengo, S., Marcarino, P. Tiziani, A. (2008) *Capabilities of a New Pressure Controller for Gas-Controlled Heat Pipes*, International Journal of Thermophysics, Vol. 29, No 5 p.1887-1895

Giunta, S., Merlone, A., Marcarino, Botta, S., Giovanetti, V. (2008) *Dedicated software package for pressure regulation at 1 ppm level using a Gas Controlled Heat Pipe*, Advanced Mathematical and Computational Tools in Metrology & Testing, Vol. 8, Series on Advances in Mathematics for Applied Sciences Vol. 78, World Scientific, Singapore, , 118-122.

- Marcarino, P., Bassani, C. (1992) *Approximation of the ITS-90 between 660 °C and 962 °C using the sodium vapour P-T relation*, Temperature: Its Measurement and Control in Science and Industry, Schooley J.F. ed., New York, American Institute of Physics, Vol. 6, p. 209-214.
- Marcarino, P., Dematteis, R., Li, X., Arai, M., De Groot M., Nubbemeyer, H.G., (1996) *Preliminary results on ITS-90 non uniqueness between freezing point of Al and Ag*, Proc. Tempmeko, Marcarino P. ed. Levrotto Bella, Torino, 1997, p. 25-32.
- Marcarino, P., Merlone, A., Coggiola, G., Tiziani, A. (1999), Proc. TEMPMEKO '99, editors Dubbeldam J. F. and De Groot M. . ed., Delft, Nmi-VSL, p. 298-303.
- Marcarino, P., Merlone, A., Dematteis, R. (2001) *Low Cost Apparatus for Accurate Comparisons of Platinum Resistance Thermometers*, Proc. Tempmeko, the “8th International Symposium on Temperature and Thermal Measurements in Industry and Science 19-21 June 2001”, Fellmuth, B., Seidel, J. Scholz, G., VDE Verlag ed. Berlin 2002, p. 641-646.
- Marcarino, P., Merlone, A. (2002) *Towards new temperature standards for contact thermometry above 660 °C*, Metrologia, , Vol. 39, p. 395-398.
- Marcarino, P., Merlone, A. (2002) *Gas-Controlled Heat-Pipes for Accurate Temperature Measurements* Proc. 12th International Heat Pipe Conference”, Moscow-Kostroma-Moscow, Russia, p. 475-479.
- Marcarino, P., Merlone, (2003) A., *On the advantages of using the "temperature amplifier" for accurate temperature measurements between 660 °C and 960 °C*. Report on the 22nd meeting of the Consultative Committee for Thermometry , May 2003, CCT/03-07.
- P. Marcarino, A. Merlone, (2003) *Gas Controlled Heat Pipes for Accurate Temperature Measurements*, Applied Thermal Engineering n. 23/9, , p. 1145-1152
- Marcarino, P., Merlone, A. (2003) *Thermodynamic Temperature Amplification By Means Of Two Coupled Gas-Controlled Heat-Pipes*. Temperature: its measurement and control in Science and Industry, Vol. 7, part 2, p. 951–956
- Merlone, A., Cavigioli, B., Marcarino, P. (2001) *A new Software for the Automation of accurate Pressure Regulation in Gas controlled Heat-Pipes*, Advanced Mathematical and Computational Tools in Metrology, Vol. 5, Series on Advances in Mathematics for Applied Sciences Vol. 57, World Scientific, Singapore, , 265-269.
- Merlone, A., Musacchio, C. (2001) *The mercury vapour pressure vs. temperature relation between 500 K and 665 K*” The Journal of Chemical Thermodynamics, Vol. 42, Issue 1, p. 38-47
- Merlone, A., (2001) *Determination of the mercury boiling point using a Heat-Pipe*, report on the 21st meeting of the Consultative Committee for Thermometry, September 2001, CCT/01-19.
- Merlone, A., Dematteis, R., Marcarino, P. (2002) *Gas controlled heat-pipes for accurate liquid-vapour transitions measurement*”, “ECTP 2002, The Sixteenth European Conference for Thermophysical Properties”, 1-4 September, 2002, Imperial College, London, UK.
- Merlone, A., Dematteis, R., Marcarino, P., (2003) *Gas Controlled Heat Pipes for Accurate Liquid-Vapour Transitions Measurements*. International Journal of Thermophysics, , Vol. 24, No. 3, 695 712.
- Merlone, A., Marcarino, P., Dematteis, R., Renaot, E., Favreau, J. O., Elgourdou, M. and Bonnier, G., (2003) *Temperature: Its measurement and control in science and industry*, Vol. 7, edited by Dean C. Ripple, AIP 957-962
- Merlone, A., Marcarino, P., Dematteis, R., Tiziani, A., Renaot, E., Elgourdou, M., Bonnier, G. (2003) *Mercury and Sodium Liquid Vapor Transitions in IMGc and BNM-INM Heat-Pipes*. “Temperature: its measurement and control in Science and Industry”, Vol. 7, part 2, , p. 957 – 962
- Merlone, A., Marcarino, P., Dematteis, R., Bassani, C. (2004) *New Gas-Controlled Heat Pipes*, Proc. Tempmeko the 9th International Symposium on Temperature and Thermal Measurements in Industry and Science, 22 - 25 June 2004 Cavtat - Dubrovnik Croatia, Vol. 1, p. 415-419
- Merlone, A., Marcarino, P., Tiziani, (2004) *A New Laboratory for Gas-Controlled Heat Pipes at*

IMGC, Proceedings of Tempmeko, the 9th International Symposium on Temperature and Thermal Measurements in Industry and Science, 22 - 25 June 2004 Cavtat - Dubrovnik Croatia, Vol. 1, p. 421-425

Merlone, A., Marcarino, P. (2004) *The "Temperature Amplifier" for very accurate temperature measurements between Al and Ag fixed points*, Proc. Tempmeko 2004, the 9th International Symposium on Temperature and Thermal Measurements in Industry and Science, 22 - 25 June 2004 Cavtat - Dubrovnik Croatia, Vol. 1, p. 227-232

Merlone, A. (2008) *The Euromet Project 772 on the Temperature Amplifier, from Its Proposal to the Present Status*, International Journal of Thermophysics, Vol. 29, No 5, p. 1858-1866

Merlone, A., Zhang, J., Giunta, S., Yan, X., Sun, J. (2008) *INRIM and NIM Cooperation on the Temperature Amplifier*, International Journal of Thermophysics, Vol. 29, No 5 / October, 2008, p. 1867-1875

Merlone, A., Giunta, S., Tiziani, A. (2008) *A New Mercury Gas-Controlled Heat Pipe for Temperature Amplifier and as Calibration Facility*, International Journal of Thermophysics, Vol. 29, No 5, p.1876-1886

Renaot, E., Elgourdou, M. and Bonnier, G., *Temperature: Its measurement and control in science and industry*, (2003) Vol. 7, edited by Dean C. Ripple, AIP 939-944

Renaot, E., Favreau, J. O., Elgourdou, M. and Bonnier, G., (2003) *Temperature: Its measurement and control in science and industry*, Vol. 7, edited by Dean C. Ripple, AIP 945-950

ENHANCEMENT OF VAPOUR CONDENSATION IN HEAT PIPES

Oleg Kabov, Igor Marchuk

Institute of Thermophysics SB RAS (IT SB RAS),
Avenue Lavrentiev 1, 630090,
Novosibirsk, Russia;
Heat Transfer International Research Laboratory
of IT SB RAS,
Avenue Lavrentiev 1, 630090,
Novosibirsk, Russia;
Center of Smart Interfaces
of Technische Universität Darmstadt,
Petersenstr., 32, 64287,
Darmstadt, Germany;
Email: okabov@ulb.ac.be, marchuk@itp.nsc.ru

Andrey Glushchuk, Yuriy Lyulin

Microgravity Research Centre
Universite Libre de Bruxelles (ULB),
Avenue F.D. Roosevelt, 50,
B-1050 Brussels, Belgium;
Heat Transfer International Research Laboratory
of IT SB RAS,
Avenue Lavrentiev 1, 630090,
Novosibirsk, Russia;
Email: aglushch@ulb.ac.be, ylyulin@ulb.ac.be

ABSTRACT

Heat pipes have found application in numerous devices used in our life. Nowadays they should have not only high performance but also have small size and minimal weight. There are several factors limiting its heat transfer capabilities. One of them is a limit of the capabilities of condenser. Presented paper describes recent progress in the solution of this problem. Heat transfer enhancement of condensation process by surface finning is a well-known method. Optimization model of condenser internal finning have been developed. It takes into account the thermal conduction coefficient of real materials. Effects of disjoining pressure and level of condensed liquid between fins have been analyzed theoretically. A dedicated space experiment to study condensation phenomena have been proposed and accepted by European Space Agency with the acronym "SAFIR". Its main goal is to obtain new quantitative local experimental data on film thickness distribution, heat flux and heat transfer coefficient. In frame work of development of this experiment the first prototype of test cell have been developed and tested on ground. Investigation of condensation process inside smooth tube has been carried out theoretically and experimentally at various gravity levels with the aim to improve condensers of loop heat pipes and capillary pumped loops.

KEY WORDS: Condensation, fining, optimization, microgravity, heat pipes.

1. INTRODUCTION

The heat pipes of various designs are used in the areas where transfer of large heat fluxes under strong limits on the size and the weight of cooling

systems are applied: space satellites, micro-electronics, air conditioning systems, etc. A lot of various types of heat pipes are presented in the literature (Groll 1989, Maydanik 2005, Vasiliev *et al.* 2005, Vasiliev 2005, Chaudhry *et al.* 2012):

tubular heat pipes, thermosyphons, variable conductance heat pipes, thermal diodes, pulsating heat pipes, loop heat pipes, capillary pumped loops, micro heat pipes and sorption heat pipes. The heat pipe is a device with very high thermal conductivity without moving parts. It can transport large quantities of heat efficiently over large distances without any external electricity input. Its main principle is based on the use of latent heat of vaporization, which is several orders of magnitude higher than the heat capacity used in single-phase mechanical cooling systems and heat conductivity used in convective cooling. Any heat pipe can be divided into three parts minimum: evaporation, condensation and adiabatic. In the first part the liquid evaporates that leads to cooling of a heat source. Generated vapor moves to the condenser through the adiabatic part due to the pressure drop. Condensed liquid flows back into the evaporator by the surface tension forces through microstructures installed into the heat pipe. There are six factors limiting heat pipe capabilities (Bejan *et al.* 2003, Serin *et al.* 2009): 1) capillary limit; 2) boiling limit; 3) entrainment limit; 4) viscous limit; 5) sonic limit and 6) condenser limit.

Presented article is focused on the last limit. At steady state, the heat rejection rate in the condenser must be equal to the heat addition rate in the evaporator. Therefore, the amount of liquid, which can be condensed in the condenser, limits the heat pipes applicability. Condenser capability is determined by two main factors: type of its cooling (convection or radiation) and its internal design. Various methods of intensification of condensation phenomena and condensers cooling are presented in the literature (Webb 1994, Bejan *et al.* 2003, Rifert and Smirnov 2004, Thome 2008). However, these methods do not take into account the additional requirements that are associated with the use of heat pipes. First of all, condensation part should not create a large pressure difference between the vapour and liquid lines. This limitation is related to the capillary limit. The large pressure drop reduces the amount of liquid entering to the evaporation part, which leads to deterioration of heat pipe capabilities. Additionally the condenser should have a minimal size and weight (Yang 2012). In modern systems it can occupy half of the weight and size. The presence of these requirements severely limits the feasible methods of intensifying the condensation part of the heat pipes.

In view of the increasing needs in producing miniaturized cooling systems in electronics, robotics and biomedical applications a deeper understanding of the physical phenomena, which occur at micro and nano-scale during film and dropwise condensation, becomes a very important aspect of research. It is quite evident that the combined effects of phase change, instabilities, thermocapillarity and solutocapillarity, interface thermal resistance, gas dynamics, gravity, as well as wettability and formation of microscopic adsorbed film on the wall, are somewhat complicated issues and have not yet been studied systematically in application to the various types of heat pipes. The main goal of the presented paper is to show the recent advances in the research of intensification of condensation phenomena by optimization of the fin profiles.

2. FIN PROFILES

Heat transfer enhancement of condensation process by surface fining is a well-known method and was reviewed by several authors: Markovich *et al.* 1972, Zener and Lavi 1974, Marto and Nunn 1983, Gogonin and Kabov 1991, Webb 1994, Cavallini 2003, Rifert and Smirnov 2004, Rose 2006. A lot of different fin shapes and condensation models have been suggested. Several authors have proposed new method of fin selection. Fin shape can be calculated theoretically with taking into account various technical requirements. This type of fins is called “optimal fin”.

Gregorig (1954) was the first who proposed to use fins of special shape to enhance film condensation on a vertical tube. He divided curvilinear tube surface into two zones: condensation area (upper part of the fin) and condensate draining area (valley between fins). Condensation process in the interfin space has been neglected because of very thick film. Thus condensation on the upper part of the fin has been considered. Using the same approach as Nusselt (1916) did for a vertical wall author obtained equation which describes the surface curvature dependence on the film thickness. He made the following statement: “If heat flux goes through a heat conductor (fin material) then each part of fin surface is equivalent. In other words, there is no zone i on the surface which is preferable than zone j ”. Using this assumption he obtained the fin profile which provides a constant film thickness distribution δ_0 :

$$\kappa = \kappa_0 - \frac{3\mu\lambda(T_f - T_v)}{2r\rho\sigma\delta_0^4} s^2 \quad (1)$$

Figure 1 shows the fin profile obtained by Gregorig. Appropriate film thickness δ_0 can be calculated from the mass balance between the condensate flow from the fin and the flow along the valley. The fin is assumed isothermal.

Adamek (1981) considered the problem of fin shape optimization from another standpoint. He proposed to search for the fin shape providing maximal condensate flow rate from its surface. Author has considered the following family of shapes:

$$\kappa(s) = b_0^1 - a_1 s^\varepsilon \quad \text{at } 0 \leq \varepsilon < \infty \quad (2)$$

$$\kappa(s) = a_2 s^\varepsilon - b_0^2 \quad \text{at } -1 < \varepsilon < 0 \quad (3)$$

Proposed shape family includes the Gregorig's fin shape ($\varepsilon = 2$). Adamek has shown that mass flow from the fin with $\varepsilon = -0.5$ is maximal (Figure 1) and therefore can be considered as optimal one. Unfortunately, obtained profile has infinite top curvature, therefore it is impossible to manufacture it. The fin is assumed isothermal.

Marchuk and Kabov (2003) considered the fin shape optimization as maximization problem of condensate flow from the fin like Adamek. They considered the fin profile of given fin surface length S , κ_0 top curvature and κ_1 the curvature at S and known ω maximal angle of the fin surface rotation. As opposed to the Adamek's family, the function of the fin curvature was not suggested a priori. This function was found from the variational problem of mass flow maximization. Authors have obtained two different fin profiles:

$$\kappa(s) = \kappa_0 + (\kappa_1 - \kappa_0) \frac{s}{S} \quad \text{at } 0.5S(\kappa_0 - \kappa_1) < \omega \quad (4)$$

$$\kappa(s) = (as + b)^{-1/2} - c \quad \text{at } 0.5S(\kappa_0 - \kappa_1) \geq \omega \quad (5)$$

Figure 1 shows profiles of obtained fins. Condensate flow from the optimal fin with finite initial curvature is less than from Adamek's optimal fin (Figure 2). But such fins can be manufactured.

Figure 2). But such fins can be manufactured.

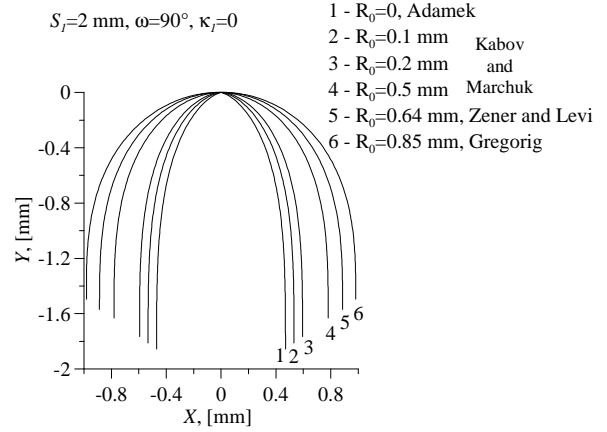


Figure 1. Optimal fins with various initial curvature.

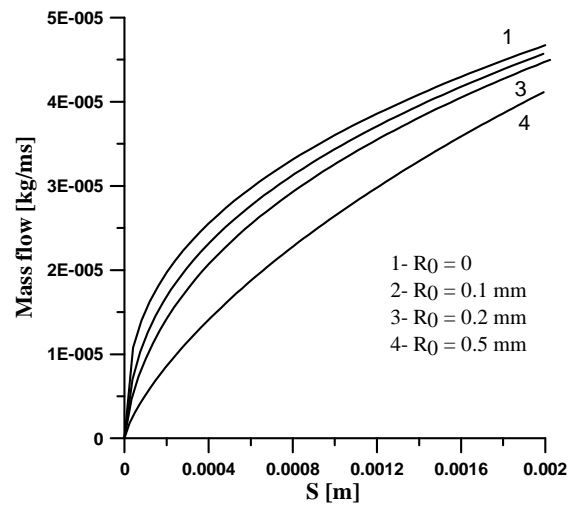


Figure 2. Mass flow distribution along the fin.

Kabov (1999) and Kabov *et al.* (2003) have proposed to extend the profiles obtained by Adamek and Gregorig to the point S_2 (Figure 3). As the coordinate s increases after the point $s = S_1$, the pressure in the film continues to decrease below the vapor pressure. This provides further motion of the film under the action of the pressure gradient. The liquid is continuously pumped out through a channel located between fins. Owing to this, intensive condensation takes place on the entire fin surface up to the point of contact of the fin surface with the base S_2 of the condenser, instead of the point S_1 . Authors investigated the influence of geometrical parameters of the fin geometry on condensation and as a result they developed the method of selection of appropriate fin parameters. Due to the use of an extended surface that can be manufactured by traditional methods, the condensate flux can be by 62% greater than at the use of the surface proposed by Adamek. But obtained fin shapes are assumed to be isothermal.

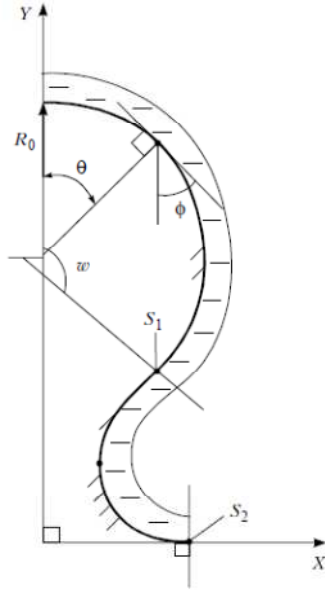


Figure 3. Extended surface of finning.

Presented fins have been obtained for the isothermal condition. The condensation capabilities of these fins will be different in reality and will depend on the condenser material. Marchuk *et al.* (2003) presented the calculation results of condensation on the extended Adamek's fins. Authors developed their own numerical method of calculation of film condensation on the non-isothermal fin. Dimensionless temperature distribution in the fin body is presented in Figure 4 for two different values of the thermal conductivity coefficient.

Dimensionless temperature $(T(x,y)-T_w)/(T_v-T_w)$ is pointed on the fin by numbers. The authors have shown that the fin becomes more non-isothermal with decreasing of heat conductivity of the fin material. Wall temperature at the fin top may reach saturation temperature for small coefficient of fin thermal conductivity, with the dimensionless temperature tending to 1. The authors have shown that the thermal conductivity of the fin essentially influences on the intensity of condensation. Even in the case of copper, there is an essential difference between calculation results with and without allowance of thermal conductivity. The fins optimized in isothermal condition are no longer optimal in the non-isothermal case. Selection of the optimum fin shape should be based on models taking into account the process of thermal conductivity in the wall of the condenser.

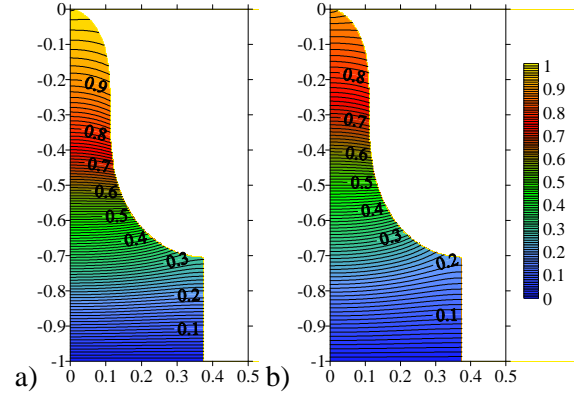


Figure 4. Temperature distribution in the fin body for different thermal conductivities: a) aluminum b) copper (steam condensation, $T_v=373.15$ K, $T_v-T_w=1$ K).

3. FIN SHAPE OPTIMIZATION

The model of fin shape optimization with taking into account heat conduction of the fin material have been developed in Marchuk *et al.* (2006). The model is described briefly below. The process of stationary condensation on a fin with variable wall temperature profile $T_f(s)$ over the surface is considered. Figure 5 shows the coordinate system used in the model.

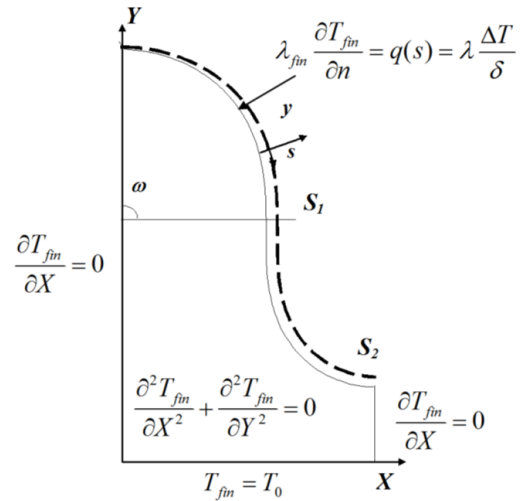


Figure 5. Schematic diagram showing the fin, the flow of condensate on its surface, system of coordinates.

The stationary flow of condensed liquid film under the action of capillary forces is described in the approximation of the lubrication model by the following system of equations:

$$\mu \frac{\partial^2 u}{\partial y^2} = \sigma \frac{\partial \kappa}{\partial s}(s) \quad (6)$$

$$\frac{\partial^2 T}{\partial y^2} = 0 \quad (7)$$

$$\int_0^s \frac{\lambda \frac{\partial T}{\partial y}(s, \delta(s))}{r} ds = \int_0^{\delta(s)} \rho u(s, y) dy \quad (8)$$

The corresponding boundary conditions express the non-slip and the absence of friction on the free surface:

$$u(s, 0) = \frac{\partial u}{\partial y}(s, \delta(s)) = 0, \quad (9)$$

$$T(s, 0) = T_f(s), \quad T(s, \delta(s)) = T_v.$$

It is assumed that the temperature on the liquid film surface equals to the vapour saturation temperature. Equation (8) describes the balance between condensed vapour and the mass m of the liquid flowing on the fin surface. Within a small length of the liquid film on the surface, the liquid flow can be considered as flat: $|\delta/R| \ll 1$. The solution of equations (6)–(8) with boundary conditions (9) yields the following expressions for the thickness of a condensed liquid film and for the flow of condensate along the fin:

$$\delta(s) = \left(-\frac{\partial \kappa}{\partial s}(s) \right)^{-\frac{1}{3}} \left(4 \int_0^s \frac{\lambda \Delta T(\tau) \mu}{r \rho \sigma} \left(-\frac{\partial \kappa}{\partial s}(\tau) \right)^{\frac{1}{3}} d\tau \right)^{\frac{1}{4}} \quad (10)$$

$$m(s) = \frac{\rho \sigma}{3\mu} \left(4 \int_0^s \frac{\lambda \Delta T(\tau) \mu}{r \rho \sigma} \left(-\frac{\partial \kappa}{\partial s}(\tau) \right)^{\frac{1}{3}} d\tau \right)^{\frac{3}{4}} \quad (11)$$

where $\Delta T = T_v - T_f(s)$.

According to approach proposed in Marchuk *et al.* (2006) the fin shape is optimal if condensate mass flow from upper part of the fin $m(S_l)$ value is maximum, where S_l is the length of the curve describing the upper (convex) part of the fin. Thus, we arrive at the problem of finding the extremum of the functional:

$$J(\kappa) = \int_0^{S_l} \Delta T(\tau) (-\kappa'(\tau))^{1/3} d\tau \rightarrow \sup \quad (12)$$

for pre-set values of

$$\kappa(0) = \kappa_0; \quad \kappa(S_l) = \kappa_1; \quad \kappa_0 > \kappa_1 \geq 0 \quad (13)$$

A solution of the Euler equation for this variational problem is:

$$\kappa(s) = -\frac{1}{C} \int_0^s \left(\frac{\Delta T(\tau)}{a\tau + b} \right)^{3/2} d\tau + \kappa(0) \quad (14)$$

Where constant C , a and b are calculated from (13). If the fin is isothermal ($\Delta T = \text{const}$) than optimal shape can be easily found from formula (14). Optimal shape of non-isothermal fin is calculated numerically using the following algorithm:

- i. The initial fin shape is determined using formula (14) for $T_f(s) = T_w$.
- ii. A stationary temperature distribution in the fin body is calculated using the algorithm developed by Marchuk and Kabov (2003).
- iii. Convergence validation. A maximum difference between the obtained temperature distribution and that determined in the preceding step is determined. If this difference is below the given accuracy, the algorithm passes to the final step (v).
- iv. The optimum fin shape is determined using formula (14) for the obtained temperature distribution $T_f(s)$, after which the algorithm returns to step ii.
- v. The calculation is terminated and the results are recorded.

The complete fin generatrix curve (Figure 5) is constructed by continuing the curvature function (obtained upon optimization of the upper convex part) to the point S_2 .

Figure 6 shows optimized fin shapes of various materials at water condensation. The main optimization parameters are: $T_v = 100$ °C, $T_w = 99$ °C, $H = 1$ mm, $S_l = 2$ mm, $\kappa_0 = 5000$ m⁻¹ ($R_0 = 0.2$ mm), $\kappa_l = 0$, $\omega = \pi/2$ rad (90°). The calculation has been done for four values of heat conductivities: isothermal case, copper 400 W/mK, aluminum 150 W/mK, black steal 50 W/mK. Black line corresponds to a profile of the optimal fin with constant surface temperature (IF). The fins obtained using presented model (OF) is wider than IF and the width increases with decreasing of material thermal conductivity. Two factors affect the optimized shape of the fin with finite thermal conductivity. From one side the fin should have the minimum fin width in order to obtain a high gradient of surface curvature. This factor explains the narrow fin shape in isothermal case. From the other side fin capability to transport condensation heat from the film reduces proportionally to thermal conductivity coefficient. Thus the fin should have the maximum as possible width. Second factor becomes more important at low thermal conductivity. For example the optimized fin made of steal is by a factor 1.4 wider than optimized isothermal fin.

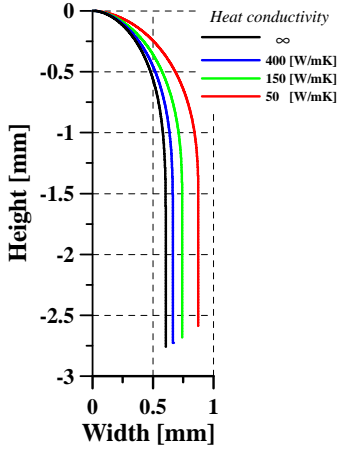


Figure 6. Effect of thermal conductivity of the fin material on fin shape.

Figure 7 shows the mass flow distribution along three different fin profiles: 1) optimized fin in isothermal case (IF); 2) the fin of IF shape manufactured of a real material with finite heat conductivity (IDF); 3) the fin with shape optimized using the proposed algorithm (OF). The IDF fin (dashed lines) cannot provide the same condensate flow as from the IF fin. The mass flow from copper IDF fin is 1.5 times less. The situation becomes worse with decreasing of thermal conductivity. The flow from aluminium IDF and steal IDF is 2.7 and 6 times less than from IF fin, respectively.

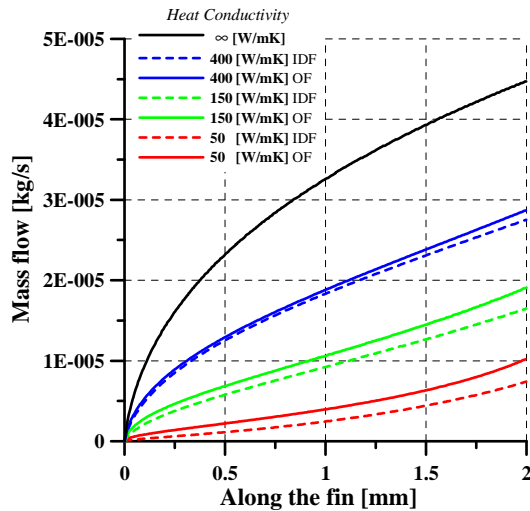


Figure 7. Effect of thermal conductivity of fin material on distributions of the mass flow along fin surface.

Solid lines on the Figure 7 (except black one) show the mass outflow from the fin optimized by the presented model. The flow from steal OF is 80% greater in

comparison with case of steal IDF. In case of aluminum OF the flow enhancement is only 20 %. Thus the optimization model allows significantly increase the condensate outflow from the fin with small heat conductivity coefficient.

4. EFFECT OF GROOVE FLOODING AND DISJOINING PRESSURE

The optimization model described above does not take into account two factors which affects on condensation on the fins: flooding the space between fins and disjoining pressure. Their effects were analysed numerically. Complete description of the analyses is written in Kabov *et al.* (2007). Let us consider condensation of pure vapour on the curvilinear fin. Condensed liquid is pumped out of the groove between fins. Pumping intensity determines the level of flooding, Figure 5. The condensate film thickness satisfies the equation:

$$-\frac{\rho\sigma\delta(s)^3}{3\mu}\partial P/\partial s = \int_0^s \frac{\lambda\Delta T(s)}{r\delta(s)} ds \quad (15)$$

Hire pressure is described as $P = P_v + \sigma\kappa - \frac{A}{\delta^3}$.

A is the Hamaker constant, which determines the disjoining pressure. The Equation (15) can be differentiated to obtain the third order ODE. Natural boundary conditions for equation (15) are as follows

$$\begin{aligned} \frac{\partial\delta}{\partial s}(0) &= 0, \\ \delta(S_2) &= \delta_S, \\ \frac{\partial\delta}{\partial s}(S_2) &= \frac{\cos(\theta(S_2))tg(\theta_F) - \sin(\theta(S_2))}{\cos(\theta(S_2)) + tg(\theta_F)\sin(\theta(S_2))} \end{aligned} \quad (16)$$

They express conditions of film symmetry on the fin top, known values of condensate film thickness δ_S and film surface rotation θ_F in valley at the end of the curve describing film surface. Curve rotation θ_F defines a symmetrical form of the film surface in the valley. It is also possible to set the condition on the surface curvature in the valley at $s=S$ instead of setting of the $\delta(S)$.

The calculations were performed for water condensation at following parameters: $T_v=373.15$ K, $T_w=368.15$ K, $\kappa_l=0$ m⁻¹, $\kappa_0=5000$ m⁻¹, $\lambda=0.677$ W/mK, $r=2270381$ J/kg, $\sigma=0.0598$ N/m, $\rho=961.7$ kg/m³, $S_f=0.001$ m, $A=-5.0E-20$ J. The fin material is copper (384 W/mK). Calculated film thickness

distributions depending on the groove flooding depth are shown in

Figure 8. Calculations show that pressure in the groove increases with flooding of the groove, consequently the pressure drop along the fin, $\Delta P = P_f(0) - P_f(S_2)$, decreases and according to this the condensate suction intensity of the groove decreases. The calculated film thickness on the fin tip is less than 0.5 μm , nevertheless, disjoining pressure influence in the carried out calculations appeared to be negligibly small. The typical value of Hamaker constant increased in two orders of magnitude almost does not have an influence on the results.

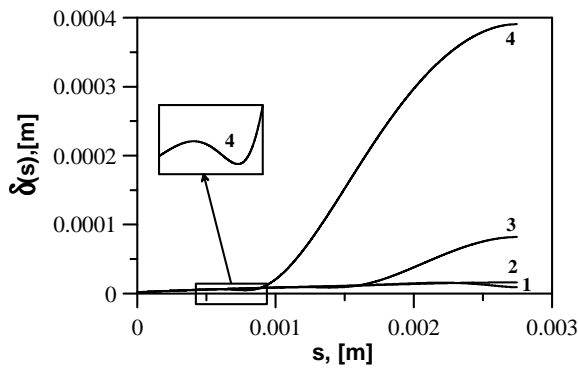


Figure 8. The film thickness distributions along the fin surface at the different values of the flooding.
 1- $\delta_s = 9.2 \mu\text{m}$, $m(S_2) = 1.53 \cdot 10^{-4} \text{ kg/ms}$, $\Delta P = 405 \text{ Pa}$;
 2- $\delta_s = 16 \mu\text{m}$, $m(S_2) = 1.47 \cdot 10^{-4} \text{ kg/ms}$, $\Delta P = 388 \text{ Pa}$;
 3- $\delta_s = 82 \mu\text{m}$, $m(S_2) = 1.17 \cdot 10^{-4} \text{ kg/ms}$, $\Delta P = 373 \text{ Pa}$;
 4- $\delta_s = 390 \mu\text{m}$, $m(S_2) = 0.78 \cdot 10^{-4} \text{ kg/ms}$, $\Delta P = 364 \text{ Pa}$.

Calculations show that disjoining pressure influence on the film thickness at the fin tip is negligibly small and may be not taken into account. Value of the groove flooding depth changes significantly the condensate outflow from the condenser. The pressure drop along the fin surface depends weakly on the groove flooding depth and condensed liquid flow rate from the convex part of the fin almost does not change. If the condensate suction pressure is the parameter regulating the condensation process is used in calculations, the insignificant condensate suction pressure change essentially influences the flooding depth in the groove and the condensate outflow from the fin. When the suction pressure drop decreases the condensation intensity decreases because of groove flooding.

5. SPACE EXPERIMENT

The widespread validation method of the theoretical models is based on comparison between

measurement of average heat transfer coefficient and one calculated by the model. In this case it is difficult to check all approaches made in the theoretical models and is impossible to estimate the influence of fin type on intensification of condensation process. For instance in most articles the fins have been considered as isothermal one and condensate film thickness at the fin top is assumed equal to zero. New accurate and local measurements (surface temperature, condensate film thickness, heat transfer coefficient...) are needed for validation of theoretical models and improvement of calculation methods of condensers with complex surfaces.

The enhancement effect can be observed if surface tension force is dominant one. On the earth the main competitor is gravity. The Bond number $Bo = \rho g / [\sigma(\partial\kappa/\partial s)]$ is used to describe relation between surface tension and gravity forces. If Bo is less than unity this surface effect is of interest. It means that a characteristic dimension of the curvilinear surface has to be less than the capillary constant: $l = (\sigma/\rho g)^{0.5}$. Table 1 shows values of this parameter for different liquids. Water has the largest l , which is about 2.5 mm. Unfortunately, it is very difficult to make any local measurements at this scale. Only average measurements can be done. As a result, we cannot check the validity of the existing condensation models by direct measurement of local film thickness and local heat transfer coefficient.

Table 1. Capillary constant of various liquids

Liquids	l [mm]	
	$g = 9.8 \text{ m/s}^2$	$g = 0.01 \text{ m/s}^2$
Water	2.5	80
Ethyl Alcohol	1.6	49
FC-72	0.7	23

The situation changes significantly if measurements are performed under microgravity conditions. The scale of the curvilinear surface can be enlarged by one order of magnitude (Table 1). For example, the size of the fin can be scaled up 30-40 time in case of water. In order to enlarge our knowledge about condensation process on a curvilinear surfaces the space experiment was proposed and accepted by the European Space Agency: "Single fin condensAtion: Film local measuReMents" (SAFIR).

The principal objectives of the experiment are to obtain new reliable local experimental data (film thickness, heat transfer coefficient...) in order to

get a better understanding of the condensation phenomenon. Experiment specific goals and detailed objectives are:

- I. Measurement of film thickness;
- II. Measurement of local heat transfer coefficient and local heat flux distributions along the fin and average heat transfer coefficient;
- III. Measurement of the effect of liquid level variations in the valley on the overall and local heat transfer performance;
- IV. Measurement of the gas-liquid interface dynamic and stability in the micro-channel (size about 10-20 μm).

The basic element of the experimental cell is the thermally controlled single-fin condenser (Figure 9). The core element of the test cell is the disk-shaped fin of special profile. The disk-shaped form is chosen to avoid the effect of the side walls of the fin on the condensate flow in microgravity. If the fin has another type of shape (for example a longitudinal one) then space between fin and covers of the test section will be filled by condensate. As a result the formed curvilinear meniscus near the fin will distort the condensate film surface. This effect may complicate the analysis of the influence of the curvilinear surface on film condensation. This effect can be neglected if fin length is much greater than its height. The longitudinal fin with length 80 mm and height 20-25 mm can be used in SAFIR experiment due to the size limits. The effects of the side walls cannot be neglected for this fin. Condensate arisen on the disk-shaped fin surface will flow axially symmetrically to the valley, where it will be pumped out from the test cell. The film will not wet any other surfaces. The effects of the side walls do not exist in the case of disk-shape form under microgravity condition.

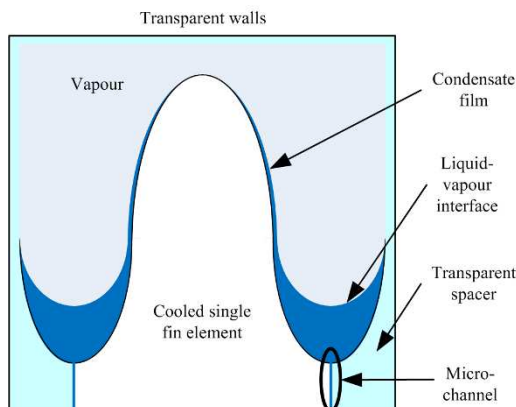


Figure 9. Single fin condenser.

Curvilinear part of the fin will have double curvature shape. Preliminary shape is shown on Figure 10. Presented profile was calculated by optimization model described in the paragraph 3. Condensed liquid will be pumped out through the channels located on both sides of the fin (Figure 9). The micro-channels will be 10 – 20 μm wide along the whole length of the fin. The external walls of channels will be transparent and will reproduce the fin geometry (profile). The symmetric (complete) interfin valleys will be created on the both sides of the fin.

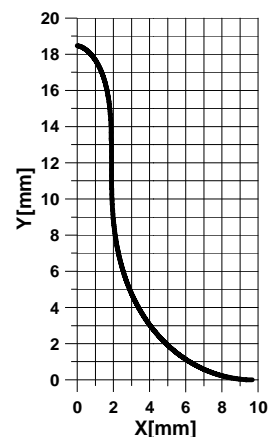


Figure 10. Preliminary fin shape.

The fin base will be cooled by Peltier elements. Several thermo sensors will be mounted along the curvilinear fin surface. A combination of the Phase-Shifting Schlieren technique and Confocal Displacement measurement system will be used to measure local film thickness on the curvilinear surface. The first system will measure the film deformation, while the second one will obtain information about local film thickness at the fin top. Using data from both systems the full distribution of the film thickness and local heat transfer coefficient will be calculated. Vapour pressure and temperature of the fin base will be varied during experiment. Third parameter, which also has scientific importance, is the height of the condensate in the valley. The shape of the liquid meniscus will affect on the film motion along the fin.

6. CONDENSATION ON DISK-SHAPED FIN

In order to make such complicated experiment under microgravity condition all experimental systems have to be tested on ground. Therefore the special set-up has been developed to carry out experimental investigation of film condensation on

the disk-shaped fin. Detailed description of this set-up is presented by Glushchuk *et al.* (2011). Here description is written very briefly. The set-up consists of cooling water loop, thermo stabilization box, optics, ventilation line and data acquisition system. The flow of distilled water is used to cool the disk-shaped fin. The heat removed with water is measured by calorimetric method. In order to decrease the heat loss the experimental cell is placed into a container with forced convection flow of hot air inside.

Experimental cell is a closed volume, in which an evaporator and single fin condenser are placed (Figure 11). Bottom part of the test cell is filled with working fluid. Coiled tube heater is used to boil the liquid. It is placed in such a way that vapour bubbles are generated uniformly in the liquid volume. An uniform evaporation from the liquid surface is provided. Generated vapour comes up and condenses on the curvilinear fin. The condensed liquid flows down. Presented designs of the heater and test cell allow obtaining quasi-stationary distribution of the vapour around the fin. All walls of the test cell are made of semi-transparent plastic LEXAN having small heat conduction coefficient (0.1944 W/mK). The optical window with diameter of 45 mm and thickness of 4 mm are mounted into the top wall to make optical investigation and visual analysis of condensation on the fin top. Vapour pressure, temperature distributions in vapour and liquid phases, heating power were measured during experiments.



Figure 11. Photo of experimental cell with disk-shaped fin.

The core element of the test cell is the disk-shaped fin of special profile. The fin in the presented experiment is made of brass. Its thermal conductivity equals to 120 W/mK. The cross section profile has the optimized shape (Figure 12) calculated using the optimization model developed by the authors. The model is described in the paragraph 3. The optimization has been done for condensation of FC-72 at atmospheric pressure and temperature drop $(T_v - T_w) = 5$ K. Geometrical parameters of optimization are following: fin top curvature 1000 m^{-1} , fin height 29.3 mm, fin base height is about 20 mm. The fin shape curvature is described by the following formula: $\kappa(s) = (as + b)^{1/2} - c$. Constants a , b and c equal to 0.002212, 6.947×10^{-7} and 199.89, respectively. Temperature distribution along the fin surface is measured by four thermocouples.

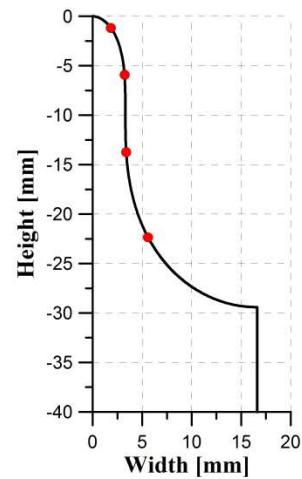


Figure 12. Cross section profile of the fin. Rounds correspond to the thermocouples location.

Confocal displacement measurement system (CDMS) is adopted to measure the film thickness at the fin top. It consists of computer, controller and a sensor. The confocal measurement principle is following. Polychromatic white light is focused onto the target surface by a multilens optical system. The lenses are arranged so that the white light is dispersed into a monochromatic light by controlled chromatic aberration. A specific distance to the target is assigned to each wavelength by a calibration. Only the wavelengths which are exactly focused on the fin and the liquid surface (target surface) are used for thickness measurement. Light reflected from the target is passed through a confocal aperture onto a spectrometer which detects and processes the spectral changes. Sensor IFS 2401-0.4 with

measurement range of 300 μm and accuracy about 1 μm is used. The measurement region is located at 9.9 mm from the sensor front site. Diameter of a measurement spot is 10 μm . Measurements carry out through the window in the upper wall of the cell.

The experimental investigation of film condensation of liquid FC-72 at atmospheric pressure has been done. Corresponding saturation temperature is 56 $^{\circ}\text{C}$. The temperature inside the fin was varied in the experiments while the vapour pressure was maintained constant. Figure 13 shows the results of the average heat transfer coefficient (HTC) measurements. Circles correspond to the experimental data. Heat transfer coefficient has been calculated using average fin surface temperature measured in the experiment. Solid line on the Figure 13 corresponds to the HTC calculated by the Nusselt's formula for condensation on the vertical square plate with height $H=100$ mm. Such linear size has been chosen using the assumption that the surface area of the plate equals to the half surface of the disk-shaped fin. Obtained experimental results are higher than HTC calculated by the Nusselt's formula on 20-25 %. This can be explained by the fact that in the experiments surface tension forces affects on the liquid film flow additionally to the gravity. In the Nusselt theory condensate film flows down under the action of gravity and the influence of the surface tension force are not taken into account. Due to this fact, there is a small intensification of the condensation process in comparison with the case of gravitational draining of the condensate.

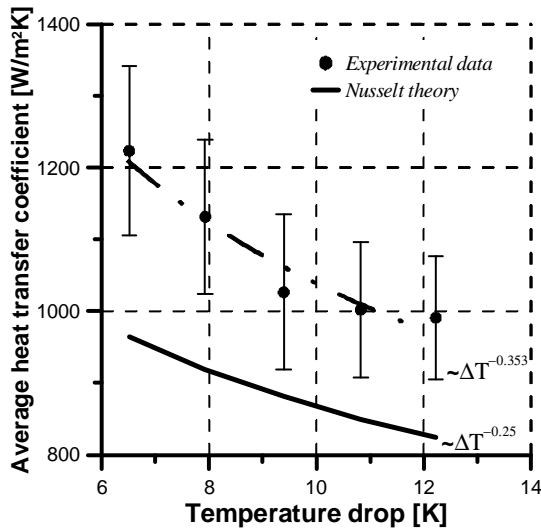


Figure 13. Average heat transfer coefficient.

Preliminary measurements of the film thickness at the fin top have been done. The reflection coefficient from the film surface was much less than one from the fin. Therefore it was difficult to distinguish the light wavelength corresponding to the condensate surface in the spectrometer signal. Only qualitative data have been obtained. The film thickness grows with decreasing of the fin surface temperature. The film thickness was about 10-30 μm at the temperature drop 12 K. Such temperature difference is maximal one which can be achieved in the developed set-up.

7. INTUBE CONDENSATION MODEL

In the works described above only the condensation process on single fin was investigated. Influence of the vapour flow and gravity acceleration effect on the condensate motion is also very important factors in condensers of loop heat pipes. In order to enlarge our knowledge about both factors the condensation process inside a smooth tube has been investigated theoretically and experimentally. Developed model is presented briefly below.

A theoretical modelling of the laminar film-wise condensation of the vapour in the condenser tube is based on the solution of the evolution equation for the condensate film thickness δ , which expresses the mass conservation of an incompressible fluid in a following form:

$$\delta_t + \text{div} \vec{q} + J_c \sqrt{\det \tilde{g}_{ij}} = 0, \quad (17)$$

$$\vec{q} = (q_1, q_2) = \left(\int_0^\delta u_1 dy, \int_0^\delta u_2 dy \right).$$

where \vec{q} is a vector of the specific volume flow rate, u_1 and u_2 are liquid velocities along the coordinate lines (ξ, ζ) of the tube surface. Figure 14 shows coordinate system used in the model.

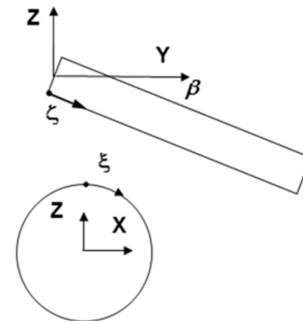


Figure 14. Coordinate system for inclined tube.

Liquid and vapor flows assumed to be laminar. In the validity of the lubrication approximation at low Reynolds numbers of condensate flow the expression for vector \vec{q} is following

$$q = \frac{\delta^3}{3\mu} f + \frac{\delta^2}{2\mu} \tau_{sur} \quad (18)$$

$f = -\nabla_1(p_v + \rho g \tilde{r} + \sigma \tilde{H})$ is a surface gradient of modified pressure, $\partial P_v / \partial \zeta = -8\mu_v G_v(\zeta) / \pi R^4$, \tilde{r} is a coordinate of the condensate film surface, \tilde{H} is the double mean curvature of the condensate film surface, $\tau_{sur} = (0, -R/2 \partial P_v / \partial \zeta)$ is the tangent shear stress induced by the vapor flow. For vapour pressure and shear stress the Poiseuille solution is used. The condensate volume flow rate through the liquid-vapour interface surface is:

$$J_c = -\lambda \Delta T / \rho r \delta \quad (19)$$

\tilde{g}_{ij} is a metric tensor of the condensate surface. The finite volume method is used for the approximation. The obtained nonlinear system of equations is solved by means of Newton method with numerical linearization.

Condensation of pure saturated ethanol vapour in circular tube of 1.5 mm diameter and 100-200 mm length has been simulated, $P_v=440$ mBar, $\Delta T=1$ K, $G_{in}=2.2$ l/min. Typical distribution of the condensate film thickness is shown in Figure 15.

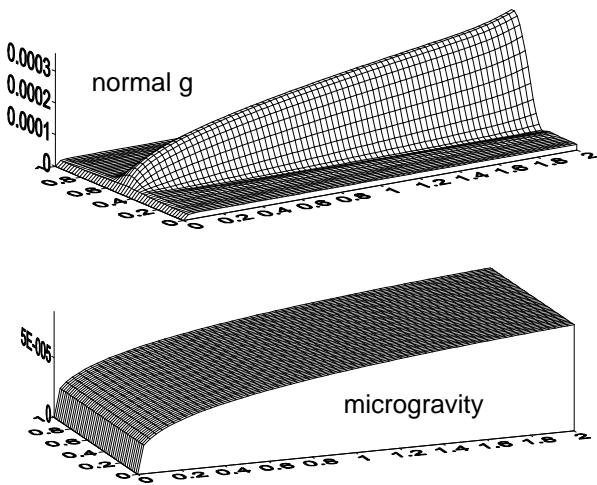


Figure 15. Condensate film thickness distribution along and across the tube.

A change in time of a heat transfer coefficient (HTC) is shown in Figure 16a. One can see that transition from normal gravity to microgravity causes a significant degradation of the heat transfer coefficient. This degradation is due to the change in the flow regime from stratified to annular. Transition time to steady state regime increases with increase in the diameter of condenser tube, Figure 16b. The time of transition to steady state regime under microgravity is greater than that under normal g for tube diameter greater than 2 mm. The capillary length of ethanol under such conditions is equal to 1.6 mm. One can see that for tubes with diameter greater than 3 mm the transition time is greater than 10 seconds.

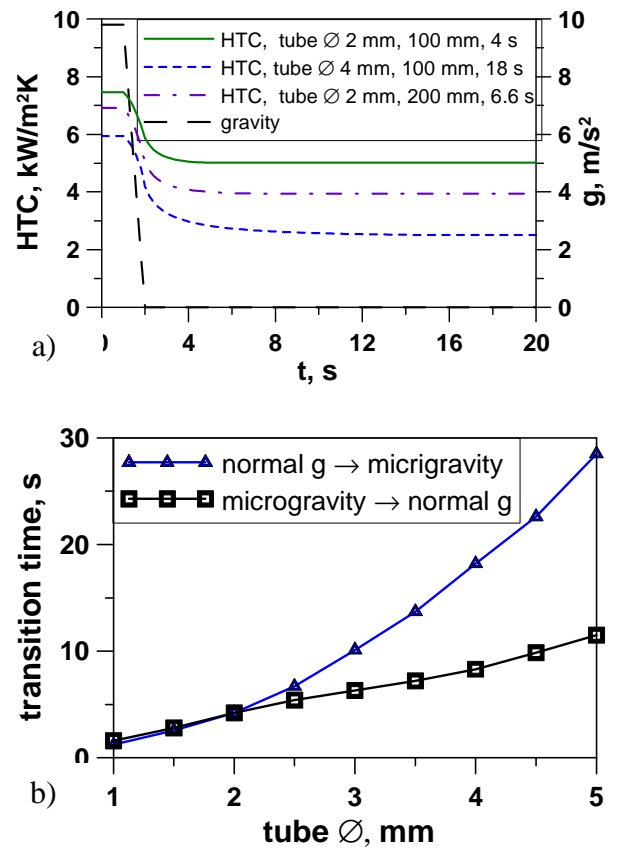


Figure 16. Dependence of the HTC on time at sudden change of gravity (a) and the time length of the transition to steady state regime (b).

8. INTUBE CONDENSATION EXPERIMENT

Experiments on convective in-tube condensation of pure ethanol vapour have been performed using an experimental rig shown in Figure 17. The goal of the experiments is to measure the average heat transfer coefficient for the in-tube condensation of pure ethanol vapour subject to the angle of the tube inclination to horizon and so to study the influence the orientation of gravity on heat transfer at flow

condensation at relatively low inlet vapour mass velocities. Also the obtained experimental data is used for validation and testing of the mathematical model for in-tube convective condensation described in the section 7.

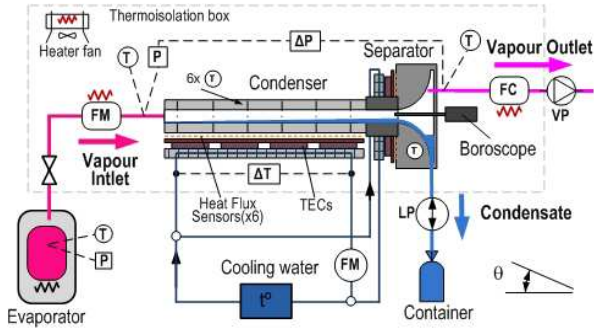


Figure 17. A schematic view of the experimental rig. FM flow meter, FC flow control, LP liquid pump.

The experiments are carried out in a smooth condenser brass tube of 4.8 mm internal diameter at saturation temperature 58 C° relevant to pressure 440 mbar. The condensation mass velocity ranges from 0.005 to 0.015 kg/(m²s). The outlet mass flow rate is constant and equals to 0.004 kg/(m²s). Pure ethanol (99.8%) is used as the working liquid. Two parameters are changed during the experiments: the difference between the saturation temperature of the vapour and the condenser tube wall temperature ranging from 0.8 to 4 K and the inclination angle of the condenser tube regards to the horizon ranging from 0.8 to 90°. The detailed description of the experiment is reported in Lyulin *et al.* (2011).

Dependency of the dimensionless heat transfer coefficient on the inclination angle at different temperature drops is plotted in Figure 18. The trends 1 and 2 represent average trends of experimental curves of dependency of the dimensionless heat transfer coefficient on the inclination angle for different values of the temperature drop. The trend 3 shows the theoretical calculation of the heat transfer coefficient. One can see in the plot that the heat transfer coefficient has a local maximum at the angle of about 30°. It is explained by the complex gravity drainage mechanisms of the condensed liquid. Slight increase of the inclination angle from zero causes expansion of the intensive condensation area due to the rivulet shallowing, but further inclination increases total condensate thickness bringing eventually to the homogenous annular flow at the vertical orientation of the tube.

The theoretical model also predicts this local maximum of heat transfer coefficient.

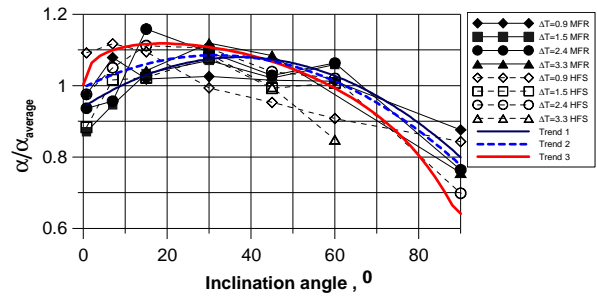


Figure 18. Dimensionless heat transfer coefficient depending on the inclination angle.

Filled symbols and Trend 1 correspond to HTC obtained using the vapour mass flow rate measurements. Unfilled symbols and Trend 2 correspond to HTC obtained by direct measurements using the heat flux sensors. Trend 1 and 2 is an approximation of the curves with filled and unfilled symbols. Trend 3 corresponds to HTC obtained by theoretical calculation. $\alpha_{average}$ average value of the heat transfer coefficient for given temperature drop.

9. CONCLUSIONS

During the last decade the model of the fin shape optimization has been developed. It takes into account surface tension forces and finite heat conductivity of the fin material. Developed model allows to significantly increasing the condensate outflow as compared with the case of the optimal isothermal fin shape at the finite thermal conductivity. Enhancement coefficient increases with fin thermal conductivity decreasing.

Effects of disjoining pressure and level of condensed liquid between fins have been analyzed theoretically that is important for condensation in grooved heat pipes. Calculations show that disjoining pressure influence on the film thickness at the fin tip is negligibly small and may be not taken into account. Value of the flooding depth changes significantly the condensate outflow from the fin. The pressure drop along the fin surface depends weakly on the liquid level and condensed liquid flow rate from the convex part of the fin almost does not change.

New type of space experiment have been proposed and accepted by the European Space Agency. Title of the experiment is “Single fin condensAtion: FIlm local measuRements (SAFIR)”. It will be carried out onboard the International Space Station. The principal objectives of the experiment are to obtain new reliable local experimental data

(film thickness, heat transfer coefficient...) in order to get a better understanding of the condensation phenomenon.

First prototype of experimental cell for the space experiment has been developed and tested. The temperature distribution along the curvilinear fin surface has been measured. The temperature drop along the surface exists and increases with growth of the difference between vapour and fin base temperatures. This temperature drop can not be neglected not only in the calculation of condensation process but also at fin shape design. The average heat transfer coefficient have been measured. The measurements of the film thickness at the fin top shows that film does not equal to zero.

The model of condensation inside a circular inclined tube at various gravity levels has been developed. In case of gravity changes transition time to steady state regime increases with increase in the diameter of condenser tube. The time of transition to steady state regime under microgravity is greater than that under normal g .

Experimental study of the laminar convective condensation of the pure vapor inside an inclined smooth tube has been performed. The average heat transfer coefficient reduces with increase in the difference between the vapor saturation and the wall temperatures. While downstream inclination of the condenser tube from 0 to 20...30° increases the average HTC the further inclination causes reducing of heat transfer coefficient. The dependency of the HTC on the inclination angle has a maximum in the range 15°–35° due to the complex gravity drainage mechanism of the condensed liquid.

Above-mentioned results could be useful for development of condensers of heat pipes, loop heat pipes and compact effective cooling systems for space and ground applications.

NOMENCLATURE

a, b, c	constant
A	Hamaker constant, [Pa m ³]
Bo	Bond number
f	surface gradient of modified pressure
g	gravitational acceleration, [m/s ²]
\tilde{g}_{ij}	metric tensor of the condensate surface
G_{in}	condensate volume flow at inlet, [m ³ /s]

J	condensate volume flow, [m ³ /s]
H	height, [m]
\tilde{H}	double mean curvature of the condensate film surface, [m ⁻¹]
l	capillary constant, [m]
m	mass flow, [kg/s]
P	pressure, [Pa]
P_l	pressure in liquid phase, [Pa]
P_v	pressure in vapour phase, [Pa]
q	heat flux density, [W/m ²]
\vec{q}	vector of the specific volume flow rate
R	curvature radius, [m]
R_0	curvature radius of fin top, [m]
R_f	curvature radius of fin surface, [m]
r	latent heat of condensation, [J/kg]
\tilde{r}	coordinate condensate film surface
S	length of curvilinear fin surface, [m]
s	axis along the curvilinear fin surface, [m]
T	temperature, [K]
T_f	temperature of fin surface, [K]
T_l	temperature in liquid phase, [K]
T_v	temperature in vapour phase, [K]
T_w	temperature of the fin base, [K]
u	velocity, [m/s]
y	axis normal to the fin surface, [m]
α	heat transfer coefficient, [W/m ² K]
δ	film thickness, [m]
δ_0	film thickness at the fin top, [m]
δ_s	film thickness at $s=S_2$, [m]
ε	geometrical parameter
ζ	coordinate lines
θ	angular coordinate, [rad]
θ_F	film surface rotation at $s=S_2$, [rad]
κ	curvature, [m ⁻¹]
κ_0	curvature of fin top, [m ⁻¹]
κ_l	final curvature, [m ⁻¹]
λ	thermal conductivity of liquid, [Wm/K]
μ	dynamic viscosity of liquid, [Pa s]
ξ	coordinate lines
ρ	liquid density, [kg/m ³]
σ	surface tension coefficient, [N/m]
τ	tangent shear stress, [kg/s ² m]
φ	angular coordinate, [rad]
ω	angle, [rad]

ACKNOWLEDGEMENT

The authors gratefully acknowledge support of this work by HEAT TRANSFER PRODEX and CIMEX PRODEX Programs (Belgium) and by the integrated projects 96 and 116 of Siberian Branch of Russian Academy of Sciences.

REFERENCES

- Adamek T. (1981). *Bestimmung der Kondensationsgrößen auf feingewellten Oberflächen zur Auslegung optimaler Wandprofile.*, Wärme - und Stoffübertragung, Vol. 15, p. 255 – 270.
- Bejan A., Kraus A. D. (2003), *Heat transfer handbook*, John Wiley and Sons, New York
- Cavallini A., Censi G., Del Col D., Doretti L., Longo G.A., Rossetto L., Zilio C. (2003), *Condensation inside and outside smooth and enhanced tubes — a review of recent research*, Int. J. of Refrigeration, Vol. 26, p. 373-392.
- Chaudhry H.N., Hughes B.R., Ghani S.A. (2012), *A review of heat pipe systems for heat recovery and renewable energy applications*, Renewable and Sustainable Energy Reviews, Vol. 16, p. 2249-2259.
- Glushchuk, A., Marchuk, I.V., Kabov, O.A. (2011), *Experimental study of film condensation of FC-72 vapour on disk-shaped fin*, Microgravity Science and Technology, Vol. 23 (SUPPL. 1), p. S65-S74.
- Gregorig R. (1954) *Hautkondensation an feingewellten Oberflächen bei Berücksichtigung der Oberflächenspannungen*, Zeitschrift für angewandte Mathematik und Physik, Bd. 5, Vol. 1, p. 36 – 49.
- Groll M. (1989), *Heat pipe research and development in western Europe*, Heat Recovery System&CHP, Vol. 9(1), p. 19-66
- Gogonin I.I., Kabov O.A. (1991), *Enhancement of Heat Transfer at Vapor Condensation by Finning*, Russian Journal of Engineering Thermophysics, Vol. 1(1), p. 51-57.
- Kabov O.A. (1999), *Capillary Effect Influence on Vapor Condensation and Heat Transfer in Falling Liquid Films*, Dr. Sci. Thesis, Institute of Thermophysics SB RAS, Novosibirsk, Russia.
- Kabov O.A., Marchuk I.V., Kolyukhin D.R. and Legros J-C. (2003), *Condensation of stationary steam on extended surfaces with suction of the liquid*, Journal of engineering Thermophysics, Vol. 12, p. 1-24.
- Kabov O., Marchuk I., Rodionova D. (2007), *Condensation on Curvilinear Fins (Effect of Groove Flooding): EMERALD Experiment of ESA*, Microgravity Sci. Technol, Vol. 19 (3-4), p. 121-124.
- Launay S., Satre V., Bonjour J. (2007), *Parametric analysis of loop heat pipe operation: a literature review*, Int. Journal of Thermal Sciences, Vol. 46, p. 621-636.
- Lyulin Yu.V., Marchuk I.V., Chikov S.B., and Kabov O.A. (2011), *Experimental study of laminar convective condensation of pure vapor inside an inclined circular tube*, Microgravity sci. technol., Vol. 23, p. 439- 445.
- Marchuk I.V., Kabov O.A. (2003). *A problem in the calculus of variations for film condensation on curvilinear fins*, Journal of Engineering Thermophysics, Vol. 12 (3), p. 199-210.
- Marchuk I.V., Kabov O.A, Legros J-C. (2003), *Steam condensation on a non-isothermal extended Gregorig - Adamek surface.*, J. of Engineering Thermophysics, Vol. 14(4), p 383-397
- Marchuk I.V., Glushchuk A.V. and Kabov O.A. (2006), *Vapour condensation on nonisothermal curvilinear fins*, Technical Physics Letters, Vol. 32 (5), p. 388-391.
- Markovich, A., Mikich, V.V., and Bergles, A.E. (1972), *Condensation on a horizontal wavy surface directed downward*, Proc. Amer. Soc. of Eng.-Mech., Ser. C, Heat Transfer, 94(3), p. 62-69.
- Marto, P.J., and Nunn, R.H. (1983), *An evaluation of film condensation on horizontal integral fin tubes*, J. Heat Transfer, 110, P. 1287-1305.
- Maydanik Yu.F. (2005), *Loop heat pipes*, Applied Thermal Engineering, Vol. 25, p. 635-657.
- Nusselt W. (1916), *Die Oberflächenkondensation des Wasserdampfes – “Zeitschrift VDI”*, Bd 60, S. 541-546, 568-575.
- Rifert V.G., Smirnov H.F. (2004), *Condensation Heat Transfer Enhancement*, WITpress.
- Rose J.W., (2006), *Enhanced Condensation Heat Transfer*, JSME International Journal, Vol. 49(3), pp. 626-635.
- Serin V., Lavieille P., Miscevic M. (2009), *Miniaturised capillary pumped loops: Design and operating limits*, Microgravity Sci. Technol, Vol. 21 (Supp 1), p. 103-109.
- Thome J.R. (2008), *Engineering Data Book III*, (www.wlv.com/products/databook/db3/DataBookIII.pdf)
- Vasiliev L., Vasiliev Jr. L. (2005), *Sorption heat pipe-a new thermal control device for space and ground application*, Int. Journal of Heat and Mass Transfer, Vol. 48, p. 2464- 2472.
- Vasiliev L.L. (2005), *Heat pipes in modern heat exchangers*, Applied Thermal Engineering, Vol. 25, p. 1–19.
- Webb R.L. (1994). *Principles of Enhanced Heat Transfer*, John Wiley and Sons, New York
- Yang A., Yan Y.Y., Mullen D. (2012), *Recent development of lightweight, high performance heat pipes*, Applied Thermal Engineering, Vol. 33-34, p 1-14.
- Zener C. and Lavi A. (1974), *Drainage Systems for Condensation*, Journal of Heat Transfer, Vol. 96, pp. 209-215.

TOWARDS QUANTITATIVE VALIDATION OF A CLOSED LOOP PULSATING HEAT PIPE NUMERICAL MODEL

Mauro Mameli, Marco Marengo

Department of Industrial Engineering, University of Bergamo, Viale Marconi 5, 24044 Dalmine (BG), Italy.
E-mail: mauro.mameli@unibg.it ; marco.marengo@unibg.it

Sameer Khandekar

Department of Mechanical Engineering, Indian Institute of Technology Kanpur, 208016 Kanpur, India.
E-mail: samkhan@iitk.ac.in

ABSTRACT

A Closed Loop Pulsating Heat Pipe (CLPHP) is one of the most recent and promising two-phase heat transfer devices, applicable for moderately high heat flux applications. It usually consists of a capillary diameter tube closed end-to-end, evacuated and then partially filled with a working fluid. In spite of the simple structure, the PHP working principles are complex. The development of a comprehensive PHP simulation tool is a contemporary problem requiring immediate attention. The present work is devoted to compare the experimental data obtained from a CLPHP test-rig with the results of a detailed numerical model, providing both qualitative and quantitative validation of the model.

KEY WORDS: two-phase flow, oscillating/circulating flow, pulsating heat pipe, numerical model

1. INTRODUCTION

In 1990, Akachi (1990) proposed a novel type of 'heat pipe' able to operate without any wick structure. Its high heat transfer capability together with the relatively simple and flexible structure (a capillary tube closed in a loop), makes it a potential competitor of conventional heat pipe technology. Many numerical models of CLPHP have been proposed in the last two decades but only a few seem to be capable of a complete thermal-hydraulic simulation.

Very recently Das *et al.* (2010) developed an evaporation/condensation model of single liquid plug/vapor bubble that allows the large amplitude oscillations (as observed experimentally) to be described. Nikolayev (2011) updated the previous model in order to treat an arbitrary number of bubbles and branches. Several phenomena occurring inside the PHP are taken into account: coalescence of liquid plugs, film merger or rupture, etc. This model captures some of the experimentally observed regimes of functioning of the PHP such as chaotic or intermittent oscillations of large amplitudes. Even though a model for the solid domain (tube wall) and a quantitative validation are absent, the use of an object oriented method represents a step forward with respect to all the previous codes.

Mameli *et. al* (2012a, 2012b) updated the model by Holley and Faghri (2005). A non-homogeneous heat transfer approach is implemented and the local pressure drops related to the presence of PHP tube bends are also accounted for. The present work is devoted to show a preliminary quantitative validation of this model by means of a direct comparison with actual experimental data of a CLPHP.

2. NUMERICAL MODEL

The numerical analysis is performed with a one-dimensional separated flow model where the control volumes representing the tube wall are treated with a Eulerian approach, while the fluid control volumes follow the liquid plugs and vapor bubbles which are moving with respect to the wall and are always traceable during the simulations (refer Fig.1).

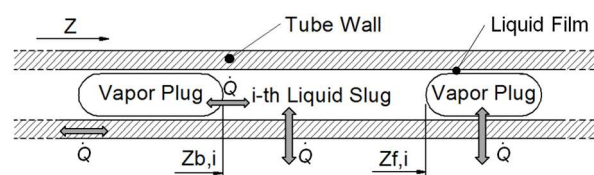


Figure 1: General scheme of the numerical model.

2.1 Assumptions in the model

The main assumptions are listed below:

- All the fluid thermo-physical properties are evaluated as functions of temperature. However, derivatives of density and viscosity are assumed to be negligible.
- The momentum equation for each liquid plug is lumped (advection term is neglected).
- The model is 1-D, with the axial dimension (z) along the flow path considered for momentum and heat transfer; heat transfer in the radial direction is lumped.
- The forward and backward menisci of the liquid plugs are assumed to be spherical with a zero apparent contact angle at the wall.
- Surface tension is evaluated at the vapor bubble temperature.
- The pressure within each vapor bubble is assumed to be uniform.
- Vapor exists at saturated conditions; each vapor bubble is treated as an ideal gas and has negligible flow friction with the wall.
- The liquid film which surrounds each vapor bubble is only considered for the heat transfer purpose, but does not play any role in the hydrodynamics and in terms of liquid mass and momentum.

2.2 Momentum equation for the i-th liquid plug

By means of assumptions a) and b), the momentum equation for incompressible flow turns into the following ordinary differential equation which is applied to each i-th liquid plug:

$$\left[\frac{d\dot{m}_l}{dt} = A_{cr} (\Delta P_g - \Delta P_v + \Delta P_\tau + \Delta P_K) \right]_i \quad (1)$$

The different pressure terms on the right hand side are, respectively, due to the gravity force:

$$\Delta P_g = \rho_l g L \cos \theta \quad (2)$$

Where $\theta[\text{deg}]$ is the angle between the gravity vector and the flow direction.

Adjacent vapour plugs expansion/compression:

$$\Delta P_v = [P_{sat}(T_v)]_{j+1} - [P_{sat}(T_v)]_j \quad (3)$$

Viscous shear:

$$\Delta P_\tau = \frac{f}{2d} \rho_l u_l^2 \quad (4)$$

where the friction factor f is evaluated for the laminar and turbulent regimes.

Minor losses due to bends and turns:

$$\Delta P_K = \sum_{k=1}^{N_t} \frac{K_k}{2d} \rho_l u_l^2 \quad (5)$$

The constant K_k is the loss coefficient due to the k-th turn according to *Darby (2001)*:

$$K_k = \frac{K_{Re}}{Re_l} + K_r \left(1 + \frac{K_d}{(d/0.0254)^{0.3}} \right) \quad (6)$$

This empirical correlation depends on three main parameters (K_{Re} , K_r , K_d), on the Reynolds number and on the exact geometry of the bend. The values adopted for the three parameters in case of 90° bend and 180° are listed in Table 1.

The new positions of the liquid plugs are calculated based on global mass conservation

2.3 Energy equation for the i-th liquid plug

The following partial differential equation accounts for heat storage and axial conduction within the fluid; the heat transfer between the wall and fluid q_{w-f} is lumped (see Section 2.6).

$$\left[c_{p,l} \rho_l A_l \frac{\partial T_l}{\partial t} = q_{w-f} p + k_l A_l \frac{\partial^2 T_l}{\partial z^2} \right]_i \quad (7)$$

Each liquid plug is divided into n_s nodes and the temperature for each node is evaluated by integrating equation (7). The remaining spatial derivative is determined using a first-order central difference. Values of heat transfer between the wall and fluid are interpolated based on the representative values of adjacent nodes.

2.4 Energy equation for the wall

Holley and Faghri (2005) assume that the internal tube surface is covered by a thin wick and that the liquid film surrounding each vapour bubble is always filling the porous structure. As most of the PHP prototypes and experimental apparati are built with smooth tubes (this is also the most attractive feature of the CLPHP with respect to the conventional heat pipe) the wick is not considered in the present work and the energy equation for the wall is:

$$c_{p,w} \rho_w A_w \frac{\partial T_w}{\partial t} = q_{ex} p_0 - q_{w-f} p + k_w A_w \frac{\partial^2 T_w}{\partial z^2} \quad (8)$$

where,

$$q_{ex} = \begin{cases} q_{ev} & \text{evaporator zone} \\ 0 & \text{adiabatic zone} \\ h_\infty (T_\infty - T_w) & \text{condenser zone} \end{cases} \quad (9)$$

The entire tube wall is divided into n_w nodes and the temperature for node is evaluated by integrating equation (8). The remaining spatial derivative is determined using a first-order central difference. Values of heat transfer between the wall and fluid are interpolated based on the representative values of adjacent grids.

2.5 Energy equation for the j-th vapour bubble

The following partial differential equation accounts for heat storage within the entire vapour bubble, for the heat transferred between vapor and the tube wall q_{w-f} and for the axial conduction with the neighbouring liquid plugs.

$$\left[(z_{f,j} - z_{b,j}) A_{cr} \frac{\partial}{\partial t} \left(H_v \frac{P_{sat}(T_v)}{RT_v} \right) = \right. \\ \left. = q_{w-f} p(z_{f,j} - z_{b,j}) + k_l A_l \frac{\partial T_l}{\partial z} \Big|_{z_{f,j-1}} - k_l A_l \frac{\partial T_l}{\partial z} \Big|_{z_{b,j}} \right] \quad (10)$$

Forward and backward first-order differences are used for conduction at the menisci.

2.6 Heat transfer between the tube wall and the working fluid

When the local Reynolds number related to the i-th liquid plug is $Re_l < 2000$ and the liquid plug is heated or cooled by means of sensible heat, the local Nusselt number is far from being constant. Thus, the correlation for thermally developing laminar flow by *Shah and London (1979)* has been implemented:

$$h_l = \begin{cases} \left(\frac{k_l}{d} \right) \cdot 1.953 \left(Re_l Pr_l \frac{D}{L_x} \right)^{1/3} & \left(Re_l Pr_l \frac{D}{L_x} \right) \geq 33.3 \\ \left(\frac{k_l}{d} \right) \left(4.364 + 0.0722 Re_l Pr_l \frac{D}{L_x} \right) & \left(Re_l Pr_l \frac{D}{L_x} \right) \leq 33.3 \end{cases} \quad (11)$$

where L_x is the thermal entry length and it is set equal to the evaporator/condenser length.

For the transient/turbulent flow ($2000 \leq Re_l \leq 10000$), the Gnielinski correlation has been implemented:

$$h_l = \left(\frac{k_l}{d} \right) \left[\frac{(f/8)(Re_l - 10^3) Pr_l}{1 + 12.7(f/8)^{1/2} (Pr_l^{2/3} - 1)} \right] \quad (12)$$

For the fully developed turbulent flow ($Re_l \geq 10000$), Dittus-Boelter correlation has been used:

$$h_l = \left(\frac{k_l}{d} \right) 0.023 Re_l^{0.8} Pr_l^n \quad (13)$$

where $n = 0.4$ if $T_w > T_{fluid}$ and $n = 0.3$ if $T_w < T_{fluid}$. Regarding the boilig/evaporation heat transfer, the *Gungor and Winterton (1987)* correlation is used:

$$h_b = h_l \left\{ 1 + 3000 Bo^{0.86} + \left[\frac{x_{ev}}{1 - x_{ev}} \right]^{0.75} \left(\frac{\rho_l}{\rho_v} \right)^{0.41} \right\} \quad (14)$$

where $Bo = \frac{q'' A_{cross}}{|\dot{m}| H_{lv}}$ is the boiling number, x_{ev} is the

vapor mass quality of the heated vapor plugs (taken from table 2) and h_l is the single phase (liquid) convection coefficient evaluated for the different flow conditions, i.e., (eq. 11,12,13).

With regards to the condenser zone, the correlation for convective condensation by *Shah (1975)* has been implemented:

$$h_l = \left(\frac{k_l}{d} \right) \left[\frac{(f/8)(Re_l - 10^3) Pr_l}{1 + 12.7(f/8)^{1/2} (Pr_l^{2/3} - 1)} \right] \quad (15)$$

Where x_{co} (taken from table 2) is the vapor mass quality of the cooled vapor plugs.

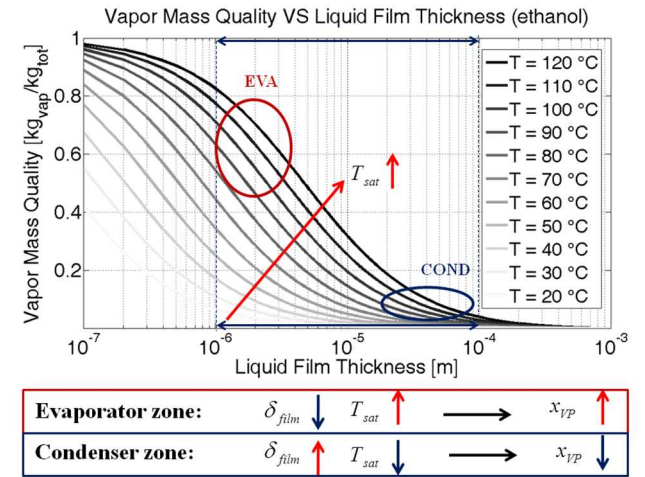


Figure 2: Vapor mass quality against liquid film thickness for ethanol at different temperatures.

From a hydrodynamic viewpoint, the bubbles are made of vapor only, while from a heat transfer point of view, a thin liquid film is supposed to wet the inner tube surface surrounding these bubbles with no inter-phase slip velocity (assumption h). Due to these assumptions, each vapor bubble is hence treated as a two-phase system in equilibrium; the local vapor mass quality x_{vp} is not calculated as the ratio of mass fluxes but simply as the ratio of masses; x_{vp} is then a function of the liquid film thickness δ_{film} and the fluid density which depends, in turn, on the temperature. If δ_{film} is assumed constant along the vapour bubble, then the local vapour mass quality can be estimated as follows:

$$x_{vp} = \frac{m_v}{m_t} = \frac{V_v \rho_v(T_{sat})}{V_v \rho_v(T_{sat}) + V_l \rho_l(T_{sat})} = \frac{\left(\frac{D}{2} - \delta_{film}\right)^2 \rho_v(T_{sat})}{\left[\left(\frac{D}{2} - \delta_{film}\right)^2 \rho_v(T_{sat})\right] + \left\{\left(\frac{D}{2}\right)^2 - \left[\left(\frac{D}{2} - \delta_{film}\right)^2\right]\right\} \rho_l(T_{sat})} \quad (16)$$

Vapor mass quality has been plotted (Fig. 2) as a function of the liquid film thickness for different fluid temperatures.

Previous numerical investigations (Mameli et al. 2012a) described the determination of the vapor mass quality for the evaporating ($x_{vp,ev}$) and condensing ($x_{vp,co}$) vapor bubbles, as a function of the heat input flux.

Heat Input [W]	$(x_{vp,ev})$	$(x_{vp,co})$
50	0.05	0.005
60	0.1	0.01
70	0.3	0.05
80	0.4	0.1
90	0.5	0.1
100	0.6	0.2

Table 1: Vapor mass quality of the vapor plugs travelling in the evaporator ($x_{vp,ev}$) and condenser ($x_{vp,co}$) for the different heat input levels.

3. EXPERIMENTAL SET-UP

The PHP apparatus consists of a closed loop with four parallel channels (Fig. 3). The copper tubes in the evaporator section ($L_{ev} = 25$ mm) are embedded in two copper plates (width = 3 mm) heated by two flat flexible heaters (Minco®, HR5383R10.7L12B). The tubes in the condenser section ($L_{co} = 35$ mm) are embedded inside a heat sink which is cooled by means of circulating water kept at 15°C. The tubes in the adiabatic section are made of borosilicate glass for the purpose of visualization ($L_{ad} = 202$ mm). O.D. = 4 mm and I.D. = 2 mm for all the tubes. The device is evacuated by means of a combo vane-turbo ultra vacuum system (Varian® DS-102; v-70) down to 0.01 Pa, partially filled with ethanol (filling ratio = 0.65) and operated in vertical position (bottom heated) at different heat input levels. The tube temperature in the evaporator zone are acquired by means of thermocouples (Omega®, K-type, bead dimension of 0.3 mm, accuracy ± 0.2 °C after calibration) and recorded with three NI-9211® modules connected to the PC via a NI-cDAQ9172® chassis. The heat input level is increased by 10W only when the evaporator wall temperature reaches a quasi steady-state condition. As shown in figure 4, the present PHP could reach a pseudo steady-state from 50W to 100W. The stable operation is characterized by a well defined flow circulation (slug flow down-comers and semi-

annular up-comers as shown in Fig. 5).

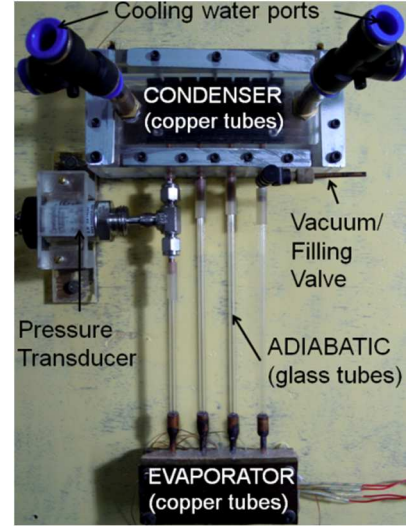


Figure 3: Pulsating heat pipe test-cell.

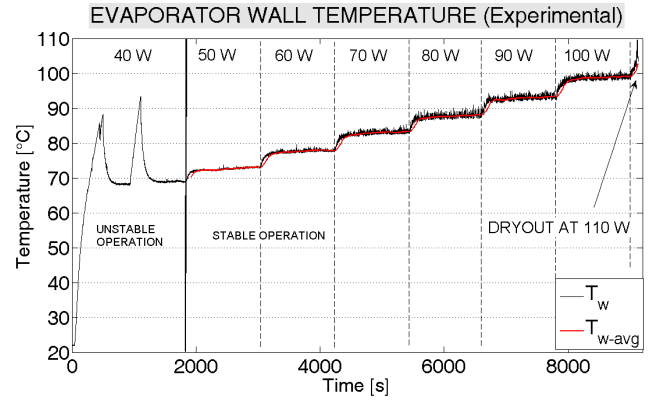


Figure 4: Temporal trend of the evaporator wall temperature T_w (Experimental result).

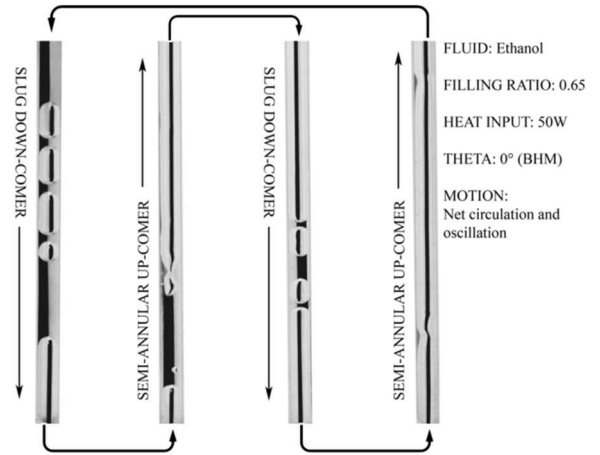


Figure 5: Flow pattern visualization.

4. MODEL VALIDATION

Finally the numerical model is set with the actual PHP test-rig characteristics, listed in Table 2 and the experiment has been simulated.

CODE INPUT PARAMETER	VALUE
Working fluid	ethanol
Tube material	copper
Internal tube diameter	2 [mm]
External tube diameter	4 [mm]
Inner surface roughness	5 [μm]
Evaporator section length	25 [mm]
Condenser section length	35 [mm]
Adiabatic section length	202 [mm]
filling ratio	0.65 [-]
Cool. medium temperature	15 [$^{\circ}\text{C}$]
Cooling medium HTC	10000 [$\text{W}/\text{m}^2\text{K}$]
Initial temperature	27 [$^{\circ}\text{C}$]
Initial n° of Liquid plugs and Vapour bubbles	6 [-]
Heat input levels	50,60,70,80,90,100[W]
Computational time step	0.0001 [s]
N° of grids for the wall	1168 [-]
N° of grids for the liquid	225 [-]
Convergence criterion	0.001 [-]

Table 2: Input parameters of the code.

The temporal trend of total liquid momentum plotted in figure 6 shows that the mean value reaches a nearly constant negative value. This means that a net circulation of the liquid plugs is occurring in the counter-clockwise direction. Circulation is always coupled with a pulsating component as observed during the experiments.

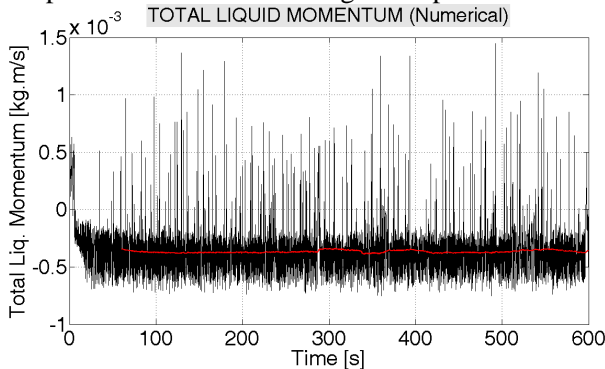


Figure 6: Temporal trend of the total liquid momentum at 50W (Numerical).

The code is able to reproduce the unsteady behavior of the CLPHP, however, since the inertia of the peripheral elements (evaporator plates, heaters, condenser heat sink and insulation) is not modeled, the PHP transient time cannot be properly reproduced. Nevertheless, the numerical average value of the evaporator wall temperature at each heat input level has been evaluated (squares symbol in Fig. 7) and compared with the average value extrapolated from the experimental data (circles in Fig. 7).

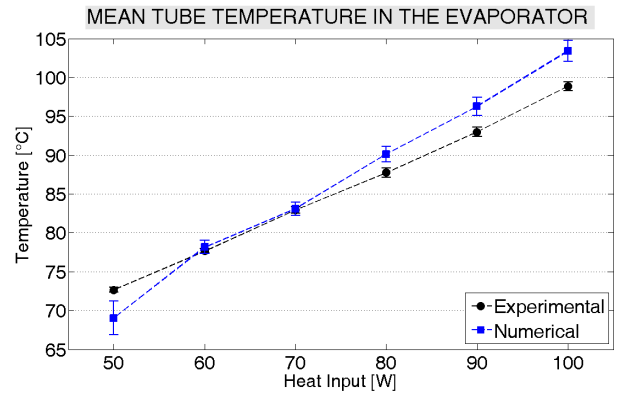


Figure 7: Comparison between numerical results and actual experimental data.

The mismatch between numerical and experimental results on the mean tube temperature in the evaporator, at each heat input level, is always less than 5°C . (please note that the bars at each heat input level is not an “error bar” but represent the temperature oscillating component). The higher error at high heat flux levels is due to two causes:

- Numerical: the model assumption of pure slug flow regime may not be suitable when the fluid up-comers go fully annular. An experimental campaign should be devoted to investigate if the transition from semi-annular to annular flow occurs at a critical heat flux level so as to update the heat transfer subroutine.
- Experimental: at high heat input level, in spite of the insulation, the evaporator loses part of the heat power to the environment, if the heat losses are not taken into account properly, temperatures are overestimated by the model.

5. CONCLUSIONS

A Closed Loop Pulsating Heat Pipe with three U-turns has been numerically and experimentally investigated and the agreement between the numerical and experimental outcomes is good.

- Qualitatively the model is able to reproduce the hydrodynamic behavior of the actual CLPHP test-rig: the fluid net circulation as well as the oscillating component is clearly recognizable from the temporal trend of the total liquid momentum.
- Quantitatively, the pseudo-steady state value of the evaporator wall temperature is also reproduced for six heat input levels with a maximum error of 5°C .

The response to many other sensible parameters (i.e. tilting angle, filling ratio) still needs to be analysed. Nevertheless, the roadmap towards quantitative validation of the numerical model is

already outlined here and future work will be devoted to further improvements.

NOMENCLATURE

A , Area [m^2];
 Bo , Boiling number [-];
 c_p , Specific heat [J/kgK];
 D , Diameter [m];
 f , Friction factor [-];
 g , Gravity acceleration [m/s^2];
 h , Heat transfer coefficient [$\text{W}/\text{m}^2\text{K}$];
 H , Enthalpy, [$\text{J}/\text{kg.K}$];
 k , Thermal conductivity [W/mK];
 L , Length [m];
 m , Mass [kg];
 \dot{m} , Mass flow rate [kg/s];
 n , Number of computational grids [-];
 P , Pressure [Pa];
 p , Tube perimeter [m];
 Pr , Prandtl number [-];
 q'' , Heat flux [W/cm^2];
 \dot{Q} , Heat input [W];
 R , Ideal gas constant [$\text{J}/\text{kg.K}$];
 Re , Reynolds number [-];
 r_{fs} , Surface roughness [m];
 T , Temperature [$^{\circ}\text{C}$];
 V , Volume [m^3];
 x , Vapor mass quality [$\text{kg}_{\text{vap}}/\text{kg}_{\text{tot}}$];
 z , Axial direction coordinate [m];
 δ , Thickness [m];
 γ , Filling ratio [-];
 μ , Dynamic viscosity [Pa s];
 ρ , Density [kg/m^3];
 σ , Surface tension [N/m];
 τ , Shear stress [N/m^2];

Subscripts

b , back meniscus;
 co , condenser/condensation;
 cr , channel cross section;
 $crit$, critical;
 ev , evaporator/ evaporation;
 f , front meniscus;
 $fluid$, related to fluid;
 $film$, liquid film;
 g , gravitational;
 i , liquid plug index;
 ∞ , Ambient;
 j , vapor plug index;
 k , turn-bend grid index

l , liquid;
 lv , liquid-vapor;
 sat , Saturation;
 s , liquid plug grid;
 t , turn;
 tot , total;
 v , vapor;
 vp , vapour plug;
 w , tube wall;

ACKNOWLEDGEMENTS

The present work was partially financed by the National Project PRIN 2009, Ministero dell'Università e Ricerca.

REFERENCES

- Akachi, H., (1990). *Structure of a heat pipe*. US Patent 4,921,041.
- Darby R., (2001). *Correlate pressure drop through fittings*. Chem. Eng., Vol. 108 (4), pp.127–130.
- Das, S.P. et al., (2010). *Thermally induced two-phase oscillating flow inside a capillary tube*. International Journal of Heat and Mass Transfer, 53(19-20), pp.3905-3913.
- Gungor, K.E. and Winterton, R.K.S., (1987). *Simplified general correlation for saturated flow boiling and comparisons of correlations with data*, Chem. Eng. Res. Des., Vol. 65, pp. 148-166.
- Holley, B. and Faghri, A., (2005). *Analysis of pulsating heat pipe with capillary wick and varying channel diameter*. International Journal of Heat and Mass Transfer, 48(13), pp.2635-2651.
- Mameli, M., Marengo, M., Zinna, S., (2012a), *Thermal Hydraulic Simulation of a Pulsating Heat Pipe Effects of Different Liquid Properties on a Simple Geometry*, Heat Transfer Engineering Int. J., Vol. 33 (14).
- Mameli, M., Marengo, M. & Zinna, S., (2012b). *Numerical model of a multi-turn Closed Loop Pulsating Heat Pipe: Effects of the local pressure losses due to meanderings*. International Journal of Heat and Mass Transfer, 55(4), pp.1036-1047.
- Nikolayev, V.S., (2011). *A Dynamic Film Model of the Pulsating Heat Pipe*, J. Heat Transfer, ASME, Vol. 133 (8), 081504.
- Shah, R.K., (1975). *Thermal entry length solutions for the circular tube and parallel plates*. Proc. 3rd Natnl. Heat Mass Transfer Conference, IIT Bombay, Vol. I, Paper HMT-11-75.
- Shah M.M., (1979). *A general correlation for heat transfer during film condensation inside of pipes*, Int. J. Heat and Mass Transfer, Vol. 22, pp. 547-556.

APPLICATION OF PHASE CHANGE SYSTEMS IN AVIONICS

C. Sarno

Thales Avionics

25 rue Jules Védrières, 26027 Valence Cedex France

Tel +33475798657, Fax +33475798606, claudio.sarno@fr.thalesgroup.com

ABSTRACT

The packaging and thermal management of electronics equipment has become an important issue because of increased power levels and the simultaneous miniaturization of the devices. With the advent of denser device packaging and faster intrinsic speeds, cost, reliability and size have been improved, but unfortunately packaging and thermal management have not followed at the same pace. As a result, it may be difficult to use the latest technology available (microprocessors for example) in avionics conditions. In order to develop products which respond to the specifications at a minimum cost, Thales performs both mechanical and thermal simulations. The simulation level depends on the phases of design (preliminary or detailed). The major challenges are encountered on thermal management problems with power higher than 100 W at the module level and with local hot spot greater to 100 W/cm². Under these conditions, standard cooling approaches using forced air are no longer applicable. To challenge these points Thales has launched many European collaboration research programs for the development of alternate options and particularly two phases cooling systems.

KEY WORDS Avionics, Loop Thermosyphon, Cooling system

1. INTRODUCTION

The packaging and thermal management of electronics equipment has become an important issue because of increased power levels and the simultaneous miniaturization of the devices. With the advent of denser device packaging and faster intrinsic speeds, cost, reliability and size have been improved, but unfortunately packaging and thermal management have not followed at the same speed. As a result, it may be difficult to use the latest technology available (microprocessors for example) in avionics conditions.

In the coming years, the electronics industry will face significant thermal management problems in the use of both existing and emerging highly integrated electronic components and modules. The heat removal capabilities of existing cooling techniques are being overtaken in three different areas:

- increased card, blade or module total heat dissipation (heat power levels higher than 100W), microprocessors presently dissipate 10W and will reach 30 W to 50 W in the coming years in avionics

- increased local heat densities for highly integrated components (heat flux greater than 10 W/cm² and up to 100 W/cm²)
- maximum use of low-cost industrial plastic components or COTS components (Component On The Shelf) in severe avionics applications.

These objectives, up to twice as high as the current practices, are associated with size limitations and higher reliability requirements. As a results packaging plays a major role in the design of the futures equipments

2. PACKAGING DESIGN

The main causes of failure in airborne equipments are due to: thermal problems, vibrations, thermo-mechanical induced stress and other environmental constraints such as fluid resistance, corrosion sand and dust...

The resulting objective of the packaging design is then to develop a product which responds to the specification at a minimum cost and in one shot, this means:

- to be able to anticipate the behavior of the equipment regarding the above mentioned specifications
- to make the good choice for the architecture and for the technologies used in the equipment
- to identify the weaknesses of the design and margins regarding fatigue effects.

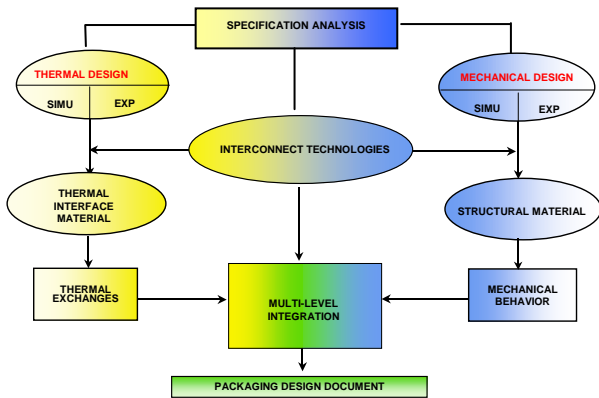


Figure 1. Packaging design procedure

In order to achieve these goals, our main solutions are to have an excellent knowledge of the involved technologies and to perform multi-physics simulations. Fig. 1 shows the design procedure used in most of our applications from the input specification up to the final design justification. Generally the mechanical and the thermal designs are performed in parallel.

2.1 Mechanical design

The complexity of the mechanical analysis will depend on the equipment function; basically the presence of sensors or sensitive equipments will require more complex simulations and justifications. The tool used within Thales is the ANSYS finite element code. The effort may vary from some ten of hours to some several thousand of hours.

In term of mechanical behavior the approach is to check that the resulting levels seen by the sensitive equipment remain below the admissible level (known or set by tests) all along the spectrum of analysis and under the solicitation generated by the carrier in the zone where the equipment is located. Example of such approach are illustrated on the Ariane Navigation Unit (Fig 2), where the power supply has been designed so that its main resonant mode be located around 500 Hz as specified in the initial frequency allocation plan. Another example

(Fig 3) is the design of the mechanical filtering function and dampers of an inertial measurement unit.

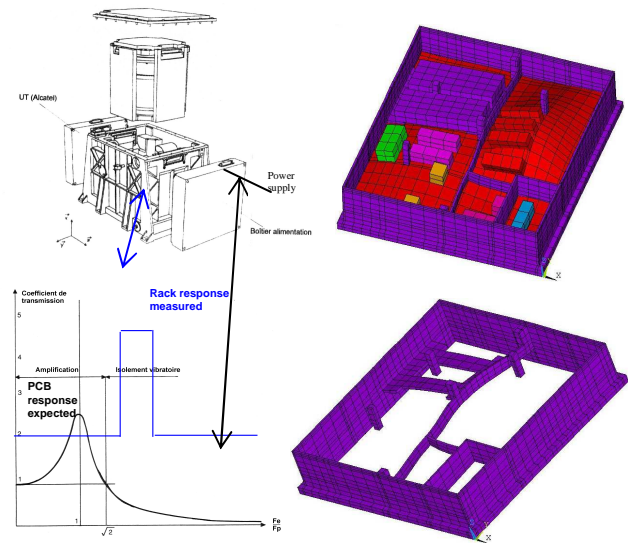


Figure 2. Ariane Navigation Unit

2.2 Thermal design

Similarly, the objectives are to take care of the equipment environment (cooling technologies, ambient temperature...) in order to keep the electronics component temperature under an acceptable level (typically 125°C for the junction temperature or 85°C for the ambient temperature).

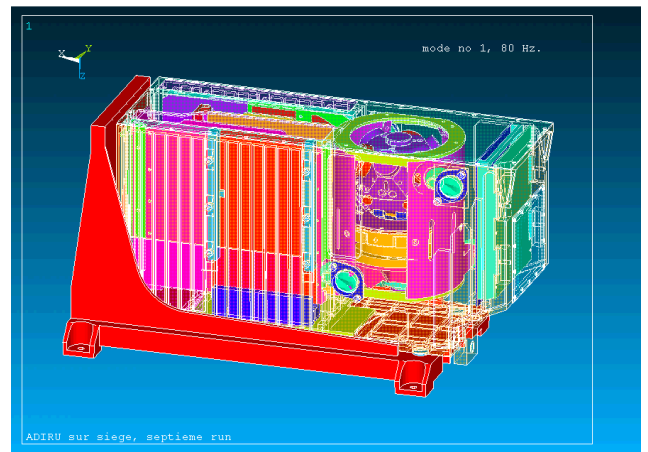


Figure 3. Inertial Reference System

During the thermal design analysis, we generally perform thermal simulations with the use of computational fluid dynamics software (FloTHERM from Mentors Graphics). Basically, we consider three levels for the simulation which

correspond to the three phases of the design (Fig 4):

- level 1, Equipment level , Preliminary design phase: the simulation just takes care of the rack external constraints. Dissipative PCBs are simulated with volumetric sources. This first algebraic or numerical approach helps us to select the most appropriate cooling technologies (free convection, conduction, forced convection) given a level of power in the package and the available cooling options. The global feasibility with associated design complexity is stated.
- level 2, PCB level, Preliminary and detailed design phases: The PCB are represented but the functional areas are just modeled as dissipative surfaces. This simulation level gives the PCB temperature and allows the optimization of the mechanical design (copper layers, specific drains, thermal wedge lock...).

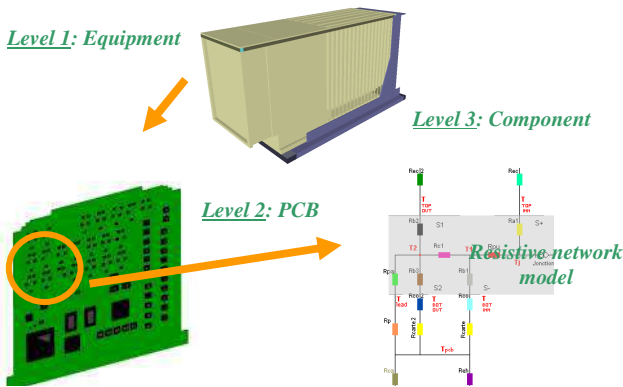


Figure 4. From the equipment to the component level

- level 3, Components level, detailed design and validation phases: All the dissipative components are modeled including their packaging technologies. Thales internal models database are used. This level allows us to reach the junction temperature for each component. The temperature will be used as an input data for the reliability and safety calculations.

3. EXISTING COOLING TECHNIQUES

The main principles, schematically depicted in Fig. 5, are implemented to cool down the components on a PC board in the aerospace domain:

- the heat load generated by the components dissipation is directly transferred from the components and the board to a cooling fluid according to various thermal transfer modes, namely radiation, free convection and forced convection with the air (direct air flow).
- the heat load is conducted from the components to the board, then from the board to heat exchanger where they are rejected to a fluid. In this case, the exchanger can be secured at the board ends or directly on the entire rear face of the board. To minimize the thermal resistance on the board, the board can be fitted with a thermal drain heat pipes. Another alternative is from the components via high thermal conductivity materials to the module shell and then via the heat exchanger surface to a gas or liquid coolant. On the board itself, the thermal transfer mode is conduction (conduction cooled, liquid flow through, air flow around).

Among all these techniques the most widespread is direct air cooling. Air is available on most of the platforms, it is simple to implement with backup options, and it does not require complex and expensive sealing devices.

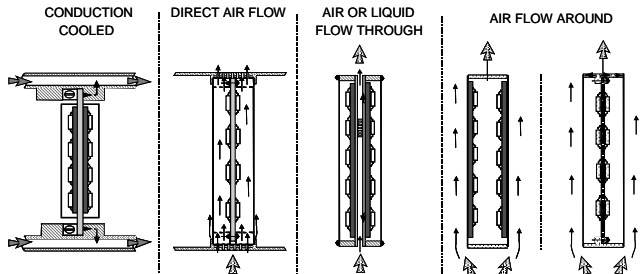


Figure 5. Cooling modes

Fig 6 gives some examples of Thales equipment using forced cooling convection. The thermal dissipation still increases: from 10 W/module, its will reach 20/30 W/module in the near future and 50 W/module in the next developments. In the same time, the module sizes are reduced or at the best remain unchanged.

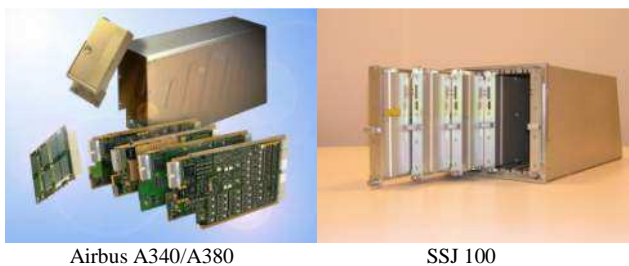


Figure 6. Computer racks

4. FUTURE COOLING TECHNOLOGIES

As mentioned already, with the increase of heat densities following Moore's law, we will face tremendous new challenges in which components heat densities are surpassing 10 W/cm² and will reach 100 W/cm². The standard approach using typical ARINC600 standard cooling conditions in the electronic bay (220 kg/h/kW mass air flow rate in forced convection) are no longer applicable. This global airflow rate cannot cope with the hot spot problems (up to three times the standard air flow rate would be required and this is not possible due to pressure drop increase). It is necessary to use novel technologies which will be able to offer alternate solutions and which will be compatible with high-integrated electronics and at affordable costs. This challenge is shared between the main US and European aerospace equipment manufacturers that are investigating new cooling options. Within Thales, European collaboration research programs have been launched on both civil and military sides about the thermal management. One of the most promising and investigated route involves phase change systems like heat pipe [1] (HP), loop heat pipe [2,3,4,5] (LHP) or loop thermosyphon [6]. These technologies have been investigated through the following European projects for avionics applications.

4.1 KHIEPCOOL Project

Carried out within the framework of the European Commission BRITE-EURAM Program, the three-year KHIEPCOOL research project was initiated to develop an alternate and more efficient cooling technique based on integrated phase change systems.

In this project [7], the proposed multidisciplinary technological development has focused on the development of integrated micro heat pipes through the following phases:

- Development of the micro heat pipe
- Development of an advanced composite materials cooling substrate
- Electronic component integration and interconnection processes
- Thermomechanical performance evaluation on technological demonstrators

The participants of the project were Sextant Avionique (Currently Thales Avionics) as coordinator, University of Lyon (INSA),

University of Stuttgart (IKE), Electrovac, and Nokia. The roles of the participants appear in Figure 7.

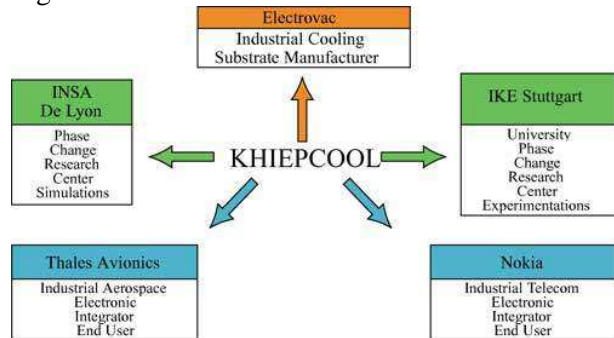


Figure 7. Structure of the KHIEPCOOL project

Heat Pipe Theoretical Study

To design a heat pipe fulfilling the requirements with the associated substrate, simulation studies were performed, thus allowing the evaluation of a great number of configurations and conditions. Using the simulation tool developed by INSA, it was possible to determine the maximum heat transfer capacity and the optimum fill charge of the micro heat pipe. The following parameters were considered: channel geometry (number of corners, corner dimensions and shape, curvature radius of the corner), fluid type and characteristics, wetting angle fluid/wall, channel fill charge, thermal operating conditions (heat flux level, cooling fluid temperature), and heat pipe tilt angle.

Heat pipe integration

Heat pipe integration must be considered according to many parameters, which define the electronic card. Among these parameters are:

- Interconnection substrate
- Component package
- Cooling principle
- Assembly techniques

One must pay close attention to different thermal interface materials, mounting techniques, and heat power levels. The required improvements in the whole system's thermal performance can be achieved by minimizing thermal resistances between the different system levels. Hence, it is important to carefully evaluate and analyze the entire system and its environment.

In the case under discussion, the electronic cards were fixed inside rack-mounted line replaceable modules (Figure 8). Each rack contained nine such modules cooled by air convection.



Figure 8. Rack and LRMs configuration

Two technological approaches (conduction cooling and convection cooling) were studied by experimentation and numerical simulation.

- Conduction cooling : The cards were fixed on an aluminum support into which the heat pipe was integrated. Heat generated by the electronic packages was transferred by conduction to the air cooler via a thermal clamp.

- Convection cooling : The electronic packages were mounted double-sided on the circuit board. Air was blown directly on the components to cool them by forced convection (Figure 9).

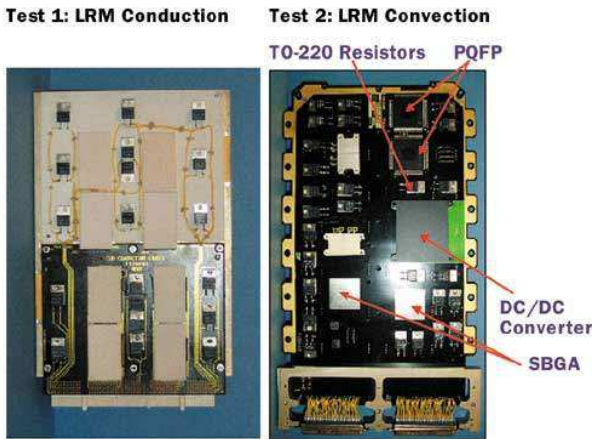


Figure 9. Conduction and convection demonstrators.

Test Results

The objectives of these tests were to check the performance of the heat pipe in a manner consistent with the specific aircraft environment and to evaluate the junction temperature benefit on actual configurations:

Static thermal performance versus position

A test setup was developed to clamp the heat pipe at both extremities (Figure 10). The results show a

good homogeneity of the heat pipe performance versus tilt angle, as illustrated in Figure 11.

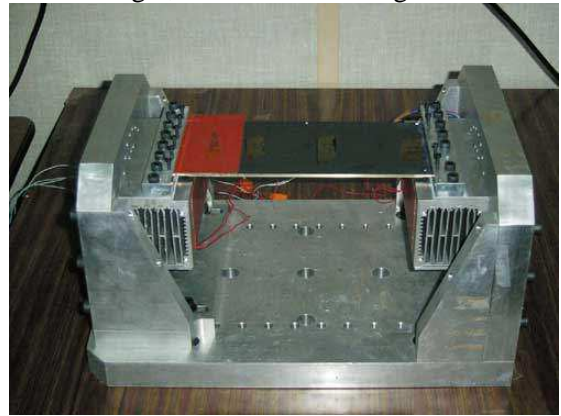


Figure 10. Heat pipe test setup.

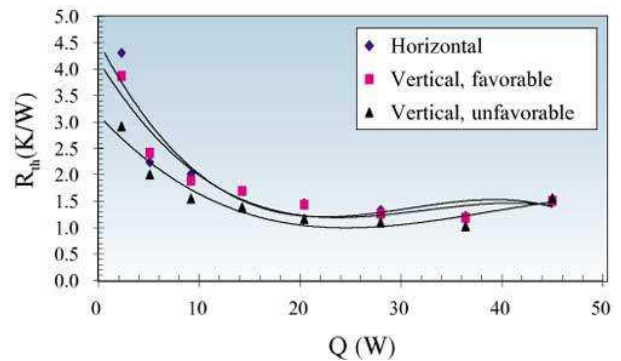


Figure 11. Heat pipe thermal resistance dependence on the tilt angle.

Thermal performance under acceleration

The main identified risk when employing heat pipes in aircraft conditions is the behavior of the heat pipe when subjected to reverse acceleration, which could prevent the liquid from returning to the evaporator section. When studying this, the setup was mounted on a centrifugal machine, as illustrated in Figure 12. The acceleration was varied using the table angular velocity up to 10G. The results in Figure 13 show a variation in the thermal resistance of about 10%, starting at 5G.



Figure 12. Test setup for acceleration.

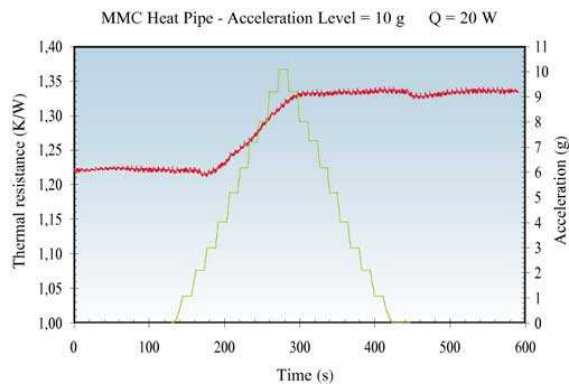


Figure 13. Thermal resistance versus acceleration.

Conclusion

Micro heat pipes have been developed to meet avionics requirements. A mathematical model was developed to simulate the triangular cross section micro heat pipe performance including wicks. The main calculated parameters were the maximum heat transfer rate and the optimum fill charge. From numerous simulations, the authors determined the final heat pipe geometry and established the manufacturing route for the heat pipes including metal matrix composite versions of the metal matrix composite heat pipe prototypes. They then carried out two different kinds of experimental investigations to determine the micro heat pipe thermal performance:

Extensive optical investigations for fluid flow visualization

Micro heat pipe design optimization.

With enhanced wick structures, a heat transport capacity of over 30W could be obtained with a heat pipe thermal resistance of less than 1.0 K/W. The heat transport capability was more than six times higher than that of an aluminum block with the same cross-section. The authors also analyzed assembly technique of heat pipes.

In the application:

The objectives of 100W dissipation at the card level was reached with 30-40W at the heat pipe level.

The chips survived the static thermal tests with hot spots densities up to 10W/cm².

Dynamic vibrations had no detrimental effects on the heat pipe thermal performance

Heat pipe depriming began at 5g when subjected to reverse acceleration

The technology has been considered applicable to avionics, provided that required complementary industrial developments and long term behavior checking occur.

4.3 COSEE Project

The COSEE Project (Cooling Of Seat Electronic Boxes and cabin Equipment) aims at the cooling of electronics equipment for the IFE (In Flight Entertainment Systems). New generations of In-flight Entertainment Systems are required to provide more and more services (Audio, video, Internet, flight services, multimedia, games, shopping, phone, etc...) at an affordable cost. But unlike other avionics systems installed in temperature controlled bays most of the IFE equipment and boxes are installed inside the cabin, they may be buried in small enclosed zones and they are not connected to the aircraft cooling system (ECS). This situation creates thermal management issues that may affect the reliability, the safety and the cost of the equipment. The most critical equipment is the seat electronic box (SEB) installed under passenger seat. To face the increasing power dissipation, the use of fans will be required with the following drawbacks: extra cost, energy consumption when multiplied by the seat number, reliability and maintenance concern (filters, failures...) The objectives of the project was therefore to develop and evaluate an alternate advanced cooling technique to the fans, based on two phase change passive systems, adequately integrated inside the seat structure and taking benefit of the seat frame as a heat sink or of the aircraft structure when installed in the ceiling. Some samples of seat electronics boxes and IFE architecture are given in Fig 14.



Figure 14. IFE Architecture and SEB samples

A community collaboration has been established due to the multidisciplinary nature of the problems to be solved and to the fact that the necessary expertise and knowledge do not lie in a sole nation (phase change simulation and design, heat pipe manufacturing, equipment cooling, seat integration and development, aircraft interfaces). The project involved Airbus, airlines, seat manufacturers, research centers and industrial companies (Fig 15).

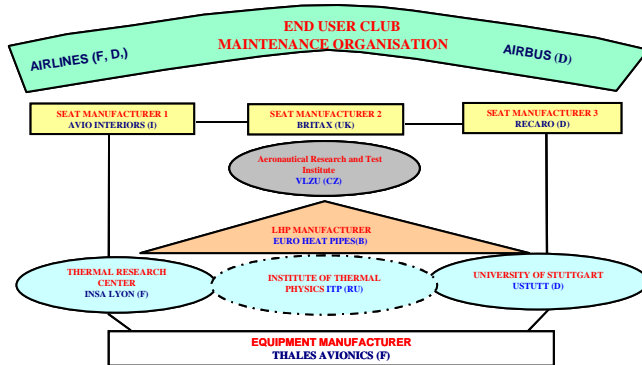


Figure 15. COSEE partnerships structure

The cooling of the SEB has been realized with the help of two kind of phase change systems : heat pipe and loop heat pipe.

- first heat pipe were used to transfer the heat from the dissipating components and the edge of the SEB. In order to increase the heat transfer and to reduce the thermal contact resistance, thermal interface materials (TIM) are used between each mechanical parts.
- then loop heat pipe were used to transfer the heat from the SEB side to the seat mechanical structure which is used as a heat sink and is cooled by natural convection with the ambient air. LHP are particularly interesting when the heat is transferred over large distance under small temperature differences.

Fig 16 gives an overview of the PCB equipped with HP. In order to test the thermal performance of these two phases technologies, we used dummy PCB with resistive components. This approach allows a correct management of the heat dissipated in each part of the demonstrator. Several thermocouples regularly distributed over the thermal path gives the thermal performance of the cooling systems.

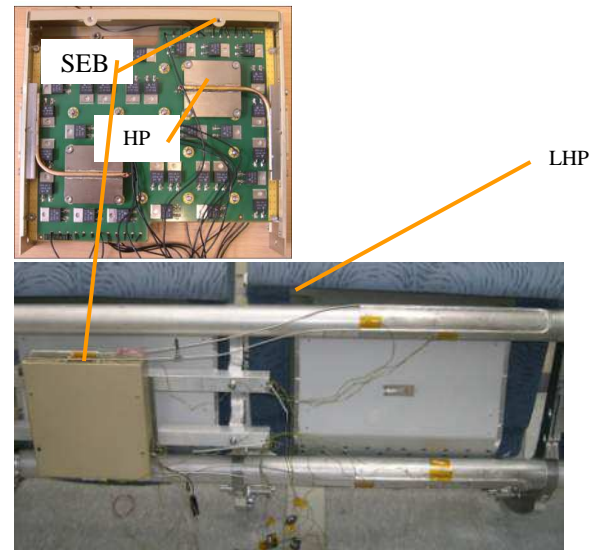


Figure 16. SEB equipped with HP and LHP

Outside the SEB, two LHPs transfer the heat from the seat to the mechanical structure composed of two mains aluminum rods.

The results [8] obtained in this configuration are presented on Fig 17. This graph gives the temperature difference between a representative point of the PCB and the ambient air according to the total dissipated power inside the SEB. Three cases are considered:

- without LHP: the SEB is only cooled by natural convection and is not linked to the seat mechanical structure,
- with LHP horizontal: the seat is in horizontal position and the two LHP are connected to the mechanical structure
- with LHP (22°tilt): the seat is tilted up the 22° in order to evaluate the sensitivity to the tilt of the plane

We can note that the use of loop heat pipe induces a tremendous improvement in the thermal management of the PCB:

- increase of 150% of the heat dissipation capability: from 40W up to 100W with a constant PCB temperature (about 60°C difference between the PCB and the ambient).
- for a same dissipated power, for example 40W, the use of HP and LHP allow 32°C decrease on the PCB temperature without the use of fans

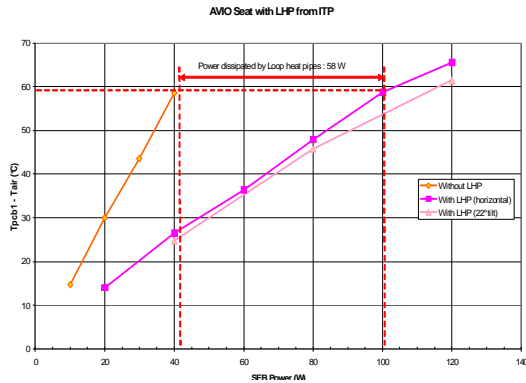


Figure 17. Thermal results

Additional tests were performed in order to check the conformity of the cooling systems with the mains avionics specifications.

These tests include:

linear acceleration (up to 9 g 3 minutes in each axis)

- vibrations (according to DO160 Curve C1)
- climatic tests (performance evaluated between 25 and 55°C ambient temperature)
- thermal shock (-45°C/+55°C, 5°C/min)

The seats have been submitted to all the different tests without damage. The loop heat pipes have had a good thermal behavior. In addition to these operational tests, long-term investigations were conducted by the phase change manufacturers without damages.

The seat mechanical structure was made from aluminum but we have also tested seat made of carbon composite structure to anticipate future developments. Compared to the aluminum, this material has a rather poor thermal conductivity, thus the results are slightly under those obtained with aluminum:

increase of 80% of the heat dissipation capability (from 38W up to 70W with a constant PCB temperature)

for a same dissipated power (40W) the use of HP and LHP allow 20°C decrease on the PCB temperature.

Nevertheless these results are of great interest in term of maximal power dissipation and reliability. Two-phase systems have a great potential for use in future avionics products.

4.4 SYSHANG Project

The SYSHANG Project is an on-going project aiming to develop loop heat pipes adapted to avionics.

It involves three partners, Thales, Atherm and the CETHIL (INSA Lyon).

The objectives of this project is to investigate low cost loop heat pipes for avionics applications and evaluate different implementations on racks and modules (IMA) configurations such as “thermal connectors” habing the capability to removes the modules or cards without disconnecting the fluid pipes.

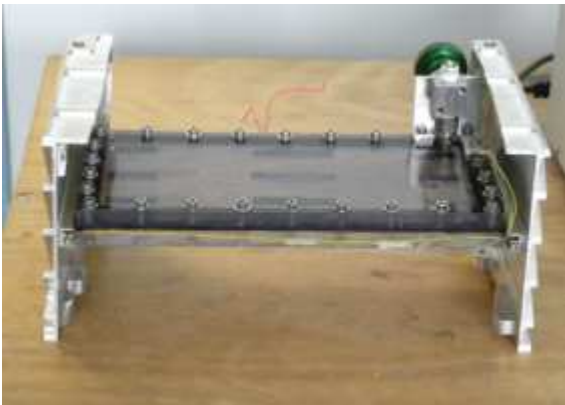
The firsts loop heat pipes have been realized, they will be tested at the CETHIL, and then integrated in a demonstrator for further testing.

The demonstrator will be composed of a representative rack populated with thermal representatives modules.

4.5 Flat plate heat pipe application in terrestrial radars

Heat pipes are well suited when the heat sources are located on one or two points like in the previous example. But for PCB where the heat is dissipated more uniformly like in numerical cards, it is better to use flat plate heat pipe (FPHP) also called Diphasic Thermal Spreader, to drain the heat from the many components toward the side and then to the rack. In FPHP, the location of the heat sources can be multiple, as well as the location of the heat sinks. Also the mass flows of liquid and vapor arrange somewhat automatically. Consequently FPHP are in competition with high thermal conductivity spreaders such as the one based on pyrolytic graphite.

A prototype was developed by CETHIL [8] to estimate the effective thermal conductivity of a FPHP with screen meshes as a capillary structure. The spreader is 260 mm x 110 mm with a total power that varies from 20 to 100 W. The effective thermal conductivity depends on the orientation of gravity but values up to $1000 \text{ Wm}^{-1}\text{K}^{-1}$ have been obtained. It showed that this type of thermal spreaders are of interest for some applications. Consequently studies go on to realize very thin FPHP that could be integrated into our equipments.

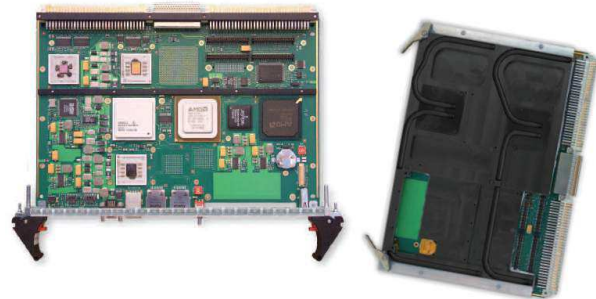


4.6 Heat pipe application for fighters

Thales has already qualified conduction boards in a 6U VME standard using heat pipes for its very demanding airborne applications.

The heat pipes inserted into the thermal drain are used to cool down more specifically 2 micro processors dissipating up to 25 W each which are located at the center of the board dissipating a total of 90W maximum.

The application meets the VITA 47 CC4 standard for the temperatures (from -40°C to 85°C on the sides of the board). In parallel the heat pipes also meet the severe vibration, shock and acceleration levels used for military application.



5. CONCLUSIONS

Packaging design in avionics applications requires a correct management of both mechanical and thermal issues. Simulation is an efficient way to improve and accelerate the design. Thales uses ANSYS finite element code for the mechanical approach and FLOTHERM finite volume code for the thermal approach. These codes help us to design at a minimum cost and in one shot. Nevertheless regarding to the integration constraints, standards solutions based on forced ventilation cannot cope with hot spot problems and new cooling technologies need to be explored. Thales has launched European collaboration research programs about thermal management. These programs mentioned concerns two phases systems for the cooling of a cabin equipments. The results exhibit a tremendous improvement in the management of the PCB with a strong increase of the heat dissipation capability of the equipment. Furthermore these systems exhibit a good behavior regarding to the mains avionics specifications. Some application of the techniques have been qualified and proposed for futures programs.

Acknowledgment

This work was supported by the EC/FP6 COSEE Project (contract no. 030800) and the EC/FP7 NANOPACK Project (contract no. 216176). The authors gratefully acknowledge the support from the EC.

NOMENCLATURE

CC	Compensation chamber
LL	Liquid line
LTS	Loop thermosyphon
VL	Vapor line
LHP	Loop Heat Pipe

REFERENCES

- [1] Peterson, G.P. (1994). An introduction to heat pipes: modeling, testing, and applications (Wiley-Interscience).
- [2] Maydanik, Y.F. (2005). Loop heat pipes. *Appl. Therm. Eng.* 25, 635–657.
- [3] Launay, S., Sartre, V., and Bonjour, J. (2007). Parametric analysis of loop heat pipe operation: a literature review. *Int. J. Therm. Sci.* 46, 621–636.
- [4] Revellin, R., Moreno, J., Bonjour, J., and Thome, J.R. (2008). Effect of local hot spots on the maximum dissipation rates during flow boiling in a microchannel. *IEEE Transactions on Components and Packaging Technologies* 31, 407–416.
- [5] S. Launay, V. Sartre, J. Bonjour, “Simulation du fonctionnement d’une boucle de fluide à pompage capillaire dans un système embarqué” Congrès français de Thermique, SFT 2007, Ile des Embiez, 29 mai - 01 Juin 2007
- [6] Gross, U., and Hahne, E. (1987). Condensation heat transfer inside a closed thermosyphon - Generalized correlation of experimental data. 6th IHPC, Grenoble 466–471.
- [7] Sarno, C., Moulin G., (2001), Thermal management of highly integrated electronic packages in avionics applications, *Electronics Cooling*, November 2001
- [8] Lefevre, F., Conrardy J.B., Raynaud, M., and Bonjour, J. (2012), Experimental investigations of flat plate heat pipes with screen meshes or grooves covered with screen meshes as capillary structure, *Appl. Therm. Eng.* 37, 95-102.

HORIZONTAL CLOSED-LOOP PULSATING HEAT PIPE WITH MULTIPLE HEAT SOURCES

Niti Kammuang-lue, Phrut Sakulchangsattajai, and Pradit Terdtoon

Department of Mechanical Engineering, Faculty of Engineering,

Chiang Mai University, Chiang Mai, 50200 Thailand.

Tel. +66 53 944144 ext. 980, Fax +66 53 226014

E-mail: pom171@hotmail.com

ABSTRACT

The objective of this study is to experimentally investigate the effect of heat source arrangements on thermal performance of a horizontal closed-loop pulsating heat pipe with multiple heat sources (CLPHP w/MHS). The CLPHP w/MHS was made of a long copper capillary tube with internal diameters of 1.0, 1.5, and 2.0 mm, and bent into an undulating tube with 32 meandering turns, in an evaporator section. Evaporator, adiabatic, and condenser section lengths were the same of 150 mm. R123, and ethanol were used as working fluid with filling ratio of 50% by volume. Working temperature was controlled at 50 ± 5 °C. The evaporator section consisted of three heat sources, which was located along the evaporator section length. Heat input was supplied by plate heaters. Input heat flux of each heat source was 1, 3, and 5 kW/m². Experiments were conducted by varying the heat source patterns in 6 possible sets of arrangements, where the heat fluxes of each heat source in the same set were always different. In each arrangement, after system was in steady state, temperatures at evaporator, condenser, and adiabatic section, and also inlet and outlet temperature of cooling medium in a condenser section were simultaneously measured in order to calculate the heat flux of the heat pipe. It was found from the study that, when the heat sources are placed in consecutive order from the highest to the lowest heat flux, beginning from the inlet of the evaporator section, the CLPHP w/MHS has the highest thermal performance.

KEY WORDS: horizontal closed-loop pulsating heat pipe, multiple heat sources, heat source arrangement

1. INTRODUCTION

The continuous increase of the average temperature of the earth in recent decades is a partial result from high temperature waste exhausted to the atmosphere. To diminish this eco-unfriendly situation; no matter where the origin of that waste is, there are many attempts to recover and reuse heat potential in the waste as much as possible. A number of methods have been proposed and applied. One of them is an application of a heat exchanger with closed-loop pulsating heat pipes as a heat transfer medium from higher temperature substance to the lower one by means of the phase change mechanism, two-phase flow of a slug-train, and the replacement mechanism between volume of expanding and collapsing vapor in the evaporator and condenser section, respectively (Soponpongpipat et al, 2009). A closed-loop pulsating heat pipe (CLPHP) was firstly introduced by Akachi et al. (1996). It is a bundle of an air-evacuated undulating capillary tube of which an internal diameter does not exceed the critical value, following the Maezawa's

criterion (Maezawa et al., 1995), and is partially filled with working fluid. Since the heat transfers through a CLPHP by the phase change of working fluid, a CLPHP has higher thermal conductivity compared with other ordinary heat exchangers. The distinctive point, that leads the CLPHP to be different from other conventional heat pipe, is the ability to transfer the heat in any orientations although the evaporator section is located higher than the condenser section, which is called "top heat mode" (THM), without the internal wick structure as in that of the conventional heat pipe (Dobson and Graf, 2003).

In general applications, a single CLPHP is frequently used to be the heat transfer medium between one heat source and one heat sink or "one-to-one CLPHP" namely. Design and fabrication of such heat pipe does not accompany with difficulty since a lot of useful information and knowledge for the design have been discovered and obtained from the studies on effects of various parameters on thermal characteristics of a CLPHP in a past decade; for example, the studies on effect of total

lengths, internal diameters, working fluids, and number of turns (Charoensawan et al., 2003; 2008). Nevertheless, in a case of more than one heat source, especially none of identical heat rate; such as an industrial steam system where waste heat from a number of steam users is recovered and recirculated to preheat feed water before supplying to a boiler, if one-to-one CLPHPs; i.e. one CLPHP with one heat source (steamer user) and all CLPHPs release heat to the same heat sink (feed water tank), are installed, this configuration causes the heat exchanger to be geometrically larger and the manufacturing cost to increase. Thus, the most suitable method to breakthrough these problems is the design and manufacturing of CLPHP which can simultaneously receive the heat from multiple heat sources, or this is named as “a closed-loop pulsating heat pipe with multiple heat sources” (CLPHP w/MHS) as shown in Figure 1. Although there is a recent study on a vertical CLPHP w/MHS; which was found that the most suitable heat source arrangement is achieved when heat sources are placed in consecutive order from the lowest to the highest heat flux, beginning from the inlet of the evaporator section (Kammuang-lue et al., 2011), the study of a horizontal CLPHP w/MHS is still limited. To extend the knowledge how to design a CLPHP w/MHS, this experimental study has been thoroughly conducted with the main objective of determining the effect of heat source arrangements on thermal performance of a horizontal CLPHP w/MHS by permuting a position of the heat sources, which are different in heat quantity, within unduplicated patterns.

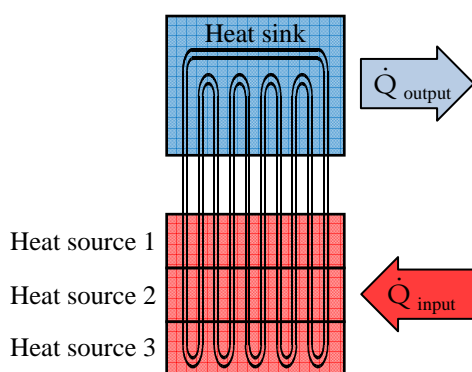


Figure 1. CLPHP with multiple heat sources

2. EXPERIMENTAL SETUP AND PROCEDURE

The CLPHPs used in the experiment were made of long copper capillary tubes with inner diameters (D_i) of 1.06, 1.50, and 2.03 mm and bent into 32

turns (N) (the number of meandering turns in this study was counted from the evaporator section). Then, both ends were connected together to form a loop. The evaporator (L_e), adiabatic (L_a), and condenser (L_c) section length was equal to 150 mm. R123, and ethanol were selected as the working fluids. The filling ratio was 50% by total volume. There were three heat sources installed along a longitudinal axis of the evaporator section. Each heat source generated the heat by using 2 electrical plate heaters (400 W, 220 VAC) with sizing of 25 mm width x 340 mm length x 3.5 mm thickness. The heaters were attached with copper bus bars, which were machined to have semi-circular grooves to fit with the outer wall of the tubes. Thermal grease was fully filled in the gap between the heaters, copper bus bars, and tubes to ensure the perfect thermal contacts. The CLPHP w/MHS was installed into a test rig and adjusted to be oriented in horizontal plane. Input heat flux of each heat source could be independently controlled by using three power controllers (Shimax, MAC3D, accuracy $\pm 0.25\%$ full scale) and simultaneously monitored for a validation of the heat flux quantity by using the watt meters (Axe, MMP, accuracy $\pm 0.25\%$ FS). Each heat source was defined to alternately change within three different input heat fluxes as of 1, 3, and 5 kW/m^2 . Therefore, the heat source arrangement could be permuted into 6 unduplicated sets. The number of each set was defined and shown in Table 1.

All of the condenser section was placed in a zinc cooling jacket with an inlet and outlet tubes. The cooling medium was a solution of water and ethylene glycol with 1:1 volume ratio. It was circulated to transfer heat from the condenser section to the heat sink, which was the cold bath (Bitzer, D7032, accuracy ± 1 °C). The temperature and flow rate of the cooling medium were directly controlled by this cold bath. The mass flow rate could be obtained after the cooling medium, which flowed in a specified time, was weighed by the digital scale (Ohaus, Adventurer, accuracy ± 0.01 g) and simultaneously counted for the time by the high precision stopwatch (Casio, HS70W-1D, accuracy ± 0.001 s). All sections including cooling medium hoses were well insulated by using a thermal-insulated sheet (Aeroflex, 3/8 in. thickness). At specified points, the temperature was monitored by a data logger (Brainchild, VR18, accuracy ± 0.1 °C). Fourteen Chromel–Alumel thermocouples (Omega, Type K, accuracy ± 0.5 °C) were installed on the outer surface of the capillary tube to measure the variations in

temperature at every part of the CLPHP. They consisted of 6 points on the middle of each tube in the evaporator section, 4 points in the adiabatic section, and 4 points in the condenser section. Two thermocouples were also placed on each inlet and outlet tube of the cooling jacket to measure the variations of the cooling medium temperature. The CLPHP w/MHS and the experimental setup were schematically shown in Figure 2.

Table 1. Heat source arrangements

Heater position	Input heat flux of each heat source (kW/m ²)					
	Set 1	Set 2	Set 3	Set 4	Set 5	Set 6
Upper	1	1	3	3	5	5
Middle	3	5	1	5	1	3
Lower	5	3	5	1	3	1

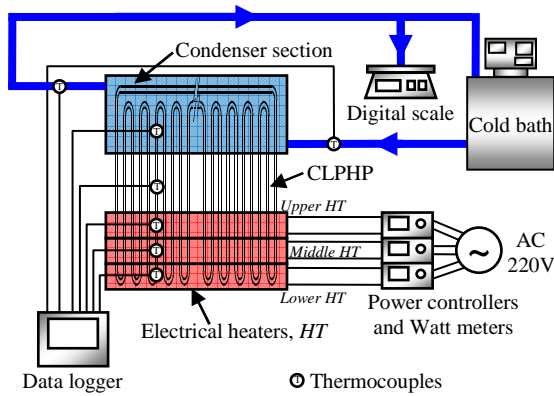


Figure 2. Experimental setup

The experiment procedure was as follows: The power controllers were started and input heat flux of each heat source was adjusted following the Set 1 in Table 1. The adiabatic temperature was controlled at 50 ± 3 °C, as this was a suitable working temperature and did not exceed the critical point of all the chosen working fluids. This was achieved by adjusting either the temperature or the flow rate of the cooling medium. When the system reached steady state, the temperature at each point in the evaporator, adiabatic, and condenser section was recorded while the variation of the inlet and outlet temperature and the mass flow rate of the cooling medium were simultaneously measured in order to calculate the heat flux at specified times by means of Equation (1). The advantage of this way of measuring is that the actual throughput heat along the CLPHP could be obtained. The experiment for the Set 1 was completely done after the test was repeatedly conducted for 5 times. The whole procedure from the beginning was conducted again by changing the input heat flux of each heat source until all set

as shown in Table 1 were successfully investigated.

$$\dot{q} = \frac{\dot{m}_c c_{pc} (T_{out} - T_{in})_c}{A_c} \quad (1)$$

when \dot{m}_c is the mass flow rate of the cooling medium

c_{pc} is the specific heat of the cooling medium

$(T_{out} - T_{in})_c$ is the difference in temperature of the cooling medium

A_c is the inner surface area of the tube in the condenser section.

After calculating the heat flux, the data were compared with the measurement error of the calculated heat flux. Only the data of which the error is less than 50% could be analyzed in the next step and subsequently brought into an account to determine “thermal resistance per unit area” (z). Since this is the first study on the horizontal CLPHP w/MHS, in order to easily understand the obtained results, the thermal resistance per unit area in this study is defined as “thermal resistance per unit area between the whole evaporator and condenser section” which can be calculated from Equation (2).

$$z = \frac{T_{e,avg} - T_c}{\dot{q}} \quad (2)$$

3. RESULTS AND DISCUSSIONS

3.1 Effect of heat source arrangements on heat flux

It was found from the study on effect of heat source arrangements on heat flux that, although heat sources were permuted to cover all 6 sets of arrangements, the heat fluxes at the condenser section, actually the heat throughputs of the CLPHP, were nearly the same. This is because the total heat input in each heat source arrangement is always the same as 9 kW/m², thus all heat source arrangements do not affect the heat flux. From this point, the heat flux cannot be directly used as the quantitative index to represent the thermal performance of the CLPHP w/MHS. Although the heat flux of every set was nearly the same and the adiabatic temperature was defined to be the same as 50 ± 3 °C in every tests to ensure that the CLPHP w/MHS operated with identical working

temperatures or in the same state, the difference in temperature between evaporator and condenser section was not necessarily identical. From this point, the ratio between this temperature difference and the heat flux per inner surface area of the tube, which is well known as “thermal resistance per unit area”, would be significantly different. This value is considerably chosen to be the quantitative index used in the analysis for the suitable heat source arrangement as discussed in the following topic.

3.2 Effect of heat source arrangements on thermal resistance

It was found from the study of the effect of heat sources arrangements on thermal resistance that when the heat source arrangement was consecutively changed from Set 1 to 6, the thermal resistance per unit area decreased as shown in Figure 3. In a case of the 1.50-mm CLPHP, when the heat source arrangement changed from Set 1 to 6, the thermal resistance per unit area tended to decrease from 14.3 to 17.4, 13.4, 16.0, 9.4, and 8.7 $\text{m}^2\text{-K/kW}$, respectively for R123 and obviously decreased from 33.5 to 30.4, 25.1, 19.0, 17.9, and 13.3 $\text{m}^2\text{-K/kW}$, respectively for ethanol. For the CLPHP with the internal diameter as of 2.03 mm, when the heat source arrangement changed from Set 1 to 6, the thermal resistance per unit area tended to decrease from 20.7 to 14.7, 16.5, 11.8, 10.3, and 9.2 $\text{m}^2\text{-K/kW}$, respectively for R123 and dramatically decreased from 39.4 to 32.0, 27.3, 15.3, 15.6, and 15.3 $\text{m}^2\text{-K/kW}$, respectively for ethanol.

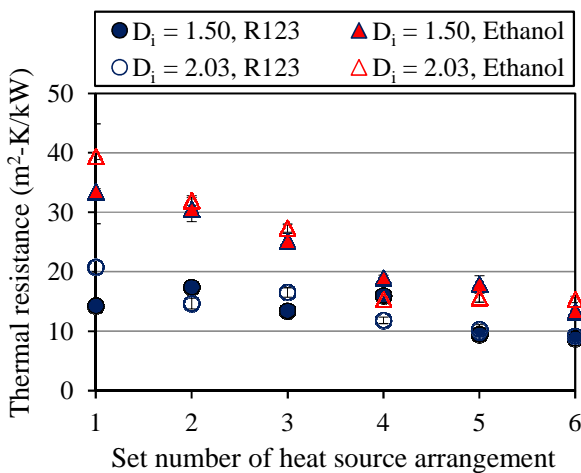


Figure 3. Effect of heat source arrangements on thermal resistance per unit area

It could be seen from the experiments that the CLPHP with the heat source arrangement in Set 1, in which the heat source with the highest input heat flux was located at the farthest end of the heat pipe, had the highest thermal resistance per unit area, in turn, this arrangement caused the CLPHP w/MHS to have the lowest thermal performance comparatively with other sets. When the heat source arrangement was orderly permuted from Set 2 to 3, 4, 5, and 6, or this was implied that the heat sources with higher input heat flux tended to be placed closer to the condenser section respectively, the thermal performance continually increased until it reached the highest value in Set 6, in which the heat source with the highest input heat flux was located close to the adiabatic section. Therefore, the most suitable heat source arrangement is Set 6, in which heat sources are placed in consecutive order from the highest to the lowest heat flux, beginning from the inlet of the evaporator section.

The reason why the horizontal CLPHP w/MHS with the heat source arrangement in Set 6 has the highest thermal performance could be discussed after working fluid’s flow phenomena inside the basically horizontal CLPHP obtained from the past visual study (Kammuang-lue et al., 2008) have been considered. It was found from the CLPHP at normal operating state that the working fluid flowed in pulsating motion and flow direction changed all the time. Intermision-stop of circulation was not observed. Condensate flowing from the condenser section, thus, could continuously flow into the evaporator section. This caused the liquid working fluid to cover entire heating surface all the time. From this point heat input could normally transfer through the CLPHP, and evaporator section temperature maintained within normal level. However, when the horizontal CLPHP operated in the just-before critical state, although main flow pattern was the same as that of the CLPHP with normal operation, intermission-stops could be more often observed as the evaporator section temperature increased. These intermission-stops could sometimes be observed when the working fluid vaporized covering the heating surface of each meandering turn. When the evaporator section was fully occupied by vapor, the liquid condensate from the condenser section could not flow to the evaporator section to receive heat. The circulation stopped until the collapsing volume of the vapor plug in the condenser section was sufficient and the vapor in the evaporator section could subsequently flow to replace the collapsing vapor, by means of the replacement

mechanism of the working fluid circulation. After that, the vapor moved out of the evaporator section, and the liquid condensate could flow into the evaporator section to receive heat as usual. It could be concluded that when intermission-stop occurs, the liquid condensate in the evaporator section is insufficient, this causes the evaporator section temperature to increase.

Past qualitative study mentioned above was considered in conjunction with the quantitative results due to various sets of heat source arrangement. As mentioned, the heat source arrangement in Set 6 has the highest heat source placed closest to the condenser section among other sets, i.e. the highest heat source was placed at an inlet of the evaporator. Therefore, when the condensate returned from the condenser section began to flow into the evaporator section, after it contacted with high heat flux, condensate suddenly evaporated into a vapor plug and it consequently expanded violently, simultaneously with the changing of working fluid's flow direction, to flow back to the condenser section. This caused the working fluid to circulate in a pulsating motion with no intermission-stop. This also corresponds with the past study when the horizontal CLPHP operated in the normal operating state (Kammuang-lue et al., 2008). According to these phenomena, heat could be continuously transferred away from the evaporator section. Possibility of the critical state to occur was absent. The evaporator section temperature, thus, was low and the lowest thermal resistance or the highest thermal performance was subsequently obtained. When the highest heat source was placed further from the inlet to the middle of the evaporator section, e.g. in a case of the heat source arrangement in Set 4, the condensate from the condenser section tended to flow into the evaporator section deeper. Due to an increase in distance of liquid's flow in the evaporator section, the liquid continuously evaporated until its quantity was low. The intermission-stop intermittently occurred; however, it was not obvious. This caused the evaporator section temperature to increase in some parts. Finally, when the lowest heat source was located at the inlet of the evaporator section as in a case of the Set 1, the liquid could flow into the evaporator section with the deepest distance. The liquid continuously evaporated until the end of the evaporator section was covered with vapor on the entire cross sectional area of a tube. This vigorous vapor plug obstructed the working fluid's flow and consequently the intermission-stop obviously

occurred. According to the intermission-stop, the working fluid's circulation had to wait until collapsing volume of vapor plugs in the condenser section was enough to continue the replacement mechanism and then the working fluid could flow again. This was agreed with the past study on the horizontal CLPHP at just-before critical state (Kammuang-lue et al., 2008). Therefore, the heat transferred intermittently, the evaporator section temperature increased, and the critical state could be observed occasionally. This caused an appearance of the highest thermal resistance or the lowest thermal performance.

Although this is a quantitative study, evidences that confirm inside flow patterns between pulsating motion with and without intermission-stop can be shown, since thermocouples in every part were attached in parallel position between adjacent tubes in the same meandering turn in this study. Therefore, T_{a1} and T_{a2} were the adiabatic temperature in left and right tube in a certain meandering turn as well as T_{a3} and T_{a4} , for another turn. Figure 4 is shown the adiabatic section temperature's variations during the steady state of a CLPHP w/MHS with internal diameter of 2.03 mm, and ethanol. It could be seen for Set 1 heat source arrangement that the left and right tubes in the same meandering turn alternated to present higher adiabatic section temperature, only one time. Since the higher temperature represents a vapor plug flowing over a certain position in the adiabatic section, and vice versa for a liquid slug, it could be implied that the working fluid also changed its flow direction one time during this 100-s steady state. The intermission-stop could be also observed with long duration of about 70 s. In a case of Set 4, the higher and lower temperature altered between the left and right tubes more frequently. In addition, the temperature difference between left and right tubes was lower than that of the first case. This showed that a changing in working fluid's flow direction could occur more continuously. Finally, it was found for the Set 6 heat source arrangement that the higher and lower temperature altered between the left and right tubes all the time. This could be deduced that the working fluid flowed in absolutely pulsating motion, changing its direction all the time, without the intermission-stop. In the mean time, average temperature between left and right tubes was almost identical. These are all important evidences to support that, when heat source are arranged in Set 6, working fluid flows in pulsating motion and changes its direction all the time without the

intermission-stop. Therefore, the highest thermal performance is consequently obtained.

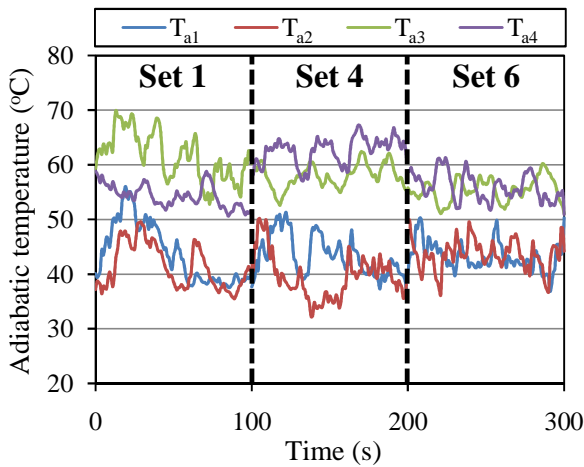


Figure 4. Variation of adiabatic temperatures depending on heat source arrangements

4. CONCLUSION

The suitable heat source arrangement and the effect of heat source arrangements on the thermal resistance per unit area of a horizontal CLPHP w/MHS have been thoroughly investigated in this study. It can be concluded that, the most suitable heat source arrangement is achieved when heat sources are placed in consecutive order from the highest to the lowest heat flux, beginning from the inlet of the evaporator section and this causes the CLPHP w/MHS to have the lowest thermal resistance per unit area or the highest thermal performance because the working fluid circulates in pulsating motion, changing its direction all the time. For this configuration, the intermission-stop is not observed. The heat, thus, transfers continuously.

NOMENCLATURE

D_i	internal diameter, mm
HT	electrical heater
L_e	evaporator section length, mm
N	number of meandering turn, turns
\dot{q}	heat flux, kW/m ²
\dot{Q}	heat transfer rate, kW
T_a	adiabatic section temperature, °C
T_c	condenser section temperature, °C
$T_{e,avg}$	average evaporator section temperature, °C
z	thermal resistance per unit area, m ² -K/kW

ACKNOWLEDGEMENT

This study was supported and cooperated by Thailand Research Fund (TRF), Office of the Higher Education Commission, Chiang Mai University, and Department of Mechanical Engineering, Faculty of Engineering, Chiang Mai University (contract no. MRG5380213). The authors would like to express their sincere appreciation for all of the support provided.

REFERENCES

- Akachi, H., Polasek, F., and Stulc, P. (1996) Pulsating heat pipes. Proc. of the 5th International Heat Pipe Symposium, Melbourne, Australia, pp. 208-217.
- Charoensawan, P., Khandekar, S., Groll, M., and Terdtoon, P. (2003) *Closed loop pulsating heat pipes - part A: Parametric experimental investigations*. Applied Thermal Engineering, 23(16), pp. 2009-2020.
- Charoensawan, P. and Terdtoon, P. (2008) *Thermal performance of horizontal closed-loop oscillating heat pipes*. Applied Thermal Engineering, 28(5-6), pp. 460-466.
- Dobson, R. T. and Graf, G. (2003) Thermal characterisation of an ammonia-charged pulsating heat pipe. Proc. of the 7th International Heat Pipe Symposium, Jeju, Korea, pp. 325-330.
- Kammuang-lue, N., Sakulchangsattajai, P., and Terdtoon, P. (2008) Effect of numbers of turns and internal diameters on internal flow pattern of a horizontal closed-loop pulsating heat pipe at maximum heat flux state. Proc. of the 9th International Heat Pipe Symposium, Kuala Lumpur, Malaysia, pp. 159-165.
- Kammuang-lue, N., Sakulchangsattajai, P., and Terdtoon, P. (2011) Multiple heat source arrangements of a vertical closed-loop pulsating heat pipe. Proc. of the 10th International Heat Pipe Symposium, New Taipei City, Taiwan, pp. 184-189.
- Maezawa, S., Gi, K. Y., Minamisawa, A., and Akachi, H., (1995) Thermal performance of capillary tube thermosyphon. Proc. of the 9th International Heat Pipe Conference, Albuquerque, USA, pp. 791-795.
- Soponpongpiat, N., Sakulchangsattajai, P., Kammuang-lue, N., and Terdtoon, P. (2009) *Investigation of the startup condition of a closed loop oscillating heat pipe*. Heat Transfer Engineering, 30(8), pp. 626-642.

Thermally induced two-phase oscillating flow in a capillary tube: theoretical and experimental investigations

Manoj Rao, Frédéric Lefèvre*, Jocelyn Bonjour

Centre de Thermique de Lyon, UMR 5008 CNRS-INSA-UCB
INSA, 20 av. A. Einstein, 69621 Villeurbanne Cedex – France

Tel.: +33 4 7243 8251; fax: +33 4 7243 8811.

E-mail address: frederic.lefevre@insa-lyon.fr (F. Lefèvre)

Sameer Khandekar

Department of Mechanical Engineering,
Indian Institute of Technology Kanpur, Kanpur (UP) 208016 India

ABSTRACT

This paper deals with thermally-induced oscillations of a meniscus in a two-phase system consisting of a liquid plug and a vapor bubble in a capillary tube of circular cross-section. This system represents the simplest version of a pulsating heat pipe (PHP). An experimental setup, made as entirely transparent to enable the observation of the meniscus oscillations, has been used to visualize the oscillations. The results are compared to a mathematical model based on the balance equations. In the model, the evaporation of a thin film left by the meniscus when it leaves the evaporator is taken into account. The presence and the evaporation of this thin film have been observed experimentally. Results from the proposed model show a good agreement with the experiment.

KEY WORDS: pulsating heat pipe, oscillating flow, thin film

1. INTRODUCTION

Research on Pulsating Heat Pipes (PHP) has received substantial attention in the recent past, due to its unique operating characteristics and potential applications in many passive heat transport situations (Zhang & Faghri 2008; Khandekar et al. 2010). A PHP is a capillary tube (with no wick structure) bent into many turns and partially filled with a working fluid. When the temperature difference between the heat source and the heat sink exceeds a certain threshold, the gas bubbles and liquid plugs begin to oscillate back and forth. The heat is thus transferred not only by the latent heat exchange like in other types of heat pipes, but also by sensible heat transfer between the wall and the fluid.

Compared to other cooling solutions, PHPs are simple and thus more reliable and cheap. However, there is no theoretical model or correlation that would predict the PHP behavior and heat exchange at present. This prevents the PHPs from being used industrially. Reliable design tools can only be formulated if the nuances of its operating principles are well understood; at present, this is rather insufficient for establishing comprehensive models.

In this context several authors have focused their efforts on the simplest pulsating heat pipe consisting of one liquid plug and one vapor bubble. Mathematical model based on the balance equations were developed for this simple system (Zhang & Faghri 2002; Dobson 2005). The vapor-phase was considered as an ideal gas. The pressure fluctuations inside the system was introduced by modeling the evaporation of a thin liquid film left on the wall when the liquid plug leaves the evaporator.

Recently (Das et al. 2010) presented the first experimental results of such a system consisting in a 2.0 mm ID capillary tube, heated at one end and cooled at the other end. They were able to obtain oscillations in this system in a definite range of experimental conditions. Vapour pressure was recorded. The oscillation of the liquid slug was observed but only in the condenser section. A satisfactory quantitative agreement was found between these experimental data and the results of an improved version of the mathematical models previously described. Nevertheless improvements were needed to increase the quality of the experimental results.

This paper presents experimental data obtained with an improved version of this bench. The objective of this new bench is to increase the understanding of the basic phenomena involved in thermally-induced two-phase oscillatory flows. Compared to the previous set-up (Das et al. 2010), the new design of the experimental bench is entirely transparent in order to observe the liquid film dynamics in the condenser but also in the evaporator, while the evaporator, made of copper, was opaque in the previous experiment. Furthermore, the tube is in vertical position, while it was in horizontal position in the previous experiment. Finally, the set-up has been improved in order to remove the singularities between the tube and the reservoir. Thus, the inner surface of the capillary tube is perfectly smooth and in a straight line from the evaporator to the reservoir.

Some preliminary experimental results are presented for Pentane as working fluid. The results are compared to a mathematical model.

2. EXPERIMENTAL SET-UP

The experimental set-up is presented in Figure 1. It is an improved version of a previous experiment presented by Das et al. (2010). It consists of a very basic PHP with one liquid plug and one vapor bubble in a vertical capillary tube of circular cross-section. The transparent capillary tube, made of glass, is closed at one side and connected to a reservoir maintained at a constant pressure at the other side. Its inner diameter is 2 mm. The liquid plug oscillates between a heat source (evaporator section length = 20 cm) located near the closed side and a heat sink (condenser section length = 20 cm) located near the reservoir. In between, an adiabatic section separates the condenser and the evaporator (length = 1 cm). The evaporator and the condenser are transparent heat exchangers, whose temperature is controlled by means of two thermostatic baths. A third thermostatic bath is used to control the temperature of the reservoir, and thus its pressure.

The two-phase oscillatory flow is characterized by vapour pressure measurements as well as meniscus displacement measurements. An absolute pressure sensor (supplied by M/s KISTLER®, piezo-resistive sensor type 4005B, operating range of 0-5 bar) is located at the closed end of the tube and a high speed camera (Fastcam-1024 PCI, 3000 frames/s) is used to record the meniscus displacement. Another tube which comes out of the

evaporator end is connected to a evacuated reservoir vacuum, with an isolation valve in between. This tube connected with the vacuum reservoir serves two purposes. It helps to remove any non-condensable gases present in the capillary tube before charging the device. Second, it helps control the position of the liquid-vapor meniscus in the beginning of the experiment.

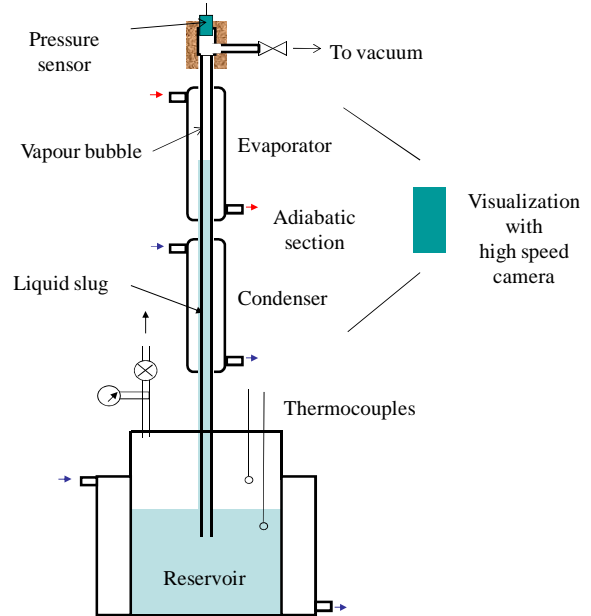


Figure 1: Experimental set-up.

Before the experiments, the system is completely evacuated to remove any non-condensable gases. The reservoir is then filled with the working fluid (Pentane).

3. EQUATIONS OF THE MODEL

This section presents the modeling of the system consisting of a vapor plug and a liquid slug oscillating in a tube closed at one end and connected to a reservoir at a constant pressure P_r at the other end (Figure 2). The equations of the model were already presented in Das et al. (2010). Some modifications are introduced in this paper to take into account the peculiarities of the new experimental set-up.

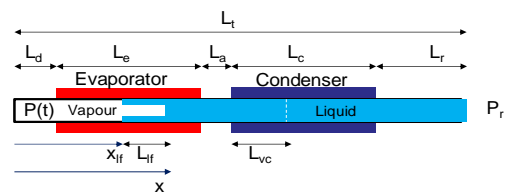


Figure 2: Geometrical properties considered in the model.

The liquid plug confines a vapour bubble at the closed end of a cylindrical tube of diameter d and cross-section area $S = \pi d^2/4$. The x axis reference is located at the closed end of the tube. The length of the tube is L_t . A dead volume is introduced in the model to take into account the volume of vapour trapped between the evaporator and the end of the tube. This dead volume is due to the presence of the pressure sensor and the connection to the vacuum reservoir. It is modeled by an equivalent length L_d . The evaporator length is L_e and the evaporator tube wall is maintained at a constant temperature T_e . The condenser length is L_c and the condenser tube wall is maintained at a constant temperature T_c . The condenser and the evaporator are separated by an adiabatic length L_a . A part L_r of capillary tube extends beyond the condenser until the reservoir at a constant pressure P_r . The pressure of the vapor bubble inside the tube P is a function of time.

When the liquid plug leaves the evaporator, a small liquid film is left on the wall. This film is responsible for a huge amount of evaporation. The thickness δ_{lf} of this film is supposed to be constant but its length L_{lf} is not constant due to evaporation or rewetting of the liquid slug, when it enters into the evaporator. The location of this film inside the evaporator is x_{lf} .

When the liquid slug is pushed into the condenser, a part of the condenser wall of length L_{vc} is in contact with the vapour and condensation occurs.

The steady state model is based on the balance equations. The momentum balance equation for the liquid slug inside the tube is written as:

$$\frac{d(m_l u)}{dt} = (F_p + m_l g \pm F_\tau) \quad (1)$$

where m_l is the mass of liquid inside the tube, which is easily derived from geometrical dimensions and the density of the liquid ρ . F_p is the difference of pressure acting on the liquid slug $F_p = S(P - P_r)$, u the velocity of the liquid plug, g the gravity and F_τ the sum of regular and singular friction forces acting on the liquid slug:

$$F_\tau = \frac{1}{2} C_f d \rho \pi (L_t - x) u^2 + \frac{1}{2} S \rho u^2 \quad (2)$$

The first term of the equation is related to the regular pressure drop while the second one stands

for the singular pressure drop due to the contraction or the enlargement at the end of the tube. The friction coefficient C_f depends on the Reynolds number Re :

$$C_f = \begin{cases} 0 & Re = 0 \\ 16 & \text{if } Re < 1 \\ \frac{16}{Re} & \text{if } 1 < Re < 1180 \\ 0.078 Re^{-0.25} & \text{if } Re \geq 1180 \end{cases} \quad (3)$$

The velocity can be related to the location $x(t)$ of the meniscus:

$$u = \frac{dx}{dt} \quad (4)$$

The length of the liquid film L_{lf} is defined only in the evaporator section since no evaporation is supposed to occur in the adiabatic section. It is expressed by considering the mass balance equation:

$$\frac{dL_{lf}}{dt} = \begin{cases} 0 & \text{if } L_{lf} = 0 \text{ and } u < 0 \\ -\frac{1}{\rho \pi d \delta_{lf}} \dot{m}_e & \text{if } x > L_e \\ u - \frac{1}{\rho \pi d \delta_{lf}} \dot{m}_e & \text{otherwise} \end{cases} \quad (5)$$

The flow rate of evaporation is:

$$\dot{m}_e = \frac{h_e \pi d L_{lf}}{h_{lv}} (T_e - T_{sat}(P)) \quad (6)$$

where h_e is the evaporation coefficient.

A fourth equation is obtained by considering the mass balance equation for the vapour:

$$\frac{dm_v}{dt} = \dot{m}_v = (\dot{m}_e - \dot{m}_c) \quad (7)$$

where the flow rate of condensation is:

$$\dot{m}_c = \frac{h_c \pi d L_c}{h_{lv}} (T_{sat}(P) - T_c) \quad (8)$$

The last equation is the energy balance equation for the volume of vapour:

$$\frac{dT}{dt} = \frac{1}{m_v C_{vv}} (\dot{m}_v R_v T + q_{\text{sens}} - P S u) \quad (9)$$

where P and T are respectively the vapor pressure and the vapor temperature. R_v is the vapor gas constant and C_{vv} the vapor specific heat at constant volume. The sensible heat flux q_{sens} is given by:

$$q_{\text{sens}} = h_{\text{sens}} (T_e - T) \quad (10)$$

where h_{sens} is the sensible heat transfer coefficient. The vapor is defined by the equation of state which is assumed to be that of ideal gas:

$$P = \frac{m_v R_v T}{S x} \quad (11)$$

Equations 1, 4, 5, 7 and 9 form a set of five coupled differential equations with five unknowns x , u , L_{lf} , m_v and T . These equations are solved using a fourth-order Runge-Kutta method. More details on the resolution process can be found in Das et al. (2010).

4. COMPARISON OF THE MODEL WITH THE EXPERIMENTAL DATA

Preliminary experimental data obtained with pentane as working fluid are presented in this part and compared to the mathematical model. The temperature of the reservoir is equal to 12 °C. The related saturation pressure is equal to 0.42 bars. The temperature of the condenser is constant and equal to -11.5 °C. Figure 3 presents the pressure variations for two different evaporator temperature ($T_e = 21$ °C and $T_e = 26$ °C) during a period of 10 s. For evaporator temperatures lower than 21 °C, it was not possible to sustain the oscillations. Above a temperature of 26 °C, the oscillations were somewhat chaotic due to nucleation inside the liquid plug at the evaporator.

Figure 4 presents the location of the meniscus versus time in the same experimental conditions. It has to be noted that for this preliminary experiment the pressure transducer and the high speed camera are not synchronized. Thus, the results of Figure 3 can only be qualitatively compared to results of Figure 4. Figure 5 focuses on one period of both the pressure oscillations and location of the meniscus.

The oscillation shape is periodic but not sinusoidal. The frequency is close to 2 Hz for both evaporator temperatures. The repetitive period is made of two

oscillations: one small for which the meniscus does not enter into the evaporator and one large where the meniscus enters into the evaporator.

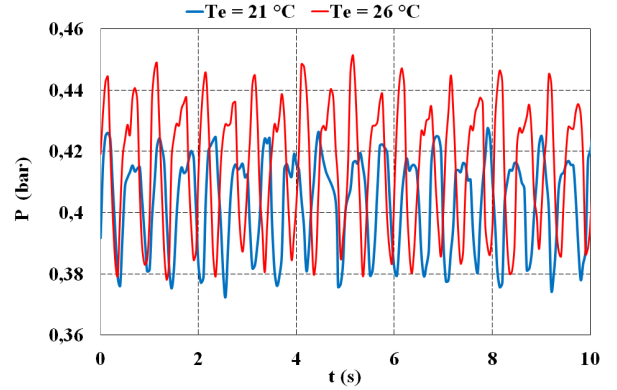


Figure 3: Experimental pressure variation
 $T_c = -11.5$ °C and $T_r = 12$ °C

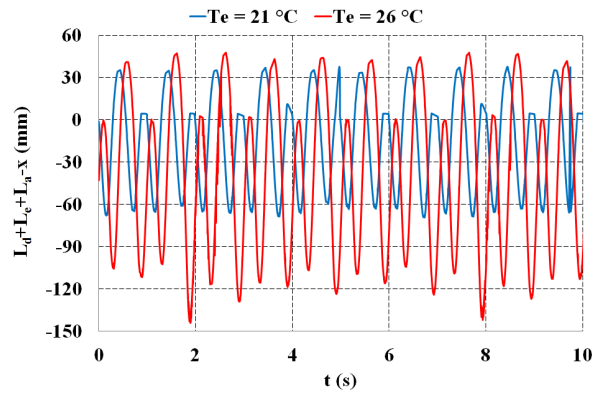


Figure 4: Experimental location of meniscus
 $T_c = -11.5$ °C and $T_r = 12$ °C

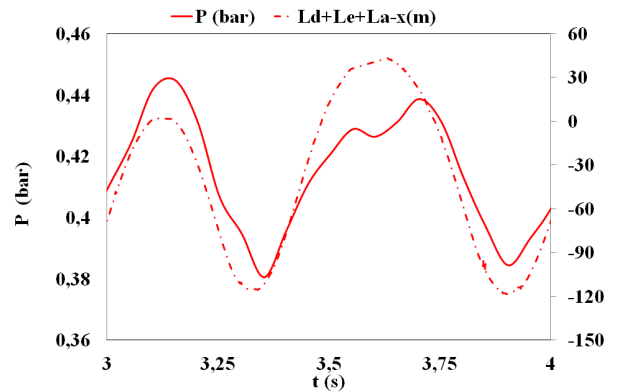


Figure 5: Experimental pressure and location of the meniscus during one period; $T_e = 26$ °C

The maximum pressure amplitude is equal to 0.07 (peak to peak) bars for $T_e = 26$ °C and 0.05 (peak to peak) bars for $T_e = 21$ °C. When the meniscus enters the evaporator, we observe a small discontinuity in the pressure increase. At the same time, the meniscus location is at its maximum depth into the evaporator. Then the pressure

increases again while the meniscus begins to leave the evaporator. This behavior can be explained by modifications in the evaporation of the thin film. When the meniscus is deep inside the evaporator the length of the thin film is equal to zero, evaporation stops and thus the pressure variation is smooth. On the contrary, when the meniscus leaves the evaporator, a thin film is left, which creates a huge amount of evaporation and is responsible for the pressure increase.

The evaporator temperature has a huge influence on the oscillation amplitude. The meniscus location at maximum amplitude is nearly equal to 20 cm for $T_e = 26\text{ }^\circ\text{C}$ and almost 10 cm for $T_e = 21\text{ }^\circ\text{C}$. It is important to note that this set-up enables to observe the thin film and its evaporation, which is an important point, since the evaporation of this film is the bases of the mathematical model. Since the evaporator was opaque in the previous experimental set-up (Das et al. 2010), this observation was not possible.

Figure 6 to Figure 8 presents the results of the mathematical model in the same thermal and geometrical conditions as the experimental set-up. The length of the dead volume L_d is estimated to 30 cm. This length is relatively important compared to evaporator length, which is due to the presence of the pressure transducer and the valve connected to the vacuum reservoir. The length L_r is equal to 24 cm. In the purpose of comparison with the experimental data some unknown parameters have to be estimated to fit at best the experimental data. The thickness of the liquid film is equal to 15 μm , the evaporator and condenser heat transfer coefficients are equal to 600 $\text{W}/\text{m}^2\cdot\text{K}$ and 200 $\text{W}/\text{m}^2\cdot\text{K}$ respectively. The sensible heat transfer coefficient in the evaporator is equal to 30 $\text{W}/\text{m}^2\cdot\text{K}$. All the parameters are the same for both experimental data except the temperature of the evaporator ($T_e = 21\text{ }^\circ\text{C}$ and $T_e = 26\text{ }^\circ\text{C}$).

The results show that the mathematical model is able to reproduce the physical behavior observed experimentally. This is mostly true for the repetitive period, which is made of one small oscillation followed by a large one, for which the pressure variation shape is very similar to the one observed experimentally.

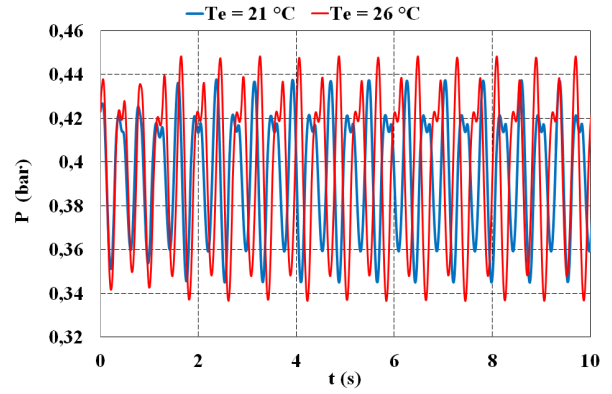


Figure 6: Numerical pressure variation
 $T_c = -11.5\text{ }^\circ\text{C}$ and $T_r = 12\text{ }^\circ\text{C}$

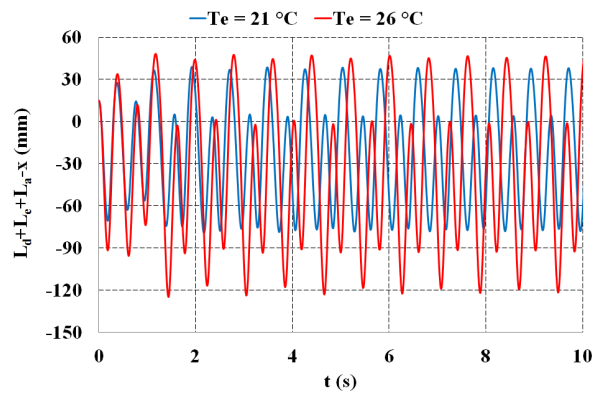


Figure 7: Numerical location of meniscus
 $T_c = -11.5\text{ }^\circ\text{C}$ and $T_r = 12\text{ }^\circ\text{C}$

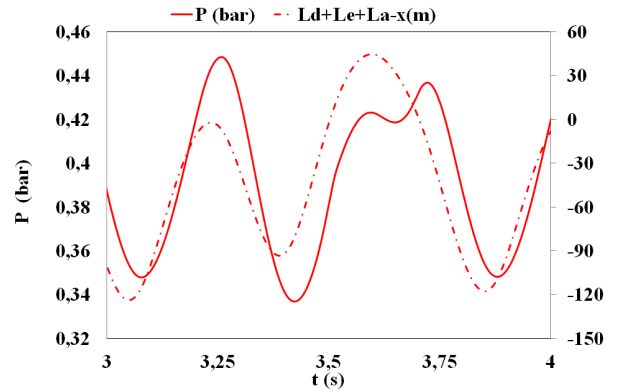


Figure 8: Numerical pressure and location of the meniscus during one period; $T_e = 26\text{ }^\circ\text{C}$

The main discrepancies are observed in the pressure amplitude, which are equal to 0.11 bar and 0.09 bar for $T_e = 26\text{ }^\circ\text{C}$ and $T_e = 21\text{ }^\circ\text{C}$, respectively. This is almost 40 % higher than that measured experimentally. Amplitude variations for both the pressure and the location of the meniscus are mostly controlled by the pressure drops inside the tube as well as the heat transfer coefficient of condensation and evaporation. Even if the sensible

heat transfer for the vapor has been introduced in the model, it is a second-order parameter.

The other discrepancy is the frequency, which is equal to 2.6 Hz numerically. The frequency of the oscillations is mainly due to the mass of vapor and liquid inside the tube. As an illustration, in the previous set-up (Das et al. 2010), the frequency was twice that observed in the present experiment, but the evaporator length and the dead volume were much smaller (~15 cm).

5. CONCLUSIONS AND PERSPECTIVES

These preliminary results are very promising. Some important parameters have still to be estimated to fit with the experimental data. At the moment, we are able to observe the presence and the evaporation of the thin liquid film, but it would be necessary to measure its thickness. Confocal microscopy could be used for that purpose, as it has already been used successfully to measure the meniscus curvature radius in the grooved capillary structure of a flat plate heat pipe but also the condensation film on the fins with thicknesses down to 2 μm (Lefèvre et al. 2010). The dead volume has to be reduced since it contributes to reduce the frequency of the oscillation and thus it is important to limit as much as possible its impact. One of the actual limitations of our approach is that the different heat transfer coefficients have also to be estimated. As their sensibility to the model is correlated to that of the pressure drops, it would be necessary to estimate accurately the pressure drops in such an oscillating device. It is planned to measure this pressure drops using the same set-up in adiabatic conditions, using a mechanical pressure oscillator. The temperature of both the evaporator and the condenser are supposed to be equal to the temperature imposed by each of the thermostatic bathes. However, heat conduction in the transparent wall is not taken into account in the equation, which could modify the numerical conditions. Finally, temperature measurement of the vapor would be important information, but this measurement is difficult due to the high frequency of the oscillations compared to the time response of the temperature sensor, and also radiative heat transfer between the wall and the sensor.

NOMENCLATURE

C_f	friction coefficient
C_v	specific heat at constant volume (J/kg.K)
d	tube diameter (m)
g	gravity (m/s^2)

h	heat transfer coefficient ($\text{W/m}^2\text{.K}$)
h_{lv}	latent heat of evaporation (J/kg)
L	Length (m)
m	mass (kg)
P	pressure (Pa)
q	heat flux (W/m^2)
Re	Reynolds number
R_v	vapour gas constant (J/kg.K)
S	tube section (m^2)
t	time (s)
T	temperature ($^{\circ}\text{C}$)
u	velocity (m.s^{-1})
x	location of the meniscus (m)
Greek letters	
δ	film thickness
μ	dynamic viscosity (Pa.s)
ρ	density (kg.m^{-3})
Subscripts	
a	adiabatic
e, c	evaporator, condenser
d	dead volume
f	film
l, v	liquid, vapour
r	reservoir
sat	saturation
sens	sensible
t	total

ACKNOWLEDGEMENT

Financial support from the Indo-French Centre for the Promotion of Advanced Research, New Delhi (Project #: 4408-1/2010), under the aegis of Indian Department of Science and Technology and the French Ministry of Foreign Affairs and from Bhabha Atomic Research Center, Department of Atomic Energy, Government of India, is gratefully acknowledged.

REFERENCES

- Das, S. et al., 2010. Thermally induced two-phase oscillating flow inside a capillary tube. *International Journal of Heat and Mass Transfer*, 53(19-20), p.3905–3913.
- Dobson, R.T., 2005. An open oscillatory heat pipe water pump. *Applied Thermal Engineering*, 25(4), p.603–621.
- Khandekar, S. et al., 2010. Local hydrodynamics of flow in a pulsating heat pipe: a review. *Frontiers in Heat Pipes*, 1.
- Lefèvre, F. et al., 2010. Confocal Microscopy for Capillary Film Measurements in a Flat Plate Heat Pipe. *Journal of Heat Transfer*, 132(3), p.031502.
- Zhang, Y. & Faghri, A., 2002. Heat transfer in a pulsating heat pipe with open end. *Int. J. Heat Mass Transfer*, 45, p.755–764.
- Zhang, Yuwen & Faghri, Amir, 2008. Advances and Unsolved Issues in Pulsating Heat Pipes. *Heat Transfer Engineering*, 29(1), p.20–44.

Intermediate Temperature Heat Pipe Life Tests

**William G. Anderson, Sanjida Tamanna,
Calin Tarau, and John R. Hartenstine**

Advanced Cooling Technologies, Inc.
1045 New Holland Ave., Lancaster, PA 17601 U.S.A.
717-295-6061, 717-295-6064 Fax, Bill.Anderson@1-act.com,
Sanjida.Tamanna@1-act.com, Calin.Tarau@1-act.com, John.Hartenstine@1-act.com

David Ellis

NASA Glenn Research Center
21000 Brookpark Road, Cleveland, OH 44135 U.S.A.
216-433-8736, 216-977-7132 Fax, David.L.Ellis@nasa.gov

ABSTRACT

There are a number of different applications that could use heat pipes or loop heat pipes (LHPs) in the intermediate temperature range of 450 to 750 K, including space nuclear power system radiators, fuel cells, geothermal power, waste heat recovery systems, and high temperature electronics cooling. Titanium/water and Monel/water heat pipes are suitable for temperatures up to 550 K, based on life tests that have been running for over 54,000 hours (6.1 years). At higher temperatures, organic or halide working fluids can be used. Long term life tests (currently 50,000 hours or 5.7 years) show that Titanium/TiBr₄ at 653 K, and Superalloys/AlBr₃ at 673 K are compatible. These results are confirmed by optical and electron microscopy, and working fluids analysis on heat pipes chosen for destructive examination.

KEY WORDS: Intermediate Temperature Heat Pipe Life Tests, Halide Life Tests, Water Life Tests

1. INTRODUCTION

There are a number of different applications that could use heat pipes or loop heat pipes (LHPs) in the intermediate temperature range of 450 to 750 K, including space nuclear power system radiators, fuel cells, geothermal power, waste heat recovery systems, and high temperature electronics cooling.

The intermediate temperature region is generally defined as the temperature range between 450 and 750 K. At temperatures above 700-725 K, alkali metal (cesium) heat pipes start to become effective. Below about 725 K, the vapor density for cesium is so low that the vapor sonic velocity limits the heat transfer. Historically, water was used at temperatures up to about 425 K. More recently, it has been shown that water can be used with titanium or Monel envelopes at temperatures up to 550 K (Anderson, Dussinger, Bonner, and Sarraf, 2006). A survey of previous life tests on intermediate temperature working fluids can be found in Anderson (2007) and Anderson et al. (2010).

2. EXPERIMENTAL PROCEDURE

Since 2004, we have been conducting life tests at temperatures up to 550 K with water and Commercially Pure Titanium Grade 2 (CP-Ti) Titanium, titanium alloys, Monel 400, and Monel K500 heat pipes. The test setup for the titanium/water and Monel/water life tests are discussed in Anderson et al. (2006). As of April 2012, several of the titanium and Monel heat pipes have been on test for over 54,000 hours (6.1 years). Periodically, the temperature is lowered to 343 K, and the pipes are tested for Non-Condensable Gas (NCG). A small amount of NCG has been noted in these pipes at 70°C, but the gas cannot be detected at the operating temperature of 550 K.

At temperatures above 550 K, the surface tension of water is so low, and the vapor pressure is so high, that water is no longer an attractive fluid. At higher temperatures, three sets of organic fluids stand out as good intermediate temperature fluids:

1. Diphenyl, Diphenyl Oxide, and Eutectic Diphenyl/Diphenyl Oxide (Dowtherm A, Therminol VP, Diphyl),

2. Naphthalene
3. Toluene.

Table 1. Heat Pipes Selected for Evaluation.

Heat Pipe	Envelope	Wick	Working Fluid	Life Test Hours
6	Hastelloy B-3	None	SnCl ₄	20,160
7	Hastelloy C-22	80 x 80 C22 Screen	SnCl ₄	20,160
8	Hastelloy C-2000	None	SnCl ₄	20,160
9	CP Ti	None	GaCl ₃	20,040
10	CP Ti	None	GaCl ₃	20,040
153	Hastelloy C-2000	None	TiCl ₄	28,560
157	Hastelloy C-22	80 x 80 C22 Screen	AlBr ₃	28,704
100	CP Ti	150x150 CP Ti Screen	Water	48,100
103	CP Ti	150x150 CP Ti Screen	Water	48,100
105	Monel K500	200x200 Monel 400 Screen	Water	48,100
107	Monel K500	200x200 Monel 400 Screen	Water	48,100
121	CP Ti	Sintered CP-2 -35+60 Mesh	Water	39,701
122	Ti Grade 7	100x100 CP Ti Screen	Water	39,701
123	Ti Grade 5	100x100 CP Ti Screen	Water	42,528
124	CP Ti with Timetal 21-S Strip	100x100 CP Ti Screen	Water	39,917
133	Monel K500	Monel 400 - 100 +170 Sinter	Water	34,344
134	Monel 400	120x120 Monel 400 Screen	Water	35,040
135	Ti Grade 9	100x100 CP Ti Screen	Water	35,544

In some cases, a non-organic working fluid is desirable, particularly for nuclear fission space

power, where the radioactivity with organic working fluids can generate gas. Since 2006, we have been conducting life tests at temperatures up to 673 K with titanium and three corrosion resistant superalloys (Hastelloy B-3, Hastelloy C-22, and Hastelloy C-2000), and five different halides working fluids: AlBr₃, GaCl₃, SnCl₄, TiCl₄, TiBr₄. The selection criteria were discussed in Anderson et al. (2007). Based on these life tests, two of the halides appear to be suitable for temperatures up to 673 K, and possibly at higher temperatures. Long term life tests are ongoing with TiBr₄/titanium at 653 K, and with AlBr₃/Superalloys at 673 K. As of April 2012, the AlBr₃ and TiBr₄ tests have been running for 50,000 hours (5.7 years).

In late 2010, several of the heat pipes were selected for destructive investigation (Table 1). One of each pair of water life test pipes was selected. The GaCl₃ and SnCl₄ pipes were known to be non-compatible, since they generated large amounts of NCG. The heat pipes containing halides were neutralized using an appropriate liquid. The neutralized fluid and water from the heat pipes using water as a working fluid were collected for chemical analysis.

To examine the cross-sections to determine the type and amount of corrosion in the wicks and heat pipes, the heat pipes were cut in half, pressure infiltrated with epoxy and sectioned at a location approximately one-third of the way above the bottom of the heat pipe. The sections were polished through 0.05-micron silica and examined using optical and scanning electron (SEM) microscopes.

3. RESULTS AND DISCUSSION

3.1 Microscopic Examination of Cross-sections

3.1.1 Titanium-Water Heat Pipes

Analysis of the cross-sections using optical and electron microscopy revealed little if any corrosion even when observed at high magnifications. When any evidence of corrosion was observed, the layer was typically around 1 micron thick. There were some indications in the backscattered electron (BSE) SEM images of changes in the structure of the Ti and Ti alloys as shown by the lighter bands near the surface in Figure 1. Energy dispersive spectroscopy (EDS) did not indicate that the layers changed composition, and they may be related to

either a change of the Ti from the α phase to the β phase or changes in grain structure from pickup of interstitial elements such as O.

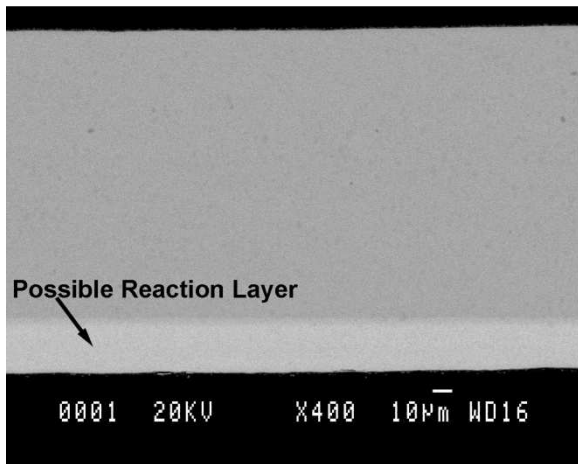


Figure 1. BSE Image of Timetal 21-S Strip Incorporated in Heat Pipe 124

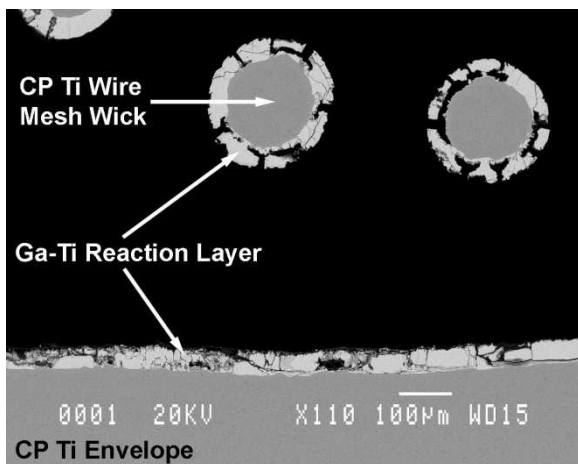


Figure 2. BSE Image of Heat Pipe 10 Envelope and Wire Mesh Wick

3.1.2 Titanium-Halide Heat Pipes

The two titanium halide heat pipes examined had very different responses. CP Ti with a TiBr_4 working fluid had minimal corrosion. There was evidence similar to the layers shown in Figure 1 of some potential change in the outer 10 microns.

CP Ti with GaCl_3 working fluid underwent extensive corrosion as seen in Figure 2. EDS analysis indicated that the corrosion layer was a Ga-29.7 wt.% Ti alloy. Examination of the Ga-Ti phase diagram (NPL, 2012) led to the conclusion that a mixture of Ga_2Ti , Ga_3Ti and Ga(l) was probably formed. Given the extensive nature of the voids, particularly on the wires, it was

hypothesized that considerable Ga(l) was present in the voids and lost during neutralization. The remaining Ga_2Ti reaction layer also exhibited evidence of brittle fracture during polishing.

3.1.3 Monel-Water Heat Pipes

Figure 3 shows an optical micrograph of the envelope and wick for Heat Pipe 136, one of the Monel-water heat pipes that underwent the most change. The formation of a dark subsurface layer and bright nodules were observed in the Monel 400 wick using BSE imaging. This was typical of all Monel 400 surfaces examined to varying but large degrees. EDS spot analysis revealed that the surface nodules were nearly pure Cu, and the dark layer was a Cu-depleted zone. Most likely, there was a phase change from α to $\alpha_1 + \alpha_2$ (ASMI, 1992) followed by diffusion of the Cu to the surface during exposure.

The Monel K500 does not show similar changes. Close examination of the envelope reveals, at most, a very thin corrosion layer. Most likely, the layer was an oxide, but it was sufficiently thin to prevent definitive identification through EDS. Apparently, the composition of the Monel K500 stabilizes the α phase.

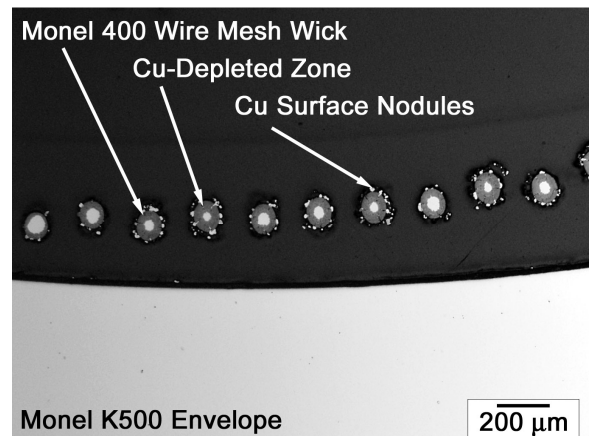


Figure 3. Optical Bright Field Micrograph of Heat Pipe 136 Envelope and Wire Mesh Wick

3.1.4 Hastelloy Superalloy-Halide Heat Pipes

Table 1 lists the five corrosion-resistant Hastelloy C-series superalloy heat pipes that were examined. As shown in Figure 4, the SnCl_4 working fluid caused considerable roughening of the C-22 envelope, up to 20-micron deep cracks in the substrate, a porous 10-micron thick corrosion layer and a thin, discontinuous Mo-W-Sn reaction layer beneath the corrosion product.

Table 2. Contaminants Found In Working Fluids (weight percent).

Heat Pipe	Working Fluid	Life Test Hours	Al	Co	Cr	Cu	Fe	Mn	Mo	Ni	Ti	V	W
6	SnCl ₄	20,160	0.007		0.38		0.038	0.012	0.79	1.78			0.02
7	SnCl ₄	20,160	0.006	0.001	0.11		0.004	0.057	0.083	0.027			
8	SnCl ₄	20,160	0.005	0.007	0.7	0.022	0.018	0.003	0.31	0.83			0.001
9	GaCl ₃	20,040									1.2		
10	GaCl ₃	20,040									1.2		
153	TiCl ₄	28,560			0.006		0.027			0.003			
157	AlBr ₃	28,704			0.013		0.018			0.002			
100	Water	48,100									0.00013		
103	Water	48,100									0.000016		
105	Water	48,100	0.000007			0.0011	0.000031	0.00021		0.00056	0.000008		
107	Water	48,100	0.000005			0.0021	0.00002	0.0016		0.00041	0.000006		
121	Water	39,701									0.000018		
122	Water	39,701									0.000012		
123	Water	42,528	0.000011								0.000025		
124	Water	39,917									0.000037		
133	Water	34,344	0.000007			0.000021							
134	Water	35,040		0.000005		0.00064	0.000015	0.00095		0.00011			
135	Water	35,544	0.000007								0.000062	0.000005	
Di Water STD	Water		<0.000005	<0.000005		<0.000005	<0.000005	<0.000005		<0.000005	<0.000005		

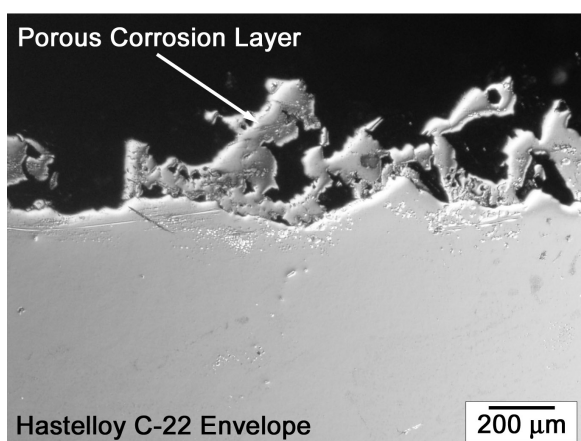


Figure 4. Differential Interference Contrast Optical Micrograph of Heat Pipe 7 C-22 Envelope

Hastelloy C-2000 also underwent extensive reaction with the SnCl₄ working fluid as shown in Figure 5. A 200-micron thick reaction layer identified as Ni₃Sn₂ with about 9 wt.% Cl was observed. In addition to the Ni-Sn-Cl reaction layer, Mo-Cl particles were observed at the

reaction layer/substrate interface during X-ray mapping.

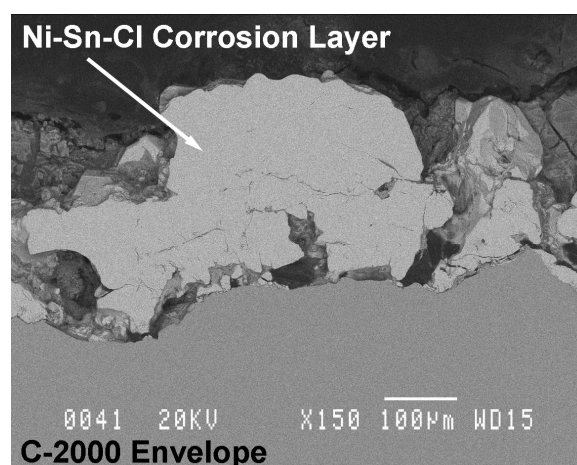


Figure 5. BSE Image of Heat Pipe 8 C-2000 Envelope Showing Thick Ni-Sn-Cl Reaction Layer Heat Pipes 153 and 157 showed good promise. Hastelloy C-2000 underwent little corrosion when used with TiCl₄ working fluid. A 1 to 2 micron

thick Ni-33 wt.% Ti-18 wt.% Mo-18 wt.%Cr-4 wt.% Cu-2 wt.% Cl corrosion layer was observed on the surface. BSE images showed that there might be a 0.5-micron thick region beneath the corrosion layer that was depleted in heavy elements.

Hastelloy C-22 exhibited a dual corrosion layer when tested with AlBr_3 working fluid as shown in Figure 6. The total thickness was 5 to 10 microns. EDS analysis of the two layers showed that the outer layer composition was Ni-11.5 wt.% Cr-11.9 wt.% Mo-3.6 wt.% Fe-9.4 wt.% W-0.6 wt.% Mn-1.7 wt.% Co-0.3 wt.% V-0.8 wt.% Si-9.5 wt.% Br. The inner corrosion layer composition was Ni-12.8 wt.% Cr-12.4 wt.% Mo-3.2 wt.% Fe-6.4 wt.% W-0.2 wt.% Mn-1.3 wt.% Co-0.3 wt.% V-21.9 wt.% Br. Based upon these analyses, it appears that AlBr_3 can slowly react with the C-22 over thousands of hours to form a relatively thin corrosion layer.

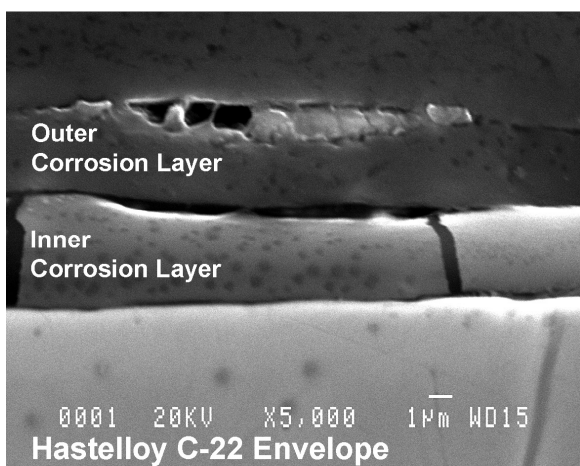


Figure 6. SE Image of Heat Pipe 157 C-22 Envelope Showing Two Corrosion Layers

3.2.5 Analysis of Working Fluids

Table 2 contains the results of the chemical analysis of the working fluids. As a standard, deionized water exposed to Ti and Monel 500 (DI Water Std.) was analyzed as well. Only the elements present in the envelope and wick alloys are listed. Minimal pickup of metals was observed for the heat pipes using water as a working fluid.

The heat pipes that used halides as a working fluid showed more contamination of the working fluids. Heat pipes 153 and 157, which appeared to form a protective layer, exhibited low total metal contents between 300 and 350 ppm. Heat Pipes 7 and 8, which used SnCl_4 , suffered more working fluid

contamination with Cr being the major metal present. The relative amounts seem to be consistent with the qualitative levels of attack observed. GaCl_3 was clearly the most aggressive working fluid when paired with Ti, which is consistent with the microscopic observations. 1.2 wt.% Ti was present in the working fluid of Heat Pipes 9 and 10. Heat Pipe 6 also exhibited large pickup of metal from the Hastelloy B-3 envelope, but no Ti was present, indicating that Ti is compatible with TiBr_4 . This is also consistent with the results for Heat Pipe 4, which showed no attack of the Ti envelope.

3. CONCLUSIONS

Titanium/water and Monel/water heat pipes are compatible at temperatures up to 550 K, based on ongoing life tests that have been running for over 54,000 hours (6.1 years) as of April 2012. Analysis of titanium/water heat pipe cross-sections using optical and electron microscopy revealed little if any corrosion even when observed at high magnifications. When any evidence of corrosion was observed, the layer was typically around 1 micron thick. Copper depleted zones, as well as copper surface nodules formed on the Monel 400 screen wick. This was not observed on the Monel K500 envelopes. An analysis of the water working fluids showed minimal pickup of metals.

A non-organic working fluid is desirable for nuclear fission space power and other applications where radioactivity can generate gas with organic working fluids. Long term life tests show that TiBr_4 /titanium at 653 K, and AlBr_3 /Superalloys at 673K are compatible. As of April 2012, the AlBr_3 and TiBr_4 tests have been running for 50,000 hours (5.7 years).

Hastelloy C-2000 underwent little corrosion when used with TiCl_4 working fluid, with the formation of only a 1-2 micron thick corrosion layer. Hastelloy C-22 exhibited a 5-10 micron thick dual corrosion layer when tested with AlBr_3 working fluid. The working fluids of these two heat pipes exhibited total metal contents between 300 and 350 ppm. The results indicate that the tested envelope materials and working fluids can form viable material/working fluid combinations.

ACKNOWLEDGEMENT

The water and halide life tests were sponsored by NASA Glenn Research Center under Contracts

NNC05TA36T, and NNC06CA74C. We would like to thank Cheryl Bowman and Ivan Locci of NASA Glenn Research Center for helpful discussions about the fluids and materials. The authors would like to acknowledge the metallographic sample preparation by Joy Buehler of NASA.

REFERENCES

- Anderson, W. G., Hartenstine, J. R., Sarraf, D. B., and Tarau, C., "Intermediate Temperature Fluids for Heat Pipes and Loop Heat Pipes," 15th International Heat Pipe Conference (15th IHPC). Clemson, USA, April 25-30, 2010.
- Anderson, W. G., "Intermediate Temperature Fluids for Heat Pipes and LHPs," Proceedings of the 2007 IECEC, AIAA, St. Louis, MO, June 25-27, 2007.
- Anderson, W.G., Bonner, R.W., Dussinger, P.M., Hartenstine, J.R., Sarraf, D.B., and Locci, I.E., "Intermediate Temperature Fluids Life Tests – Experiments" Proceedings of the 2007 IECEC, AIAA, St. Louis, MO, June 25-27, 2007.
- Anderson, W.G., Dussinger, P.M., Bonner, R.W., and Sarraf, D.B., "High Temperature Titanium-Water and Monel-Water Heat Pipes," Proceedings of the 2006 IECEC, AIAA, San Diego, CA, June 26-29, 2006.
- ASM International (ASMI), Cu-Ni Phase Diagram, ASM Handbook, Vol. 3, Alloy Phase Diagrams, ASM International, Materials Park, OH (1992), p. 2-173.
- National Physical Laboratory (NPL), Calculated Ga-Ti Phase Diagram, London, UK, <http://resource.npl.co.uk/mtdata/phdia/grams/gati.htm> , retrieved March 12, 2012.

AN EXPERIMENTAL STUDY OF LOCAL NUSSLETT NUMBER FOR GAS-LIQUID TAYLOR BUBBLE FLOW IN A MINI-CHANNEL

Abhik Majumder, Balkrishna Mehta and Sameer Khandekar

Department of Mechanical Engineering

Indian Institute of Technology Kanpur

Kanpur (UP), 208016 India

Tel: +91-512-259-7038; Fax: +91-512-259-7408; E-mail: samkhan@iitk.ac.in

ABSTRACT

Taylor bubble flow or capillary slug flow takes place when a low density fluid flows through another relatively high density fluid in a tube of capillary dimensions. This kind of flow pattern is observed in many engineering devices like pulsating heat pipes, gas-liquid-solid monolithic reactors, micro-two-phase heat exchangers, digital micro-fluidics, micro-scale mass transfer process etc. The flow pattern in such device is very complex and is subjected to several unresolved issues. Hence, the understanding of the local and global behavior of such flow is important. In the present work, the temperature profile of gas-liquid (a) isolated Taylor bubbles and (b) Taylor bubble train flows has been studied on the basis of varying gas and liquid Reynolds numbers and input heat flux to understand the local and global heat transfer phenomena under specified boundary condition in a horizontal square channel. The experimental setup consists of square channel of cross section 3.3 x 3.3 mm and 350 mm in length with one side heating at constant heat flux and other boundaries are kept insulated. The heater length is 175 mm. The variation of local wall and fluid temperature are recorded to evaluate the local and average Nusselt number.

KEY WORDS: Taylor bubble flow, Mini-channels, Local Nusselt number, Heat Transfer enhancement

1. INTRODUCTION

Capillary slug flow or Taylor bubble flow is one of the sub-classes of conventional slug flow; this special pattern appears when surface tension dominates over gravitational body force, typically in mini-/micro-scale systems. In such geometries, the flow is essentially laminar and predominantly viscous [Bretherton 1961; Taylor, 1961; Cox, 1964]. The understanding of species transport under such a flow configuration is a challenging problem. In recent years, research on Taylor bubbles has increased due to the development of mini/micro scale systems in diverse branches of engineering wherein Taylor bubble flow is the dominant flow pattern. [e.g., refer Triplett *et al.*, 1999; Ghiaasiaan and Abdel-Khalik, 2001; Taha and Cui, 2006; Angeli and Gavrilidis, 2008; Wörner, 2010]. Pulsating heat pipes represent an important field of application, utilizing self-sustained thermally driven passively oscillating Taylor bubble flows for enhanced heat transfer [Khandekar *et al.*, 2010].

Taylor slug flow conditions are typically characterized by a sequence of long bubbles which are trapped in between liquid plugs; such flows therefore have strong geometric constraints. A thin

liquid film, thickness of which depends on flow parameters and thermophysical properties of the fluids involved, usually always separates the bubbles from the channel wall. The presence of the film that separates the bubble from the wall means that the bubble velocity is not equal to the liquid one [Fabre and Liñe, 1992]. The presence of bubbles in front and at the back of the slugs, modifies the flow field in the liquid slug compared with single-phase flow and toroidal vortices extending the length of the slug can form [Thulasidas *et al.*, 1995, 1997]. The recirculation patterns within the liquid slugs enhances heat and mass transfer from liquid to wall and interfacial mass transfer from gas/vapor to liquid. The transport mechanisms are thus influenced by the dynamics of isolated 'unit-cell', consisting of a Taylor bubble and the adjoining liquid plug. Understanding transport mechanism necessitates localized experimental observations of slug-bubble systems, with synchronized measurements of the resulting fluctuations in local conditions such as temperature, pressure and wall heat flux [King *et al.*, 2007]. Such information is vital for designing micro-thermofluidic and micro-chemical reactor systems that operate in this regime.

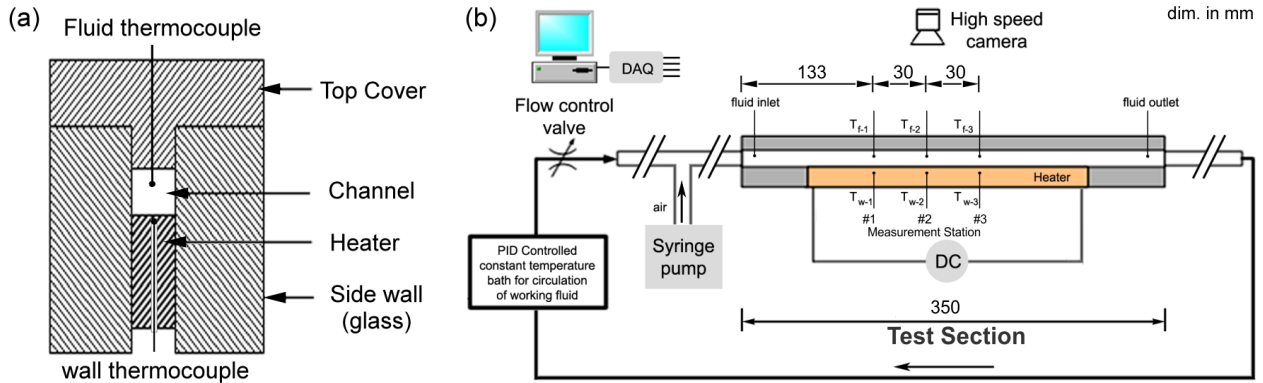


Figure 1. (a) Details of the test section and (b) Schematic details of the experimental test rig.

Bao et al. [2000] experimentally investigated non phase-change air-water flow in a circular channel of diameter 1.95 mm under constant heat flux boundary condition and observed enhancement in heat transfer coefficient due to the presence of gas. Narayanan and Lakehal [2008] conducted numerical simulation of sensible heat transfer during gas-liquid flow in small-diameter pipes and found that overall heat removal is significantly increased due to the presence of circulation as compared to the corresponding single-phase flow. Walsh et al. [2010] experimentally investigated the heat transfer rate in non-boiling two phase flow problem in a circular channel of 1.5mm of internal diameter under constant heat flux boundary conditions. They used infra red thermography to record the change in substrate temperature, to calculate the Nu. They showed that such flow pattern can be very useful for augmentation of Nu in fully developed flows, whereas, in contrast the performance degrades in case of entrance region flow. However, these observations were made without measurement of the local fluid temperature; the fluid temperature was extrapolated. In this work, we undertake local heat transfer measurements of isolated air-water Taylor bubble/ Taylor bubble-train flow, in a square channel (aspect ratio ≈ 1). A square channel is chosen as it provides the least wetted perimeter, for a given cross sectional area and therefore is preferable from an overall pressure drop point of view. Flow Reynolds number and the volumetric flow rate of air are the variable parameters. Benchmarking of the setup is first done against single phase data before performing the actual tests.

2. EXPERIMENTAL DETAILS

The schematic of the setup is shown in Figure 1. The channel dimensions were 3.3 mm X 3.3 mm.

A constant heat flux boundary condition was applied at the bottom channel wall (DC-strip heater), while the other three channel sides were kept insulated. Heat loss to the surroundings was $\sim 10\%$ - 17% of the input heat. The side walls were made of glass for visualization of Taylor bubbles (Photron-Fastcam[®]-SA3 camera). The temperature profile of gas-liquid (a) isolated Taylor bubble flows and, (b) Taylor bubble train flows, was studied by varying gas and liquid Reynolds numbers and input heat flux. A precisely controlled single syringe pump (Cole-parmer-WW-74900) was used to inject air at the T-junction, as shown. The junction was located sufficiently upstream of the heated test section for achieving flow stability. Micro-Thermocouples (0.13 mm bead diameter; Type-K-Omega[®]) were used to measure the local wall/ fluid temperature at the three measurement stations, as shown. Thermocouples measuring the fluid temperatures were inserted from the top of the channel and were centrally located in its cross-section. Interfacial distortion of Taylor bubbles was not observed due to these thermocouples; however, they did disturb the liquid flow, as discussed later. A 24 bit DAQ (NI[®]-9213) was used at a sampling frequency of 20 Hz. Constant inlet temperature of distilled, degassed and deionized water was maintained within $\pm 0.01^\circ\text{C}$ by a circulator (Julabo[®] ME-26). The liquid flow Reynolds number was kept such that the flow was hydrodynamically fully developed but thermally developing inside the channel. The experiment was conducted in two steps. At first, the data was recorded for single-phase (water) steady-state flow at a defined flow rate. Keeping the liquid flow rate same, in the next step, air was injected to create either (i) a single isolated bubble flow or, (ii) alternately, a quasi-periodic Taylor bubble train flow; thermocouple data at the three measurement stations and image acquisition was simultaneously done.

3. RESULTS AND DISCUSSIONS

3.1 Single-phase experimental results

A typical non-dimensional plot of normalized wall and fluid temperatures versus non-dimensional axial streamwise coordinate, with constant heat flux applied to the heater, under single-phase laminar flow of water at three different Reynolds number viz. 120, 180 and 220, is shown in Figure 2. The results clearly show that the flow is developing in nature. For hydrodynamically fully developed but thermally developing flow, London and Shah [1978] suggest a thermal entry length of $z_{th} = 0.066 \text{ Re Pr } d_h$. It follows that for $\text{Re} \leq 40$, all the three measurement stations are in hydrodynamic as well as thermally fully developed regions, whereas for $\text{Re} \geq 115$ all of them are in hydrodynamically developed but thermally developing region. As all the results presented here are for $\text{Re} > 115$, it follows that these cases represent Graetz type flow. It is evident from Figure 2 that as the flow Re increases, thermal transport increasingly takes place in the thermally developing region. For $\text{Re} = 120$, the difference between the wall and fluid temperature tends to become constant towards the downstream direction suggesting the completion of the flow development phenomena. Several independent tests were conducted under these flow conditions and the quantitative variation in the data was within the experimental scatter range. Estimation of single-phase Nu , from this raw data, is discussed later.

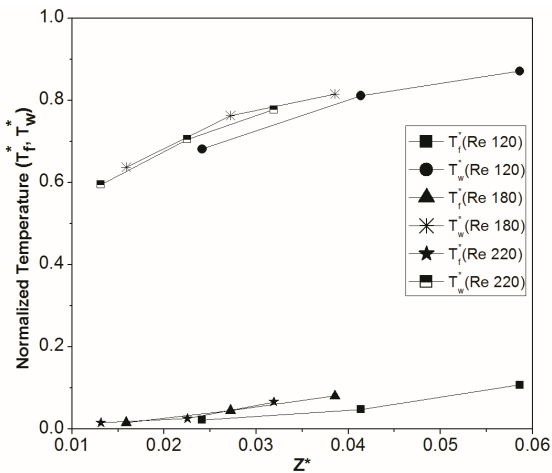


Figure 2. Streamwise variation of normalized steady state fluid and heater wall temperatures.

3.2 Single Taylor bubble flow

When steady state is reached in single-phase water flow at a given flow rate, a single isolated Taylor bubble is injected in the flow at the T-junction,

which, as noted earlier, is located far upstream in the tube leading to the test section. This ensures that any flow perturbations created by sudden injection of the bubble get dissipated by the time the bubble reaches the heated test section. Typical results for the wall and fluid temperature profile respectively, at $\text{Re} = 130$ and heat input of 8.0 W, is shown in Figure 3(a), (b), for two bubble lengths respectively. In the present experiment, the wall temperature does not show any appreciable change as the isolated bubble passes through the three measurement stations. This is primarily because of the thermal inertia of the heater wall, its response time scale being slower than the disturbance time scale of the bubble. However, once the Taylor bubble reaches the point of measurement, the bubble temperature is seen to be higher than the surrounding liquid. This is attributed to the low thermal capacity of air as compared to water. The heat flux input being constant along the streamwise direction, air temperature rises. Thus, there is a momentary apparent increase of the local heat transfer coefficient, as the difference between the wall and fluid temperature goes down. After the bubble passes, the water temperature comes back to its original level.

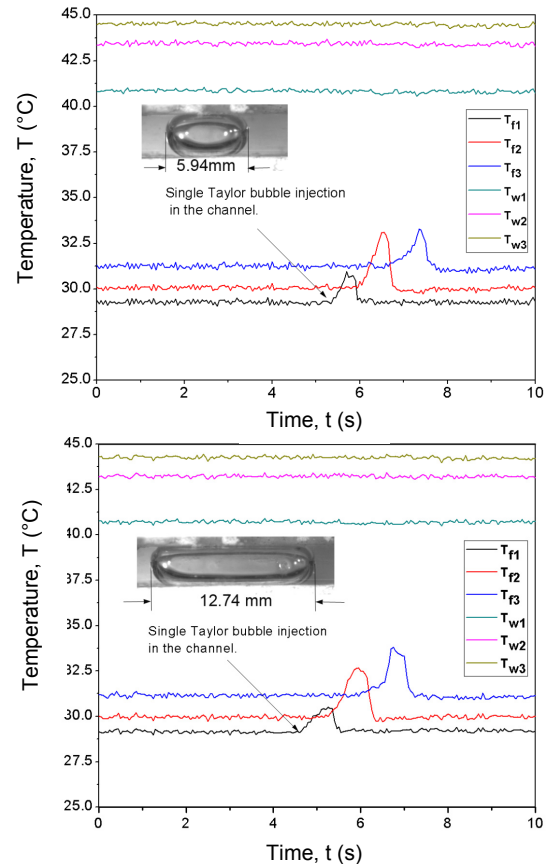


Figure 3. Temporal variation of wall and fluid temperature for a single Taylor bubble flow ($\text{Re} = 130$; heat input = 8.0 W).

3.3 Slug/Taylor bubble train flow

The continuous introduction of a quasi-periodic Taylor bubble train into a Graetz type flow provides the opportunity to study its effect on the effectiveness of the heat removal capability. As noted earlier, Taylor bubble train flow is achieved by injecting air from a syringe through a regulated syringe infusion pump, supplying air to the T-junction which is located far upstream. The flow rate of the air and therefore its volumetric flow ratio (ξ = the ratio of air flow rate to the total flow rate of air and water) is controlled. Results reported here are from experiments carried out at different ξ and with two flow Re, viz. 180 and 196. The fully developed flow of the Graetz-solution suggests an asymptotic constant value of Nusselt number under the said boundary condition [Shah and London, 1978]. Hence, fully developed flows saturate the heat transfer coefficient. Thermal transport enhancement under such flow conditions can be achieved by creating local flow disturbances. In the present case, this is achieved by the injection of a quasi-periodic Taylor bubble train into the liquid flow. Figure 4 (a), (b) and (c) show the temporal variation of the fluid and wall temperature versus time at the measurement station 1, 2 and 3 for a volumetric flow rate ratio (ξ) of 0.424, 0.387 and 0.321, respectively. The thermocouple data acquisition frequency is 20 Hz.

Experiments starts with (i) single-phase water flow with no air-injection, followed by (ii) the commencement of air injection from the T-junction, (iii) continuation of Taylor bubble train flow till a quasi-steady state is reached and (iv) closing of the air-injection to restore the single-phase water flow. In this experimental sequence, the evolution of Nusselt number is as shown in Figure 4 (d).

No sooner the Taylor bubble train reaches the measurement stations, it causes the wall temperature to decrease at all the measurement station 1, 2 and 3, respectively. Respective wall temperatures at the measurement stations located in the streamwise direction are progressively higher. Simultaneously, an increase of the average fluid temperature is also noted, the phenomenon being similar to the single Taylor bubble case (Section 3.2). However, in the present case, as there is a continuous train of Taylor bubbles, achievement of a quasi-steady state is possible. For this large flow time scale, the wall temperature also decreases due to enhanced localized radial mixing caused by the local circulation in the liquid plugs trapped between the Taylor bubbles [Taha and Sui, 2006]. Typically, for such flow conditions toroidal vortices are present in the flowing liquid plugs which enhance the heat transfer coefficient. Due to the intermittent nature of the flow and the difference of thermal capacities of the air and

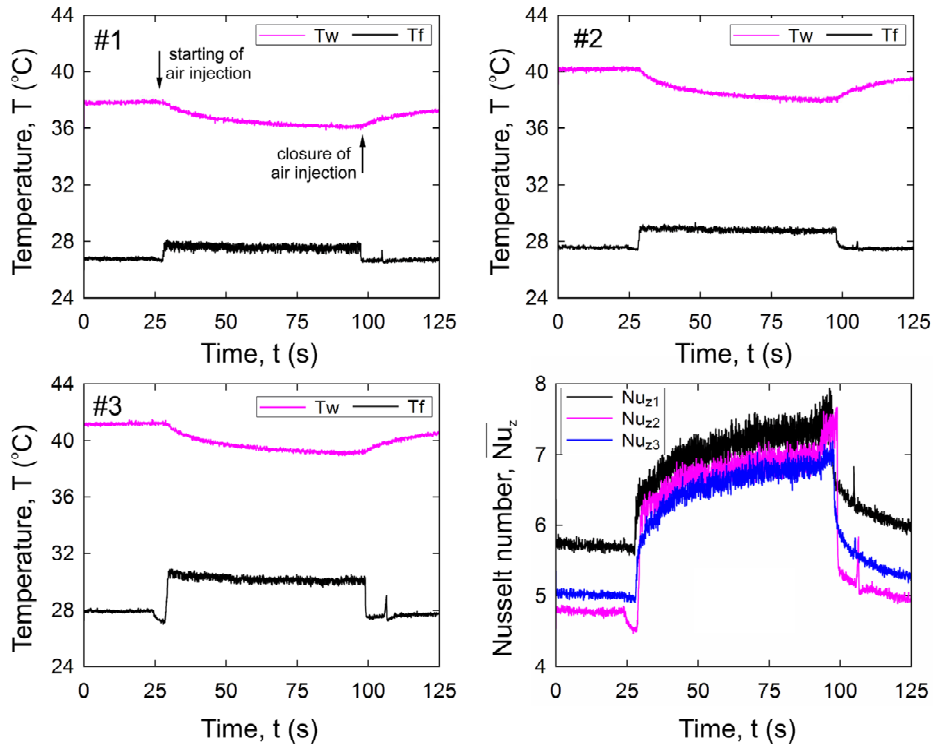


Figure 4. Transient temperature distribution of fluid and wall at measurement station 1, 2 and 3 are shown for void fraction of 0.217 in (a), (b) and (c), respectively. The liquid Reynolds number is 196. Variation of local Nu at measurement stations 1, 2 and 3 is simultaneously shown in (d).

water, the fluid temperature fluctuates quasi periodically with a dominant frequency which matches with the bubble flow time scale. The frequency spectrum analysis of the temperature data is not described here due to lack of space. The alternating pattern of liquid plug and bubble flow continually disrupts the formation of the thermal boundary layer, which gets renewed every time an air bubble passes. As can be seen in the figures, the wall and fluid temperatures come back to the original level once air injection is stopped and flow returns back to single-phase water. As can be seen from Figure 4 (d), air injection induces strong enhancement in local Nusselt number, which settles down to a new asymptotic high level once quasi-steady state is attained. Stopping the air flow brings the Nusselt number back to the level corresponding to the single-phase water flow.

For the present range of experiments, the steady-state time averaged local Nusselt number, computed at three measurement stations at various void fractions, are plotted against the non-dimensional streamwise coordinate, are shown in Figure 5. Both, results obtained from single-phase water flow experiments and Taylor bubble train flow experiments are included. Keeping the water flow rate fixed, volumetric flow ratio of air is increased by increasing flow rate of air; this results in longer lengths of Taylor bubbles. The ξ values equal to 0.451, 0.413 and 0.346 are obtained at liquid Reynolds number 180 while for $Re = 196$, we obtained ξ values equal to 0.424, 0.387 and 0.321, respectively. For benchmarking and comparison of the data, the average local Nusselt number for hydrodynamically fully developed but thermally developing as well as simultaneously developing flows in a square channel, under H1 boundary condition, as respectively obtained by Wibulswas [Shah and London, 1978], are also included. Results obtained from the Ansys[®] Fluent based CFD simulation for hydrodynamically fully developed but thermally developing flows are also shown (for brevity, details of the CFD simulations are not given here).

First, looking at the single-phase heat transfer results of the present study, it is noticed that the heat transfer coefficient is lying between simultaneously developing flow and thermally developing flow. This is predictable as, although the design of the experiment is expected to provide hydrodynamically fully developed flow, the three micro-thermocouples located in the flow path disturb the velocity boundary layer and tend to increase the local heat transfer. Overall, the single-phase results are quite satisfactory and depict the

developing nature of the flow, Nusselt number gradually decreasing in the streamwise direction, as the boundary layer develops.

The results obtained for the Taylor bubble train flow clearly show that there is a significant enhancement in heat transfer when the flow is subjected to non-boiling two-phase Taylor bubble flow. It is also evident that as the void fraction decreases, \overline{Nu}_z also decreases and tends to finally approach the values obtained during single-phase flow. The percentage enhancement with respect to the single-phase flow is not high in the early part of the channel. In this part of the thermal entry length, the developing nature of the single phase flow itself provide sufficiently high transport coefficient. In the latter part of the channel ($Z^* \sim 0.04$), the advantage of Taylor bubble train flow is clearly visible. Also, it is clear that for a given flow Reynolds number, increasing volumetric flow ratio of air flow improves the Nusselt number, in the range of the present experiments.

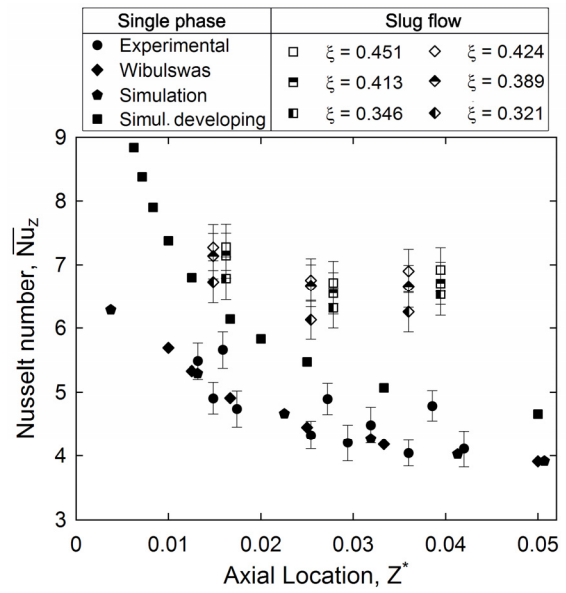


Figure 5. Variation of experimental \overline{Nu}_z along the channel at various void fractions of Taylor bubble train flows, and its comparison with single-phase flow experiments, and other benchmark solutions.

Decreasing air flow rates brings the transport situation asymptotically closer to single-phase liquid flow. In contrast, as ξ increases, the liquid plug length trapped between the Taylor bubbles goes down. This increases the time scale of the recirculating toroidal vortices, improvising the Nusselt number. Logically, such an enhancement of Nusselt number with ξ will not be monotonous as after a threshold value of ξ , the flow morphology may change to churn/ annular flow.

4. SUMMARY AND CONCLUSIONS

The major conclusions of the study are as follows:

- Injection of Taylor bubbles provides an efficient means of heat transfer enhancement, up to 1.5 to 2 times, as compared to fully developed laminar single-phase. The relative enhancement may not be attractive when compared to developing single-phase flows.
- At any given location in the streamwise direction, injection of Taylor bubble train flows results in lowering of the wall temperature and increase of the average fluid temperature. Fluctuations of the wall temperature were not detectable due to the thermal inertia compared to the ensuing time scales of the transport process, when an isolated Taylor bubble is injected.
- Increasing volumetric fraction (ξ), for a fixed liquid mass flow rate, the T-junction flow mixing system resulted in longer air bubbles, i.e. smaller liquid plugs entrapped between the bubbles. This increased the time averaged local Nu, for the present range of experiments. However, such an increase may not be monotonous; this aspect needs further exploration.

NOMENCLATURE

d_h	Hydraulic diameter (m)
H1	Boundary condition refers to the constant axial and peripheral wall heat flux
Nu_z	Local Nusselt number
$\overline{Nu_z}$	Time averaged local Nusselt number
Pr	Prandtl number
Re	Reynolds number (based on liquid superficial velocity)
T_{fi}	Temperature of the fluid (°C)
T_{wi}	Temperature of the substrate (°C)
Z^*	Thermal entry length
ξ	Volumetric flow ratio (air flow/total flow)

ACKNOWLEDGEMENT

Financial grants from the Indo-French Center for Promotion of Advanced Research (IFCPAR) are gratefully acknowledged (Project 4408-E).

REFERENCES

Angeli P. and Gavriilidis A., *Hydrodynamics of Taylor flow in small channels: A review*, Proc. IMechE, Part C: J. Mech. Engg. Sc., 222, p. 737-751, 2008.

Bao Z., Fletcher D. and Haynes B., *An experimental study of gas liquid flow in a narrow conduit*, Int. J. Heat Mass Trans., 43, p. 2313-2324. 2000.

Bretherton F. P., *The motion of long bubbles in tubes*,

J. Fluid Mech., 10, 166-188, 1961.

Cox B. G., *An experimental investigation of streamlines in viscous fluid expelled from a tube*, J. Fluid Mech., 20, p. 193-200, 1964.

Fabre J. and Liñe A., *Modeling of two-phase slug flow*, Ann. Rev. Fluid Mech., 24, p. 21-46, 1992.

Fairbrother F. and Stubbs A. E., *The bubble tube method of measurement*, J. Chem. Soc., 1, p. 527-529, 1935.

Ghiaasiaan S. M., and Abdel-Khalik S. I., *Two-phase flow in microchannels*, Adv. in Heat Transfer, 34, p. 145-254, 2001.

Harmathy T. Z., *Velocity of large drops and bubbles in media of infinite or restricted extent*, AIChE Journal, 6(2), p. 281-288, 1960.

Khandekar S., Panigrahi P. K., Lefevre F. and Bonjour J., *Local hydrodynamics of flow in a pulsating heat pipe: A review*, Frontiers in Heat Pipes, Vol. 1, pp. 023003(1-20), 2010.

King C., Walsh E. and Grimes R., *PIV measurements of flow within plugs in a microchannel*, Microfluids and Nanofluids, 3, p. 463-472, 2007.

Kolb W. B. and Cerro R. L., *The motion of long bubbles in tubes of square cross sections*, Phy. Fluids-A, 5, p. 1549-1557, 1993.

Narayanan C. and Lakehal D., *Two phase convective heat transfer in miniature pipes undernormal and micro gravity conditions*, J. Heat Transf, 130, 2008.

Shah R. K. and London L. A., *Laminar flow forced convection in ducts*, Academic Press, 1978.

Taha T. and Cui Z. F., *CFD modeling of slug flow inside square capillaries*, Chem. Engg. Sc., 61, p. 665-675, 2006.

Taylor G. I., *Deposition of a viscous fluid on the wall of a tube*, J. Fluid Mech., 10, p. 161-163, 1961.

Thulasidas T. C., Abraham M. A. and Cerro R. L., *Flow patterns in liquid slugs during bubble train flow inside capillaries*, Chem. Engg Sc., 52(17), p. 2947-2962, 1997.

Thulasidas T. C., Abraham M. A., and Cerro R. L., *Bubble train flow in capillaries of circular and square cross section*, Chem. Engg. Sc., 50 (2), p. 183-199, 1995.

Triplett K. Ghiaasiaan S., Abdel-Khalik S. I., Le-Mouel A. and McCord B., *Gas-liquid two-phase flow in microchannels. Part I: Two-phase flow pattern*, Int. J. Multiphase Flow, 25, p. 377-394, 1999.

Walsh A. P., Walsh J. E. and Muzychka S. Y., *Heat transfer model for gas-liquid slug flows under constant flux*, Int. J. Heat Mass Transf., 53, p. 3193-3201, 2010.

Wörner M., *A key parameter to characterize Taylor flow in narrow circular and rectangular channels*, Proc. 7th Int. Conf. Multiphase Flow (ICMF 2010), Tampa, USA, 2010.

AUTOMATED FILLING AND SEALING OF EMBEDDED HEAT PIPES

Wessel W. Wits

Faculty of Engineering Technology, University of Twente
P.O. Box 217, 7500 AE, Enschede, The Netherlands
+31 (0)53 489 2266, +31 (0)53 489 3631, w.w.wits@utwente.nl

Johannes van Es

Dutch National Aerospace Laboratory
P.O. Box 153, 8300 AD, Emmeloord, The Netherlands
+31 (0)88 511 4230, +31 (0)527 248210, Johannes.van.es@nlr.nl

Gert Jan te Riele

Thales Nederland B.V.
P.O. Box 42, 7550 GD, Hengelo, The Netherlands
+31 (0)74 248 2294, +31 (0)74 248 4058, gertjan.teriele@nl.thalesgroup.com

ABSTRACT

High performance electronics cooling moves from utilizing modular heat pipes to fully integrated heat pipes. Filling and sealing of these non-tubular embedded heat pipes is a challenge, since traditional methods as evacuate, fill and pinch do not suffice. This paper presents a charging station that is able to fill and seal embedded heat pipes in a reliable manner. A small, low-cost charge component is connected to the heat pipe. This allows the fill head of the charging station to mount the heat pipe in an automated manner. The charging station uses specially designed zero dead volume valves to minimize internal fluid volumes and thus increase the fill accuracy. Inside the fill head, the internal fluid line for filling and the plunger performing a pressed plug seal alternate position during the charging process. Prototype testing shows that the charging station is able to charge heat pipes in around 5 minutes with a final fill accuracy of 1.5 μ l.

KEY WORDS: Heat pipes, Automated charging, Heat pipe filling station

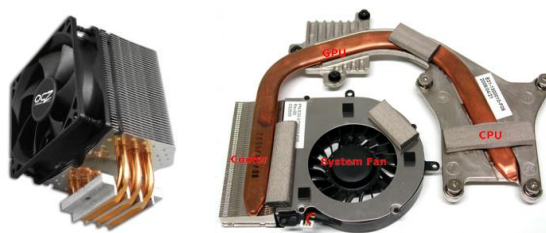
1. INTRODUCTION

Thermal management plays an increasingly dominant role in the design process of electronic products. The increasing local heat fluxes constrain the design of electronic products. Nowadays, quite often traditional cooling methods, such as air cooling and single phase liquid cooling, no longer suffice due to the high power density.

1.1 Electronics cooling with heat pipes

Two-phase cooling techniques are an effective and reliable solution for high power density cooling. Especially interesting are heat pipes; as these are passive systems heat is transported in a very efficient manner. Heat pipes require no pump, power or moving parts to function and the temperature gradient across its length is extremely low; typical <10°C. By now the electronics industry has fully embraced the advantages of heat pipes in the thermal design of notebooks, game

consoles and other high performance devices, as shown in Figure 1.



a) heat sink [OCZ] b) notebook cooling [Tom]

Figure 1. Heat pipes in electronics cooling.

Figure 1 shows applications where heat pipes are build-in to either improve the spreading and/or transport of the heat from local hotspots. As shown, in most cases conventional tubular heat pipes are bent in the right shape and sometimes even flattened to get a good thermal connection. The use of a modular heat pipe to improve the cooling system is a very typical design solution.

1.2 Full integration of electronics cooling

This study focuses on the full integration of thermal management functions into the design process of electronic products. This will lead to more functionality and performance in a smaller form factor. In addition, by smart integration products can be realized at a lower cost; altogether leading to smaller, lighter and more affordable electronics products. A working demonstrator of this research was first presented in Wits (2006) and a comprehensive paper was presented at the IHPC 2007 (Wits, 2007) and published in Wits (2011).

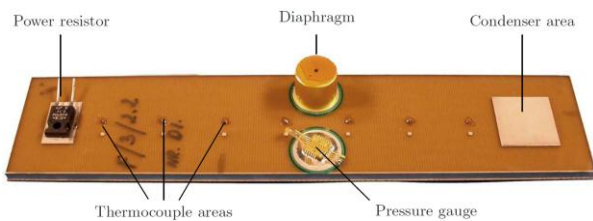


Figure 2. Heat pipe fully integrated into a PCB.

The working demonstrator consisted of a Printed Circuit Board (PCB) with a heat pipe designed as an integral part of the laminated board structure, as shown in Figure 2. Prototype measurements showed that the initial thermal performance of these heat pipe integrated PCBs was excellent; however, long term stability was an issue. This was likely due to the chosen approach of charging and sealing the heat pipe. To seal the heat pipe the design featured a diaphragm device filled with an airtight elastomeric barrier. Both evacuation and fluid filling was done through a (separate) needle.

1.3 Outline

This paper presents a new and reliable method to charge and seal non-conventional, integrated heat pipes. Typical for such heat pipes is that they are not modular as the examples of Figure 1; therefore, traditional evacuate, fill and pitch strategies cannot be applied. Integrated heat pipes are fully embedded into the electronics assembly, enabling direct access to local and even embedded hotspots. The next chapter describes the developed charging station, Chapter 3 describes the charging process and finally Chapter 4 describes the sealing method.

2. HEAT PIPE CHARGING STATION

To enable high speed filling and sealing of non-tubular, embedded heat pipes a special apparatus is developed. In literature several charging devices and procedures are described. In Faghri (1995) a device with interstage containers is described through where the working fluid is distilled into

the heat pipe. For high-speed filling however usually the working fluid is injected into the heat pipe in its liquid form. For this, different methods are known. Probably most common is filling through a T-junction: one leg for evacuation, one leg for fluid injection and the last leg running to the heat pipe. In this case, sealing is usually done by pinching the tube from the outside. In practice, heat pipes charged using this method are usually overfilled and purged. By purging, unwanted Non-Condensable Gas (NCG) is blown out the heat pipe before permanent sealing. Due to the many valves and channels (and other reasons) it is difficult to reach a high accuracy; therefore, in practice heat pipes are often overfilled to about 10%.

To enable high-speed filling, the developed charging apparatus also injects the working fluid in its liquid phase. The complete station, as shown in Figure 3, is designed for high precision, automated and reliable filling of embedded heat pipes.

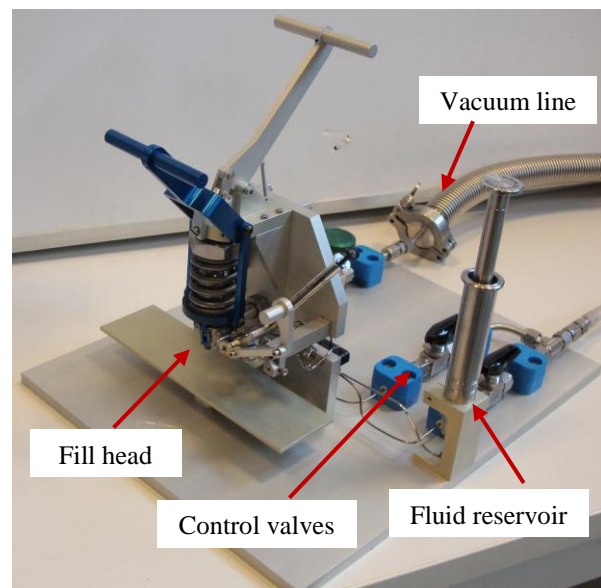


Figure 3. Heat pipe charging station.

Working fluid is transported from the fluid reservoir to the fill head using the control valves. Charging is done in 4 steps: mounting, evacuating, filling and sealing.

In the mounting phase, the heat pipe is clamped to the fill head. The clamp, clamp mechanism and charge component are shown in Figure 4. A specially design charge component is used for clamping. This part must be soldered, brazed or welded to the heat pipe prior to the charging process. The clamp mechanism automatically aligns the fill head to the charge component allowing for a quick and automated process.

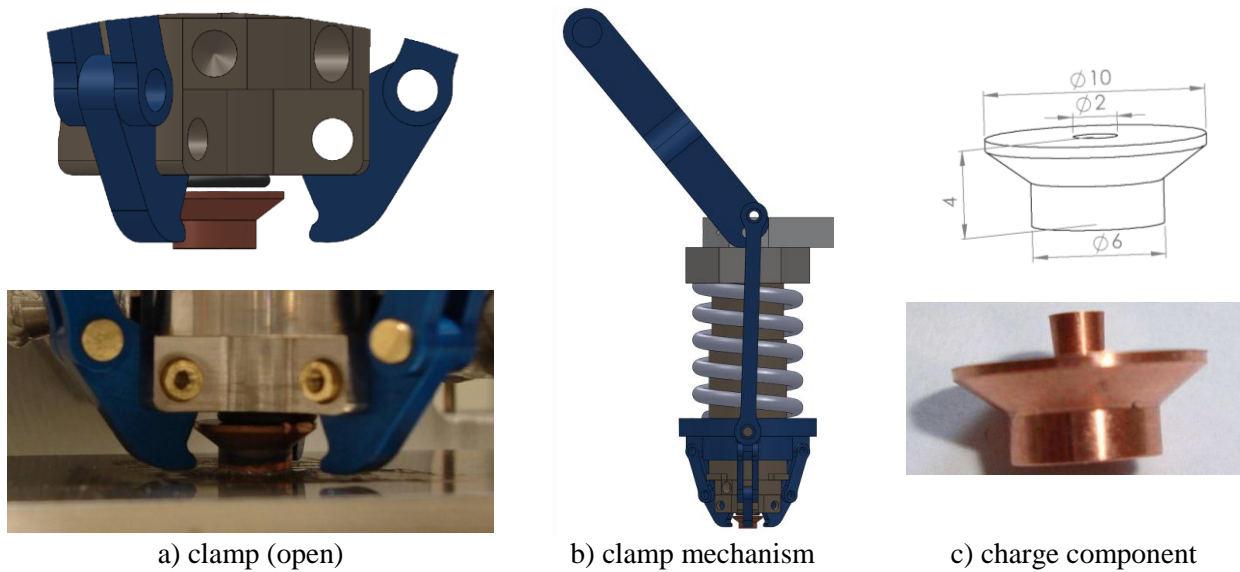


Figure 4. Mechanism connecting the fill head to the heat pipe.

The charging station is designed to guarantee a reliable temporary seal during the charging process. The clamp mechanism is calibrated to put sufficient pressure on the O-ring between the fill head and the component. Clamp forces are guided through the charge component only and not through the entire heat pipe and electronics assembly. In Figure 4c the charge component is depicted with an inserted pin. This pin is used to hermetically seal the heat pipe after filling (see Chapter 4). Since the charge component is required for every heat pipe, it is designed as a small, low-cost part measuring only $\text{Ø}10 \times 4 \text{mm}$.

3. HEAT PIPE CHARGING

Charging of heat pipes can be done in many ways (Peterson, 1994; Chi, 1976; Dunn, 1994), ranging from vaporizing a totally liquid filled heat pipe (large volume heat pipes) to filling heat pipes with supercritical vapor (micro-heat pipes). The most common technique is to evacuate the heat pipe after which it is filled through either the liquid or vapor phase. For high accuracy filling, charging is done through the vapor phase of the working fluid. Since vapor densities are relatively low compared to liquid densities it is much easier to meter the fluid entering the heat pipe accurately.

The main process steps in most charging procedures of low&high temperature heat pipes are

1. Baking out of the heat pipe internals
2. Working fluid purification; in parallel with 3&4
3. Flushing / cleaning sometimes operation in reflux mode (optional)
4. Evacuation

5. Working fluid insertion
6. Operating and venting of NCG (optional)

Baking out of the heat pipe internals can be done off-line and is not discussed in this paper. For working fluid purification the use of distilled water is chosen combined with a freeze-thaw cycle to remove any dissolved gasses (Chi, 1976). In this case, purified water is stored into the fluid reservoir and attached to the charging station. Cleaning is already implemented in the embedded heat pipe manufacturing process and is therefore not foreseen as a separate step during the charging process. This step can however be implemented when deemed necessary.

For this research critical focus is put on the design and trade-off of steps 4 (evacuation) and 5 (fluid insertion). The additional requirement of this research compared to conventional heat pipe filling is that filling is possible for a small series production line with a high accuracy. Typically for our application a 5% accuracy on a filling volume of around $300 \mu\text{l}$ is demanded. Further, the formation of NCG and leak should be limited to 6% of the condenser volume for 25 years of heat pipe operation: 5% is reserved for leak during operational life time and 1% during filling.

Two possible sources of NCG are identified during filling. Firstly, the initial vacuum quality before liquid insertion and secondly the leak during filling through the O-rings and soldered connections. For both sources a maximum of 0.5% condenser volume of NCG is allowed. The vacuum level required to meet this requirement for the embedded

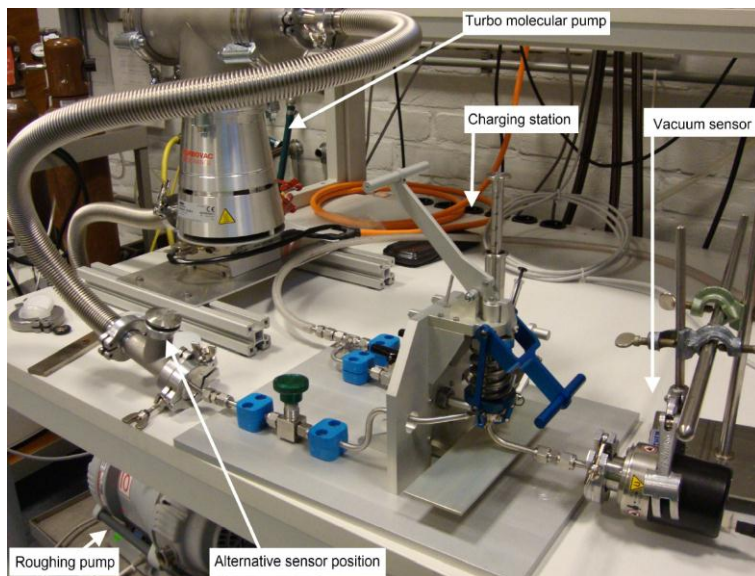


Figure 5. Vacuum test set-up.

heat pipes as shown in Figure 2 is 0.18mbar assuming the baking out of the heat pipe materials is done in advance and off-line. The leak tightness for the filling system during filling is $2.1 \cdot 10^{-6}$ mbar·l/s assuming a charging time of 10 minutes.

3.1 Evacuation

The heat pipe is evacuated through the fill head after it is mounted to the charging station. The process time to reach the required vacuum level will be the most time consuming step for series production. The pump system of the charging station consists of a rough vacuum pump (BOC Edwards XDS10) connected in series with a turbo molecular pump (Oerlikon Leybold Turbvac TW 250S).

To estimate the required time for evacuation, tests have been performed with a vacuum sensor connected to the fill head (see Figure 5). The vacuum sensor is mounted to charging station using the same charge component as will be used to charge the heat pipe. The vacuum line runs through the fill head and charge component. The time to reach the required 0.18mbar is about 3½ minutes. In first instance this is acceptable for series production.

The vacuum level was also measured at the alternative position before the charging station to determine the pressure drop induced by the charging station. This proved to be about 2 decades. In a future design of the charging station, the design of channel and opening diameters, and charge component can be optimized to further reduce the required evacuation time.

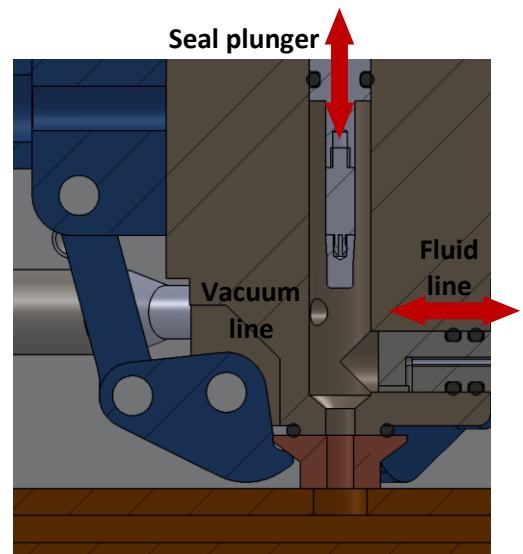


Figure 6. Fill head internals.

Also, a leak test was performed using a helium mass spectrometer (Oerlikon Leybold UL200). Helium was sprayed around the charging station, but leaks were below the detection limit of $1 \cdot 10^{-10}$ mbar·l/s. Thus fulfilling the leak tight system requirement of $2.1 \cdot 10^{-6}$ mbar·l/s.

3.2 Working fluid insertion

After creating the required vacuum the pump system is disconnected from the charging station by closing the (green) valve. To start the fluid insertion phase, the fluid line is slid in horizontally (Figure 6). This way the fill opening is positioned above the charge component and the working fluid is dispensed directly into the heat pipe.

The driving requirement for the filling process is an accuracy of 5%; i.e. 15µl on a total of 300µl. Two main factors contribute to the filling error, namely the error of the metering device and dead volume inside the filling system. An accurate 500µl syringe is chosen as metering method with an error of less than 2% (6µl) of the syringe volume. The biggest source of error in filling accuracy for micro-heat pipes are dead volumes and the main contributors are normally the valves. The internal volume of the most accurate valve at the moment of writing is 16.5µl, which consumes already the whole accuracy budget available.

3.3 Zero dead volume valve

To tackle this problem two specially designed Zero Dead Volume Valves (ZDVs) are incorporated into the design of the charging station. The ZDVV is derived from an expired patent by Hunkapiller, 1985. A schematic view, explaining the principle,

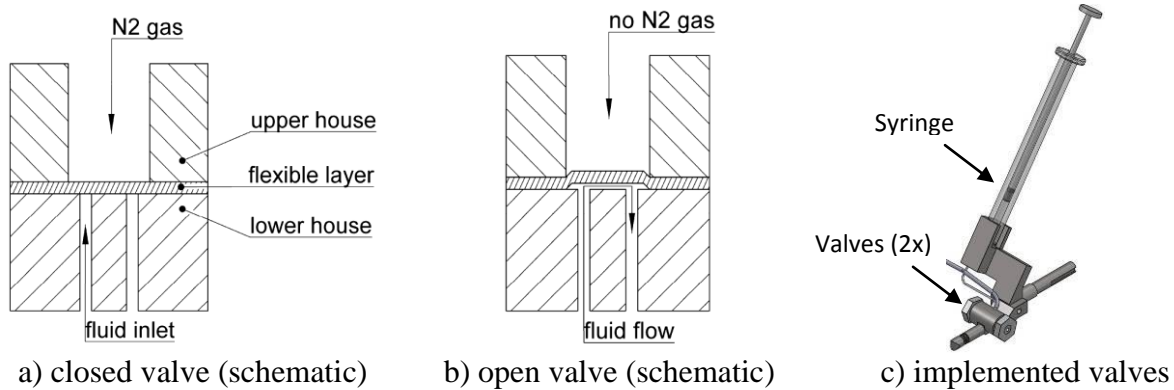


Figure 7. Working principle of the zero dead volume valve.

is given in Figure 7. The valve consists of 3 components: a lower house, a flexible layer and an upper house. The small channels inside the lower house are used for fluid pumping. The flexible layer enables opening and closing of the valve. The ZDVV is closed pneumatically by applying a gas pressure, in this case nitrogen, above the flexible layer (Figure 7a). Opening is done by releasing the nitrogen pressure. Fluid inside the small inlet channel can now be pumped into outlet channel (Figure 7b). The ZDVV can also function as a pressure relief valve.

By operating 2 ZDVs in series the error in fill accuracy is reduced to the volume uncertainty in the connection lines between the 2 ZDVs and the heat pipe, indicated in grey in Figure 8. These connection lines have capillary dimensions and by heating them it can be assured that they only contain a minimum of vapor. In the figure, S2 refers to the fluid reservoir and S1 refers to the accurate 500 μ l syringe. By operation the nitrogen pressure valves V2 & V3, the working fluid can be transported from S2 to S1, accurately metered and finally transported from S1 into the heat pipe.

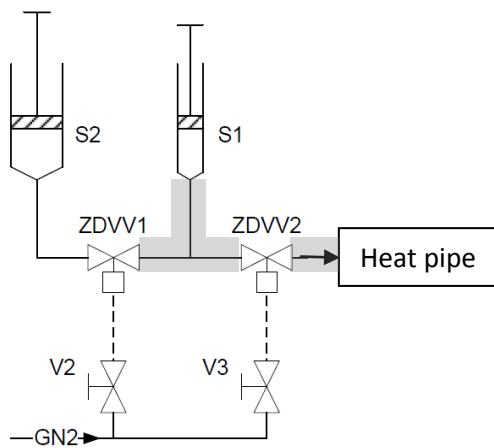


Figure 8. Operational filling scheme.

3.4 Fill accuracy

The fill accuracy is verified by filling a number of test tubes (see Figure 9) connected to the fill head. The inserted mass is verified by measuring before and after filling with an accurate mass balance.

Measurement results show that on average 99.5% of the intended fill volume was actually inserted into the test specimens. For the intended heat pipe application this means a fill accuracy of 1.5 μ l, well below the required specifications.



Figure 9. Test items for fill accuracy testing.

4. HEAT PIPE SEALING

To prevent unwanted gases entering the heat pipe, a permanent seal has to be made after the pipe is fully charged. Traditionally, heat pipes are sealed by pinching the fill tube. This is an efficient way for conventional tubular heat pipes. However, for embedded heat pipes or vapor chambers this method is not very suitable. Due to a lack of alternatives sometimes a small protruding tube is connected and used for charging and sealing.

As mentioned, 5% of the condenser volume is allowed as leak during the operational life time of 25 years. For the intended application this means the maximum leak rate of the heat pipe seal is $4.3 \cdot 10^{-11}$ mbar·l/s. Next to this requirement, the seal procedure should not impede the filling process and series production.

As mentioned before, this research explores another method of sealing, namely the pressed plug seal. Here, the seal is formed by forcing a plug into a housing, in this case the charge component. Similar to the traditional pinched tube, this forms a cold weld seal. After forcing down the plug, soldering or welding can improve the long-term reliability of the seal. Inside the fill head, the fluid line is first slid back to make room for the plunger that forces down the plug (see Figure 6).

There are a number of advantages of using this method. The combination of a plug and housing is more compact than a protruding tube. Also, the process of sealing by inserting a plug is better controlled and industrialized. The cost of the charge component is negligible to the system cost. Finally, as the charge component can be positioned and soldered automatically as many other electronics components, the proposed method is very suitable for integration with common electronics manufacturing processes.

4.1 Seal test results

A number of experiments have been done to prove and optimize the pressed plug seal concept. The plugs are tapered and the internal diameter of the charge component was set to 2mm for evacuation and filling requirements. Copper is chosen for both the plug and charge component. The plugs are pressed into the hole using a workbench and a load cell was used to measure the insertion force (see Figure 10a). After insertion, the seals were tested for leakage right away and also 4 days later.

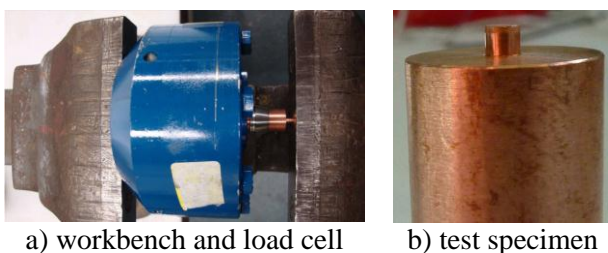


Figure 10. Pressed plug seal experiment.

The insertion length varied from 0.2-2.6mm, but this proved to be no clear indicator of a good seal. The insertion force was however critical and had to be over 100N to guarantee a hermetic seal. This threshold was also used to engineer the plunger.

Pressurized helium leak tests show that the concept of heat pipe sealing by means of inserting a plug into a compact counterpart is robust and reliable. Combined with a cost efficient process integration, this makes for an overall attractive solution.

5. CONCLUSIONS

This paper presents a new apparatus for quick, accurate and reliable filling of non-tubular embedded heat pipes. The charging station uses specially designed zero dead volume valves to minimize internal fluid volumes. A small, low-cost charge component is connected to the heat pipe. It allows the fill head to be mounted to the heat pipe in an automated and reliable manner. Inside the fill head the fluid line and plunger alternate position during the charging and sealing processes.

Prototype testing shows that the charging station, for which a patent is pending, performs well. Sealed heat pipes are leak tight well below their requirements. Heat pipe charging can now be done in an automated manner within about 5 minutes with a final fill accuracy of 1.5 μ l.

ACKNOWLEDGEMENT

The authors would like to acknowledge the great support and enthusiasm of Harm Jan ten Hoeve (design), Sander Weitkamp, Wim den Ouden, Corné Lof (filling) and Danny Ellermann (sealing).

REFERENCES

- Chi, S.W. (1976) *Heat pipe theory and practice*. Series in thermal and fluids engineering
- Dunn, P.D., Reay, D.A. (1944) *Heat pipes*. Elsevier Science Ltd, Oxford
- Faghri, A. (1995) *Heat pipe science and technology*. Taylor & Francis, London
- Hunkapiller, M.W. (1985) *Zero dead volume valve*. Patent number 4558845
- OCZ technology. (2012) CPU cooler with heat pipe. <http://www.ocztechnology.com>. 16 March 2012.
- Peterson, G.P. (1994) *An introduction to heat pipes: modeling, testing and applications*. Series in thermal management of microelectronic & electronic systems. Wiley, New York
- Tom's guide. (2012) Notebook cooling with heat pipe. <http://www.tomsguide.com>. 16 March 2012.
- Wits, W.W., Legtenberg, R., Mannak, J.H., Van Zalk, B. (2006) *Thermal management through in-board heat pipes manufactured using PCB multilayer technology*. Proc. 31st Int. Conf. on Electronic Manufacturing and Technology, Petaling Jaya, Malaysia, pp. 55-61.
- Wits, W.W., Kok, J.B.W., Legtenberg, R., Mannak, J.H., Van Zalk, B. (2007) *Manufacturing and modelling of flat miniature heat pipes in multilayer printed circuit board technology*. Proc. 14th Int. Heat Pipe Conf. (IHPC), Florianópolis, Brazil, pp. 169-175.
- Wits, W.W., Kok, J.B.W. (2011) *Modeling and validating the transient behavior of flat miniature heat pipes manufactured in multilayer printed circuit board technology*. Journal of Heat Transfer, Vol. 133.

MULTILAYER SINTERED POROUS MEDIA MINI HEAT PIPE

FLOREZ, J.P.M.; NUERNBERG, G.G.V.; PAIVA, K.V.; VELASQUEZ, S.T.R.; MANTELLI, M.B.H.

Department of Mechanical Engineering, Bloc. A3, Third floor, Federal University of Santa-Catarina (Heat Pipe Laboratory), Florianopolis, Santa-Catarina, ZIP CODE: 888040-900, Brazil. Tel: +55 (48) 3721-9937, Fax: +55 (48) 3721-7615, E-mail: jpablo@labtucal.ufsc.br

ABSTRACT

The main objective of this work is to evaluate the thermal performance of mini heat pipes produced with multilayer capillary structures. Multilayered sintered porous media is able to produce high working fluid pumping capacity while keeps the pressure drops in low levels, optimizing the heat pipe thermal performance. Multilayer heat pipes are made of overlapping layers of sintered copper powder. The tested mini heat pipes have the nominal dimensions: 100 mm × 30 mm × 2 mm and their porosities vary between 42 and 52%. Flat copper plates are used as the closing sheets and wires of 1.70 mm of diameter are used to improve the mechanical resistance of the system. These sintered materials are produced with atomized copper powder of 95% of purity and average particle sizes of 20 and 50 μm. A particle circularity factor of 70% is observed for the powder. Distilled water is used as working fluid. The effective thermal conductivity and permeability are experimentally measured using an experimental apparatus especially designed and built for this purpose. The thermal performances of multilayered and conventional mini heat pipes are compared. Models available in literature are used to evaluate the mini heat pipe. A simple hydraulic resistance model is proposed to evaluate the capillary limit in multilayer mini heat pipes. The wick porous size distribution and porosity are determined by image analyses using software IMAGO[®].

KEY WORDS: mini heat pipes, multilayer porous media.

1. INTRODUCTION

Mini heat pipes (MHP) can be employed as thermal control devices for electronic equipment cooling, in the aerospace, automotive, computer, and other industries (Faghri, 1995). LABTUCAL (Heat Pipe Laboratory) of UFSC (Federal University of Santa Catarina - Brazil) works in the development of MHP with sintered wick structure since 2005.

Conventional porous media shows a limited heat transfer capacity in mini heat pipes. A porous media with small pores presents high working fluid pumping capacity, but on the other hand, a large liquid pressure drop. Actually, the fluid pumping capacity improvement is obtained by reducing the pore diameter, which, in turn, reduces the media permeability. One of the possible ways to achieve the mini heat pipe maximum performance, is to construct porous media composed with layers of different permeabilities. These arrangements show

a high capillary pumping capacity and no significant decrease in the global permeability.

The main objective of the present work is the application of a novel wick technology in heat pipes, to improve its thermal performance. Wicks formed by multilayers of sintered metal with different characteristics are studied. These media are able to combine high capillary pumping capacity with low pressure drops, enhancing, therefore, the heat transfer capacity of the device.

2. LITERATURE REVIEW

Most of the research in heat pipes around the world has been focused on developing new structures and capillary pumping configurations for porous media. The literature shows that different types of grooves, sintered porous media (metallic and ceramic) and screens are employed.

Groove wicks have attracted great interest, as reported by Cao and Faghri (1993) and Peterson

(1990), due to its high permeability and low manufacturing costs, compared to other wicks. However, sintered materials have higher pumping capacity that compensates the lower permeability, as stated by Vasiliev (2006).

Berre et. al (2003) produced a micro heat pipe, with mini V-shaped channels. Adjacent smaller channels below the main channel, or arteries, are assembled. Their micro heat pipe tube was made of thin silicon wafers. These micro channels further allowed an independent path for the flow of condensate to the evaporator. The experimental results using methanol as the working fluid showed that the artery arrangements increased the conductivity of mini heat pipe, compared to the conductivity of silicon.

Paiva (2007) developed a mathematical model and an experimental prototype of a mini heat pipe formed by wires and copper blades. These mini heat pipes were tested in gravity and micro-gravity environment. In his work, a methodology for manufacturing mini heat pipes was developed, as described by Mantelli et al. (2002). Tests using distilled water as working fluid showed that these devices were able to deliver 55 W with thermal resistance of 0.5 °C/W.

Xiao and Franchi (2008) used a combination of different porous structures to improve the capillary pumping characteristics, by increasing the surface area between the solid and the working fluid and enhancing the amount of open pores. These researchers designed and manufactured different hybrid structures, using copper screen and sintered powder of copper and nickel, arranged in different compositions. The tests were conducted using distilled water as the working fluid. Different configurations showed an increase of around 70% of the working fluid pumping capacity. All these measurements were made with the heat pipes in a vertical position. A maximum power of 15 W was transported.

The direct mixing of powders in the fabrication of sintered porous media has been studied and reported by Yeh et al. (2009). These researchers produced a capillary structure formed by "biporos". According to the authors, this structure provides greater interconnection among the formed pores, providing a greater heat transfer capacity due to phase-change (evaporation) of the working fluid in the evaporator.

3. EXPERIMENTAL TESTS

In the present work, the thermal resistance and the capillary limit of multilayer MHPs are evaluated. MHP samples with four different combinations of sintered material layers are experimentally studied. The samples are tested in two conditions: vacuum of 0.001 mbar (no working fluid) and filled with several different volumes of saturated distilled water. Factorial design of experiments 2^4 is employed, with two replicates in a single level. The MHP wicks are produced by loose sintering metallurgy process. Atomized copper powder is employed to produce the multilayer and the conventional porous media. These selected powders have commercial names PAC and PAM. PAC has a fine and PAM a coarse average particle sizes. Copper is selected for the reason that it is commonly used in MHP wick structures and is compatible with water. Other copper interesting characteristics are the high thermal conductivity and low cost (Dunn and Reay, 1994).

The MHP produced presents a parallelepiped shape with nominal dimensions of 100 mm × 30 mm × 2 mm. The closing cases are built using 0.3 mm thickness copper sheets. Before closing, the case is filled with a controlled amount of powder and them sintered in an oven, forming the first layer. The second layer was deposited over the first layer and sintered again. After the porous media is ready, the cover sheet is diffusing welded to the base, using the same oven.

The resulting samples are denominated as: 100PAM, PAM75PAC25, PAM50PAC50 and PAC100, according to the thickness of the layers, respectively: 100% PAM, 75% PAM plus 25% PAC, 50% PAM plus 50% PAC and 100% PAC, as depicted in Figure 1.

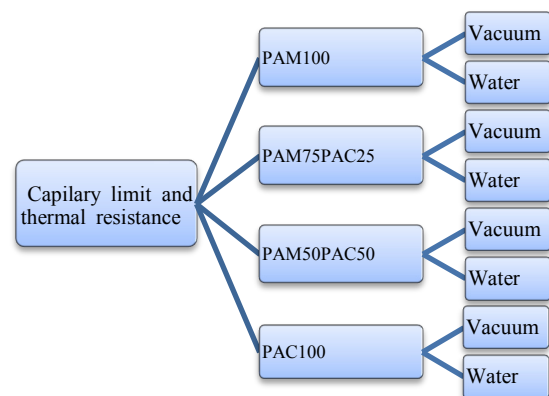


Figure 1. Tests description

The sintering heating rate is 5°C/min and the system is left inside the oven for 50 minutes, after reaching the 850°C. The sintering process is conducted in a vacuum furnace with commercial H₂ controlled atmosphere, available at the UFSC Materials Laboratory. In the final step, the MHP case walls receive a oxy-acetylene welding to guarantee the vacuum. A capillary tube is provided to allow the selected working fluid filling.

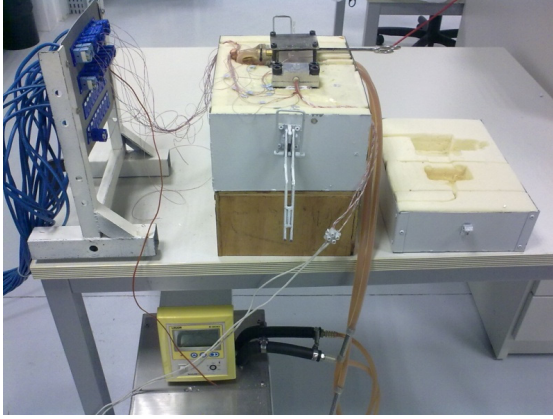


Figure 2. Experimental apparatus

An experimental apparatus is designed and built especially for testing the thermal performance of MHP. Heating plates are connected to the evaporator and a small heat exchanger is attached to the condenser. This assembly is housed inside a metallic box filled with polyurethane foam as insulating material, according to Figure 2. The heat is removed by cooled water from a thermostatic bath, maintaining the temperature condition set in 40°C during the tests.

The temperatures are measurement by type T thermocouples. The position of the thermocouples can be seen in Figure 3. The left rectangle represents evaporator, the center rectangle adiabatic and the right rectangle condenser sections.

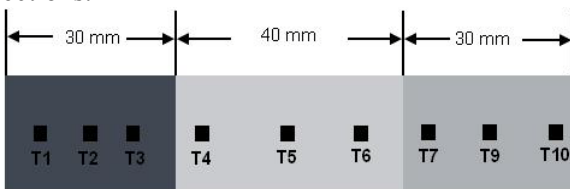


Figure 3. MHP Thermocouple distribution

The power is supplied to the four electric heaters, with a total capacity of 50 W, by a power supply. The software Labview 8.6 is used as the graphical interface for recording the thermocouple readings.

4. THEORETICAL ANALYSIS OF MHP

4.1 Capillary limit model

To determine the MHP capillary limit, the Faghri (1995) and Chen (2001) models, with the addition of two terms is employed, resulting in Equation 1. One of the added terms, in the left side of the equation, is relative to the capillary pumping for each layer of the porous material. It is considered that the two porous media layers work as capillary pumps in series. In the right hand side of the equation, one term is added to the fluid pressure drop term, consisting of pressure losses of parallel paths, according to Darcy's law, resulting in:

$$2\sigma \cos \theta \left(\frac{1}{r_{c1}} + \frac{1}{r_{c2}} \right) = \left(\frac{C(f_v Re_v) \mu_v}{2r_{h,v}^2 A_v \rho_v h_v} \right) l_{ef} q + \frac{1}{\left(\frac{\mu_l l_{ef}}{\rho_l K_1 A_{w1}} \right)^{-1} + \left(\frac{\mu_l l_{ef}}{\rho_l K_2 A_{w2}} \right)^{-1}} \left(\frac{q}{h_{lv}} \right) + \rho_l g d \quad (1)$$

The following hypotheses are considered: laminar flow regime; Darcy's equation is valid and vapor is incompressible (Mach number less than one). The properties are considered constant and obtained for the adiabatic section temperature. The MHP operates in steady state.

4.2 Global thermal resistance

The global thermal resistance is defined as the ratio between condenser and evaporator temperature difference and the power transferred, being given by:

$$R_t = \frac{\bar{T}_{eva} - \bar{T}_{cond}}{P_e} \quad (2)$$

where \dot{Q} is the heat transfer for the MHP, \bar{T}_{eva} and \bar{T}_{cond} are the average temperatures of the evaporator and condensation sections, respectively. The heat loss through the insulation was determined to be around 4%.

5. TEST RESULTS AND DISCUSSION

5.1 Wick properties

The results of measurements of the properties of porous media are present in Table 1. The properties were measured according to procedures

described in Florez et al. (2011) and Nuernberg et al. (2011).

Table 1. Wick properties

Property	PAC	PAM
Permeability [m ²]	3.71E-13± 0.15	2.89E-12± 0.42
Critical radio [μm]	9.4	19.7
Porosity [%]	41.31 ± 0.60	51.95 ± 0.71
Effective thermal conductivity [W/(m · K)]	52	36

The thicknesses of the two layers are controlled during the fabrication process and measured later by image analysis. It is observed that, between these layers, there is a third transition interfacial layer, which thickness was determined applying statistical image analysis, using software IMAGO[®], as proposed by to Nuernberg et al. (2011). Porosity was employed as parameters of evaluation of the produced layered wick. Table 2 shows the thickness of each sintered material layer. The thickness of the interfacial layer is of the order of magnitude of the sum of the particles average diameters of each layer.

Table 2. Wick thickness.

Thickness wick [μm]	PAM	PAC
PAM100	670±10	0
PAM50PAC50	260±10	330±10
PAM75PAC25	430±10	170±10
PAC100	0	670±10

5.1 Analysis of fluid working volume for multilayer sintered porous media

The wicks of the MHP are filled with distilled water in different volumes. The resulting MHP are tested with several power input levels. The working fluid volume varied starting form values below the theoretical amount needed to saturate the porous medium. Table 3 shows the theoretical working fluid volumes for each sample, obtained from the image analysis.

Table 3. Theoretical working fluid volume.

Theoretical amount water [ml]	Total	PAM	PAC
PAM100	1.65	1.65	0
PAM50PAC50	1.50	0.83	0.67
PAM75PAC25	1.57	1.24	0.33
PAC100	1.33	0	1.33

The tested MHP tubes were gradually loaded with working fluid and its thermal resistance measured until the optimum operation conditions were

achieved. The measurement uncertainties obtained were calculated to be around ± 12% for the start up period. For steady state, the overall thermal resistance uncertainty was approximately ± 3%. A confidence level of 95% was used in the uncertainty calculations.

In Figures 4, 5 and 6, the x-axis represents the power input while the y-axis represents the overall thermal resistance.

Figure 4 shows that the thermal resistance in vacuum conditions was approximately 4°C/W for sample PAM100. Approximately the same resistance for vacuum conditions can be observed for other samples, as it can be seen in Figures 5 and 6. For PAM 100, the lowest thermal resistance is obtained for 1.2 ml of working fluid, reaching values below 0.5 °C/W, for heat transfer powers varying from 50 W to 80 W. This fluid volume was about 72.7% of the theoretical fluid amount enough to saturate the porous media.

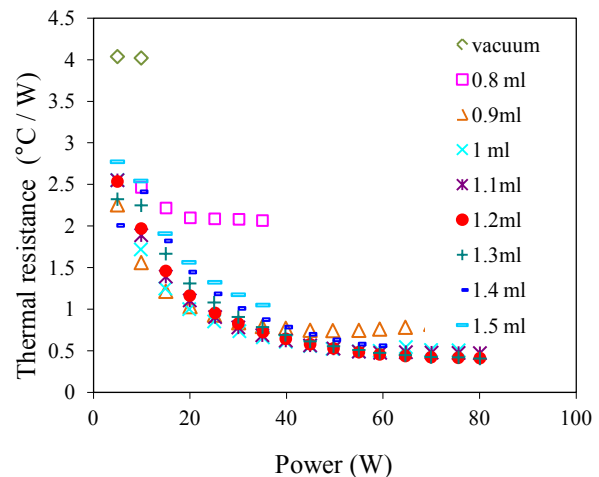


Figure 4. Experimental data for MHP PAM100 for several working fluid loads

Figure 5 shows the experimental thermal resistance for PAM50PAC50 sample, for different amounts of fluid. The lower thermal resistance observed was around 0.35 °C/W, for heat transfer power larger than 60 W, with 1.5 ml of distilled water. This amount of fluid showed the best performance, being able to transfer up to 104 W. This working fluid amount represents 100% of the volume necessary to saturate the porous wick.

Figure 6 presents the data for PAM75PAC25. The results show a higher thermal resistance related to the other two MHP samples. For this configuration, the best result was obtained for a load of 1.4 ml, which corresponds 89.2% of the

amount needed to saturate the porous media. This low thermal performance can be explained by the fact that the PAC layer does not provide the appropriate capillary pumping.

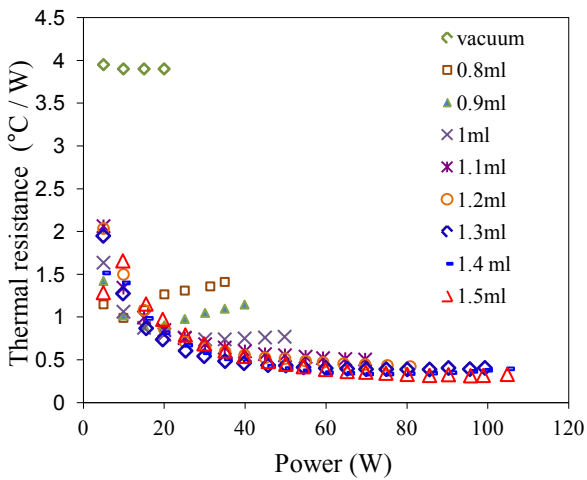


Figure 5. Experimental data MHP PAM50PAC50 several working fluid loads

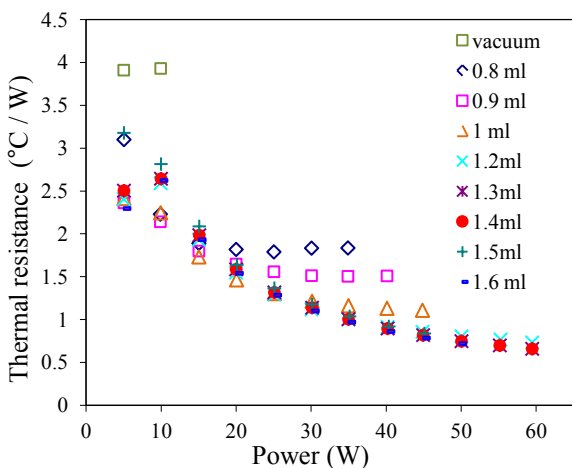


Figure 6. Experimental data PAM75PAC25 several working fluid loads

In Figure 7, it is presented a comparison between the best configurations for each sample studied, in terms of thermal resistance. From all tested samples, the lower thermal resistance is obtained is for PAM50PAC50, which is 20% lower than the MHP built with a single layer PAM100.

In Figure 7, it is also possible to observe the dry-out for PAM100, PAM75PAC25 and PAM50PAC50 samples. According to Paiva (2007), this behavior can be observed by a change in the slope of the resistance curve against thermal power input. Usually, as the heat power increases, the thermal resistance tends to decrease and a sudden increase shows that the capillary limit is reached. The PAM100 MHP reaches its capillary limit for a power input approximately 20% lower

than that observed for PAM50PAC50. In this figure, one can also observe that the smallest resistance is obtained for the PAM50PAC50 sample.

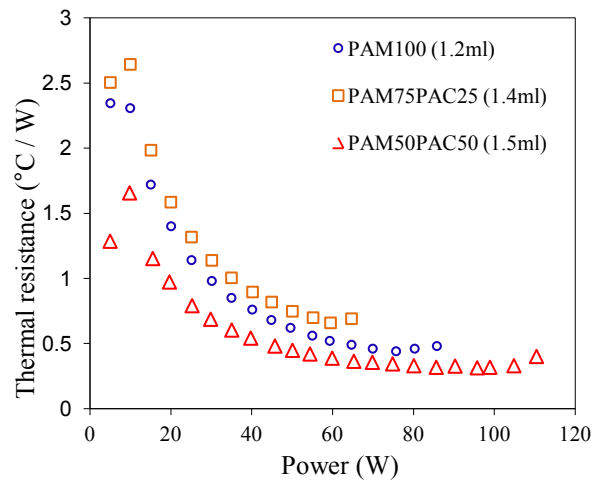


Figure 7. Compare of the thermal resistance of the three MHP

Figure 8 shows the temperature profiles for different power inputs for the PAM50PAC50 samples. The evaporator achieves a temperature of 76 °C for a power of 100 W.

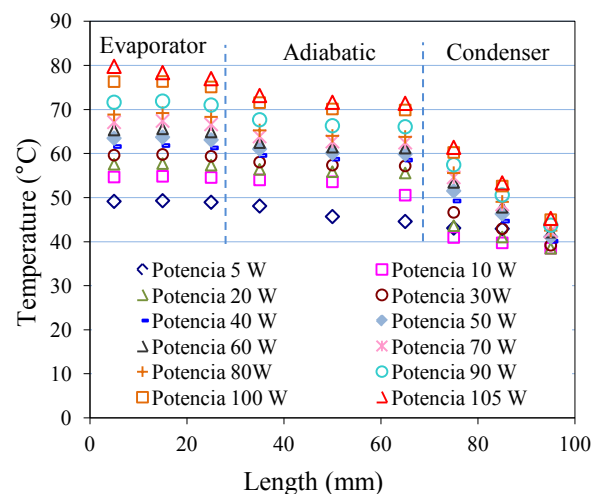


Figure 8. Experimental data sample PAM50PAC50 1.5 ml

For the working fluid volume of 1.5 ml, the MHP has the lower the thermal resistance 0.35 °C/W. The model expressed by equation 1, when applied to this configuration and to operating temperature of 75 °C, predicts a capillary limit of the 108 W. The experimental data indicate that the tube is able to transport up to 100 W, for an average evaporator temperature of 76 °C. As already observed, for the 104 W power level, the evaporator temperature quickly increases, showing the beginning of dry-out. The capillary limit calculated by Equation 1 present an accuracy of approximately 8% for this

configuration. However for PAM75PAC25 sample, the comparison between model and data is not good.

6. CONCLUSIONS

In the present paper, it was demonstrated that the use of layers of different porosities modify the thermal behavior of mini heat pipes, showing that this is an interesting configuration as they can combine high pumping capacity and low pressure drop. Tests conducted on the PAM50PAC50 MHP (two layers of same thickness, made of powder of different sizes), showed a 20% increase of the maximum power transported (100 W) in comparison to the conventional tube with a single layer of PAM material.

NOMENCLATURE

K	Permeability	[m ²]
k_e	Effective thermal conductivity	[W/(m · K)]
q	Power	[W]
R_t	Total thermal resistance	[°C/W]
r_c	Critical radius	[m]
C	Fluid constant	
f_v	Friction factor	
Re_v	Reynolds number in vapor	
$r_{h,v}$	Hidráulic radius in vapor	[m]
A_v	Transversal area in vapor	[m ²]
A_w	Transversal area in liquid	[m ²]
h_v	Enthalpy of vapor	[kJ/kg]
h_{lv}	Enthalpy of saturation	[kJ/kg]
l_{ef}	Effective length	[m]
g	Acceleration of gravity	[m/s ²]
P_e	Power inlet	[W]
\bar{T}_{eva}	Average temperature in the evaporator	[°C]
\bar{T}_{cond}	Average temperature in the condenser	[°C]

ACKNOWLEDGEMENT

The authors acknowledge the National Council for Scientific and Technological Development (CNPq) for financial support through Universal Project and scholarships. They also acknowledge CAPES for the financial support via scholarships and EES

Company for supplying the image analysis software IMAGO® license.

REFERENCES

- Berre, M. L., Launay, S., Sartre, V., Lallemand, M. (2003) *Fabrication and experimental investigation of silicon micro heat pipes for cooling electronics*. J. Micromech. Microeng. 13, p. 436-441.
- Cao, Y., Faghri, A., Mahefkey, T. E. (1993) *Micro/Miniature Heat Pipes and Operating Limitations*. HTD-Vol. 236, ASME.
- Chen Y. M., Wu S. C., Chu C. I. (2001) Thermal performance of sintered miniature heat pipes. Heat and Mass Transfer 37, pp 611-616.
- Dunn, P. D.; Reay, D. A. (1994) *Heat Pipes*, Pergamon. 4. ed.
- Faghri, A. (1995) *Heat Pipe Science and Technology*. Ed. Taylor & Francis, 874p, Washington, USA, 1995.
- Florez, J. P. M., Nuernberg, G. G. V., Mantelli, M. B. H., Almeida R. S. M., Klein A. N. (2011) *Effective Thermal Conductivity of Layered Porous Media*. Proc. of 10th Int. Heat Pipe Symp., Taipei, Taiwan.
- Mantelli, M. B. H., Buschinelli, A. J. A., Nascimento, R. M., Paiva, K. V. (2002) *Diffusion welding of wire micro heat pipe arrays*. Proc. 12th Int. Heat Pipe Conf., Moscow-Kostrona-Moscow, Russia.
- Nuernberg, G. G. V., Florez, J. P. M., Mantelli, M. B. H., Almeida R. S. M. (2011) *Experimental Permeability of Sintered Porous Media Multilayer*. Proc. 21st Brazilian Cong. of Mech. Eng. ABCM, Natal RN, Brazil.
- Paiva, K. V. (2007) *Thermal behavior of mini heat pipes kind wire and flat plate in gravity and microgravity conditions*. Dissertation. Pós-Mec UFSC. (in Portuguese).
- Peterson, G. P., Babin, B. R., Wu D. (1990) *Steady-State Modeling and Testing of a Micro Heat Pipe*, J. Heat Transfer, Vol 112, p. 595.
- Vasiliev, L. L. (2006) *Micro and Miniature Heat Pipes – Electronic Component Coolers*. App. Thermal Eng.
- Xiao, H., Franchi, G. (2008) *Design and Fabrication of Hybrid Bi-modal Wick Structure for Heat Pipe App*. J. Porous Mater, 15, p. 635-642.
- Yeh, C. C., Chen C. N., Chen Y. M. (2009) *Heat Transfer Analysis of a Loop Heat Pipe with Biporous Wicks*. Int. J. Heat and Mass Transfer, 52 (2009), p. 4426–4434.

ATV ACTIVE THERMAL CONTROL WITH VARIABLE CONDUCTANCE HEAT PIPES: DESIGN DESCRIPTION AND IN FLIGHT RESULTS

Patrick Oger

ASTRIUM Space Transportation
66, Route de Verneuil B.P. 3002 78133 Les Mureaux Cedex - France
Phone: +33 1 39 06 24 50, Fax: +33 1 39 06 39 93
Patrick.oger@astrium.eads.net

Frank Bouckaert

ESA/ESTEC
Keplerlaan 1, 2201 AZ Noordwijk - The Netherlands
Phone: +31 71 565 64 93, Fax: +31 71 565 50 92,
Frank.Bouckaert@esa.int

ABSTRACT

This paper presents the thermal control of the Automated Transfer Vehicle (ATV) Spacecraft and more particularly the active control of the heat rejection using 40 Variable Conductance Heat Pipes (VCHP) that has been developed in order to optimize the overall energy balance of the vehicle during the all the phase of its flight. First a short overall description, of the vehicle, its mission and its overall thermal control, is presented. Then the definition of the active thermal control design is given in more details as well as the associated thermal tests performed during the development and qualification phases that have allowed characterizing and validating the principle of the thermal control. Finally the performances of the active thermal control during the two first flights ATV1 Jules Verne in 2008 and ATV2 Johannes Kepler in 2010 are exposed and some comparison between post flight predictions and the flights measurements are presented showing the good global accuracy of the mathematical models built during the development phase and validated on the ground test results.

KEY WORD: VCHP, spacecraft thermal control, heat rejection management

1. INTRODUCTION

The Automated Transfer Vehicle (ATV) is a space transport vehicle developed by ESA with ASTRIUM Space Transportation as prime contractor for the logistic servicing of the International Space Station (ISS) on the Russian segment side through delivering of dry cargo, water gas and propellants, contributing to the ISS attitude control and reboost and disposing of ISS wastes.

During its whole mission the ATV is exposed to very variable internal and external thermal conditions (high or low dissipation phases, wide range of solar directions exposure, shadowing periods induced by ISS, ...). These conditions drove to develop a thermal control system based on VCHP technology to control the rejection of the heat generated by the avionic items and on actively controlled heaters lines for thrusters and pressurized module.

The design has been validated by ground tests at sub assembly and vehicle level and the flight performances have been verified during the two first flights (ATV1 Jules Verne in 2008 and ATV2 Johannes Kepler in 2010).

2. ATV GENERAL DESCRIPTION

2.1 General design description

The ATV is composed of two main parts: the Integrated Cargo Carrier (ICC) and the Spacecraft (SC) as shown on figure 1.

The ICC is designed to transport the dry cargo inside the Pressurized Module (PM) and fluids and gases inside the non-pressurized External Module (EM). It accommodates also the Russian Docking System (RDS) for connecting the ATV to the ISS as well as the optical sensors used to perform the rendezvous with the ISS.

The Spacecraft is an unpressurized module that accommodates most of the functions and resources needed to perform the ATV mission. It is composed of:

- The Equipped Avionics Bay (EAB) that accommodates most of the avionic items mounted on 10 Active Fluidic Cooling Units (AFCU)
- The Equipped Propulsion Bay that accommodates the propulsion system composed of 8 propellants tanks, 4 main thrusters and 4 clusters of attitude control thruster and the Solar Generator System (SGS) composed of 4 rotating Solar panels

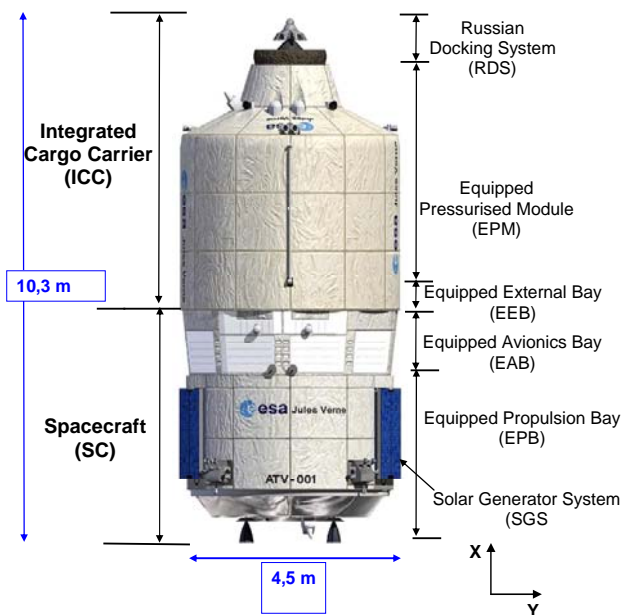


Figure 1: ATV general layout

2.2 Mission and main thermal requirements

After launch, the ATV performs a phasing and a rendezvous with the ISS on an orbit inclined at 51.6° and with an altitude between 300 km and 460 km.

During free flight, the vehicle has two main attitudes:

- Yaw steering used the most of the time (+ZATV toward Earth and XATV in the plane ATV/Earth/Sun, with -XATV towards the Sun)
- LVLH used for boost and final rendezvous phase (+ZATV toward Earth and +XATV towards velocity)

During attached phase the ISS attitude is most of the time close to LVLH attitude.

Due to the high inclination of the orbit, the angle between sun direction and orbital plane called Beta angle is varying between -75° and $+75^\circ$ in one year. Combined with the various attitudes, it induces a very large range of Sun directions on ATV.

The internal power dissipation level is of about 1100 W during phasing phase up to 2000 W during final rendezvous phase and down to 700 W during dormant attached phases.

The main thermal requirements are shown in table 1 and 2 for both temperature range and heater power allocation.

Table 1: Temperature range requirements

Temperature requirements °C	Min T	Max T
Avionics items	-20	+50
Rechargeable Batteries	+10	+17
Internal propulsion items	0	+40
Water cargo at delivery	16	+30
Fuel cargo at delivery	0	+38
PM internal surfaces	16	+45

Table 2: maximum heater power allocation

	Heater power (orbital average) W
Free flight	750
Attached	630

2.3 Overall thermal control description

The ATV thermal control baseline is shown on figure 2 and consists of:

- Passive external Multi Layers Insulation (MLI) to protect all the internal compartments and structure from the external environment
- 240 heater's lines, to compensate the heat leakage towards space. The heater's lines are controlled individually by the Flight Applicative Software via thermistors. They are installed externally on the structure of the pressurized module, on the thruster platform and on external items (thrusters and rendezvous sensors),
- Controlled heat rejection of spacecraft dissipation loads. This rejection is controlled by 40 Variable Conductance Heat Pipes, so as to control the overall vehicle heat balance and minimize the heater power budget

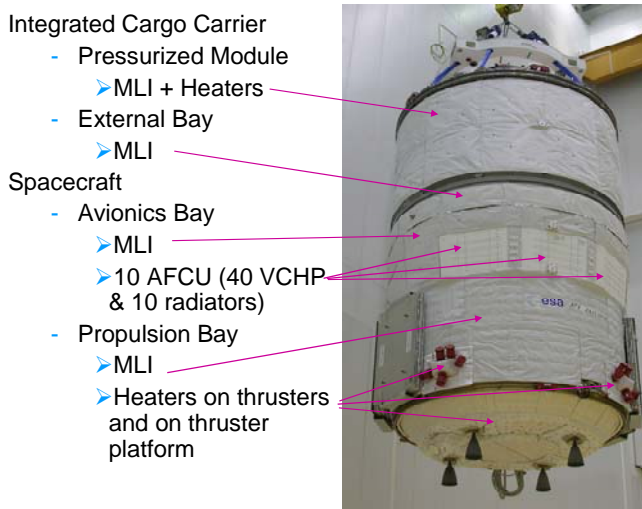


Figure 2 Overview of the thermal control

3. ACTIVE THERMAL CONTROL DEFINITION

3.1 General description

The active thermal control implemented in the EAB consists of 10 Active Fluidic Cooling Units (8 for avionics and 2 for batteries). Each AFCU includes (see also Figure 3):

- 4 internal equipment support tray,
- 1 external radiator plate (PSB white paint),
- 4 VCHP,
- 4 specific radiators and heater lines to control the temperature of each VCHP reservoir

The radiators are thermally insulated from the structure via non conductive brackets and MLI

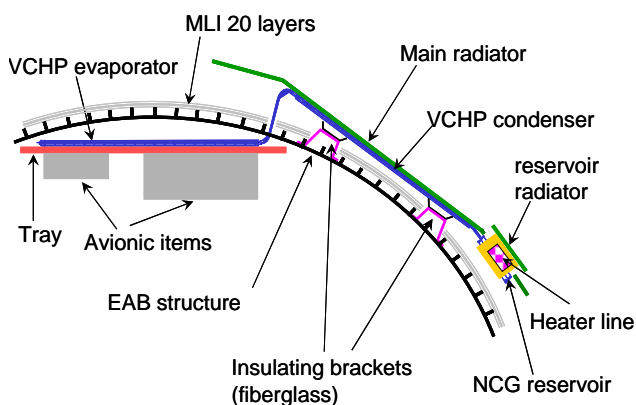


Figure 3 AFCU-A layout principle

The Batteries AFCU have in addition 4 CCHP installed between the support tray and the VCHP evaporators to homogenize the batteries cells

temperatures and an internal MLI tent to ensure thermal insulation between batteries and EAB internal environment.

3.2 VCHP definition

The VCHP and CCHP are provided by Euro Heat Pipe (EHP) (Mullender 2005). The VCHP are of the type A95 in stainless steel with aluminum saddles and NH3 as working fluid and N2 as non condensable gas and the BCCHP are of type AG110

Due to the various environments and internal conditions, 4 types of NCG loading of the VCHP have been defined, depending of the requested conditions (temperatures of NH3 vapor, condenser and NCG reservoir) in full ON and full OFF states.

3.3 VCHP control principle

The control of the conductance of each Avionics VCHP is done through the heating of the reservoir. The heater line is switched ON or OFF according to the algorithm shown on figure 4 using the reservoir and evaporator temperature measurements.

Each 10s the temperatures are measured and the following test is done:

- If the evaporator temperature is higher than the control temperature, the heater is switched OFF so as to cool the reservoir and increase the VCHP conductance.
- If the evaporator temperature is lower than the control temperature and the temperature difference between evaporator and reservoir is lower than 3°C the heater is switched ON in order to heat the reservoir and reduce the VCHP conductance.

The test on the temperature difference between evaporator and reservoir is performed in order to optimize the reservoir heater power consumption considering that when that difference is lower than 3°C the VCHP is full OFF and any additional heating of the reservoir is wasted.

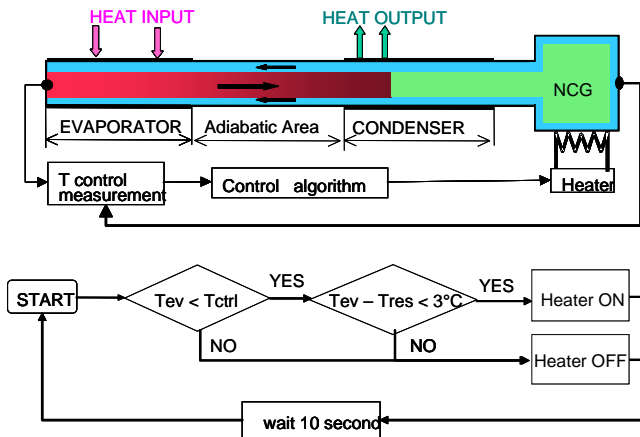


Figure 4 control algorithm of the VCHP-A

The conductance control of Battery VCHP is achieved according to similar principles except that the control temperature is compared to the battery temperature, instead of the evaporator temperature.

The thermal analyses and the tests performed during development and qualification of ATV have lead to define a common temperature control value of 15°C for all avionics AFCU and all the mission phases, with an option to increase it up to 20°C in case of failure.

For batteries AFCU, the temperature control has been set to 15°C for optimization of the charge/discharge cycle.

4. THERMAL QUALIFICATION TESTS

The following thermal test program has been settled.

4.1 VCHP test

The VCHP technology at EHP had been qualified from a long time. A program of qualification complement tests has been made in 2002 for the qualification of ATV specificity like shape, conductance and conductance control temperature values. Each VCHP type has been tested and the data issued from those test have been used for the development and validation of the VCHP Thermal Mathematical Model.

4.2 AFCU-A test

This development test has been achieved in February 2002 at INTESPACE SIMDIA Chamber (Toulouse France). The test objective was to

validate the VCHP control architecture and algorithm and to characterize the assembly thermal properties under a number of various environmental conditions. This test is presented in Vincent, Rochas et al (2003).

The test item was one avionic AFCU with thermally representative dummy equipments. The radiator was exposed to a controlled variable IR environment using IR lamps. Some extreme conditions have been tested like iced condenser, avionic over dissipation, over heating of the gas reservoir or de-priming.

The data from the various phases of this test have been used to validate the detailed AFCU Thermal Mathematical Model (TMM) as well as a simplified VCHP TMM (4 thermal nodes) that has been implemented inside the ATV Overall TMM. The figure 5 shows the comparison between test results and predictions for a case with VCHP full OFF.

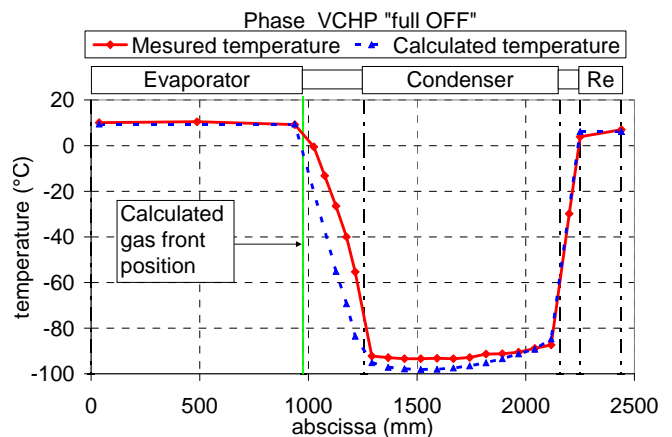


Figure 5: AFCU test – case VCHP full OFF

4.3 STM test

This qualification thermal balance test has been achieved in July 2002 in the Large Space Simulator of ESTEC (Noordwijk, The Netherlands) on the Structural Thermal Model (STM) of the ATV (presented in Vincent, Joulot et al. 2003). The test objectives were to validate the SC control architecture, to characterize the assembly thermal properties and to correlate the mathematical thermal model. The thermally tested item was limited to the unpressurised parts of the ATV, excluding the Pressurized Module for test simplification purpose and the solar generator. The vehicle was installed in a vertical position and was exposed to:

- the low temperature of chamber shrouds (< 100 K)

- an Earth flux simulator composed of 45 panels thermally controlled regulated by heaters
- a temperature controlled panel on the aft ATV side that was either cooled by liquid Nitrogen (<100 K) or heated by heaters to reproduce the sink temperature in sun pointing mode
- the solar flux simulator (6 meters diameter) of the chamber.
- variable dummy equipment dissipation representative of the avionics dissipation.

This test set-up allowed achieving several thermal balances and transients' representative for various mission phases. This test validated the global TCS architecture and resulted in a very satisfactory correlation of the OTMM of the ATV vehicle for prediction of temperature and heater power budget.

An interesting test observation was done on the Battery Variable Conductance Heat Pipes that were working in thermo siphon .After around two hours of effective control in OFF mode; the heat transfer restarted whatever the temperature of the NCG reservoir.

5. IN FLIGHT RESULTS

During the first ATV flight (Jules Verne), the active thermal control has demonstrated excellent performances with a very stable control during the entire mission whatever the dissipation level and the vehicle attitude. The temperatures at evaporator level for avionic trays have been generally controlled within a range of +/-0.5°C and the batteries temperature in a range of +/- 1°C. The flexibility of the system has also been validated by the reconfiguration of the control of AFCU from 15°C to 20°C during free flight in order to reduce the negative effects of the degraded MLI on ICC. The flight results of the second ATV Johannes Kepler have confirmed the performances of the system.

The figure 6 shows the temperature evolution of one VCHP on the AFCU1 during the launch and first orbits phase. It can be observed the start of the VCHP heat transfer when the condenser reaches a sufficient cold temperature; then, after a cooling period, the control starts and the evaporator temperature stays very stable at 15°C although, externally, the condenser temperature is cycling following the day/night orbital cycle and, internally, the dissipation inside the Power

Conditioning and Distribution Unit (PCDU) is also cycling.

The figure 7 shows the temperatures evolution for the batteries AFCU10 from launch until stabilization. It can be shown that, when the control starts the regulation of the VCHP is cycling between full ON and full OFF mode instead working at a stabilized point like the VCHP on avionic AFCUs. This specific behavior is due to the high thermal inertia of the batteries and of the position of the regulation point on the batteries (far from the VCHPs). It is in accordance with the temperature behavior predicted by the TMM as shown on figure 8.

Regarding the heater power budget needed to perform the control of the VCHP, the flight results for both flights are very close to the predicted values with difference of about 10% on the total budget as shown on figure 9. Its demonstrate that the correlation of the simplified AFCU TMM made during the qualification test campaign is valid for flight prediction

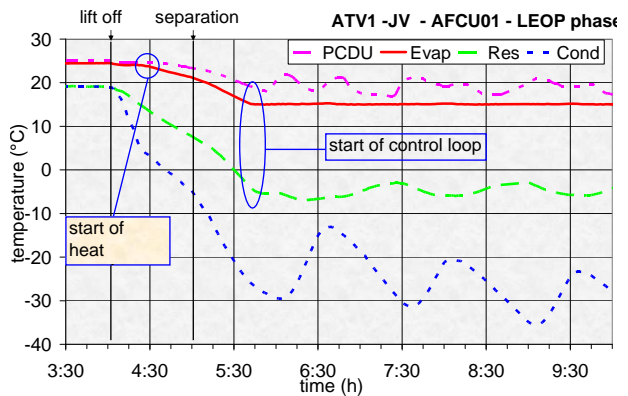


Figure 6: ATV1 flight results on AFCU1 avionics

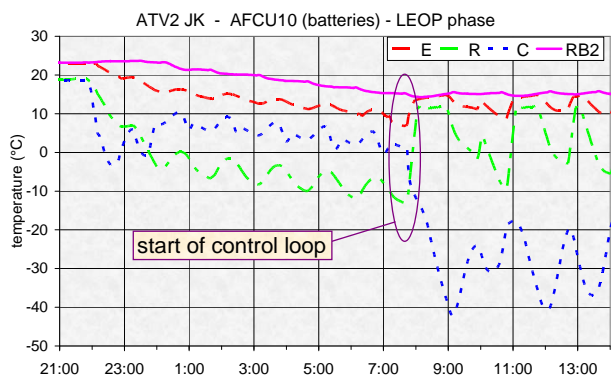


Figure 7: ATV2 flight results on AFCU10 batteries

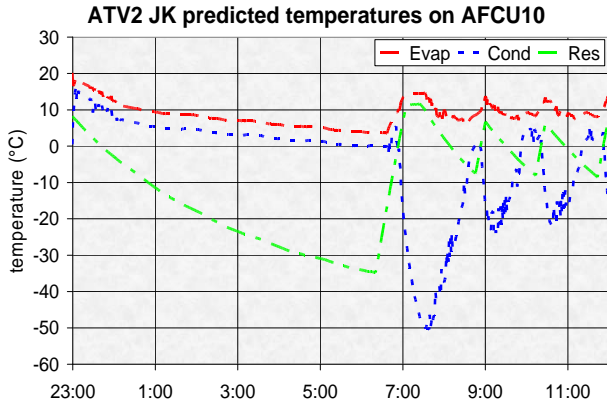


Figure 8 predicted temperatures on AFCU10

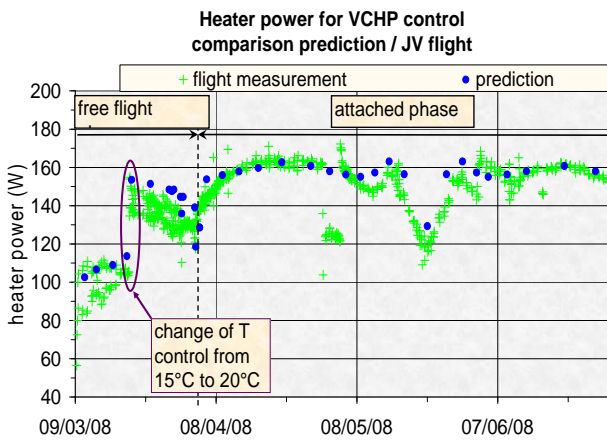


Figure 9: heater power for control

6. CONCLUSIONS

The innovative active thermal control of the ATV based on VCHP technology has successfully fulfilled its mission during the two first ATV flights in 2008 (ATV Jules Verne) and in 2010 (ATV Johannes Kepler).

It has shown a very accurate temperature control of the avionics equipments and rechargeable batteries and it has demonstrated robustness in the margins allowing flexibility on the temperature control level.

The exploitation of the flight measurements has also shown the quality of the simplified Thermal Mathematical Model of VCHP allowing to predict with a good accuracy the heater power budget for VCHP control all over the mission.

For future space applications derived from ATV the use of Loop Heat Pipe instead of VCHP is considered because this technology is now mature enough and is offering more flexibility with

respect to the physical implementation inside the vehicle.

NOMENCLATURE

AFCU: Avionic Fluidic cooling Units
 ATV: Automated Transfer Vehicle
 CCHP: Battery Constant Conductive Heat Pipe
 EAB: Equipped Avionic Bay
 EM: External Module
 EPB: Equipped Propulsion Bay
 FM: Flight Model
 HP: Heat Pipe
 ICC: Integrated Cargo Carrier
 ISS: International Space Station
 LVLH: Local Vertical Local Horizontal
 MLI: Multi Layer Insulation
 NCG: Non Condensable Gas (here Nitrogen)
 NH₃: Ammonia
 PM: Pressurized Module
 RDS: Russian Docking System
 SC: Spacecraft
 SGS: Solar Generator System
 STM: Structural and Thermal Model
 TMM: Thermal Mathematical Model
 VCHP: Variable Conductive Heat Pipe

REFERENCES

- Mullender. B (2004) Design and Manufacturing of Heat pipes on ATV. Proc. 13th Int. Heat Pipe Conf., Shanghai.
- Vincent P., Rochas L. Menut P. and Romera-Perez JA., (2003) "Thermal Test of the Active Fluidic Cooling Unit of ATV", 03ICES-276.
- Vincent P., Joulot A., Ruffino F., Romera-Perez JA. and Signetti. M. (2003) "Structural Thermal Test – Thermal Balance Test of ATV ". 03ICES-277

AUTONOMOUS HEAT PIPE THERMAL CONTROL SYSTEMS FOR CCD COOLING OF SPACE SCIENTIFIC EQUIPMENT

Baturkin V.

Heat Pipe Laboratory, National Technical University of Ukraine "KPI", Kyiv, Ukraine &
Department of System Conditioning, Institute of Space Systems, Bremen, Germany
Pr. Peremogy, 37, 03056, Kyiv, Ukraine
Robert-Hooke-Str. 7, 28359 Bremen, Germany
Phone: +49421 – 2442011610, fax: +49421 244201120, email: baturkinvm@mail.ru

ABSTRACT

The approach of heat pipes' implementation into passive radiative cooling system is considered for optical sensors (CCD), operating on the temperature level of 180...240 K in unsteady regime. Heat pipes have shown themselves as effective heat transfer element used for heat moving from sensor to radiator on distance up to 0.5 m and as heat redistribution element, being integrated into low temperature radiator. In order to avoid the negative influence of the external heat fluxes the system design with a set of thermally coupled radiators, interconnected with heat pipes (conventional and thermodiodes) is proposed. This design allows to keep the low temperature level of CCD at spacecraft maneuvers and to widen the operation range of solar constant.

KEY WORDS: sensor, passive, cooling, thermal control, heat pipe

1. INTRODUCTION

Required temperature level of sensitive elements of optoelectronic devices, which are widely used at the Earth observation and in IR astronomy, depends on type of optical sensor, acceptable signal-to-noise ratio and makes 80...260 K. Own heat generation in sensitive element is small enough (tens-hundreds milliwatts – watts), however heat leakage to sensor from mounting place, having the temperature within 253...323 K, could be one order more.

At the space exploitation of sensors the temperature level of 80...260 K can be reached by thermoelectric coolers (partly), radiation systems, systems with expendable substances and others ways (Donabedian et al. (2004)). The boundary conditions for heat sink, power consumption and operation duration play the key role at choice of cooling principle.

Design of sensor module, having CCD (charge couple device), for example, with sizes of 15 x 11 mm is characterized by additional heat inputs from mounting place in the range of 0.3...1 W in vacuum at 240 K (Avanesov et al. (1989)). This value rises with enlarging the CCD array size. For passive radiative system one of important parameter is the distance between CCD module and radiator, which defines the length of heat

transfer, mass and dimension of transfer line (figure 1). Heat pipe (HP) is the promising candidate for this task (Gilmore et al. (2002)).

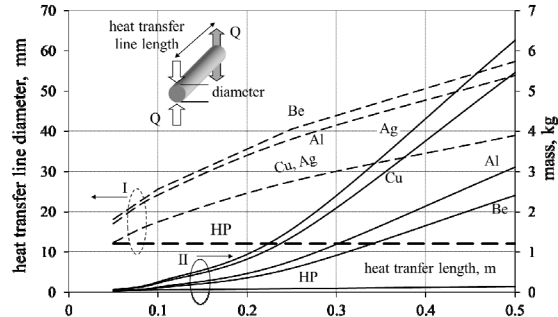


Figure 1. Comparison of mass and diameter of heat transfer line at fixed thermal resistance of 1K/W (configuration - rod) made of solids (Ag, Al, Be, Cu) and axial grooved heat pipe on temperature level of 183 K. Group I corresponds to external diameter of rod, group II – to mass.

2. THE BASIC PRINCIPLES OF RADIATIVE COOLING SYSTEM WITH HEAT PIPES

There are the following possible approaches to thermal control system (TCS) design for CCD cooling. The first one (active) deals with the use of thermoelectric cooler. The sensor or sensor module has perfect thermal contact with cold junction of the thermoelectric cooler, which ensures the

required temperature level. Hot junction has connection with heat sink like device mounting places on spacecraft (SC), radiator or liquid cooling line. Heat leakage Q_{mp} and heat released in matrix Q_d are input to thermoelectric cooler (they are its cooling productivity). Heat rejection from hot junction Q_{TB} is higher than heat input ($Q_{mp} + Q_d$) in 4...15 times. This heat has to be rejected by additional cooling system to mounting place, where device is installed, or to radiator. The temperature of hot junction is on the level of 270...360 K. Heat pipe could transfer the heat from sensor to thermoelectric cooler or from thermoelectric cooler to radiator.

Radiative TCS uses the low temperature of environment as a heat sink and is passive (figure 2). Heat energy ($Q_{mp} + Q_d$) is removed from CCD by heat conductors of any type with the thermal resistance R_c, R_1, R_2, R_3 towards low temperature radiator (or radiators) and is scattered to the space. In this scheme the main difficulty is to achieve the temperature of radiator(s) 180...250 K taking into account the external light disturbances (solar flux, planet fluxes, reflection from nearby devices) and heat leakage to radiator via mechanical stands-off (st) and multilayer insulation (MLI).

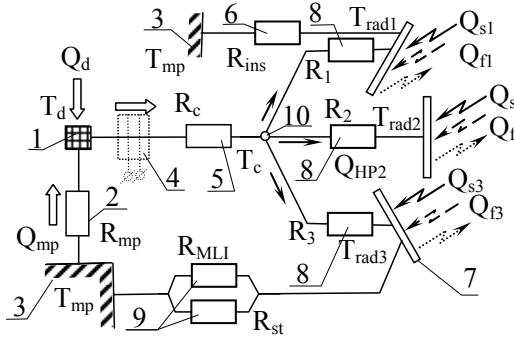


Figure 2. Thermal scheme of passive radiative TCS: 1 – CCD or device to be cooled; 2 – thermal resistance “mounting place – device”; 3 – mounting places; 4 – thermoelectric cooler (optional), 5 – resistance of heat conductor; 6 – resistance R_{ins} “radiator – mounting place”; 7 – radiators (temperatures $T_{rad1}, T_{rad2}, T_{rad3}$); 8 – resistances R_1, R_2, R_3 between central point and dedicated radiator(s); 9 – components of resistance R_{ins} : R_{st} and R_{MLI} ; 10 – central point; Q_s, Q_f – absorbed by radiator heat fluxes in Sun spectrum and IR range. 1-3 radiators could be considered.

Minimization of TCS mass and its overall sizes requires the reduction of the thermal resistance of

all conducting lines (one of variant is the use of heat pipe with resistance less than 0.1...1 K/W), decrease of all contact resistances, increase of radiator efficiency by optimizing its thickness, to optimize thermal scheme, to enhance the optical coating parameters, and to limit the external fluxes to radiator. Mechanical connection of CCD with heat transfer line has to be flexible in order to provide the adjustment of optical axis and to avoid the excessive mechanical loads.

The typical specimen of passive radiative system with heat pipe was presented by Semena et al. (1986). TCS serves two CCD modules, functioning in parallel. Heat leak to every module from mounting place is collected by flexible cooper conductor, then it is transferred to heat pipe (external diameter 8 mm, stainless steel shell/metal fiber wick/refrigerant R22) and, finally, the heat is radiated into the space. TCS was designed to operate not less than 30 min in conditions of Sun light illumination. The compensation of heat inputs to radiator is realized by increasing the radiator mass and by use of melting type heat accumulators (3 units, mass 0.08 kg each, melting temperature 239 K). Figure 3 presents the operation function of such system (Avanesov et al. (1989)).

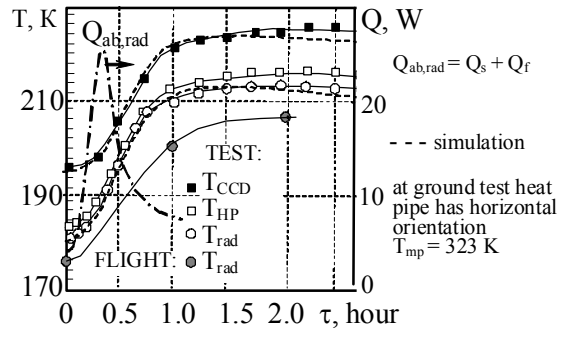


Figure 3. Thermal behavior of system in vicinity of Venus orbit. Flight telemetric radiator temperature for regime K-4 for spacecraft “VEGA-1” is being compared with ground thermal vacuum test. T_{CCD}, T_{rad}, T_{HP} – temperatures of CCD, radiator, connection of flexible with heat pipe.

Research of TCS with four CCDs modules, attached to one radiator (figure 4), has shown that without heat pipe, which re-distributes the heat over the radiator surface, not uniformity of places, where the flexible elements are attached, could reach 14 K (Baturkin et al. (1988)).

At integration of heat pipe (external diameter 10 mm, stainless steel shell/metal fiber wick capillary

structure/refrigerant R22) into radiator design this difference is reduced by 3.5 K at heat load of 1.5 W per CCD module.

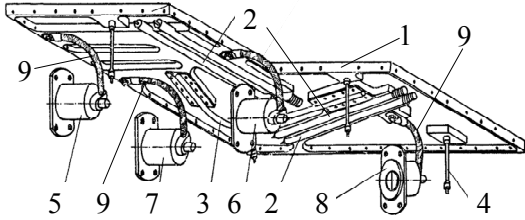


Figure 4. TCS with HP for four CCDs (figure by Dr. Kostenko V.): 1 – radiator (0.3 x 0.3 x 0.01 m); 2 – heat accumulators; 3 – HP; 4 – stands-off; 5, 6, 7, 8 – CCD modules; 9 – flexible transfer lines.

Choice of heat capacity and reducing the temperature non uniformity by embedded heat pipe allows to keep its temperature in steady and unsteady conditions, which occur at illumination of radiator by the Sun (angle of incidence of sunbeams φ_s). For this regime it was shown an ability to keep the radiator temperature $T_{rad} < 223$ K during 11 hours of TCS functioning at Phobos scanning by videospectrometric complex (figure 5).

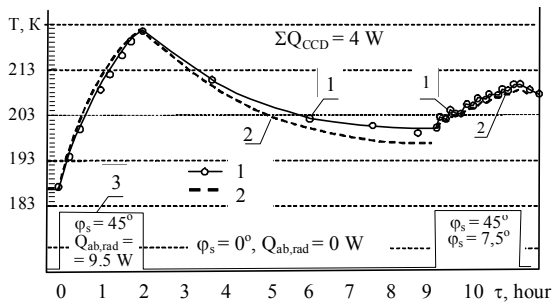


Figure 5. Average radiator temperature of TCS with 4 CCDs in regime, simulated movement of spacecraft near Phobos and approach with the surface: 1 – experimental data; 2 – simulation; 3 – profile of flux, absorbed by radiator $Q_{ab,rad} = f(\tau)$.

HPs in TCSs have bent configuration, the metal fiber wick with stepwise porosity change in evaporator, transport and condenser zones in order to reduce the total thermal resistance, saving heat transfer ability. Refrigerant R22 was selected due to its low melting temperature (113 K), possibility to operate in wide temperature range (170...300 K) and its compatibility with stainless steel, long life stability against factors of space and successful space qualification (Alekseev et al. (2006)).

In ground thermal vacuum tests of the assembly

“TCS + device” and “device together with spacecraft”, there is the obligatory requirement to provide heat pipe operation against gravity forces where heat has to be lifted up to $\Delta h = 250$ mm. Due to insufficient value of surface tension and heat of evaporation the refrigerants could not operate because of hydrodynamic crisis (figure 6). For such tests the subsidiary heat pipes with ammonia have been designed, having the same thermal resistance.

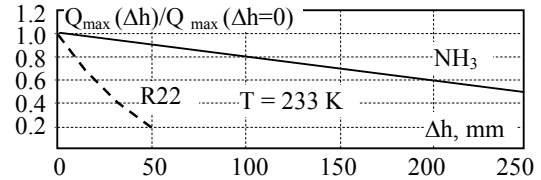


Figure 6. Comparison of maximal heat transfer ability of heat pipe with refrigerant R22 and ammonia NH_3 at different tilts against gravity.

Considered TCS operates only for a limited time, if the radiator is illuminated with the Sun. Before an operation starts the radiator should be cooled down. In the cases, if spacecraft should have the freedom in an orientation relative to the Sun, and the sensor should be in constant readiness for a long time, the considered principle of TCS design meets the evident difficulties in realization and a new approach should be elaborated.

3. CONCEPTION OF TCS WITH REDUCED SENSITIVITY TO EXTERNAL HEAT FLUXES

The major restriction of passive radiative systems to achieve the temperature level of 180...250 K is the effect of heat fluxes Q_s and Q_f , which cause the radiator temperature rise, and increasing of radiator sizes does not keep its required temperature. This limitation could be estimated by the following heat balance equation for the radiator:

$$Q_d + Q_{mp}(T_{CCD}, T_{mp}) + \frac{T_{mp} - T_{rad}}{R_{st}(F_{rad})} + \frac{T_{mp} - T_{rad}}{R_{MLI}(T_{rad}, F_{rad})} + Q_s(\tau, F_{rad}) + Q_f(\tau, F_{rad}) \leq C_{rad} \frac{dT_{rad}}{d\tau} + \varepsilon F_{rad} \eta \sigma (T_{rad}^4 - T_o^4),$$

where T_{rad} – feasible radiator temperature; R_{st} , R_{MLI} – thermal resistances of mechanical stands-off and MLI package, insulating the radiator; C_{rad} , ε , F_{rad} , η – heat capacity, IR emittance, area and thermal efficiency of radiator, correspondently; σ – Boltzmann constant. The most important

magnitude, defining T_{rad} in the majority cases, is Q_s . particular the direct Sun illumination.

The TCS, having several radiators, variously oriented relative to the Sun, and having thermal interconnection between radiators, is one of the promising technical solutions to overcome the restriction of direct solar illumination. In this design one of radiators will always reside in favorable conditions (in shadow), provide heat removal and keep the demanded temperature level as well (figure 7).

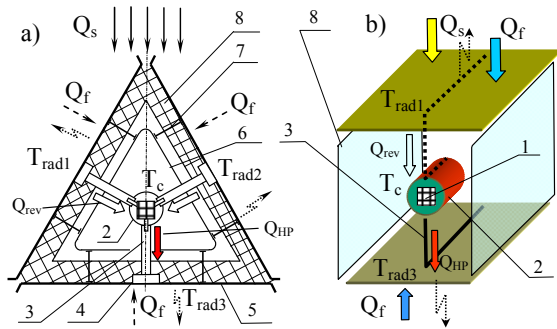


Figure 7. Design of passive multi-radiators' cooling system: a) with three radiators; b) with two radiators: 1 – CCD module; 2 – positioner and central point; 3 – heat pipe – thermal diode (TD); 4 – heat pipe attachment to radiator; 5 – radiator; 6 – inner support structure; 7 – stands-off; 8 – MLI blankets.

An analysis of such TCS with 2-3 radiators (curve $R_{HP} = const$, figure 8) has shown that such approach is more effective as compared with one radiator system. But to obtain essential reducing of CCD temperature, element which thermally joints CCD and the radiator, has diode type thermal resistance, depending on direction of heat flux (curve $R_{HP} = var$).

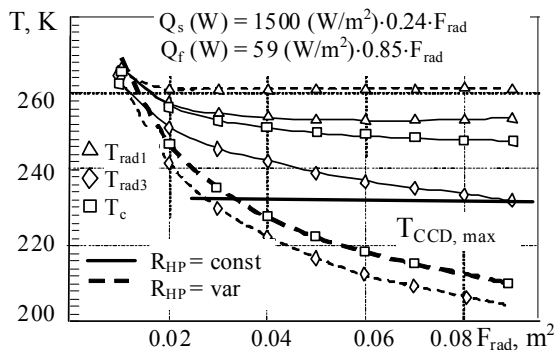


Figure 8. Required radiator area for three-radiators' system on near-Earth orbit at $Q_{mp} + Q_d = 2W$.

2W. Solid lines – heat pipes of constant resistance, $R_{HP} = const = R_1 = R_2 = R_3 = 2 K/W$ in direct and reverse mode, dashed – variable resistance heat pipe with 2 K/W in direct mode and 100 K/W in reverse mode ($R_{HP} = var$).

This property is intrinsic to the heat pipe, named as thermal diode (Groll et al. (1978), Williams et al. (1978)), which has essential thermal resistance in reverse mode, when heat is transferred from hot (exposed on the Sun) radiator to a cold central point, and low resistance – in direct mode. The system will operate if the Sun changes its position relative to radiators, one of them should be in shadow.

The temperature of optical sensor could be less than 233 K at external heat fluxes in the range of 500...2700 W/m² that corresponds to the operation in vicinity of Mars, Earth and Venus (figure 9).

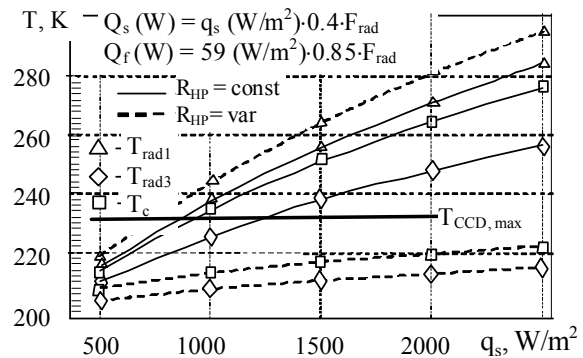


Figure 9. Achieved sensor temperatures for orbits of Mars, Earth, Venus for three-radiators' system with heat generation $Q_{mp} + Q_d = 2W$. Solid lines are related to the heat pipes of constant resistance, $R_{HP} = const = R_1 = R_2 = R_3 = 2 K/W$ in direct and reverse mode, dashed – to the variable resistance heat pipes with 2 K/W in direct mode and 100 K/W in reverse mode ($R_{HP} = var$).

One can find that the system, operating with thermal diodes could provide much low temperature of central point T_c as compared with constant resistance heat pipe system in considered range of external heat fluxes. For example, for Venus orbit these temperatures are 223 K and 275 K, correspondently.

4. VERIFICATION OF PROPOSED CONCEPTION OF MULTI-RADIATORS TCS

The theoretic approach has been proved on the thermal mock-up of star tracker TCS with two

radiators (figure 10). In this system the heat generated by optical element, and heat leak are removed by constant conductance heat pipe to central point and then by two thermal diodes towards the radiators. The heat pipe system seats on the device cabinet, using low conductance stands-off. The radiators and heat pipe are protected from external fluxes by MLI.

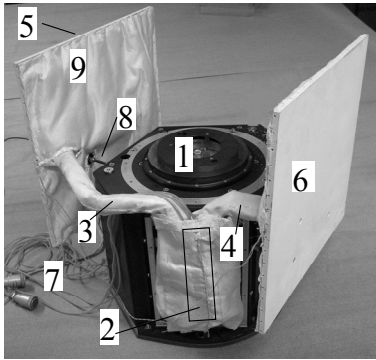


Figure 10. Design of passive two-radiators' cooling system: 1 – cabinet for sensor (CCD); 2 – central point and contact with constant conductance heat pipe; 3, 4, – thermal diodes; 5, 6 – radiators 1 and 2; 7 – harness; 8 – low thermal conductance stands-off; 9 – MLI blankets.

Thermal diode design uses the principle of liquid trap located in the evaporation zone (placed in central point). Material of heat pipe shell – stainless steel 12X18H9T, capillary structure – metal sintered fibers made of the same stainless steel, heat carrier refrigerant R22 (figure 11). Thermal diode shell was made of tube OD 10 mm and is bent in two planes according to the geometric requirements to be adapted to the device configuration.

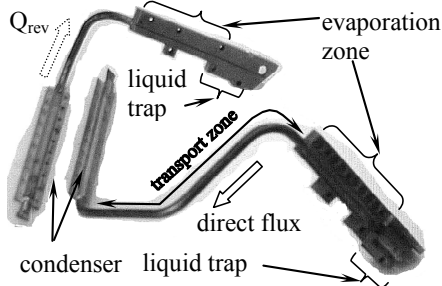


Figure 11. View of thermal diodes for two heat conductive lines.

The experimentally defined thermal resistance R_{rev} and heat flux Q_{rev} in reverse direction of heat transfer are given on figure 12. In initial moment

the TD runs as conventional heat pipe with the changeable heat-carrier mass. After accumulation of the major quantity of working liquid in liquid trap the complete drying of the radiator zone and adiabatic zone occurs and heat transferred in this direction is decreased essentially.

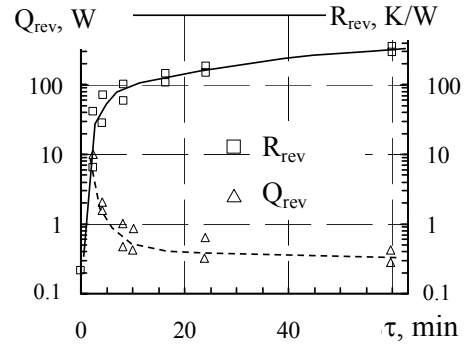


Figure 12. Summarizing of the heat flux (Q_{rev}) and thermal resistance of TD (R_{rev}) in reverse mode.

For chosen conditions the computation displays that thermal diode resistance grows up to the values of 100 K/W in the first 10 minutes that well agrees with experiment. Analyzing the common operation of two thermodiodes as components of thermal control system, it should be noted that when the system changes the orientation of radiator relative to the Sun, there is the time period, when one TD begins to close, and the second one yet is closed, because this radiator has not been cooled less than the temperature of the central point (figure 13, zone I).

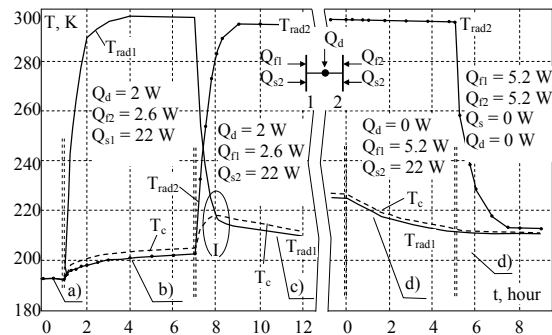


Figure 13 Experimental study of two-radiators' system with thermal diodes, functioning in regimes without sun flux (a, d) and with illumination of one of the radiators (b, c): $F_{rad} = 0.052 \text{ m}^2$, emittance $\varepsilon = 0.85$, solar absorptance $\alpha_s = 0.24$, I – zone of $dT/d\tau > 0$.

The system ensures the temperature level of 190...210 K for major regimes of optical sensor operation associated with the orientation changing: a) without solar illumination; b) direct solar rays hit on radiator 1; c) changing of the object orientation, and solar rays hit on the radiator 2; d) system is in non-working condition.

At stepwise change of radiator orientation relative to the Sun the derivative $dT_c/d\tau > 0$ for the temperature of central point (thermal joint of TD) T_c for zone I. This is explained by absence of heat output from this point for a short period of time as $T_c < T_{rad1}$ and $T_c < T_{rad2}$. After reaching the condition $T_c > T_{rad1} + (2...4 \text{ K})$ value $dT_c/d\tau < 0$. The simulation of this transfer regime at different heat capacity of central point C_c/C_{rad} has shown (figure 14) that the minimization of $\Delta T_c = T_{c(\text{point B})} - T_{c(\text{point A})}$ takes place at reducing the radiator heat capacity C_{rad} and increase in heat capacity of central point C_c , but to avoid absolutely this effect is impossible. The value of ΔT_c is within 4...20 K.

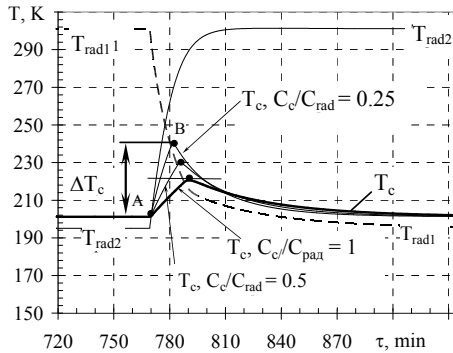


Figure 14. Dynamics of TCS at different heat capacity ratios $C_c/C_{rad} = 0.25...1$.

3. CONCLUSIONS

Principles of passive radiative thermal control system design with heat pipes for optical-electronic devices are proposed.

The tasks, which could be decided by the implementation of heat pipes into space thermal control radiative systems are the following:

- heat transfer from a device to a radiator with low thermal resistance;
- equalization of the radiator temperature field for its higher thermal effectiveness;
- providing of similar temperature level for several attached CCD modules;
- organization of directional heat fluxes in multi-radiators' systems by heat pipes – thermal diodes

and reducing the thermal control system sensitivity to external light disturbances.

The heat pipes made of stainless steel metal felt wicks and refrigerant R22 are designed for operation in the temperature range of 180...300 K. The heat pipes with ammonia as heat carrier have been used in ground tests of scientific equipment on the system level when heat has to be lifted against gravity forces.

ACKNOWLEDGEMENT

The heat pipes for TCSs have been elaborated and fabricated in the National Technical University of Ukraine “Kyiv Polytechnic Institute” (Kyiv, Ukraine) in cooperation with the Institute of Space Research of Russian Academy of Sciences (Moscow, Russia) and the Institute of Space Research (Berlin, Germany) for several International space missions.

REFERENCES

- Alekseev, S., Prokopenko, I., Ribkin, B. (2006) *Low temperature heat pipes for space technique (in 2 volumes)*. Novosti, Moscow.
- Avanesov, G. et al. (1989) *TV surveying of comet Halley*. Nauka, Moscow.
- Baturkin, V. et al. (1988) *The cryogenic cooling system for videospectrometrical complex VSK of Phobos project*. Preprint Пp-1409, Space Research Institute, Moscow, 39 p.
- Donabedian, M. et al. (2004) *Satellite Thermal Control Handbook. Vol. 2: Cryogenics*. Aerospace Corporation Press, El Segundo, USA.
- Gilmore, D. et al. (2002) *Satellite Thermal Control Handbook. Vol. 1: Fundamental Technologies*. The Aerospace Corporation Press, El Segundo, USA.
- Groll, M. et al. (1978) *Development of an axial groove aluminium/ammonia liquid trap heat pipe thermal diode*. A collection of technical papers. 3rd Int. heat pipe conf., Palo-Alto, p. 184-193.
- Semena, M. et al. (1986) *Working out of the cryogenic cooling system on the base of heat pipes for VEGA television camera*. Preprint Пp-1072, Space Research Institute, Moscow, 36 p.
- Williams, R. et al. (1978) *Investigation of a cryogenic thermal diode*. A collection of technical papers. 3rd Int. heat pipe conference, Palo-Alto, p. 177-183.

VARIABLE CONDUCTIVE HEAT PIPES FOR SPACE RADIATORS

K. Goncharov, A. Golikov, V. Antonov,
The Heat Pipe Centre Lavochkin Association,
24, Leningradskaya st., Khimki, Moscow region, 141400, Russia
Tel/Fax: +7 495 5736374; heatpipe@laspace.ru

A. Rukovishnikov, N. Tarnovsky,
OEKN CNII "Cometa", St. Petersburg, Russia

ABSTRACT

Research and development results of Variable Conductive Heat Transfer Device (VCHTD) on the base of loop heat pipe (LHP) design are presented in this paper.

Taking into account our experience in LHP development and application; we decided to develop VCHTD on the base of LHP. Condenser of original design was developed for the LHP for connection it with radiators heat pipes. Condenser was attached directly to Compensation Chamber. Such design provides start up of LHP without applying additional heat power to the Evaporator. Heater was mounted to Compensation Chamber for control of working fluid circulation.

Considered design versions and test results of VCHTD are described in this paper. Developed device will be used on board of spacecraft that will be put into the orbit in the nearest future.

1. INTRODUCTION

Infrared sensors are used in spacecraft systems intended for earth surface monitoring. Infrared sensors operation ability is kept by cooling and temperature control of optoelectronic devices.

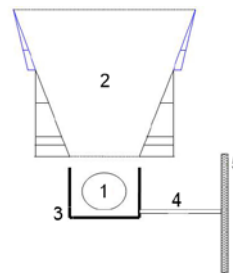
Variable Conductive Heat Transfer Device (VCHTD) developed on the base of loop heat pipe (LHP) is considered in this paper. VCHTD is a key element of thermal control system (TCS) of a spacecraft payload. TCS (see Fig. 2) consists of Optical System, Sun Blend, Thermal Screen, VCHTD, Radiator, Electrical Heaters, Temperature Sensors and Thermal Insulation.

Sun Blend is mounted in front of the Optical System. Thermal Screen keeps stable temperature of the Optical System by means of thermal re-radiation. VCHTD provides thermal connection between Thermal Screen and Radiator. For temperature equalization Thermal Screen and Radiator are equipped with heat pipes.

TCS shall keep the temperature of Optical System in specified temperature range at any orientation of the Spacecraft relative to the Earth and Sun. When Optical System is exposed to direct solar flash it is closed by a special cover. Heat exchange between Optical System, Sun Blend and Thermal Screen is carried out by radiation. VCHTD provides

thermal connection of the Thermal Screen with Radiator.

At initial stage of operation VCHTD thermal resistance shall be large in order to avoid rapid cooling of the Optical System. Then VCHTD shall provide cooling of the Optical system from initial temperature to calculated value of $\text{minus } 10 \pm 1^\circ\text{C}$ with gradient that is not more than 1K/hour . When operating TCS shall strictly keep the specified temperature of $\text{minus } 10 \pm 1^\circ\text{C}$.



1 – Optical System, 2 – Sun Blend, 3 – Thermal Screen, 4 – VCHTD, 5 – Radiator
Figure 2. TCS Layout.

In hot case, when the Sun Blend is exposed to Earth and Sun flash, it is necessary to cool the Thermal Screen to the temperature of $\text{minus } 40^\circ\text{C}$ removing the heat power of 110W through VCHTD to Radiator and providing minimum thermal resistance (not more than 0.1 K/W) of VCHTD. System the

minimum temperature of the Thermal Screen shall be of 20°C. Such temperature value is provided by Electrical Heaters mounted to the Thermal In cold case Optical System radiates heat power into space through opened objective. For keeping stable temperature of the Optical Screen and by increasing VCHTD thermal resistance up to 40 K/W. In this case no heat power is transferred to Radiator and Radiator temperature decreases to -153°C.

Such TCS design sets very unusual requirements to VCHTD:

1. At low Evaporator temperature (minus 40°C) minimum transferred heat power should be of 110 W and VCHTD thermal resistance should be minimum (not more than 0.1 K/W).

2. At high Evaporator temperature (20°C) maximum transferred heat power should be less than 5 W and VCHTD thermal resistance should be maximum (more than 40 K/W).

3. When running from hot to cold case the value of heat power to be transferred by the VCHTD should be more than 110 W because dynamic component of heat power is added to the value of nominal heat power due to thermal capacity of Thermal Screen and Radiator. Dynamic component of heat power may be of essential value and depends on velocity of the Thermal Screen temperature change. Velocity of the Thermal Screen temperature change determines indirectly the accuracy of the Optical System thermal stabilization. To avoid the capillary structure drying out, the total heat power to be transferred in dynamic mode shall not exceed heat transfer ability of VCHTD. The calculated value of maximum heat power to be transferred by VCHTD is 200 W at the temperature of 20°C.

4. To provide specified accuracy of the Optical System thermal stabilization, VCHTD shall respond quickly to the Thermal Screen running from hot to cold case and vice versa. In other words, changing of thermal resistance from large to small value shall be realized quickly, during some minutes.

1. VCHTD DESIGN ON THE BASE OF VCHP WITH NCG.

Initially, VCHTD was developed basing on gas controlled variable conductive heat pipe (VCHP).

Gas-controlled VCHP differs from traditional HP by the presence of

noncondensable gas (NCG) and the gas Reservoir. The Reservoir shall be directly connected to the end of the condenser. During VCHP operation NCG is captured by vapor and is transferred to the end of condenser and gas Reservoir. Presence of NCG in part of the condenser prevents vapor condensation in this zone. When heat input to the evaporator increases the vapor pressure increases and the NCG is compressed, this results in an increase of the active condensation zone. Therefore, evaporator temperature of VCHP can be changed slowly though heat power changes essentially Golovin et al. (1999).

Layout of traditional VCHP is presented in Figure 3.

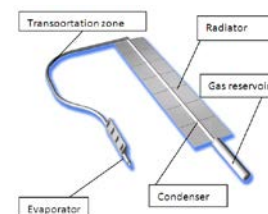


Figure 3. VCHP layout

VCHP with passive reservoir cannot solve the task as its thermal resistance increases when the temperature decreasing. But we need to have high thermal resistance at high vapor temperature and minimum thermal resistance at low temperature.

Perhaps this task can be solved using VCHP with active reservoir when a heater is mounted to the reservoir for controlling gas heating.

Propylene (C₃H₆) was chosen as a working fluid and Argon was chosen as NCG. For calculations it was assumed that Condenser length was 0.8 m and Condenser inner diameter was 10 mm. The calculations showed that active reservoir with NCG has too high volume (some liters) and shall be heated in hot case to the temperature higher than 100°C that requires high power consumption and is not safety for the components of spacecraft. Thus, it is obviously that VCHP of such design cannot be used for the task solving.

2. VCHTD DESIGN ON THE BASE OF ARTERIAL HP.

After Gas Controlled VCHP was excluded from the analysis we decided to develop controlled Arterial Heat Pipe (ArHP). For control of its operation it was suggested to use

controlled drying out of artery in transport zone.

Large experience of Lavochkin Association in the development and space application of ArHP allowed to hope that the task can be solved Golovin et al. (1999), Antonov et al. (2006).

The main problem that shall be solved when artery capillary structure designing is boiling of working fluid in the artery and blocking of the working fluid circulation by vapor and gas bubbles. As David Antoniuk says: “No bubble –no trouble!” Specialists of Lavochkin Association learned to fight efficiently with the problem of the artery blocking by vapor and gas bubbles. When designing controlled ArHP we should stop to fight with bubbles and working fluid boiling and allow the bubbles to block artery and stop the working fluid circulation at certain moment.

To check this idea ArHP experimental sample with diameter 12 mm was developed. It is presented in Figure 4. ArHP length is about 1 meter. Thermal conductive flanges with the length 140 mm each are mounted in evaporating and condensing zones. Propane was used as a working fluid. Before Evaporator there was made a zone of artery without design elements that protect ArHP from the working fluid boiling. Heater with heat flux more than 2 W/cm^2 was mounted in this zone.

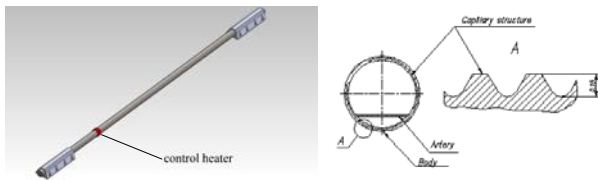


Figure 4. ArHP with control heater

Obtained test results of ArHP experimental sample shows that ArHP can solve the task. ArHP experimental sample transfers the heat power of 50 W at condenser temperature of minus 45°C . At stationary heat transfer mode different power values were applied to control heater and ArHP response to control action was investigated. ArHP dries out when heat power of 10 W is applied to control heater. After heat power is taken away from the heater ArHP starts up again.

VCHTD differed from the experimental sample by shortened transport zone and six contact flanges mounted to condensing zone. Dimensions of each contact flange are 70 mm x 40 mm.

Test results of VCHTD developed on the base of ArHP shows that stable control of ArHP by means of film heater mounted to transport zone was not obtained. Increasing of condensing zone and shortening of transport zone changed to the worth ArHP performance. In gravity conditions it was impossible to stop ArHP operation using control heater with rather small power consumption. It is possible to achieve ArHP drying out if heat flux at the heater is increased multiply but then ArHP restart does not occur.

Obtained test results forced us to reject such control method and we should develop more complicated VCHTD basing on Loop Heat Pipe design.

3. VCHTD designed on the base of LHP.

When designing VCHTD on the base of LHP it is necessary to solve the following tasks:

LHP shall start at zero or even negative heat power applied to Evaporator i.e. start autonomously.

LHP working fluid freezing temperature shall be lower minus 150°C .

LHP control shall be done with low electrical power consumption.

As far as possible LHP shall save overall and port dimensions set down when developing previous VCHTD designs (Arterial Heat Pipe (ArHP)).

To meet the requirements presented above there was designed LHP with the following peculiarities:

1. LHP compensation zone is joined to LHP Condenser directly. It allows to provide LHP autonomous start.

2. Propane (C_3H_8) with freezing temperature minus 183°C is used as LHP working fluid.

3. Condenser is designed as coaxial gap, liquid channel passes inside coaxial gap. It allows to decrease condensate subcooling and power consumption necessary for LHP control.

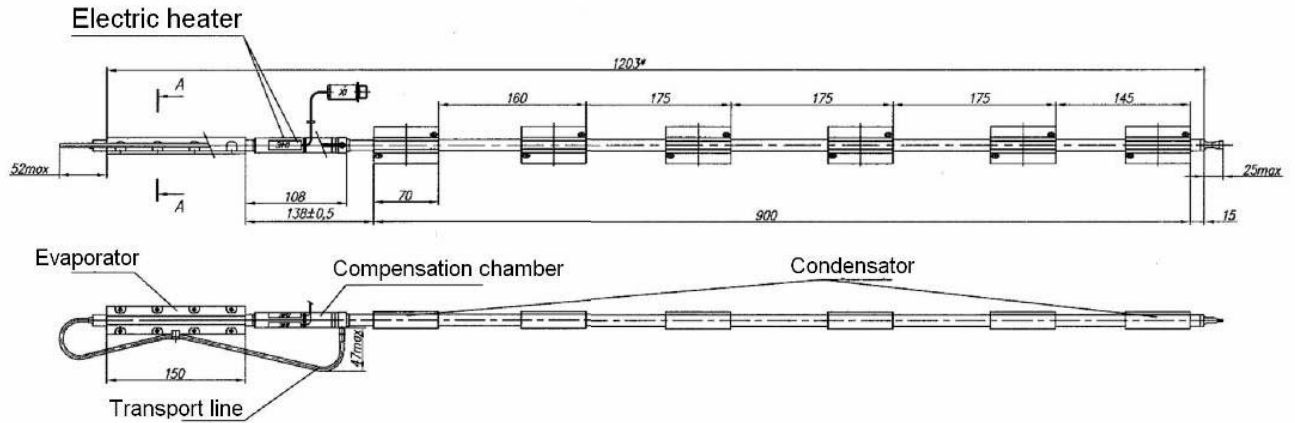


Figure 5. Configuration of VCHTD developed on the base of LHP

4. Body with thermal conductive saddles (from previous VCHTD design (ArHP)) for connection with heat pipes of Radiator was used as LHP Condenser.

Configuration of VCHTD developed on the base of LHP is presented in Figure 5.

LHP thermal calculation was made using EASY-2.1 package V.Buz and K.Goncharov (2002).

Calculation result of maximum transferred heat power in LHP components is presented in figure 6.

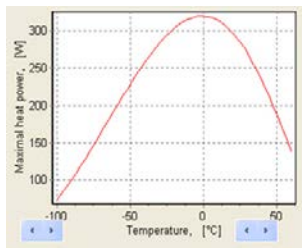


Figure 6. Calculation of maximum transferred heat power by EASY2.1 package

Analysis of obtained calculation results shows that VCHTD developed on the base of LHP excels ArHP in maximum transferred heat power and thermal resistance and meets the requirements set in VCHTD Specification.

Calculation of power consumption necessary for LHP control Buz et al.(1996), Buz et al.(2002), Goncharov et al.(1994), Goncharov et al.(1996),

According to Specification requirements the heater of 15 W power shall stop working fluid circulation in VCHTD when Evaporator temperature is of minus 40 °C and heat power of 110W is applied to evaporator.

One of the methods of control of thermal resistance and accordingly temperature of Evaporator attached to the cooled equipment is heat supply to Compensation Chamber or Liquid Line. Such control method is similar to regular triode with amplification coefficient from 10 to 100. The coefficient value depends on kind of working fluid and value of condensate subcooling.

Such process of LHP temperature control is described by the equation

$$Q_{\text{contr}} = k \cdot C_p \cdot Q \cdot \Delta T / L - Q_R, \quad (1)$$

where Q_{contr} – heat power applied to condensate returning to Evaporator through Liquid Line; Q – heat power transferred by LHP; C_p – thermal capacity of the working fluid liquid phase; ΔT – temperature difference between cold condensate and vapor in the evaporator; L – heat of vaporization of the working fluid; k – coefficient that describes heat exchange between cold condensate and working fluid in Compensation Chamber; Q_R – parasitic heat flow between evaporating and absorbing surfaces of the wick.

Value of parasitic heat flow was calculated by the equation:

$$Q_R = \frac{2\lambda_w \pi l_w (t_{SE} - t_{SR})}{\ln(R_w / r_w)}, \quad (2)$$

where λ_w – thermal conductivity of Evaporator wick; l_w – length of Evaporator wick; t_{SE} – Evaporator temperature; t_{SR} –

Compensation Chamber temperature; R_w – wick outer diameter; r_w – wick inner diameter.

Value of coefficient k in the equation (1) can be from 0 to 1 and depends on LHP configuration and area of heat power supply. For example, $k = 0$ if heat power is applied directly to Compensation chamber; $k = 1$ if heat power is applied to LHP Liquid Line when Compensation Chamber has no thermal contact with Liquid Line and Evaporator.

Analysis of the dependence of heater power necessary for LHP control (the heater is mounted to Liquid Line ($k=1$)) versus heat power rejected from Evaporator at Evaporator temperature of minus 40°C shows that power of the heater shall be of 25 W.

To decrease power necessary for LHP control (coefficient k) the control heater was mounted to Compensation Chamber and thermal link between Vapor and Liquid Lines was arranged. These measures allowed to decrease power necessary for LHP control to the required value.

4. VCHTD autonomous startup

Very important peculiarity of this device is its ability of autonomous startup. Known drawback of LHP is a problem with startup when low heat power is applied to Evaporator. Developed VCHTD is able to start when 0W heat power is applied to Evaporator. The problem was solved by joining Compensation Chamber directly to Condenser which is cooled by Radiator. At low transferred heat power Radiator temperature is very low (Radiator temperature may decrease to minus 150°C). Compensation Chamber joined to Condenser is cooled and LHP starts. Thermal resistance of the walls is chosen in such a way that heat flow transferred from Compensation Chamber to Condenser is enough for secure startup but not too large as this heat flow is rejected from the system to open space and shall be compensated by means of electrical heaters.

5 Thermal vacuum test results of VCHTD developed on the base of LHP.

Assembly for thermal vacuum tests included two VCHTD mounted to honeycomb panel Radiator with 6 embedded Axial Groove

Heat Pipes. The assembly was placed into vacuum chamber in horizon and was coated with MLI excluding Radiator working surface. Service heater imitating thermostated payload with maximum mass of 0.13 kg was mounted to Evaporator of each VCHTD. Thermal couples were mounted to the assembly.

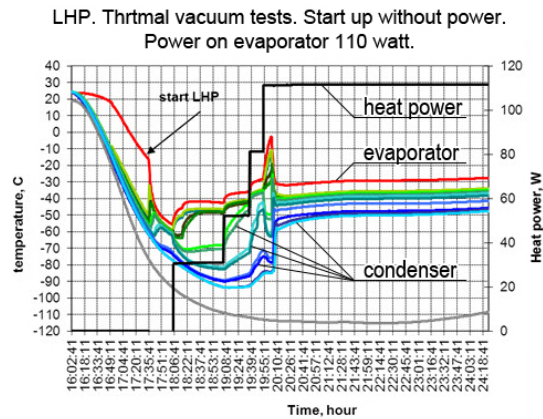


Figure 7. Thermal vacuum tests for LHP startup.

Thermal vacuum test results of VCHTD when it starting are presented in Figure 7. Initially VCHTD does not operate. When Condenser attached to Radiator is cooled to the temperature of minus 50°C circulation of LHP working fluid starts. It is necessary to emphasize that LHP startup occurs without applying heat power to Evaporator (see time 17:35 on the graph).

After VCHTD startup the heat power of 110 W was applied to Evaporator and VCHTD reached stationary mode successfully. At this time heat power was applied to the control heaters of the second VCHTD (the second VCHTD was included into the system for redundancy). It allowed to keep the second VCHTD out of operation.

Results of thermal vacuum tests for the working fluid shutdown are presented in the Figure 8. VCHTD reached the stationary mode when heat power of 110 W was applied to Evaporator. At the time of 26:15 the control heater with power of 15 W was switched on. Shutdown of the working fluid circulation was observed and Evaporator temperature decreased and reached 20°C. After switching off of the control heater the working fluid circulation in LHP was recovered immediately and Evaporator temperature decreased to its initial temperature.

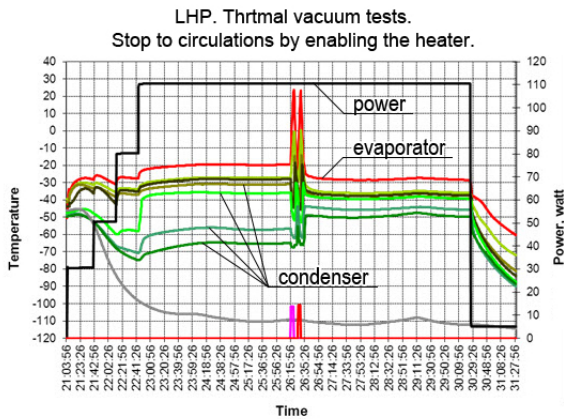


Figure 8. Thermal vacuum tests for the working fluid shutdown and recovery

This mode was repeated twice (see the time 26:15 and 26:36). Obtained test results prove possibility and stability of the working fluid shutdown and recovery in the developed VCHTD by means of heaters with low electrical power consumption.

CONCLUSIONS

1. Calculations showed that for thermostating of Optical System using Radiation Screen, gas-controlled VCHP shall have a reservoir with too large volume and shall heat in the hot case to the temperature exceeding 100°C. It requires high electrical power consumption and is not safe for components of spacecraft. Obviously that such heat pipe cannot have practical application.

2. We could not obtain stable control of Arterial Heat Pipe (ArHP) by means of a film heater mounted to transport zone. It is impossible to shut down ArHP operation by means of a control heater mounted to transport zone. In ground conditions ArHP does not dry out. If ArHP dryout is achieved by multiple increasing of heat flux on a control heater then ArHP restart does not occur. It ought to continue studying of arterial structure and methods of its control and maybe will possible to develop a unit more simple and reliable than LHP in the nearest future.

3. There was developed VCHTD on base of LHP. Overall dimensions and appearance of the VCHTD are similar to regular heat pipe. The VCHTD is able to start autonomously and excel regular heat pipes in transferred heat power, thermal resistance and possibility of stable shutdown and recovery of the working

fluid circulation. Test results of VCHTD prototype and TCS fragment developed on its base proved possibility of stable temperature control in wide range and with high accuracy by means of electrical heaters with low power consumption.

REFERENCES

- Antonov V., Goncharov K., Kochetkov A. (2006) Development of the low-temperature arterial heat pipes.// 36th International Conference on Environmental Systems. July 17-20, Norfolk, Virginia, USA, 06ICES-252.
- Golovin O., Goncharov K., Orlov A., Kochetkov A., Kolesnikov, (1999) Arterial Heat Pipes Application in Russian Spacecrafts. IHPC11, Tokio.
- Buz V., Goncharov K., Smirnov H. (1996) Thermal control two-phase system statically and dynamical characteristics analysis // 2nd European Thermal-Sciences and 14th National Heat Transfer Conference. Rome, Italy, p. 1381-1388.
- Buz V., Goncharov K. (2002) Modeling of LHP Performances by Means of Specialized EASY Package Program // IHPC 12. Moscow, Russia, May 19-24.
- Goncharov K., Maidanik Yu., Fershtater Yu. (1991) Capillary pumped loop for the systems of thermal regulation of spacecraft // ICES 4th. Florence, Italy, October 21-24, P. 125-129.
- Goncharov, K., Fershtater, Y., Maidanik, Y., Vershinin, S. (1994) Russian patent № 2015483: Method of LHP thermal resistance control. Published, bulletin № 12.
- Goncharov K., Fershtater Y., Maidanik Y., Kotlyarov E. (1996) Russian patent № 2062970: Method of LHP temperature control. Published, bulletin № 18.
- Goncharov K., Golovin O., Panin J., Korzhov R., Perrez R. (2007) Arterial Variable Conductive Heat Pipe. 14th International Heat Pipe Conference (14th IHPC), Florianopolis, Brazil, April 22-27.

VISUAL AND INSTRUMENTAL INVESTIGATIONS OF A COPPER-WATER LOOP HEAT PIPE

E. Bartuli, S. Vershinin, Yu. Maydanik

Institute of Thermal Physics, Ural Branch of the Russian Academy of Sciences,
Ekaterinburg, 620016, Amundsen st. 106

Tel. 7(343)267-91-19, Fax. 7(343)267-87-99, e-mail: ebartuli@gmail.com

ABSTRACT

Visual and instrumental investigations of the processes of condensation and redistribution of a working fluid in a loop heat pipe have been carried out. This paper presents the results of an experimental investigation of the heat transfer and hydrodynamics during the condensation of water vapor in a flat gap condenser measuring 80x40x1 mm. Investigations have been conducted at a condenser cooling temperature of 20, 40 and 60 °C. During all operating modes a stratified two-phase flow and film condensation have been observed. The temperature field in the condenser has been measured, and the heat-transfer coefficients and the thermal resistances have been determined.

KEY WORD: copper-water loop heat pipe, flat gap condenser, condensation, heat transfer coefficient, thermal resistance.

1. INTRODUCTION

Heat transfer and hydrodynamics processes in loop heat pipes (LHPs) accompanying the phase changes of a working fluid have a complex character. The traditional approach used to study these processes employing temperature measurement at different points of the device does not allow obtaining a comprehensive physical picture. In turn, this lack of physical information impedes the formulation of an adequate physical model, which serves as the basis for calculations of LHP operating characteristics at different modes and conditions of its operation. Visual investigations make it possible to obtain additional information and better disclose the “secrets” of the operation of these devices.

The processes in LHP condensers as well as the processes of redistribution of a working fluid between the compensation chamber (CC) and the condenser, which strongly depend on the cooling conditions of the condenser, are of some interest for visual investigations. But these investigations are not numerous considering that they require significant efforts for their preparation. Besides, they are seldom compared with results of temperature measurement. In the paper by D’Entremont and Ochterbeck J.M. (2008) the use was made of the fiber-optic equipment which made it possible to observe visually the processes proceeding in the central channel of the wick from the side of the CC. The paper by Cimbalá et al.

(2004) described a method of neutron radiography which made it possible to observe the process of partial drying of the wick as well as the phase boundary in the condenser. Li et al (2010) investigated the temperature distribution in the LHP at different heat loads was investigated by means of an infrared camera with an accuracy of $\pm 2^\circ\text{C}$.

The purpose of this study is to perform visual investigations of the processes in the LHP and their comparison with the results of temperature measurements at characteristic points at different heat loads and cooling conditions of the condenser. A copper-water LHP with a flat evaporator and a flat gap condenser was chosen as the object of the study.

2. DESCRIPTION OF THE EXPERIMENTAL DEVICE

Fig. 1 presents the scheme of the experimental device.

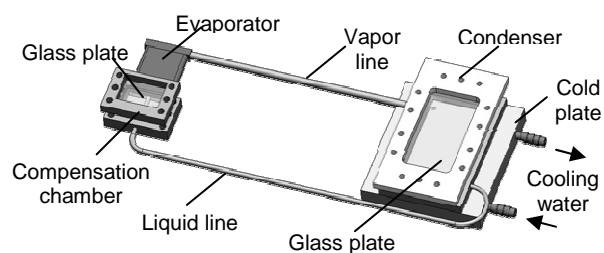


Figure 1. Experimental LHP.

The LHP had a flat evaporator 7 mm thick supplied with a thermal interface measuring 30x35 mm. The length of the liquid line was 550 mm and the length of the vapor line was 250 mm. The inner diameter was equal to 3 mm and 4 mm, respectively. The active section of the condenser was the multilayer object shown in Fig. 2.

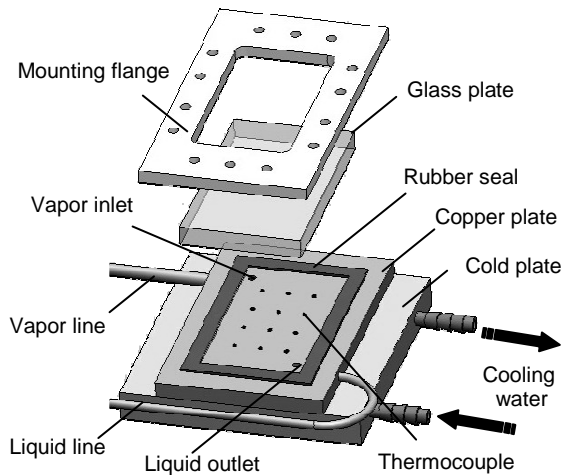


Figure 2. Scheme of the condenser.

There was a rubber seal between the lower copper and the upper glass plate. The inner space of the gap condenser measured 80x40 mm. The thickness of the gap was determined by the degree of compression of the seal and was set to 1 mm. This condenser allowed making visual observations as well as photography and video recording of the process of condensation. The lower side of the copper plate contacted a cold plate cooled by running thermostatted water. To intensify heat transfer in the condenser between the incoming vapor and the smooth cooled surface two types of intensifying insertions were used: guide insertions made of rubber and spiral insertions made of copper wire 0.4 mm in diameter. The general view and the location of these insertions are presented in Fig. 3.

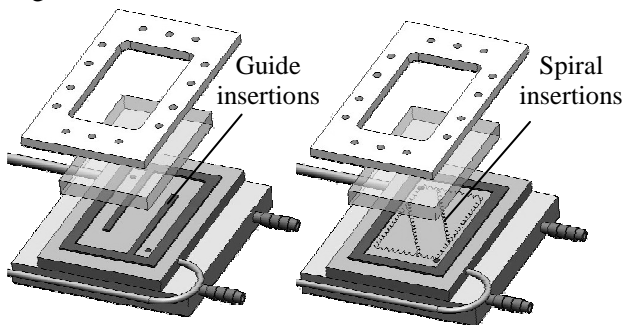


Figure 3. Scheme of the condenser with guide and spiral insertions.

The insertions provided vapor flow turbulization at the inlet of the condenser as well as suction of the liquid film from the condensation surface. The compensation chamber, shown in Fig. 4, had an analogous design.

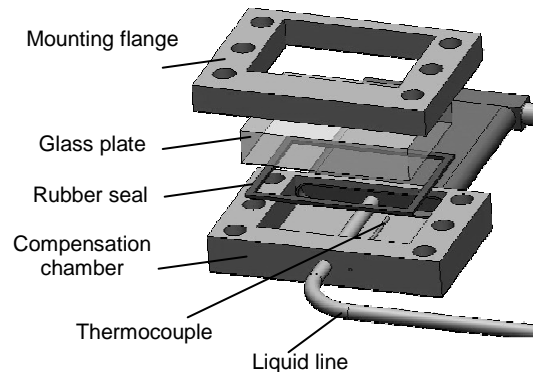


Figure 4. Scheme of the compensation chamber.

3. TESTING PROCEDURE

The experiment began with preparation of the working fluid and the loop heat pipe to avoid the effect of non-condensable gases, air and contamination on the LHP operation. This stage included cleaning and degassing of the working fluid as well as vacuum pumping and charging of the LHP. Then the cooling system of the condenser and evaporator heat source were turned on. The heat load source was an aluminum block in which two 250 W heating cartridges were installed. The heater had a surface area measuring 30x35 mm. The heat load changed stepwise with the help of a laboratory autotransformer from 20 to 500 W. The condenser was cooled by running thermostatted water with a temperature of 20, 40 and 60 °C. The temperature was measured with the help of copper-constantan thermocouples OMEGA TT-T-30. The temperature on the copper plate surface, where condensation of the working fluid took place, was measured at 12 points which are shown in Fig. 2. In addition, the temperature inside the CC was also measured. Data collection and processing was performed with the help of an Agilent 34970A data acquisition unit. The readings of the thermocouples were recorded after transient processes were complete and equilibrium was established. The optical instruments placed above the condenser and the CC registered the visual images of the processes of condensation and redistribution of the working fluid between the condenser and the CC. The area of the condensation zone was determined by means of computer photographic processing.

4. TEST RESULTS

4.1 Processes in the condenser

Visual investigations of the processes in the condenser made it possible to see that in the whole range of heat loads and condenser cooling temperatures the character of condensation remained the same. During all operating modes of the LHP a stratified two-phase flow and film condensation took place. Under constrained conditions determined by the height of the gap, the flow of oncoming vapor actively influenced a film of the condensate running along the cooper plate surface. There was a distinct, well-defined boundary between the condensation zone and the zone occupied with the liquid. The boundary fluctuated in a wavy manner, but exhibiting oscillations were short-term and changed the area of condensation no more than 5 %. These oscillations were too small to influence the temperature distribution at the condensation surface and the LHP operating temperature. At the condenser inlet, where vapor velocity was maximum, small perturbations were observed at the film surface. Wave flows of the film decayed downstream and in the direction of the periphery of the condensation zone.

4.2 Redistribution of the working fluid in the LHP

Visual investigations showed that before heat was applied to the evaporator, two variants of the initial working fluid distribution within the LHP were possible. These distributions were determined by the temperature of the condenser cooling. When this temperature was higher than the ambient the working fluid in the condenser was driven to the CC by the increased water vapor pressure in the condenser, almost filling the CC with working fluid. On the contrary, when the condenser cooling temperature was lower than the ambient, the increased vapor pressure in the CC drove the working fluid into the condenser, emptying the CC. Values of the area of the condensation surface at different heat loads and condenser cooling temperatures were obtained with the help of image processing software. Fig. 5 shows relative areas of the condensation surface at a cooling temperature of 20°C, determined by the formula:

$$S^* = \frac{\bar{S}_{\text{cond } i}}{S_{\text{tot}}} \quad (1)$$

From the graph it is seen that at low heat loads the

condensation surface is about 3-4 % from the total surface of the condenser. With the further increasing of the heat load, the condensation surface increases and is equal to about 50 % and does not depend on the presence of the intensifying insertions.

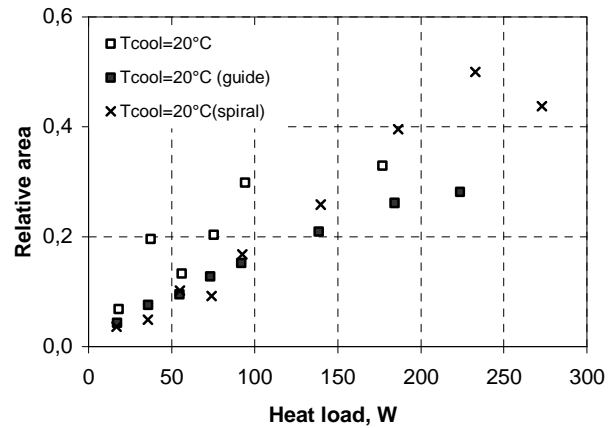


Figure 5. Heat load dependence of a relative area of the condensation surface, $T_{\text{cool}} = 20^\circ\text{C}$.

In Fig. 6 there are photographs of the compensation chamber and the condenser with the spiral insertions at a heat load of 60 W and 300 W and a cooling temperature of 20°C.

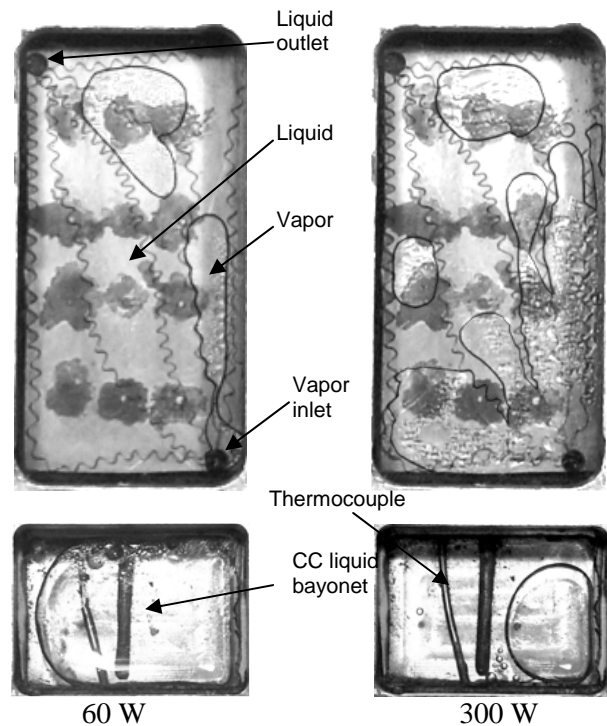


Figure 6. Redistribution of the working fluid between the condenser and the compensation chamber at a cooling temperature of 20°C.

It can be seen that at 60 W the condenser is almost completely filled with the liquid and at the same time the compensation chamber remains almost “empty”. As the heat load is increased the working fluid is displaced from the condenser, filling the compensation chamber. However, even at the maximum heat load, the complete filling of the CC does not take place.

Fig. 7 presents the heat load dependence of a relative area of the condensation zone at a cooling temperature of 40°C and 60°C. It appears that the condensation area even at a heat load of 20 W is more than 60%. In the range of heat loads from 200 to 500 W the relative area of condensation reaches 90% and more.

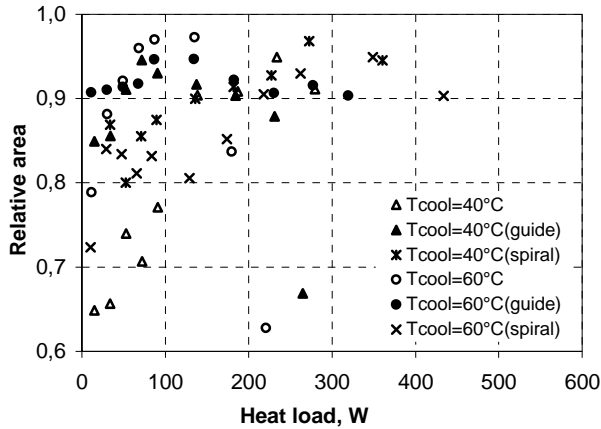


Figure 7. Heat load dependence of a relative area of the condensation surface, $T_{cool} = 40^{\circ}\text{C}$ and 60°C .

It may also be noticed that the guide insertions do not noticeably change in the condensation area as the cooling temperature goes from 40 to 60°C : it remains around 90% for the whole range of heat loads.

Fig. 8 shows the photographs of the compensation chamber and the condenser with the spiral insertions at a heat load of 60 W and 300 W at a cooling temperature of 60°C . Here one can see that in the whole range of heat loads there is no redistribution of the working fluid in the LHP because the compensation chamber is initially filled with the liquid. A small bubble, which was observed in the CC, does not change its volume and is probably related to the presence of a small amount of non-condensable gases.

At high heat loads for some LHP operating modes, an abrupt reduction of the condensation area was observed. At the same time the CC remained filled

with the working fluid. This happens when liquid leaves the wick, blocking the condensation surface.

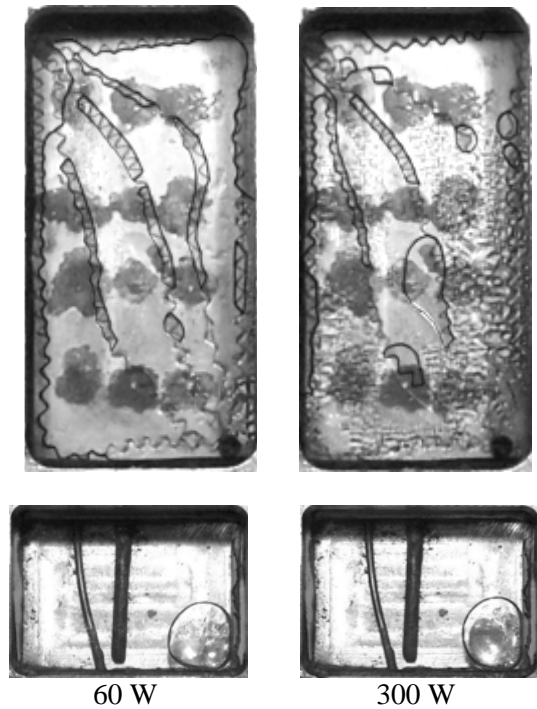


Figure 8. Redistribution of the working fluid between the condenser and the compensation chamber at a cooling temperature of 60°C .

This effect is not observed when spiral insertions are used. As a matter of fact, because of capillary forces and the effect of ejection the liquid coming from the evaporator to the condenser is removed and does not block the active condensation surface.

4.3 Thermal resistance of the condenser

The heat-exchange processes during condensation strongly impact the thermal resistance of the condenser expressed by the formula:

$$R_{tot} = R_{int} + R_{w-c} = \frac{T_v - \bar{T}_{cond}}{Q} + \frac{\bar{T}_{cond} - T_{cool}}{Q} \quad (2)$$

In our case, the thermal resistance R_{w-c} is constant. It is determined by the material and the thickness of the condenser wall as well as the cooling intensity and does not depend on the heat-exchange processes occurring in the condenser. Therefore, in this study only the component R_{int} determined by the intensity of heat exchange at the condensation surface was considered. Fig. 9 presents the heat load dependence of the condenser thermal resistance at a cooling temperature of 20°C .

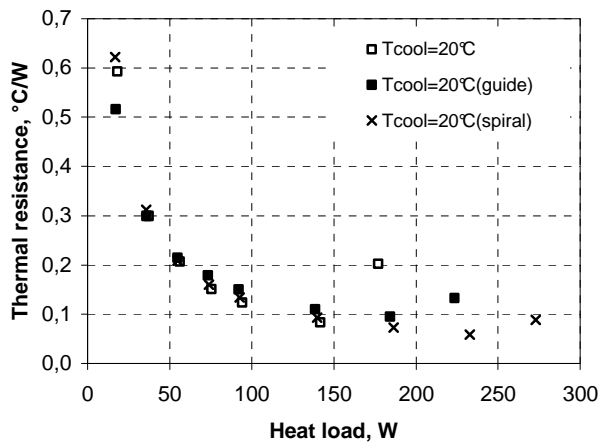


Figure 9. Heat load dependence of the condenser thermal resistance, $T_{cool} = 20^{\circ}\text{C}$

It appears that at heat loads up to 150 W the thermal resistance decreases sharply and does not depend strongly on the intensifying insertions. Its minimum value is equal to $0.06^{\circ}\text{C}/\text{W}$. However, at a heat load of more than 150 W the thermal resistance of the condenser without the insertions increases dramatically. It is explained by the reduction of the condensation surface area caused by the filling of the condenser with the liquid from the wick.

The heat load dependence of the condenser thermal resistance at cooling temperatures of 40°C and 60°C is plotted in fig 10.

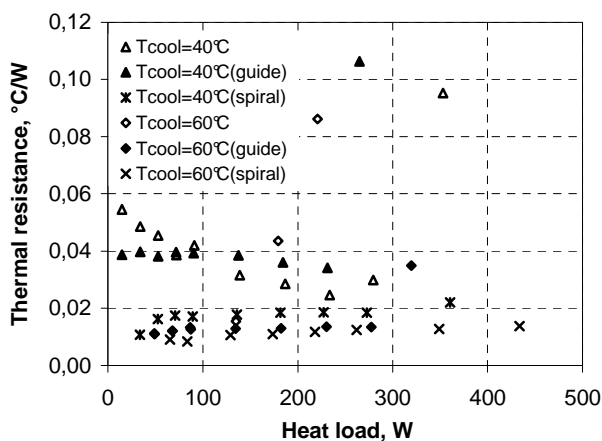


Figure 10. Heat load dependence of the condenser thermal resistance, $T_{cool} = 40^{\circ}\text{C}$ and 60°C

It is seen that at a cooling temperature of 40°C the thermal resistance of the condenser with the spiral insertions is twice lower than without the insertions and does not exceed the value of $0.025^{\circ}\text{C}/\text{W}$ in the whole range of heat loads. At a cooling temperature of 60°C the condenser thermal

resistance with the spiral insertions is also lower. At a heat load of more than 200 W, cases arise in which there is a sharp increase in the condenser thermal resistance. This is linked to the filling of the condenser, but this effect was not observed with spiral inserts.

The presence of the intensifying insertions promotes a decrease of the liquid film thickness at the condensation surface. The film employs capillary forces to pull up to the intensifying insertions and moves to the condenser outlet along the insertions. In this case, continuity of liquid flow in the condenser is not disturbed. However, in spite of the presence of the guide insertions in the condenser, the process of condensation is more intense and the thermal resistance of the condenser does not decrease. This is due to the fact that the guide insertions block a part of the active condensation zone. The spiral insertions, which are made of a thin heat-conducting copper wire, are more efficient. They intensify the heat-exchange process but at the same do not block the condensation surface.

4.4. Heat-transfer coefficients during condensation

Fig. 11 presents the heat load dependence of the heat transfer coefficient at a cooling temperature of 20°C .

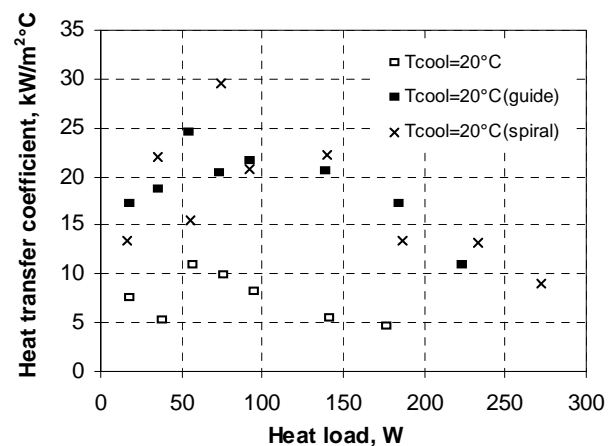


Figure 11. Heat load dependence of the heat transfer coefficient, $T_{cool} = 20^{\circ}\text{C}$.

Calculation of the heat-transfer coefficients was performed with the condenser surface being free of the liquid. It is seen that the use of both types of the intensifying insertions at heat loads above 80 W leads to a doubling of the heat-transfer coefficients during condensation.

The heat load dependence of the heat transfer coefficients at cooling temperatures of 60°C and 40°C is shown in Fig. 12. At these temperatures the spiral insertions result in a large increase of the heat-transfer coefficients over the whole range of heat loads. The guide insertions have an intensifying effect only at a cooling temperature of 60°C.

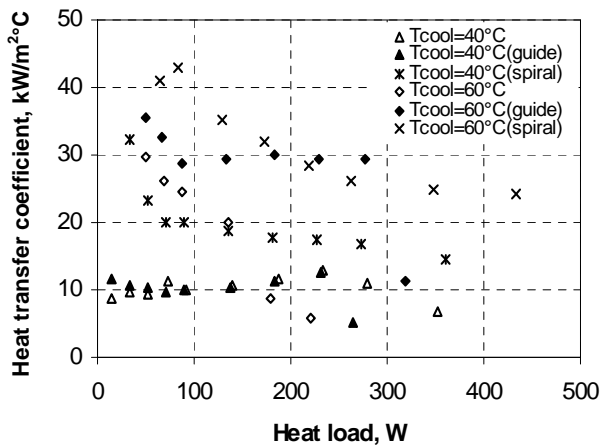


Figure 12. Heat load dependence of the heat transfer coefficient, $T_{cool} = 40$ and 60°C .

5. CONCLUSIONS

1. The active redistribution of the working fluid from the compensation chamber to the condenser takes place only at condenser cooling temperatures below or close to the ambient temperature. Film condensation and a stratified two-phase flow with unstable boundary were observed in the condenser.
2. Even at high heat loads, the condenser freed no more than 50% of its working fluid at a cooling temperature of 20°C . At cooling temperatures of 40°C and 60°C the condenser freed close to 90% of its working fluid.
3. The use of intensifying insertions in the condenser makes it possible to increase the intensity of heat-exchange processes. It is the result of the efficient removal of the liquid film from the condenser caused by capillary forces as well as the ejection effect and turbulization of the liquid film.

4. The heat-transfer coefficients during condensation without the intensifying insertions varied in the range from 5.1 to $29.8 \text{ kW/m}^2\text{C}$, with the guide insertions they ranged from 5.2 to $35.4 \text{ kW/m}^2\text{C}$ and with the spiral insertions from 9.0 to $42.9 \text{ kW/m}^2\text{C}$.

NOMENCLATURE

- Q – heat load,
 R_{tot} – total thermal resistance of the condenser,
 R_{int} – thermal resistance, connected with internal heat-exchange processes in the condenser,
 R_{w-c} – thermal resistance, determined by the thickness and the material of the condenser wall, as well as the intensity of condenser cooling,
 S^* – relative area of condensation,
 $\bar{S}_{cond\ i}$ – average area of the condensation surface for an i -heat load,
 S_{tot} – total area of the active condenser surface,
 T_{cool} – condenser cooling temperature,
 \bar{T}_{cond} – average temperature of the total area of the condenser surface.
 T_v – vapor temperature at the condenser inlet.

REFERENCES

- Cimbala John M. et al. (2004) Study of a loop heat pipe using neutron radiography. *Applied Radiation and Isotopes*, 61, p. 701-705.
D'Entremont B.P., Ochterbeck J.M. (2008) *Investigation of loop heat pipe startup using liquid core visualization*. Proc. Of the ASME Summer Heat Transfer Conference, 2, p. 387-393.
Li Ji, Wang Daming, Peterson G.P. (2010) Experimental studies on a high performance compact loop heat pipe with a square flat evaporator. *Applied Thermal Engineering*, 30, p. 741-752.
Maydanik Yu.F. (2005) *Loop heat pipes*. *Applied Thermal Engineering*, 25, p. 635-657.

A CAPILLARY AND GRAVITY PUMPED TWO-PHASE-TWO-LOOP-SYSTEM FOR COOLING OF ELECTRONIC DEVICES

Peter Stephan^{a,b} and Boris Schilder^{a,b}

^a Institute for Technical Thermodynamics, ^b Center of Smart Interfaces
Technische Universität Darmstadt, Petersenstrasse 32, 64287 Darmstadt, Germany
Phone +49 6151 163159, Fax +49 6151 166561, E-mail pstephan@ttd.tu-darmstadt.de

ABSTRACT

The trend to miniaturize electronic devices requires novel high performance cooling techniques. Heat pipes (HP), loop heat pipes (LHP) and capillary pumped loops (CPL) have proven their potential to remove high heat fluxes. Here, a novel two-loop system is presented, similar in design to CPLs but with a secondary buoyancy driven two-phase loop. Specific advantages compared to a standard CPL are: the working fluid can be filled in a non-degassed state due to the large system tolerance towards non-condensable gases; easy filling procedure; easy start-up; the amount of fluid in the system can be varied in a broad range without affecting the heat transfer performance. For the present study methanol was used as working fluid and three different inverted meniscus type evaporators have been employed. A maximum heat transfer rate of $35\text{W}/\text{cm}^2$ at the evaporator has been obtained. The maximum heat transfer coefficient was $16.5\text{ W}/(\text{cm}^2\text{ K})$ at a very small wall superheat of $0.45\text{ }^\circ\text{C}$. Oscillations of pressure, temperature and the liquid vapour interface occurred for all experimental conditions. These oscillations triggered a periodical wetting/dewetting process within the evaporator structure which obviously contributes to an enhancement of the evaporative heat transfer coefficient.

KEY WORDS: Loop heat pipes, capillary pumped loops, evaporation, non-condensable gases, oscillations

1. INTRODUCTION

The trend to miniaturize electronic devices and to increase their performance goes along with strongly increasing dissipated heat fluxes. The heat flux of high performance computer chips, e.g., is expected to reach up to $140\text{ W}/\text{cm}^2$ soon [1]. Novel cooling techniques with high heat transfer coefficients are required because the maximum chip surface temperatures are at a moderate level below 100°C for performance and reliability reasons [2]. Forced convection air cooling, the state of the art technology to remove the dissipated heat from computer chips, is capable to remove heat fluxes of less than $2\text{ W}/\text{cm}^2$ at this temperature level [1]. Therefore, two-phase cooling technologies with high heat flux heat spreaders are required. Microchannel evaporators, spray coolers, heat pipes, LHPs and CPLs seem to be capable to transfer the desired heat fluxes [3-7]. A miniature heat pipe with water as a working fluid demonstrated the capability to remove heat fluxes of more than $140\text{W}/\text{cm}^2$ [8]. However, a rather high wall superheat of more than 60°C occurred at these high heat fluxes. Jung-Yeul et al. [9]

obtained a heat transfer coefficient of about $0.09\text{ W}/(\text{cm}^2\text{ K})$ at a heat flux of $6\text{W}/\text{cm}^2$ with a CPL with FC-72 as working fluid. Maydanik et al. developed miniature LHPs with water and ammonia as working fluids [7]. With ammonia they reached a maximum heat transfer coefficient of $7.8\text{ W}/(\text{cm}^2\text{ K})$ at $21.2\text{ W}/\text{cm}^2$ and a maximum heat flux of $69.1\text{W}/\text{cm}^2$. For the water LHP a maximum heat transfer coefficient of $3.17\text{ W}/(\text{cm}^2\text{ K})$ was obtained at $35\text{W}/\text{cm}^2$ and a maximum heat flux of $44.5\text{W}/\text{cm}^2$. With a specially designed high heat flux LHP using ammonia as a working fluid they reached a maximum heat flux of $130\text{W}/\text{cm}^2$ and a maximum heat transfer coefficient of $4.4\text{ W}/(\text{cm}^2\text{ K})$.

The design of the capillary structure of a conventional heat pipe requires a compromise regarding radial heat transfer coefficient (fine structure), capillary pressure difference (fine structure), and axial flow resistance (coarse structure). Contrary to heat pipes, CPLs and LHPs need to be equipped with capillary structures only in the evaporator zone, and thus, flow resistance and radial heat transfer coefficient are decoupled.

Higher heat fluxes can be obtained. The liquid in the inlet port of the evaporator remains subcooled due to the relatively high thermal resistance of the capillary structure. An inverted meniscus type evaporator is typically used in CPLs and LHPs. The liquid flow is directed from the cold end into the capillary structure while the heat flows in the opposite direction. A comprehensive review of LHP parametric studies can be found in [10]. The majority of loop heat pipes and capillary pumped loops are designed and used for cooling purposes in space and aerospace applications. They can be rarely found in low cost applications for terrestrial applications. Reasons can be found e.g. in the following characteristics: Preventing non-condensable gases from diffusing into and working fluid diffusing out of the system requires a ‘perfectly’ sealed and thus costly system. LHPs and CPLs usually require a well-defined start-up procedure. The novel two-phase-two-loop system described in the present study is an alternative cooling system with low sensitivity in this respect.

2. CONCEPT AND SETUP OF THE TWO-LOOP SYSTEM

Figure 1 schematically shows the loop design. The system consists of two fluid loops. The first loop (evaporator loop) is a classical CPL type loop with an inverted meniscus evaporator. A porous capillary structure (1) separates the liquid inlet port (2) from the vapour removal channels (3) and provides the capillary pumping force. The generated vapour is transported from the porous structure through vapour removal channels to the evaporator exit from where it flows along the vapour line (4) into condenser A. The condensed fluid is transported back via the liquid line (5) into

the liquid inlet port. The second loop (reservoir loop) enables to remove non-condensable gases and/or vapour bubbles from the liquid inlet port to avoid liquid supply blockage. Therefore, the usage of non-degassed working fluid is unproblematic. Buoyancy is the acting pumping force in the reservoir loop. Vapour and/or non-condensable gases that might occur in the liquid inlet port rise against gravity and leave the inlet port with a two-phase flow towards condenser B. The condensed working fluid together with non-condensable gases is guided into a reservoir where liquid and gas are separated. Working liquid is transported back into the liquid inlet port. The fluid in the reservoir is captured by a flexible silicon membrane, thus enabling pressure equalization between the fluid inside the reservoir and the environment. Reservoirs with different volumes have been tested (110 cm^3 and 200 cm^3). Methanol has been used as working fluid (i) because of its high merit number in the relevant temperature range and (ii) because the same evaporator design was applied in another project with the aim to produce methanol vapour for a micro-combustion process [11]. Prior to the test runs non-degassed methanol has been filled into the reservoir.

Three evaporator types (E1, E2, E3) with two different porous structures and two different vapour removal channel geometries have been tested. Major design parameters of the evaporators are summarized in Table 1.

The capillary structure in evaporator E1 is a spherical bronze sinter structure. Vapour is removed by 18 parallel rectangular copper channels, each 1mm in depth and 0.5 mm in width. Two windows at the top of evaporator E1 (6 in Figure 1) allow optical access to the liquid inlet

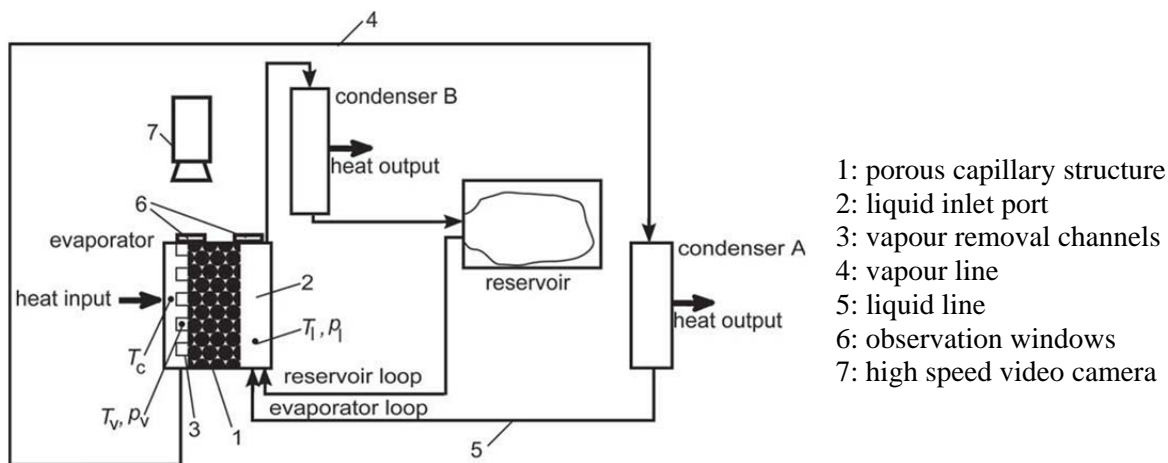


Figure 1. Two-phase-two-loop flow scheme and the system components

chamber and the vapour removal channels with a high speed video camera (7 in Figure 1). Evaporators E2 and E3 have the same sintered stainless steel felt as porous structure. Evaporator E3 has the same rectangular vapour removal channels as E1, the vapour removal channels of E2 consist of 10 triangular copper channels, each 1.5mm in depth and 1 mm in width. The liquid inlet chamber is made of stainless steel.

Table 1: Design parameters of the evaporators

Type	Capillary structure			Vapour removal channels
	Material	Mean pore size	Thick-ness	
E1	bronze	40 μm	5 mm	rectangular
E2	stainless steel	37 μm	1 mm	triangular
E3	stainless steel	37 μm	1 mm	rectangular

The condensers A and B are made of copper blocks with eight parallel fluid channels of 15mm length each. The diameters of the channels are 1mm for condenser A and 1.3mm for condenser B. Heat is supplied to the evaporator by an electrically heated copper block. The condensers are attached to an external cooling loop. The interface area between the heater block and the evaporator is 15mm x 20mm and equal to the projected surface area of the porous structure inside the evaporator. Conductive paste (thermal conductivity 9.2W/(m K) is used for a low and reproducible thermal resistance at the interface.

The coolant temperature was held constant for each test run, -5 °C or 15 °C, respectively. With that the condenser wall temperatures were always kept below 50 °C, even for the highest heat flux. The heat fluxes supplied to the evaporator q_e and removed from the condensers q_{cA} and q_{cB} are calculated based on the temperature difference between thermocouples at different locations in the walls. The evaporator wall superheat is defined as temperature difference $T_c - T_s$, where T_c is the measured temperature inside the evaporator wall and T_s the saturation temperature of methanol at the mean pressure inside the vapour removal channels p_v . The heat transfer coefficient then is defined as

$$h_e = \frac{q_e}{T_c - T_s}$$

Temperatures are measured by 0.5mm diameter K-type thermocouples calibrated with an accuracy of 0.15 °C. The vapour pressure is measured with

$\pm 250\text{Pa}$ accuracy. A differential pressure sensor with $\pm 40\text{Pa}$ accuracy is used for measuring the pressure difference between the vapour removal channel section and the liquid inlet port.

3. RESULTS AND DISCUSSION

3.1. Heat transfer performance

The heat fluxes supplied to the evaporators E1 and E2 in a test sequence with stepwise increase of the heating power are presented in Figure 2.

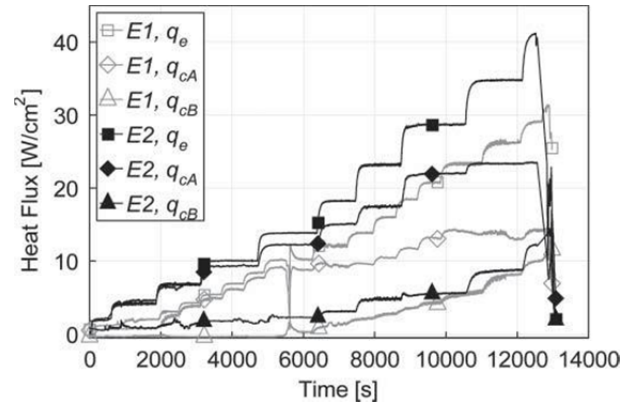


Figure 2: Heat fluxes at evaporators E1 and E2 and condensers A and B in a typically test sequence

At low heat flux (up to 10W/cm²) almost the total heat supplied to the evaporators is removed from condenser A. At mean evaporator heat fluxes (E1: 10...20W/cm², E2: 10...28 W/cm²) the heat removed from both condensers is increasing with rising evaporator heat flux. At high heat fluxes (E1: >20W/cm², E2: >28W/cm²) the heat removed by condenser B is increasing with rising evaporator heat flux, while the heat removed by condenser A remains approximately constant. The pressure drop inside the evaporator loop is equal to the capillary pressure provided by the porous structure. While an increase of heat above the capillary limit results in a dryout and failure for CPLs and LHPs, the present system is still able to reject some heat at dryout conditions with the gravity-driven two-phase flow in the reservoir loop. Dryout of the porous structure occurred at 31W/cm² for E1 and 41 W/cm² for E2.

The mean evaporator heat fluxes and heat transfer coefficients under steady state conditions are shown in Figures 3 and 4. A steep increase of the heat flux at low wall superheat up to 3 °C can be observed in all cases. For higher wall superheat the gradient is less pronounced. The maximum steady

state heat fluxes reached were: $29\text{W}/\text{cm}^2$ at a wall superheat of $36\text{ }^\circ\text{C}$ for evaporator E1, $34.5\text{W}/\text{cm}^2$ at a wall superheat of $26\text{ }^\circ\text{C}$ for E2, and $32\text{W}/\text{cm}^2$ at a wall superheat of $9\text{ }^\circ\text{C}$ for E3. Since the pore size and thus the capillary force is about the same for all evaporators, the lower flow resistance of the steel felt and the triangular vapour removal channels compared to the bronze structure and the rectangular channels is felt to be the reason for these differences in maximum heat flux.

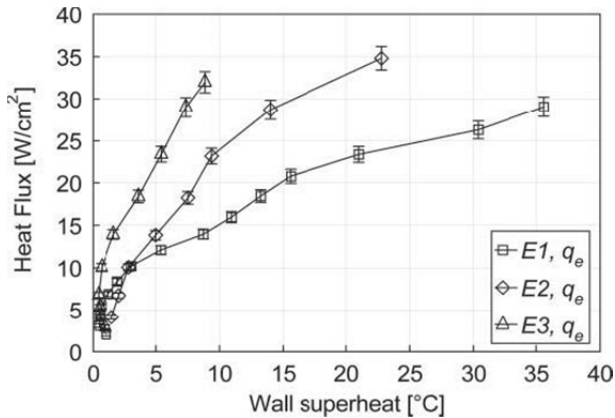


Figure 3: Heat flux vs. wall superheat for evaporators E1, E2, and E3

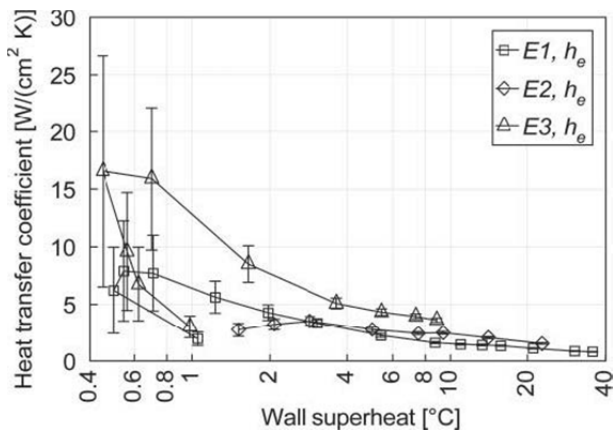


Figure 4: Heat transfer coefficient vs. wall superheat for evaporators E1, E2, and E3

The heat transfer coefficients seem to have maximum values for the evaporators E1 and E3 equipped with rectangular vapour removal channels at low wall superheats $<1\text{ }^\circ\text{C}$: $8\text{ W}/(\text{cm}^2\text{ K})$ for E1 and $16.5\text{ W}/(\text{cm}^2\text{ K})$ for E3. However, the potential measurement error is rather high at these low superheats (see later comments). For $>1\text{ }^\circ\text{C}$ superheat the heat transfer coefficient is monotonously decreasing with rising wall superheat for these two evaporators. The maximum heat transfer coefficient of evaporator E2 is only

$3.5\text{ W}/(\text{cm}^2\text{ K})$ at a superheat of $3\text{ }^\circ\text{C}$, and the decrease of the heat transfer coefficient with rising superheat is less pronounced than for evaporator E1. Obviously the steel felt used in E2 and E3 enables higher heat transfer coefficients than the bronze structure applied in E1, probably due to its lower thickness and thus shorter residence time of the liquid inside the structure. A shorter residence time means less heat is transferred from the heat source through the porous structure towards the liquid inlet port. As a consequence less liquid evaporates inside the porous structure and more evaporates close to or even inside the vapour removal channels. This keeps the evaporator wall at a lower temperature. The difference in the heat transfer coefficients of the two steel felt evaporators E2 and E3 cannot be attributed to the thermal resistance of the vapour removal channel geometry only. The conductive heat transfer resistance in the solid copper from the location of the thermocouple in the evaporator wall (T_c) to the surface of the vapour removal channels is about two times higher for E2 (triangular vapour removal channels) compared to E3 (rectangular vapour removal channels). For E2 the conductive heat transfer resistance contributes only to about 30% to the overall heat resistance (calculated based on the measured heat transfer coefficient of $2.5\text{ W}/(\text{cm}^2\text{ K})$). Taking into account the lower thermal resistance of the channel structure in E3, one would expect about 20% higher heat transfer coefficient for evaporator E3 compared to E2. However, much higher performance differences have been measured (see Figure 4).

Experiments with different reservoir volumes (110 cm^3 and 200 cm^3) and different filling levels showed no influence of the reservoir volume on the steady-state heat transfer performance.

The error bars in Figures 3 and 4 display the standard deviation of the heat flux and the heat transfer coefficient. They have been calculated following the Gaussian error propagation formula accounting for the measurement uncertainties (temperature, thermocouple position, thermal conductivity of the heater block) and based on rather conservative assumptions. While the uncertainty of the derived heat flux is rather low, the uncertainty of the heat transfer coefficient is considerably high at low wall superheat.

In comparison to the heat fluxes and heat transfer coefficient measured by Maydanik et al. [7] with an ammonia LHP and a water LHP the performance data here is on a similar level.

However, it should be kept in mind that ammonia and water potentially have a higher latent heat of vaporization, higher surface tension, and lower viscosity compared to methanol.

3.2. Oscillations and their influence on heat transfer

The observation windows on top of the evaporator together with high speed video recording allowed some insight into the evaporation process at the interface between porous structure and vapour removal channels. Oscillations of the liquid-vapour interface positions were observed under all experimental conditions. Two vapour removal channels are within the camera's field of view. It could be seen that liquid-vapour phase change in the inverted meniscus type evaporator occurred only partly inside the porous structure but also in the vapour removal channels. Liquid coming out of the porous structure periodically wetted and dewetted the channel walls. The frequency of these liquid oscillations was about 3 to 10 Hertz. Simultaneously to the menisci oscillations, also oscillations of pressure and temperature were observed. The pressure difference p_v-p_l and the temperatures measured in evaporator E1 during and after a start-up are shown in Figure 5.

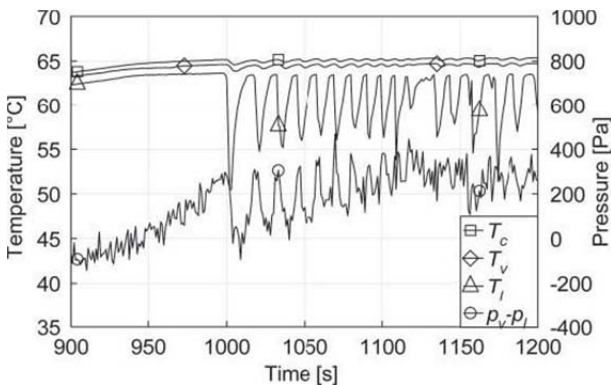


Figure 5: Oscillations of pressure difference p_v-p_l and temperatures (evaporator E1 at 2 W/cm^2)

Until about $t=1000 \text{ s}$ after start-up the pressure difference is increasing until saturation conditions are reached and the fluid starts to circulate. Then pressure oscillations and simultaneous temperature oscillations in the liquid inlet port (T_l) start and further develop. First, the frequency of the oscillations is increasing while the amplitude is decreasing with time, then a periodically steady-state is reached. Observations of the flow in the liquid inlet port indicate that each drop of T_l appears at the same moment when a gas or vapour

bubble leaves the liquid inlet port towards condenser B. These bubbles already occurred at liquid temperature below saturation in the liquid inlet port. Thus, it is assumed that the bubbles consist mainly of non-condensable gases during start-up and later on, at higher temperatures, more and more of vapour. Whenever such a bubble leaves the liquid inlet port, its volume is rapidly replaced by cold liquid coming from the reservoir and condenser A, causing a sudden liquid temperature drop in the inlet port. The observed pressure drops follow the temperature drops and induce a periodically moving liquid-vapour interface in the porous structure reaching out to the vapour removal channels. More details of the oscillatory behaviour are given in [12]. The periodically local wetting/dewetting process seems to lead to an enhanced heat transfer performance by a stimulation of a rather efficient thin film evaporation especially at low heat flux operation. At high heat flux this effect should be of minor importance because of higher wall superheat.

4. CONCLUSIONS AND OUTLOOK

The novel capillary pumped two-loop system for cooling of electronic devices presented here shows the following major characteristics:

- Very basic sealing requirements due to large tolerance towards non-condensable gases. Evacuation before the filling procedure is not needed.
- The amount of working fluid can be varied in a broad range without affecting the heat transfer performance.
- Easy system start-up procedure.
- A maximum heat flux of 35 W/cm^2 has been obtained at a wall superheat of 23°C . A maximum evaporator heat transfer coefficient of $16.5 \text{ W}/(\text{cm}^2 \text{ K})$ has been achieved at a wall superheat of about 0.45°C .
- The evaporators with a thinner capillary structure show better heat transfer performance. Likely reasons are the reduced flow resistance and the reduced residence time of the liquid inside the capillary structure.
- Oscillations of pressure, temperature and liquid-vapour interface position inside the evaporator were observed. The periodically wetting/dewetting process of the liquid in the porous structure and the vapour removal channels seems to contribute to an enhancement of heat transfer performance.

Further fundamental experimental studies with different working fluids and design variations are planned.

A technology demonstrator with the novel two-phase-two-loop system is currently tested in a high performance PC as shown in Figure 6. Here, the evaporator is attached directly to the chip. The system replaces the conventional cooling system based on single phase forced convection. The novel cooling system is working reliably without any failure and at moderate chip temperatures up to now. No external energy is required to drive the cooling loop, and no noise is emitted.

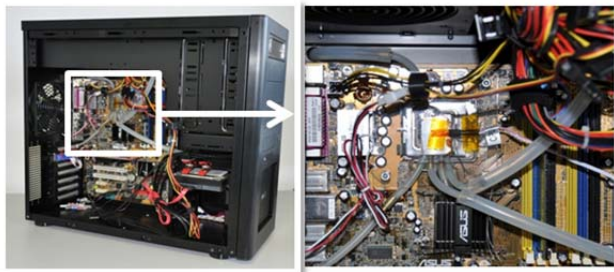


Figure 6: Two-phase-two-loop system tests within a high a PC replacing the standard chip cooling system

ACKNOWLEDGEMENT

The authors thank the Fritz & Margot Faudi Stiftung as well as the German Science Foundation for their financial support.

REFERENCES

- [1] Anandan, S. S., Ramalingam, V. (2008) *Thermal management of electronics: A review of literature*. Thermal Science, 12(2), p. 5-26
- [2] Hannemann, R. J. (2003) *Thermal control of electronics: Perspectives and prospects*. Rohsenow Symposium on Future Trends in Heat Transfer, Massachusetts Institute of Technology
- [3] Sobhan, C. B., Garimella, S. V. (2001) *A comparative analysis of studies on heat transfer and fluid flow in microchannels*.

- [4] Kandlikar, S. G., Bapat, A. V. (2007) *Evaluation of jet impingement, spray and microchannel chip cooling options for high heat flux removal*. Heat Transfer Engineering, 28(11), p. 911-923
- [5] Yeom, J., Shannon, M. A., Yogesh, G., Osamu, T., Hans, Z. (2008) *Micro-coolers*. In Comprehensive Microsystems, Elsevier, Oxford, p. 499
- [6] Reay, D. A., Kew, P. A., Dunn, P. D. (2006) *Heat Pipes*. Butterworth-Heinemann, Oxford, Burlington, MA, 5th edition
- [7] Maydanik, Y. F. (2005) *Loop heat pipes*. Applied Thermal Engineering, 25(5-6), p. 635-657
- [8] Lin, L., Ponnappan, R., Leland, J. (2002) *High performance miniature heat pipe*. International Journal of Heat and Mass Transfer, 45(15), p. 3131- 3142.
- [9] Jung, J. Y., Oh, H. S., Lee, D. K., Choi, K. B., Dong, S. K., Kwak, H. Y. A (2008) *A capillary-pumped loop (CPL) with microcone-shaped capillary structure for cooling electronic devices*. Journal of Micromechanics and Microengineering, 18(1), p.017002
- [10] Launay, S., Sartre, V., Bonjour, J. *Parametric analysis of loop heat pipe operation: A literature review*. International Journal of Thermal Sciences, 46(7), p. 621-636
- [11] Kania, T., Dreizler, A., Janicka, J., Schilder, B., Hardt, S., Stephan, P. (2006) *Conceptual Study of a Micro Energy Converter using Thermoelectric Materials*. Proc. 6th Int. Workshop on Micro and Nanotechnology for Power Generation and Energy Conversion Applications (PowerMEMS), Berkeley
- [12] Schilder, B., Stephan, P. (2012) *Design and operation of a novel capillary pumped two loop system for cooling of electronic devices*. Journal of Heat Transfer Engineering, 33(1), p. 12-20

EFFECTS OF ACCELERATION FORCES ON THE THERMAL PERFORMANCES ON FLAT HEAT PIPES WITH DIFFERENT CAPILLARY STRUCTURES

M. C. Zaghdoudi

Université de Carthage

Institut National des Sciences Appliquées et de Technologie (INSAT)

Laboratoire Matériaux, Mesures et Applications (MMA)

Centre Urbain Nord – BP N° 676 – 1080 Tunis Cédex - Tunisia

(+216) 71 704 309 – Ext. 6448, (+216) 71 704 329, chaker.zaghdoudi@insat.rnu.tn

C. Tantolin, C. Sarno

Thales Avionics

Packaging Department, Navigation Competence Center

25, Rue Jules Védrines – 26027 Valence – France

Phone : (+33) 4 75 79 86 57 – Fax : (+33) 4 75 79 86 06

E-mail : christian.tantolin@orange.fr, claude.sarno@fr.thalesgroup.com

ABSTRACT

This paper reports on the effects of acceleration forces on the thermal performance of Flat Heat Pipes (FHP) including different capillary structures under constant heat load. Transient accelerations are generated using a centrifuge table in order to simulate acceleration forces corresponding to aircraft maneuvering in frequency, amplitude, duration, and direction. The capillary structure plays a significant role in the heat transport potential of the FHP subjected to accelerations. There is a decrease in the FHP thermal performance with increasing acceleration as a result of partial dry-out of the evaporator and flooding in the condenser section. Dry-out, which is demonstrated as a result of increased acceleration, depends on the input heat power, the acceleration type, and the acceleration direction. The FHP repriming with a suppression of acceleration is observed only for capillary structures including sintered powder metal.

KEY WORDS : Flat Heat Pipes, Acceleration, Avionics

1. INTRODUCTION

An alternate and efficient cooling technique for electronic components is based on integrated phase change heat pipes. These systems are very active and promising for electronics cooling applications because they offer many advantages: (1) highly reliable systems because they are sealed passive devices, (2) high thermal efficiency, (3) nearly isotherm systems (hot spots of high power densities are spread), (4) no energy consuming because no external force is necessary for operation, (5) silent systems with no acoustic noise, (6) light weight systems, (7) they could be interchangeable with existing cards in such a way that several cooling technologies could be mixed in standard electronic racks, and (8) they could be located closer to the chips in the central core of the electronic cards.

The typical cooling techniques for avionics are based on cooling with conduction and with forced or natural convection (Assouad, 1997, Mudawar, 2000, Sarno & Moulin, 2001). These techniques may provide no convenient source of cooling to prevent the electronics from operating at temperatures surpassing those required for maximum component life. New cooling techniques will have to be developed to maintain components within the temperature limits. Heat pipe technology may be able to provide sufficient cooling in these situations. Heat pipes have traditionally been operated in environments free of adverse body forces such as vibrations and high acceleration forces. Recently, heat pipes have been proposed to be used aboard military aircraft to act as heat sinks for electronic packages (Sarno, 2010, Zaghdoudi et al., 2011a, 2011b, 2011c). During combat, transient acceleration fields up to 10 g

could be present on the aircraft. Acceleration force fields may be transient and coupled with transient heat loads. Therefore, characterizing the steady state and transient performance of heat pipes under elevated acceleration fields is of importance to designers of the electronics packages in need of cooling and will require experimental approaches.

The results of previous published experimental studies have indicated a need for improved thermal performance under acceleration fields. In addition, a capillary wick is sought to provide an adequate behavior of the working fluid within heat pipes under these conditions. Therefore, to address these points, FHPs with different capillary structures are tested under acceleration fields.

2. DESCRIPTION OF THE TESTED FHPs

Six types of FHPs are considered:

- (1) a FHP including screen meshes (SM FHP). It is constructed from rectangular extruded copper tube. The maximum axial heat transport of this FHP is about 35 W at 30 °C when it is oriented horizontally.
- (2) a FHP including a sintered powder metal (SP FHP). The maximum axial heat transport of this FHP is about 45 W at 30 °C for the horizontal position.
- (3) a FHP including six embedded copper/water heat pipes (EMB FHP). The FHP envelope is in aluminum. The maximum heat transport is nearly 120 W with a typical center to cold wall temperature difference of 20 °C or less when cooling at both edges is assured.
- (4) a pulsating FHP (PULS FHP). It can dissipate 30 W at 30 °C for the horizontal position.
- (5) a FHP with screen meshes and axial grooves (SMAG FHP).
- (6) a FHP with sintered powder metal and axial grooves (SPAG FHP).

The main dimensions of these FHPs are listed in Table 1.

Table 1. FHP dimensions

FHP type	Length (mm)	Wide (mm)	Thickness (mm)
SM	120	10	2.1
SP	120	10	2.1
EMB	240	120	3
PULS	150	60	2
SMAG	127	37	2
SPAG	127 </tr		

3. EXPERIMENTAL SET UP

The FHP is clamped as indicated in Figures 1 and 2. Heat input is delivered by thermofoil electric resistor attached at one end of the FHP (Table 2). Contact resistance at the resistor-wall interface is reduced by applying a 3M high thermal conductive interface material. The power input to the heaters is controlled through a variable transformer. Both the evaporator and the adiabatic sections are thermally insulated. The heat loss from the insulation surface to the ambient is determined by evaluating the temperature difference and the heat transfer coefficient of natural convection between the insulated outer surface and ambient. Heat losses to the environment of a functioning heat pipe are than closely approximated versus operating temperature. Heat is removed from the FHP by air convection. A thermally conductive paste is used to enhance the heat transfer between the FHP and the aluminum blocks. The heat sink area can be varied so that FHP thermal performance for different condenser lengths can be determined. In order to measure the evaporator and condenser temperatures, grooves are practiced in the heater and the condenser blocks and thermocouples are inserted along the grooves so that the thermocouples are in contact with the FHP wall.

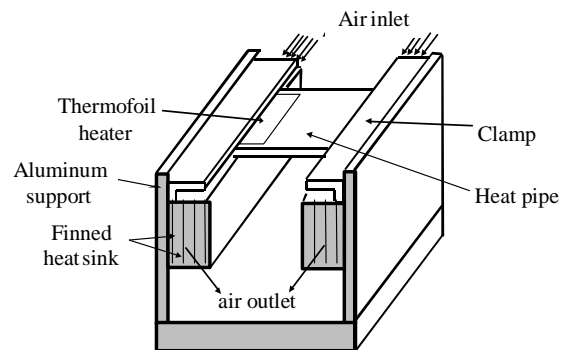


Figure 1. Sketch of the experimental set-up

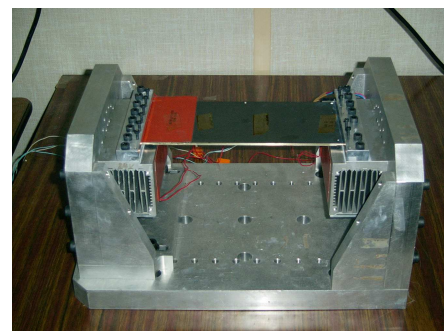


Figure 2. View of the experimental set-up

Table 2. Heat source and heat sink dimensions

FHP	Heat Source (cm ²)	Heat Sink (cm ²)	Heating Area (cm ²)	Cooling Area (cm ²)
SM	1 × 6.6	1 × 1	5.741	1
SP	1 × 6.6	1 × 1	5.741	1
EMB	5.7 × 11.4	1 × 12	56.9	12
PULS	1.5 × 7.6	1 × 6	6.064	6
SMAG	1.5 × 3.7	1 × 3.7	3.741	3.7
SPAG	1.5 × 3.7	1 × 3.7	3.741	3.7

Acceleration forces are generated after mounting the previously described set-up on a centrifuge table (Fig. 3). Transient acceleration forces consisting of step changes are generated by controlling the angular velocity of the centrifuge table. An accelerometer is used to monitor the time variant acceleration forces. For these experiments, the heat pipe is mounted so that only axial accelerations are considered. Since the heat pipe assembly is subjected to great air velocities due to the rotation of the table, the entire heat pipe is insulated in order to reduce convective heat losses from the exterior of the heat pipe and to provide a reasonable adiabatic operating environment. Heat losses are estimated to be less than 2 % of the input heat power. The output thermocouple signals are amplified and linearized to 0-10 V signal on the centrifuge table prior to data acquisition through the rotating contactors. Conditioning the temperature signals prior to leaving the centrifuge table avoids the disturbance of the thermocouple signal by the voltage drop in the rotating contactors. The acceleration test consists of increasing and decreasing the acceleration level after thermal stabilization. This test is the longest one since it depends on the time needed to reach the steady-state heat pipe operation for each acceleration level. The experiments are carried out for different constant heat loads and the acceleration is applied for each heat load level. The heat pipe is mounted on the centrifuge table in such a way that acceleration forces are opposite to the liquid flow (unfavorable heat pipe mounting).

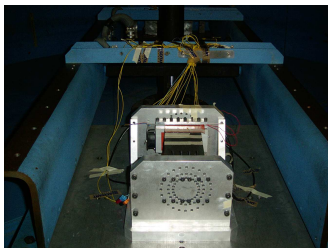


Figure 3. View of the experimental set-up on the accelerometer

The acceleration is generated using a step change in the centrifuge table angular velocity, ω . The speed, at which the centrifuge table angular velocity is increased or decreased, is fixed at 1 rpm/s. This results in the centrifuge table angular velocity and acceleration profiles depicted in Figure 4. A stabilization of 10 seconds is considered for each acceleration level. The overall duration of this test is about 300 seconds and 10-g acceleration level is reached in 140 seconds.

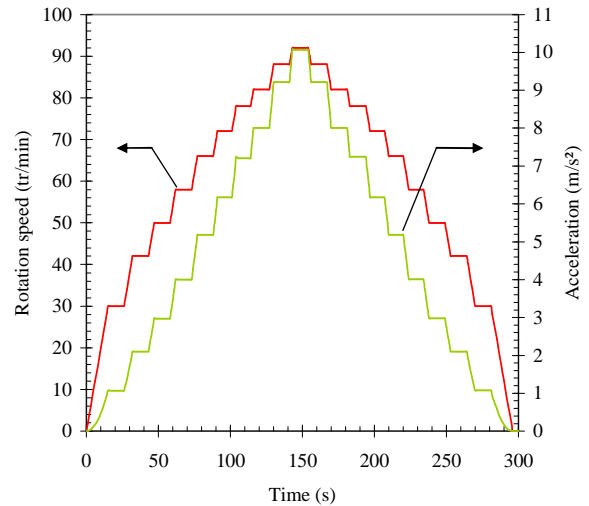


Figure 4. Acceleration profile

4. EXPERIMENTAL RESULTS AND ANALYSIS

FHP temperatures for the heater, evaporator and condenser are plotted with time for an input power of $Q = 20$ W in Figure 5.

For the SM FHP (Fig. 5a), the acceleration initiating the dry-out is nearly 1g, and the FHP depriming starts from this acceleration level. The heater and the evaporator temperatures increase as the acceleration level increases, however, the condenser temperature decreases. When the acceleration level increases from 0 g to 10 g, the heater and the evaporator temperatures increase from 160 °C and 145 °C to 193 °C and 180 °C, respectively. These values are beyond the limits for a safe operation of the electronic component. When the acceleration decreases, these temperatures continue to increase (199 °C and 185 °C for the heater and the evaporator, respectively), and the repriming of the FHP is not observed when the acceleration is suppressed. The thermal resistance of the FHP increases from 5.5 K/W to 7.8 K/W when the acceleration varies from 0 g to 10 g, which corresponds to a 42 % increase.

For the SP FHP (Fig. 5b), the acceleration initiating the dry-out is less than 1 g. When the acceleration level increases from 0 g to 10 g, the heater and the evaporator temperatures increase from 98 °C and 78 °C to 120 °C and 101 °C, respectively. When the acceleration decreases, these temperatures start to decrease, and the repriming of the FHP is observed when the acceleration is suppressed. The thermal resistance of the FHP increases from 2.1 K/W to 3.4 K/W when the acceleration varies from 0 g to 10 g, which corresponds to a 66 % increase. For this FHP, it is observed that a total repriming of the FHP occurs whatever the heat input power level. The duration of the FHP thermal response (DTR), which is defined as the time spent between the instant when the acceleration is applied and that when the FHP reprimed, that is when the initial thermal performances before the applications of the acceleration are reached, is greater than the duration of the acceleration. Indeed, for $Q = 20$ W, the DTR is 400 seconds which is 1.3 times higher than the duration of the acceleration (300 seconds). It can be also noticed that there is a delay (DSR) between the instant when the acceleration is suppressed and that when there is a total FHP repriming. Indeed, for $Q = 20$ W, the total repriming of the FHP occurs 100 seconds after the acceleration suppression. DTR and DSR depend on the heat input power.

For the EMB FHP (Fig. 5c), the acceleration initiating the dry-out is 2 g. When the acceleration level increases from 0 g to 10 g, the heater and the evaporator temperatures increase from 44 °C and 40 °C to 47 °C and 41 °C, respectively. When the acceleration decreases, these temperatures start to decrease, and the repriming of the FHP is observed when the acceleration is suppressed. The thermal resistance of the FHP increases from 0.49 K/W to 0.58 K/W when the acceleration varies from 0 g to 10 g, which corresponds to a 18 % increase. A similar behavior as that observed for the SP FHP is noticed. That is the repriming of the FHP happens whatever the input power level, and there is a hysteresis phenomenon (delay between the suppression of the acceleration and the repriming of the FHP). Other tests under higher input powers are carried out, and the experimental results show that input power as high as 100 W can be applied under 10 g acceleration level (Zaghdoudi et al., 2011a).

For the PULS FHP (Fig. 5d), the acceleration initiating the dry-out is 2 g. When the acceleration

level increases from 0 g to 10 g, the heater and the evaporator temperatures increase from 74 °C and 60 °C to 100 °C and 87 °C, respectively. When the acceleration decreases, these temperatures continue to increase, and the repriming of the FHP is not observed when the acceleration is suppressed. The thermal resistance of the FHP increases from 0.9 K/W to 2.6 K/W when the acceleration varies from 0 g to 10 g, which corresponds to a 180 % increase.

For the SMAG (Fig. 5e), the acceleration initiating the dry-out is 5 g. When the acceleration level increases from 0 g to 10 g, the heater and the evaporator temperatures increase from 57 °C and 51 °C to 60 °C and 54 °C, respectively. When the acceleration decreases, these temperatures continue to increase, and the repriming of the FHP is not observed when the acceleration is suppressed. The thermal resistance of the FHP increases from 0.72 K/W to 0.95 K/W when the acceleration varies from 0 g to 10 g, which corresponds to a 30 % increase. Other tests with higher heat input power under the same acceleration profile show that the repriming of the FHP could happen (Zaghdoudi et al., 2001).

For the SPAG FHP (Fig. 5f), the acceleration initiating the dry-out is 5.5 g. When the acceleration level increases from 0 g to 10 g, the heater and the evaporator temperatures increase from 112 °C and 83 °C to 115 °C and 90 °C, respectively. When the acceleration decreases, these temperatures start to decrease, and the repriming of the FHP is observed when the acceleration is suppressed. The thermal resistance of the FHP increases from 0.82 K/W to 1.063 K/W when the acceleration varies from 0 g to 10 g, which corresponds to a 30 % increase.

When subjected to axial unfavorable acceleration, a redistribution of the working fluid within the capillary structure occurs. The excess working fluid is pooled into the condenser section. This is evidenced by the decrease in condenser temperature with a subsequent increase in acceleration. This pooling, which is a direct result of the mounting configuration of the FHP on the centrifuge table, reduces the effective condensation area implying that there should be an increase in the evaporator temperature which occurs for a certain critical level of the acceleration depending on the input heat load. Onset of dry-out occurs with evaporator temperature increase. For this case, a subsequent reduction in the acceleration,

while maintaining power to the FHP, has no immediate effect on the operating temperature once dry-out has started. This results in a plateau in the operating temperature until there is a sufficient reduction in the acceleration to reprime or not the FHP thereby reducing or not the operating temperature. This hysteresis, which significantly altered the FHP transient behavior once dry-out is initiated, can be explained by the rewetting

behavior of the capillary structure under different input heat loads and acceleration. This can be explained by the effect of the acceleration profile on the liquid distribution within the FHP and the hydrodynamics aspects relative to the liquid and vapor flow within the capillary structure under acceleration forces. Hence, the duration of the FHP thermal response (DTR) depends on the heat input power.

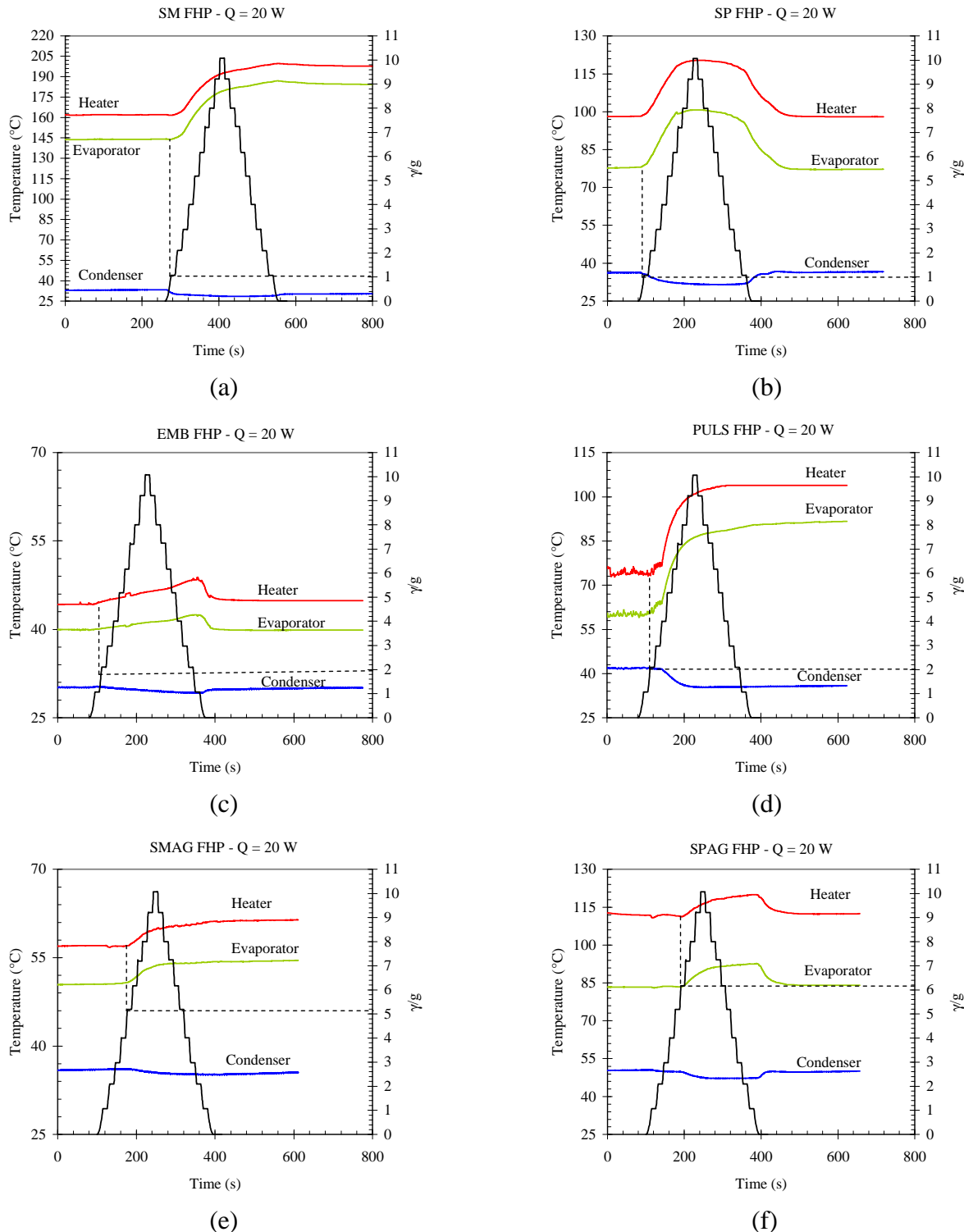


Figure 5. Effect of the acceleration on the heater, evaporator and condenser temperatures

3. CONCLUSIONS

An experimental investigation into the effects of accelerations with constant input heat loads on the performance of flat heat pipes with different capillary structures has been carried-out. The following conclusions can be made:

- (1) There is a decrease in the FHP thermal performance with increasing acceleration as a result of partial dry-out of the evaporator and flooding in the condenser.
- (2) The dry-out, which is demonstrated as a result of increased acceleration, depends on the input heat power, the acceleration profile, and the capillary structure which plays a significant role in the heat transport potential of the FHP subjected to accelerations.
- (3) FHP including screen meshes (SM FHP) is not reprimed when the acceleration forces are suppressed whatever the heat input power and the acceleration profile. The depriming of the FHP starts from low acceleration level (1g).
- (4) FHPs including both screen meshes and axial grooves is reprimed when the acceleration is suppressed for high heat fluxes. This result is obtained with a specific arrangement for meshes and grooves. The experimental tests show also that the depriming of the FHP starts from 5g.
- (5) FHP including sintered powder structures (SP FHP) allows for repriming when the acceleration is suppressed whatever the heat input power, and the FHP depriming starts from 1g acceleration.
- (6) FHP including embedded (EMB FHPs) heat pipes including sintered powder metal as capillary structures is reprimed whatever the heat input power and the acceleration profile. These FHPs are very sensitive to acceleration forces and their depriming starts from 2g. However, it allows for low thermal resistance and high transport capacity.
- (7) FHPs including combined capillary structures (sintered powder metal and axial grooves, SPAG) is reprimed whatever the heat input power. Their depriming starts from an acceleration level (5.5 g), which is higher than that obtained for the SMAG ones.

NOMENCLATURE

g	Gravitational acceleration (m/s ²)
Q	Input heat power (W)
<i>Greek symbols</i>	
ω	Angular velocity (rd/s)

ACKNOWLEDGEMENT

This work was supported by Thales (Valence, France). The first author would like to acknowledge the technical and financial supports provided by the Manufacturing Department. and CAD Design Department. Special Thanks go to Mr Sarno, Head of the Electronic Packaging Department, for his permanent assistance and guidance.

REFERENCES

- Assouad, Y. (1997) *Forced convection cooling of airborne electronics*, Electronics Cooling, Vol. 3, N° 2, pp. 30-35.
- Mudawar, I. (2000) *Assessment of high heat flux thermal management schemes*, IThERM 2000, Las Vegas, Nevada, USA, May 23-26, Vol. 1, pp. 1-20.
- Sarno, C., Moulin, G. (2001) *Thermal management of highly integrated electronic packages in avionic industry*, Electronic Cooling, Vol. 7, N° 4, pp. 12-20.
- Sarno, C., Tantolin, C. (2010) *Integration cooling and packaging issues for aerospace equipments*, Design, Automation & Test in Europe (DATE 2010), March 8-12, Dresden, Germany, pp. 1225-1230.
- Zaghdoudi, M.C., Sarno, C. (2001) *Investigation on the effects of body force environment on flat heat pipes*, J. Thermophysics and Heat Transfer, Vol. 15, N°4, p. 384-394.
- Zaghdoudi, M.C., Tantolin, Sarno, C. (2011a) *Acceleration and vibration effects on the thermal performance of a two-phase heat spreader with embedded flat mini heat pipe*, International Review of Aerospace Engineering (IREASE), Vol. 4, N° 2, pp. 109-121.
- Zaghdoudi, M.C., Tantolin, C., Sarno, C. (2011b) *Experimental investigation on the use of flat mini heat pipes for avionics electronic modules cooling*, International Review of Mechanical Engineering (IREME), Vol. 5, N° 4, pp. 770-783.
- Zaghdoudi, M.C., Tantolin, C., Sarno, C. (2011c) *Use of flat mini heat pipes for the thermal management of high dissipative electronic packages for avionic equipments*, International Review of Mechanical Engineering (IREME), Vol. 5, N° 5, pp. 843-855.

HORIZONTAL VAPORDYNAMIC THERMOSYPHONS, FUNDAMENTALS AND PRACTICAL APPLICATIONS

L.L. Vasiliev and L.L. Vasiliev Jr.,

Luikov Heat and Mass Transfer Institute
15 P. Brovka Str., 220072, Minsk, Belarus
Tel/Fax: +375-17-284-21-33, E-mail: Leonard_Vasiliev@rambler.ru

ABSTRACT

Vapordynamic thermosyphons (VDT) have a principal distinction from conventional thermosyphons and heat pipes of the same diameter. VDT can transfer the heat flow in horizontal position over a long distance. Its condenser is near isothermal with the length of tens of meters. One of the original particularities of VDT is the **long annular gap** between the vapor transport pipe line and the condenser (tube-in-tube). The innovations in VDT design were related with the porous coating of the outer surface of the vapor pipe. The data obtained on a flooded and partially flooded vapor pipe in confined space (annular channel 0.2 to 2 mm thick) testify the phenomena of micro heat pipe inside a porous structure and mini heat pipe in the annular gap. Visual analysis (glass condenser) and experimental results obtained with Propane as a working fluid show, that such combination is favorable for the enhancement of the heat transfer (up to 2.5-3 times as high) in the VDT condenser at heat fluxes $< 50 \text{ kW/m}^2$. Some practical applications of VDT were considered.

KEY WORDS: Vapordynamic thermosyphon, long horizontal condenser, heat transfer intensification.

1. INTRODUCTION

Two-phase conventional thermosyphons and loop thermosyphons have been developed for many years. The most famous publications, Imura, H., et al., (1979, 1994) and Piro L.S., Piro I.L. (1997), were mentioned in some papers on this topic. Two-phase loop thermosyphons were used for several applications, such as electronics cooling (Garner S., and Patel C. 2001, Khrustalev D. 2002, Haider et al. 2002, Khodabandeh R., 2005, Gima et al. 2005, Hartenstine et al., 2007), nuclear power plants (Sabharwall, 2008; Sviridenko et al. 2011), waste heat recovery (Dube et al. 2004), asphalt tank heating (Milanez and Mantelli, 2006), miniature compressors cooling (Possamai et al. 2009, Aliakhovich et al., 2011) among many others.

Vapordynamic thermosyphons (VDT) Vasiliev, L.L., Morgun V.A., Rabetsky M.I. were patented in 1985 and have a principal distinction from conventional thermosyphons and heat pipes of the same diameter. VDT can transfer the heat in horizontal position over a long distance. Its condenser is near isothermal with the length of tens of meters, Vasiliev et al., (1986, 1994). The VDT evaporators may have different form and

length. The heat transfer intensification in VDT evaporators is related with the porous coating of the heat loaded surface, Vasiliev et al., 2012. The VDT with porous coating of the evaporator ensures a heat transfer enhancement up to 5 times compared with the plain tube thermosyphon and started to work without a temperature overshoot typical for conventional thermosyphons.

Recent innovations to VDT design related to nano technologies anticipate a significant impact on heat pump/cooler and heat/cold accumulator's designs and its thermal solutions. The first main distinction of VDT is the **long annular gap** between the vapor pipe line and the tubular condenser (tube-in-tube). The vapor generated in the VDT evaporator pass through the long pipe line and enters into the annular gap of the condensation zone, where it condenses. The vapor pipe is made from metal with high thermal conductivity. There is an intense radial heat transfer with phase change between the vapor pipe and the condenser envelope. The data obtained on a flooded and partially flooded vapor pipe in confined space (annular channel 0.2 to 2 mm thick) testify the phenomena of micro heat pipe inside a porous structure and mini heat pipe in the annular gap. Visual analysis (glass condenser) and

experimental results show, that such combination is favorable for the enhancement of the heat transfer in the VDT condenser. The hydraulic diameter of the condenser annular channel has two options: 1. it is more than, or equals the capillary constant; 2. it is less than a capillary constant of the working fluid.

The second VDT fundamental difference consists in the fact that the motion of vapor and liquid flow is separated spatially (tube in tube).

This makes it possible to avoid a negative hydrodynamic interaction between the opposite flows of the vapor and liquid typical for the conventional thermosyphons. The picture of the VDT is shown on Fig. 1. When heat load is supplied to the evaporation zone, the vapor through vapor transport pipe 3 flows into the condensation zone, where it condenses and gives up heat to an external heat sink.

The condensate returns through a short liquid transport pipe 2 into the evaporator 1, Fig.1, under the action of the hydrostatic pressure difference $H_0 = h_2 - h_1$. ΔP_g – is the difference of the liquid levels in the evaporation and condensation zones:

$$\Delta P_g = g (\rho_l - \rho_v) (h_2 - h_1), \quad (1)$$

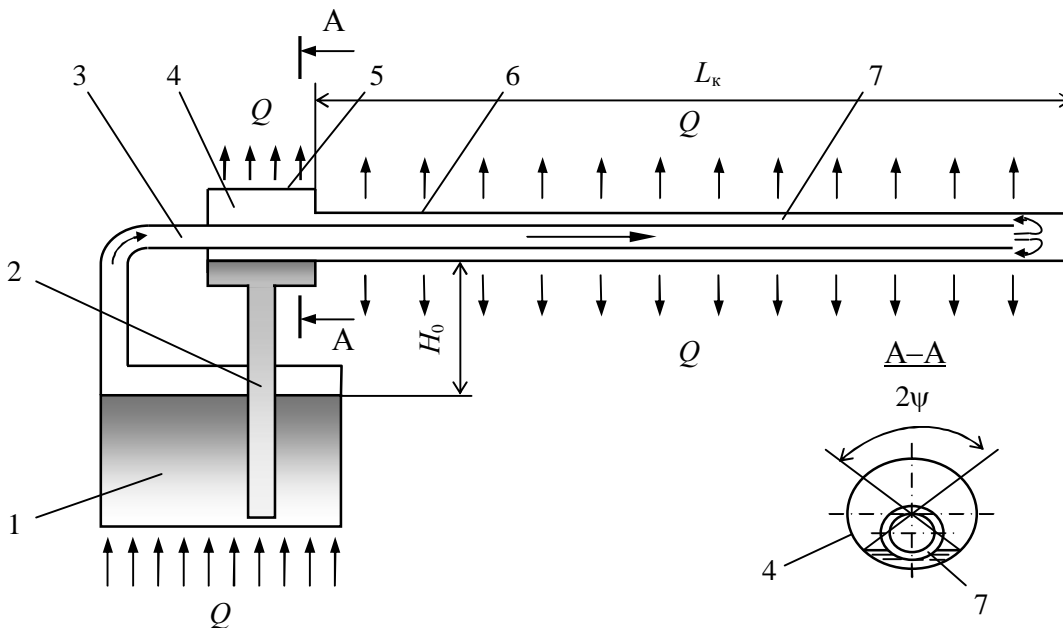


Figure 1. Vapordynamic thermosyphon: 1 – evaporator, 2 – liquid pipe, 3 – vapor pipe, 4 – compensation chamber, 5 – heat sink, 6 – condenser, 7 – annular channel, H_0 – hydrostatic pressure drop [US Patent No. 4554966] .

where the ρ_l and ρ_v are the liquid and vapor densities, respectively; h_1 and h_2 are the heights of the liquid levels in condenser and evaporator; g is the gravity constant.

The maximum allowable difference is Δh_{max} , i.e., the vertical distance between the evaporator liquid surface and the condenser bottom. The pressure drop in the liquid pipe due to the working fluid flow must be compensated by a hydraulic head of condensate above the evaporator. The total pressure drop ΔP_t is the summation of the pressure drops due to fluid flow at the evaporator ΔP_{evap} , the vapor line ΔP_v , the condenser annular channel ΔP_{cond} and the liquid transport pipe ΔP_l , i.e.:

$$\Delta P_t = \Delta P_{evap} + \Delta P_v + \Delta P_{cond} + \Delta P_l \quad (2)$$

The procedure of heat and mass transfer in such VDT annular mini channel is interesting to visualize to be sure in what way the vapor bubbles are interacting with the liquid flow.

There are two options of the VDT condenser design:

a. When the hydraulic diameter is less than a capillary constant, there is no fluid stratification in the channel, Fig.2. Fluid transport to the annular channel occurs from the vapor transport pipe covered by the micro porous coating on the outside. This porous coating provides a large surface area and enhances heat transfer inside the annular channel due to mini bubble generation in the pores. The dynamic vapor bubbles pressure on the two-phase flow is the additional force that induces liquid influx. Do they serve as mini compressors to push the two-phase flow along the condenser?

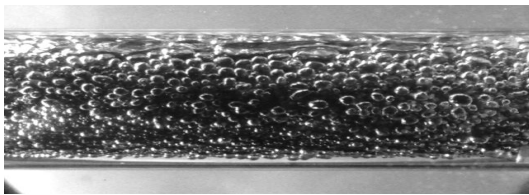


Figure 2. Fluid flow (Propane) visualization in annular mini-channel

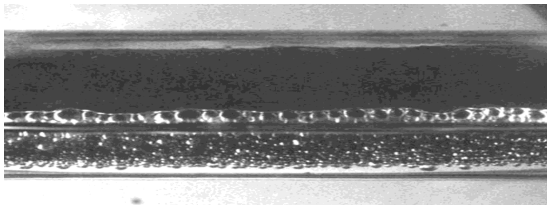


Figure 3. Fluid flow (Propane) visualization in annular mini-channel; hydraulic diameter is more than the capillary constant (stratification).

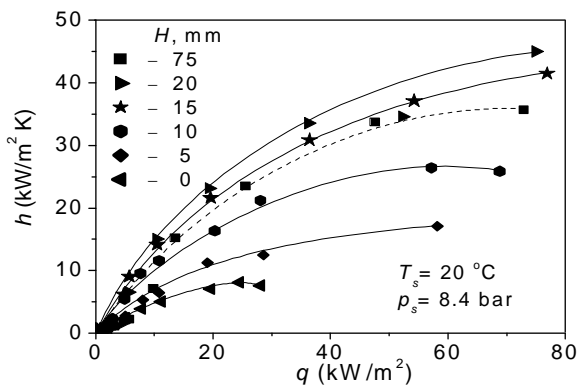


Figure 4. Heat transfer in the VDT annular channel as the function of heat flux in the evaporator.

b. The hydraulic diameter of the annular channel is more than the capillary constant. The stratification of the vapor and liquid flow occurs in the channel, Fig.3.

There is an intense heat transfer between the liquid flow, porous coating of the vapor transport pipe, Fig.4, saturated with liquid due to the capillary forces and the wall of the VDT condenser (mini heat pipe effect). The difference of the height between the liquid interface and the top of the vapor transport pipe inside the condenser is denoted as H . At the optimal height $H = 20$ mm for Propane, the heat transfer between the saturated vapor and the condenser wall is close to $45 \text{ kW/m}^2\text{K}$ at the heat load equal to 80 kW/m^2 .

2. VAPORDYNAMIC THERMOSYPHON MAIN THERMAL PARAMETERS

The main VDT thermal parameters are: the maximum heat load Q_{\max} , the heat flux in the evaporation zone q and thermal resistance R . To determine the thermal resistance of VDT the formula (3) is used:

$$R = (T_e - T_c) / Q , \quad (3)$$

where T_e and T_c are the average wall temperatures of the evaporator and the condenser, respectively, and Q is the heat load. The VDT wall temperatures of the evaporator and the condenser, and the temperatures of the vapor and condensate pipes are necessary to be known. Standard Copper-Constantan thermocouples with data acquisition unit were used for the measurements. When the thermosyphon exceeds the heat transfer limit Q_{\max} due to pressure drop, the condensate blocks part of the condenser, increasing the overall thermal resistance of the system.

3.1 Heating devices based on vapor - dynamic thermosyphons

Long vapordynamic thermosyphons are used for the floor heating in houses, timber drying, roof snow melting, etc. A VDT with long horizontal condenser (10 m) is shown on Fig. 5.

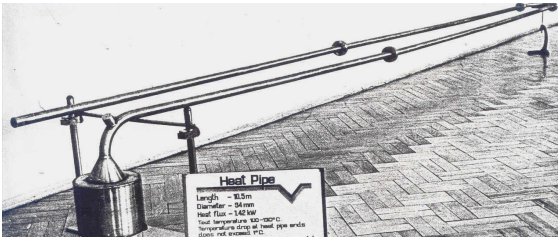


Figure 5. Vapordynamic thermosyphon, condenser length - 10 m.

The VDT thermal resistance R as a function of the heat load is shown on Fig.6. The working fluids are water and Propane. The VDT envelope is made from stainless steel.

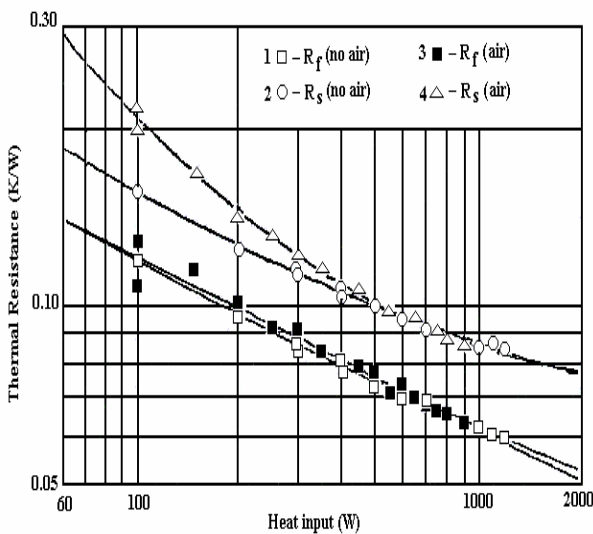


Figure 6. Thermal resistance R of VDT as a function of heat load W : 1- water; 2 - Propane; 3 - water with air; 4 - Propane with air in the gas trap

3.2. Vapordynamic thermosyphon as the thermal control system for adsorbers of solid sorption heat pump.

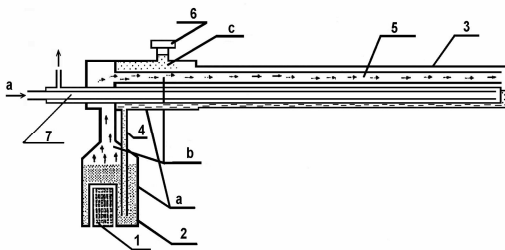


Figure 7. VDT with liquid mini heat exchanger (tube-in-tube) inside. 1- cartridge heater; 2 - evaporator; 3 - condenser; 4 - liquid pipe; 5 - vapor pipe ; 6 - NCG trap C ; 7- liquid heat exchanger; a - liquid; b -vapor.

Solid sorption heater/cooler with VDT thermal control has a good potential to be used in the air-conditioning and transport cooling applications, Vasiliev et al. (2001).

The main feature of such heater/cooler is the possibility to heat (desorption) sorbent canister and to cool (adsorption) it, using miniature liquid heat exchanger (tube-in-tube) inside the VDT condenser, Fig.7.

VDT condenser is covered by the sorbent material (activated carbon fibre) disposed between fins of condenser, Fig. 8.



Figure 8. VDT (stainless-steel/water) with mini gas burner. Sorbent material in disposed between fins.

3.3. Vapordynamic thermosyphon as the thermal control system for solar solid sorption cooler.

VDT was successfully used for thermal coupling of solar collector and two adsorbers of the solid sorption cooler, Alyousef et al., 2012.

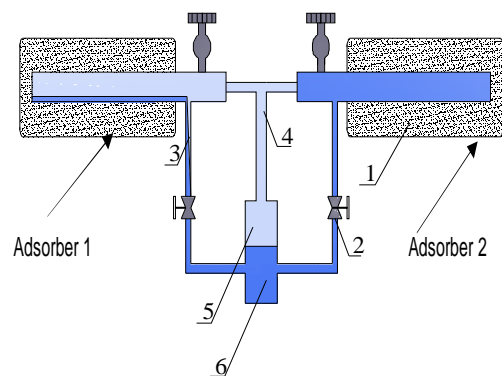


Figure 9. Two condensers of VDT are placed inside the Adsorber 1 and Adsorber 2 : 1-condensers, 2-valves, 3-liquid line, 4-vapor line, 5-evaporator, 6- liquid pool of the evaporator

VDT condensers were placed inside the Adsorber 1 and Adsorber 2, Fig.9-10. The working fluid was water. The system of thermal management

based on VDT, was used to heat the sorbent material inside the adsorbers. VDT evaporators were disposed inside the glass vacuum tubes of solar collector. Two VDT condensers were placed inside the Adsorber 1 and Adsorber 2. Two vapour and liquid transport mini pipes were used as the link between VDT evaporators and condensers. VDT condensers are switched on and off alternatively by valves 2, Fig.9. Such VDT has low thermal resistance ($R = 0.01-0.05 \text{ K/W}$), the condenser length is one meter. The constant heat flow (solar energy) in the thermosyphon evaporators is transformed into intermittent heat flow in condensers, Fig. 9, Fig.10.

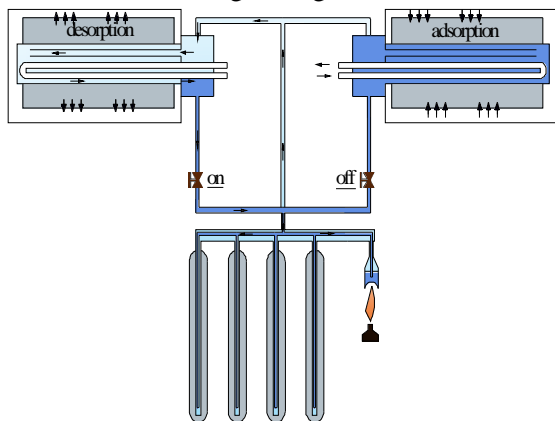


Figure 10. Solar heater with two adsorbers, solar collectors (with flame as the back-up), five evaporators vapor-dynamic thermosyphon and two valves.

The cooling of the sorbent material inside the adsorbers of the solar cooler was performed by miniature liquid heat exchanger, Fig. 7, Fig.10. The heat exchanger was made as a 2 mm SS tube placed inside the annular channel of the VDT condenser.

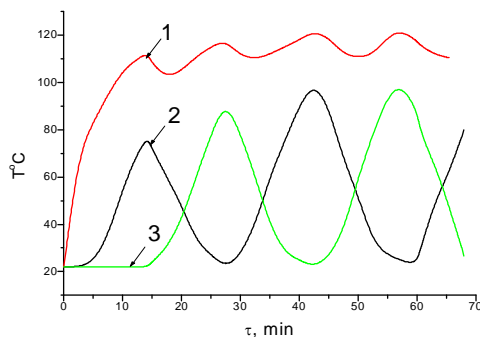


Figure 11. The temperature evolution of VDT evaporator 1, adsorber 2 and adsorber 3 envelopes of the solar cooler.

When the thermosyphon is closed (valve closed) the liquid heat exchanger actively cools the sorbent bed, realizing two-phase heat transfer (vapor condensation) inside the annular gap. The time of the cycle (adsorption/desorption) was close to 12 minutes, Fig.11. During the tests the temperature of the evaporator envelope (curve 1) was constantly near $110 \text{ }^{\circ}\text{C}$, while the temperature of adsorbers envelope (curves 2-3) was periodically changing from ambient temperature $20 \text{ }^{\circ}\text{C}$ (adsorption) up to $90 \text{ }^{\circ}\text{C}$ (desorption). The heat transfer intensity between the thermosyphon condenser and the adsorber is limited by the thermal conductivity of the sorbent bed.

Among the additional advantages of VDT is the possibility to use small diameter flexible condensers Fig.12.



Figure 12. VDT with flexible condenser of small diameter.

3.4. Vapordynamic thermosyphon as a thermal control system for snow thawing.

Such VDT design is used to heat the railway switches in winter (snow thawing), Fig.13, green houses, floor in buildings and pavements.

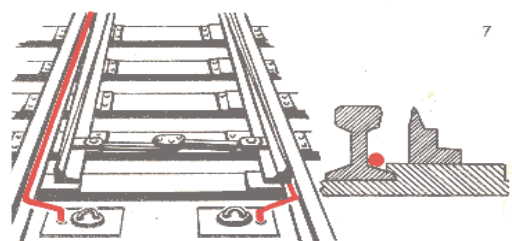


Figure 13. VDT for snow melting, length – 4.5 m, heat flow 2 kW.

The VDT condenser diameter is 16 mm. At the ambient temperature minus of $7-10 \text{ }^{\circ}\text{C}$, the snowfall intensity of 100-150 mm and wind velocity 5-10 m/s the vapordynamic heater

ensures complete snow thawing. After the switch on of the VDT heater the snow between the stock and points rail disappears within one hour.

4. CONCLUSIONS

Vapordynamic thermosyphons are rather simple and efficient heat-transfer devices capable of operating in a wide range of temperatures and heat loads. The constantly increasing interest of using such devices in various fields of technology both for heating and for cooling testifies its thermodynamic efficiency.

NOMENCLATURE

F surface, m^2
h heat-transfer coefficient, W/m^2
Q heat load, W
P pressure, kPa
R thermal resistance, $^{\circ}C/W$
T temperature, $^{\circ}C$
H, h height, mm

Subscripts

c condenser
e evaporator
l liquid
tot total
v vapor

REFERENCES

Aliakhnovich V.A., Kireichik D.G., Vasiliev L.L., Konev S.V., Zikman A.B. (2011), Cooling system for hermetic compressor based on the loop thermosyphon, Proc. 6th International Seminar "Heat Pipes, Heat Pumps, Refrigerators, Power Sources", Minsk, Belarus, September 12-15, v.2 p.101-110.
Alyousef Y., Antukh A., Tsitovich A., Vasiliev L. (2012), *Three adsorbers solar cooler with sorbent bed and heat pipe thermal control*, App. Thermal Engineering 38 (2012), p.124-130.
Dube, V., Akbarzadeh, A., Andrews, J. (2004), *The Effects of Non-condensable Gases on the Performance of Loop Thermosyphon Heat Exchangers*, Applied Thermal Engineering, 24, p. 2439-2451.
Garner, S., and Patel, C. (2001), "Loop Thermosyphons and their Applications to High Density Electronics Cooling", Proc. of IPACK'01 The Pacific Rim/ASME International Electronic Packaging Technical

Conference and Exhibition, July 8 - 13, Kauai, Hawaii. IPACK2001-15782.

Imura, H., et al. (1979), *Heat transfer in two-phase thermosyphons*, Heat Transfer Japanese Research, p. 41-53.

Imura H., Takeshita K., Doi K., Noda K. (1994) The Effect of the Flow and Heat Transfer Characteristics in a Two-Phase Loop Thermosyphon. Proc. 4th Int. Heat Pipe Sym., Tsukuba, Japan, p. 95-106.

Khodabandeh, R., (2005) *Pressure Drop in Riser and Evaporator in an Advanced Two-Phase Thermosyphon Loop*, International Journal of Refrigeration, 28(5), p. 725-734.

Khrustalev D. (2002), Loop Thermosyphons for Cooling of Electronics. Proc. 18th SEMI-THERM Symp., San Diego, California, USA, p. 145-150.

Milanez, F. H., Mantelli, M. B. H., (2010), *Heat transfer limit due to pressure drop of a two-phase loop thermosyphon*, Heat Pipe Science and Technology, An International Journal 1(3), p.237-250.

Pirol L.S., Pirol I.L. (1997), Industrial Two-phase Thermosyphons, Begell House Inc.

Possamai F.C., Setter I., Vasiliev L.L. (2009), *Miniature heat pipe as compressor cooling devices*, Applied Thermal Engineering 29, 3218-3223.

Sviridenko I., Shevelov D. (2011), Autonomous thermosyphon system for WWER-1000 pressurizer cooldown, Proc. 8th International Seminar "Heat Pipes, Heat Pumps, Refrigerators, Power Sources", Minsk, Belarus, September 12-15, v.2, p.71-78.

Vasiliev, L.L., Morgun V.A., Rabetsky M.I. (1985), US Patent No. 4554966, 26.11.1985.

Vasiliev L.L., Rabetsky M.I., Kiselev V.G. (1986), *Vapordynamic thermosyphons*, Journ. Appl. Thermophysics, v. 52, № 1. p. 62-66.

Vasiliev L.L. (1994), Heat Pipes Technology in CIS Countries, Proc. 4th International Heat Pipe Symposium – Tsukuba, Edited by Y. Kobayashi, K. Oshima, 16 – 18 May, p. 12 – 24.

Vasiliev L.L., Mishkinis D.A., Antukh A.A. and Vasiliev L.L. Jr. (2001), *A solar-gas solid sorption refrigerator*, Adsorption, 7, p.149-161.

Vasiliev L., Zhuravlyov A., Zhapovalov A. (2012), *Heat transfer in mini channels with micro/nano particles deposited on a heat loaded wall*, Journal of Enhanced Heat transfer, 19 (1), p.13-24.

EXPERIMENTAL INVESTIGATION OF FLAT HEAT PIPES TO REMOVE HIGH HEAT FLUXES

Valerij Derevyanko, Denis Nesterov

Institute of Computational Modelling SB RAS
Russia, 660036, Krasnoyarsk, Akademgorodok

phone: +7 (391) 243-17-39, fax: +7 (391) 290-74-76; e-mail: ndanda@mail.ru, dv@icm.krasn.ru

Sergey Suntsov

Joint Stock Company "Academician M.F. Reshetnev's "Information Satellite Systems"

Russia, Krasnoyarsky Krai, Zheleznogorsk
e-mail: sbsun@iss-reshetnev.ru

ABSTRACT

The results of experimental investigation of two different copper/water flat heat pipes are presented. Capillary structure of both heat pipes is made of sintered powder, but the configurations of wick and vapor channels are differ. The maximum heat fluxes for concentrated heat input on the area of 2 cm^2 were determined for both flat heat pipes. For the first flat heat pipe of T-shaped form the maximum value of heat flux is essentially less than for the second one. The first flat heat pipe provides heat flux removal more than 10 W/cm^2 at temperature of $35 \text{ }^\circ\text{C}$. This value depends on temperature of heat pipe and location of heater. The second flat heat pipe has more complex configuration of wick and vapor channel, which provide more effectively heat spread in plane of flat heat pipe. For the most favorable configuration of heat source and sink, when cooler covers whole heat pipe surface, the maximum heat flux reached up to 60 W/cm^2 at heat pipe temperature of $60 \text{ }^\circ\text{C}$.

KEY WORDS: flat heat pipe, electronic cooling, high heat flux

1. INTRODUCTION

Heat pipes are effective solution for thermal management in many industrial applications. Interesting review can be found in paper of Masataka Mochizuki et al (2011). The most commonly used is classical tubular heat pipes because of its simple design and low cost. However the flat heat pipes offer the solution with significant advantages, especially for electronic cooling. Compared to one-dimensional heat pipe, the width of flat heat pipe allows an adequate cross-section for heat flow with small thickness. Moreover, several heat sources can be located on flat surfaces with low thermal resistance.

A lot of works devoted to the flat heat pipes have been carried out: Vadakkan U., Garimella S.V., Murthy J.Y. (2004); Aghvami M., Faghri A. (2011) and many others. Although the most of the works devoted to the theoretical analysis and numerical simulation, many experimental papers demonstrate the facilities of flat heat pipes. Wang & Vafai (2000) presented the experimental investigations results, which show that temperature distribution along the flat heat pipe surfaces is

quite uniform. The flat heat pipes can be effectively used as heat spreader for high heat flux electronic cooling. Wessel Wits (2010) presented the investigations of the flat miniature heat pipe embedded in the printed circuit board, which able to effectively remove heat from several hot spots. Hirofumi Aoki, Masami Ikeda and Yuichi Kimura (2011) developed ultra thin heat pipe (less than 1 mm thickness) which can be applied to compact electronic equipments. Lefèvre F. et al. (2012) presented the results of flat heat pipes investigations with different sizes and capillary structures. It was showed the ability of using the flat heat pipes to cool several electronic components located on a printed circuit board.

This paper presents the results of experimental investigations of two copper-water flat heat pipes, with different configurations of wick and vapor channels. The detailed measurements of heat transfer parameters were performed. The main focus was on the measurements of the maximum value of heat flux, which can be removed without droyout of capillary structure and reducing efficiency of heat transfer. The flat heat pipes under investigation were designed for thermal

management of electronic equipment. The printed circuit boards with electronic components are to be installed on the flat surfaces of heat pipes. The distribution of input heat power on the heat pipe surface is uneven, because the power of each electronic component is various. Moreover the bulk of heat power is usually dissipated by a few most powerful miniature components. Therefore the maximum value of heat flux is the important parameter determining the maximum acceptable power of each single electronic component (transistor, chip), for which cooling the considered flat heat pipes can be used.

2. DESCRIPTION OF FLAT HEAT PIPES

The flat heat pipes under investigation have thin leak-tight construction containing a wick of sintered powder and vapor channels. The heat pipes are made of copper and filled with pure water. It is investigated two different types of flat heat pipes, which differ from their outward appearance and configuration of wick and vapor channels.

2.1 Flat heat pipe of type 1 (T-shaped)

Fig. 1 presents the sample of flat heat pipe of type 1. The copper heat pipe is nickel plated for corrosion protection. It is of T-shaped form with sizes: width and height equals $110 \times 130 \text{ mm}^2$, thickness is equal to 2.3 mm and bottom side width is equal to 30 mm. T-shaped flat heat pipe is designed for cooling electronic components. Printed circuit boards with electronic components as heat sources are installed on the surfaces of the flat heat pipe. The bottom side is used as heat sink area.



Figure 1. Flat heat pipe of type 1 (T-shaped)

The configuration of wick and vapor channels provides effective transport of working fluid along direction to bottom side (vertical direction in

fig. 1). The working fluid can move and in transversal direction (horizontal direction in fig. 1) but less effectively.

2.2 Flat heat pipe of type 2

Fig. 2 presents the samples of flat heat pipe of type 2. It is of rectangular form with length and width equals $360 \times 80 \text{ mm}^2$ (working area is $350 \times 70 \text{ mm}^2$), thickness equals 3.5 mm. The heat pipe of type 2 has more complex configuration of wick and vapor channels than type 1. The capillary structure provides moving of working fluid in lengthwise and transversal directions equally effectively. The flat heat pipe of type 2 can be used for heat removal from high heat flux sources.



Figure 2. Flat heat pipe of type 2

2. INVESTIGATION OF FLAT HEAT PIPE OF TYPE 1 (T-SHAPED)

The main purpose of experimental investigations with flat heat pipe of type 1 was to determine maximum heat load at various size of heat sources. In the first series of experiments the heater with area of 20 cm^2 was used. The results demonstrate thermal performance of heat pipe and influence of gravity forces on the operation of heat pipe at vertical orientation when heat source is above heat sink. The second series of experiments were conducted with using heater of small area about 2 cm^2 . The maximum heat fluxes at local intensive heating in center and corner of the heat pipe surface were determined.

3.1 Heater $30 \times 70 \text{ mm}^2$

In the course of experiments the maximum heat load was determined at various orientations and temperature of T-shaped flat heat pipe. The location of heat source and sink on the heat pipe has shown on fig. 3. The electric heater of size $30 \times 70 \text{ mm}^2$ was installed on the heat pipe at the maximum distance of 100 mm from a cooler. The water heat exchanger as the cooler was installed on the bottom side of heat pipe. The cooling water flow rate was constant and the inlet temperature

was controlled by means of a thermostatic bath. The heater, cooler and heat pipe were thermally insulated except on opposite from heater side of heat pipe. The temperature field of not insulated surface was recorded by infrared imager. The use of infrared imager allows observing the appearing of hot spot, the changing its form and size. Not insulated surface led to additional outflow of heat by convection and radiation. Estimations have shown that under experimental conditions the heat loss to ambient air amounted to about 2.5 watts of heat at temperature surface at 40 °C.

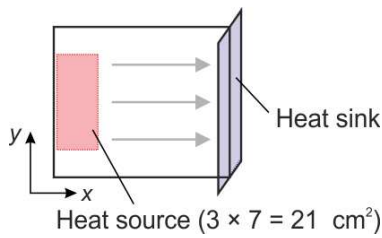


Figure 3. Heat source and sink location

Fig. 4 presents temperature profiles of the heat pipe surface along center line and temperatures of cooler at various heat loads after steady state was reached in horizontal orientation. Temperature of inlet cooling water was equal to 27 °C. With the growing power of heater the surface temperature of heat pipe increased uniformly, remained nearly isothermal within 2.5 degrees. After exceeding the heat load of 100 W there was a sharp increase of surface temperature in area of heater. The sharp overheating provides evidence of the wick is drying out and the maximum heat load has been achieved. With further grows of heating power the maximum surface temperature and the size of overheating area increases.

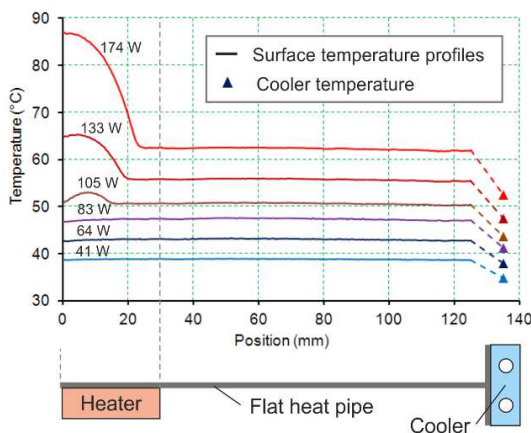


Figure 4. Temperature profiles along heat pipe

Fig. 5 presents differences between maximum surface and cooler temperatures vs. power of

heater at two various temperatures of cooling water for horizontal orientation of heat pipe. For the cooling water temperature of 27 °C the wick dryout was occurred at 100 W heat load at the temperature of the heat pipe was 50 °C. For the cooling water temperature of 42 °C the wick dryout was occurred at 130 W heat load at the temperature of the heat pipe was 68 °C.

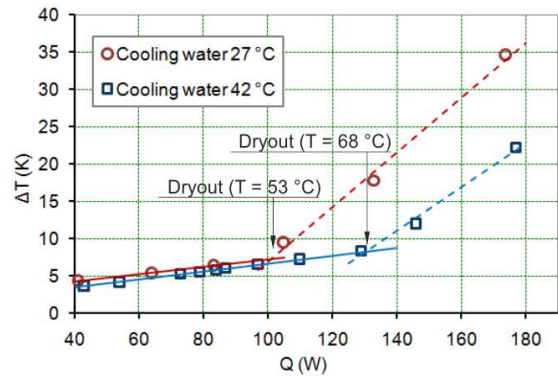


Figure 5. Temperature difference vs. power in horizontal position

Fig. 6 presents same dependences for vertical orientations of heat pipe, when the heater is above the cooler. For the cooling water temperature of 27 °C the wick dryout was occurred at 24 W heat load at the temperature of the heat pipe was 35 °C. For the cooling water temperature of 42 °C the wick dryout was occurred at 30 W heat load at the temperature of the heat pipe was 49 °C.

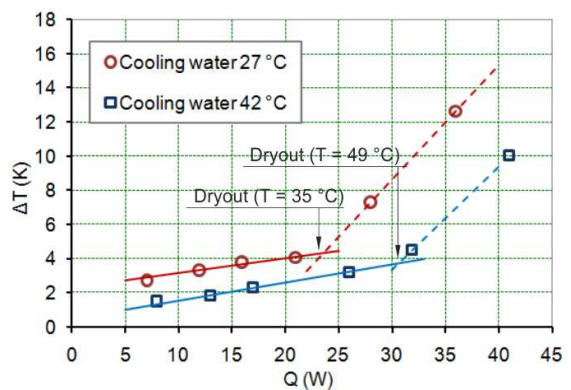


Figure 6. Temperature difference vs. power in vertical position

The conducted experiments showed, that when using heat source with area of 21 cm², the T-shaped flat heat pipe operates effectively without dryout of wick up to heat load of 100 W (at T ≈ 50 °C) at horizontal orientations. At vertical orientation, when heater is above cooler, at same other conditions the maximum heat load is of

30 W. The thermal resistance between maximum surface temperature of heat pipe (on the opposite side from heater) and cooler is less than 0.1 W/K.

3.2 Heater 2 cm²

The objective of experiments was to determine maximum heat power, which can be removed with using T-shaped flat heat pipe without wick dryout. The high power transistor was used as a heat source with size of 14 × 16 mm² (2.2 cm²), which capable to providing heat power up to 100 W. The experiments were conducted for horizontal orientations of heat pipe for various heat source locations on the surface (Fig. 7). With a central location of heater distance to cooler was 60 mm, with the location in the corner - 105 mm. The conditions of the experiments were same as with using heater 30 × 70 mm².

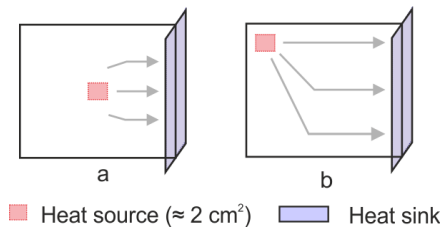


Figure 7. Heat source and sink location

Fig. 8 presents differences between maximum surface and cooler temperatures vs. power at two various locations of heat source. The results are presented for cooling water temperature of 27 °C. For the central location of heater the wick dryout was occurred after 25 W heat load at the temperature of the heat pipe was 35 °C. For the location in the corner the wick dryout was occurred at 13 W heat load at the temperature of the heat pipe was 32 °C.

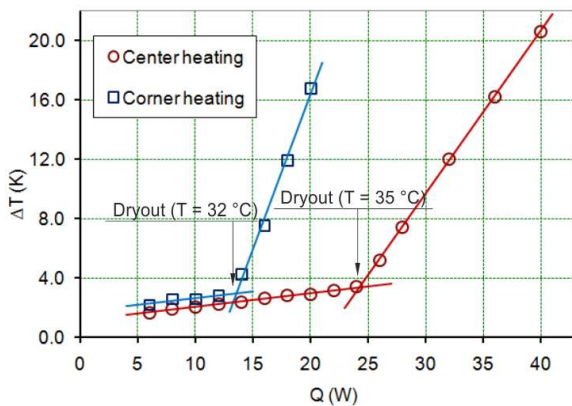


Figure 8. Temperature difference vs. power for area of heat source is equals 2.2 cm²

Fig. 9 presents examples of obtained by infrared imager temperature fields of heat pipe surface. The left image (fig. 9a) demonstrates almost uniform temperature field at values of heating power of 24 W. A slight decreasing temperature less than 2.5 degrees observed in area of corners near cooler. The right image (fig. 9b) demonstrates overheated spot on the surface at power of 28 W, this means dryout of wick.

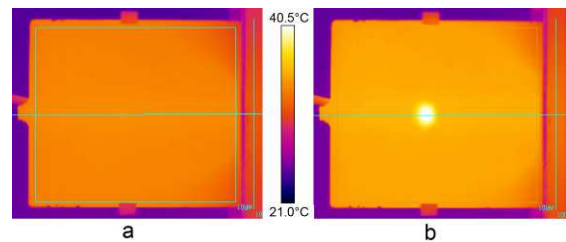


Figure 9. Temperature fields of heat pipe surface with central location heater of 2 cm²: a – uniform temperature field, b – overheating area.

The results of experiments show that with concentrated heat input (~ 2 cm²) in center of T-shaped flat heat pipe, the maximum heat flux is more than 10 W/cm² at temperature of 35 °C. With increasing distance between heat source and cooler the maximum heat flux reduces. Apparently, the reason for wick dryout is classical capillary limitation. When the heat source with a larger area is used (~ 20 cm²), the maximum heat load is much higher. This is due to the fact that the configuration of wick and vapor channels provides efficient movement of working fluid only along the direction to the cooler (to bottom of T-shaped flat heat pipe on fig. 1). The transverse motion of the working fluid is carried out with much more resistance. Therefore, the flat heat pipe almost doesn't spread the heat in transverse direction, and only narrow part of heat pipe area works effectively.

4. INVESTIGATION OF FLAT HEAT PIPE OF TYPE 2

4.1 Long distance between heater and cooler

The objective of experiments was to investigate thermal performance of heat pipe of type 2 (fig. 2) with high heat flux source. The location of heat source and sink on the heat pipe has shown in fig. 10. Heater of size 14 × 16 mm² (high power transistor) and cooler of size 50 × 70 mm² were mounted on the one side of horizontal heat pipe at distance L from each other. The experiments were

conducted for various values of L . The heater, cooler and heat pipe were thermally insulated from ambient air, except on some small areas of heat pipe surfaces from the opposite side from heater and cooler for observation temperature field by infrared imager. Temperatures of heater and cooler were measured by thermocouples.

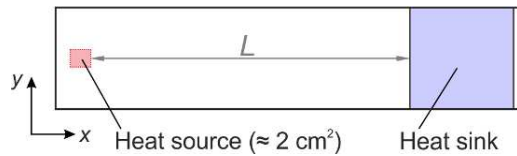


Figure 10. Heat source and heat sink location

Fig. 11 presents differences between heater and cooler temperatures vs. power of heater at two values of L . For the distance L of 240 mm the dryout of wick was revealed at heat load of 25 W. Temperature of heat pipe was 45 °C. For the distance L of 105 mm the wick dryout was revealed at heat load of 60 W. Temperature of heat pipe was 55 °C. The corresponding heat flux was more than 27 W/cm².

The conducted experiments showed that flat heat pipe of type 2 allows removing much more heat power from concentrated heat input ($\sim 2 \text{ cm}^2$) as opposed to flat heat pipe of type 1. The configuration of wick and vapor channels in heat pipe of type 2 provide effective heat spreading in transverse direction, therefore all width of heat pipe involved in the heat transfer.

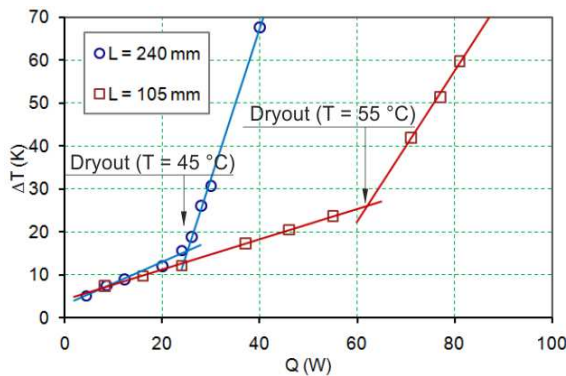


Figure 11. Difference heater and cooler temperatures vs. power.

4.2 Heat pipe as heat spreader

The purpose of these experiments was to determine the maximum heat flux of flat heat pipe of type 2 for the most favorable configuration of heat source and sink, when the heat pipe operates as a heat

spreader. The scheme of experiment is shown in fig. 12. Flat heat pipe was installed horizontally on a heater with maximum heat power up to 1 kW. The heat input area has form of circle with diameter of 16 mm (2 cm^2). The temperature of heater in the vicinity of contact with heat pipe surface was measured by thermocouples. The water heat exchanger as a cooler was installed on the heat pipe, covering almost entire its surface. The difference between inlet and outlet temperatures of cooling water and its mass flow rate were measured for evaluating heat power of cooler.

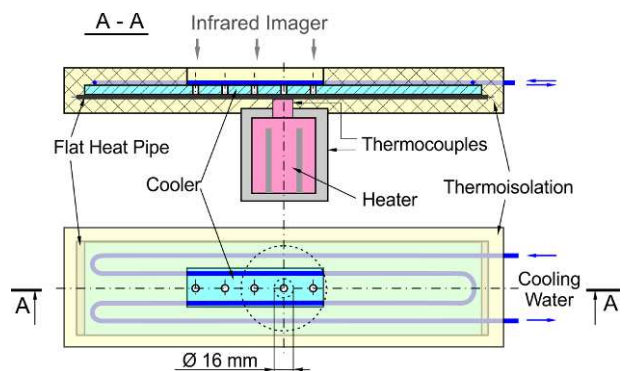


Figure 12. Experiment scheme

Fig. 13 presents the temperatures of heat pipe surface, which observed through holes in the cooler, for various values of power after reaching steady state. The temperature of cooling water was 41 °C. With heat power growing, the temperature of heat pipe surface in area of heat source increases uniformly and stays isothermal within 0.2 degree. After heat power (removing by cooler) has reached a value of 160 W, the surface temperature opposite heater begins to grow rapidly.

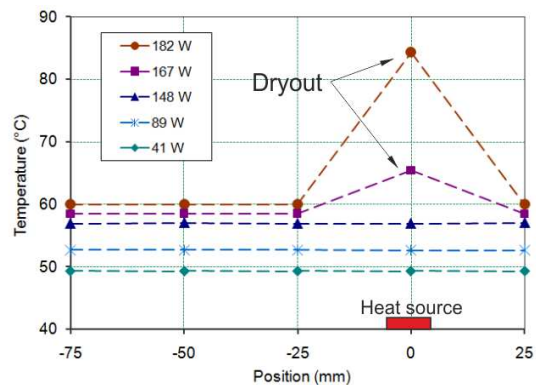


Figure 13. Temperatures of heat pipe surface

Fig. 14 presents two dependences of temperature differences vs. power: between heater (in the vicinity of heat pipe) and cooler; and between

temperatures of heat pipe surface (on the opposite side of heater) and cooler. With increasing power the temperature of heater grows linearly until heat power of 115 W. The corresponding thermal resistance is about 0.25 K/W. With further power increasing the temperature of heater grows more rapidly, but the growing rate of heat pipe surface temperature doesn't change. This indicates that the wick is drying out partially, not on full thickness. The hot spot on the surface of heat pipe appeared only at power of 160 W. It means that the wick is dried out on full thickness.

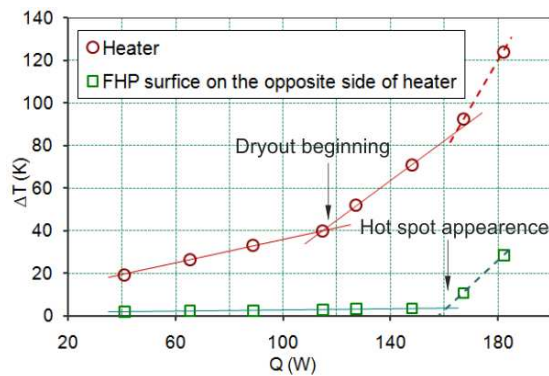


Figure 14. Differences temperatures heater - cooler and heat pipe surface - cooler vs. power

The experiments were conducted at various cooling water temperatures. It is revealed, that the maximum heat flux grows with increasing temperature. The dryout of wick arises at heat flux of 60 W/cm² at the temperature of flat heat pipe of 60 °C and at heater temperature of 90 °C. The overheating of the heat pipe surface from the opposite side from heater arises at heat flux of 80 W/cm² at heater temperature of 135 °C. The flat heat pipe of type 2 can be effectively used as heat spreader for heat sources with area ~ 2 cm² of more than 120 W.

3. CONCLUSIONS

The maximum heat fluxes for concentrated heat input on the area of about 2 cm² were determined for both flat heat pipes. For the flat heat pipe of type 1 (T-shaped) the maximum heat flux is essentially less than for the flat heat pipe of type 2. This is due to different configurations of wicks and vapor channels. The capillary structure of flat heat pipe of type 2 provides effectively heat spreading in plane of flat heat pipe.

The results of experiments with T-shaped flat heat pipe show that for the heat sources with area of 21 cm² the maximum heat load can be more than

100 W at horizontal orientation and heat pipe temperature about 50 °C. The maximum power of the center location heat source (the distance between heater and cooler is 60 mm) with area 2.2 cm² can be more than 20 W (heat flux 10 W/cm²) at the heat pipe temperature of 35 °C. The maximum heat loads decreases with increasing the distance from cooler down to 13 W for location in the farthest corner. It is revealed, that gravity forces can be essentially influences on the thermal performance of T-shaped heat pipe. For operation of heat pipe against gravity forces when heater is above the cooler for 100 mm the maximum heat load at vertical orientation is less then at horizontal orientation about 3 times.

For the flat heat pipe of type 2 the maximum heat flux is more than 27 W/cm² at distance of 105 mm between heat source and cooler. This value increases with decreasing distance to cooler. For the most favorable configuration of heat source and sink, when flat heat pipe operating as heat spreader (cooler covers the whole heat pipe surface), the wick dryout arises at heat flux of 60 W/cm² at heat pipe temperature of 60 °C.

REFERENCES

- Aghvami M., Faghri A. (2011) *Analysis of flat heat pipes with various heating and cooling configurations*. Applied Thermal Engineering, 31, p. 2645-2655
- Hirofumi Aoki, Masami Ikeda and Yuichi Kimura (2011), *Ultra thin heat pipe and its application*. Frontiers in Heat Pipes, Vol. 2, No. 4 (2011)
- Lefèvre F., Lips S., Rullière R., Conrardy J., Raynaud M., Bonjour J. (2012) *Flat plate heat pipes: from observations to the modeling of the capillary structure*. Frontiers in Heat Pipes (FHP), 3, 013001.
- Masataka Mochizuki et al. (2011) *Review of heat pipe application including new opportunities*. Frontiers in Heat Pipes (FHP), 2, 013001 (2011)
- Vadakkan U., Garimella S.V., Murthy J.Y. (2004) *Transport in flat heat pipes at high fluxes from multiple discrete sources*. ASME J. Heat Transfer, 126, p. 347-354
- Wang Y., Vafai K. (2000) *An experimental investigation of the thermal performance of an asymmetrical flat plate heat pipe*. Int. J. Heat and Mass Transfer, 43, p. 2657-2668
- Wessel Wits (2010) *Advances in Integrated Heat Pipe Technology for Printed Circuit Boards*. 40th International Conference on Environmental Systems, AIAA 2010-6007.

LOOP HEAT PIPE THERMAL MODEL

C. FIGUS, T. COQUARD, A. LECOSSAIS

ASTRIUM
 Tel 33-5-62-19-57-61
 Fax 33-5-62-19-58-00
 Christophe.figus@astrium.eads.net
 31 Av. des cosmonautes
 31402 Toulouse Cedex
 FRANCE

ABSTRACT

Modeling a Loop Heat Pipe (LHP) at spacecraft system level could be carried out - at first approximation - by simply using a constant thermal conductance on the complete range of the evaporator power : from the lowest possible power up to the maximum value depending on the available capillary pumping capability. This approach leads however to an overestimation of Loop Heat Pipe performance, especially at low power. Moreover, the sub-cooled condenser zone could reach the temperature level such that the radiator heaters are activated to prevent the LHP working fluid from freezing. Then, the precise determination of equipment temperatures functioning at low dissipation rate as well as the activation of radiator heaters at satellite cold mode requires a quite accurate modeling of the LHP. Astrium has developed a simplified thermal model for LHP architecture design and justification. This model is currently used for the development of different thermal bus for the cooling and temperature regulation of instruments and equipments. The LHP module software is compatible with any standard system level thermal model, without requiring the use of any dedicated heavy hydraulic software. The software has to be included in the satellite system model, allowing to predict the LHP specific operations such as: instabilities and performance oscillations; start & stop operations depending on environment variations and dissipative source conditions, active performance control via LHP heat leak regulation. Owing to a wide test campaign of different technologies and architectures, it has been possible to achieve a very high level of accuracy in the simulation results. An overview of different tested cases and simulations is presented. Moreover, a correlation of an active regulation with a mini-Loop Heat Pipe is shown and discussed.

KEY WORDS Loop heat pipe, thermal, model

1. INTRODUCTION

Astrium as the third worldwide spacecraft manufacturer develops technologies with strong system interactions. Thus, convinced of the thermal architecture impact on the spacecraft performances, Astrium has decided in 1989 to start the development of capillary pumped loop thermal transfer devices (LHP). This development has led to in-orbit qualification and use of micro (less than 1 cm²), mini (less than 10 cm²), medium (less than 100 cm²) and macro capillary evaporators.

In parallel to the product development, the Astrium team has developed a strong expertise in “new” passive thermal architectures using LHP. These LHP architectures could be thermal regulation of an equipment; multi-radiators or multi-LHPs configurations; deployable radiator; ...

In order to develop and predict impacts and thermal performances of these architectures, it was

necessary to have a simulation tool compatible with large spacecraft thermal model and enough detailed for a good description of the different physical phenomena.





Micro-LHP: Evaporator : 3x5 mm ² 0.5 / 10 W	
Mini-LHP: Evaporator : 3x3 cm ² 2 / 50 W	
Medium LHP: Evaporator : 5x10 cm ² 20 / 200 W	
Macro LHP: Evaporator : 5x40 cm ² 50 / 800 W	

Figure 1: Astrium/EHP Ammonia Loop Heat Pipes

2. MODEL DEFINITION

2.1 Model requirements

In order to support the design, development and use of Loop Heat Pipe in a large thermal system, some main requirements were established:

- Physical phenomena inside a Loop Heat Pipe are thermal, hydraulic and thermodynamic. The used model should take into account these physical phenomena.
- The model should be enough detailed for a comprehensive behavior of the LHP and enough reduced for running in larger thermal model (like spacecraft thermal model) without impacting the global running time.
- The model should be able to simulate transient and steady states.
- The model should predict on-ground and in-orbit performances whatever is the LHP orientation.
- The model should allow simulating active or passive LHP conductance variation.

Based on these requirements, no commercial software did provide satisfactory performance, and it was decided to develop our own LHP model.

2.2 Main hypotheses

2.2.1 Time constants

A thermal system using Loop Heat Pipe, as heat carrier, has three major time constants:

- The Loop time constant (τ_{Loop}) defines the time scale for the fluid to flow around the complete loop. It is a hydraulic time constant.
- The Evaporator time constant (τ_{Evapo}) defines the time scale for the fluid to modify the operating temperature of the evaporator. It is a thermodynamic time constant.
- The equipment time constant (τ_{Eq_t}) defines the time scale for heat to modify the equipment temperature. It is a thermal time constant.

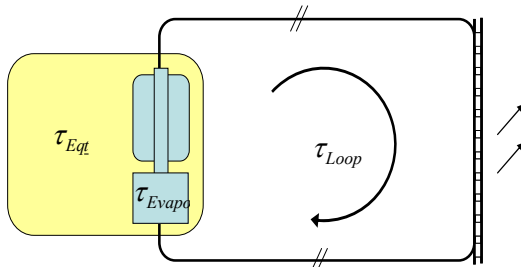


Figure 2 : Thermal system with LHP time constants

Concerning the equipment time constant it is defined by the following law:

$$\tau_{Eq_t} = \frac{M_{eq} \times C_p}{C_{LHP}} \quad (1)$$

with M_{eq} the equipment mass, C_p the equipment specific heat and C_{LHP} the LHP thermal conductance.

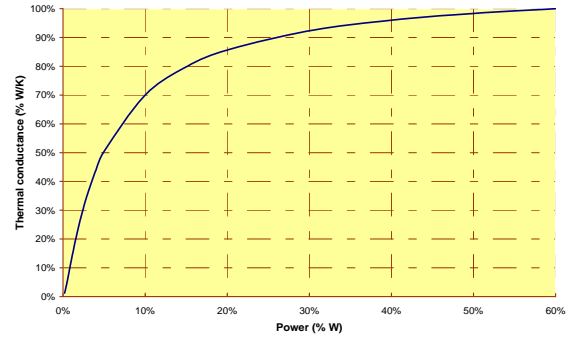


Figure 3 : Typical LHP thermal conductance

The Loop time constant is defined by the fluid flow, thus the following law is obtained:

$$\tau_{Loop} = \frac{L \times \pi \times d^2}{4 \times Q} (\ell_v \times \rho_v + \ell_l \times \rho_l) \quad (2)$$

$$\tau_{Loop} \approx \frac{\pi \times L \times d^2 \times \rho_l \times \ell}{8 \times Q} \quad (3)$$

With L the latent heat of vaporization, d the LHP tube internal diameter, $\ell_{v,l}$ respectively vapor and liquid line length (ℓ is the total LHP tubing length and the assumption is done that $\ell_v = \ell_l = \frac{\ell}{2}$), $\rho_{v,l}$ respectively vapor and liquid density (the assumption is done that $\rho_v \ll \rho_l$), Q the heat transported by the LHP.

The evaporator time constant is defined with the energy balance at evaporator level.

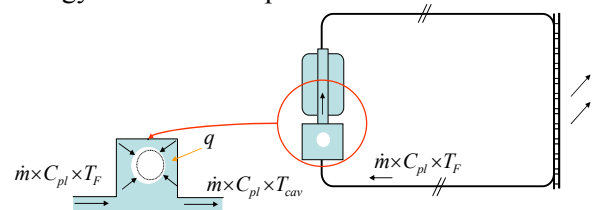


Figure 4 : Evaporator energy balance

Thus the following expression can be written:

$$\frac{dT_{evapo}}{dt} \approx \frac{dT_{cav}}{dt} \quad (4)$$

Where T_{evapo} is the evaporator temperature, T_{cav} is the cavity temperature. Then

$$\frac{dT_{cav}}{dt} \approx \frac{\dot{m}}{M} \times (T_{cav} - T_F) + \frac{L}{C_{pl}} \times \frac{dx}{dt} - \frac{dq}{M \times C_{pl}} \quad (5)$$

Where \dot{m} is the LHP fluid mass flow rate, M is the cavity thermal mass, T_F is the LHP cold fluid temperature, C_{pl} is the LHP liquid specific heat, x is the LHP cavity vapour title, q is the heat flux to the cavity when LHP is operating.

Concerning variation of the vapour title, it is:

$$\frac{dx}{dt} \approx \frac{Q_{out}(t) - Q_{in}(t)}{M \times L} \approx \frac{Q_{out}(t) - Q_{out}(t - \tau_{Loop})}{M \times L} \quad (6)$$

$$\text{So } \frac{L}{C_{pl}} \times \frac{dx}{dt} \approx \frac{Q}{M \times C_{pl}} \times \frac{\tau_{Loop}}{\tau_{EqL}} \quad (7)$$

For the variation of the cavity heat flux, it is:

$$\frac{dq}{M \times C_{pl}} \approx \alpha \times \frac{dQ}{M \times C_{pl}} \quad (8)$$

$$\text{And } dQ = \int_{\tau_{Evapo}}^{\tau_{EqL}} \frac{Q}{\tau_{EqL}} \times dt \quad (9)$$

$$\text{So } \frac{dq}{M \times C_{pl}} \approx \alpha \times \frac{Q}{M \times C_{pl}} \times \frac{\tau_{Evapo}}{\tau_{EqL}} \quad (10)$$

If we suppose that

$$T_{cav} = A \times \text{Exp}\left(\frac{-t}{\tau_{Evapo}}\right) + B \quad (11)$$

Then using relations (5), (7), (10) and (11) the following relation is then obtained:

$$\tau_{evapo} \approx \frac{M \times L}{Q} \quad (10)$$

Based on these results some main conclusions can be performed.

At low heat load, the LHP thermal conductance is low and the LHP cavity is sub filled. Thus, the equipment time constant is long, the evaporator time constant is short and the following relation is obtained.

$$\tau_{EqL} \gg \tau_{evapo} \approx \tau_{Loop} \quad (12)$$

At large power, the LHP thermal conductance is large, the LHP cavity is filled. Thus the following relation is obtained.

$$\tau_{EqL} > \tau_{evapo} > \tau_{Loop} \quad (13)$$

It has to be noticed, that most of the time the Loop time constant is short in comparison to Equipment

and evaporator time constant. But in some configurations, for micro-Loop heat pipe device (see figure 1) or for long distance heat transport the time constant of the Loop at low power load can be longer than the evaporator time constant, leading to some oscillatory behaviour.

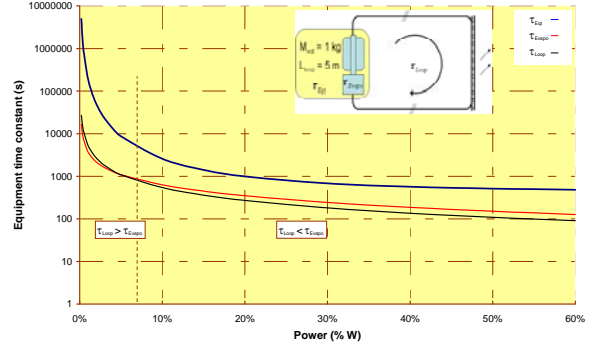


Figure 5 : Example of time constant comparison for 1kg equipment cooled with mini-LHP

Thus, use of a quasi-static Loop Heat Pipe thermo-hydraulic model in order to describe transient behaviour is acceptable as long as equipment time constant is larger than Loop and Evaporator time constants.

2.2.2 Momentum and Energy balance

In order to perform the momentum and energy balance equations, the heat and mass transfer at evaporator porous wick [1] should be performed.

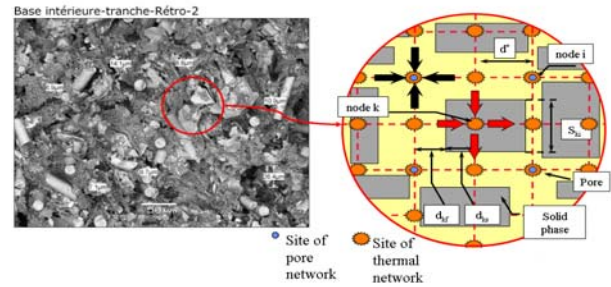


Figure 6 : Pore network simulation of wick

In contrary to Faghri [2] definition, the transfers are not in one dimension, but in two dimensions, with the displacement of the vapor mass production along the porous wick.

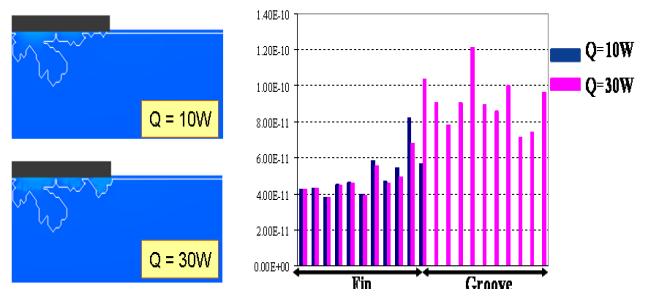


Figure 7 : Vapor production at wick/fin level

Such a two dimensional model is not compatible with a complex system (spacecraft) thermal model, as it would lead to too long running time. Momentum and energy balance equations, impact directly the evaporation heat transfer (C_{evap}) and pressure drop budget (vapour flow through the porous media). As indicated on figure 8, the evaporation heat transfer can be considered as constant in the LHP operating range as soon as the pressure drops through the complete loop are much smaller than the evaporator maximum capillary pressure ($P_{c_{\text{max}}}$).

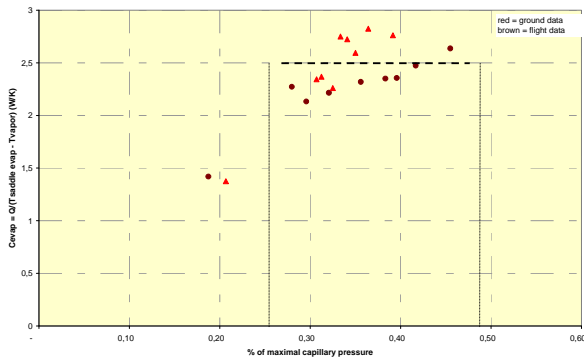


Figure 8 : Evaporation conductance for a mini-LHP

The thermo-hydraulic model can be simplified in a unidirectional model as soon as the pressure drop through the complete LHP are much lower than the evaporator maximum capillary pressure ($P_{c_{\text{max}}}$). The limit is defined using a pressure head (Hydrostatic for example) for which the evaporation heat transfer starts decreasing.

2.3 Model

The thermo-hydraulic model is based on the mass, heat and momentum balance equation on several LHP nodes (see figure 9):

- The evaporator saddle,
- The vapour at wick meniscus (A),
- The condenser in vapour and liquid phase (B, C, D),
- The LHP cavity (E),
- The liquid at wick meniscus (F).

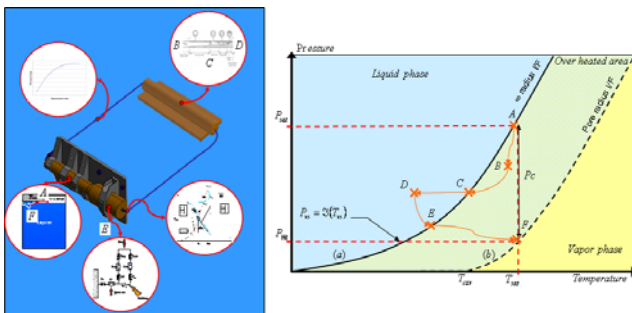


Figure 9 : Sensitive LHP thermal nodes

Such balance leads to an explicit relationship at evaporator level:

$$T_{Eqt} - T_F = \frac{\alpha * Q^2 + \beta * Q + \delta}{\xi * Q + \varepsilon} \quad (14)$$

Where $\alpha, \beta, \delta, \xi, \varepsilon$ are explicit parameters of the LHP and operating conditions (fluid, pressure drops,...); T_F is the cooled liquid temperature. And thus the only implicit relationship is obtained at condenser level with the enthalpy variation along the condenser.

$$T_{sat} - T_F = \pi \times d \times \int_{l_{condenser}} h(x) \times (T_x - T_w) dx \quad (15)$$

Where h is obtained with a Travis formulation and T_{sat} is the vapor temperature of the LHP. Such semi-explicit formulation allows limiting the running time. The only restriction is provided by the condenser and the vapour front displacement in transient, which has to be minimized between two time steps in order to not generate high liquid cold temperature variation and thus evaporator oscillations.

Indeed the LHP is an “oscillator”. At large power, the system operates as a constant conductance device and time steps can be increased. At low power, the system operates in variable conductance mode and small perturbations are amplified by the evaporator behaviour as shown on figure 10.

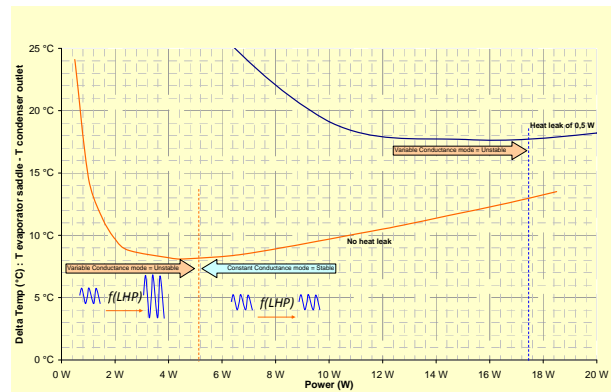


Figure 10 : LHP oscillator behaviour

For this model, some additional closure laws are also established in order to take into account effect gravity on the cavity, condenser or evaporation heat transfers. These relationships are very dependant of the LHP design and local Bond number. Thus gravity has nearly no effect on mini (for a limited cavity size) and micro LHP heat transfer, which is not the case for medium and macro LHP, or for mini-LHP with large cavity volume.

3. RESULTS AND DISCUSSION

A complete representative mock-up has been extensively tested in order to deliver flight hardware for an observatory spacecraft. The mock-up was composed of 8 mini-LHPs dedicated to several instruments cooling. The mock-up was tested in vacuum conditions for several orientations (horizontal and against gravity head), with several equipment inertia and power loads.

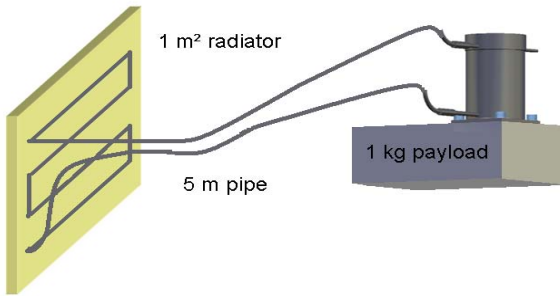


Figure 11 : Tested mock-up

In a first step, only LHP heat transfer capacity was tested and correlated. At low power (less than 10W), the system is oscillating. The Loop and evaporator time constants are close to the equipment time constant. Thus, even if the LHP should operate in constant conductance mode (transition between constant and variable conductance mode is around 6W for mini-LHP), the system conditions provides a resonance between the condenser front displacement and the equipment inertia variation.

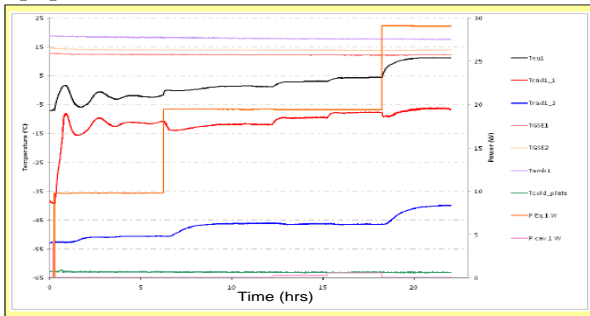


Figure 12 : Test results at different power

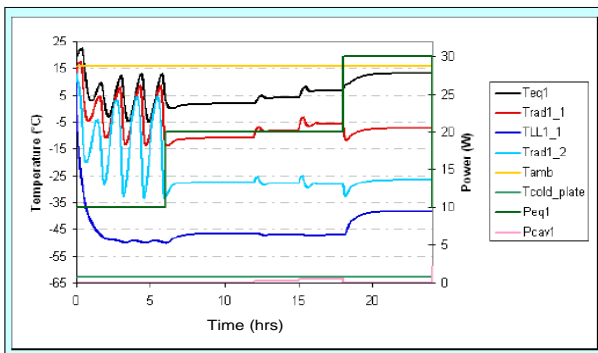


Figure 13 : Test simulation in same conditions

At low and large power load, the thermal model predicts correctly the system behaviour, test correlations are performed with accuracy better than 2°C.

In a second step, the system is tested in temperature regulation mode. LHP thermal conductance is adjusted by means of a cavity heater in order to maintain the equipment temperature constant. The regulation is performed in a mono-stage (only radiator temperature variation are filtered, the vapour temperature is maintained constant) and in a two stages (= cascade, radiator temperature and payload power variations are filtered, the vapour temperature is adjusted in order to maintain a constant equipment temperature).

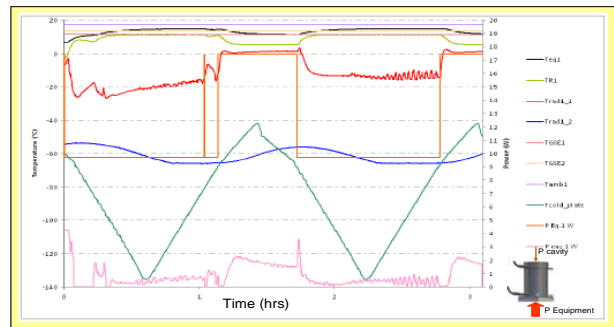


Figure 14 : Test results in cascade regulation mode

As shown on figure 14, even with radiator temperature variation of several tens of degree and equipment power variation from 10 to 18 W, the equipment is maintained in a temperature range lower than 2°C. Thermal correlations are also with accuracy better than 2°C. Calculation of the active power on the cavity side in order to regulate the LHP temperature is better than 10% compared with test results.

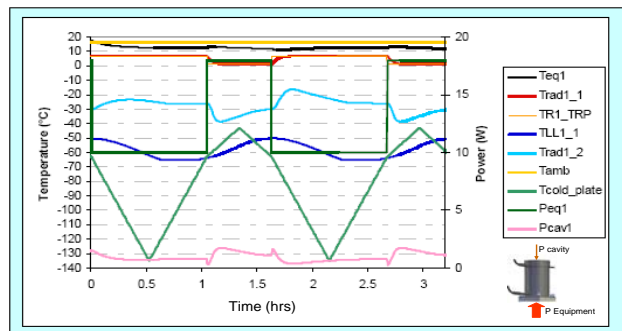


Figure 15 : Test simulation in cascade regulation mode

Moreover, one can observe, that with heat applied on the LHP cavity, the thermal system is stabilised. Even when operating at 10W, no more oscillations are observed. By heating the evaporator cavity, the evaporator time constant becomes negligible compared to the equipment one.

Owing to this model, Astrium has developed and correlated advanced thermal systems using LHP. Thus, it has been possible to develop advanced thermal bus using 8 mini-LHPs and single radiator. Start-up conditions; heat sharing rules and stability of such configuration were studied and used in the frame of project like Atlid cooling instrument. It was also possible to demonstrate and correlate thermal regulation with less than 1°C accuracy with large equipment power load (100% variation) and radiator thermal environment (60°C variation) variations. This function has been implemented on another observatory spacecraft.

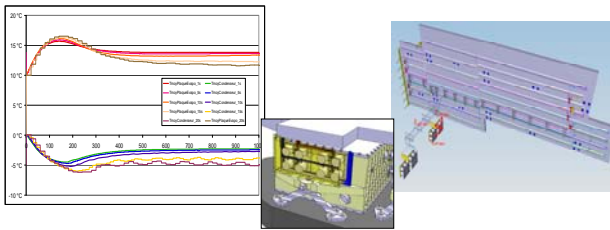


Figure 16 : Parallel multi LHPs / single-radiator architecture (courtesy from ATLID ESA/Astrium)

A multi-LHPs with multi-radiators (4) configuration was studied and developed. Tests were performed with a representative transient sun illumination. Heat sharing rules and stability were tested and correlated. The benefits of this architecture were demonstrated and its extension to a larger spacecraft analyzed. Based on the test results and the model it was demonstrated the very good reliability of the LHP device, and the large benefits of such solution. The architecture stability criteria were defined and validated.

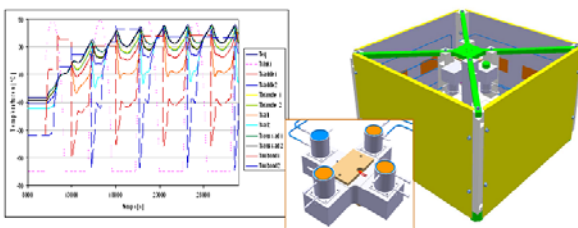


Figure 17 : Multi-LHPs with multi-radiators architecture (courtesy from MRAD CNES/Astrium)

In the same way, a double side deployable radiator (DPR) with 4 dedicated LHPs attached to a same heat pipe network is being studied in the frame of the Alphas extension program development. This multi-LHPs with multi-radiators (double side) configuration requires to predict at system level (spacecraft) impacts of the environment (antenna; solar array, spacecraft, sun illumination, payload dissipation...) on the radiator dissipation and Loop

Heat Pipe heat sharing. The global thermal conductance of the DPR can be affected by these different parameters. A thermal model of the DPR has been established, and test on a representative mock-up are on-going.

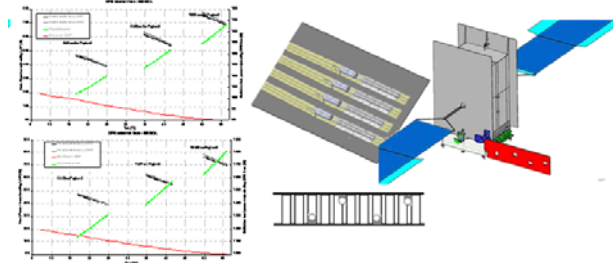


Figure 18 : Deployable radiator: Parallel multi LHPs / multi-radiators architecture (courtesy from Alphas ESA/EHP/Astrium)

4. CONCLUSIONS

Based on a physical definition of some Loop Heat Pipe nodes, Astrium has developed a LHP semi-explicit thermo-hydraulic model. This model is used in transient and steady state environment, and is deeply used for the implantation of “advanced” thermal control system into complex system (Spacecraft) without impacting the running time. Owing to this model, the team has developed high accuracy multi-LHPs active regulations for three different observatory spacecrafts, multi-radiators and multi-LHPs architecture for three phase-A demonstrators and one proto-flight model. The thermal model has been in-orbit validated with 6 different applications.

NOMENCLATURE

LHP	Loop Heat Pipe
M	Mass
Q	Heat
T	Temperature
ρ	Density
t, τ	Time

ACKNOWLEDGEMENT

Astrium wants to acknowledge CNES and ESA for their support.

REFERENCES

- [1] Figus, C and Al (1998) *Heat transfer in porous media considering phase change capillarity and gravity*. Int. Jour. of Heat and Mass transfer
- [2] Faghri (1994) *Heat pipe science and technology*. Taylor & Francis, London

SIMULATION OF THE OPERATING CHARACTERISTICS OF A CASCADED LHP WITH THERMAL CONNECTOR FOR ON BOARD ELECTRONIC COOLING

Nathanaël Rivière, Valérie Sartre, Jocelyn Bonjour

INSA-Lyon, CETHIL, UMR5008,
F-69621 Villeurbanne, France

Phone: + 33 (0)4 72 43 64 27, Fax: + 33 (0)4 72 43 88 11, E-mail: valerie.sartre@insa-lyon.fr

ABSTRACT

For avionic applications, heat can be transferred from the electronic cards to the heat sink in a totally passive way by Loop heat pipes (LHP). In order to keep the possibility of easily connecting or disconnecting the electronic box, a cascaded LHP is envisaged, including a “card LHP” which transports heat from the electronic components to a thermal connector and an “aircraft LHP” which links the connector to the aircraft structure. The connector ensures the thermal link between the condenser of the card LHP and the evaporator of the aircraft LHP. The objective of the present work is to design this cascaded LHP, in the operating conditions corresponding to avionic applications. A simplified analytical model is used (Launay et al., 2008). The selection of the geometry, fluid and materials is performed by means of a sensitivity analysis to these parameters. Four fluids were compared - methanol, ethanol, water, acetone - and two materials for the evaporator body – copper, stainless steel. Wicks made of sintered powder of nickel or copper and a polypropylene wick are simulated. Some relevant geometrical parameter are varied, the tube diameter and the wick thickness. With the proposed cascaded LHP, the evaporator temperature does not exceed the maximum allowable limit in the whole operating range.

KEY WORDS: Loop Heat Pipe, thermal connector, analytical model, sensitivity analysis

1. INTRODUCTION

Loop heat pipes are thermo-capillary-driven two-phase heat transport systems which have already proved their efficiency for the thermal management of electronic devices under space or ground environmental conditions. For avionic applications, the opportunities for cooling the electronic boxes are generally limited due to the small external surface area of the boxes. Therefore, it is necessary to find an external heat sink on the aircraft structure itself. The heat can be transferred from the electronic cards to the heat sink by a LHP, in a totally passive way. In order to keep the possibility of racking the electronic box, a thermal connector is envisaged which, like an electrical connector, should transfer the heat with a minimal thermal resistance. Transferring heat by a conventional LHP is not feasible, because the tight fluidic loop cannot be separated in two parts. Another solution is to design a cascaded LHP (figure 1). The “card LHP” transports heat from the electronic components to the thermal connector, and the “aircraft LHP” links the connector to the aircraft structure which acts as the

terminal heat sink. The connector ensures the thermal link between the condenser of the card LHP and the evaporator of the aircraft LHP.

The objective of the present work is to design this cascaded LHP, in the operating conditions corresponding to avionic applications. A sensitivity analysis is performed on various LHP geometrical parameters, on working fluids and LHP materials.

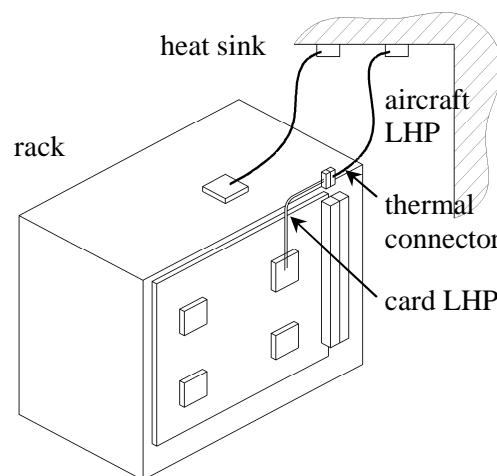


Figure 1. Rack equipped with the cascaded LHP

2. LHP GEOMETRY AND MODEL

The card LHP and aircraft LHP have about the same design. The evaporators have a cylindrical shape in order to enhance the mechanical resistance under pressure. Due to the flat shape of electronic components, a saddle must be added to the evaporator of the card LHP which supports the component (figure 2). The reservoir is integrated laterally in the evaporator body. The condenser of the card LHP is a tube wired around an annular copper cylinder, in which the evaporator of the aircraft LHP is inserted (figure 3).



Figure 2. Cross section of the card LHP evaporator

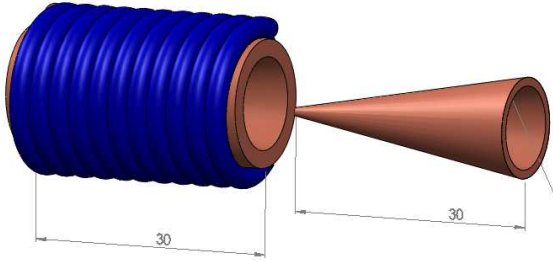


Figure 3. Concept of the thermal connector

A numerical model was developed for each LHP, solving the conservation equation of momentum and energy for the evaporator wall, the wick, the reservoir, the liquid line, the condenser, the region of subcooled liquid and the condenser wall (Launay et al., 2007). The system of equations is closed by thermodynamic equations applied to the liquid-vapour interfaces. In this work, a simplified analytical model is used (Launay et al., 2008). It mostly consists of general simplified equations for predicting the LHP reservoir temperature in variable conductance mode (eq. 1) or fixed conductance mode (eq. 2):

$$T_R = \frac{T_{Sink} + \frac{l_v}{c_{p,l}} \left[\frac{R_E}{R_{wall}} + \frac{T_A}{R_A Q_i} \right] + (T_A - T_{Sink}) \left[1 - \exp \left(- \frac{\pi D_L L_L K_L}{Q_i} \frac{l_v}{c_{p,l}} \right) \right]}{1 - \frac{1}{Q_i} \left[\frac{1}{\rho_v c_{p,l}} \left(\frac{1}{R_w} + \frac{1}{R_{wall}} \right) (\Delta P_v + \Delta P_l - \rho_l g \Delta H) - \frac{l_v}{c_{p,l} R_A} \right]} \quad (1)$$

$$T_R = T_{Sink} + \frac{Q_i}{\pi D_{C,i} L_C K_C} \frac{1 + \frac{R_E}{R_{wall}} \frac{K_C}{K_{sub}}}{1 + \frac{R_E}{R_{wall}}} \quad (2)$$

The evaporator body temperature is deduced from the heat balance at the evaporator wall:

$$Q_i = \frac{T_E - T_R}{R_{wall}} + \frac{T_E - T_v}{R_E} \quad (3)$$

A thermodynamic relationship links the vapor and reservoir temperatures:

$$T_v - T_R = \left(\frac{\partial T}{\partial P} \right) (\Delta P_v + \Delta P_l - (\rho_l - \rho_v) g \Delta H) \quad (4)$$

The calculation of the pressure losses due to friction and hydrostatic forces in the LHP is based on usual relationships which depend on the flow regime. The thermal resistance corresponding to the axial heat leak, R_{wall} , and the thermal resistance between the evaporator wall and the interface, R_E , are deduced from the LHP geometry, assuming that the porous medium is saturated by the liquid. The model also includes the calculation of the capillary limit. The reservoir is designed according to the method recommended by Ku et al. (1999). The thermal resistance of the connector was calculated with a 2D model based on a finite volume method, not presented here. Its value is of 0.15 K/W.

The aircraft LHP operation is first simulated, since its boundary conditions are known: fixed heat flux at the evaporator, Fourier condition at the condenser. Knowing the heat dissipation, the connector thermal resistance, and the evolution of the aircraft LHP evaporator temperature as a function of the heat input (output data of the first simulation), the condenser wall temperature of the card LHP can be calculated. The card LHP operation is then simulated, using a fixed temperature condition at the condenser wall and a fixed heat flux at the evaporator. Due to the electronic component temperature limits, the maximum permitted evaporator wall temperature of the card LHP is 110 °C.

3. SENSITIVITY ANALYSIS

2.1 Simulation parameters

The reference geometrical parameters used in the numerical simulations are given in table 1. In the following numerical simulations, the ambient and

heat sink temperatures are fixed to their maximal values in avionic applications, i.e. 70 °C. The heat transfer coefficient between the condenser wall and the heat sink is 4000 W/m².K. As the LHP tubing and the compensation chamber are not thermally insulated, a heat transfer coefficient of 10 W/m².K with the ambient is assumed. An adverse elevation of 0.4 m of the evaporator with respect to the condenser is considered. The sensitivity analysis is conducted for the aircraft LHP only. The evolutions of the LHP evaporator wall temperature with the heat input rate are compared by varying one parameter at a time, the other parameters being fixed to their reference value. The total LHP pressure drops are compared to the capillary pumping pressure.

Table 1. LHP geometry.

Evaporator	
I.D./O.D./length	10/13/30 mm
vapor channels size	1 × 1 mm ²
vapor channel spacing	1 mm
saddle size	30 × 30 × 2 mm ³
Capillary structure	
I.D./O.D./length	2/10/30 mm
porosity	75 %
pore radius	4 μm
Compensation chamber	
I.D./O.D./length	12/13/30 mm
Liquid and vapor lines	
I.D./O.D./length	2/2.4/0.5 mm
Condenser	
I.D./O.D./length	2/2.4/0.6 mm

2.2 Effect of the working fluid

The effect of the working fluid is investigated using four fluids commonly used in LHPs, i.e. ethanol, methanol, water and acetone. Whatever the fluid and input power, the total pressure drops are lower than the capillary pumping pressure provided by the sintered nickel wick (fig. 4). The evaporator wall temperature is much more affected by the fluid type at low than at high heat flux (fig. 5). The highest temperatures are reached with water, because the LHP operates at variable conductance mode in the whole heat flux range: due to the high latent heat of water, the mass flow rates are lower as compared to other fluids. For heat fluxes greater than 50 W, methanol is the best working fluid. But as it is a toxic compound, ethanol is preferred for avionic applications.

2.3 Effect of the porous material

In the LHP filled with ethanol, three types of sintered porous wicks are simulated, whose properties were found in the literature: copper ($\lambda = 98$ W/m.K, $\varepsilon = 69$ %, $r_p = 8$ μm), nickel

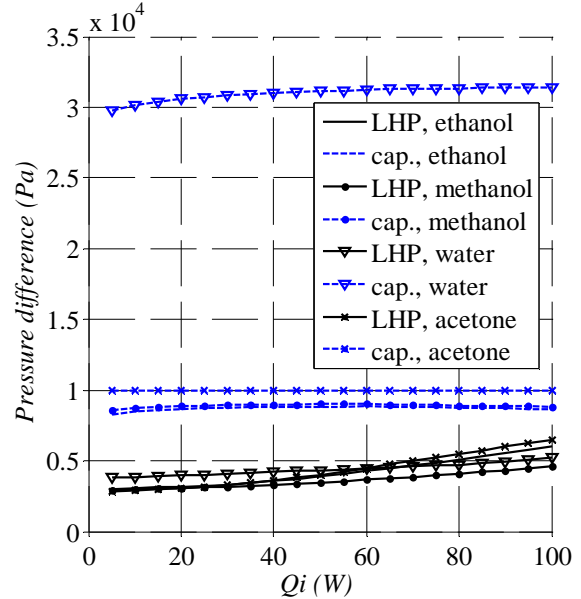


Figure 4. Total pressure drops along the LHP and capillary pumping pressures for various fluids

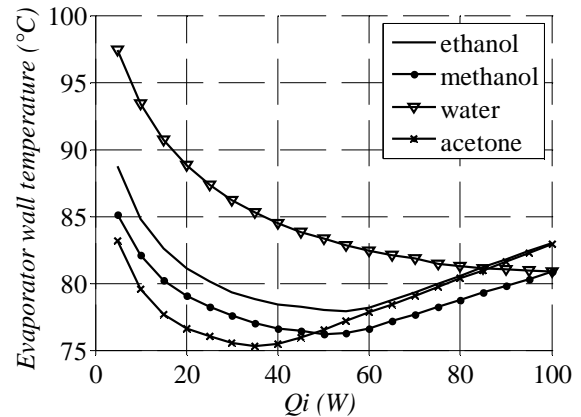


Figure 5. Evaporator wall temperatures for various working fluids

($\lambda = 90$ W/m.K, $\varepsilon = 75$ %, $r_p = 4$ μm) and polypropylene ($\lambda = 0.2$ W/m.K, $\varepsilon = 45$ %, $r_p = 0.5$ μm). The polypropylene wick is the most favorable material. Due to the small pore radii, the capillary pumping pressure is very high (fig. 6); its low thermal conductivity reduces the radial heat leak (fig. 7), so that the evaporator wall temperature does not exceed 85 °C in the whole heat flux range (fig. 8). The main disadvantage of polypropylene lies in its low tolerance to high temperatures (Boo & Chung, 2004). Therefore, the porous nickel wick is more convenient for such application, although

the evaporator reaches higher temperatures in variable conductance mode (fig. 8). The copper wick is not suitable, since the capillary limit may be reached at large heat dissipations (fig. 6).

2.4 Effect of the wick thickness

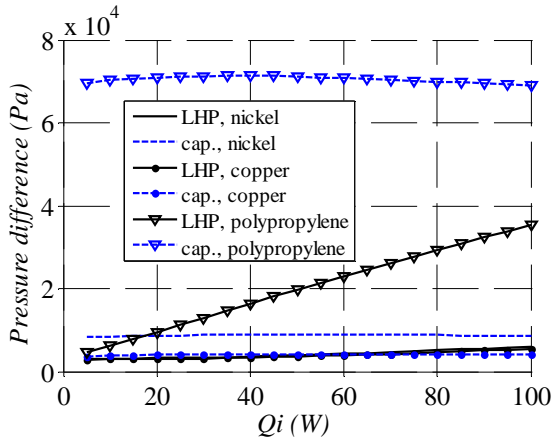


Figure 6. Total pressure drops along the LHP and capillary pumping pressures for various wicks

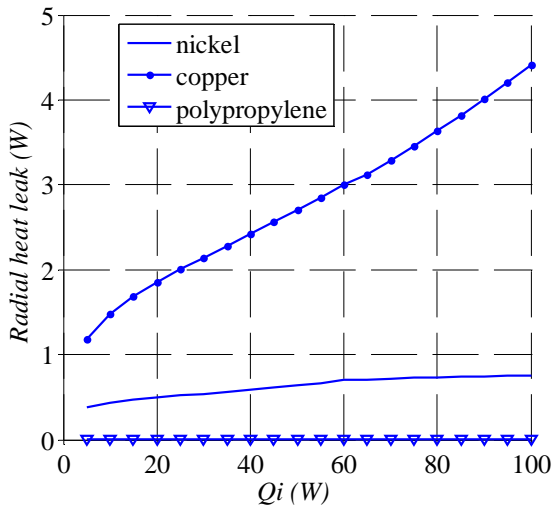


Figure 7. Radial heat leaks for various wicks

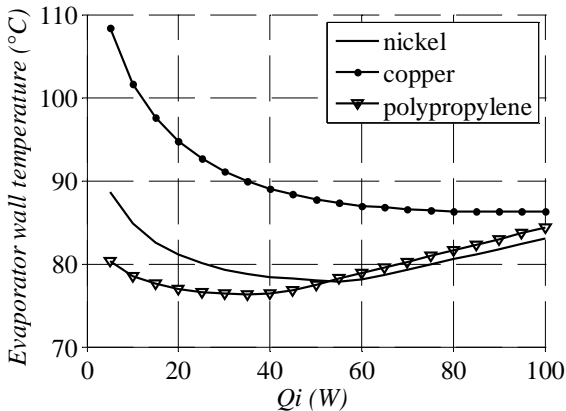


Figure 8. Evaporator wall temperatures for various wicks

The LHP performance is very sensitive to the wick thickness, as shown in figure 9. Reducing the wick thickness increases the radial heat leak (fig. 10) and hence, the evaporator wall temperature becomes higher. This effect seems to vanish at large heat fluxes.

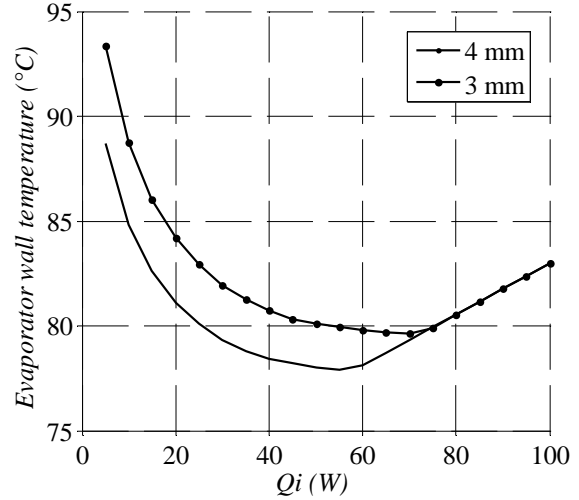


Figure 9. Effect of the wick thickness on the evaporator wall temperature

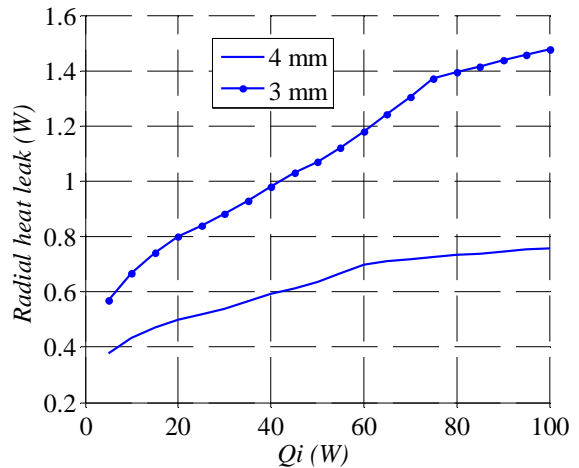


Figure 10. Effect of the wick thickness on the radial heat leak

2.5 Effect of the evaporator body material

We compare here the performance of LHPs whose bodies (evaporator and compensation chamber) are made of copper or stainless steel. In both cases, the other elements (tubes, condenser) are made of copper. Due to the lower thermal conductivity of stainless steel as compared to copper, the axial heat leaks are reduced in the whole heat flux range (fig. 11), so that the evaporator wall temperature is lowered at low heat inputs (fig. 12). When the heat power reaches 20 W, the temperature curves meet together. In the energy balance of the evaporator wall (eq. 3), the heat input is shared into the axial

heat leak and the heat fraction transferred to the interface. Since the axial heat leak absolute variation is always very small even at large heat dissipation (lower than 0.5 W), the strong variation of the thermal resistance R_{wall} induces an increase of the evaporator wall temperature T_E .

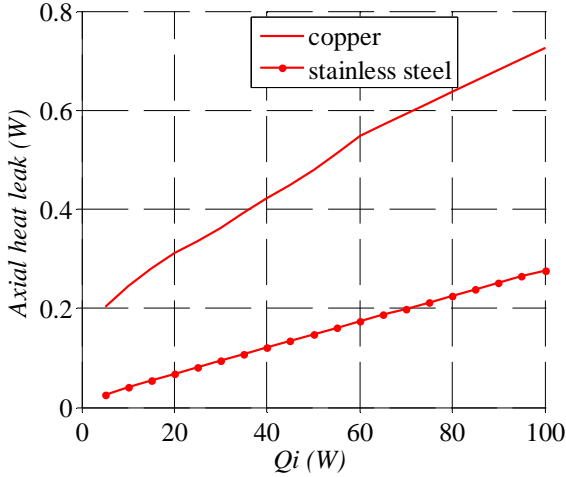


Figure 11. Effect of the evaporator body material on the axial heat leak

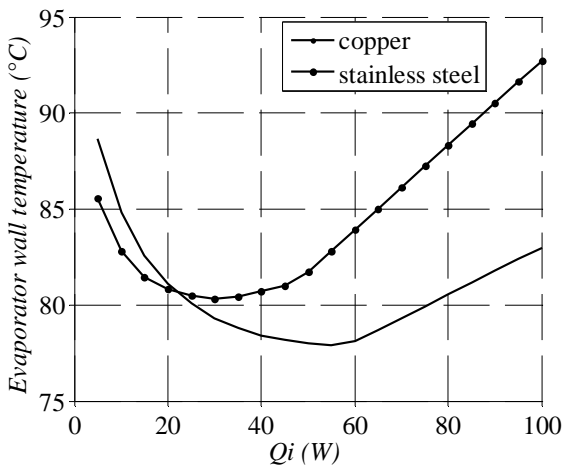


Figure 12. Effect of the evaporator body material on the evaporator wall temperature

2.6 Effect of the tube internal diameter

A reduction of the tube diameter has a negative effect as soon as the heat input exceeds 25 W. The decrease of the heat exchange surface area at the condenser leads to an increase of the condensation temperature and consequently, to the evaporator wall temperature (fig. 13). The pressure drops increases too, so that the capillary pressure may be reached (fig. 14). The slight decrease of evaporator wall temperature at low heat flux results from the decrease of the pitch between the turns of the card LHP condenser (fig. 3), that induces a reduction of the length of the aircraft LHP evaporator and hence, an increase of the radial heat flux.

4. SIZING OF THE CASCADED LHP

For the cascaded LHP, ethanol is selected as the working fluid and copper is the material of the evaporator / compensation chamber. The 4 mm

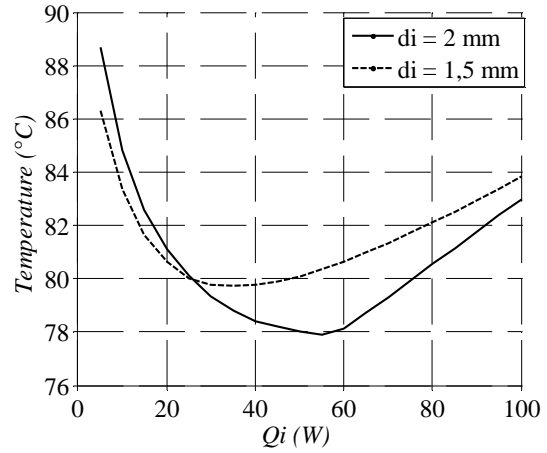


Figure 13. Effect of tube diameter on the evaporator wall temperature

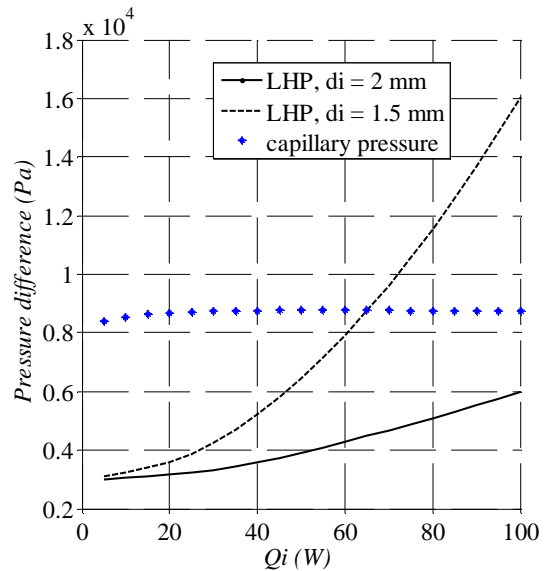


Figure 14. Effect of tube diameter on the total pressure drops and capillary pumping pressure

thick wick is made of sintered nickel powder. Fig. 15 shows the temperature variation of the evaporator wall, of the compensation chamber and of the heat sink, as function of the heat flux. The evaporator wall and reservoir temperature profiles are close together. For the aircraft LHP, the transition between variable and fixed conductance modes occurs at 55 W and at 30 W for the card LHP. The highest temperatures of the aircraft LHP appear at low heat fluxes, contrarily to those of the card LHP which are higher at large heat fluxes. The highest temperature, reached at 100 W, does not exceed the maximum allowable value of 110 °C. In any situation, the capillary pumping

pressure is always higher than the total pressure drops occurring in each LHP (fig. 16). Both LHPs operate far from their capillary limit.

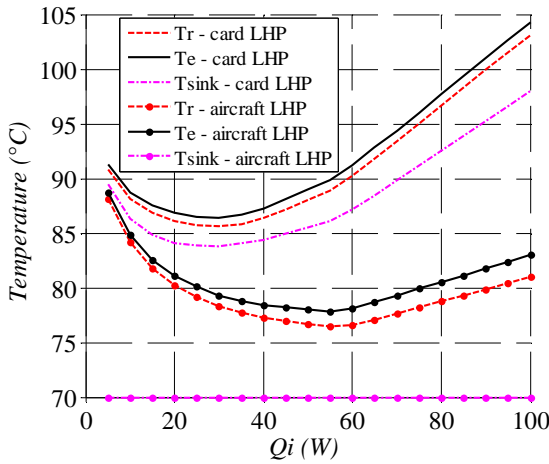


Figure 15. Temperatures of the cascaded LHP

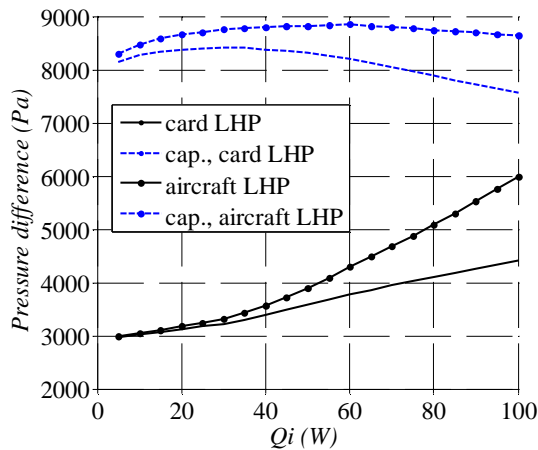


Figure 16. Total pressure drops along the cascaded LHP and capillary pumping pressures

5. CONCLUSIONS

The performance of the cascaded LHP is sensitive to the fluid, the body material, the wick type, the wick thickness and the tube diameter. Based on capillary limit and evaporator temperature limitations, the most convenient LHP parameters were selected.

NOMENCLATURE

c_p	specific heat, $J kg^{-1} K^{-1}$
D	diameter, m
ΔH	relative elevation, m
K	overall heat transfer coefficient, $W K^{-1}$
l_v	latent heat of vaporization, $J kg^{-1}$
L	length, m
P	pressure, Pa
Q	heat transfer rate, W
r_p	pore radius, m

R	thermal resistance, $K W^{-1}$
T	temperature, K

Greek

ε	porosity
λ	thermal conductivity, $W m^{-1}K^{-1}$
ρ	density, $kg m^{-3}$

Subscripts

A	ambient
C	condenser or condensation
E	evaporator
i	input or inlet or inner
l	liquid
L	liquid line
R	reservoir
$Sink$	heat sink
sub	subcooled zone
v	vapour
V	vapour line
w	wick
$wall$	wall

ACKNOWLEDGEMENT

This work was conducted in the frame of the SYSHANG project funded by the DGA, in partnership with ATHERM and THALES Avionics companies.

REFERENCES

- Boo, J. H., Chung, W. B. (2004) Thermal performance of a small-scale loop heat pipe with PP wick, Proc. 13th Int. Heat Pipe Conf., Shangai, p. 259-264.
- Faghri, A. (1995) *Heat pipe science and technology*. Taylor & Francis, London
- Hopkins, R., Faghri, A., Khrustalev, D. (1999) *Critical heat fluxes in flat miniature heat sinks with micro capillary grooves*. J. Heat Transfer, 121(5), p. 217-220
- Ku, J. (2009) Operating characteristics of loop heat pipes, Int. Conf. On Environmental Systems, Denver, SAE paper 1999-01-2007, 16 p.
- Launay, S., Sartre, V., Bonjour, J. (2007) Effect of fluid thermophysical properties on loop heat pipe operation, Proc. 14th Int. Heat Pipe Conf., Florianopolis.
- Launay, S., Sartre, V., Bonjour, J. (2008) *An analytical model for characterization of Loop Heat Pipes*. Journal of Thermophysics and Heat Transfer 22(4), p. 623-631
- Maydanik Yu. F. (1999) State-of-the-art of CPL and LHP technology. Proc. 11th Int. Heat Pipe Conf., Tokyo, p. 19-30

Theoretical and Experimental Study of CPL and LHP with Ceramic Wicks

Paulo Henrique Dias dos Santos

Federal University of Technology Paraná, Department of Mechanical Engineering
84016-210, Ponta Grossa, PR, Brazil
Tel: +55 42 98003861, e-mail: paulosantos@labcet.ufsc.br

Amir A. M. Oliveira and Edson Bazzo

Federal University of Santa Catarina, Department of Mechanical Engineering, LabCET - Laboratory of
Combustion and Thermal Systems Engineering - 88040-900, Florianópolis, SC, Brazil
Tel: +55 48 37219390, Fax: +55 48 37219390, e-mails: amir.oliveira@gmail.com, ebazzo@emc.ufsc.br

ABSTRACT

First, the heat and mass transfer in a flat capillary evaporator formed by a single porous wick is analyzed. The wick has a shape of a flat disc and is assembled between the liquid and vapor channels. The mass and heat transfer are modeled using the mass and energy macroscopic conservation equations. The model developed allows to verify the effect of the thermal conductivity of the wick in order to calculate the onset of drying of the porous wick. Next, experimental results using a ceramic wick (80 % Mullite and 20% Alumina) are reported for one LHP and one CPL both using water as working fluid. The theoretical and experimental results are compared. Besides, further numerical results are also reported for ceramic wicks with varying composition: (i) 50% Mullite and 50% Alumina and (ii) 20% Mullite and 80% Alumina. Additional experimental work is planned in order to validate the numerical results.

KEY WORDS: LHP, CPL, Water, Modeling, Thermal Conductivity

1. INTRODUCTION

The electronics industry has grown at a rapid pace seeking the miniaturization and better performance of components. At the scales reached nowadays, the thermal control of electronic equipment has become an important issue. There is a need to develop heat transfer devices that are capable of transferring large amounts of heat with a minimal temperature drop. In this context, Heat Pipes (HP), Loop Heat Pipes (LHP) and Capillary Pumping Loops (CPL) are reliable and feasible alternatives as heat transfer devices. They are passive two-phase devices that utilize the evaporation and condensation of a working fluid to transfer heat. The thermal fluid circulation is accomplished by the capillary forces generated in a porous wick. To the authors' knowledge, there are few capillary pumping systems (LHPs and CPLs) using a ceramic porous wick as a porous structure of the capillary evaporator (Santos et al., 2010; Berti et al., 2010). Most LHP and CPL use polyethylene or metallic porous wicks. It is expected that ceramic wicks become more advantageous, because they are less expensive and easier to machine without damaging the pores in the external surface of the structure.

Here in this work, first a mathematical model for the heat and mass transfer problem which occurs

within the porous wick of evaporators of capillary pumping systems is developed. This model allows to verify the effect of design variables, such as working fluids, dimensions, permeability, average pore radius and thermal conductivity of the wick, in the performance of the capillary evaporator and it allows for establishing a rigorous criterion for the wick dry-out limit. Next the results obtained with the model are compared with the experimental results obtained with one LHP and one CPL which use water as working fluid and a ceramic porous wick as capillary structure.

2. PROBLEM FORMULATION

The geometry of interest here is shown in Fig. (1) which depicts a capillary evaporator with a ceramic porous wick.

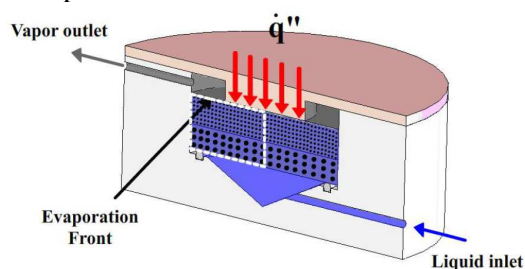


Figure 1. Cut of the flat capillary evaporator with a ceramic porous wick in the shape of a flat disc. The operation of the LHP or a CPL can be described as follows. Heat is supplied to the

evaporator so that the liquid saturating the surface pores of the wick evaporates. The vapor, which has been generated, flows via the vapor transport line to the condenser, where heat is rejected, causing the condensation of the vapor. Saturated liquid flows back to the evaporator by the capillary-driven flow (essentially Poiseuille flow). Detailed information on the operation, thermodynamic behavior, selection of working fluids and pressure losses of CPLs and LHPs can be found in Maydanik (1999).

In this work, the wick is a flat circular disc and is assembled between the liquid feeding channel and the vapor outlet. The upper part of the wick is heated by an external heat flux. After start-up, the evaporation of the working fluid that takes place around the fin occurs in three regimes, depending on the magnitude of the applied heat flux: (1) evaporation in microfilm, (2) evaporation in the external surface of the wick and (3) evaporation within the wick. Here, the evaporation in the external surface of the wick is considered the normal operation mode of capillary pumping systems, as verified experimentally by Li and Ochterbeck (1999) and assumed also by Cao and Faghri (1994). Also, this evaporation front is assumed sharp.

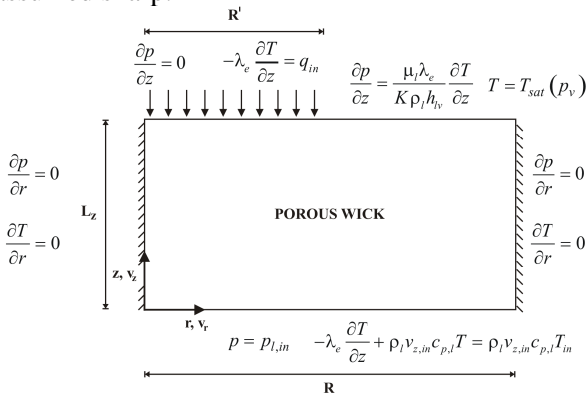


Figure 2. Schematic of the calculation domain.

Here, the equations of conservation of energy and mass are provided in cylindrical coordinates with the following assumptions: (1) The process is steady state, (2) The porous layers forming the wick are isotropic and homogeneous, (3) There is a negligible influence of gravity, (4) There is no heat transfer by radiation, (5) The solid phase is inert and stationary, (6) The fluid (liquid and its vapor) is incompressible, (7) The vapor in the vapor chamber is in a saturated state, (8) The thermophysical properties are constant, (9) The solid phase is in local thermal equilibrium with the liquid phase and (10) There are no chemical

reactions. The physical domain of interest and the boundary conditions are represented schematically in Fig. (2). Due to the cylindrical symmetry, only the section represented by a dotted line in Fig. (1) is modeled.

From the hypothesis listed above, the volume-averaged equation for the conservation of mass of liquid in cylindrical coordinates is

$$\frac{1}{r} \frac{\partial}{\partial r} (r v_r) + \frac{\partial v_z}{\partial z} = 0. \quad (1)$$

Here, the volume averaged notation is omitted for simplicity. The formulation of the conservation of linear momentum depends on the flow velocity. It has been shown before by Cao and Faghri (1994); Figus et al. (1999) that the flow velocity in the application of interest here is small. The pore Reynolds number ($Re_p = \rho_l v_{z,in} 2r_p / \mu_l$) ranges from 4×10^{-5} to 4×10^{-4} . Therefore, macroscopic and microscopic (Forchheimer) inertia terms are negligible when compared to the microscopic viscous terms. Also, since boundary effects penetrate distances that are of the order of a few particle diameters, the macroscopic (Brinkman) viscous term is also neglected. Finally, neglecting the influence of gravity, the r and z components of the equation for the conservation of linear momentum reduce to Darcy's Law, i.e.,

$$v_r = -\frac{K}{\mu} \frac{\partial p}{\partial r}, \quad v_z = -\frac{K}{\mu} \frac{\partial p}{\partial z}. \quad (2)$$

Substituting the conservation of momentum in the conservation of mass and assuming constant properties, we obtain a Laplace equation for the pressure, i.e.,

$$\frac{1}{r} \frac{\partial}{\partial r} \left(r \frac{\partial p}{\partial r} \right) + \frac{\partial}{\partial z} \left(\frac{\partial p}{\partial z} \right) = 0. \quad (3)$$

The equation for the conservation of the thermal energy is also written neglecting the convective terms. Following Cao and Faghri (1994), the characteristic Peclet number ($Pe = RePr = v_{z,in} R' / \alpha_e$) for the application of interest here is of the order of 10^{-2} . Then, the equation for the conservation of thermal energy, assuming isotropic media and constant properties, is written as

$$\frac{1}{r} \frac{\partial}{\partial r} \left(r \frac{\partial T}{\partial r} \right) + \frac{\partial}{\partial z} \left(\frac{\partial T}{\partial z} \right) = 0. \quad (4)$$

Following Fig. (2), the boundary conditions are: At the surface at $r=0$, cylindrical symmetry requires that

$$\frac{\partial p}{\partial r} = 0 \quad \text{and} \quad \frac{\partial T}{\partial r} = 0. \quad (5)$$

At the surface at $r=R$, the boundary is assumed impermeable to liquid flow and adiabatic. Then,

$$\frac{\partial p}{\partial r} = 0 \quad \text{and} \quad \frac{\partial T}{\partial r} = 0. \quad (6)$$

At the inlet surface at $z=0$, the porous wick is fed with a liquid flow with far end temperature $T_{l,in}$, i.e.,

$$p = p_{l,in} \quad \text{and} \quad -\lambda_e \frac{\partial T}{\partial z} + \rho_l v_{z,in} c_p T = \rho_l v_{z,in} c_p T_{l,in} \quad (7)$$

In the volume-averaged sense and assuming local thermal equilibrium between the liquid and solid phases, λ_e is the effective thermal conductivity of the fully liquid saturated porous medium. Finally, at the outlet surface, two sections are observed. First, underneath the metallic fin ($z = L_z$, $0 \leq r \leq R$)

$$\frac{\partial p}{\partial z} = 0 \quad \text{and} \quad -\lambda_e \frac{\partial T}{\partial z} = q_f. \quad (8)$$

Second, assuming that the pore size is not extremely small, from Kelvin's Law the surface temperature is approximately equal to the vapor saturation temperature in the bulk of the vapor channel. Also, the conduction heat transfer from the fin is responsible for the liquid evaporation. Therefore, the boundary condition at the evaporation surface can be written as,

$$\frac{\partial p}{\partial z} = \frac{\mu_l \lambda_e}{K \rho_l h_{lv}} \frac{\partial T}{\partial z} \quad \text{and} \quad T = T_{sat}(p_{sat}) \quad (9)$$

In the evaporation front (liquid-vapor interface), located in the external surface of the wick, the pressure difference between the phases is the capillary pressure, which can be expressed by the Young-Laplace's equation. Assuming cylindrical capillaries, the maximum capillary pressure that the wick can withstand is therefore,

$$\Delta p_{cap,max} = p_v - p_{l,min} = \frac{2\sigma}{r_p} \quad (10)$$

This maximum capillary pressure is related to the threshold for percolation of the non-wetting phase and is commonly identified as the wick bubbling pressure. In the operation of a capillary evaporator, when the pressure losses of the system exceed the maximum capillary pressure, the system fails. Therefore, the capillary limit of capillary pumping systems reflects its maximum pumping capacity.

2.1 Nondimensional Equations

Udell (1983) studied the heat and mass transfer in a problem that resembles the operation of a heat pipe. Following Udell (1983), the nondimensional variables are proposed:

$$p_{ref} = \frac{\sigma}{(K/\varepsilon)^{1/2}}, \quad v_{ref} = \frac{(K\varepsilon)^{1/2} \sigma}{\mu_l L_z}, \quad q_{ref} = \frac{\lambda_e (T_v - T_l)}{L_z}, \quad r^* = \frac{r}{R}$$

$$z^* = \frac{z}{L_z}, \quad v_r^* = \frac{v_r}{v_{ref}}, \quad v_z^* = \frac{v_z}{v_{ref}}, \quad q_{in}^* = \frac{q_f}{q_{ref}}, \quad p^* = \frac{p}{p_{ref}}$$

$$r_p^* = \frac{r_p}{(K\varepsilon)^{1/2}}, \quad E_v = \frac{\lambda_e (T_v - T_l) \mu_l}{\rho_l h_{lv} (K\varepsilon)^{1/2} \sigma}, \quad Pe = \frac{\rho_l c_{p,l} (K\varepsilon)^{1/2} \sigma}{\mu_l \lambda_e}$$

$$T^* = \frac{T - T_l}{T_v - T_l}, \quad \Delta p_{cap}^* = \frac{(p_v - p_l)(K/\varepsilon)^{1/2}}{\sigma}, \quad r_{p,crit}^* = \frac{2\sigma}{(p_v - p_l)(K/\varepsilon)^{1/2}}$$

2.2 Results

For the results presented here, water was used as working fluid and a ceramic wick was used as porous wick. The thermodynamic properties of the wick and the working fluid and the main nondimensional parameters are presented in Table (1). In the analysis that follows, the properties were kept constant.

Table 1. Thermophysical properties of the porous wick and working fluid and nondimensional parameters.

	ε (%)	K (m ²)	$\lambda_{e,l}$ (W/m-K)	$\lambda_{e,v}$ (W/m-K)	r_p (mm)
Wick	0.5	35 x 10 ⁻¹⁵	4.0 – 8.0	4.0	3.0 - 15.0
	σ (N/m)	h_{lv} (kJ/kg)	c_p (kJ/kg-K)	ρ (kg/m ³)	μ (kg/m-s)
Water	0.07119	2382	4.18	995.60	0.0007977
	p_{ref} (Pa)	v_{ref} (m/s)	E_v	Pe	L_z/R
	269073	0.00118	0.00143	12.28	0.67

It is expected that an increase in the heat flux at the fin causes an increase in the mass flow rate. Figures (3) and (4) present the nondimensional isotherms and heat flux lines for two increasing heat fluxes. Figure (3) presents the results for a nondimensional inlet heat flux of 5.0. The fin ends at $r^* = 0.5$. The isotherm with $T^* = 1.0$ ($T = T_v$) is also shown. Note that surface evaporation occurs only in the first few millimeters of the outlet surface, very close to the end of the fin. For the remaining of the fin, the heat flux lines turn around and heat flows right to the liquid channel.

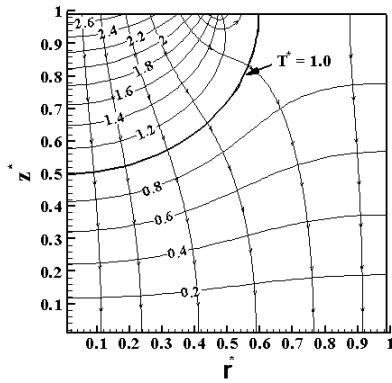


Figure 3. Nondimensional isotherm and heat flux lines for a nondimensional inlet heat flux of 5.0.

As the nondimensional heat flux is increased, Fig. (4), an increased amount of heat flows to the outlet surface, causing the liquid evaporation. When the heat flux is increased, the isotherm $T^* = 1.0$ penetrates deeper in the porous wick.

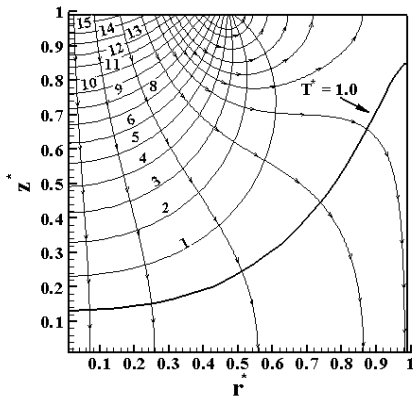


Figure 4. Nondimensional isotherm and heat flux lines for a nondimensional inlet heat flux of 37.5.

The heat transfer rate imposed in the fin is transferred to the outlet surface, causing evaporation, and also to the inlet surface, resulting in heating of the liquid channel. Both these heat transfer paths have their characteristic thermal resistances. As a result of these thermal resistances, the fin surface reaches a temperature which can be reasonably large in certain conditions. For instance in Fig. (4), we observe that for a nondimensional inlet heat flux of 37.5, the fin surface reaches nondimensional temperatures above 15 which are about 14 times above the nondimensional saturation temperature of the fluid (for infinite radius of curvature). Then, a question remains whether the fluid would remain liquid or evaporate under this temperature. This can be tested by observing the capillary pressure at the top surface of the wick and comparing it to the maximum capillary pressure that the wick can sustain.

Figure (5) presents the nondimensional capillary pressure (Δp_{cap}^*) at the top surface as a function of properties for two nondimensional heat fluxes, 10.5 and 5.0. All properties were kept constant and correspond to the properties of the porous wick with nondimensional average pore radius of 11.34. The horizontal lines represent the maximum nondimensional capillary pressure for each characteristic nondimensional pore size, from 11.34 to 56.69 as shown. We note that for the nondimensional inlet heat flux of 5.0 all media would remain saturated by liquid except those with the larger nondimensional pores of 37.80 and 56.69. For these two sizes, the local capillary pressure exceeds the maximum allowed capillary pressure and, therefore, the region underneath the fin would dry and the evaporation front would seek a new equilibrium position within the wick.

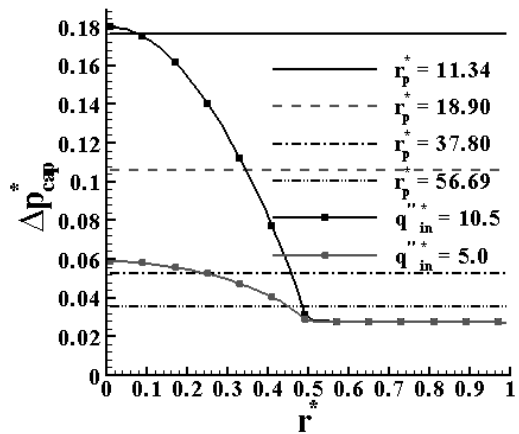


Figure 5. Nondimensional capillary pressure profiles at $z^* = 1.0$.

For a given nondimensional heat flux there will be a local maximum nondimensional average radius needed to avoid the drying of the wick in the region underneath the fin, which will be called critical nondimensional average radius ($r_{p,crit}^*$) which is presented in Fig. (6).

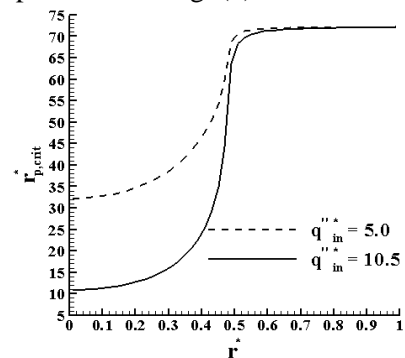


Figure 6. Critical nondimensional average radius profiles at $z^* = 1.0$.

It is noticed in Fig. (6) that the minimum critical nondimensional average radius is located in the region underneath the fin at $z^* = 1.0$ and $r^* = 0.0$. Thus, the Fig. (7) presents the critical nondimensional average radius as a function of the nondimensional heat flux at this position. The curve shown in this figure represents the capillary limit, *i.e.*, below this curve the capillary limit is not reached and there is no vapor breakthrough and above the curve occurs the vapor invasion of the porous wick.

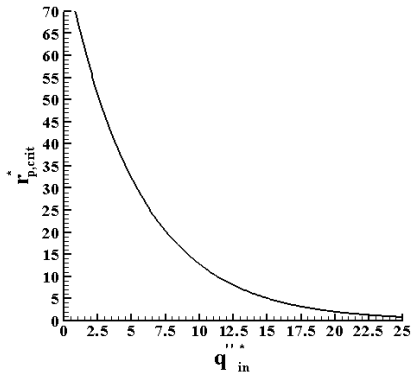


Figure 7. Critical nondimensional average radius at $z^* = 1.0$ and $r^* = 0.0$.

3. EXPERIMENT

In this work one LHP, Fig. (8), and one CPL, Fig. (9), were manufactured and tested in order to evaluate their thermal performance and applicability in thermal control of microprocessors and electronic components in general. They used water as working fluid and a ceramic wick in the capillary evaporators.

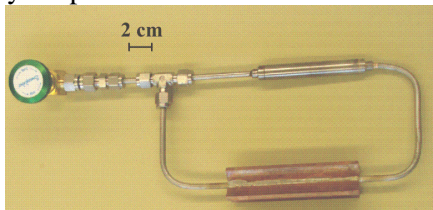


Figure 8. General view of the LHP.

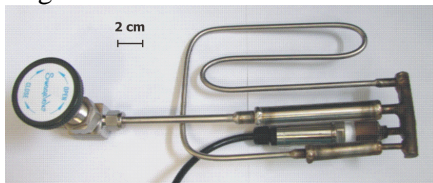


Figure 9. General view of the CPL.

The uncertainty of the temperature measurement is estimated at ± 0.41 °C for the LHP and ± 1.8 °C for the CPL. Further information concerning the estimate of the experimental uncertainty can be found in Santos (2010). Figure (10) depicts the temperatures of the LHP for stepwise increase in heat load in the range from 5 to 15 W. Figure (11)

depicts the temperatures of the CPL for stepwise increase in heat load in the range from 5 to 30 W.

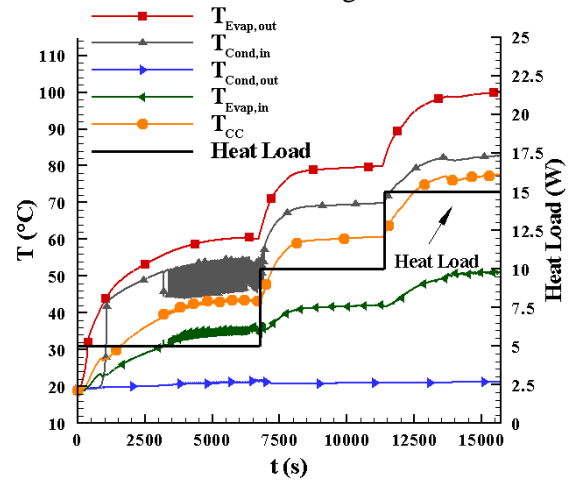


Figure 10. Temperatures of the LHP.

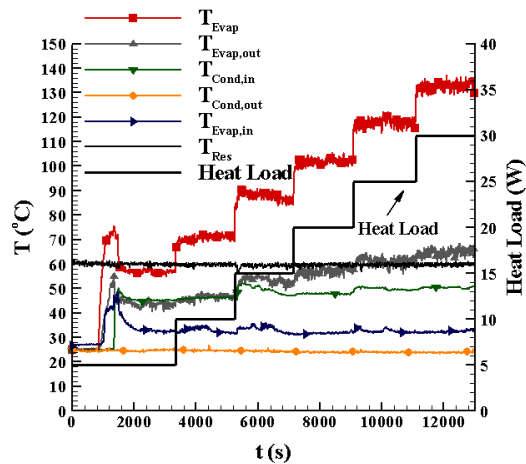


Figure 11. Temperatures of the CPL.

4. COMPARISON OF THE RESULTS

This section presents a comparison between the experimental and theoretical results. Figure (12) presents this comparison.

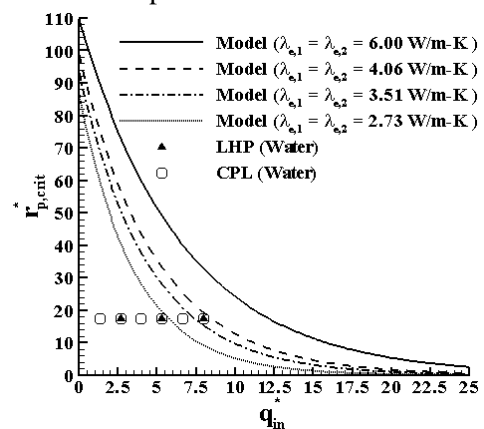


Figure 12. Comparison between the experimental and theoretical results.

The curves of the critical nondimensional average radius at $z^* = 1.0$ and $r^* = 0.0$ as a function of the

nondimensional inlet heat flux are compared to the experimental nondimensional average radius for each heat flux applied to the LHP and CPL tested in this work.

The ceramic wick used in the LHP and CPL has 80% of Mullite ($\lambda_{s,Mullite} = 4$ W/m-K) and 20% of Alumina ($\lambda_{s,Alumina} = 40$ W/m-K) and its effective thermal conductivity was estimated as $\lambda_{e,1} = \lambda_{e,2} = 2.73$ W/m-K.

Note in Fig. (12) that this ceramic wick presented the lower capillary limit. In this figure, it can be noticed that both LHP and CPL have reached the capillary limit, but the LHP continued working for the heat load of 15 W and the CPL continued working from 25 until 30 W. So, according to the model, the evaporation front invaded the porous wick and established a stable position within it.

The ceramic wick composition was varied in order to evaluate the effect of the effective thermal conductivity on the capillary limit. The composition was varied as follows: (i) 50% Mullite and 50% Alumina ($\lambda_{e,1} = \lambda_{e,2} = 3.51$ W/m-K) and (ii) 20% Mullite and 80% Alumina ($\lambda_{e,1} = \lambda_{e,2} = 4.06$ W/m-K). It is also noticed in Fig. (12) that the higher the effective thermal conductivity of the wick the higher the capillary limit. Accordingly, high effective thermal conductivity underneath the fin is desirable for LHPs and CPLs.

5. CONCLUSIONS

The LHP and CPL using water and ceramic porous wick worked satisfactorily in the range from 5 to 15 W and from 5 to 30 W, respectively.

The experimental results were compared with the theoretical results. Despite the LHP and CPL having reached the capillary limit, they continued working for increasing heat loads. Therefore, according to the model, the evaporation front invaded the porous wick and established a stable position within it. However, this comparison should be taken only as a first approximation since the theoretical model does not reproduce completely the geometry of the tested LHP and CPL. Nevertheless, the physical trends remain the same. It was also observed that the higher the thermal conductivity underneath the fin the higher the capillary limit for both capillary systems.

NOMENCLATURE

c_p	specific heat [J/kg-K]	λ	thermal conductivity [W/m-K]
E_v	evaporation-cooling number	μ	dynamic viscosity [Pa-s]

h_v	latent heat of evaporation [J/kg]	ρ	mass density [kg/m ³]
K	permeability [m ²]	σ	surface tension [N/m]
L_z	wick thickness [m]	θ	contact angle [rad]
p	pressure [Pa]	Subscripts	
Pe	Peclet number	cap	capillary
q	heat flux [W/m ²]	e	effective
R'	fin radius [m]	f	fin, fin/wick interface
R	wick external radius [m]	in	inlet
Re	pore Reynolds number	l	liquid, liquid side
r_p	pore radius [m]	max	maximum
T	temperature [K]	out	outlet
v	liquid velocity [m/s]	r	coordinate r

Greek Symbols

$\alpha = \frac{\lambda}{\rho c_p}$	thermal diffusivity [m ² /s]	v	vapor
ε	porosity	z	coordinate z

ACKNOWLEDGEMENT

The authors thank the CNPq, UFSC and UTFPR for the financial support granted to this research.

REFERENCES

- Berti, L., Santos, P., Bazzo, E., Janssen, R., Hotza, D. and Rambo, C. (2010). *Evaluation of permeability of ceramic wick structures for two phase heat transfer devices*. Applied Thermal Engineering, Vol. 31, pp. 1076–1081.
- Cao, Y. and Faghri, A. (1994). *Analytical solution of flow and heat transfer in a porous structure with partial heating and evaporation on the upper surface*. Int. J. of Heat and Mass Transfer, Vol. 37, pp. 1525 – 1533.
- Figus, C., Bray, Y.L., Bories, S. and Prat, M. (1999). *Heat and mass transfer with phase change in a porous structure partially heated: continuum model and pore network simulation*. Int. J. of Heat and Mass Transfer Vol. 42, pp. 2557 –2569.
- Li, T. and Ochterbeck, J.M. (1999). *Effect of wick thermal conductivity on startup of a capillary pumped loop evaporator*. AIAA, Vol. 993446, pp. 10–20.
- Santos, P.H.D. (2010). *Theoretical and Experimental Study of the Application of a Ceramic Porous Wick in LHP and CPL*. Ph.D. thesis, Federal University of Santa Catarina, Brazil.
- Santos, P.H.D., Bazzo, E., Becker, S., Kulenovic, R. and Mertz, R. (2010). *Development of lhps with ceramic wick*. Applied Thermal Engineering, Vol. 30, pp. 1784–1789.
- Udell, K.S. (1983). *Heat transfer in porous media heated from above with evaporation, condensation and capillary effects*. ASME, Vol. 105, pp. 485–492.

A THEORETICAL ANALYSIS OF THE TRANSIENT BEHAVIOR OF A CPL FOR TERRESTRIAL APPLICATION

A. Kaled and S. Dutour

Université de Toulouse; UPS, INPT; CNRS; LAPLACE (Laboratoire Plasma et Conversion d'Energie);
118 route de Narbonne, F-31062 Toulouse cedex 9, France.
ahmed.kaled@laplace.univ-tlse.fr (corresponding author)

V. Platel

LaTEP, Université de Pau et des Pays de l'Adour,
Quartier Bastillac, 65000 Tarbes, France

L. Lachassagne , V. Ayel

Institut Pprime, CNRS-ENSMA-Université de Poitiers,
1 avenue Clément Ader, 86961 Futuroscope-Chasseneuil Cedex, France

ABSTRACT

The present study focuses on a theoretical analysis of the dynamic behavior of a CPL. A transient model has been developed and compared to an experimental test. This model is then used to highlight the effect of liquid flow inertia on CPL dynamics. It shows that the liquid motion can amplify the pressure drop overshoot during fast transients (about 20%). In a second part, an analysis of the CPL pseudo-periodic behavior is proposed based on the linearized model approach.

KEY WORDS: Transient model, inertia effects, linear stability analysis

1. INTRODUCTION

Capillary pumped loop (CPL) and loop heat pipe (LHP) are passive heat transport devices that are gaining importance as a part of the thermal control system for ground applications. Figure 1 shows the schematic of a Capillary Pumped Loop for Integrated Power (CPLIP) developed by Euro Heat Pipe, Belgium. A CPL is basically composed of the following components: a capillary evaporator (responsible for generating capillary forces that drive the working fluid), a condenser, a two-phase reservoir (to control the loop saturation pressure) and the liquid and vapor lines (figure 1). The heat load applied to the evaporator is transported to the condenser where it is rejected to the heat sink.

Because of the efficiency of vaporization and condensation heat transfer and the flexibility of the fluid transport process, passive two-phase closed systems are very attractive for transferring large heat fluxes with small temperature differences. However, these heat transfer devices will encounter specific constraints such as acceleration, vibration and different orientations vs. gravity, which may

significantly perturb their performances (Gottschlich, 1996). Therefore, CPL and LHP technologies continue to be an important area of research and there is a need for the development of models in order to understand and control such CPL and LHP dynamic behaviors in the gravity field.

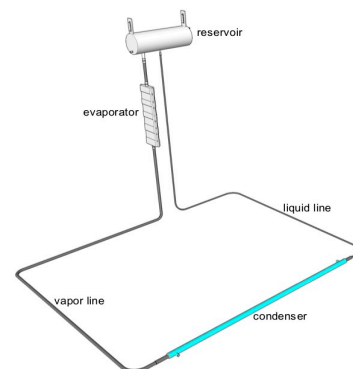


Figure 1. Schematic of a CPLIP.

In this work, a theoretical analysis of the dynamic behavior of a CPL is proposed. A transient model has been developed to reproduce the CPL dynamic behavior in ground conditions and has been used to:

- examine the system's sensitivity to the effects of

the liquid motion in the loop following fast heat load steps.
- analyze the stability of steady-state solution.

2. MODELING APPROACH

The model is based on mass, momentum and energy balances for evaporator, condenser and fluid lines. The theoretical development of this transient model is essentially based on the previously laboratory modeling investigations (Pouzet et al, 2004 and Launay et al, 2007).

2.1 Reservoir

The CPLIP reservoir is divided into two parts: the lowest part is assumed to be full of liquid and the highest part is at two-phase state. The particular CPLIP design, as well as classical CPLs, allows to control the temperature of the two-phase part thanks to a Proportional Integral Derivative regulator (PID regulator) and, so, the reservoir pressure is assumed to be maintained constant:

$$p_R = p_{sat}(T_R) \text{ with } T_R = C^{st} \quad (1)$$

2.2 Condenser and liquid line model

The transient behavior of the condenser and of the liquid flow is modeled through the variation of condensation zone length $L_{2\varphi}$ and mass flow rate at the condenser outlet m_l . The following assumptions are made:

- the void fraction α in the two-phase flow region of the condenser is assumed to be constant; the vapor flow is supposed to be incompressible.
- the global condensing heat transfer coefficient $h_{2\varphi}$ is determined to consider an annular flow condensation.

The following equations are obtained:

$$\frac{dL_{2\varphi}}{dt} = \frac{m_v l_v - h_{2\varphi} \pi D_c L_{2\varphi} (T_{2\varphi} - T_f)}{A_c \rho_v \alpha l_v} \quad (2)$$

$$\frac{dm_l}{dt} = \left[\frac{(L_c - L_{2\varphi})}{A_c} + \frac{L_R}{A_R} + \frac{L_l}{A_l} \right]^{-1} \left[(p_{2\varphi} - p_R) - \Delta p_l - \Delta p_g \right] \quad (3)$$

$$T_{2\varphi} = T_f + \frac{l_v}{h_{2\varphi} \pi D_c L_{2\varphi}} \left[m_v - \rho_v \frac{m_v - m_l}{\rho_v - \rho_l} \right] \quad (4)$$

$$p_{2\varphi} - p_R = \frac{dp_{sat}}{dT} \Big|_{T_R} (T_{2\varphi} - T_R) \quad (5)$$

where $T_{2\varphi}$ is the working fluid average temperature in the condensation zone, Δp_l is the

pressure drop in the liquid line and Δp_g the gravity pressure drop.

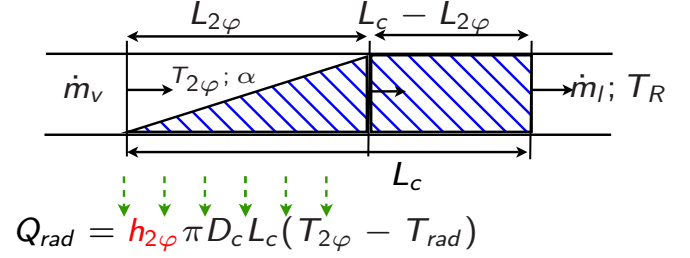


Figure 2. Variables of condenser model

2.3 Evaporator model

The evaporator is composed of the metal masses, the vapor grooves and the capillary wick. The model is based on capacitive transient model of evaporator body, which transfers the heat source Q_{load} from exterior wall until the vaporization interface. This model allows determining the vaporization mass flow rate at the porous wick surface m_v and the mean temperature of the evaporator metal masses T_m .

$$\frac{dT_m}{dt} = \frac{Q_{load} - G_{eq}(T_m - T_v)}{(\rho C p \Omega)_m} \quad (7)$$

$$T_v = T_{2\varphi} + \frac{\Delta p_v}{\frac{dp_{sat}}{dT} \Big|_{T_R}} \quad (8)$$

$$m_v = \frac{G_{eq}(T_m - T_v)}{l_v + C_{pl}(T_v - T_l)} \quad (9)$$

where G_{eq} is the equivalent conductance from exterior wall until the vaporization interface (calculates from experiment results), and Δp_v the pressure drop in the vapor line.

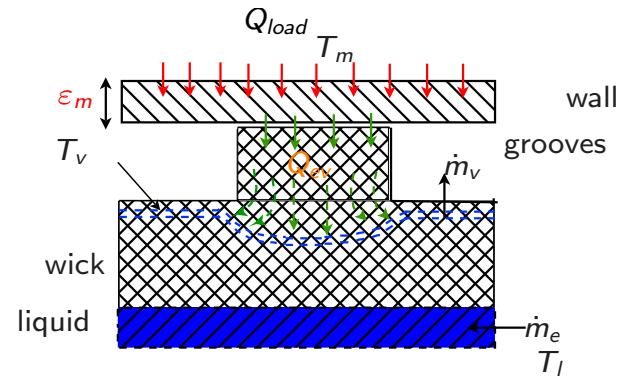


Figure 3. Variables of evaporator model

3. CONFRONTATION WITH DATA

3.1 CPLIP test set-up description

An experimental test bench has been developed at PPRIME Institute with the evaporator/reservoir assembly designed by EHP society for power electronics cooling in terrestrial applications. The fully detailed description of this test bench can be found in (Lachassagne, 2012). Figure 2 presents a view of this prototype and its instrumentation. The two-phase part of the reservoir is controlled thanks to a PID regulator and is instrumented by a platinum thermal sensor allowing verifying the saturated state (Eq. (1)). It is separated from the lower part of the reservoir by a stainless steel plate. The whole loop is made of stainless steel and the working fluid is ethanol.

The condenser is a 5 m long counter-current heat exchanger where ethanol flows in the inner pipe (12 mm inner diameter) and the water/ethylene glycol mixture, provided by a chiller, flows in the outer annular channel (between 14 mm and 17.3 mm diameters). The liquid and vapor lines are respectively 1.92 m and 1.94 m long with 6 mm and 12 mm inner diameters.

The evaporator dimensions are of 320x81x20 mm³ including a sintered nickel wick. The heated area of 148 cm² is covered with a thermal interface and eight copper heating blocks linked to four power supplies of 1500 W, allowing total heat charge to reach 6000 W on this test bench.

T-type thermocouples ($\pm 0.5^\circ\text{C}$) of 0.1 mm wire diameter are located along the whole loop as shown on figure 2. In addition, 32 T-type sheathed thermocouples of 0.5 mm wire diameter have been inserted between the copper blocks and the evaporator body. Concerning the hydraulic measurements, absolute pressure transmitters are located at each ends of major loop components. Finally, the major advanced feature of this test bench is the Coriolis flowmeter (*Micromotion elite CMF010*) located at the condenser outlet.

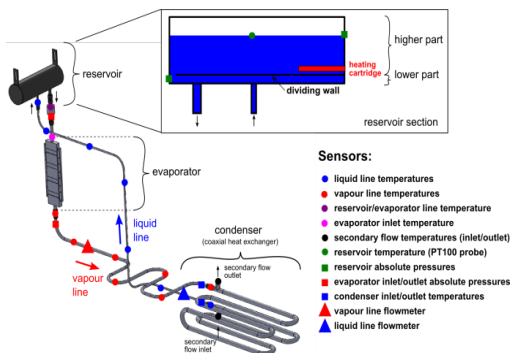


Figure 4. Schematic of the CPLIP test bench.

3.2 Transient test

As an example of experimental results, a transient response of the CPLIP to a heat load rising step from 400 W to 800 W is given in figure 3 (condenser coolant temperature: 20°C; reservoir temperature: 73°C). This figure represents various temperature recordings at different locations of the loop, together with the applied power. Note that these experimental curves correspond to that of figure 4 in which the liquid mass flow rate is drawn for the same experiment. One can see on this figure that the applied power rising step has only few influence on the temperature levels: only the maximal evaporator metal mass $T_{m,max}$ and the reservoir-evaporator line temperatures are subject to a noticeable change, of less than 3°C. On the contrary, one can see on figure 4 that the applied power rising step leads to a significant overshoot of the liquid mass flow rate at the outlet of the condenser. This behavior will be discussed below.

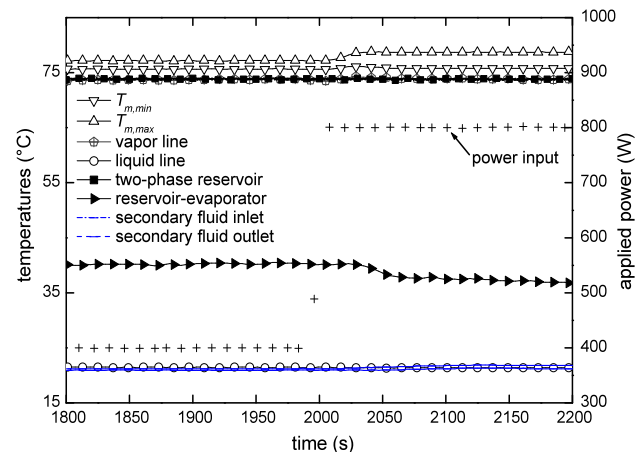


Figure 5. Transient response of the CPLIP to a rising step of heat load

3.3 Comparison with data

The experimental study has demonstrated that the transient behavior is mainly observable through the fluid motion. Therefore, we choose to compare the model results with the variation of the liquid mass flow rate in the loop over a rising step of heat load from 400 W to 800 W following by a downward from 800 W to 400 W. Figure 4 shows both calculated and experimental mass flow rate. We can see that, both the overshoot and the undershoot are satisfactorily reproduced. It is important to note that any model parameters (G_{eq} and $h_{2\varphi}$) have been estimated from data, it was only to match the steady state regime and thus no adjustment have been made for the transient.

4. THEORETICAL ANALYSIS

4.1 Influence of the liquid flow inertia

To examine and quantify the role of the inertial effect of the liquid motion, the approach consists in comparing the trajectories of the presented model for a case where the liquid flow is considered in a quasi-static mode. This is actually made by exchanging the equation (3) with the corresponding pressure drop relation. Figure 5 presents the pressure difference (across the evaporator) and liquid mass flow rate trajectories resulting from both model versions during a severe heat loading (from 400W to 1200W and back to 400W).

It can be noticed first that the overshoot and the undershoot are observable in every case, demonstrating that these non-linear behaviors are due to a thermal coupling between the evaporator and the condenser. However, the accelerating or decelerating of the liquid mass in the lines amplifies significantly the pressure drop between the two sides of the evaporator: we denote that the maximum pressure drop deviation between both trajectories can reach about 1000 Pa. Moreover, the peak width appears larger. The early response times are slightly slow down while the relaxation time increases. Focusing on the mass flow rate results, the previous tendencies are confirmed except for the overshoot and undershoot mass flow rate amplitude which is somewhat smoothed by the liquid inertial effect.

4.2 Study of system response times

In this section, approach linear stability analysis is used to determine, from the set of the nonlinear model equations, the response times, when the loop is subjected to small perturbations, close to the steady state regime. This approach gives the opportunity to find explicit analytical relation between the system relaxation times and parameters.

Considering only the first order of some perturbations about the steady state:

$$\begin{aligned} T_m(t) &= T_{ss} + \delta T_m(t) \\ \eta(t) &= \eta_{ss} + \delta \eta(t) \\ m_l(t) &= m_{ss} + \delta m_l(t) \end{aligned}$$

we obtain the following linear system of equations governing the dynamics of the perturbations:

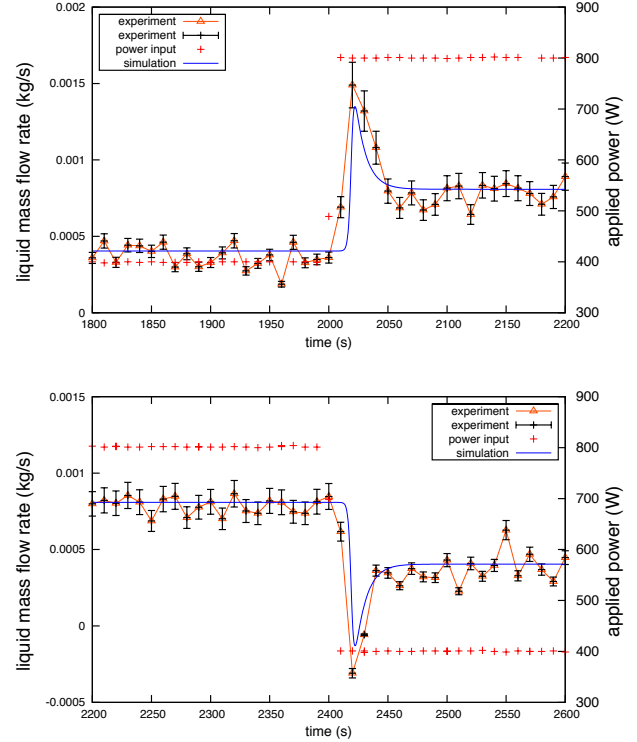


Figure 6. Calculated and experimental liquid mass flow rates.

$$\begin{pmatrix} \frac{d\delta T_m}{dt} \\ \frac{d\delta \eta}{dt} \\ \frac{d\delta m_l}{dt} \end{pmatrix} = J \begin{pmatrix} \delta T_m \\ \delta \eta \\ \delta m_l \end{pmatrix}$$

where J refers to the Jacobian matrix. An algebra procedure leads to the computation eigenvalues of J.

The first major result is that among the three eigenvalues, one is real and negative and the two others are complex conjugate with a negative real part. This feature shows a potentially oscillatory system behavior (pseudo-periodic). This is consistent with the conclusions of Hoang et al. (1995) with a somewhat simple CPL model.

Table 1 collects the time responses τ_1 and τ_2 (respectively calculated from the first real and from the real part of complex conjugate) and the period τ_3 (calculated from the imaginary part) for different heat loads. The ratio of the two relaxation times of the order of 4 to 5. The greatest value is close to 10s. The damping time corresponding to the real part of the complex eigenvalues is two times higher than the period (1s). Moreover, it can be observed that the heat load does not influence these times.

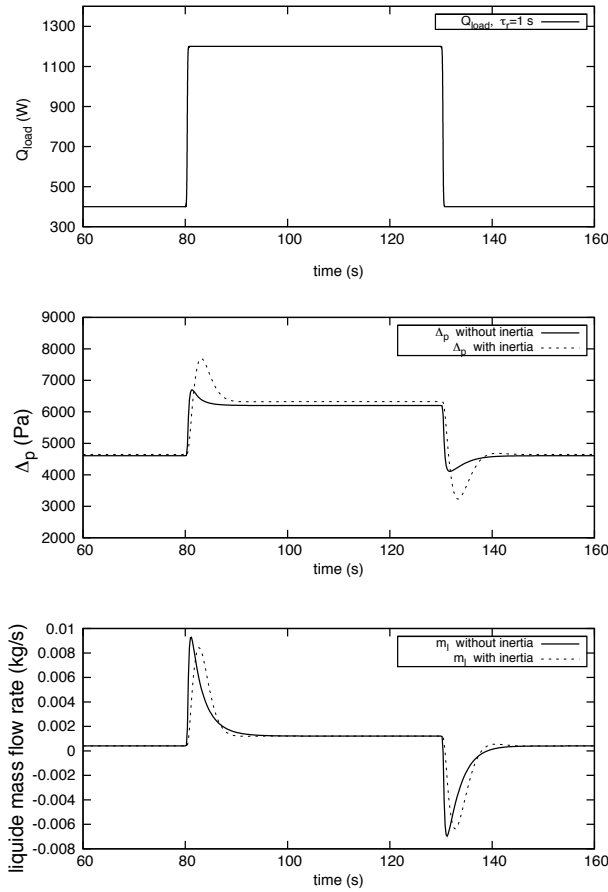


Figure 7. Influence of the liquid flow inertia.

Table 1. Time responses and the period for different heat loads

ε_m (mm)	$h_{2\varphi}$ ($W.m^{-2}.K^{-1}$)	Q_{load} (W)	τ_1 (s)	τ_2 (s)	τ_3 (s)
15	1000	100	-8.88	-2.37	1.03
		400	-8.98	-2.37	1.03
		800	-9.10	-2.36	1.03
		1000	-9.17	-2.36	1.03
		1200	-9.24	-2.36	1.03
		1600	-9.38	-2.35	1.03
		1800	-9.45	-2.34	1.03
		2000	-9.53	-2.34	1.03

4.3 Response time sensitivities

Using the relations obtained in the previous part, the sensitivity of the loop dynamics is explored through the linearized system. This is achieved regarding to the variation of (i) $h_{2\varphi}$, the global heat transfer coefficient in the condensation part of the condenser and (ii) ε_m the saddle evaporator thickness. This latter parameter is actually a way to modulate the ratio $\frac{G_{eq}}{(\rho C_p \Omega)_m}$ in equation (7).

Figures 6 show the first set of response times versus the heat load from $h_{2\varphi}=200 \text{ W.K}^{-1}.\text{m}^{-2}$ to $2000 \text{ W.K}^{-1}.\text{m}^{-2}$. This interval includes the range of variation of $h_{2\varphi}$ with the condensation heat transfer regime (bubbly, annular, stratified, ...). It can be seen that τ_1 is insensible to a change of this parameter revealing that the long-time variation seems to be independent of the condensation regime. However, the complex eigenvalues are affected by a variation of $h_{2\varphi}$: the damping time increases while the period decreases. This tendency shows that an intensification of the heat transfer in the condenser increases the opportunity for pseudo-oscillations with a frequency close to 10 s^{-1} .

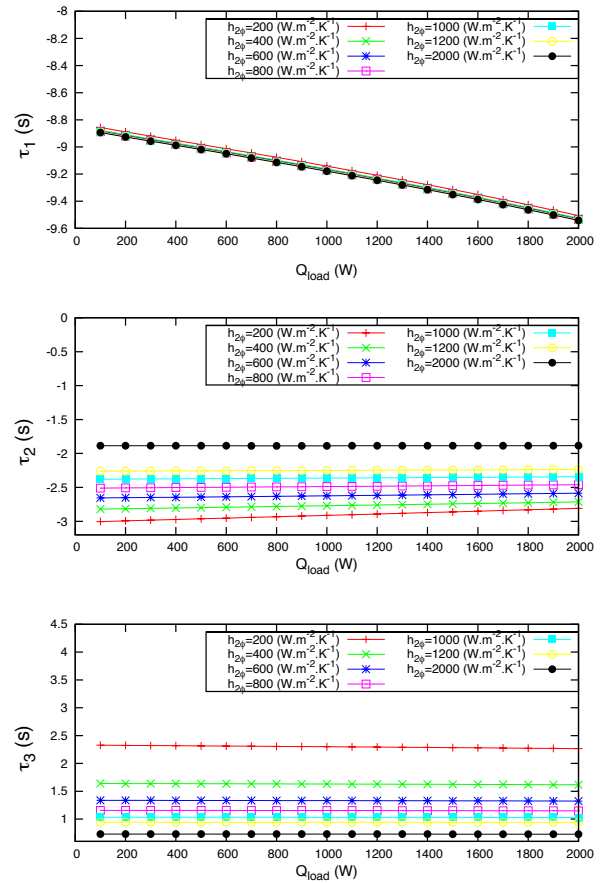


Figure 8. Response times vs the heat load for different condensation heat transfer coefficients ($h_{2\varphi}$)

Figures 7 show the second set of response times versus the heat load from $\varepsilon_m=1 \text{ mm}$ to 20 mm . The two extreme cases correspond respectively to an evaporator with low thermal mass inertia and great conductivity and one with greater thermal mass inertia and smaller conductivity. Here, we found

that the relaxation times are more influenced with a decrease of the order of 5 for τ_1 and an increase of the order of 3 for τ_2 . On the other hand, the pseudo period is almost insensitive to a variation of ϵ_m . The tendency corresponds to the fact that the system response time is improved and damping is smoothed when the evaporator thermal inertia decrease. However, what is finally more surprising is that the opportunity to observe a pseudo-periodic behavior is still true on all over the range of variations of the parameter.

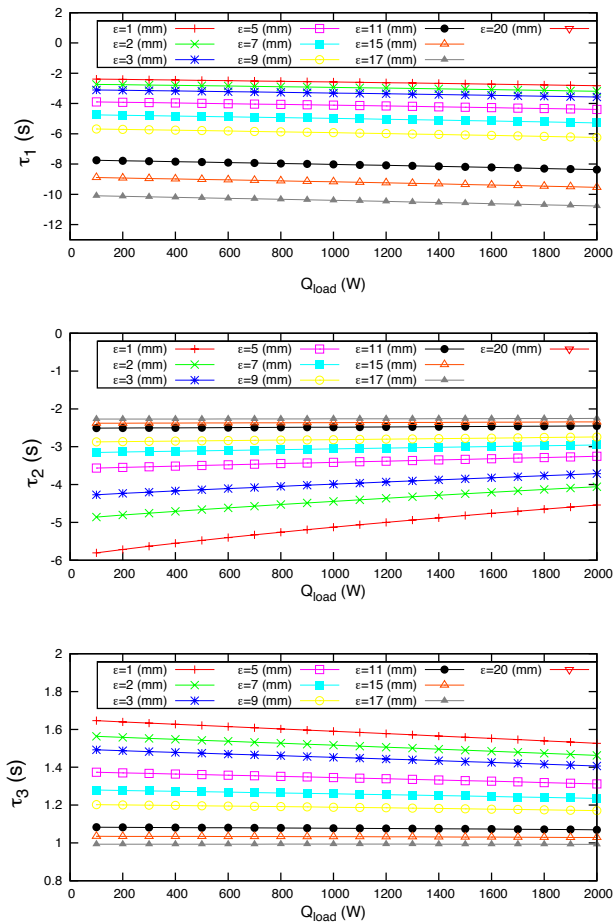


Figure 9. Response times vs the heat load for different evaporator thicknesses ϵ_m .

5. CONCLUSION

We have presented a theoretical analysis of the dynamic behavior of a CPL based of a new transient model. The results show that the fluid motion plays a significant role in the amplification of the pseudo-periodic behavior of the system. We found that this effect mainly influences the pressure drop in the loop (about 20% of amplification) so that a fast heat load step can mechanically

destabilize the system. On the second part of the analysis, the pseudo-periodic behavior through the linearized model has been examined: on the explored range of the parameters, the system keeps its pseudo-periodic intrinsic properties even in the case of an important thermal mass inertia.

NOMENCLATURE

- A section (m²)
- C_p specific heat (J.kg⁻¹.K⁻¹)
- C^{st} constant
- D diameter (m)
- G conductance (W.K⁻¹)
- L length (m)
- l_v latent heat of vaporization (J.kg⁻¹)
- p pressure (Pa)
- T temperature (K)
- ϵ thickness (mm)

Subscripts

- c condenser
- g gravity
- l liquid
- m metal
- R reservoir
- ss steady state
- v vapor
- eq equivalent

REFERENCES

- Gottschlich, J.M., Baldassarre, G.J., Gernert, N.J. (1996) *Loop heat pipe for avionics thermal control*. SAE, (961318).
- Hoang, T.T., Ku, J., (1995) *Theory of hydrodynamic stability for capillary pumped loops*, National Heat Transfer Conference, 307 p.33-40.
- Lachassagne, L., Ayel, V., Romestant, C., Bertin, Y. (2012) *Experimental study of capillary pumped loop for integrated power in gravity field*, Applied Thermal Engineering, 35, p. 166-176
- Launay, S., Platel, V., Dutour, S., (2007) *Transient modeling of loop heat pipes for the oscillating behavior study*, Journal of Thermophysics and Heat Transfer, 21 p. 487-495.
- Pouzet, E., Joly, J.-L., Platel, V., Grandpeix, J.-Y., Butto, C. (2004) *Dynamic response of a capillary pumped loop subjected to various heat load transients*. International Journal of Heat and Mass Transfer, 47 p. 2293-2316.

A THEORETICAL INVESTIGATION OF PHASE DISTRIBUTION IN THE EVAPORATOR CAVITY OF A LOOP HEAT PIPE

H.T. Phan, S. Dutour

Université de Toulouse; UPS, INPT, CNRS; LAPLACE (Laboratoire Plasma et Conversion d'Energie)
 118 route de Narbonne, F-31062 Toulouse cedex 9, France.
 Phone: +33 (0)5 61 55 69 87 - Fax: +33 (0)5 61 55 60 21
 sebastien.dutour@laplace.univ-tlse.fr (corresponding author).

V. Platel

Université de Pau et des Pays de l'Adour, LaTEP
 Quartier Bastillac, 65000 Tarbes, France.

A. Larue de Tournemine

Centre National d'Etudes Spatiale (CNES)
 18 avenue Edouard Belin, 31055 Toulouse Cedex, France.

ABSTRACT

This work focuses on the influence of phase distribution on the heat and mass transfers in the evaporator cavity of a LHP. The discussion is based on the results from a LHP model including some recent efforts to represent the phase distribution. Different patterns of the phase distribution in the core are predicted at steady state and sensitivities with the heat exchange. These results notably highlight the role of the phase distribution in temperature hysteresis.

KEY WORDS : Model, Two-phase flow pattern, Temperature hysteresis.

1. INTRODUCTION

The LHP operating temperature is very sensitive to the amount of heat load which is not absorbed by vaporization of the working fluid taking place in the primary wick of the evaporator. This heat leak (also known as parasitic heat) spreads by diffusion through the wicks, the fluid and the evaporator casing, reaches the inner surface of the capillary structure where it is transferred to the fluid contained in the evaporator cavity (i.e. the compensation chamber and the evaporator core) leading to an increase of the loop temperature.

During this process, vaporization/condensation may appear and generate a relatively complex phase distribution in the cavity (see figures 1a to 1c for a schematic view of the mass transfer corresponding to 3 configurations: with a vapor flow from the core to the compensation chamber (CC), with an isolated two phase flow in the core and a liquid full core). This makes the loop sensitive to several factors such as : the gravity environment, the evaporator orientations in gravity field, the operating conditions of heat loading (eg.

the temperature hysteresis can be observed with an increase or a decrease step of the heat load),...

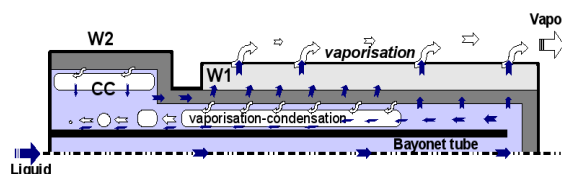


Figure 1.a : Mass transfer in a LHP evaporator with a vapor flow from the core to the CC.

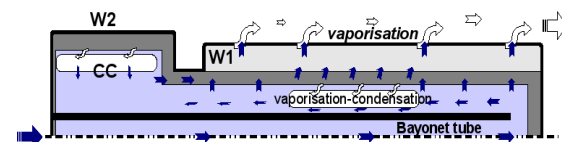


Figure 1.b : Mass transfer in a LHP evaporator with an isolated two-phase flow in the core.

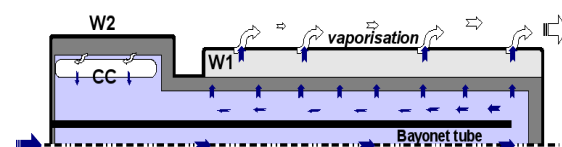


Figure 1.c : Mass transfer in a LHP evaporator with a liquid full core.

In the past, some experimental study have attempted to highlight the phase distribution in the evaporator by direct visualization (d'Entremont et al., 2008). Only a few theoretical approaches have attempted to predict the heat and mass distributions inside the evaporator (Hoang and Ku, 2003), (Dutour et al. 2010).

This study focusses on the description of the phase distribution resulting in the heat and mass transfers structure in the evaporator cavity of a LHP integrating a cylindrical evaporator and a bayonet tube. The discussion is based on the extension of a one dimensional LHP model including some recent efforts to represent different configurations of the cavity phase distribution at steady state.

2. MODELING APPROACH

2.1 The evaporator core

We assume that a two-phase flow can be modeled by an uniform saturation temperature and pressure region. Therefore, the fluid phase distribution in the evaporator cavity can be modeled by a more or less complex partition of sub-cooled liquid and saturation domains. The objective is then to determine the length of each zone in a consistent way with the global heat and mass transfer model.

It is thereby necessary to have a preset idea of phase structures encountered in the cavity. In this work, we explore two possible configurations as follows :

- pattern 1 (P1) : vapor enters the CC (figure 2), a heat pipe effect between the core and the CC which can exist over a distance $L_2=L_w-L_1$, where L_w is the primary wick length and L_1 is the sub-cooled liquid zone lasting at the inlet of the core.

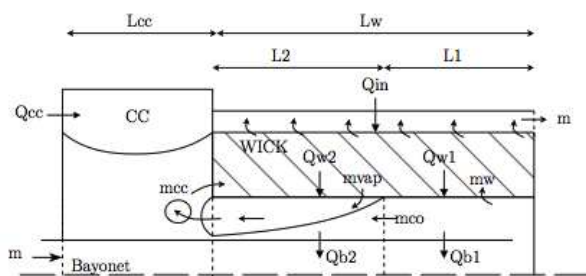


Figure 2. Schematic view of the model of heat and mass transfers in the evaporator cavity for the pattern P1 (with vapor entering the CC).

- pattern 2 (P2) : no vapor enters the CC (figure 3) but a two-phase flow under the wick persists over a portion L_2 of the core. There is then an additional sub-cooled region of length L_1^* at the outlet of the core taking into account that the vapor can be condensed before reaching the CC.

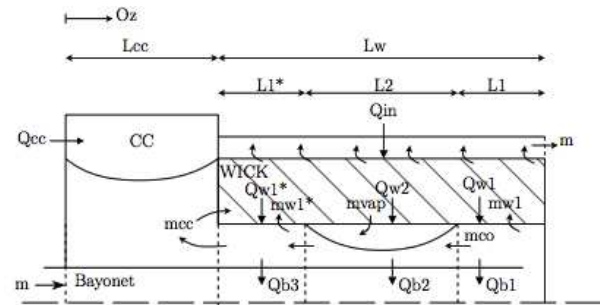


Figure 3. Schematic view of the model of heat and mass transfers in the evaporator cavity for the pattern P2 (no vapor is entering in the CC).

Moreover, we assume that, in each condition, the capillary structure (i.e. the primary and the secondary wicks) is always full of liquid and ensures perfectly all the mass transfers needed for the proper functioning of the system. This hypothesis is valid even when a secondary mass flow rate loop appears between the wick and the CC due to the fluid vaporization in the core. The global mass exchanges were then established assuming that the capillary pumping is uniform in the sub-cooled domains.

The heat leaks Q_{w1} , Q_{w1}^* and Q_{w2} are correlated with the physical parameters of the primary wick considering the heat diffusion and the transport through an equivalent porous medium as well as the heat convection at the inner surface of the wick.

The continuity between the two patterns is provided by a condition for the heat transfer on the two-phase domain : if the heat leak Q_{w2} is greater than the heat removed along the corresponding bayonet portion (Q_{b2}) then vapor is entering the CC (model with P1); else, the solution is given by the model with P2.

2.2 LHP Model

The evaporator cavity model was developed for a full steady state loop model. See Launay et al. (2007) for a detailed description of the condenser and transport-line models.

3. RESULTS

3.1 Steady state solutions

At steady state, the heat and mass balances can be solved analytically except for the sub-cooled liquid in contact with the wick. We assumed, then, an additional hypothesis that the heat transport at the inner surface of the wick (due to the capillary pumping) is negligible compared to the heat leaks and the axial-core heat transport. As a result for each phase distribution configurations, the steady state of the loop model are provided for a given set of operating conditions (Q_{in}, T_{amb}, T_{sf}) by the solutions of one phase distribution equation :

- for the configuration P1 :

$$f1(L1, L2) = 0 \quad (1)$$

where $f1$ is given by the heat and mass transfer model with the P1 phase distribution in which $L2$ can be replaced by $L_w - L1$.

- for the configuration P2 :

$$f2(L1^*, L1, L2) = 0 \quad (2)$$

$$f3(L1^*, L1, L2) = 0 \quad (3)$$

where $f2$ and $f3$ are given by the heat and mass transfer model with the P2 configuration in which $L2$ can be replaced by $L_w - L1 - L1^*$.

The first major result is that the second system of equations (equations (2) and (3)) admits a trivial solution that is $L2=0$. This implies that the configuration P2 consistently includes the liquid full core distribution (P2-liquid).

3.2 Numerical results

The model is solved for a classical configuration of a LHP for space applications. The fluid is ammonia and the primary wick is metallic. The cold source temperature is about 10°C which is lower than the ambient temperature (maintained at 25°C). The loop design properties are summarized in table 1.

The heat exchange coefficients between the liquid and the bayonet tube is estimated by the classical Nusselt number correlations used for liquid convective heat transfer in cylindrical tube. When

condensation takes place, the heat transfer coefficient is chosen as a constant value of 3000 W/K.m^2 since this value is well known as a good order of magnitude of condensation heat transfer regime.

Table 1. Loop properties.

Wick	
Material	Sintered Nickel
Dry Conductivity	5 W/mK
Outer diameter	18 mm
Core diameter	12 mm
Active length	400 mm
Compensation Chamber	
Volume	60 ml
Length	50 mm
Lines	
Outer diameter	4.76 mm
Inner diameter	3.64 mm
Vapor line	5 m
Liquid line	5 m
Condenser	2 m

3.21 Core phases distributions

Figure 4 shows the solutions of the phase distribution in the evaporator core through the variation of the two phase ratio $L2_r = L2/L_w$ versus the heat load. It is observed that :

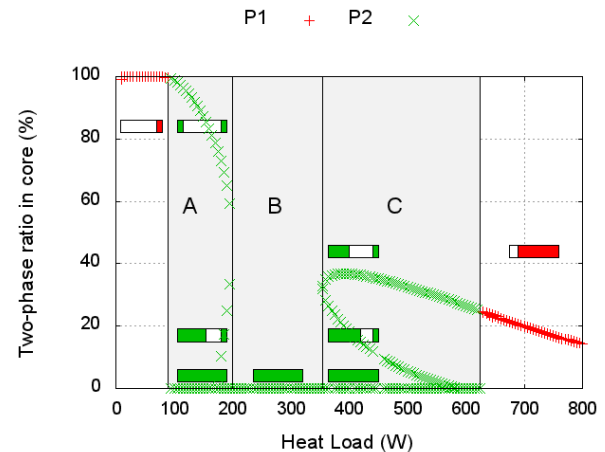


Figure 4. Two-phase ratio versus the heat load.

i) at very low heat loads ($Q < 100\text{W}$), the only solution is that a major part of the core is in a two-phase state and there is a heat pipe effect between the wick and the CC. This result is in good agreement with the visualization of

d'Entremont (2008) (with an intermittent bubbly flow) and can be understood as the bayonet tube acts as an exchanger of infinite length : no significant sub-cooling is produced at the inlet of the core and thus, the heat leaks, even if they are very small, vaporize the fluid under the wick;

ii) at high heat load ($Q > 600W$), we find again that the configuration P1 is the only solution and thus vapor enters the CC. However, the sub-cooled region at the inlet of the core is more significant. Increasing heat load, the two-phase ratio decreases from 25% to 15% : the liquid seems to gradually and significantly invades the core with heat loading;

iii) at the intermediate range of heat load ($100W < Q < 600W$), different behaviors appear : there are one or more solutions corresponding to the configuration P2 i.e. a liquid full core (P2-Liquid) or an isolated two-phase flow confined in an internal portion of the core (P2-Isolated). Moreover, 3 subdomains can be observed (figure 4) :

- zone A : the steady state phase structure can be either a liquid full core or a large isolated two-phase flow or a smaller isolated two-phase flow located at the outlet of the bayonet;

- zone B : here a liquid full core is the only steady state solution;

- zone C : on a larger heat load range, the phase structure can be either a liquid full core, a large isolated two-phase flow or a smaller isolated two phase flow located at the outlet of the bayonet; the difference with the subdomain A is that the liquid fraction is greater.

It is important to note that these solutions correspond to the steady state and moreover that, with the present model, we do not have the opportunity to determine the stability of each solutions. For instance, an unsteady regime with a isolated two-phase flow alternating with a liquid full core can be in fine the real behavior.

3.22 Phase distribution sensitivity

Figure 5 and figure 6 show the solutions of the phase distribution in the evaporator core for two distinct values of the global heat transfer coefficient between the fluid in the bayonet and the fluid in the CC. We chose two different orders of magnitude $h = 1500 W/Km^2$ (figure 5) and $h = 15 W/Km^2$

(figure 6) in order to highlight the sensitivity to the heat transfer regime between bayonet and the CC (involving condensation or only convection). Moreover, the condenser is two-time smaller in the second case.

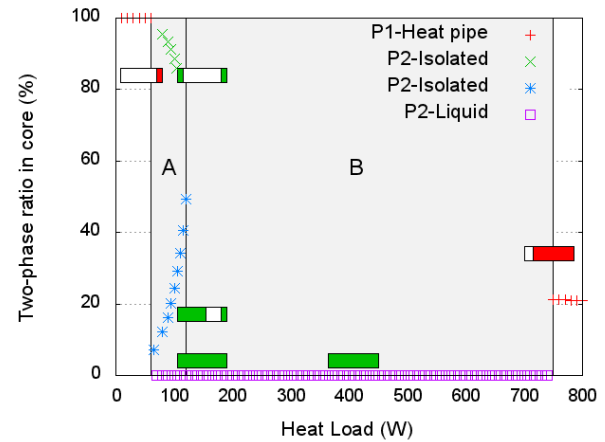


Figure 5. Two-phase ratio versus the heat load in the case of a condensation regime on the portion of the bayonet in contact with the CC ($h = 1500 W/Km^2$).

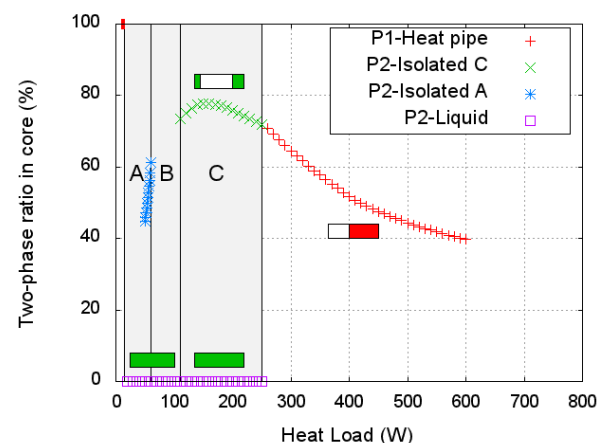


Figure 6. Two-phase ratio versus the heat load in the case of a convection regime on the portion of the bayonet in contact with the CC ($h = 15 W/Km^2$).

We find that in both cases vapor is entering the CC at very load heat load and for the upper range of heat loads. However, the interval corresponding to the patterns P1 and P2 is significantly modified :

i) in the case of intensive heat transfer with bayonet (figure 5), the P2 sub-domain extends beyond 700W and is mainly reduced to the liquid full solution. Note that we don't manage to

observe the C subdomain (but this can be to insufficient numerical convergence);

ii) in the case of a low heat transfer with the CC portion of the bayonet tube (figure 6), the region with an heat pipe effect is greater and start before 300 W. The patterns P2 are confined to a smaller interval in the lower heat load range.

3.23 Temperature sensitivity and hysteresis

Figure 7 and figure 8 show the corresponding saturation temperature of both previous cases.

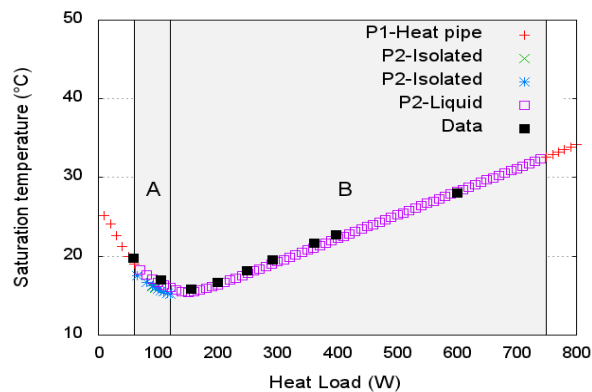


Figure 7. Saturation temperature versus the heat load in the case of a condensation regime on the portion of the bayonet in contact with the CC ($h=1500W/Km^2$).

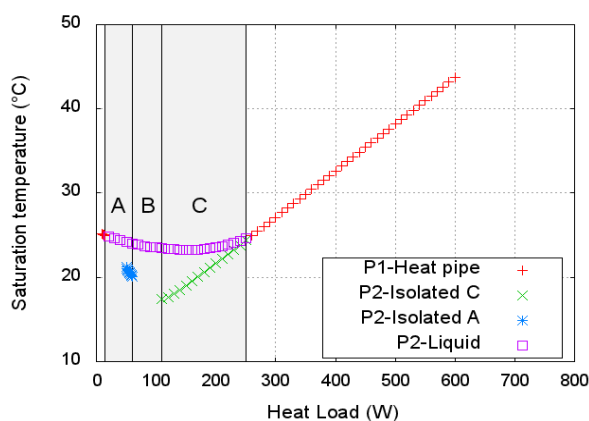


Figure 8. Saturation temperature versus the heat load in the case of a convection regime on the portion of the bayonet in contact with the CC ($h=15W/Km^2$).

These graphs contribute to determine the steady state loop performance sensitivities with this parameter including the feed-back of the flow patterns in the core. It can be noticed that they incorporate some experimental data from the test

of a ammonia LHP made available by the French Spatial Agency (CNES). The properties of this loop are very similar to the ones given in Table 1.

These results demonstrate two drastically different sensitivities to the phase distribution :

i) in the case of intensive heat transfer with bayonet (figure 7), the temperature saturation appear almost unaffected by the large phase distribution shown in figure 5. In the zone A, an isolated two-phase flow in the core or the liquid full solution will lead to a temperature difference of about 2K ;

ii) in the case of a low heat transfer with the CC portion of the bayonet tube (figure 8), both the subdomain A et C exhibit a difference of 5K to 10K demonstrating a high sensitivity of the loop to the phase distribution in the core. These results can get close to the temperature hysteresis observed in some experimental studies (d'Entremont, 2008): any design options or operating conditions (like a CC hard filling, orientation in the gravity field) that would lead to a low heat transfer between the fluid in the CC and sub-cooled liquid in the corresponding portion of bayonet tube, expose the system to a high sensitivity to the phase distribution in the core and thus large temperature hysteresis.

4. CONCLUSIONS

A theoretical contribution for the determination of the nature of fluid behavior in the evaporator cavity has been presented in this paper. We found that over its operating heat load range, a LHP encounters a variety of phase patterns in the core : a two-phase flow up to the CC, different isolated two-phase flows limited in a portion of the core and a liquid full core. The sensitivity study has demonstrated that these phase patterns are involved in temperature hysteresis.

ACKNOWLEDGEMENT

Funding for this work was provided by CNES.

NOMENCLATURE

L1 sub-cooled liquid length in the core
 L1* sub-cooled liquid length in the core

L2 two phase flow length in the core
Lw primary wick length
Qin heat load
Tamb Ambient temperature
Tsf Cold source temperature
m mass flow rate

REFERENCES

d'Entremont B.P., Ochterbeck J.M. (2008)
“*Investigation of loop heat pipe startup using liquid core visualization*”, proc. of the 2008 ASME Summer Heat Transfer Conference, Jacksonville, Florida, USA.

Hoang T.T., Ku, J. (2003), “*Heat and mass transfer in loop heat pipe*”, ASME Summer Heat Transfer Conference, Las Vegas.

Dutour S., Soler Ph., Platel V., Joly JL., Tadrist L., Larue de Tournemine A. (2010) “*A theoretical investigation of the influence of phase distribution in the evaporator cavity on the performance of A Loop Heat Pipe*”, proc. of the 15th IHPC, Clemson, USA.

Launay, S., Platel, V., Dutour, S., (2007) “*Transient modeling of loop heat pipes for the oscillating. behavior study*” Journal of Thermophysics and Heat Transfer, 21 p. 487–495.

The Influence of Groove Shape on Loop Heat Pipes' Performance

Masakazu Kuroi and Hosei Nagano

Department of Aerospace Engineering, Nagoya University
Furo-cho Chikusa-ku Nagoya, Aichi 464-8603 Japan

Phone: +81-(0)52-789-4403

Fax: +81-(0)52-789-3281

kuroi@prop2.nuae.nagoya-u.ac.jp

ABSTRACT

The influence of groove shape on loop heat pipes' performance has been investigated by analysis and experiment. In analysis, the effects of width, depth, and the number of axial grooves on steady-state performance were examined. Calculation results indicated the existence of optimum width and depth to get down the evaporator temperature. The smaller the width and the depth become, the higher the evaporator temperature becomes due to the growth of pressure drop at the grooves. The increase of width and depth of the grooves result in the rise of evaporator temperature due to the decreasing of contact area between the evaporator case and the wick, and the increase of heat leak from the grooves to the core. Experimental investigations were conducted with a same LHP, which is able to exchange wicks. The wicks which have different groove shapes were examined. The parameters of groove shapes are the number of axial grooves and the existence of circumferential grooves. In the case of only axial grooves, there is the optimum number of axial grooves. The circumferential grooves have thermal uniformity effect, and with a small heat input, evaporator temperature becomes lower than the wick which has only axial grooves. However, with a large heat input, evaporator temperature becomes higher. This is due to the reduction of contact area and the increase of heat leak from the grooves to the core. About start-up time, the larger the axial groove passage area becomes, the shorter the start-up time becomes.

KEY WORDS: Two-phase heat transfer, start-up, circumferential groove

1. INTRODUCTION

Loop heat pipes (LHPs) attract attentions as next generation thermal control device. LHPs are two-phase heat transfer devices whose operating principle is based on the evaporation/condensation of working fluid, and use the capillary pumping forces to ensure the fluid circulation. LHPs are semipermanent devices which need no electric power nor mechanical body. Compared to similar two-phase devices such as traditional heat pipes and thermosyphons, they have superior heat transfer capability and reliable operation in gravitational field. This is due to structural differences such as a wick being located only in an evaporator. However, the existence of a wick in an evaporator makes it the most complex component in a LHP, and the design of the evaporator has great influence on the LHP's operating performance.

In the past, the relationship between the wick design and maximum heat transfer rate was investigated by analysis and experiment (Chu,

2004). It was reported that maximum heat transfer rate become greater with growing the number and flow passage area of grooves due to reduction of pressure drop at grooves. However, as the ratio of pressure drop at grooves against total pressure drop is small, it is considered that the upper limit of maximum heat transfer exists. Yiding (1994) simulated the liquid flow in the wick and three-dimensional vapor flow in the grooves. It was found that vapor flow in the grooves is highly dependent on the working fluid used. Valeri and Roger (2006) developed the wick which has axial and circumferential grooves and conducted analysis and experiment. It was reported that the circumferential grooves have efficiency to collect the vapor and capability to reduce the presence of localized dryout. However, since their evaporator also has micro grooves inside evaporator, it is difficult to evaluate the effects of groove shape separately.

In this way, only few studies have so far been made about groove shape. The purpose of this research is to clarify the influence of groove shape

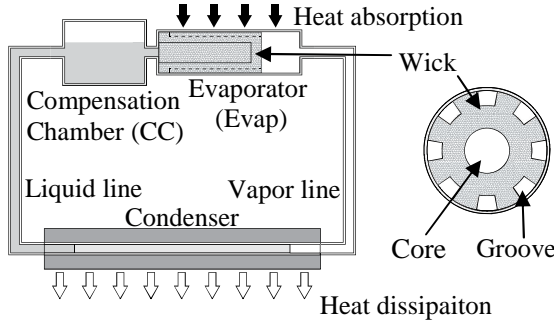


Figure 1. Schematic the LHP and cross section of an Evaporator

on LHP performance and establish the design method of groove shape. In this paper, the parameters width depth, and the number of axial grooves and the existence of circumferential grooves, are investigated by steady-state model and experiment.

2. STEADY STATE MODEL

A steady-state model was established to examine the influence of groove shape on the LHP performance. This numerical model is based on one dimensional energy and momentum equations. The working fluid assumes uncompressed and viscous fluid.

2.1 Vapor and Liquid lines

The vapor and liquid lines of the LHP are usually made of small diameter smooth pipes with long transport length. As it was assumed that they are insulated, there is no heat exchange between these lines and outside. The energy and momentum equations are as follows:

$$-\dot{m}c_p \frac{dT}{dL} = -\pi D_i \tau_w u \quad (1)$$

$$-\frac{dp}{dL} = \tau_w \frac{4}{D_i} \quad (2)$$

In a single phase, the wall shear stress τ_w is given with friction coefficient of a pipe f , i.e.

$$\tau_w = f \times \frac{1}{2} \rho u^2 \quad (3)$$

$$f = \begin{cases} 16/Re & \text{Laminar flow} \\ 0.0791/Re^{0.25} & \text{Turbulent flow} \end{cases} \quad (4)$$

2.2 Condenser

At the condenser, the term of heat exchange with outside was added to energy equation because the condenser is mounted on a cold plate.

$$-\dot{m}c_p \frac{dT}{dL} = -\pi D_i \tau_w u + G'_{\text{sink}} (T - T_{\text{sink}}) \quad (5)$$

The thermal conductance per unit length between the condenser and the cold plate G'_{sink} is as follow:

$$\frac{1}{G'_{\text{sink}}} = \frac{1}{h_i \pi D_i} + \frac{\ln(D_i/D_o)}{2\pi k_w} + \frac{1}{h_o \pi D_o} \quad (6)$$

In two phase flow, heat transfer coefficient h_i and the frictional pressure drop are calculated by the Lockhart-Martinelli method (Lockhart, 1949).

2.3 Evaporator and CC

Figures 2 and 3 show cross sections of an evaporator and a CC. Figure 4 shows thermal network around the evaporator and the CC. Heat load from a heat source to the evaporator case Q_{load} transports along three paths: one part is transferred to the evaporation front Q_{wi} , another is transferred to the grooves Q_{gr} , and the other is transferred to the CC casing Q_{case} , as shown by

$$Q_{\text{load}} = Q_{\text{wi}} + Q_{\text{gr}} + Q_{\text{case}} \quad (7)$$

$$Q_{\text{wi}} = G_{\text{ev}} (T_{\text{ec}} - T_{\text{ev}}) \quad (8)$$

$$Q_{\text{gr}} = G_{\text{gr}} (T_{\text{ec}} - T_{\text{gr}}) \quad (9)$$

$$Q_{\text{case}} = G_{\text{case}} (T_{\text{ec}} - T_{\text{cc}}) \quad (10)$$

The thermal conductance between the evaporator case and the grooves G_{gr} is as follow:

$$\frac{L_{\text{gr}}}{G_{\text{gr}}} = \frac{1}{h_i \pi D_i} \quad (11)$$

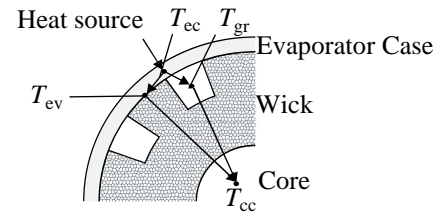


Figure 2. Cross section of an Evaporator

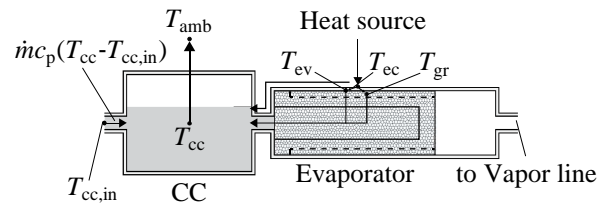


Figure 3. Cross section of Evaporator and CC

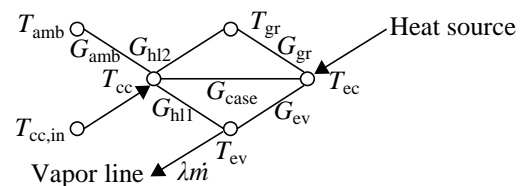


Figure. 4 Thermal network of Evaporator and CC

The thermal conductance between the evaporator casing and the CC casing G_{case} is given by thermal conductivity of the casing. The thermal conductance between the evaporator casing and the evaporation front G_{ev} is given by Zhao, Liao method (Zhao and Liao, 2000). Like Fig. 5, for the cylindrical geometry adopted for pores of wick, liquid and vapor of a meniscus are defined as an equivalent pipe (the area of dash line) and a cylinder from condition of equivalency of volumes. The thermal conductance G_{if} , G_{wi} and G_{vap} are given by contact thermal resistance, thermal conductivity of wick material and vapor, respectively. The thermal conductance G_1 is as follow:

$$G_1 = \frac{k_1 2\pi h_m}{\ln\{r_p/(r_p - \delta)\}} \quad (12)$$

The curvature radius of a meniscus is as follow:

$$r_m = r_p \frac{P_{\text{cap}}}{\Delta p_m} \quad (13)$$

Δp_m is a pressure difference between the back and forth of a meniscus, and equal to the total pressure drop of the LHP. The pressure drop through the wick is as follows:

$$\Delta p_{\text{wi}} = \frac{\mu_1 u}{K_p} L(\theta) \quad (14)$$

The permeability of the wick is estimated by the following equation (Lizhan, 2009):

$$K_p = \frac{(2r_p)^2 \phi^3}{150(1-\phi)^2} \quad (15)$$

$L(\theta)$ is the length of liquid flow through wick, and different in three areas; (i) the area where liquid flow in a radial direction, (ii) a direct course, (iii) radial and circumferential direction like. They can be expressed as:

$$L(\theta) = \begin{cases} r_o - r_i & \text{: (i)} \\ ((r_o \cos \theta - (r_i^2 - h^2)^{1/2})^2 + (r_o \sin \theta + h)^2)^{1/2} & \text{: (ii)} \\ ((r_o \cos \theta - r_i \cos(\theta - \cos^{-1}(r_i/r_o)))^2 + (r_o \sin \theta - r_i \sin(\theta - \cos^{-1}(r_i/r_o)))^2)^{1/2} & \text{: (iii)} \\ + r_i(\theta + \pi/2 - \cos^{-1}(r_i/r_o) - \cos^{-1}(h/r_o)) & \end{cases} \quad (16)$$

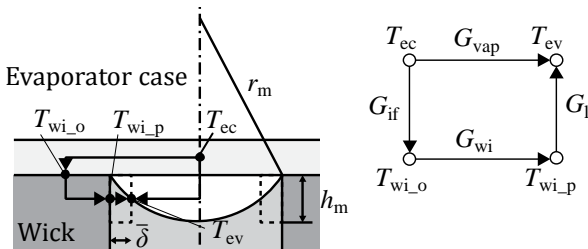


Figure 5. Schematic and network of interface

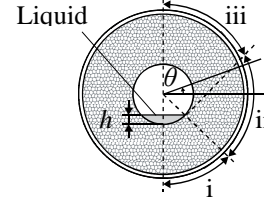


Figure 6. Cross section of Evaporator

The heat rate to the evaporation front Q_{wi} is the sum of liquid evaporation Q_{ev} and the heat leak to the core through wick Q_{hl1} :

$$Q_{\text{wi}} = Q_{\text{ev}} + Q_{\text{hl1}} \quad (17)$$

Q_{hl1} is calculated as follows:

$$Q_{\text{hl1}} = \frac{2\pi L_{\text{wi}} k_{\text{eff}}}{\ln(D_o/D_i)} (T_{\text{ev}} - T_{\text{cc}}) \times Ra_{\text{wi}} \quad (18)$$

k_{eff} is calculated as follows (Lizhan, 2009):

$$k_{\text{eff}} = k_{\text{max}}^{0.42} + k_{\text{min}}^{0.58} \quad (19)$$

$$\begin{cases} k_{\text{max}} = \phi k_f + (1-\phi) k_{\text{wi}} & \text{parallel} \\ k_{\text{min}} = (k_f k_{\text{wi}}) / [\phi k_{\text{wi}} + (1-\phi) k_f] & \text{serial} \end{cases} \quad (20)$$

The heat rate to the vapor grooves Q_{gr} is the sum of the heat rate of the vapor heating Q_{vap} and the heat leak to the core through the wick Q_{hl2} .

$$Q_{\text{gr}} = Q_{\text{vap}} + Q_{\text{hl2}} \quad (21)$$

$$Q_{\text{hl2}} = \frac{2\pi L_{\text{gr}} k_{\text{eff}}}{\ln(D_o/D_i)} (T_{\text{gr}} - T_{\text{cc}}) \times Ra_{\text{gr}} \quad (22)$$

$$D_o = D_o - 2d_{\text{gr}} \quad (23)$$

In the grooves, the vapor mass flow rate is grows with the down stream, i.e.

$$\begin{aligned} \dot{m}_i h_{\text{ec-gr}} A_{\text{ec-gr}} (T_{\text{ec}} - T_i) + dp_i \dot{m}_i / \rho \\ = \dot{m}_i c_p (T_{i+1} - T_i) + d\dot{m}_i c_p (T_{i+1} - T_{\text{ev}}) \end{aligned} \quad (24)$$

The first term of the left part is the heat input from the evaporator case, and the second is the pressure drop. The right part is the increase in temperature, the first accounts for about the flowing vapor until then, the second accounts for the increasing vapor $d\dot{m}_i$. It is assumed that the fluid inside the CC is always saturated. The energy conservation equation in this section is expressed as follows:

$$\dot{m} c_p (T_{\text{cc}} - T_{\text{cc.in}}) + Q_{\text{amb}} = Q_{\text{hl1}} + Q_{\text{hl2}} + Q_{\text{case}} \quad (25)$$

These calculations are conducted for discretization of 1 mm. At first, arbitral values of T_{ev} and Q_{ev} are assumed as inputs and calculation continue until that all of T and Q balance out.

3. EXPERIMENTAL SETUP

A LHP, able to exchange the wick, was fabricated. Figure 7 shows a photograph of the experimental LHP, and Table 1 indicates the LHP geometry. The LHP temperatures are measured by 18 T-type thermocouples. 4 thermocouples are attached on the evaporator, 2 on the CC, 3 on the vapor line, 3

on the liquid line, and 6 on the condenser. Aluminum heater blocks are attached to the evaporator to simulate the instrument mass as shown in Fig. 8. Four cartridge heaters are inserted into the thermal mass to apply the heat load to the evaporator. 2 types of heat input mode were tested: the equal heat input mode, with 4 cartridge heaters (Equal), and the one surface heat input mode with 2 cartridge heaters (Top and Bottom). The condenser is mounted on an aluminum cold plate. The cold plate has a good contact with a copper plate and the anti freeze liquid from the chiller unit flows through the pipe behind the copper plate for sink temperature control. The experiments were conducted at sink temperature of 5 °C and the average ambient temperature of 23 °C. All tests were conducted at least two times to evaluate their repeatability.

Table 2 shows the wick geometry for experiments. The parameters are the number of axial grooves and the existence of circumferential grooves. The number is decided under conditions of constant ratio of constant area against the wick outer surface Ra_{wi} , and constant ratio of passage flow area against the wick cross section S_{gr} . The width, depth, and the number of circumferential grooves are 0.8mm×1mm×8, respectively.

4. RESULTS AND DISCUSSIONS

At first, the parameters are set to the width, depth and number of axial grooves based on shape $n=4$ in Table 2. Figure 9 shows the calculation result of the evaporator temperature and pressure drop at the grooves. As Fig. 9 indicates, the evaporator temperature becomes higher with the reduction of the width and depth. This is due to the growth of pressure drop with the narrowing of the flow passage area. The expanding of the flow passage area also leads to the increase in evaporator temperature, because of the reduction of the contact area between the evaporator casing and the wick, and the growth of heat leak from the grooves to the core. Figure 10 presents the measured evaporator and CC temperature. $n=1, 2, 4, 20$ experiments were broken up due to the rapid uplift of evaporator temperature with 10, 20, 30, 25W respectively. In the case of shapes $n=1, 2, 4$, a few axial grooves lead vapor leak to the core because

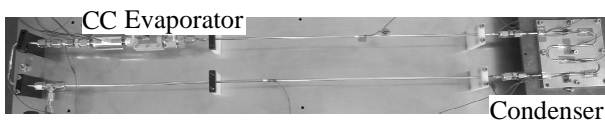


Figure 7. Photograph of the LHP

Table 1. LHP geometry characteristics

Heater Blocks (AL5052)	Length[mm]	40
	Height[mm]	16
	Width[mm]	24
Evaporator case (SUS304)	Length[mm]	75
	O.D.[mm]	13
Wick (PTFE)	Length[mm]	50
	O.D.[mm]	11
	Pore radius[μm]	1.2
	Porosity[%]	34
CC (SUS3004)	Length[mm]	40
	O.D.[mm]	22
Vapor line (SUS304)	Length[mm]	500
	O.D.[mm]	3.2
Liquid line (SUS304)	Length[mm]	900
	O.D.[mm]	3.2
Condenser (SUS304)	Length[mm]	350
	O.D.[mm]	3.2
Working fluid	ethanol	

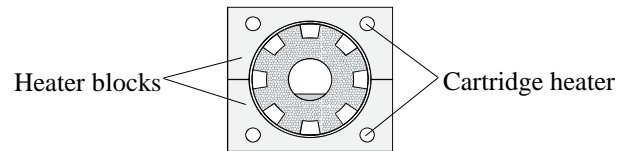


Figure 8. Cross section of Heater blocks and the Evaporator

Table 2. Wick geometry

Name	$n=1$	$n=2$	$n=4$	$n=8$	$n=20$	$cn=1$	$cn=2$
n	1	2	4	8	20	1	2
W_{gr} [mm]	4	2	1	0.5	0.2	4	2
D_{gr} [mm]	1	1	1	1	1	1	1
Ra_{wi} [%]	88	88	88	88	88	76	76
S_{gr} [%]	7	7	7	7	7	7	7
cn	0	0	0	0	0	1	1
Cross Section							

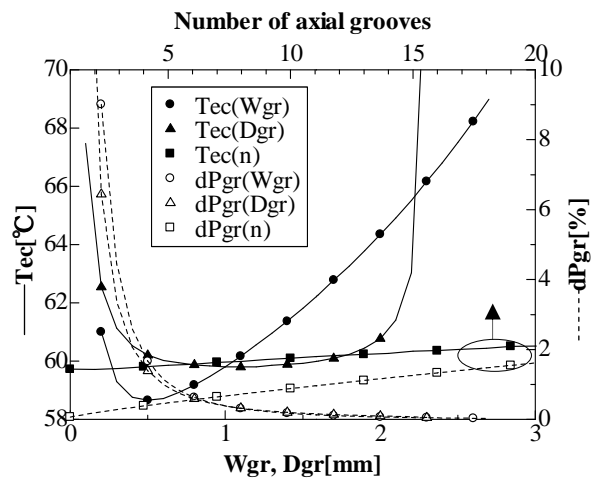


Figure 9. Calculated evaporator temperature and pressure drop at grooves

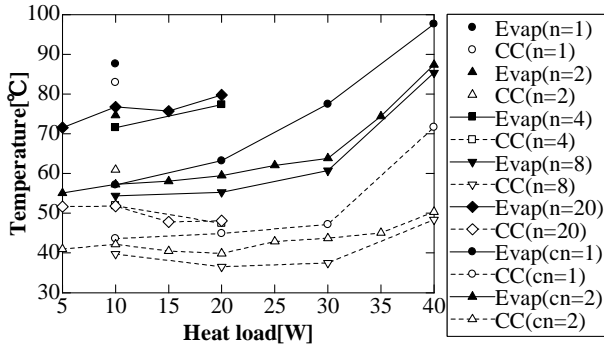


Figure 10. Experimental results

there is the point whose distance from the axial grooves is longer than that from the core on contact surface. In the case of $n=20$, it becomes difficult for vapor to flow out to the vapor line with the vapor increase because of the too narrow passage area. $n=8$, $cn=1$, 2 operated stably up to 40W, and operating temperature of $n=8$ was the lowest. This reason is that the contact area of $cn=1$, 2 is smaller than that of $n=8$ due to the circumferential grooves. As compared to $cn=1$, $cn=2$ prevented from vapor leak because $cn=2$ has more axial grooves. Table 3 lists steady-state temperature and temperature distribution in the evaporator with equal and one surface heat input, and start-up time with equal heat input. Temperature distribution of $n=8$ is the largest, and evaporator temperature with 5W input of $cn=1$ is the lowest. These results can reasonably come from the thermal uniformity effect of circumferential grooves. $cn=1$ started the earliest, this reason is possibly that its passage area of axial groove is the largest. It can be said that the large passage area of axial grooves is capable of vapor flowing to the vapor line at early phase when vapor content is small.

Turning to the comparison between calculation and experimental results, the comparison of steady-state temperature is shown in Fig. 11. The calculated maximum heat transfer rate is 36W. In experiments, $n=8$, $cn=1$ and 2 can transfer 40W. However, in experiments, the CC temperature of all shape increases at 40W, and this is sufficient evidence of vapor leak at the upside of wick. Additionally, $cn=1$ evaporator temperature is high also at 20, 30W while the CC temperature is not increased. This is thought to be due to as the backdown of evaporation front at the contact away from the axial groove. The increase of vapor amount makes it impossible to discharge vapor to the axial groove through narrow circumferential grooves. Because the backdown of evaporation front is not taken in account in steady-

Table 3. Evaporator temperature and Start-up time

	$n=8$		$cn=1$		$cn=2$	
	5W	40W	5W	40W	5W	40W
Equal[°C]	54.5	59.4	52.9	77.5	52.7	64.9
Top[°C]	54.3	63.2	51.8	76.2	53.7	64.0
Bottom[°C]	58.9	59.5	52.1	73.8	54.0	63.3
max ΔT [°C]	4.6	3.8	1.1	3.7	1.3	1.6
Start-up time[sec]	588	58	501	51	1075	52

state model, there is the difference between calculation and experimental results. By contract, in the case of $n=8$, $cn=2$, the calculated temperature agreed well with the experimental data. The order of evaporator temperature between calculation and experimental results for $cn=1$, $cn=2$, $n=8$ agreed well. About $n=8$ and $cn=2$, each calculated ratio of heat amount against heat load is shown in Fig. 12. It was clarified that heat leak from grooves to the core Q_{hl2} of $cn=2$ is larger than that of $n=8$. This is thought to be due to the addition of the heat leak from circumferential grooves. Because the distance between the grooves and the core is shorter than that between the contact area and the core, Q_{hl2} becomes larger than the heat leak from the contact area Q_{hl1} . It can be said that this is one of the reasons for the temperature increase of $cn=2$.

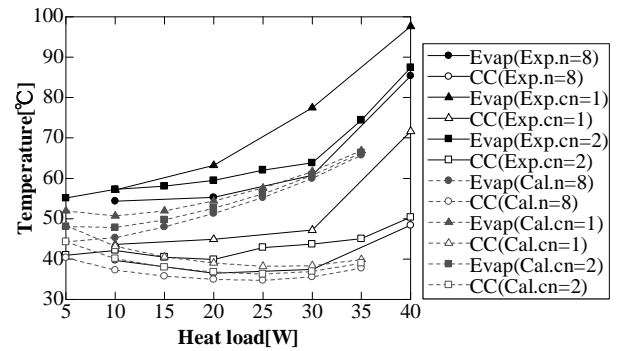


Figure 11. Comparison of analysis and experiment

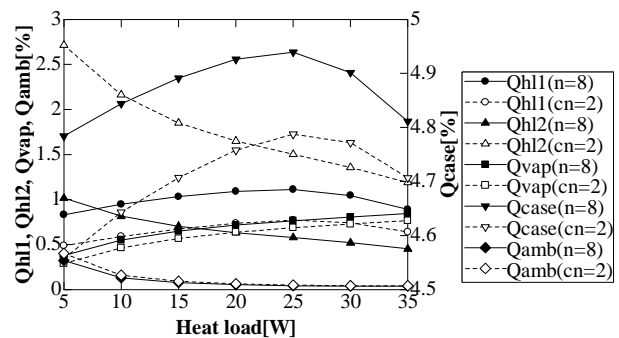


Figure 12. Distribution ratio of heat load

5. CONCLUSIONS

The influence of the groove shape on the LHP performance was investigated by analysis and experiments. The numerical model could estimate the optimum width and depth of axial grooves in order to decrease evaporator temperature. Experiments were conducted with a miniature LHP which is able to exchange the wicks, whose parameters are the size, the number of axial grooves and the existence of circumferential grooves. In the case of only axial grooves, there was an optimum number of axial grooves. Additionally, the circumferential grooves have thermal uniformity effect, and with a small heat input, the evaporator temperature becomes lower than the wick which has only axial grooves. However, with a large heat input, the evaporator temperature becomes higher. This is due to the reduction of contact area and the increase of heat leak from the grooves to the core. About start-up time, the larger the axial groove passage area becomes, the shorter the start-up time becomes.

NOMENCLATURE

A	= area, m^2
cn	= number of circumferential grooves
c_p	= specific heat capacity at constant pressure, $J/(kg \cdot K)$
D	= diameter, m and depth, m
f	= friction coefficient
G, G'	= thermal conductance, W/K , $W/(K \cdot m)$
h	= heat transfer coefficient, $W/(K \cdot m^2)$
	height, m
k	= thermal conductivity, $W/(K \cdot m)$
K_p	= permeability, m^2
L	= Length, m
\dot{m}	= mass flow rate, kg/s
n	= number of axial grooves
p	= pressure, Pa
Q	= rate of heat transfer, W
r	= radius, m
Ra	= ratio of contact area
Re	= Reynolds number
S	= ratio of cross section
T	= temperature, K
u	= velocity, m/s
W	= width, m
Greek	
δ	= thickness of liquid film, m
λ	= latent heat, J/kg
μ	= dynamic viscosity, $Pa \cdot s$
ρ	= density, kg/m^3
\emptyset	= porosity

Subscript

amb	= ambient
cap	= capillary
cc	= compensation chamber
ec	= evaporator case
eff	= effective
ev	= evaporation
f	= fluid
gr	= groove
hl	= heat leak
i	= inner, discrete number
if	= inter face
in	= inlet
l	= liquid
m	= meniscus
o	= outer
p	= pore
vap	= vapor
w	= wall
wi	= wick

ACKNOWLEDGEMENT

This research is partially supported by Industrial Technology Research Grant Program in 2008 (Grant No. 08E51515d) from New Energy and Industrial Technology Development Organization (NEDO) of Japan.

REFERENCES

- C. I. Chu, S. C. Wu, P. L. Chen, Y. M. Chen (2004) *Design of Miniature Loop Heat Pipe*, J. Heat Transfer-Asian Research, 33(1), p. 42-52
- Lizhan Bai, Guiping Lin, Hongxing Zhang, Dongsheng Wen, (2009), *Mathematical modeling of steady-state operation of a loop heat pipe*. J. applied thermal engineering, 29, p. 2643-2654
- R. W. Lockhart, R. C. Martinelli, (1949) *Proposed Correlation of Data for Isothermal Two-phase, Two-Component Flow in Pipes*, Chemical Engineering Progress, 45, p.39-48.
- Valeri V. Vlassov, Roger R. Riehl, (2006) *Modeling of a Loop heat Pipe with Evaporator of Circumferential Vapor Grooves in Primary Wick*. 36th Int. Conf. Environmental Systems, Norfolk, paper # 2066-01-2173
- Yiding Cao, Amir Faghri, (1994) *Conjugate analysis of a flat-plate type evaporator for capillary pumped loops with three-dimensional vapor flow in the groove*. J. Heat and Mass Transfer. 37(3). p. 401-409
- Zhao T.S., Liao Q. (2000) *On capillary-driven flow and phase-change heat transfer in a porous structure heated by a finned surface: measurement and modeling*. J. Heat and Mass Transfer, 43, p. 1141-1155.

ON THE LOWERING OF THE OPERATING TEMPERATURE OF A COPPER-WATER LOOP HEAT PIPE

Yushakova S., Chernysheva M., Maydanik Yu., Vershinin S.

Institute of Thermal Physics, Ural Branch of the Russian Academy of Sciences

Amundsen St., 106, 620106, Ekaterinburg

Phone: +7(343)267-87-91, Fax: +7(343)267-87-99, E-mail: s.yushakova@gmail.com

ABSTRACT

The problem of reducing the operating temperature of copper-water loop heat pipes (LHPs) used to cool computers is considered in the paper. An analysis of the factors determining the vapor temperature in an LHP has shown that this problem can be solved by decreasing heat flows into the compensation chamber, reducing pressure losses in the vapor line as well as optimizing working fluid charge volume. Experimental studies of the influence of these factors on the operating temperature of an LHP were carried out. Seven copper-water LHPs with a flat evaporator were made and tested for that purpose. The tests were conducted in the range of heat loads from 20 to 250 W with the LHP oriented horizontally.

KEY WORDS: copper-water loop heat pipe, operating temperature, computer cooling system.

1. INTRODUCTION

One of the crucial problems which can be solved with the help of loop heat pipes (LHPs) relates to the development of the energy efficient cooling system of central processing units (CPUs) and graphics processor units (GPUs) housed in densely packed computer servers. The maximum heat these CPUs can currently dissipate is between 130-150W (You and Lee, 2004). The problem is particularly acute for cooling systems of 1U servers or blades, where owing to free space constraints it is quite difficult to find the space above CPUs and GPUs to install large heat exchange surfaces. In air cooled servers the lack of space causes the use of more powerful fans, which increases the energy needed to run the fans. LHPs are able to move heat from the CPUs and GPUs to peripheral areas or the server enclosure where there is more room to dissipate the heat to either air or water and simultaneously reduce the energy required to cool the unit. Experiments with an air-cooling system based on ammonia LHPs were carried out in a commercial 1U server (Maydanik et al., 2010). The experiments were successful mainly because of the fact that ammonia as a working fluid makes it possible to use rather long vapor and liquid lines with a diameter of the order of 2-2.5 mm. Such lines can be easily configured in any manner which is necessary for the LHP arrangement in constrained conditions. However, the use of ammonia is very often restricted by environmental requirements. Therefore it becomes necessary to use

ecologically clean and safe working fluids, the best of which is water. Copper LHPs with a ceramic wick and water as a working fluid were tested in a 1U server for the cooling of 100-watt CPUs (Zimbeck et al., 2008).

From the point of view of chemical compatibility copper is the most suitable structural material for water. However, on the way to the creation of copper-water LHPs there is a problem connected with the thermophysical properties of water at 40-50°C. Such vapor temperature should be maintained in the LHP to prevent the temperature of the object being cooled from exceeding 60-70°C. The problem is connected with the realization of the thermodynamical condition of LHPs operability, which can be expressed by formula:

$$\Delta P = \left. \frac{\partial P}{\partial T} \right|_{T_{v-cc}} \cdot \Delta T_{v-cc} \quad (1)$$

where ΔP is the vapor pressure drop between the evaporating wick surface and the phase interface in the compensation chamber and ΔT_{v-cc} is the difference of the corresponding temperatures. The value of ΔP can be defined as the value of the pressure losses which occur during the motion of a working fluid in the circulation loop area, including the vapor-removal channels in the wick, the vapor line, the condenser and the liquid line. With regard to $\partial P/\partial T$, this value is determined by the Clausius-Clapeyron equation connecting pressure changes with temperature changes on the saturation line of the working fluid. In the

temperature range of 40-50°C on the saturation line, water has a relatively small value of $\partial P/\partial T$ when compared to working fluids like ammonia. For the fulfillment of the condition (1) it is necessary either to create high temperature head (to increase $\Delta T_{v,cc}$) or to decrease ΔP . In its turn, $\Delta T_{v,cc}$ depends on the value of parasitic heat flows into the compensation chamber, while ΔP is generally determined by pressure losses in the vapor line. However, it is rather difficult to keep the pressure losses small in copper-water LHPs as the pressure losses in the vapor line are rather high owing to low vapor density at the indicated temperature, while the high thermal conductivity of copper impedes the decrease of the $\Delta T_{v,cc}$ value (Maydanik et al., 2011).

The vapor temperature in the LHP also depends on the temperature of the fluid used to cool the condenser T_{cool} , on the thermal resistance of the condenser R_{cond} , as well as pressure losses in the vapor line ΔP_{vl} (Chernysheva et al., 2007):

$$T_v = T_{cool} + R_{cond} \cdot Q + \frac{\partial T}{\partial P} \cdot \Delta P_{vl} \quad (2)$$

The aim of this paper is to determine and investigate different factors influencing the operating temperature of copper-water LHPs and search for ways for its reduction at the optimum device design.

2. DESCRIPTION OF EXPERIMENTAL DEVICES

The main factors that determine the LHP operating temperature are:

- the condenser cooling temperature;
- the volume of the working fluid in an LHP;
- the hydraulic resistance of the vapor line;
- the thermal resistance of the wick barrier layer.

This study is based on tests of seven copper-water loop heat pipes differing in the characteristics of the wick and the diameter of vapor lines. The general view of the LHPs is presented in Fig. 1. Structural characteristics of the LHPs are given in Table 1. All LHPs had a flat-oval evaporator 7 mm thick equipped with a thermal interface with a heat-supply zone measuring 30x30 mm. The LHP condenser had a plastic cooling jacket for pumping the cooling water.

The heat load source was an aluminum block in which 4 heating cartridges of 75 W each were installed. The heater had a square heating surface measuring 30x30 mm. The electrical load changed stepwise with the help of a laboratory autotransformer from 20 to 250 W. The LHP tests were conducted at the horizontal orientation of the device in the gravity field.

Temperature measurement was carried out with the help of copper-constantan thermocouples OMEGA TT-T-30, the location of which is shown in Fig.1. Readings of the thermocouples were recorded by a data acquisition unit "Agilent 34970A".

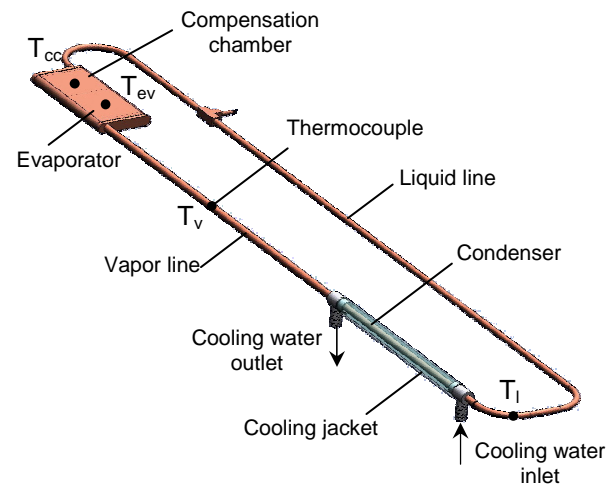


Figure 1. General view of the copper-water LHPs.

3. TEST RESULTS AND ANALYSIS

3.1 Influence of the condenser cooling temperature

The temperature of the medium, cooling the LHP condenser, determines the minimum basic level below which the vapor temperature in the LHP cannot be decreased. Depending on whether the condenser cooling temperature is higher or lower than the ambient temperature, the type of the LHP operating characteristic and the relative temperature level, which is connected with the initial distribution of the working fluid, can change. If the condenser cooling temperature is above the ambient temperature, the compensation chamber is initially filled more than at $T_{cool} = 20^\circ\text{C}$, and there is the minimum amount of the working fluid in the condenser.

Table 1. Structural characteristics of the copper-water LHPs.

Basic component	LHP-1	LHP-2	LHP-3	LHP-4	LHP-5	LHP-6	LHP-7
<i>Evaporator</i>							
Thickness x length x width, mm	7x 80 x 42	7x 80 x 42	7x 80 x 42	7 x 75 x 42	7 x 75 x 42	7 x 75 x 42	7 x 75 x 42
Pore radius, μm	15	15	15	27	27	27	27
Porosity, %	68	68	68	43	43	43	43
Barrier layer material	copper	copper	copper	copper	copper	copper	copper
Barrier layer thickness, mm	8	8	8	9	9	9	9
Additional barrier layer	-	yes	yes	-	-	-	-
Additional barrier layer material	-	copper	titanium	-	-	-	-
Additional barrier layer thickness, mm	-	10	10	-	-	-	-
<i>Vapor line ID/OD x length, mm</i>	4/5 x 305	4/5 x 305	4/5 x 305	2/3 x 305	3/4 x 305	4/5 x 305	5/6 x 305
<i>Condenser ID/OD x length, mm</i>	4/5 x 160	4/5 x 160	4/5 x 160	4/5 x 160	4/5 x 160	4/5 x 160	4/5 x 160
<i>Liquid line ID/OD x length, mm</i>	3/4 x 800	3/4 x 800	3/4 x 800	3/4 x 800	3/4 x 800	3/4 x 800	3/4 x 800

The LHP-1 test results at two condenser cooling temperatures $T_{\text{cool}}=20^{\circ}\text{C}$ and $T_{\text{cool}}=40^{\circ}\text{C}$ are presented in Fig. 2. The upper curve corresponds to a higher condenser cooling temperature. The graph shows that the reduction of the condenser cooling temperature from 40 to 20°C leads to the LHP vapor temperature decrease by 20°C in the region of relatively high heat loads. However, in the region of low heat loads this decrease is equal only to $10\text{-}15^{\circ}\text{C}$. This is explained by the fact that there is a vapor-liquid interface in the compensation chamber at $T_{\text{cool}}=20^{\circ}\text{C}$ and presence of vapor impedes the decrease of the LHP operating temperature. Therefore, the influence of heat flows into the compensation chamber has a greater effect on the LHP vapor temperature.

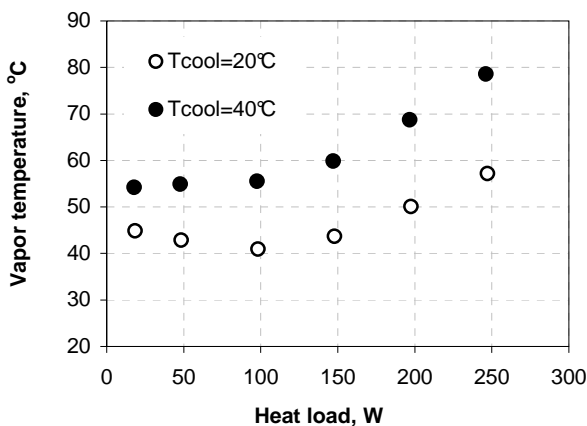


Figure 2. Vapor temperature vs. heat load for different condenser cooling temperature.

3.2 Influence of the wick barrier layer thermal resistance

One of the ways to decrease the LHP operating temperature at the expense of design

modifications in the device is the reduction of heat leaks into the compensation chamber. The value of heat flows into the compensation chamber can be reduced by increasing the thermal resistance of the region of the wick that separates the evaporation zone from the compensation chamber (the wick barrier layer). This can be accomplished by increasing the barrier layer thickness or reducing the thermal conductivity of the material used. However, the influence of these heat leaks on the LHP operating temperature takes place only if the compensation chamber is not completely filled with liquid. When the compensation chamber is filled with liquid, the influence of these heat flows becomes insignificant.

The effect of a barrier layer thickness on an LHP performance was studied in the paper (Wang et al.). The authors investigated start-up characteristics of copper-water LHPs with a flat evaporator having wick barrier layers 3, 5 and 7 mm thick. The experimental results showed that with an increase of the sintered capillary barrier layer thickness, the performance of the LHP becomes better because the heat leaks to the compensation chamber are reduced.

The effect of the thermal conductivity of the wick barrier layer on the operating temperature of a copper-water LHP was studied in this work. Two LHPs with a barrier layer thickness increased up to 18 mm were made for this purpose. The barrier layer of the LHP-2 evaporator was completely made of copper. The evaporator of the LHP-3 had a composite barrier layer which consisted of a copper layer 8 mm thick and an additional titanic

layer 10 mm thick, whose thermal conductivity is almost an order less, than that of a copper wick.

The test results for the LHP-2 and LHP-3 are given in Fig. 3. The graph shows that in the heat load range of 20-200 W reduction of the barrier layer thermal conductivity did not considerably influenced the LHP operating temperature. Slight difference in operating temperatures of LHP-2 and LHP-3 at heat loads over 200 W is explained by minor difference in charge volumes of the devices. Based on the obtained date, it can be concluded that the use of thickened wick barrier layer made it possible to so reduce the heat leaks into the compensation chamber that the effect of its further reduction at the expense of decrease of the barrier layer thermal conductivity was slight.

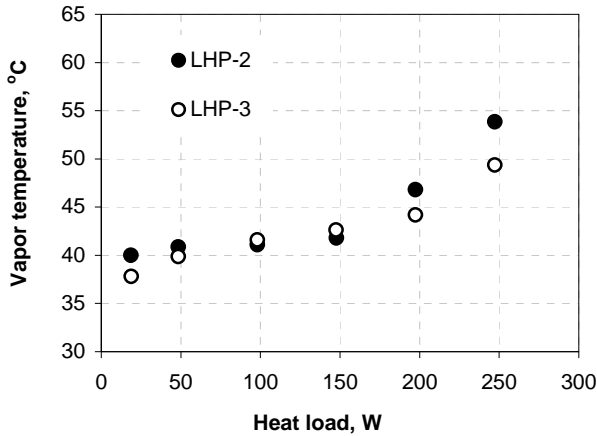


Figure 3. Vapor temperature vs heat load for different wick barrier layer.

3.3 Influence of the LHP charge

Another way of decreasing the LHP vapor temperature is to optimize the charge of a working fluid. With its reduction additional condensation surface area arises in the condenser and the operating vapor temperature decreases. The results of the LHP-5 tests at different charges are shown in Fig. 4. Charge 1 corresponds to its maximum value, charge 4 is minimum. It is seen that the vapor temperature decreases as the charge volume is reduced. This effect becomes more evident with increasing heat load. So, in the range of heat loads from 100 to 150 W the charge volume change from the minimum to the maximum value results in the temperature decrease from 7 to 11°C.

After obtaining a certain charge volume its further reduction causes pulsations of the operating temperature. The charge which minimizes vapor

temperature and provides a stable LHP operation without producing temperature pulsations can be considered as optimum.

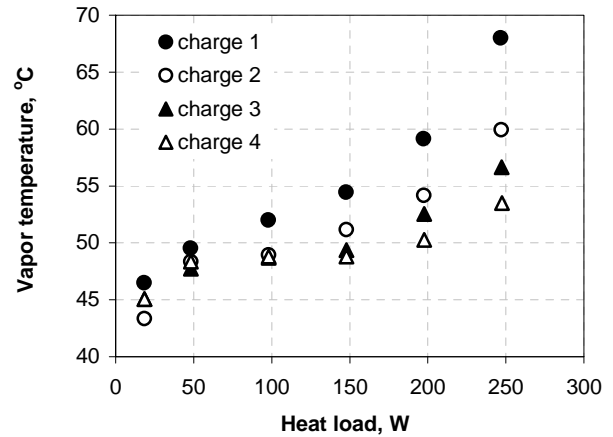


Figure 4. Vapor temperature vs. heat load for different charge of LHP-5.

3.2 Influence of the vapor line diameter

According to (2), the vapor temperature T_v can be decreased by reducing the hydraulic losses during the vapor motion in the vapor line ΔP_{vl} . The value of these losses is determined by the formula:

$$\Delta P_{vl} = \xi \cdot C \cdot \frac{\mu_v}{\rho_v \cdot k} \cdot \frac{2 \cdot L_{vl}}{\pi \cdot d_{vl}^4} \cdot Q \quad (3)$$

where ζ is the friction factor and C is the coefficient of vapor compressibility. The coefficients ζ and C depend on the vapor flow regime, that relies on the Reynolds number. From eq. (3) it is seen that among the factors influencing the value of ΔP_{vl} are the geometrical parameters of the vapor line such as its length and diameter. Between them, the influence of the diameter is more considerable because of the dependence of ΔP_{vl} on d_{vl} ($\Delta P_{vl} \sim d_{vl}^{-4}$), while $\Delta P_{vl} \sim L_{vl}$.

Considering this, tests of LHPs with different diameters of vapor lines were carried out. For this purpose the LHPs numbered 4, 5, 6 and 7 were used; the inner diameters of their vapor lines were 2, 3, 4 and 5 mm, respectively. The experimental results are presented in Fig. 5. It can be seen that the lowest vapor temperature was obtained in the LHP-7, whose vapor line inner diameter was 5 mm. In the range of heat loads of 100-150 W the increase of the vapor line diameter from 2 to 5 mm results in the vapor temperature decrease by 13-15°C. However, it should be underlined that

the increase of the vapor line diameter reduces the LHP compactness and restricts possibilities for its configuring that is necessary for the LHP arrangement in the constrained context of computer servers. In this situation, with this specific length of vapor line, a diameter of 3-4 mm can be considered as optimum because the vapor temperature is within the range of 40-50°C at all heat loads.

In Fig. 5 there is also a theoretical line presenting the results of the vapor temperature calculations for the ideal case when the condenser is completely free of liquid and the pressure losses in the vapor line determined by the third term of the formula (2) are not significant. It is seen that in this case the vapor temperature does not exceed 25°C even at the maximum heat load.

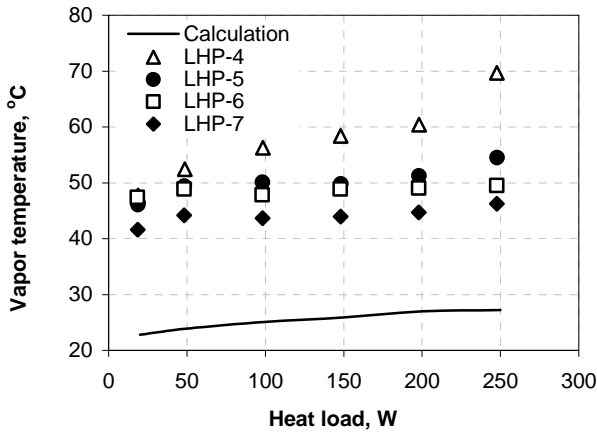


Figure 5. Vapor temperature vs heat load for different vapor line inner diameters.

3.4 Influence of the wick thermal conductivity

The wick thermal conductivity depends on the thermal conductivity of the material from which it is made as well as on its porosity. Its value can be estimated with the help of the Odolevskiy formula:

$$k_{wick} = k_{comp} \cdot \frac{(1-\varepsilon)}{(1+\varepsilon)^b} \quad (4)$$

where ε is the wick porosity and k_{comp} is the thermal conductivity of the compact material. The index b for sintered copper capillary structures is equal to 2.1. According to eq. (4), the thermal conductivity of a copper wick with a porosity $\varepsilon=0.43$ is 105 W/m·K, whereas the wick with a porosity of 0.68 has lower thermal conductivity (42 W/m·K).

The tests results for two LHPs are shown in Fig. 6. The porosity of the LHP-1 wick was 0.68 while the porosity of the LHP-6 wick was 0.43. From the graph it is clear that the vapor temperature of LHP-1, whose wick thermal conductivity is 2.5 times lower than for LHP-6, is lower than the vapor temperature of the LHP-6. Indeed the increase of the barrier layer thermal conductivity promotes the increase of parasitic heat leaks into the compensation chamber. In addition, because of the wick porosity reduction, the surface of evaporating menisci decreases and the heat exchange efficiency in the evaporation zone drops. According to eq. (1), both these processes result in the increase of the compensation chamber temperature and the vapor temperature in the LHP, correspondingly.

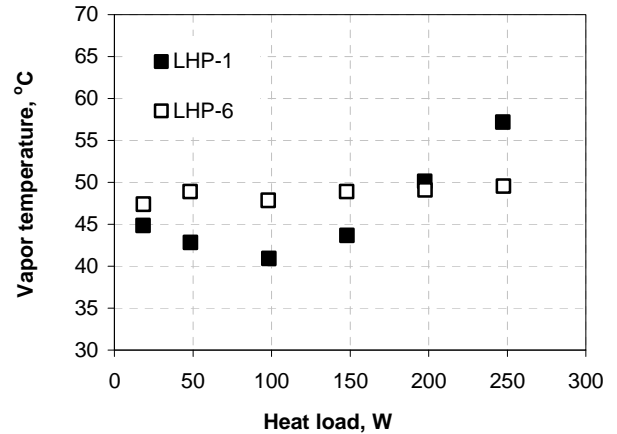


Figure 6. Vapor temperature vs heat load for different wick porosity.

4. CONCLUSIONS

Experimental studies of the influence of different factors on the operating vapor temperature in copper-water LHPs are presented in the paper.

The test results have shown that:

1. A decrease in the operating temperature of the device, particularly in the region of high heat loads, can be reached by a proper optimization of the fluid charge.
2. An increase of the vapor line inner diameter from 2 to 5 mm results in the temperature decrease by 5°C in the region of low heat loads up to 22°C in the region of high heat loads. The vapor temperature in LHPs with a vapor line 3-4 mm in diameter is acceptable because it stays within the range of vapor temperature values of 40-50°C at all heat loads.
3. An increase in thermal resistance of the wick barrier layer leads to a vapor temperature decrease

if there is a vapor-liquid interface in the compensation chamber.

NOMENCLATURE

C – coefficient of vapor compressibility;
ID – inner diameter, m;
L – length, m;
OD – outer diameter, m;
P – pressure, Pa;
Q – heat load, W;
Re – Reynolds number;
T – temperature, °C;
d – diameter, m;
h – heat of evaporation, J/kg;
k – thermal conductivity, W/m·K;
 ε – porosity of wick;
 μ – viscosity, Pa·s;
 ρ – density, kg/m³.
 ζ – constant of friction.

Subscripts

cc – compensation chamber;
comp – compact material;
cool – cooling water;
ev – evaporator;
l – liquid;
v – vapor;
vl – vapor line.

ACKNOWLEDGEMENT

This work was supported by the Russian Foundation for Basic Research, Grant № 11-08-00369-a.

REFERENCES

- Chernysheva M., Vershinin S., Maydanik Yu. (2007) *Operating temperature and distribution of a working fluid in LHP*. Int. Journal of Heat and Mass Transfer, 50(13-14), p. 2704-2713.
- Maydanik Yu.F., Vershinin S.V., Pastukhov V.G., Fried S. (2010). *Loop heat pipes for cooling systems of servers*. IEEE Transactions on Components and Packaging Technologies, 33(2), p. 416-423.
- Maydanik Yu., Vershinin S., Chernysheva M., Yushakova S. (2011). *Investigation of a compact copper-water loop heat pipe with a flat evaporator*. Applied Thermal Engineering, 31(16), p. 3533-3541.
- You S.M., Lee S. (2004). *High-power microelectronics thermal management and packaging fundamentals*. Proc. of the 9th. IEEE Intersociety Conference on Thermal Thermomechanical Phenomena in Electronic Systems, Las Vegas, NV, short course N°1.
- Wang S., Zhang W., Zhang X., Chen J. (2011). *Study on start-up characteristics of loop heat pipe under low-power*. Int. Journal of Heat and Mass Transfer, 54, p. 1002-1007.
- Zimbeck W., Slavik G., Cennato J., Kang S., Yun J., Krolczek E. (2008). *Loop heat pipe technology for cooling computer servers*. Proc. of the 11th. IEEE Conference on Thermal Thermomechanical Phenomena in Electronic Systems, Orlando, FL, p. 19-25.

PERFORMANCE OF AN AMMONIA LOOP HEAT PIPE OPERATING AT TEMPERATURES UP TO 125° C

P. Prado¹, D. Mishkinis, A. Kulakov, A. Radkov, A. Torres
IberEspacio

C/ Magallanes 3 4º, 28015, Madrid, Spain

¹ Phone: (+34) 91 444 1500 (Ext 7535), Fax: (+34) 91 445 17 64, E-mail: ppn@iberespacio.es

T. Tjiptahardja

ESA (ESTEC)

Postbus 299 2200 AG Noordwijk, The Netherlands

A. S. Merino

Thales Alenia Space

100, Boulevard du Midi 06150 - Cannes la Bocca Cedex, France

ABSTRACT

The potential increase of the operational and non-operational temperature limit for spacecraft electronics in the nearest future is demanding heat transfer devices able to operate up to 125° C. In this line, an Elevated Temperature Loop Heat Pipe has been developed. The selection of the LHP materials and working fluid is based on an extensive trade-off which takes into account the compatibility of the materials and working fluid. A dedicated compatibility test and preliminary testing in LHP breadboards have been carried out for the selection of components. The selected LHP prototype consists of titanium and stainless steel envelope, stainless steel wick and ammonia as the working fluid. The extension of the temperature range of the ammonia LHP has been studied by modeling and testing. The LHP has undergone an extensive test campaign including performance in different orientations, maximum power, transient, regulation, start-up tests and thermal cycling. Results of the test campaign show stable operation of the LHP in most operational regimes, with heat transport capability >500W and global thermal conductance >30W/K at 125°C. A simulation model has been developed in EcosimPro and correlated to the test results.

KEY WORDS: Ammonia, Loop Heat Pipe, elevated temperature range

1. INTRODUCTION

Loop Heat Pipes (LHPs) are two-phase capillary pumped heat transfer devices, which are being used more and more often for thermal control in a number of application fields including space and aircraft industries. Current LHP technology for space is based on the use of ammonia as the working fluid. Ammonia is the most efficient working fluid in the temperature range from -30° C to 80° C, and it is compatible with wall materials commonly used in space, such as aluminum and stainless steel. Moreover, it is also compatible with the commonly used wick materials: polyethylene, nickel, titanium and stainless steel.

However, an increase of the operating temperature of the next generation of on-board equipment is expected in the near future. Analysis based on equipment suppliers expertise, indicates that the

maximum expected operating temperature at qualification level can reach +125° C for passive equipments (OMUX, antenna feeds) and +110° C for active equipments (GaN SSPAs, TWT). The increase of the operating temperature of on-board equipment is demanding heat transport devices being able to work in a higher range of temperatures, up to 125° C. An extension of the LHP and radiator technology to temperatures above 100° C will provide the means for an optimized thermal design with reduced radiator areas. Other potential applications have been identified by Mishkinis et al. (2010).

An extensive trade-off on different LHP materials and working fluid combinations was performed (Mishkinis, 2010). The objective of the trade-off was the selection of an optimal LHP design to operate efficiently in an extended temperature range, up to 125° C. Dedicated compatibility test

and preliminary testing in LHP breadboards were carried out for the selection of components.

2. SELECTION OF THE LHP WORKING FLUID AND MATERIALS

2.1 Compatibility Test

The compatibility test set-up consists of set of thermosyphons (which reproduce the characteristics of each potential solution for the elevated temperature LHP) with three main components: wick, envelope and working fluid. These thermosyphons are submerged in a thermostatic bath so that the adiabatic zone of the thermosyphons is regulated $\sim 125^\circ\text{C}$. The heat is removed from the condenser region by convection. The temperature difference increase between the adiabatic zone and the condenser is indicative of the presence of NCG in the pipe. The NCG is indicative of incompatibility of the related working fluids and materials. As a result of the more than three years compatibility test, the following combinations, presented in Table 1, have been found compatible:

Table 1. Compatible combinations.

Fluid	Wick	Envelope
Acetone	SS	SS
Acetone	Ti ¹	Ti
Acetone	Cu	Ti
Acetone	Cu	Monel
Methanol ²	Ti	Ti
Methanol	Cu	Monel
Water	Ti ¹	Ti
Ammonia	Ti	Ti
Ammonia	SS	Ti
Ammonia	SS	SS

The combination Ammonia – SS wick – SS envelope (evaporator) – Ti envelope (transport lines and condenser) was submitted to the testing in a LHP breadboard. Preliminary testing showed stable performance and no degradation was detected. Thus, this combination was selected to undergo the full test campaign described hereafter.

2.2 Elevated Temperature LHP design

Main features of the LHP design are summarized in Table 2.

¹ Titanium purity (>99%) is required.

² Anhydrous methanol can cause stress corrosion cracking of Ti and Ti alloys (Titanium Information Group, 1999).

An overview of the tested prototype is shown in Figure 1.

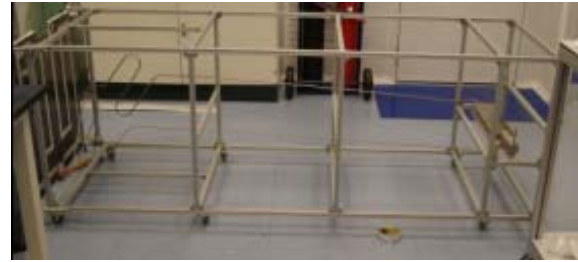


Figure 1. Elevated Temperature LHP prototype.

Table 2. LHP Prototype Main Features.

LHP component	Feature	Value
Evaporator case	Material	SS 316
	OD	24 mm
	Length	0.418 m
Primary Wick	Material	SS 316
	Porosity	0.60
	Pore Diameter	< 2.5 μm
Vapor Line	Material	Ti Grade 2
	Length	3.057 m
	ID	4.6 mm
	OD	6.4 mm
Liquid Line	Material	Ti Grade 2
	Length	3.057 m
	ID	4.6 mm
	OD	6.4 mm
Condenser	Material	Ti Grade 2
	Length	4.506 m
	ID	4.6 mm
	OD	6.4 mm
Radiator (Composite Radiator)	Skin Material	CFRP
	Core Material	Al
	Area	0.7 x 0.7 m ²

The LHP condenser consists of two lines in parallel. A capillary blocker consisting of a T-connector with an internal porous structure, similar to the one described by Dussinger et al. (2009) is implemented to prevent the vapor flow from one to other branches of the condenser and to the liquid line. The titanium lines are connected to the SS components by bimetallic joints.

3. TEST CAMPAIGN

The prototype has been submitted to an extensive test campaign including the tests shown in Table 3. The measurement plan is shown in Figure 2. The evaluation of the LHP performance is based on the assessment of the heat transport capability and the

thermal conductance, in addition to the characteristic parameters of each test (i.e. start-up capability, maximum tilt, maximum static head, etc.).

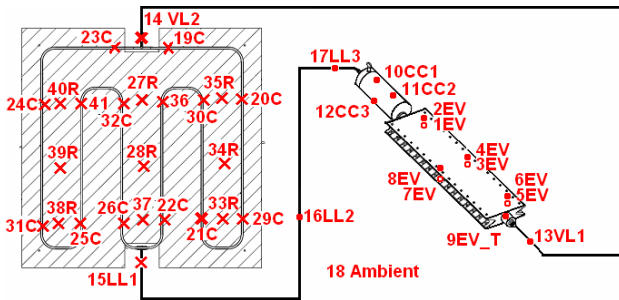


Figure 2. Thermocouples Location.

Table 3. LHP Test Sequence.

Orientation	Test Description / TRP temperature
Horizontal	Performance / 15° C; 50° C; 115° C; 125° C
	Perfo. Qll = 5 W & 20 W / 125° C
	Max Power / 125° C
	Regulation / 125° C
	Transient / 125° C; -30° C (CN)
	Tilt / 125° C
	10 cycles from -40° C to 125° C followed by Performance / 50° C
Start-up / 110° C; -5° C	
Adverse	Performance / 15° C; 50° C; 125° C
Reflux	Performance / 15° C; 50° C; 125° C

The calculation of the LHP conductance is performed considering the temperature at the middle of the evaporator saddle flange width (TRP), the temperature at the vapor line inlet (operation temperature) and the condenser average temperature as a reference.

3.1 Performance in Horizontal

The performance of the LHP has been tested at four temperatures: 15° C, 50° C, 115° C and 125° C. Different power levels have been defined in the test procedure: 50 W, 100 W, 300 W and 500 W. The tests were performed in climatic chamber to minimize the effects of the environment (as a rule, the temperature of the climatic chamber is the LHP operation temperature). The test results show that the LHP is able to transport the power at the four temperature levels without dry-out. The LHP thermal conductance as a function of the input power is shown in Figure 3. The performance test at 125° C is show in Figure 4.

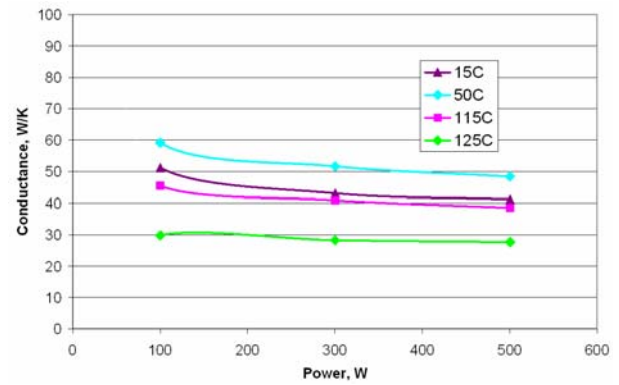


Figure 3. Conductance in Horizontal.

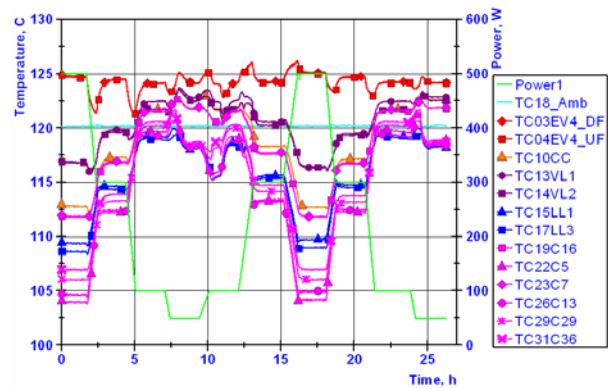


Figure 4. Horizontal, 125° C, Temp. Profile.

3.2 Test with a heat input into the Liquid Line

This test is performed to evaluate the effect of the heat leakages to the liquid line on LHP operation. Two power levels were tested: 5 W and 20 W. The temperature at the TRP was 125° C. No dry-out was observed when applying up to 500 W to the evaporator. The global thermal conductance is decreased for the lowest power steps (<10 W/K, 50 W at evaporator). The additional heat leak in the liquid line requires more sub-cooling. The condenser conductance is reduced to be able to compensate the heat back from the evaporator to the reservoir.

3.3 Maximum Power Test

It is known that ammonia efficiency as working fluid is decreased when the LHP operating temperature is close to ammonia critical temperature. In spite of this decrease, ammonia is still more efficient than other working fluids. According to the testing, the maximum power that the LHP is able to transport at a temperature of 125° C on the TRP, is higher than 800 W.

3.4 Regulation Tests

These tests have been conducted to evaluate the ability of the evaporator temperature regulation with a heater on the compensation chamber. The test results show that the regulation is possible in these conditions, but a significant power input has to be applied to the reservoir (>50 W). High power inputs applied to the reservoir increase the risk of shutting down the LHP. Moreover, the control laws to regulate the evaporator temperature and to prevent large overshoot are complex.

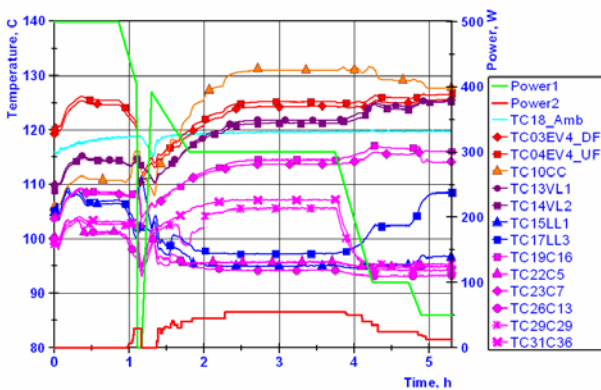


Figure 5. Regulation at 125° C, Temp. Profile.

Other methods such as the regulation by a PRV (Torres et al., 2011) could be an alternative to reduce the mentioned risks during the regulation.

3.5 Transient Tests

The LHP was subjected to transient regimes, with sharp power variations from 50 W to 500 W. Two test conditions were defined: hot case (125° C at the TRP with a power input of 500 W) and cold case (-30° C at the condenser with the lowest power input, 50 W). The tests were performed with and without an additional 5 kg aluminum thermal mass (attached to the evaporator). The LHP is able to sustain sharp power variations without dry-out.

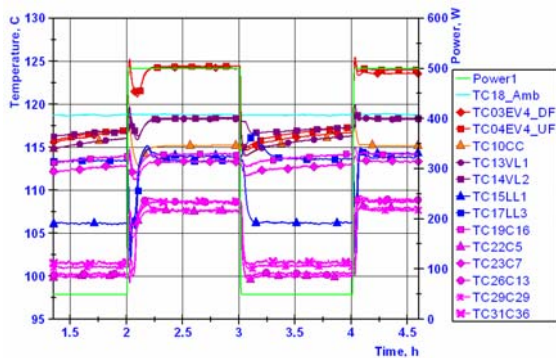


Figure 6. Transient (hot case), Temp. Profile.

3.6 Tilt Tests

The LHP was also tested with different evaporator tilts to evaluate the efficiency of the fluid link provided by the secondary wick. It was observed that the LHP sustained more than 28 mm tilt, the compensation chamber below the evaporator, with 125° C at the TRP and 500 W.

3.7 Thermal Cycling

This test allows assessing if there is any degradation of the LHP performance when sustaining cycles between the mNOT and the MNOT. Ten cycles from -40° C to 125° C were performed. After the thermal cycling, the performance test at 50° C was carried out to compare with previous tests. No degradation of the LHP performances was observed.

3.8 Start-up Tests

The LHP start-up has been tested in hot (initially 115° C at the TRP) and cold (initially -5° C at the TRP) conditions. In both cases, it has been verified that the LHP is able to start-up with less than 50 W applied to the evaporator. The shut-down power is <20 W (applied to the compensation chamber).

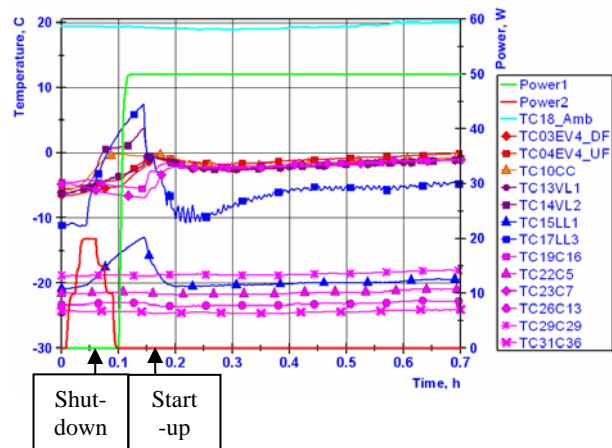


Figure 7. Start-up cold conditions, Temp. Profile.

3.9 Performance in Adverse Elevation

In general, the LHP heat transport capability is reduced due to the gravity forces, which are opposite to the fluid flow. The present LHP was able to sustain 500 W at 125° C with the condenser 1 m below the evaporator. At 50° C and 15° C it was able to sustain the 500 W with the condenser 2 m below the evaporator. The LHP conductance is also reduced, especially at the low power levels. Therefore, the global thermal conductance values

with 2 m of adverse elevation is not higher than 30 W/K (at 50° C and 15° C it achieved 40-50 W/K in horizontal orientation) for the maximum power (500 W). It decreases to 3 W/K for the lowest power (50 W).

3.10 Performance in Reflux

In reflux orientation, the gravity forces assist the flow into the LHP. Therefore, the heat transport capability and the LHP conductance are the same or higher than in horizontal conditions. The tested LHP was able to sustain 500 W at all the three temperature levels (15° C, 50° C and 125° C) with the condenser 2 m above the evaporator. The thermal conductance was the same or better than the conductance in horizontal conditions. It achieves a global thermal conductance ~40 W/K at 125° C for the highest power and ~50 W/K at 50° C and 15° C for 500 W. The most significant increase is noticed for 125° C and 50 W, when the LHP achieves a global conductance of 75 W/K.

4. TMM CORRELATION

In addition to the testing, a TMM model of the LHP was built and correlated to the obtained test results. The software EcosimPro was used to develop the model. An overview of the mathematical formulation used for the modeling can be seen in Gregori et al. (2005).

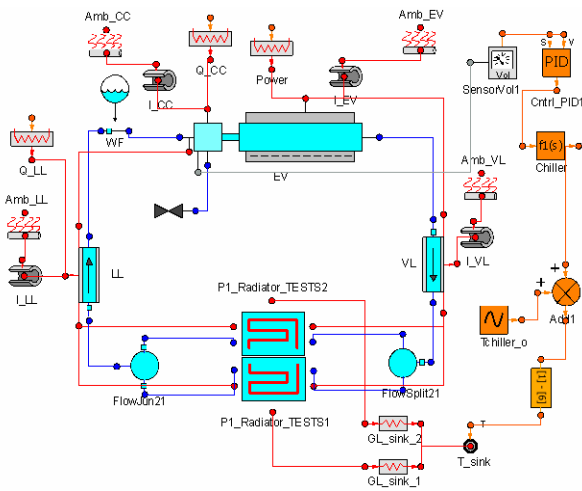


Figure 8. TMM Schematic.

The model is representative of the tested LHP, including the condenser with two parallel lines configuration. The heat exchanges with the environment are included taking into account the temperature of the climatic chamber and the insulation. Some parameters are adjusted to have a

difference in the steady state temperatures lower than ~3° C between the test and the simulation results.

In general, the model is able to predict and reproduce the LHP performance in the different test regimes, as shown in the graphs in Figure 9 and Figure 10.

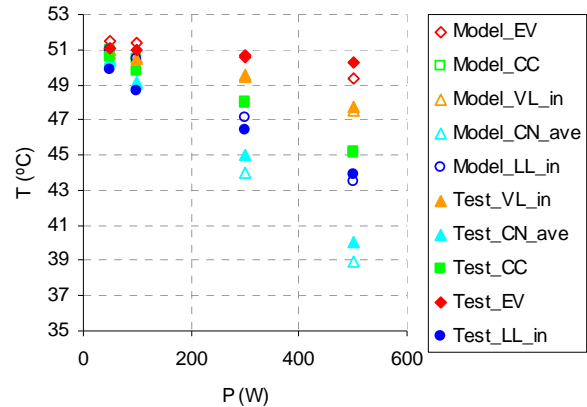


Figure 9. Model correlation, performance 50° C.

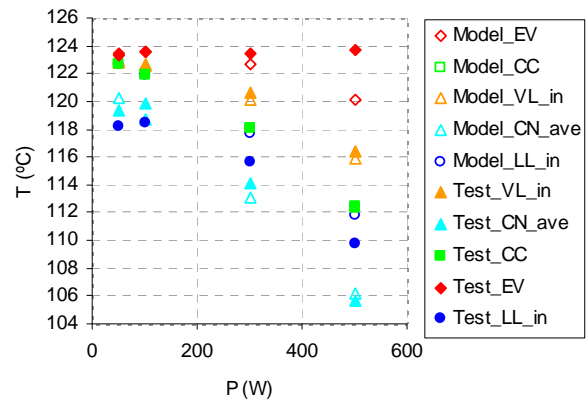


Figure 10. Model correlation, performance 125° C.

5. CONCLUSIONS

A LHP prototype (Ammonia – SS evaporator (wick & case) – Ti lines) has been developed by IberEspacio and extensively tested for an extended temperature range (up to 125° C at the TRP). The LHP prototype demonstrates stable operation and compliant with the requirements for the potential space applications (Mishkinis et al., 2010) in most of the test scenarios.

In the performance tests in horizontal it was observed that the LHP is able to operate at all power regimes in the complete temperature range, including 125° C at the TRP. It operates with high global thermal conductance (>30W/K) and high

evaporator thermal conductance (in general >150W/K). The LHP is able to transport more than 800 W.

Other tests in horizontal configuration were conducted, including performance with heat input to the liquid line, regulation with a heater on the reservoir, transient regimes, tilt and start-up in different conditions. In all the tests the LHP showed proper and stable operation. As far as regulation is concerned, some drawbacks have been found (power need > 50 W, complex control laws and risk of significant overshoot) and alternative regulation methods such as the use of PRV should be studied.

Also, the LHP was tested in adverse and reflux configurations. It showed proper performance in both configurations, being able to sustain 500 W with 125° C at the TRP and 1 m of adverse elevation

Furthermore, the LHP was subjected to thermal cycling. No degradation after 10 cycles between -40° C and +125° C was observed.

In addition to the testing, a simulation model of the LHP has been developed and correlated to reproduce the performance of the real device. The model can predict and reproduce the main characteristics of the LHP performance.

The successful test campaign has demonstrated feasibility of extending of the operational upper limit from +80-90°C (today technology state-of-the-art) to +115-125°C (future needs for space applications) for ammonia LHPs. This approach allows rather quickly re-qualify current ammonia LHP technology for elevated temperatures and gives certain advantages over other alternative solutions with other working fluids (acetone, methanol, water, etc.).

NOMENCLATURE

CC: Compensation Chamber
CFRP: Carbon Fiber Reinforced Plastic
CN: Condenser
EV: Evaporator
ID: Inner Diameter
LHP: Loop Heat Pipe
LL: Liquid Line
mNOT: minimum non operating temperature
MNOT: maximum non operating temperature
NCG: Non Condensable Gas

OD: Outer Diameter
OMUX: Optical Multiplexer
PRV: Pressure Regulating Valve
SS: Stainless Steel
SSPA: Solid State Power Amplifier
TC: Thermocouple
Temp.: Temperature
TMM: Thermo-Mathematical Model
TRP: Temperature Reference Point
TWT: Travelling Wave Tube
VL: Vapor Line

REFERENCES

- Dussinger, P. M., Sarraf, D. B., Anderson, W. G. (2009) *Loop Heat Pipe for TacSat-4*, AIP Conf. Proc. 1103, 91
- Gregori, C., Torres, A., Pérez, R., Kaya, T. (2005) *LHP modeling with EcosimPro and experimental validation*, Proc. 35th Conf. on Environmental Systems, Rome, Italy, SAE Paper 2005-01-2934.
- Torres, A., Mishkinis, D., Kulakov, A., Romera, F., Gregori, C., Kaya, T. (2010) *Thermal Control of Loop Heat Pipe with Pressure Regulating Valve* Heat Pipe Science and Technology, an International Journal, Volume 1/Issue 4, pages 329-357 .
- Mishkinis, D., Prado, P., Sanz, R., Torres, A., Merino, A. S., Tjptahardja, T. (2010) *Loop Heat Pipe for Intermediate Temperature Range: from -40° C to +125° C* Proc. 15th Int. Heat Pipe Conf., Clemson, USA.
- Titanium Information Group (1999), *Titanium and Methanol Data Sheet* No 5 (Issue 3) <http://www.titaniuminfogroup.co.uk/>

HIGH HEAT TRANSPORT CAPILLARY EVAPORATOR DEVELOPMENT FOR LOOP HEAT PIPES

Randeep Singh, Masataka Mochizuki, Kazuhiko Goto, Thang Nguyen, Tien Nguyen, Koichi Mashiko,
Yuji Saito, Vijit Wuttijumnong

Thermal Technology Division, R&D Department, Fujikura Ltd.,

1-5-1, Kiba, Koto-ku, Tokyo 135-8512, Japan

Phone: +81-3-5606-1174, Fax: +81-3-5606-1514,

randeep.singh@jp.fujikura.com, mmotizuk@fujikura.co.jp, kaz_goto@fujikura.co.jp,

thang007@bigpond.net.au, tien2@optusnet.com.au, mashikok@fujikura.co.jp, y_saito@fujikura.co.jp,

vijit@fujikura.com

ABSTRACT

In the present paper, design discussion and development activities on the capillary evaporator with high heat flux transport capability has been presented. Cylindrical evaporator with nickel as high performance capillary pump, copper as high conductivity containment material and water as superior heat transfer working fluid was designed to transport 500 W heat load up to distance of 250 mm. Nickel powder with average particle diameter of 12 μm was sintered at 750 – 1000 $^{\circ}\text{C}$ to obtain soft (750 – 850 $^{\circ}\text{C}$) and hard wicks (850 – 1000 $^{\circ}\text{C}$) with 59% (at 1000 $^{\circ}\text{C}$) to 78% (at 750 $^{\circ}\text{C}$) porosity, $2 - 9 (x 10^{-13}) \text{ m}^2$ permeability and pore radius $< 7.2 \mu\text{m}$. High volumetric shrinkage (4 – 50% @ 750 – 1000 $^{\circ}\text{C}$ respectively) of the sintered wick results in poor control over the sample dimensions which makes wick integration inside evaporator difficult. Special procedures were conducted to develop machined nickel wick with good dimensional control ($\pm 0.15 \text{ mm}$) and high roughness surface morphology, which provide high evaporation area and high surface porosity. These machined wick were successfully integrated inside the evaporator using different methods. In summary, high performance capillary wicks developed in this study can be used to fabricate miniature to large-scale loop heat pipes with high heat flux management capabilities.

KEY WORDS: Loop heat pipe, capillary evaporator, passive pump, porous structure, heat transfer

1. INTRODUCTION

Loop heat pipe (LHP) is the structurally modified version of heat pipe with fine pore wick structure confined inside the evaporator section and separated vapour and liquid flow passages (Singh et al, 2008). Constructively, these structural differences bestow LHPs with superior functionalities as heat transfer device however, these transformations poses number of performance and fabrication challenges in their promotion. At present, LHPs are gaining significant research attention for performance improvement and cost reduction to implement them successfully in the commercial areas of interest. High heat flux handling capability, long distance heat transfer and orientation independent operation are the unique characteristics of loop heat pipe. These are some of the competing application domains for passive loop systems when compared to the conventional heat pipes and electrically operated mechanical pump. Highly developed capillary evaporator with evaporation from inverted meniscus inside fine pore wick and branched system of vapour removal channels provide LHPs with high heat flux management capability. Bare transport lines complemented by

microporous wick gave LHP with long distance heat transfer and orientation independent (against gravity) operation.

Operational characteristics of the loop heat pipe including start-up time, steady state temperature profile within range of applied heat load and component/overall thermal resistance are principally dictated by the loop evaporator design and configuration. Unlike conventional heat pipe, in which evaporator structure, that comprises of wick layer sintered attached to the tube internal surface, has simpler design and structurally identical to the other sections of pipe, the LHP evaporator has much more complicated geometry and structural altogether different from the rest of the loop. In essence, majority of the LHP performance issues are associated with the loop evaporator design considerations and construction. In this paper, structure, sizing and fabrication of the capillary evaporator, particularly the wick, has been discussed in details to address the critical parameters that are vital in LHP system design. Measurement methods to qualify the integrity of the manufacturing techniques has also been presented.

2. LOOP EVAPORATOR DESIGN

Evaporator is the integral part of the loop heat pipe system and structurally most complex component of the loop heat pipe system. By definition, the evaporator assembly includes containment vessel with 1) grooved section for vapour flow (active evaporator section) and 2) bare section for liquid storage (compensation chamber) both separated by 3) fine pore porous structure. Two prime functions of the evaporator are 1) heat load acquisition and 2) pumping working fluid around the loop. There are number of design parameters for the evaporator, as whole, and for its components, individually. In this research work, mainly development on cylindrical evaporator, with 25 mm diameter and 150 mm total length (Figure 1), has been discussed. It should be noted that abovementioned evaporator dimensions were application specific.

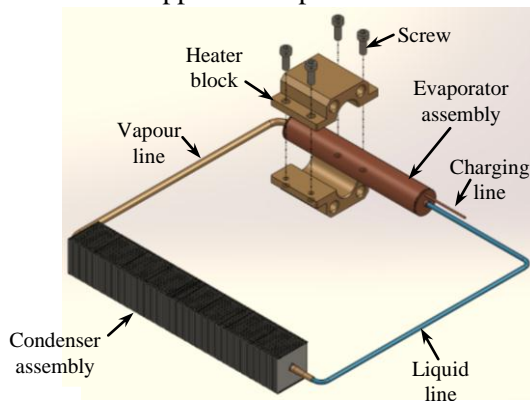


Figure 1. Schematic of Loop Heat Pipe Prototype

3. EVAPORATOR CONTAINMENT

3.1 Evaporator Shape

Two most typical profiles for evaporator are cylindrical and flat shape. The choice of one shape over the other is largely dependent on the heat source footprint and shape, available space constraints, structural/strength requirements, junction thermal resistance considerations and application specific requirements. In most applications, aforesaid factors favours the domination of one profile type over the other. In electronic cooling, heat dissipating semiconductor modules are flat shape with restricted space and requirement for least junction (source to evaporator active surface) thermal resistance therefore flat shape is best. In another instance, for automotive thermal management, thermal footprint is large, space constraints are not as tight however structural strength is important therefore cylindrical evaporator can be favoured over flat evaporator. In general, cylindrical evaporator are easy to seal against leaks (internally from evaporator to compensation chamber and

externally from evaporator to ambient) and are structurally more stronger than flat evaporator (particularly for high pressure working fluids like ammonia). Flat evaporators are very space conservative and generally provide low thermal resistance from source to evaporator surface (unlike cylindrical shape that needs metal interface for attachment with the flat surfaces). Flat disk shape (Singh et al, 2008) is one of optimum evaporator shape that shares some of these advantages for both flat and cylindrical shapes.

3.2 Evaporator Materials

For loop system, evaporator containment material should have high heat conductivity (e.g. copper) to acquire heat with least thermal resistance, good strength to maintain structural integrity and should be compatible with the working fluid. Normally, evaporator material choice is very application specific. For example, for very high temperature ($> 200\text{ }^{\circ}\text{C}$) and rugged applications, stainless steel is preferred container material over copper. Container and wick materials should not possess any galvanic potential (to avoid material depreciation) and should have close thermal expansion coefficient (to minimize interfacial stresses). Copper containment with nickel wick and water as working fluid can be considered as one of the potential material fluid combination for loop heat pipes (Singh et al, 2007). With ammonia, aluminium and stainless steel are compatible materials.

3.3 Evaporator Design

Evaporator, normally referred as evaporator active zone, is the portion of the loop heat pipe where actual heat is applied, phase change from liquid to vapour takes place; and vapour are collected and exhausted to the vapour line. Evaporator design should consider containment structure, internal system of vapour flow channels and any captive hardware, if needed, to mount evaporator body to the heat source. For containment structure, strength is the main design requirements which depends on the application (simple or rugged), working fluid (low or high operating pressure) and therefore dictates the evaporator wall thickness. The system of vapour removal channels (or evaporator grooved portion) must address 1) proper heat conduction path from wall to wick structure and 2) lower pressure drop for the vapour phase, which are optimized on the basis of the evaporator containment thermal conductivity and wick pumping capability respectively. As a general rule of thumb, flow channel can consider 50% void

fraction i.e. 50% area for vapour flow and 50% for heat flow. This factor can be relaxed or tightened depending on the containment heat conductivity and working fluid surface tension at operating temperatures.

4. COMPENSATION CHAMBER

Generally, compensation chamber (or liquid reservoir) adds to the length of the cylindrical evaporator or thickness of the flat evaporator. The material and shape of the chamber is dictated by the evaporator containment design. In particular, the chamber sizing (or total volume) is an important design parameter and effects the overall thermohydraulics of the loop system. Factors that effects the chamber size are loop internal volume (excluding chamber volume), loop operational orientation (horizontal, top heat or bottom heat mode) and expected temperature response with heat load (variable or constant conductance). A point of optimization between these factors should be based on fact that chamber size should provide continuous wick hydration (in operational as well as cold state) and should be able to accommodate any displaced liquid from loop (particularly during start-up and transient states). Here, as general rule, chamber can be size same as loop internal volume however depending on the operational orientation that size can be altered. For top heat mode, loop liquid inventory is generally large, to gurantee wick hydration, therefore chamber size should be large enough to perform its intended displaced liquid containment function. For bottom heat mode, chamber can be relatively undersized due to low liquid charge and high filling probability of evaporator at all times. To provide variable conductance (or self regulating characteristic) to LHP, i.e. constant source temperature with changing heat load, chamber size should be oversized.

5. WICK STRUCTURE

Wick is the heart of the loop heat pipe that provides necessary capillary pumping of the working fluid around the loop. Additionally, wick should help to minimise heat leaks from evaporation zone to liquid reservoir or compensation chamber (heat barrier), separate liquid and vapour phases inside the evaporator (internal sealing) and spread liquid in the evaporator active or heated zone for evaporation (liquid distribution). In order to satisfy these roles, the wick structure should possess appropriate physical properties: 1) Fine pore size: To generate

capillary pressure greater than or equal to the total pressure loss by fluid around the loop at maximum heat load, 2) High porosity: For effective wick hydration and lower effective thermal conductivity of liquid saturated wick (to reduces heat leaks from active zone to liquid reservoir), 3) High permeability: To reduce pressure drop of fluid while filtering through the wick, 4) Low effective thermal conductivity: To reduce heat leak from evaporation zone to compensation chamber and 5) Small geometrical tolerance: To establish good thermal contact between wick and vapour flow passages and to provide internal sealing or separation of liquid phase (on compensation chamber side) and vapour phase (on vapour removal channel side). In order to transfer 500 W heat load up to distance of 250 mm, in horizontal orientation, cylindrical wick structure, as shown in Figure 2, with dimensions for active zone $\phi 18$ mm, thickness 4 mm & total wick length of 100 mm, and with mean pore radius $< 12 \mu\text{m}$, porosity $> 50\%$ and permeability $> 10^{-13} \text{ m}^2$ should be installed inside the loop evaporator.

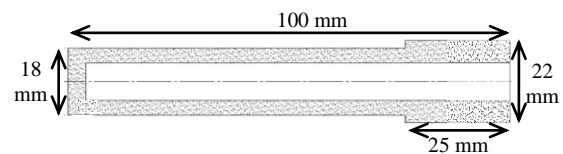


Figure 2. Cross section of cylindrical wick

5.1 Wick Development

In order to develop porous structure with required geometrical dimensions and physical properties, four types of highly pure ($> 99.5\%$) nickel powder that differ in powder size and shape were considered for sintering experiment (Vijit et al, 2012). Nickel has been considered as wick material for LHP due to its 1) lower thermal conductivity (to avoid heat leaks) 2) sinterable with high porosity and fine pore size and 3) availability in high assay level at reasonable cost and in different powder sizes. Creteria for optimization was to achieve best combination of porosity, permeability, pore size, shrinkage and strength for sintered wick so as to qualify the wick as efficient passive pump for designed loop heat pipe. Measurement techniques for porosity (soaking method), pore radius (U-tube bubble point method) and permeability (Darcy's law) are detailed in reference (Singh et al, 2009). On the basis of the sintering runs, 750 – 1000 °C temperature and one hour time period was chosen as optimum sintering conditions. The lower end of temperature range provides higher porosity, higher permeability and

lower volumetric shrinkage whereas the upper end provides higher strength and finer pore size. Based on the measured porosity and volumetric shrinkage, powder with 12 μm average particle size was chosen as best powder which has irregular chain like structure with large surface area for material diffusion during sintering process thereby providing high porosity but at the expense of larger volumetric shrinkage (Vijit et al, 2012). In Figure 4, variation of porosity and volumetric shrinkage with sintering temperature for wick made from chosen powder has been presented. Within the sintering temperature range (650 to 1000 $^{\circ}\text{C}$), it is evident from the graphs that porosity reduces from 78 to 59% and shrinkage increases from 4 to 50% with temperature rise. Here, the incentives of using higher sintering temperatures is to gain high wick strength with reasonable porosity.

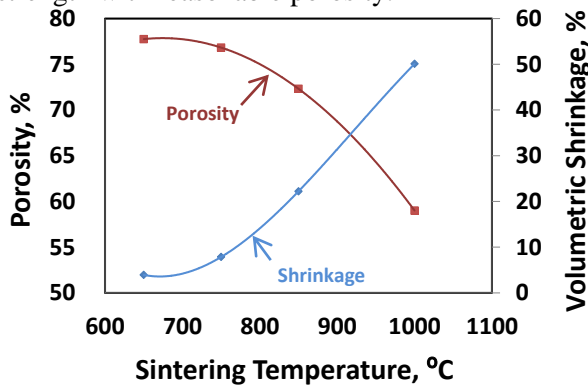


Figure 4. Dependence of wick porosity & shrinkage on temperature

For wicks sintered at 750 $^{\circ}\text{C}$, specific permeability was measured to be within 2 to 9 ($\times 10^{-13}$) m^2 range and largest pore size was below 7.2 μm . At higher sintering temperature, permeability as well pore size will reduce whereas strength will increase due to volumetric compaction. It is worth noting that for loop heat pipes, the largest pore size in the given wick sample is very significant parameter because the back flow of vapour from the evaporation zone to compensation chamber will commence through the pore with maximum radius owing to inverse dependence of capillary pressure on pore radius. It should be noted that expected wick strength is very much application dependent e.g. for electronic cooling low strength can be acceptable, however, for automotive application high strength will be a necessity. In these experiments, compressive stress tests were conducted on wick structures sintered at different temperatures to establish their strength characteristics. The test sample consists of 15 mm cylindrical section of wick with uniform diameter on which compressive stress was applied in radial

direction, using load arm with constant speed, until the sample yields. It was observed that the wick strength is direct dependent and linear function of the sintering temperature. For 750 $^{\circ}\text{C}$, the yield load was as low as 5 kg whereas at 1000 $^{\circ}\text{C}$ the wick load taking capability increases to more than 45 kg. Wick strength should be decided by two prime factors that includes 1) wick integration method inside evaporator tube and 2) application specific requirements. In summary, the wick samples, developed as part of this research investigation, exhibited appropriate physical properties to qualifying it as high performance capillary pump for loop heat pipe.

5.2 Wick Integration

Wick integration inside the evaporator tube is one of the most critical step in the proper integrity of the loop heat pipe system. Two functions that wick integration process should guarantee are 1) good thermal contact between the wick and vapour channels and 2) good internal sealing between evaporation zone (vapour side) and compensation chamber (liquid side). In the sintered product, wick diametric shrinkage was the highest and the wick diameter is the most critical dimensions in the proper integration of wick into evaporator container. Figure 5 plots the diametric profile along the length of the wick at different sintering temperatures. It is observed from the graph that volumetric shrinkage reduces the wick diameter below the required value of 18 mm at active zone and 22 mm at sealing portion.

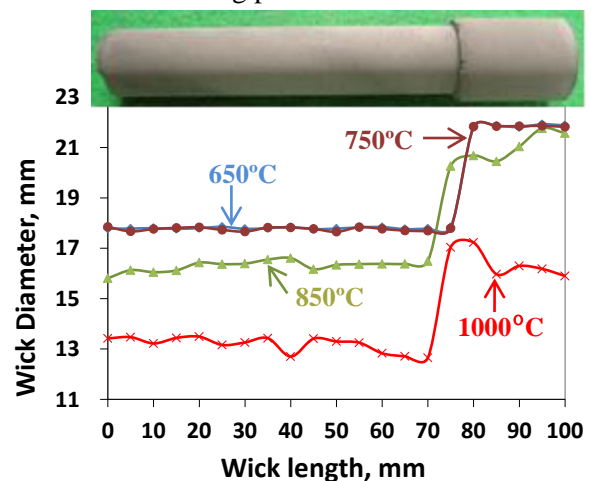


Figure 5. Diametric variation of sintered wick at different temperatures

To address this issue, two new carbon moulds with 10% and 20% oversize as compared to the original mould, which has dimensions conforming to actual wick geometry, were designed. In this case, the 10% oversize was based on the diametric

shrinkage at 1000 °C (force fit type wick) and 20% oversize consider diameter shrinkage at 1000 °C with definite machining tolerance (machined type wick). Wick structures sintered from these large moulds were able to provide force fit tolerance of ~ +0.1 to 0.7 mm (with 10% oversize) and machining tolerance of +1 to 3 mm (with 20% oversize). The variability in tolerance was controllable by sintering temperature and time with largest tolerance at 950 °C and 20 minute heating time. Two important attributes that the wick must possess for successful integration includes 1) uniform diameter (for proper thermal contact with vapour channels) and 2) good straightness (for successful insertion process). Here, straight wick will be easy to insert inside the containment tube and will provide proper alignment between 1) wick active length and evaporator grooved portion and 2) wick sealing portion and evaporator ungrooved portion. It should be noted that force fitting of sintered wick with positive tolerance was possible however owing to the unequal shrinkage there was larger waviness along the wick length (Figure 5) that might 1) damage the grooved portion of evaporator tube and 2) provide unequal thermal contact between the wick evaporating face and the vapour removal channels. Nonetheless, this technique, using direct force fitting of sintered wick inside evaporator tube, is viable for soft wick which were obtained at lower sintering temperatures (750 to 850 °C) and with 10% oversize mould. Owing to the fact that 1) soft wick structure can be easily force fitted without damaging grooved portion of tube and 2) lengthwise straightness of soft wick was better than high temperature hard wick. The applicability of this method is limited to stationary applications with lower wick strength requirements e.g. desktop computer, datacenter cooling. The second integration method utilises hard wick, obtained at high sintering temperature (850 – 1000 °C) and with 20% oversize mould, that is machined to obtain highly straight lengthwise profile (uniform diameter) of wick to install inside the evaporator tube. Two types of machining method used include 1) high speed lathe machining using sharp tool and 2) centerless machining that consists of two grinding wheels rotating in opposite direction with work piece placed between them. Sintered nickel is a very brittle material and therefore the incidence of wick breakage under machining load was very high (1 in 3 samples). To address this issue, a center stainless steel rod support was used inside the wick core to provide additional wick strength and material removal rate was decreased to reduce tool loading.

Out of two methods, lathe machining presented better results with good surface morphology and low sample breakage incidence rate. Figure 6 shows the diameter profile along the length of the nickel wick before and after the machining process. It is clear that the machining process improved the straightness of the wick dramatically.

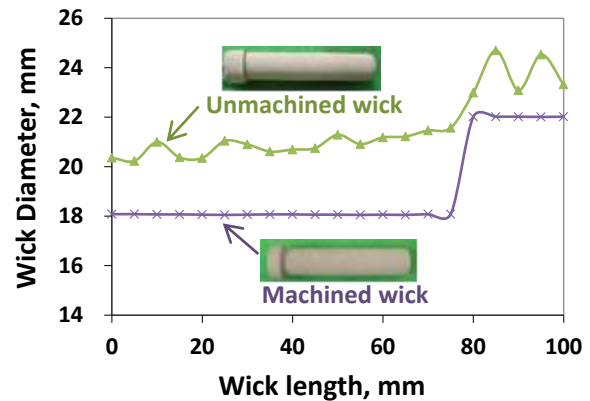


Figure 6. Diametric profile of the sintered wick before and after machining process

Machined wicks were measured to have diametric and straightness control within ± 0.15 mm and ± 0.075 mm respectively. Nickel wick due to its brittle nature was easily machined without affecting the surface porosity of the sample. In Figure 7, SEM surface morphology of wick exposed face before and after machining clearly shows that pore structure and surface porosity remains intact. Nickel particles on the machined surface, as seen in Figure 7, will not have any effect on the functionalities of the porous structure.

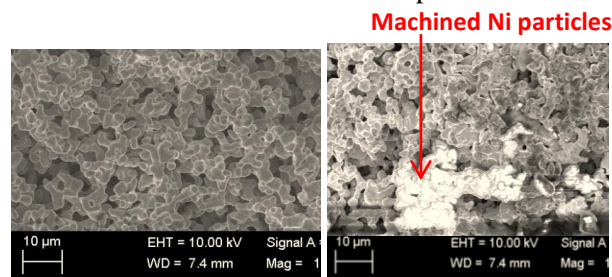


Figure 7. SEM profile of sintered wick before (left) and after (right) machining process

This was confirmed by conducting the wettability test using pure water throughout the stretch of the machined face. It was observed that the machined face exhibited a better wettability response than the unmachined surface. On close observation and quantitative test, it was established that machining increases the surface roughness of the wick. For the machined face, the average surface roughness increases by 4 times, which will provide twofold advantages: 1) increase evaporation surface area 2) improve wick surface wettability. It should be

noted that unmachined sintered wick outer (diametric) face has low roughness (low porosity) due to close proximity of exposed face to the sintering mould that results in higher temperature (and thus material diffusion) of the face. For wick insertion inside the evaporator tube, different technique that includes evaporator tube thermal expansion, cryogenic wick shrinkage or force fitting of tapered machined wick can be employed. The chosen method should guarantee good contact between wick external surface and evaporator tube interior. Figure 8 shows the wick successfully integrated inside the evaporator tube. Also, in Figure 8, snapshot of the integrated wick after extraction from tube shows contact footprint of the channel portion which validate superior wick-tube contact. To establish proper internal sealing between evaporator and compensation chamber, capillarity test or appropriate sealing inspection tests should be conducted on wick integrated evaporator.

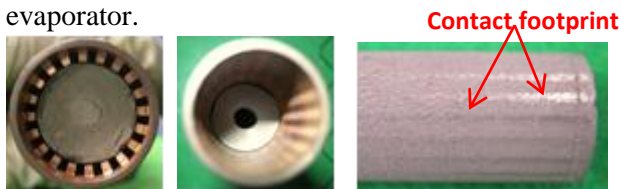


Figure 8. Wick integrated inside evaporator (vapour side (left), liquid reservoir side (center), visual view after wick extraction showing contact footprint (right))

As an example, Figure 9 presents the thermal characteristics of the loop heat pipe with designed material-fluid combination i.e. nickel wick, copper containment and water as the working fluid. The loop heat pipe design include flat disk evaporator (Singh et al, 2007), wick structure with flow properties as discussed above, chamber size equal to loop volume and charged with liquid inventory equal to ~ 60% of loop total internal volume.

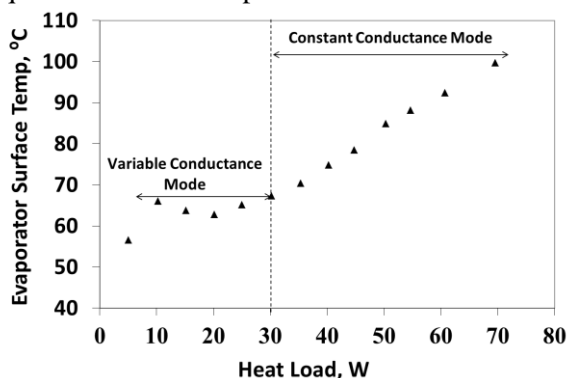


Figure 9. Evaporator temperature versus heat load characteristics for copper water LHP with nickel wick
It is observed from graph that the loop presented variable conductance mode for input power less than 30 W whereas for higher heat load constant

conductance mode was realized. At maximum heat flux of $\sim 18 \text{ W/cm}^2$ (70 W), minimum LHP thermal resistance (evaporator to condenser surface) of $0.17 \text{ }^\circ\text{C/W}$ was achieved with evaporator temperature maintained at $99.6 \text{ }^\circ\text{C}$. The present investigation validates the nickel wick as superior capillary pump for loop heat pipe with copper containment and water as working fluid.

6. CONCLUSIONS

In summary, the present paper addresses the design and development of the cylindrical evaporator for LHP with high heat transport capacity. The capillary evaporator, with 150 mm length and 25 mm diameter, utilises nickel wick, copper containment and water as working fluid. Nickel wicks as passive pumps with 59 – 78% porosity, 2 to 9 ($\times 10^{-13}$) m^2 permeability and pore size $< 7.2 \text{ } \mu\text{m}$ were sintered at $750 - 1000 \text{ }^\circ\text{C}$ with variable strength (5 to 45 kg compressive load over 15 mm cylindrical section). High strength porous samples (sintered at $850 - 1000 \text{ }^\circ\text{C}$) were machined to obtain wicks with good surface porosity, good diametric ($\pm 0.15 \text{ mm}$) and straightness control ($\pm 0.075 \text{ mm}$) that were successfully integrated inside the partially grooved evaporator tube. As an outcomes of this research investigation, sintered nickel wick structures with superior thermal and hydraulic characteristics will help to develop capillary evaporators with high heat flux transport capability.

REFERENCES

- Singh, R., Akbarzadeh, A., Mochizuki, M., (2008), *Operational characteristics of a miniature loop heat pipe with flat evaporator*, Int J Therm Sci, 47(11), pp. 1504-1515
- Singh, R., Akbarzadeh, A., Dixon, C., Mochizuki, M., (2007), *Novel Design of a Miniature Loop Heat Pipe Evaporator for Electronic Cooling*, J. Heat Transfer, 129(10), pp. 1445-1452.
- Wuttijumnong, V., Singh, R., Mochizuki, M., Goto, K., Nguyen, T., Nguyen, Ti., Mashiko, K., High-Performance Nickel Wick Development for Loop Heat Pipes, (2012), Proc. 28th IEEE SEMI-THERM Symp., CA, USA, March 18-22, 2012
- Singh, R., Akbarzadeh, A., Mochizuki, M., (2009), *Experimental Determination of Wick Properties for Loop Heat Pipe Applications*, (2009), J Porous Mat, 12(8), pp. 759 – 776.
- Singh, R., Akbarzadeh, A., Dixon, C., Mochizuki, M., Riehl, R.R., (2007), *Miniature Loop Heat Pipe with Flat Evaporator for Cooling Computer CPUs*, IEEE T Compon Pack T, 30(1), pp. 42 – 49

A HIGH POWER DENSITY AND LOW WATER CONTENT HEAT PIPE NATURAL CONVECTION HEAT EXCHANGER FOR DOMESTIC HEATING APPLICATION

K. Kerrigan, G.E. O'Donnell, H. Jouhara, A. J. Robinson*

Department of Mechanical & Manufacturing Engineering, Trinity College Dublin, Ireland

*+353 85 156 3366 (ph), +353 1 679 5554 (fax) arobins@tcd.ie

ABSTRACT

The introduction of geothermal renewable energy sources such as geothermal heat pumps into domestic central heating systems will demand that new technologies be developed to dissipate the required heat loads into homes. The main reason for this is the lower operating temperatures associated with these energy sources, which can be as low as 35°C and rarely exceed 55°C. Unless the appropriate heat exchanger is deployed, expensive and intrusive alternatives such as forced air convectors, under floor heating and home insulation retrofitting must be considered. This work details the development of a turn-key heat pipe based naturally aspirated convector for domestic central heating applications. The results show that the heat pipe convector design has a power density of nearly 3 times that of a popular off the shelf panel radiator. Furthermore, the low water content associated with the heat pipes results in a unit with a much reduced thermal response time.

KEY WORDS: Heat pipe, domestic heating, natural convection

1. INTRODUCTION

Energy conservation is an important part of national energy strategies, whose growth in importance will continue into the future. This is due to the significant, if not crucial, role played by energy in the social and economical development of societies (Kaynakli, 2008). Geothermal heat pumps (GHP) have become a popular choice for people building new homes and retrofitting old ones to ensure that renewable energy is acquired efficiently and cost effectively. GHPs operate by using the ground around a building as the heat source, or in some cases the ambient air. By installing a suitably sized GHP loop in the ground or in the air, heat energy can be taken from a low-temperature source and upgraded to a higher temperature at which it can be usefully employed for domestic heating purposes (Ochsner, 2007).

The conventional household hydronic-based radiator design has changed very little over the last hundred years. In these types of units the hot source water flow is channeled within the radiator housing. The hot fluid spreads across and heats a large enough internal surface area within the device that sufficient heat can be dissipated into the room air passively by buoyant natural convection and radiation. Newer devices operate on the same principle, though may include external fins to decrease the overall size and weight of the units.

With regards to the heat transfer, the main drawbacks of having the hot water flowing within a large internal volume are that the velocities are quite low causing a non-negligible thermal resistance on the water-side and the flow can be poorly distributed causing stagnation zones and large temperature variations across the radiator (see Fig. 1). Further to this the heat transfer is negatively influenced by the height of traditional radiators, which are typically well in excess of 50 cm. For panel radiators with rear vertically aligned fins, this height is longer than the length required for the thermal boundary layers on each opposing wall of the channel to merge. As a result, beyond this point the local driving temperature differential for heat transfer continually decreases which is not ideal from a convective heat exchanger design standpoint.

Conventional radiators are not ideal for use in GHP domestic heating applications because of the low source water temperatures generated, which are generally lower than 55°C. Their power densities are typically so low that oversized radiators would be required. A standard panel radiator output is given in Fig. 1. The unit is rated at 750W for an operating temperature of 80°C, though is found to underperform somewhat. At an inlet water temperature of 55°C, which is rather high for a GHP, the output reduces to ~300W meaning that two radiators would be required to perform the

equivalent task which negatively influences cost and occupies more space within the room. Preferable options for low temperature GHPs are enhanced building insulation, under floor heating systems or fan-based forced convection heat exchangers. In terms of retrofitting existing buildings neither the re-insulating nor the under floor heating options are attractive due to the large added cost and disruptive nature of the installation (Rawling, 2004). Fan-based convectors are beginning to hit the market for this application though retrofitting for electrical connections at water points, fan noise and long term reliability are an ongoing concern for retrofit domestic applications.

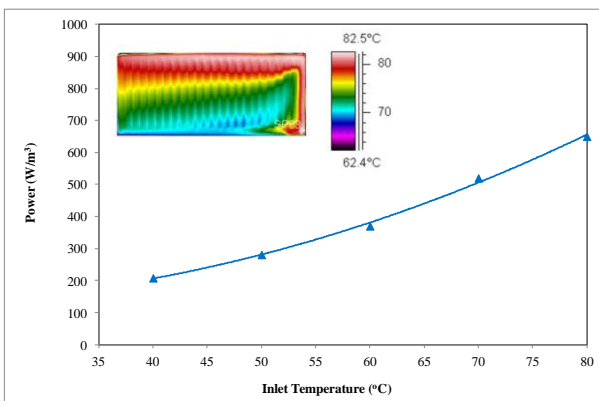


Figure 1. Heat transfer and temperature distribution of a popular panel radiator.

Heat pipe technology has a proven track record in space technology (Savage, 1969, Swanson & Birur, 2003), thermal storage (Caruso et al., 1989, Zalba, 2003), harnessing of renewable energy (Mathioulakis & Belessiotis, 2002, Sodha & Bansal, 1986) and in waste heat recovery of various processes (Vasiliev, 1989, Sun et al., 2002). As in domestic air conditioning systems, its advantages and economics are proven (Jouhara, 2009) with an expanding number of applications which utilize such technology to ensure that heat energy is transferred effectively (Noie, 2005, Dunn & Reay, 1994).

The primary objective of this research is to design, construct and test a naturally aspirated heat pipe based radiator prototype that would be suitable for GHP retrofit installations. The overarching objective is to construct a prototype technology that mitigates the need for expensive and disruptive building retrofits, such as re-insulating the home and/or installing under floor heating. Specifically the objective is to reach a heat transfer rate of 750 W at an inlet water temperature of 55°C

and do so in a much reduced space compared with conventional panel radiators.

2. DESIGN AND MANUFACTURE

2.1 Design Concept

The design concept of the heat pipe-based radiator is given in Fig. 1. The heat exchanger is comprised of two naturally aspirated air side tube bundles whose fins are heated by being in thermal contact with the condenser ends of six heat pipes (per side). The heat pipes are press fit to the aluminum fins in a staggered arrangement. In order to increase the heat transfer per channel the fins were wavy, as depicted in Fig. 3.

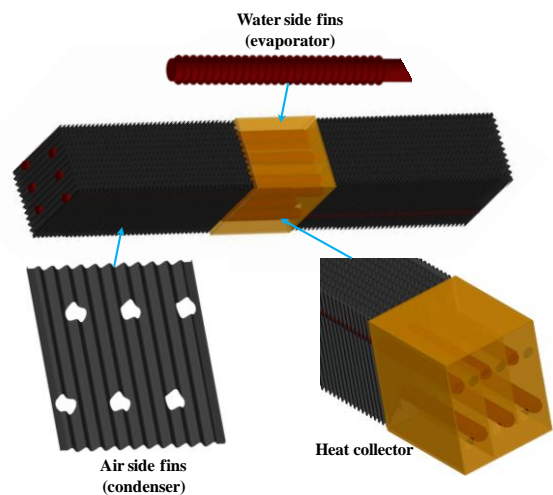


Figure 2. Heat pipe prototype design.

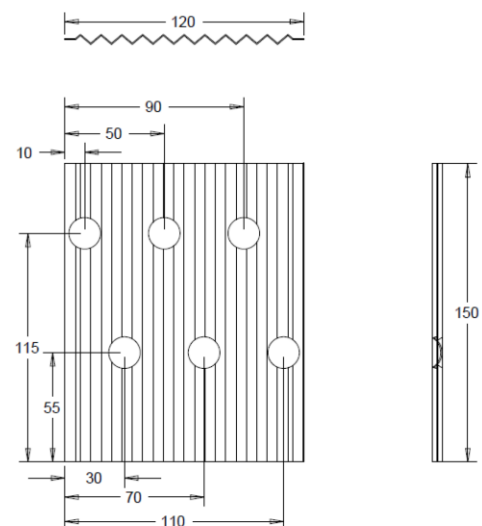


Figure 3. Aluminum wavy fin design.

Heat is absorbed into the heat pipes at a centrally located hot water manifold. The evaporator ends are immersed in the flow of hot water which is

routed through a serpentine channel to increase the water side heat transfer coefficient. The heat pipe evaporator ends are fitted with annular copper fins and are arranged in a cross flow arrangement with four heat pipes per channel (two per side).

2.2 Simulation Driven Design

Simulation Driven Design was used to determine the geometric aspects of the fins and channels within which the air flows. The commercial CFD package CFX was utilized to model a half of a single 3D channel and various arrangements (heat pipe spacing, channel width etc.) were simulated until enough heat was transferred per channel that the overall size of the heat exchanger was acceptable. The main geometric constraint was that the fin width could not exceed 12 cm (Fig. 3) since this is a wall mounted device and this is considered by industry to be an acceptable intrusion into the room.

For a given scenario the CFD model involved applying a constant temperature on the cylindrical heat pipe segments within the channels as well as at the circular interface where the heat pipes connect with the fins. Room temperature air is assumed at a given distance from the periphery of the fins. Within the fins the heat equation is solved in order to get a sense of the fin efficiency dependence on the heat pipe size and spacing. Within the air the full Navier-Stokes equations were solved implementing the Boussinesq approximation. More detail with regard to the simulation strategy can be found in Kerrigan et al. (2011).

Figure 4 shows a sample result of the simulation for a heat pipe temperature of 50°C. The top figure shows the temperature distribution within the fin and shows that for this configuration it is very uniform and thus the fin efficiency is very high. The bottom figure shows the predicted air velocity distribution at the mid plane within the channel. The figure indicates slight blockage in the centre of the tube bundle though this was anticipated. However, this staggered tube arrangement was found to be adequate and significantly better than a fully in-line arrangement.

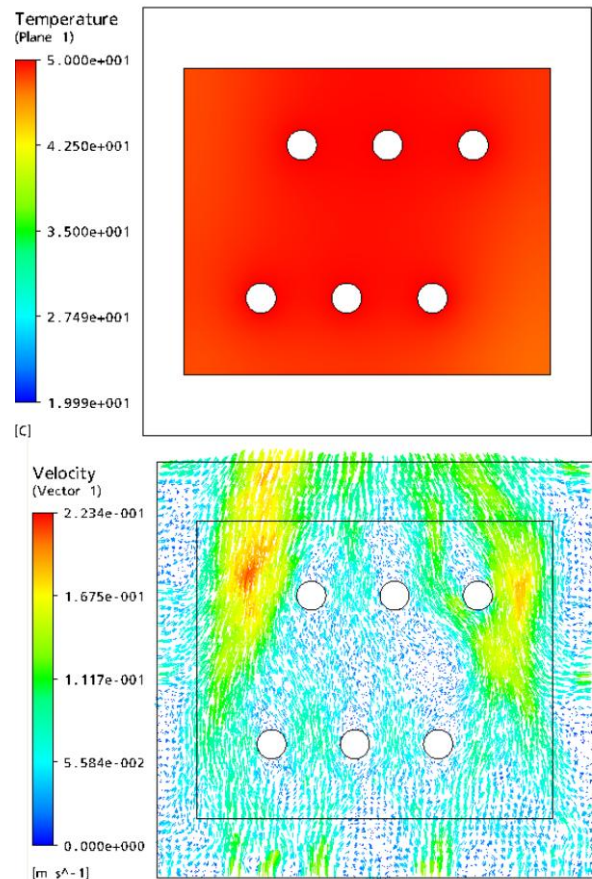


Figure 4. CFD simulation of a single channel. (Top) Temperature distribution within a fin, (Bottom) Air velocity distribution at the channel mid plane.

A prototype heat pipe radiator was fabricated in-house and is shown in Fig. 6. The convector consists of 12 1.6 cm diameter water charged heat pipes. The heat pipes were designed so that each could transport over 100 W in the horizontal orientation without reaching the capillary limit. To achieve this, the interior of the heat pipes are lined with 3 wraps of MESH145 copper screen mesh. The evaporator end is 15 cm long and the condenser ends are 35 cm long, each fitted with 12 cm x 15 cm aluminium fins of 0.5 mm thickness (Fig. 3). The heat pipes were charged with a small quantity of pure water and subsequently purged of non-condensable gas by boiling off a small quantity of vapour and immediately sealing. Once cooled, this creates a partial vacuum within the heat pipe so that it will operate at low temperatures, in this case around 35°C. The overall volume of the heat exchanger is 0.0176 m³.

3. TEST FACILITY & DATA REDUCTION

A thermal performance test facility was constructed to evaluate the overall performance of the radiator. The main features of the test rig are illustrated in Fig. 5. A circulation pump draws hot water from a storage tank fitted with electrical immersion heaters. The heaters are wired to a control box that regulates the water temperature to a preset value. The volume of flow is controlled by a simple bypass valve and is measured with an in-line flow meter. Flexible hoses are then fixed to the inlet and outlet fitting of the radiator being tested. Calibrated thermocouples are placed in the hot water flow at the inlet and outlet of the radiator.

Fig. 6 shows a thermal image of the heat pipe radiator in operation for an inlet source water temperature of $\sim 55^\circ\text{C}$. The actual temperatures illustrated should not be taken as universally accurate across the entire unit as the surface emissivities of the different materials are quite different (aluminium, copper, brass). What is important to observe is that the heat is spread uniformly from the inner to outer most fins on the finned tube bundles of each arm of the convector: this is a unique characteristic of heat pipes which makes this radiator unique and facilitates such high power densities which will be discussed.

The heat transfer, Q , dissipated by the radiator is related to the volumetric flow rate of the water and the net temperature drop across the radiator unit through the equation:

$$Q = \rho \dot{V} (T_{w,in} - T_{w,out}) \quad (1)$$

where ρ is the water density, \dot{V} is the water volumetric flow rate and $T_{w,in}$ and $T_{w,out}$ are the water inlet and outlet temperatures respectively. The figure of merit for comparing different radiators of different overall volume, V , is related to the measured power density, given by:

$$PD = \frac{Q}{V} \quad (2)$$

for a given water-to-room temperature differential:

$$\Delta T = T_{w,in} - T_{room} \quad (3)$$

where the room temperature, T_{room} , was approximately 20°C for all tests performed.

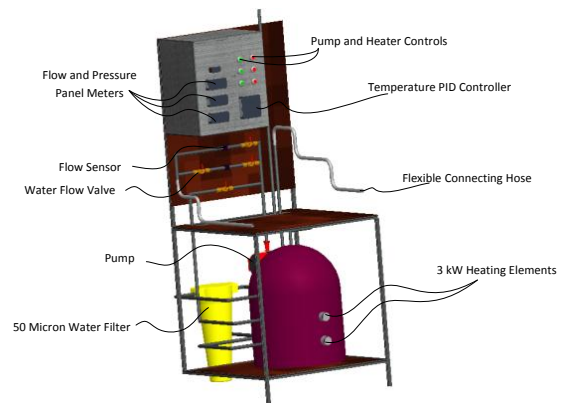
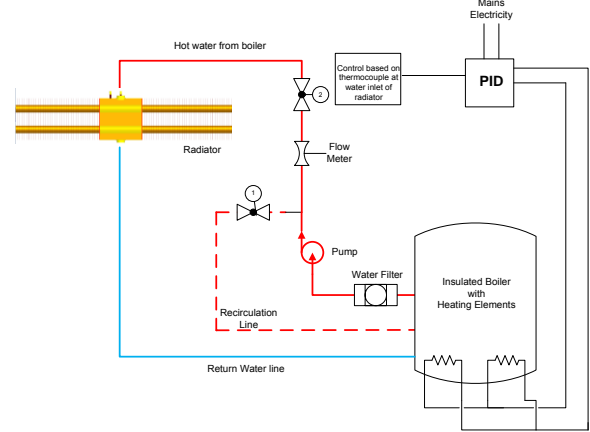


Figure 5. Test facility for thermal performance testing of hydronic radiators.

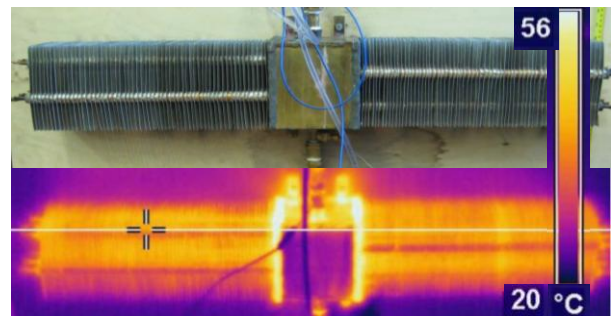


Figure 6. Photograph (top) and thermal image (bottom) of the heat pipe based radiator.

The uncertainty on the heat transfer for a nominal flow rate of 5 L/min, an inlet temperature of 55°C and a power output of ~ 750 W was determined to be better than $\pm 10\%$.

3. RESULTS AND DISCUSSION

Figure 7 shows plots of the thermal performance tests carried out on the prototype heat pipe radiator. The net heat transfer from the heat

exchanger is plotted for different inlet water temperatures and two flow rates, 2.5 L/min and 5 L/min. Also indicated in the figure is the design point to which the unit was designed. The figure shows that the unit under performs by about 100 W at the lower flow rate. At the higher flow rate the design set point is reached as the convective thermal resistance on the water side is lowered.

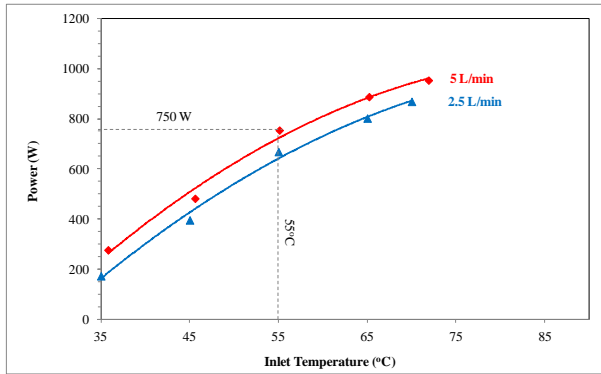


Figure 7. Heat transfer from the heat pipe prototype for different water flow rates and inlet temperatures.

Fig. 8 shows the net thermal output for the heat pipe prototype and a popular commercially available unit of nearly equivalent overall length (<100 cm). The important feature of this comparison plot is that the heat pipe prototype outputs significantly more power (~750 W @55°C) compared with the standard panel radiator (~300 W @55°C), which is a 2.5 fold improvement for nearly the same wall space claim.

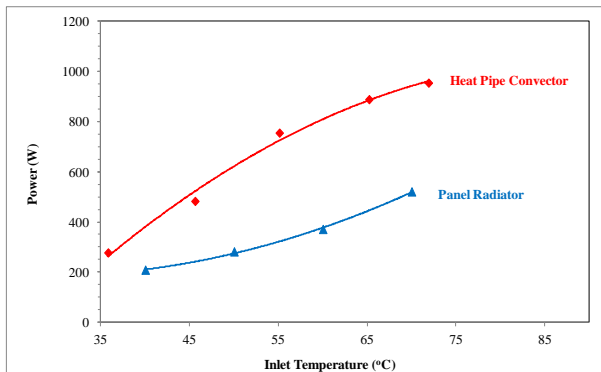


Figure 8. Comparison of the heat transfer from the heat pipe radiator with a popular panel radiator.

A truer performance metric for comparing the thermal performance of the two heat exchangers such as these is the power density, PD, defined in Eq. 2, since it relates the overall power throughput to its overall size or footprint. Both the heat pipe radiator and the panel radiator units were within 13 cm from the wall, including mounting. However,

the overall physical volume of the heat pipe prototype is only 0.0176 m³ whilst the commercially available panel radiator is 0.0208 m³. As a result, the higher heat transfer and the smaller volume of the heat pipe prototype results in it having a significantly higher power density, as depicted in Fig. 9. It is evident that the heat pipe prototype outperforms the panel radiator 2.9 fold at 55°C, which is significant. It is also clear that this level of improvement is observed over the entire range of water inlet temperatures tested, though tends to drop somewhat at the lower temperatures.

As discussed, the large internal volume of panel radiator is required in order that the hot liquid accesses a significant internal surface area, in the sense that the water itself acts as the heat spreader. As a result, the volume of liquid water it contains is relatively large. Also, the panel radiator is constructed of mild steel for cost and built strength considerations. On the other hand, the heat pipe prototype radiator only contains heated water in the manifold, in the sense that the heat dissipating ends of the unit do not contain any notable amount of liquid. This combined with the fact that the finned heat pipe tube bundle is constructed from copper and aluminum, means that the thermal mass of the heat pipe prototype should be much less than the panel radiator.

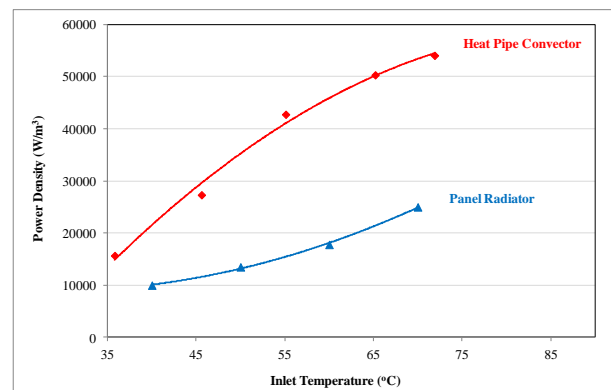


Figure 9. Comparison of the power density of the heat pipe radiator with a popular panel radiator.

To prove this a simple test was performed whereby a valve on the hot water supply was quickly closed and the maximum temperature on each unit was monitored over time with a thermal imaging camera. The results are plotted in Fig. 10. Clearly, the panel radiator with the higher water content responds much slower to fairly abrupt changes in its thermal environment. The low water content heat pipe radiator takes 1.3 minutes to cool by 5°C whilst the panel radiator takes 5 minutes to cool

the same amount. This quicker response characteristic of the heat pipe radiator would be desirable when tight thermostatic control of the room temperature is required.

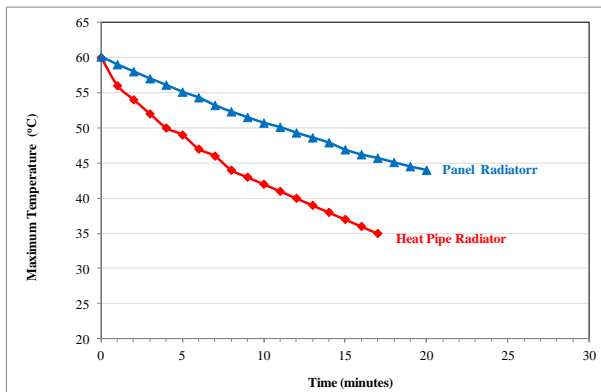


Figure 10. Cooling curves as a result of abruptly stopping the hot water inlet flow.

3. CONCLUSIONS

The prototype heat pipe based double convector radiator has proven the concept that using heat pipes as heat spreaders for effective heat dissipation in domestic applications has many advantage over conventional wet panel radiators, including nearly tripling of the power density and significantly reduced thermal mass for improved controllability. Overall, the heat pipe based naturally aspirated radiator achieved its design goal of 750 W at an inlet water temperature of 55°C and is a possible candidate for turn-key retrofit of traditional panel radiators subsequent to domestic heat pump installations.

ACKNOWLEDGEMENT

We gratefully acknowledge the support from Enterprise Ireland under the grant CFTD -07 -IT -307.

REFERENCES

- Caruso, A., Grakovich, L.P., Pasquetti, R., Vasiliev, L.L., (1989) *Heat Pipe Storage Performance*, Heat Recovery Systems & CHP, 9, p. 407-410.
- Dunn., P., Reay, D. (1994) *Heat Pipes*, 4th ed. New York: Pergamon, 1994.
- Jouhara, H., (2009) *Economic Assessment of the Benefits of Wrap-around Heat Pipes in Ventilation Processes for Hot and Humid Climates*, International Journal of Low Carbon Technology, 9, p. 52-60.

- Kaynakli, O. (2008) *A study on residential heating energy requirements and optimum insulation thickness*, Renewable Energy, 33, p. 1164-1172.
- Kerrigan, K., Robinson, A.J., O'Donnell, G.E., Jouhara, H., (2011) *Heat Pipe Based Radiator for Low Grade Geothermal Energy Conversion in Domestic Space Heating*, Simulation, Modelling, Practice and Theory, 19 (4), p. 1154-1163.
- Mathioulakis E., Belessiotis, V. (2002) *A new Heat-pipe Type Solar Domestic Hot Water System*, Solar Energy, 72, p. 13-20.
- Noie, S.H., (2005) *Heat Transfer Characteristics of a two-phase closed thermosyphon*, Applied Thermal Engineering, 25, p. 495-506.
- Ochsner, K. (2007), *Geothermal Heat Pumps: A guide to planning and installation*. Trowbridge: Cromwell Press.
- Rawling, R. (2004) *Energy Efficiency Best Practice in Housing Domestic Ground Source Heat Pumps: Design and installation of closed-loop systems*, E. S. Trust, Ed.: E&OE.
- Savage, C. J. (1969) *Heat pipes and vapour chambers for satellite thermal balance.*, R. T. R. 69125, Ed., June 1969.
- Sodha, M.S., Bansal, N.K. (1986), *Solar Passive Building: Science and Design*. Oxford: Pergamon..
- Sun, Q.P., Chen, X.H., Chen, J.F., (2002) *The Development and Application of Solar Energy Heat-pipes*, Energy Technology, 23, p. 110-112.
- http://www.sei.ie/Publications/Statistics_Publications/Fuel_Cost_Comparison/Domestic_Fuel_Cost_Comparison_January_2009.pdf.
- Swanson, T. D., Birur, G. C. (2003) *NASA Thermal Control Technologies for Robotic Spacecraft*, Applied Thermal Engineering, 23, p. 1055-1065..
- Vasiliev, L.L. (1989) *Heat-pipe research and development in the USSR*, Heat Recovery Systems & CHP, 9, pp. 313-333.
- Zalba, B., Marin, J.M., Cabeza, L.F., Mehling, H., (2003) *Review on thermal energy storage with phase change: Materials, heat transfer analysis and applications*, Applied Thermal Engineering, 23, p. 251-283.

COMPARATIVE ANALYSIS OF TWO-PHASE THERMOSYPHONS SOLAR COLLECTORS

D. Del Col, A. Padovan

Dipartimento di Ingegneria Industriale – Università di Padova
Via Venezia, 1 – 35131 Padova – Italy
davide.delcol@unipd.it, a.padovan@unipd.it

S. Filippeschi

Department of Energy and Systems Engineering – Università di Pisa
Largo L. Lazzarino – 56122 Pisa – Italy
s.filippeschi@ing.unipi.it

ABSTRACT

This paper deals with two-phase thermosyphons used in glazed flat plate solar collectors. It analyses the performance of thermosyphons solar collectors by means of a steady-state mathematical model based on the lumped capacitance method. The model simulates the thermal behaviour of a single tube and of the whole collector at various operating conditions.

The present mathematical model has been validated experimentally using data taken on a copper thermosyphon. A test section has been set up, which is made of a single ended copper thermosyphon, where the input power at the evaporator is supplied by an electrical heater.

The validated model is finally applied to an analysis of two-phase thermosyphons solar collectors with variable configuration.

KEY WORDS: Solar collector, Two-phase thermosyphon

1. INTRODUCTION

Glazed flat plate solar collectors are largely employed in different applications, such as heating of domestic water, space of buildings and swimming pools. The main issues in the solar collector design are cost reduction, efficiency increase and limitation of the operating conditions leading to stagnation.

Heat pipes are largely used in the solar collectors and their characteristics are well-known in the literature (Hammad, 1995; Chaudhry et al., 2012). They show high performances, especially if applied together evacuated tube collector, quick thermal responses, thermal diode behaviour.

In the last decades a strong interest in the use of wickless devices as the two-phase thermosyphons, or pulsating heat pipes (Rittidech et al., 2007) has been reported.

Two-phase thermosyphons applied to the solar collector can be an interesting solution, because of their simplicity, low cost and good performance.

Several kinds of wickless two-phase solar evaporators have been proposed in the literature. They can be divided into three main groups: loops with remote condensation, closed loops

thermosyphons and single ended thermosyphons. They show different peculiarities.

In the first group the solar evaporator produces vapour which condenses in a remote condenser (tank) displaced above (Ordaz-Flores et al., 2011) or below the evaporator (Filippeschi, 2006). In these devices the condenser can be displaced at a very long distance from the evaporator.

The second group of devices enrolls all the solar collectors where the heat removal is located at the top of the device, close to the evaporator. These devices are loop thermosyphons and the upcomer is heated by the solar radiation, while the downcomer is placed on the back of the collector. Usually these loops have lower head load than the previous devices and therefore lower mass flow rates. These loops are widely investigated in the literature.

Esen and Esen (2005) analysed the thermal performances of a closed loop two-phase thermosyphon in a flat plate solar collector, under clear sky conditions, using different refrigerants. They constructed three small-scale solar water heating systems, and evaluated R134a, R407C and R410A as working fluids. They found that the latter offered the highest solar energy collection.

Chen et al. (2009) investigated experimentally the long-term thermal performance of a loop two-phase thermosyphon solar water heater with a check valve inserted in the downcomer and compared the results with the conventional systems, finding 18% increase in efficiency.

With the same device Chien et al. (2011) obtained thermal efficiency of 82%. They showed a mathematical model based on a resistive-capacitive model with prediction errors on the thermal efficiency of 6%.

However, the most investigated and simulated solar thermosyphon collectors are shell and tube systems with single ended thermosyphons.

Hussein et al (1999) theoretically analysed the transient thermal behaviour of a thermosyphon solar collector. They showed that the condenser section aspect ratio and the thermosyphons inclination angle had a considerable effect on the condensation. Hussein et al. (2007) experimentally investigated the effect of thermosyphon pipe cross section geometry and the working fluid filling ratio on the performance of the flat plate solar collectors. The experimental results indicated that the elliptical cross section has better performance than the circular cross section at low water filling ratios. Amatachaya & Srimuang (2010) compared the performance of a conventional copper pipe thermosyphon with an internal diameter of 32 mm with those of a flat pipe obtained by pressing the previous diameter. They experimentally analysed the effect of the heat load, the filling ratios and the thermal resistance. The flat pipe provided higher temperature and higher optimal filling ratio (60%). Xiao et al (2011) presented a theoretical analysis of a shell and tube solar collector with two-phase thermosyphons. They propose a 1D plus 1D differential equation system and validated it with experimental tests. A good agreement between model and experiments was reported.

From the literature it is possible to conclude that thermosyphon solar collector showed high efficiency if joined with evacuated pipes technology. The most of devices proposed presented thermal efficiency comprised in the range 40-70%.

The present paper deals with the use of two-phase thermosyphons in glazed flat plate solar collectors. The thermosyphon solar collector, which has been experimentally and theoretically studied here, consists of copper pipes which are welded on a flat selective copper absorber. Each pipe is a single ended thermosyphon.

2. EXPERIMENTAL TESTS

A copper thermosyphon pipe for applications in solar collectors has been instrumented to experimentally characterize its thermal behaviour. The thermosyphon is 1560 mm long and is charged with water. The test thermosyphon has been installed with an inclination angle of 30° respect to the horizontal plane. This inclination has been chosen because it is common in solar installations at values of latitude of the Southern Europe and also for roof-integrated applications.

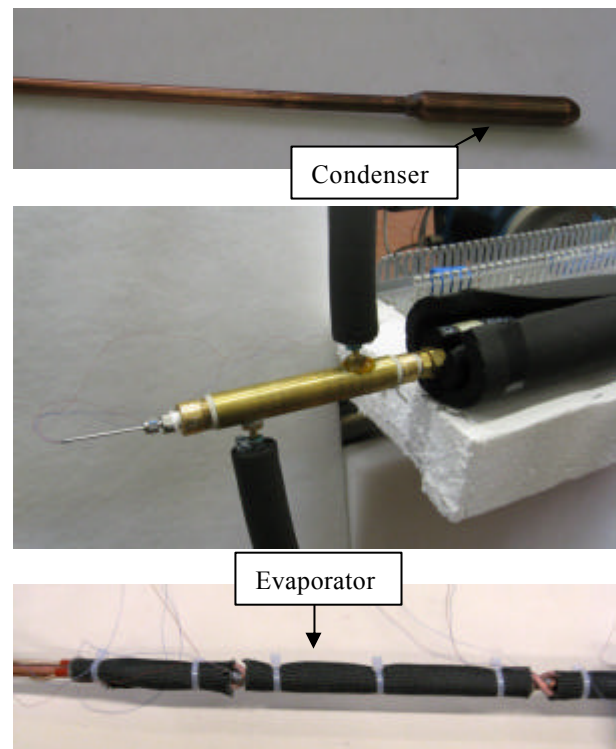


Figure 1. Thermosyphon pipe (top), water jacket at the condenser (center) and part of the evaporator (bottom).

The test tube has been divided in three sections: the evaporator, 1065 mm long, an adiabatic section, 415 mm long and the condenser, 80 mm long. The outer diameter of the evaporator and adiabatic sections is 8 mm, whereas it is equal to 14 mm at the condenser. An electrical resistance wire has been wrapped around the evaporator and the input power ($Q_{in, ev}$) is provided by a DC power supply. Both the voltage and current are measured, the latter by means of an instrument shunt with $\pm 0.1\%$ accuracy. A water jacket, made of brass, has been built to remove the heat from the condenser. Some photographs of the test thermosyphon are reported in Figure 1. The electrical wire is wrapped with a high-temperature resistant fiber glass sheet and then the whole test

section is thermally insulated. The cooling water flows in the annulus, having the inner diameter equal to 18 mm. The inlet and outlet water temperature and the temperature difference, ΔT_w , are measured in adiabatic mixing chambers by two type T thermocouples and a four junction thermopile, respectively. The volumetric flow rate of water V_w is also measured, thus the heat flow rate exchanged at the condenser is obtained as:

$$Q_{cond} = \rho_w V_w c_{p,w} \Delta T_w \quad (1)$$

where ρ_w and $c_{p,w}$ are the water density and specific heat capacity obtained from Refprop 8.0 (Lemmon et al., 2002).

Type T micro-thermocouples have been built, calibrated and installed to measure the wall temperature of condenser, evaporator and adiabatic sector. At the evaporator the thermocouples have been attached on the outer surface of the wall in six different axial positions. At each position two thermocouples are installed to measure the wall temperature at the top and bottom of the tube.

The saturation temperature is measured by three thermocouples (top, bottom and side) attached in the middle point of the adiabatic section. The wall temperature of the condenser is measured by two thermocouples attached on the ends of the condenser. All the thermocouples and the thermopile have been calibrated on site by comparison with two thermistor probes, getting an expanded uncertainty at 95% of confidence level of ± 0.05 K.

The volumetric flow rate of cooling water is measured with a magnetic flow meter with a value of expanded uncertainty equal to $\pm 1\%$.

The test runs have been carried out by varying the inlet temperature of the cooling water between 18 °C and 39 °C and the input power between 60 W and 170 W.

Figure 2 reports the temperature values measured along the test tube at four different test conditions. The three zones (evaporator, adiabatic sector and condenser) are identified in the figure. The average temperature value between top and bottom position is reported.

By measuring the heat flow rate and the wall temperatures, it is possible to calculate the overall thermal resistance in the heat pipe as:

$$R = (T_{wall,ev} - T_{wall,cond}) / Q_{cond} \quad (2)$$

where the wall temperature at the evaporator ($T_{wall,ev}$) and condenser ($T_{wall,cond}$) are spatial

average values of the direct measurements. As a result of the evaluation of the heat losses, Q_{cond} is equal to the effective power at the evaporator.

It is also possible to determine the heat transfer coefficient at the condenser (eq. 3) and at the evaporator (eq. 4):

$$HTC_{cond} = Q_{cond} / [Area_{cond} (T_{sat} - T_{wall,cond})] \quad (3)$$

$$HTC_{ev} = Q_{cond} / [Area_{ev} (T_{wall,ev} - T_{sat})] \quad (4)$$

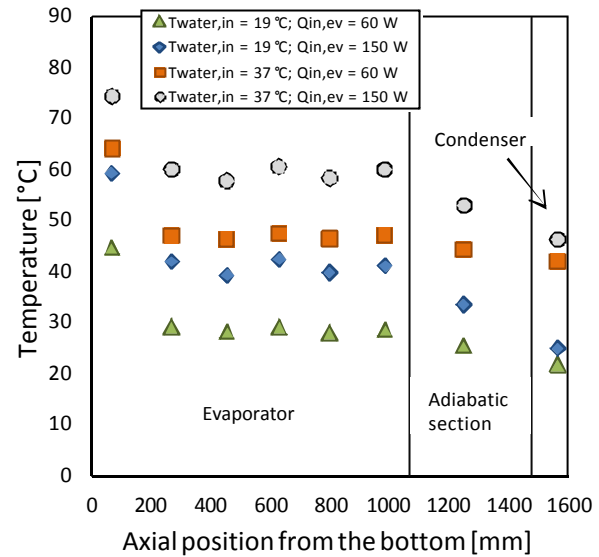


Figure 2. Measured temperature vs. axial position of the thermocouples from the bottom of the thermosyphon tube.

3. MATHEMATICAL MODEL

A steady-state mathematical model based on the lumped capacitance method was developed to predict the performance of thermosyphons solar collectors. The model is able to simulate the thermal behaviour of a single tube and of the whole collector at various operating conditions subjected to a constant input power. The mathematical model has been developed in a Matlab platform, using available correlations to estimate the heat transfer coefficients at the evaporator and condenser.

The thermosyphon pipe is schematized as a copper tube that is divided in three sections: the evaporator, an adiabatic sector and the condenser. The heat transfer in the evaporator is modeled using the Cooper (1984) correlation: it has been implemented to calculate the nucleate boiling heat transfer coefficient, with a value of the roughness factor equal to 1, as suggested for plain surfaces. The vapor is supposed to be in saturated

conditions. The correlation by Grooten & Van der Geld (2009) is also implemented.

When vapor moves from the evaporator to the condenser, the pressure drop is responsible for a slight decrease of the saturation temperature in the condenser. The vapor pressure drop consists of a friction part along the entire pipe and the inertia effects in the evaporator and condenser. The pressure drops are evaluated following the approach described in VDI (2010). When the inertia effects have to be taken into account a total pressure recovery in the condenser is assumed. However, the estimated pressure drop is small and can be here neglected.

The heat transfer in the condenser is modeled with the efficiency - NTU method. The condensation heat transfer is modeled using the Nusselt theory modified for inclined thermosyphons as reported in Faghri (1995).

The input data to the model are the supplied power, the inlet temperature and mass flow rate of the cooling water, the ambient surrounding temperature and the tilt angle of the thermosyphon pipe. The calculation process is based on an iterative procedure, which ends when the two-phase fluid reaches the conditions that allow removing the supplied power.

The operating conditions established inside the thermosyphon are finally compared with the heat transfer limitations, due to flooding, dry-out and boiling. Equations reported in Faghri (1995) for two-phase thermosyphons are used.

4. SIMULATIONS VS. EXPERIMENTAL DATA

The experimental heat transfer coefficients in condensation have been compared with the Nusselt equation modified for inclined thermosyphons:

$$Nu^* = 0.925 Re_j^{-1/3} \quad (5)$$

where the modified Nusselt number, Nu^* , is a function of the modified Reynolds number of the liquid film Re_j . Both the non-dimensional numbers are here defined as reported in Gross (1992) and Faghri (1995).

The Nusselt correlation overestimates most of the measured values and this is in agreement with the results reported in literature for low values of the film Reynolds number (Chen et al., 1984; Gross, 1992; Hashimoto & Kaminaga, 2002).

The heat transfer coefficient at the evaporator is underpredicted by the Cooper (1984) correlation.

A more significant underestimation is provided by the Grooten & Van der Geld (2009) correlation.

The present model (Sec. 3) is used to simulate the thermal behaviour of a two-phase closed thermosyphon with a single tube configuration, which operates under steady state conditions. The geometric characteristics are the same as in the test heat pipe (Sec. 2). The model is applied as described in Sec. 3, but adding a proper correction to the heat transfer coefficient correlation at the evaporator. As a consequence of the experimental results, and as a first approximation, the heat transfer coefficient is calculated with the equation by Nusselt (eq. 5) in the condenser, while in the evaporator the value calculated by Cooper (1984) has been multiplied by 1.5.

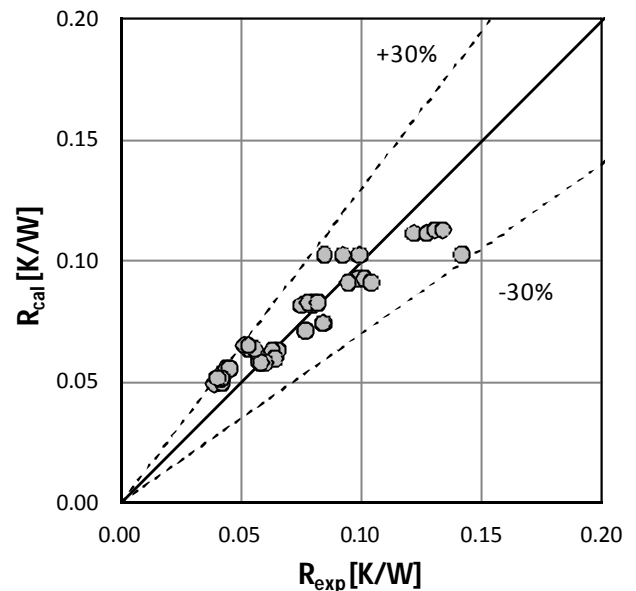


Figure 3. Calculated vs. experimental thermal resistance. The inlet temperature of cooling water is 22 °C and 37 °C.

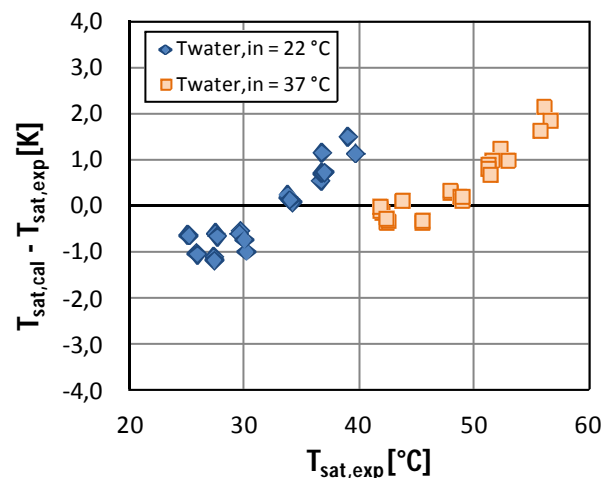


Figure 4. Difference between calculated and experimental saturation temperature vs measured saturation temperature.

Figure 3 displays the calculated overall thermal resistance (eq. 2) plotted versus the experimental values. It can be seen that on average the present model is able to predict the overall performance of the thermosyphon. The thermal resistances are fairly well predicted at both the two ends of the heat pipe (condenser and evaporator), and this can be deduced from Figure 4, which presents the saturation temperature agreement between simulations and experiments.

From the analysis of the present experimental heat transfer data at the condenser and at the evaporator, it comes out that neither model is able to correlate the present data when varying the operating conditions. However, a larger database would be necessary to provide new fitting correlations of the heat transfer coefficients. The agreement in terms of overall thermal resistance and saturation temperature is good enough to use the present model for the prediction of thermal efficiency of solar collectors.

5. SIMULATIONS OF SOLAR COLLECTORS

The same modeling approach has been used to simulate the thermal performance of the thermosyphon pipe applied to a flat plate solar collector. The difference is on the side of evaporator, because here the useful input power comes from an energy balance which accounts for the heat losses through the glass cover during operation. Equations reported in Duffie & Beckman (2006) are implemented. In the first design of solar collector, ten thermosyphons, like the one tested, are welded on a selective copper absorber plate. The condenser of each thermosyphon is cooled by means of water in a tube-in-tube heat exchanger. On the water side, the condensers are connected in series: the water from the first condenser enters the second one and so on. The heat transfer coefficient on the water side is based on the results of the experimental tests.

Figure 5 reports the efficiency curve obtained from the model as a function of the reduced temperature difference, that is the difference between the average temperature of the cooling water in the collector and the ambient temperature divided by the solar irradiance. The efficiency is the ratio of the useful heat flow rate and the input radiative power on the aperture area of the collector. Simulations refer to a value of solar irradiance of 1000 W/m^2 and a mass flow rate equal to 0.02 kg/s per square meter of collector area (Zambolin & Del Col, 2010). In the present collector the

aperture area is 1.48 m^2 . The effect of the size of the condenser can be observed in the graph.

Figure 6 reports the efficiency curve of a second design: this solar collector consists of twenty thermosyphon pipes with 3 mm inner diameter, charged with R134a. The evaporator and the condenser of each thermosyphon are 1480 mm and 200 mm long, respectively. The aperture area of the collector is 1.48 m^2 .

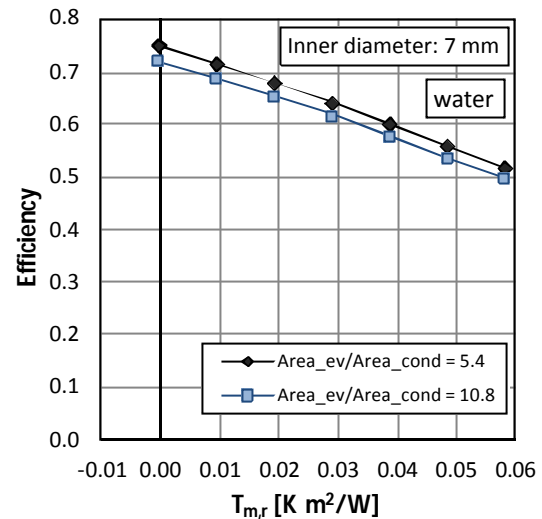


Figure 5. Thermal efficiency of solar collector using thermosyphons charged with water.

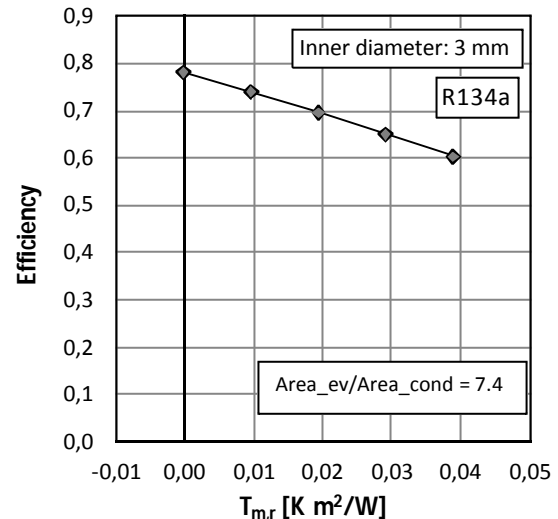


Figure 6. Thermal efficiency of solar collector using small diameter thermosyphons charged with R134a.

6. CONCLUSIONS

A mathematical model for two-phase thermosyphons has been developed using available correlations to estimate the heat transfer coefficients at the evaporator and condenser. The present model is able to evaluate the operating limitations of the heat pipe when applied to a solar

collector. Experimental tests on an instrumented thermosyphon have been performed in order to validate the prediction capability of the model. The experimental tests cover the operating conditions of solar collectors.

The preliminary results show that the present model is able to simulate the operation of two-phase closed thermosyphons applied to the flat plate solar collectors. Future work will be addressed to enlarge the experimental database used for assessing the simulations: the goal is to obtain a tool for the design and the modeling of new high performance solar absorbers.

ACKNOWLEDGEMENT

The financial support of the Regione Veneto through the project FSE 2105/1/6/1102/2010 is acknowledged.

REFERENCES

- Amatachaya P., Srimuang W. (2010) *Comparative heat transfer characteristics of a flat two-phase closed thermosyphon (FTPCT) and a conventional two-phase closed thermosyphon (CTPCT)*. International Communications in Heat and Mass Transfer, 37, p. 293-298.
- Chaudhrya H.N., Hughesa B.R., Ghanib S.A. (2012) *A review of heat pipe systems for heat recovery and renewable energy applications*. Renewable and Sustainable Energy Reviews, 16, p. 2249-2259.
- Chen B.R., Chang Y.W., Lee W.S., Chen S.L. (2009) *Long-term thermal performance of a two-phase thermosyphon solar water heater*. Solar Energy, 83, p. 1048-1055.
- Chien C.C., Kung C.K., Chang C.C., Lee W.S., Jwo C.S., Chen S.L. (2011) *Theoretical and experimental investigations of a two-phase thermosyphon solar water heater*. Energy, 36, p. 415-423.
- Cooper M.G. (1984) *Saturation nucleate pool boiling - a simple correlation*. Proceedings of 1st UK National Conference on Heat Transfer, Leeds, UK.
- Duffie A., Beckman W.A. (2006) *Solar engineering of thermal processes*. 3rd ed., Wiley&Sons, New Jersey.
- Esen M., Esen H. (2005) *Experimental investigation of a two-phase closed thermosyphon solar water heater*. Solar Energy, 79(5), p. 459-468.
- Faghri A. (1995) *Heat pipe science and technology*. Taylor & Francis, London.
- Filippeschi S. (2006) *On periodic two-phase thermosyphons operating against gravity*. International Journal of Thermal Sciences, 45, p. 124-137.
- Grooten M.H.M., van der Geld C.W.M. (2009) *Predicting heat transfer in long R-134 filled thermosyphons*. Journal of Heat Transfer, 131, 051501 1-9.
- Gross U. (1992) *Reflux condensation heat transfer inside a closed thermosyphon*. International Journal of Heat and Mass Transfer, 35, p. 279-294.
- Hammad M., (1995) *Experimental study of the performance of a solar collector cooled by heat pipes*. Energy Conversion and Management, 36 (3), p. 197-203.
- Hashimoto, H., Kaminaga, F. (2002) *Heat transfer characteristics in a condenser of closed two-phase thermosyphon: effect of entrainment on heat transfer deterioration*. Heat Transfer - Asian Research, 31, p. 212-225.
- Hussein H.M.S, Mohamad MA., El-Asfour A.S. (1999) *Transient investigation of a thermosyphon flat plate solar collector*. Applied Thermal Engineering, 19(7), p. 789-800.
- Hussein H.M.S. (2007) *Theoretical and experimental investigation of wickless heat pipes flat plate solar collector with cross flow heat exchanger*. Energy Conversion and Management, 48(4), p. 1266-1272.
- Lemmon E.W., McLinden M.O., Huber M.L. (2002) *NIST Standard Reference Database 23, Version 80*. NIST National Institute of Standard and Technology, Boulder, Colorado, US.
- Ordaz-Flores A., García-Valladares O., Gómez V.H. (2011) *Experimental characterisation and technical feasibility of a closed two-phase vs a conventional solar water heating thermosyphon*. Applied Thermal Engineering (31) p. 1313-1322.
- Rittidech S., Wannapakne S. (2007) *Experimental study of the performance of a solar collector by closed-end oscillating heat pipe (CEOHP)*. Applied Thermal Engineering, 27, p. 1978-1985.
- VDI-Gesellschaft (2010) *VDI Heat Atlas*. 2nd Edition, Springer Verlag, Berlin, Heidelberg, Germany.
- Xiao L, Wu S.H., Zhang Q.L., Li Y.R. (2012) *Theoretical investigation on thermal performance of heat pipe flat plate solar collector with cross flow heat exchanger*. Heat Mass Transfer DOI 10.1007/s00231-012-0972-3.
- Zambolin E., Del Col D. (2010) *Experimental analysis of thermal performance of flat plate and evacuated tube solar collectors in stationary standard and daily conditions*. Solar Energy, 84, p. 1382-1396.

COMPLETELY PASSIVE HEAT PIPE BASED EMERGENCY CORE COOLING SYSTEM FOR NUCLEAR POWER REACTOR

Masataka Mochizuki, Randeep Singh, Thang Nguyen, Tien Nguyen, Koichi Mashiko, Yuji Saito, and Vijit Wuttijumnong

Thermal Technology Division, Fujikura Ltd.,
1-5-1, Kiba, Koto-ku, Tokyo 135-8512, Japan
Phone: +81-3-5606-1174, Fax: +81-3-5606-1514,
mmotizuk@fujikura.co.jp, randeep.singh@jp.fujikura.com, thang007@bigpond.net.au,
tien2@optusnet.com.au, mashikok@fujikura.co.jp, y_saito@fujikura.co.jp, vijit@fujikura.com

ABSTRACT

On March 11th, 2011, a natural disaster created by earthquakes and Tsunami caused a serious potential of nuclear reactor meltdown in Fukushima due to the failure of Emergency Core Cooling System (ECCS) powered by diesel generators. In this paper, heat pipe based ECCS has been proposed for nuclear power plants. The designed loop type heat pipe ECCS is composed of cylindrical evaporator with 62 vertical tubes, each 150 mm diameter and 6 m length, mounted around the circumference of nuclear fuel assembly and 21 m x 10 m x 5 m naturally cooled finned condenser installed outside the primary containment. Heat pipe with overall thermal resistance of $1.44 \times 10^{-5} \text{ }^\circ\text{C/W}$ will be able to reduce reactor temperature from initial working temperature of 282 $^\circ\text{C}$ to below 250 $^\circ\text{C}$ within 7 hours. The overall ECCS also includes feed water flooding of the core using elevated water tank for initial 10 minutes which will accelerate cooling of the core, replenish core coolant during loss of coolant accident and avoids heat transfer crisis phenomena during heat pipe start-up process. The proposed heat pipe system will operate in fully passive mode with high runtime reliability and therefore provide safer environment to nuclear power plants.

KEY WORDS: *Nuclear Power Reactor, ECCS, Loop type heat pipe, BWR, PWR, Leidenfrost phenomenon*

1. INTRODUCTION

Nuclear power has the potential to support the electric energy needs of the growing population. Nuclear energy share in global electricity production is growing fast due to its high energy density, advanced reactor technology, low greenhouse gas emissions, ease of installation and plant expansion. In nuclear power plants, kinetic energy produced by the nuclear fission of the radioactive material (usually uranium-235 or plutonium-239) is converted to heat and thereby to useful electrical power. Nuclear fission provides very high density energy, for example one kg of U-235 can produce 3 million times of energy generated by equivalent mass of coal. Japan has total of 54 nuclear power reactors with total electric power capacity of 49 GW (30% of country's demand) and there is proposal for 19 new reactors with total capacity of 13 GW to be built in the near future.

Two most commonly used reactors in nuclear power plants are pressurized water reactor (PWR) and boiling water reactor (BWR). PWR pumps high pressure coolant (water) to the reactor core to extract energy from the nuclear fission reaction. The hot water is then passed through the steam generator where it heats up the secondary coolant

and produce steam which is passed through turbine to generate electricity. Unlike PWR, in BWR the steam ($\sim 282 \text{ }^\circ\text{C}$) is generated in the nuclear core that is directly used to drive the turbine. In case of an accident, BWR is more susceptible to radiation leak than PWR, due to direct utilisation of the contaminated steam in the turbine located outside the primary containment. The BWR containment consists of drywell that houses reactor with related cooling system and wet well or suppression pool. The suppression pool contains water charge for core cooling during emergency reactor shutdown and for dumping excess heat (nuclear reaction control) during reactor operation. Fig. 1 presents the schematic of the BWR based nuclear power plant showing reactor vessel with fuel and control rods assemblies, turbine and generator arrangement, sea water cooled condenser, suppression pool and, most importantly, electrically driven ECCS with pumps. Nuclear power plants normally use sea water for cooling purpose. In case of any malfunctioning, the nuclear reactors are automatically shut down by using control rod mechanism. After shutdown, the ECCS is required to transfer and dissipate the residual heat from the core and maintain reactor temperature within safer limits ($< 100^\circ\text{C}$). The ECCS, which is activated

after reactor shutdown, typically uses diesel generators to power number of pumps for spraying high pressure water on the hot core. If the active water cooling system stops due to loss of electrical power, then the reactor internal temperature and pressure will build-up due to steam formation from accumulated residual heat causing fuel meltdown ($\sim 1,800\text{ }^{\circ}\text{C}$) and reactor vessel damage.

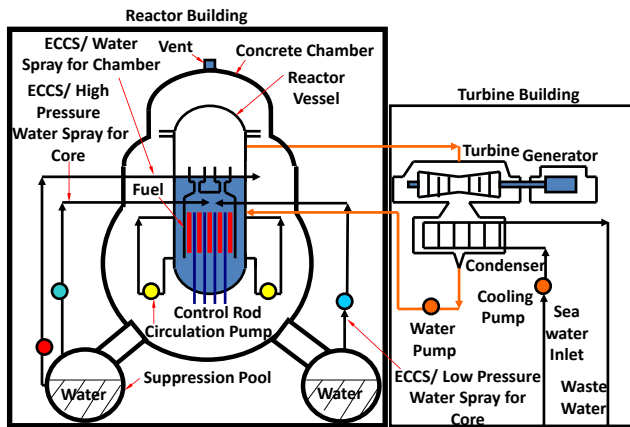


Figure 1. Boiling Water Reactor with ECCS system

One of the worst nuclear accident at Fukushima nuclear power plant resulted from the failure of electric generators for ECCS that was caused by M9 earthquake and Tsunami triggered by it. The system described in Fig. 1 is similar to the BWR used in Fukushima nuclear power plants. Active ECCS is not reliable due to their dependence on the electric power and therefore is prone to failure during adverse natural calamities. Passive cooling systems are more potential to enhance plant safety through system reliability and eliminate cost associated with the installation, maintenance and operation of the active cooling system that consists numerous electric pumps with independent and dedicated power supplies.

Sviridenko and Shevelov (2011) proposed a passive two-phase heat transfer thermosiphon system to remove residual heat for the Pressurised Nuclear Power Plant WWER-1000 during emergency shutdown. Analytical analysis for variables such as heat removal, temperature and pressure with time were given. For example, temperature in the core reduced from about $350\text{ }^{\circ}\text{C}$ to $220\text{ }^{\circ}\text{C}$ and pressure reduced from about 16 MPa to 2.5 MPa in approximately 8 hours. Most of the existing safety (or ECCS) systems are category D type (need initiate signal, energy from stored sources and limited active components to control) and utilises gravity assisted fluid (single phase or two phase) circulation through the core to remove decay heat (IAEA, 2009). In the present investigation, heat pipe based decay heat removal system (Kaminaga et al, 1988) from reactor core

has been proposed and analyzed as safety system for nuclear reactors. The proposed heat pipe ECCS will operate passively with high runtime reliability.

2. DECAY HEAT

The decay heat output by reactor after shutdown process, $P(t)$, can be expressed as shown in Eq. (1) (Glasstone & Sesonske, 1967)

$$\frac{P(t)}{P_0} = 0.066[t^{-0.2} - (t_s + t)^{-0.2}] \quad (1)$$

It depends on the nominal thermal power before shutdown (P_0), time for which the reactor was in operation before shutdown (t_s) and time since reactor shutdown (t). The decay heat variation after shutdown for nuclear reactor, similar to Fukushima No. 1 reactor, with 1,350 MW thermal power, 460 MW electric output and operating for last 5 years, is calculated and presented in Fig. 2. It is observed that immediately after reactor shutdown the decay heat is around 6.4% of total thermal power at normal operating conditions ($\sim 87\text{ MW}$), it is reduced to 0.5% of total thermal power ($\sim 7\text{ MW}$) after a day and continues to reduce exponentially with time.

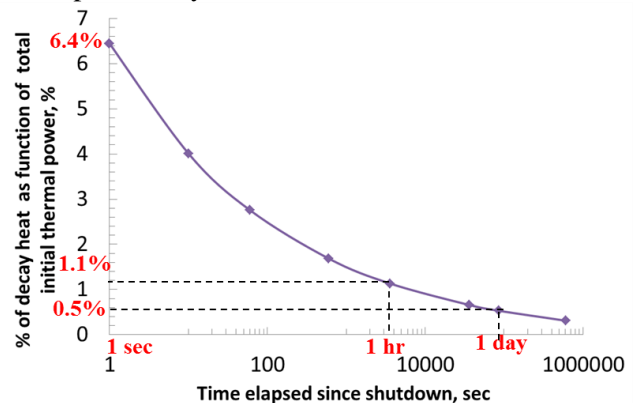


Figure 2. Decay heat output by nuclear reactor, with 1,350 MW thermal power output, after shutdown

3. HEAT PIPE ECCS

Fig. 3 shows the proposed loop-type heat pipe based emergency core cooling system for BWR.

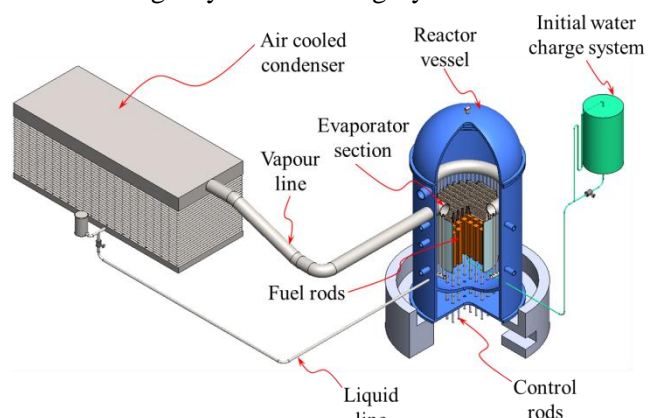


Figure 3. Proposed Heat Pipe ECCS with Gravity Assisted Feed Water System

There are two components of the overall ECCS system 1) Gravity assisted feed water tank and 2) Loop type heat pipe assembly. The concept uses elevated water tank for initial flooding of core with water, by gravity feed, for specific time (~10 min) and passive core cooling using loop type heat pipe.

3.1 Gravity Assisted Water Charging

The feed water flooding of the core using elevated water tank helps to:

- Replenish the coolant inside the core during loss of coolant accident (LOCA)
- Provide initial accelerated cooling of the core
- Complements additional cooling backup system
- Avoids Leidenfrost phenomenon during loop-type heat pipe start-up

One of the main purpose of the initial water charge is to avoid Leidenfrost effect that is a phenomenon in which liquid coming in contact with a surface significantly hotter than liquid's boiling point produces an insulating vapour layer which keeps the liquid from boiling rapidly thereby limiting heat transfer from hot surface to be cooled. Here, the gravity assisted initial flooding of core with water will provide cooling for heat pipe evaporator thereby limiting the occurrence of Leidenfrost phenomenon. The feed water tank with 18 m³ capacity is located at 5.1 m higher level above reactor water level and drains through 8 cm tube at 10 m/s flow velocity. This will accounts to 32 kg/second of water flow rate for initial 10 minutes interval. Such a system design will reduce the decay heat to less than 27 MW at the end of the water charging phase.

3.2 Loop Type Heat Pipe System

The loop heat pipe system with evaporator mounted inside the reactor vessel and condenser installed outside the primary containment building, as shown in Fig. 3, is designed to continually dissipate the decay heat output by the nuclear fuel. The evaporator consists of 62 vertical tubes, 0.15 m outer diameter and 6 m long, placed circumference around the fuel core and connected via top and bottom ring shaped header. The natural convection cooled condenser (21 m x 10 m x 5 m) consists of 840 tubes, each 0.15 m outer diameter and 5m long, with aluminium fins (300 mm diameter, 3 mm thickness at 20 mm pitch) arranged in triangular flow arrangement. Each of these tubes is connected to top and bottom rectangular header. Heat pipe material is stainless steel SUS-316L with internal Ti lining to make system compatible with water as working fluid.

3.2.1 Heat Pipe Thermal Analysis

In this section, thermal performance of the loop type heat pipe has been estimated on the basis of the reactor thermal data and heat pipe system geometry. From reactor hot water with initial temperature of 282°C to ambient air at 40°C, there are number of conduction and convection based thermal resistances to heat transfer via heat pipe as shown in thermal network in Fig. 4. Conduction heat resistance through cylindrical tube is given by Eq. (2).

$$R_{cond} = \frac{\ln\left[\frac{D_o}{D_i}\right]}{2\pi kL} \quad (2)$$

Where D_o , D_i and L are the outer diameter, inner diameter and length of tube, and k is the thermal conductivity for the tube material (16 W/m.K for SUS).

Convection heat resistance can be expressed by Eq.(3)

$$R_{conv} = \frac{1}{hA} \quad (3)$$

Where, A is heat transfer surface area and h is the evaporative or condensation (h_e or h_c) heat transfer coefficient or natural convection heat transfer coefficient (water to evaporator external surface (h_{w-e}), condenser external surface to air (h_{c-a})). These coefficients can be calculated using following correlations.

Heat pipe evaporator, boiling heat transfer coefficient (h_e) can be calculated from Imura's correlation. (JAHP, 1985)

$$h_e = 0.32\chi\left(\frac{P_{in}}{P_o}\right)^{0.3} \quad (4)$$

Where, P_{in} , P_o are the heat pipe inside pressure and ambient pressure respectively and

$$\chi = \frac{\rho_l^{0.65}\lambda_l^{0.3}c_{pl}^{0.7}g^{0.2}q_e^{0.4}}{\rho_v^{0.25}L^{0.4}\mu_l^{0.1}} \quad (5)$$

ρ_l , ρ_v , μ_l , λ_l , c_{pl} , q_e , L and g are liquid/vapour density, liquid dynamic viscosity, liquid thermal conductivity, liquid specific heat, evaporator heat flux and acceleration due to gravity.

Heat pipe condenser, condensation heat transfer coefficient (h_c) can be calculated from Nusselt's correlation. (JSME, 1986).

$$h_c = 0.925\left(\frac{\lambda_l^3\rho_l^2gL}{\mu_l q_c l_c}\right)^{1/3} \quad (6)$$

Where, ρ_l , μ_l , λ_l , q_c , L and g are liquid density, liquid dynamic viscosity, liquid thermal conductivity, condenser heat flux, latent heat and acceleration due to gravity.

Water side natural heat transfer coefficient from reactor water to evaporator (h_{w-e})external surface is estimated by Eq.(7)-(11) (JSME, 1986)

$$h_{w-e} = \frac{Nu_x \lambda_l}{l} \quad (7)$$

Where,

$$Nu_x = \left\{ C_1 \left(\frac{\nu_\infty}{\nu_w} \right)^{0.21} Ra_x^{\frac{1}{4}} \right\}; 10^4 \leq Ra_x \leq 4 \times 10^9 \sim 3 \times 10^{10} \quad (8)$$

$$C_1 = \frac{3}{4} \left(\frac{Pr}{2.4 + 4.9\sqrt{Pr} + 5Pr} \right)^{1/4} \quad (9)$$

$$Ra_x = Gr_x Pr \quad (10)$$

$$Gr_x = \frac{g\beta(T_w - T_\infty)x^3}{\nu_\infty^2} \quad (11)$$

Subscripts ∞ and w represents the properties of liquid (water) at reactor bulk (T_∞) and evaporator wall (T_w) temperatures. $x = \frac{l}{2}$, where l is evaporator tube length. T , ν , Pr , g , β and are temperature, liquid dynamic viscosity, Prandl Number, acceleration due to gravity and thermal expansion coefficient of water (at mean temperature i.e. $T_m = \frac{(T_\infty + T_w)}{2}$) respectively.

Air side heat transfer coefficient from condenser external surface to ambient air (h_{c-a}) can be calculated from Eq.(12) (Obana, 1982).

$$h_{c-a} = 0.45 \left(\frac{\lambda_a}{D_o} \right) \left(\frac{D_o G_{max}}{\mu_a} \right)^{0.625} \left(\frac{A_f}{A_o^*} \right)^{-0.375} \left(\frac{C_{pa}\mu_a}{\lambda_a} \right)^{-0.375} \quad (12)$$

Where, λ_a , C_{pa} , μ_a , D_o , G_{max} , A_f and A_o^* are air thermal conductivity, air specific heat capacity, air dynamic viscosity, condenser tube outer diameter, air mass flow rate (in kg.m².hr), fin area per meter and unfinned area per meter of condenser tube respectively. h_{c-a} value from Eq. (12) will be in Kcal/hr.°C.m² which can be converted to W/m².K by multiplying with 1.163. Eq. (12) is valid for:

$$5 < \left(\frac{A_f}{A_o^*} \right) < 12 \quad (13)$$

For finned heat exchanger, the effective finned area for heat transfer is determined by fin efficiency which depends on the fin properties and fin to air heat transfer coefficient (h_{c-a}). In the present heat exchanger design, annular fins with rectangular profile has been considered for which overall fin efficiency (η_o) can be calculated from reference. (Incropera & DeWitt, 2002)

Overall thermal resistance (R_o) of the loop type heat pipe can be expressed as:

$$R_o = \frac{1}{h_{w-e}A_{eo}} + \frac{\ln\left[\frac{D_{eo}}{D_{ei}}\right]}{2\pi k_e L_e} + \frac{1}{h_{e-ai}A_{ei}} + \frac{1}{h_{c-ai}A_{ci}} + \frac{\ln\left[\frac{D_{co}}{D_{ci}}\right]}{2\pi k_c L_c} + \frac{1}{h_{c-a}A_{ct}\eta_o} \quad (14)$$

Where, Subscripts eo, ei, co, ci denotes the evaporator outer, evaporator internal, condenser outer and condenser internal respectively. A , D , L , k_e and k_c are area, diameter, length and thermal conductivity of evaporator and condenser tubes (stainless steel) respectively.

Based on the above approach, the calculated values for:

- Heat pipe evaporator boiling coefficient (h_e) = 14,000 W/m².K,
- Condensation heat transfer coefficient (h_c) = 5,200 W/m².K,
- Water to evaporator external surface natural heat transfer coefficient (h_{w-e}) = 1,180 W/m².K and
- Condenser external surface to ambient air heat transfer coefficient (h_{c-a}) = 7.9 W/m².K (for air velocity, $V_a = 1$ m/s)

The overall calculated thermal resistance of heat pipe (R_o) was 1.44×10^{-5} °C/W.

4. REACTOR THERMAL ANALYSIS

In this section, the reactor vessel is analysed for different core cooling conditions.

4.1 ECCS Failure: No Cooling

If the cooling function of the ECCS fails, there will be continuous increase in the temperature of the reactor vessel under the impact of the decay heat released by the nuclear fuel inside core. Under no cooling condition, the thermodynamic state of reactor can be expressed by Equation (15).

$$MC_{pw}(T_{rf} - T_{ri}) = P\Delta t \quad (15)$$

Where, M is the water mass inside the reactor (~ 200 tons), C_{pw} is water specific heat capacity, T_{ri} is the reactor initial temperature (~ 282 °C) and T_{rf} is the reactor final temperature after Δt time. P is the rate of decay heat output by reactor, with 1,350 MW heat output, as per Eq. (1). Fig. 4 presents the transient thermal response of water inside reactor which will reach nuclear meltdown situation (> 1,800 °C) within 2 day time period, due to accumulation of decay heat inside vessel.

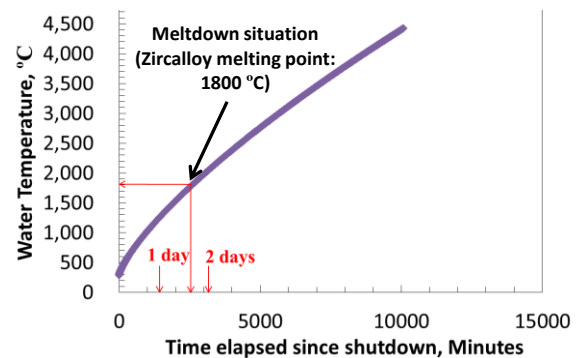


Figure 4. Transient response of reactor water temperature under ECCS failure condition

4.2 Heat Pipe ECCS

Heat pipe will be able to provide reliable and powerless two-phase heat transfer system for the

removal of the decay heat without any failure consequences. With the proposed loop type heat pipe system, the overall system energy balance can be expressed by Eq.(16).

$$MC_{pw}(T_{rf} - T_{ri}) = (P - Q_{hp})\Delta t \quad (16)$$

Where, Q_{hp} is the heat pipe heat removal rate from reactor given by Eq.(17).

$$Q_{hp} = \frac{(T_{ri} - T_a)}{R_o} \quad (17)$$

Where, T_a is the ambient temperature $\sim 40^\circ\text{C}$ and R_o is thermal resistance from reactor coolant to ambient air via heat pipe system ($1.44 \times 10^{-5}^\circ\text{C/W}$). Fig. 6 shows the transient response of the reactor vessel (or water) temperature, T_{rf} , with heat pipe heat removal system, as calculated from Eq. (16). It is observed from the graph that, after reactor shutdown, the water temperature continues to rise for first 60 minutes reaching maximum of 305°C from initial 282°C , followed by gradual drop in temperature with time. The initial rise in reactor temperature is due to larger quantity of decay heat from reactor core after shutdown process which exceeds the heat pipe heat dissipation capacity. As the decay heat reduces exponentially with time and drops below heat pipe capacity, gentle drop in reactor vessel temperature is noted. If the overall thermal resistance of heat pipe unit is doubled ($\sim 2.88 \times 10^{-5}^\circ\text{C/W}$) by reducing heat pipe system size, then the extent of temperature rise and time taken to reduce reactor temperature below certain value will increase accordingly. In this case, the reactor will achieve highest temperature of 404°C in 7 hours before commencement of cooling down operation.

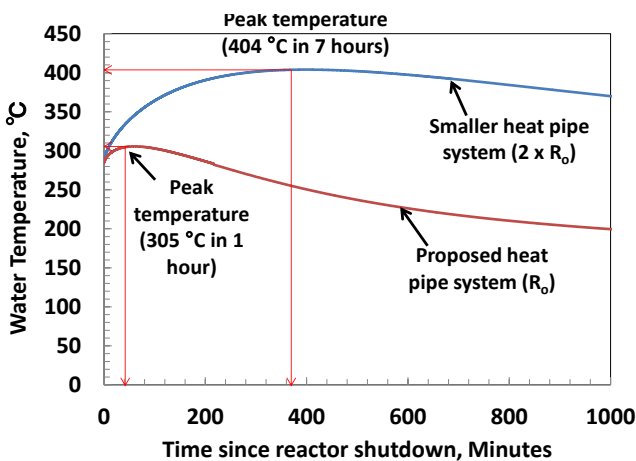


Figure 6. Transient response of reactor water temperature with loop type heat pipe cooling

Fig. 7 presents the extended cooling operation for two different heat pipe system sizes. Here, it is estimated that to achieve temperature below

250°C , proposed heat pipe system will take less than 7 hours whereas with reduced system size the cooling time will increase to 4.5 days. As safety is one of the prime requirements in the nuclear plants, therefore heat pipe unit will shorter cooling time will provide more reliable and secure system.

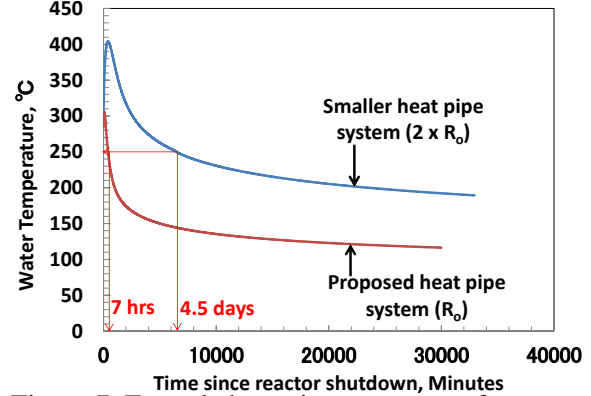


Figure 7. Extended transient response of reactor water temperature with loop type heat pipe cooling

4.3 Heat Pipe ECCS with Initial Water Charge

The proposed heat pipe based ECCS system with initial water charge represent more advanced and safer ECCS for nuclear reactor by providing reliable and passive heat pipe core cooling system and by injecting gravity feed additional water quantity inside core for 10 minutes which can replenishing lost coolant and address high temperature heat transfer limiting issues (Leidenfrost effect). Fig. 8 represents the thermal model of the proposed system with its energy balance represented by Eq. (18).

$$MC_{pw}(T_{rf} - T_{ri}) = \{(P - Q_{hp}) + m_w C_{pw}(T_a - T_{rf})\}\Delta t \quad (18)$$

Where, m_w is the gravity feed water mass flow rate.

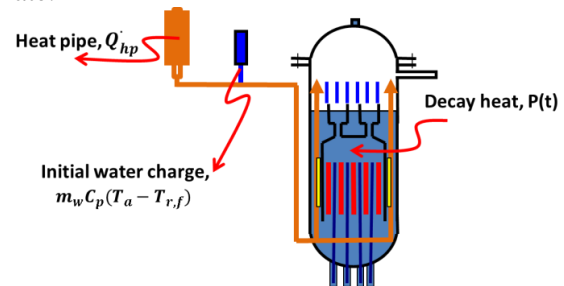


Figure 8. Thermal model of reactor with heat pipe cooling and initial water charge

Fig. 9 presents the reactor water temperature response with and without initial 10 minutes water feeding (32 kg/s) and with heat pipe cooling. It is observed from Fig. 9 that during initial water charging process, reactor cooling is accelerated.

The gravity feed water offers additional cooling capacity for the core that helps to reduce highest reactor temperature achieved, provide initial temperature drop after shutdown procedure and reduce reactor cooling time. In Fig. 10, system operation for larger span of time is provided that shows that with water injection, the reactor can achieve temperature below 250 °C within 4.3 hours which is 1.6 times less than without water charging case. It should be noted that, other than reducing cooling time, water feeding provides coolant replenishment and addresses heat transfer limiting issues during heat pipe start-up.

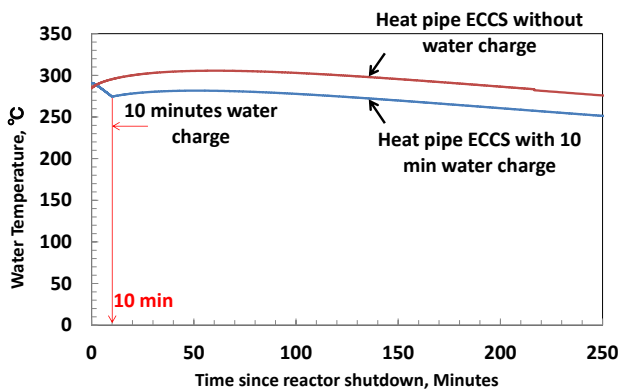


Figure 9. Reactor water temperature variation with and without initial water charge and heat pipe ECCS

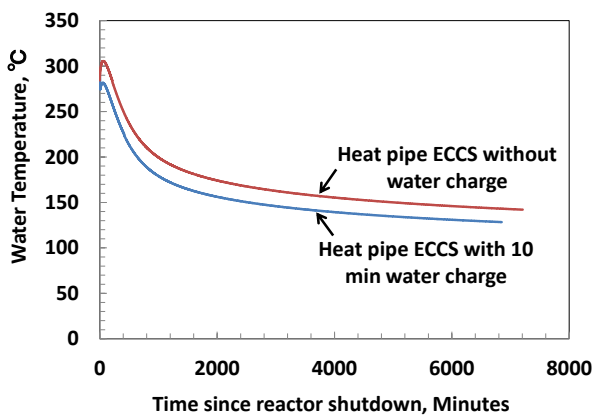


Figure 10. Extended transient response of reactor water with and without initial water charge and heat pipe ECCS

5. EXPERIMENTAL APPROACH

In order to validate the concept of cooling nuclear reactor core using loop-type heat pipe with initial gravity water charging, a lab prototype with 1:10,000 scale will be fabricated and tested. The proof of concept prototype will be expected to transfer heat load up to 3 kW and will be downscale on the basis of 1) evaporator length to diameter ratio, 2) evaporator active heat flux and 3) evaporator axial heat flux criteria, to simulate experimental conditions close to real scale model.

Heat pipe container material and working fluid will be similar to the proposed configuration.

6. CONCLUSIONS

On the basis of present research, it is concluded that loop type heat pipe can be successfully utilized for dissipating decay heat from nuclear reactor core. The proposed heat pipe emergency core cooling system with cylindrical evaporator composed of 62 vertical tubes, each 150 mm diameter and 6 m length, mounted around the periphery of nuclear fuel assembly and 21 m x 10 m x 5 m finned condenser installed outside the primary containment was designed to dissipate decay heat from reactor vessel with 1,380 MW full load thermal capacity to ambient air at 40 °C. Overall thermal resistance of the heat pipe unit was 1.44×10^{-5} °C/W. within 6-7 hours, the proposed heat pipe system can reduce the reactor temperature below 250 °C from initial working temperature of 282 °C. It is recommended to use initial water charge of 32 kg/s for 10 minutes to accelerate the cooling time of the core and provide safer ECCS cooling system. With heat pipe ECCS and 10 minutes water charge, the core cooling time was reduced. The proposed heat pipe system can be operated completely passive which will provide safer operational environment to nuclear power plants.

REFERENCES

- International Atomic Energy Agency (IAEA), (2009), Passive Safety Systems and Natural Circulation in Water Cooled Power Plants, IAEA-TECDOC-1624, ISBN:978-92-0-111309-2, Austria
- Kaminaga, F., Okamoto, Y., Keibu, M., Ito, H., Mochizuki, M., Sugihara, S., (1998) Application of Heat Pipe to JSPR Safety, Proc. of Design Feasibility for JSPR, UTNL-R0229, pp. 31-39,
- Glasstone S., Sesonske, A., (1967), Nuclear Reactor Engineering, 2nd Ed., Van Nostrand Reinhold Japan Society of Heat Pipes (JAHP) (1985), Heat Pipe Applications, 1st Ed. Chapter:2, JSME, (1986), JSME Databook: Heat transfer, 4th Ed., Chapter:2
- Obana H., (1982), Heat Exchanger Design Handbook, 1st Edition, Chapter:27, Kogaku Tosho
- Incropera F.P., DeWitt D.P., (2002), Fundamentals of Heat and Mass Transfer, 5th. Edition, Wiley, ISBN: 0-471-38650-2
- Sviridenko I., Shevelov D., (2011), Autonomous Thermosiphon System for WWER-1000 Pressuriser Cooldown, 8th International Seminar "Heat Pipes, Heat Pumps, Refrigerators, Power Sources", Minsk, Belarus, Sept 12–15, 2011

WETTING AND FILM BEHAVIOR OF PROPANE INSIDE GEOTHERMAL HEAT PIPES

Thomas Storch, Tom Weickert, Thomas Grab, Ulrich Gross

Institute of Thermal Engineering, Technische Universität Bergakademie Freiberg

Gustav-Zeuner-Strasse 7; 09599 Freiberg, Germany

Phone: +49-(0)3731-393185; fax +49-(0)3731-393963; E-mail: thomas.storch@iwtt.tu-freiberg.de

Manja Kasper

BLZ Geotechnik Service GmbH

Industriepark Str. A Nr. 1; 39245 Gommern, Germany

Phone: +49-(0)39200-7020; E-mail: geothermie@blz-geotechnik.de

ABSTRACT

The knowledge of the efficiency of a heating system is essential for engineering. The efficiency of geothermal heat pipes depends, e.g., on the wetted inner tube surface due to the principle of falling film evaporation. To achieve a high evaporation rate a nearly closed liquid film down to the lower end of the pipe is required. To investigate the real processes inside a geothermal heat pipe and the wetting behavior of Propane on solid materials more in detail, two experimental plants were used. The experimental setups are presented as well as the first results of visual investigations inside a geothermal heat pipe during the starting process. Furthermore first results of wetting investigations with liquid Propane on selected solid surfaces are shown.

KEY WORDS: geothermal plant, thermosyphon, wetting behavior, falling film, evaporation

1. INTRODUCTION

Increasing prizes for fossil fuels indicate the need for alternative and sustainable energy resources for cooling and heating of buildings. In Germany, e.g., 33% of the final energy consumption is used for room heating applications, Kaltschmitt et al. (2007). Shallow geothermal energy is obtained at depths of up to 400 meters and it is usable as energy source for cooling and heating of buildings. There exist various closed systems of borehole heat exchangers, like geothermal u-tubes, coaxial tubes, heat pipes and energy piles. For heating applications, ground heat pumps are necessary to increase the temperature level up to the required heating temperature, (VDI 4640 standard, 2010).

Heat pipes in general have been widely investigated in the past. The first applications for extracting heat from the ground by means of heat pipes were used to stabilize pipeline and railway fundamentals, e.g. Vasiliev et al. (1982), or to heat highways and bridges, e.g. Nydahl et al. (1987), Tanaka et al. (1982). Nowadays gravitational driven heat pipes combined with heat pumps are an alternative solution for geothermal energy use for heating applications. The principle of a heat pipe cycle which is connected to a heat pump cycle by a heat exchanger (heat sink) is shown in fig. 1.

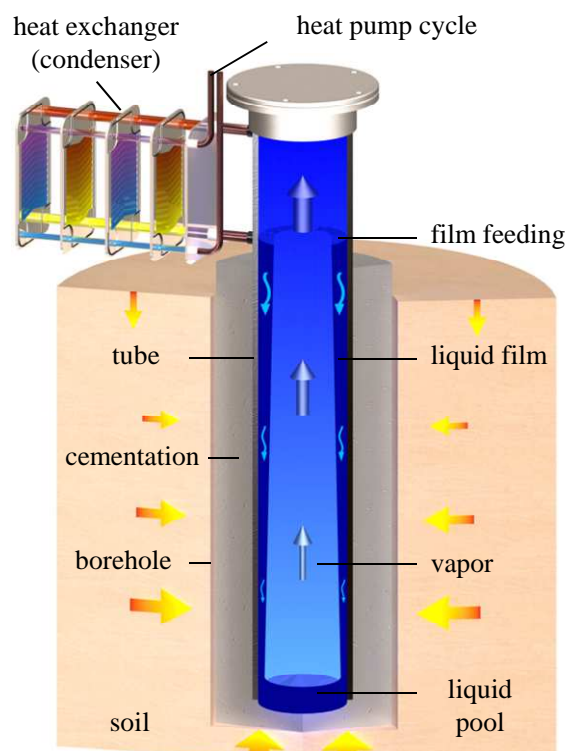


Figure 1. Schematic of a geothermal heat pipe

Actual geothermal heat pipes are up to 250 m in length, 15 - 65 mm in diameter and operate with Propane or carbon dioxide. During operation the

liquid flows down the tube due to gravity and cools the surrounding rock by evaporation. Thereby the heat pipe mechanism transfers heat very efficiently which can be a big motivation for users, e.g. house owners, see Grab et al. (2011) and Ochsner (2008).

The efficiency of heat pipes depends, e.g., on the wetted inner tube surface due to the principle of falling film evaporation. To achieve a high evaporation rate a nearly closed liquid film down to the lower end of the pipe is required. The liquid film spreading depends on several properties of the heat pipe, like pipe material, surface roughness, inclination angle, length as well as the operating regime, see also Weickert et al. (2011).

The present contribution is focused on two research topics. First, processes inside geothermal heat pipes were investigated where the working fluid is Propane. These processes were observed visually by the help of a miniature camera inside the heat pipe. Second, the wetting behavior of Propane was studied on several pipe materials in a laboratory autoclave. The present paper contains short explanations of the experimental setups, first results from the visual observations inside the geothermal heat pipe and temperature log of the surrounding soil. Furthermore first results of the wetting research with Propane are presented.

2. EXPERIMENTAL

2.1 Setup A: geothermal heat pipe

For the visual investigations inside a geothermal heat pipe a new heat pipe was installed in Freiberg (Germany). The heat pipe consists of outside coated steel pipes welded every 6 m with an inner diameter of 53 mm and a total length of about 91.5 m (incl. head of the heat pipe, see Fig. 2). Above, a camera chamber with a special pressure lock system is installed, see also Storch et al. (2011). This system with integrated pressure maintenance is needed to provide the visual observations during operation without leakages. For extracting heat from the rock a heat sink is generated by a heat pump cycle. It consists of thermostatic expansion valve, compressor (3.5 kW) and heat exchanger.

Further the test plant is equipped with extensive measurement technique consisting of several temperature sensors and pressure transmitters. In addition a fibre optical temperature measurement system (FOM) is installed along the heat pipe's length. It enables long-time measurements and

temperature monitoring during the different experimental settings. In the heat pipe cooling cycle a flow meter is installed (fig. 2). Therewith the heat extracted from the ground and the system efficiency can be calculated and checked.

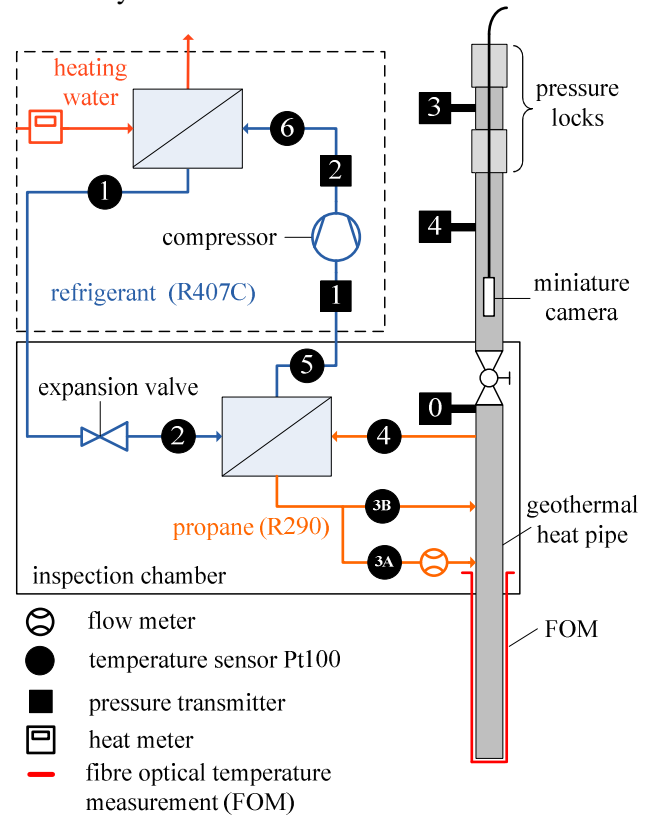


Figure 2. Cycles and instrumentation of test plant

2.2 Setup B: Wetting investigations with liquid Propane

The wetting behavior of a liquid on a solid surface is characterized by the contact angle and alternatively the contact area of a liquid droplet. Contrary to many other liquids the contact angle of Propane could not be found in the considered literature. Hence a laboratory facility was developed which enables investigations of the Propane wetting behavior on metallic and synthetic surfaces. The key component is a $12 \cdot 10^{-3} \text{ m}^3$ pressure vessel ("autoclave"), see fig. 3. Two different gas types are used for the experiments: Propane 2.5 (purity 99.5 %) and technical nitrogen for inert purging after the tests.

The experimental setup was designed to measure the contact area of single liquid Propane droplets on various materials. Therefore it is necessary to evacuate with a vacuum pump and generate a saturated vapor atmosphere first. Subsequently liquid drops (fig. 4) with defined volume

($5.6 \cdot 10^{-9} \text{ m}^3$) are dripped onto the solid samples through a capillary tube, regulated by two needle valves. The saturation state is identified by means of temperature and pressure sensor.

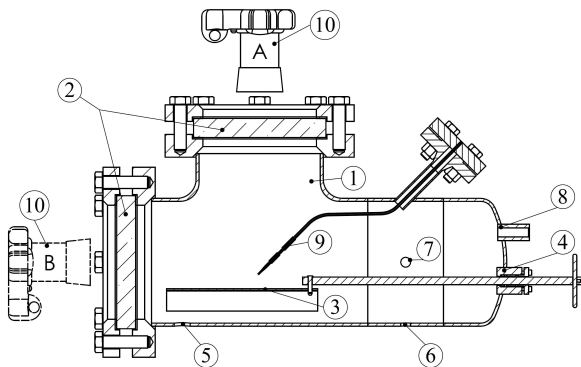


Figure 3. Autoclave (cross-sectional view)

- | | | | |
|-----|---|---|---------------|
| 1 | autoclave | 2 | sight glasses |
| 3 | object slide | 4 | slideway |
| 5 | gas inlet | | |
| 6 | connection to outlet and vacuum pump | | |
| 7/8 | connection pressure sensor / thermocouple | | |
| 9 | capillary for drop generating | | |
| 10 | CCD camera (position A or B) | | |

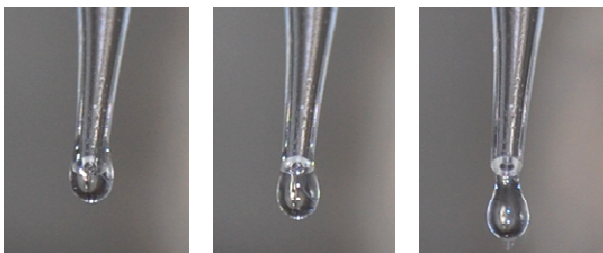


Figure 4. Propane droplet detaching from a glass capillary

Two sight glasses are located on the top and the left side of the autoclave. At the outside of the sight glasses an LED-ring light for illumination of the samples and a CCD-camera for photographic documentation of the wetting droplets can be installed. The camera can be placed either in position A (fig. 3) to detect the wetted area or position B for a profile-view of the droplet. The samples are located on a moveable object slide. Before the experiments the samples have to pass a cleaning process to remove oil-residues and dust.

The aim is to measure the wetted area of droplets. Hence the drop is photographed perpendicular from above by the CCD camera and evaluated by image analysis software. The contour line of the drop has to be framed manually and the software

afterwards calculates the wetted area from a defined scale. To determine this scale for the conversion of the measured pixel to an area, a rule is photographed together with the sample.

3. RESULTS AND DISCUSSION

3.1 Investigations of a geothermal heat pipe

The first experimental period was focussed on visual observations of the starting process next to the liquid pool. Furthermore the temperature distribution over depth was investigated.

Starting process

In fig. 5 a view on the liquid pool during the starting process is shown whereby fig. 5 (1a) presents the situation before the heat pump start. Approximately one sixth of the inner pipe surface is wetted, due to the first test runs. When starting the heat pump system the pressure inside the heat pipe decreases rapidly in the first seconds due to the highly subcooled heat sink at the heat pipes head. Propane vapor rises to the heat sink and condenses. The liquid Propane residues evaporate from the tube surface and the wetted area decreases rapidly in few seconds ($t < 25 \text{ s}$), fig. 5 (1b – 2a), until the dry surface is visible, fig. 5 (2b). Thus for the arriving liquid film it is always a first wetting.

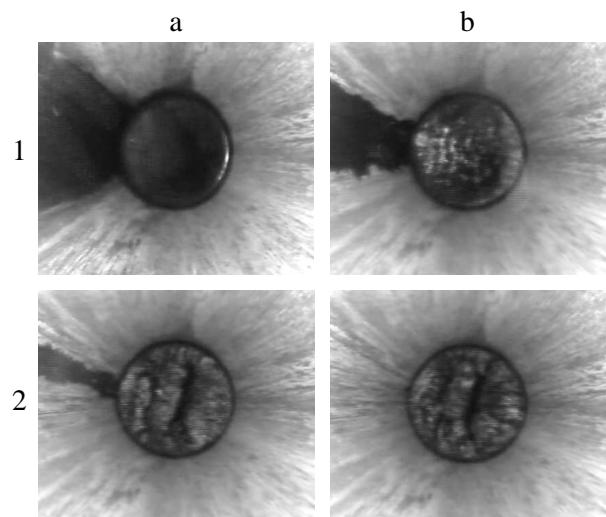


Figure 5. View on liquid pool during starting process: dry out, start pool boiling (86.5 m depth)

During the starting process evaporation starts from the liquid pool surface followed by transition to pool boiling – visible in fig. 5 (1b) – (2b), whereby the surface becomes cumulative billowy. Due to the rapid pressure decrease the liquid pool becomes superheated. Consequently a geyser-like

rising of the pool level up to 1 m in height by bubble and churn flow is visible (fig. 6). This state is time-limited ($100 \text{ s} < t < 240 \text{ s}$). Hence the pool level decreases in height (depth of camera position increases) and the bubble activity drops whereby the wetted surface dries out again (fig. 6 (b - c)).

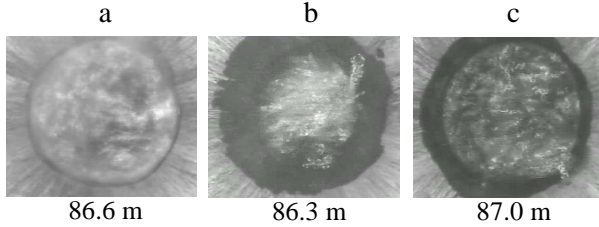


Figure 6. Liquid pool activity: increase from (a) - (b) with eruptive pool boiling, decrease (b) - (c)

Depending on several system parameters, e.g. T_{heatsink} and T_{rock} , etc., the liquid film created by the condensation process arrives at the liquid pool as a rivulet ($600 \text{ s} < t < 1000 \text{ s}$). Thereby the edges of the rivulet pulsates with continuous spreading and shrinking by evaporation. Besides that the arriving film is accompanied by a nebulous vapor (fig. 7 (a - b)). Temporally the nebulous vapor gets more transparent until it is only visible next to the rivulet edges, see fig. 7 (c).

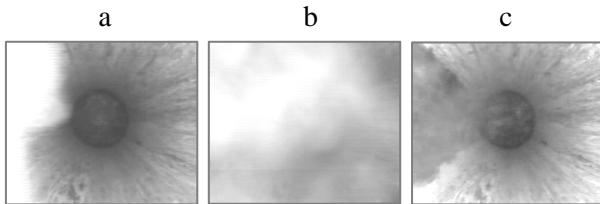


Figure 7. Arriving liquid film with nebulous vapor

In fact next to the liquid pool with respect to the low residual mass flow rate no closed liquid film was detectable. This effect is supported in case of an inclination of the heat pipe.

Long term operating regime

As mentioned above the first experimental period was focussed on visual observations of the starting process. Secondly, a continuous long term run of about 140 h of heat extraction without visual observations was realised. The temperature distribution over depth and the circulating mass flow rate were measured. The main data are given in table 1. No. (A) represents the beginning ($t = 4 \text{ min}$, $T_{\text{Propane}} \approx 273 \text{ K}$) and (B) the end of run ($T_{\text{Propane}} \approx 263 \text{ K}$). By assuming that the whole inner wall is wetted uniformly at the liquid inlet, Re_{film} (eq. 1) is about 1000 in maximum.

$$Re_{\text{film}} = \frac{\dot{m}_{\text{propane}}}{\pi \cdot d \cdot \mu_{\text{liquid}}} \quad (1)$$

$$Re_{\text{vapor}} = \frac{u_{\text{vapor}} \cdot d_{\text{equivalent}}}{\nu_{\text{vapor}}} \quad (2)$$

Table 1. Data of heat extraction with geothermal heat pipe (length = 91.5 m, $t \sim 140 \text{ h}$)

No.	\dot{m}_{Propane} (kg/h)	\dot{Q}_{source} (kW)	Re_{film} (1) (entrance)	Re_{vapor} (2) (head of heat pipe)
A	76	> 9.0	1000	66400
B	54	5.8	640	49100

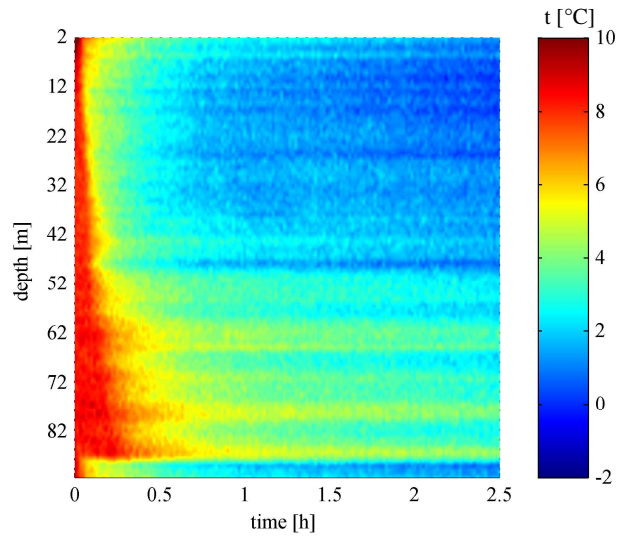


Figure 8. Temperature profile during first 2.5 h of heat extraction (measured with FOM)

At the beginning, the rock is thermally regenerated, e.g. the initial temperature profile has been reestablished. The extracted heat flow decreases in time from 9 to 5.8 kW after 6 days, as expected. In fact, for this short period the heat extraction rate was about 63 to 70 $\text{W}/\text{m}_{\text{length}}$. This is in the upper range for shallow geothermal systems, (VDI 4640 standard, 2010). Subsequently the temperature of the rock next to the heat pipe drops, see fig. 8. Though the decrease in temperature is not uniform over the depth, which is clearly visible for the first $\frac{1}{2}$ h. This compares very well with the visual findings about the liquid distribution and the period until the film arrives at the pool. Thus, during the first minutes ($t < 1000 \text{ s}$) pool boiling is the dominating heat transfer mechanism next to the bottom of the tube. This is important for the heat pipe design in case of cyclic operation.

3.2 Wetting of solid materials by liquid Propane

The smaller the surface tension of a liquid, the better wetting of a solid surface. Propane has a relatively low surface tension (7.5 mN/m at 20°C (VDI Heat Atlas, 2010)) and it belongs to the group of alkanes, thus it is completely nonpolar (Carter (2007)). A method called “Wetting Envelope” is known in the literature to predict the wetting behavior, see Feigl et al. (2010), Janssen et al. (2006). The wetting envelope is a special procedure to describe the relation between the contact angle and the polar (p) and dispersive (d) part of a solid’s surface energy. The correlation is defined by eq. 3, Feigl et al. (2010):

$$\frac{(1 + \cos \theta) \sigma_1}{2\sqrt{\sigma_i^d}} = \sqrt{\sigma_s^p} \sqrt{\frac{\sigma_i^p}{\sigma_i^d}} + \sqrt{\sigma_s^d} \quad (3)$$

If the polar and dispersive parts of the solid’s surface energy (σ_s) is known (from measurements), the wetting envelope can be plotted by setting the contact angle (θ) for example to zero and calculating pairs of values for the surface tension parts of the liquid (σ_l). The diagram has the format $\sigma_l^p = f(\sigma_l^d)$ and the curve is independent of any liquid. If a liquid’s surface tension pair of values σ_l^p , σ_l^d is located inside/under the curve, complete wetting is predicted; outside its contact angle would be larger than 0°.

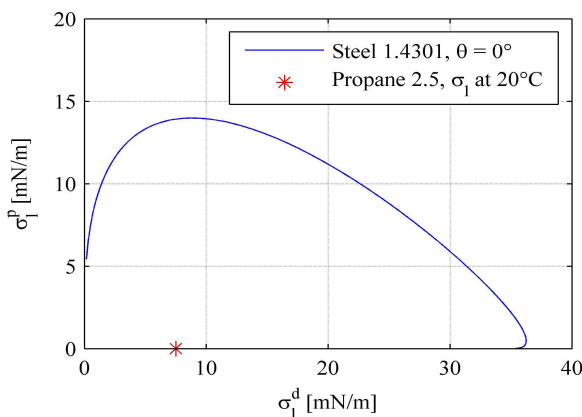


Figure 9. Wetting Envelope for steel 1.4301¹, Propane² is predicted to wet completely ($\theta = 0^\circ$)

Fig. 9 shows a wetting envelope for steel 1.4301 with surface energy values provided by Feigl et al. (2010). The surface tension of Propane is indicated, too. In consequence it is expected that the static contact angle of a Propane droplet is 0°.

¹ Feigl et al. (2010)

² σ_l from VDI Heat Atlas (2010)

That means the droplet will spread on the solid surface and result in complete wetting.

One aim of the present investigation was to compare various materials and surfaces concerning their wettability with liquid Propane. Materials of real heat pipes were investigated: steel, high grade steel, polyamide. Because the contact angle of Propane on the considered materials is too small for measurements with conservative methods, the contact area wetted by a liquid droplet on the sample was defined as the wetting criterion. The larger this area is, the better the samples wettability.

As predicted by the wetting envelope, experiments showed, that Propane wets very well on the examined surfaces. Once a single drop is positioned on the surface, the wetted area extends very fast with time, strongest within the first seconds and subsequently decreasing. This general behaviour was observed on all examined materials, see fig. 10. However there are differences in wettability of the various materials and surfaces. The experiments showed a better wettability of metallic surfaces compared to Polyamide (PA12).

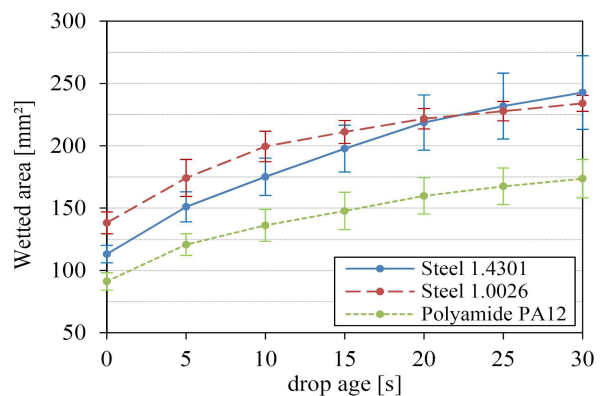


Figure 10. Measured wetted area of a liquid Propane droplet ($5.6 \cdot 10^{-9} \text{ m}^3$) on various materials

It has to be considered, that the measurements were done on samples of actual geothermal heat pipe tubes. In fact the surfaces are curved with equal curvature, however, the absolute areas are non-transferable to planar surfaces.

4. CONCLUSIONS

The starting process inside a special equipped geothermal heat pipe next to the liquid pool was investigated visually for the first-time. By starting the heat pump system the wetted pipe areas dries out immediately ($t < 25 \text{ s}$). Thus for the arriving

residual liquid film ($t > 600$ s), depending on several system parameters ($T_{\text{heat sink}}$, T_{rock} , etc.), it is always a first wetting situation. Simultaneously the liquid pool gets superheated and pool boiling starts with a geyser-like rising of the pool level at the beginning. The time dependent liquid distribution is also detectable in the temperature profile measured outside the pipe over depth with FOM. Thus, in the first period of time only the pool is cooled down by pool boiling. This is important for heat pipe design in case of cyclic operation.

For wetting research with liquid Propane an experimental facility was developed. It allows single droplet generation and the comparison of different surfaces regarding their wettability with optical measurement. The contact area between liquid droplet and solid sample is used as wetting criterion. The theory of Wetting Envelopes predicts complete wetting on steel ($\theta = 0^\circ$). Indeed, experiments on the first examined materials and surfaces (steel, high grade steel, polyamide) showed almost complete wetting. Liquid Propane droplets spread on all investigated materials and the contact area is strongly time-dependent. Nevertheless, differences in wettability are measurable. It appears that the wettability of the metallic samples (steel, high grade steel) is better than that of polyamide PA12.

Further work is concentrated on the time-dependent liquid distribution along the heat pipe length and on the processes inside in comparison to heat output and temperature profiles.

NOMENCLATURE

d	Diameter	[m]
\dot{m}	Mass flow rate	[kg/h]
Q	heat flow	[W]
Re	Reynolds number	
t	Time	[s]
T	Temperature	[K]
u	Velocity	[m/s]

Greek symbols

μ	Dynamic viscosity	[Pa·s]
θ	Contact angle	[°]
σ	Surface tension	[mN/m]
ν	Kinematic viscosity	[m ² /s]

Indices

d	dispersive;	l	liquid
p	polar;	s	solid

ACKNOWLEDGEMENT

We want to thank H. Fischer, A. Wahl, S. Schreiter and C. Zieger for their contributions.



REFERENCES

- Carter, K. (2007) *Organic chemistry*, 1. Ed., Global Media, Delhi.
- Feigl, M., Nofz, M., Sojref, R., Kohl, A. (2010) *Improved wetting of bare and pre-coated steels by aqueous alumina sols for optimum coating success*, J Sol-Gel Sci Technol 55, p. 191–198.
- Grab, T., Storch, T., Braune, S., Gross, U., Wagner, S. (2011) *Performance of a geothermal heat pipe using Propane*, in: Proc. of VIII Minsk Int. Seminar.
- Janssen, D., Depalma, R., Verlaak, S., Heremans, P., Dehaen, W. (2006) *Static solvent contact angle measurements, surface free energy and wettability determination of various self-assembled monolayers on silicon dioxide*, Thin Solid Films 515, p. 1433–1438.
- Kaltschmitt, M., Streicher, W., Wiese, A. (2007) *Renewable Energy: Technology, and Environment Economics*, Springer-Verlag Berlin Heidelberg.
- Nydahl, J., Pell, K., Lee, R. (1987) *Bridge deck heating with ground-coupled heat pipes: analysis and design*, ASHRAE Trans. 93, p. 939–958.
- Ochsner, K. (2008) *Carbon dioxide heat pipe in conjunction with a ground source heat pump (GSHP)*, Applied Thermal Eng. 28, p. 2077–2082.
- Storch, T., Grab, T., Zieger, C., Kupka, M., Gross, U., Wagner, R.M. (2011) *Visual observations inside a geothermal heat pipe*, in: Proc. of VIII Minsk Int. Seminar.
- Tanaka, O., Yamakaga, H., Ogushi, T., Murakami, M., Tanaka, Y. (1982) *Snow melting using heat pipes.*, in: D. Reay (Ed.), *Advances in heat pipe technology*, Pergamon Pr, Oxford, p. 11–23.
- Vasiliev, L.L., Vaaz, S.L., Grakovich, L.P., Sedelkin, V.M. (1982) *Heat transfer studies for heat pipe cooling and freezing ground.*, in: D. Reay (Ed.), *Advances in heat pipe technology*, Pergamon Pr, Oxford, p. 63–71.
- VDI Heat Atlas (2010), Ed.: VDI Gesellschaft, Springer Verlag, Berlin Heidelberg.
- VDI 4640 standard (2010), *Thermal use of the underground: fundamentals, approvals, environmental aspects*. Ed.: VDI, Beuth, Berlin.
- Weickert, T., Grab, T., Storch, T., Gross, U. (2011) *Investigations regarding the wetting behaviour of Propane on the surfaces of geothermal heat pipes*, in: Proc. of VIII Minsk Int. Seminar.

THERMOSYPHONS FOR HIGH POWER LED LIGHTING PRODUCTS

Valery M. Kiseev, Victor G. Cherkashin

Ural Federal University, Institute of Natural Science,
Lenin av. 51, 620083, Ekaterinburg, Russia,
Phone: (+7) 343-261-6775, Fax: (+7) 343-261-6778
e-mail: Valery.Kiseev@usu.ru

ABSTRACT

Extensive development of the light-emitting diode (LED) devices on the basis of LED matrix offers capabilities to occupy LED at the top place for the street and industrial lighting as one of the most reliable and energy-efficient devices. However, there are not enough experimental data on the optimization of the cooling systems for LED devices. Traditionally, the cooling systems for LED devices are designed with even pitch of LED locations on the radiator's surface. With the increase of LED power the radiator's surface and the distance between the LED locations grows correspondingly. It results in the increase of mass and size of the LED device. This paper presents some designs of two-phase thermal control systems for LED cooling on the basis of conventional thermosyphon (TS) and loop thermosyphon (LTS) and studies the experimental data, which were investigated for the two-phase systems considering the gravity influence. Additionally, the paper presents a comparative study between different working fluid, LED power and the radiators.

KEY WORDS: Two-phase thermal control system, conventional thermosyphon, loop thermosyphon, heat pipe, LED lamp, radiator, working fluid, heat transfer

1. INTRODUCTION

The main attractive quality of LED devices is its high level of luminous efficiency in comparison to alternative light sources. Therefore, employing LED technology may result in different economic and social effects. The most important effect among others is a considerable reduction in electrical energy consumption, used for illumination purposes, which, according to different estimations, is about 18-20% of overall produced electricity (http://thecleanrevolution.org/assets/files/LED_report_web1.pdf). The comparison of available light sources is presented in Table 1.

Although LED lamps are more than 50 times as expensive as bright white lamps and about 7 times as expensive as compact luminous lamps, the price has been decreasing recently. Assuming that the characteristics improve and the price reduces, it is predicted that within a few years LED sources will be used in the majority of lighting systems.

However, some of the factors that prevent LED from wide application should be taken into

account. Thus, diode's parameters are very sensitive to working temperature, applied voltage, current etc. (<http://www.osram-os.com>). For example, when the temperature of a diode is more than 80°C the luminous efficiency reduces, while at 120 C° it tends to zero (Staroverov K., 2008).

Table 1. Characteristics of light sources

Light source type (LS)	Luminous efficiency of LS, lm/W	Efficiency of lamps with respective LS, lm/W	Life time, hours
Glow lamp	8-13	6-10	1 000
halogen lamp	16-37	12-20	50-6 000
Compact luminous tube lamp	50-70	35-50	6 000-15000
metal-halide lamp	60-100	<40	6 000-10 000
luminous tube lamp	60-100	55-70	15 000-32000
Semiconductor LED (Cree XR-E)	100-110	90-100	>50 000
Sodium high-pressure lamp	90-130	<50	15 000-32000

Moreover, the lifetime decreases significantly. In order to deal with all the above mentioned problems it is required to develop and employ an efficient method of heat removing, i.e. new LEDs or LED matrices which possess the maximal heat diffusion ability are needed.

Similar problems with thermal control exist in other fields such as space and aircraft industry, semiconductor industry, etc. In order to deal with these problems two-phase thermal control systems – heat pipes and devices based on them are often used (Dan P., Ray D., 1979; Faghri A., 1995)

Therefore, the goal of this work was to develop and study cooling technologies of LED matrices that have the output of more than 30 W using effective heat sinks – loop heat pipes (Gerasimov Yu.F. et al., 1975), including the most simple of them: loop thermosyphons (Kiseev V. M. et al, 1992) and conventional thermosyphons (Pioro A. S., Pioro I. L., 1988;).

2. DEVELOPMENT AND STUDY OF TWO-PHASE THERMOSYPHONS FOR LED MATRICES COOLING

2.1. The schematic diagram of a loop two-phase thermosyphon (LTS).

The schematic diagram of a loop two-phase thermosyphon is shown in Figure 1. When voltage is applied on diode 2 it begins to glow and produces heat energy, which then is passed through substrate 9 to the liquid located at liquid cavity 7 of evaporator 1. Depending on the density of heat flux, the liquid boils or evaporate and becomes vapor, consuming latent heat of vaporization. During this process the vapor's pressure in a vapor cavity 8 is higher than the one in condenser because of the temperature difference between them, so the vapor travels through the vapor line 3 to the condenser 4, where it condenses with release of latent heat of condensation and becomes a liquid. Then the released heat is transferred to the condenser 4 and eventually by means of the radiator 6 to the environment. The liquid, influenced by gravity or capillary forces, drains through liquid line 5 back into the liquid cavity 7 and, therefore, encloses the evaporation-condensation heat transfer cycle.

The proposed LTS design allows to transform the heat energy from light emitting diodes compactly situated on metal substrate, which has smaller size

than the radiator, as well as, it allows to spatially separate the heat input and output. The lack of moving parts as well as the benefits mentioned above positively affect LED devices, allowing to easily arrange the radiator at places with the most intensive heat transfer and where natural or forced convection takes place. This results in lower power consumption, illumination efficient increase of LED matrix and lifetime expansion alongside the overall rise of reliability.

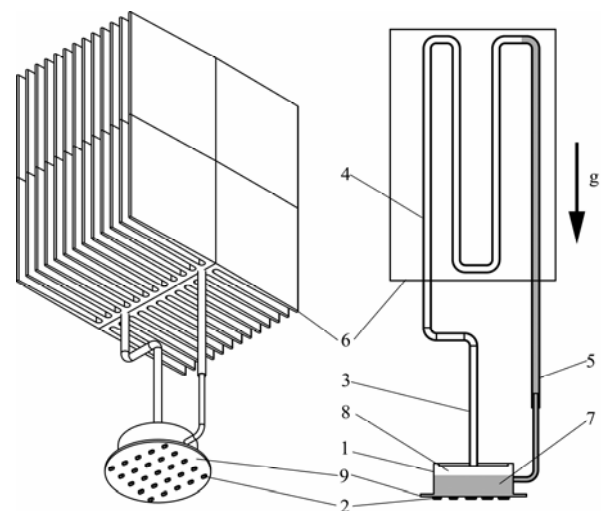


Figure 1. The schematic diagram of loop two-phase thermosyphon (LTS) for LED cooling. 1 – evaporator, 2 – diodes; 3 – vapor line; 4 – condenser; 5 – liquid line; 6 – radiator; 7 – liquid cavity of evaporator; 8 – vapor cavity of evaporator; 9 – LED matrix

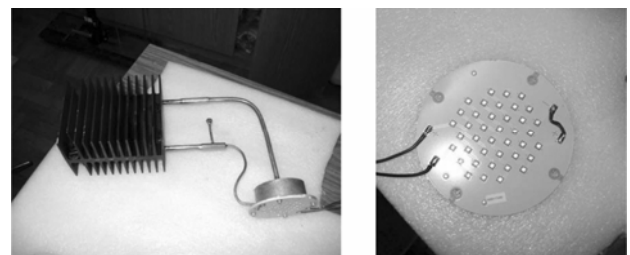


Figure 2. Loop thermosyphon (LTS No 1) with LED matrix (on the right)

Figure 2 shows the photograph of developed experimental LTS for cooling LED matrices (on the left) and a LED matrix with 20 to 40 diodes (Osram. Germany) located on the aluminum plate, which is 1.7mm in thickness and 80mm in the diameter (on the right). To reduce the number of light emitting diodes and correspondingly the overall price of the device, the nominal load per diode has been increased up to 3.6 W, whereas in

most cases 1 Watt per diode is used. The reduction of luminous efficiency, caused by the increase of nominal load from 0.35 A to 1 A, were about 24% of the nominal.

The evaporation chamber of the studied LTS was made of copper, tablet-shaped with 60mm inner diameter and 25mm wall thickness respectively. The vapor line and the coil condenser (4 loops with step 25mm) were made of copper tube with inner diameter of 4, 1mm thickness. For the condenser line a copper 2x0.5mm tube was used.

Radiator 6 is composed of two standard finned radiators, which are 125x98 mm and 125x196 mm with the fin's length of 39mm and 46mm for LTS No 1 and LTS No 2 respectively. The total finned surface of radiator was 0.20 m² for the LTS No 1 and 0.48 m² for the LTS No 2 respectively. On the finless surfaces of radiators grooves for the coil condenser were made. Two halves of the radiator with applied thermal interface were fastened together by bolts so that the coil condenser was between the halves, inside the radiator as it is shown in Fig 1.

The material of LTS No 2's radiator is aluminum. In order to test thermal characteristics of heat-conducting composite plastic with thermal conductivity of 8 W/m K (Krivatkin A., Sakunenko Yu., 2010) (Teplostok T6-E5-7, SpecPlast-M ltd, Russia), the comparison of the aluminum radiator and the radiator made of the plastic have been conducted. The dimensional parameters of the radiators were the same.

2.2. The schematic diagram of the conventional two-phase thermosyphon (CTS)

The schematic diagram of the conventional two-phase thermosyphon is presented in Figure 3. The illuminating device works in the following way. When voltage is applied on diodes 4, they begin to glow and produce heat energy, which then is passed through substrate 3 to liquid 2 located at the bottom part of chamber 1. Depending on the density of heat flux, the liquid boils or evaporates and becomes vapor, consuming latent heat of vaporization that for most liquids exceeds the thermal conductivity for hundred times. After that, the vapor travels to the above part of chamber 1, where it condenses and becomes a liquid with release of latent heat of condensation, which is then transferred to environment by means of radiator 5. The originated condensate 6 drains on

the inner wall surface back into the bottom part of chamber 1, thereby enclosing the evaporation-condensation heat transfer cycle.

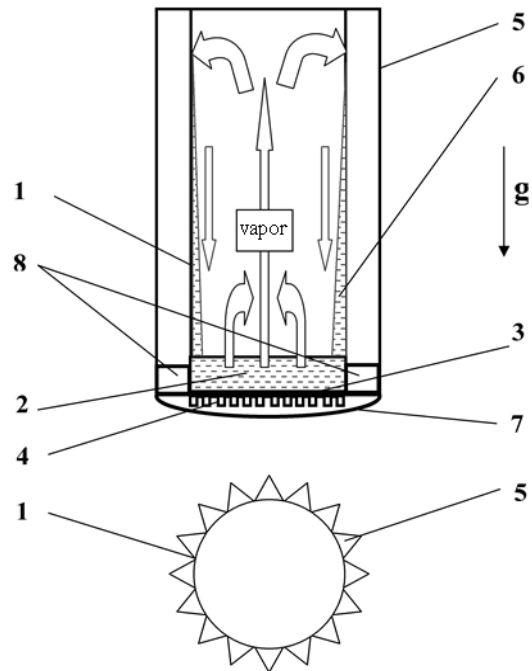


Figure 3. The schematic diagram of conventional thermosyphon (CTS)

1 – evacuated hermetic chamber – two-phase closed thermosyphon, 2 – working fluid, 3 – heat-conductive metal substrate, 4 – LEDs, 5 – radiator's fins, 6 – condensate, 7 – optically transparent cover, 8 – power supply with functional sensors

The heat-transfer system, from which the air has been evacuated, is filled with working fluid that has a freezing point lower than the lowest climatic temperature specific for the region. For instance, in southern regions, where the air temperature in winter time is not lower than +5 °C, pure distilled water might be used as a working fluid, while in northern regions, where the air temperature could possibly be below +5 °C, the working fluid might be methanol, acetone and ethanol, the freezing temperature of those are below – 60 °C.

The proposed CTS design allows to transform the heat energy from light emitting diodes compactly situated on metal substrate, which has smaller size than the radiator, as well as to spatially separate the heat input and output. The lack of moving parts as well as the benefits mentioned above positively affect LED devices, allowing easily arrange the radiator at places with the most intensive heat

transfer and where natural or forced convection takes place. This results in lower power consumption, illumination efficient increase of LED matrix and lifetime expansion alongside the overall rise of reliability. Figure 4 shows the photograph of developed experimental CTS for cooling LED matrices and a LED matrix with 20 to 40 diodes (Osram, Germany) located on the aluminum plate, which is 1.7mm in thickness and 80mm in the diameter. To reduce the number of light emitting diodes and correspondingly the overall price of the device, the nominal load per diode has been increased up to 3.6 W, whereas in most cases 1 Watt per diode is used. The reduction of luminous efficiency, caused by the increase of nominal load from 0.35 A to 1 A, were about 24% of the nominal.

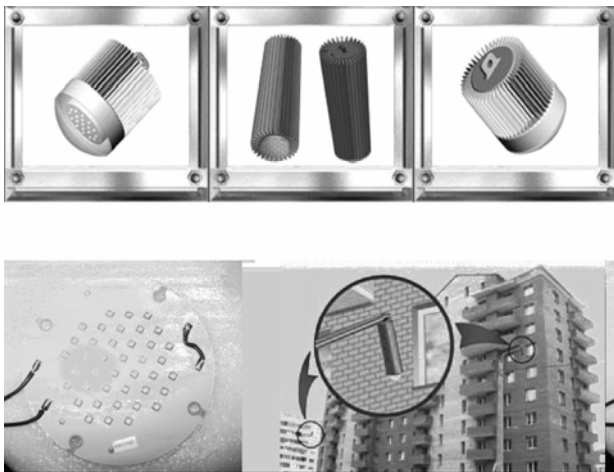


Figure 4. The conventional thermosyphon with LED matrix and the LED matrix (left-bottom)

3. EXPERIMENTAL APPARATUS AND PROCEDURE

The experimental setup was designed to measure temperature on different points of thermosyphon versus nominal power load N applied directly to LED matrix or versus a heat load Q . The local temperatures on LTS characteristic points were measured by thermocouples or the infrared imager (Fluke Ti32). Thermocouples were located as follows. One thermocouple was placed on the heat input zone, on the middle part of the LED matrix or on the middle part of the evaporator's shell between the electric heater and the evaporator. (label T_h). Two thermocouples were mounted on the vapor line and the liquid line, one on the outlet of the evaporator (label T_v) and one on the inlet of the evaporator (label T_l) respectively. The

environmental temperature T_{env} was measured as well. All thermocouples were connected to data acquisition system (Owen TRM-148).

The experimental LED illuminating device based on a conventional thermosyphon and the locations of thermocouples is shown in Figure 5. For this series of experiments the device were made of aluminum and the total external surface for heat exchange with environment was $S_p = (0.336 \pm 0.004) \text{ m}^2$, while the CTS's mass was $m_{cts} = (2.40 \pm 0.05) \text{ kg}$.

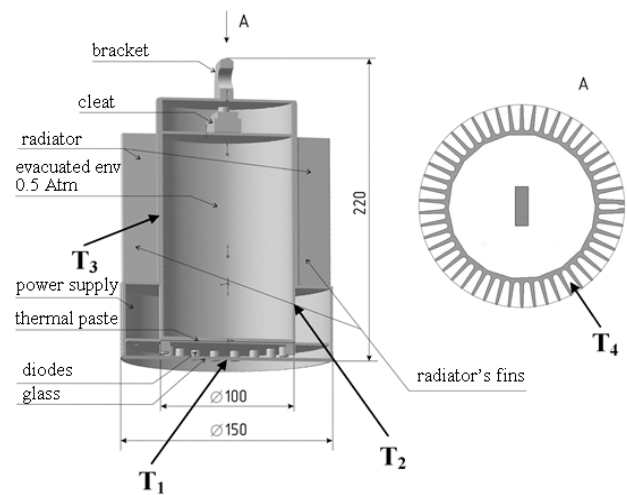


Figure 5. Experimental LED illumination device and the thermocouples' locations

4. RESULTS AND DISCUSSION

Figure 6 represents a typical experimental curve for LTS No 2 with water as a working fluid. From the graph it is seen, that under a low heat load the oscillations of measured temperature with the magnitude up to 3-4 degrees occur. However, the magnitude considerably decreases with a rise of the heat load.

One of the goals of this work was to compare the thermal characteristic of heat conductive plastic against the ones of traditional materials, such as aluminum. To do so, two geometrically identical radiators, one of the plastic and the other of traditional aluminum, were made. Figure 7 below shows the results of the comparison.

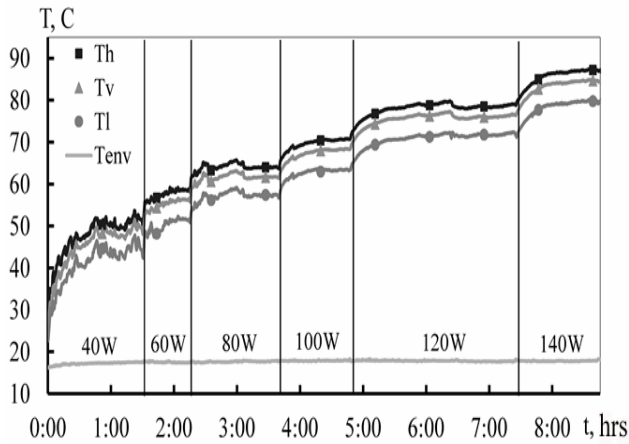


Figure 6. Working temperatures (T) of LTS No 2 (working fluid - water) for various heat loads (Q)

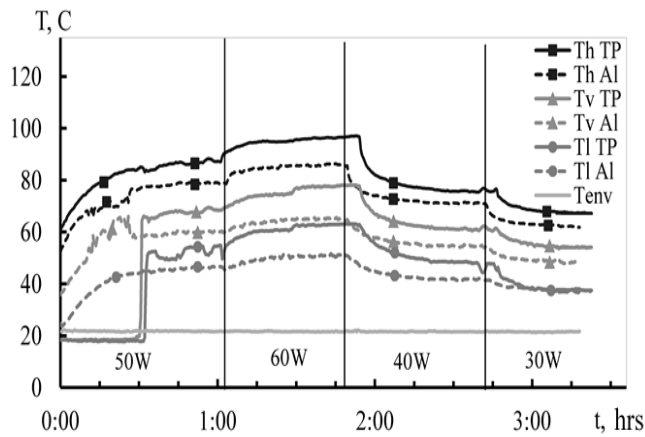


Figure 7. Working parameters for LTS No 1. Comparison of aluminum (Al) radiator and heat-conductive plastic (TP) radiator.

From the data above it is followed that the heat conductive plastic, having a relatively low thermal conductivity of 8 W/m K compared to aluminum and its alloys ($220 - 180 \text{ W/m K}$), is suitable for heat sink within a natural convection condition. During these series of experiments, when the aluminum radiator was replaced by the TP radiator, the temperature on heat input zone increased by 4-8 per cent depending on the heat load (other conditions were kept the same).

Figure 8 represents the results of test for the conventional thermosyphon with acetone as a working fluid depending on an input power. In addition, a possibility to employ water as a working fluid, supposing its chemical compatibility with thermosyphon's materials and

the ability to work under temperatures below 0°C , is of interest as water is non-toxic and easy-to-work with.

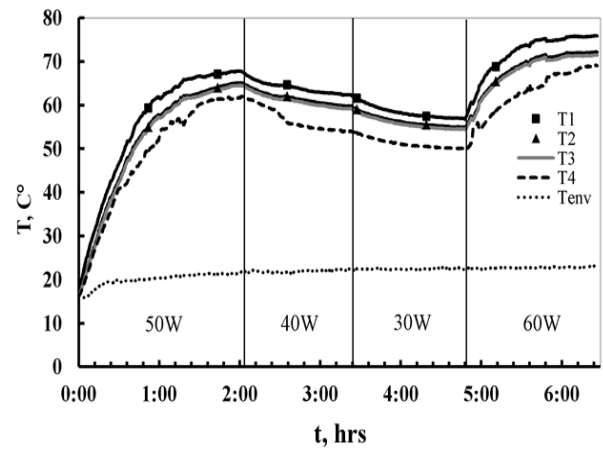


Fig. 8. The temperature field as a function of time and power. Working fluid – acetone.

Below, in Fig. 9 a typical experimental dependence of the heat zone temperature on time t is shown. In this experiment the working fluid was frozen and the heat load on thermosyphon Q was 50 W . When the temperatures are about 0°C the phase transition "ice-water" occurs, which is seen as a small step on the curve. Then, with the rise of temperatures the device's working regime changes to the normal two-phase one.

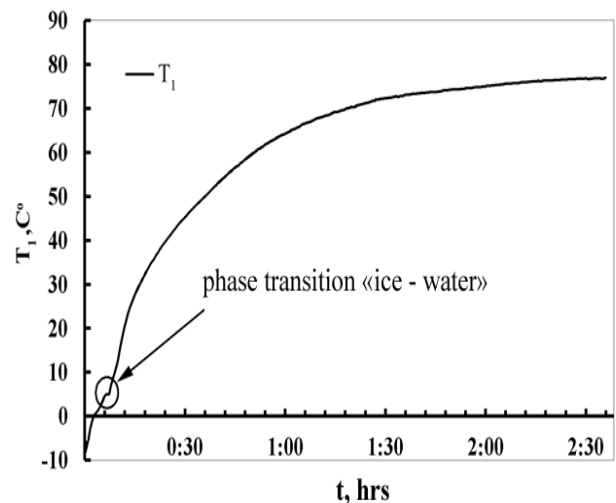


Fig. 9. Startup diagram $T_1 = f(t)$ from frozen state of working fluid (water) under nominal heat load $Q = 50 \text{ W}$ and the environmental air temperature $T_{env} = (24 \pm 1)^\circ\text{C}$

This study has shown that all working parameters of thermosyphon filled with water remained the

same for both normal conditions and when the phase transitions occurred. Additionally, no mechanical damages or changes in the geometry of the thermosyphon were observed. This can be explained by a relatively small portion of the water in the internal volume of the device, about 2.5 per cent of the volume. Considering all the factors, water may be recommended as a working fluid for two-phase thermosyphons; however, some of limits such as chemical compatibility, relatively small volume of liquid, should be taken into account.

5. CONCLUSIONS

1. A thermal control system for LED cooling based on the loop thermosyphons has been proposed. The advanced study of loop thermosyphons has been performed and it has been shown that these systems might be applied in the LED device's cooling.
2. A thermal control system for LED cooling based on the conventional thermosyphons has been proposed. The diverse study of conventional thermosyphons with flat end heat input has been performed and it has been shown that these systems might be applied in the LED devices cooling.
3. The comparative analysis of aluminum radiators and heat-conductive plastics has been performed. It was shown that the heat conductive plastics, low-cost, low-weight and easy-to-process material, have a great potential in thermal applications.
4. Using of thermosyphons allowed to raise the nominal load per diode to 3.5 W (as a rule 1 W) by decreasing the number of diodes more than tree times, while the reduction of luminous efficiency was no more than 24%.

REFERENCES

- http://thecleanrevolution.org/assets/files/LED_report_web1.pdf. WWW.CLEANREVOLUTION.ORG
<http://www.osram-os.com/>
Staroverov K. (2008) *Cooling systems for LED*.
Novosty Elektroniky. v. 17. p. 21–23 (In Russian)
Dan P., Ray D. (1979) *Heat pipes*. Energia, Moscow, (in Russian)
Faghri, A. (1995) *Heat pipe science and technology*. Taylor & Francis, London
Gerasimov Yu.F., Maydanik Yu.F., Shegolev G. T., Filippov G. A., Starikov L. G., Kiseev V. M., Dolgirev Yu. E. (1975) *Low temperature heat pipes with separated channels for vapor and*

liquid. Inzhenerno-Fizicheskii Zhurnal. v. 6. p. 957 (in Russian)

Kiseev V. M., Pogorelov N.P., Menkin L. I. (1992) *The study on two-phase thermosyphon application for mock-up fuel elements temperature regime modeling*. Proc. of the 8th IHPC. Beijing. p.673.

Pioro A. S., Pioro I. L. (1988) *Two-phase thermosyphons and its applications in industry*. Naukova dumka, Kiev (in Russian)

Krivatkin A., Sakunenko Yu. (2010) *Heat conductive plastics - challenge to aluminum*. Solid-state lightning. v. 1. p. 54. (in Russian)

A STUDY ON THERMAL CONDUCTANCE IN A LOOPED PARALLEL THERMOSYPHON

Fumito Kaminaga, Kunihiro Matsumura, Ryo Horie
Department of Mechanical Engineering, Ibaraki University
4-12-1 Nakanarusawa, Hitachi 316-8511 Japan

Phone: +81-294-38-5035, Fax: +81-294-5047, E-mail: kaminaga@mx.ibaraki.ac.jp

Akira Takahashi

Fukushima National College of Technology

30 Nagao, Kamiarakawa, Taira, Iwaki, 970-8034 Japan

Phone: +81-246-46-0784, Fax: +81-246-46-0792, E-mail: a-taka@fukushima-nct.ac.jp

ABSTRACT

The purpose of this study is to experimentally examine a practical heat transfer performance of the looped parallel thermosyphon which consists of two single tube thermosyphons connected by two U tubes at the top and bottom ends. Experiments are conducted in the thermosyphon and also a conventional single tube thermosyphon with a similar size and arrangement for different cooling temperature and charge ratio using water and ethanol working fluids. The major findings are as follows: Wall temperature profile in an evaporator section is more flat for ethanol working fluid in the loop type, but for the water working fluid it is almost similar between the thermosyphons. The thermal conductance variation relating to heat transfer rate is almost similar between the thermosyphons. For the water working fluid the effect of cooling temperature and charge ratio on the conductance is distinct, but for the ethanol the effect is negligibly small. The amount of thermal conductance shown in the present study is about one third of that shown in the previous study in which a thermosyphon with small heat capacity evaporator and condenser sections was tested. The advantage of the loop type as a heat transfer device is to produce an increase of maximum heat transfer rate.

KEY WORDS: Thermosyphon, thermal resistance, heat transfer rate

1. INTRODUCTION

In order to remove a large heat rate from electric or electronic devices such as a power transistor a multiple installation of a single tube type thermosyphon, which is referred to a single type in this paper, as shown in Fig.1(a) is commonly used as a compact and efficient heat exchanger. But current large increase of the heat rate, such as a heat release from a power transistor used in an electric vehicle, has made a conventional single type to have an insufficient performance to transmit the heat from the devices. Since the maximum heat transfer rate in the conventional thermosyphon is mainly determined by a countercurrent flow limitation between upward vapor flow and downward liquid film flow, the rate is not large enough. Other defects of the conventional thermosyphon consisted of a single tube are non-uniform wall temperature of an evaporator section and large deterioration effect of non-condensable gas on condensing heat transfer. At an upper part of an evaporator section boiling or film evaporation is fully developed, but at a lower part of it boiling is

partially developed or does not occur. The wall temperature in an evaporator section, therefore, has a profile such as low at the upper part and high at the lower part. Non-condensable gas which gives large heat transfer deterioration is normally accumulated in an upper part of a condenser section since a top of thermosyphon tube is a dead end. Those defects can be resolved by giving a circulation of a working fluid in a thermosyphon using a loop thermosyphon as shown in Fig.1 (b).

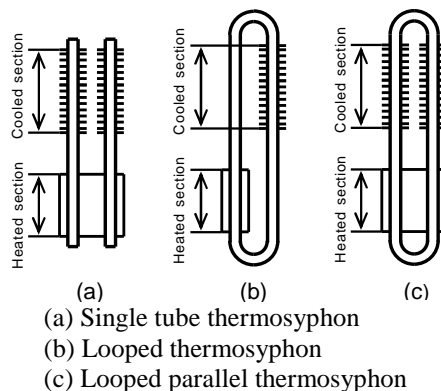


Fig.1 Types of thermosyphon

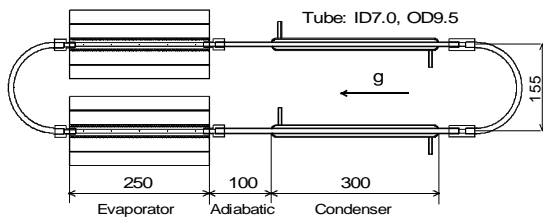


Fig.2 Loop type thermosyphon used in the previous study

But the evaporator and condenser section area is half of the single type, which is a problem for compact space application. In order to make use of the total heat transfer area in the loop thermosyphon, a looped parallel thermosyphon, which is referred to a loop type in this paper, having a combination of two single types joined at top and bottom by two U-tubes, has been developed (Kaminaga, 2003). A fluid flow fluctuation by boiling in the evaporator section is observed, which improves the inside heat transfer characteristics.

In previous studies (Kaminaga, 2003, 2004, and 2007, Takahashi, 2008) fundamental heat transfer characteristics in the loop type were investigated. In those studies wall temperature distribution in evaporator section, heat transfer in evaporator and condenser sections, maximum heat transfer rate, and non-condensable gas effect were experimentally examined using the test loop shown in Fig. 2.

In the present study heat transfer performance of the loop type thermosyphon is experimentally examined using a test loop which is designed for a practical application for electric or electronic device cooling. The single type with the same geometry as the loop type is also tested for comparison.

2. EXPERIMENTAL APPARATUS

The schematic diagram of the experimental apparatus is shown in Fig. 3. The thermosyphon test loop consists of three sections, evaporator, adiabatic, and condenser and is vertically oriented. Detailed dimensions of the thermosyphons, the loop and the single types, are shown in Fig. 4. The evaporator section is made of a copper block, 100mm high, 100mm wide, and 16mm thick. In a center of the block two copper tubes, 9.5mm OD and 7.5 mm ID, are inserted and a gap between the block and the tubes are soldered to have a good thermal contact. To measure wall temperatures on the evaporator section six sheathed K-type thermo-

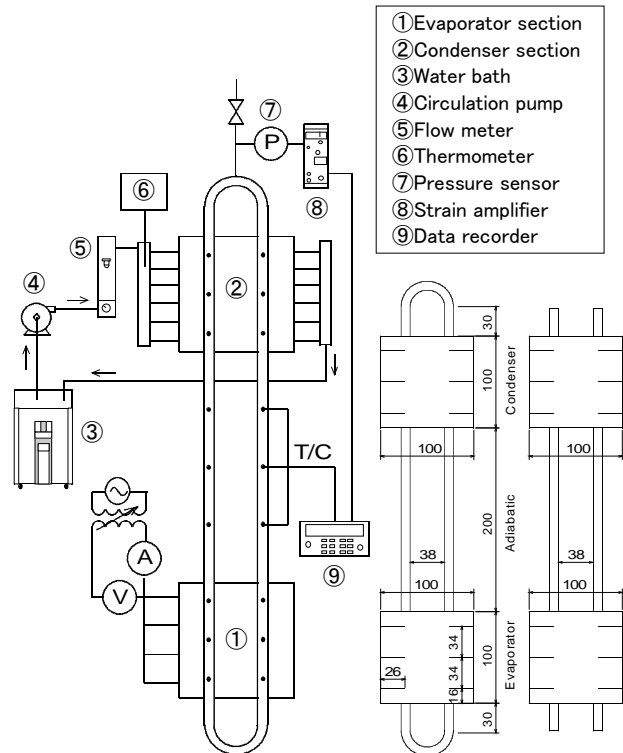


Fig.3 Experimental apparatus Fig.4 Dimensions of thermosyphons

couples with a 0.5 mm diameter are embedded in grooves at three elevations and both sides. The measured points are located at the center of the tubes. The block and tubes at the condenser section are fabricated with the same size and arrangement as the evaporator and the thermocouples are also attached at the same locations. For the loop type, the both tubes are connected by U-tubes with the same inside diameter at the top and the bottom and for the single type, both ends of two tubes are plugged. The adiabatic section, 200mm long, is made by the same copper tube. To measure wall temperatures on the adiabatic section six K-type bare thermocouples with a 0.1 mm diameter are attached on the tube at three locations on each side. The evaporator section is heated from both sides by two same size heater blocks, 100mm high, 100mm wide, and 15mm thick, including four 400W cartridge heaters. The heater block is pinched by a ceramic plate and an auxiliary rubber heater to compensate a heat loss. The power of the rubber heater is controlled for the difference between wall temperatures on both sides of the ceramic plate to be negligibly small. The condenser section is cooled from both sides by two same size cooling jackets, 100mm high, 100mm wide, and 16mm thick, each of which includes six horizontal holes, 8.6mm in diameter, for a water coolant flow path. A phase change material is used

Table 1 Experimental conditions and their ranges

Working Fluid	Charge Ratio, V^+	Coolant Temp., T_f ($^{\circ}\text{C}$)
Ethanol	0.3	25
Water	0.6	35
	0.9	35

to reduce a contact resistance between the condenser plate and the cooling jacket. A water coolant flows in the holes through an inlet header of the jacket with a constant temperature and flow rate. Coolant temperatures in the inlet and outlet header are measured by a thermistor thermometer. Two conditions for the inlet coolant temperature, 25 and 35 $^{\circ}\text{C}$, are tested. The whole of the test loop is insulated by a rock wool insulator with a 30 mm thickness. To measure time variations of system pressure an absolute pressure sensor is installed at the top end of the U-tube for the looped and of one tube for the single type. A vacuum pump is equipped at the top of the loop to remove non-condensable gas contained in the tube before the experiments.

An input power to the heater in the evaporator section is increased stepwise. The power is increased until the wall temperature on the evaporator plate is round 200 $^{\circ}\text{C}$. The measurements are made under a steady state condition at each input power. Water and ethanol are used as working fluids. The experimental parameters are a fill charge ratio and a coolant temperature. The range of the parameters is shown in Table 1.

3. RESULTS AND DISCUSSIONS

3.1 Operating system pressure

To estimate an operating system pressure in a thermosyphon a wall temperature at an adiabatic section is normally used since in that section a saturated condition is nearly obtained. Figure 5 (a) and (b) show comparison of measured wall temperature with saturated temperature corresponded to measured pressure in the loop type for ethanol and water working fluids, respectively. These figures indicate that for the ethanol working fluid, the saturated temperature is at most 5% larger than the wall temperature and this tendency is independent of the coolant temperature and the charge ratio. For the water it is about 3 to 7 % larger and the difference is larger for the charge

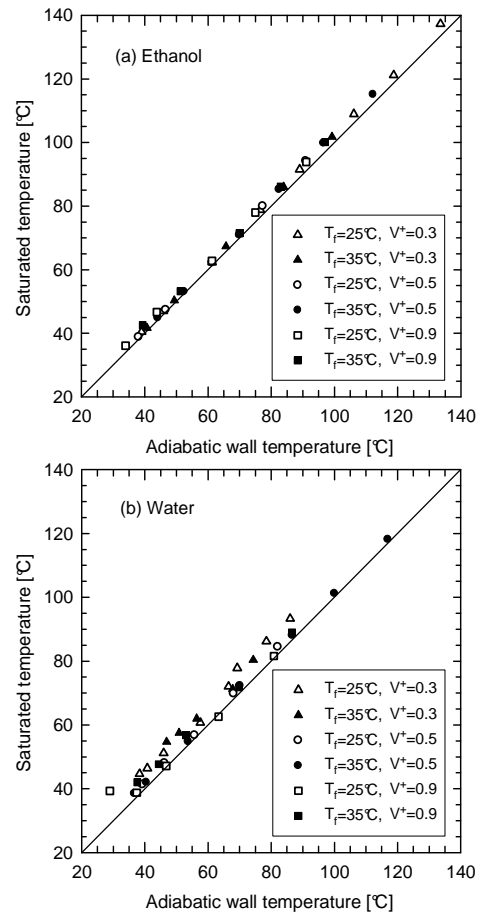


Fig.5 Saturated temperature versus adiabatic wall temperature

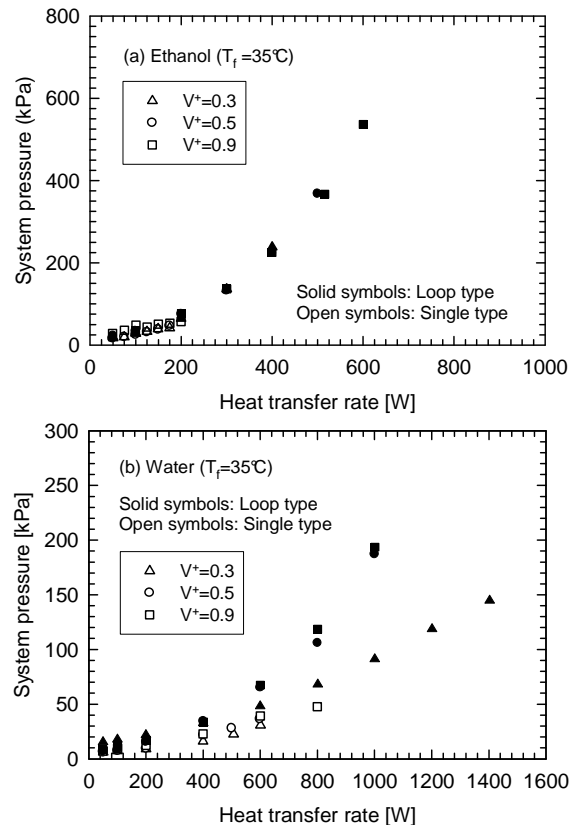


Fig.6 System pressure variations

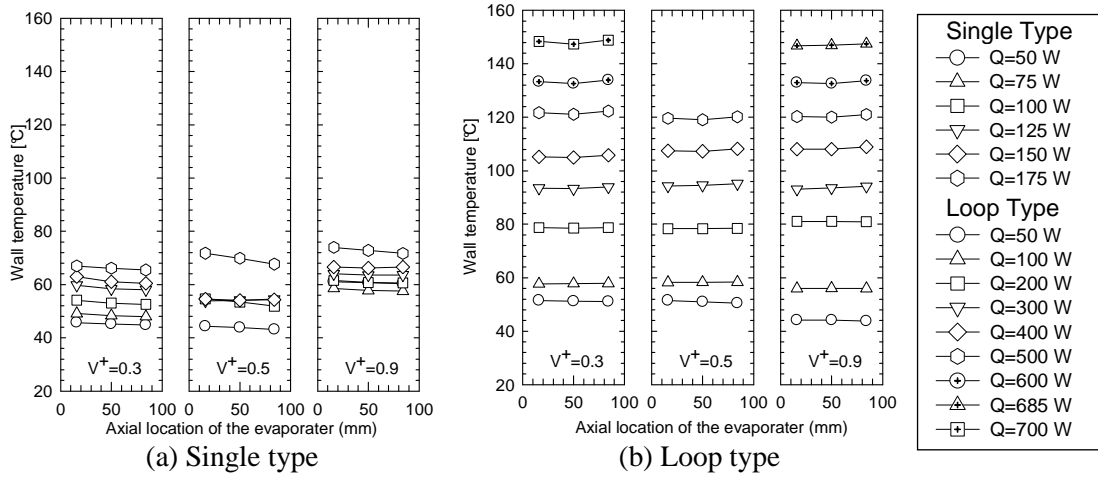


Fig.7 Wall temperature profiles in evaporator section for ethanol working fluid

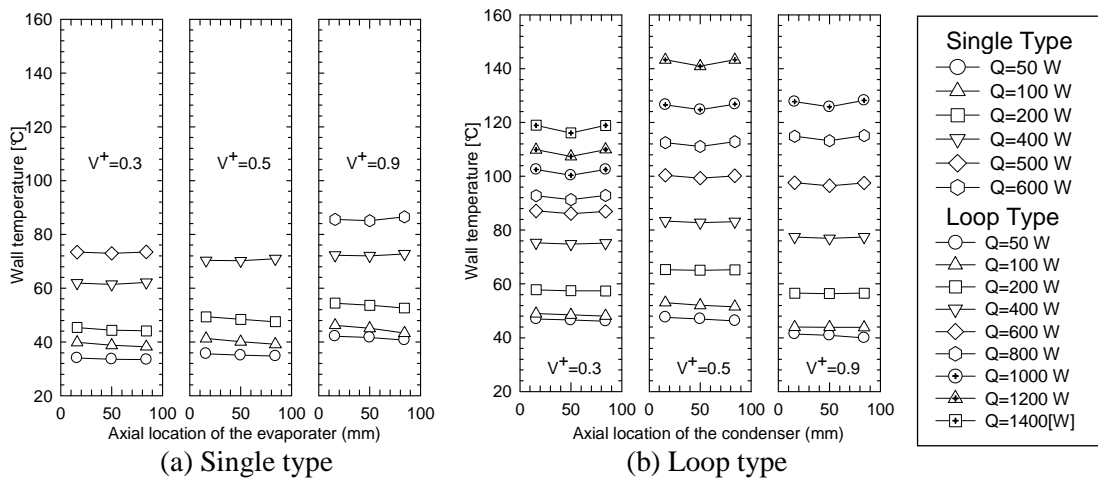


Fig.8 Wall temperature profiles in evaporator section for water working fluid

ratio of 0.3. The larger difference shown in the small charge ratio might be due to less enough mixing between subcooled fallback liquid from the condenser section and upward vapor from the evaporator section. These two figures indicate that the wall temperature in an adiabatic section can be used to estimate the inside pressure of the loop type thermosyphon, based on an assumption of a thermal equilibrium.

The operating system pressure variations relating to heat rate transferred from evaporator to condenser at a condition of 35°C coolant temperature are shown in Fig.6 (a) and (b) for the ethanol and the water working fluids, respectively. For the ethanol shown in (a), the variations are similar between the single and the loop types and it is independent of the charge ratio. For the water, the variations at $V^+ = 0.3$ condition in the loop type is similar to those at all charge ratios in the single type, but those at $V^+ = 0.5$ and 0.9 condition in the

loop type are different from the others. This tendency is similarly shown at a condition of 25°C coolant temperature.

3.2 Wall temperature profile on evaporator

Figures 7 and 8 show wall temperatures measured at three elevations in the evaporator section for the single and the loop types for ethanol and water working fluids, respectively. For the ethanol working fluid as shown in Fig. 7 the temperature at a lower part of the evaporator section for the single type shows a little larger value than that at an upper part, and for the loop type the temperature difference between lower and upper parts is a little smaller. Compared at same heat transfer rate, the profiles are not so different between both types since the volume of the evaporator section made by copper is large enough to obtain a uniform wall temperature. However, at a high heat transfer rate and low charge ratio condition, the profile gradu-

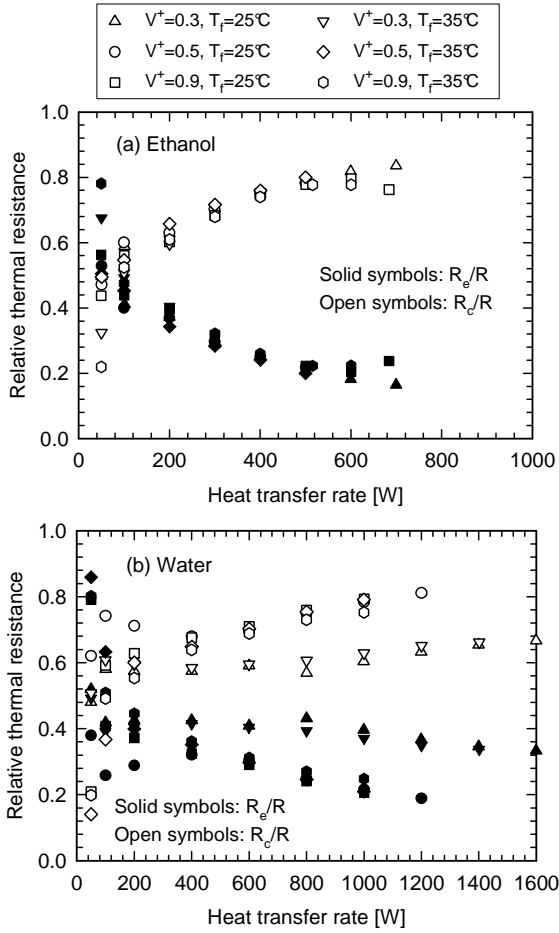


Fig.9 Relative thermal resistance in evaporator and condenser sections

ally changes to be one with a higher temperature at a lower and higher part. For the water working fluid as shown in Fig. 8, the temperature profiles are more similar between single and loop types at the same heat transfer rate, but beyond the maximum rate for the single type the temperature shows the profile which is indicated at a higher heat rate for the single type. This result is quite different from the result in the previous study (Kaminaga, 2004 and 2007) in which the loop type gave much more flat profiles for the water working fluid since in the previous study a heat capacity in the evaporator section is much smaller than that in the present study.

3.3 Thermal conductance

To evaluate heat transfer performance a thermal conductance, C , which is defined by Eq.(1) for the single and the loop type is examined.

$$C = \frac{1}{R} = \frac{1}{R_e + R_c} \quad (1)$$

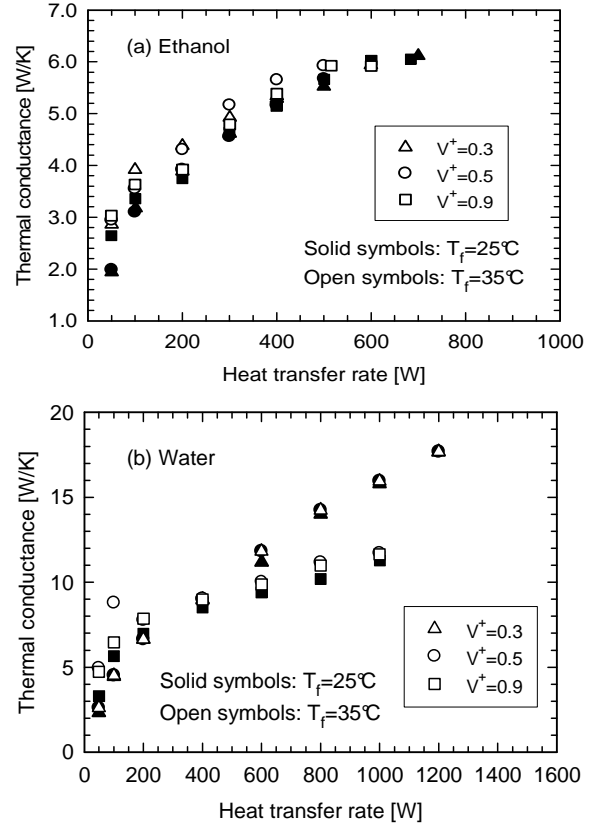


Fig.10 Total thermal conductance

where, R_e is thermal resistance in the evaporator section and R_c is in the condenser section defined by Eqs. (2) and (3), respectively.

$$R_e = \frac{T_e - T_s}{Q} \quad (2)$$

$$R_c = \frac{T_s - T_c}{Q} \quad (3)$$

where, Q is heat transfer rate from evaporator to condenser sections, T_e is an average value of wall temperatures measured on the evaporator section, and T_c is an average value of wall temperatures measured on the condenser section.

Figure 9 (a) and (b) show relative thermal resistances in the evaporator section, R_e/R , and in the condenser section, R_c/R , on conditions of three charge ratios and two coolant temperatures in the loop type for the ethanol and water working fluids, respectively. For the ethanol fluid, the effect of the charge ratio and coolant temperature on both thermal resistances is small. For the water fluid, the effect of those parameters is different such as the effect of the coolant temperature is small but the charge ratio's effect is large. At a low charge

ratio, $V^+=0.3$, the thermal resistance is different from that at the other charge ratios. This indicates the charge ratio of 0.3 is insufficient for appropriate operation.

Figure 10 (a) and (b) show variations of total thermal conductance, C , related to the heat transfer rate in the loop type for the ethanol and the water working fluids, respectively. For the ethanol shown in (a), the conductance is not quite affected by charge ratio and coolant temperature. But for the water shown in (b) it is affected by them. The variations can be categorized into two groups. One is obtained on conditions of $V^+=0.3$ with $T_f=25$ and 35 °C and $V^+=0.5$ with $T_f=25$ °C, the other is of $V^+=0.9$ with $T_f=25$ and 35 °C and $V^+=0.5$ with $T_f=35$ °C. The effect of these parameters on the variations is different from that on the variations of each thermal resistance shown in Fig. 9 (b). This different effect has not been cleared yet.

Figure 11 (a) and (b) shows the thermal conductance obtained in the previous study (Takahashi, 2008) using the test loop shown in Fig. 2. In these figures the similar tendency for the parameter effect to that obtained in the present study is shown such as there is less effect of those parameters on the conductance for the ethanol and distinct effect for the water. Comparing the results shown in Fig. 10 with those shown in Fig. 11, the absolute value of the thermal conductance in the present study is about one third of that obtained in the the previous study since, in this test loop, the heat conduction between the thermosyphon tube and the surface of the copper plate, which functions as a heat spreader, in both sections of evaporator and the condenser, might produce a large thermal resistance.

4. CONCLUSIONS

Experimental studies for thermal performance of the looped parallel thermosyphon give the following findings:

- (1) Wall temperature profile in an evaporator section is a little more flat in the loop type.
- (2) The thermal conductance variation relating to heat transfer rate is almost similar between the loop and the single types. For the water working fluid the effect of cooling temperature and charge ratio on the conductance is distinct, but for the ethanol the effect is negligibly small.
- (3) The amount of thermal conductance is about one third of that shown in the previous study. The

major advantage of the loop type as a heat transfer device is to give a larger heat transfer rate.

REFERENCES

Kaminaga, F., Chowdhury, F., Watanabe, H., Matsumura, K. (2003) *Heat transfer characteristics in an evaporator section of a looped parallel thermosyphon*. Proc. 7th Int. Heat Pipe Symp., Jeju, p.169-174.

Kaminaga, F., Tokuhara, A., Matsumura, K, Chowdhury, F. (2004) *Heat transfer characteristics in a looped parallel thermosyphon*. Proc. 13th Int. Heat Pipe Conf., Beijing, p. 62-67.

Kaminaga, F., Matsumura, K., Takahashi, A. (2007) *Heat transfer performace in a looped parallel thermosyphon*. Proc. 14th Int. Heat Pipe Conf., Florianopolis, p. 57-62.

Takahashi, A., Kaminaga, F., Matsumura, K. (2008) *Study on thermal conductance of looped parallel closed thermosyphon*. Proc. 2nd Int. Forum on Heat Transfer, Tokyo, Paper No. 119, p.1-9.

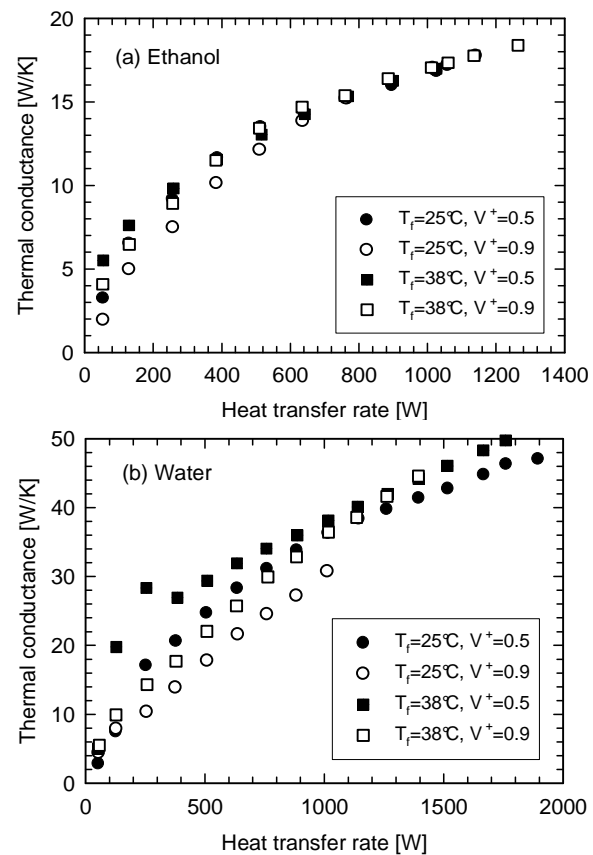


Fig.11 Thermal conductance in previous studies (Takahashi 2009)

RELATIVE THERMAL PERFORMANCE OF SUPER-CRITICAL CO₂, H₂O, N₂ AND HE CHARGED CLOSED-LOOP THERMOSYPHON-TYPE HEAT PIPES

Dobson RT

Department of Mechanical Engineering, University of Stellenbosch
Private Bag X1, MATIELAND 7602, South Africa
Telephone 27 21 808 4268 Fax 27 21 808 4958 Email rtd@sun.ac.z

ABSTRACT

Compared with water, CO₂'s relatively high density at high temperatures and pressures makes it significantly more efficient as a working fluid for trans-critical power generation, and also, much smaller physically sized pipes and turbo machinery can be used. As such this paper considers the use of CO₂ as the working fluid for closed and closed-loop two-phase thermosyphon heat pipes. It also compares the relative performance of CO₂ compared with superheated and supercritical water, helium, nitrogen and sodium. A time-dependent (transient) computer simulation program of a typical closed loop thermosyphon has been developed. The simulation requires the discretisation of the loop into a series of control volumes, the application of the equations of change (mass, motion and energy) to each control volume and the solution of the set of non-linear partial differential equations so generated using an explicit numerical formulation technique and appropriate properties and equations of state for closure. The assumptions made include one-dimensional and quasi-equilibrium flow conditions and upwind differencing. The results of this analysis are collated in a tabular and graphical form thereby allowing the relative performance and scaling characteristics of the various working fluids to be readily established. It is also envisaged that such information will be useful in the design of high performance heat transfer systems, especially in the light of a greater awareness of and the ever-increasing imperative for sustainable and pollution-free energy and heat transfer solutions.

KEY WORDS: Supercritical heat transfer, Closed loop thermosyphon-type heat pipe, Thermofluid modelling

1. INTRODUCTION

In this paper a simple yet appropriate and accurate methodology will be presented whereby the transient performance of a single-phase natural-circulation closed-loop thermosyphon-type heat pipe may be characterised under supercritical (superheated) and transcritical operating conditions. The working fluids considered include carbon dioxide (CO₂), water (H₂O), helium (He), nitrogen (N₂) and sodium (Na). There are a number of reasons why such a heat transfer device needs to be studied:

- Technology has in general been steadily progressing and heat loads and temperatures have been increasing and hence better heat transfer devices are needed. Heat pipes are already extensively used in the cooling of electronic equipment; modern Rankine cycles operate in the region of 20 MPa and 650 °C. However, using CO₂ at these conditions, efficiencies of 43 to 46% are possible (Singer, 2011). These efficiencies are thus obtained at a much lower temperature than the 950 °C

operating temperatures necessary for comparable closed Brayton cycle power generation equipment.

- Although the excessive generation of CO₂ by industrial activity is considered as being a major contributing factor towards global warming; CO₂ with its so-called *global warming potential* of "1" is never-the-less the lowest of all known substances. Further, because of its higher density and high specific heat at these high temperatures and pressures, under these conditions, it is the working fluid of choice. Sandia Laboratories (Singer, 2011) claim that the supercritical-CO₂ (S-CO₂) Brayton cycle could increase electrical power produced per unit of fuel consumed by 43%!
- A requirement of all next-generation nuclear reactors (so-called GEN IV reactor technology) is that the use of passive cooling, because of its acceptably high reliability, needs to be considered a priori, over mechanically pumped and actively controlled devices. Not only can heat pipes transfer large quantities of heat over relatively long distances, they are also self-

controlling – as the temperature difference increases so too does the heat transfer rate.

- Although a plethora of published literature regarding CO₂ is available, it is generally overly complicated and does not specifically apply to closed loop natural circulation, often called *gravity assisted*, heat pipes.

2. OBJECTIVES

The preceding considerations in the Introduction lead to the objective of this paper, which is, to

- present the theory of operation of a closed loop natural circulation thermosyphon-type heat pipe and how its thermal performance may be simulated using a series of partial differential equations,
- give a computer algorithm showing how these equations may be solved as a function of time and thereby being able to capture transient effects and behaviour.
- undertake a thermofluid dynamic analysis showing the response of the heat transfer loop to sudden changes in operating conditions, and to
- establish the relative heat transfer rate performance efficacy of a number of working fluids (CO₂, H₂O, He, N₂ and Na) under super- and trans-critical conditions.

3. THEORY

Consider a rectangular loop of internal diameter d , length (height) L , and width W , containing a working fluid and orientated in a vertical plane, relative to gravity, as shown in figure 1. The loop may be operated at constant pressure using a relatively-large expansion tank maintained at a constant pressure P . The loop may be heated along the one vertical side and cooled along either the top horizontal side and/or the other vertical side, using tube-in-tube heat exchangers for instance. By introducing a temperature induced density gradient along the loop the less dense side of the loop will tend to rise and the more-dense sink, due to the effect of gravity (buoyancy). [Heating along the horizontal bottom side and cooling along the top side has to be avoided as then, at least in theory, there will be either no flow, flow from left to right or from right to left. If the top portion is heated and the lower portion cooled there will normally be no natural circulatory flow.]

The loop is discretised into a series 1 to N_{14} of one-dimensional cylindrical control volumes containing

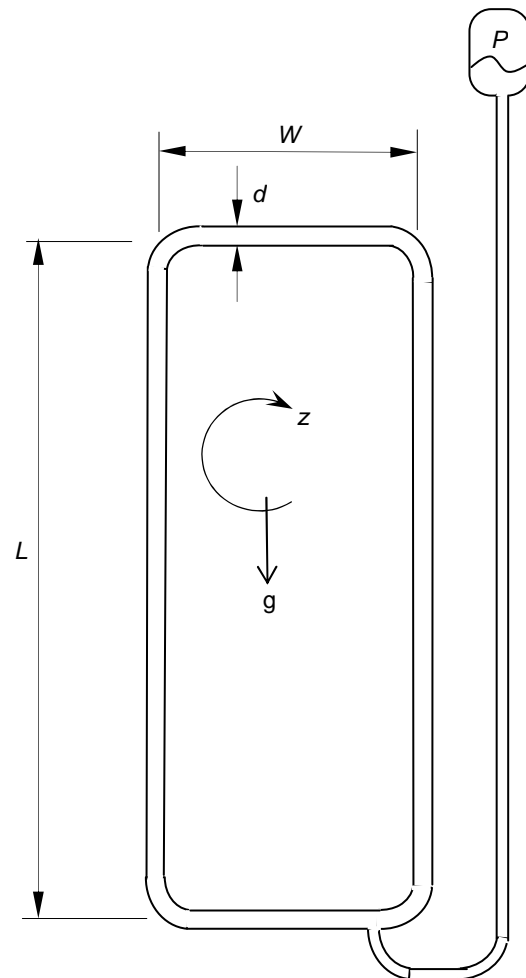


Figure 1. Constant pressure closed loop natural circulation-thermosyphon-type heat pipe

the working fluid as shown in figure 2. By applying the equations of change, namely mass (continuity), motion and energy, to each control volume (see figure 3) a set of partial differential equations characterising the thermo-fluidic behaviour of the working fluid in the loop may be derived. This set of equations may then be solved having a suitable equation of state and properties of the working fluid. To do so however a number of simplifying assumptions are necessary:

- One-dimensional or so-called *plug flow* in a pipe is assumed. This implies that the velocity is constant over the cross-sectional area A_x and is taken as $v = \int_0^R v(r)2\pi r dr / A_x$.
- The initial state of the working fluid in the heat pipe is assumed to be either superheated (super critical) or trans-critical and hence does not undergo a change in its phase over the working temperature and pressure range.

- Any pressure differences of the fluid in the loop, due to temperature induced density gradients, are small compared to the high (≥ 2 MPa) operating absolute-pressure. This implies that at any height-level or elevation in the loop that the pressure is essentially constant, and thus is a so-called *hydrostatic* problem; and thus the *Boussinesqu* approximation for natural convection for the volumetric expansion coefficient in the buoyancy term of the equation of motion may be applied, if so desired.
- The speed of sound in the working fluid is assumed to be considerably greater than the particle or average velocity. This implies that at any instant in time, although the density and average velocity of the working fluid might change around the loop, that the volumetric flow rate $G = vA_x$ is constant for all positions z around the loop, and hence the mass flow rate at any position is $\dot{m} = \rho(z)G$. This assumption thus assumes a so-called *quasi-equilibrium* condition.

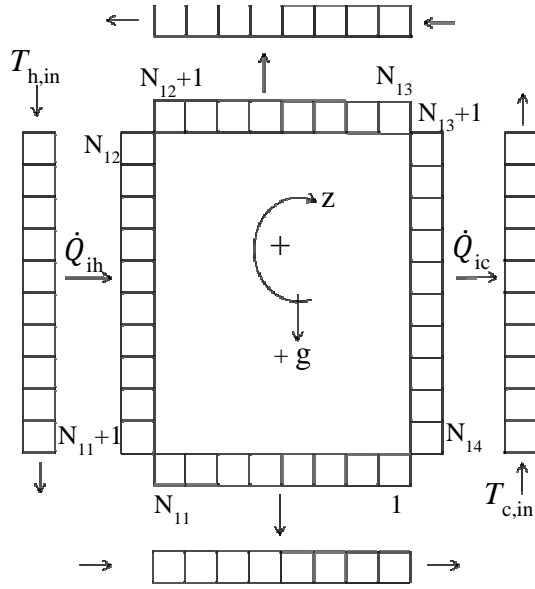


Figure 2. Discretised loop

3.1 Conservation of mass

By applying the general statement of the conservation of mass

$$\frac{\Delta m}{\Delta t} = \Sigma \dot{m}_{in} - \Sigma \dot{m}_{out} \quad [\text{kg/s}] \quad (1)$$

to the control volume shown in figure 3(a), in the limit as Δm and Δt tend to zero

$$\frac{\partial m}{\partial t} = \partial \dot{m} \quad [\text{kg/s}] \quad (2)$$

where $m = \rho A_x \Delta z$, $A_x = \pi d^2/4$ and $\dot{m} = \rho v A_x = \rho G$ since $v = G/A_x$

3.2 Conservation of momentum

By applying the general statement of the conservation of momentum to the control volume shown in figure 3(b)

$$\frac{\Delta m v}{\Delta t} = (\Sigma \dot{m} v)_{in} - (\Sigma \dot{m} v)_{out} + (P_{in} - P_{out}) A_x - mg - \tau A_z \quad [\text{N}] \quad (3)$$

where $\tau = C_f \rho (G/A_x)^2/2$, $A_z = \pi d \Delta z$, but dividing by A_x (assumed constant in this case) and noting that G is also constant for all z at any instant in time and summing-up for all the control volumes around the loop, the pressure terms cancel out and the equation becomes

$$\frac{\Delta G}{\Delta t} \Sigma \frac{m}{A_x^2} = (G/A_x)^2 \Sigma (\rho_{in} - \rho_{out}) + \Sigma \rho g \Delta z \sin \theta - \Sigma \tau A_z / A_x \quad [\text{N/m}^2] \quad (4)$$

where the angle θ equals $-\pi/2$ if gravity is acting against the flow (ie in the left hand side of the loop) and $+\pi/2$ if gravity is acting in the positive direction of z . Dividing equation 3 by A_x and Δz , and in the limit, as Δz and A_x tend to zero and integrating around the loop

$$\oint \frac{\partial \rho v_z}{\partial t} = - \oint \frac{\partial \rho v_z^2}{\partial z} - \oint \frac{\partial P}{\partial z} - \oint \rho g_z - \oint \frac{\partial \tau_{zz}}{\partial z} \quad (5)$$

$$\text{and } \oint \frac{\partial P}{\partial z} = 0 \quad [\text{N/m}^3]$$

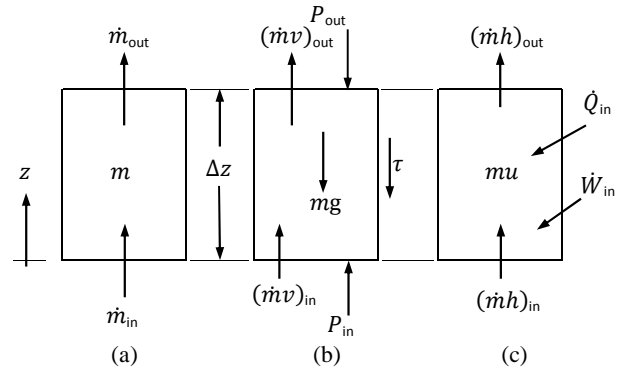


Figure 3. One-dimensional mass, momentum and energy control volumes

3.3 Conservation of energy

Applying the general statement of the conservation of energy to the control volume shown in figure 3(c) and ignoring kinetic and potential energy

$$\frac{\Delta m u}{\Delta t} = (\Sigma \dot{m} h)_{in} - (\Sigma \dot{m} h)_{out} + \dot{Q}_{in} - \dot{Q}_{out} - P \Delta V \quad [\text{W}] \quad (6)$$

Noting that the enthalpy $h = u + P \Delta V$, this equation becomes

$$\frac{\Delta m h}{\Delta t} = (\Sigma \dot{m} h)_{in} - (\Sigma \dot{m} h)_{out} + \dot{Q}_{in} - \dot{Q}_{out} \quad (7)$$

and, in the limit for each control volume

$$\frac{\partial m h}{\partial t} = \partial \dot{m} h + \partial \dot{Q} \quad [\text{W}] \quad (8)$$

The heat transfer rate $\dot{Q} = (T_{\text{surface}} - T_{\text{fluid}})/R$ where typically for a convection boundary condition (heating mode HM=1) and $R = 1/(\alpha A_z)$ where α is a convection heat transfer coefficient and A_z is the heat transfer area in contact with the fluid. For electrical resistance heating (assuming no heat loss to the environment) a constant heat flux boundary condition (heating mode HM=2) is used as $\dot{Q} = \dot{Q}'_{elec} \Delta z$ where \dot{Q}'_{elec} is the electrical power input per unit length.

3.4 Fluid properties

For uniformity and ease of programming simple property equations, based on NIST published information, were determined using relatively simple correlations (at constant pressure) as follows: density $\rho = a \ln T + b$, enthalpy $h = cT + d$, temperature $T = (h - d)/c$, dynamic viscosity $\mu = eT + f$, thermal conductivity $k = gT + h$, Prandtl number $Pr = i \ln T + j$ for CO₂, H₂O and Na but $Pr = iT + j$ for He and N₂. The constants a to j for 2 and 10 MPa are given in Table 1.

4. SOLUTION ALGORITHM

An explicit numerical solution method is used to solve equations 1, 2 and 3 applied in turn to each of the discretised control volumes shown in figure 3. This procedure is similar to the solution approach as outlined in Dobson (1993), and which also references a number of applicable papers, as of that date.

Input the geometrical and initial values

$L_1 = L_3 = 1.0$ m, $L_2 = L_4 = 1.0$ m, $N_1 = N_3 = 11$, N_2

$= N_4 = 21$, $N_{11} = N_1$, $N_{12} = N_1 + N_2$, $N_{13} = N_1 + N_2 + N_3$, $N_{14} = N_1 + N_2 + N_3 + N_4$, $\Delta z_1 = L_1/N_1$, $\Delta z_2 = L_2/N_2$, $\Delta z_3 = L_3/N_3$, $\Delta z_4 = L_4/N_4$,

$D_1 = D_2 = D_3 = D_4 = 0.010$ m, $\Delta t = 0.0001$, $t_{\text{stop}} = 50$ s

$T_{\text{initial}} = 600$ °C, $P_{\text{initial}} = 2$ MPa, $G = 0$

If HM = 1 then $T_{\text{hw}} = 700$ °C, $T_{\text{cw}} = 600$ °C and $\dot{Q}_{elec} = 0$ W, If HM = 2 then $\dot{Q}'_{elec} = 1000$ W, $T_{\text{cw}} = 600$ °C

Start the calculational procedure

1 $t = t + \Delta t$

For $i = 1$ to N_{14}

Calculate the property values:

$\rho_i = f(T_i, P_i)$, $h_i = f(T_i, P_i)$, $\mu_i = f(T_i, P_i)$, $k_i = f(T_i, P_i)$ and $Pr_i = f(T_i, P_i)$ and set the density and enthalpy for the 0th and $(N_{14}+1)$ th control volumes as

$\rho_0 = \rho_{N_1}$ and $\rho_{N_{14}+1} = \rho_1$ and $h_0 = h_{N_1}$ and $h_{N_{14}+1} = h_1$

Calculate the Reynolds number

$Re_i = 4\rho_i |G| / (4\rho_i |G|)$

Calculate the heat transfer coefficients

if $Re_i \leq 2300$ and HM= 1 then $\alpha = 3.66k/d$

if $Re_i \leq 2300$ and HM= 2 then $\alpha = 4.36k/d$

if $Re_i > 2300$ then $\alpha = 0.023kRe^{0.8}Pr^{0.35}/d$

Calculate the heat transfer rates

If $i > 0$ and $i < N_{11}+1$ then $\dot{Q}_{in,i} = 0$ and $\dot{Q}_{out,i} = 0$

If $i > N_{11}$ and $i < N_{12}+1$ and HM = 1 then $\dot{Q}_{in,i} = \alpha_i A_{z_i} (T_{\text{hw}} - T_i)$ and $\dot{Q}_{out,i} = 0$ If $i > N_{11}$ and $i < N_{12}+1$ and HM = 2 then $\dot{Q}_{in,i} = \dot{Q}'_{elec} \Delta z_i / L_i$ and $\dot{Q}_{out,i} = 0$

If $i > N_{12}$ and $i < N_{13}+1$ then $\dot{Q}_{in,i} = 0$ and $\dot{Q}_{out,i} = 0$ If $i > N_{13}$ and $i < N_{14}+1$ then $\dot{Q}_{out,i} = \alpha_i A_{z_i} (T_i - T_{\text{cw}})$ and $\dot{Q}_{in,i} = 0$

Calculate the mass and enthalpy flow rates (using up-wind differencing)

$\dot{m}_{out,i} = \rho_i |G|$ ($\dot{m}h$)_{out,i} = $\dot{m}_{out,i} h_i$}

If $G \geq 0$

Table 1. Property constants at 2 and 10 MPa

	P (Mpa)	CO ₂	H ₂ O	He	N ₂	Na
a	2	-8.844	-3.829	-0.8133	-5.721	-147.0
b	2	69.04	29.56	6.312	44.32	1750
c	2	1114	2248	5192	1110	1278.2
d	2	445600	234800	1430100	267490	4952
e	2	0.0367x10 ⁻⁶	0.0405 x10 ⁻⁶	0.03606 x10 ⁻⁶	0.03160 x10 ⁻⁶	0.036742 x10 ⁻⁶
f	2	15.17 x10 ⁻⁶	8.220 x10 ⁻⁶	20.15 x10 ⁻⁶	18.98 x10 ⁻⁶	15.17 x10 ⁻⁶
g	2	0.0754 x10 ⁻³	0.1270 x10 ⁻³	0.2806 x10 ⁻³	0.05553 x10 ⁻³	-0.04676
h	2	0.01652	5.935 x10 ⁻³	0.1593 x10 ⁻⁶	0.02594	92.38
i	2	0.04403	-1.007	6.18 x10 ⁻⁶	0.02167 x10 ⁻³	-0.001576
j	2	0.9980	1.553	0.6583	0.7203	0.01463
a	10	-65.69	-28.37	-3.914	-27.73	-147.0
b	10	478.8	208.5	30.52	2148	1750
c	10	1203	2611	5191	1129	1278.2
d	10	385716	2042900	1430089	267490	4952
e	10	0.03199x10 ⁻⁶	0.04164x10 ⁻⁶	0.03588 x10 ⁻⁶	0.03160 x10 ⁻⁶	0.036742 x10 ⁻⁶
f	10	18.49 x10 ⁻⁶	7.8512 x10 ⁻⁶	20.36 x10 ⁻⁶	18.98 x10 ⁻⁶	15.17 x10 ⁻⁶
g	10	0.067 x10 ⁻³	0.104 x10 ⁻³	0.2792 x10 ⁻³	0.05553 x10 ⁻³	-0.04676
h	10	.02313	0.027306	0.1637	0.02594	92.38
i	10	-0.1452	-0.4673	0.01329 x10 ⁻³	0.02167 x10 ⁻³	-0.001576
j	10	1.6747	3.958	0.6478	0.7203	0.01463

then $\dot{m}_{in,i} = \rho_{i-1}|G|$ and $(\dot{m}h)_{in,i} = \dot{m}_{in,i}h_{i-1}$
else

$\dot{m}_{in,i} = \rho_{i+1}|G|$ and $(\dot{m}h)_{in,i} = \dot{m}_{in,i}h_{i+1}$

Calculate the control volume mass

$$m_i^{t+\Delta t} = m_i + \Delta t(\dot{m}_{in,i} - \dot{m}_{out,i})$$

Calculate the new enthalpy, temperature and density

$$h_i^{t+\Delta t} = \frac{h_i + \Delta t((\dot{m}h)_{in,i} - (\dot{m}h)_{out,i} + \dot{Q}_{in,i} - \dot{Q}_{out,i})}{m_i^{t+\Delta t}}$$

$$T_i^{t+\Delta t} = f(h_i^{t+\Delta t}, P) : \rho_i^{t+\Delta t} = f(T_i^{t+\Delta t}, P)$$

$$m_i^{t+\Delta t} = \rho_i^{t+\Delta t} V_i$$

next i

Calculate the volumetric flow rate

For i = 1 to N₁₄

Calculate the shear stress acting on each control volume

If Re_i ≤ 0.1 then C_f = 160

If Re_i > 0.1 and then Re_i ≤ 1181 then C_f = 16/Re_i

If Re_i > 1181 C_f = 0.079Re_i^{-0.25}

$$\tau_i = C_f \rho_i (G/Ax_i)^2 / 2$$

next i

Calculate the sum of the friction terms

$$F = \sum_{i=1}^{N_{14}} (\tau_i \pi d_i (\Delta z_i + \Delta z_{minor}) / Ax_i)$$

[Δz_{minor} = 77d for a smooth bend]

If G ≥ 0 then F = -F else F = F

Calculate the sum of the buoyancy terms

B = $\sum_{i=1}^{N_{14}} (\rho_i g \Delta z_i \sin \theta_i)$ [For i = 1 to N₁₂ and N₁₂₊₁ to N₁₃ to θ_i = 0, for N₁₁₊₁ to N₁₂ θ_i = -π/2, and for N₁₃₊₁ to N₁₄ θ_i = π/2]

Calculate the sum of the momentum flux difference terms

$$M = \sum_{i=1}^{N_{14}} ((\rho_{in,i} - \rho_{out,i}) (G/Ax_i)^2)$$

Calculate the new volumetric flow rate

$$G^{t+\Delta t} = G + \Delta t \frac{(M \pm B - F)}{\sum_{i=1}^{N_{14}} (m_i^{t+\Delta t} / Ax_i^2)}$$

Set the old values of the mass, temperature, density and volumetric flow rate equal to the new values

For i = 1 to N₁₄, m_i^t = m_i^{t+Δt} and T_i^t = T_i^{t+Δt}

Print out or store data

If t > t_{stop} then stop else go back to 1 and repeat until time = t_{stop}

5 RESULTS

Considering the loop shown in figure 1 with L = W = 1.0 m and d = 0.01m but with different heating and cooling temperatures T_{hot} and T_{cold}, respectively then the rate at which heat is transferred by the loop for CO₂, H₂O and N₂ at a loop pressure of 2 MPa is given in table 1. It is seen that at typical so-called *supercritical*

conditions of about 2 MPa and 600 °C that the CO₂ loop transfer some 5.64 W at a temperature difference of 50 °C and this is some 94.5% better than the 2.90 W for H₂O. At so called *trans-critical* conditions at say 10 MPa and 600 °C it is 96.6% better.

Table 2. Heat transferred for L = W = 1 m and d = 0,01 m at different temperatures and temperature differences between the hot and cold sides for CO₂, H₂O and N₂

P	T _{hot}	T _{cold}	ΔT	CO ₂	H ₂ O	N ₂
MPa	°C	°C	°C	W	W	W
2	610	590	20	1.11	0.41	0.25
2	625	575	50	5.64	2.90	2.75
2	650	550	100	16.7	10.6	9.46
2	700	500	200	44.0	34.3	29.2
10	610	590	20	5.89	6.8	4.17
10	625	575	50	40.5	20.6	13.0
10	650	550	100	111	44.7	28.4
10	700	500	200	305	94.0	158
25	650	550	100	216	184	-

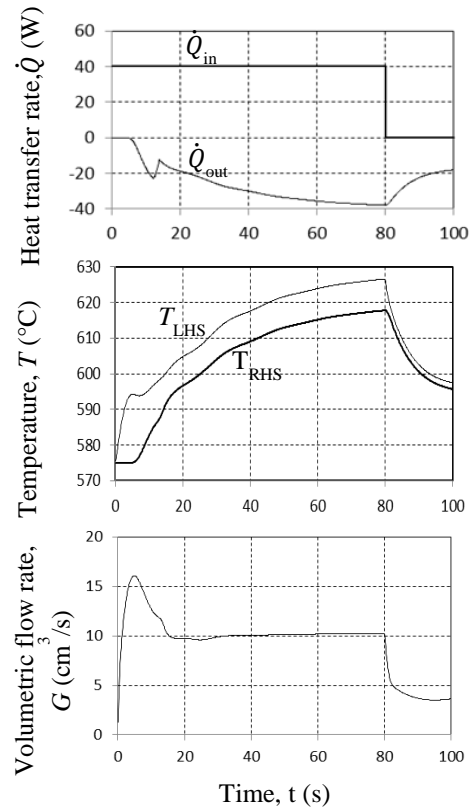


Figure 4. Thermal performance response of the loop to a step-wise change in power input.

The numerical procedure outlined in section 4 is also able to compare the heat transfer for different geometries. For instance, the rate of heat transferred at 10 MPa for different CO₂ loop diameters are given in table 3.

Tabel 3. Heat transferred for different CO₂ loop diameters d for a hot and cold side temperature differences of 100 °C.

P	T _{hot}	T _{cold}	ΔT	.005	0.01	0.02	0.03
MPa	°C	°C	°C	m	m	m	m
10	650	550	100	22.5	111	216	283

Representative graphs of volumetric flow rate G , average hot and cold side temperatures and heat transfer rates as a function of time are shown in figure 4 for a 40 W heat input and a $L = W = 1.0$ m and $d = 0.01$ m CO₂ loop; the initial and cooling temperatures being both 575 °C and operating pressure 10 MPa.

6. CONCLUSIONS / RECOMMENDATIONS

- Using the theory and solution procedure and analysis described in this paper indicates that CO₂ as the working fluid in a natural circulation heat transfer loop is able to transfer some 95% more heat than a similar H₂O loop, all things being equal.
- It is recommended that the experimental validation of the analysis procedure as outlined in this paper now be considered. It is further recommended that the property functions and solution procedure be extended to include phase changes and that a constant volume geometry also be considered.

NOMENCLATURE

A area, m²
 c specific heat, K/kg°C
 d diameter, m
 G volumetric flow rate, m³/s
 g gravitational constant, 9.81 m/s²
 h specific enthalpy, J/kg
 k thermal conductivity, W/m°C
 L length, m
 m mass
 \dot{m} mass flow rate, kg/s
 P pressure, Pa
 Pr Prandtl number, $Pr = c_p \mu / k$
 R radius

Re Reynolds number, $Re = \rho v d / \mu$
 \dot{Q} heat transfer rate, W/s
 \dot{Q}' power input per unit length, J/m
 r r-direction
 T temperature, °C
 t time, s
 u specific internal energy, J/kg
 V volume, m³
 v velocity, m/s
 W width
 \dot{W} rate of work, W
 z axial-direction (in cylindrical coordinates)
 α heat transfer coefficient, W/m²°C
 θ angle
 τ shear stress, N/m²
 μ dynamic viscosity, Pas
 ρ density, kg/m³

Subscripts

v constant volume
 p constant pressure
 x cross section
 z z-direction

ACKNOWLEDGEMENTS

The assistance of the South African Heat Pipe Association is greatly appreciated.

REFERENCES

- Dobson, RT (1993) Transient response of a closed loop thermosyphon, *R&D Journal*, Vol 9, No 1, pp 32-38.
- NIST (2011) Thermophysical Properties of Fluid Systems. National Institute of Standards and Technology, *U.S. Secretary of Commerce on behalf of the United States of America*, <http://webbook.nist.gov/chemistry/fluid/>
- Singer, N, (2011) Supercritical carbon dioxide Brayton Cycle turbines promise giant leap in thermal-to-electric conversion efficiency, *Sandia news media release* March 4, 2011, Sandia Corporation, Albuquerque.

ANALYSIS RESULTS OF A TEN YEAR SODIUM HEAT PIPE LIFE TEST

John H. Rosenfeld

Thermacore Inc.

780 Eden Road, Lancaster, PA 17601 USA

Phone 717.569.6551, Fax 717.569.8424, E-mail j.h.rosenfeld@thermacore.com

James L. Sanzi

Sest Inc.

18151 Jefferson Park, Suite 104, Middleburg Heights, OH 44130 USA

Phone 216.433.5036, james.l.sanzi@nasa.gov

ABSTRACT

High temperature heat pipes are being evaluated for use in energy conversion applications such as fuel cells, gas turbine re-combustors, Stirling cycle heat sources; and with the resurgence of space nuclear power both as reactor heat removal elements and as radiator elements. Long operating life and reliable performance are critical requirements for these applications. Long-term materials compatibility is being evaluated through the use of high temperature life test heat pipes. A ten year sodium heat pipe life test has been conducted to establish long term operating reliability. A representative one-tenth segment Stirling Space Power Converter heat pipe with an Inconel 718 envelope and a stainless steel screen wick has operated for over 87 000 hours (ten years) at nearly 700°C. These life test results have demonstrated the potential for high temperature heat pipes to serve as reliable energy conversion system components for power applications that require long operating lifetime with high reliability. Detailed design specifications, operating history, and post-test analysis of the heat pipe and sodium working fluid are described. The heat pipe operated successfully without failure during the ten year life test. Changes to the sodium working fluid composition and the envelope and wick surfaces were measured, but these changes did not appear to adversely affect normal heat pipe operation.

KEYWORDS: Heat Pipe, Life Test, Sodium, High Temperature, Stirling Engine, Space Power

1. INTRODUCTION

High temperature heat pipes are being evaluated for use in energy conversion applications such as fuel cells, gas turbine re-combustors, Stirling cycle heat sources. The resurgence of space nuclear power has created renewed interest in their use as reactor heat removal components and as radiator components. In the temperature range between 500°C and 1000°C, heat pipes can offer the favorable features of passive, reliable operation, effective thermal coupling between non-contacting fluid streams, and modest cost (Rosenfeld and Ernst, 1999). Long operating life and reliable performance are critical requirements for these applications. Reliability for space-based applications is particularly critical because component replacement is generally difficult or impossible.

Heat pipes are a key component under consideration for the higher-power dynamic power systems. NASA Glenn Research Center has been

involved in the development of dynamic power converters for both nuclear and solar power conversion systems. Of particular current interest are: 1) the development of a Stirling Radioisotope Generator (SRG) as a possible high efficiency alternate to Radioisotope Thermo-electric Generators (RTGs) for deep space missions and unmanned Mars rovers, and 2) higher-power Brayton and possibly Stirling or Rankine power systems for nuclear electric propulsion and power applications. Thermal energy is generally supplied at a high temperature (>1000K) to the power conversion system. High temperature heat pipes are one option to efficiently transfer thermal energy from the nuclear reactor heat source to the dynamic power converter. Heat pipes may also be useful for transferring waste heat from the power converter to the radiator. Heat pipes and other passive two-phase technologies are currently being considered for the purpose of transferring heat from the power converter to the radiator with minimal temperature drop and to spread heat within the radiator panels isothermally.

Stirling heat engines are being developed for electrical power generation on manned and unmanned earth orbital, planetary missions, and terrestrial applications for utility and remote power generation. Dish Stirling solar systems and nuclear reactor Stirling systems are two promising applications of Stirling engine technology. Sources of thermal energy used to drive the Stirling engine typically have non-uniform temperatures and heat fluxes. Liquid metal heat pipe receivers are often used as heat transformers to uniformly deliver thermal energy at high temperatures to the heater heads of these Stirling engines. The use of heat pipe receivers can greatly enhance system efficiency and potential life span.

One issue that needed to be addressed during the design phase of heat pipe receivers is the potential solubility corrosion of the heater head section by the liquid metal working fluid. Stainless steels and nickel-based superalloys are standard materials of construction for high temperature heat pipes and heater heads operating in the temperature range 823-1073K. At these operating temperatures, some components of these materials are appreciably soluble in working fluids such as sodium, potassium, and NaK. Over a typical life span of seven to ten years, essentially pure working fluid condensate will condense on the heater head surfaces. The condensate will leach the soluble components of the heater head material and transport them to the evaporator section of the heat pipe. When the working fluid is evaporated again, the soluble materials are precipitated and essentially pure working fluid is returned to the condenser section to leach more material. The condensation heat flux for a Stirling heater head is typically 20-25 W/cm². For a 33% efficient 25kW_e Stirling engine this corresponds to approximately 760 m³ of sodium per year, condensing on a heater head.

To establish long term operating reliability for sodium heat pipes, long-duration sodium heat pipe life tests were performed. This paper describes the design and performance results from these tests, which collectively establish the capability of sodium heat pipes in applications requiring high reliability over long time durations.

2. ONE TENTH SEGMENT STIRLING SPACE POWER HEAT PIPE LIFE TEST: TEST ARTICLE DESCRIPTION

A representative one-tenth segment Stirling Space

Power Converter heat pipe with an Inconel 718 envelope and a stainless steel screen wick was operated for over 87 000 hours (ten years) at nearly 700°C. Detailed design specifications, operating history, and post-test analysis are described for the sodium heat pipe.

2.1 Heat Pipe Design

Glenn Research Center funded a dual phase program to investigate solubility corrosion and to develop coatings that would essentially eliminate the solubility corrosion potential. A complete description of the work performed on the first phase of work can be found in the Final Report for Contract No. NAS3-26925 (Dussinger and Lindemuth, 1997). The final task of the program was to fabricate a 1/10th segment of the current Stirling Space Power Converter (SSPC), Starfish heater head heat pipe, utilizing the coatings and coating processes developed during the program. This heat pipe would then be life tested for up to ten years by Thermacore as Phase 3. Unfortunately, the heat pipe intended for life testing had several weld failures after charging and processing. Because this pipe was no longer available, NASA acquired the original 1/10th segment heat pipe from Mechanical Technology Incorporated (MTI) and provided it for testing in the Phase 3 effort. The 1/10th segment heat pipe, fabricated by Thermacore for the SSPC project under MTI Subcontract No. 003-05034, was returned to Thermacore for testing on this program.

The 1/10th segment is a 36° slice of the overall heater head and heat pipe. Design specifications for the heat pipe are given in Table 1.

2.2 Life Test Supporting Equipment Design

A cart-mounted supporting equipment arrangement was used to complete the life test on the heat pipe. The heat pipe was heated primarily by radiation from twelve silicon carbide heating elements. In order to minimize heat loss, the heating elements were surrounded by a nine-inch thick graded insulation package. The insulation package was formed to fit and support the heat pipe/calorimeter package. The power was controlled with a phase angle power controller in conjunction with a PID temperature controller. The silicon carbide heating elements were operated in series at a relatively low voltage, approximately 30 volts. A 10kVA step down transformer was used to reduce the primary 208V to 35V.

Table 1. Design Specifications for the Tenth Segment Heat Pipe.

Parameter	Specification
Operating Temperature	1023K (750°C)
Working Fluid and Fluid	100g, High Purity
Calorimetric Heat	4500 W
Condenser Surface Heat	20 W/cm ²
Envelope Material	In 718 Envelope
Wick Structure Material	316LSS; 2 Layers of 100 Mesh Screen
Fill tube Material	316 Stainless Steel
Arteries	Four; 0.318 cm ID
Artery Material	316L SS; 325 Mesh
Coating	None

The desired operating temperature was set on the temperature controller. The temperature controller also had a latching, over temperature alarm feature. In addition, the temperature controller had a second control feature that is being used to energize the hour meter when the temperature is within five degrees of the set point.

The power that the heat pipe transfers is extracted and measured using a gas gap calorimeter. The gas gap calorimeter consists of small diameter water tubes that are inserted into the heater head gas passage holes. The temperature rise of the water flowing through the tubes and the flow rate are used to calculate the heat pipe power throughput. The distilled water coolant is pumped from a tank under the test setup, through a 50 micron filter, and into the calorimeter. The coolant exiting the calorimeter then flows through two liquid-to-air heat exchangers, which are also mounted under the test setup.

2.3 Life Test Operating Results

The program goal was successfully reached through ten years of operation at 700°C. The test operations began in summer 1996 and were completed on June 1, 2010. A total of 87 783 hours (10.0 years) of operation at 700°C were accomplished over this time period. The heat pipe continued to operate without apparent variation in thermal performance for the entire duration of the life test program.

3. POST TEST ANALYSIS RESULTS

This section of the paper describes the post-test analysis of the sodium and the heat pipe envelope. The goal of this task was to measure and evaluate changes to the sodium chemistry and envelope metallurgy incurred during the long term operation of the heat pipe. At the conclusion of testing, a sodium sample was removed from the heat pipe for analysis.

A sample of the sodium was also collected from the source vessel, to compare the initial composition with the composition after ten years of operation. Lastly, a sample of the de-ionized water was collected to confirm that no contamination occurred due to impurities in the water. The aqueous samples were placed into Nalgene bottles and sent to a certified testing laboratory for chemical analysis. A sample concentration of 2000 mg/l was used to quantify the elemental concentration data. The solution concentration in ppm is equal to the concentrations of other elements found in the sodium sample.

3.1 Sodium Analysis Results

Fifteen trace elements were found in the initial sodium composition, compared to nineteen that were found present in the composition after ten years of operation. Table 2 shows the complete sodium analysis results. The deionized water was determined to be essentially free of trace metal contaminants, which verifies the accuracy of the results. The largest changes to the sodium composition included increased concentrations of boron, aluminum, silicon, iron, and barium. The source of these elements would be the Inconel and stainless steel vessel materials in contact with the sodium. A decrease in the potassium, phosphorus, and nickel concentration was also measured.

Review of the Inconel alloy composition shows that boron, manganese, iron, chromium, silicon, and aluminum may have dissolved into the sodium from the envelope inner surface. Similarly, iron, chromium, manganese, and silicon are present as alloying elements in the 316 stainless steel screen wick material. The envelope and wick materials can account for all of the trace element increases except barium. It is possible that barium is present in small concentrations in either the wick or wall material, or that the sodium sample removed from the heat pipe had barium concentrated in the excess fluid charge, because as a heavy element it would have settled to the bottom of the vessel from where the sample was removed.

Table 2. Sodium Composition Analysis.

Element	Sodium Source (ppm)	Sodium After 10 yrs (ppm)	DI Water Source (ppm)
Boron	41	713	0.1
Magnesium	5	15	< 0.0001
Aluminum	26	286	< 0.02
Silicon	< 14	7171	0.03
Potassium	430	177	< 0.04
Calcium	25	86	< 0.0004
Chromium	4	39	0.01
Manganese	1	4	< 0.0007
Iron	14	198	0.06
Copper	84	98	< 0.002
Zinc	37	78	0.004
Strontium	0.5	0.6	< 0.0002
Barium	48	949	< 0.002
Phosphorus	22	< 1	< 0.04
Nickel	114	< 1	< 0.01
Lithium	0	18	0
Zirconium	0	5	0

Table 3. Heat Pipe Sample Location Descriptions.

Sample Number	Location on Heat Pipe	Specific Features Comments
1A	Evaporator	Screen Wick / Screen Artery
1B	Adiabatic	Screen Wick
2A	Evaporator / Adiabatic	Internal Support Divider / Weld
2B	Evaporator / Adiabatic	Internal Support Divider / Weld
3	Fill tube	Fill tube
4	Corner/ Adiabatic	Corner with Other Fill Tube
5A	Evaporator	Screen Wick / Screen Artery
5B	Adiabatic	Screen Wick
6	Condenser	Screen Wick / Artery

3.2 Post-test Analysis of the Envelope and Wick Materials

Several sections of the heat pipe envelope were selected from which to remove samples for analysis. The heat pipe was first cut into two pieces; smaller samples were then removed from the two halves. A wire electron discharge machining (EDM) approach was used to remove the test samples. The outer surface of the envelope retained a natural dark oxide coating. Figure 1 shows the heat pipe after it was cut into two sections and the samples were removed.

The sample analysis was performed by NASA Glenn Research Center (GRC). Each envelope/wick sample was then prepared for analysis. The individual samples were sectioned then nickel-plated, mounted, and polished.

A total of six envelope/wick samples were removed for analysis. Sample regions included envelope samples taken from the heat pipe evaporator, adiabatic, and condenser regions. For some samples, a single wire EDM cut removed two samples, i.e. the lower side (evaporator) sample and an upper (adiabatic) sample. These were designated A and B, respectively. Table 3 describes the location of each sample. Smaller samples were sectioned for metallographic and electron microscopy analysis. Samples were nickel-plated, mounted, and polished.

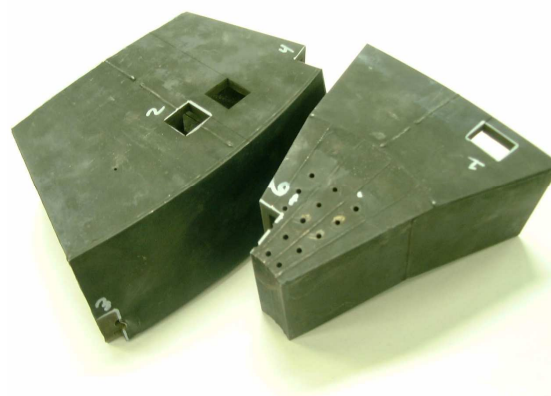


Figure 1. Sectioned Heat Pipe

3.3 Heat Pipe Evaporator Region Envelope

Electron microprobe microstructural analysis was done on evaporator samples 1A and 5A. The analysis of the inner surface of the envelope in the heat pipe evaporator section showed about 30µm near the interface that was significantly affected. The principal effect was a loss of nickel from this layer. Microprobe wavelength dispersive spectroscopy (WDS) maps show that other elements were present in increased concentration, including niobium, iron, silicon, and titanium. Sample 5A showed similar result. Microprobe analysis also showed an increase in nickel and a decrease in molybdenum and iron near the outer surface of the envelope wall, in a region about 100

μm in thickness. This surface was exposed to air and to direct radiation from the silicon carbide heaters during the life test. Most of the envelope thickness was not substantially affected by the test.

Because nickel was apparently removed from the inner envelope surface in the evaporator region, an effort was made to determine if nickel was transported by the sodium to other regions of the heat pipe. No evidence of nickel deposition was observed in any sample; in fact, nickel removal to a 30 μm depth was typically observed near the inner envelope surface in all of the analyzed samples (Figures 2 and 3). This result suggests that the nickel migrated deeper into the envelope, and that diffusion from the inner surface toward the outer surface was the predominant method of transport. The outer surface of the heat pipe envelope was covered with a dark oxide that typically forms from long exposure to air at high temperature.

3.4 Heat Pipe Adiabatic Region Envelope

Microprobe analysis was performed on samples taken from the adiabatic region of the heat pipe, e.g. Samples 1B and 5B. Analysis of test samples showed similar metallurgy changes to those found in the evaporator region; a 30 μm thick region near the inner envelope surface was depleted of nickel, and other alloying elements had migrated in a similar manner.

3.5 Heat Pipe Condenser Region Envelope

Microprobe analysis was also performed on a sample taken from the condenser region of the heat pipe, i.e. Sample 6. Analysis of test sample showed element migration and other changes similar to those found in the evaporator and adiabatic regions; a 30 μm thick region near the inner envelope surface was depleted of nickel, and other alloying elements had migrated in a similar manner.

3.6 Heat Pipe Wick Structure Analysis

The screen wick material was analyzed to determine the effects of long term exposure to the sodium working fluid. Observations of the electron beam welds indicated no evidence of corrosion in the weld metal or heat affected zone. Electron beam weld penetrations were measured to be between 3.5 and 5.4 mm. Microprobe analysis indicated deposition of sodium, oxygen, and carbon on the surface of the screen. These elements were most likely residues of sodium

hydroxide and sodium methoxide that remained from the sodium removal and disposal process. Some evidence was seen of species migration in the screen wires; this effect did not seem to affect the integrity of the wires. Physical observation showed that the wires retained ductility and did not separate from the envelope inner surfaces near the tack-weld locations.

4. CONCLUSIONS

A sodium heat pipe demonstrated favorable materials compatibility and heat transport characteristics at 700°C while operating in air for over ten years. A representative one-tenth segment Stirling Space Power Converter heat pipe with an Inconel 718 envelope and a stainless steel screen wick has operated for over 87 000 hours at nearly 700°C. Post-test analysis revealed no significant degradation of the envelope or screen wick material as a result of the life test. The life test provides strong evidence for long-term chemical compatibility of sodium heat pipes at high operating temperatures. A detailed report has been completed to document this work (Rosenfeld et al, 2012).

Chemical composition was determined for the source sodium and for the fluid charge removed from the tenth segment unit after 87 000 hours of operation. The analysis of the sodium working fluid from the tenth segment unit showed small quantities of more than a dozen other elements, some of which were originally present in the source sodium. Migration of some alloying elements was observed, though the end effect on the envelope was minimal. A 30 μm region of the inner surface was significantly depleted of nickel; it appeared to migrate outward through the envelope, since no region of the envelope inner surface or wick contained re-deposited nickel. These metallurgical changes did not appear to adversely affect the integrity of the heat pipe envelope or operational characteristics of the heat pipe.

NOMENCLATURE

EDM = electron discharge machining
GRC = Glenn Research Center
MTI = Mechanical Technology Incorporated
NASA = National Aeronautics and Space Administration
RTG = Radioisotope Thermoelectric Generators
SRG = Stirling Radioisotope Generator
WDS = wavelength dispersive spectroscopy
NaK = Sodium/Potassium Eutectic Alloy

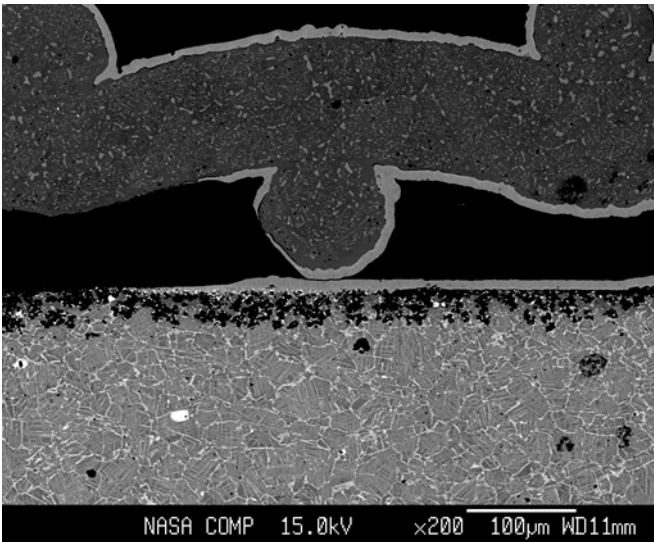


Figure 2. Electron Microprobe Images of the Sodium (Inner) Side of Sample 1A.

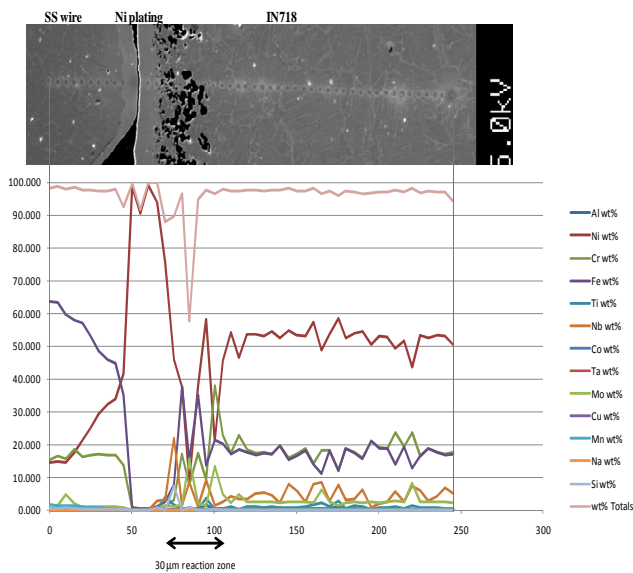


Figure 3. Electron Microprobe Image and Wavelength Dispersive Spectroscopy (WDS) Quantitative Line Scan of Major Elements for Test Sample 1A Near the Sodium (Inner) Surface.

ACKNOWLEDGMENTS

The work described in this paper was performed by Thermacore, Inc., for NASA Glenn Research Center. The one-tenth segment heat pipe life test was designed and built under NASA Contract No. NAS3-26925 and has been tested under a series of extensions through NASA Glenn Research Center. The program was monitored by Dr. Steven M. Geng. The following NASA persons are acknowledged for their contributions to this work: Ivan E. Locci (University of Toledo at the NASA Glenn Research Center), David R. Hull (NASA/GRC), and James L. Sanzi (Sest Corporation). The authors also wish to acknowledge the many engineers and technicians who participated in the design, fabrication, and testing work described herein. Special appreciation is expressed to Mr. Kenneth G. Minnerly, who tended the life test support equipment for over 10 years.

REFERENCES

- Dussinger, P. M., and Lindemuth, J. E., *Insoluble Coatings for Stirling Engine Heat Pipe Condenser Surfaces*, final report NASA CR-202323, NASA Contract No. NAS3-26925, July 1997.
- Rosenfeld, J. H., and Ernst, D. M., "Advances in Refractory Metal Heat Pipe Technology," in *Heat Pipe Science and Technology: Proc. 11th Int. Heat Pipe Conf., Tokyo-Japan 1999*, pp. 407-413.
- Rosenfeld, J. H., Ernst, D. M., Lindemuth, J. E., Sanzi, J. L., Geng, S. M., and Zuo, J., "An Overview of Long Duration Sodium Heat Pipe Tests," *STAIF 2004*, M. E. El-Genk, Ed.
- Rosenfeld, J. H., Minnerly, K. G., and Dyson, C.M., "Ten Year Operating Test Results and Post-Test Analysis of a 1/10th Segment Stirling Sodium Heat Pipe," Phase III Final Report, Report Number NASA/CR-2012-217430, June 2012.

AUGMENTING CAPILLARY SUCTION BY ELECTROWETTING FOR COOLING APPLICATIONS

Soubhik Kumar Bhaumik, Sunando DasGupta*

Department of Chemical Engineering, Indian Institute of Technology, Kharagpur

E-mail: soubhikge@gmail.com and sunando@che.iitkgp.ernet.in

Suman Chakraborty

Department of Mechanical Engineering, Indian Institute of Technology, Kharagpur

E-mail : suman@mech.iitkgp.ernet.in

ABSTRACT

Spreading and wetting play important roles in the performance of miniature cooling devices that utilize the phase change heat transfer mechanism for cooling. The wetting characteristics of partially wetting liquids over silicon surfaces covered with native oxides are investigated herein in the presence of electric field and heat transfer. The experiments are performed in a specially designed experimental cell with provisions of applying electric field and heating. The shape change of the curved liquid meniscus and its advancement on application of electric field are monitored in situ. Image analyzing interferometry technique is used to measure the shape and thickness of the film in the microscopic contact line region. The results of only electrowetting (without heat transfer) show substantial advancement of the meniscus as a result of Maxwell stress at interline due to the electric field. However, the film retracts from the hot spot on application of an external heat flux to the system. Experiments involving the simultaneous application of electrowetting and heat input demonstrate that the effects of electrowetting can potentially counter the retraction tendency of the meniscus due to heating. This will have important applications in micro heat pipes where externally applied electric field can increase the capillary limit and thus delay the dry-out of such devices.

KEY WORDS: CAPILLARY, ELECTROWETTING, CONTACT LINE DISPLACEMENT

1. INTRODUCTION

Miniaturized cooling devices such as micro-heat pipes, grooved evaporators and capillary fed heat exchangers rely on the capillary action of the coolant, typically a wetting/partially wetting liquid to form a self sustaining cooling system. Cooling efficiency of these devices is related to the wetting characteristics of the thin liquid film on various substrates, including microgrooved surfaces, where the microgrooves provide the capillary suction necessary to draw the liquid towards the hot-spot/region. This is further assisted by the inherent spreading tendency of the liquid on the substrate. Hence, for efficient cooling of a hotspot in miniature systems, the spreading of the liquid towards the hotspot needs to be augmented using a variety of techniques.

Means of enhancing the spreading of liquids include electrowetting which has recently emerged as an extremely flexible method for modifying the surface property from hydrophobic to hydrophilic through the application of electric field. Electrowetting is popularly conducted in the 'Electrowetting on Dielectric' (EWOD)

configuration in which electric fields are applied across a dielectric layer placed between a conducting liquid and a planar electrode below (Berge, 1993, Mugele & Baret (2005)). In fact, a whole branch of 'digital microfluidics' is devoted to manipulating flow of discrete liquid droplets over substrates using configurable electrode patterns. Diverse applications of EWOD include lab on a chip (Fair, 2007; Pollack et al. (2002)), liquid display (Kuiper & Hendriks (2004)) and cooling applications. The phenomenon of electrowetting is explained by a reduction in the liquid-solid interfacial tension leading to the reduction of the apparent contact angle.

Despite the vast literature on electrowetting of drops, only recently electrowetting has been implemented on partially wetting liquids with contact angle tending to zero. Unlike the case of drops where the phenomena are macroscopic, the scale of the contact line for partially wetting liquid is microscopic ($\sim\mu\text{m}$) and any experimental technique to examine the transport processes taking place in the sub-micron contact line region needs to be non-intrusive in nature (DasGupta et al. (1995), Argade et al. (2007), Gokhale et al.

* Corresponding Author

(2004)). Using such a technique, namely image analyzing interferometry, Bhaumik et al. (2011) investigated the electrowetting of surfactant (SDS) laden NaCl solution over Si-SiO₂ (native oxide) substrate, adopting an EWOD configuration. Considerable advancement of the contact line (~100 μm) has been observed for voltages as low as 4V. It is felt that the scope of using electrowetting in heat pipes for electronic circuitry cooling is immense. The phenomenon incurs no power loss due to the open circuit capacitive configuration involved in EWOD.

This paper compiles recent studies related to electrowetting of thin films of partially wetting liquids along with new experimental data on the effects of heat transfer during electrowetting. The studies include investigations on the electrowetting of thin liquid films of partially wetting liquids and also electrowetting as a means to counter the retraction of liquids during cooling application.

2. EXPERIMENTAL SECTION

2.1 Set up

The EWOD cell is fabricated using circular stainless steel plates and Teflon gaskets as shown in Figure 1. The lower stainless steel plate has a sleeve for holding a metallic plate over which Si wafer is placed. On top of the wafer a Teflon gasket is placed with provisions of O-rings for sealing. The Teflon gasket with O rings, form an enclosure for a liquid pool. The liquid is injected through the micro-tube on the Si substrate to form a liquid pool. The top SS plate has a glass window for viewing the meniscus. Voltage is applied across an electrode dipped in the bulk (thicker region) of the liquid pool and the metallic plate placed below the Si wafer. The cell is mounted on the microscope stage below the objective with CCD camera attached to a image processing computer. The whole set up is tilted at an angle so that the meniscus is formed halfway on the substrate. The behavior of the meniscus under the application of electric field and heat transfer can be analyzed in-situ using a monochromatic light and subsequent processing of the images of the interferometric fringes formed at the curved meniscus.

The Si substrate acts as a conductor whereas the native oxide SiO₂ constitutes the dielectric layer. The working liquid used is 0.1 M critical micellar concentration (CMC) Sodium Dodecyl Sulphonate

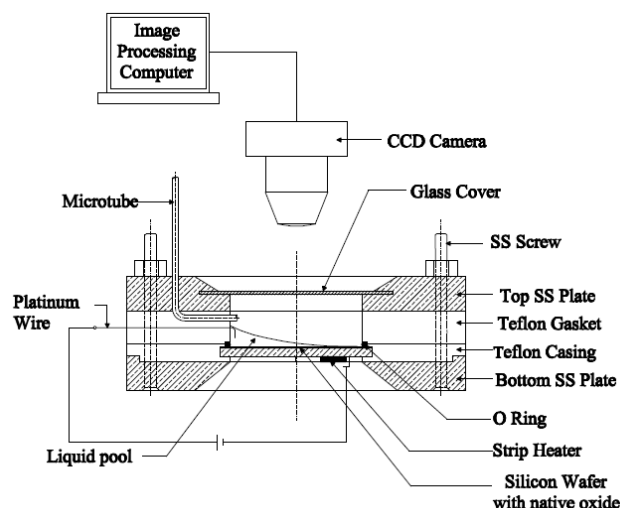


Figure 1. Schematic of experimental set up.

(SDS) and 0.1 M NaCl solution characterized by low surface tension (0.027 N m⁻¹) and high conductivity (1.34 S cm⁻¹). The presence of SDS renders the water partially wetting on Si/SiO₂ surface and ensures that discernible fringes are obtained for interferometry. A small quantity (0.1 CMC) of SDS is added to the solution to render the interference fringes clearly visible. Changing the SDS slightly may bring only nominal changes in the electrowetting behavior and hence the results are insensitive to the amounts of SDS present within the ranges used herein. The amount of NaCl should be sufficient to render the liquid conducting and is taken to be 0.1M.

2.2 Procedure

The meniscus is allowed to equilibrate first and for about 30 minutes and monochromatic light ($\lambda = 543$ nm) is focused on the contact line region. An interference pattern results due to the interference of reflected light from the substrate and the liquid vapor interface. Two separate studies involving electrowetting are conducted namely i) electrowetting without heat input and ii) evaporating thin films where a constant heat flux is applied externally along with application of electric field.

In the former case, the meniscus is subjected to electric fields in increments of 0.5 V (0-4V). The equilibrium states for the different voltages are captured by a CCD camera. The non-isothermal experiments consist of the following sequence. The isothermal stable meniscus is subjected to a constant heat input. The contact line starts to

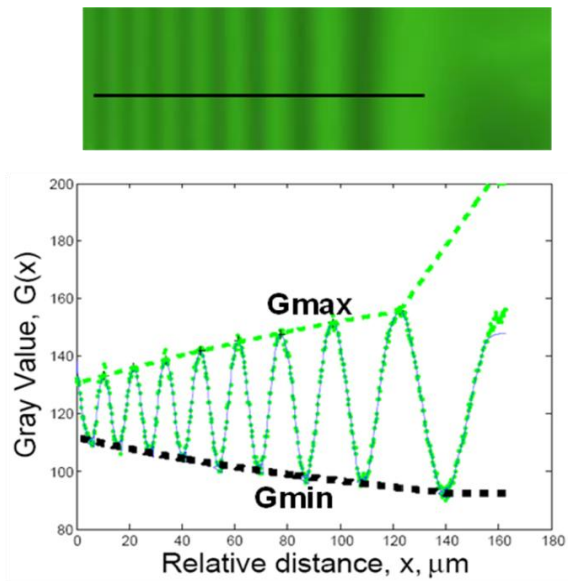


Figure 2. Typical interferometric image and gray value pattern extracted from image.

retract till it reaches a steady state when evaporation from the meniscus is balanced by replenishment from the adjacent thicker zones. Keeping the heat source on, the meniscus is subjected to gradually increasing electric fields of 4V, 6V and 8V respectively. The images of the interferometric fringes are captured and analyzed to obtain the thickness profiles and hence the effect of electric field and heat on the meniscus shape.

2.3 Image analysis

The reflectivity images (Figure 2) captured from the microscope through the CCD camera are digitized and assigned one of 256 possible gray values representing intensity from zero (black) to 255 (white). The gray value at each pixel is a measure of the reflectivity and the local film thickness over a region of $0.29 \mu\text{m}$ diameter (20 X objective magnification). For each image, line profiles of the gray values are extracted in a direction normal to the contact line, using Image-Pro-Plus software version (6.0). The real peaks/valleys are identified by scanning after filtering noise from the raw data. The relative gray values are calculated by drawing interpolatory envelopes drawn to maximas and minimas (DasGupta et al. (1995), Argade et al. (2007), Gokhale et al. (2004)). Using the relation for relative gray value with thickness, thickness profiles are obtained from experimental data.

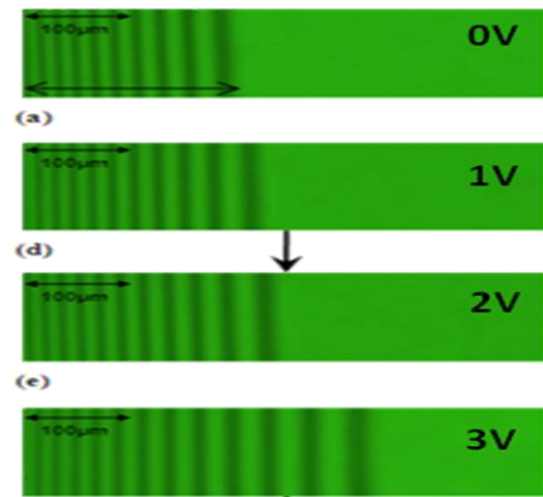


Figure 3. Interferometric images of equilibrium meniscus

3. RESULTS AND DISCUSSION

3.1 Meniscus Subject to Electric Field

Reflectivity images of the equilibrium meniscus at different applied voltages between 0-3.5 V are shown in Figure 3. In the figure, the fringes move forward with increasing voltage, indicating advancement of the contact line. A shift of $135 \mu\text{m}$ is observed for an applied voltage of 3.5 V. Along with the overall shift in the fringe pattern, inter-fringe spacing increases as well, indicating a reduction of meniscus curvature and therefore enhanced spreading. The film retracts towards its original position on withdrawal of voltage, with marginal hysteresis in most of the cases. The thickness profiles of the equilibrium meniscus are

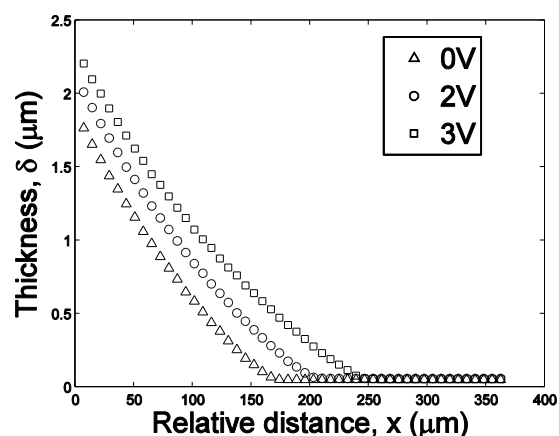


Figure 4. Thickness profiles of the equilibrium meniscus (reproduced with permission from Bhaumik et al. (2011))

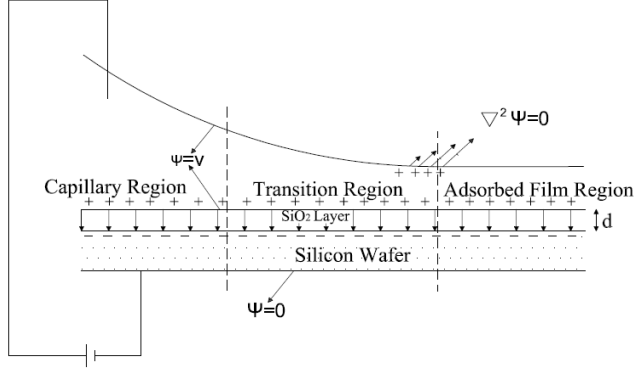


Figure 5. Illustration of the electrowetting mechanism (reproduced with permission from Bhaumik et al. (2011))

plotted in Figure 4 for applied voltages of 0V, 2V, and 3 V. As can be seen from the figure, the meniscus advances with increase in voltage, however, the adsorbed film thickness remains nearly unchanged.

The mechanism of electrowetting is illustrated in Figure 5. Since the liquid is conducting due to the presence of NaCl, the liquid-vapor and the solid-liquid interfaces become iso-potential surfaces with a potential equal to the applied potential V . The voltage at the Si-SiO₂ interface is 0 V. The dielectric constant of the ambient phase is assumed to be same as that of the dielectric. The potential in the dielectric and surrounding is given by (Li, 2008)

$$\nabla^2 \phi = 0 \quad (1)$$

where ϕ is the electric field potential. The relevant boundary conditions are

$$\text{At l-v \& s-l interfaces } \phi = V \quad (2)$$

$$\text{At Si-SiO}_2 \text{ interface } \phi = 0 \quad (3)$$

where subscript s, l and v represent solid, liquid and vapor phase respectively. Solving equation 1 with the relevant boundary conditions (Eq. 2 and 3), fringe electric fields appear concentrated at the contact line tip of the meniscus. In order to screen these fields, charges accumulate at the liquid-vapor interface. The electrostatic pressure arising as a result, is given as $P_{el} = \rho_e E/2$, where ρ_e is the charge density and $E = -\nabla\phi$ is the electric field. Using Gauss theorem, the effective electrostatic pressure is given as

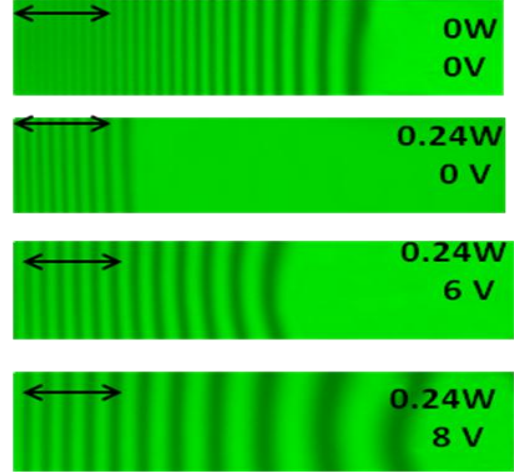


Figure 6. Interferometric images of evaporating meniscus. Heat applied 0.24 W.

$$P_{el} = \frac{1}{2} \epsilon E^2 \quad (4)$$

where ϵ is the dielectric permittivity of the dielectric layer. The effect of the electrostatic force is highly localized and singular at the contact line region (Kang, 2002, Li, 2008) Hence the net effect is a horizontal force expressed as

$$F_{el} = \frac{1}{2d} \epsilon V^2 \quad (5)$$

where d is the dielectric layer thickness. This force pulls the interline away from the capillary meniscus resulting in increased spreading. Thus the extent of spreading is a function of the applied voltage and inversely proportional to the thickness of the dielectric layer. It is to be noted that this capacitive system remains unaffected by the polarity of the voltage applied. This is because force acting at the meniscus tip is always directed normally outwards acting to pull the interline forward (as illustrated in Fig. 5) irrespective of the location of the electrode and polarity. The intensity of field is given by the voltage applied divided by the dielectric layer (SiO₂) thickness and is equal to 2×10^9 V/m for this specific case.

3.2 Meniscus Subject to Heat and Electric Field

Figure 6 shows the typical interference pattern for a combined heat transfer and electrowetting experiment with an applied heat of 0.24 W. The heat is applied to the strip heater by a precision

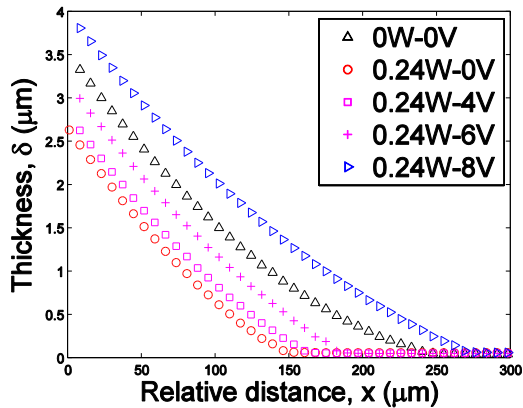


Figure 7. Thickness profiles of evaporating meniscus (at 0.24 W) for different applied voltages.

power supply system (TESTRONICS) with an accuracy of $\pm 2\%$. The values at the right corner of each sub-figure indicate the applied heat flux and voltage respectively. The images are in the following sequence from top: isothermal meniscus with no applied voltage, meniscus subjected to heat alone (0.24 W), and then the constant application of heat (0.24 W) but with progressive increases of applied voltages. It is clear that with heat application, the meniscus recedes and finally attains a steady state. On application of electric field, the meniscus advances thereby countering the effect of heat.

Figure 7 represents the film thickness profiles under conditions described above. It is apparent that the film retracts considerably and becomes more steep (higher curvature) on application of heat but the final figure (0.24W and 8V) shows that the film has advanced even beyond the position of the isothermal meniscus with less curvature. The situation is more clearly depicted in the next figure where the beneficial effects of the applied field (in terms of spreading) become clear.

In this figure for simultaneous heat transfer and electrowetting (Figure 8), the contact line displacement is plotted for both isothermal and evaporating meniscus. The vertical line is the datum line at the initial state. As was presented before (Figure 3), during electrowetting the meniscus advances monotonically with applied voltages. The results for experiments involving electrowetting of an evaporating meniscus demonstrate that the effects of electrowetting can potentially counter the retraction tendency of the meniscus due to heating. Electrowetting will also

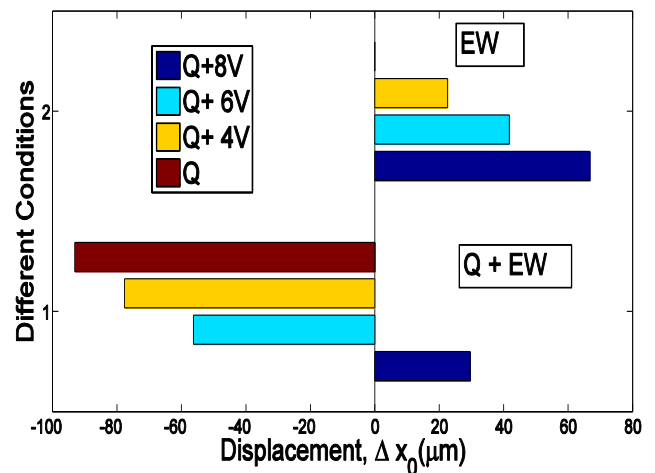


Figure 8. Displacement of the contact line of the meniscus during electrowetting and heat transfer

occur if dilute NaCl solution is used as opposed to the SDS+ NaCl solution. SDS is added specifically to view the interferometric images more clearly for analysis purpose. The electrowetting phenomena is generic for any partially wetting liquid as long as it is made electrically conductive by suitable addition of small quantities of any electrolyte (NaCl is used herein). The above holds huge promise in applications in micro-heat pipes where externally applied electric fields can increase the capillary limit and thus delay the dry-out of such devices.

4. CONCLUSIONS

Electrowetting of a partially wetting liquid film (an aqueous solution of 0.1 M NaCl with 0.1 CMC SDS) over Si substrate, with passivating oxide is explored using image analyzing interferometry. The contact line displacement and the shape of the meniscus are measured for isothermal and non-isothermal conditions. For the isothermal case, the experimental results demonstrate considerable advancement of the meniscus front with applied voltages (0-3.5V). The advancement for an applied voltage of 3.5 V is measured to be about 135 μm . The results of subsequent experiments involving simultaneous electrowetting and heat transfer confirm that electrowetting offsets the retraction tendency of the meniscus due to heating even for relatively smaller values of applied voltages. These results underscore the applicative potential of electrowetting in micro-cooling devices e.g., to counteract capillary limitations in micro-heat pipes.

5. ACKNOWLEDGEMENTS

This work is partially supported by a grant from the Department of Biotechnology (DBT) (Sanction number: BT/PR13931/MED/32/141/2010 dated 22.12.2010).

References

- Argade, R., Ghosh, S., De, S., DasGupta, S. (2007) *Experimental investigation of evaporation and condensation in the contact line region of a thin liquid film experiencing small thermal perturbations*. *Langmuir*, 23, p. 1234–1241.
- Berge, B. (1993) *EÄ lectrocapillarite ´ et mouillage de films isolants par l'eau*. C R. Acad. Sci, 2nd ed., 317, p. 157-163.
- Bhaumik, S. K., Chakraborty, M., Ghosh, S., Chakraborty, S., DasGupta, S. (2011) *Electric field enhanced spreading of partially wetting thin liquid films*, *Langmuir*, 27, p. 12951-12959.
- DasGupta, S., Plawsky, J. L., Wayner, P. C., Jr. (1995) *Interfacial force field characterization in a constrained vapor bubble thermosyphon*. *AICHE J.*, 41, p. 2140–2149.
- Fair, R. B. (2007) *Digital microfluidics: Is a true lab-on-a-chip possible?* *Microfluidics and Nanofluidics*, 3, p. 245-281.
- Gokhale, S. J., Plawsky, J. L., Wayner, P. C., Jr. DasGupta, S. (2004) *Inferred pressure gradient and fluid flow in a condensing sessile droplet based on the measured thickness profile*. *Phys. Fluids*. 16 (6), p. 1942–1955.
- Kang, K. H. (2002) *How electrostatic fields change contact angle in electrowetting* *Langmuir* 18, p. 10318–10322.
- Kuiper, S., Hendriks, B. (2004) *Variable-focus liquid lens for miniaturized cameras* *Appl Phys. Letter*, 85, p. 1128–1135.
- Li, D., (2008) *Encyclopedia of Microfluidics and Nanofluidics*. Dongking Li (ed). , Springer: Nashville, TN, USA.
- Mugele, F., Baret, J.C. (2005), *Electrowetting: from basics to applications*. *J. Phys. Condens. Matter* 17, p. R705-774.
- Pollack, M. G., Shenderov, A. D., Fair, R. B. (2002) *Electrowetting-based actuation of droplets for integrated microfluidics*, *Lab Chip*, 2, p. 96–101.

INCREASING THE CPL POWER AT STARTUP BY USING A CHECK VALVE

V. DUPONT, S. VAN OOST, L. BARREMAECKER

Euro Heat Pipes SA,

Rue de l'Industrie 24, B-1400 Nivelles, Belgium.

Tel: +32 67 88 94 71 Fax: +32 67 88 94 99 Email : vincent.dupont@ehp.be

ABSTRACT

Capillary Pumped Loop can be used for cooling of high power electronics. The present paper describes a new simple and passive way to secure high power and high heat fluxes startups of CPL evaporators i.e. a "float check valve". This solution has been extensively tested, first on a single evaporator CPLIP-1 demonstrator, and after, on a four-evaporator CPLIP-2 demonstrator, both using methanol as working fluid. The investigated heat flux ranges from 10 to 100 W/cm², the power per evaporator from 0.5 to 5.5 kW, the saturation temperature from 69.4 to 75.8 °C and the subcooling before heat application from 14 to 56K.

KEY WORDS CPL, methanol, high power, high heat flux, startup.

1. INTRODUCTION

The CPL concept, developed originally for space applications, has been customized to cool high power electronics modules on earth (Dupont 2007) and (Dupont 2010). A major improvement is the flat mechanical interface at evaporator wall level. The flat wick is directly assembled on a nickel wall and this unique design minimizes the overall thermal resistance of the evaporator.

During the startup phase heat is applied at evaporator wall level. If the vapor phase is already present inside the evaporator and directly in contact with the heated wall, then the CPL (or the LHP) startups successfully (Ku 1995). If the evaporator is in subcooled condition i.e. fully flooded with liquid then startup can be more difficult. In this case, the part of the heated wall in contact with the fluid must be superheated above the boiling incipience superheat $\Delta T_{sat,i}$ to start the system (Dupont, 2003). During the time needed for the capillary wall to reach $\Delta T_{sat,i}$ the metastable liquid, the pay load, the heated wall itself and the porous wick store extra-heat. When the first bubble appears in the evaporator, this extra-heat is released very fast by phase change. A large quantity of vapor flows suddenly to the condenser and push the liquid from vapor line and condenser to the reservoir. At this moment, the pressure spike inside the evaporator

might exceed the pumping capability of the primary wick and the vapor goes to the reservoir through the porous media: the capillary evaporator deprimed and startup is unsuccessful.

Different methods has been developed to improve the CPL startup:

a - design. The diameter of the liquid and vapor lines are enlarged in order to reduce the pressure drop between the capillary evaporator and the reservoir.

b - limitation of the power at startup. The power limit is set below the steady state transfer capability of the system or the thermal inertia of the heat load is increased.

c - startup heater (SUH). This well-known device in space market is an additional heater located at capillary evaporator level that permit to superheated locally the liquid and avoid a global superheating of the evaporator during the application of the main heat load.

d - auxiliary capillary evaporator. This device is an additional capillary evaporator placed in parallel to the main capillary evaporator. The vapor created by the auxiliary capillary evaporator purges the vapor side in the capillary evaporator before the application of the main heat load (Butler 1995).

e- electrohydrodynamically enhanced CPL. An electrode is inserted inside the capillary evaporator and an electrical field is generated through the porous wick. In such a configuration instability-induced Maxwell

stresses and contribute to reduce the startup time and boiling incipience superheat (Mo 1999).

These solutions induce generally an increase of the cost, mass and complexity (dedicated reliable power supply, additional wires, etc.) of the thermal solution that might be penalizing for the technology, in particular for “non-space market”.

In the present study, a new simple and passive way of increasing the power at startup is proposed. A check valve is added at the liquid inlet of the evaporator in order to block the vapor front outside the porous wick during the boiling incipience stressing event.

2. EXPERIMENTAL SET-UP

2.2 CPLIP-1 design and experimental setup

The CPLIP-1 loop is described in figure 1. A 5 kW flat vertical evaporator is connected to a liquid cooled exchanger. The pressure inside the reservoir is precisely regulated with a simple heating cartridge that permits a constant operating temperature of the modules whatever the temperature fluctuations of the cold source. The working fluid is methanol to avoid freezing and pressure issues.

In the present paper startup issue is investigated through four configurations:

1. Evaporator in nominal configuration
2. a startup heater (SUH) located on the upper part of the evaporator side (Fig. 2 et 3a)
3. a startup heater located on the lower part of the evaporator side (Fig. 2 et 3b)
4. a check valve (CV) located at the liquid inlet of the evaporator (Fig. 4)

2.3 Design of the startup heater

The SUH is a High Power Resistor assembled on a aluminum block. The contact area with the lateral side of the evaporator is 5.6 cm² and the maximum power 64W. Thermal grease is use to improve the thermal transfer between the SUH and the evaporator.

The SUH is powered before the application of the main heat load at evaporator level in order to “trig” the vaporization.

Table 1. Summary of CPLIP-1 design.

Components	Material	Value
Evaporator	Nickel & SS	473 x 83 x 19 mm ³ 4 pockets : 48 x 81 mm ² ep. wall : 1 mm mass : 1.3 kg
Primary wick	Nickel	porosity : 0.73 pore dia. : 6.8 μm permeability : 6.53 x 10 ⁻¹³ m ²
Evaporator exit tube	SS	o.d. : 15.88 mm length : 179 mm
Reservoir	SS	o.d. : 101.6 mm length : 308 mm
Vapor line	SS	o.d. : 14 mm length : 2200 mm
Liquid line	SS	o.d. : 8 mm length : 2600 mm
Condenser tube	SS	o.d. : 16 mm length : 3500 mm
Subcooler tube	SS	o.d. : 8 mm length : 650 mm
Working fluid	Methanol	mass : 1.4 kg

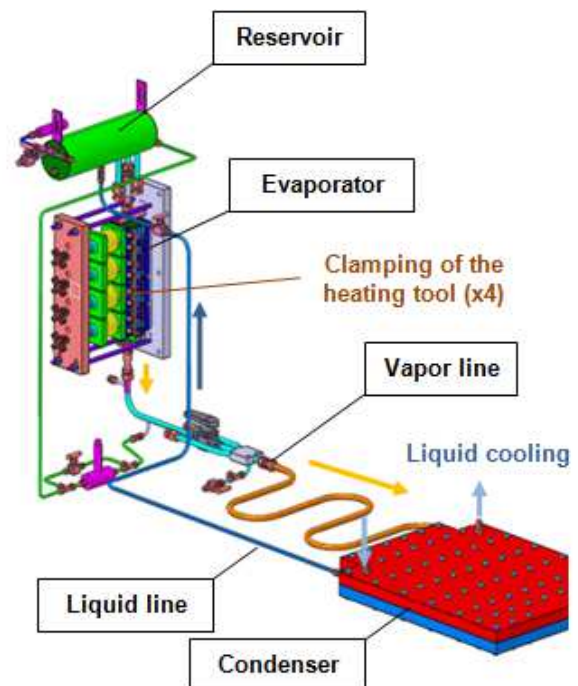


Figure 1. CPLIP-1 equipped with a 5 kW evaporator

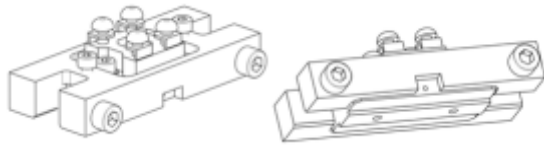


Figure 2. Global design of the SUH.

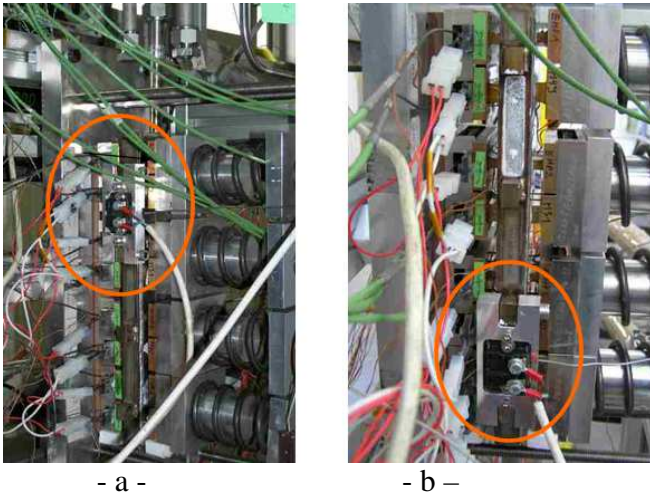


Figure 3. Location of the SUH on the evaporator side: above (a) and below (b).

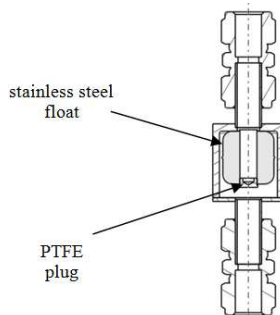


Figure 4. Design of the stainless float tested.

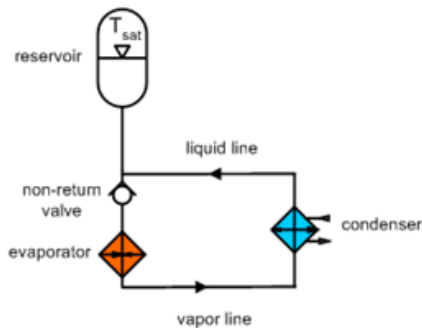


Figure 5. CPLIP-1 evaporator equipped with the check valve at inlet.

2.3 Design of check valve

The proof-of-concept of the check valve solution is designed around a stainless steel float equipped with a PTFE plug. The float force is 3.5 grams, the outside diameter 28 mm. The CAR is located on the liquid line between the evaporator and the reservoir, it performs 3 functions:

- avoid flows from the evaporator at startup when the evaporator and the valve are fully flooded with liquid,
- allow liquid flows to the main wick,
- allow vapor or NCG bubbles to escape from the evaporator core to the reservoir. This design of CAR must be placed vertically to perform this goal and is suitable only for non-space application.

2.3 Heating tool and data acquisition device

The 8 pockets of the evaporator are equipped with the heating tool presented in (Dupont 2010). The heating elements consist of two ceramic glow igniters made of silicon nitride (active part: $50 \times 14.6 \times 4.3 \text{ mm}^3$) with a maximum contact temperature of 580°C and a maximum power of 600W. The two heaters are clamped on two copper blocks (1.5 kg of copper per evaporator) with a total contact area of 15.16 cm^2 per pocket. The 16 heaters are electrically connected to 6 Xantrex 600V-10A power supplies. To reach very high heat flux several power supplies could be connected on the same heat element.

The data acquisition device is an Agilent 34970A connected to the PC via a GPIB connection and a Labview interface. The evaporator temperatures are given indirectly by the temperature of the copper block of the heating elements (16 type-K thermocouples). Thermal grease and copper material are present between the thermocouple and the surface of the evaporator. Typical precision of the EHP calibration process is $\pm 0.3^\circ\text{C}$. The other thermocouples are located on the system according to Fig. 6. P_{res} is measured with an absolute pressure transducer Keller PAA-33X, 0-10 bars pressure transducer with an accuracy of 0.10% EM i.e. $\pm 10 \text{ mbar}$, on the measurement range. P_{res} is used to determine the saturation temperature $T_{\text{sat}}(P_{\text{res}})$ inside the loop and to regulate the pressure inside the reservoir.

ΔP_{loop} is measured between the vapor outlet and the liquid inlet with a differential pressure transducer

Keller PD23 0- 200 mbars with an accuracy of 0.5%, i.e +/- 100 Pa, on the measurement range

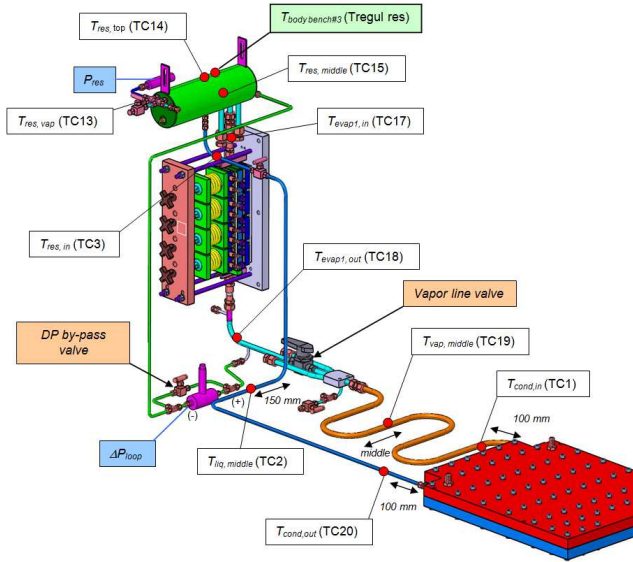


Figure 6. Location of the thermocouples of the system and the pressure transducer at reservoir level.

3. EXPERIMENTAL RESULTS

3.1. Test procedure

Before heat load application, the reservoir temperature is set to 73°C. The power cycle is applied on the evaporator: full power during 20 minutes and no power during 20 min, etc. The success of the startup is determined by the pressure evolution inside the reservoir. In case of success the pressure decrease a little bit and stabilizes at the set point level. In case of failure, the evaporator deprimizes and the vapor flows directly to the reservoir through the porous wick. In this case pressure spike in the system is clearly visible (Fig. 8).

The boiling incipience superheat and the maximum subcooling before startup are determined as described in Fig. 9:

$$\Delta T = T_{\text{heating tool}} - T_{\text{sat}}(P_{\text{res}}) \quad (1)$$

Where the saturation law for methanol is given by :

$$T_{\text{sat}}(P_{\text{sat}}) = 5.209388E-06 \ln(P_{\text{sat}})^6 + 7.795873E-04 \ln(P_{\text{sat}})^5 + 1.571637E-02 \ln(P_{\text{sat}})^4 + 1.899360E-01 \ln(P_{\text{sat}})^3 + 2.131387 \ln(P_{\text{sat}})^2 + 25.33618 \ln(P_{\text{sat}}) + 64.14863$$

with P_{sat} in expressed in bar and T_{sat} in °C.



Figure 7. Pressure evolution during startup cycling at 1 kW (19 w/cm²) : 2 failures for 14 startups.

3.2. Test campaign

A large range of parameters given by Table 2 have been investigated during the experimental validation. Very high heat fluxes have been reached (up to 100 W/cm² based on a contact area of 15.16 cm² per pocket). Figure 9 shows the value of the pressure spike for 104 startups. Only the check valve solution was 100% successful. The failure rates as summarized in Table 3. It is very important to perform a large number of run (typically over 20) to be sure that a two-phase cooling system is robust to high power startup.

Figure 10 gives more detail on the superheat reach by the heating tool at time t_i (not the evaporator wall itself) during the tests at 80W/cm². The SUH located at the top side of the evaporator exhibit a statically effect on the boiling incipience superheat. The other configuration (SUH below and CAR) have no impact with respect to “the natural discrepancy” of the boiling incipience phenomena.

3.3. Physical interpretation

CPL evaporator deprimizes at startup due to high boiling incipience superheat. The SUH is located on the side of the evaporator and the vapor created here is not able to propagate to the superheated liquid inside the grooves just in front of the heating tool and to reduce efficiently the boiling incipience superheat. To be efficient a SUH must purge all the vapor part of the evaporator but operating conditions and power available make this design impossible.

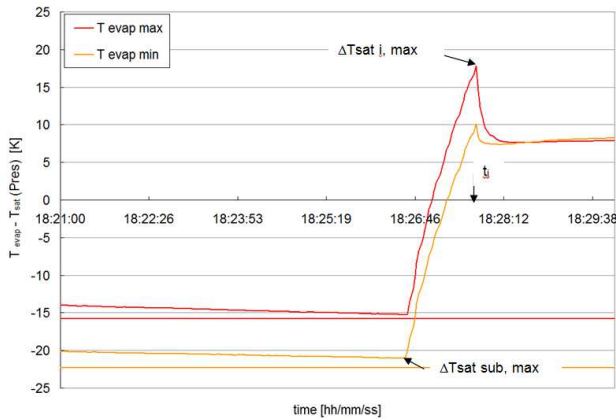


Figure 8. Definition of boiling incipience superheat time t_i and subcooling.

Table 2. Range of the investigated parameters.

	Q loop [W]	T sat [°C]	Psat [mbar]	Psat, max [mbar]	DPloop [Pa]	
Natural	540	69.4	1227	1386	1276	min
	5575	73.7	1443	5051	16938	max
SUH - top	3829	72.3	1366	1392	4886	min
	4587	73.7	1438	3331	14345	max
SUH - bellow	1060	65.8	1068	1398	5099	min
	4560	72.8	1393	3055	22861	max
Anti-return	4534	71.7	1335	1374	4501	min
	4568	75.8	1559	1605	22532	max

	Q loop [W]	DTsat,i max [°C]	q flux max [W/cm²]	DTsub max [°C]	
Natural	540	10	9.5	14	min
	5575	42	99.9	59	max
SUH - top	3829	24	73	23	min
	4587	33	82	55	max
SUH - bellow	1060	21	19	21	min
	4560	42	82	56	max
Anti-return	4534	27	82	23	min
	4568	42	82	56	max

Nevertheless, the check valve works well because it supports the porous media during the duration of the high stress event i.e. the pressure spike at boiling incipience. The CAR must work during few tenths of seconds and after, during the “normal” behavior, the float remains in the back of its body and allow the flow of subcooled liquid to the porous wick and, if needed, the outgassing from the evaporator core.

5. TEST ON THE CPLIP-2 LOOP

The check valve solution has been applied to CPLIP-2 i.e. a CPL equipped with four evaporators able to transfer up to 27kW and described in details in (Dupont 2010). In the frame of the present study, this CPL has been modified with the two following configurations.

Configuration 1: 4 check valves (one for evaporators).

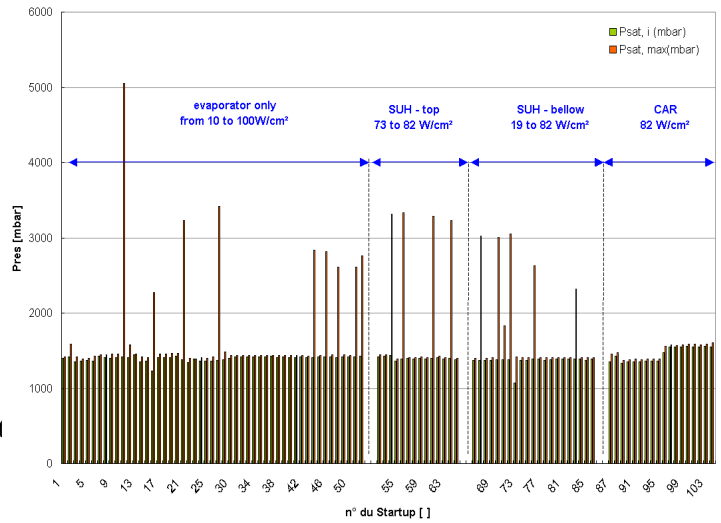


Figure 9. CPLIP-1 maximum pressure after startup.

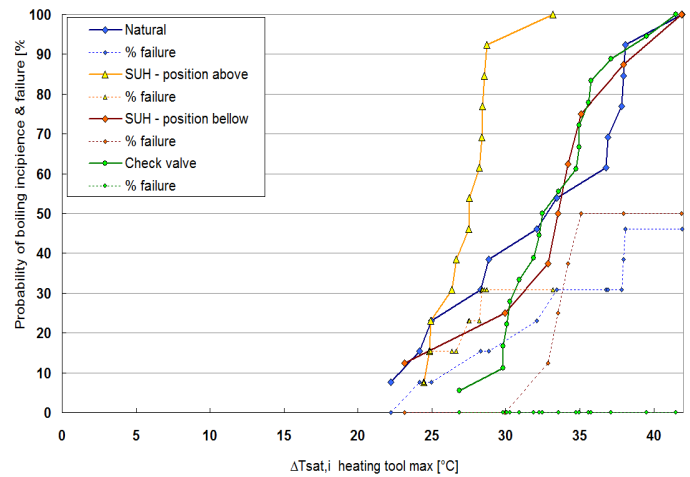


Figure 10. Probability of boiling incipience and failure rates versus heating tool superheat at startup.

Table 3. Failure rate for the evaluated configuration.

	total []	failure []	% failure [%]
Natural	51	9	17.6%
SUH - top	14	4	28.6%
SUH - bellow	21	6	28.6%
Car	18	0	0.0%
Global without CAR	86	19	22.1%

The test procedure is close to those of §3.1. During 3 days, the 4 evaporators are cycled from 0 to 22.2 kW. The duration of each phase is, respectively, 20 and 10 minutes: 100% of the 150 startups have been successful.

Additional tests have been done with startup shift between evaporators i.e. heat load is applied on

evaporator n°1, after 30s on evaporator n°2, etc. For these tests only the 3 upper pockets are used because of power supplies architecture: 100% of the 150 startups have also been successful.

Thus, the system is robust at startup. The number of active evaporator has no impact on reliability.

Configuration 2: a unique check valve for the 4 evaporators as described in Fig. 11.

More than 120 tests have been run for the two configurations and all startups are 100% successful.

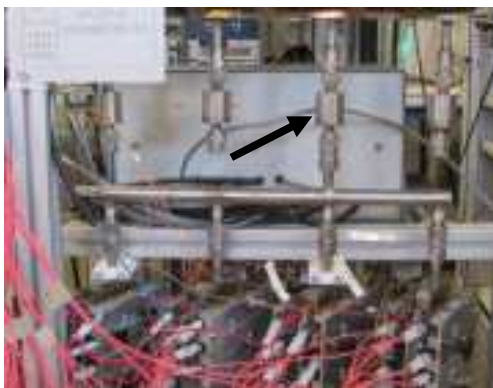


Figure 11. CPLIP-2 single CAR configuration.

5. CONCLUSIONS

The maximum power at startup is lower than the transport capability of the CPL during less severe heat load application. This phenomenon is due to the pressure spike at boiling incipience superheat that induces a vapor penetration inside the porous wick.

In the present study a “float check valve” has been added to the evaporator liquid inlet of a methanol CPL in order to avoid this vapor invasion inside the porous material.

This check valve has been successfully tested in various CPL configurations (with hundreds of runs):

- single evaporator,
- multi-evaporator with a four or single check valve,
- multi-evaporator with a single check valve,
- multi-evaporator with time-shifted startup of each evaporator.

Comparison with an evaporator equipped with a startup heater located in the top or in the bottom part of the evaporator has been performed. Until now the

check valve is the only way to insure a 100% successful start-up of the CPL at high heat flux and power.

Patent pending (FR 1158202 and FR 1158203).

NOMENCLATURE

$\Delta T_{sat, i}$	tooling superheat at boiling incipience time
CAR	check valve (Clapet Anti-Retour)
CPL	capillary pumped loop
$q_{l/F}$	evaporator external wall heat flux [W/cm ²]
o.d.	outside diameter [m]
P_{res}	absolute pressure inside the reservoir [Pa]
SUH	Startup Heater
TRL	Technical Readiness Level
T_{sat}	Saturation temperature [°C]
t_i	time of boiling incipience [s]

ACKNOWLEDGEMENT

The authors thank the Region Wallonne in Belgium for its strong and determining support.

REFERENCES

1. Ku J. (1995) *Startup issues of capillary pumped loop*, Proc of the 9th IHPC Albuquerque, New Mexico, p. 994-1001.
2. V. Dupont, J. L. Joly, M. Miscevic, V. Platel, (2003). *Capillary Pumped Loop startup: effects of the wick fit on boiling incipience*, J. Thermophysics Heat Transfer 17 (2), p. 138-144.
3. Butler D., Ottenstein L et Ku J. (1995), *Flight testing of the capillary pumped loop flight experiment*, SAE Transact., no. 951566, p 750-764.
4. Mo B., Ohadi M. M., Dessiatoun S. V., Cheung K. H. (1999) *Startup time reduction in an electrohydro-dynamically enhanced capillary pumped loop*, J. Thermophysics Heat Transfer, 13 (1), p. 134-139.
5. Dupont, V., Van Oost, S., Barremaecker, L., Legros, J.C. (2007), *EBoWIT characterization device for capillary evaporator development*, Proc. of the 14th IHPC, Florianopolis, pp. 95-100.
6. Dupont, V., Van Oost, S., Barremaecker, L., & S. Nicolau (2010), *Experimental investigations on a methanol capillary evaporator equipped with four flat evaporators*, Proc. of the 15th IHPC, Clemson, pp. no printed version.

DEVELOPMENT AND EXPERIMENTAL INVESTIGATION OF A HEAT-TRANSFER SYSTEM ON THE BASIS OF A LOOP AND A PULSATING HEAT PIPE

Pastukhov V.G., Maydanik Y.F.

Institute of Thermal Physics, Ural Branch of the Russian Academy of Sciences

Amundsen st.106, Yekaterinburg 620016, Russia

Phone: +7(343) 267-87-91, Fax: +7(343) 267-87-99, E-mail: pastukhov@itp.uran.ru, maidanik@etel.ru

ABSTRACT

The paper presents the results of development and experimental investigation of a heat-transfer system consisting of a pulsating and a loop heat pipe. The pulsating heat pipe (PHP) was made of a copper capillary tube and located on an aluminum plate measuring 260×200×1 mm, had a thermal contact with the evaporator interface of a loop heat pipe (LHP). A heat load source was located on the PHP, and its heat was transferred to the LHP evaporator. The working fluid of the PHP was R141b. The LHP was filled with ammonia. Tests have shown the fundamental possibility of creating a combined heat-transfer system which can be operable in a wide range of ambient conditions and have a thermal resistance of about 0.3-0.4 °C/W.

KEY WORDS: heat-transfer system, loop heat pipe, pulsating heat pipe.

1. INTRODUCTION

The necessity of developing combined heat-transfer systems consisting of heat pipes of different types may be caused by the peculiarities of thermal management problems and searching for their optimum solution. The present paper solves the problem of cooling a source of heat distributed over a sufficiently large surface when the heat sink is at a distance which exceeds considerably the dimensions of the source. A heat-transfer system must be operable at any orientation in the gravity field and have minimum mass-and-size parameters. The solution of such a problem with the help of any one type of heat pipe either is impossible or leads to a design with unsatisfactory thermal and mass-and-size characteristics. This is connected with the fact that every type of heat pipes has its own structural and heat-transfer characteristics, which determine the area of application best suited for them.

The problem mentioned above may be solved with help of an appropriate combination of a pulsating and a loop heat pipe.

LHPs are characterized by a local arrangement of the capillary structure in the heating zone and separate channels for vapor and liquid, which connect the evaporator and condenser. Such a design ensures high heat-transfer characteristics,

and the ability to transfer heat for sufficiently large distances at any orientation in the gravity field (Maydanik, 2005). Their considerable advantage is also fine mass-and-size characteristics. These merits, however, are realized at relatively high heat fluxes in the evaporation zone. Besides, a thermal interface made of a heat-conducting material is often required for realizing a thermal contact of the LHP evaporator with the heat source. If the heat source has a large surface, the dimensions of the thermal interface increase, which leads to an increase in thermal resistance of the system as a whole and its mass. The use of the LHP multievaporator scheme or a synthesis of an LHP evaporator with a conventional flat heat pipe (Maydanik et al., 1998) complicates considerably the design of the system.

A PHP is a bundle of a repeatedly bent capillary tube (or channels in a solid material) partially filled with a working fluid (Akachi, 1990). A PHP does not contain any capillary structure and is one of the simplest designs of a two-phase heat-transfer design. Besides, the diversity of constructional embodiments and the ability to operate at any orientation (Khandekar et al., 2004) make it quite interesting for application in cooling systems of electronics (Akachi et al., 1996; Maydanik et al., 2009). However, the potentialities of PHPs in transferring heat for sufficiently large distances are quite limited.

Of considerable interest is the use of PHPs as inset structures in various panels of solid materials. Katoh et. al. (1999) investigated the possibility of reducing the thermal resistance of a chassis wall (height \times length: 157 \times 318 mm) with help of a PHP during heat removal from printed-circuit boards (PCBs). The evaluations of the authors have shown that the thermal resistance of a chassis wall can be reduced approximately 6 times as compared with an aluminum wall 2.5 mm thick.

Cal et. al. (2007) investigated by experiment a cooling system which consisted of two PHPs placed between the PCBs and in the chassis wall. The PHPs were made of a copper tube with OD/ID=3.18/1.65 mm (outside/inside diameter) and had 7 turns for the PCBs and 12 turns for the chassis. Thermal tests were conducted with different working fluids (water, ethanol and acetone) and different filling ratios (from 40 to 70%). It has been shown that PHPs have the capability to transfer heat efficiently and to considerably reduce the temperature drop as compared with conductive cooling.

The aims of the present work were the development of an experimental combined heat-transfer system on the basis of a loop and a pulsating heat pipe and the determination of its operating characteristics at different orientations in the gravity field and heat sink temperatures.

2. DESCRIPTION OF THE HEAT-TRANSFER SYSTEM

The configuration of the system and its general view are presented in Fig.1. Figs. 2 and 3 show schemes of the PHP and LHP and the arrangement of measuring thermocouples.

A PHP of the closed loop type was made of a copper tube and bent in one plane. The PHP geometry was caused by the necessity of its location on the supporting plate and the limitation of the minimum radius of the tube bend equal to \sim 10 mm. Besides, such a geometry made it possible to compact the turns in the zone of the contact of the PHP with the LHP and to create there a sufficiently high heat flow concentration. The PHP was soldered with a tin-lead solder to one side of nickel-coated aluminum plate. The opposite smooth side of the plate was intended for the location of a heat source and joining with the LHP. The design parameters of the PHP are given in Table 1.

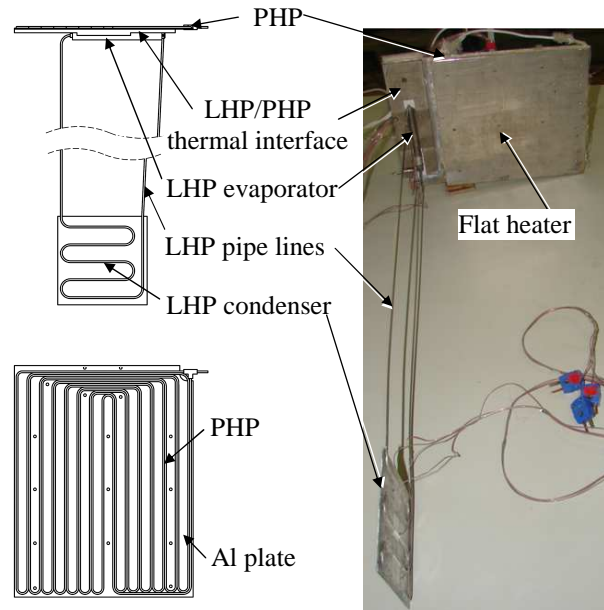


Fig.1. Scheme and general view of the heat-transfer system.

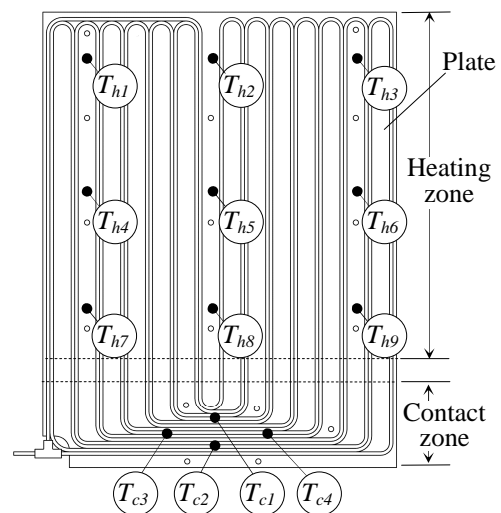


Fig.2. Scheme of the PHP.

Table 1. Constructive parameters of the PHP.

Parameter	Value
PHP:	
- material	cooper
- ID/OD, mm	1.3/2.0
- total length, m	8.08
- turns number	7
Plate:	
- material	aluminum
- length \times width \times thickness, mm	260 \times 200 \times 1
Heating zone (L \times W), mm	200 \times 200
Contact zone (L \times W), mm	200 \times 50
Working fluid /Filling ratio,%	R141b/ 50
Total weight, g	465

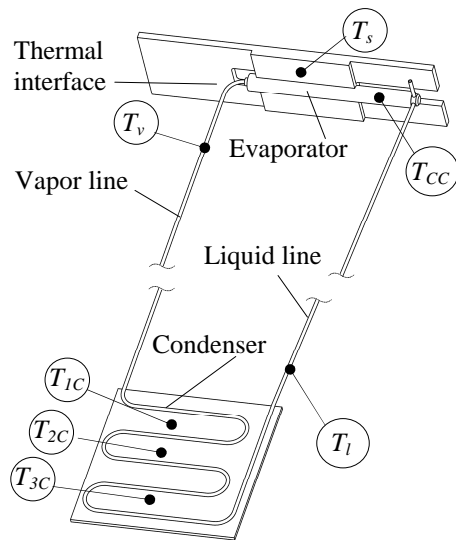


Fig.3. Scheme of the LHP.

The LHP had a cylindrical evaporator equipped with a thermal interface and a serpentine condenser joined to a thin plate. The pipelines and the LHP condenser were made from an integral tube. The design parameters of the LHP are given in Table 2.

Table 2. Constructive parameters of the LHP.

Parameter	Value
Evaporator:	
- material	nickel
- outside diameter \times wall, mm	10 \times 0.4
- total length, mm	100
- active zone length, mm	60
Wick:	
- material	nickel
- porosity, %	61
- breakdown pore radius, μm	4.6
Pipe lines:	
- material	ss
- ID/OD, mm	1.5/2.0
- vapor line length, mm	502
- liquid line length, mm	489
- condenser length, mm	554
Evaporator thermal interface:	
- material	aluminum
- length \times width \times thickness, mm	180 \times 50 \times 7
Condenser plate:	
- material	aluminum
- length \times width \times thickness, mm	100 \times 100 \times 1
Working fluid	ammonia
Total weight, g	216

The joint of the LHP thermal interface with PHP was dismountable and was realized with the help of screws. A heat-conducting paste with an

effective thermal conductivity of about 1 W/m·K was used in the contact zone. The total weight of the system with fastening elements was about 690g.

The working fluid in the PHP was R141b. The LHP was filled with ammonia. Such a choice of working fluids was caused by the chemical compatibility with the structural materials of the devices and, besides, by the required operating temperature range from -50°C to $+50^\circ\text{C}$.

3. TESTING TECHNIQUE

Originally the PHP and the LHP were tested separately. In testing the LHP a heat load was supplied to the thermal interface by a special heater with a heating surface measuring 50 \times 50 mm, which was located at the center of the contact surface of the evaporator interface. Heat from the condenser was removed to a cold plate, through which the thermostatted liquid was pumped. Investigations were conducted at three main orientations: $+90^\circ$ (vertical, heater-up), 0° (horizontal), $0^{*\circ}$ (horizontal, on the side).

In testing the LHP the heat load was created by an electric heater located in the heating zone and removed to a cold plate which served as a heat sink. The PHP was investigated at the same orientations as the LHP. Besides, tests were conducted at the orientation -90° (heater-down). In testing the system use was made of the same PHP heater and cold plate as in individual tests. The test orientations of the system are shown in Fig.4.

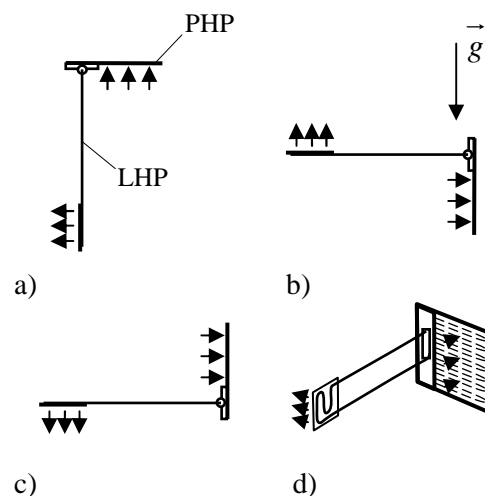


Fig.4. Test orientations of the system ($\varphi = \varphi_{\text{LHP}}/\varphi_{\text{PHP}}$): a) $+90^\circ/0^\circ$, b) $0^\circ/-90^\circ$, c) $0^\circ/+90^\circ$, d) $0^{*\circ}/0^{*\circ}$.

During the trials the temperature was measured at various point of the system at different heat loads and heat sink temperatures. The heat load was changed stepwise in the range from 10 to 170W. The heat sink temperature was taken equal to -20°C, 0°C and +20°C. Within the limits of every experiment temporal records of temperatures were made at the points shown in Figs. 2 and 3. The readings were averaged over the data of stable (quasi-stationary) regimes, and were later used for presenting the operating characteristics of the system and calculation of thermal resistances. The thermal resistances of the PHP (R_{PHP}), LHP (R_{LHP}) and the system as a whole (R_{syst}) were calculated by the following relations:

$$R_{PHP} = \frac{\overline{T}_h - \overline{T}_c}{Q}, \quad (1)$$

$$R_{LHP} = \frac{T_s - \overline{T}_C}{Q}, \quad (2)$$

$$R_{syst} = \frac{\overline{T}_h - \overline{T}_C}{Q}, \quad (3)$$

where: \overline{T}_h is the average temperature value in the PHP heating zone determined by thermocouples T_{hi} ($i=1-9$), °C; \overline{T}_c is the average temperature value of the PHP contact zone determined by thermocouples T_{ci} ($i=1-4$), °C; T_s is the temperature of the LHP thermal interface, °C; \overline{T}_C is the average temperature value of the LHP condenser plate determined by thermocouples T_{iC} ($i=1-3$), °C; Q is the heat load, W.

The effect of the environment was minimized at the expense of the thermal insulation of the system elements. The presence of heat losses in evaluations of thermal resistances were not taken into account.

4. TEST RESULTS AND DISCUSSION

Individual tests of a PHP have shown that without a working fluid its thermal resistance is 0.77 ± 0.04 °C/W. In a filled state this parameter is estimated at 0.14 ± 0.02 °C/W in the range of heat loads from 50 to 100 W. From the data presented in Fig.5 it can be seen that in this range of heat loads the PHP thermal resistance was minimum. The PHP start-up was successfully realized from a heat load of 20 W at orientations 0° , $0^{*\circ}$, -90° . At the orientation $\varphi = +90^\circ$ (heater-up) for reliable start-up it was necessary to increase the heat load to 40-50 W. The most favorable orientation for the

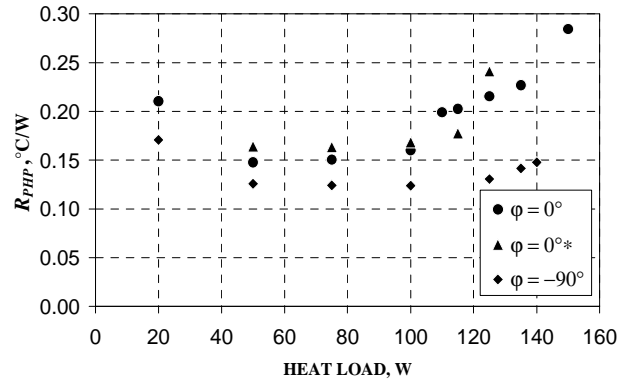


Fig.5. Heat load dependence of the PHP thermal resistance at different orientations ($T_{cool}=20^\circ\text{C}$).

PHP was orientation $\varphi = -90^\circ$ (heater-down), at which the thermal resistance was the lowest, and the working range of the heat loads was wider.

For the LHP maximum range of heat loads was from 10 to 175 W. A start-up from 10 W was successfully realized at all orientations and cooling conditions. A peculiarity of start-ups at low cooling temperatures (0°C and -20°C) was initiation of the oscillating regime, which disappeared when the heat load was increased to 25 W. This regime of LHP operation is well known (Vershinin et al., 2007; Goncharov et al., 2008) and is connected with the presence of two interfaces, which exist in the compensation chamber of the evaporator and in the condenser. From the data presented in Fig.6 one can see that from approximately 50 W the LHP thermal resistance is independent of both the heat load and the orientation. In the range of heat loads from 50 to 150 W the LHP thermal resistance was estimated at 0.17 ± 0.04 °C/W for all orientations and cooling temperatures.

With allowance for the fact that each of the devices has its own start-up peculiarities connected with

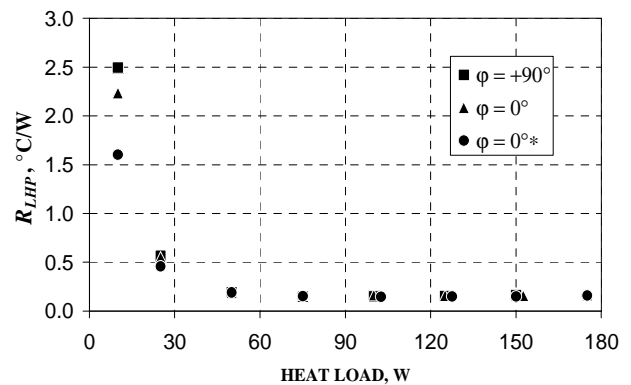


Fig.6. Heat load dependence of the LHP thermal resistance at different orientations ($T_{cool}=0^\circ\text{C}$).

the presence of a minimum starting load, it would be quite interesting to clarify the behavior of a heat-transfer system during a start-up. Tests showed that in starting the system with a heat load of 20 W one could observe oscillating regime, in which there superimposed low-frequency pulsations in temperature characteristic of the LHP start-up and high-frequency temperature pulsations of the PHP. The typical temperature-time diagram is given in Fig.7. Here it is well seen that a system start-up began with certain heating of the PHP, which was followed by a rapid temperature drop. It is interesting that in individual LHP tests there was no oscillatory operating regime at this heat load. It may be suggested that such a behavior is connected with an additional thermal resistance between the heat source and the evaporator of the LHP created by the PHP. It can also be seen that in the range of heat loads from 40 to 120W the system operation was stable. At 120W one could observe a PHP crisis, which was accompanied by a rapid increase of the temperature gradient in heating zone.

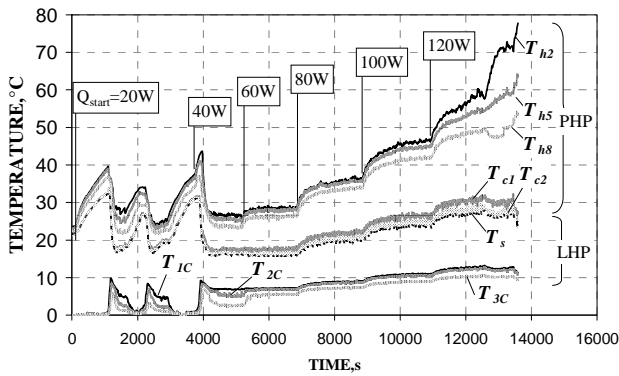


Fig.7. Temperature-time diagram for the system at orientation $\phi = +90^\circ/0^\circ$ and $T_{cool} = 0^\circ\text{C}$.

System start-up with a higher heat load of 50W proceeded without low-frequency temperature pulsations. The same heat load was minimum for start-up at the system orientation $\phi = 0^\circ/+90^\circ$, when the PHP was in the “heater-up” position. The data for this regime are presented in Fig.8. It is seen that for this orientation the maximum heat load was equal to 90W and it was lower than at other orientations. The maximum heat-transfer capacity of the system was 140W at the orientation $\phi = 0^\circ/-90^\circ$. Evidently, the potentialities of the system under consideration were limited by those of the PHP.

Data on the total thermal resistance of the system at all orientations are given in Fig.9. It is seen that

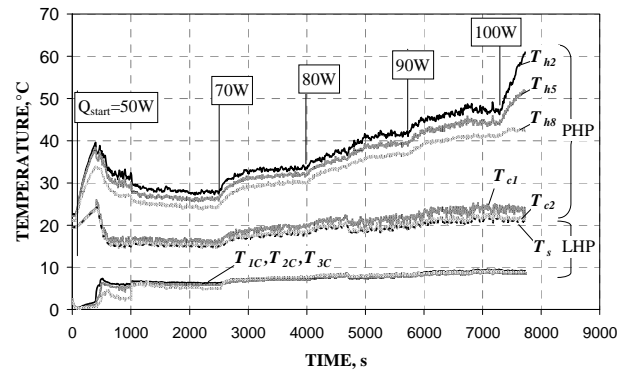


Fig.8. Temperature-time diagram for the system at orientation $\phi = 0^\circ/+90^\circ$ and $T_{cool} = 0^\circ\text{C}$.

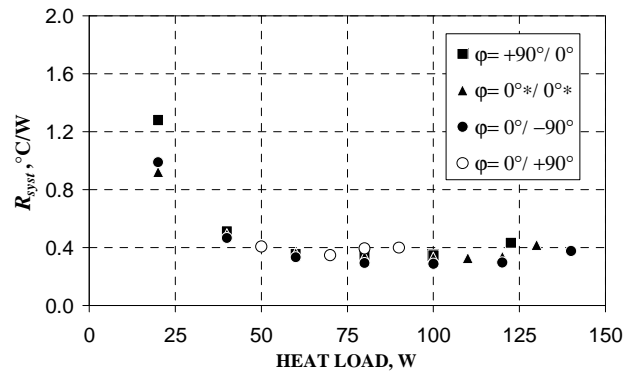


Fig.9. Heat-load dependence of the system thermal resistance at different orientations ($T_{cool} = 0^\circ\text{C}$).

in range of heat loads from 50 to 90W the system was little sensitive to the orientation. A minimum thermal resistance of 0.28°C/W was achieved in this range of heat loads at the orientation $\phi = 0^\circ/-90^\circ$.

The individual contributions of the PHP and the LHP to the thermal resistance of the system depended on the value of the heat load. From the data presented in Fig.10 it is seen that in the range of heat loads from 60 to 100W the PHP thermal resistance had a minimum, whereas the LHP thermal resistance continued to decrease. Here the thermal resistances of the devices were practically equal and were evaluated at about 0.12°C/W . The contact thermal resistance between the thermal interface of the LHP evaporator and the PHP was estimated at $0.05 \pm 0.01^\circ\text{C/W}$. Noteworthy is the discrepancy in the evaluations of the LHP thermal resistance in individual tests and included in the system, which was equal to 30-40%. This may be explained by different conditions of the heat load supply to the LHP thermal interface. Besides, in the case of great nonuniformity of the temperature

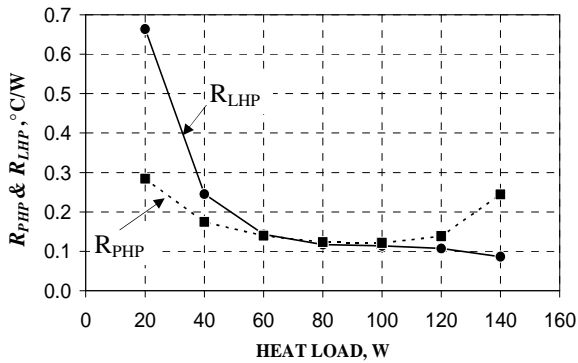


Fig.10. Thermal resistances of PHP and LHP in the system at orientation $\varphi=0^{\circ}/-90^{\circ}$ and $T_{cool}=0^{\circ}\text{C}$.

field of the interface measuring its temperature was obviously insufficient and resulted in a methodological error.

Thus, tests showed that the degree of the orientation effect on the characteristics of the system was mainly determined by the PHP operation. We can assume with assurance that the tangible effect of orientation on the PHP operation was connected with the small number of the tube turns. It should be expected that an increase in the number of turns will contribute to the reduction of the PHP sensitivity to changes in the orientation and enhance the stability of its operation (Zhang&Faghri, 2008).

3. CONCLUSIONS

The results of the work have shown the fundamental possibility of creating a combined heat-transfer system on the basis of a loop and a pulsating heat pipe which can be operable in a wide range of ambient conditions and slightly dependent on the orientation in the gravity field.

The experimental system developed has made it possible to remove heat from a large surface at advantageous mass-and-size parameters and a sufficiently low thermal resistance. The optimum range of heat loads, in which the system was low-sensitive to the orientation and had a minimum thermal resistance, was within the limits of 50...90W.

A topical problem determining the efficiency of such a system is the problem of agreement between the characteristics of the devices it consist of. First of all, it concerns starting and limiting heat loads.

In the system examined the main effect of the orientation was connected with the operation of the PHP and may be reduced by increasing the number of its turns.

REFERENCES

- Akachi, H.(1990) *Structure of a Heat Pipe*, United States Patent No. 4921041
- Akachi, H., Polasek, F. and Stulc, P. (1996) *Pulsating Heat Pipes*, Proc. of the 5th IHPS, Melbourne, Australia, p. 208-217
- Goncharov, K.A., Kochetkov, A.Yu., Buz, V.N. (2008) *Analysis of Thermal and Hydraulic Autooscillations in Loop Heat Pipe*, Proc. of the 7th Minsk Int. Seminar “Heat Pipes, Heat Pumps, Refrigerators, Power Sources”, Minsk, Belarus, p. 104-109
- Cai, Q. et. al. (2007) *Experimental Investigations of an Avionics Cooling System for Aerospace Vehicle*, Journal of Spacecraft and Rockets, V.44, No.2, March-April, p. 439-444
- Katoh, T. et. al. (1999) *New Heat Conductor for Avionics Cooling*, Proc. of the 11th IHPC, Tokyo, Japan, p. 452-457
- Khandekar, S. et. al. (2004) *Closed and open pulsating heat pipes*, Proc. of the 13th IHPC, Shanghai, China, September 21-25, p. 36-48
- Maydanik, Y. et al. (2009) *Compact cooler for electronics on the basis of a pulsating heat pipe*, Applied Thermal Engineering, V. 29, p. 3511–3517
- Maydanik, Yu. (2005) *Loop heat pipes*, Applied Thermal Engineering, Vo 25, p. 635–657
- Maydanik, Y.F and Goncharov K.A. (1998) *Heat transfer device*, Russian Patent No. 2120593
- Vershinin, S.V. and Maydanik, Yu. F. (2007) *Investigation of Pulsations of the Operating Temperatures in a Miniature Loop Heat Pipe*, Int. J. Heat and Mass Transfer, V.50, Issues 25-26, p. 5232-5240
- Zhang, Y. and Faghri, A. (2008) *Advances and Unsolved Issues in Pulsating Heat Pipes*, Heat Transfer Engineering, 29(1), p. 20 – 44

EXPERIMENTAL STUDY ON THE EFFECTS OF THE VAPOUR PRESSURE LOSSES ON A CAPILLARY PUMPED LOOP FOR TERRESTRIAL APPLICATION

Vincent Ayel, Laurent Lachassagne, Yves Bertin, Cyril Romestant

Institut Pprime, CNRS-ENSMA-Université de Poitiers, UPR 3346

1, avenue Clément Ader 86961 Futuroscope Chasseneuil Cedex

Phone: (+33) 5 49 49 81 12, Fax: (+33) 5 49 49 81 01, vincent.ayel@ensma.fr

ABSTRACT

In this experimental study, a specific CPL designed for power electronics cooling has been tested. Because of its use under gravity, the reservoir is located above the evaporator. Thanks to a setting valve situated on the vapour line, tests have been performed in order to assess the influence of the vapour pressure losses on this CPLTA operation. The vapour pressure losses have been increased by gradually closing the valve, until the failure of the loop. Steady-state measurements show that the mean evaporator wall temperature $T_{w,m}$ increases as the vapour pressure losses increase. Theoretical calculations have been used to determine the saturated evaporation temperature, T_E , and pressure, P_E , for every experimental result. It was found that, for lowest heat power applied, the increase of $T_{w,m}$ can be directly attributed to the temperature glide of T_E on the saturation curve, due to the increase of vapour pressure losses, ($T_{w,m} - T_E$) remaining constant whatever the closure of the valve is. For highest heat power applied, the increase of $T_{w,m}$ can be attributed to the recession of the evaporation front, leading to increasing heat conductive resistance between $T_{w,m}$ and T_E .

KEY WORDS: Capillary Pumped Loop (CPL), gravity, vapour pressure losses, saturation curve

1. INTRODUCTION

Capillary Pumped Loops, as well as Loop Heat Pipes, highly performing devices in regard to heat transfers, are both sensitive to the vapour pressure losses (d'Entremont, 2007). Pressure and temperature at two-phase points of the loops are linked together by the saturation curve. Increasing the pressure difference thus generates an increase of the temperature difference between the evaporation front and the reservoir. Practically speaking, the increase of pressure drop, mostly due to increasing vapour pressure losses, leads to an increase in evaporation temperature on the saturation curve.

In LHPs, such an effect strongly depends upon interactions among the fluid inventory, tilt and evaporator power (Ku, 2002). For example, Ku et al. (2002) conducted an experimental study on a 2 m long LHP filled with ammonia, on which a control valve was installed on the vapour line. They concluded that the operating temperature increases with increasing pressure drop caused by the closure of the valve. From this fact, Mishkinis et al. (2011) have used this property for LHP

thermal control purpose. They have in fact valves that adjusted automatically the hydraulic resistance of the circuit by adjusting that of the vapour line, hence varying the LHP pressure drop. The temperature of the evaporator has thus been maintained closed to constant and independent of the cold source temperature. Launay et al. (2010) have deduced a criterion from the pressure balance all over the LHP in which the liquid pressure drops are neglected. This criterion is based on turbulent vapour flow pressure losses that must remain under the capillary limit.

In CPLs, the effect of the vapour pressure losses increase is direct, due to the fact that the thermodynamic cycle is established from the reference point in the two-phase reservoir, since its temperature is imposed. However, in CPLs like in LHPs, a large increase of the vapour pressure losses may also lead to new pressure balance around the menisci in the porous wick. Such new balance may be associated with a recession of the evaporation front in the wick, therefore accompanied by a temperature difference increase between the evaporator wall and the evaporation

front, for same external conditions (heat transfer rate across a higher conductive heat resistance).

In this study, a specific capillary pumped loop (figure 1), designed for operation under gravity field, is considered to examine the effects of the vapour pressure losses. It differs from traditional CPL in that the circulating fluid passes through the reservoir, instead of being attached to the liquid line by a small diameter line (Nikitkin, 1994). The reservoir is located above the evaporator, taking advantages of gravitational forces to ensure the hydraulic connection between the reservoir and the evaporator. Lachassagne et al. (2012) have performed a steady-state modeling of this loop, showing *inter alia* that increasing vapour pressure losses has a significant effect on the evaporator wall temperature. Thus, the aim of this work was to perform an experimental study on the influence of the vapour pressure losses on the operation of this specific CPL by means of a setting valve installed on the vapour line.

2. EXPERIMENTAL APPARATUS

The specific *Capillary Pumped Loop for Terrestrial Application* (CPLTA or CPLIP, figure 1) has been already precisely described in (Ayel, 2011) and (Lachassagne, 2012). Its evaporator and reservoir have been developed by Euro Heat Pipe (Nivelles, Belgium). The main difference with regard to classical CPL is that the liquid flows through the lower part of the reservoir, located above the evaporator, before entering the latter. The whole loop is made of stainless steel, with external dimensions: $H = 0.74$ m and $L = 1.55$ m.

The reservoir is a 10.2 cm external diameter and 30.8 cm length cylinder, the higher part of which is thermally controlled by a PID regulator connected to a cartridge heated by an electrical power supply. A platinum thermal sensor (T_R , $\pm 0.1^\circ\text{C}$) and a GE druck PDCR3500 pressure sensor allow verifying the saturated state: $P_R = P_{sat}(T_R)$.

The vertical flat-plate evaporator (nickel and stainless steel) external dimensions are of $296 \times 83 \times 18$ mm³ and it includes a plane-parallel nickel porous wick whose dimensions are of $283 \times 68 \times 16$ mm³. Note that the mean pore diameter d_p is of $6.8 \mu\text{m}$, the porosity 73% and the permeability 6.53×10^{-13} m². Sixteen cartridge heaters (of global electrical resistance 14.4Ω and maximal power 6 kW) have been inserted in eight

copper blocks, divided into four blocks on each side and are heated by an electrical power supply of 11 kW maximal power.

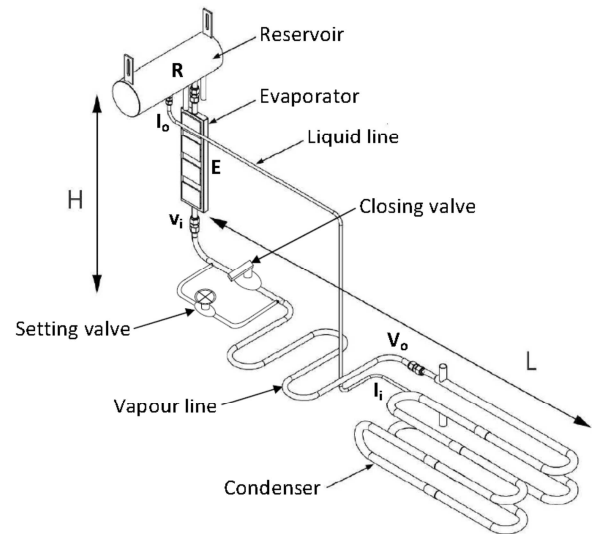


Figure 1. Schematic view of the CPLTA.

The condenser is a 12 mm inner diameter and 4 m long counter-current heat exchanger. The water/ethylen glycol mixture flows in the external annular channel (between 14 mm and 17.3 mm diameters) and is cooled by a cryostat of nominal cooling capacity of 5 kW. The liquid -and vapour- lines are 1.48 m -and 1.81 m- long with 6 mm -and 12 mm- inner diameters, respectively. All the lines of the loop have been thermally insulated. All parts of the loop, except evaporator, are made of stainless steel. In the vapour line, a bypass, in which a setting valve (Swagelok SS-12BG-MM) has been disposed in parallel with a closing valve (figure 1), let us the possibility to increase vapour pressure losses by closing gradually this valve. The CPLTA was tested with ethanol as a working fluid. The evaporator body has been accurately instrumented by 32 T-type thermocouples of 0.5 mm diameter ($T_{w,j}$, $1 \leq j \leq 32$) inserted between the copper blocks and the evaporator external wall. Ten other T-type thermocouples (0.1 mm diameter, $\pm 0.5^\circ\text{C}$ uncertainty) instrument different locations on outer tube surfaces: T_{li} to T_{lo} for the liquid line temperatures (three thermocouples), T_{vi} to T_{vo} for the vapour line temperatures (four thermocouples), T_R for the reservoir diphasic part, T_{R-E} for the line situated between the outlet of the reservoir and the inlet of the evaporator, and $T_{II'i}$ and $T_{II'o}$ for the secondary fluid temperatures at both ends of the condenser.

Figure 2 presents a theoretical thermodynamic operating curve of the working fluid inside the

CPLTA (corresponding to figure 1): first, the liquid evaporates in the porous wick (E_i - E); the vapour flows and is heated through the evaporator grooves (E - v_i) and flows in the vapour line (v_i - v_o); in the condenser, the vapour is first cooled (v_o - C) until saturation state (C), condensates, and the resulting liquid is subcooled until the exit of the condenser (C - l_i); note that the pressure increase between C and l_i is mainly due to gravitational forces, the outlet of the condenser being located 10 cm below the inlet; after, the liquid flows to the reservoir with decreasing pressure due to viscous and gravitational pressure drops (l_i - l_o); through the lower part of the reservoir the liquid also flows (l_o - RE), being partially heated by this latter; the liquid leaving the reservoir then enters the evaporator (RE - E_i) with increasing pressure due to gravitational forces; from the evaporator inlet, the liquid is heated while flowing through the porous media until evaporation (E_i - E). R is defined as the upper part of the reservoir, in saturated equilibrium. The pressure link between R and l_o is due to the gravitational pressure drop $\rho_l g H_{l,R}$, with $H_{l,R}$ the height of liquid in the reservoir. Note that the presence of non-condensable gazes in the reservoir leads to a pressure drop between P_R and $P_{sat}(T_R)$. In that case it is P_R that must be considered as a reference, due to the fact that the saturation points are linked the ones to the others only by pressure drops.

3. RESULTS AND DISCUSSION

3.1 Direct influence of the valve closure

During every test, the CPLTA was kept under constant conditions:

- heat power applied: Q_{el} ;
- secondary fluid temperature: $T_{II^o_i} = 20^\circ\text{C}$;
- two-phase reservoir temperature: $T_R \approx 73^\circ\text{C}$.

Note that, in the following, N is defined as the number of opening turns of the setting valve ($N = 0$: closed valve; $N = 4$: fully opened valve). So, a typical running test consisted of applying a constant heat power to the evaporator, turning off the closing valve, starting from a fully opened valve ($N = 4$) and closing gradually this latter until the loop started to fail. Steady-state measurements were recorded every half turn of the setting valve. The following parts will present results for Q_{el} values of 1000 W, 1500 W and 2000 W. Beyond 2000 W, the CPLTA stopped working as soon as

the closing valve was turned off (even if the setting valve was fully opened).

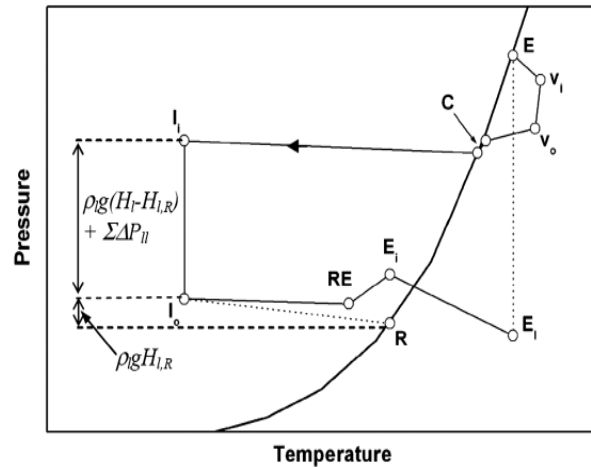


Figure 2. Theoretical cycle of the CPLTA.

First of all, the direct influence of the setting valve closure is shown on figure 3: one can see that the mean evaporator wall temperature $T_{w,m}$ increases when N decreases. The failure of the CPLTA has been instantly attained for a number of turns just below the lower value of each curve ($N = 0.5, 1$ and 2 for $Q_{el} = 1000$ W, 1500 W and 2000 W, respectively). Already in the beginning of the figure ($N = 4$), the curves are shifted the ones to the others: this can be mainly attributed to the progressive recession of the evaporation front in the porous media with increasing heat power applied, leading to increasing conductive heat resistance between the evaporator wall $T_{w,m}$ and the evaporation front T_E . This particular point has been already discussed in (Ayel, 2011). However, the curves of figure 3 show that the vapour pressure drop has a first order importance on the CPLTA operation, since they reach a sufficient level.

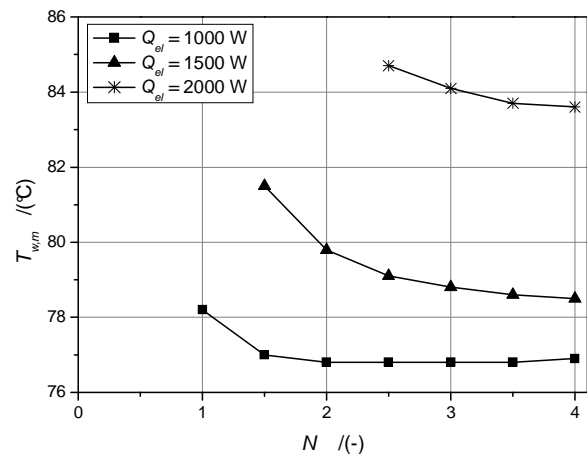


Figure 3. Evaporator mean wall temperature as a function of N .

Starting from these results, a question arises: as well as the influence of the heat power applied, can the increase of $T_{w,m}$ with decreasing values of N be attributed to the recession of the front in the porous wick, leading to higher temperature difference ($T_{w,m} - T_E$) (with increasing conductive heat resistance at constant heat power level), or to the temperature glide on the saturation curve (with increasing vapour pressure losses, *cf.* figure 2)?

3.2 Theoretical evaluation of T_E and P_E

In order to answer this question, a theoretical analysis has been performed on every result, trying to identify by postprocessing the evaporation temperature T_E and its corresponding pressure P_E . The methodology has already been presented by Ayel et al. (2011). It consists in calculating all pressure losses in the CPLTA, for every experimental test, starting from the known values of (T_R, P_R), determined experimentally, until the evaporation point (T_E, P_E) on the saturation curve:

$$P_E - P_R = \sum \Delta P_l + \sum \Delta P_g + \sum \Delta P_v \quad (1)$$

The first term of right-hand side of Eq. (1) corresponds to the overall singular and linear pressure losses of the liquid flow; the second term corresponds to gravitational pressure drops; the last term corresponds to the overall singular and linear pressure losses of the vapour flow. From the known values of $T_R, P_R, T_{li}, T_{RE}, T_{vi}$ and T_{vo} identified experimentally, the calculations allowed the identification of all other parameters that can be seen on the theoretical cycle of figure 2. The following assumptions have been adopted here:

- the vapour pressure losses in porous wick have been neglected;
- all linear and singular one-phase viscous pressure losses have been evaluated using classical correlations;
- the two-phase pressure losses at condensation have been estimated by taking into account only vapour properties;
- the condensation length has been calculated thanks to Chato correlation (1962), involving condensation of water in pipes;
- the height of liquid in the reservoir $H_{l,R}$ has been evaluated by mass balance in the loop, taking into account the condensation length for each heat power applied.

Starting from the pressure/temperature of the two-phase high part of the reservoir, the flow path has been monitored counterflow (see figure 2), until determining the value of the evaporation pressure P_E and its corresponding temperature T_E on the saturation curve. For example, the pressure of the liquid entering the reservoir, P_{lo} , is linked to P_R by gravitational pressure drop:

$$P_{lo} = P_R + \rho_l g H_{l,R} \quad (2)$$

The setting valve pressure drop $\Delta P_{v,v}$ is given by the following relation (Swagelok, 1994), as a function of the mass flow rate \dot{m} :

$$\Delta P_{v,v} = \left[\frac{\dot{m}}{C_v \rho_v \left(1 - \frac{2\Delta P_{v,v}}{3P_{vi}}\right)} \right]^2 \frac{G_v T_{vi}}{P_{vi}} \times 10^{10} \quad (3)$$

with C_v the flow coefficient and G_v the vapour density. The mass flow rate \dot{m} of the fluid flow in the loop is given by:

$$\dot{m} = \frac{Q_{el} - Q_{losses}}{h_{lv} + c_{p,l}(T_E - T_{RE})} \quad (4)$$

where Q_{losses} are the heat losses of the evaporator to the ambient, evaluated with empty CPLTA. In Eq. (4), the evaporation temperature T_E is still unknown, so that an iterative loop on \dot{m} permits determination of T_E until thermal/hydraulic balance on the saturation curve (figure 2).

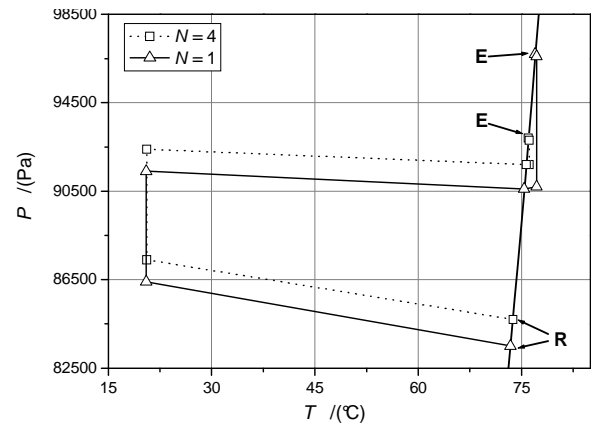


Figure 4. Thermodynamic operating curves of the CPLTA for $Q_{el} = 1000$ W.

Resulting thermodynamic cycles can be seen on figure 4 for $Q_{el} = 1000$ W and on figure 5 for $Q_{el} = 2000$ W. On each figure have been represented the curves for the fully opened valve ($N = 4$, dotted lines) and the lower value of N attained before the loop started to fail (continuous

lines). The effect of the valve closure is clearly noticeable on figure 4 for 1000 W: the vapour pressure drop is multiplied by more than four between $N = 4$ and $N = 1$. Thus, the mean pressure of evaporation P_E is significantly raised on the saturation curve and the evaporation temperature, T_E , is thereby increased up to 1°C. On the contrary, for a heat transfer rate of 2000 W (figure 5), the vapour pressure losses are already initially high, so that the increase of P_E and T_E caused by the closure of the valve before the loop stops working is not relevant.

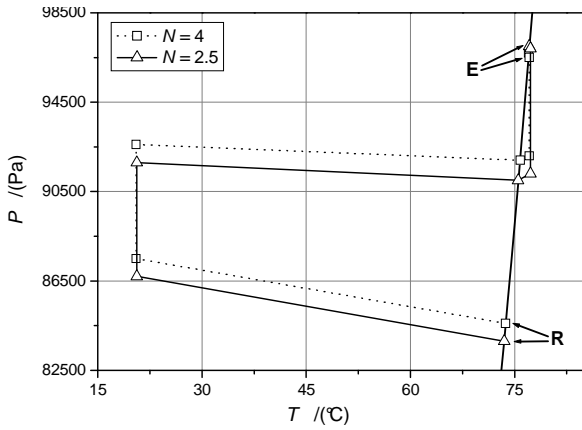


Figure 5. Thermodynamic operating curves of the CPLTA for $Q_{el} = 2000$ W.

3.3 Discussion and analysis

From these results, it is now possible to compare on figure 5 the curves of $(T_E - T_R)$ (dotted lines) and $(T_{w,m} - T_R)$ (continuous lines) for every test. One can see that gradually closing the valve causes a slight increase of $(T_E - T_R)$. Compared to $(T_{w,m} - T_R)$, for $Q_{el} = 1000$ W, the slopes of the curves corresponds with each other, suggesting that the increase of $T_{w,m}$ can be attributed to the temperature glide on the saturation curve only. This assertion can be confirmed by figure 7: the value of $(T_{w,m} - T_E)$ remains constant until $N = 1$: one can suppose that the heat conductive resistance between $T_{w,m}$ and T_E remains constant (for constant heat power applied), showing a stability of the evaporation front in the porous wick.

On the contrary, for higher heat powers applied, figure 7 clearly shows that the closure of the valve is linked to an increase of $(T_{w,m} - T_E)$. In these cases, considering constant heat flux through the dry part of the wick, the mean thickness of this latter necessarily grows to carry out such an increase of the temperature difference. The pressure difference around the menisci is equal to

the overall pressure drop in the loop ΔP_{tot} . Thus, increasing the pressure difference around the menisci leads to a recession of the evaporation front for high values of ΔP_{tot} .

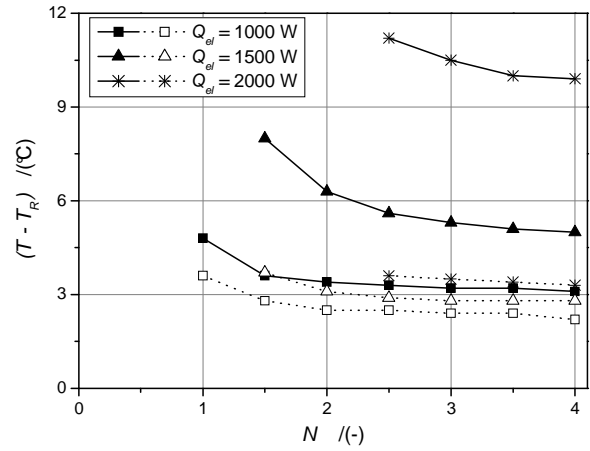


Figure 6. $(T_E - T_R)$ (---) and $(T_{w,m} - T_R)$ (—) as functions of N .

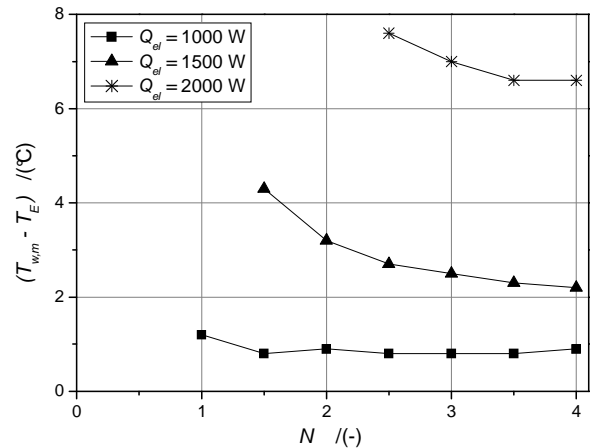


Figure 7. $(T_{w,m} - T_E)$ as a function of N .

Finally, figure 8 presents the evolution of the overall pressure drop ΔP_{tot} as a function of N for all the tested configurations. Referring to figure 2, ΔP_{tot} can be written as:

$$\Delta P_{tot} \approx (P_E - P_{lo}) + \rho_l g H_{RE} + \Delta P_{w,l} \quad (5)$$

where H_{RE} is the height between the bottom of the reservoir and the high part of the evaporator, and $\Delta P_{w,l}$ are the liquid pressure losses in the porous wick calculated thanks to Darcy law. ΔP_{tot} is calculated at the highest part of the evaporator because it reaches its maximal value here.

On figure 8 has also been represented the maximal capillary pressure drop of the loop, $\Delta P_{c,MAX}$, calculated at evaporation temperature. It is clear that, for the three heat power tested, the lower

value of N has resulted in overall pressure drop just below the capillary limit. The dotted lines completing each curve represent the calculation for an extra half a turn with previous operating conditions: one can see that the pressure drop is greatly beyond the capillary limit for 1000 W and 1500 W, while it is just exceeded for 2000 W. This suggests that the capillary limit was actually reached in all cases.

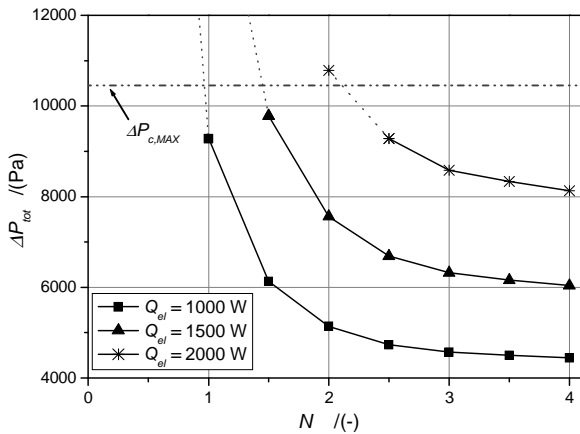


Figure 8. ΔP_{tot} as a function of N .

4. CONCLUSIONS

The specific Capillary Pumped Loop, designed to work under gravity field, has been tested here in order to assess the influence of the vapour pressure losses on its operation by means of a setting valve. It has been found that the evaporator mean wall temperature increases with the vapour pressure losses. Thanks to a theoretical study allowing us to determine the temperature/pressure of the evaporation front, it was found that:

- the mean wall temperature increases with the closure of the valve following the temperature glide on the saturation curve for the lowest heat powers applied;
- beyond 1500 W, mean wall temperature rather increases due to the recession of the evaporation front in the porous wick;
- the calculation of the overall pressure drop shows that the capillary limit has been reached for all tested cases.

NOMENCLATURE

c_p	mass heat capacity ($J.K^{-1}kg^{-1}$)
g	gravitational acceleration ($m.s^{-2}$)
G	density (-)
h_{lv}	latent heat of evaporation ($J.kg^{-1}$)

H, L	height, length (m)
\dot{m}	mass flow rate ($kg.s^{-1}$)
P	pressure (Pa)
Q	heat transfer rate (W)
T	temperature ($^{\circ}C$)
ρ	density ($kg.m^{-3}$)

Subscripts:

C	condenser
E	evaporator
el	electrical
i,o	inlet, outlet
l,v	liquid, vapour/valve
m	mean
R	reservoir
w	wall
II ^o	secondary fluid

REFERENCES

- Ayel, V., Lachassagne, L., Bertin, Y., Romestant, C., Lossouarn, D. (2011) *Experimental Analysis of a Capillary Pumped Loop for Terrestrial Application*, Journal of Thermophysics and Heat Transfer, 25(4), p. 561-571
- d'Entremont, B.P., Ochterbeck, J.M. (2007) *Vapor Pressure Limit in Capillary Pumped Loop*, Proceedings of the 14th IHPC, Florianopolis, p. 365-372
- Ku, J., Ottenstein, L., Rogers, P., Cheung, K. (2002) *Effect of Pressure Drop on Loop Heat Pipes Operating Temperature*, Proceedings of the 12th IHPC, Moscow, p. 153-158
- Lachassagne, L., Ayel, V., Romestant, C., Bertin, Y. (2012) *Steady-state Modeling of Capillary Pumped Loop in Gravity Field*, accepted for publication in Int. J. Thermal Sciences.
- Launay, S., Sartre, V., Bonjour, J. (2010) *Selection Criteria for Fluidic and Geometrical Parameters of a LHP Based on an Analytical Approach*, Proceedings of the 15th IHPC, Clemson, 6 p.
- Mishkinis D., Kulakov, A., Romera, F., Gregori, C., Torres, A. (2011) *Thermal Control of Loop Heat Pipe with Pressure Regulating Valve*, Proceedings of the VIII Minsk International Seminar "Heat pipes, Heat Pumps, Refrigerators, Power Sources, Minsk, p. 340-351
- Nikitkin, M., Cullimore, B. (1998) *CPL and LHP Technologies: What are the Differences, What are the Similarities?*, SAE Paper 981587, p. 400-408
- Swagelok (1994) *Valve Sizing - Technical Bulletin*, www.swagelok.com

Dependence of Liquid Reservoir Orientation on Behavior of Temperature Controllable Oscillating Heat Pipe

Hiroyuki OGAWA, Naoko IWATA

Japan Aerospace Exploration Agency

3-1-1 Yoshinodai, Sagamihara-shi, Kanagawa, 252-8510, Japan

+81-50-3362-3592, +81-42-759-8068, iwata.naoko@jaxa.jp, ogawa.hiroyuki@jaxa.jp

Yoshiro MIYAZAKI

Fukui University of Technology

3-6-1, Gakuen, Fukui-shi, Fukui, 910-8505, Japan

+81-776-29-2675, +81-776-29-7891, miyazaki@fukui-ut.ac.jp

ABSTRACT

Experiments were conducted to verify an Oscillating Heat Pipe (OHP) with liquid reservoir works as a temperature controllable thermal control for the inner pressure of the OHP is controlled by the saturated vapor pressure of the liquid reservoir. We set the liquid reservoir in 3 ways (vertical, horizontal, and vertically inverted directions) and measured the pressure of both the OHP and the liquid reservoir. The temperature of the heating section was maintained almost constant by regulating the temperature of the liquid reservoir and the inner pressure of the OHP is equivalent to that of the liquid reservoir even when the heat input changed and the liquid reservoir set in different ways. It was confirmed that the OHP operates as a variable conductance heat pipe in each case. It was concluded that the OHP with the liquid reservoir operates as a variable conductance heat pipe as its inner pressure is controlled by the liquid reservoir.

KEY WORDS: Oscillating Heat Pipe, Liquid Reservoir, Pressure Measurement, Variable Conductance

1. INTRODUCTION

An oscillating heat pipe (OHP), also known as a pulsating heat pipe or a loop-type heat pipe, was invented by Akachi et al. in the 1990s^[3-5]. It consists of a meandering capillary tube that does not need an internal wick. The capillary tube goes back and forth many times between a heating section and a cooling section. The working principle of an OHP is described in detail in the literatures. OHP operation relies on the oscillation and/or circulation of vapor plugs and liquid slugs in the capillary tube. Vapor bubbles are generated and grow in the heating portion (evaporator) and collapse in the heat radiating portion (condenser). The generation and collapse of vapor bubbles pump the liquid slugs, thus causing pressure and temperature fluctuations. As a consequence of thermo-hydrodynamic coupling of pressure and temperature fluctuations with the void fraction, the entrapped liquid slugs and vapor bubbles undergo complex translational oscillatory movement. This leads to transfer of both sensible heat and latent heat.

An OHP connected a liquid reservoir can operate as a variable conductance heat pipe, i.e. VC-OHP^[6].

The operation temperature of the OHP is maintained by the reservoir temperature that is controlled by an active control such as a heater as the inner pressure of the OHP is controlled by the vapor saturated pressure of the liquid reservoir. Experimental studies have been conducted to demonstrate the assumption. The inner pressure of both the liquid reservoir and the OHP is measured. The liquid reservoir is set in three directions: vertically, horizontally, and vertically inverted.

2. EXPERIMENTAL SETUP

The test specimen consists of an OHP and a liquid reservoir. The reservoir is connected to the OHP via a polytetrafluoroethylene (PTFE) tube with inner diameter of 1 mm and length of 600 mm. The OHP is a closed-loop type: A stainless steel capillary tubes with inner and outer diameters of 0.8 mm and 1 mm, respectively, meanders between a heating section and a cooling section 15 times in each direction (30 times in total), with both terminals interconnected. Fifteen check valves are inserted between the two sections, at every other line, to direct the flow from the cooling section to the heating section. The working fluid circulates in

one direction, and more working fluid is transported as liquid phase than as vapor per unit volume flow rate. The check valves are installed in the tubes of the adiabatic section close to the heating section where liquid slugs flow from the cooling section to the heating section so that the liquid slugs are steadily supplied to the heating section. Figure 1 shows the OHP apparatus. The upper panel shows a top view, and the lower panel shows a lateral view. At the heating section and the cooling section, the tube is set in grooves in the aluminum plates and joined by diffusion bonding. The plates of both the heating and cooling sections are 100 mm by 100 mm, and 3 mm in thickness. A 100 mm by 70 mm sheet heater is attached to the heating section plate. The heating section plate and the heater are pinched between two pieces of phenolic resin insulation by C clamps. An aluminum block, in which the 10 °C coolant flows, is attached to the cooling section, and the aluminum block and the cooling section are pinched by C clamps. The whole system, except the liquid reservoir and the PTFE tube, is covered with rock wool insulation. The liquid reservoir is a stainless steel tank with volume capacity of 50 mL, around which a silicone rubber heater is wound for temperature control. The liquid reservoir is covered with elastomeric foam insulation.

For temperature measurements, thermocouples are attached on the liquid reservoir, as well as to the OHP. The silicone rubber heater and the thermocouple (T_E in Fig. 1) are connected to an AC temperature controller. The heater is turned on or off by the temperature controller to keep the temperature T_E constant. A pressure sensor is set above the reservoir to measure the pressure of the vapor in the liquid reservoir. A pressure sensor is also set by the OHP to measure the inner pressure of the OHP.

There is a valve located on each side of the reservoir: the top valve and the bottom valve. The liquid line bifurcates downstream of the bottom valve. A valve is located on each of the bifurcated lines: the filling valve and the evacuating valve. The OHP is connected to the filling valve via the above-mentioned 600-mm-long PTFE tube.

1,1,1,2-Tetrafluoroethane (HFC-134a) is used as a working fluid. The liquid inventory is 50 mL. The method of filling the reservoir with HFC-134a is as follows: (1) the liquid reservoir is evacuated, filled with liquid HFC-134a, and then closed by the top and bottom valves, (2) the PTFE tube from the OHP is connected to the filling valve, (3) air is evacuated from the OHP, the PTFE tube, and the line downstream of the bottom valve, from the

evacuating valve, and (4) the evacuating valve is closed and the bottom valve is opened. After the bottom valve is opened, a liquid-vapor distribution is established in the OHP, as well as in the liquid reservoir. The liquid-vapor distribution depends on environmental factors (e.g., ambient temperature).

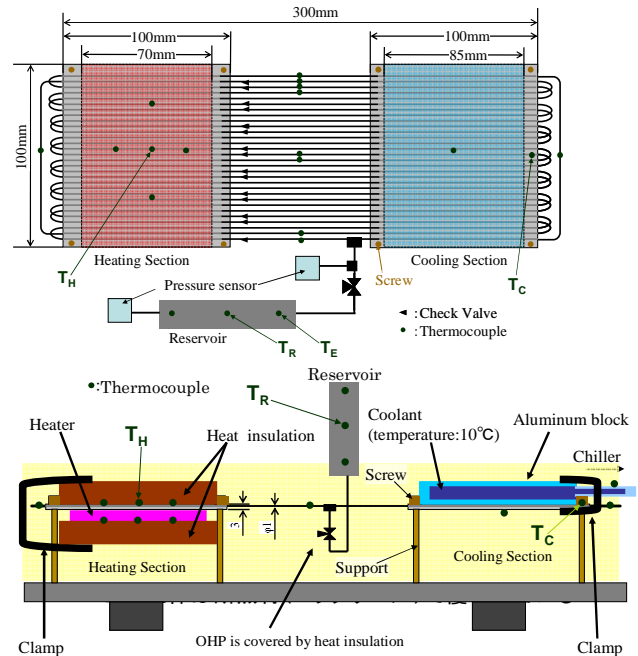


Fig. 1 Schematic of OHP

3. EXPERIMENTAL CONDITION

Table 1 shows the experimental conditions. The liquid reservoir is set in three ways: horizontally, vertically (i.e., the PTFE tube is placed at the reservoir's bottom) and vertically inverted (i.e., the PTFE tube is placed at the reservoir's top). The OHP without the reservoir (i.e., a fixed conductance OHP) is also tested. The coolant temperature is set to 10 °C in all experiments. The heat input to the heating section is increased from 0 to 70 W in 10 W increments. The liquid reservoir temperature is kept 40 °C.

Table 1 Experimental Conditions

Reservoir Orientation	No Reservoir	Vertical	Horizontal	Vertically Inverted
Reservoir Temperature [°C]	40			
Heat Input [W]	10, 20, 30, 40, 50, 60, 70			
Coolant Temperature [°C]	10			

4. EXPERIMENTAL RESULTS

4.1 Result of the OHP without the reservoir

Fig.2 shows the temperatures and the pressures of the OHP without the reservoir. The temperature and the pressure of the reservoir that is maintained at 40°C by the heater are also measured and shown in Fig.1 to compare the other results while the valve between the reservoir and the OHP is closed. The temperatures of the heating section and the cooling section are measured at the locations T_H and T_C shown in Fig 1. The temperatures of both the heating section and the cooling section rise and the OHP pressure is also increased as the heat input is increased. The OHP pressure is equal to the saturated pressure at the temperature of the heating section. The error bars in the figure indicate the amount of heat leak from the heating section to the surroundings. Note that the net amount of heat transferred by the OHP is the difference between the heat input and the heat leak. This also applies to the remaining results. The experimental configuration is also shown in the figure.

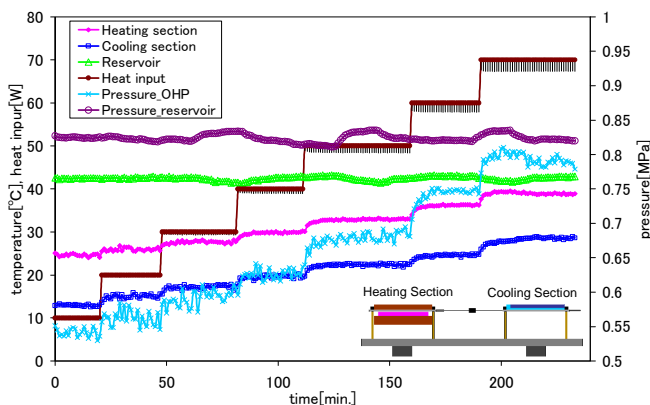


Fig.2 Experimental result of the OHP without the reservoir

4.1 Result of the OHP with the reservoir in vertical direction

Fig. 3 shows the test result for the OHP with the vertical liquid reservoir. The heating section temperature rises slightly as the heat input is increased, and the temperature increase with increasing heat input is much smaller in comparison with the results shown in Fig. 2. The heating section temperature is maintained at about 40 °C, which is the temperature of the liquid reservoir. The OHP pressure is continually same as the reservoir pressure and is equal to the saturated pressure at 40°C. The saturated vapor pressure of the liquid reservoir regulates the operating

temperature of the OHP and therefore the conductance of the OHP. The liquid reservoir is in a two-phase state when its temperature is kept at 40 °C. The amplitude of the pressure oscillation of the OHP with the vertical direction reservoir is smaller than that of the OHP without reservoir as the OHP pressure is controlled by the reservoir. It is also assumed that the liquid reservoir is contributed to regulate the liquid amount in the OHP. As the heat load increases, excessive vapor builds in the OHP and displaces the liquid from the OHP into the liquid reservoir: The amount of vapor in the cooling section increases and the excess working fluid is stored in the liquid reservoir.

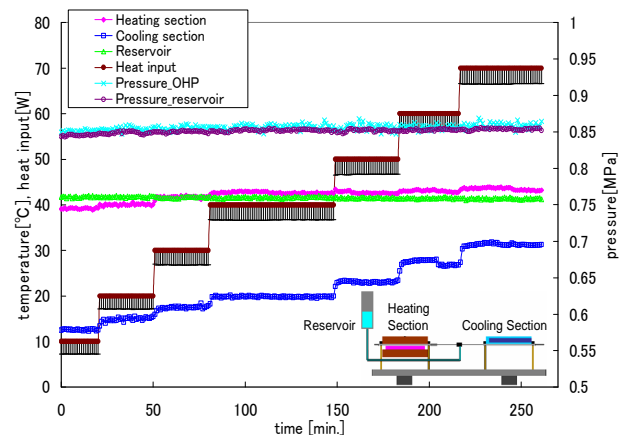


Fig.3 Experimental result of the OHP with reservoir in vertical direction

4.2 Result of the OHP with the reservoir in horizontal direction

Fig. 4 shows the test result for the OHP with the horizontal liquid reservoir. The temperature of the heating section and the pressure of the OHP is kept at those of the reservoir same as the OHP with the vertical direction reservoir.

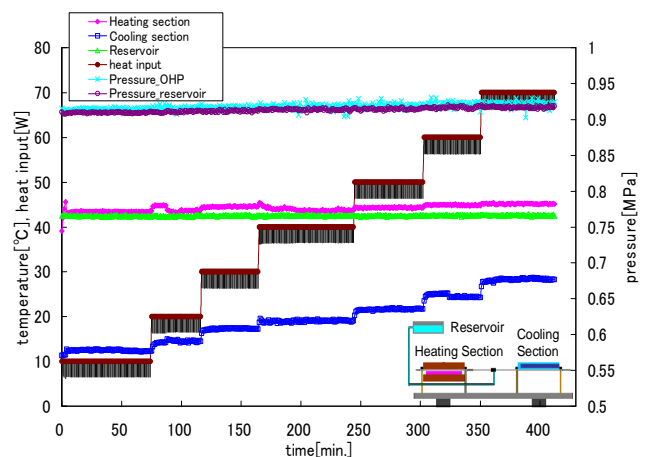


Fig.4 Experimental result of the OHP with reservoir in horizontal direction

4.3 Result of the OHP with the reservoir in vertically inverted direction

Fig. 5 shows the test result for the OHP with the vertically inverted direction reservoir. The temperature of the heating section and the pressure of the OHP is kept at those of the reservoir same as the former two cases. However, the heating section temperature is 2°C or 3°C higher than that of the OHP with the reservoir in vertical or horizontal direction. The liquid amount in the OHP is regulated with the liquid slugs in the tube between the reservoir and the OHP in this case, i.e. the OHP with the vertically inverted reservoir. The temperature of the liquid slugs in the tube is lower than that of the reservoir because the liquid slugs exist intermittently from the reservoir in vertically inverted direction and it is cooled from the ambient. The oscillation is occurred not only in the OHP but also in the tube. The heating section temperature becomes lower than the reservoir temperature as the liquid slugs in the tube flow into the OHP.

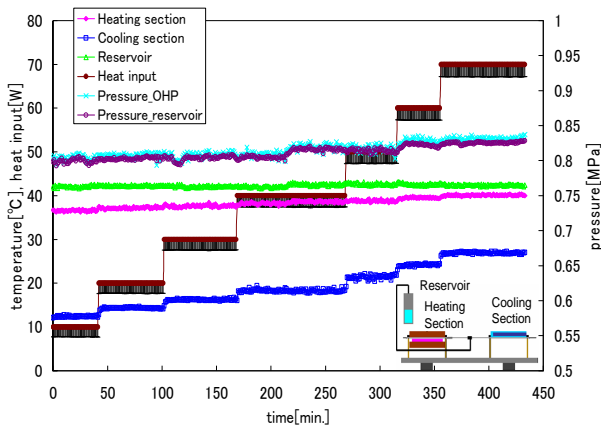


Fig.5 Experimental result of the OHP with reservoir in vertically inverted direction

5. CONCLUSIONS

The operation temperature, i.e. the heating section temperature the OHP is kept at the same temperature of the reservoir when the heat input to the heating section is changed. The OHP pressure is also continually same as that of the reservoir while the pressure of the OHP without the reservoir is increased with increasing of the heat input. The saturated vapor pressure of the liquid reservoir regulates the operating temperature of the OHP and therefore the conductance of the OHP. The OHP pressure is controlled not only by the vertical direction reservoir but also by the horizontal or vertically inverted reservoir.

REFERENCES

- [1] Kobayashi, Y., Okumura, A., and Matsue, T., "Effect of Gravity and Noncondensable Gas Levels on Condensation in Variable Conductance Heat Pipe," *Journal of Thermophysics and Heat Transfer*, Vol.5, No.1, 1991, pp. 61-68.
- [2] Kaya, T., and Ku, J., "Thermal Operational Characteristics of a Small-Loop Heat Pipe," *Journal of Thermophysics and Heat Transfer*, Vol.17, No.4, 2003, pp. 364-470.
- [3] Akachi, H., U.S. Patent, Patent Number 4921041, May 1, 1990.
- [4] Akachi, H. U.S. Patent, Patent Number 5219020, June 15, 1993.
- [5] Akachi, H., Polasek, H., Stulc, P., "Pulsating heat pipes," *Proceedings of the 5th International Heat Pipe Symposium*, Melbourne, Australia, 1996, pp. 208-217
- [6] Iwata, N., Ogawa, H., and Miyazaki, Y., "Temperature-Controllable Oscillating Heat Pipe", *Journal of Thermophysics and Heat Transfer*, Vol.25, No.3, pp.386-392, 2011

MODELING TRANSIENT ACCELERATION EFFECTS ON HEAT PIPE PERFORMANCE

Jay Ambrose

Lockheed Martin Space Systems Company
1111 Lockheed Martin Way, Sunnyvale, CA 94089
jay.h.ambrose@lmco.com

ABSTRACT

Acceleration forces are an important factor in the design of heat pipes for space systems. Since typical aerospace heat pipes have a low capillary pumping head, they can be affected by relatively small accelerations. In some spacecraft acceleration forces are negligible once on-orbit. Manned spacecraft tend to have higher thrust propulsion systems and therefore higher acceleration loads. This coupled with the stringent operational requirements associated with manned systems has limited the application of heat pipes to such systems. In the current work, the application of heat pipes in a spacecraft with a known acceleration environment will be addressed. The generic acceleration problem will be discussed. Specific methods used for treating acceleration deprime and recovery will be presented along with example simulations and comparisons with available data. The current work is intended to describe on-orbit acceleration forces on heat pipes and how they may be addressed in typical spacecraft systems.

KEY WORDS: accelerations, heat pipes, transient operation

1. INTRODUCTION

The effect of uniform adverse acceleration forces on the operation of heat pipes is well understood. Adverse accelerations (acting from the evaporating toward the condensing end) reduce the available (capillary) pumping head and result in a predictable decrease in heat transport capability. Favorable accelerations increase the available pumping head and increase heat transport, until the point at which they exceed capillary forces and disrupt the liquid-vapor surface. The heat pipe then becomes a thermosyphon, for which transport modeling becomes more complex. Most heat pipes are ground tested at normal gravity with a slight adverse acceleration. Once on-orbit, accelerations are usually orders of magnitude lower. Typical spacecraft heat pipes (aluminum/ammonia, axial groove) have capillary pumping capability of the order of 100 Pa, and therefore elevation differences of the order of 1 cm in normal gravity will significantly impact transport capacity. This is equivalent to an acceleration of ~ 0.01 g acting along the axis of a 1 meter long heat pipe.

This paper deals with heat pipes operating under the influence of transient accelerations of relatively short duration, as is commonly the case in spacecraft. Such heat pipes operate continuously under negligible acceleration levels which are interrupted by intermittent, larger accelerations. The objective is to adequately describe the transient

thermal behavior of the system when subjected to a known acceleration profile. The acceleration levels can be large enough that body forces in the fluid exceed the capillary forces, resulting in redistribution of the working fluid.

Transient operation of heat pipes during periods when heat transport capacity is temporarily exceeded has been studied by various authors (Beam, 1985, Ambrose et al., 1989, Reagan, 1994). It has been found in general, that the fluid behavior can be treated as quasi-steady, since the thermal time constants of the surrounding system tend to dominate the response. Most of the prior work focused on the case when the thermal boundary conditions were used to exceed the heat transport capacity of the heat pipes. Reagan (1994) also considered the case when accelerations caused a temporary decrease in heat transport capacity (with fixed thermal boundary conditions). Although it is generally accepted that the quasi-steady fluid assumption is valid, a more general treatment useful for engineering design of spacecraft systems has not been presented.

2. DESCRIPTION OF THE PROBLEM

Consider a heat pipe in a spacecraft under the influence of acceleration forces. When the spacecraft is orbiting a planet, the centripetal acceleration of motion exactly balances the gravitational pull exerted such that the net

accelerations are nearly zero. When the spacecraft moves at a constant velocity at a great distance from gravitational forces, the accelerations are likewise negligible. However, when the control system produces thrust to accelerate or re-orient the vehicle, or if the spacecraft spins about its axes, non-negligible accelerations are produced. The 2 simplest cases are considered here.

2.1 Linear Thrusting

This type of acceleration, represented in Figure 1, can be derived directly from the spacecraft propulsion system burns, given a known thruster force, thrust direction and vehicle mass properties. The acceleration along the axis of a heat pipe of interest can be resolved from the geometry of the vehicle, with the linear acceleration acting through the center of mass. An example based on a realistic crew vehicle mission is shown in Figure 2. Two thruster types (OME and Aux) are used in this example. The accelerations are given in fraction of normal (earth) gravity (g's). Such accelerations would cause transient depriming if oriented (adversely) along the axis of conventional heat pipes.

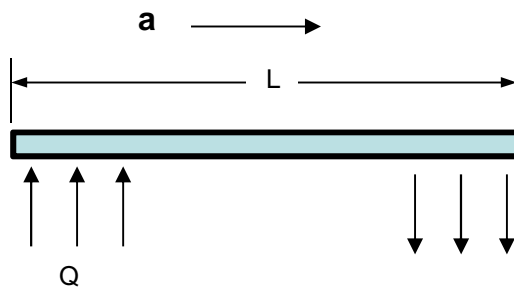


Figure 1. Configuration for Linear Thrust Acceleration

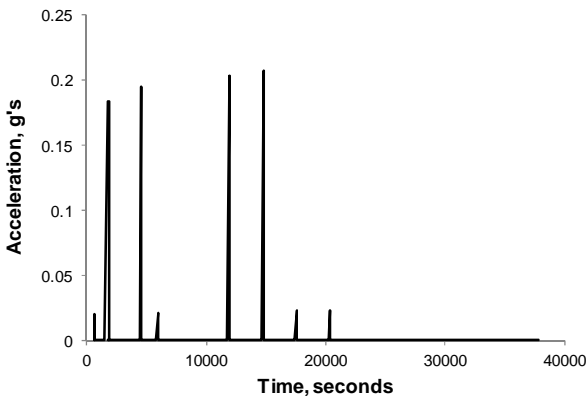


Figure 2. Predicted Acceleration Profile for Linear Thrusts

2.2 Re-Orientation

In this case, shown in Figure 3, the vehicle rotation rates/accelerations about the system Center of Gravity (C.G.) are known. These are given as a combination of rotation rate and rotational accelerations. Note that rotational accelerations and higher order jerk (time rate of change of rotational acceleration) usually operate over negligible time periods in such systems. Again, the acceleration along the axis of a heat pipe of interest can be resolved from the geometry of the vehicle.

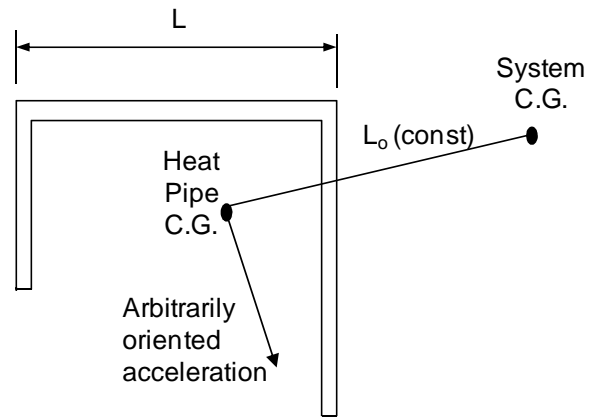


Figure 3. Configuration for Centrifugal Acceleration

Consider the case of the heat pipe in Figure 3 at fixed radius L_0 from the system Center of Gravity (C.G.), with rotations about orthogonal axes in directions θ and ϕ . The resolution of these rotation rates into an approximate linear acceleration along the heat pipe axis is given (by spherical coordinates) as:

$$a_r = \ddot{r} - r\dot{\Phi}^2 - r\dot{\theta}^2 \cos^2 \Phi \tag{1}$$

$$a_\theta = \frac{\cos \Phi}{r} \frac{d(r^2 \dot{\theta})}{dt} - 2r\dot{\theta}\dot{\Phi} \sin \Phi \tag{2}$$

$$a_\phi = \frac{\cos \Phi}{r} \frac{d(r^2 \dot{\phi})}{dt} - 2r\dot{\phi}\dot{\Phi} \sin \Phi \tag{3}$$

Since r represents the constant dimension L_0 , dr/dt and higher terms are zero. It can be readily shown that for a length L_0 of the order of 1 meter, rotation rates of a few degrees per second will induce accelerations of the order of 1 mg at the heat pipe C.G. Operation of subsystems during such reorientation events must be considered in the spacecraft design.

3. HEAT PIPE THERMOHYDRAULIC MODEL

Accelerations primarily impact the heat transport capacity. Large adverse accelerations greatly reduce the heat transport capacity and cause dryout of the evaporator. The transport capacity can be represented as a function of acceleration as shown in Figure 4, where a_{max} is given by $\Delta P_c / (\rho_l L_{tot})$. A constant conductance may be assumed unless the transport capability is exceeded. Two cases should be considered: adverse acceleration levels less than or greater than a_{max} . When the accelerations are less than a_{max} , a flat front dryout/rewetting model is assumed. When the transport capacity (including the effect of any acceleration) is exceeded, wetted length is reduced until required heat flow and transport capacity balance. When the transport capacity exceeds the required transport, wetted length is likewise increased. This is the so-called quasi-steady fluid assumption, as the fluid response is assumed to be instantaneous. The basic approach has been described previously (Ambrose et al. 1991).

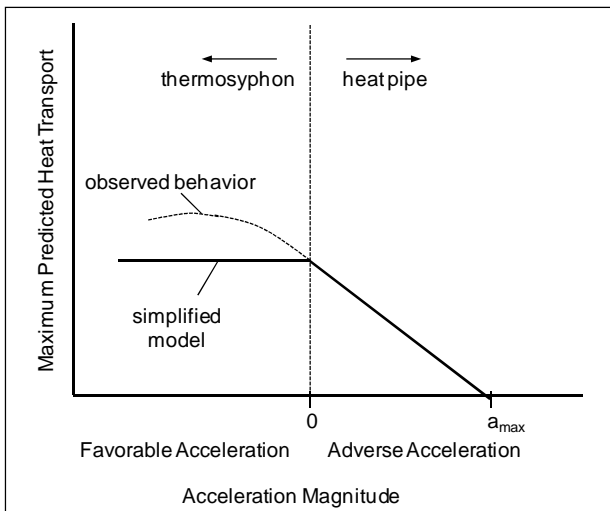


Figure 4. Assumed Maximum Heat Transport versus Acceleration

For accelerations which exceed a_{max} (i.e. zero transport capacity), an adiabatic deprime/reprime model is added. In this case, the liquid may be relocated away from the evaporator section and must rewet a significant length of the pipe.

Consider the control volume shown in Figure 5, which moves with the liquid front. A force balance on either fluid phase gives:

$$\frac{d(\rho U)}{dt} = -\frac{dP}{dx} - \frac{4\tau}{D_h} \quad (4)$$

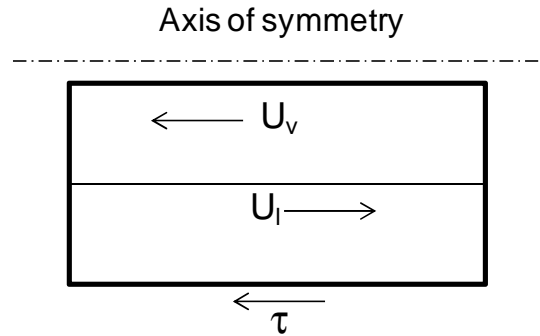


Figure 5. Control Volume for Reprime Model

Assuming laminar flow, $\tau = 8\mu U/D$. Using Eqn (4) and subtracting the vapor and liquid components, we have:

$$\frac{d(\rho_l U_l - \rho_v U_v)}{dt} = \frac{dP_v}{dx} - \frac{dP_l}{dx} - \frac{32\mu_l}{D_{hl}} + \frac{32\mu_v}{D_{hv}} \quad (5)$$

Introducing continuity as $(\rho U)_v = -(A_l/A_v)(\rho U)_l$, (5) becomes:

$$c_1 \frac{dU_l}{dt} = c_2 - c_3 U_l \quad (6)$$

Where:

$$c_1 = (1 + A_l/A_v), \quad c_2 = \frac{\Delta P_c}{\rho_l L_{tot}}, \text{ and}$$

$$c_3 = 32 \left\{ \frac{\mu_l}{D_{hl}^2} + \frac{A_l \mu_v}{A_v D_{hv}^2} \right\}$$

Here it is assumed that the minimum average axial pressure gradient may be used, which is represented by the ratio of capillary pressure drop to total length, $\Delta P_c / L_{tot}$. This value of the forcing term is the value at the moment of deprime and is conservative relative to reprime results since it is a minimum. Inclusion of a more realistic assumption results in a higher order equation for momentum which must be solved numerically (e.g. Reagan, 1994).

A particular solution to Eqn (6) is:

$$U = \frac{c_2}{c_3} (1 - \exp(-c_3 t / c_1)) + U_0 \exp(-c_3 t / c_1) \quad (7)$$

Where the velocity U_0 at $t = 0$ is specified.

For a conservative deprime/reprime model, all liquid is assumed to be relocated instantaneously to one end of the heat pipe once a_{max} is exceeded, and the initial reprime velocity is set equal to zero. The liquid velocity and wetted length are allowed to increase once a $\ll a_{max}$ using Eqn (7) until wetted length reaches a maximum value (either the length of the pipe or a partially wetted length due to transport limitation described earlier). A sample prediction using this approach is shown in Figure 6.

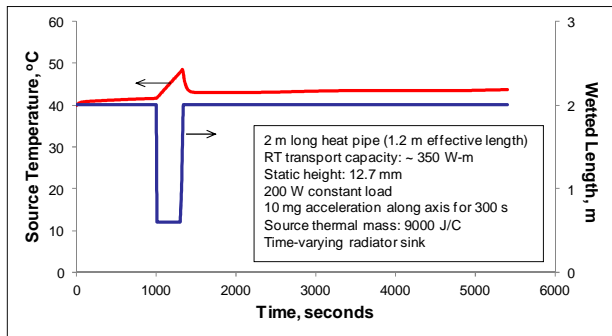


Figure 6. Example of Predicted Heat Pipe Thermal Response to Acceleration Pulse

4. COMPARISON TO FLIGHT DATA

4.1 Centrifugal Deprime

Fleischman et al. (1994) reported results for two grooved heat pipe designs (0.46 m overall length) subjected to rotational accelerations on-board the Space Shuttle during STS 52. Accelerations were induced by spinning the heat pipes using a special apparatus at rates of 0 to 12 revolutions per minute, while the heat pipes were operating at a constant heat load. Dryouts were observed when the centrifugal force exceeded the available capillary pumping capability, consistent with the theory. Detailed performance time histories were not reported, but re-wicking times of less than one minute were observed following removal of the rotational accelerations. The groove geometries, dimensions and charge quantities were reported for the water and Freon-113 filled heat pipes. The predicted adiabatic rewetting periods are shown in Figure 7 for typical test conditions. The minimum rewetting length in this analysis assumed that the entire heat pipe charge was located at the cold end of the heat pipe, which is the worst case. Although the period of application of the accelerations was not reported, it was likely insufficient to fully deprime the heat pipes. Heat load was maintained during the deprime/reprime period. As can be seen from the predictions, the observed rewetting times

are consistent with the predictions, less than one minute.

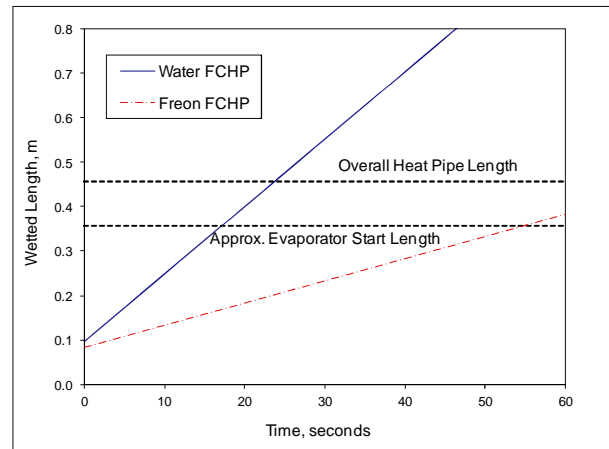


Figure 7. Predicted Adiabatic Rewetting Behavior, HPP Experiment

4.2 Linear Thrust Deprime

During the SHARE II heat pipe flight experiment on the Space Shuttle during STS 43 (Ambrose et al., 1992), very long (6.8 m overall length) high-performance heat pipes were tested under a variety of stressing conditions, including large linear accelerations. Shuttle thruster firings produced an acceleration of approximately 0.09 m/s^2 along the axis of the heat pipes ($\sim 0.01 \text{ g}$). The heat pipes had a unique single groove geometry with a split passage near the evaporator end (1 m in length) which created a discrete change in capillary pumping. The effective capillary pumping dimension was approximately 3.8 mm in the evaporator, increasing to 5 mm over the rest of the pipe. The predicted adiabatic deprime/rewetting behavior is shown in Figure 8 for the Deprime 2 case, in which thrusters were fired for 5 seconds with a 240 W heat load on the heat pipe. The model term dP/dx was modified to include the discrete change in capillary pumping dimension when the wetted front was predicted to enter the split passage. The wetting velocity abruptly increases at this point. The wetted front reaches the evaporator start at ~ 230 seconds. A transient thermal analysis was used to predict the observed thermal response of the heat pipe during this test (Ambrose et al., 1991). In that work, an empirical time dependence of the transport capability was used to fit the data. In order to correlate the Deprime 2 data take, transport capacity was increased from zero to 100% in ~ 180 seconds. The current predicted adiabatic rewetting response is conservative, since it assumes the absolute maximum rewetting time. In the actual

experiment, complete deprime likely did not occur within the short duration of the thruster firing. The current results are in good agreement with the measured data based on the observed and predicted thermal response.

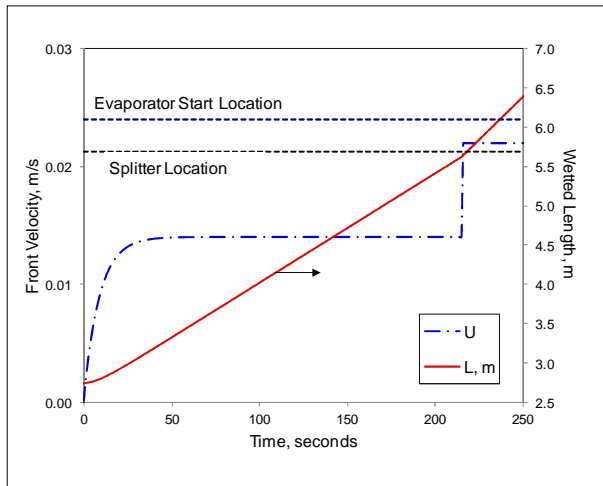


Figure 8. Predicted Adiabatic Deprime/Rewetting Behavior, SHARE II Experiment

A more recent set of flight data was reported by Baker et al (2010) for the Lunar Reconnaissance Orbiter (LRO) insertion burns. The LRO had a 40 minute burn required during orbit insertion maneuvers, which induced an acceleration of $\sim 0.18 \text{ m/s}^2$ along the avionics heat pipe radiator. The large avionics heat pipe radiator has a network of spreader heat pipes, with 11 per side fed by a central header heat pipe system. The observed thermal response indicated a substantial dryout as observed by a thermal excursion of a maximum $33 \text{ }^\circ\text{C}$ in the measured avionics radiator temperatures lasting $\sim 42\text{-}44$ minutes. This indicates that full recovery of the induced thermal gradients took approximately 2-4 minutes following termination of the induced accelerations. For the magnitude of these accelerations, it is estimated that complete deprime would take less than one minute. This estimate is based on replacing the capillary forcing term in Eqn (5) with a term modified to account for acceleration force. Therefore the assumed worst case initial conditions of the adiabatic reprime analysis are accurate for this data. The authors did not provide complete design details of the LRO heat pipes, so the pipes were assumed be similar in design to other aluminum-ammonia axial groove heat pipes used in many spacecraft. Based on this assumption and the approximate dimensions of the heat pipes, the predicted adiabatic rewetting behavior is shown in Figure 9. It is seen that the

rewetting into the short evaporator sections takes approximately 120 seconds. Recovery of the thermal gradients would take slightly longer. The predicted behavior is in good agreement with the flight data.

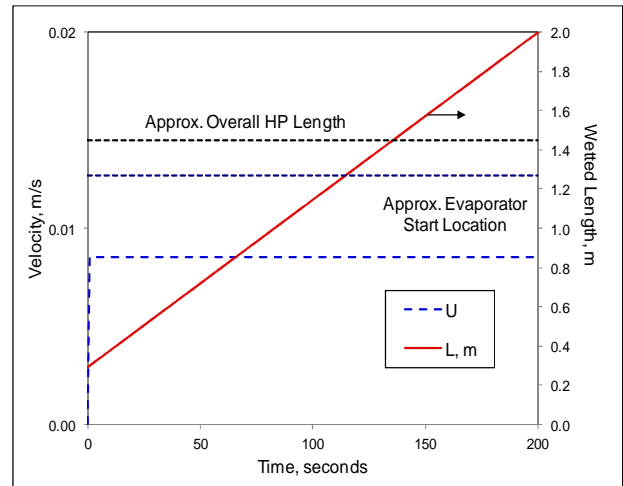


Figure 9. Predicted Adiabatic Rewetting Behavior, LRO Avionics Heat Pipes

5. CONCLUSIONS

A general approach for treating the impact of accelerations on spacecraft heat pipes has been presented. The approach assumes quasi-steady fluid behavior for the thermal analysis, but includes important details of the dryout and rewetting process. Comparisons with available flight data provide support to the current approaches.

NOMENCLATURE

- a - acceleration along heat pipe axis
- a_{max} - acceleration balancing static capillary pumping, corresponding to zero transport capability
- A - flow area
- C.G. - center of gravity
- D_h = liquid groove hydraulic diameter
- L - wetted length
- L_o - dimension from system C.G. to heat pipe C.G.
- L_{tot} - total length of heat pipe
- N - number of liquid grooves
- ΔP_c - maximum capillary pumping
- r - radial coordinate
- t - time
- U - flat front deprime/rewetting velocity
- Greek symbols
- r, θ, ϕ - spherical coordinates
- ρ - fluid density
- τ - shear stress
- μ - liquid viscosity
- ν - liquid kinematic viscosity

Subscripts

l - liquid

v - vapor

REFERENCES

- Ambrose, J.H, Chow, L.C., Beam, J.E. (1987) *Transient Heat Pipe Response and Rewetting Behavior*, AIAA J. Thermophysics and Heat Transfer, 1(3), p.222-227 .
- Ambrose, J.H, Holmes, H.R., (1991) *Transient Response of a High-Capacity Heat Pipe for Space Station Freedom*, AIAA 26th Thermophysics Conf., Honolulu, AIAA-91-1403.
- Ambrose, J.H, Holmes, H.R., Cima, R.M., Kapolnek, M.R. (1992) *Flight Test Results for a High-Capacity Single-Groove Heat Pipe*, AIAA 27th Thermophysics Conf., Nashville, AIAA-92-2887.
- Baker, C., Garrison, M., Cottingham, C., Peabody, S. (2010) *Lunar Reconnaissance Orbiter (LRO) Thermal On-Orbit Performance*, 40th Int. Conf. on Environmental Systems, Barcelona, AIAA-2010-6000.
- Beam, J.E. (1985) *Unsteady Heat Transfer in Heat Pipes*, PhD Dissertation, Univ. of Dayton, Dayton, OH.
- Fleischman, G.L., Gier, K.D. and Wong, L.S. (1994) *Heat Pipe Performance In-Space Technology Experiment (HPP)*, 6th AIAA/ASME Joint Thermophysics and Heat Transfer Conf., Colorado Springs, AIAA-94-2030.
- Reagan, M.K., (1994) *Transient Body Force Effects on the Dryout and Rewet of a Heated Capillary Structure*, PhD Dissertation, AF Inst. Technology, WPAFB, OH.

Variable Conductance Heat Pipes for Variable Thermal Links

William G. Anderson, John R. Hartenstine, and Christopher J. Peters

Advanced Cooling Technologies, Inc.

1045 New Holland Ave., Lancaster, PA 17601 U.S.A.

717-295-6061, 717-295-6064 Fax, Bill.Anderson@1-act.com, John.Hartenstine @1-act.com

ABSTRACT

Variable Conductance Heat Pipes (VCHPs) for spacecraft thermal control typically have a cold-biased reservoir at the end of the condenser. During operation, electrical heat is supplied to the reservoir to provide $\pm 1\text{-}2^\circ\text{C}$ temperature control over widely varying powers and sink temperatures. A second application for VCHPs is as a variable thermal link for lunar landers and rovers, while minimizing the required electrical power. During the long lunar day, the VCHP must remove waste heat from the electronics and batteries to prevent overheating. During the long lunar night, the variable thermal link must passively limit the amount of heat removed from the electronics and radiated to space since little to no power is available for temperature regulation. A VCHP was developed to act as a variable thermal link for lunar landers and rovers, passively minimizing heat losses during the lunar night, without requiring electric power to shut off. In addition to acting as a thermal link, the VCHP was able to withstand multiple freeze/thaw cycles without performance degradation. Short-duration, full-power bursts were demonstrated during -60°C and -177°C cold shutdown. Startup of the VCHP with a frozen condenser was also demonstrated.

KEY WORDS: Variable Conductance Heat Pipes, VCHPs, Variable Thermal Links

1. INTRODUCTION



Figure 1. A typical VCHP with an evaporator, a single condenser, and an electrically heated reservoir at the end of the condenser.

A typical Variable Conductance Heat Pipe (VCHP), shown in Figure 1, has an evaporator, a single condenser, and an electrically heated reservoir at the end of the condenser. This system is commonly used in spacecraft thermal control to provide $\pm 1\text{-}2^\circ\text{C}$ temperature control over widely varying powers and sink temperatures.

While the standard VCHP is used for tight temperature control, this paper will discuss VCHP applications where a variable thermal link is desired instead. In most of these applications, liquid in the condenser can freeze. VCHPs or gas-loaded heat pipes simplify start-up with a frozen condenser.

2. VCHP DESIGN FOR LUNAR LANDERS AND ROVERS

The lunar environment presents a number of

challenges to the design and operation of thermal management systems. The heat rejection sink can be 330 K during daytime and can drop down to 50 K at night or in dark craters (Swanson and Butler, 2006). Instruments and equipment, such as batteries, will need to be maintained within -20°C to 40°C throughout the large diurnal temperature swings (Birur and Tsuyuki, 2009). In addition, depending upon the mission, the thermal system will be required to work both on the lunar surface after deployment, and during the transit time from the earth to the moon. Due to the wide temperature swings, future lunar landers and rovers will require a variable conductance thermal link that can reject heat during the day and passively shut off during the lunar night without requiring any electrical power. During the long lunar day, the thermal management system must remove waste heat from the electronics and batteries to prevent overheating. During the long lunar night, the

variable thermal link must passively limit the amount of heat removed from the electronics and radiated to space since little to no power is available for temperature regulation. For solar powered systems, the variable link design is complicated by the heavy mass penalties associated with providing continuous power throughout the 14-day-long lunar night: It is estimated that 5 kg of batteries, solar cells, etc., are required to supply 1 W of electricity. Therefore, designs that operate without electrical power are highly desirable. The Lunar Anchor Node design targets are shown in Table 1.

Table 1. Anchor Node Design Targets.

Minimum Electronics Temperature	-10°C (263 K)
Maximum Electronics Temperature	50 °C (323 K)
Maximum Radiator Load (Moon)	73 W at lunar noon (30 % margin: 94.9 W)
Power During Transit (Space)	90 W during cruise (30 % margin: 117 W)
Mission Length	~ 6 years
Warm Electronics Box Geometry	61cm x 104cm x 36cm (height)
Distance from WEB to Radiator	36cm to side mounted vertical radiator
Minimum Sink Temp.	96 K
Maximum Sink Temp.	269 K
Maximum Tilt	±14° (8° slope, 6° obstruction)

The Anchor Node VCHP design is shown in Figure 2. The VCHP evaporator is nominally horizontal, and the condenser is nominally vertical during operation on the Lunar Surface. An important design target consideration for Lunar Landers and Rovers is that the VCHP must work both in space and in a gravity-aided mode on the lunar surface. For the Lunar Anchor Node, the VCHP needs to operate against a maximum slope. For the Anchor Node, it is ±14° (due both to the general tilt of the terrain, as well as any local rock or depression). The maximum slope for rovers can be as high as ±45°. The basic VCHP layout is shown in Figure 2 (a). The VCHP evaporator sits on the WEB enclosure base plate. The adiabatic section is tilted so that it is always gravity aided on the moon.

Due to the ±14° slope, the conventional spacecraft all-grooved wick is not suitable in the evaporator

section. Typically, grooved heat pipes are tested on earth with an adverse tilt (evaporator above condenser) of 0.1 inch (2.54 mm). As shown in Figure 2 (b), the lander evaporator can have an adverse tilt of several cm. To accommodate this high adverse elevation, a hybrid wick was developed. All of the condenser and most of the adiabatic section employ axial grooves for liquid return. A small portion of the adiabatic section and all of the evaporator use wrapped screen mesh as the wicking structure. The screen mesh wick, which has higher capillary pumping pressure than grooves, enables the evaporator to operate against the tilt caused by the uneven lunar surface.

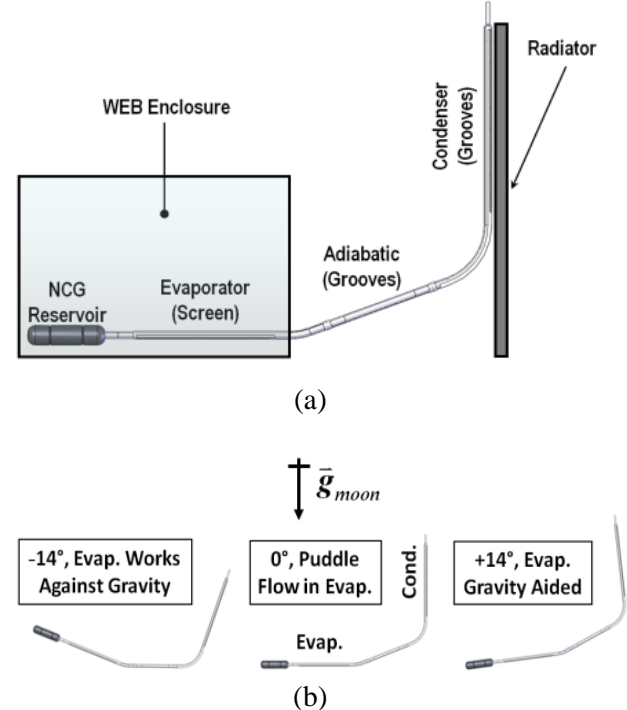


Figure 2. a. Schematic of the VCHP layout from the WEB to the radiator. b. Depending on the terrain, the evaporator can have a ±14° tilt relative to horizontal. In some cases, the evaporator wick must work against gravity on the lunar surface, which is not possible with a conventional grooved wick.

A schematic of the VCHP is shown in Figure 3. The VCHP incorporates three novel features in order to achieve the design targets of the ILN program:

1. Hybrid-Wick, discussed above.
2. Reservoir near Evaporator, to prevent the reservoir temperature from dropping during the lunar night.

3. Bimetallic Adiabatic Section, to minimize heat losses during the lunar night.

A stainless steel heat pipe section of 12.7 cm (5 inches), which replaces the original aluminum portion in the adiabatic section, acts as a thermal dam, and minimizes axial heat leak to the cold radiator during shutdown.

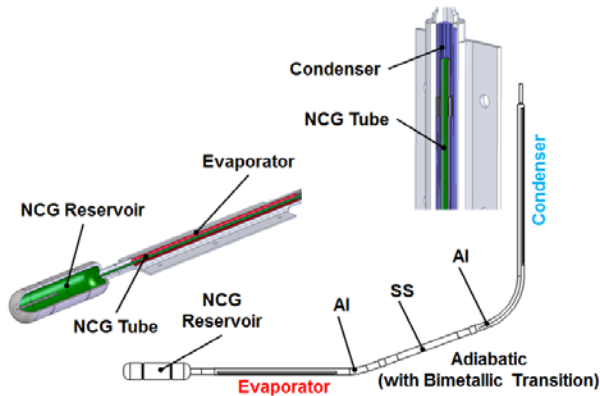


Figure 3. Schematic of the VCHP with a hybrid wick, to allow operation at different tilts. Placing the reservoir near the evaporator keeps the reservoir warm, minimizing the required reservoir size. Also, part of the adiabatic section is stainless steel, which minimizes heat leaks when the VCHP is turned off.

The heat pipe uses anhydrous ammonia as the working fluid, since it is the best working fluid when the heat pipe is operational. The Non-Condensable Gas (NCG) has two purposes: 1. Provides a variable thermal link that turns off as the evaporator temperature drops, and 2. Suppresses the freezing of ammonia in the condenser during the lunar night. The freezing point of ammonia is 195 K, while the radiator could conceivably cool down to 96 K. In a CCHP, ammonia would tend to freeze in the condenser. However, in a VCHP, the gas in the adiabatic and condenser sections blocks the flow of ammonia from the evaporator to the condenser. Ammonia can only slowly diffuse through the gas. The NCG also aids in starting up the heat pipe after sunrise (Ellis and Anderson, 2009).

VCHPs typically use argon as the NCG. Due to the low temperatures, neon was selected for this VCHP instead. The reason is that the critical temperature of Argon is 151 K, so the argon would not be a perfect gas during the lunar night, and could actually condense. Neon, with a critical temperature of 44 K, will behave like a perfect gas.

2.1 Reservoir Location

Placing the NCG reservoir near the evaporator, as opposed to the traditional location near the condenser, keeps the gas reservoir warm and minimizes the reservoir size. A conventional VCHP, shown in Figure 1, has the reservoir located next to the condenser. The VCHP reservoir temperature is controlled by tying it thermally to another portion of the spacecraft to cold bias the VCHP, then adding heaters on the reservoir to control power.

In contrast, no electrical heating is available to control the VCHP temperature in a lunar lander or rover. If the VCHP reservoir was located at the top of the condenser in Figure 2 (a), then the VCHP reservoir would operate near the sink temperature of 96 K during the lunar night. Anderson, Ellis, and Walker (2009) developed the equations to size this type of radiator, and showed that with a wide variation in sink temperature, there is a minimum ΔT_{VCHP} , even with an infinite reservoir.

Placing the NCG reservoir near the condenser would necessitate a very large reservoir that can only provide coarse temperature control ($\Delta T_{VCHP} \geq 30 \text{ }^\circ\text{C}$). ΔT_{VCHP} is defined as the difference between the operating and shutdown temperatures of the evaporator ($\Delta T_{VCHP} = T_{On} - T_{Off}$). A very precisely controlled VCHP would have a very small, but finite ΔT_{VCHP} . Such temperature control is only possible with a reservoir near the evaporator. Figure 4 illustrates these principles.

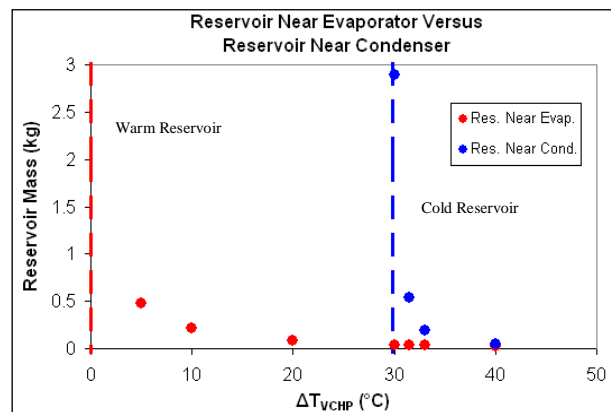


Figure 4. Comparison between NCG Reservoir Locations.

In Figure 4, items colored red correspond to a warm reservoir placed near the evaporator and items colored in blue correspond to a cold reservoir

located near the condenser. The two dashed vertical lines represent the asymptotes for either the warm or cold reservoir. In both reservoir types, the mass of the system trends exponentially towards infinity as the degree of control increases and ΔT_{VCHP} decreases. Observe that an infinitely large cold reservoir provides $\Delta T_{VCHP} \approx 30$ °C and an infinitely large warm reservoir provides $\Delta T_{VCHP} = 0$ °C. For this reason, the reservoir is located in the WEB, next to the evaporator, where it can be kept warm by the heat pipes used to transfer heat in the WEB. A small NCG tube passes through the entire length of the heat pipe to pneumatically connect the NCG reservoir to the condenser (see Figure 3). This NCG tube allows the NCG reservoir to be located near the evaporator rather than the condenser. While this heat pipe design has been theoretically discussed as far back as Marcus (1971), to the best of our knowledge this is the first time that this type of VCHP has been fabricated.

3. VCHP TEST SETUP AND TESTING

3.1 Test Setup

The VCHP had the following specifications:

- 30.5 cm (12 inch) Condenser / \approx 48.3 cm (19 inch) Adiabatic Section – Grooved aluminum extrusion (6063-T6 Al)
- Bimetallic Transition – 1.25 inch 6061-T6 Al \times 5 inch 304 SS \times 1.25 inch 6061-T6 Al
- 22.9 cm (9 inch) Evaporator – Nickel 200 50 \times 50 screen mesh
- NCG Tube (304 SS) – 0.32 cm (0.125 inch) outer diameter

- NCG Reservoir (304 SS) – 73.7 cm³ (4.5 inch³) internal volume
- Working Fluid (Ammonia) – 20.8 grams
- Non-Condensable Gas (Neon) – \approx 0.65 grams

The completed hybrid wick VCHP is shown in Figure 5. In addition to an intrusive thermocouple in the reservoir, thermocouples were attached every 5 cm to the evaporator, adiabatic, and condenser sections. Heat was supplied to the evaporator with electric cartridge heaters embedded in an aluminum block. Heat was removed from the condenser with a cold plate, cooled with liquid nitrogen to a fixed temperature.

3.2 Test Objectives

The first major test objective was a simulated Lunar Freeze/Thaw test: Demonstrate the ability of the VCHP to act as a variable thermal link on the moon, and minimize the heat transfer as the condenser temperature dropped below the freezing point of ammonia. In addition, verify that the VCHP can operate for short periods with a cold condenser (which can occur in some lander and rover scenarios).

The second major test objective was to demonstrate that the VCHP will act as a diode in space, preventing heat from solar insolation from heating the WEB.

3.3 Variable Thermal Link and Freeze/Thaw Testing

For the simulated lunar tests, the VCHP was mounted in a test fixture on an optical table that set the condenser vertical and allowed the evaporator

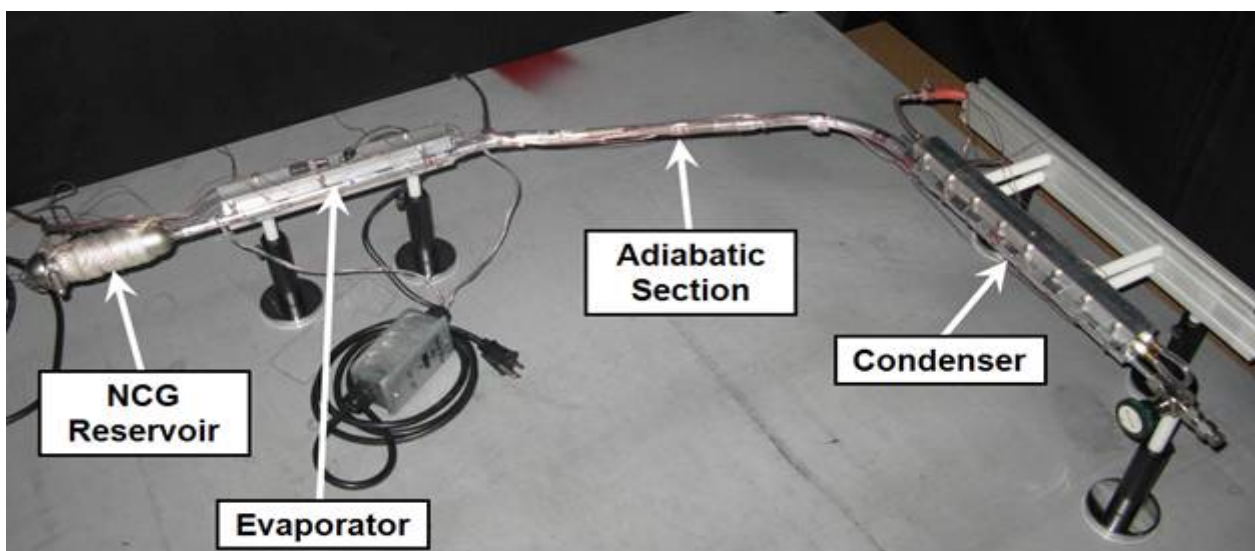


Figure 5. Hybrid wick VCHP with reservoir adjacent to the evaporator.

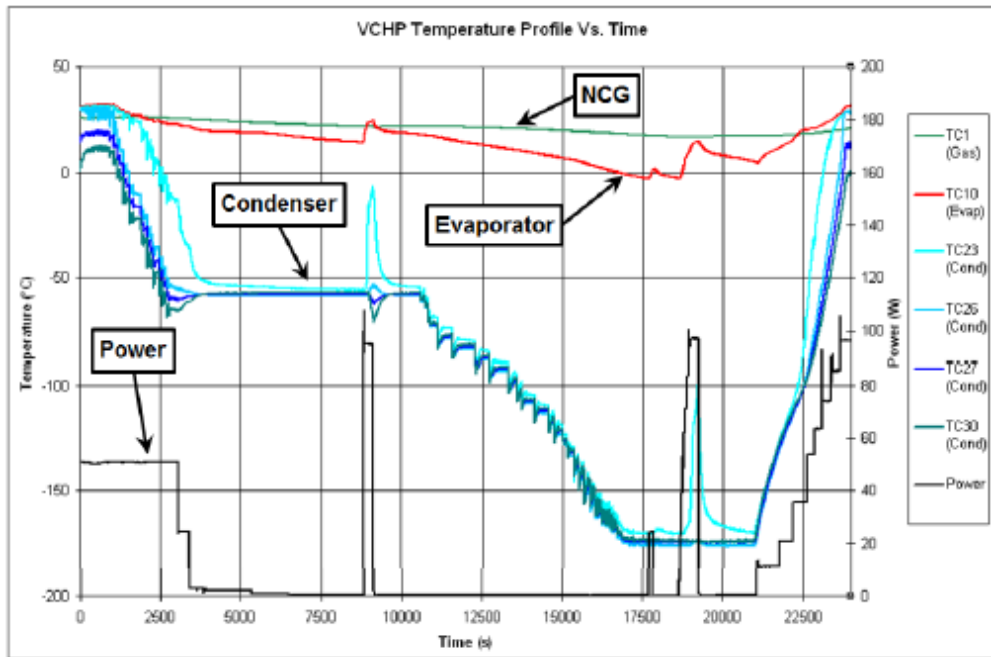


Figure 6. VCHP Temperature Profile as a Function of Time (-2.3° Orientation).

to be configured for gravity aided (+2.3°), gravity neutral (0°) and gravity adverse (-2.3°) inclinations (2.3° on earth is equivalent to a 14° inclination on the moon).

Figure 6 plots VCHP temperatures as a function of time during the lunar freeze/thaw test. TC1 corresponds to the gas temperature in the NCG reservoir. TC10 measures the vapor temperature of the evaporator. TC23, TC26, TC27 and TC30 detect the vapor temperature of four locations within condenser, with TC23 at the entrance of the condenser and TC30 close to the tip of the condenser. The power curve shows the electrical power input into the heater block of the evaporator.

Initially, the pipe is operating at a nominal 25 °C and 50 W. At about 6000 seconds the pipe temperature and power input are reduced to -60 °C and 0.2 W, respectively. The purpose of 0.2 W of heat input was to maintain the evaporator above -10°C. At around 9000 seconds, power is temporarily increased to the full 95 W, to simulate a brief period of activity during the lunar night. After this power increase, the pipe was returned to the -60 °C shutdown state. Next, the sink temperature is further reduced to -177 °C (96 K, ammonia freezes at 195 K). The pipe reaches a steady-state shutdown at -177 °C and 0.1 W. At approximately 17,500 seconds, the power is briefly increased to 25 W and the transient response of the frozen pipe was observed. With no indication of problems, the pipe is returned to -177 °C shutdown. Power is then increased to a full 95 W

for a short duration. After the full power increase, the pipe is returned to a state of shutoff until around 21000 seconds when the power is gradually increased and heat pipe startup begins. Finally, the VCHP is brought to nominal steady-state operation at 95 W and 25 °C. Overall conductances for the heat pipe during normal operation, and with -60 and -177°C sinks, given in Table 2, show that the heat pipe operates as a variable thermal link.

Table 2. Heat Pipe Overall Conductances for Freeze/Thaw, -2.3° Inclination.

Testing Condition	Overall Conductance (W/°C)
25 °C Operation	4.7
-60 °C Shutdown	0.00310
-177 °C Shutdown	0.00057

3.4 Diode Operation in Space

During transit, at some times the radiator will be hotter than the WEB due to solar insolation. During these times, it is desirable for the VCHP to act as a diode, preventing overheating of the WEB. A conventional VCHP would behave like a gas-loaded diode in this situation. Tests were conducted to verify that a VCHP with the reservoir near the evaporator would also act as a diode. During these tests, the ILN VCHP was kept in a

horizontal orientation; however, the adverse elevation and heat input/output were reversed compared to the space thermal performance test. The goal of this test was to verify that the pipe inhibited heat transfer in the reverse direction; therefore, the test intentionally attempted to operate the heat pipe backwards. Heat was input into the condenser and rejected from the evaporator. Since the capillary flow would travel from the evaporator to the condenser, the adverse elevation was defined as the condenser being 0.1, 0.2, and 0.3 inch (2.54mm, 5.08mm and 7.62mm) above the evaporator.

During these tests, the power into the nominal condenser was adjusted until a steady-state temperature difference of 20 °C was observed between the evaporator and condenser. Once this temperature difference was achieved, the input power was recorded as the reverse heat transfer rate.

Table 3 lists the results of the thermal diode experiments. All of the reverse powers are low (less than 4 % of the 117 W target for space) and the conductances are minimal (two orders of magnitude less than the values of the space thermal performance test). The conductances are negative because the condenser is hotter than the evaporator, which is the opposite of normal operation.

Table 3. VCHP Results for Space Thermal Diode (Evaporator at 25 °C; Condenser at 45 °C).

Adverse Elevation (in)	Reverse Heat Transfer Rate (W)	Overall Conductance (W/°C)
0.1	4.3	-0.205
0.2	3.2	-0.165
0.3	3.2	-0.168

3. CONCLUSIONS

A VCHP was developed to act as a variable thermal link for lunar landers and rovers, passively minimizing heat losses during the lunar night, without requiring electric power to shut off. Differences from a conventional spacecraft VCHP include 1. A hybrid wick, to allow the evaporator to operate when tilted at adverse orientations of up to 14°. 2. The reservoir was located next to the evaporator, to minimize the reservoir size and mass, while using no electrical heaters, and 3. The addition of a bimetallic adiabatic section, with a

length of grooved stainless steel to minimize heat leaks during the lunar night.

The simulated lunar performance testing demonstrated that the VCHP shut off as the condenser temperature was lowered, so the system acted as a variable thermal link. The VCHP was able to withstand multiple freeze/thaw cycles without performance degradation. Short-duration, full-power bursts were demonstrated during -60°C and -177°C cold shutdowns. Startup of the VCHP with a frozen condenser was also demonstrated. As expected, the VCHP behaves as a gas diode heat pipe when the condenser is heated in a simulated space environment.

ACKNOWLEDGEMENT

This program was sponsored by NASA Marshall Space Flight Center under Purchase Order No. NAS802060. We would like to thank the technical monitor, Jeffery Farmer of NASA Marshall, for many helpful technical discussions.

REFERENCES

W. G. Anderson, M. C. Ellis, and K. Walker, "Variable Conductance Heat Pipe Radiators for Lunar and Martian Environments," SPESIF 2009, Huntsville, AL, February 24 - 27, 2009.

Birur, G., Tsuyuki, G., "JPL Advanced Thermal Control Roadmap – 2009", presented at the Spacecraft Thermal Control Workshop, March 10-12, 2009.

M. C. Ellis and W. G. Anderson, "Variable Conductance Heat Pipe Performance after Extended Periods of Freezing," SPESIF 2009, Huntsville, AL, February 24 - 27, 2009.

Hartenstine, J. R., Walker, K. L., and Anderson, W. G., "Loop Heat Pipe with Thermal Control Valve for Variable Thermal Conductance," 41st International Conference on Environmental Systems (ICES 2011), Portland, OR, July 17-21, 2011.

Marcus, B. D., "Theory and Design of Variable Conductance Heat Pipes: Hydrodynamics and Heat Transfer," NASA Report No. NASA-CR-146195, April 1971.

Swanson, T., and Butler, D., "NASA/Goddard Thermal Control Technology Roadmap-2006", 17th Aerospace Spacecraft Thermal Control Workshop, Los Angeles, CA, March 14-16, 2006.

THEORETICAL AND EXPERIMENTAL STUDY OF THE THERMAL RESISTANCES IN THE UNIT, INCLUDING TWO AXIAL HEAT PIPES JOINED TO EACH OTHER.

K. Goncharov, Yu. Panin, V. Antonov, A. Kochetkov
The Heat Pipe Centre Lavochkin Association,
24, Leningradskaya st., Khimki, Moscow region, 141400, Russia
Tel/Fax: +7 495 5736374; heatpipe@laspace.ru

ABSTRACT

There was carried out the research of thermal resistance and heat-transfer coefficient in the contact between two AGHP. 3D model of a contact between two AGHP (see Fig. 3) was developed and the temperature distribution study was carried out.

Experimental research for theoretical results proof of the heat-mass transfer between two AGHPs with various outer diameters at different temperature ranges and applied heat power was conducted. Thermal resistance of AGHP assembling was researched in different positions in the gravity conditions. Thermal and physical characteristics of AGHP and their collateral contact were obtained basing on the experimental data.

Calculation results, experimental data and operational data were compared in the paper.

1. INTRODUCTION

Most of the Thermal Control Systems (TCS) used in the design of modern spacecrafts are developed on the base of honeycomb panels with Heat Pipes (HP). Last years Lavochkin Association developed TCS for numerous SC: KazSat, KazSat-2, Express MD-1, Express MD-2, Canopus-B, Belka, Electro-L, Spectrum-RG, Phobos-Ground and other. Honeycomb Panels with embedded and collector HP are used in all these SC.

The temperature field equalization on the honeycomb panel surface for space application is important and actual task of the thermal design. The problem is often solved by use of the collector axial grooved heat pipes (AGHP) mounted on the top THP surface perpendicular to the panel embedded heat pipes (see Fig. 1). The AGHP provides the heat power redistribution between embedded heat pipes.

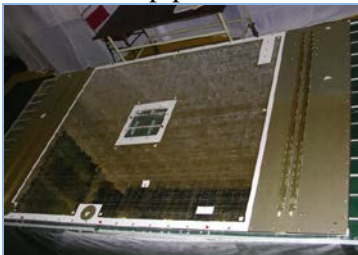


Figure 1. Panel with AGHP from SC KazSat”.

First results of this research were presented in the paper «Thermal resistance research of two axial grooved heat pipes assemblage» at the 8th Minsk international seminar.

There was carried out the research of thermal resistance and heat-transfer coefficient in the contact between two AGHP with various outer diameters and also between the AGHP and the liquid loop.

The temperature field equalization on the panel surface is important and actual task of the thermal panel design. The problem is often solved by use of the collector AGHP mounted on the heat panel surface perpendicular to the panel internal heat pipes. The AGHP provides the heat power redistribution between the panel internal heat pipes. The valid data on the internal and collector heat pipes interface is the most important component of the spacecraft thermal control system design process.

The experiment for determination of thermal resistance along HP was carried out earlier. Its results are presented in the paper Barantsevich et al. (1998). Determination of thermal resistance in the contact area of two HP is more complicated task for calculation. Therefore, we tried to determine thermal resistance of such joint experimentally and then prove obtained results in the conditions of SC operation Bazhan et al. (1989).

2. THE TEST UNIT

The experimental assembly consisting of two AGHPs cross joint is produced for the test devoted to the joint interface thermal resistance.

The unit consists of the two AGHP and aluminum plate inserted between them. Both AGHPs are produced from the same aluminum profile of 12,5 mm diameter (the AGHP cross-section is presented in the Fig.2). The AGHP1 length is 818mm and the AGHP2 length is 643mm. The plate was produced from the 7075 aluminum alloy. Its thickness is 0,5 mm. The plate size is 140x140mm. The ammonia of high purity was used as the AGHPs heat fluid.

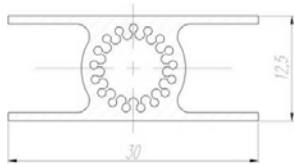


Figure 2 The AGHP cross-section.

The AGHPs are joined in cross direction between each other and to the aluminum plate with the heat-conducting polymerizing paste. The paste coefficient of heat conductivity is $\lambda = 2,0 \text{ W/m}^2$. The paste layer thickness is from 0,01 up to 0,05 mm. The AGHP arrangement is shown in the Fig.3.

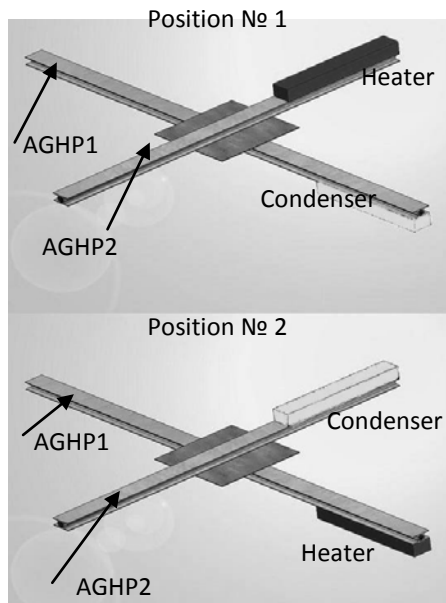


Fig.3. The AGHP experimental assemble.

Length of the AGHP1 and AGHP2 heating and cooling zone is 200 mm. The zones are located out of the aluminum plate. The heat power up to 100W is supplied by the facility heater. The heat power is dissipated by the liquid nitrogen cooler (see Fig.4).

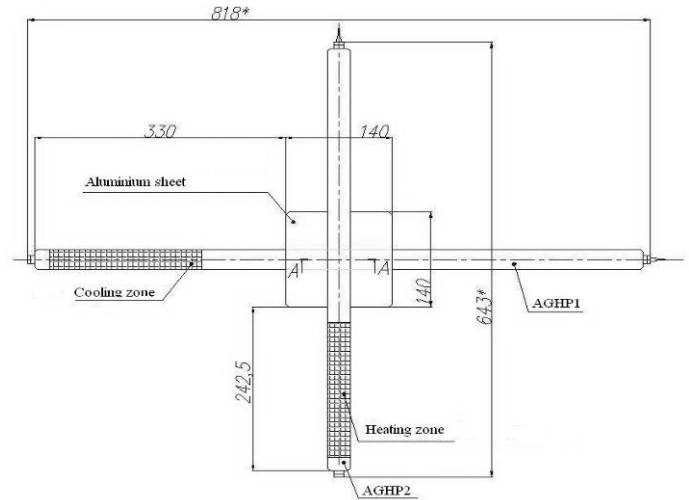


Figure 4. The test facility.

The testing was performed on the two typical positions of the AGHP assembly location. At the first case the heater was mounted at the AGHP2 top. The AGHP2 was mounted on the aluminum plate. The AGHP1 was mounted on the plate bottom. The cooler was mounted in the AGHP1 bottom. Such heater and cooler arrangement provides better heat exchange comparing to the real heat exchange observed in space at the zero-gravity condition Ivanovsky et al. (1978).

At the Position 2 while the construction remained the same the heater was mounted at the AGHP1 bottom and the cooler was located at the top of the AGHP2. The heat exchange of the Position 2 is comparatively weaker than the real heat exchange in the zero-g condition.

The test was performed for 3 thermal modes. Each mode was defined by the temperature in the transportation zone of the colder AGHP (the one with the condenser). The following temperature values were selected for the test: minus 20°C, plus 20°C, plus 40°C.

The test was started at the heater initial power 10W. After the AGHP1 and AGHP2 stationary mode achievement the heat load was increased with step 10W. In case when the temperature difference between the AGHP2 heating zone and AGHP1 cooling zone has exceeded 20°C the test

was stopped and the next thermal mode has been begun.

The temperature values were measured by the thermocouple sensors. The measurement tolerance was $\pm 0,3$ °C. Each heat pipe surface was divided into several zones. Each zone was provided with 4 thermocouples. The thermocouples placing scheme is presented in the Fig.5.

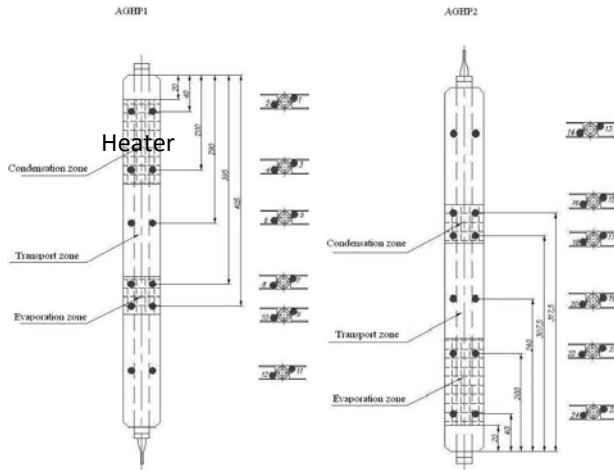


Figure 5. Thermocouple sensors placing scheme.

The test was performed at the atmospheric test facility.

The tested unit was mounted on the turntable with the supports through the heat insulation gaskets and was covered with thermal insulating.

3. THE METHOD OF THE AGHP THERMAL RESISTANCE AND HEAT DISSIPATION FACTOR DETERMINATION

The thermal resistance is a very important thermal engineering parameter used for the spacecraft TCS design. It shows the temperature gradient of the heat flux propagation in the studying structural element. The valid analytical value of the thermal resistance can be received only for the simplest structures. Therefore the thermal resistance of the tested unit was calculated as the temperature difference at the specified section of the AGHP, related to the transmitted heat power.

The thermal resistance along the AGHP (Chi (1976), Dunn and Reay (1979)):

$$R_{AGHP} = \frac{(T_{vap.av.} - T_{cond.av.})}{Q_{AGHP}}, \quad (1);$$

where:

$T_{vap.av}$ – the average temperature in the AGHP evaporation area;

$T_{cond.av}$ – the average temperature in the AGHP condensing area;

Q_{AGHP} – the heat power, transmitted by the AGHP, W

The thermal resistance between the AGHP1 and AGHP2 in the contact area:

$$R_x = \frac{(T_{cond.av.AGHP2} - T_{vap.av.AGHP1})}{Q_{AGHP}} \quad (2);$$

where:

$T_{vap.av.AGHP1}$ – the average temperature in the AGHP1 contact area;

$T_{cond.av.AGHP2}$ – the average temperature in the AGHP2 contact area;

Q_{AGHP} – the heat power, transmitted by the AGHP, W.

The thermal resistance between the vapor in AGHP1 and the vapor in AGHP2:

$$R_{vap} = \frac{(T_{tr.AGHP2} - T_{tr.AGHP1})}{Q_{AGHP}} \quad (3);$$

where:

$T_{tr.AGHP1}$ – the temperature in the AGHP1 transport zone;

$T_{tr.AGHP2}$ – the temperature in the AGHP2 transport zone;

Q_{AGHP} – the heat power, transmitted by the AGHP, W.

4. THE TEST RESULTS

The test results include the stationary operational mode for all operational temperature values (minus 20°C, plus 20°C, plus 40°C). The thermocouple sensor indications were recorded for each mode and the maximal AGHP powers at the given temperature differences were determined.

The Figs. 6, 7 present the tested unit temperatures distributions on the thermocouple sensor indications for the thermal mode plus 20°C in both positions.

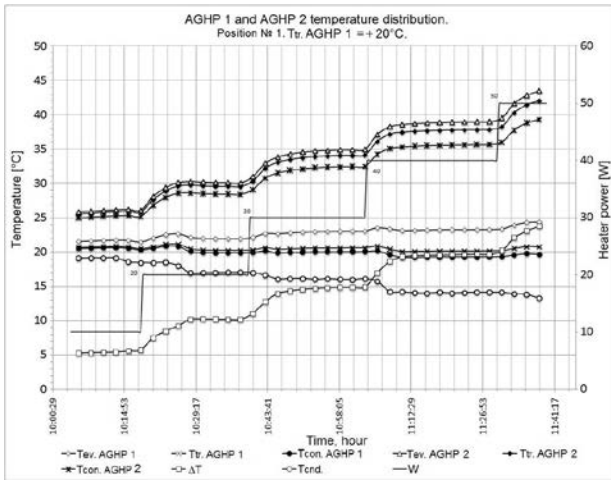


Figure 6. The temperature distribution for Position 1 on the mode plus 20°C.

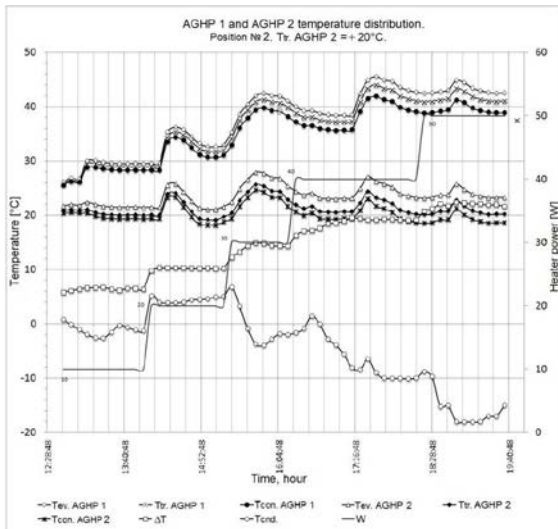


Figure 7. The temperature distribution for Position 2 on the mode plus 20°C.

The given test mode monitoring was performed with the thermocouples of the cold AGHP1 transport zone. The test result analysis shows that during all thermal modes and various power values the AGHP stationary operational mode has been achieved. At that the temperature difference between the heat input zone and heat dissipation zone was not more than 23°C (see Figs. 6, 7) at the power not more than 50W.

The temperature jumps of all thermocouple sensors are stipulated by the heater input power increase. The required thermal mode in this case was restored by the heat fluid rate regulation.

Analysis of the AGHP thermal resistance calculated values for different temperature modes, and the experimental curve analysis (presented in

the Figs. 8, 9) shows the following. External heat flows are typical for the temperature mode minus 20°C. Therefore the received thermal resistance values exceed the real values. The mode plus 40°C is presented with heat dissipations and the thermal resistance values are lower than real values. Most valid from the practical point of view is the thermal resistance value for the mode plus 20°C. In this case the temperature of testing was corresponded to the ambient temperature and therefore the heat inputs and heat dissipations were minimum.

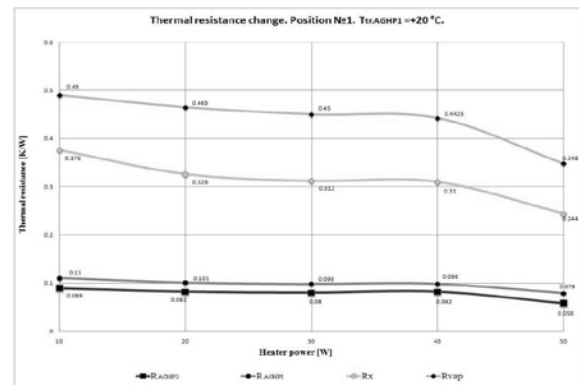


Figure 8. The AGHP1 and AGHP2 cross joint thermal resistance depending on the heat input. Position 1. The mode – plus 20°C.

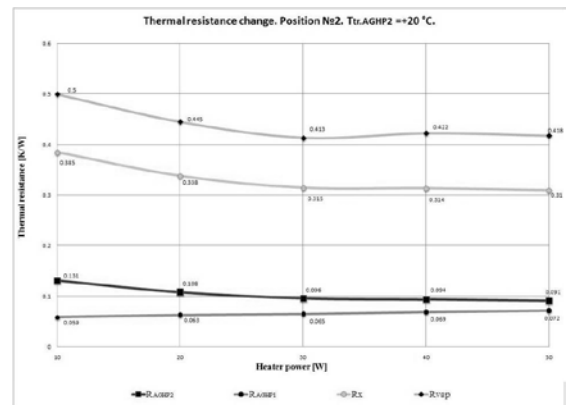


Figure 9. The AGHP1 and AGHP2 cross joint thermal resistance depending on the heat input. Position 2. The mode – plus 20°C.

Based on the test results the following thermal resistance values for the Position 1 were received (the heat input was provided from the unit top and the heat output was provided from the bottom of the unit):

$$\begin{aligned}
 R_{av,AGHP1} &= 0,097 \text{ K/W}; \\
 R_{av,AGHP2} &= 0,078 \text{ K/W}; \\
 R_{av,x} &= 0,313 \text{ K/W}; \\
 R_{av,vap} &= 0,438 \text{ K/W}.
 \end{aligned}$$

For the Position 2 the received values are the following (the heat input was provided from the bottom of unit and the heat output was provided from the top of the unit):

$$\begin{aligned} R_{av,AGHP1} &= 0,066 \text{ K/W}; \\ R_{av,AGHP2} &= 0,1 \text{ K/W}; \\ R_{av,x} &= 0,332 \text{ K/W}; \\ R_{av,vap} &= 0,439 \text{ K/W}. \end{aligned}$$

Calculated as the test data processing results the AGHP average thermal resistance in the contact area in Position 1 differs from the AGHP average thermal resistance in the contact area of Position 2 insignificantly (the difference is 6%). At that the considered thermal model of the heater and cooler position (see Fig. 3) provides the better heat exchange than the real heat exchange in the zero-g space environment. The thermal model of Position 2 provides heat exchange worse than the real heat exchange in the zero-g space environment. So the real thermal resistance value in the zero-g space environment will be in the range between the two above mentioned values of the thermal resistances $R_{av,x}$.

AGHP cosmic operation takes place in microgravity conditions and existence of noncondensable gas. Moreover, there is a possibility of liquid plug generation in the AGHP. It is very difficult to take into account all these factors when AGHP modeling. AGHP experimental refining is more simple and valid method for estimation of considered factors influence on AGHP operation ability.

5. LIQUID PLUGS

The possibility of liquid plug generation is caused by excess of liquid phase of the working fluid which accumulates in condensation zone and blocks vapor condensation. HPs are designed for certain operation temperature range. In order to avoid drying out of the capillary structure, often mass of charged working fluid is chosen for minimum operation temperature. At high operation temperature excess of the working fluid liquid phase is observed. Excess of liquid is located in the coldest HP zone – condensation zone. For HP cross joint there is possible the situation when all condensation zone is filled with excess of liquid (Fig. 10). In this situation thermal resistance may increase multiply

Isachenko et al. (1975), Vargaftik (1971), Dunn and Reay (1979).

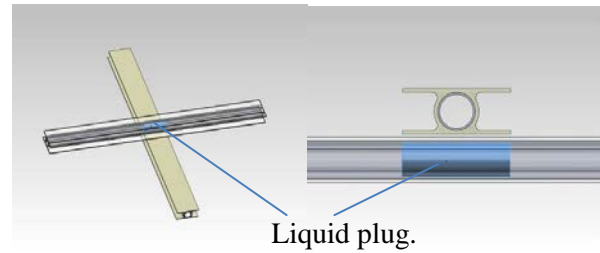


Figure 10. Generation of liquid plug in HP condensation zone.

The calculations carried out in accordance with the paper show that for Ammonia HP with operation temperature range from minus 20 to plus 40 °C and made of the profile with diameter 10 mm and length 1.5 m, the length of liquid plug can reach 50 mm. During ground testing liquid plugs spread along HP and their influence is imperceptible. In microgravity conditions liquid plugs will block condensation zone. It can lead to the system failure.

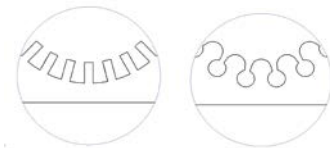


Figure 11. Profiles with rectangular-shape and Ω-shape grooves.

Calculation of the working fluid charging mass was made using the relation presented in the paper Brennan et al. (1993). This relation takes into account linear variation of liquid meniscus shape along AGHP. The calculation is made for the profile rectangular -shape grooves. It is assumed that heat flow in the profile cross section is uniform and one-directional.

$$G = L \cdot [n \cdot \rho_l \cdot (F_l - \pi \cdot a^2 \cdot / 16) + \rho_v \cdot (F_v + n \cdot \pi \cdot a^2 \cdot / 16)], \quad (4)$$

where: G – mass of charged working fluid; ρ_l, ρ_v – density of liquid and vapor phase of the working fluid; F_l, F_v – cross section area of longitudinal groove and vapor channel (respectively); a – width of longitudinal groove slit; n – quantity of longitudinal grooves.

Fragment of TCS developed for “Electro” SC that was launched on January 20, 2011 is presented on Fig. 12.

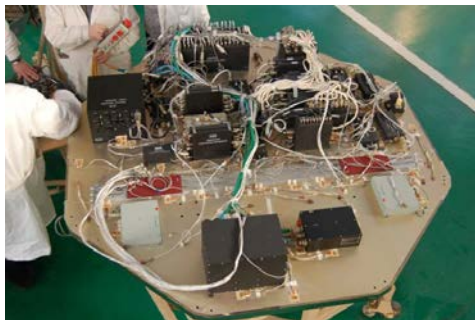


Figure 12. Electro – M panel

The data obtained during verification nature tests of “Electro” SC showed that in microgravity conditions TCS performance is close to its performance during ground testing. Thus, microgravity does not have essential influence on TCS performance.

Obtained flight telemetric data shows that temperature drop in the contact area of embedded and collector HPs is close to the temperature drop obtained during ground tests.

Additional analysis of honeycomb temperature fields allows us to conclude that there are no liquid plugs in condensation zones of embedded HPs.

Our experimental test results show that to the end of HP operation life, amount of noncondensable gas in the HP does not exceed 30 – 45 mm. Therefore, it is possible not to take into account influence of noncondensable gas on HP performance.

CONCLUSIONS

The thermal resistance between panels heat pipes and collectors heat pipes is the most important component of the spacecraft thermal control system design.

The experimental research was performed on the two typical positions of the AGHP in the gravity and in the flight. At the first case the heater was mounted at the AGHP2 top. The AGHP1 was mounted bottom. The cooler was mounted in the AGHP1 bottom. Such heater and cooler arrangement provides better heat exchange comparing to the real heat exchange observed in space at the zero-gravity condition. At the Position 2 while the construction remained the

same the heater was mounted at the AGHP1 bottom and the cooler was located at the top of the AGHP2. The heat exchange of the Position 2 is comparatively weaker than the real heat exchange in the zero-g condition.

The thermal resistance is 0,44K/W between vapor and vapor the AGHPs with outer diameter 12 mm. Deviation of thermal resistance depended from the heater location is less then 10%.

REFERENCES

- Bazhan P., Kanevets G., Selivestrov V. (1989) Handbook on Heat Exchange Apparatus. - M.: Mashinostroenie Press, (in Russian).
- Chi S. W. (1976) Heat Pipe. Theory and Practice, Washington-London: Hemisphere Publishing Corporation.
- Dunn P., Reay D. (1979) Heat Pipes. - M.: Publisher “Energia“ (in Russian).
- Vargaftik N. (1971) Gases and liquids thermophysical properties handbook - M.: Publisher “Nauka” (in Russian)
- Isachenko V., Sukomel A., Osipova V. (1975) Heat-transfer process. Third issue. - M.: Publisher “Energia“ (in Russian)
- Barantsevich V., Golovin O., Goncharov K., Orlov, A. (1998) Investigation Results of Axial Grooved Heat Pipes with High Thermal Capacity - 31th International Conference on Environmental Systems. Orlando, Florida, USA
- Ivanovsky M., Iagodkin I., Sorokin V. (1978) Physical Basics of Heat Pipes. - M.: Atomizdat Press (in Russian)
- Brennan P, Kirkpatrick J., Schlitt K. (1993) Parametric performance of extruded axial grooved heat pipes from 100 to 300 K. AIAA Paper-724-74, pp.1-9.

GROOVED HEAT PIPE EVAPORATORS WITH POROUS COATING

L.L. Vasiliev L.P. Grakovich, M.I. Rabetsky
and L.L. Vasiliev Jr.,

Luikov Heat and Mass Transfer Institute
15 P. Brovka Str., 220072, Minsk, Belarus
Tel/Fax: +375-17-284-21-33, E-mail: Leonard_Vasiliev@rambler.ru

ABSTRACT

Grooved heat pipes (GHP) are the most convenient two-phase heat transfer devices for the space vehicles thermal control. The thermo-vacuum tests and comparative analysis of the GHP with smooth grooves and grooves with porous deposit (GHPPC) is the subject of this paper. An ammonia and Propane are used as the working fluid for the GHPPC. Experimental results show that the porous coating in the GHPPC evaporator significantly affects the heat transfer performance and depends on the form and shape of grooves. The main aim of the experiments is to improve the cooling capability of GHPPC, applying thin (Al_2O_3 nano particles) deposit ($25\ \mu\text{m}$ - $150\ \mu\text{m}$) on the surface of mini fins inside the heat pipe evaporator.

KEY WORDS: Heat pipe, nano-porous coating, evaporation, capillary grooves, heat transfer coefficient

1. INTRODUCTION

Two-phase heat transfer in mini and micro channels is a fast-progressing field of science. In recent years the advances in micro scale heat transfer and fluid flow were remarkable and applications using micro scale phenomena have become popular. Especially, innovations in space, electronic technology and biotechnology are striking. The ratio of the heat transfer area to the volume of the channel is inversely proportional to the lateral size of the channel and its decrease stimulates the high intensity of heat transfer. It is the reason why considerable emphasis was devoted last time to the study of the evaporation and condensation phenomena in the open and closed microchannels. However, this heat transfer enhancement is still poorly understood due to the large number of determinative parameters influencing the rate of evaporation/boiling and condensing enhancement in the confined space [1-3]. It is known that the coefficients of heat transfer on evaporation in thin liquid films and porous coating greatly exceed the coefficients on liquid evaporation and pool boiling. Capillary-porous coatings are often used for creation and maintenance of thin liquid films. Porous materials as the wick for heat pipes provide not only heat transfer enhancement but also transportation of liquid into the evaporation zone by capillary forces. Many studies on the upward and horizontal

gas-liquid flows in mini channels and pipes were done in recent years. These studies showed that the two-phase flow in a channel with hydraulic diameter less than the capillary constant differs significantly from that in the conventional tube. In heat pipes responsible for the thermal management in spacecrafts the capillary structures in the form of capillary grooves are often used. The properties of these structures and heat pipes employing them have been studied rather adequately. A modern improvement of them is in optimization of shapes and dimensions of capillary grooves depending of the purpose and specific conditions of its application. At the same time, though capillary grooves possess indisputable advantages, they present certain restrictions in evaporation and boiling of liquid that are related to the special features of heat transfer in the grooves. The possibility of coating the groove surface with an additional thin (25 - $100\ \mu\text{m}$) porous layer forms next stage of heat transfer enhancement. The authors of [4-6] showed both theoretically and experimentally that deposition of a porous coating on the groove surface positively affects the heat transfer coefficient. This related to the specific of liquid evaporation from the capillary groove. At present the model of liquid evaporation predominantly in a very limited zone of a transient thin film of the liquid meniscus in

the groove is the proved evaporation model [7- 9]. The intensity of evaporation is not high in the region of the main meniscus (large thickness of the liquid layer) and in the zone of an equilibrium film (large effect of surface intermolecular interactions). A mean intensity of evaporation in the capillary groove can be increased if we increase the porous surface of the groove edge, where a thin liquid film is constantly maintained by capillary forces.

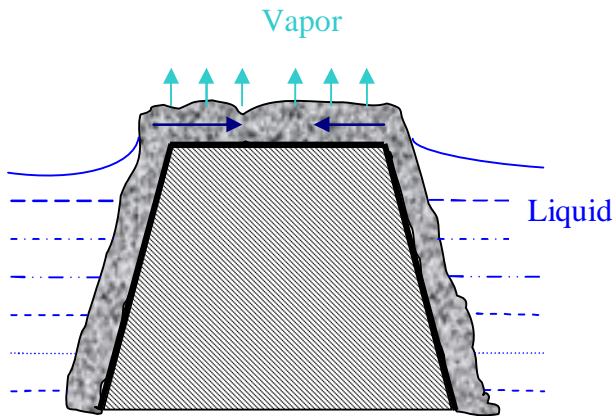


Figure 1: Schematic of the liquid evaporation in a capillary groove with porous coating

A large surface of evaporation can be provided by a thin capillary-porous coating on the inner surface of the groove edge and its crest, Fig.1. It is evident that the coating thickness must be much smaller than the characteristic dimensions of capillary grooves designated for transport of liquid along the groove without problems. The porous coating thickness and permeability should provide the necessary flow rate of the liquid. This method of heat transfer enhancement was at first suggested and experimentally checked in [4, 5] and later confirmed in [6]. Porous coating ensures a uniform distribution of the liquid over the volume due to the capillary forces action. In this case, the whole surface of the groove edge beyond the liquid meniscus in the groove turns to be wetted uniformly and the area of the effective evaporation can be increased manifold. Unlike the heat transfer with boiling on the smooth surface the liquid evaporation/boiling on the porous deposit (like aluminum oxide nanoparticles coating) is characterized by the fixed number of sources of nucleation, Fig.2. These local sources of vapor generation inside the porous coating are constant; its number depends on the heat flow density in the heat loaded zone of the heat pipe.

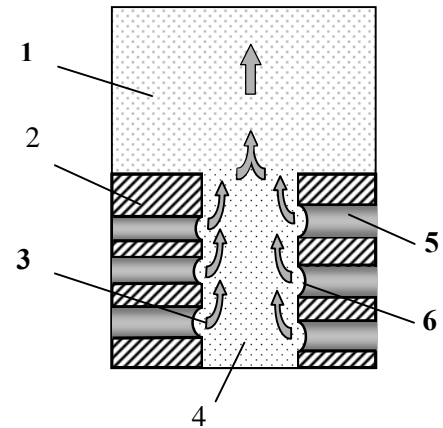


Figure 2: Model of heat transfer on the upper part of the mini groove with porous coating. 1 – vapor channel, 2 – solid part of the wick, 3,6 – vapor flow, 4 – macropore free of liquid, 5 – micropore with capillary liquid flow

In porous coatings the liquid/vapor interface consists of menisci situated inside the macropores and numerous menisci between macro and micropores. The menisci of the evaporation disposed on the macropore interface liquid/vapor are typical for low heat flux, when the wick is completely saturated with liquid. For such a case the heat transfer is realized by conduction through the wick.

The menisci of the evaporation in micropores are typical for high heat flux and the case, when the menisci in macropores recede and are open for the vapor flow. For such a case many nucleation sites (micro menisci exist on the interface between macro and micropores), are becoming the centers of vapor generation inside the macropore, Fig.2 . The possibility of coating the groove surface with a thin (25-100 μm) porous layer forms next stage of heat transfer enhancement

2. EXPERIMENTAL RESULTS

The heat flux q through the wall of the GHP evaporator can be written as:

$$q = \frac{T_w - T_{sat}}{\frac{\delta_{wick}}{k_{eff}} + \frac{1}{h_e}}, \quad (1)$$

where $T_w - T_{sat} = \Delta T_t$ and is determined

$$\text{as: } \Delta T_t = \frac{2\sigma T_{sat}}{h_{lv}\rho_v} \left(\frac{1}{r_v} - \frac{1}{r} \right) \quad (2)$$

The effective thermal conductivity k_{eff} of porous systems has been a source of interest over the last two centuries. As for now, numerous experimental materials have been devised and a large number of formulae have been put forward

to calculate the effective thermal conductivity of porous systems (Luikov *et al.*, 1968) [10]. Following the experimental data, the upper part of the groove has more intense heat transfer compared to the bottom part of the groove, Fig.2.

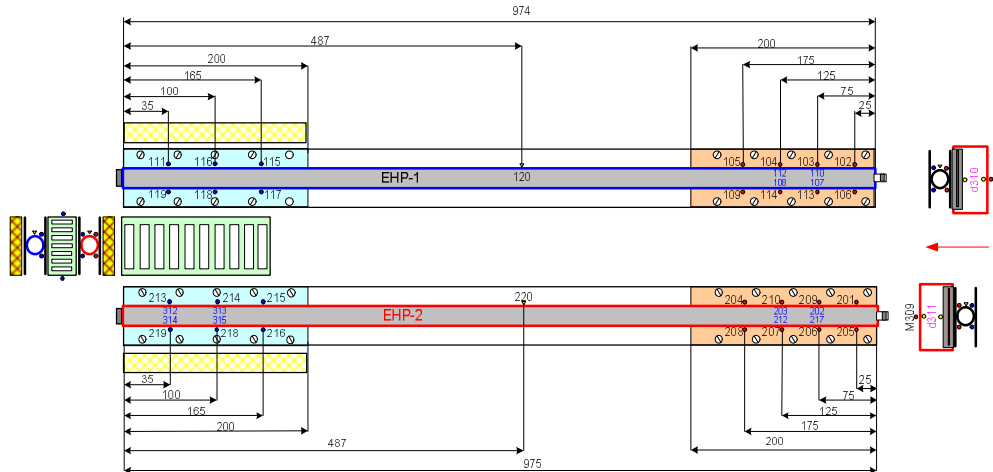


Figure 3. Schematic view of two tested GHPs with thermocouples, heaters and heat exchangers.

2.1 Experimental set-up

The experimental set-up, Fig.3, was suggested and designed to investigate the thermal performance of different kinds of GHP with maximum length up to 2 meters. The experimental set-up consists of a 10 m³ vacuum chamber, two thermal baths, liquid flow meters, Agilent Data Acquisition system with a set of thermocouples and basement support with an optical system of sample space orientation. The experimental

studies were aimed to obtaining quantitative dependences of the heat transfer parameters in evaporation and boiling for the surfaces with capillary grooves of different shape. We ought to know the extent to which these parameters are affected by the thin capillary coatings (Al₂O₃ particles, 30-100µm). The heat load, temperature of the GHP evaporator and vapor were registered during experiments. The characteristics of different capillary grooves are shown in Table 1.

TABLE 1: Characteristics of the GHP different capillary grooves (smooth and with porous coating)

Structure designation	Groove type	Groove depth, mm	Edge width at the crest, mm	Porous coating thickness, µm
S-1		2	0.54	
S-1-1		2	0.54	50
S-2		2	1	
S-2-1		2	1	50
S-3		1.3	0.36	
S-3-1		1.3	0.36	50

Ammonia was the main working fluid selected for such experiments. In Figs. 4-7 the heat transfer coefficients for the evaporators of GHPs S1-(S1-1), S2-(S2-1), and S3-(S3-1) are presented. An appreciable increase in the heat transfer coefficients is noted for all GHP with porous

coating to compare with GHPs with smooth grooves. For grooves of different shapes and dimensions this increase is within the range of 1.3-1.6 times. As has been already mentioned, the heat transfer enhancement depends on the increase of the porous surface of the groove edge, Fig.1.

This increase is the highest for the GHP S2-1 surface for which the portion of the total area occupied by the crests of edges is the largest and is close to 0.6. For S1 surfaces it is 0.43 and for S3 surfaces it equals 0.33. These data are in agreement with those given in [6].

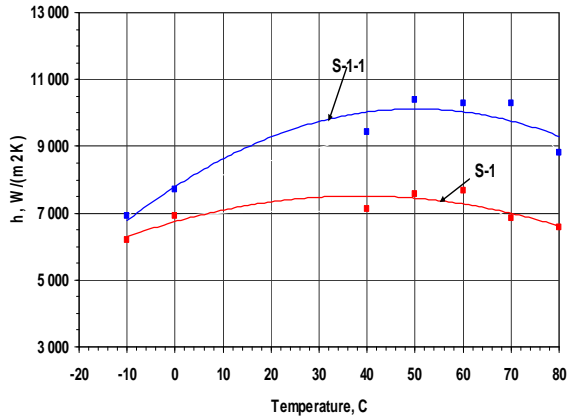


Figure 4. Heat transfer intensity in the evaporator of GHPs S1 and S1-1 (ammonia) as a function of the temperature of saturated vapor

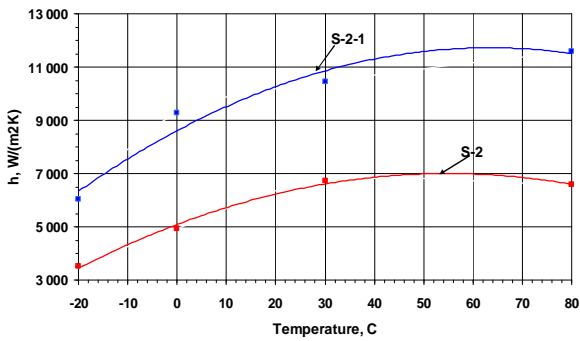


Figure 5. Heat transfer intensity in the evaporator of GHPs S2 and S2-1 (ammonia) as a function of the temperature of saturated vapor

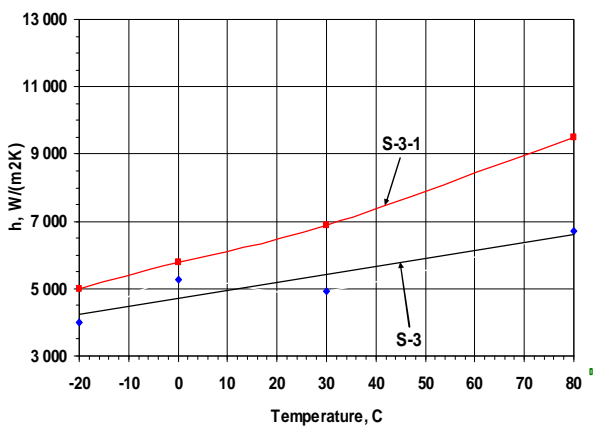


Figure 6. Heat transfer intensity in the evaporator of GHPs S3 and S3-1 (ammonia) as a function of the temperature of saturated vapor

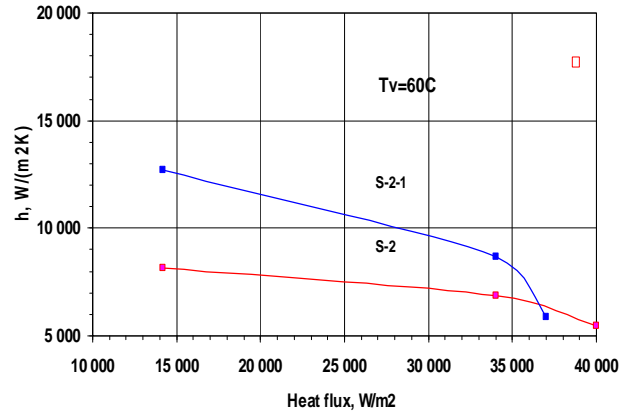


Figure 7. Heat transfer coefficient as a function of heat flux for S2 evaporator. $T_v = 60^\circ\text{C}$.

Propane was the alternative (to ammonia) working fluid to compare the efficiency of the nano porous technology application. Propane (R290) was chosen as a beneficial working fluid for heat pipes due to its good thermodynamic properties, low cost, availability, compatibility with constructional materials, and environmental friendliness. The latest circumstance is very important because of the ozone depletion by chlorofluorocarbons (CFC) and hydrochlorofluorocarbons (HCFC). The heat transfer intensity in the GHP S1-1 evaporator via the heat load is presented on Fig.8.

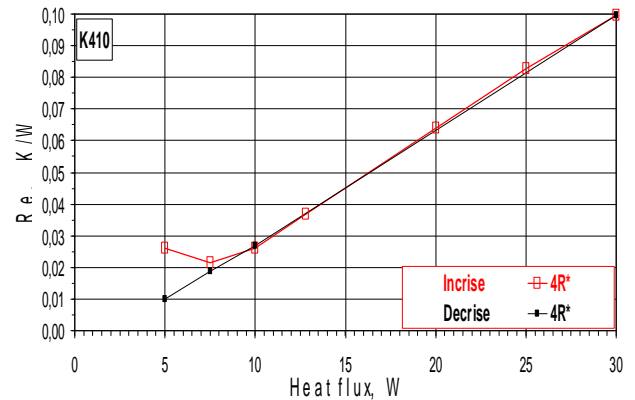


Figure 8. GHP S1-1. The evaporator thermal resistance R_e as a function of the heat load. Working fluid-**Propane**

Capillary coatings of the GHP enhance the heat transfer not only in the regime of thin liquid film evaporation, but also when there is a boiling in the liquid pool and flooded surfaces, Fig.9. In this case porous coating plays the role of additional and stable centers for the vapor generation, which do not require high superheating of the surface.

To prove this hypothesis the experiments were carried out not only with cylindrical GHP evaporators but with **plane aluminum GHP evaporators** having triangular grooves with the depth 0.5 mm and pitch 1 mm. Both grooves and edges have a porous coating made from aluminum oxide particles. The particle size dispersion was from 5 to 7 μm and the coating thickness was 20-30 μm . The pore diameter in the porous layer was 0.1-2 μm . The coating porosity - 50%. The height of the Propane film above the porous coating was 2 mm.

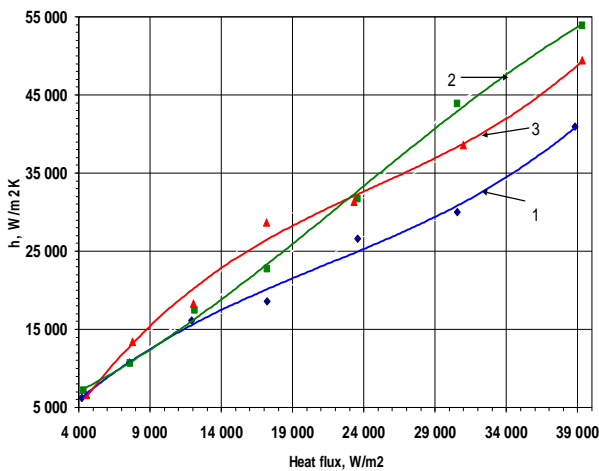


Figure 9. Heat transfer coefficients as a function of the heat flux on the flat GHP evaporator with smooth capillary grooves (1) and grooves with Al_2O_3 nanoporous coating (2, 3).

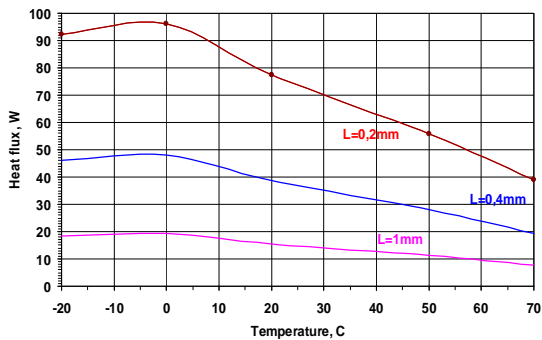


Figure 10. Heat flow removed from one edge of the capillary groove with porous coating as a function of temperature. L is the edge width, mm; temperature of ammonia vapor -20°C .

Heat flux removed from the porous layer of certain thickness and length can be determined, using formula:

$$q = \frac{\frac{2\sigma \cos \theta}{R_p} - \rho_l g L \sin \varphi}{\left(\frac{\mu_l}{\rho_l K A_w} + \frac{1}{n_{\max}} \frac{8\mu_v \delta_v}{\rho_v r_v^4 L} \right) \frac{L A_e}{h_{fg}}} \quad (3)$$

Capillary transport of liquid in thin coatings with microporous structure can become an appreciable factor that limits the heat removal. A maximum curvature of the meniscus is determined by the dimensions of the nano particles. For a fin with a rather wide edge or in the case of liquid meniscus deepening inside the mini channel the capillary potential of the coating may turn to be insufficient. In this case, a portion of the edge surface can be dried and the effect of the porous coating is decreasing. Figure 10 shows the estimated dependence of maximum heat flux that can be removed from one crest of the groove edge, when the groove is wetted completely. The heat flux value depends on the liquid temperature. It is assumed that the main meniscus of the liquid lies at the groove base. The capillary structure used in the experiments is shown in Fig. 11. It was manufactured from the aluminum oxide particles.

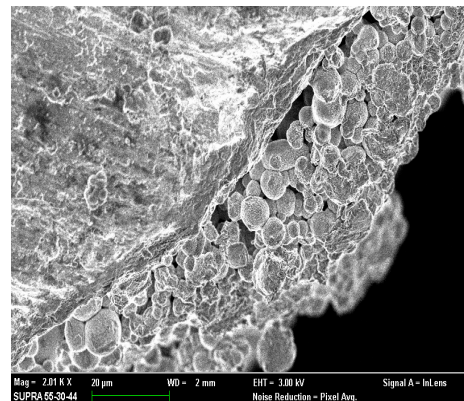


Figure 11. Aluminum oxide porous coating of GHP mini groove

Visual analysis and experimental validation of the heat transfer intensity using nano-porous technology testify the heat transfer enhancement (2.5 to 3 times) compared to heat transfer occurring on the same GHP with smooth grooves. Nanoporous coating of mini-fins completely modifies the hydrodynamics of two-phase flow in mini grooves. A micro-scale effect is essential inside a porous body, and a mini-scale effect is available in the groove. A porous coating with open pores can be considered as a medium in which a particularly large number of micro heat pipes with zones of evaporation and condensation

are active, Fig.2. Mini/micro porous coating on the GHP heat-loaded wall helps to enhance heat transfer [11-12]. It means that the heat flux increasing may occur with a slight increase of the wall temperature.

3. CONCLUSIONS

The parameters of the evaporators with smooth capillary grooves and capillary grooves having porous coating of walls with a thickness of 20-100 μm were experimentally analyzed.

Comparative studies of the heat transfer coefficients of the evaporators with different types of capillary grooves testify the efficiency of the nano porous coating of the GHP mini channels.

Within the entire studied range of temperatures and heat loads the heat transfer coefficients of all types of evaporators with the porous coating are 1.3-1.8 times higher than of similar evaporators with a smooth surface of capillary grooves.

On determining the required parameters of the porous coating one should, along with the structural characteristics, take into account the geometry and dimensions of capillary grooves, the temperature and heat load of the evaporator.

The change in the height of the liquid/vapor interface above the surface of edges of capillary grooves does not result in appreciable changes of the heat transfer coefficient

NOMENCLATURE

F surface, m^2
 k heat-transfer coefficient, $\text{W}/\text{m}^2\text{ }^\circ\text{C}$
 Q heat load, W
 P pressure, kPa
 R thermal resistance, $^\circ\text{C}/\text{W}$
 T temperature, $^\circ\text{C}$
 Subscripts
 c condenser
 e evaporator

REFERENCES

1. Triplett K.A., Ghiasian S.M., Abdel S.I. Khalik, Sadowski, D.L.,(1999), Gas-Liquid Two-Phase Flow in Microchannels Part I: Two-Phase Flow Patterns, *Intern. Journal of Multiphase Flow*, 25, pp. 377–394
2. Revellin, R. and Thome, J.R.,(2006), New Diabatic Flow Pattern Map for Evaporating Flows in Microchannels, *Annals of the Assembly for 13 International Heat Transfer Conference*, 13-18 August, Sydney, Australia

3. Kawahara A., Chung P. and Kawaji P., (2002), Investigation of Two Phase Flow Pattern, Void Fraction and Pressure Drop in a Microchannel, *Int. J. Multiphase Flow*, 28 (9), 1411-1435
4. Vasiliev, L. L., Khrustalev, D. K., and Grakovich, L. P., (1988), *Heat Pipes in the Systems with Renewable Energy Sources*, Minsk: Nauka i Tekhnika Press, (in Russian).
5. Khrustalev, D. K. and Denisevich, S. V., (1986), Heat transfer in evaporation and condensation in a heat pipe with a combined capillary-porous structure, in: *Heat Pipes with Capillary-Porous Structures*, pp. 39-50, Minsk, HTMI, (in Russian)
6. Wang, J. and Catton, I., , (2001), Enhanced evaporation heat transfer in triangular grooves covered with a thin porous layer, *J. Appl. Thermal Eng.*, vol., 21, pp. 1721-1737.
7. Khrustalev, D. and Faghri, A., (1995), Heat transfer during evaporation on capillary grooved structures of heat pipes, *J. Heat Transfer*, vol. 117, pp. 740-747
8. Ma, H. B. and Peterson, G. P., (1996), The interline heat transfer of evaporating thin film along a micro grooved surface, *ASME J. Heat Transfer*, vol. 118, pp. 747-755
9. Wang, J. and Catton, I., (2004), Vaporization heat transfer in biporous wicks of heat pipe evaporators, *Proc. 13 Int. Heat Pipe Conf. "Heat Pipe Theory and Applications,"* pp. 96-104
10. Luikov A.V., Shashkov A.G., Vasiliev L.L., Fraiman Yu.E., (1968), *Thermal Conductivity of porous systems*, Int. Journ. Heat Mass Transfer, Vol. 11, pp. 117-140
11. Vasiliev L., Zhuravlyov A., Zhapovalov A., (2012), Heat transfer in mini channels with micro/nano particles deposited on a heat loaded wall, *Journal of Enhanced Heat transfer* 19(1), pp. 219-236
12. Vasiliev L., Grakovich L., Rabetsky M., Romanenkov V., Vasiliev L., Jr., Ayel V., Bertin Y., Romestant C., Hugon J., (2010), Grooved heat pipes with a nanoporous deposit in an evaporator, *Heat Pipe Science and Technology, An International Journal* 1(3), 219-236

Evaporation from micro-porous surfaces in a mechanically pumped two-phase loop

M. Winter^{a,b}, P. Stephan^{a,b}

^a Institute for Technical Thermodynamics, Technische Universität Darmstadt
Petersenstrasse 17, 64287 Darmstadt, Germany

^b Center of Smart Interfaces, Technische Universität Darmstadt
Petersenstrasse 17, 64287 Darmstadt, Germany

Phone: +49 6151 16-3159, Fax: +49 6151 16-6561, pstephan@ttd.tu-darmstadt.de

ABSTRACT

The increasing application of high power density electronic components, for example in space applications or data processing centers, causes the need of heat transfer devices that can handle the high heat fluxes dissipated by these components. A prototype of a mechanically pumped two-phase loop has been developed at the Institute for Technical Thermodynamics in cooperation with OHB System AG and ESA/ESTEC. The loop incorporates miniature evaporators that can be mounted directly on the heat dissipating device minimizing temperature differences between heat dissipating part and cooling device. Three evaporators are arranged in parallel to investigate the performance of the loop during multi-evaporator operation at different heat loads at the evaporators.

In this study the heat transfer coefficients of the new sintered surface could be increased up to 20 W/(cm²·K). The fouling of the surface slows down due to a higher porosity (bigger grain size, here: 60µm). The CHF of the porous surfaces measured is limited to approx. 90 W/cm² and does not increase with the volume flux (above 30 ml/min) as it happens with the smooth reference and a new micro-structured surface. The micro-structured surface reaches a critical heat flux of 152.6 W/cm² and a heat transfer coefficient of 6.5 W/(cm²·K) which is the best overall performance of all tested structures inside this evaporator type up to now. System tests with three evaporators at different heat loads show stable system behavior. The saturation pressure inside the evaporators depends on the system heat load.

KEY WORDS: spacecraft thermal control, two-phase loop, porous surface, miniature evaporator

1. INTRODUCTION

The demand for thermal systems to cool high power electronics has increased significantly. Mechanically pumped two-phase cooling loops have been developed to meet these requirements since the state-of-the-art capillary pumped systems extragate, Schweizer et al. (2008).

Current research activities in this field indicate that mechanically pumped loops are very suitable for high power electronics cooling. Mechanically pumped two-phase systems incorporating convective boiling in regular and small channel sizes have been developed. Recently there is an increasing interest in the use of mini- and microchannel evaporators, Kandlikar (2002) and Thome et al. (2004).

According to Schweizer et al. (2008) the most significant parameters of such systems are the pressure drop and flow instabilities that affect the system reliability.

Hybrid pumped loops utilize capillary forces to transport and equally distribute the liquid to the place of evaporation. These systems differ from flow boiling but are similar to evaporation in capillary pumped systems.

This paper focuses on single evaporator measurements with different heat transfer surfaces and the performance of the complete two-phase loop with three parallel evaporators working the same time at different heat loads.

2. EXPERIMENTAL SETUP

2.1 Experimental rig

The loop operates as follows: the liquid working fluid (methanol) is pumped by a magnetically coupled micro annular gear pump through the liquid line and spread to three parallel lines. Each line has a lock valve, a flow meter, a control valve and an evaporator.

The vapor of all three evaporators is collected in one tube and flows to the condenser where it is re-condensed and sub-cooled. The condenser is tempered by a thermostat. The configuration of the different components of the experiment is shown in Figure 1.

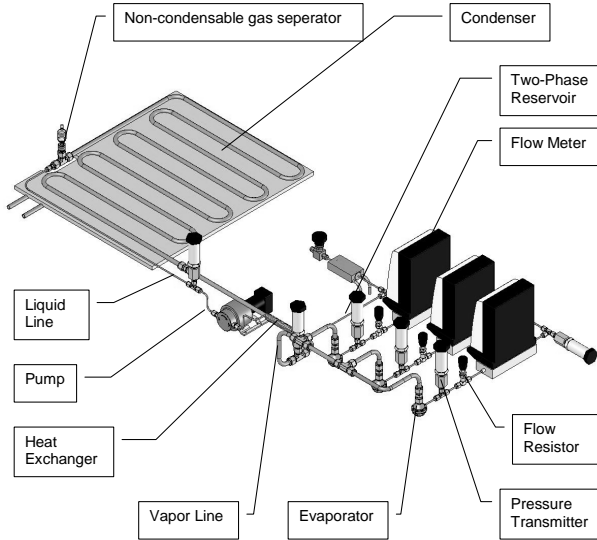


Figure 1: CAD model of the loop

The structure of the heat transfer surface inside the evaporators can be varied by changing the pot at the bottom. The tested surface has several functions:

(1) to distribute the liquid uniformly, (2) to increase the number of nucleation sites if working in pool boiling mode, (3) to increase the length of the contact line.

The aim is to have a heat transfer surface that fulfills all the three aspects (1) to (3) best possible. Control valves are placed in front of the inlet of each evaporator to act as the dominating resistance of the line to guarantee a uniform distribution of the fluid to all evaporators, even at different heat loads that create different pressure losses inside the evaporators. A more detailed description of the setup can be found in Winter et al. (2010).

The volume of the system is approx. 475 ml, the liquid charge is approx. 285 ml \pm 15 ml which corresponds to a liquid filling degree of approx. 60% \pm 3%.

2.2 Measurement instrumentation

The operation conditions of the loop are determined by six absolute pressure transmitters (accuracy \pm 8 mbar), three flow meters (accuracy \pm 2.5% of value) and several thermocouples (accuracy \pm 0.5 K). There is one pressure transmitter upstream and downstream the pump

and one between each control valve and evaporator as well as one before the condenser. To determine the volume flux, the system has been newly equipped with three flow meters; schematically shown in Figure 1, to measure the liquid volume flux to each evaporator. Since the results in Winter et al. (2010) give more qualitative results, due to the lack of the correct volume flux due to changing pressure losses of the different surfaces, the flow meters give now the possibility to get also quantitative results. The thermocouples are located at the inlet and outlet and 0.75 mm below the heat transfer surface of each evaporator. Additionally, temperatures are measured upstream and downstream the condenser.

2.3 Heat transfer surfaces

Different heat transfer surfaces inside the evaporator have been manufactured and tested. An overview and a short description of the surfaces presented in this study is given in Table 1.

Table 1: Listing of tested heat transfer surfaces

<i>identifier</i>	<i>description</i>
smooth	smooth (turning process), <i>here</i> : distance needle-to-surface 200 μm
MFR	circular channels with width 300 μm , fin width 300 μm , depth 300 μm
C3 & C4 Si60	sintered powder, purity 99.99% Cu, mean grain size 60 μm , layer thickness 350 μm
CNstack	stacked copper nets, 1x D50/S200/T104 μm^* (bottom) 2x D90/S300/T186 μm^*

* D=wire diameter; S=span; T=thickness single net

The distance of the needle-tips to the heat transfer surface is 200 μm for the smooth surface, since a distance tending to zero would cause a blocking of fluid flow. The distance for micro-structured and porous surfaces is in the range of 50 to 100 μm .

3. MEASUREMENTS

3.1 Proceeding of the measurements

After degassing and setting the system pressure to 260 mbar, the pump speed is set to a constant value for the desired volume flux. The condenser temperature is constant at 25° C (=temperature at evaporator inlet t_{ei}) for all measurements presented in this study. The *single evaporator tests* to investigate the different surface structures are done as follows: Starting from 0 W, the heat load is increased in steps of 50 W until steady state condition is reached for min. 5 min.

The heat load is increased repeatedly to the next step until the critical heat flux (CHF) is reached.

To investigate the system performance the *multiple evaporator tests* are done as follows:

The control valves of the liquid lines are set to an equal value for the volume flux at each evaporator. Following the heat load is set to a medium value for all evaporators the same. After steady state condition is reached for min. 5 min, the heat loads of the single evaporators are changed randomly in steps, while the overall heat load of all evaporators is kept constant. The heat loads are set within the working range (below CHF) with the CNstack surface that was tested with single evaporator tests before.

3.2 Evaluation

The heat transfer coefficient h characterizes the intensity of the heat transfer from the test surface to the heat transport medium and is defined by:

$$h = \frac{\dot{Q}}{A \cdot (t_{surf} - t_{eo})} \quad (1)$$

with \dot{Q} as the heat load, A the heat transfer area inside the evaporator, the temperature of the heat transfer surface t_{surf} and the temperature at the evaporator outlet t_{eo} ($=t_{sat}$, saturation temperature). Giving the efficiency of evaporation a boiling-number is defined as:

$$N_{bm*} = \frac{\dot{q} - \dot{m} \cdot c_{p,liq} \cdot (t_{surf} - t_{eo})}{\dot{m} \cdot \Delta h_v} \quad (2)$$

with \dot{q} as the heat flux, \dot{m} the mass flux, the liquid heat capacity $c_{p,liq}$, the enthalpy of evaporation Δh_v and the temperature difference of the heat transfer surface t_{surf} and the temperature at the evaporator outlet t_{eo} .

3.3 Single evaporator test results

The results of the *single evaporator tests* with a variation of the heat transfer surface are as follows: For the smooth surface the result of one exemplary measurement is shown in Figure 3. The flow rate is 15 ml/min and the critical heat flux (CHF) for this smooth evaporator is 350 W.

The temperature of the surface t_{surf} increases with increasing heat load \dot{Q} . The surface temperature starts to deviate at a heat load of 250 W. The deviations (ca. 1-3 K) increase with each step of increasing heat load, until the CHF is reached and the temperature of the surface increases very fast

and exceeds 100°C (stop criterion). This behavior can be observed in almost all of the measurements.

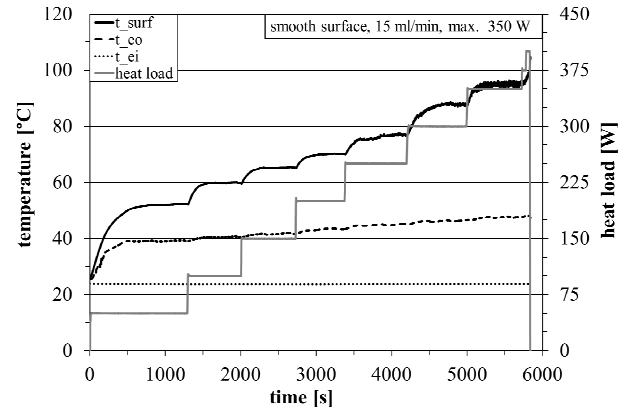


Figure 3: Trend of temperatures of smooth surface at $\dot{v} = 15$ ml/min

Measurements with a variation in volume flux from 10 to 35 ml/min have been done for the smooth surface. They are all accounted to calculate an average value as reference case (in the following called “smooth_avg”) for the other surfaces. The maximum deviation to the smooth_avg is 0.1 W/(cm²·K). The heat transfer coefficient of the smooth surface increases with increasing heat flux. The CHF at $\dot{v} = 35$ ml/min is 96 W/cm² with a maximum $h = 2.6$ W/(cm²·K). These values are higher than the ones measured in Winter et al. (2010). The needles of the evaporator now have a distance of 200 μm to the smooth surface. In Winter et al. (2010) the distance was nearly zero, which lead to blocking of some liquid supply tubes that have a deviation in length due to the manufacturing.

The micro-milled surface MFR consists of circular channels (geometry see Table 1). The trends of h versus \dot{q} for the MFR are shown in Figure 4.

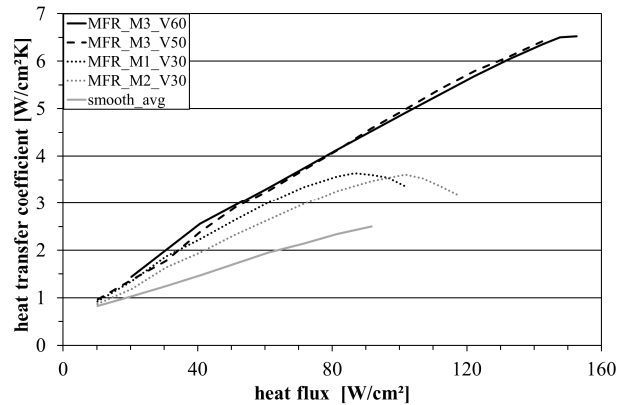


Figure 4: h versus \dot{q} for micro-milled surfaces

The h of the MFR is always above the smooth_avg and increases with a higher gradient. The CHF for MFR at $\dot{v} = 60$ ml/min is 152.6 W/cm² with a maximum $h = 6.5$ W/(cm²·K). For $\dot{q} = 90$ W/cm² and $\dot{v} = 30$ ml/min the MFR $h = 3.5$ W/(cm²·K) compared to the smooth_avg $h = 2.5$ W/(cm²·K) which is an increase of 40%. The offset between M1_V30 and M2_V30 can be explained with different content of non-condensable gases (NCG) in the system, due to a leakage and may also be influenced by deposits.

The trends of h versus \dot{q} for the sintered surfaces C3 and C4 (properties see Table 1) are shown in Figure 5.

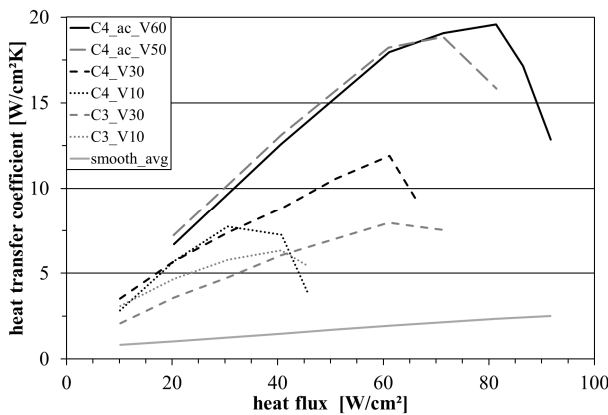


Figure 5: h versus \dot{q} for sintered surfaces

The trends of the h versus \dot{q} for the sintered surfaces show an increase of h with increasing \dot{q} . After reaching a maximum h , the value of h decreases until the CHF is achieved. This behavior is similar to observations by Winter et al. (2010) and by Kim et al. (2009) in experiments on porous surfaces. The heat transfer on the sintered surfaces goes through different boiling modes: Starting with low heat flux, the film on the surface is at its maximum thickness. The heat transfer takes place as single-phase convection and with increasing heat flux nucleate boiling occurs since the sintered surfaces contain many nucleation sites that can be activated. With further increasing heat flux, the film thickness decreases until the liquid film breaks up. Here the heat is mainly transferred by evaporation at the three-phase contact-lines that shape within the porous surface.

The h for the C3 is always below the one for C4 at the same \dot{q} . This is due to aging and fouling effects on the surface C3, that was used in tests before this study, while C4 was unused. Additional measurements have been done with the C4 surface after cleaning in an ultrasonic bath with acetone,

indicated as ‘C4_ac’ in Figure 5. The maximum values for the sintered surfaces are $h = 19.6$ W/(cm²·K) and $\dot{q} = 91.75$ W/cm². For $\dot{q} = 61$ W/cm² and $\dot{v} = 30$ ml/min the C4 reaches $h = 11.9$ W/(cm²·K) compared to the smooth_avg $h = 1.9$ W/(cm²·K) which is an increase of 526%.

The trends of h versus \dot{q} for stacked copper nets (CNstack; see Table 1) are plotted in Figure 6.

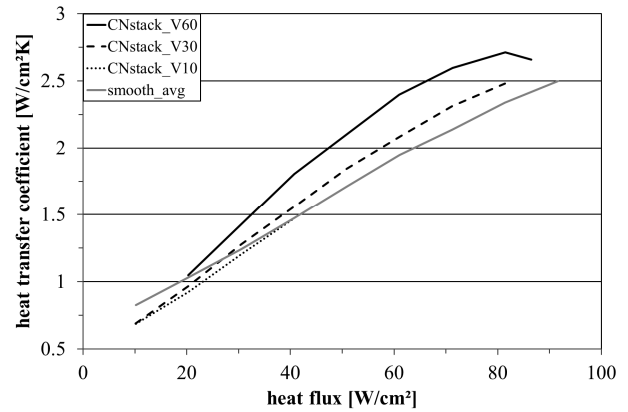


Figure 6: h versus \dot{q} for stacked copper nets

Since one copper net surface worked well in Winter et al. (2010), a structure with stacked copper nets of different values (wire diameter & span) has been tested. One fine net is placed at the bottom covered by two less fine ones. The h increases with increasing heat flux. The CHF for the CNstack at $\dot{v} = 30$ ml/min is 81.4 W/cm² with a maximum $h = 2.49$ W/(cm²·K). Above $\dot{v} = 30$ ml/min the CHF and h do not change significantly even with $\dot{v} = 60$ ml/min (CHF = 86.5 W/cm²; $h = 2.66$ W/(cm²·K)). This may be explained with the thickness (476 μ m) of the porous structure. It is supposed that the vapor cannot exit the porous structure fast enough so that the vapor layer inside the structure acts like an isolator and retards the fresh liquid to reach the hot surface.

For $\dot{v} = 30$ ml/min and $\dot{v} = 60$ ml/min the CHF and h are listed in Table 2.

Table 2: listing of CHF and maximum h at different volume fluxes

surface	flux [ml/min]	CHF [W/cm ²]	max. h [W/cm ² K]
smooth	30	96.7	2.6
MFR	30	122.2	5.1
MFR	60	152.6	6.5
C4	30	66.3	9.3
C4ac	60	91.8	19.6
CNstack	30	86.5	2.4
CNstack	60	86.5	2.7

For $\dot{v} = 30$ ml/min the h for the MFR is approx. two times and for the C4 more than 3.5 times the value, while the h for the CNstack is quite similar to the value of the smooth_avg.

The maximum boiling numbers N_{bm*} for $\dot{v} = 10$ ml/min and $\dot{v} = 30$ ml/min are listed in Table 3.

Table 3: listing of boiling numbers of the surfaces at different volume fluxes

surface	flux [ml/min]	max. N_{bm*}
smooth	10	0.224
smooth	30	0.161
MFR	10	0.222
MFR	30	0.182
C4	10	0.267
C4	30	0.092
CNstack	10	0.234
CNstack	30	0.139

The N_{bm*} for $\dot{v} = 10$ ml/min is between 0.222 and 0.267 for all surfaces while for $\dot{v} = 30$ ml/min the N_{bm*} is smaller for each surface. The porous structures reach lower N_{bm*} than smooth and MFR.

3.4 Three evaporator system test results

Measurements with three evaporators working in parallel are shown in Figure 7, Figure 8 and Figure 9. Each evaporator is equipped with the similar CNstack surface and is heated by a heater that is equipped with seven independently switchable heating cartridges to vary the heat load of the evaporators.

Table 4: listing of number of switched on heating cartridges for the different steps

step	number of cartridges switched on in evaporator		
	evap_1	evap_2	evap_3
1	4	4	4
2	5	5	2
3	6	5	1
4	5	6	1
5	5	1	6
6	2	5	5
7	4	4	4

The numbers of cartridges switched on are listed in Table 4 for the different steps. Each cartridge has a heat load of 33.3 W for the measurement plotted in Figure 7 and 62.5 W for the measurement plotted in Figure 8.

A measurement with $\dot{v} = 10$ ml/min for each evaporator is shown in Figure 7.

The maximum heat load for one evaporator is limited to 200 W, while the overall system heat load is kept constant at 400 W.

The measurement starts and ends at an equal heat load of 133.3 W for each evaporator.

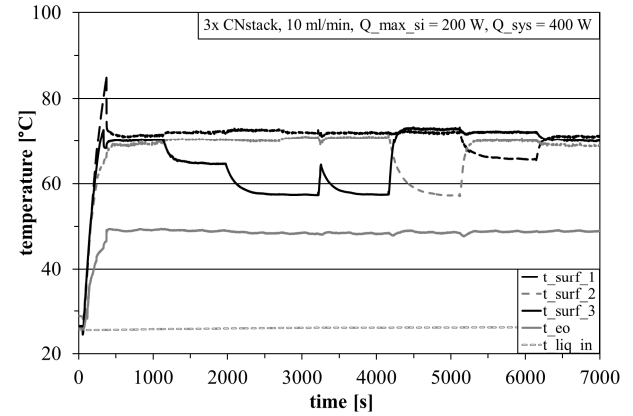


Figure 7: 3 evaporators with constant system heat load of 400 W at $\dot{v} = 10$ ml/min per evaporator

The system heat load affects the system pressure and therefore the saturation temperature (t_{Sat}), that is constant. All evaporator outlet temperatures are similar (± 0.8 K), one representative is plotted as $t_{co}=t_{Sat}$. The temperatures of the heat transfer surfaces t_{surf} are affected by the heat load of the individual evaporator. The pressure drop of a single evaporator increases up to 15 mbar during the measurement.

A measurement with $\dot{v} = 20$ ml/min for each evaporator is shown in Figure 8.

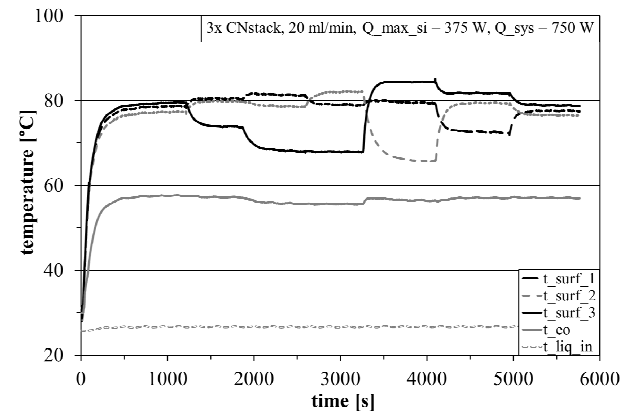


Figure 8: 3 evaporators with constant system heat load of 750 W at $\dot{v} = 20$ ml/min per evaporator

The maximum heat load for one evaporator is limited to 375 W, while the overall system heat load is kept constant at 750 W. The measurement starts and ends at an equal heat load of 250 W for each evaporator and is varied random in between. The pressure drop of a single evaporator increases up to 12 mbar during the measurement. A measurement with variable system heat load at $\dot{v} = 20$ ml/min for each evaporator is shown in Figure 9.

The maximum heat load for one evaporator is 345 W, while the overall system heat load is kept maximum 1025 W.

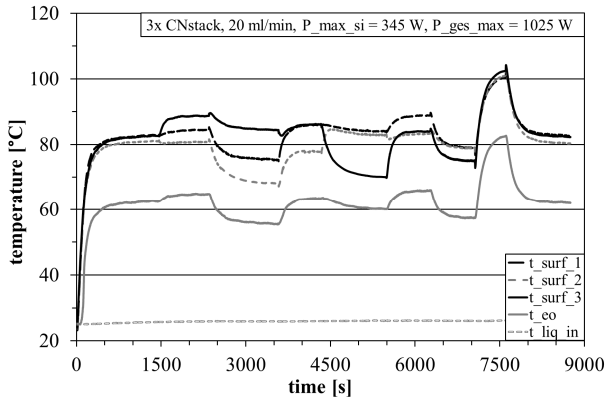


Figure 9: 3 evaporators with variable system heat load at $\dot{v} = 20$ ml/min per evaporator

The measurement starts and ends at an equal heat load of 200 W for each evaporator and is varied random in between. The system works stable without any anomalies. The pressure drop of a single evaporator increases up to 14 mbar during the measurement.

4. CONCLUSIONS

(1) For this special evaporator design it is important to consider that the distance of the needles to the surface/structure plays an important role on the performance of the evaporator. For the smooth surface it is required, that the distance is $>0\mu\text{m}$ (here $200\mu\text{m}$), otherwise blocking of the liquid flow would occur.

(2) Compared to Winter et al. (2010) the heat transfer coefficients of the sintered surface with bigger grain size (here: $60\mu\text{m}$, before: $36\mu\text{m}$) could be increased up to $20\text{ W}/(\text{cm}^2\cdot\text{K})$. Also fouling of the surface slows down due to a higher porosity.

(3) The CHF of the porous surfaces C4 and CNstack is limited. It is supposed that the vapor cannot exit the porous structures fast enough so that a vapor layer forms inside the structure that acts like an isolator and retards the fresh liquid to reach the hot surface.

(4) Regarding heat transfer it is very important to enable a good junction from the surface to the structure and conduction of the heat inside the structure to the three-phase contact-line (less good for porous surfaces, better for MFR).

(5) The MFR reaches a CHF of $152.6\text{ W}/\text{cm}^2$ and $h = 6.5\text{ W}/(\text{cm}^2\cdot\text{K})$ which is the best overall heat transfer performance of all tested structures inside this evaporator type up to now.

(6) System tests with three evaporators show stable system behavior. The saturation pressure inside the evaporators depends on the total system heat load.

NOMENCLATURE

symbol	unit	meaning
A	cm^2	area of heat transfer surface
$c_{p,\text{liq}}$	$\text{J}/\text{g}\cdot\text{K}$	liquid heat capacity
Δh_v	J/g	enthalpy of evaporation
h	$\text{W}/(\text{cm}^2\cdot\text{K})$	heat transfer coefficient
\dot{m}	g/min	mass flux
$M'1'$	#	test series number '1'
\dot{q}	W/cm^2	heat flux
\dot{Q}	W	heat load
t	$^\circ\text{C}$	temperature
\dot{v}	ml/min	volume flux
$V'10'$	ml/min	volume flux $\dot{v} = '10'$

ACKNOWLEDGEMENT

The authors would like to thank Mr. Hannes Wiegand and Gunter Wittlich for doing measurements. For the financial support the authors would like to thank ESA/ESTEC who supported the buildup of the setup in cooperation with OHB System AG within the "Innovation Triangle Initiative". Part of this study was funded by the German Excellence Cluster 'Smart Interfaces' (EXCL 29), Deutsche Forschungsgemeinschaft.

REFERENCES

- Schweizer, N., Stephan, P., Schlitt, R., 'A concept for a miniature, mechanically pumped two-phase cooling loop', Proceedings of the 38th Int. Conf. On Environmental Systems, San Francisco, USA, 2008
- Winter, M., Schweizer, N., Stephan, P., Schlitt, R., 'Mechanically pumped two-phase loop for space application', Contribution to the 15th International Heat Pipe Conference, Clemson, USA, 2010
- Kandlikar, S.G., 'Fundamental issues related to flow boiling mini channels and microchannels', *Exp. Thermal Fluid Science*, 26, pp. 389-407, 2002
- Thome, J.R., Dupont, V., Jacobi, A.M., 'Heat transfer model for evaporation in microchannels. Part I presentation of the model', *Int. J. Heat and Mass Transfer*, 47, pp. 3375-3385, 2004
- Kim, Y., Choi, C., Lee, K., Han, D., 'experimental study of spray cooling performance on micro-porous coated surfaces', *Heat Mass Transfer*, 2009

A HIGH THERMAL DISSIPATION PERFORMANCE POLYETHYLENE TEREPHTHALATE HEAT PIPE

Guan-Wei Wu, Wen-Pin Shih

Department of Mechanical Engineering, National Taiwan University, Taipei
No. 1, Sec. 4, Roosevelt Road, Taipei, 10617 Taiwan(R.O.C)

Tel: +886-2-33664511, Fax: +886-2-23631755, E-mail: d96522025@ntu.edu.tw, wpsih@ntu.edu.tw

Sih-Li Chen

Department of Mechanical Engineering, National Taiwan University, Taipei
No. 1, Sec. 4, Roosevelt Road, Taipei, 10617 Taiwan(R.O.C)

Tel: +886-2-23631808, Fax: +886-2-23631755, E-mail: slchen01@ntu.edu.tw

ABSTRACT

In this research, polyethylene terephthalate (PET) is applied as the container material for heat pipe which is different from conventional copper heat pipe. PET is a thermoplastic polymer resin which can be easily bonded together with another PET laminating film by hot lamination. The copper mesh and methanol are sealed inside the middle of two PET films as the wick structure and working fluid, respectively. The experiment results reveal that the minimum thermal resistance in this PET heat pipe is 0.146 ($^{\circ}\text{C}/\text{W}$) at 36.9% filling ratio and 26W input power. However, when input power is larger than 30W, the laminated PET will debond because of higher methanol vapor pressure. The endurable critical pressure of PET heat pipe is 14.06 kPa. Although the thermal conductivity of PET ($0.15\text{-}0.24 \text{ W}\cdot\text{m}^{-1}\text{K}^{-1}$) is much smaller than copper ($401 \text{ W}\cdot\text{m}^{-1}\text{K}^{-1}$), the PET heat pipe still has greatly low thermal resistance. Besides, compare with the copper pipe, PET is an inexpensive, lighter and simple sealing material. The high thermal dissipation performance PET heat pipe can be applied in electronic devices cooling with power consumption smaller than 30W in the future.

KEY WORDS : PET, thermoplastic polymer resin, hot lamination, critical pressure

1. INTRODUCTION

In recent years, the heat pipe is always used for high power heat dissipation because of its high efficiency cooling performance than heat sink. As the processing speed of central processing unit (CPU) progress from MHz to GHz, the single phase air cooling system is not suitable for high power heating source application no more. Heat pipe is a two-phase heat transfer exchanger with very high thermal dissipation efficiency.

When the working fluid absorbs heat from the heat source, it evaporates at the boiling point and the vapor delivers to the cooling end. Then the vapor releases latent heat (enthalpy) and condenses to liquid. The wick structure provides capillary force for facilitating the liquid return to the heat source again. This closed two-phase thermal cycle enables transmitting large amounts of heat energy with only minimal temperature gradient. Though heat pipe is a very efficient cooling system, it will be dominated some heat transfer limitations such as viscous limit, sonic limit, entrainment limit, capillary limit, condenser limit, boiling limit etc.

[1]. In regular operating conditions of heat pipe, the viscous limit, sonic limit and entrainment limit are not regarded. The capillary limit is usually encountered in flat or micro heat pipe. When the sum of vapor and condensing liquid pressure drop exceeds the capillary pressure, the capillary limit will be occurred. If this situation continues, there is no sufficient liquid deliver to evaporator. As a result, the heat pipe will dry out and the cooling efficiency will decay seriously [2].

Conventionally, the container materials of heat pipe are made of metal such as aluminum, stainless steel and copper (Cu) [3,4]. Many researches focus on micro heat pipe fabrication using Cu or silicon and patterned hundred-micrometer microchannels on its surface for wick structures [5,6]. In this experiment, we purpose to develop a relative simple approach to fabricate heat pipe by hot lamination. The polyethylene-terephthalate (PET) plastic films are used to replace the metal as the container material of heat pipe. In this paper, a number of operating parameters such as filling ratio, input power and critical pressure will also be discussed.

2. FABRICATION PROCESS

2.1 Heat pipe container and wick structure fabrication

The fabrication process of PET heat pipe is illustrated in Figure 1. First a thin film of PET is used and two windows are cut out and attached to a copper tape (Figure 1a-b). The function of these two hollow region can let the Cu tape contact the heat source and heat sink directly. Then the Cu mesh, rubber and another Cu mesh are stacked layer-by-layer (Figure 1c-e). The another PET laminating film is covered on the upper Cu mesh. At last, a hot laminator is used for bonding the top and bottom PET layers (Figure 1f). The width, length and thickness of PET heat pipe are 20 mm, 120 mm and 1.7 mm, respectively.

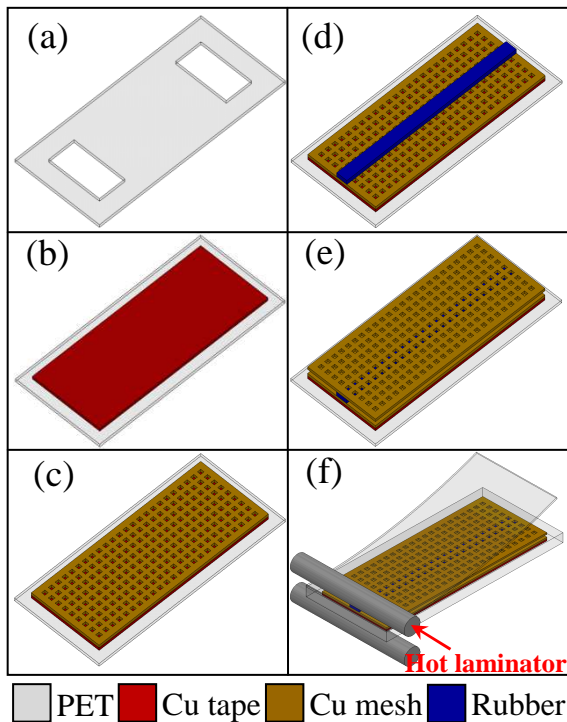


Figure 1. PET heat pipe fabrication process

2.2 Filling working fluid and vacuum packaging

The finally fabrication process of heat pipe includes filling working fluid and vacuum packaging. In PET heat pipe, it is difficult to insert a filling tube for pumping the non-condensed gas (air) out which inside the container. For this reason, vapor pumping method is adopted in this experiment. The heat pipe is firstly filled with methanol and then immerses in a hot water bath. Because the boiling point of water is higher than

methanol which will evaporate first and the air will be pumped out together with the methanol vapor (Figure 2). The filling ratio is determined by evaporation time. After the specific filling ratio is obtained, an adhesive tape is pasted on the filling hole for sealing package.

3. EXPERIMENTAL SETUP AND PROCEDURES

A thermal infrared (IR) camera is used to detect thermal radiation of heat pipe which connect to the personal computer. From IR thermal images, the temperature distribution will be obtained in real time. The temperature measurement range and maximum resolution of IR camera are $-40\sim 500\text{ }^{\circ}\text{C}$ and $18.5\cdot 18.5\text{ }\mu\text{m}^2$ at single pixel size (mount microscope lens), respectively. A power supply provides the power to the polyimide film heater as the heat source for transferring heat to the working fluid which inside the PET heat pipe. The condensation section is cooled by natural convection with $25\text{ }^{\circ}\text{C}$ ambient temperature (Figure 3).

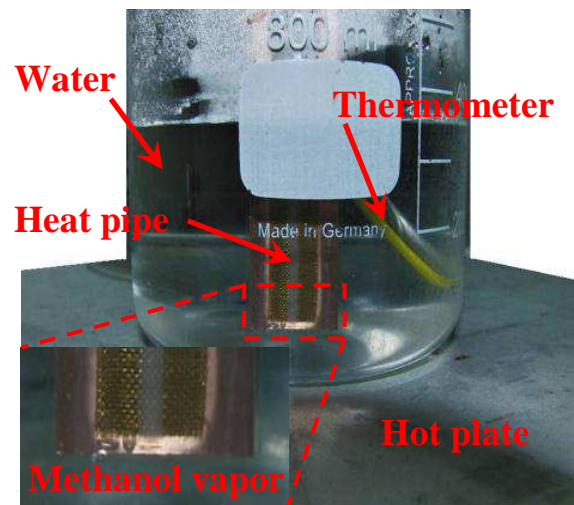


Figure 2. Vapor pumping method for pumping non-condensed gas out

4. EXPERIMENT RESULTS AND DISCUSSION

4.1 Influence of filling ratio on the thermal resistance

The IR thermal image of PET heat pipe with 26W input power and 36.9% filling ratio is shown in Figure 4. The red and black numbers are the highest and lowest temperature of single pixel in the black rectangular area, respectively. The

average temperature of evaporator and condenser are sum of each pixel temperature value divide by sum of pixel numbers at black areas. The thermal resistance (R_{th}) is calculated by

$$R_{th} = \frac{T_e - T_c}{Q_{in}} \quad (1)$$

where T_e and T_c are the average temperature of evaporator and condenser, respectively, Q_{in} is the input power.

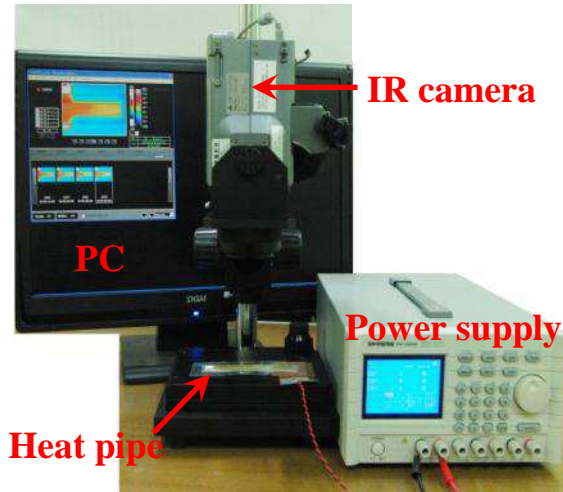


Figure 3. Experimental setup

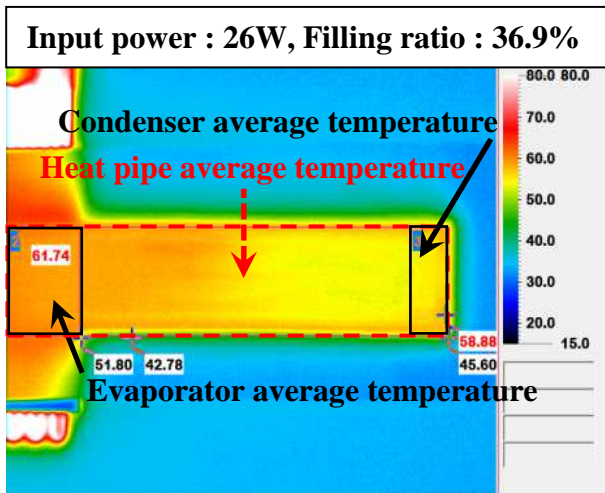


Figure 4. IR image for calculation the average temperature of evaporator and condenser

The IR thermal images of PET heat pipe with 36.9% filling ratio at different input power are illustrated in Figure 5. If input power larger than 10W, the heat will deliver initially from evaporator to condenser. The average temperature in the evaporator and condenser are 58.94 °C and 54.86 °C at 26W input power. Therefore, the minimum thermal resistance of PET heat pipe is 0.146 (°C/W)

which is suitable for practical applications. The effects of different input power and filling ratio operating conditions on thermal resistance are investigated in this experiment (Figure 6).

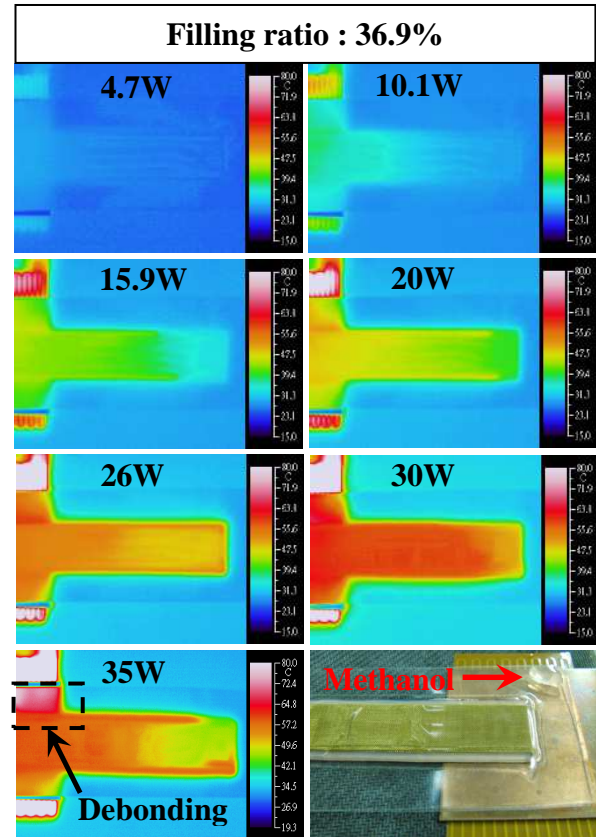


Figure 5. IR thermal images of PET heat pipe at different input power

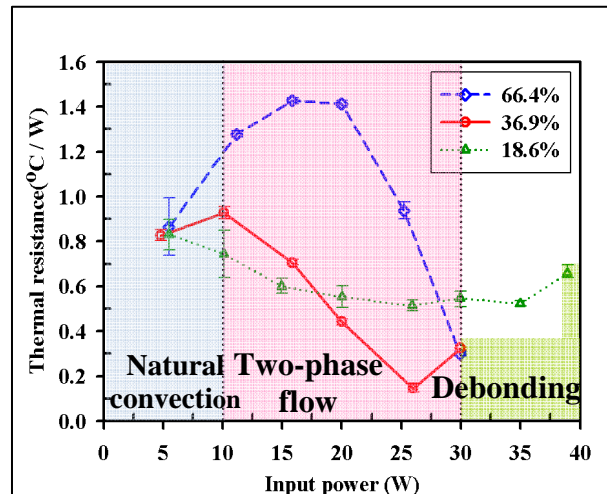


Figure 6. Thermal resistance variation with different input power

Three experimental phenomenons can be observed in the PET heat pipe from IR thermal images. As input power is below than 10W, the methanol is simply natural convection in liquid phase. If input power rises to 10-30W, the two-phase flow heat transfer cycles are generated inside the heat pipe. The heat is rapidly transferred from evaporator to condenser and the thermal resistance will reduce with increasing input power. However, when input power is larger than 30W, the laminated PET will debond because of high methanol vapor pressure and methanol will leak out from debonding position (see Figure 5. 35W).

4.2 Non-condensed gas inside the PET heat pipe

Vapor pressure is the pressure of a vapor in thermodynamic equilibrium with its condensed phase in a closed container. Liquid will evaporate when the vapor pressure below its saturated vapor pressure. As the liquid methanol absorbs heat which evaporates to the vapor and the vapor pressure will greatly increase in temperature rise. The Antoine equation indicates the correlation between vapor pressure and temperature for pure liquid [7]. The equation is described as below:

$$P_v = e^{\left(\frac{a-b}{T_v-c}\right)} \quad (2)$$

where a , b and c are experimental constants, T_v is the temperature, and P_v is the vapor pressure. If vapor pressure higher than the endurable critical pressure of PET laminating film, the heat pipe will debond immediately. In this fabricated PET heat pipe, the laminating film debonds with input power larger than 30W at 36.9% and 66.4% filling ratio (Figure 7).

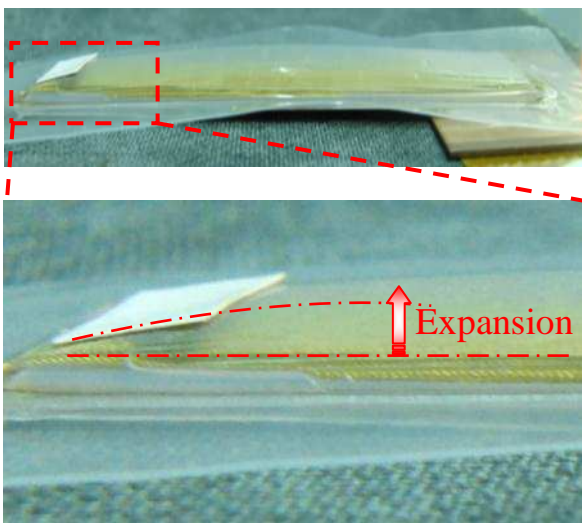


Figure 7. Debonding in PET heat pipe

To determine the vapor pressure of methanol, we grab the heat pipe average temperature from IR image (See Figure 4). The temperature of methanol rise with increasing input power. From Antoine equation, the methanol vapor pressure will be obtained at specific temperature (Figure 8). Since the package process of heat pipe is performed under vacuum condition, there are methanol vapor pressure (P_v) and one atmosphere pressure (1 atm, P_a) loading on it. If heat pipe crack, the vapor pressure must be larger larger than 1 atm pressure. However, the vapor pressure of 36.9% and 66.4% filling ratio is lower than 1 atm pressure at 35W input power when heat pipe debonding (Figure 9).

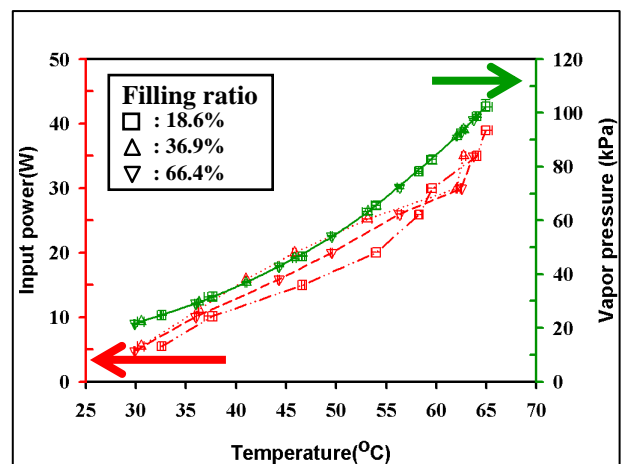


Figure 8. The correlation between input power-temperature and temperature-vapor pressure

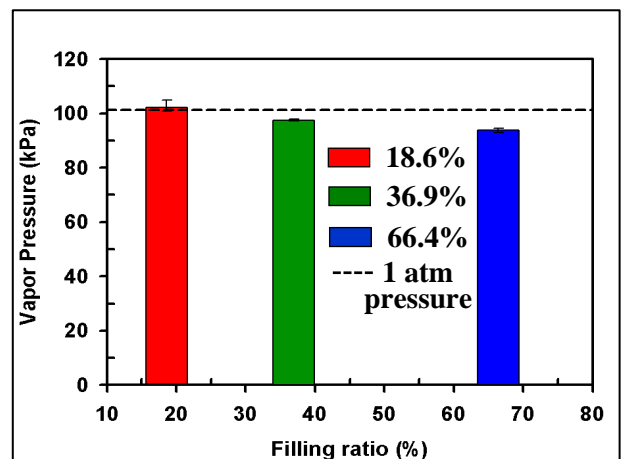


Figure 9. The vapor pressure of different filling ratio at heat pipe debonding state

In this experiment, only the vapor pressure of 18.6% filling ratio is larger than 1 atm pressure actually at 39W input power. It means a few residual non-condensed gas (air) still inside PET

heat pipe even if vapor pumping method has been used. This is why the vapor pressure lower than 1 atm pressure the PET laminating film will debond. Therefore, the pressure which loading on heat pipe has to consider the effect of gas pressure (P_g) (Figure 10).

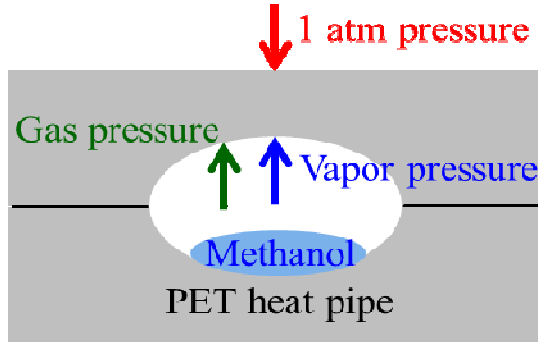


Figure 10. The pressure loading on heat pipe with non-condensed gas inside

4.3 The correlation between PET bonding energy and critical pressure

As a matter of fact, the structure of laminating film mainly consists of two components, PET and Ethylene Vinyl Acetate (EVA). The EVA is one kind of thermosoftening plastic polymer which is usually coated on PET substrate as the commercial laminating film product. After hot rolling process by thermal laminator, the EVA is changed phase from non-stick dry film to hot-melt adhesive. As a result, the PET/EVA/PET will bond together with high bonding energy. Generally speaking, the hot rolling temperature is around 110 °C. In previous research, the strain energy release rate of the interface debonding was obtained by assuming that the debonded portion can be modeled as elastic beams [8-10]. It is found that the bonding interface fails when the internal applied pressure reaches a critical value. This assumption allows the bonding energy is determined by evaluating the strain energy release rate at the critical pressure. The heat pipe bonding interfac (PET/EVA/PET) and dimensions are shown in Figure 11. If channel height (h) is much smaller than the channel width (w) ($h \ll w$), this mechnism model can be defined as a crack in finite solid for pressurized channel. The h and w of heat pipe are 1.7 and 20 mm and the thickness (t) of PET is 75 μm . The effective modulus (E^*) is defined by [11]

$$\frac{1}{E^*} \equiv \frac{(1-\nu_1^2)}{E_1} + \frac{(1-\nu_2^2)}{E_2} \quad (3)$$

where E_1 , ν_1 and E_2 , ν_2 are Young's modulus and Poisson's ratio of the upper channel wall and the substrate respectively. Because the upper channel wall and substrate of heat pipe are all PET, the E^* can be simplified as follow

$$E^* = \frac{E}{2(1-\nu^2)} \quad (4)$$

where E and ν are Young's modulus and Poisson's ratio of PET.

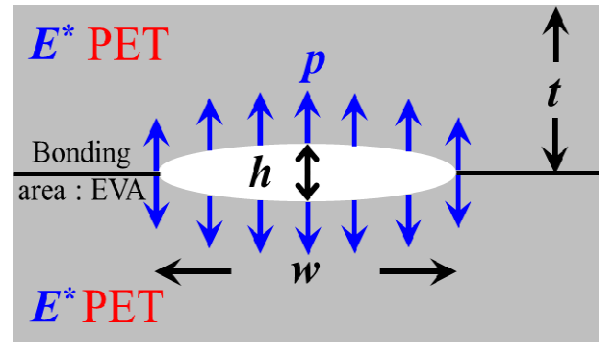


Figure 11. PET heat pipe bonding interface and dimensions

Initiation of interface debonding occurs when the sum of internal (P_v and P_g) and external (P_a) pressure larger than the critical pressure which is determined by bonding energy ($\Delta\gamma_b$). The correlation between bonding energy and critical pressure are expressed as [11-13]

$$\Delta\gamma_b = \frac{\pi P_{crit}^2 w}{2E^*} \left(\frac{2}{\sqrt{3\pi}(2t/w)^{3/2}} + 1 \right)^2 \quad (5)$$

where p_{crit} and π are the critical pressure and the ratio of a circle's circumference to its diameter. For wide channel, $w/t \gg 1$, and according to (4), the (5) can reduce to

$$\Delta\gamma_b = \frac{w^4 P_{crit}^2 (1-\nu^2)}{6t^3 E} \quad (6)$$

In our mechnism model, the critical pressure is equal to $P_c = P_v + P_g - P_a$ (see Figure. 12). Equation (6) can be expressed as

$$\Delta\gamma_b = \frac{w^4 [P_v + P_g - P_a]^2 (1-\nu^2)}{6t^3 E} \quad (7)$$

How to measure or calculate the gas pressure directly is quite difficult in this research. We have to determine the bonding energy of laminating film at first. In 3M™ EPE films (Product type: 212-C) technical data [14], they point out that the bonding energy of interlayer adhesion (EVA/PET) is 3500 (J/m^2). Substituting the bonding energy listed above into equation (5), the critical pressure of EVA/PET is 14062.5 (Pa). Each pressure value

when PET heat pipe debonding are calculated as shown in Table 1.

Table 1. Each pressure value when PET heat pipe debonding

Filling ratio		18.6%	36.9%	66.4%
P_{crit}	Unit:(Pa)	14062.5		
P_a		101325		
P_v		102221	97456	93693
P_g		13167	17931	21695

5. CONCLUSIONS

A high thermal dissipation PET heat pipe has been fabricated successfully in this research. Different from previous research works focusing on heat pipe with metal, Si or polymer container, we use PET as the container material for heat pipe fabrication. The hot laminator is applied to bond two pieces of PET together for heat pipe package. This laminating method can both reduce the fabrication time and cost. Although the thermal conductivity of PET is much smaller than others metal container of heat pipe, the PET heat pipe still have low thermal resistance (0.146 ($^{\circ}\text{C}/\text{W}$)) at 36.9% filling ratio and 26W input power.

A crack in infinite solid mechanism model is applied to explain the PET debonding when input power large than 30W. After hot lamination, PET laminating film has a bonding energy. The structure dimensions and bonding energy will determine the critical pressure magnitude. In this PET heat pipe, the pressure factors include vapor, gas and atmosphere pressure. As the input power increase, PET laminating film will debond when sum of internal and external pressure reach its critical pressure. Therefore, this PET heat pipe is suitable for cooling electronic devices with power consumption smaller than 30W.

REFERENCES

[1] Reay, D., Kew, P. (2006) *Heat pipes theory, design and applications*. Butterworth-Heinemann, Boston

[2] Lim, H. T., Kim, S. H., Im, H. D., Oh, K. H., Jeong, S. H. (2008) *Fabrication and evaluation of a copper flat micro heat pipe working under adverse-gravity orientation*. J. Micromechanics and Microengineering, 18, p. 105013

[3] Take, K., Webb, R. L. (2001) *Thermal performance of integrated plate heat pipe with a heat spreader*. J. Electronic Packaging, 123, p. 189-195

[4] Lips, S., Lefèvre, F., Bonjour, J., (2010) *Combined effects of the filling ratio and the vapour space thickness on the performance of a flat plate heat pipe*. Int. J. Heat and Mass Transfer, 53, p. 694-702

[5] Hwang, G. S., Nam, Y., Fleming, E., Dussinger, P., Ju, Y. S., Kaviany, M. (2010) *Multi-artery heat pipe spreader: Experiment*. Int. J. Heat and Mass Transfer, 53, p. 2662-2669

[6] Launay, S., Sartre, V., Lallemand, M. (2004) *Experimental study on silicon micro-heat pipe arrays*. Applied Thermal Engineering, 24, p. 233-243

[7] Theodore, L., Ricci, F., Vanvliet, T. (2009) *Thermodynamics for the practicing engineer*. John Wiley and Sons

[8] Maszara, W. P., Goetz, G., Caviglia, A., McKitterick, J. B. (1988) *Bonding of silicon wafers for silicon-on-insulator*. J. Applied Physics, 64, p. 4943-4950

[9] Blom, M. T., Tas, N. R., Panraud, G., Chmela, E., Gardeniers, J. G. E., Tijssen, R., Elwenspoek, M., Berg, A. Ven den (2001) *Failure mechanisms of pressurized microchannels, model, and experiments*. J. Microelectromechanical Systems, 10, p. 158-164

[10] Murakami, Y., Hanson, M. T., Itoh, Y., Kishimoto, K., Miyata, H., Miyazaki, N., Terada, H., Tohgo, K., Yuuki, R. (1992) *Stress intensity factors handbook*. Pergamon press, Oxford

[11] Wu, G. W., Shih, W. P., Hui, C. Y., Chen, S. L., Lee C. Y. (2010) *Bonding strength of pressurized microchannels fabricated by polydimethylsiloxane and silicon*. J. Micromechanics and Microengineering, 20, p. 115032

[12] Hills, D. A., Kelly, P. A., Dai, D. N., Korsunsky, A. M. (1996) *Solution of crack problems: the distributed dislocation technique*. Kluwer Academic Publishers, London

[13] Tong, Q. Y., Cha, G., Gafiteanu, R., Gosele, U. (1994) *Low Temperature Wafer Direct Bonding*. J. Microelectromechanical Systems, 3, p. 29-35

[14] www.3M.com/solar

Simulation of Heat Transfer in Liquid Plugs Moving Inside Dry Capillary Tubes

Ashish Kumar Bajpai and Sameer Khandekar*

Department of Mechanical Engineering
Indian Institute of Technology Kanpur, Kanpur 208016, India
*E-mail: samkhan@iitk.ac.in

ABSTRACT

The present work numerically simulates the flow of a single isolated liquid plug of glycerin and water, respectively flowing in a round dry capillary tube (ID = 2.0 mm), to understand its local thermal transport behavior. When an isolated liquid plug moves in a capillary tube, there is a difference in the advancing and receding dynamic contact angles of the two menisci, respectively. This has been considered in the simulations. The linearized simplification of Hoffman-Tanner's law is used to model the variation in the two respective apparent contact angles, with the velocity of the liquid plug (i.e., $Ca = \mu U/\sigma$). Simulations are carried out for a range of Capillary number and length of liquid plugs. It has been found that variation in dynamic contact angle leads to enhanced local and average heat transfer coefficient in the moving liquid plug; the local fluid circulation gets affected by meniscus deformations. In addition, as the length of the liquid plug is increased, average heat transfer coefficient decreases and finally shows the asymptotic transport behavior of Poiseuille flow. Other than Capillary number, the fluid Prandtl number strongly affects the local thermo-hydrodynamics.

KEY WORDS: Taylor bubble flow, contact angle hysteresis, plug flow, capillary tube, transport coefficients

1. INTRODUCTION

Micro-scale two-phase flow is an active research area because of its application in many engineering devices like microreactors, catalyst coating in capillaries, electronics cooling, refrigeration industry, flow in blood vessels, porous media etc. [Gunther et al. (2004), Kolb et al. (1991), Zheng et al. (2007)]. Taylor flow or slug flow, characterized by long bubble slugs separated by liquid plugs, constitutes the typical regime under such conditions. Many groups have worked on Taylor flow regime [e.g., Triplett et al. (1999), Zhao et al. (2001)] and tried to understand the thermo-hydrodynamic properties of such flows. A recent review of local hydrodynamics in such flows, especially in the context of pulsating heat pipes, can be found in Khandekar et al. (2010). Internal circulations in liquid plug have been found to be the major cause of enhanced heat (and/or mass) transfer in such flows. However, not many studies have reported the impact of the dynamic local meniscus level deformations due to the imposed plug velocity on local plug transport behavior.

When a liquid plug flows in a small diameter tube ($Bo < 2$), the capillary forces play a major role and gravity become relatively insignificant. In such a case, the interfacial tension between solid-liquid (σ_{SL}) and solid-gas (σ_{SG}) should also be taken into account during analysis; surface wettability of the tube wall becomes a critical factor in determining

local transport behavior. A single moving liquid plug inside a capillary tube is enclosed by two menisci. During its motion, the dynamic contact angle formed between the flowing liquid meniscus and the solid surface is achieved by a balance between the capillary and the viscous forces. Thus, the moving menisci of the liquid plug are characterized by advancing and receding contact angles, which are different from the static contact angle because of the interplay between surface tension and viscous forces. The relative scaling of these two forces is represented by the Capillary number ($Ca = \mu U/\sigma$). Rose and Heins (1962) were amongst the first to highlight the relation between the advancing contact angle and average velocity U of three-phase contact line. Later on, various researchers like Hoffman (1974), Tanner (1991) and Blake (2006) studied the wetting behavior and dependency of advancing contact angle on Ca and the static contact angle. Researchers like Barajas et al. (1992), Lee et al. (2008), Walsh et al. (2011) have tried to analyze the surface wettability and heat transfer but none of them incorporated the real dynamic interface. Tripathi et al. (2010) and Shekhawat et al. (2009) previously tried to experimentally understand such phenomenon in oscillating contact line motion in a square capillary tube and presented hydrodynamics of oscillating meniscus. This work is an attempt to analyze the heat transfer in isolated Taylor bubble flow by including the effect of contact angle hysteresis.

Glycerine and water have been chosen to get a range of Prandtl number, so also the static wettability characteristics. Further, Taylor flow conditions can occur either as (i) wet plug flow regime where a liquid thin film exists at the wall around the bubble (pre-wetted capillary) and (ii) dry plug flow regime where no such film exists. We focus only on the latter case while the former is intended for future scrutiny.

2. PROBLEM FORMULATION

2.1 Physical description

A liquid plug of length L is moving inside a previously dry capillary tube of inner diameter D with a constant velocity U . It is subjected to either a constant temperature or a constant heat flux boundary condition at the tube wall. Because of low Bond number ($Bo < 2$), gravity effect is negligible and surface tension plays an important role in determining the thermo-hydrodynamic behavior of the plug. Figure 1 explains the physical problem under consideration, where θ_s is the static contact angle and θ_a and θ_r are the advancing and receding contact angles of the interface, respectively, when liquid plug moves with velocity U .

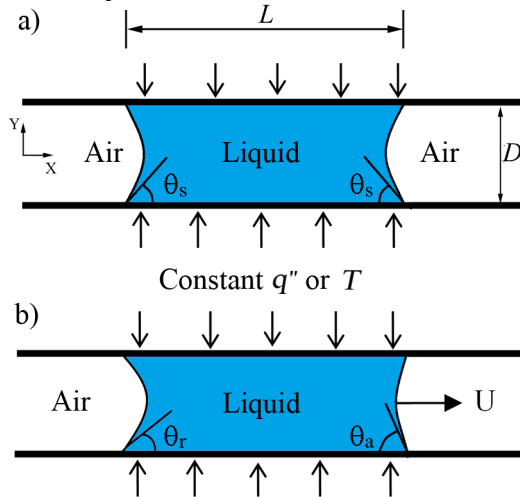


Figure 1. Problem description (a) static plug where θ_s is static contact angle (b) moving plug, where θ_a is the advancing and θ_r is the receding contact angle

2.2 Modeling of dynamic contact angles

Modified Hoffman-Tanner's law is used to determine the dynamic contact angles. According to this law, dynamic contact angle is given as [Berthier (2008)]:

$$\theta_d^3 - \theta_s^3 = ACa \quad (1)$$

where, θ_d and θ_s are dynamic and static contact angles respectively, Ca is Capillary number and A is a constant whose value is approximately equal to 94 when angles are taken in radians. Berthier (2008) further simplified this model and linearized Eq. (1) by series expansion, under the assumption of small Capillary number ($\sim Ca < 0.1$). Hence, the dynamic advancing and receding contact angles (θ_a and θ_r respectively) are given as:

$$\theta_a = \theta_s + \frac{A|Ca|}{3\theta_s^2} \quad (2a)$$

$$\theta_r = \theta_s - \frac{A|Ca|}{3\theta_s^2} \quad (2b)$$

2.3 Governing equations

The governing transport equations i.e. continuity, momentum and energy equations for a Newtonian incompressible fluid with constant properties respectively, can be written as:

$$\nabla \cdot \vec{V} = 0 \quad (3)$$

$$\rho \frac{D\vec{V}}{Dt} = -\nabla p + \mu \nabla^2 \vec{V} \quad (4)$$

$$\rho C_p \frac{DT}{Dt} = k \nabla^2 T \quad (5)$$

Nusselt number, Nu , is defined as

$$Nu = \frac{hD}{k} \quad (6)$$

where, D is the diameter of the tube. The heat transfer coefficient h is given by:

$$h = \frac{q''}{(T_w - T_{avg})} \quad (7)$$

where, q'' is the heat flux at the wall, T_w is the wall temperature and T_{avg} is the local mean temperature of the fluid in the plane perpendicular to the wall. In case of constant heat flux, q'' is known to us, T_{avg} and T_w is obtained from the solution data at the wall. In case of constant temperature boundary condition, T_w is known, and T_{avg} and the ensuing heat flux are obtained from the solution. Average Nusselt number along the length of the plug is then given by (see Figure 2 for axes index):

$$Nu_{avg} = \frac{1}{L} \int_0^L Nu_x dx \quad (8)$$

2.4 Numerical method

Lagrangian approach of moving frame is used to analyze the heat transfer and simulate the flow with moving walls, while keeping the plug stationary. The circular wall is given a velocity in the negative X direction while the plug is kept at rest, as shown in Figure 2. Symmetric boundary condition is used at plane $Z=0$ while no slip boundary condition is used at the wall. The interface is simulated with zero heat flux and zero shear stress i.e. free surface boundary condition. Both, constant heat flux ($q'' = 10,000 \text{ W/m}^2$) and constant temperature boundary conditions ($T_w = 350 \text{ K}$) at the wall, have been solved, respectively. Initial temperature of the fluid is taken to be 300 K ; fluid properties are kept constant. Table 1 gives the range of parameters used for the study. Geometry and mesh is created using Gambit[®]-2.3 with unstructured tetrahedral elements. The model is solved using unsteady pressure based solver in Ansys-Fluent[®]-v12.0 for water and glycerin. PISO algorithm is used for pressure-velocity coupling while the PRESTO interpolation is used for computing the face pressure. Momentum and energy equations are discretized using a second-order upwind scheme while temporal discretization is done using second-order implicit scheme for better accuracy. Green-Gauss node-based averaging scheme is used to evaluate gradients and derivatives as recommended [Ansys-Fluent[®] manual].

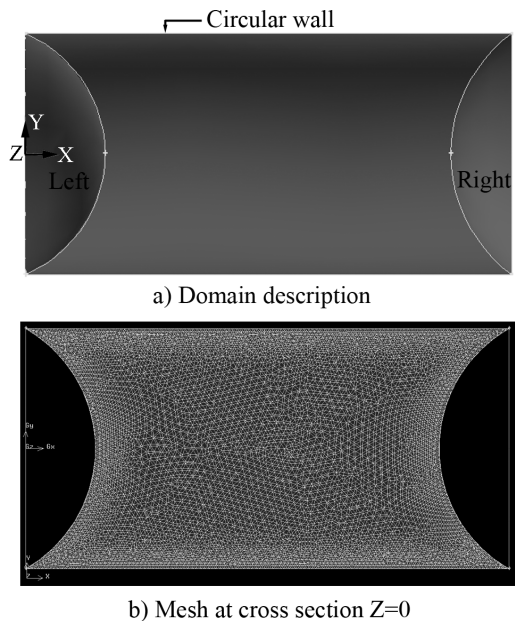


Figure 2. (a) Domain description and, (b) mesh at symmetric plane for a glycerin plug of $L/D = 2$ at $Ca = 10^{-3}$, finer mesh near interfaces and coarser in center

Table 1: Range of parameters

Fluid	Ca	Pr	Re_D	Bo
Water	10^{-5}	3.56	1.42-142	0.737
Glycerine	to 10^{-3}	6780	2.5×10^{-6} - 2.5×10^{-4}	0.883

3. PROCEDURE

3.1 Experimental investigation of contact angle

To determine the initial static contact angle of the working fluids, water and glycerin were carefully introduced in dry capillary tubes so as to produce isolated single plugs, respectively. The capillary tubes were made of Pyrex glass of inner diameter 2.0 mm and were thoroughly cleaned and rinsed before the experiment. Images were captured using high resolution digital camera fitted with a macro lens. Figure 3 shows the captured liquid plug images, with respective static contact angle for water and glycerin plugs. Hence, average static contact angle for water is taken to be 67° and that for glycerin is taken to be 30° , during simulations.

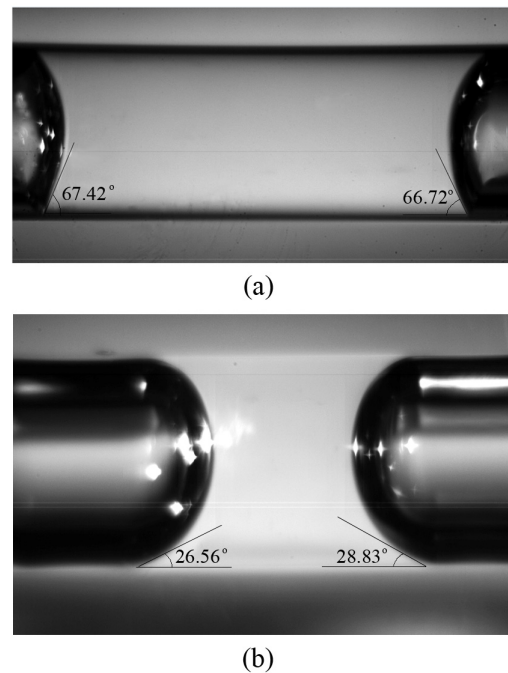


Figure 3. Captured images of liquid plug of (a) water and (b) glycerin in the capillary tube ($ID = 2.0 \text{ mm}$)

3.2 Numerical simulations

Numerical simulations are carried out using the technique described above for different L/D ratios of the liquid plugs, i.e., $L/D = 1, 2$ and 4 and for different Capillary numbers, i.e., $Ca = 10^{-5}, 10^{-4}$ and 10^{-3} for water and glycerin liquid plugs. Grid independence test is carried out for four different

grid element sizes at $Ca = 10^{-3}$ and $L/D = 2$, taking glycerin as the working fluid. Figure 4 (a) and (b) show the grid independence and validation test, respectively. In Figure 4(a), non-dimensional centerline velocity is plotted against the distance from entrance. It is clear that the numerical results are independent of grid after smallest element size 0.04. Hence, all other simulations are carried out taking this as the initial smallest element size. To validate the present model, a test is carried out against fully-developed Poiseuille flow. Figure 4(b) shows the results for this simulation. The maximum error between the theoretical results and simulation results is 0.05% at the point of maximum velocity which is satisfactory.

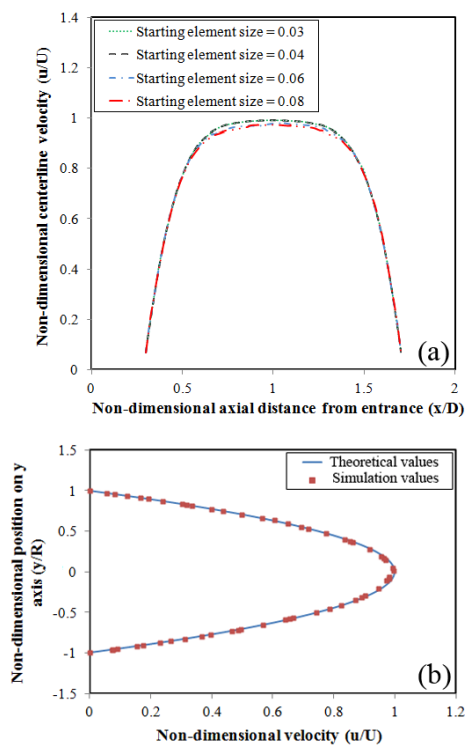


Figure 4. (a) Grid independence test for glycerin plug at $L/D = 2$ and $Ca = 10^{-3}$ and (b) validation test against fully developed Poiseuille flow

4. RESULTS AND DISCUSSION

Figure 5 shows the temporal variation of Nu_{avg} (as per Eq. (8)) for glycerin and water plug with $L/D = 2.0$, $Ca = 10^{-3}$ and constant heat flux condition. The re-circulation time scale, $(D + 2L_s)/U$, defined as the time taken by a fluid element inside the liquid plug to circulate once through it, is used as non-dimensional time scale. Two cases are reported for comparison (i) taking dynamic contact angle variations, as per Eq. 2 and, (ii) fixed contact angles, equal to the respective static contact angles, irrespective of the plug velocity.

Several important aspects are noted from Figure 5. Firstly, steady state Nu_{avg} is attained very early in the case of glycerin plug. Another notable feature is the initial fluctuations observed in the Nu_{avg} in case of water plug; these are absent in the glycerin system. Both these transport features are a direct consequence of higher Prandtl number of glycerin. In the case of water, the initial climb in Nu_{avg} is attributed to the rapid motion of the cold fluid in the central core of the plug which comes in contact with the tube wall because of greater propensity of frequency of internal circulations, which are present in the water plug. Thus, Nu_{avg} reaches a maximum and then starts declining as the fluid that has previously been heated completes its circulation and again comes in the contact of the wall. The cycle keeps on repeating with decreased amplitude. After some time, an asymptotic steady-state is reached and there are no more oscillations in Nu_{avg} . As explained earlier, owing to high Pr for glycerin, such fluctuations are absent in its plug. Similar observation is also reported by Walsh et al. (2011) and Young et al. (2008) with different Prandtl number fluids. Finally it is noted that an increase of about 16% in the steady-state Nu_{avg} due to contact angle hysteresis is observed in case of glycerin plug while for water plug, this value is approximately 33%.

Figure 6 (a) and (b) shows the variation of Nu_{avg} with Ca , for $L/D = 2$, under constant wall temperature boundary condition.

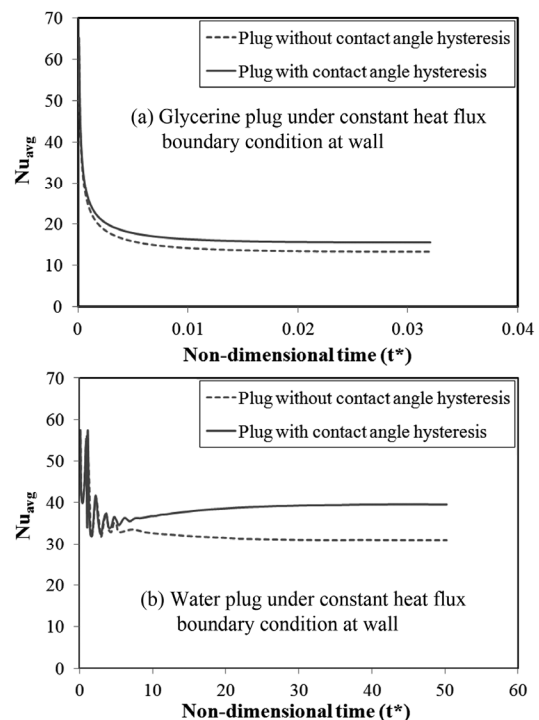


Figure 5. Nu_{avg} for $L/D = 2$ and flow $Ca = 10^{-3}$ for (a) glycerin plug (b) water plug

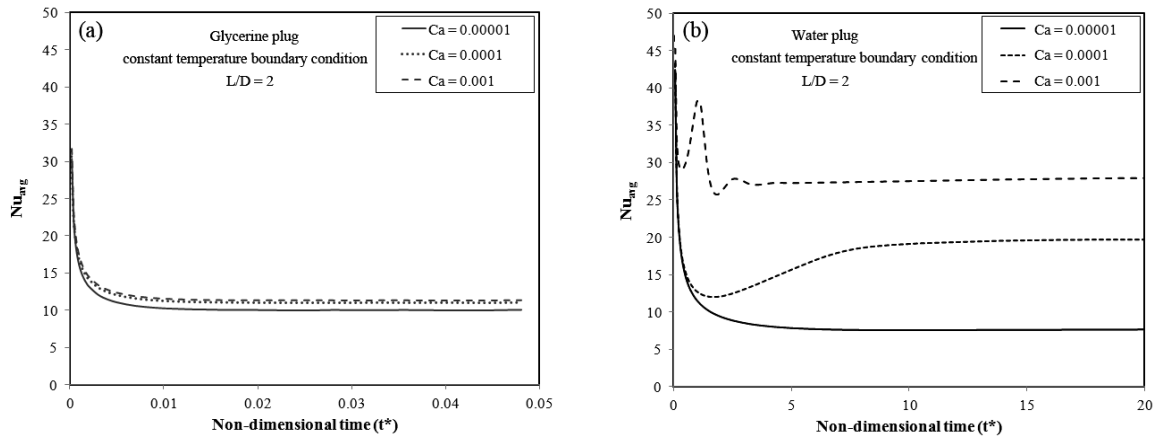


Figure 6. Temporal variation of Nu_{avg} with Ca at $L/D = 2$ under constant wall temperature $T_w = 350$ K

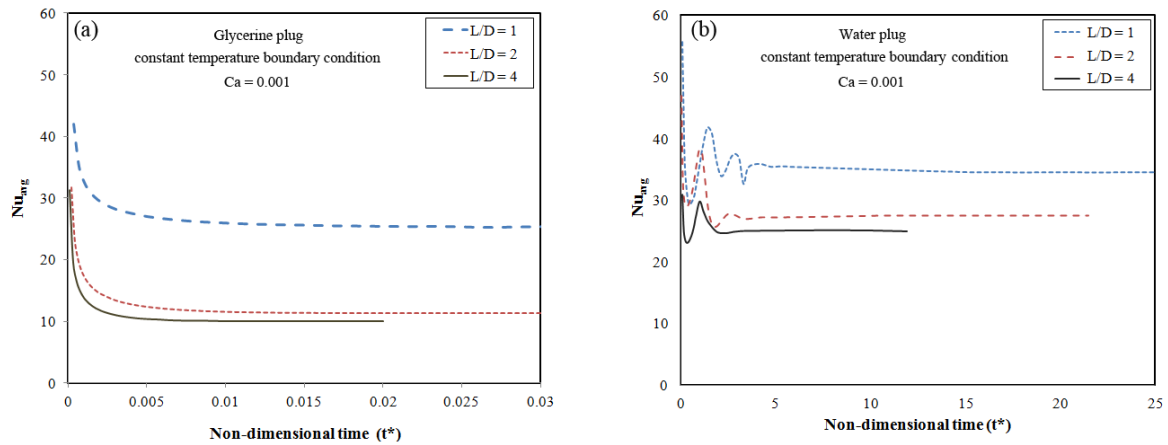


Figure 7. Temporal variation of Nu_{avg} with L/D at $Ca = 0.001$ under constant wall temperature $T_w = 350$ K

It is clear from these results that, at a constant L/D ratio, Nu_{avg} increases with Ca for both the liquids, though the increase in Nu_{avg} with Ca is more in water compared to that of glycerin. Because of high momentum diffusivity, there is no significant effect of increased velocity in case of glycerin and convection is more or less not much effected. In case of water, increase in Ca , and thus velocity has significant impact on Nu_{avg} and around 50% increment is observed. Thus, Ca plays an important role in determining the effective heat transfer coefficient in case of water.

Figure 7 (a) and (b) shows variation of Nu_{avg} with L/D ratio at $Ca = 0.001$ for glycerin and water plug, respectively, under constant wall temperature case. Most important feature to be noted here is that the heat transfer coefficient increases as the length of the plug decreases (we have not checked whether this is monotonous). Higher heat transfer coefficient in case of low L/D is because of the decrease in recirculation time scale (amount of time required for a typical fluid element to circulate once in the liquid plug) because of which relatively cooler fluid from inside the droplet core is able to reach the walls at a faster rate. Another fact which needs attention is that, for any given

Ca , there will be reduced oscillations of Nu_{avg} as L/D increases. Alternately, for any given L/D , reducing Ca will eventually reduce oscillations. In fact, when the cooler liquid travels a few times of its plug length, the peak, and thus amplitude of Nu_{avg} oscillations, gets reduced. Eventually Nu_{avg} stabilizes to a constant asymptotic value.

5. CONCLUSIONS

Transport parameters of isolated single liquid plugs moving inside dry capillary tubes is analyzed. The study clearly reveals that it is important to include the variations in the dynamic contact angles while determining the heat transfer coefficient in isolated Taylor slug flows. Dynamic contact angle hysteresis plays a critical role in local transport behavior. Furthermore, effect of Ca and L/D ratio of the plug is investigated and it is observed that high velocity (high Ca) and low L/D ratio of liquid plugs results in significant higher heat transfer coefficients than corresponding Poiseuille flow. Together, Ca , L/D , Pr , contact angle and its hysteresis are the governing parameters of system transport.

NOMENCLATURE

Bo	Bond number ($Dg(\rho_l-\rho_v)/\sigma$) ^{0.5}
Ca	Capillary number (-)
Cp	Specific heat (J/kgK)
D	diameter of the plug (m)
g	acceleration due to gravity (m/s ²)
h	heat transfer coefficient (W/m ² K)
k	thermal conductivity of fluid (W/mK)
L	length of the liquid plug (m)
Nu	Nusselt number (hD/k)
Pr	Prandtl number ($\mu Cp/k$)
q''	heat flux (W)
T	temperature (°C or K)
t	time (s)
t^*	non-dimensional time ($tU/(D+2L_s)$)
U	mean velocity of liquid plug (m/s)

Greek Symbols

μ	dynamic viscosity of liquid (Pa·s)
ρ	density of fluid (kg/m ³)
σ	surface tension (N/m)
θ	contact angle (rad)

Subscripts

a	advancing
d	dynamic
m, avg	mean/ average
r	receding
s	static
w	wall
l	liquid
v	vapor

ACKNOWLEDGEMENTS

Financial support from Indo-French Center for Promotion of Advanced Research (IFCPAR) is gratefully acknowledged (Project #: 4408-E).

REFERENCES

- Anslys Fluent® 12.0 manual
- Barajas, A.M., Panton, R.L. (1992), *The effect of contact angle on two-phase flow in capillary tubes*, Int. J. Multiphase Flow 19 (2), p. 337-346
- Berthier J. (2008) *Microdrops and Digital Microfluidics*, William Andrew, NY USA
- Blake, T. (2006) *The physics of moving wetting lines*, J. Colloid Interf. Sc. 299 (2006), p. 1-13
- Fermigier, M., Jenffer, P. (1991) *An experimental investigation of the dynamic contact angle in liquid-liquid systems*, J. Colloid Interface Sc. 146(1), p. 226-241
- Gunther, A., Khan, S.A., Thalmann, M., Trachsel, F., Jensen, K.F. (2004) *Transport and reaction in microscale segmented gas-liquid flow*, Lab on a

Chip 4, p. 278-286

- Hoffman, R. (1974) *A study of advancing interface*, J. Colloid Interface Sc. 50(2), p. 228-241
- Kolb, W.B., Cerro, R.L.(1991) *Coating the inside of a capillary of square cross section*, Chem. Engg. Sc. 46(9), p. 2181-2195
- Khandekar, S., Panigrahi, P.K., Lefevre, F., Bonjour, J. (2010) *Local hydrodynamics of flow in a pulsating heat pipe: A review*, Frontiers in Heat Pipes 1, 023003 (2010)
- Lee C.Y., Lee S.Y. (2008) *Pressure drop of two-phase plug flow in round mini-channels: Influence of surface wettability*, Exp. Thermal Fluid Science 32, p. 1716-1722
- Rose, W., Heins, R.W. (1962) *Moving interfaces and contact angle rate-dependency*, J. Colloid Science 17(1), p. 39-48
- Rosengarten, G., Cooper-White, J., Metcalfe, G. (2006) *Experimental and analytical study of the effect of contact angle on liquid convective heat transfer in micro channels*, Int. J. Heat Mass Transf. 49, p. 4161-4170
- Shekhavat, S., Khandekar, S., Panigrahi, P.K. *Hydrodynamic study of an oscillating meniscus in a square mini-Channel*, Proc. Micro/Nano-scale Heat Mass Transf. Int. Conf., Shanghai, China
- Tripathi, A., Khandekar, S., Panigrahi, P.K. (2010) *Oscillatory contact line motion inside capillaries*, Proc. 15th Int. Heat Pipe Conf., Clemson, USA
- Triplett, K.A., Ghiaasiaan, S.M., Abdel-Khalik, S.I., Sadowski, D.L. (1999) *Gas-liquid two-phase flow in micro channels*, Int. J. Multiphase Flow 25(3), p. 377-394
- Walsh, P.A., Walsh, E.J. and Muzychka, Y.S. (2011) *Prandtl and capillary effects on heat transfer performance within laminar liquid-gas slug flows*, Int. J. Heat Mass Transf. 54, p. 4752-4761
- Young, P., Mohseni, K. (2008) *The effect of droplet length on Nusselt numbers in digitized heat transfer*, IEEE 978-1-4244, p 1701-1708
- Zheng, Y. Fujioka, H. Grotberg, J.B. (2007) *Effect of gravity, inertia and surfactant on steady plug propagation in a two dimensional channel*, Phy. Fluids 19, p. 082107-1-082107-16
- Zhao, T.S., Bi, Q.C. (2001) *Co-current air water two phase flow patterns in vertical triangular micro channels*, Int. J. Multiphase Flow 27(5), p. 765-782

INDUSTRIAL MANUFACTURING OF LOOP HEAT PIPE POROUS MEDIA

Thomas Albertin, Jean-François Savard

Atherm

1 rue Charles Morel, 38420 Domène, France

Phone: +33 (0)4-76-77-23-24, Fax: +33 (0)4-76-77-09 03, t.albertin@atherm.com, jf.savard@atherm.com

Valérie Sartre

Centre de Thermique de Lyon (CETHIL) UMR5008 CNRS-INSA-Univ. Lyon 1

INSA de Lyon, Villeurbanne, France

Phone: + 33 (0)4 72 43 81 66, Fax: + 33 (0)4 72 43 88 11, E-mail: valerie.sartre@insa-lyon.fr

ABSTRACT

One of the most important parts of the LHP is the porous wick which provides the capillary force to circulate the working fluid. To achieve good thermal performance, capillary wicks with high permeability and porosity and fine pore radius are requested. Unfortunately, there are only few papers in the literature describing with details the fabrication of wicks adapted to LHPs. The objective of the present work is to develop the machining procedure and tool for LHP porous wicks, and to develop the assembling methods for a complete LHP evaporator equipped with this capillary structure. The wick porosity is estimated by the weight method and the pore size is determined using Scanning Electronic Microscopy and Confocal Microscopy. The effects of the sintering temperature, sintering time, speed of temperature rise, powder size and powder type, powder vibration are investigated. The optimum wick properties – porosity of 65-70%, pore diameter of 8-9 μm - are obtained by sintering a nickel type 2 powder at 0.6 time the melting temperature, for 20 minutes. A cylindrical capillary structure was fabricated and inserted into the evaporator body. The tests of this LHP are in progress.

KEY WORDS: Sintered metal capillary wick, porosity, pore size

1. INTRODUCTION

Continuous progress and improvement of electronic components bring new thermal constraints for users. Indeed, the increase of component power and their miniaturization generate the need to dissipate more and more increasing power densities. Embedded electronics (civil and military aircrafts applications for example) follow this trend.

Beyond thermal performances, cooling system users in the field of aeronautics add other constraints on operating conditions: hard environmental conditions, large scale of operating temperatures, use of passive systems, systems working against gravity and under acceleration, minimal weight and dimensions...

Proper qualities of Loop Heat Pipes (LHPs), allow them to bring suitable answers to above needs. LHPs are two-phase heat transfer devices that utilize the evaporation and condensation of a working fluid to transfer heat, and the capillary

forces developed in fine porous wicks to circulate the fluid. Hence, LHPs are totally passive systems. They have gained increasing acceptance in spacecraft applications because of their high pumping capability and robust operation (Ku et al., 1999). They are able to transfer high heat fluxes over long distances with a low thermal resistance. They also have a self-adjustment capability: when the external conditions vary, LHPs regulate their operating temperature. To achieve good thermal performance, capillary wicks with high permeability and porosity and fine pore radius are requested. For sintered metallic powders, these parameters closely depend on the manufacturing process. Unfortunately, there are only few papers in the literature describing with details the fabrication of wicks adapted to LHPs. The most frequently used wicks are made from sintered metal, like copper, titanium, nickel, stainless steel. Li et al. (2010) fabricated nickel wicks with porosity up to 80 % and found that the pore size distribution ranges become wider and the mean pore diameters increase by adding an increasing quantity of a space-holder material. The porosity

increases when the temperature or the forming pressure decrease. For Xin et al. (2009), the optimal capillary wick was found to be sintered at 650 °C for 30 minutes, using direct loose sintering technique, with 90% nickel and 10% copper. The wicks reach the porosity of 70% and a mean pore radius of 5 μm. Li et al. (2012) fabricated biporous nickel wicks. A porosity of 77.4% was achieved using cold pressing sintering method, at a temperature of 700 °C, with a pore former content of 30% in volume. Three kinds of pore were observed, the biggest ones of 60 μm radii made by the pore former, the smallest ones of 1 μm radii between the powder grains, the last ones of 5 μm generated by the grains agglomeration.

The objective of the present work is to develop the machining procedure and tool for LHP porous wicks, and to develop the assembling methods for a complete LHP evaporator equipped with this capillary structure. The sintering methods and sintering parameters are detailed, as well as the method used to determine the porous wick thermophysical properties. The effect of the metal and powder size is investigated. Then, the fabrication methods for the preformed wick are presented. Finally, the first experimental results are shown.

2. MANUFACTURING AND CHARACTERIZATION OF METALLIC SINTERED SAMPLES

2.1 Experimental means

In order to achieve powder sintering, it is necessary to use a vacuum or neutral atmosphere furnace: the aim is to ensure a reducing atmosphere during the sintering process to avoid any oxidization of powders. The furnace we used for the study (Carbolite BCWF12/23C) is equipped with an inonel box allowing a work under reducing gas.

Three types of powders have been used during the trials:

- Copper: grain sizes ϕ 5, 50 and 160 μm
- Nickel: grain sizes ϕ 3-7, 45 and 150 μm
- Bronze: grain sizes ϕ 150 μm.

A graphite tool (mold) has been designed (figure 1) for the realization of calibrated porous samples:

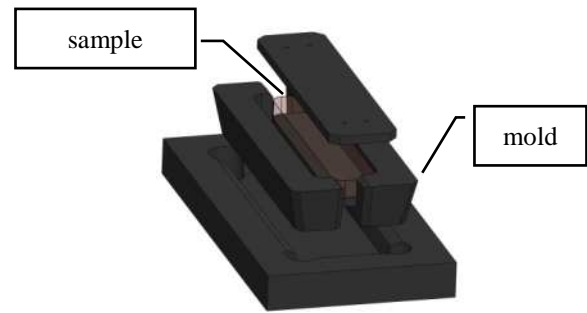


Figure 1. Sample sintering tool

dimensions 50 mm × 10 mm with possible thickness variation between 2 and 4 mm. The aim of the project is the manufacturing of wicks with a porosity around 75% and pore diameters lower than 10 μm.

2.2 Measurement of sample properties

Pores size

For the measurement of pore sizes, a binocular lens associated with a digital camera and a specific software for image post treatment is utilized. This method allows not only the measurement of pore sizes (minimal value of 10 μm) but also an estimation of their shape. For smaller sizes, the samples are measured using Scanning Electronic Microscopy and Confocal Microscopy.

Porosity ϵ

For the porosity measurement, the weight method is used. First, the sample is weighed in dry state. Secondly, the sample is soaked with isopropyl alcohol ($\rho_{\text{propanol-2}} = 0.785 \text{ g}\cdot\text{cm}^{-3}$ at 20°C). The weight of absorbed alcohol is estimated by the difference between both values, and then a deduction of the "empty space" (thus the total pore volume) and the porosity.

$$\epsilon = \frac{M_{\text{soaked sample}} - M_{\text{dry sample}}}{V_{\text{total}} \rho_{\text{propanol-2}}} \quad (1)$$

2.3 Influence of sintering parameters

Parameters with an influence on the porous wick characteristics are the following: sintering time, sintering temperature, temperature increasing speed, grain sizes and material type.

Sintering time and temperature

A study based on the factorial method is conducted on those two parameters in order to find a behavior law. Trials have been performed on bronze powder

(grain sizes 40 μm) for sintering times of 20 and 90 minutes and temperatures of 0,6 T_f and 0,9 T_f . T_f is the melting temperature of the considered material.

Results are summarized in table 1. Pore size decreases when sintering time increases and when the sintering temperature increases. The following law is deduced for the porosity (ϵ):

$$\epsilon = 39.75 - 11.75 t - 12.25 T - 7.75 t T \quad (2)$$

Table 1. Effect of temperature and sintering time

Sintering temperature	0.6 T_f	0.6 T_f	0.9 T_f	0.9 T_f
Sintering time (min)	20	90	90	20
porosity (%)	56	48	8	47
pores size (μm)	19	15	11	14

Temperature increasing speed

The study on this parameter is conducted with copper and bronze powders. The results show that a slow increase up to the sintering temperature gives a good mechanical cohesion of the sintered material.

Grain size

Nickel powder is sifted to obtain three different particle size scales: lower than 50 μm , between 50 and 100 μm , greater than 100 μm . It seems that particle size has no significant influence on the porosity (table 2). However, it has a logical influence on pore size: pore size decreases with particle size.

Table 2. Effect of the grain size

particule size (μm)	>100	50 - 100	<50
porosity (%)	45	48	47
pore size (μm)	70	28	26

Material type

The material type has a very important influence on the sintering results. For example, when sintering bronze powder and copper powder with equivalent parameters, we can notice some differences between copper and bronze porosity and pore diameters (table 3). The porosity and pore diameter of copper and bronze sintered powder are not as interesting as nickel powder for LHP porous wicks [requested porosity: 65-70%/pore diameter 8-9 μm , reached with Bronze 45%/12 μm , reached with Copper 30%/25 μm]. In addition, the wicks must be preferably made of low conductivity metals in order to limit the parasitic radial heat flux

[Copper 400W/mK, Bronze 50 to 60 W/mK, Nickel 90W/mK]. These aspects guided the selection of nickel powder in the following work.

Table 3. Effects of the material type

Material type	Powder size (μm)	Sintering time (min)	Sintering temperature ($^{\circ}\text{C}$)	Porosity (%)	Pore diameters (μm)
Copper	<50	20	0.6 T_f	30	25
			0.8 T_f	25	20
Bronze	<50	20	0.6 T_f	50	14
			0.8 T_f	45	12

2.4 Realization and analysis of samples (nickel powder)

A lot of trials have been performed with several different powders. Only the nickel results for powder type 1 (figure 2) and type 2 are presented. Particle size is described in table 4. Properties of manufactured samples (figure 3) are presented in table 5. It appears that samples 3 and 4 (with nickel type 2, sintering temperature of 0.6 T_f and a sintering time of 20 min) give the best compromise in terms of porosity (65 to 70%) and pore diameters (8 to 9 μm).

Table 4. Powder size of Ni

Ni type	1	2	3
mean size (μm)	4-6	1.8-2.8	40
maximum size (μm)	14	23.5	100

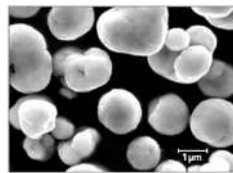


Fig. 2. Photo of Ni type1 powder



Fig. 3. Photo of sintered nickel samples

Samples 3 and 4 have been analyzed with Scanning Electronic Microscopy (figure 4 and 5). It appears that powders have two different behaviors. On a first scale (around 20 μm) the powder seems to agglomerate like bigger grains, giving some pores with mean diameters of 8 μm . Inside the grains agglomeration, we can observe smaller pores with size around 1 - 2 μm .

A second analysis of the sample has been performed with the confocal microscope (figure 6). The 1D picture of the surface (realized on a portion

Table 5. Properties of the sintered Ni samples

Sample	Grains size (μm)	Sintering time (min)	Sintering Temperature (°C)	Porosity (%)	Pore Diameters (μm)
1	4 to 6	20	0.6 T_f	55	9.9
2	4 to 6	20	0.6 T_f	56	6.8
3	1.8 to 2.8	20	0.6 T_f	67	8.8
4	1.8 to 2.8	20	0.6 T_f	72	8
5	4 to 6	20	0.9 T_f	43	8.3
6	4 to 6	20	0.9 T_f	45	7
7	1.8 to 2.8	20	0.9 T_f	55	7.7
8	1.8 to 2.8	20	0.9 T_f	53	8.2
9	4 to 6	40	0.6 T_f	55	8.7
10	4 to 6	40	0.6 T_f	56	9
11	1.8 to 2.8	40	0.6 T_f	65	7
12	1.8 to 2.8	40	0.6 T_f	67	8
13	4 to 6	40	0.9 T_f	36	9.7
14	4 to 6	40	0.9 T_f	39	8.1
15	1.8 to 2.8	40	0.9 T_f	43	6.8
16	1.8 to 2.8	40	0.9 T_f	45	8

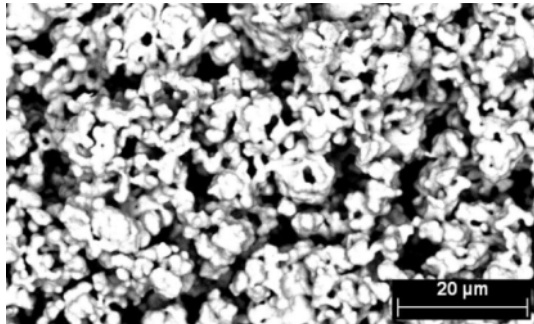


Figure 4. MEB picture of Nickel sample n°3

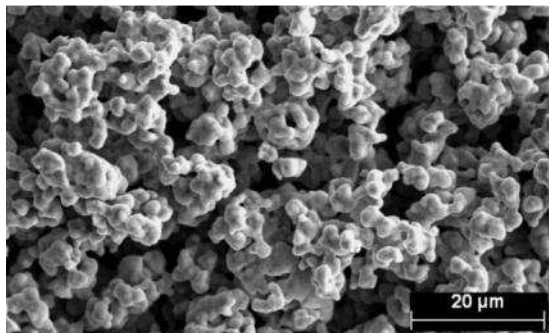


Figure 5. MEB picture of nickel sample n°4

of 0.3 mm length) shows around 30 "holes" corresponding to pores. The pore diameters vary

between 2 and 15 μm but the large size pores are the result of gathering of several smaller pores. A certain regularity is noticed in the pore distribution and dimensions.

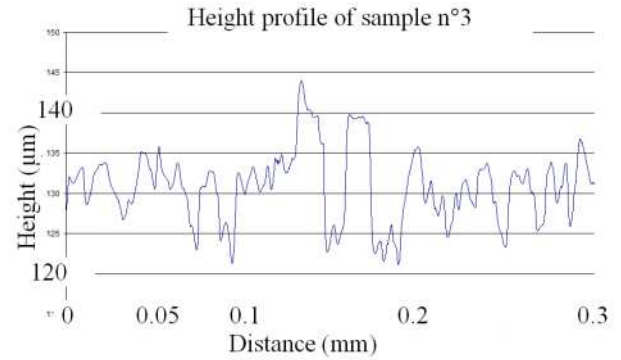


Figure 6. Surface analysis of a Ni type 2 sample with the confocal microscope

3. MANUFACTURING OF PRE-SHAPED WICKS AND FINAL SHAPING FOR A LHP EVAPORATOR

The wick structure, in sintered nickel, is designed for a LHP evaporator, with a cylindrical shape, made of copper. Length of the wick structure is 30 mm, the external diameter is 10 mm, and the wick has a 2 mm cylindrical hole in the center. The sintering cycle used for its manufacturing is described on figure 7. The nickel powder is first brought to 400 °C and after a plateau, to the sintering temperature of 0.6 T_f during 20 min. Then, the sample is abruptly cooled to 20 °C for a period of time.

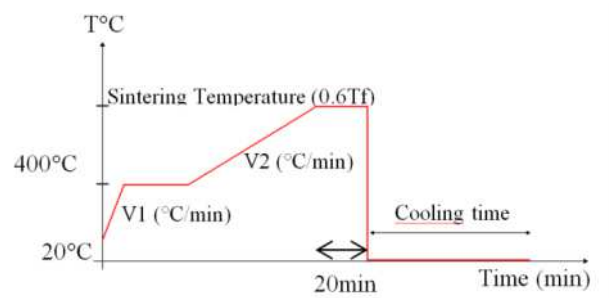


Figure 7. Temperature cycle for the cylindrical wick structure sintering process

3.1 Influence of mechanical vibration during preparation on the wick properties

During the several trials performed, we have noticed that the way of implementation of powder into the mold has a very important influence on the dimensional characteristics of the parts (especially

on the shrinkage phenomenon). A study is then carried out to estimate the influence on the shrinkage phenomenon of a vibration process during filling of the mold. A mechanical vibration is applied on the mold while the powder is inserted and shrinkages of manufactured samples with this process are compared to samples realized without any vibration. Powders used are nickel type 2 and nickel type 3 and also spherical copper powder with particles of 100 to 150 μ m.

Copper powder is sensible to vibrations (table 6): the particles are reordered creating a decreasing of porosity and pore size. Shrinkage is slightly affected. The nickel powder vibration brings an important decreasing of the shrinkage phenomenon. On the other side, the decreasing of porosity is quite important while pore size doesn't change a lot. We can then say that a reorganization of powders by mechanical vibrations gives a better control on shapes and dimensions of samples.

Nevertheless, vibrating process doesn't allow the realization of wicks with the requested porosity. Finally, this process is not retained for the manufacturing of wicks for LHP.

Table 6. Effect of mechanical vibration on the wick shrinkage

		Porosity (%)	Pore ϕ (μ m)	Shrinkage (%)
spherical Copper	Basic sample	38	59	0.5
	Vibrated sample	16.8	39.5	4
Nickel Type 2	Basic sample	67	8.8	10
	Vibrated sample	54	11	1.9
Nickel Type 3	Basic sample	80	24.5	6.5
	Vibrated sample	60	21	3.5

3.2 Manufacturing process

For the manufacturing of a porous wick dedicated to the concerned LHP (cylindrical shape), a cylindrical graphite mold is machined (figure 8). The assembly of a porous wick in the evaporator of a LHP requires a great control of the tolerances of the parts. In order to avoid tolerance problems due to dimensional variations by shrinkage phenomenon during sintering process, a traditional stock removal manufacturing process is considered

on pre-shaped parts (figures 9 and 10). A study driven on capillary structures sintered with bronze and nickel powders shows the feasibility of such a process. The pores are not obstructed by traditional



Figure 8. Cylindrical mold for porous wick manufacture



Figure 9. Sintered part / machined part (nickel)



Figure 10. Machined porous wick (nickel)

machining like drilling, milling or turning (figure 11). Machined parts present a surface porosity really satisfying (figure 12) and capillary pumping capacities are not affected. Those results are different from the ones obtained by Li and al. (2012) who have observed the obstruction of the porous media after machining by traditional means, hence their proposition to use electro erosion process.

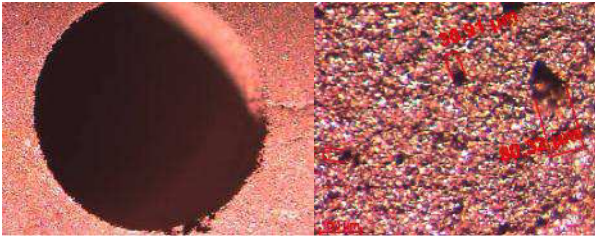


Figure 11. Detail of a drill and machined surface (bronze)

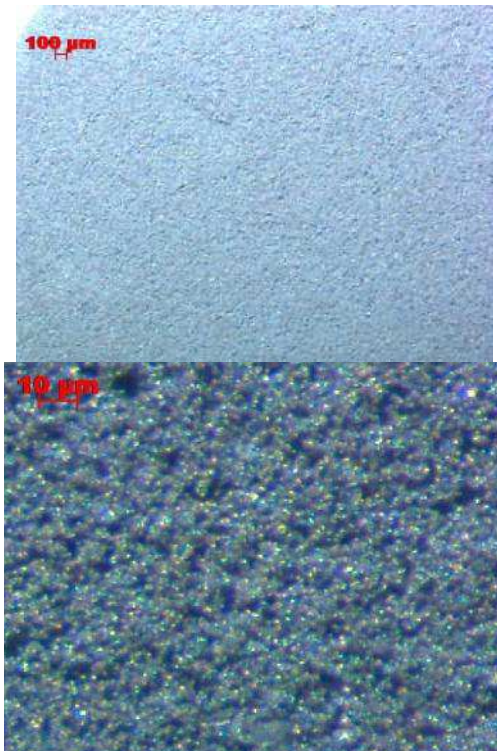


Figure 12. Machined surface (nickel)

4. CONCLUSIONS

The several studies realized on different materials for the manufacturing of porous wicks have finally guided our choice on nickel powder for the realization of primary LHP porous wicks.

Indeed, original objectives regarding the thermophysics characteristics of the primary porous wick have been reached with this material: Sintering at $0.6 T_f$ during 20 min gives a porosity of 70% and pore size of $8\mu\text{m}$, and thus allow needed capillary performances.

Trials on bronze and copper sintered wicks and characteristics obtained are also implementable for the manufacturing of secondary wicks in the case of LHP.

Regarding the assembling of LHP evaporator, after first successful assembling of evaporators,

machining process of sintering wicks seems to be a good option to reach the dimensional, geometrical characteristics and tolerances needed to give the best interfaces with evaporator casing.

NOMENCLATURE

M	mass, kg
T	sintering temperature, K
T_f	melting temperature, K
t	sintering time, s
V	volume, m^3
ε	porosity
ρ	density, kg m^{-3}

ACKNOWLEDGEMENT

This work was conducted in the frame of the SYSHANG project funded by the DGA, in partnership with the CETHIL and the THALES Avionics company.

REFERENCES

- Ku, J. (2009) Operating characteristics of loop heat pipes, Int. Conf. On Environmental Systems, Denver, SAE paper 1999-01-2007, 16 p.
- Li, J., Zou, Y., Cheng, L., Singh, R., Akbarzadeh, A. (2010) *Effect of fabricating parameters on properties of sintered porous wicks for loop heat pipe*, Powder Technology, 204(2-3), p. 241-248
- Xin, G., Cui, K., Zou, Y., Cheng, L. (2009) *Development of sintered Ni-Cu wicks for loop heat pipes*, Sci China Ser E-Tech Sci, 52(6), p. 1607-1612
- Li, H., Liu, Z., Chen, B., Liu, W., Li, C., Yang, J. (2012) *Development of biporous wicks for flat-plate loop heat pipe*, Experimental Thermal and Fluid Science, 37, p. 91-97

COOLING SYSTEM FOR HERMETIC COMPRESSOR BASED ON THE PULSATING LOOP THERMOSYPHON

Aliakhnovich V.A., Vasiliev L.L.

Luikov Heat and Mass Transfer Institute
National Academy of Sciences of Belarus
15, Str. P.Brovka, 220072 Minsk, Belarus

Tel: +375 17 2842133/ Fax: +375 017 2322513

e-mail: aliakhnovich@gmail.com, leonard.vasiliev@gmail.com

ABSTRACT

In the design of small hermetic compressors used in air conditioning and refrigeration the thermal management is one of the most important issues that determine overall performance and reliability of the system. In hot climate countries this problem is more difficult and usual internal oil spray cooling of the working compressor is not enough. In this paper the simple solution of the hermetic compressor thermal control by means of the pulsating loop thermosyphon is offered. And also a description of the pulsating loop thermosyphon is given. The experimental data on the critical temperature decrease of the working compressor are received and presented.

1. INTRODUCTION

Small hermetic reciprocating compressors are used in air conditioning, refrigeration and heat pump systems. When the compressor operates in the conditions of poor ventilation and high surrounding temperature its efficiency goes down (weak degree of compression in the cylinder).

Besides, heat flux which is evolved by the working compressor partially is carried away by the coolant from the compressor to the refrigerator condenser. That leads to the temperature increase of the condenser and reduces efficiency of a whole heat pump system. Therefore in the design of small hermetic compressors the thermal management is one of the most important issues that determine overall performance and reliability of system. In hot climate countries this problem is more difficult and usual internal oil spray cooling of the working compressor is not enough. Earlier experimental works on use of a heat pipes for cooling of the small hermetic compressor (Possamai et al. (2009)), and use of a loop thermosyphon with a porous insert (Aliakhnovich et al. (2011)) have been carried out.

In this paper the simple solution of the small hermetic compressor thermal control by means of the pulsating loop thermosyphon (PLT) is offered.

2. EXPERIMENTAL SET-UP

2.1 Experimental compressor with PLT

The experimental compressor represented the standard hermetic piston compressor batch-produced by Embraco. For convenience of the experiment realization the top cover of the compressor has been made demountable (figure 1).



Figure 1. Photo of the compressor with PLT

On figure 2 the cross-section of the hermetic compressor with PLT is shown. The flat PLT evaporator was fastened to the flat polished surface of a compressor cylinder head. The condenser of the PLT was outside of the compressor and cooled by two flat aluminium heat sinks with fins.

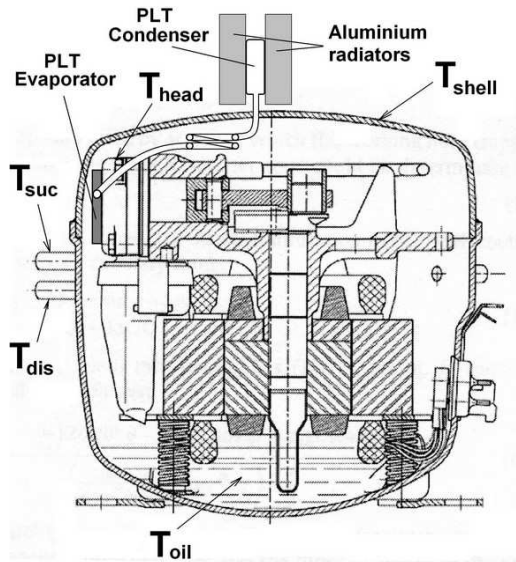


Figure 2. Cross section of the compressor with pulsating loop thermosyphon (PLT)

2.2 Pulsating loop thermosyphon (PLT)

PLT consists of a tube of a small diameter and a hollow condenser chamber (the condenser) located above (figure 3).

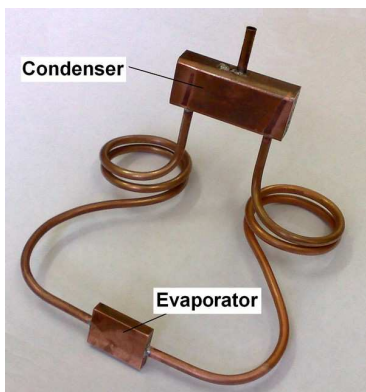


Figure 3. Photo of PLT for the compressor cooling

Both ends of the tube are connected to the condenser in its bottom part. The condenser has the internal volume forming a loop with the internal channel of the tube. The internal volume of the thermosyphon was evacuated and filled by a certain quantity of the working liquid. The

minimum volume of the liquid filling was defined by a condition that the level of working liquid in the condenser was above the entrance of the tube. As the evaporator the bottom part of the tube is used. Water as a working fluid for the PLT was chosen.

The preliminary test of this PLT has shown the thermal resistance $R = 0.31 \text{ K/W}$ for 100W heat input and $R = 0.19 \text{ K/W}$ for 160W.

The operation mechanism of the pulsating loop thermosyphon was in detail described by Aliakhnovich & Konev in 2008.

On figure 4 the top cap of the compressor with fitted PLT is shown. Two coils of the PLT transport zone (as a vibration isolator) prevent the thermosyphon from destruction during the compressor vibrations.



Figure 4. Top cap of the compressor with fitted PLT

2.3 Experimental heat pump

The experiment with hermetic compressor with PLT was carried out on the experimental set-up (figure 5), which represented a heat pump (HP).



Figure 5. Experimental set-up

The compressor has a demountable top cover. This set-up was performed to reproduce the mode of the compressor application close to realistic. The tests of the compressor were performed with such parameters:

- ambient temperature – 26 °C;
- gas outlet pressure – 23 bar;
- gas suction pressure – 1,5 bar;

The temperature measurements were made as:

- T_{head} – cylinder head;
- T_{shell} – compressor shell;
- T_{oil} – oil;
- T_{dis} – gas temperature at the compressor exit;
- T_{suc} – gas temperature at the compressor entrance;
- T_{con} – HP condenser entrance;
- T_{evp} – HP evaporator entrance;

Before each test, the heat pump system has been evacuated and then filled with the necessary quantity of the Freon-22.

3. EXPERIMENTAL RESULTS

The tests of the compressor have been made: test of the compressor without any additional cooling; test of the compressor with built in PLT; test of the compressor with PLT and fan.

The obtained data is presented in tables 1, 2.

Table 1. The experimental data of the temperature distribution inside the compressor

	T_{head} °C	T_{shell} °C	T_{oil} °C	T_{dis} °C	T_{cond} °C
Without cooling	143.2	76.5	93.1	128,0	63,3
With PLT	119.5	75.2	89.5	117,6	60,1
PLT with Fan	110.3	72.4	85.9	112,6	59,9

Table 2. The temperature drop of the working compressor with additional cooling

	ΔT_{head} °C	ΔT_{shell} °C	ΔT_{oil} °C
With PLT	-23,7	-1,3	-3,6
PLT with Fan	-32,9	-4,1	-7,2

3. CONCLUSIONS

The carried out experiment has shown that the temperature of a cylinder head of the compressor working under load exceed 140 °C. Using PLT it has allowed to decrease the cylinder head temperature by 23,7 °C, and with fan by 32,9 °C. Such decrease in temperature of the cylinder increases compression ratio that raises efficiency of the compressor. In addition the condenser temperature has gone down by 3,4 °C that will lead to increase in efficiency of the refrigerator.

Thus, some effective application of the pulsating loop thermosyphon in thermal control of the small hermetic piston compressor has been shown, which can be advantageously applied high temperature operation conditions of refrigerators.

REFERENCES

- Aliakhnovich V.A., Kireichik D.G., Vasiliev L.L., Konev S.V., Zikman A.B. (2011) “Cooling system for hermetic compressor based on the loop thermosyphon”, VIII Minsk International Seminar “Heat Pipes, Heat Pumps, Refrigerators, Power Sources”, Minsk, Belarus, September 12–15
- Aliakhnovich V.A., Konev S.V. (2008) “Heat transfer device for microelectronic cooling”, MIF-VI, May 19-23, Minsk, Belarus (in russian).
- Possamai F.C., Setter I., Vasiliev L.L. (2009) “Miniature heat pipe as compressor cooling devices”, Applied Thermal Engineering 29 3218-3223

SINTERED ALUMINUM HEAT PIPE (SAHP)

Ameli M^{a*}, Agnew B^a, Leung P S^b, Ng B^a, McGlen R^c, Sutcliffe C J^d, Singh J^d

^a School of the Built and Natural Environment, Northumbria University, Wynne Jones Building
Ellison Place, Newcastle upon Tyne, NE1 8ST, Tel: (0191) 227 4060, seied.ameli@northumbria.ac.uk

^b School of Computing, Engineering and Information Sciences, Northumbria University

^c Thermacore Europe, 12 Wansbeck Business park, Ashington, NE63 8QW, UK, Tel: (01670)859500

^d School of Engineering, University of Liverpool, Tel: (0151)7944316

ABSTRACT

This work is the product of an ongoing PhD project in the School of the Built and Natural Environment of Northumbria University in collaboration with University of Liverpool and Thermacore of Ashington. This paper is a summary of the achievements at the end of the first year. The main objective of the project is to develop an aluminum ammonia heat pipe with a sintered wick structure. Currently available ammonia heat pipes mainly use extruded grooved aluminum tubes. There have been a few attempts of employing porous steel or nickel wicks in steel tubes with ammonia as the working fluid (Bai, Lin et al. 2009) but there is no report of aluminum heat pipes with ammonia and a porous wick structure. The main barrier is the difficulty of sintering aluminum powders to make porous wicks. So far during this project promising sintered aluminum heat pipe samples have been manufactured using the Selective Laser Melting (SLM) technique with various wick characteristics. This new method is proved to be capable of manufacturing very complicated wick structures with different thickness, porosity, permeability and pore sizes in different regions of a heat pipe in addition to the solid walls while the entire heat pipe including the end cap, tube wall, wick and the fill tube can be generated in a single process.

KEY WORDS: Ammonia Heat Pipe, SLM, Sintered Aluminium Heat Pipe

1. INTRODUCTION

The first investigation of ammonia as a working fluid for heat pipes was done in late 60s and the first use of an ammonia heat pipe was in the early 1970s. They have been used in spacecraft as a mean for managing internal temperature conditions. To date, nearly all space radiator systems have used grooved aluminium/ammonia heat pipes or loop heat pipes (Anderson, Dussinger et al. 2008).

Axially grooved heat pipes offer relatively simple industrial fabrication and greater reliability than other wick designs, such as artery heat pipes. Their principal function is to transport heat from dissipative equipment to radiative panels. They equalise the temperature over the surface of a panel. Thus north and south panels each require a network of heat pipes (Hoa 2003).

There is no record of an aluminium ammonia heat pipe with a porous wick structure in the literature.

The main reason for this seems to be in the fact that almost all the existing heat pipe porous wicks are made by the powder sintering method while aluminium powder sintering is a much more complicated process than sintering particles like copper or nickel and is not practical for making heat pipe wick structures. Also, making the porous wick from other materials and applying it on the internal walls of an aluminium heat pipe has many other complications including compatibility and wick-wall thermal resistance.

Developing an aluminium ammonia heat pipe with a porous wick structure is the main subject of this project and this paper reports the results of this project at the end of year one. For simplification, during the project this type of heat pipe is called SAHP or Sintered Aluminium Heat Pipe. However it is understood that this short name is subject to controversy as the porous structures which are discussed through this project are not developed by sintering method but with Selective Laser Melting (SLM) technique.

As this is the first time that a heat pipe has been fabricated using this SLM technique, there are numerous questions that must be answered and of parameters which must be analysed or tested before the design rules for manufacturing heat pipes using this new method can be developed.

There are two groups of these parameters. First are the SLM machine settings in order to make acceptable solid structures (heat pipe container) and also porous structures (heat pipe wick). The other group are the characteristics of the heat pipe itself especially with regard to the porous wick structure e.g. the maximum heat removal, porosity, permeability and pore radii.

So far, during this project, solid and porous structures have been made by SLM to characterise their basic parameters. Then dummy heat pipes were manufactured to prove SLM capability in making different types of aluminium porous wick structures with the container, end cap and fill tube all in a single process.

Building operational heat pipe samples, filling and venting them and testing their thermal performance in various orientations is the ongoing activity and the results of this work will be presented in the future.

2. Manufacturing of the samples

2.1 Selective Laser Melting (SLM)

Selective Laser Sintering/Melting (SLS/SLM) manufacturing process utilises a laser beam to locally melt a thin layer of metal powder. By applying additional powder layers and using 3D CAD and a custom beam control software to melt a pattern across each layer, complex 3D components that are not able to be manufactured using conventional machining are produced (Almeida 2004).

SLM process begins with a completely defined CAD model of the part to be made. Divided into cross-sections by special software, the model is then directly involved in the process. The essential operation is the laser beam scanning over the surface of a thin powder layer previously deposited on a substrate. The forming process goes along the scanning direction of the laser beam. Each cross-section (layer) of the part is sequentially filled with elongated lines (vectors) of molten powder (Yadroitsev, Bertrand et al. 2007).

Different aspects of the laser treated surfaces have been studied in literature e.g. corrosion (Liu,

Chong et al. 2006), optimum value of the process parameters (Yadroitsev, Bertrand et al. 2007) and residual stresses (Merzelis and Kruth 2006).

The samples for this project were manufactured by MCP Realizer 100 (MTT Tooling Technologies, UK) SLM machine. A ytterbium fibre laser with maximum laser output of 200 W having continuous wavelength (CW), $\lambda=1.071\mu\text{m}$ and nominal beam diameter of $50\mu\text{m}$ was employed in the machine. The optical system controls the movement of the focused laser beam on the build substrate having accuracy of $\pm 5\mu\text{m}$.

The processing chamber operated at a positive argon pressure of 14 mbar with oxygen levels kept between 0.1% - 0.2%. The atmosphere within the chamber is circulated and filtered to remove processed bi-products such as particles formed from condensed metal vapour, from the recycled gas. The specimens were manufactured layer by layer on an aluminium substrate plate secured on an elevator plate that moved vertically downwards allowing the controlled deposition of powder layers at $50\mu\text{m}$ intervals. The power and exposure time of the laser during each layer projected in spots is set from a defined process window. These parameters control the degree of melting at each laser contact spot and the melt pool, which in turn controls the strut diameter of the porous structures and consequently their porosity and strength. Porous structures are generated by formation of octahedral units, repeated in a constrained boundary representing structural geometry. The build substrate plate is removed from the build chamber after completion of build and un-fused powder is removed by applying a vibratory action to the up-turned plate. Test pieces are then cut from the substrate plates using a wire erosion process to avoid excessive smearing of the pores. Figure 1 shows a substrate with some random geometry fabricated on it;



Figure 1: In SLM machine, objects are made on a substrate and then are cut using a wire erosion process. A substrate is shown here with some random geometry fabricated on it.

To prepare a CAD model for the SLM machine first the entire geometry is enclosed in a bounding box. The box is then filled with cuboids of a defined unit cell size (in this project, 300, 500 and 700 μm).

For those parts which meant to be porous these cuboids are populated with a 3-D octahedral geometry. Then the entire geometry is sliced into layers with specific thickness (in this project, 50 μm). Specific commands are applied to change the Cartesian coordinates of the octahedral structure's centre point if randomising of the structures is required (to obtain porous structures with a mix of pore radii as opposed to homogeneous porous structure).

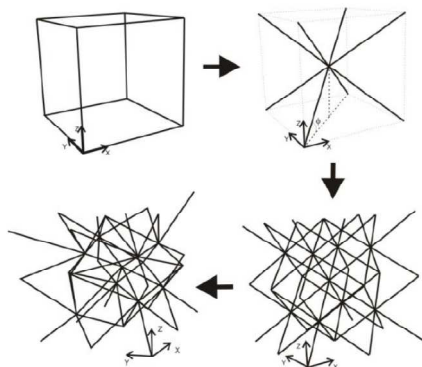


Figure 2: Transformation of the unit cell into a regular or randomised porous structure. [ref: Stamp, R. C., (2007) "The Rapid manufacturing Of Hierarchical Structures For Orthopedic Applications." PhD. University of Liverpool.]



Figure 3: Randomised and regular (in inset) geometry structures

2.2 Manufacturing of the prototypes

SLM solid structures are defined by the laser point distance, hatch distance and exposure time of the laser beam. A series of thin walls were manufactured to understand the relation between these as shown in Figure 4.

Then a series of solid blocks were fabricated using a point distance of 0.01mm with various exposure times and hatch distances as shown below.

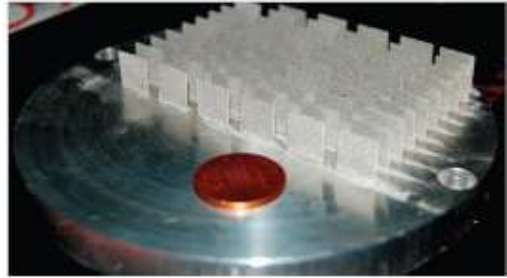


Figure 4: Al6061 thin walls made by SLM

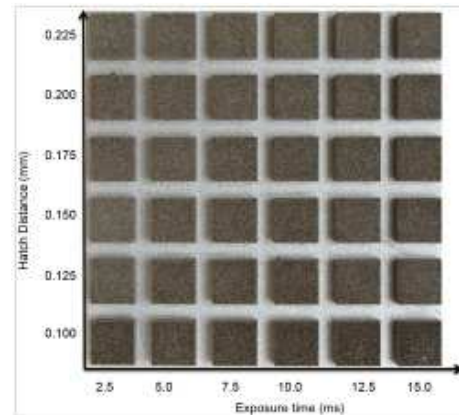


Figure 5: Al6061 solid blocks fabricated with different exposure times and hatch distances

SLM has previously been used for making porous structures e.g. porous finned heat sinks but only in the course of this project it has been used, for the first time, to make porous structures to work as a heat pipe capillary wick.

Initially, regular porous structures of 15x15x15 mm block of 300, 500 and 700 μm octahedral unit cell sizes were manufactured. The porous structures with 500 μm and 700 μm unit cell porous structures were brittle, requiring higher energy for melting. This was achieved by manufacturing them at a higher exposure time. Figure 6 shows regular and 30% randomised porous structures manufactured from Al6061.

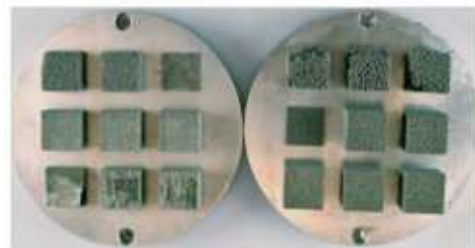


Figure 6: Al6061 regular (left) and 30% randomised (right) blocks fabricated with 300, 500 and 700 μm unit cell sizes from bottom row to the top row respectively

A set of porous samples were also manufactured for permeability testing. These specimens were

manufactured in $\phi 13$ mm porous structures surrounded by thin solid wall of 0.2 mm, Figure 7. Therefore during permeability test, water will flow through top and bottom surfaces of the porous specimen, but there is no leakage along its length and through side walls.



Figure 7: Porous samples made for permeability measurements. Different tries improved the quality as shown above from first build on the left to the 3rd build on the right

After analysing the solid and porous structures various designs were proposed for manufacturing heat pipes on SLM. In order to check the feasibility to manufacture the proposed designs, specifically axial grooved heat pipe (AGHP), a preliminary 20 mm section of heat pipe was built in titanium. Then the same geometry was made from Al6061 and 60mm length.

Al6061 was being used in SLM for the first time while there is a lot more knowledge about handling AlSi12 in SLM process so other samples were made using AlSi12. These samples were to prove the ability of SLM in manufacturing complicated wick structures. In total four different wicks structures were manufactured, axial grooved wick (porous fins), annular wick, graded wick (different thickness and porosity in the evaporator and condenser sections of the pipe) and arterial wick (small ducts fabricated into an annular porous wick to facilitate the return of the working fluid condensate from the condenser). These are shown in Figure 8 and 9.



Figure 8: Arterial wick heat pipe made from AlSi12. (Small ducts inside the wick can be seen)

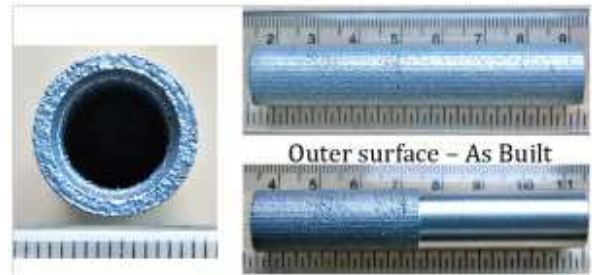


Figure 9: Annular wick heat pipe from AlSi12. Right top shows the outer surface of the pipe as built and right bottom after getting machined partially

One end of these heat pipes is already sealed and the whole heat pipe including the bottom cap, solid walls and porous wick is built in a single process. Obviously the top cap and fill tube can also be made as integrated parts of the heat pipe.

3. Analyzing the samples and prototypes

The density of the SLM solid structures was measured for different SLM machine settings. This value changes from 74.03% to 98.87% for different exposure times and hatch distances. These are the average of density measurements on several samples of each type. This was a comparative study. The main interest was to figure out how changing the machine settings affect the density of the solid parts rather than the absolute values of the densities.

Considering the high vapour pressure of ammonia it is still not known if this density is enough for the pipe solid walls to provide required strength and leak freeness.

Heat pipe samples all passed the bubble leak test. The air inside the pipe was pressurised up to five bars under water and no bubble was observed. Samples were also tested for helium porosity. In this method the pressure inside the tube is brought down to 10^{-7} Torr and helium is blown over the outer surface. Any helium leakage into the pipe is detected by the instrument.

Overall permeability of all the porous samples was measured by a test rig specifically made for these samples. Water flow rate through the sample was measured at a constant back pressure (constant water level above the sample) and assuming a unidirectional and steady flow Darcy's law (Equation 1 below) was used to calculate the bulk permeability;

$$V = \frac{Q}{A} = \frac{K}{\mu} \left(\frac{\Delta P}{l} \right) \quad 1$$

Measured permeability for different samples are shown in table 1;

Table 1 Measured permeability for different SLM made porous structures

Sample	Description	Permeability	Sample	Description	permeability
1	500µm, Random	1.12×10^{-10}	11	300µm, Regular	2.22×10^{-13}
2	500µm, Random	1.47×10^{-10}	12	300µm, Regular	3.31×10^{-13}
3	500µm, Random	2.06×10^{-10}	13	300µm, Regular	3.23×10^{-13}
4	500µm, Random	1.93×10^{-10}	14	300µm, Regular	2.70×10^{-13}
5	500µm, Random	1.53×10^{-10}	15	300µm, Random	2.95×10^{-13}
6	500µm, Regular	2.74×10^{-10}	16	300µm, Random	3.80×10^{-13}
7	500µm, Regular	2.85×10^{-10}	17	300µm, Random	7.80×10^{-13}
8	500µm, Regular	2.86×10^{-10}	18	300µm, Random	4.70×10^{-13}
9	500µm, Regular	2.86×10^{-10}	19	300µm, Random	2.85×10^{-13}
10	500µm, Regular	2.52×10^{-10}	20	300µm, Random	1.65×10^{-13}

Permeability changes from 10^{-10} m^2 for 500µm unit cell samples to 10^{-13} m^2 for 300µm samples and no meaningful difference was observed between the random and regular porous structures.

SLM porous structures are believed to have negligible number of isolated pores due to the nature of the process thus almost-identical effective porosity and total porosity.

Porosity of the SLM porous samples was measured by imbibition method. In this method a sample is immersed in a preferentially wetting fluid under vacuum for a sufficiently long time to let the fluid to imbibe into all the pores. The sample is weighed before and after imbibition. These two weights, coupled with the density of the fluid, permit calculation of the pore volume. By knowing the sample's bulk volume and pore volume the porosity can be directly calculated. The samples were kept inside oven at 125°C for several hours to make sure that they are completely dry and then weighed. Then each sample was immersed in water inside a vacuum chamber for 5 minutes and was weighed again.

Porosity value changes from around 20% in 300µm regular structures to about 60% in 500µm regular samples with a sensible difference between regular and random structures.

4. CONCLUSIONS

In continuation of this project the pore radii of the porous samples will be analysed under electronic microscope. Then SLM machine settings will be specified to achieve the most optimum set of permeability, porosity, pore radii values and another set of heat pipes will be built using those settings.

Special separate fill tubes have been made and the very complicated process for welding them to the heat pipe samples is being developed. Once these all are done, heat pipe samples will go through the filling, venting and thermal performance test process and the results will be presented in future papers.

NOMENCLATURE

A: Cross sectional area of the porous sample, m^2

K: Bulk permeability, m^2

l: Porous sample length, m

ΔP : Hydrostatic pressure drop of the liquid along the length, l, of the sample, Pa

Q: Fluid volume flow rate, m^3/s

V: Fluid velocity, m/s

μ : Fluid dynamic viscosity, Pa.s (kg/m.s)

ACKNOWLEDGEMENT

Ameli gratefully acknowledges the support provided for this project by the School of the Built and Natural Environment at Northumbria University and Thermacore of Ashington UK.

REFERENCES

- Almeida, R. (2004). NOVEL, COMPOSITE WICKS (FOR TWO-PHASED LOOPS), European Space Research and Technology Centre.
- Anderson, W. G., P. M. Dussinger, et al. (2008). "High Temperature Titanium-Water and Monel-Water Heat Pipes." *Aerospace*: 1-12.
- Bai, L., G. Lin, et al. (2009). "Experimental investigation of startup behaviors of a dual compensation chamber loop heat pipe with insufficient fluid inventory." *Applied Thermal Engineering* 29: 1447-1456.
- Ho, C. (2003). "Roadmap for developing heat pipes for ALCATEL SPACE's satellites." *Applied Thermal Engineering* 23: 1099-1108.

Liu, Z., P. Chong, et al. (2006). "Fundamental understanding of the corrosion performance of laser-melted metallic alloys." *Surface and Coatings Technology* 200: 5514-5525.

Mercelis, P. and J.-P. Kruth (2006). "Residual stresses in selective laser sintering and selective laser melting." *Rapid Prototyping Journal* 12: 254-265.

Yadroitsev, I., P. Bertrand, et al. (2007). "Parametric analysis of the selective laser melting process." *Applied Surface Science* 253: 8064-8069.

PRESSURE CONTROLLED HEAT PIPE APPLICATIONS

William G. Anderson, John R. Hartenstine, David B. Sarraf, Calin Tarau, and Kara L. Walker

Advanced Cooling Technologies, Inc.

1046 New Holland Ave., Lancaster, PA 17601 U.S.A.

717-295-6061, 717-295-6064 Fax, Bill.Anderson@1-act.com, John.Hartenstine@1-act.com,

Calin.Tarau@1-act.com, Kara.Walker@1-act.com

ABSTRACT

In a Variable Conductance Heat Pipe (VCHP), a Non-Condensable Gas (NCG) is added to the heat pipe to vary the condenser length, and hence the conductance. A Pressure Controlled Heat Pipes (PCHP) is a modified VCHP, where the heat pipe operation is controlled by varying either the gas quantity or the volume of the gas reservoir. This paper will discuss two applications for PCHPs: 1. Precise temperature control, and (2) Switching thermal power between multiple sinks. A prototype aluminum/ammonia PCHP was built and tested to demonstrate the capability of controlling the temperature of the evaporator section of an aluminum/ammonia pressure controlled heat pipe to milli-Kelvin levels over an extended period of time, while the heat sink temperature and evaporator power were varied. In a second program, a heat pipe solar receiver was designed to accept, isothermalize and transfer the solar thermal energy to reactors for oxygen production from lunar regolith. The receiver has two PCHPs and two Constant Conductance Heat Pipes (CCHPs) to supply heat to two reactors. During operation, one reactor is producing hydrogen at low solar power, while the other reactor is warming up a fresh batch of regolith. The PCHPs are used to switch power between the two reactors as required.

KEY WORDS: Pressure Controlled Heat Pipes, PCHPs, Precise Temperature Control, High Temperature Power Switching

1. INTRODUCTION

In a Variable Conductance Heat Pipe (VCHP), the non-condensable gas (NCG) mass and volume are fixed. When the heat load increases or the radiator sink temperature increases, the temperature (and pressure) of the heat pipe also increases. The increase in vapor pressure forces more of the NCG gas into the reservoir, which moves the vapor/NCG gas interface further into the condenser, and increases the effective condenser conductance. This change in conductance allows a VCHP to maintain a relatively constant temperature as the power or heat sink conditions change. With a heater on the reservoir, the VCHP temperature can be maintained within a few degrees Celsius.

Pressure Controlled Heat Pipes (PCHPs) are similar to VCHPs. The vapor/NCG interface position in the condenser moves to vary the conductance of the heat pipe. The control mechanism in a PCHP, however, is active. This provides much closer control of conductance and can allow changing of the set point temperature after assembly of the heat pipe. Two different control mechanisms are possible: actively injecting or removing NCG, or by varying the volume of the

reservoir by contracting or expanding a bellows. PCHPs were initially developed for precise temperature control of annular heat pipes operating in the region of 1300K. Using a gas injection mode of control, the PCHP operating temperature was stabilized against changes of input power or heat loss to within 0.001K for several hours (Bienert, 1991).

Modulation of the reservoir volume is the other method of controlling the PCHP. In this concept, the NCG reservoir includes a bellows structure. A linear actuator is used to drive the position of the movable end of the bellows, thus modulating the volume of the reservoir; see Figure 1. The bellows system was selected for the PCHPs below, since it is simpler to implement for space applications.

2. PCHPS FOR PRECISE TEMPERATURE CONTROL

Regardless of the method used, it is the variable reservoir volume or variable NCG charge that allows the PCHP to define a set point (over a wider temperature range), and to control temperature precisely about that set point. In contrast, even with an unusually large reservoir, conventional

VCHPs in a thermal network have a fixed set point, and are not capable of precision temperature control to the milli-Kelvin level.

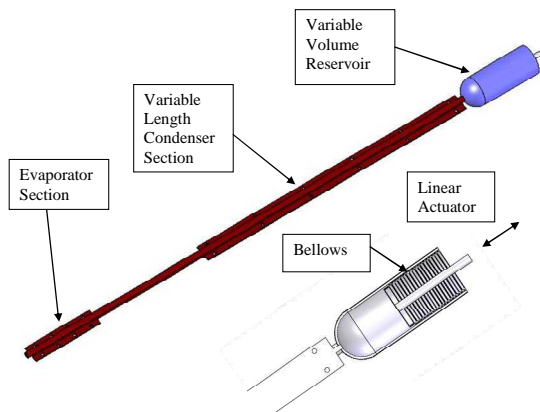


Figure 1. Volume Modulated PCHP.

Pressure Controlled Heat Pipes have three major advantages over conventional CCHPs, VCHPs, and Loop Heat Pipes (LHPs):

- Precise temperature set point control to the milli-Kelvin level without power-wasting trim heaters and without a massive reservoir.
- Nearly instantaneous reaction to changes in the environmental conditions (low thermal mass lag).
- Ability to adjust the set point in-situ. Thermal analysis and ground testing can differ by as much as $\pm 10K$ from the results in space. The PCHP compensates for these discrepancies in real time after the satellite has been placed in orbit.

The control scheme for the PCHP for precise temperature control is shown schematically in Figure 2. With a suitable feedback control system, the PCHP can achieve milli-Kelvin temperature control of evaporator temperature while compensating for changes in sink temperature or input power without the need for the large VCHP reservoir.

2.1 PCHP Design for Precise Temperature Control

The design requirements, shown in Table 1, were selected for a hypothetical but typical spacecraft cooling application in low earth orbit. The design parameters for the PCHP are shown in Table 2.

One of the flight-weight devices is shown in Figure 3. It is mounted on a test fixture with electrical heaters at the evaporator and a liquid nitrogen (LN) chill block at the condenser. Heat from the stepper motor is rejected to the condenser through the

cooling strap. The bellows is contained in the bellows capsule, which assures alignment and prevents overstressing due to accidental over-travel. The PCHP body is bent to fit into a particular thermal-vacuum system.

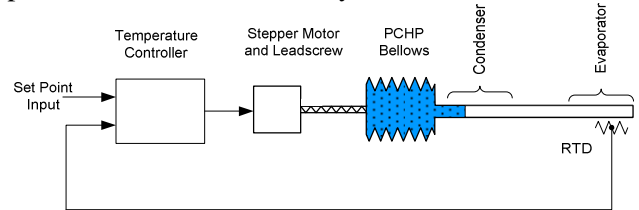


Figure 2. Schematic of Pressure Controlled Heat Pipe showing feedback control of reservoir volume and condenser thermal resistance.

Table 1: Temperature control PCHP design requirements.

Parameter	Value
Evaporator Temperature Stability	0.001K
Evaporator Input Power	50-150 Watts
Evaporator Temperature	20°C
Sink Temperature	-40°C to 0°C
Life	10 years minimum
End Use	Small Satellite on Low-Earth Orbit
Number of Orbits	~58,400
Working Fluid	Ammonia
Evaporator	3.8cm wide x 15.2cm long
Condenser	3.8cm wide by 30.5 cm. long

2.2 PCHP Qualification Tests

One of the objectives of the program was to demonstrate that the components used can be flight qualified and that they will have a long life in a flight environment. In addition to the thermal control tests, discussed below, the following tests were conducted:

- Proof pressure testing.
- Bellows assembly cycle testing to demonstrate the ability to withstand the number of flexures required over a 10 year life.
- Cycle testing the selected stepper and drive to demonstrate operation in vacuum.
- Shock and vibration testing.

Details of these qualification tests are given in Anderson et al. (2011).

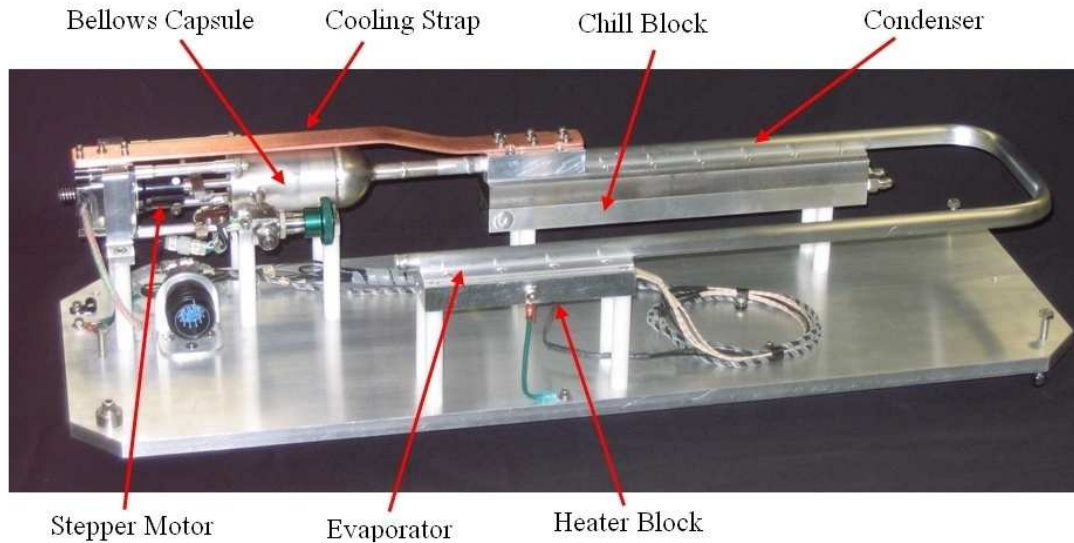


Figure 3. Photograph of PCHP on its test fixture.

Table 2: Temperature control PCHP parameters.

Evaporator Length	6" (150 mm)
Condenser Length	6" (150 mm)
Overall Length	16" (400 mm)
Extrusion diameter	½" (12.5 mm)
Flange Width	1.5" (38 mm)
Working Fluid	Ammonia, 7.4 gm ⁽¹⁾
Stepper Motor	Size 23
Bellows	SS-1000-50-44
Bellows Displacement	8.98 cm ³
Reservoir Average Volume	110 cm ³
Condenser Volume	5.22 cm ³
Reservoir/Condenser Volume Ratio	29:1

2.2 PCHP Temperature Control

For testing, the PCHP was mounted to a rigid aluminum fixture with screws at each corner to precisely adjust the PCHP inclination. The PCHP evaporator and condenser flanges were bolted to rectangular aluminum blocks that supply heat and serve as a heat sink. The whole system was then inserted in a thermal vacuum chamber. Details of the test setup are given in Anderson et al. (2011). The PCHP had excellent temperature control during the thermal vacuum tests. Figure 4 compares the open-loop and closed-loop response of the PCHP over variations of input power. This PCHP is able to maintain a steady evaporator temperature (measured by the RTD) over input powers ranging from 50 to 125 Watts. In the figures, Open Loop refers to the no control case, or

behavior as a passive VCHP, and SP refers to the Set Point Temperature in closed loop mode.

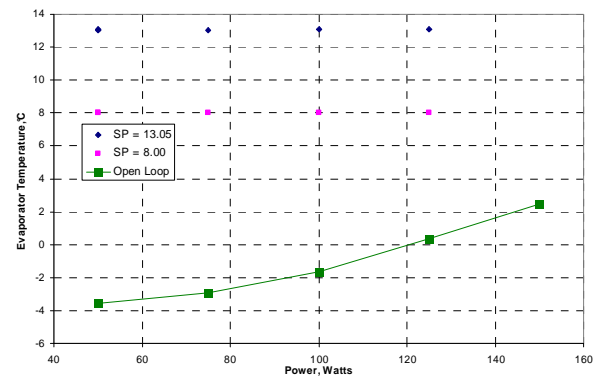


Figure 4. Comparison of Open Loop and Closed Loop response of the PCHP in vacuum over changes of input power.

3. PCHPs FOR POWER CONTROL AT HIGH TEMPERATURES

A second application for PCHPs is their ability to switch power between different reactors at high temperatures for In-Situ Resource Utilization (ISRU). The lunar soil consists of approximately 43% oxygen that is contained within the oxides of the lunar soil. Oxygen is produced by heating the regolith to 1050°C, then flowing hydrogen through the regolith. The hydrogen reacts with the oxygen in the lunar regolith to produce water. The water is then electrolyzed to produce oxygen, and the hydrogen recycled into the process. The mass of the overall system can be minimized if one solar concentrator supplies a constant rate of power to two reactors, with the power switched from one reactor to the other as fresh batches of regolith are added.

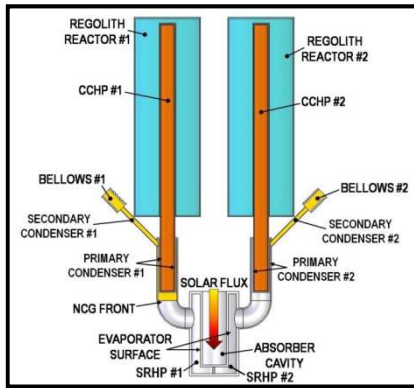


Figure 5. Schematic of the PCHPs (shown as SRHP #1 and #2) and CCHPs used to transfer heat to the two reactors.

3.1 PCHP for Lunar Regolith Design

A Pressure Controlled Heat Pipe (PCHP) is a viable solution to utilize a single energy source to provide heat to two separate reactors; see Figure 5. The assumed base location is near the lunar South Pole, so the sunlight is always coming from near the horizon. The sunlight is focused with a solar concentrator that directs the solar energy down into the central Solar Receiver Heat Pipe (SRHP). The system components include:

1. Two SRHPs, one for each regolith processing reactor.
2. Two CCHPs, one for each reactor.
3. A primary condenser on each SRHP.
4. A secondary condenser on each SRHP, with bellows to vary the reservoir volumes.

The SRHPs are used to control the gas front location, and therefore control the power delivered to each reactor. The CCHP transfers the thermal load to the reactor from the variable conductance SRHP. CCHPs are used to provide uniform heating to the regolith. The change in the exposed length of the two condensers of each SRHP would vary as the power was transferred. The secondary condensers provide a method to reject excess heat, so that the concentrator can always deliver the full heat load to the SRHP.

The SRHP is divided into two halves that are thermally connected, with Non-Condensable Gas (NCG) added to each side. Each half has a side arm which serves as a primary condenser, a secondary condenser and a bellows. During steady-state operation, one reactor is gradually heating the regolith, while the other reactor is extracting oxygen. The bellows are used to control the location of the gas fronts on each side, and hence the heat supplied to each side.

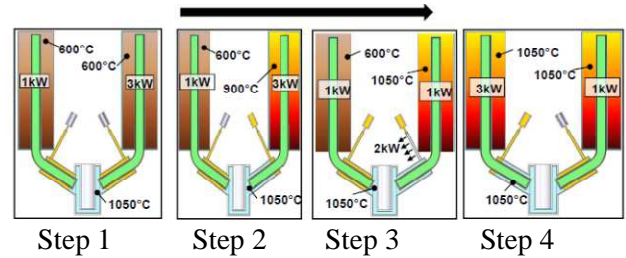


Figure 6. Schematic of the initial Lunar regolith PCHP startup. The NCG is shown in yellow

A projected operational scenario for the start up and operation of a multiple reactor system is shown in Figure 6:

Step 1. The SRHPs are at 1050°C, and cold regolith (600°C) is loaded into the reactors. During the loading, the bellows are fully extended, so gas blocks the CCHP evaporators. This is done to maintain the temperature of the SRHPs, which otherwise would quickly drop to 600°C, due to the high power capabilities of the heat pipe. Once the regolith is loaded, the gas in the Right Hand Side (RHS) is withdrawn slightly, so that 3 kW is supplied to warm up the RHS reactor.

Step 2. As the RHS reactor warms up, the driving force between the heat pipes and the regolith diminishes. The RHS bellows is gradually withdrawn to maintain the 3 kW heating. The picture in Step 2 shows the NCG gas completely withdrawn from the RHS CCHP evaporator.

Step 3. As the RHS temperature approaches the final 1050°C temperature, the ΔT diminishes so that less than 3 kW of power can be conducted into the RHS reactor. The excess power is radiated from the secondary condenser. The picture in Step 3 shows the condition when the RHS reactor is at 1050°C: 1 kW is supplied to the reactor to make up thermal losses, and the other 2 kW is radiated. At this point, the RHS reactor is at temperature. Hydrogen then flows through the reactor to produce water, which is electrolyzed to produce oxygen.

Step 4. The 3 kW of heat is then supplied to the LHS reactor to warm up the regolith, while the RHS reactor produces oxygen. When the oxygen has been removed, fresh regolith is added, and the cycle repeats.

3.2 PCHP for Lunar Regolith Fabrication

The high-temperature double-sided system has an annular SRHP split in two halves, each with its own side arm, CCHP, secondary condenser and bellows/stepper motor assembly; see Figure 7. The evaporator for the system is located on the exterior surface of the inner vertical pipe. Each SRHP has

a separate evaporator, with the vapor space split into two halves by welding a thin Haynes 230 plate on the inside, so that each side of the SRHP (represented in Figure 5 as #1 and #2) has a fixed amount of NCG.

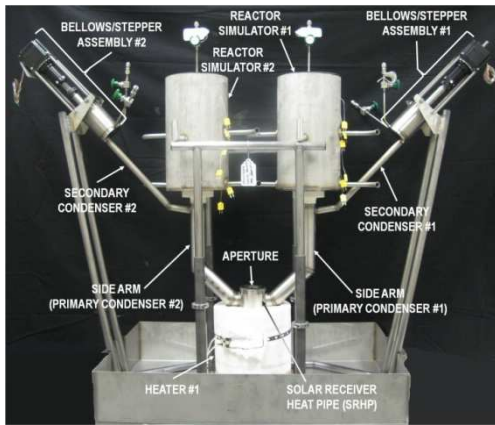


Figure 7. Dual sided Haynes 230 demonstration system test setup.

3.1 High Temperature PCHP Testing

Prior to testing, the side arms (primary condensers) were covered with 5 cm of Microtherm insulation. The vertical, annular portion of the system was insulated using the insulation package provided with the ceramic heater. Kaowool was also used as extra insulation and covered the entire system with the exception of the secondary condensers.

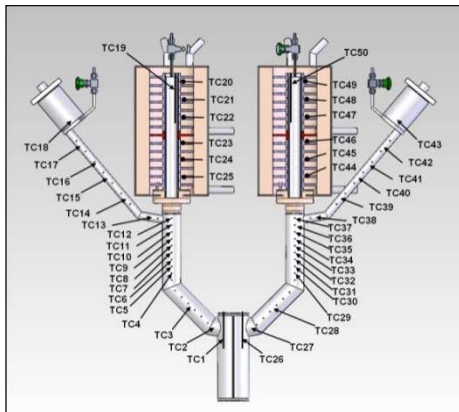


Figure 8. TC map for the dual sided Haynes 230 demonstration system.

The thermocouple locations for the test setup are shown in Figure 8. The temperature of the “regolith” is the average of 6 intrusive TCs at equidistant locations along the vertical direction inside the “regolith” at the mid distance between the cylindrical case and the central axis. During testing, the total power between the two heaters was set to approximately 3.5kW, and was held constant. This power represents the constant power the system would receive from a solar concentrator during actual operation. The transient

behavior of the dual sided system during a dual cycle time period is shown in Figure 9 (left side) and Figure 10 (both sides). The left side of the system was operated through two full cycles (charging-processing-replenish represents one full cycle) while the right side was operated through one and a half cycles. Four temperatures are represented on the primary ordinate axis for each reactor:

- SRHP vapor temperature, TC1 & TC26
- Vapor temperature at the entrance of the secondary condenser, TC13 & TC38 (indicates when NCG front enters the secondary condenser)
- Vapor temperature in the CCHP condenser, TC19 & TC50
- Average “regolith” temperature.

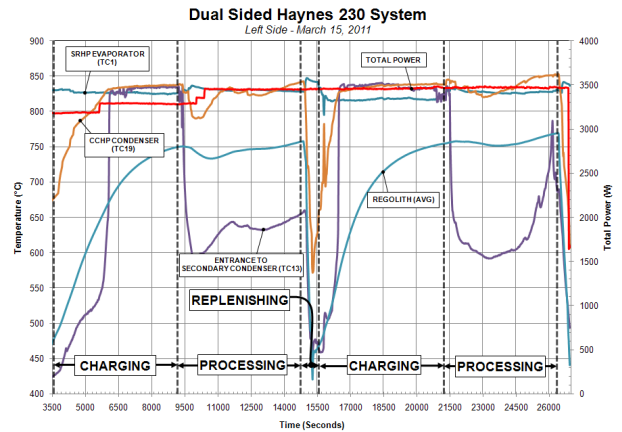


Figure 9 Dual sided Haynes 230 & sodium demonstration system - left side operation.

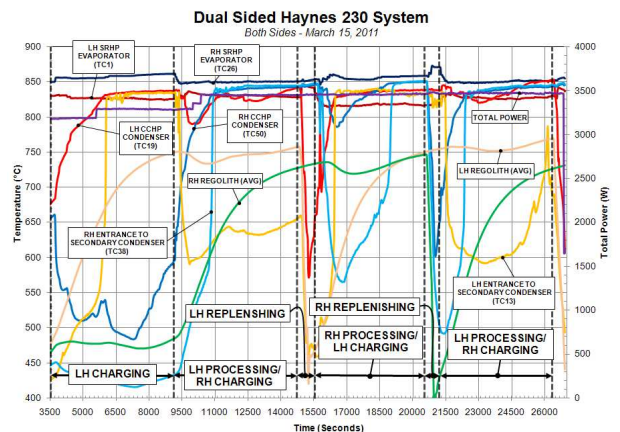


Figure 10. Dual sided Haynes 230 & sodium demonstration system - both sides operating.

Testing of the dual sided system was conducted at lower temperatures than the nominal operating temperature of 1050°C. This decision was made to be conservative and protect the heaters from an over temperature condition. Another reason for lowering the operating temperature was to decrease the heat losses from the system, since it was tested

in air rather than vacuum. An operating temperature of 850°C was chosen. Testing of the dual sided system was performed manually. The temperature set points were designated as follows:

- Regolith preheat temperature ~ 470°C
- SRHP vapor temperature ~ 850°C
- Regolith processing temperature ~ 750°C

As seen in the figures, the SRHP evaporator vapor temperature was maintained relatively constant for both sides through all stages of the cycle. A roughly 10°C ΔT was experienced across the wall that separates the two SRHP vapor spaces, as a result of the heat flux transmitted through the splitting plate from one evaporator to the other because of the unbalanced heat load through the two SRHPs. The first charging stage for both the left and right hand sides of the system took approximately 92 to 94 minutes. Charging for the second cycle took approximately 84 to 86 minutes. A ΔT of approximately 100°C was experienced for both sides between the CCHP vapor temperature and the average regolith temperature. The fluidized bed used in a true regolith reactor would greatly reduce this ΔT due to the higher effective thermal conductivity.

Soon after charging starts, a sharp increase in the secondary condenser temperature is experienced in TCs 13 and 38 for the left and right sides, respectively. This occurs when the NCG front reaches the entrance of the secondary condenser, rejecting the excess power that cannot be conducted into the regolith. This can be seen graphically as the CCHP vapor temperature at this moment has reached approximately 830°C for the left hand side and 840°C for the right side. A drastic drop in temperature is observed in the CCHP vapor, regolith and secondary condenser during the replenishment stage of the cycle. At this moment the forced air cooling systems for the regolith reactor simulator was turned on to simulate the removal of processed regolith and addition of new regolith. The regolith temperature was maintained near constant for all processing cycles for both the left and right hand sides of the system. A slight dip in temperature is observed in both reactors during processing due to more power being transferred to the opposite side to aid in charging, which is the power heavy stage in the full cycle. To summarize, testing of the dual reactor system was completely successful.

4. CONCLUSIONS

PCHPs are a variant of VCHPs, where the amount

or volume of NCG in the heat pipe can be adjusted for control of the thermal conductance. PCHPs can be used for precise temperature control at the milli-Kelvin level, and for switching power at high temperatures, where there are no known alternatives.

PCHPs for Precise Temperature Control: A series of aluminum/ammonia PCHPs were fabricated that achieved good closed-loop feedback control. The ammonia PCHP was able to maintain a constant evaporator temperature over changes of input power from 50-150 Watts and changes of sink temperature from -10°C to -40°C. The ammonia PCHP met the goal of milli-Kelvin control, by demonstrating a standard deviation of 0.006K in evaporator temperature over time.

PCHPs for Power Switching: Two PCHPs with integral CCHPs were used to control the thermal loading from a single solar source to multiple lunar regolith oxygen processing reactors. The amount of thermal energy was adjusted between multiple reactors by varying the volume of non-condensable gas (NCG) in the PCHP using a bellows or piston and stepper motor.

ACKNOWLEDGEMENT

The PCHPs for Precise Temperature Control program was sponsored by NASA Goddard under Contract No. NNX08CA35C. Laura Ottenstein of NASA GSFC was the program technical monitor. The PCHPs for Lunar Regolith program was sponsored by NASA Glenn Research Center under Purchase Order No. NNX09CA48C. Don Jaworske, NASA/GRC, was the technical monitor for the program.

REFERENCES

- Anderson, W.G., Hartenstine, J.R., Sarraf, D. B., and Walker, K. L., *Pressure Controlled Heat Pipes*, 41st International Conference on Environmental Systems (ICES 2011), Portland, OR, July 17-21, 2011.
- Bienert, W., *Isothermal Heat Pipes and Pressure-Controlled Furnaces*, *Isotech Journal of Thermometry*, 2(1), pp. 32-52, 1991.
- Hartenstine, J. R., Walker, K. L., Tarau, C., and Anderson, W. G., "PCHP Solar Receiver for Regolith Oxygen Production with Multiple Reactors," 49th AIAA Aerospace Sciences Meeting, Orlando, FL, January 4-7, 2011.

Experimental performance comparison of axially grooved heat pipes charged with acetone and ammonia

Jorge Bertoldo Junior, Valeri V. Vlassov, Pedro Antônio Cândido, Gino Genaro
Instituto Nacional de Pesquisas Espaciais – INPE,
São José dos Campos – SP, Brasil.
jorge.bertoldo@inpe.br

Valery M. Kiseev
Ural State University - USU
Ekaterinburg, Russia

ABSTRACT

To validate proposed axially grooved heat pipe, designed to work with acetone, comparative characterization tests have been conducted for two heat pipes, having the same profile height of 19.1 mm, and length of 730 mm. First heat pipe is charged with acetone and has unique core however the second heat pipe, charged with ammonia, has two cores. Both heat pipes are directed to Space application and have profiles with similar flat interfaces to fit inserting in honeycomb satellite panels. Two different characterization tests were performed. First, an inclination test conducted by means of a motorized table; second, a dry-out test in horizontal position at different temperatures. The characteristic curves were obtained for both HP profiles under symmetrical heating/cooling

KEY WORDS :heat pipe, thermal stabilization of satellite panels, HP performance test, ammonia, acetone.

1. INTRODUCTION

Historically, when heat pipes (HPs) first were recognized in 1960's as promising devices for thermal control in space applications, aluminum HPs with different fluids began to be developed and tested. The fluids were mainly freons, ammonia, methanol, and propylene. Soon after the aluminum-ammonia HP demonstrated best heat transport capability, which allowed the producing of light HPs with very small diameter (about 10 - 20 mm); the technology was space-qualified and other technologies were restricted for special applications. Traditionally, aluminum-ammonia HPs are used in thermal control systems, because ammonia has appropriate temperature range and high Liquid Transport Factor.

There are two main kinds of heat pipe applications in satellites: (i) for transferring heat to radiator over large distances from areas where are equipment with high heat dissipation or; (ii) for spreading heat over a structural panel to minimize the thermal gradients over it and finally reduce the equipment temperature. In many cases where HPs are embedding in honeycomb panels, larger diameter tubes are quite desirable because they can provide higher area of thermal contact with the panel face-sheet and fits the panel thickness.

In such applications the acetone heat pipes can compete with ammonia HPs; their lack of performance can be compensated by a particular design, as increasing the cross section area of the tube. Also, other criteria may be adopted on working fluid choice, in terms of vapor pressure, toxicity and dangerousness.

As quoted by Nakamuro et al, 1984, ammonia heat pipe need to have a wall thickness high enough to endure the vapour pressure at temperature of ~120°C which is the imbedding process temperature to cure adhesive. Acetone heat pipe would not have this problem because the pressure inside the tube don't offer explosion risks during imbedding process.

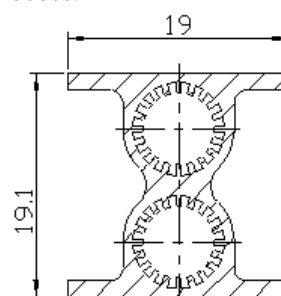


Figure 1.a) Ammonia Heat Pipe Profile

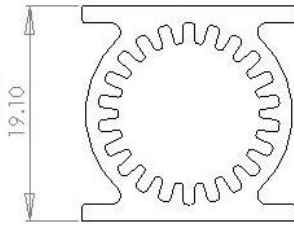


Figure 1.b) Acetone Heat Pipe Profile

Acetone-copper heat pipes already have been used in thermal control of the Mageon 4 and 5 satellites, which was in operation for more than 4 years (Baturkin et al, 2002); flat aluminium-acetone mini HPs are produced to cool electronics for domestic and industrial applications. Al-acetone groove HPs have never designed no produced and qualified for Space applications up to now, as we can monitor through available publications.

In order to exploit the advantages and disadvantages of heat pipes charged with low-pressure fluids, INPE adopted a research program CONTER (when PJHPACETONA), which includes the development of two phases technologies employing low-pressure and low hazardous working fluids (Vlassov, 2008).

Finally, a HP axially groove profile was designed and optimized to have the acetone as a working fluid and to fit the honeycomb satellite panels of 20 mm thickness, see Fig. 1b. This profile is suitable for a low-pressure fluids and is a less dangerous alternative of ammonia HPs (Fig. 1a) used in CBERS series satellites.

2. EXPERIMENTAL SETUP

The HP thermal performances are investigated using the classical test setup, presented in the Fig. 2.

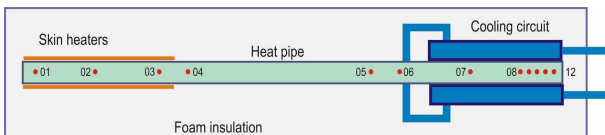


Figure 2. Heat Pipe test setup

The heat pipe is held with a supporting insulation fixture. Heat is applied to one end symmetrically from above and from below of heat pipe with a skin electrical heater and is removed from the opposite end by a coolant circuit controlled by thermostat. Thermocouples are attached along the

length of the heat pipe to measure the axial vapour temperature along the heat pipe at different positions, see Figure 2. An insulation system is used over the heat pipe to minimize the parasitic heat losses or inputs, see Figure 4 (Brennan P. & Krociczek, E., 1979).

The heat pipe is fixed firmly through insulation supports on structure of a motorized table (see Figure 3). Motorized test table can rotate in very slow angular velocity, 3.40 deg./min. Inclination angle is measured by a digital inclinometer, within 0.1 degree accuracy. Performance tests is conducted under different inclination angles and cooling liquid temperatures -20oC, 0oC and 20oC,

During preliminary tests, two types of dry-out were detected, like was purposed by Busse and Kemme, 1979, analysing the physical mechanism of the dry out in gravity assist heat pipes. There are two different types of dry out; first is when power is set at a fixed value and the motorized test table is rotated in very slow angular velocity, until the dry-out phenomenon occurs. This dry-out is characterized as complete, once the condenser temperature gets fast drop down following the fast rising up at evaporator end. Second type is when HP is set at horizontal position and power is gradually increased. In this case the dry-out is partial, which is detected following the PSS-49 standard criteria, where was take in consideration that partial dry out phenomena occurs when the difference between two consecutive points of the evaporator is at least five degrees.



Figure 3. Both heat pipes installed on rotation table

The heat transport characteristics, including maximum heat transfer capability and conductance, are determined through the measuring temperature distribution along both heat pipes under same heat load conditions.

We believe that the 1st type of dry-out (fixed power and increasing angle) corresponds the dry-out

mechanism that could take place under microgravity (0-G) condition, when the Marangony effect does the same work as the dynamic liquid moving, driven by slow test table rotation, which provokes a complete drying of the evaporation area. Busse & Kemme, 1979, proposed this way of dry-out conditions, keeping heat flux, temperature and all other design and operating parameters.

The 2nd mechanism, of partial dry-out, may only take place under 1-G condition, when the gravity effect on the excess liquid pool contributes to the liquid return. This phenomenon arises from a lack of hydrostatic driving force in grooves and appears when the heat flux increases (Busse & Kemme, 1979).

3. SIMPLIFIED ANALYTICAL MODEL FOR PERFORMANCE EVALUATION

We developed a simplified analytical model to predict basic HP performance, used well-known relationships for axially grooved HPs, presented in (Chi and (Faghri, 1995). The basic system of equations, used to compare with experimental data, is presented below.

Under maximal heat load, the capillary pressure must sustain hydraulic lost of liquid flow in grooves and vapor flow in HP core, as well as hydrostatic tilting component because of possible HP inclination. The capillary balance is expressed by

$$\Delta P_c^{\max} = \Delta P_l + \Delta P_v \pm \Delta P_g \quad (1)$$

Other components of pressure balance like interfacial shear pressure drop are neglected. Assuming the Darcy flow and conception of effective HP length to account variable mass flow rate in evaporator and condenser zones, the balance can be expressed as following

$$\frac{2\sigma \cos\theta}{w} = \frac{\mu_l Q_{\max} L_{\text{eff}}}{K\lambda\varepsilon\delta_p \pi D_v \rho_l} + \frac{128\mu_v Q_{\max} L_{\text{eff}}}{\lambda \pi D_v^4 \rho_v} \pm \rho_l g L \sin\beta \quad (2)$$

The simplified geometry presented in Fig. 4 was adopted.

Permeability is expressed by

$$K = \frac{d_{hg}^2}{2(f \text{ Re})} \quad (3)$$

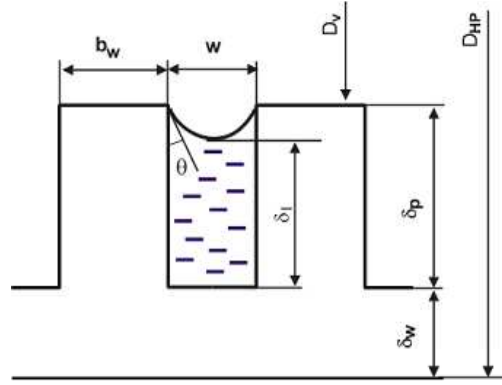


Figure 4. HP cross section parameters.

Shah and Bhatti in 1987 have found that for the rectangular channels

$$(f \text{ Re})_l = 24(1 - 1.3553a + 1.9467a^2 - 1.7012a^3 + 0.9564a^4 - 0.2537a^5) \quad (4)$$

This equation is applicable to the configuration shown in Figure 4 (Faghri, 1995).

The equation components are:

$$a = \frac{w}{\delta_p}; \quad \varepsilon = \frac{w}{w + b_w}; \quad \delta_l \cong \delta_p - \frac{w}{2};$$

$$L_{\text{eff}} = \frac{1}{2}(L_e + L_c) + L_a;$$

The groove hydraulic diameter expression is modified to account the average meniscus recession under maximal heat load:

$$d_{hg} = \frac{4\delta_l w}{(2\delta_p + w)} \quad (5)$$

Finally we have the expression for maximal heat transport capability:

$$(QL) = Q_{\max} L_{\text{eff}} = \frac{2\sigma \cos\theta \mp w \rho_l g L \sin\beta}{w \left(\frac{\mu_l}{K\lambda\varepsilon\delta_p \pi D_v \rho_l} + \frac{128\mu_v}{\lambda \pi D_v^4 \rho_v} \right)} \quad (6)$$

This expression is used to compare with experimental data for both acetone and ammonia HP; the last is factored by 2 in order to account two-core performance.

4.RESULTS

Fig 5 and 6 show the axial temperature distribution along the length for both HPs analysed, ammonia and acetone, at horizontal HP position and under different heat loads. It is possible to observe, that acetone HP presents elevated temperature differences between evaporator wall and vapor temperature and between vapor temperature and condenser zone. At the same time the temperature differences along the adiabatic sections are very small.

It can be explained by the following. Because of relatively wide grooves of acetone HP profile, the liquid phase does not fill all upper grooves, which provokes the liquid pool at the bottom of HP of significant volume. Such phase redistribution forms additional thermal resistances from both sides: liquid pool from the bottom and empty grooves from the above. Finally, this phenomena makes the temperature differences between evaporator and condenser sections to be significantly higher than for ammonia HP.

The heat pipe performance curve, that is the relation of average temperature difference between the evaporator and condenser zone to the maximal heat transport capability (QL), are presented in Figs. 7 and 8 for tests in horizontal position. The maximum heat transfer rate Q_{max} is defined as the heat load when dry-out occurs. The maximum heat transfer capability (QL) is defined as the product of Q_{max} and L_{eff} , L_{eff} is the effective length of the heat pipe (Nakamaru et al, 1984).

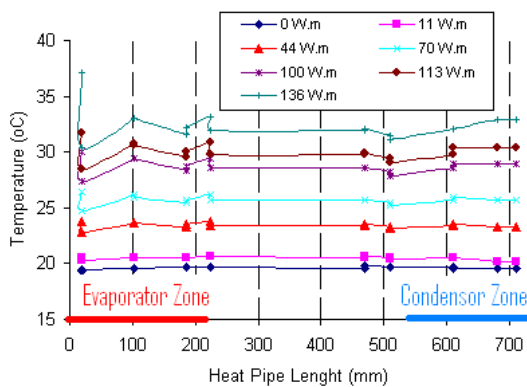


Figure 5. Temperature distribution along the ammonia heat pipe length.

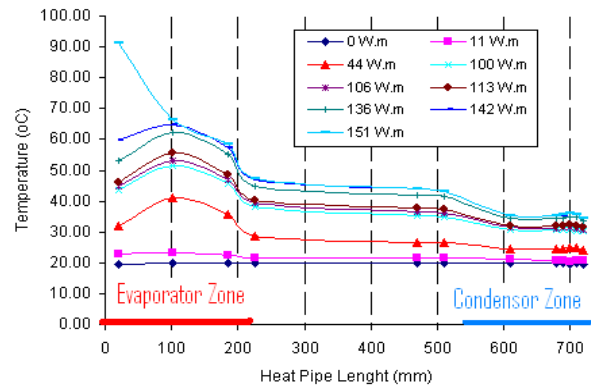


Figure 6. Temperature distribution along the acetone heat pipe length.

Predicting the maximum heat transfer capability under 0-G condition would be possible by a measurement of (QL) under different inclination angles. It is generally conducted for reason of the theoretical linear relation between the maximum heat transfer capability and the inclination of the heat pipe (Brennan P. & Krolczek, E., 1979) (Nakamaru et al, 1984).

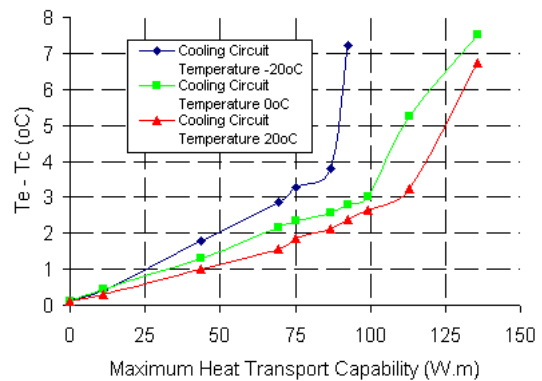


Figure 7. Ammonia Heat Pipe performance curve

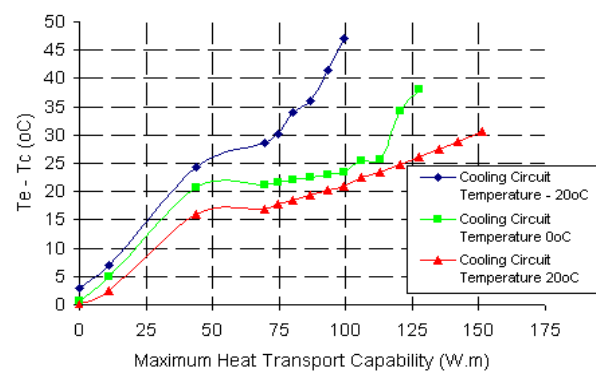


Figure 8. Acetone Heat Pipe performance curve.

The characteristics curves of the inclination test are presented in Figs 9 and 10 under different vapor temperatures. The tendency performs as expected: ammonia HP is less sensitive to inclination, then acetone HP. Acetone HP becomes still more sensitive to inclination under lower temperatures. .

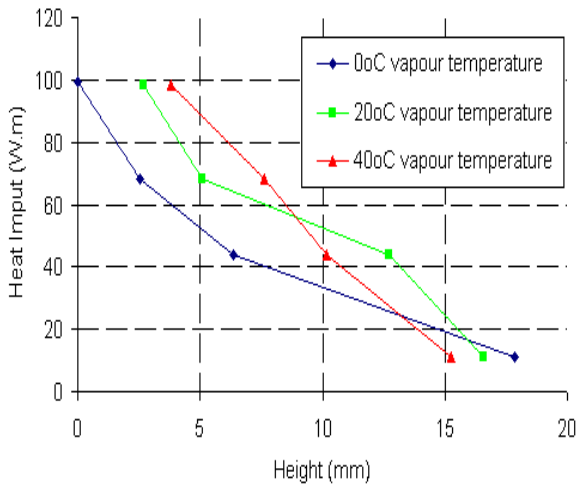


Figure 9. Ammonia Heat Pipe Inclination Test

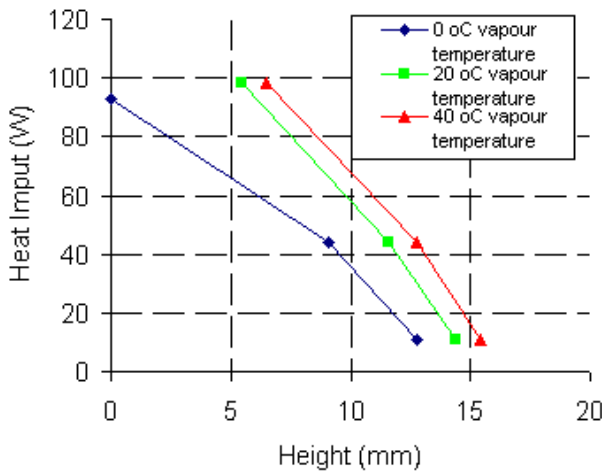


Figure 10. Acetone Heat Pipe Inclination Test

Next, the maximum heat transfer capability is taken up as function of vapor temperature. In figure 11 it is possible to see the theoretical and experimental results for both HPs. Obtained magnitudes of maximal heat transport capability (QL) are similar within about $\pm 30\%$ for both HPs, having acetone HP QL better values under higher temperatures (above +30C) and vice-versa in lower temperatures

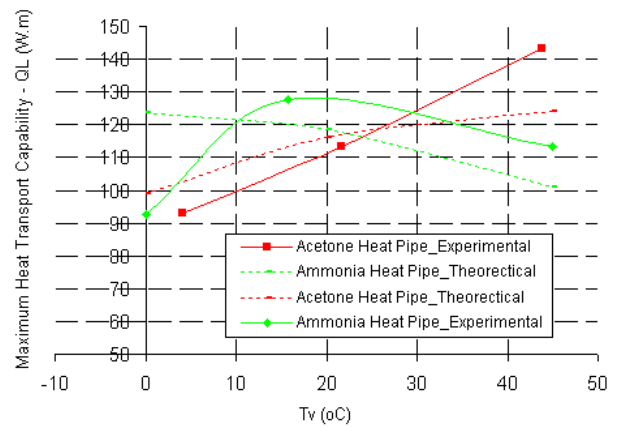


Figure 11. Comparison between theoretical and experimental maximum heat transport capability.

In case of axial grooved heat pipes, in higher temperature ranges, the excess of liquid of the working fluid forms liquid puddle at lowest point of the heat pipe because of the variation of liquid density and non connection between groove. Probably not all upper grooves are filled with liquid, that contributes to the volume of the puddle. The bottom grooves, which are partially submerged, shows a reduction in their effective transport length and the actual effective elevation increases the maximum heat transfer capability (Nakamaru, et al, 1984). This situation partly explains the observed discrepancies between the theoretical and experimental results.

5. CONCLUSIONS

The conducted tests confirm that two-cores ammonia HPs can be substituted with one-core acetone HP for the application in honeycombs satellite panels of specified thickness of 20 mm. Obtained magnitudes of maximal heat transport capability (QL) are similar within about 30% for both HPs, having acetone HP QL better values under higher temperatures (above 30C) and vice-versa in lower temperatures, that is expected through fluid properties.

At the same time, acetone HPs presents additional difficulties for testing in 1G conditions as well as to interpret the test results. Because of relatively wide grooves, the liquid phase does not fill all upper grooves, which provokes the liquid pool at the bottom of HP of significant volume. Such phase redistribution forms additional thermal resistances that make the temperature differences between evaporator and condenser sections to be significantly higher than for ammonia HPs. In

inclination test the Acetone HP presents more sensitivity to tilting that establishes more exigent requirement for leveling when testing at 1G conditions.

Anyway, in 0G conditions it is expected all grooves of acetone HP being filled with liquid, and these thermal resistances do not appear.

NOMENCLATURE

σ – surface tension
 μ - dynamic viscosity
 ρ - density
 λ -latent heat
 ε - porosity
 β - inclination angle
 δ - thickness
 θ - contact angle

ACKNOWLEDGEMENT

Authors would like to acknowledge the support of CNPq organization, Brasil, through Research Project 560092/2010-5, Edital MCT/CNPq/AEB 33/2010.

REFERENCES

Baturkin, V., Zhuk, S., Vojta, J., Lura, F., Biering, B., Lötze, H – G (2003) *Elaboration of thermal control systems on heat pipes for microsatellites Magion 4, 5 and BIRD*. Applied Thermal Engineering 23, p.1109–1117.

Brennan, P., Krolczek, E. (1979) *Heat Pipe Design Handbook*. B&K Engineering, Inc., Contract No NAS5-23406, June 1979.

Busse, C. A., Kemme, J. E. (1980) *Dry-Out Phenomena in Gravity – Assist Heat Pipes with Capillary Flow*. International Journal of Heat Mass and Transfer, 23, p. 643 – 654.

Chi, S. W. (1976) *Heat pipe theory and practice*, McGraw-Hill Book Company, London.

Faghri, A. (1995) *Heat pipe science and technology*. Taylor & Francis, London

Fleischman, G. L., Chiang, T. C., Ruff, R.D. (1991) *Oxygen Heat Pipe 0 – G Performance Evaluation Based on 1 – G Tests*. AIAA 26th Thermophysics Conference, Honolulu.

Hoa, C., Demolder, B., Alexandre, A. (2003) *Roadmap for developing heat pipes for ALCATEL SPACE's satellites*. Applied Thermal Engineering 23, p. 1099–1108.

Nakamaru, K., Kanamori, Y., Kimura, H., Masumoto, H., Ogushi, T. (1984) *Development of Fixed Conductance Heat Pipe for Spacecraft Application*. 5th International Heat Pipe Conference, Tsukuba, p. 465 – 472.

Qualification requirements to heat pipes (1983) *ESA PSS-49 (TST-01)*. Issue 2.

Shah, R.K., Bhatti, M.S. (1987) *Laminar Convective Heat Transfer in Ducts*, in: S. Kakac, R.K. Shah, W. Aung (Eds.), *Handbook of Single-Phase Convective Heat Transfer*, Wiley, New York, Chapter 3, pp. 3.1–137.

Vlassov, V. V. (2008) *Analysis of Heat Spreading Performance of Acetone-Filled Heat Pipe at Low Temperatures for using in Satellite Honeycomb Panels*. Journal of Aerospace Engineering, Sciences and Applications, 1, p. 1 – 17.

EXPERIMENTAL STUDY OF PULSATING HEAT PIPES TESTED IN LOOPED AND UNLOOPED CONFIGURATIONS

Jean-François Bonnenfant, Vincent Ayel, Yves Bertin, Cyril Romestant

Institut Pprime, department Fluide, Thermique et Combustion, UPR 3346

1, avenue Clément Ader 86961 Futuroscope Chasseneuil Cedex

Phone: (+33) 5 49 49 81 36, Fax: (+33) 5 49 49 81 01, jean-francois.bonnenfant@ensma.fr

ABSTRACT

Beside the fact that pulsating heat pipes (PHP) are very effective and promising two-phase heat transfer devices, the complexity of their behavior, and the high number of parameters involved in their operation still limit their development. Among these parameters, the present work focuses on the influence of looped or unlooped configuration: an experimental set-up has been developed, consisting of two pulsating heat pipes, having the same external dimensions, made of single smooth copper tubes of 1.2 mm inner diameter – 40 turns, and of 2.5 mm inner diameter – 20 turns, respectively. The working fluids studied are water and pentane for the first PHP, and ethanol for the second one. The other varying parameters are the temperature of the secondary fluid (cold source) and the heat power applied. Results show that, in some specific conditions and at low heat powers, the closure of the PHP has a significant influence on its overall performances. At higher heat powers, the influence is significantly reduced with respect to dynamic effects. It has also been noticed, during experiments, that different quasi-steady states could occur in only one configuration.

KEY WORDS: Pulsating heat pipes, looped and unlooped configurations, slug flow

1. INTRODUCTION

Pulsating heat pipes (PHP) are very effective two-phase heat transfer devices, widely studied in the last twenty years. A PHP consists of a meandering capillary tube partially filled with a working fluid. The spontaneous formation of vapour bubbles in the evaporator (hot section) and the condensation in the condenser (cold section) creates the oscillating motion of the bubble-plugs structure, which characterizes the PHP operation.

However, an accurate comprehension of the functioning of these devices is limited by the high number of parameters involved in the oscillating flow of the fluid (Charoensawan, 2003): influence of the tube inner diameter/length and number of turns, influence of the filling ratio and physical properties of the working fluid, influence of the cold source temperature, heat power, and inclination. Though, the influence of the closure or not of the overall loop is almost unknown.

Many of the parameters mentioned above have been studied in closed loop configuration (Charoensawan, 2003). Studies show that some aspects, such as flow direction and phase

distribution in the loop, influence the performances of the system (Tong, 2001). Thus, a homogeneous two-phase distribution generally leads to an improved performance (Khandekar, 2009). It has even been experimented that several flow regimes could be observed in only one configuration, keeping all the operating conditions fixed (Khandekar, 2009). Concerning the unlooped configuration, it seems to be unfavourable for the fluid circulation (and phase distribution) in some cases, compared to the loop configuration (Zhang, 2004). However, this assessment needs more investigations. Indeed, few unlooped configurations have been studied and, to our knowledge, no direct experimental comparison between the two cases can be found in literature. Only numerical study comparing both configurations can be cited (Shafii, 2001).

One can underline that the effect of the closure or not of the loop will be strongly linked to other parameters. For example, if the tube diameter decreases very below the critical value, the influence of the surface tension will become predominant compare to the other parameters, including looped or unlooped configurations. On the other hand, close to the critical diameter value,

the influence of these parameters will increase. The number of turns is another key parameter in a PHP operation. Lips et al. (2010) pointed out that increasing the number of turns, and therefore the number of interconnections, also tends to decrease the effects of the other parameters.

The present work aims to emphasize on effect of closure on the other parameters for two PHPs presenting different geometrical characteristics. Thereby, the study will be limited to the following parameters: the couple (D, N) (internal diameter and number of turns), the heat transfer rate Q , and the cold source temperature T_{cryo} .

2. EXPERIMENTAL SETUP

An experimental set-up (figure 1), was developed (Ayel, 2010) in order to test two kinds of pulsating heat pipes, both of them having the same external geometrical dimensions (lengths: $L_e = 0.18$ m, $L_c = 0.2$ m, $L_a = 0.19$ m, width: $l = 0.122$ m). These PHPs, made of single smooth copper tubes, differ from their inner diameter and number of turns (**PHP 1**: 2.5 mm inner diameter – 20 turns; **PHP 2**: 1.2 mm inner diameter – 40 turns). The evaporator and the condenser are made of copper blocks of same dimensions (evaporator length: 180 mm, condenser length: 200 mm), around which the capillary tubes are wound. A so-called “adiabatic zone” exists between the evaporator and the condenser. Closing the valve leads to an open - or unlooped - PHP, whereas opening it leads to a close - or a looped - PHP.

The two PHPs have been instrumented by nine cartridge heaters (of maximal power 6 kW), linearly inserted in the evaporator block from the end into the adiabatic zone; on the opposite, the condenser is cooled by an ethylene-glycol/water mixture flow crossing the copper block and whose temperature is controlled by means of a cryostat allowing maintaining it very closed to a fixed consign (stabilized between $\pm 0.1^\circ\text{C}$). Moreover, the evaporator and the adiabatic zone have been insulated (with glasswool - $\lambda \approx 0.035 \text{ Wm}^{-1}\text{K}^{-1}$ and rockwool - $\lambda \approx 0.04 \text{ Wm}^{-1}\text{K}^{-1}$). Attachments between the pulsating heat pipes and the bench are made with ertalonTM 4.6 ($\lambda \approx 0.3 \text{ Wm}^{-1}\text{K}^{-1}$) in order to minimize the conductive heat losses.

The evaporator and the condenser of both PHPs have been instrumented by means of 24 K-type thermocouples of 1.5 mm diameter distributed all along the length of each component. 18, and 6,

thermal sensors instrument each side of the evaporator, and of the condenser, respectively, all of them inserted at 30 mm from the borders of the copper blocks. It is worth emphasizing that the measured temperatures are in the copper blocks, and not in the cartridge heaters, neither in the cooling fluids nor in the working fluid in the tubes of the PHPs. The interface between all components (thermal sensors, electrical power supply, cryostat) have been developed with Labview[®].

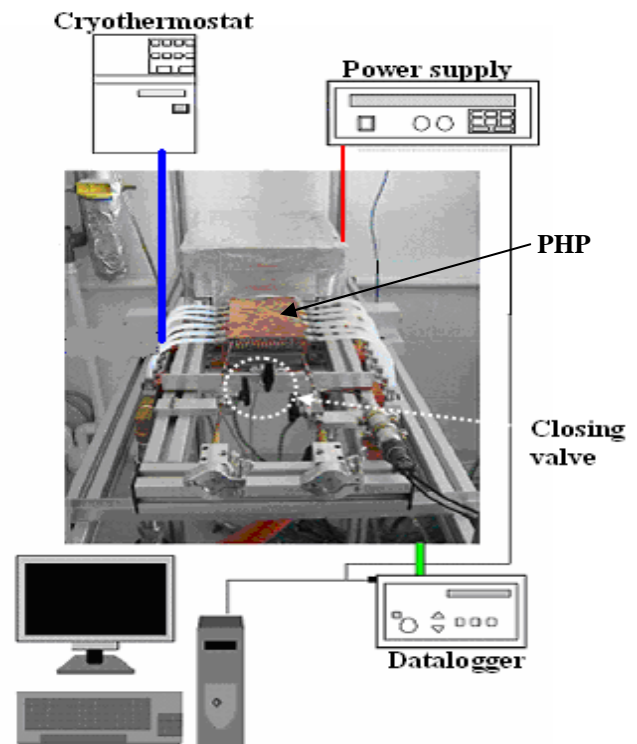


Figure 1. Schematic view of the PHP and experimental apparatus.

The parameters that were fixed during experiments were: the tube diameters, the length of each part, the unclosed configuration and the filling ratio that was equal to 50%. Both PHP have been tested in horizontal inclination. Several experiments have been led with three different fluids (ethanol for PHP 1, water and pentane for PHP 2), in order to examine the differences in performance between closed and open loop PHP. Note that experiments were planned to test PHP 1 with water and pentane, so as to have more relevant comparisons between the PHPs, particularly the influence of the inner diameter and the number of turns. Unfortunately, tests were interrupted due to a rupture of one tube of PHP 1.

3. EXPERIMENTAL RESULTS

3.1 PHP 1 (2.5 mm – 20 turns)

The following results compare the evolution of the overall performances of the pulsating heat pipe for the looped and unlooped configurations, as functions of the heat power applied and the cold source temperature. The curves present the thermal resistance R as a function of the heat load. It is defined as:

$$R = (T_e - T_{cryo})/Q' \quad (1)$$

Where Q' is the effective thermal power, subtracting the evaluated values of heat losses to the electrical power, T_e the average copper block temperature at the evaporator, and T_{cryo} , the average coolant temperature of the fluid cooling the condenser.

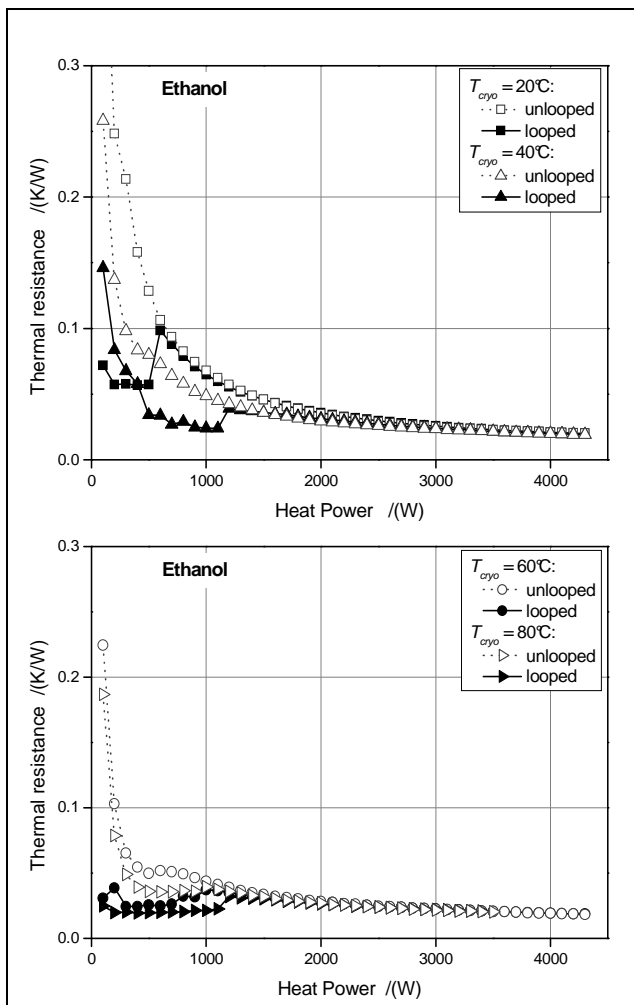


Figure 2. Thermal resistances vs. heat power for looped and unlooped configurations (PHP 1, ethanol, $D_i = 2.5$ mm, $N = 20$).

For a large enough diameter (PHP 1 diameter being relatively close to the critical value), and ethanol as a working fluid, curves of figure 2 show better performances with the looped configuration, particularly at low heat power applied, and whatever the cooling temperature value. Beyond a certain value of heat power applied, the two curves are superimposed, showing that there is no more effect on the performances of the PHP. The flow regime occurring at these heat powers levels allows a better homogenization of the temperature field along the evaporator, whatever the configuration. The dynamics effects related to pressure forces predominate over other effects.

One can notice that, for the unlooped configuration, the thermal resistance decreases smoothly with the heat power applied. On the contrary, for the looped configuration, particularly at 20°C and 40°C, the thermal resistance first decreases, before a slight increase occurs at a threshold value (depending on the value of T_{cryo}) of heat power, reaching the curve of unlooped configuration.

One can add that, for ethanol, the higher T_{cryo} , the lower the thermal resistance. Thus, the best performances are observed at 80°C. At this temperature, the thermal resistance is globally constant, compared to other cases, whatever the heat power beyond 300W. The main observation with ethanol as a working fluid is that, in an interval of heat power applied of [0-1000 W], approximately, the closure of the PHP leads to an enhancement of its performances, whatever the value of T_{cryo} .

3.2 PHP 2 (1.2 mm – 40 turns)

As mentioned earlier, giving the fact that this PHP has a higher number of turns and a smaller inner diameter, it is expected to be less sensitive to the variation of other parameters. Starting from this, tests have been done with two working fluids: water and pentane.

Water

Water has been tested for a secondary fluid temperature from 40°C to 90°C. An example is given at 60°C and 500 W on figure 3, illustrating the transitory regime of temperatures along the PHP (condenser, adiabatic and evaporator zones) as function of time. According to the curves, the alternation of unlooped and looped configurations has very little influence on the overall temperature

field of the evaporator. Note that this assessment remains the same whatever the cold source temperature T_{cryo} . Thus, one can see on figure 4, illustrating the evolution of the overall thermal resistance of the system at 40°C and 90°C , that the performances of this PHP, filled with water, are very close to one another with both configurations. However, one can notice a little gap between the two configurations for $T_{cryo} = 40^{\circ}\text{C}$ at very low heat powers applied (100 W). Except this observation, thermal resistances decrease smoothly with heat power applied.

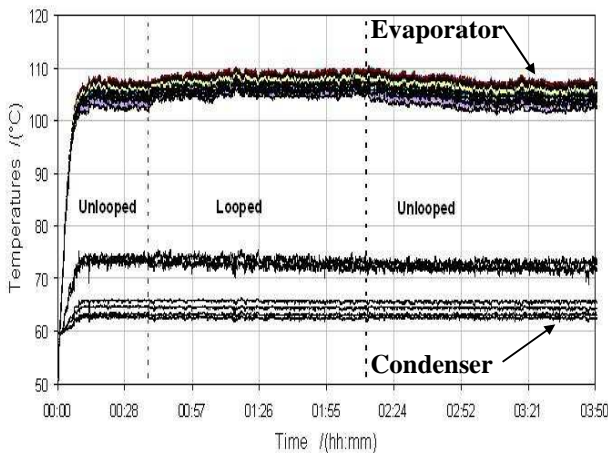


Figure 3. Transitory temperatures vs. time with looped and unlooped alternation (PHP 2, water, $T_{cryo} = 60^{\circ}\text{C}$, $Q = 500\text{ W}$).

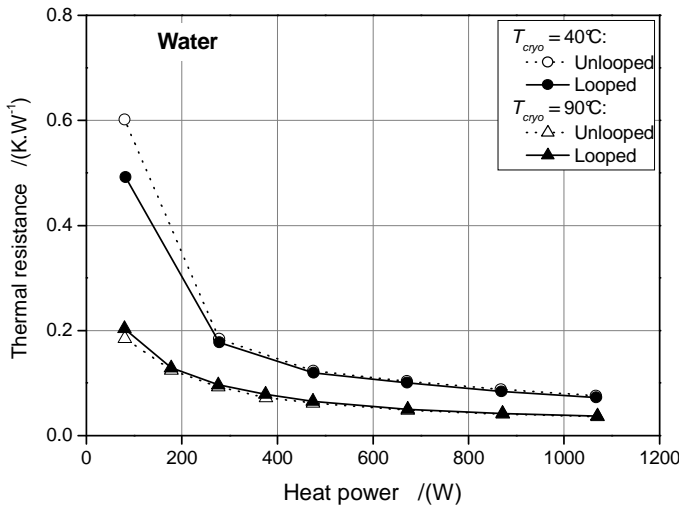


Figure 4. Thermal resistances vs. heat power for looped and unlooped configurations (PHP 2, water, $D_i = 1.2\text{ mm}$, $N = 40$).

In that case, it is noticeable that, for this PHP, the closure of the valve has no effect on its operation at first order. It can first be explained, once more, by the high number of turns which reduced

the effects of looped and unlooped configurations. It is also important to notice that critical inner diameter for water at these temperature ranges is around 5 mm for this temperature range. The inner diameter of PHP 2 ($D_i = 1.2\text{ mm}$) is therefore far under this critical value, suggesting that it has a weak sensitivity to other parameters. One can expect that other fluids with different characteristics (physical and chemical properties, critical diameter) will give different results for the same operating conditions.

Pentane

Indeed, experiments have been led with pentane as a working fluid. First, figure 5 presents results for secondary fluid temperature from 40°C to 80°C . One can see that closing the PHP has hardly any influence on the overall thermal resistance of the PHP in the three cases. When increasing the heat power, all the curves are superimposed, whatever T_{cryo} . All the studied parameters seem to have no effect on the overall performances of the PHP in these operating conditions. Though, at 40°C and 100 W heat power applied, it has been observed through the transitory temperature evolutions (figure 6) that switching from the looped configuration to the unlooped one leads to a slight increase of the temperatures in the evaporator. According to figure 5, this little variation does not affect significantly the overall thermal resistance of the system. One can also notice on figure 6 that the looped configuration leads to an increase of instabilities in the evaporator section, compared to water (figure 3), this later giving a better stability of the temperatures through the time.

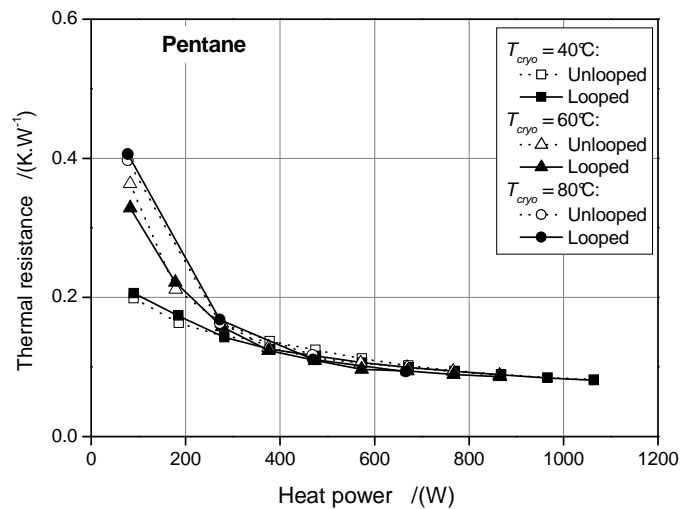


Figure 5. Thermal resistances vs. heat power for looped and unlooped configurations (PHP 2, pentane, $D_i = 1.2\text{ mm}$, $N = 40$).

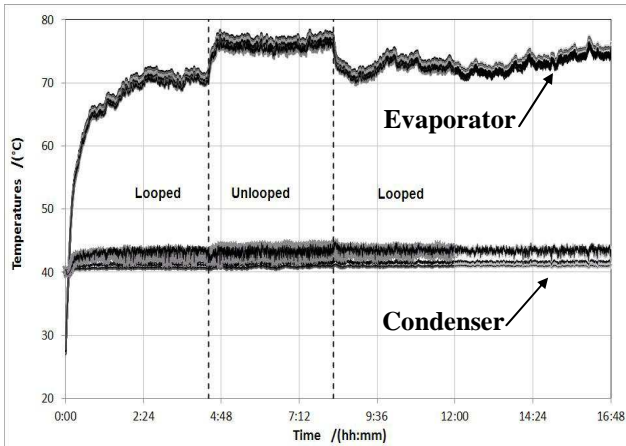


Figure 6. Transitory temperatures vs. time with looped and unlooped alternation (PHP 2, pentane, $T_{cryo} = 40^{\circ}\text{C}$, $Q = 100\text{ W}$).

Despite the weak influence of the closure in these cases, the overall performances of the PHP seem to be more sensitive to the varying parameters (looped/unlooped, T_{cryo} , Q') at low heat powers (under 200 W). This last observation has been confirmed by tests led with $T_{cryo} = 20^{\circ}\text{C}$ (figure 7). These tests have been done at different times, but they present the same operating conditions.

Firstly, like in the other cases illustrated on figure 5, the thermal resistance smoothly decreases when the heat power increases. One can notice that, for two unlooped curves, there is a sharp decrease of the thermal resistance between 100 W and 400 W approximately. Starting from around 400 W, thermal resistance of the PHP is totally independent on other parameters, and is the same for the three curves. The configuration, looped or unlooped, has then no more influence on the performances of the PHP when Q' increases. The stress will hence be put on what happens at 100 W. It is clear on figure 7 that, in these conditions, the “looped/unlooped” parameter has a strong influence on the overall thermal resistance of the PHP. This influence is effective on the three tests carried in the same conditions. Nonetheless, the obtained values appear to be different from one test to another, although the operating conditions are identical. This non-reproducibility of the results confirms the instabilities of the evolution of temperatures at low heat power, already observed at 40°C , especially with pentane.

In order to highlight the influence of the closure at $T_{cryo} = 20^{\circ}\text{C}$ and $Q' = 100\text{ W}$, figure 8 illustrates the evolution of the transitory regime. The transition from the looped configuration to the unlooped one shows a straight increase of the

average temperature in the evaporator section. This difference of temperatures has obviously a significant influence on the overall performances of the PHP, as already been on figure 7.

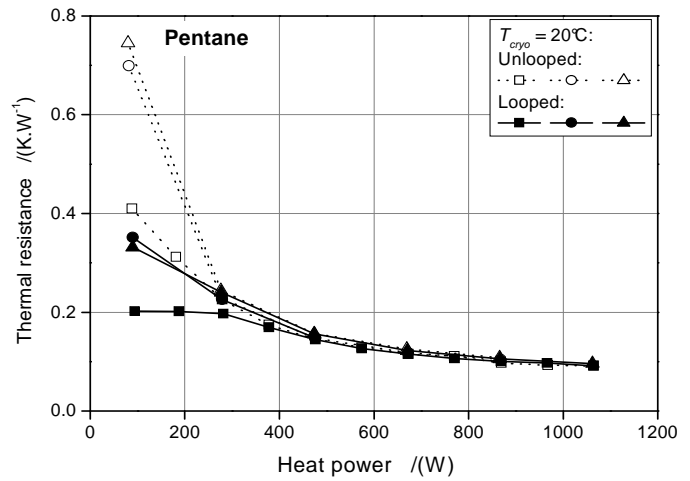


Figure 7. Thermal resistances vs. heat power for looped and unlooped configurations (PHP 2, pentane, $T_{cryo} = 20^{\circ}\text{C}$).

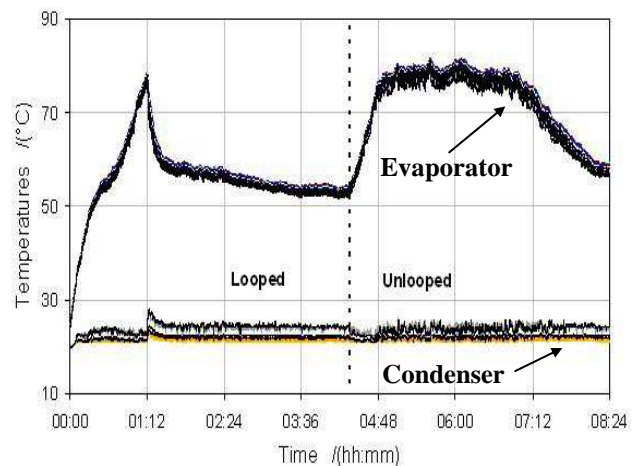


Figure 8. Transitory temperatures vs. time with looped and unlooped alternation (PHP 2, pentane, $T_{cryo} = 20^{\circ}\text{C}$, $Q = 100\text{ W}$).

After this change, the evolution of the temperatures seems to reach a quasi-steady state, corresponding to the unlooped configuration. However, one can notice that after several hours, the temperature regime changes itself, without touching any parameter. The mean temperature decreases slightly before stabilising (apparently) at another value! This assessment tends to confirm the work of Khandekar et al. (2009), proving the existence of multiple quasi-steady states in a heat pipe in only one configuration, keeping all the operating conditions fixed.

4. CONCLUSIONS

Two similar pulsating heat pipes have been tested in this work in order to characterize their performances according to two configurations: looped and unlooped. The varying parameters were the heat power applied, the cold source temperature, the working fluids and the dimensions (inner diameter and number of turns), different for the two PHPs. It is important to notice that the influence of the configuration may be strongly linked to these other parameters, particularly the geometry of the PHP.

Thus, some results confirm, in specific conditions, that the looped configuration tends to increase the overall performances of the system significantly. Such is the case at low heat powers for PHP1 filled with ethanol, or for PHP2 filled with pentane under specific conditions: $Q' = 100 \text{ W}$ and $T_{cryo} = 20^\circ\text{C}$. However, most of the time, the closure of the pulsating heat pipes has a weak effect on its performances, mostly when the heat power applied increases. Indeed, starting from a threshold value of heat power applied, the behavior of the system is independent on the configuration, and even on T_{cryo} for ethanol and pentane. One can also notice that instabilities are more important with pentane compared to water, this latter giving smoother variations of temperatures. A better homogenization of the temperatures in the evaporator may explain the low influence of the closure of the PHP on its performances, in the case of water. Finally, the instabilities with pentane are highlighted in the last transitory curves, showing the existence of multiple quasi-steady states without changing any parameter. This last assessment is in agreement with previous works.

NOMENCLATURE

D	diameter (m)
l	width (m)
L	length (m)
N	number of turns (-)
Q'	effective heat power (W)

Subscripts

a	adiabatic
c	condenser, critical
$cryo$	cryostat
e	evaporator

REFERENCES

- Ayel V., Bertin Y., Romestant C., Burban G., (2010) *Experimental study of pulsating heat pipes tested in horizontal and vertical positions*, 15th International Heat Pipe Conference, Clemson, USA, April 25-30.
- Charoensawan P., Khandekar S., Groll M., Terdtoon P., (2003) *Closed loop pulsating heat pipes, Part A: parametric experimental investigations*, Applied Thermal Engineering 23 2009-2020.
- Khandekar S., Gautam A.P., Sharma P.K., (2009) *Multiple quasi-steady states in a closed loop pulsating heat pipe*, International Journal of Thermal Sciences 48 535-546.
- Lips S., Bensalem A., Bertin Y., Ayel v., Romestant C., (2010) *Experimental evidences of distinct heat transfer regimes in pulsating heat pipes (PHP)* Applied Thermal Engineering
- Shafii, M.B., Faghri, A., Zhang, Y. (2001) *Thermal modeling of unlooped and looped pulsating heat pipes* J. Heat Transfer, 123(6), 1159-1172
- Tong B.Y., Wong T.N., Ooi K.T., (2001) *Closed loop pulsating heat pipe*, Applied Thermal Engineering 21 1845-1862.
- Zhang X.M., Xu J.L., Zhou Z.Q., (2004) *Experimental study of a pulsating heat pipe using FC-72, ethanol and water as working fluids*, Experimental Heat Transfer 17 47-67.

Investigation on operational characteristics of the miniature loop heat pipes with flat evaporators based on diverse vapor removal channels

Jeehoon Choi, Yunkeun Lee

Zalman Tech Co., Ltd. /School of Mechanical Engineering, Sungkyunkwan University
Seoul, 153-803, Republic of Korea

+82-70-4480-7875, +82-2-2107-3333, choijeehoon@gmail.com/jhchoi@zalman.co.kr and lyk@zalman.co.kr

Byungho Sung, Chulju Kim

School of Mechanical Engineering, Sungkyunkwan Univ.

Suwon, 440-746, Republic of Korea

+82-31-290-7434, +82-31-290-5889, bh03@chol.com and cjkim@me.skku.ac.kr

ABSTRACT

Thermal design and fabrication of an evaporator play the dominant roles in governing the development of a competitively priced miniature loop heat pipe (mLHP) application in order to successfully deploy on a commercially computing hardware cooling scales. Among the evaporator design factors, vapor removal channel(VRC) is a crucial factor that can influence the thermal regime inside the evaporator. This study proposed four models of VRC to investigate experimentally the operational characteristic of the mLHPs with flat evaporators. Geometric shapes of VRCs were the triangular and trapezoidal grooves protruding from the outer of a sintered wick. A sinter-bonding method was devised to improve the quality of the contact area of the grooves in contact with the base plate. Practical applications of the results are discussed in relation to the design and manufacturing process of the mLHP.

KEY WORDS : mLHP, flat evaporator, the vapor channel characteristics (VRCs)

1. INTRODUCTION

For the last two decades, a loop heat pipe(LHP) system has been proven to be an effective thermal management system for electronic devices mounted in several commercial communications satellites, Russian spacecrafts and NASA space shuttles (Maidanik *et al.*, 1985; Kozmin *et al.*, 1996; Baker & Grob, 2001). On the basis of these successful LHP outcomes, a miniature LHP(mLHP) has come into the spotlight since the early 2000s, as it enables to achieve a large amount of heat removal rates over a long distance, capableness of confined space and low temperature in high power density chips (Pastukhov *et al.*,2003; Maydanik, 2005; Singh *et al.*, 2007; Pastukhov & Maydanik, 2009). Nevertheless, most of the mLHP reviews do not reach a commercially computing hardware cooling scale since the cooling performance of active heat sinks combined with several conventional heat pipes is better than one of the mLHP (Choi *et al.*, 2012). One of the main reasons is related to its operational problems such as high thermal resistance, instability behavior, startup

failure, and etc., and they have yet to be solved. Previous literature reports (Riehl & Siqueria, 2006; Launay *et al.*,2007; Vershinin *et al.*, 2007; Launay & Vallee ,2011) pointed out that these problems are associated with the parasitic heat transferred to a compensation chamber (CC).

As shown in Fig.1 and 2, a non-negligible amount of heat escapes through the evaporator chamber walls to the CC and a liquid transport line affecting the performance of the CC because of the high contact thermal resistance between the wick structure and the base plate of the evaporator. This manner may lead to the temperature rise of working fluid inside the CC, which contributes ultimately to an increase in the overall operating temperature of mLHP (Adoni *et al.*, 2010). It is important how the operational temperature of the mLHP can be effectively down at given design constraints parameters, i.e., confined integration space, low cost, low acoustic level, etc. To deal with this tough situation, it may be necessary to retrofit other cooling module parts into the evaporator chamber wall or take complex refinements (Pastukhov *et al.*,2007).

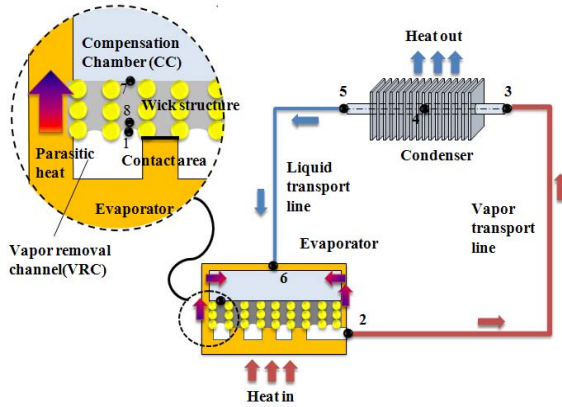


Figure 1. Schematic of mLHP with flat evaporator: Parasitic heat transferred to the CC.

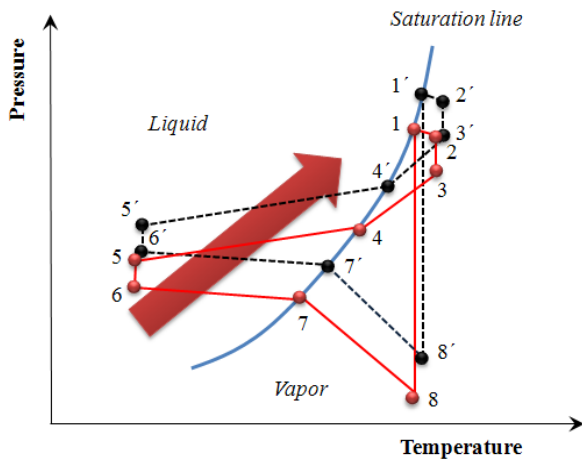


Figure 2. Pressure-Temperature curve of mLHP: the temperature rise of CC contributes to increase in the operation temperature.

Both of which are inconvenient because would necessitate significant expense. This increased cost has made it difficult to deploy on a commercial scale. Therefore, the successful mLHP implement in the computer hardware cooling scale is riding on the evaporator design and fabrication at low cost to lower the CC temperature as well as the overall operating temperature.

This study sought to get some answers in a vapor removal channel (VRC) inside the evaporator. The VRC composed of vapor grooves provides a path for the conductive heat transfer from the base plate of the evaporator to the liquid-vapor interface of the wick structure. In addition, the VRCs play the role in the vapor collection and removal from the evaporation zone to the vapor transport line. Thus, the shape, the position and the dimension of the VRCs are crucial factors that can influence the thermal regime inside the evaporator (Altman et al.,

Table 1. Physical Properties of wick structures

	Model 1,2 and 3	Model 4
Material	Nickel	Bronze
Particle size	~ 3 μm	~ 120 μm
Porosity	0.65	0.35
Max capillary pressure	37.4kPa	59kPa
Permeability	$5.3 \times 10^{-13} \text{ m}^2$	$1.0 \times 10^{-13} \text{ m}^2$
Effective thermal conductivity	8.62 W/m $^{\circ}\text{C}$	8.43 W/m $^{\circ}\text{C}$

2002; Delil et al., 2002). Evaporation rates and the contact area of the wick structure in contact with the base plate are closely related to the geometric shape of the vapor groove. Therefore, the features of the vapor groove can respond to the thermal design criterion of the evaporator.

In this study, the experimental investigations were carried out on the operational characteristic of the mLHP with flat evaporators based on diverse VRCs considering simplified fabrication which is directly correlated to the system cost must be maintained at or below that of current computer hardware cooling systems. The geometric shapes of the vapor groove were triangular and trapezoidal. Practical applications of the results are discussed in relation to the design and manufacturing process in order to define the optimal VRCs between the technological fabrication complexity and thermal efficiency.

2. DESCRIPTION OF VRCs

Typically, the VRCs have been engraved either at the inner surface of the evaporator base plate or at the outer surface of the wick structure. The VRCs at the outer surface of the wick have an advantage to obtain more efficient evaporation rates because this shape enables to secure more vaporization surface area in VRCs engraved on the wick. However, this geometry needs to be precisely machined and involves expense.

In this study, the wicks with VRCs sintered at a time by using carbon graphite moulds and a hot pressing to minimize the process of fabrication. As shown in Fig.3, the geometric shapes of VRCs were the two types: the triangular and trapezoidal vapor grooves which both geometric shapes are so friendly-manufacturing to be handled easily.

Table 2. Main shape parameters of VRCs

	Wick material	Groove shape	The ratio of contact area to wick cross-sectional area	The ratio of contact area to the grooved surface area	Contact condition
Model 1	Nickel	Triangular	1:4	1:8	Mechanical contact
Model 2	Nickel	Trapezoid	1:2	1:4	Mechanical contact
Model 3	Nickel	Trapezoid	1:2	1:4	Sinter-bonding
Model 4	Bronze	Trapezoid	1:2	1:4	Sinter-bonding

Competitive materials such as pure nickels and commercial bronze powders were selected to fabricate the wicks. As provided in Table 1, the physical properties of the wicks were determined based on demands of the mLHP in terms of capillary pressure, porosity, permeability and effective thermal conductivity. These parameters are able to be capable of heat dissipation over approximately 14.44 W/cm^2 of computing hardware chips (Sung *et al.*, 2008).

A simplified one-dimensional thermal resistance network of the evaporator consists of the conduction in the base plate, conduction and evaporation in the wick structure and the contact resistance between the two. The thermal resistance of evaporator is determined by the heat load (Q_0), the temperature of the evaporator base plate (T_h), and the temperature of the saturated vapor in the VRCs (T_v). The resistance is inversely proportional to the product between the contact area of the grooves in contact with the base plate (A_c) and the thermal contact conductance (h_c). The following formula can be used to estimate h_c :

$$h_c = \frac{Q_0}{A_c(T_h - T_v)} \quad (1)$$

When increasing the contact area between the wick structure and the base plate, h_c is expected to decrease the evaporator resistance. Once again, h_c affects the cooling performance of the entire system.

In the present study, the wicks with trapezoidal grooves (models 2, 3 and 4) were designed to obtain the ratio of A_c to the cross-sectional area of the wick stands at 1:2 and the ratio of A_c to the grooved surface area of the wick stands at 1:4. In contrast, the vaporization surface area of the triangular grooves (model 1) was devised to expand twice more than one of the trapezoidal grooves. The diameter of all wicks is $\Phi 38 \text{ mm}$ and the height of them is 4.5 mm.

In order to improve the contact quality of A_c , the wicks of models 3 and 4 were coupled to the base plate by a sinter-bonding method in a vacuum of 1 mTorr to prevent oxidization. To avoid changing the design properties of the wick, the metal powders sintered into the carbon graphite moulds to form a required geometry wick structure shape at low temperature condition and then the sinter-bonding step was conducted to bond the formed wick at the

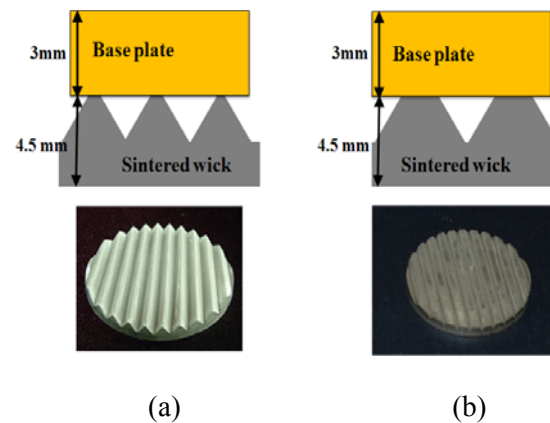


Figure 3. Geometric shape of vapor grooves: (a) Triangular; (b) Trapezoid.

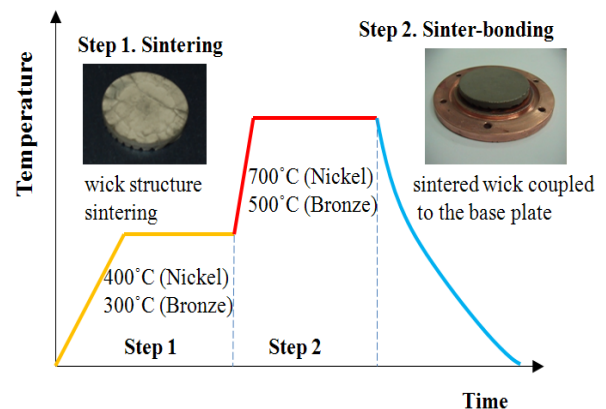


Figure 4. Schematic of the sinter-bonding method to fabricate model 3 and 4.

base plate. Schematic of the sinter-bonding method is shown in Fig. 4. This method has simplified the packaging process to combine the wick with the base plate at the same time.

3. TESTING METHOD

Experimental tests were carried out with the mLHP employing flat evaporators based on four models; mLHP components were otherwise identical and the tests were performed using the same conditions and parameters. The evaporator housing was made of stainless steel with an outside diameter of 41mm, while the base plate was made of copper. Furthermore, the base plate was designed to fit into a 3 x 3 cm² CPU chip. A secondary wick, composed of stainless steel fibers with a porosity of 85%, was adopted inside the CC as the secondary wick which assisted stable startup and operation in our previous study (Choi *et al.*, 2010). The vapor and liquid transport lines containing 3/16" and 1/4" were made of copper. A fin-tube condenser was capable of dissipating 250W by running an axial fan of 120 mm at a maximum speed of 2150 rpm. The overall dimensions of the fin-tube condenser were 100 x 90 x 20 mm. Water was used as the working fluid.

As practical application tests of a cooling device, a dummy ohmic heater with controllable electronic power supply was used as a heat source. The heater consisted of a copper block spreader (30 x 30 mm) with an embedded carbon film resistor. The carbon film resistor was soldered to the copper spreader, while its back side was insulated with a 1.5mm layer of glass fiber ($k = 0.046\text{W/m}^\circ\text{C}$) followed by a 3.5mm of bakelite ($k = 0.232\text{W/m}^\circ\text{C}$). The heater was estimated with $\pm 5\%$ accuracy. T-type thermocouples were used to measure the temperature of each component. The tests were performed under normal environmental conditions at the ambient temperature of $24 \pm 1^\circ\text{C}$. The voltage and the current applied to the heater were continuously monitored during the tests to determine the applied power. All temperature data were automatically collected by a computer via data acquisition system (Yokogawa Ltd., Co.).

4. RESULTS AND DISCUSSION

Experimental results were obtained for four flat evaporator models with one using triangular vapor grooves and the other three using trapezoidal grooves as the VRCs. The intensity of the heat transfer processes inside the evaporator was

estimated using the temperature difference (ΔT) between T_h and the vapor inlet temperature (T_{vi}).

$$\Delta T = T_h - T_{vi} \quad (2)$$

Figure 5 presents the ΔT of the investigated models measured at steady-state. As can be seen from Fig.5, for model 1, when heat load exceeded 50W, ΔT was much shaper compared with others. This causes the temperature rise of liquid inside the CC. On the other hand, it is observed that most of the applied heat load was concentrated at the vaporization zone in front of the wick through the trapezoidal grooves of models 2, 3 and 4 using increased contact areas. As pointed out above, the contact area is dependent on the evaporator performance.

It was observed that the ΔT of models 3 and 4 was lower than one of the model 2. One possible explanation of this trend is the poor contact quality. Due to the high thermal contact resistance of the poor contact area, the heat escaped to the evaporator chamber walls is relatively higher than the heat transferred to the vaporization zone. Hence it is necessary to elevate T_h so as to reach an evaporation condition, which leads to the increase of ΔT depending on the CC temperature. However, the use of sinter-bonding can provide locking the parasitic heat to the CC, which concentrates heat on supplying the wick and thus makes it possible to maintain relatively low operating temperature.

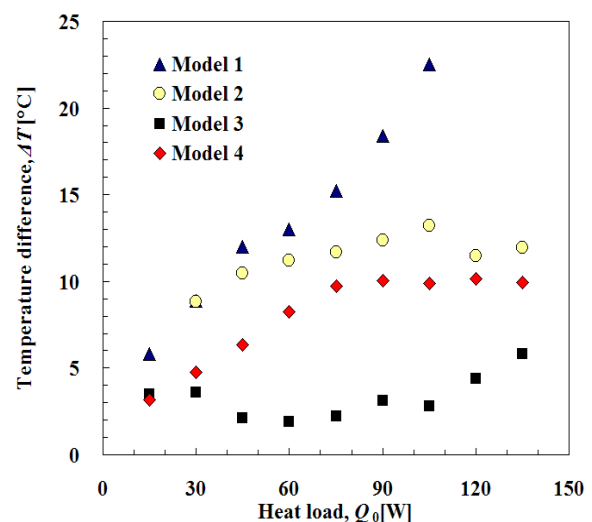


Figure 5. Temperature difference associated with heat transfer from the base plate to the vapor inlet temperature, ΔT , as function of applied heat load.

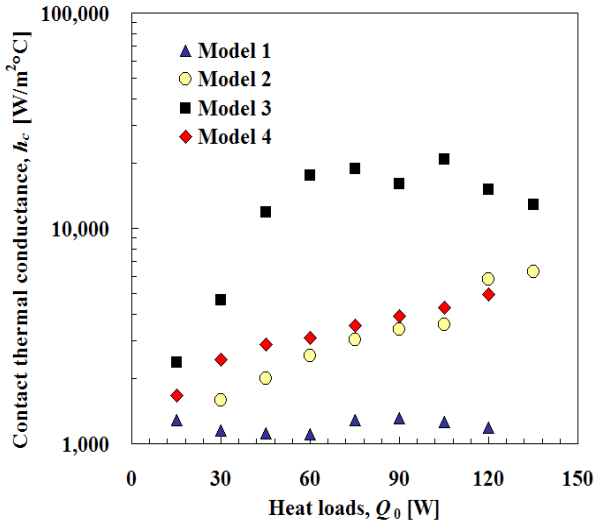


Figure 6. Thermal contact conductance, h_c , as function of applied heat load.

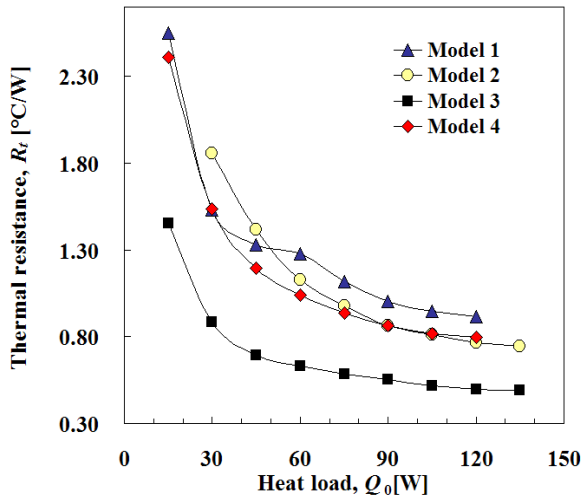


Figure 7. Total thermal resistance, R_t , as function of applied heat load.

It is noteworthy that the ΔT of model 3 was lower than one of model 4 although model 4 has the same geometric shape with respect to model 3. More insight into the heat transfer of evaporators can be obtained from Fig. 6 which depicts the experimentally determined h_c as a function of applied heat loads for each model. As can be seen from the figure, the h_c of model 3 is superior to one of model 4. The h_c of model 3 varied from 2,380 to 20,820 $W/m^2°C$ but one of model 4 varied from 1,675 to 4,925 $W/m^2°C$. Besides, the two curves of models 2 and 4 are slightly different and even at 120W the h_c of model 2 was higher than one of model 4. This can be ascribed that models 2 and 3 have better wick wetting characteristics to supply

liquid well to the liquid-vapor interface at the vapor grooves compared with model 4.

Figure 7 explains the total thermal resistance associated with the entire system, R_t . R_t is usually used to characterize the overall performance of the mLHP and it is defined as:

$$R_t = \frac{T_h - T_a}{Q_0} \quad (3)$$

where, T_a is the ambient temperature. As plotted in Fig. 7, R_t of mLHP employing model 1 is 2.55-0.92 $°C/W$ at heat loads of 15-120W while that of model 2 is 1.86-0.75 $°C/W$ at heat loads of 30-135W. As explained above, this order of magnitude difference between the thermal resistances of models 1 and 2 reflects the contact area size of the two VRCs. At a glance, the total thermal resistances of model 3 is less than 0.49 $°C/W$ at the highest load and is up to about 37% lower than that of model 2 and up to 38% less than that of model 4. It can be inferred that when the porosity and permeability of the wick are higher, they induce less hydraulic resistance for liquid flowing in the wick and also can cause more evaporation. Thus, it is evident that the contact area and the contact quality corresponding to VRCs are dependent on the changes in the temperature of the sub-cooled working fluid inside the CC, which affects the overall operating temperature.

3. CONCLUSIONS

This study proposed mLHPs with flat evaporators based on diverse VRCs, denoted by models 1, 2, 3 and 4, respectively. The VRCs of all models were protruding from the outer surface of the wick. Models 1, 2 and 3 possessed the same physical properties but model 4 was different. The geometric vapor shape of models 2, 3 and 4 were trapezoidal grooves except for model 1 with triangular groove shapes. To improve the quality of the contact area of the grooves in contact with the base plate, the sinter-bonding method was devised and applied to models 3 and 4.

The thermal contact conductance of model 3, which varied from 2,380 to 20,820 $W/m^2°C$, is superior to the others. The total thermal resistance of model 3 is less than 0.49 $°C/W$ at the highest heat load and is significantly lower than that of other models. All results of model 3 thus suggest a potential configuration for computing hardware cooling to enhance the cooling performance and simplify the evaporator manufacturing process.

NOMENCLATURE

A_c Contact area of the grooves in contact with the base plate
 h_c Thermal contact conductance
 Q_0 Heat load
 R_t Overall thermal resistance
 T_a Ambient temperature
 T_h Temperature of the evaporator base plate
 T_v Temperature of the saturated vapor
 T_{vi} Vapor inlet temperature

REFERENCES

- Adoni, A. A., Ambirajan, A., Jasvanth, V. S., Kumar, D., Dutta, P. (2010) *Theoretical and experimental studies on an ammonia-based loop heat pipe with a flat evaporator*, IEEE Trans. Compon. Packag. Technol., 30 (2), p. 478–487.
- Altman, E. I., Mukminova, M. I., Smirnov, H.F. (2002) *The loop heat pipe evaporators theoretical analysis*. Proc. 12th Int. Heat Pipe Conf., Moscow, p. 159-164
- Baker, C., Grob, E. (2001) *System Accommodation of Propylene Loop Heat Pipes for the Geoscience Laser Altimeter System (GLAS) Instrument*. Proc. 31st Int. Conf. on Environment system, Orlando, SAE Paper no. 2001-01-2263
- Choi, J., Sung, B., Yoo, J., Nguyen, X., Kim, C. Koh, H. (2010) *A study on the operation stability improvement of mLHP*. 15th Int. Heat Pipe Conf., Clemson
- Choi, J., Jeong, M., Yoo, J., Seo, M., (2012) *A new CPU cooler design based on an active cooling heatsink combined with heat pipes*, Appl. Therm. Eng., 44, p. 50-56
- Delil, A., Baturkin, V., Fridrichson, Y., Khmelev, Y., Zhuk, S. (2002) *Experimental results of heat transfer phenomena in a miniature loop heat pipe with a flat evaporator*. Proc. 12th Int. Heat Pipe Conf., Moscow, p. 126-133
- Kozmin, D., Goncharov, K., Nikitkin, M., Maidanik, Y.F., Fershtater, Y., Smirnov, F. (1996) *Loop heat pipes for space mission Mars 96*. Proc. 26th Int. Conf. on Environment system, Monterey, p. 961-602
- Launay, S., Satre, V., Bonjour, J. (2007) *Parametric analysis of loop heat pipe operation: a literature review*, Int. J. Therm. Sci., 46, p.621–636
- Launay, S., Vallee, M. (2011) *State-of-the-art experimental studies on loop heat pipes*. Frontiers in Heat Pipes, DOI: 10.5098/fhp.v2.1.3003
- Maidanik, Y. F., Vershinin, S. V., Kholodov, V., Dolgirev J. (1985) *Heat Transfer Apparatus*. U.S. Patent No.4515209
- Maydanik, Y. F. (2005) *Review:loop heat pipes*. Appl. Therm. Eng., 25, p. 635-657
- Maydanik, Y.F., Vershinin, S.V., Korukov M.A., Ochterbeck, J.M. (2005) *Miniature loop heat pipes: A promising means for cooling electronics*. IEEE Trans. Compon. Packag. Technol., 28 (2), p. 290–296
- Pastukhov, V.G., Maydanik, Y.F., Vershinin, S.V. (2003) *Miniature loop heat pipes for electronics cooling*. Appl. Therm. Eng., 23, p.1125-1135
- Pastukhov, V. G., Maydanik, Y. F. (2007) *Low noise cooling system for PC on the base of loop heat pipes*, Appl. Therm. Eng., 27, p. 894–901
- Pastukhov V. G., Maydanik Y. F. (2009) *Active coolers based on copper-water LHPs for desktop PC*. Appl. Therm. Eng., 29, p. 3140-3143
- Riehl, R. R. Siqueria, T. (2006) *Heat transport capability and compensation chamber influence in loop heat pipes performance*. Appl. Therm. Eng., 26, p. 1158-1168
- Singh, R., Akbarzadeh, A., Dixon C., Mochizuki, M., Riehl, R. R. (2007) *Miniature loop heat pipe with flat evaporator for cooling computer CPUs*. IEEE Trans. Compon. Packag. Technol., 30 (1), p.42-49
- Sung, B., Choi, J., Ki, J., Yoo, J., Seo, M., Kim, C. (2008) *The sintered porous metal media development and measurement of LHP systems for electronic cooling device*, Proc. ASME IMECE, Boston
- Vershinin, S. V., Maydanik, Y. F. (2007) *Investigation of pulsations of the operating temperature in a miniature loop heat pipe*. Int. J. Heat Mass Transfer, 50, p. 5235-5240

ON THE USE OF HEAT PIPE PRINCIPLE FOR THE EXPLOITATION OF MEDIUM - LOW TEMPERATURE GEOTHERMAL RESOURCES

Alessandro Franco, Maurizio Vaccaro

Department of Energy and System Engineering (DESE) - University of Pisa

address: Largo Lucio Lazzarino, 1, 56122 PISA (Italy)

Phone: +39-050-2217154, Fax: +39-050-2217160

e-mail: alessandro.franco@ing.unipi.it

ABSTRACT

In geographical areas characterized by geothermal anomalies (such as a lot of area in Italy which comprehend active volcanic basins) the geothermal heat could be exploited directly as hot source using heat exchanger without fluid withdrawal from the reservoir and with no alteration of the natural balance of the basin. An interesting solution could be the use of heat pipe principle. In geothermal reservoirs with temperature below 100 °C, the heat pipe mechanism and in particular the two phase closed loop thermosyphon can transfer heat very efficiently, with vapor rising and liquid falling in comparable quantities, driven by gravity. In this case the most important the task is an efficient heat transfer from the aquifer or reservoir to the heat exchanger in the well. A review of particular application connected to the geothermal heat pipe applications is presented and guidelines for power systems sizing are provided.

KEY WORDS:

Geothermal energy, Two phase Thermosyphons, Geothermal Energy, Single well systems, Heat Pipe Turbine

1. INTRODUCTION

The conventional utilization plants for low and medium temperature (60 ÷ 150 °C) geothermal reservoirs have three considerable inconveniences. The mass withdrawal from the aquifer alters the natural balance of the basin, while over-exploitation causes a temperature and pressure reduction during the lifetime of the plant (Axelsson et al. 2005). The use of extraction pumps operating with very corrosive geothermal fluids leads to high installation and operation costs and short machinery useful life. Moreover a second well is usually necessary for reinjection, due to technological and environmental request.

These problems can be avoided using devices that only allow heat transfer with the aquifer, basing on the concept of the Single Borehole Extraction System. For this utilization layout a secondary fluid (e.g. water or a low boiling point organic fluid) will be needed and a down-hole heat exchanger (DHE) is necessary. A DHE consists of a simple coil or of a U-tube located in a well, through which the working (or secondary) fluid circulates. The secondary fluid is pumped or circulated by natural convection (thus eliminating the problem of disposal of geothermal fluid, since only heat is taken from the well). The use of DHE has been discussed in the literature along a period of 35 years (Lund, et al., 1975; Culver and Lund, 1999; Boyd and Lund, 2010).

Several types of DHE, like thermosyphon type heat pipe, concentric tube thermosyphon, downhole coaxial heat exchanger (DCHE), U-tube downhole heat exchanger, as well as others, have been proposed in order to extract heat directly from shallow geothermal aquifers. Several concepts or designs of DHE have been successfully tested. In U.S. over 500 DHE installations exist in Klamath Falls (Chiasson, 2006). Existing applications include space heating and snow melting, mainly in U.S., Turkey and New Zealand, Iceland, Hungary, Russia, Italy, Greece, Japan (Boyd and Lund, 2010).

DHEs has some disadvantage respect to fluid extraction systems, mainly regarding the absence of heat flow induced by extraction into the aquifer. The heat flow that can be extracted from the well is tied only to the natural convection that occurs in the aquifer-well system. In case of low aquifer permeability, the convective transport can be particularly weak and the heat extraction can reach limited values. However, even in favourable conditions, that is for permeability greater than 10^{-4} m/s⁻¹, DHEs are suitable systems for moderate heat transfer applications (Allis, 1980). An alternative pathway with respect to DHE is the application of the heat pipe concept both in the basic version and (in particular) as in the Closed Loop Two Phase Thermosyphons (CLTPT) version. The utilization of the thermosyphon concept in the DHE avoids the need of a downhole pump. Downhole pumps

have two different drawbacks: firstly, in the harsh downhole environment they have relatively short lifetimes and secondly, it is less efficient thermodynamically to pump and pressurize the fluid and then exchanging heat on the surface (DiPippo, 2008). Compared with the conventional systems based on the extraction of water, CLTPT permits to exchange heat at a constant temperature and it has other advantages:

- it can be used even in a dry geothermal reservoir;
- a loop type heat pipe can control the heat transfer rate by controlling the flow rate of the returning working liquid.

The principle of Geothermal heat pipe has been proposed in applications to renewable energy sources (geothermal heat, underground water, hot-spring water and solar heat), city waste heat (waste heat from subway, river, drainage, building, etc.), and utilization of deep underground heat.

A particular case of CLTPT, named geothermal convector (GTC) to extract heat from geothermal aquifers was proposed by Carotenuto et al. (1999). Researches were carried out to understand the technical and thermodynamic problems that the device gave in this type of application and to determine solutions to them. Recently the use Thermosyphon Loops has been proposed for heat extraction from the ground and for heating of railway points (Rudorf et al., 2008).

The use of heat pipe technology has been proposed also for geothermal power production since the early 1990s (Mc Guinness et al., 1993, Nguyen et al., 1995; Kusaba et al., 2000; Akbarzadeh et al., 2001). Interest to the utilization of two phase thermosyphon is demonstrated in connection with development of Enhanced Geothermal Systems (EGS) for power production by Wang et al. (2009).

2. GEOTHERMAL SYSTEMS WITHOUT FLUID EXTRACTION

In geothermal heat utilization a balance between fluid/heat extraction and natural recharge has to be identified, in order to maintain the renewability of the source. Fig. 1 summarizes the main strategies and practices for geothermal resources utilization.

In many utilizations in the past the “open-cycle” scheme was followed, fluid extraction and surface discharge (no fluid reinjection).

This leads to limited production rates (in many cases not economical for utilization) and geothermal resource impoverishment.

High production rates can exceed the natural long-term recharge rate causing a resource depletion.

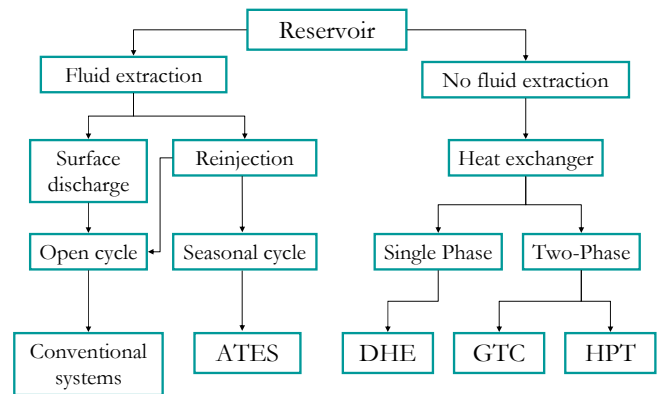


Figure 1. Pathways for the use of geothermal energy

For this reason in the majority of the utilization schemes the fluid reinjection is considered, to replenish the fluid content and to help sustaining or restoring reservoir pressure.

A completely different pathway is represented by the schemes without fluid extraction: these can be used both for direct energy utilization and for power production with the single phase thermosyphon principle (like in DHE) or the heat pipe principle (like in Geothermal convector or Heat Pipe Turbine). This principle encounters the aim of geothermal sustainable utilization, by keeping the fluid in the reservoir avoiding the drilling of a reinjection well. Furthermore problems related to the chemical properties of fluid extracted (scaling, corrosion) are avoided. Heat extraction from a geothermal reservoir can occur by two methods:

- a) heat transfer from a water body flowing through the aquifer;
- b) extraction of the stored heat from the rocks surrounding the well.

Let us schematize this process. Once the evaporator section is extracting heat and a convection cell is established, a portion of the convecting water (surrounding the heat pipe) will be fresh water entering the well from the aquifer.

The same amount of cooled water leaves the well and gets back to the aquifer. DHEs are generally set up by putting in a well a simple U-Tube (or double U or coaxial tubes), through which the operating fluid circulates. The heat flow extracted from the reservoir is regulated by the Law

$$\dot{Q} = n\pi h D_e U \Delta T_{lm} \quad (1)$$

where Q is the heat transferred per unit time, $n\pi h D_e$ represents the heat exchange area (n tubes, D_e the external diameter of the pipes and h the length of the tube), U the overall heat transfer

coefficient, ΔT_{lm} , the mean temperature difference between aquifer and working fluid in the extraction device. CLTPT is generally a simple pipe, that constitutes the external shell for the heat exchanger and extends itself for a certain length of the well. In geothermal applications, CLTPT works with a downhole evaporator and a condenser at the ground level. The heat flow rate that can be extracted from the well is tied only to the natural heat transfer occurring in the aquifer-wells-system. For this reason, to improve the mass transfer between aquifer and well, the use of a natural circulation promoter is necessary (Fig. 2).

The heat transfer between aquifer and well and between geothermal fluid and the external surface of DHE has been object of wide analysis and optimization. The formation of strong temperature gradients along the well axis imposes limits on the heat power rate (generally less than 100 kW). Carotenuto et al. (1997) derived an analytical expression to define the heat flow rate that can be transferred in the evaporator zone. This correlates heat rate to mass flow rate in the aquifer \dot{m}_a and to temperature difference between unperturbed aquifer and well output temperature ($T_\infty - T_{ow}$):

$$Q = m_a \cdot c_p \cdot \exp\left[-a(c_p m_a)^b\right] \cdot (T_\infty - T_{ow}) \quad (2)$$

where a and b are coefficients depending on the permeability and on the hydraulic conductivity, on the temperature difference and on the dimensionless length of the convection promoter. A maximum rate value has been identified. It depends on the mixing ratio R_m defined as:

$$R_m = 1 - \frac{m_a}{m_t} \quad (3)$$

where m_a is the aquifer renewed mass flow-rate, and m_t the total mass flow rate of the fluid circulating within the well and on the short circuit effect in the flow of the geothermal fluid.

The theoretical maximum steady state amount of transferred heat from the aquifer would be when the mixing ratio is zero. Mixing ratios lower than 0.5 have never been observed and mainly it is in the range 0.5-0.95 (Culver and Lund, 1999).

3. APPLICATION HEAT PIPE PRINCIPLE FOR GEOTHERMAL ENERGY USE

In a conventional heat pipe consisting of a single tube, thermal performance is restricted by entrainment and flooding phenomena.

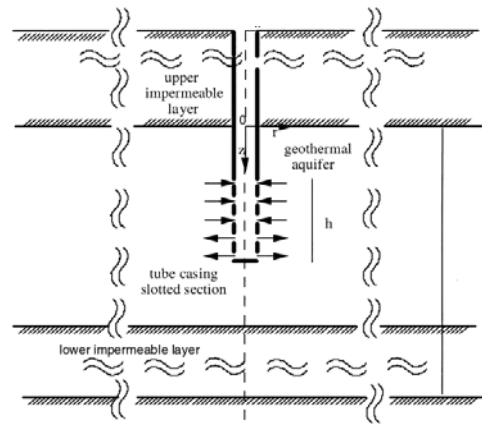


Figure 2. Geothermal well with convection promoter

Several variants of heat pipes for utilization of geothermal energy and underground rock heat have been studied. Vasiliev (1990) proposes a first interesting analysis of the problem. Several factors, like operating temperature range, vapor pressure, thermal conductivity, compatibility with the wick and case materials, stability and toxicity, affect the selection of the working fluid. The heat transfer “quality” of working fluids can be expressed by a Merit Number, defined as (Peterson et al, 1994):

$$M = \frac{\rho \cdot \sigma \cdot h_{fg}}{\mu} \quad (4)$$

where σ is the surface tension of the working fluid, h_{fg} is the latent heat of vaporization, and μ is the viscosity. In order to improve the thermal performances (mainly for a large scale heat pipe), loop type and gravity assisted heat pipe (where vapour and liquid flow passages are separated) represent a better option. The interaction between the fluid flow in the well and to the aquifer, and the interaction with the rocks surrounding the well is the real keypoint of the problem. It is known that the heat output can be significantly increased if a convection cell could be set up in the well.

3.1 Experiences on geothermal convector use

A particular type of DHE is the geothermal convector (GTC), which is a special geothermal application of the two-phase closed thermosyphon (Faghri, 1995, and Reay and Kew, 2006).

The CLTPT is a device operating in a gravity field able to transfer high heat flow rate in a simple way. In the bottom part the operating fluid evaporates, the vapour rises to the top where it condenses, then the condensate returns by gravity to the evaporator section. Thus, the heat transfer occurs by phase

change with negligible thermal gradients. In geothermal applications the CLTPT works with a downhole evaporator and with a condenser at the ground level. The GTC shares the advantages and disadvantages with common DHEs but it does not require mechanical energy for fluid extraction and it can reduce the chemical deposition (scaling) phenomena, since it keeps a better control of the DHE surface temperature.

The GTC described by Carotenuto et al. (1999) has been tested in the Campi Flegrei geothermal field (Ischia island) in an aquifer with fluid at 70-80 °C at a depth of 10 m from ground level (10 - 25 kW heat rate, R11 as working fluid).

In recent time Jeong and Lee (2008) tested a two-phase thermosyphon system using CO₂ as working fluid. The total length of the thermosyphon was of 1 m with inside and outside diameters of 9.9 mm and 12.7 mm respectively. However the use of heat pipe for direct heat extraction from geothermal aquifers has not been developed in a practical way.

3.2 Heat Pipe Turbines (HPT) experiences

The Heat Pipe Turbine (HPT) or Thermosyphon Rankine Engine (TSR) is a concept proposed for power generation purposes. The basis of the engine is the modification of a heat pipe to incorporate a turbine. This system, which is also known as GEESOR (Geothermal Energy Extraction System Organic Rankine), overcomes the necessity of a reinjection well. The main innovation is the combination of two separate cycles, the heat pipe connected directly to the ORC without the need for a heat exchanger. This system could represent an interesting alternative to the classical binary plant, mainly for small plant size (50-100 kW).

HPT have been object of various analysis in the literature (Mc Guinness et al., 1993, Nguyen et al., 1995; Wang et al., 2009;) even if no real development has been observed and only some design schemes or prototypes are available (Table 1). Kusaba et al. (2000) and Akbarzadeh et al. (2001) proposed HPT for power generation using geothermal low grade heat sources with temperatures in the range 80 - 150 °C for application in specific geothermal sites. The heat pipe extracted quite high heat power (about 100 kW) but with efficiency level of 3-5%.

They analyzed a particular HPT using a modification of the thermosyphon cycle with a turbine in the adiabatic region. They also calculated the extraction rate for different of heat pipe lengths and different temperatures of the geothermal source.

Table 1. Various Heat Pipe Turbine systems

Authors	T _{geo} [°C]	P [W]	Fluid
McGuinness et al. (1993)	No available data		
Nguyen et al. (1995)	> 80	5,5	water
Kusaba et al. (2000)	120-150	7800	R123
Akbarzadeh et al. (2001)	80-120	3000	R114
Wang et al. (2009)	ground	-	isopentane

The same authors studied the performance of a turbine which can be installed on top of a heat pipe (using a binary fluid). The configuration involves a closed, vertical cylinder functioning as an evaporator, an insulated section and a condenser. The turbine is placed near the upper end between the insulated section and a condenser section; a plate is installed to separate the higher pressure region from the lower pressure region in the condenser (Fig. 3). Conversion of the fluid enthalpy to kinetic energy is achieved through a nozzle. It is important to notice that between the systems analyzed (Table 1) the expected performances are very low (below 1%). This is because a single pipe is used and the power extraction is mainly related to the kinetic effect.

3.3 CLTPT systems for power production

It would be more efficient (for power production purposes) the use of the concept of CLTPT (see Fig. 4), with a pump to increase the pressure of the fluid and a classical turbine working on a Δp (Single well binary cycle). In this case the enthalpy drop in the turbine can be referred to the operating pressure in the loop thermosyphon. The operating principles of heat pipe and CLTPT have been tested by the author (Franco and Filippeschi, 2010; 2011) with special attention to small size systems.

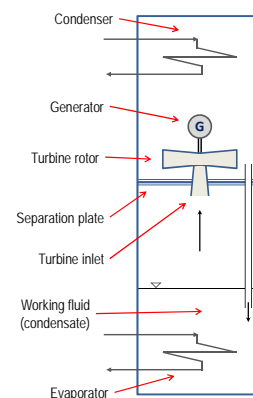


Figure 3. The operating principle of HPT

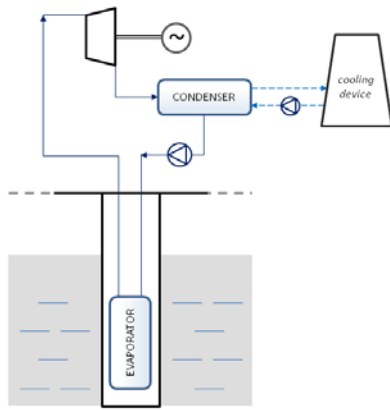


Figure 4. The operating principle of advanced HPT

In CLTPT, several key parameters influences the heat transport together with the heat flow Q (at the evaporator section, from the source), as:

- diameter of riser and downcomer tube (d);
- distance evaporator-condenser (H);
- length of the heat input zone (h);
- thermophysical properties of working fluid;
- operating pressure;
- volumetric filling ratio or driving head;
- pressure drops and thermal resistances.

To analyze the technical feasibility of power production using CLTPT concept (Fig. 4), a Rankine cycle has been calculated. The analysis has been referred to the data of Carotenuto et al. (1999). The temperature of the geothermal source was fixed at 70 °C (15 m depth) and the maximum heat flow rate to maintain the temperature is assumed at 15 kW. Considering a Rankine cycle, operating between 30 °C and 60 °C and considering an isentropic efficiency of 0,85 it is possible to foresee power production unit of 1 kW. Table 2 provides gross power P , mass flow rate m and efficiency η_I with different working fluids.

Table 2. Rankine cycle results with different operating fluids

Fluid	Δp [bar]	P [kW]	m [kg/s]	η_I %
R134a	9,112	1,064	0,08	7,1
R152a	8,175	1,076	0,05	7,2
R123	1,774	1,064	0,08	7,1
R21	3,07	1,078	0,06	7,2
R600	3,499	1,060	0,04	7,1
R600a	4,714	1,060	0,04	7,1

4. DISCUSSION

The use of geothermal energy extraction systems based on DHE shows remarkable differences with respect to the traditional geothermal utilizations.

These differences are in positive as for example the use of single well systems instead of a multiwell systems (no reinjection), the use of a gravity head two-phase thermosyphon in place of downhole pumps and the possibility of using a secondary working fluid that permits the utilization of sources at temperatures below 100 °C. Moreover the thermosyphon can be beneficial in providing a more advantageous energy cycle even if some problems must be solved for the engineering development of these systems:

- the estimation of heat flow rate in the aquifer Q ;
- the maximization of the mass flow rate.

It is difficult to define the heat transfer equilibrium between the aquifer and the evaporator of the thermosyphons. First of all, without the benefit of fracture circulation the system capacity would be limited and heat extraction would quickly decline. Convection promoters are devices proposed to increase the fluid (and heat) transport between aquifer, well and DHE. Heat flow rate is a function of the mass circulation rates and it shows a maximum. Near to this maximum, the Q values show a small difference from the maximum for a large range of mass circulation rates. Anyway, it is important that the device operates in the way such that the maximum of the heat flow is obtained. The determination of an equilibrium point between heat transfer well-evaporator and well-aquifer and mass transfer in the thermosyphon requires further research activity, mainly if the development of a HPT systems is considered.

5. CONCLUSIONS

The use of heat pipe principle for geothermal energy extraction can be an interesting pathway for geothermal systems available at reduced depth and temperature below 100 °C. A real advantage consists in the direct solution of resource depletion and reinjection problems. The concept can be used both for direct heat uses, like in Geothermal Convective Systems and for power production.

The idea has been critically reviewed starting from an analysis of various applications. Though if a reduced number of installations can be observed, the development of CLTPT appears to be interesting, both for direct heat used and also in connection with small (single well) power systems (HPT) of 1-2 kW. In this last case, considering a solution similar to that proposed for binary cycle, an energy efficiency up to 7% can be obtained. This results is surely interesting if compared with those obtained with the conventional HPT systems.

NOMENCLATURE

c_p	Specific heat at constant pressure
d	Pipe diameter
g	acceleration due to gravity
h	height of the downhole heat exchanger
h_{fg}	evaporation enthalpy
H	distance evaporator-condenser
m	mass flow rate
M	merit number
Q	heat flow
R_m	mixing ratio
T	temperature
U	Mean heat transfer coefficient
σ	surface tension of the working fluid
η	Thermodynamic efficiency
μ	viscosity

Acronyms and Abbreviations

CLTPT	Closed Loop Two Phase Thermosyphon
DHE	Downhole Heat Exchanger
GEESOR	Geothermal Energy Extraction System Organic Rankine
GTC	GeoThermal Convectore
HPT	Heat Pipe Turbine
ORC	Organic Rankine Cycle
TSR	Thermosyphon Rankine Engine

REFERENCES

- Allis R.G., (1980). *A study of the use of downhole heat exchanger in the moana hot water area, Reno.* GHC Report. Oregon Institute of Technology.
- Akbarzadeh A., Johnson P., Nguyen T., Mochizuki M., Mashiko M., Sauciu I., Kusaba S., Suzuki H., (2001). *Formulation and Analysis of the Heat Pipe Turbine for Production of Power from Renewable Sources*, App. Ther. Eng. 21, p. 1551-1563.
- Axelsson, G., Stefansson V., Björnsson G., Liu J., (2005). *Sustainable Management of Geothermal Resources and Utilization for 100-300 Years*. Proc. of World Geothermal Congress, Antalya, Turkey.
- Boyd T., Lund J.W., (2010). *Use of Promoter Pipes with DHE in Klamath Falls, Oregon*, Proc. of World Geothermal Congress, Bali, Indonesia.
- Carotenuto A., Casarosa C., Martorano L., (1999). *The geothermal convectore: experimental and numerical results*. App. Ther. Eng. 19, p. 349-374.
- Carotenuto A., Casarosa C., Dell'Isola M., Martorano L., (1997). *An aquifer-well thermal and fluid dynamic model for downhole heat exchanger with a natural convection promoter*. Int. Journal of Heat and Mass Transfer 40, p. 4461-4472
- Chiasson, A., (2006). *A Simplified Design Method for PEX Plastic Downhole Heat Exchangers*, GRC Annual Meeting San Diego, CA
- Culver, G.G., Lund J.W., (1999). *Downhole Heat Exchangers*, GHC Bulletin, vol. 20, no. 3
- DiPippo, R.D., (2008). *Geothermal Power Plants* Second Edition, Elsevier, Oxford.
- Faghri A., (1995). *Heat Pipe Science and Technology*. 6, Taylor & Francis, London.
- Franco A., Filippeschi S., (2010). *Experimental Analysis of Heat and Mass Transfer in Small Dimension, Two phase Loop Thermosyphons*, Heat Pipe Science and Technology, 1, p. 163-182.
- Franco A., Filippeschi S., (2012). *Closed Loop Two-Phase Thermosyphon of Small Dimensions: a Review of the Experimental Results*, Microgravity Sci. Technol. 24 (3) p. 165-179.
- Jeong S.J., Lee K.S., (2008). *Performance of a Two-Phase Carbon Dioxide-Filled Thermosyphon*, Materials Science Forum 569, p. 345-348.
- Kusaba S., Suzuki H., Hirowatari K., Mochizuki M., Mashiko K., Nguyen T., Akbarzadeh A., (2000). *Extraction of Geothermal Energy And Electric Power Generation Using a Large Scale Heat Pipe*, Proc. of World Geothermal Congress, Kyushu, Japan
- Lund, J.W., Culver, G.G., Svanevik L.S., (1975). *Utilization of Intermediate Temperature Geothermal Water in Klamath Falls, Oregon*. Proc. of the 2nd U.N. Symp. in the Development and Use of Geothermal Resources, San Francisco, CA, Vol. 2, p. 2147-2154.
- McGuinness M.J., Blakeley M., Pruess K., O'Sullivan M.J., (1993). *Geothermal heat pipe stability: solution selection by upstreaming and boundary conditions*, Transport in Porous Media, 11, p. 71-100.
- Nguyen T., Johnsson P., Akbarzadeh A., Gibson K., Mochizuchi M., (1995). *Design, Manufacture and Testing of a Closed Cycle Thermosyphon Rankine Engine*, Heat Recovery Systems & CHP 15 (4), p. 333-346.
- Peterson G.P., (1994). *An Introduction to Heat Pipes: Modeling, Testing, and Applications*, Wiley.
- Reay D, Kew P., (2006). *Heat Pipes* 5th ed., Elsevier.
- Rudorf J., (2008). *Thermosiphon Loops for Heat Extraction from the Ground*, PhD dissertation, Royal Institute of Technology, Sweden.
- Vasiliev L.L., (1990). *Geothermal energy utilization with heat pipes*, Journal of Engineering Physics and Thermophysics, 59, p. 1186-1190.
- Wang Z., McClure M.W., Horne R.N., (2009). *A Single-Well EGS Configuration Using a Thermosiphon*, Proc. of the 34th Workshop on Geoth. Reservoir Engineering, Stanford, USA.

CRYOGENIC THERMAL LINK WITH TWO PHASE COLD RESERVOIRS

P. Gully, F. Bonnet

CEA-INAC/SBT

UMR_E 9004 CEA-UJF

17 Rue des Martyrs, 38054 Grenoble Cedex 9

Phone: +33 (0)4 38 78 32 40, Fax: +33 (0)4 38 78 51 71, E-mail address: philippe.gully@cea.fr

ABSTRACT

The need of thermal links in cryogenic applications is increasing, especially because of the use of mechanical cryocoolers which offer a reduced size cold finger to cool any object located at large distance. We have designed, manufactured and tested a laboratory prototype of a new two phase thermal link using helium as working fluid. It features a closed circuit with two heated cold reservoirs thermally shunted to the cold source, two condensers and an evaporator connected with a small pipe. The heat is transported from the evaporator to one of the condensers by applying small electrical heating power to the other side cold reservoir which acts as a liquid pump. As soon as the reservoir empties, the heating power is switched to another reservoir. This system can cool down efficiently any warm object. It can also be used to remove heat at constant cryogenic temperature. Experimental results of the cool down of a 950 J thermal mass from 60 K to 4 K are presented. The thermal performance of the thermal link at constant temperature between 3 K and 4.3 K are also presented and discussed.

KEY WORDS : Cryogenics, two phase heat transfer

1. INTRODUCTION

Efficient passive thermal links are needed to ease the distribution of the cold power in any cryogenic systems where mechanical cryocoolers are used. When the distance between the object to be cooled and the cryocooler becomes large, typically on the order of one meter or more, copper links are heavy or lead to significant temperature gradients.

Two phase thermal links become attractive in such a situation and developments have been made at cryogenic temperature in the last ten years, among them capillary pumped two phase systems (Hoang, 2002, Yun 2002, Khruslatev, 2003, Mo, 2006 and Gully, 2011), pulsating heat pipes (Chandratilleke, 1998, Jiao, 2006 and Bonnet, 2011) and thermo siphons (Benkhera, 2006).

The use of a two phase thermal link at cryogenic temperature requires precooling of the objet before operation. In the precooling systems the gravity force or capillary pressure are used to push liquid towards the evaporator to cool the object. We present the thermal performances of a new cryogenic thermal link with two phase cold reservoirs acting alternatively as liquid pumps. Helium is used as working fluid. The result of the cool down of a warm thermal mass is presented.

The thermal performance of the thermal link at constant temperature between 3 K and 4.3 K is also presented and discussed.

2. THE CRYOGENIC THERMAL LINK WITH TWO PHASE COLD RESERVOIRS

2.1 Description

A laboratory prototype has been designed manufactured and tested at the Divison of low temperatures of Institute for Nanosciences and Cryogenics (INAC/SBT). It is a closed two phase system (Figure 1). It consists of two cold reservoirs, two thermal resistances used to heat the reservoirs, an evaporator thermally connected to a thermal mass (object) and a single pipe that connects together all the components.

Starting from a warm evaporator and cold reservoirs with liquid inside, the cool down is performed as follows. When applying a small heating power Q_{R1} to the reservoir 1, both its temperature T_{R1} and pressure increase slightly and a pressure difference between the reservoirs appears. The gas in the heated reservoir acts as a liquid pump. It pushes the liquid towards the other

reservoir. The sub cooled liquid flows towards the evaporator where it is evaporated.

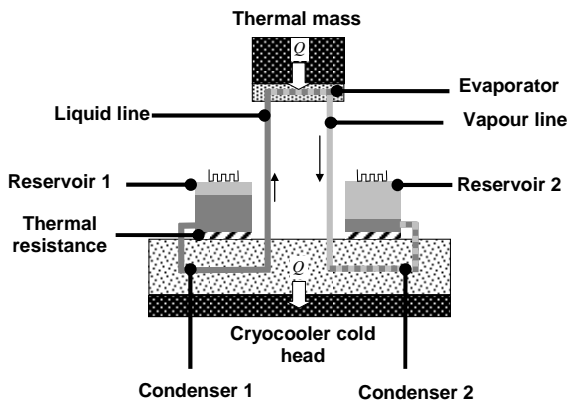


Figure 1. Principle of the thermal link with two cold reservoirs.

The vapor penetrates into the condenser 2 where it is condensed and the reservoir 2 fills up. During this process, a significant cooling power Q can be removed from the object due to the latent heat. When the reservoir 1 empties, its heater is switched off and the heater Q_{R2} of the reservoir 2 is turned on. As a consequence, a similar process occurs and the flow changes direction.

This system can be also used for any heat removal at constant temperature. If such a system is used alone, the evaporator temperature T_{EVAP} is not constant because of the change of flow direction when switching the heaters. This limitation can be overcome by using for instance two identical systems connected in parallel of the object (Figure 2). With a controlled heat management, a liquid flow rate of at least one evaporator can be maintained at any time.

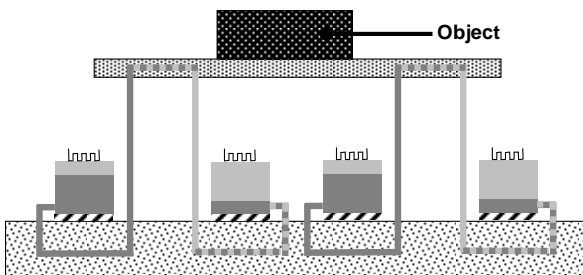


Figure 2. Two identical systems in parallel.

The system setting is presented in Figure 3. The reservoirs (5 cm^3 each), the condenser and

evaporator blocs are made of copper. The pipe (1 mm outer diameter) is brazed in grooves machined in the copper blocs. The pipe ends are brazed close to the bottom of each reservoir to use their full liquid capacity. The system is equipped with electrical heater on each reservoir and with thermometers (Cernox sensors) mounted on the reservoirs, on the condenser bloc and on the evaporator.

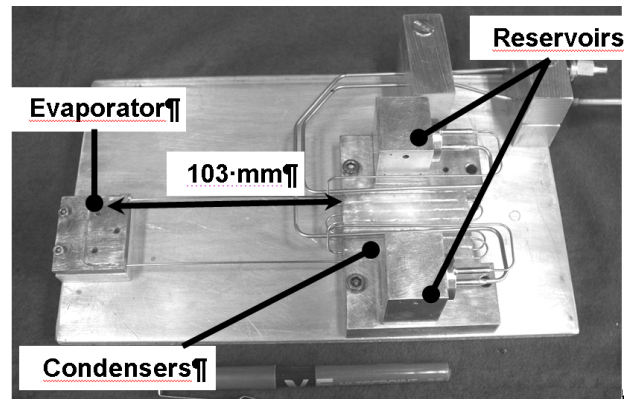


Figure 3. Photograph of the cryogenic thermal link with two phase reservoirs.

2.2 Experimental set up

The system was tested in horizontal position in a test cryostat (Figure 4). It comprises a vacuum vessel with a double stage pulse tube cryocooler as a cold source. The first stage is used to cool the first copper thermal shield. The second stage cools the internal cold thermal shield and a large, thick and isothermal copper cold plate whose temperature T_{CP} is kept constant at a required value (3.0 K, 3.4 K or 4.2 K) using a heater and a PID regulation.

The condenser bloc is mechanically anchored to the cold plate. The evaporator and the thermal mass are mechanically and thermally coupled together. They represent the total mass of 0.37 kg to be cooled down. Two types of tests have been performed:

- Cool down test starting with the evaporator at 60 K and the condenser at 4.3 K.
- Thermal performance in stationary condition at different cold plate temperatures and transferred powers Q .

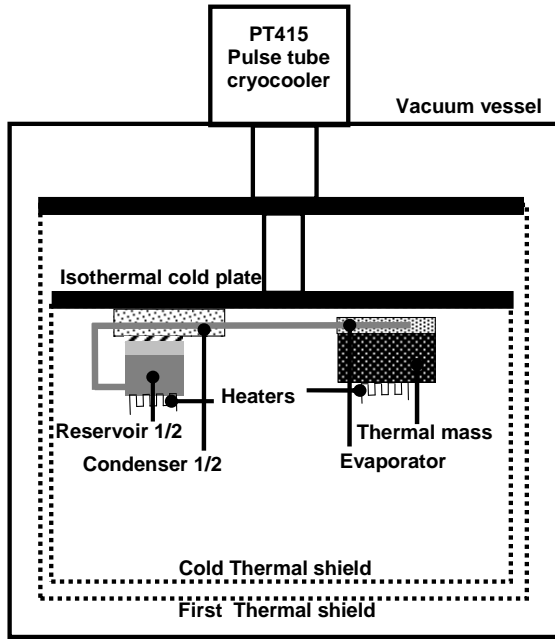


Figure 4. Experimental set up.

3. RESULTS AND DISCUSSION

3.1 Cool down test

The thermal mass takes about 1.7 h to be cooled (Figure 5). During the transient a small heating power (5 mW) is alternately applied to the two-phase reservoirs (Figure 6). The temperature of the heated reservoir rises (up to 4.4 K) and fixes the pressure of the system. As a consequence, the temperature of the other (not heated) reservoir is close to that of the heated reservoir because of negligible pressure drop in the pipe. When the heated reservoir empties, the vapor starts flowing out of it instead of the liquid. Therefore the reservoir temperature starts to decrease. This phenomenon is used as an indicator for the switching of the reservoirs heaters. In the experiment, the use of such a process allows removing a total energy of 950 J (value calculated from the total mass of the evaporator and the thermal mass and the specific enthalpy of copper) from the evaporator. This corresponds to the mean transferred power of 150 mW.

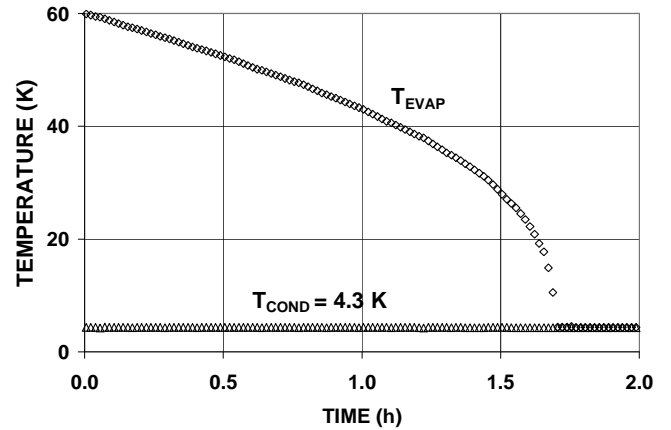


Figure 5. Cool down of the thermal mass from 60 K to 4.3 K. General results.

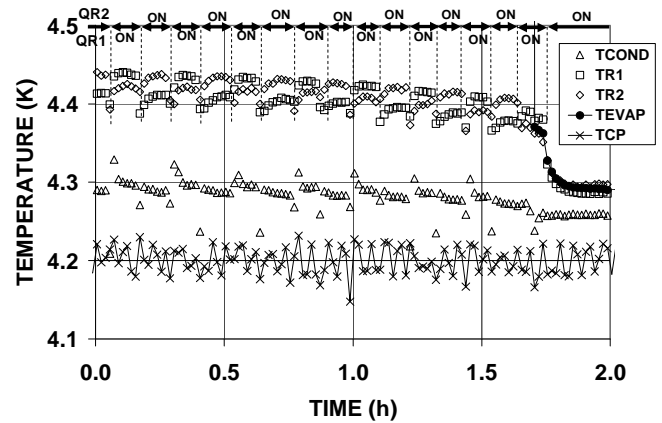


Figure 6. Cool down of the thermal mass from 60 K to 4.3 K. The temperatures as functions of time are shown.

3.2 Thermal performance in stationary condition

The temperatures in stationary condition are measured after thermal stabilization during several test series. For each run, a constant heating power ($Q_R = 1 \text{ mW}$) is applied to one reservoir; the heating power Q applied to the evaporator is increased step by step. The test is aborted when the evaporator temperature T_{EVAP} becomes unstable or diverging. The results of a typical run are shown in Figure 7.

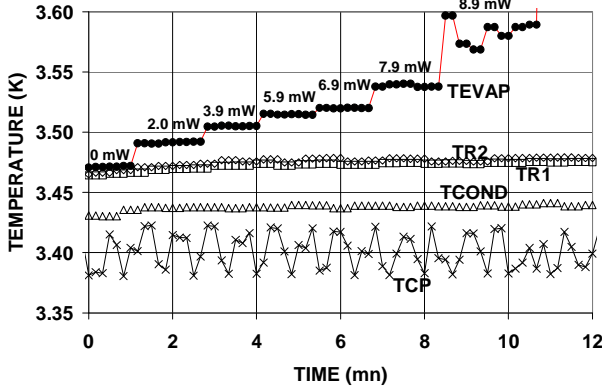


Figure 7. Typical run. Temperatures as functions of time are shown.

The two reservoirs are at the same temperatures T_R . This means that pressure drop between them is negligible. For this test, the maximum transferred power Q_{MAX} is 7.9 mW above which the evaporator temperature T_{EVAP} is no more stable. Using the temperatures measured after stabilization, the thermal performance of the thermal link can be plotted (Figure 8).

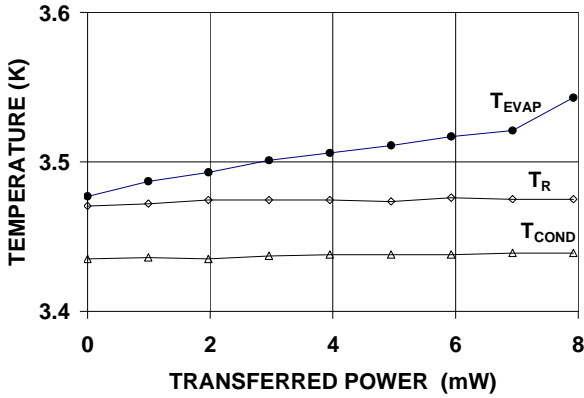


Figure 8. Condenser, reservoirs and evaporator temperatures as functions of transferred power for the 3.4 K cold plate temperature test series.

The whole system temperature difference $T_{EVAP} - T_{COND}$ consists of two different contributions. The first contribution $T_{EVAP} - T_R$ is the temperature difference between the evaporator and the reservoirs which are at saturation. It is the results of heat transfer in the evaporator. The second contribution $T_R - T_{COND}$ is the consequence of the heat transfer in the condensers. This latter temperature difference induces a heat flow Q_{RTH}

through the thermal resistance. The difference $Q_R - Q_{RTH}$ is used to generate a pure liquid mass flow rate \dot{m} at the heated reservoir outlet. The mass and energy balance applied on the heated reservoir reads

$$\dot{m} = \frac{Q_R - Q_{RTH}}{h_{LV}} \left(\frac{\rho_L}{\rho_V} - 1 \right), \quad (1)$$

where h_{LV} , ρ_L and ρ_V are respectively the evaporation latent heat and the liquid and vapor densities. The mass and energy balance on the non-heated reservoir leads to

$$Q_{RTH} = \frac{\dot{m} h_{LV}}{\frac{\rho_L}{\rho_V} - 1} \left[\frac{1}{\alpha \left(\frac{\rho_V}{\rho_L} - 1 \right) + 1} + 1 \right], \quad (2)$$

where α is the void fraction of the two phase fluid entering the non-heated reservoir. Combining (1) and (2), one obtains

$$Q_{RTH} = (Q_R - Q_{RTH}) \left[\frac{1}{\alpha \left(\frac{\rho_V}{\rho_L} - 1 \right) + 1} + 1 \right]. \quad (3)$$

Finally assuming $\rho_V \ll \rho_L$ and a small void fraction $\alpha \ll 1$ of the fluid entering the non-heated reservoir, i.e. efficient condensation process in the condenser, we can obtain simple expressions for the heat flow Q_{RTH} through the thermal resistance and for the maximum transferred power Q_{MAX} which corresponds to the total evaporation of the liquid flow in the evaporator:

$$Q_{RTH} = \frac{Q_R}{2} \quad (4)$$

$$Q_{MAX} = \dot{m} h_{LV} = \frac{Q_R}{2} \left(\frac{\rho_L}{\rho_V} - 1 \right) \quad (5)$$

Figure 9 shows a good agreement on Q_{MAX} between the experimental results and equation (5). A significant temperature effect on Q_{MAX} is observed. This effect is due to the dependence of $\frac{\rho_L}{\rho_V}$ on the temperature. For given

Q_R this ratio acts as an amplifier to achieve large Q_{MAX} . This means that this kind of thermal link is

suitable for cryogenic fluids which have large $\frac{\rho_L}{\rho_V}$ to achieve very large transferred power using a limited reservoir heating. The interest of the design is that the maximum transferred power depends only on the fluid properties and not on the geometry of the thermal link, in particular on the distance between the condenser and the evaporator.

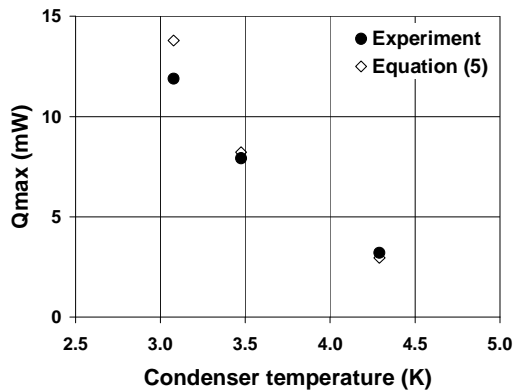


Figure 9. Maximum transferred power Q_{MAX} (experimental results and equation (5)) for different reservoir temperatures.

4. CONCLUSION

A cryogenic thermal link with two phase cold reservoirs using helium as working fluid has been designed, manufactured and tested at INAC/SBT. An efficient cool down of warm objects down to 4.3 K transferring a mean power of 150 mW has been demonstrated. This system can be used to remove heat and maintain any object at a constant cryogenic temperature. The maximum transferred power mainly depends on the liquid-vapor density ratio and is independent of the geometry and of the distance condenser-evaporator.

NOMENCLATURE

Parameter

T	Temperature
Q	Heating power
\dot{m}	Mass flow rate
x	Vapor quality
h_{LV}	Evaporation latent heat
ρ	Fluid density

Subscript

$R1$	Reservoir 1
$R2$	Reservoir 2
$EVAP$	Evaporator
$COND$	Condenser
CP	Cold plate
RTH	Thermal resistance
L	Liquid
V	Vapor

ACKNOWLEDGEMENT

The authors gratefully acknowledge the help of D. Garcia, J. Inigo, Y. Poultriniez and all technical support staff of INAC/SBT in manufacturing, commissioning, and testing the cryogenic system.

REFERENCES

- Benkhera L., et al. (2006), *Régimes d'ébullition convective d'un écoulement thermosiphon en hélium normal (4,2 K)*. Proc. Congrès Français de Thermique, SFT 2006, Île de Ré, France
- Bonnet F., Gully P. (2011), *Development and test of a cryogenic pulsating heat pipe and a pre-cooling system*. Proc. CEC-ICMC 2011, Conf., Spokane (USA)
- Chandratilleke R., et al (1998), *Development of multi-loop heat pipes for superconducting magnet applications*. Proc. Cryogenic Engineering Conference, 1998, Advances in Cryogenic Engineering, Vol. 43, Edited by P. Kittel, Plenum Press, New York
- Gully P., MO Q., Yan T., Seyfert P., Guillemet L., Thibault P. (2011), *Thermal behaviour of a cryogenic loop heat pipe for space application*. Cryogenics 51 p. 420-428
- Hoang T.T., Khruslatev D., Ku J. (2002), *Cryogenic advanced loop heat pipe in temperature range of 20-30K*. Proc. 12th IHPC, pp. 201-205
- Jiao A.Z. J. et al. (2009), *Experimental investigation of cryogenic oscillating heat pipes*. Int. J. Heat Mass Transfer, Volume 52, Issues 15-16, July 2009, p. 3504-3509
- Khruslatev D. (2003), *Cryogenic loop heat pipes as flexible thermal links for cryocoolers*. Proc. 12th Int Cryocoolers Conf, pp. 709-716
- Mo Q., Liang J.T (2006), *A novel design and experimental study of a cryogenic loop heat pipe with high heat transfer capability*. Int. J. Heat Mass Transfer 49 p. 770-776

Yun J., Kroliczek E. and Crawford L. (2002),
*Development of a Cryogenic Loop Heat pipe
(CLHP) for Passive Optical Bench Cooling
Applications*. Proc. 32nd ICES, SAE paper n°
2002-01-2507, Conf., San Antonio, Texas

PERFORMANCE OF A GRAVITY-DRIVEN AND CAPILLARY-SIZED THERMOSYPHON LOOP WORKING WITH AMMONIA

Mathieu Habert*

ABB Ltd. Switzerland, Corporate Research, Segelhofstrasse 1K, 5405 Daettwil, Switzerland
mathieu.habert@ch.abb.com, tel. +41 (0)586 80 57, fax. +41 (0)586 40 06

Bruno Agostini

ABB Ltd. Switzerland, Corporate Research, Segelhofstrasse 1K, 5405 Daettwil, Switzerland
bruno.agostini@ch.abb.com, tel. +41 (0)586 80 42, fax. +41 (0)586 40 06

ABSTRACT:

The current trend in power electronics as in microelectronics is a continuous increase of heat losses and heat density. As a consequence the performances of these devices are often thermally limited. Two-phase cooling technologies based on the thermosyphon principle are a promising solution because they can comply with long operation time without maintenance. However their use for power electronics is still not widespread. Ammonia is a promising natural refrigerant for the replacement of HFCs in low charge systems but no experimental data or models are available at the required working conditions. This study presents a comparison of the performance of ammonia in a gravity-driven and capillary-sized thermosyphon loop designed for power electronics cooling compared with three fluorinate fluids: R134a, R245fa and Novec 649. The influence of heat load, filling ratio, coolant temperature and flow rate were investigated and compared. The results show enhanced performance using Ammonia with 20% decrease in thermal resistance, a 20% increase of manageable heat load with 50% less fluid charge.

KEYWORDS: thermosyphon, heat pipe, power electronics, refrigerant, ammonia

1. INTRODUCTION

The current trend in power electronics is a continuous increase of heat losses and heat density. As a consequence the performances of these devices are often thermally limited and traditional cooling technologies like heat sinks are unable to cope with this increasing trend in heat dissipation. Two-phase cooling technologies based on the thermosyphon principle are a promising solution because, being entirely passive and simple equipments, they can comply with 30 years of operation without maintenance. Furthermore their simple design makes them cheap to produce.

The choice of the working fluid is an important design issue as it will condition the global performance of the system. The “ideal fluid” should have good thermal properties, be environment friendly, safe, non-toxic, chemically stable, cheap and available. Water is the most common working fluid used in two-phase thermosyphon loop, but its use is usually not well accepted in power electronics.

HFCs (chlorine-free hydrofluorocarbons) and natural fluids such as ammonia are nowadays used in large quantities in refrigeration systems and exhibits most of the above-mentioned characteristics. However their use in power electronics is still not widespread and no experimental data or models are available at the required working conditions.

Palm et al. (2003) simulated the performance of water, ammonia, R134a, R32, R142b and R600a in a thermosyphon loop and conclude that for their specific design, channel dryout would occur at much higher heat loads for higher reduced pressure fluid: 90W for water, 250W for R134a and 600W for ammonia.

Franco (2008) has compared the performance of a closed loop thermosyphon with water, R11, R113, R141b and FC72 showing a higher mass flow and bumble pump efficiency for higher saturation temperature fluids FC72, R113 and R141b.

ABB has developed its own improved compact two-phase thermosyphon technology for

power electronics. The choice of the working fluid should cope with the technical requirements specific to power electronics application.

2. ABB THERMOSYPHON COOLER

Heat sinks are currently used in air cooled converters to remove heat losses from the power electronics modules. An increase in the heat transfer rate would mean an increase in size and air velocity, which would in turn increase cost and noise. Furthermore, the heat spreading from the semiconductor into the heat sink base is a limiting factor. ABB developed a compact thermosyphon cooler, shown in Figure 1, manufactured using automotive technologies, in order to increase the heat transfer removal from the semiconductors and increase the maximum ambient temperature at which the converter can operate.

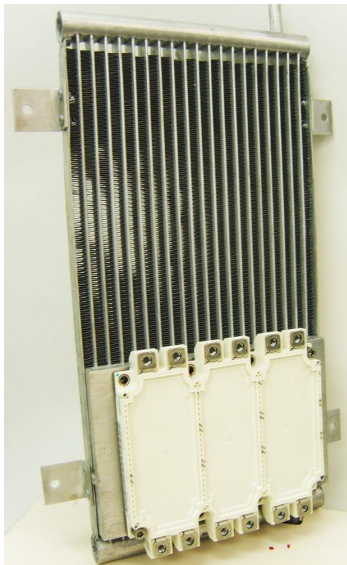


Figure 1: ABB compact thermosyphon cooler.

Figure 2 shows the details of the design and the working principle. The cooler is made of parallel aluminium multi-port extruded (MPE) tubes whose ends are connected to a manifold tube at the top and bottom. The cooler is divided into an evaporator plus riser section at the bottom and a condenser plus downcomer section at the top. The MPE tube is composed of several mini-channels in parallel. Part of these channels are dedicated to the evaporation and therefore brazed into a baseplate where the power electronics is fixed while louvered air fins are fixed on the remaining channels for condensation. Thus each of the MPE tubes behaves like an individual thermosyphon. This design allows having a large number of MPE

tubes in a given volume and therefore yields a higher heat density than classical heat pipe coolers.

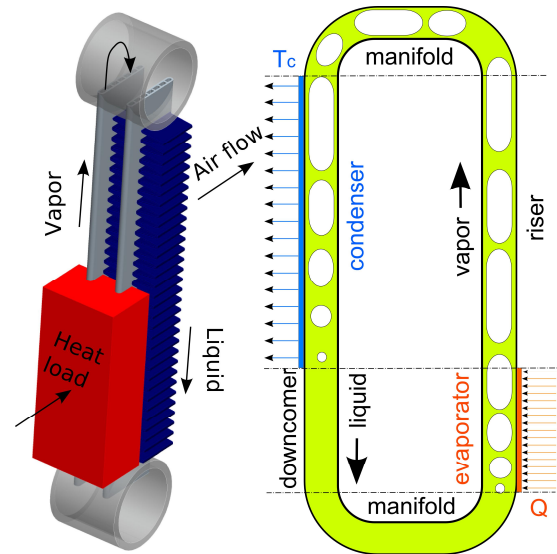


Figure 2: design and working principle.

3. MATERIAL AND METHODS

The test facility, shown in Figure 3, is equipped to monitor and acquire the top and bottom temperatures, pressure and level of working fluid. The cooler baseplate was equipped with 6 thermocouples in order to measure the temperature non-uniformity and detect hotspots under the heating power module. The air flow temperature was controlled using an air tunnel equipped with a frequency-controlled fan, an air flow meter and a PID-controlled chiller. Air temperature is measured at one location, in the middle of the stream for the inlet, and at 3 locations (centre left, centre middle and centre right) at the outlet to take into account flow non-uniformity. The heating was provided with a 6MBI450U-120 IGBT module. All the instruments used for these measurements and their relative uncertainties are shown in Table 1.

The energy balance, calculated as the relative difference between the electrical power injected in the baseplate and the heat extracted by the air stream, was kept below 8%. The uncertainty of the measured electrical power and calculated air enthalpy change are $\pm 0.8\%$ and $\pm 1.4\%$ respectively. Working fluids thermo-physical properties are taken from the software NIST REFPROP 9.0.

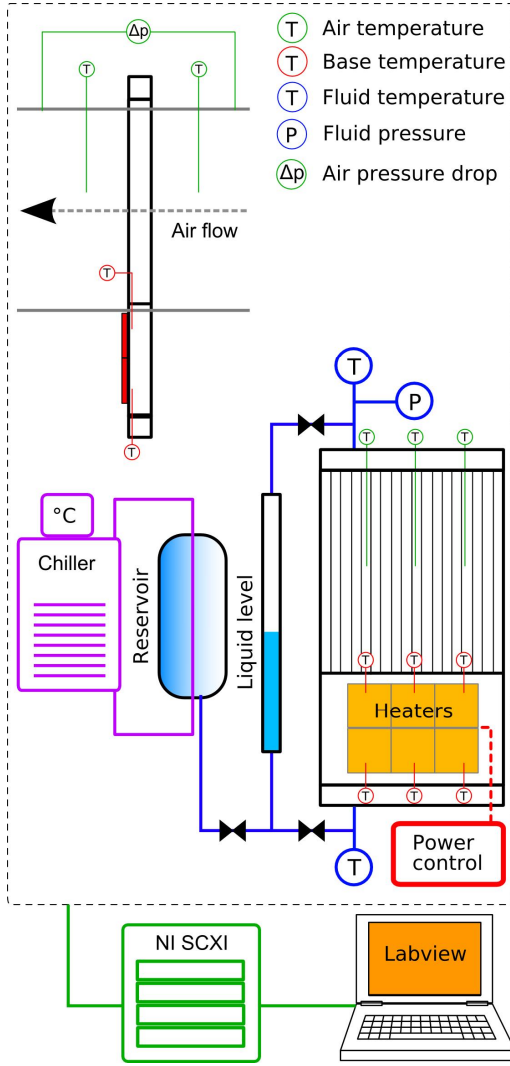


Figure 3: test setup.

Table 1: instrumentation and uncertainties

Instrument	Type	Range	Error
thermo-couple	Thermocoax type K (calibrated)	0–200 °C	0.1 K
pressure sensor	ABB 261AS	0-30 bar	0.15 %
data acquisition	NI SCXI 1000 + module 1102	0-10 V	0.02 %
pressure drop	Huba control	0-100 Pa	2 %
air flow rate	ABB Topaz	80-4000 kg/h	0.1 %
power supply	Xantrex XDC 1200	0-10 V, 0-1200 A DC	0.3 % 0.5 %

The chosen data reduction procedure was to calculate the average thermal resistance, together with an associated uncertainty that

represents the measured temperature non uniformity. When there is a hotspot, the average thermal resistance will be well below the maximal one. This is useful to optimize the thermosyphon and usually the minimal average thermal resistance also yields the minimal temperature difference over the base plate.

The total average thermal resistance is calculated as follows:

$$R_{th} = \frac{\bar{T}_b - T_{air,in}}{Q} \quad (1)$$

where $\bar{T}_b = \frac{1}{6} \cdot \sum_1^6 T_{b,i}$ is the average base-plate temperature.

The condenser thermal resistance is calculated as follows:

$$R_{th,c} = \frac{T_{f,top} - T_{air,in}}{Q} \quad (2)$$

The evaporator thermal resistance is calculated as follows:

$$R_{th,e} = \frac{\bar{T}_{w,e} - T_{f,top}}{Q} \quad (3)$$

where $T_{w,e} = \bar{T}_b - \frac{Q \cdot e_b}{k_b \cdot A_b}$ is the average channel wall temperature.

The filling ratio was obtained using a glass tube to observe and measure the liquid level.

The uncertainties on the measurement of the average thermal resistance as a function of the heat load are displayed on Figure 4. For heat load above 200W, they are acceptable because below 10%.

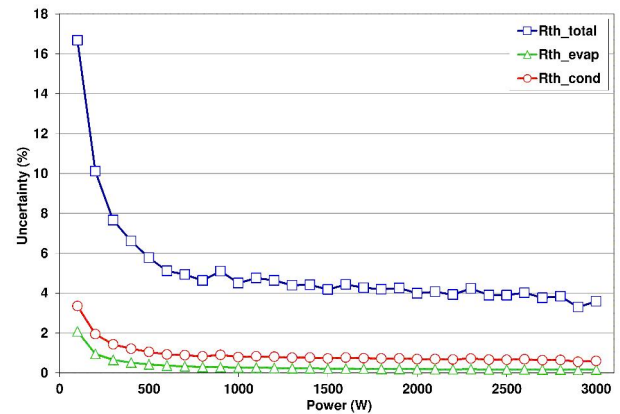


Figure 4: uncertainties on thermal resistances.

4. MEASUREMENTS

Initially, the effect of fluid filling on the thermosyphon performance was tested as shown on Figure 5.

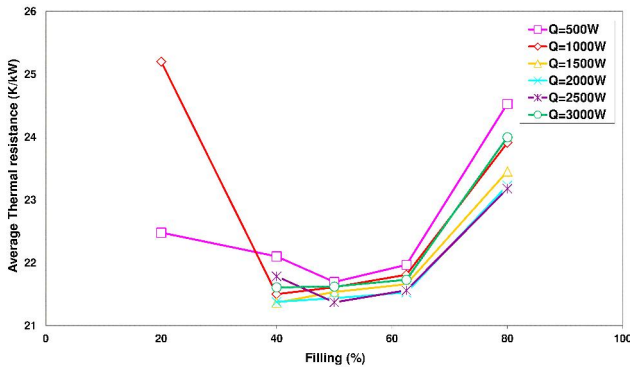


Figure 5: Influence of filling ratio on thermal performance

It is obvious that there is an optimal range of filling ratio (between 40 and 60%) where the cooler performance remains the same. Outside of this range a decrease of performance is observed for low filling ratio due to dry-out of the evaporator channels and for high filling ratio due to the flooding of the condenser. These observations are similar to the one made by Agostini et al. (2012) when using R134a. Only 50 g of ammonia are required in the cooler, compared to 100-150g using R134a, R245fa or Novec-649.

The evolution of the average thermal resistance calculated with equation (1) is shown on Figure 6 as a function of the heat load. It is remarkable to see that 3000W of heat were dissipated using ammonia before dry-out occurs. For the other fluids, dry-out had already appeared for 2500W and the experiment stopped.

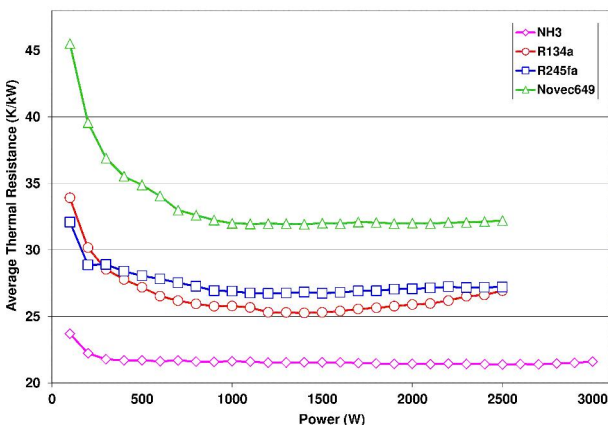


Figure 6: Influence of heat load on average thermal resistance

If we compare the average thermal resistances obtained for the different fluids, ammonia is the one performing the best: at 2500W, the improvement is 20.4% compared to R134a, 21.3% compared to R245fa and 33.5% compared to Novec649.

A more detailed analysis can be made using Figs 7 and 8 showing respectively the evaporator and condenser thermal resistance calculated with Eqs. (2) and (3).

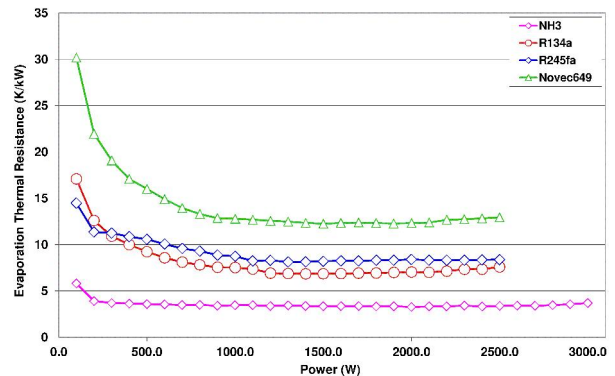


Figure 7: Influence of heat load on evaporator thermal resistance

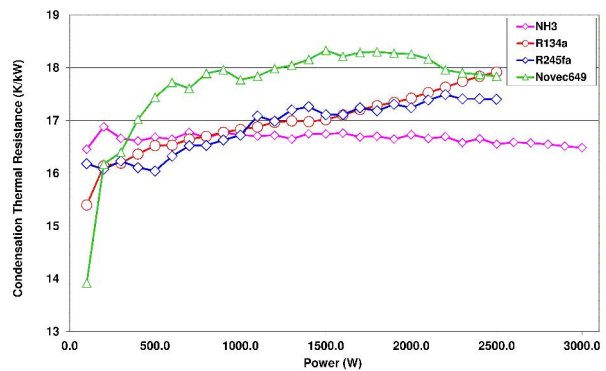


Figure 8: Influence of heat load on condenser thermal resistance

For ammonia, thermal resistances are constant over the range of heat load tested. The condensation thermal resistance has a similar value for the 4 different fluids which means that the dominating resistance is on the air side. On the evaporator side, large differences can be observed between the fluids. The evaporator thermal resistance is improved by 2 to 3 times using ammonia. The evaporator performance seems to be improving when increasing reduced pressure.

Figure 9 shows the evolution of the maximum temperature difference on the baseplate as a function of the heat load and fluid. The trends observed for each fluid show clearly a better temperature uniformity when using ammonia: at

2500W, 3°C with ammonia compared to 9°C with R134a, 10°C with R245fa and 14°C with Novec649. The change of slope represents the occurrence of dry-out within the channel of the baseplate: 1200W for Novec649, 1600W for R134a and R245fa compared to 2500W for ammonia.

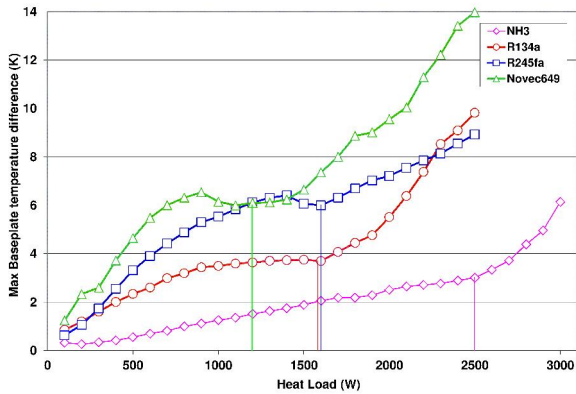


Figure 9: Influence of fluid on onset of dry-out

Figures 10 and 11 show respectively the effect of air flow rate and ambient temperature on the thermosyphon performance for a heat load of 1800W.

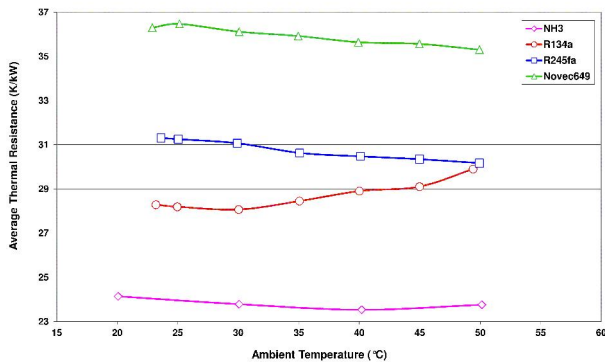


Figure 10: Influence of air inlet temperature on thermal performance

The effect of the air inlet temperature is limited on the average thermal resistance compared to the other parameters.

On the other hand, better performance were observed when increasing air flow rate, mainly due to the improvement of the air side thermal resistance.

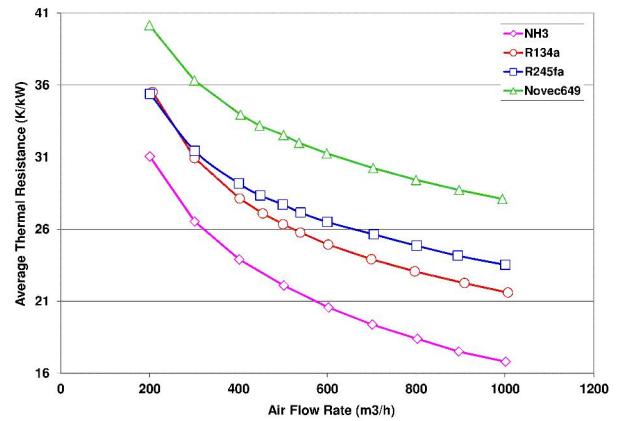


Figure 11: Influence of condenser air flow rate on thermal performance

Finally, the transient behaviour of the thermosyphon cooler was tested with ammonia and R134a for comparison. An example of load cycle for power electronics application was applied to the power module: 4 min at 1800W nominal load followed by 1 min at 50% overload. This cycle was repeated 3 times. The evolution of the fluid and maximum baseplate temperatures with time is displayed on Figure 12.

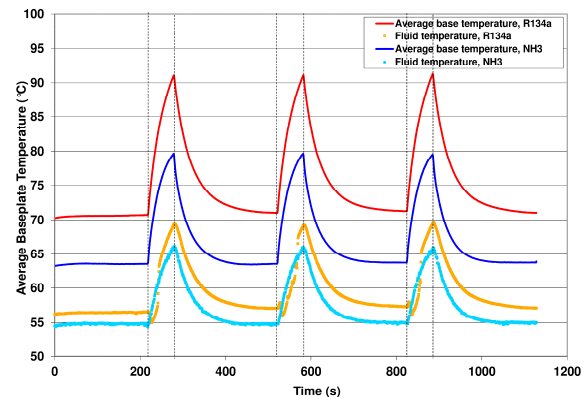


Figure 12: Transient behaviour of ammonia compared to R134a

At nominal load, an improvement of 7.5°C on the maximum baseplate temperature is observed using ammonia. This improvement even reaches 15°C during overload. This can be explained by the fact that Dry-out occurs earlier for R134a, giving a steeper increase of temperature during the overload

5. CONCLUSIONS

The results show enhanced performance using Ammonia with 20% decrease in thermal resistance, a 20% increase of manageable heat load with 50% less fluid charge, more uniform

baseplate temperature and better transient behavior.

The use of ammonia as working fluid can bring a large advantage in power electronics because of its excellent thermal behavior and low environmental impact, but even in small quantities, its safety classification as B2 (high toxicity, low flammability) makes it practically difficult to implement.

NOMENCLATURE

A_b	base plate area	(m ²)
e_b	base plate thickness	(m)
k_b	base plate thermal conductivity	(W/m K)
Q	heat load	(W)
R_{th}	thermal resistance	(K/kW)
T	temperature	(K)

Subscripts

air	air	-
b	base plate	-
bot	bottom	-
c	condenser	-
e	evaporator	-
f	fluid	-
in	inlet	-
top	top	-
w	channel wall	-

REFERENCES

Palm B., Khodabandeh R. (2003) *Choosing Working Fluid for Two-Phase Thermosyphon Systems for Cooling of Electronics*. Journal of Electronic Packaging, Vol. 125, p. 276-281.

Franco A. (2008) *Heat Transfer and Flow pattern in two-phase loops: Experimental Investigation*. 5th European Thermal-Sciences Conference, The Netherlands, 2008

Agostini B., Habert M. (2012) *Compact Thermosyphon Heat Exchanger for Power Electronics Cooling*. 16th International Heat Pipe Conference, France, 2012

STUDY ON HEAT TRANSFER CHARACTERISTICS OF LOOP HEAT PIPE FOR SOLAR COLLECTOR

Shigeki Hirasawa, Shota Sato, and Tsuyoshi Kawanami

Department of Mechanical Engineering, Kobe University

1-1, Rokkodai, Nada-ku, Kobe, Hyogo 657-8501 Japan

Tel/Fax: +81-78-803-6153

hirasawa@kobe-u.ac.jp, shota.sato.0505@gmail.com, kawanami@mech.kobe-u.ac.jp

ABSTRACT

We experimentally studied the thermal conductance of single-tube and loop heat pipes for a solar collector. The evaporator of the heat pipe is 1 m long, 6 mm in diameter and has 30° inclination. The thermal conductance is defined as the heat transfer rate divided by the temperature difference of the evaporator-wall and the condenser-wall. Effects of heat transfer rate, saturation temperature of the working fluid, liquid fill ratio, and inclined angle on the thermal conductance are examined. We found that the thermal conductance of the inclined loop heat pipe is 40-50 (W/K), which is 10 % higher than that of a vertical loop heat pipe and three times higher than that of a single-tube heat pipe. Thus, the inclined loop heat pipe is preferable for a solar collector. There is an optimum liquid fill ratio, which is a function of heat transfer rate. When the liquid fill ratio is too small, a dry-out portion appears in the evaporator. When the liquid fill ratio is too large, the liquid flows into the condenser to decrease heat transfer area. Also we numerically analyze the thermal conductance of a vertical loop heat pipe.

KEY WORDS: Loop Type Thermosyphon, Thermal Conductance, Inclined Angle

1. INTRODUCTION

To reduce consumption of fossil fuel and to decrease CO₂ emission, alternative energy systems have been developed. Solar energy is one form of clean energy. If all houses use more solar energy for their heat source, much fossil fuel can be saved. To expand the usage of solar energy, a highly efficient solar collector system needs to be developed. Heat pipe solar collector system, which uses heat pipes to transfer heat from the collector plate to the heat storage tank, has high collector-efficiency (Tanaka, 2003). Figure 1 schematically shows a heat pipe solar collector system. The evaporator of the heat pipe is attached to the collector plate, and the condenser of the heat pipe is attached to the heat storage tank. We use loop wickless thermosyphon heat pipe.

Many researches on a loop heat pipe have been reported. McDonald et al. (1977) studied the effect of liquid fill ratio, inclination angle, and saturation temperature of working fluid (R-11 and R-113) on the thermal conductance of a loop heat pipe. Vincent et al. (1992) analyzed transient performance of a loop heat pipe using the control volume approach and reported the dynamic oscillation phenomena. Takahasi et al. (2008)

experimentally studied the effect of the working fluid and the heat transfer rate on the thermal conductance. Koito et al. (2010) reported experimental result of a 2-m-long closed loop heat pipe with valves to circulate working fluid.

In this paper, we experimentally study the thermal conductance of a heat pipe for a solar collector system. We examined effects of the liquid fill ratio, heat transfer rate, and inclination angle on the thermal conductance. We examined single-tube

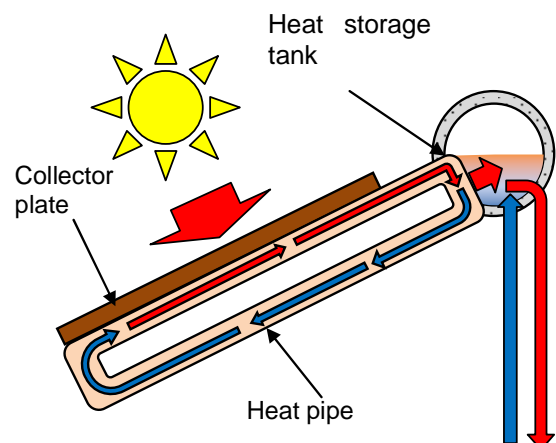


Fig. 1 Solar collector system

and loop heat pipes. Also we numerically analyze the thermal conductance of a loop heat pipe.

2. EXPERIMENTAL APPARATUS

We study thermal performance of a heat pipe for the solar collector system shown in Figure 1. The collector plate for home usage is 1-2 m long with 30°-inclination, and the solar heat flux is less than 1000 W/m². Therefore, we study a heat pipe with a 1-m-long evaporator and heat transfer rate of 100-300 W. Water is used as the working fluid for safety. Figure 2 schematically shows experimental apparatus of a single-tube type and a loop type. The heat pipe is a copper pipe with a 6-mm-outside diameter and 4.4-mm-inside diameter. The evaporator is 1 m long, and the condenser is 0.25 m long. The outside of the heat pipe is covered with a wool insulator. A flexible heater is attached to external surface of the evaporator, and the heating rate of the heater is controlled. A copper cooling plate is soldered to the condenser and the cooling rate is controlled by changing heat transfer area and flow velocity of cooling air in order to adjust the saturation temperature of the working fluid. Vertical and 30°-inclination of the heat pipe are studied. T-type thermocouples are attached at 19 positions of the heat pipe, and the temperatures at steady state are measured. Liquid fill ratio V is defined as the ratio between the height of the working fluid filled in the evaporator and the length of the evaporator before heating. Thermal conductance C (W/K), evaporator heat transfer coefficient α_e (W/m²K), and condenser heat transfer coefficient α_c (W/m²K) are defined as Eqs. (1)-(3).

$$C = Q/(T_e - T_c) \quad (1)$$

$$\alpha_e = Q/\{A_e(T_e - T_{sat})\} \quad (2)$$

$$\alpha_c = Q/\{A_c(T_{sat} - T_c)\} \quad (3)$$

where, Q (W) is the heat transfer rate, A_e and A_c are the evaporator and condenser heat transfer area, T_e and T_c are the mean wall temperatures of the evaporator and condenser, and T_{sat} is the saturation temperature of working fluid. The maximum heat transport Q_{max} (W) is defined as the heat transfer rate just before thermal conductance suddenly decreases.

3. EXPERIMENTAL RESULTS OF VERTICAL SINGLE-TUBE TYPE

Figure 3 shows the experimental results for the relationship between the heat transfer rate Q and the thermal conductance C of a vertical single-tube type heat pipe for liquid fill ratio $V = 0.5$ and saturation temperature $T_{sat} = 110-130^\circ\text{C}$. Thermal conductance is almost constant at 14 W/K when the heat transfer rate is less than 150 W. But thermal conductance decreases when heat transfer rate is 180 W. This is because the single-tube heat pipe was flooded. Flooding is the phenomenon in which the vapor flow turns back the liquid flow from the condenser to the evaporator when the vapor flow increases as the heat transfer rate increases. Figure 3 shows that the maximum heat transfer rate Q_{max} of a single tube type heat pipe is 150W.

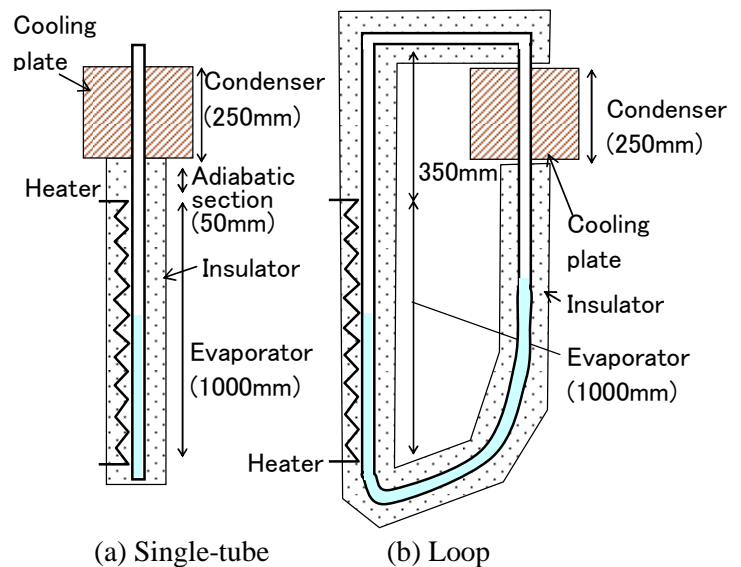


Fig. 2 Experimental apparatus

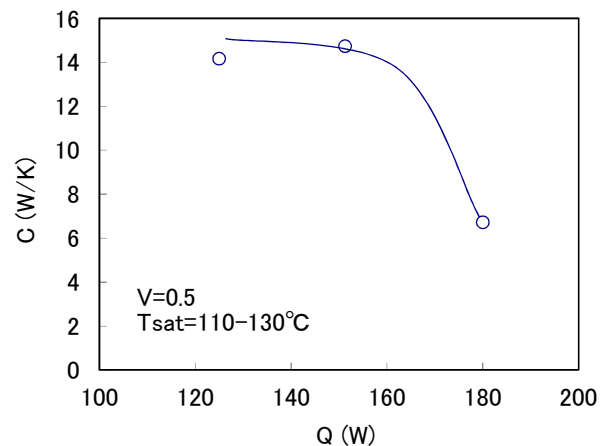


Figure 3. Relation between heat transfer rate and thermal conductance of single-tube type.

4. EXPERIMENTAL RESULTS OF VERTICAL LOOP TYPE

Figure 4 shows the experimental results for the relationship between the heat transfer rate Q and the thermal conductance C of a vertical loop heat pipe for liquid fill ratio $V = 0.3-0.5$ and saturation temperature $T_{sat} = 115-130^\circ\text{C}$. The thermal conductance is about 35-45 W/K for the liquid fill ratio 0.4-0.5, and it is 2.8 times as large as that of a single-tube type. When the heat transfer rate is larger than 210 W with the liquid fill ratio 0.3, thermal conductance decreases. This is because the dry-out appears in evaporator. The maximum heat transfer rate Q_{max} is more than 300 W for the liquid fill ratio 0.4-0.5, and it is higher than a single type. The boiling heat transfer coefficient α_e of the experimental results shown in Figure 4 is about 5-6 kW/m²K for the liquid fill ratio 0.4-0.5. The condensation heat transfer coefficient α_c is about 20-40 kW/m²K.

Figure 5 shows the experimental results for the relationship between the saturation temperature of working fluid T_{sat} and the thermal conductance C of a vertical loop type for liquid fill ratio $V = 0.4$ and heat transfer rates $Q = 210$ W. The thermal conductance is almost constant at 40 W/K.

Figure 6 shows the experimental results for the relationship between the liquid fill ratio V and the thermal conductance C of the vertical loop type for saturation temperature $T_{sat} = 113-130^\circ\text{C}$ and heat transfer rate $Q = 180-280$ W. There is the optimal liquid fill ratio according to heat transfer rate, that maximizes thermal conductance. Figure 7 shows the wall temperature distribution T_e of the

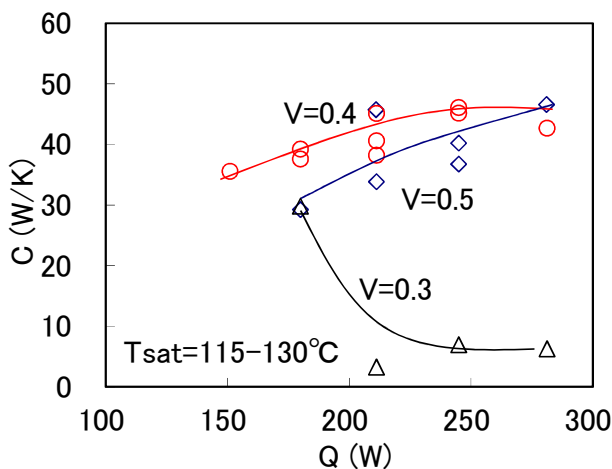


Figure 4. Relation between heat transfer rate and thermal conductance of vertical loop type.

evaporator at liquid fill ratio $V = 0.3-0.4$ and heat transfer rate $Q = 250$ W. The saturation temperature of working fluid T_{sat} is also shown in Figure 7. When the liquid fill ratio is too small, dry-out portion appears in the evaporator and the wall temperature increases. It decreases the thermal

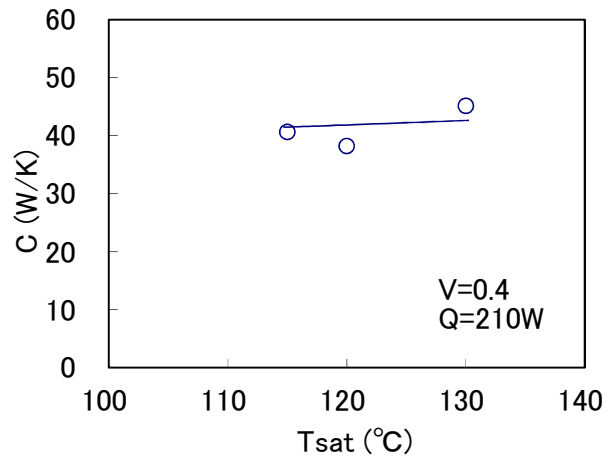


Figure 5. Relation between saturation temperature and thermal conductance.

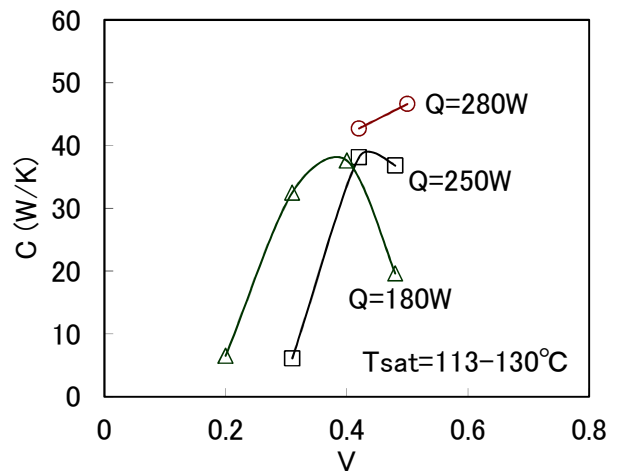


Figure 6. Relation between liquid fill ratio and thermal conductance of vertical loop type.

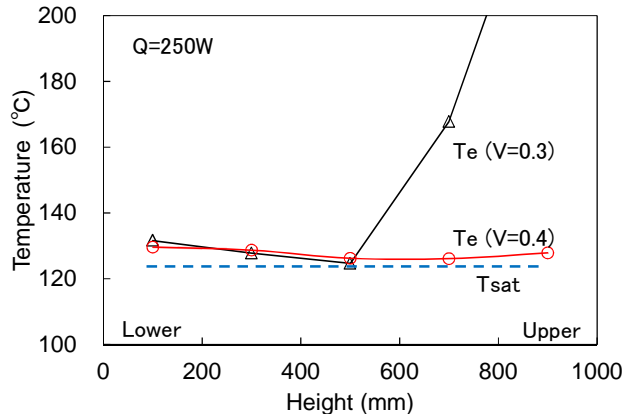


Figure 7. Wall temperature distribution of evaporator.

conductance. Figure 8 shows the wall temperature distribution T_c of the condenser at liquid fill ratio $V = 0.4-0.5$ and heat transfer rate $Q = 180W$. When the liquid fill ratio is too large, the liquid enters in the condenser and the wall temperature decreases. It decreases the thermal conductance.

5. EXPERIMENTAL RESULTS OF INCLINED LOOP TYPE

Figure 9 shows the experimental results for the relationship between the heat transfer rate Q and the thermal conductance C of an inclined loop type for liquid fill ratio $V = 0.3-0.5$ and saturation temperature $T_{sat} = 115-130^\circ C$. The thermal conductance of the inclined loop heat pipe is 40-50 W/K, which is 10 % higher than that of a vertical loop type and 3 times higher than that of a single-tube type. When the heat transfer rate is larger than 210 W with the liquid fill ratio 0.3, the thermal conductance of the vertical type decreases in Figure 4, but the thermal conductance of the inclined type does not decrease. It shows that the maximum heat transfer rate Q_{max} of the inclined

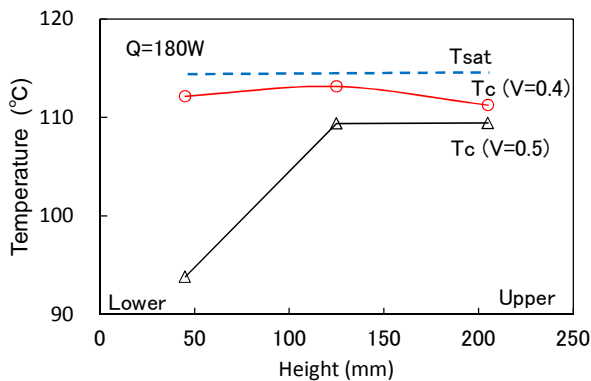


Figure 8. Wall temperature distribution of condenser.

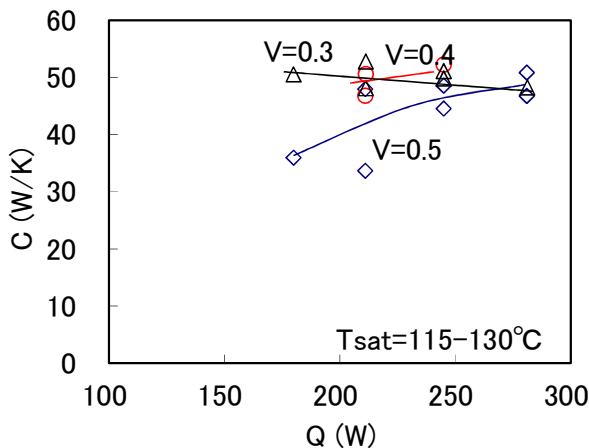


Figure 9. Relation between heat transfer rate and thermal conductance of inclined loop type.

type is higher than that of the vertical type in case of small liquid fill ratio. Figure 10 shows the boiling heat transfer coefficient α_e . The boiling heat transfer coefficient does not depend on a liquid fill ratio V and heat transfer rate Q . The value is about 5-6 kW/m²K, and is almost equal to that of a vertical type. Figure 11 shows the condensation heat transfer coefficient α_c . The condensation heat transfer coefficient of the inclined type is about 30-50 kW/m²K, and is about 20% higher than that of the vertical type.

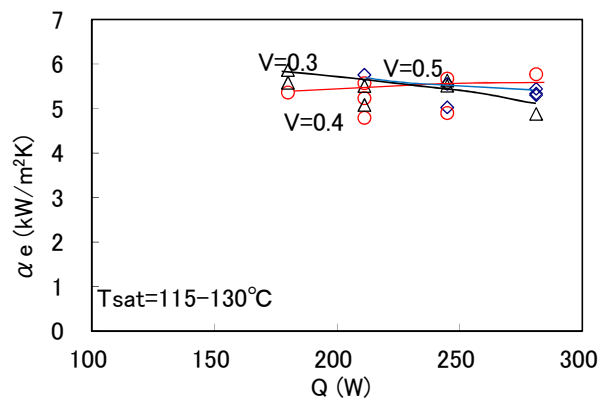


Figure 10. Relation between heat transfer rate and boiling heat transfer coefficient.

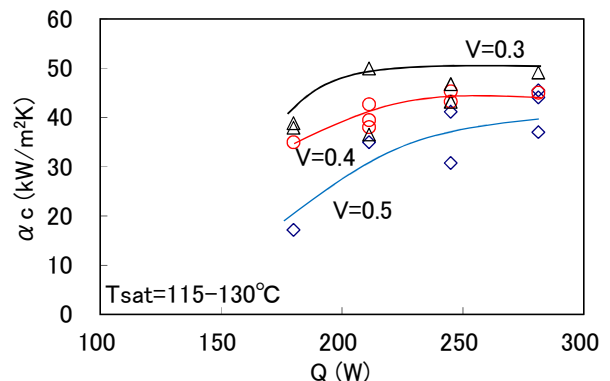


Figure 11. Relation between heat transfer rate and condensation heat transfer coefficient.

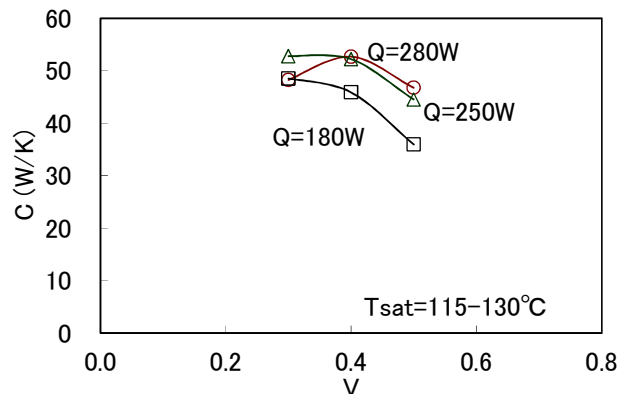


Figure 12. Relation between liquid fill ratio and thermal conductance of inclined loop type.

The condensation heat transfer coefficient is small when the heat transfer rate is low. This is because that vapour flow velocity of the working fluid is small. Moreover, the condensation heat transfer coefficient is small, when the liquid fill ratio is large. This is because that the more liquid flows into the condenser.

Figure 12 shows the experimental results for the relationship between the liquid fill ratio V and the thermal conductance C of a inclined loop type for saturation temperature $T_{sat} = 115-130^{\circ}\text{C}$ and heat transfer rate $Q = 180-280 \text{ W}$. The thermal conductance is high at wider range of the liquid fill ratio than that of the vertical type in Figure 6. So we conclude that the inclined loop type with the optimum liquid fill ratio is preferable for a solar collector.

6. ANALYSIS OF VERTICAL LOOP TYPE

Steady state thermal conductance of a vertical loop heat pipe is numerically calculated for the experimental condition. Local boiling heat transfer coefficient α_e in a vertical tube is calculated with Eq. (4) proposed by Schrock et al. (1962).

$$\alpha_e = 0.023 \frac{\lambda}{D} \text{Re}_L^{0.8} \text{Pr}^{0.4} \left[10^4 \text{Bo} + 1.5 \left(\frac{1}{X_{tt}} \right)^{0.667} \right] \quad (4)$$

where, λ is thermal conductivity, D is diameter, Re_L is Reynolds number for liquid alone flow, Pr is Prandtl number, Bo is Boiling number, and X_{tt} is Martinelli parameter. Local condensation heat transfer coefficient α_c in a tube is calculated with Eq. (5) proposed by Shah (1979) for $\text{Re}_L > 350$ and Eq. (6) proposed by Chato (1962) for $\text{Re}_L < 350$.

$$\alpha_c = 0.023 \frac{\lambda}{D} \text{Re}_{L0}^{0.8} \text{Pr}^{0.4} \left[(1-x)^{0.8} + \frac{3.8x^{0.76}(1-x)^{0.04}}{(P/P_{cr})^{0.38}} \right] \quad (5)$$

$$\alpha_c = 0.56 \left[\frac{g\rho^2 \lambda^3 L}{\mu D (T_{sat} - T_w)} \right]^{0.25} \quad (6)$$

where, x is quality, P is pressure, P_{cr} is critical pressure of working fluid, ρ is density, μ is viscosity, L is latent heat, and T is temperature. Pressure drop is calculated with the equation for viscous-viscous flow proposed by Lockhart et al. (1949). Void fraction is calculated with the drift-flux model proposed by Zuber et al. (1965). Flow direction of the loop heat pipe is divided with 80

elements and local heat flux, quality, void fraction, saturation temperature, and pressure are calculated. As the flow rate is small, most liquid is assumed to stay in the lower part of the loop. Liquid-head below condenser is higher than that in evaporator due to the pressure drop in the loop. Calculation scheme is that the saturation temperature of working fluid is calculated using repeated calculation so that heat balance of the system is kept for a given liquid fill ratio.

Figure 13 shows calculation results for the relationship between the liquid fill ratio V and the thermal conductance C . Experimental results in Figure 6 are also shown in Figure 13. The calculation results almost agree with the experimental results. When the liquid fill ratio is small, dryout appears in the evaporator as shown in Figure 14(a). When the liquid fill ratio is large, the liquid flows into the condenser to decrease heat transfer area as shown in Figure 14(b).

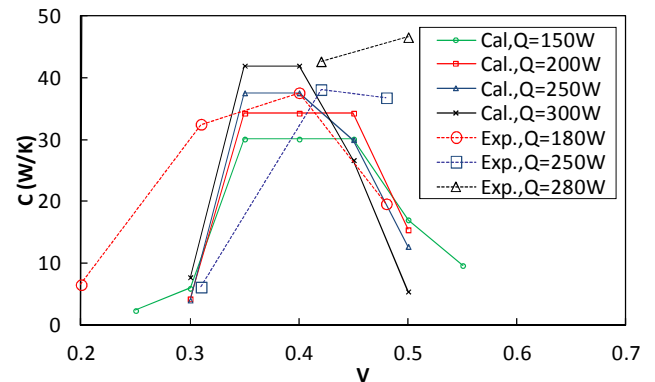


Figure 13. Calculation result of relation between liquid fill ratio and thermal conductance.

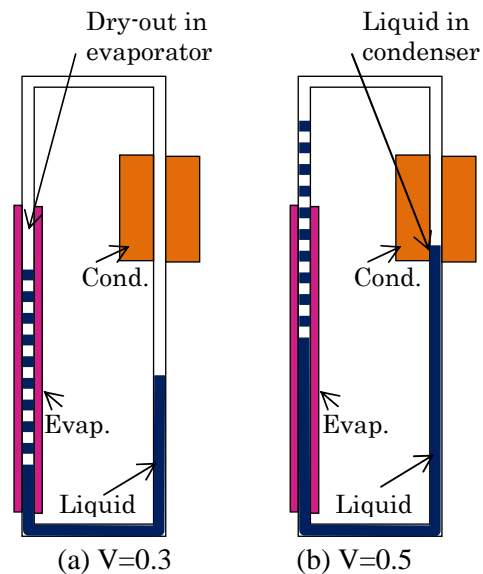


Figure 14. Model of liquid in loop.

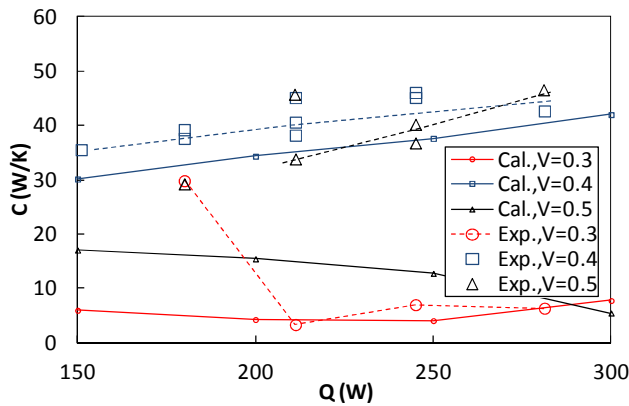


Figure 15. Calculation result of relation between heat transfer rate and thermal conductance.

Figure 15 shows calculation results for the relationship between heat transfer rate Q and thermal conductance C . Experimental results in Figure 4 are also shown in Figure 15. The calculation results almost agree with the experimental results with some differences. We will improve calculation model and will calculate for an inclined loop type.

7. CONCLUSIONS

Thermal conductance of a heat pipe for a solar collector system was studied, and the following results were obtained.

1. The thermal conductance of an inclined loop heat pipe is 40-50 (W/K), which is 10 % higher than that of a vertical loop type and 3 times higher than that of a single-tube type. So the inclined loop heat pipe is preferable for a solar collector.

2. There is the optimum liquid fill ratio, which is a function of heat transfer rate. When the liquid fill ratio is too small, dry-out portion appears in the evaporator. When the liquid fill ratio is too large, the liquid flows into the condenser to decrease heat transfer area.

NOMENCLATURE

C : thermal conductance (W/K)
 D : diameter (m)
 Pr : Prandtl number
 Re_L : Reynolds number for liquid alone flow
 Q : heat transfer rate (W)
 Q_{max} : maximum heat transfer rate (W)
 V : liquid fill ratio
 T_c : wall temperature of condenser ($^{\circ}C$)
 T_e : wall temperature of evaporator ($^{\circ}C$)

T_{sat} : saturation temperature of working fluid ($^{\circ}C$)
 α_c : condensation heat transfer coefficient (W/m^2K)
 α_e : boiling heat transfer coefficient (W/m^2K)

REFERENCES

- Chato, J.C. (1962) American Society of Heating, Refrigerating and Air Conditioning Engineers, ASHRAE Journal, February 1962, p.52
- Koito, Y., Ikemizu, Y., Tomimura, T., Mochizuk, M., (2010) *Vapor-Pressure-Driven Heat Pipe for Sideward Long-Distance Heat Transfer*, *Frontiers in Heat Pipes*, 1, 013005, p.1-7
- Lockhart, R.W. and Martinelli, R.C. (1949) *Proposed Correlation of Data for Isothermal Two-Phase Two-Component Flow in Pipes*, *Chemical Engineering Progress*, 45, p.39-48
- McDonald, T.W., Hwang, K.S., Diccio, R. (1977) *Thermosiphon Loop Performance Characteristics: Part-1 Experimental Study*, *ASHRAE Transaction*, 83,2, p.250-259
- Schrock, V.E. and Grossman, L.M. (1962) *Forced Convective Boiling in Tubes*, *Nuclear Science and Engineering*, 12, p.474-481
- Shah, M.M. (1979) *A general correlation for heat transfer during film condensation inside pipes*, *International Journal of Heat and Mass Transfer*, 22(4), p.547-556
- Takahasi, K., Kaminaga, F., Matsumoto, K. (2008) *Study on the heat transfer characteristic in Looped Parallel Closed Thermosiphon* (in Japanese), *Transaction of Japan Society of Mechanical Engineers*, 74(741), p.1128-1135
- Tanaka, H., Nakatake, Y. (2003) *A newly designed vertical multiple-effect-diffusion type solarstill coupled with heat-pipe solar collector* (in Japanese), *Journal of Japan Solar Energy Society*, 29(5), p.49-55
- Vincent, C.C.J., Kok, J.B.W. (1992) *Investigation of the Overall Transient Performance of the Industrial Two-Phase Closed Loop Thermosiphon*, *International Journal of Heat and Mass Transfer*, 35(6), p.1419-1426
- Zuber N. and Findlay, J.A. (1965) *Average Volumetric Concentration in Two-Phase Flow System*, *Transaction of ASME, Journal Heat Transfer*, 87, p.453-468

THERMAL PERFORMANCE OF HEAT PIPE-HEAT SOURCE USED FOR TEMPERATURE STABILIZATION IN EXTENDED TEMPERATURE RANGE

N. Koneva, L. Domorod

A.V. Luikov Heat & Mass Transfer Institute NAS Belarus

P. Brovka str. 15, 220072, Minsk, Belarus

Tel: +(37517) 2842244/Fax:+(37517) 2922513; E-mail: nsk@hmti.ac.by

ABSTRACT

The present research was devoted to the study of heat and mass transfer intensification in temperature stabilization systems. The paper provides an analysis of the heat source benefits with evaporation-condensation heat transfer for accurate repeated temperature stabilization in climatic test chambers. The proposed condenser temperature estimation method takes into account the constructive features, used instruments and applied thermal control loops. Numerical experiments were performed using an adequate analytical model for heat exchange in cylindrical vertical heat pipe-heat sources (HPS). The calculation method takes into account potential changes in the external and internal boundary conditions caused by the presence of thermal screens, thermal bridges and measuring units both on the condenser side and in vapor channel. A series of heat transfer devices with optimal thermal performance in a wide cooling temperature range have been proposed. HPS were proposed as variants of the technical realization of accurate surface temperature stabilization method in temperature range from 253 to 623 K. The paper also presents the results of an experimental study of the samples temperature stability. The preliminary tests show the possibility of using heat pipe as the heat source in test chambers of different application.

KEY WORDS: heat pipe, flat condenser, test chamber conditions

1. INTRODUCTION

At the present time the most common methods for measuring of the thermal physical properties involves using controlled thermo-stabilization conditions. Operation and regulation principles of measuring equipment used for these purposes should take into account all possible factors causing deformation of temperature fields in working area. Most important factors include immersed and contact sensors, geometrical, technological and structural parameters of material being studied and of system components. The technical realization of measuring equipment should have minimal deviation in parameters from mathematical model describing it. Optimal design of system for this purpose provides boundary conditions of one-dimensional temperature fields and spatially uniform temperature in heat sources. Precision measurement and control allows to study and to adjust the majority of device parameter fluctuations from accepted model.

Heat pipes based on the closed evaporation-condensation provide one-dimensional and two-dimensional uniform temperature field boundary conditions by uniform release of latent heat of

evaporation. The complex experiments of such heat transfer devices generally are aimed to analysis of the fluctuation of their thermal characteristics under repeated temperature stabilization modes, including the thermal contact of working surface with various objects.

2. HPS THERMAL PERFORMANCE IN TEST CHAMBER CONDITIONS

2.1 Temperature ranges analysis

Many types of cycles have been analyzed to choose for the construction of heat pipe with flat isothermally heated condenser in temperature range from 253 to 623 K. As it is follows from the analysis of compatibility and maximum heat accumulated, the heat pipe for thermal stabilization can be divided into narrow working ranges, which are described in table 1. For the analysis of compatibility, durability and repeated reproducibility, the operational characteristics of potential designs were estimated.

According to experimental results of the wide variety of constructions (Dan & Reay, 1982) heat pipe-heat sources have the following limitations.

Table 1. HPS working ranges.

Temperature range (K)	Material	Potential fluid
[253~323]	Al, St	C ₃ H ₆ O, NH ₃
[333~393]	Ni, Cu	CH ₄ O
[373~523]	Ni, Cu	H ₂ O
[423~623]	St	DowthermA

Combination Al-Acetone is best suited when a minimal total thermal resistance and a small wall thickness are required. For Al-C₃H₆O and Al-CH₄O combinations a traces of water vapor absence and the chemical purity is required. Long-term thermal performance reproducibility and compatibility have been reported for the Al-NH₃ devices up to temperature of 333 K only. According to life tests (Dan & Reay, 1982), (Koneva & Domorod, 2005) a two-phase Cu-H₂O device provides good stability of calculated temperature and heat transfer characteristics during about eighteen thousand of operational hours. The experimental data (Semena et al., 1984) presented for copper constructive heat pipe elements prove the stability of thermal performance of Cu/Acetone combination up to heat transfer limit. Methanol as unstable organic compound normally causes the corrosion of copper structure at temperatures of 393 K and higher. Dowtherm A may be used within a temperature range from 423 to 623 K, due to its low contact angle on the solid copper surface. Experimental study of numerous isotropic structures (Semena et al., 1984) shows the connection between the capillary structure elements and heat pipe container, which remains stable both during the extended period of storage and during the cyclic switching to different operating regimes, including low temperatures. Heat pipe maintains its accurate reproducible thermal characteristics also in the case of using grooves instead of capillary structures.

From the above mentioned results, it can be concluded that structure and technological characteristics of heat pipe-heat sources will stay invariable in case of using the grooves and powder materials. In close proximity to sensors either being introduced or being in contact with the device, the temperature field deformation can be minimized by choice of the evaporation-condensation principle.

2.2 Transfer processes for axisymmetric model

Figure 1 shows a model of closed cycle for HPS with isothermal flat condenser.

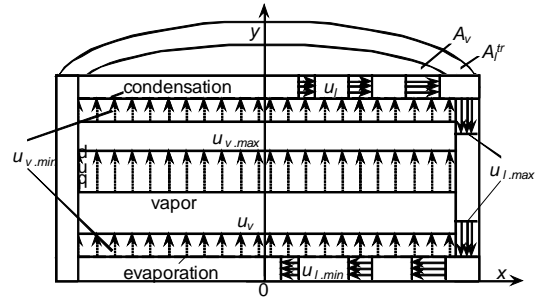


Figure 1. Scheme of the mass transfer in HPS.

Construction was employed (Koneva & Domorod, 2005), (Konev et al., 2008), (Rosso et al. 2009) for providing an accurate thermal control and a high repeatability of operational thermal characteristics in the narrow temperature range. The maximum temperature field deformation in liquid and vapor channels is determined by particular features of cycle. The mass flow along liquid transport lines occurs in evaporator and condenser at an outflow and an inflow and variable cross section conditions. The stability of mass flow is caused mainly by hydraulic viscous limitation of laminar condensate flow.

Any sensor being in contact with evaporator and condenser surfaces is placed in conditions of maximal homogeneous temperature field for the heat source. The vapor passes to the vapor channel through the porous structure. Velocity distribution for a vapor cross section A_v depends on outlet liquid velocity profile ($u_{l,max}$) and on evaporation rate. In the condensation region, the vapor flow slows down to a minimum value ($u_{v,min}$). The nominal vapor velocity ($u_{v,max}$) can be estimated for a fixed vapor temperature and thermal load of cycle. It is important to note that, that in proposed model the recovery of velocity profile occurs close to a flat parallel interfaces. Thus, any sensor being introduced into vapor channel is situated in boundary conditions of maximal homogeneity and isotropy of the vapor flow. Such sensor is located along the vapor isotherm lines and is parallel with heat exchange evaporator surface. Dimensions of in-homogeneity regions in axial direction are fixed between the external surfaces and the liquid-vapor or vapor-liquid interfaces. In case of condenser temperature estimation T_c in axial heat transfer direction the accuracy of extrapolation method will depend on axial anisotropy of an evaporator and condenser and on the precision measurement of saturated vapor T_v and evaporator or heater T_e temperatures.

The method is based on precision control of thermal resistance at different thermal stabilization regimes. The maximal and minimal differential temperatures in axial and radial direction can be evaluated in the course of optimization design.

A method of detailed design of the HPS includes following steps:

- 1) an evaluation of the nominal heat flows and axial differential temperatures for the opened and closed type of thermal control, for regimes of limit axial differential temperature, for total or partial screening the condenser surface; for liquid trapping in evaporator;
- 2) an estimation of the pressure differentials in axial and radial directions with radial temperature differentials for a number of fixed cross-sectional areas;
- 3) a calculation of the maximal radial differential temperatures and isothermicity in typical operational conditions;
- 4) an estimation of the ability to reproduce a fixed surface temperature under test chamber various conditions.

The calculation method has been suggested (Koneva, 2011) for a designing and analysis of the main characteristics of HPS operated with different types of thermal control. Computer code is used for the estimation of the condenser temperature uniformity under changes in external and internal boundary conditions caused by the presence of thermal screens, thermal bridges and measuring units both on the condenser side and in vapor channel. Numerical code has been optimized for an accurate computation of the axial and radial differential temperatures and heat transfer coefficient of heat source in various test chamber cooling regimes and vapor temperatures. The program includes features for calculation of the thermal characteristics of heat pipes (Konev & Koneva, 2002), (Koneva et al., 2003).

2.3 Numerical results

The HPS was proposed to the study the repeatable temperature characteristics in test chamber cooling boundary conditions, to use for the condenser temperature stabilization in extended temperature range. The heat sources whole temperature range was subdivided onto narrow intervals due to the necessity of designing a robust thin-wall construction working under the low operation pressures.

The above mentioned combinations of heat pipe were analyzed to provide an optimal vapor velocities and minimal condensate pressure differences. The optimal structures of capillary porous material and grooved inner surfaces (figure 2) have been developed after the detailed design.

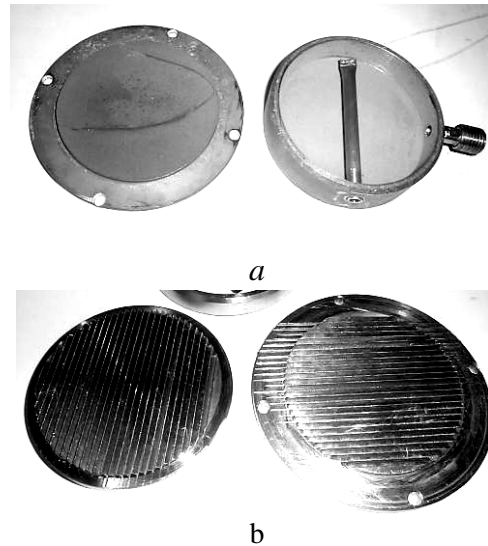


Figure 2. HPSs structure with a copper sintered powder (a) and stainless steel grooves (b).

The copper sintered powder structure is compatible with fluids C_3H_6O , CH_4O , H_2O and Dowtherm A; the stainless steel grooves could be used with C_3H_6O and Dowtherm A. Optimization of the characteristics of transport structures was carried out to estimate a versatility of heat pipe construction under working with variety of heat transfer fluids (table 2).

Table 2. HPS samples.

Type	Configuration	Diameter/Height/ /Thickness (mm)
HPS1	Cu/methanol/ /porous copper	100x25x3
HPS2	Cu/water/ /porous copper	100x25x3
HPS3	Dowterm/ /St.Steel	100x25x5
HPS4	NH_3 /St.Steel	100x25x5

The numerical results given below (figures 3, 4) show the influence of constructive parameters onto a heat transfer under the critical heat exchange conditions for the external condenser boundary. In particular, by using of proposed calculation method the comparison of temperature characteristics has been performed for different

screening factors (b) and for screenless (b=1) condenser heat exchange surface. The axial temperature differentials have been calculated in fixed control points within the whole vapor temperature range under variable cooling loads of HPS1.

As it follows from calculation results (figure 3) the copper sample provides in test chamber conditions a steady heat transfer with the minimal axial temperature difference. For example, in intensive cooling mode of free convection ($\alpha = 14 \text{ W/m}^2\text{K}$, $T_o = 280 \text{ K}$), for the heater temperature changing T_h from 323 to 403 K, the axial temperature difference varies.

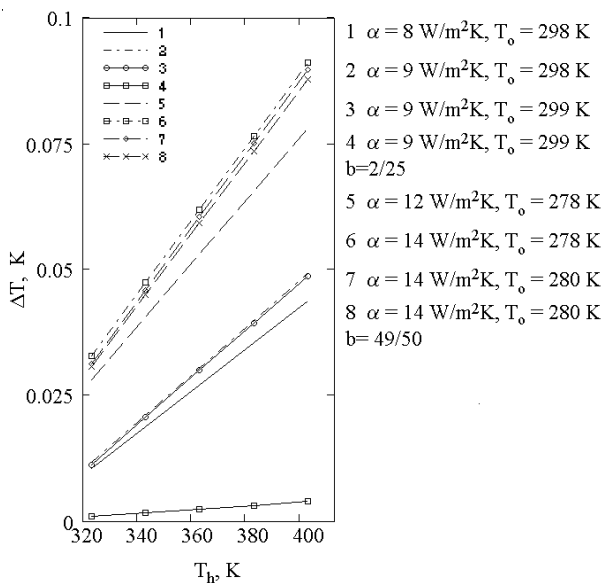


Figure 3. Axial temperature difference for HPS1 in different test conditions.

In such conditions the condenser temperature varies within the range from $T_c = T_h \pm 0.02 \text{ K}$ to $T_c = T_h \pm 0.05 \text{ K}$, while an additional thermal load Q of HPS increases from 4 to 14 W. The operating at the same cooling regime but with partial screening of condenser (b=49/50), due to the presence of contact sensors with low heat transfer characteristics, it requires small thermal load adjustment. For decreased intensity of the free convective cooling mode ($\alpha = 8 \text{ W/m}^2\text{K}$, $T_o = 298 \text{ K}$) the temperature of condenser stabilizes within the range $T_c = T_h \pm 0.008 \text{ K}$ to $T_c = T_h \pm 0.002 \text{ K}$. The heat exchange of low-intensity may be considered as a critical regime since the heat pipe operates under the drastically reduced heat flows.

On figure 4, the temperature characteristics are given for a HPS2 with the same evaporation-condensation principle. Water as a working fluid

allows reproducing an operating temperatures T_h within extended range from 313 to 473 K. With using such heat pipe combination in conditions of low-intensity cooling of the test chamber ($\alpha = 6 \text{ W/m}^2\text{K}$, $T_o = 308 \text{ K}$) the temperature of condenser can be maintained within the range from $T_c = T_h \pm 0.008 \text{ K}$ to $T_c = T_h \pm 0.03 \text{ K}$.

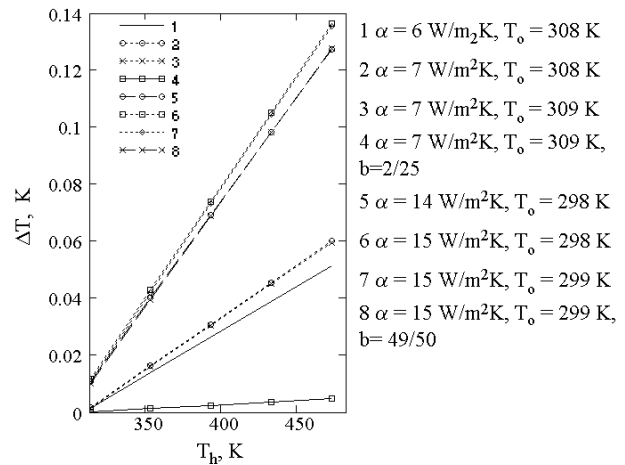


Figure 4. Axial temperature difference for HPS2 in various test conditions.

Temperature stabilization can be achieved by adjustment of the additional heat load within a range from 2 to 10 W. It can be concluded, from numerical results, that the operating of the HPS below the temperature of 383 K is critical for the minimum thermal loads. With an intensive grow of cooling heat exchange a thermal load of the heat source increases up to 20 W and the condenser surface temperature is stabilized within the range from $T_c = T_h \pm 0.005 \text{ K}$ to $T_c = T_h \pm 0.06 \text{ K}$. Numerical experiments allowed studying the maximum thermal performance of samples and corresponding condenser surface oscillation under free convection in the test chamber. Results of optimization of thermal characteristics of stainless steel models HPS3 and HPS4 for a various heat input and heat output have been presented on figures 5, 6. The thermal load dependence from a working temperature is presented on figure 5 for different test chamber boundary conditions for combination of St.Steel – DowtermA – porous steel. Numerical experiments illustrate the thermal performance of HPS for typical heat exchange rates and temperatures of test chamber T_o , for various screening factors. The thermal load Q has to be adjusted in that case within the range from 5 to 35 W. Under intensive cooling of the condenser ($\alpha = 15 \text{ W/m}^2\text{K}$, $T_o = 335 \text{ K}$) within temperature range T_h from 423 to 623 K the typical axial temperature differences will correspond to the condenser

surface temperature fluctuations between $T_c = T_h \pm 0.8$ K and $T_c = T_h \pm 2.5$ K for the same construction of HPS. Within the same temperature range for decreased intensity of cooling the heat source, the condenser temperature stabilization occurs between $T_c = T_h \pm 0.6$ K and $T_c = T_h \pm 1.3$ K.

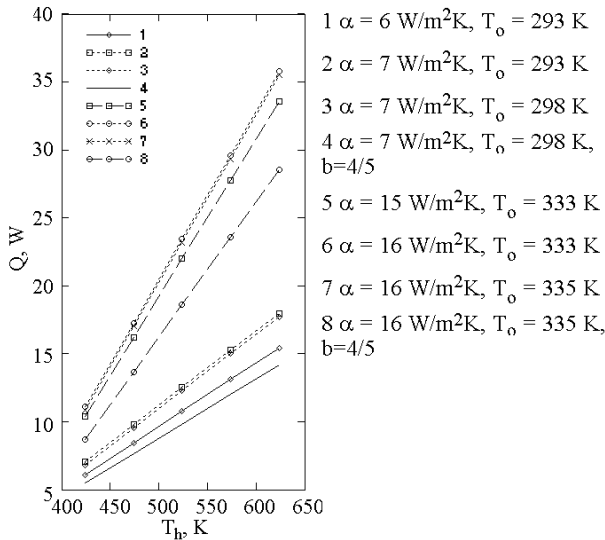


Figure 5. Thermal performance of HPS3 in different test conditions.

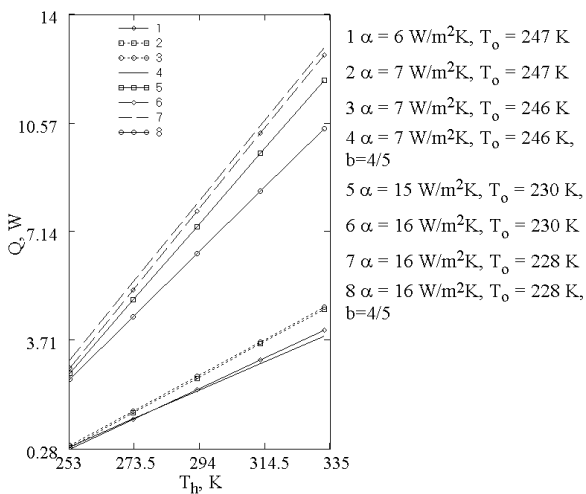


Figure 6. Thermal performance of HPS4 in different test conditions.

Thermal performance of the same construction of heat pipe but with using a low temperature working fluid and with the cooling in low temperature test chamber is given at figure 6. With an accurate thermal control it is possible to maintain the condenser temperatures. In case of intensive cooling condenser ($\alpha = 15$ W/m²K, $T_o = 228$ K) the accurate thermal control provides both the heater temperatures T_h between 253 and 333 K and the corresponding condenser surface

temperatures within the range from $T_c = T_h \pm 0.25$ K to $T_c = T_h \pm 0.6$ K. Typical condenser temperature fluctuation for the low intensive heat exchange ($\alpha = 6$ W/m²K, $T_o = 253$ K) such heat pipe maintains within the temperature range between $T_c = T_h \pm 0.03$ K and $T_c = T_h \pm 0.9$ K. Numerical experiments for every construction and provide a temperature and thermal performance data for the cases of critical and typical heat sinks on condenser boundaries. For verification of the heat pipe characteristics the accurate heat sink temperature measurements were also performed.

According to the method described by the authors (Koneva, 2011) the axial and radial temperature differences and the maximum spatial isothermicity parameter can be estimated for each type of heat pipe.

2.4 Experimental study of HPS

The investigation of the grooved HPS gave following results. The accurate estimation of axial temperature gradient for any control points of evaporator or condenser surface depends on accuracy of structural parameters measurement (including thickness and spatial distribution) and requires the preliminary marking up the heat exchange surfaces. The investigation of grooved condensers proved a stability of the calculated thermal performance and working temperatures for cases of partially screened and wholly unscreened heat exchange surface.

The long-term tests have been performed for the temperature characteristics of the heat sinks having thermal contacts with the heat-pipe heat sources (figure 7). In this case, long-term thermal performance tests of heat pipe provided the data for a various modes of temperature stabilization. The temporal temperature profiles for stabilization heater temperature T_h and condenser temperature T_c were presented on figure 7,a for three samples of copper HPS having an identical construction and porous capillary structures. Figure 7,b illustrates a temperature profiles of the same HPS after a exploitation period of two years.

Both thermal characteristics and time stabilization are kept constant. It is also important that the results of metrological certification confirm the stability and repeatability of a predicted temperature characteristics during the eighteen thousand of operational hours.

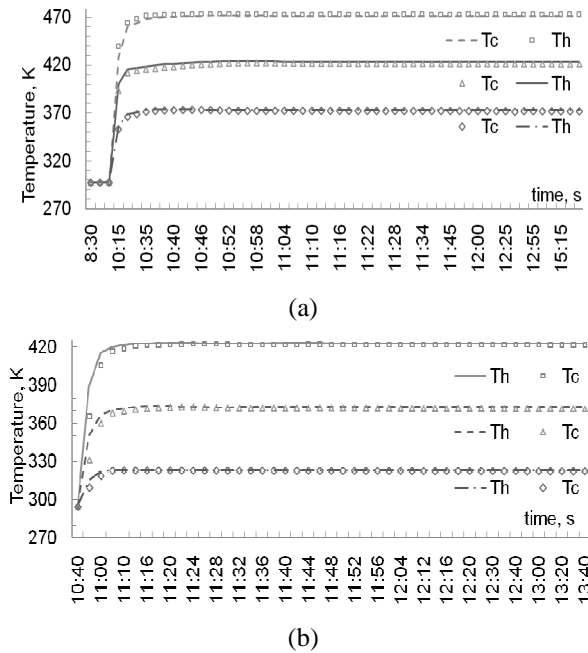


Figure 7. Temperature profiles from primary tests (a) and after two years of exploitation (b)

3. CONCLUSIONS

By using of proposed type of heat pipe in accurate thermal physical experiments, it is possible to provide a detailed study of heat exchange conditions on surface of various materials. In comparison with temperature stabilization by using a single-phase heat transfer devices the HPS has a number of advantages. In particular, it increase the accuracy of temperature estimation on control points of surface, it also reduces in two times the period of temperature stabilization. Reproducible temperature stabilization function of the HPS2 is confirmed by tests performed within more than six year. Its calculated temperature characteristics (up to 523 K) have been verified in metrological test chambers with following parameters: varied humidity (65-93)%, heat exchange rate α varied from 8 to 25 W/m²K, cooling media temperature T_0 varied from 288 to 301 K.

The HPS being studied within the framework of the present research expands a series of two-phase heat transfer devices that had been developed till now for electronics (Konev et al., 1990), for microscopy and medicine (Konev et al., 2008), and for metrology (Rosso et al., 2009)

NOMENCLATURE

- A_l – cross section for liquid
- A_v – cross section for vapor
- b – screening factor
- Q – thermal load
- T_c – condenser temperature
- T_h – heater temperature
- T_v – vapor temperature
- T_v – test chamber temperature
- u_l – condensate velocity
- u_v – vapor velocity
- α – heat exchange rate
- x, y – coordinate

REFERENCES

Dunn, P.D. and Reay, D.A. (1982) *Heat Pipes*. 3rd Edition, Pergamon Press.

Konev, S., Koneva N. (2002) *An analysis & development of the thermal control systems on heat pipe-thermal switch for space application*. Proc. 12th Int. Heat Pipe Conf., Yekaterinburg, Russia. p. 260-263

Konev, S.V., Chizhik, S.A., Domorod, L.S., Koneva N.S. (2008) *Isothermally heated platform for microscopy*. Annual proc. Heat & Mass transfer, Minsk, p. 442-445

Konev, S.V, Vasiliev, L.L., Khrustalev, D.K., Rabetsky, M.I. (1990) *Heat pipes for electronic equipment cooling systems*. Proc. 7th Int. Heat Pipe Conf., Minsk, p. 131-138

Koneva, N. S., Domorod, L. S. (2005) *Study of the isothermicity of Cu-Water flat heat pipe as surface source*. Proc. 6th Int. Heat Pipe Seminar, Minsk. p. 167-174

Koneva, N. S. (2011) *Temperature distribution prediction for two-phase plate under contact thermal resistance test conditions*. Proc. 8th Int. Heat Pipe Seminar, Minsk. p. 128– 133

Koneva, N.S., Dragun, V.L., Koneva, E.S. (2003) *The analysis and numerical calculations of gravitational heat diodes*. Proc. 4th Baltic Heat Transfer Conf., Kaunas. p. 523-530

Semena, M.G., Gershuni A.N., Zaripov, V.K. (1984) *Heat pipes with fibermetallic capillary structures*, Vishcha Sk., Kiev (in Russian)

Rosso, L., Koneva, N., V Fernicola, V. (2009) *Development of a Heat-Pipe-Based Hot Plate for Surface-Temperature Measurements*. Int. J. Thermophysics, 30(1), p. 257-264.

RESEARCH OF FACTORS INFLUENCING HEAT TRANSFER CHARACTERISTICS OF MINIATURE HEAT PIPES

V.Yu. Kravets, Ia.V. Nekrashevych

Heat Pipes Laboratory

National Technical University of Ukraine "Kiev Polytechnic Institute"

off. 903, 6 Polytechnichna Str., Kyiv, 03056, UKRAINE

tel/fax: +380444068098, kravetz_kpi@ukr.net, niav@i.ua

ABSTRACT

Results of an experimental research of thermal resistance of miniature heat pipes (MHP) with metal fibrous capillary structure are presented. It is shown that heat transfer characteristics of a MHP influence both geometrical and regimes factors. Calculations of the vapour velocity in the adiabatic section and in this connection change of the vapour flow regime are presented.

KEY WORDS: Miniature heat pipe, thermal resistance, heat transfer coefficient

1. INTRODUCTION

It is known that the principle of functioning of MHP is the same of the majority of the heat pipes. However, in view of the MHP small sizes, there are difficulties in the organization of vapour and liquid flows. On one hand, it is necessary to provide a free exit of steam from the evaporator to the condenser, on the other hand – it is necessary to create conditions to pump liquid by capillary forces, from a zone of condensation to the evaporation zone. Thus, the main objective of capillary-porous structure is to return working fluid from evaporator to condenser. There are many capillary structures (powder, mesh, constructional, metal fibrous, etc.) which develop different a capillary pressure, sufficient for delivery of the working fluid liquid phase to the zone of evaporation of the MHP.

The difficulties caused with placing capillary structure inside a MHP, have led to creation constructional structure which are made by rolling round pipes, in square or triangular cross section shapes [2]. Authors [2] investigated MHP with the triangular form, where the working fluid, under the influence of capillary forces, settled down on corners, allowing separate movement of the vapour and liquid. In [3] a MHP with a square form, made from copper or silver, filled with the distilled water was studied. The basic advantage for such kinds of the MHP cross section is the separate movement of the various phases of the working fluid, even for thin channels. The sharper corner, the higher

capillary force, which keeps the liquid phase in the channel. Comparative researches [5] of the heat transfer characteristics of MHP of triangular and square cross section have been conducted. It has been shown that a MHP thermal resistance of square cross section was lower pumping capacity than at MHP with triangular cross section. In [6] a constructional capillary structure was installed in a round pipe compared bundle of thin wires, to create more capillary pumping conditions for the transporting the working fluid to the evaporator.

For increase in transferred heat fluxes in [7,8] have suggested to use a MHP arrays which settle down on one substrate. Such arrays allow transfer heat fluxes up to 45W, which results to lower temperature of cooled object and to provide its uniform cooling.

Along with round, triangular and square miniature heat pipes also used flat heat pipes with various types of the capillary structures. Authors [9] used as structure squared shape grooves on all perimeter of a pipe. Such flat MHP remove considerably big specific heat fluxes (to 10^4 W/m²) in comparison with triangular MHP. It is possible to note that they practically do not work against gravity as lack of such design.

The most effective capillary structures now are metal fibrous and powder structure which allow to improve MHP heat-transfer characteristics [9,10,11]. The capillary structure saturated with the working fluid allows to solve a problem of separate

movement of the different phases, possesses sufficient capillary force for liquid movement in capillary structure, even if pipe placed in space against gravity.

2. EXPERIMENTAL SET-UP

The present research is aimed at investigating the intensity of heat transfer in a zone of evaporation of the copper MHP with metal fibrous capillary structure. As the working fluid water was used. On Fig. 1 samples of the MHP made in Heat Pipes Laboratory at NTUU “KPI” are presented.

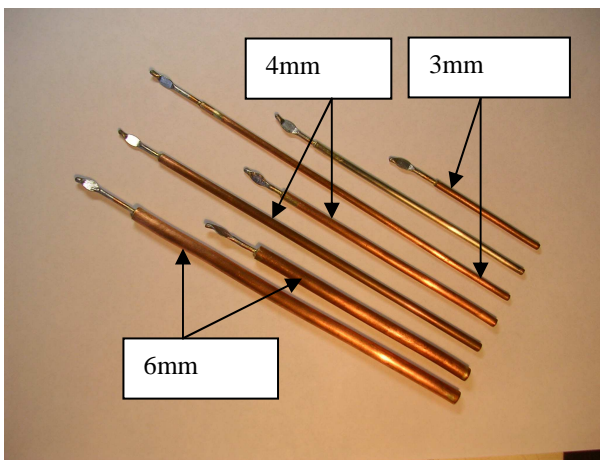


Figure 1. Tested miniature heat pipes

Geometrical characteristics of investigated copper MHP with metal fibrous capillary structure are presented in Table 1.

Table 1. Geometrical characteristics of the investigated MHP.

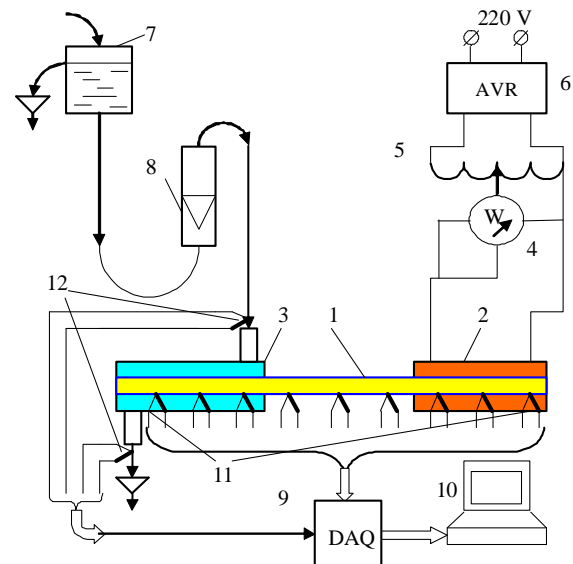
d_{mhp}, mm	3	4	6	6
d_v, mm	1,2	2	4,0	4,0
L_{mhp}, mm	300	150	230	200
L_{evap}, mm	60	60	70	60
l_c, mm	162	68	40	82
δ, mm	0,4	0,5	0,5	0,5
$e, \%$	88	82	88	80

Experimental research of the MHP heat transfer characteristics was carried out on the installation presented in [12] and schematically shown on Figure 2. The miniature heat pipe equipped with a heater 2 and condenser 3 was mounted, depending on the research problem, with angles of inclination $+90^0, 0^0, -90^0$. On all the length of MHP, T-type thermocouples 11 were installed, three units both

in evaporation and condensation zones and two pcs in the transport zone. The signal from thermocouples was transmitted on digital acquisition system (DAQ) 9 and further on to the personal computer 10. This system collecting signals from thermocouples and allowing establishing temperature with frequency 1Hz. For the purpose of minimization of thermal losses into environment MHP were completely insulated by a basalt fiber with factor of heat conductivity of 0,04 W/m·K.

The condensation zone was washed by water with constant liquid flow rate m (kg/sec) which was supported by means of a pressure head tank 7 and controlled by flow meter 8.

Water temperature at entry in the condenser and at exit from it was measured by two thermocouples 12 the signal from which was also transmitted to DAQ and further on to computer software.



1 - MHP; 2 - heater at zone of evaporation; 3 - condenser «a pipe in a pipe»; 4 - wattmeter; 5 - lab autotransformer; 6 - voltage stabilizer; 7 - tank pressure head; 8 - flowmeter; 9 - DAQ; 10 - computer; 11,12 – thermocouples, type T.

Figure 2. Experimental set-up for research of the MHP heat transfer characteristics

Water temperature at entry in the condenser during experiment was held constant with accuracy $\pm 0,2^0C$. According to indications of thermocouples 6 (t_{out} and t_{in}) at a known specific heat c_p and the liquid flow rate m a real heat flux, transferred by MHP, was calculated $Q = c_p m [t_{out}(\tau) - t_{in}(\tau)]$.

In accordance with values of average temperatures in evaporation and condensation

zones, and also value of heat flux, thermal resistances were further calculated:

$$R = \frac{\Delta t}{Q} = \frac{t_{evap} - t_{cond}}{Q} \quad (2)$$

Since the average temperature in a transport zone practically corresponds to saturation temperature in a MHP, thermal resistance and average heat-transfer coefficients in a heating zone were calculated in accordance with the known values of average temperatures in zones of evaporation, transport and condensation, and also with the real value of the heat flux transferred by a MHP:

$$\alpha_{evap} = \frac{Q}{(t_{evap} - t_{ad})A_{evap}} = \frac{q}{t_{evap} - t_{ad}} \quad (3)$$

3. RESULTS DISCUSSION

As the size of miniature heat pipe thermal resistance is one of the basic characteristics of the heat transfer ability and it is necessary to know its minimum value (heat flux will be maximum). The size of thermal resistance is influenced by enough considerable quantity of factors (a thickness of capillary structure, porosity, diameter of the vapor channel, angle of inclination, a type of the working fluid, etc.). Decrease in porosity and increase in a thickness of capillary structure reduces influence of gravitation forces on thermal resistance [13].

Diameter of steam space d_v and effective length L_{eff} makes considerable impact on R_{mhp} . Increase L_{eff} and reduction d_v leads to substantial increase R_{mhp} and, accordingly, to essential decrease in maximum heat fluxes Q_{max} . Besides it, conditions of cooling a condenser also influence.

So on figure 3 influence of temperature of a cooling liquid in a condenser on size of MHP thermal resistance a MHP in diameter 3mm and 300mm ($d_v=1,2mm$) length is shown. There it is visible that with increase in heat flux, R_{mhp} monotonously decreases to some minimum. The further slight increase Q led to sharp growth R_{mhp} . It is connected with the beginning of drainage of an extreme point of an evaporator region (length 60mm) and fast distribution of this phenomenon on all region.

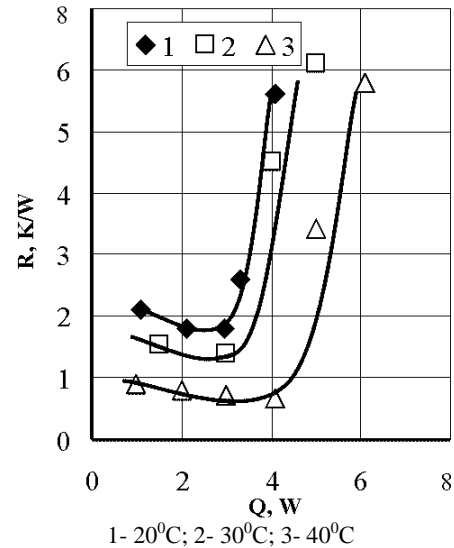


Figure 3. Influence of t_{in} on the R_{mhp} at horizontal orientation
($l_{mhp}=300mm$, $d_v=1,2mm$, $m=4,9 \cdot 10^{-3} kg/s$).

With temperature increase t_{in} the minimum value of thermal resistance considerably decreases and Q_{max} increases. It is possible to explain such influence t_{in} on R_{MHP} if to consider processes occurring inside a MHP. At increase t_{in} also the saturation temperature inside a MHP (pressure also increases) accordingly increases. And as in evaporation zone there is a nucleate boiling separate diameters of steam bubbles at pressure increase, decrease also quantity of a steam phase, thus, also decreases. It leads to decrease in speed of steam movement on the vapor channel and process of transfer of thermal energy improves that accordingly leads to growth Q_{max} and decrease R_{min} .

On figure 4 influence of gravitation forces on thermal resistance a MHP with diameter 4mm ($d_v=2mm$) is shown. Character of curves specifies in a major factor which essentially reduces a pipe heat transfer – gravitational forces counteraction.

Apparently from drawing the size of thermal resistance monotonously decreases with simultaneous increase in a heat flux to some minimum value, and then starts to increase slowly. At a horizontal arrangement of a pipe ($\varphi=0^\circ$) when action of forces of gravitation is absent, MHP heat transfer ability will be defined basically only at the expense of capillary forces which in turn depend on constructional characteristics of capillary structure. Pressure p_{cap} , created in capillary structure, depends on surface tension force σ and the main radiuses of curvature of a meniscus R_1 and R_2

$$p_{cap} = \left(\frac{1}{R_1} + \frac{1}{R_2} \right) \sigma \cos \Theta \quad (4)$$

With an inclination of an arrangement a MHP from the horizontal forces of gravitation which or help working fluid movement in an evaporation zone start to operate, or counteract it.

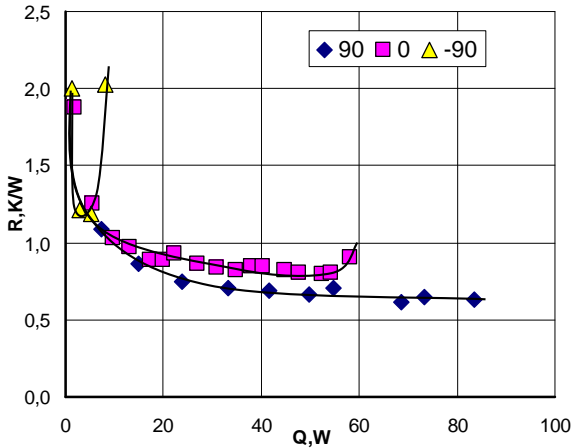


Figure 4. Gravity forces influence on R_{mhp} ($l_{mhp}=150\text{mm}$, $d_{mhp}=4\cdot 10^{-3}\text{m}$, $m=4,9\cdot 10^{-3}\text{kg/s}$).

These forces can be considered by expression for a hydrostatic pressure Δp_l [13]

$$\Delta p_l = \rho_l g L_{eff} \sin \phi \quad (5)$$

Apparently from expressions (4) and (5) heat-transfer characteristics of the MHP strongly depend on the pores sizes and effective length L_{eff} . Thus influence of an angle of inclination will be lower, when it's smaller pores radius and higher working fluid surface tension coefficient. Also, when less distance between evaporator and condenser L_{eff} .

From figure 4 it's visible that at an arrangement a MHP against gravity ($\phi = -90^\circ$) the minimum value of thermal resistance is $R_{min}=1,2\text{K/W}$, and the maximum transferred heat flux $Q_{max}=5,2\text{W}$. When gravitational forces help working fluid movement in an evaporation zone ($\phi = +90^\circ$), R_{min} decreases to $\sim 0,62\text{K/W}$, and Q_{max} increases to 85W .

The increase in diameter of steam space leads to considerable growth of transferred heat fluxes; however thermal resistance changes a little. So on figure 5 it is shown that the MHP with $d_v=4\cdot 10^{-3}\text{m}$ and with total length $0,2\text{m}$ at a vertical arrangement transfers heat fluxes up to 280W and R_{mhp} does not exceed $0,4\text{K/W}$. At a horizontal

arrangement at 220W thermal resistance increases to $0,7\text{K/W}$ that testifies to the worsened mode of heat exchange and to the possible beginning of drainage in an extreme point of a evaporator region.

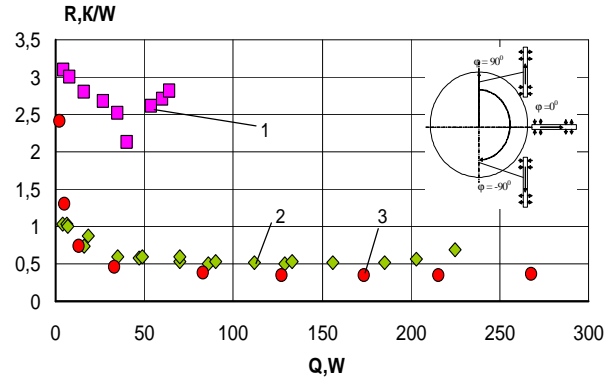
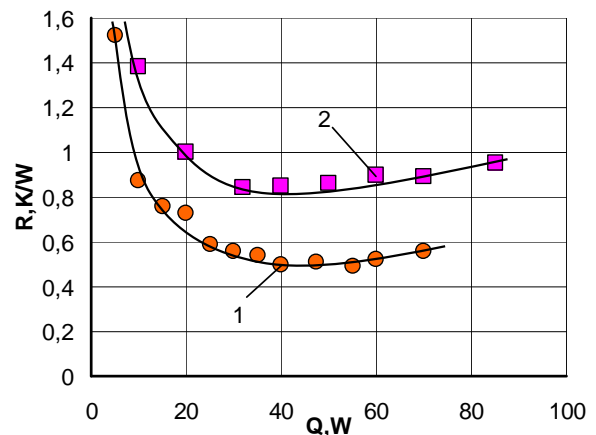


Figure 5. Dependence of R_{mhp} for the MHP with total length $0,2\text{m}$ and diameter $6\cdot 10^{-3}\text{m}$ from Q , inclination angles: 1- $\phi=-90^\circ$; 2 - 0° ; 3 - $+90^\circ$.

The type of working fluid also plays an essential role in the transfer of thermal energy in the MHP. So on figure 6 it is shown that the MHP ($\phi=+90^\circ$, $l_{mhp}=230\text{mm}$, $d_{mhp}=6\text{mm}$, $t_{in}=20^\circ\text{C}$) filled with ethanol reduces the heat transfer ability. In comparison with water such MHP transfers approximately in three times smaller heat fluxes, however thermal resistance remain approximately at one level.

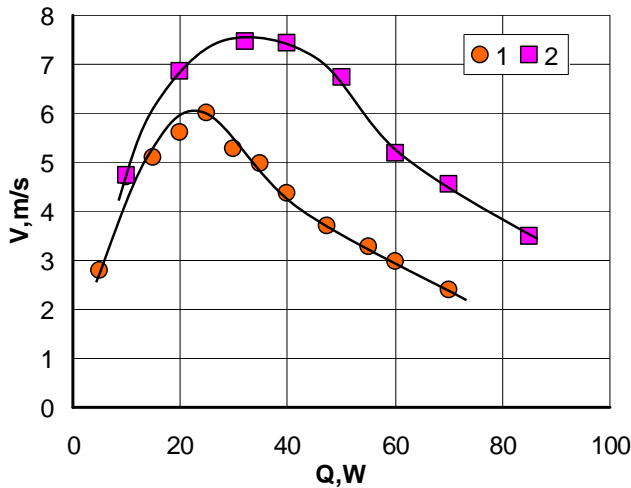


1 - $m=1,8\cdot 10^{-3}\text{kg/s}$; 2 - $m=7,5\cdot 10^{-3}\text{kg/s}$

Figure 6. Influence of the factor m on the R_{mhp} at vertical MHP arrangement.

One of influencing factors is also the expense of the cooling water m washing a zone of condensation. Deterioration of external conditions of heat transfer in a condensation zone results to increase in temperature level of all MHP and

accordingly pressure in it. And, as shown above, steam speed decreases that leads to corresponding decrease in hydraulic resistance and increase in a transferred heat flux. On figure 7 settlement values of speed of movement of steam in an adiabatic region are resulted.



1 – $m = 1,8 \cdot 10^{-3} \text{ kg/s}$; 2 – $m = 7,5 \cdot 10^{-3} \text{ kg/s}$
 Figure 7. Influence flow rate m on the vapour speed in adiabatic zone of MHP ($\varphi = +90^\circ$, $l_{mhp} = 230 \text{ mm}$, $d_{mhp} = 6 \text{ mm}$, $t_{in} = 20^\circ \text{ C}$, ethanol)

Speed of movement of steam is defined on dependence (6)

$$W = \frac{Q}{h_{fg} \cdot \rho_v \cdot A_v} \quad (6)$$

With growth of a heat flux speed of steam increases to some value then its monotonous decrease is observed. The increase in the expense of a cooling liquid approximately four times m leads to insignificant growth of speed of movement of steam. Thus the maximum value of speed moves in area of higher values of heat fluxes. As have shown experiments, to the maximum values of speed of movement of steam there correspond the maximum factors of heat transfer in an evaporation zone.

3. CONCLUSIONS

Thus, research has shown that heat transfer ability of miniature heat pipes is influenced by a considerable quantity of factors. In our opinion, it is possible to carry diameter of steam space, MHP effective length L_{eff} , a type of the working fluid and an arrangement a MHP in space concerning forces of gravitation. Authors, on the basis of the

calculated speeds of steam, shown that at vapor flow in the steam channel probably existence of a turbulent mode of a flow. Therefore calculations of heat transfer characteristics in miniature heat pipes need to be spent taking into account possible change of a vapor flow regime.

NOMENCLATURE

d	diameter, m
A	cross-sectional area, m^2
c_p	specific heat
ρ	density, kg/m^3
g	gravitational acceleration, m/s^2
σ	surface tension, N/m
l	length, m
L_{eff}	effective length
K	permeability coefficient
δ	capillary structure thickness, m
e	porosity
t	temperature, $^\circ\text{C}$
\bar{t}	average temperature, $^\circ\text{C}$
h_{fg}	latent heat of vaporization, kJ/kg
m	mass flow rate, kg/s
R	thermal resistance, K/W
Q	heat flux, W
q	heat flux density, W/m^2
α	heat-transfer coefficient, $\text{W/m}^2\text{K}$
φ	inclination angle, degree
W	velocity, m/s
Re	Reynolds number
Bo	Bond number
p	pressure, N/m^2
r	radius, m

Subscripts:

ad	adiabatic
cond	condensing, condenser
cap	capillary
evap	evaporating, evaporator
in	incoming
l	liquid
mhp	miniature heat pipe
max	maximum
min	minimum
out	outgoing
v	vapour

REFERENCES

1. Ha J. M., Peterson G. P. The maximum heat transport capacity of micro heat pipes // ASME J. Heat Transfer. 1998. Vol. 120, №4. pp. 1064 – 1071.

2. Moon S.H., Hwang G., Ko S.C., Kim Y.T. Experimental study on the thermal performance of micro-heat pipe with cross-section of polygon // *Microelectronics Reliability*. 2004. Vol. 44. pp. 315 – 321.
3. B. R. Babin, G. P. Peterson, and D. Wu, “Steady-State Modeling and Testing of a Micro Heat Pipe,” *Journal of Heat Transfer*, vol. 112, no. 3, pp. 595-601, Aug. 1990.
4. Schneider M., Yoshida M., Groll M. Investigation of interconnected mini heat pipe arrays for micro electronics cooling // 11th International Heat Pipe Conference, Sept. 14, 1999, Tokyo, Japan, Vol.1. pp. 7-9.
5. S. H. Moon, G. Hwang, S. C. Ko, and Y. T. KIM, “Experimental study on the thermal performance of micro-heat pipe with cross-section of polygon,” *Microelectronics Reliability*, vol. 44, no. 2, pp. 315–321, Feb. 2004.
6. S. S. Launay, V. V. Sartre, M. B. H. M. B. H. Mantelli, K. V. K. V. de Paiva, and M. Lallemand, “Investigation of a wire plate micro heat pipe array,” *International journal of thermal sciences*, vol. 43, no. 5, pp. 499–507, 2004.
7. G.P. Peterson, Investigation of micro heat pipes fabricated as an integral part of silicon wafers, Proc. 8-th. Int. Heat Pipe Conf., Beijing, China, 1992, pp.1-11.
8. Hopkins R., Faghri A., Khrustalev D. Flat miniature heat pipes with micro capillary grooves// *Journal of heat transfer* .1999. Vol. 121, №1, pp. 102 – 109.
9. Pat. 50435 A. UA. Micro heat pipe / V.Yu. Kravets, Yu.E. Nikolaenko; 2002.
10. Vasiliev L.L., Kulakov A.G., Rabetsky M.I., Antukh A.A. Miniature heat pipes for electronic equipment thermal control// Proceeding of the V Minsk International Seminar “Heat pipes, Heat Pumps, Refrigerators”, September 4-7, 2002, Minsk, Belarus, pp. 270 – 278.
11. Kravets V.Yu., Nikolaenko Yu.E., Nekrashevich Ya.V. Experimental studies of heat-transfer characteristics of miniaturized heat pipes// *Heat Transfer Research*. 2007, Vol. 38, № 6. pp. 553 – 563.
12. Kravets V.Yu., Nekrashevych Ia.V., Goncharova A.P. Research thermal resistance of miniature heat pipes/ *Eastern European Journal Enterprise Technologies*. 2011. Vol. 1/9(49), pp. 55 – 60.
13. Semena M.G., Gershuni A.N., Zaripov V.K. Heat Pipes with metal felt capillary structures/ Kiev. Vyscha shcola, 1984. 215 p.

EFFECT OF COMPENSATION CHAMBER COOLING ON THE OPERATION OF A FLAT EVAPORATOR LOOP HEAT PIPE

Tae Hee Kim*, Wukchul Joung**, Sung pil Ma*, Chun Bae Choi***, Jinho Lee*⁺

*School of Mechanical Engineering, Yonsei University

**Korea Research Institute of Standards and Science

***Daehan Engineering Company

⁺School of Mechanical Engineering, Yonsei University, Seoul, Shinchon-dong, Seodaemun-gu, yonsei-ro 50
120-749, Republic of Korea

Phone : +82-2-2123-2816, Fax : +82-2-312-2159, E-mail : jinholee@yonsei.ac.kr

ABSTRACT

Loop heat pipes (LHPs) are highly promising passive two-phase heat transfer devices, and due to their superior heat transfer capability, they have been actively used as thermal control devices for satellites and highly integrated electronic devices. In general, in order to start up the LHPs, certain amount of heat load above a minimum start-up heat load is needed to circulate the working fluid throughout the loop. Therefore, at low heat load, it is difficult to start up the LHPs and guarantee a stable operation, limiting extensive application of these devices. In this work, in order to solve this problem, active thermal control of the compensation chamber was attempted. Particularly, employing commercially available heat sink-fan assemblies, it was aimed to extend operating range of the LHPs with relatively low-cost and simple means. The effect of compensation chamber cooling was found to decrease the minimum start-up heat loads and thus to extend the operating range of the LHPs.

KEY WORDS : Loop heat pipe (LHP), Start-up, Compensation chamber cooling

1. INTRODUCTION

Loop heat pipes (LHPs) are highly efficient passive two-phase heat transfer devices utilizing phase change of the working fluids and fast vapor flow to transfer large amount of heat quickly. Due to this heat transfer capability, the LHPs have been actively utilized as thermal control devices of satellites and highly integrated electronic devices [1-4].

The LHPs are known to have a minimum start-up heat load, and below this a stable start-up is not guaranteed. This limitation on the operating heat load range of the LHPs is mainly attributed to the insufficient saturation temperature difference between the evaporator and the compensation chamber(CC). Thus, in order to solve this problem, most of the reported works were focused on the increase of the temperature difference between these components at low heat load. The simplest approach is to increase the thickness of the wick [5,6], but usually resulting in the increased system dimension and restricted working fluid supply to the evaporator.

The other way of achieving required saturation temperature difference at low heat load is to cool

the compensation chamber actively, thus lowering the compensation chamber temperature. Ku et al. [7] utilized thermoelectric converters (TECs) in order to maintain the CC at the desirable set point temperature and operate a LHP at low heat load. However, as the use of thermoelectric modules requires high parasitic power and additional cooling scheme to dissipate heat, another simple way of compensation chamber cooling is needed for practical importance.

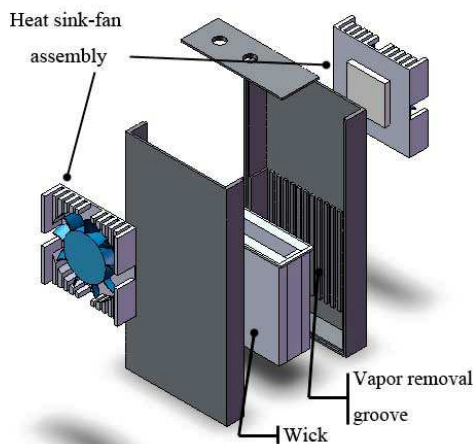
In this work, in order to resolve the aforementioned problem, active thermal control of the compensation chamber was attempted. Particularly, employing commercially available heat sink-fan assemblies, it was aimed to extend operating range of the LHPs with relatively low-cost and simple means.

2. Experimental set-up

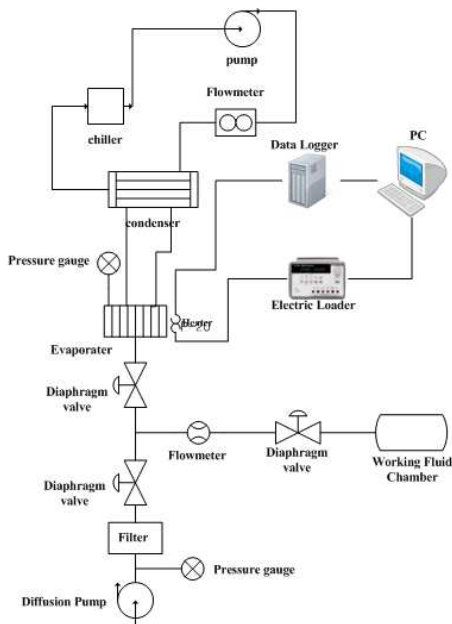
The LHPs mainly consist of the evaporator, compensation chamber, wick, condenser, and the working fluid transport lines. Figure 1 (a) shows the schematic of the flat evaporator LHP and the compensation chamber cooling with heat sink-fan assembly employed in this work. The evaporator

and the wick were made of stainless steel, and had dimensions of $60 \times 22 \times 121$ mm and $52.4 \times 52.4 \times 5$ mm ($w \times h \times t$). The mean pore size and porosity of the wick are $5 \mu\text{m}$ and 0.5, respectively. The heat sink-fan assemblies, which cooled down the compensation chamber, were attached to the outer surfaces of the compensation chamber. The condenser was designed to have enough cooling capacity, and consisted of a counter-flow concentric-tube heat exchanger.

The working fluid transport lines were connected



(a) Explosion view of LHP



(b) Schematics of test set-up

Figure 1. Experimental apparatus of LHP

to the evaporator and the condenser using rigid tubes (stainless tube, 1/4 in). Methanol was chosen as the working fluid, and injected to fill around 60 % of the total loop volume.

The test set-up consisted of the working fluid charge part, the data acquisition part, and the LHP. The test set-up is shown in Figure 1 (b). To measure the operating temperature, T-type thermocouples were attached on the components of the LHP. The temperature of the coolant supplied to the condenser of the LHP was set at $25 \text{ }^\circ\text{C}$. The heat load was supplied by an electric loader through a film heater, which was attached on the either side of the evaporator.

3. Experimental procedure

In this work, the compensation chamber cooling was achieved by applying power of 1.6 W to the each heat sink-fan assembly. To investigate the effect of the compensation chamber cooling on the start-up of the LHP, the applied heat load was decreased below the minimum start-up heat load of 35 W.

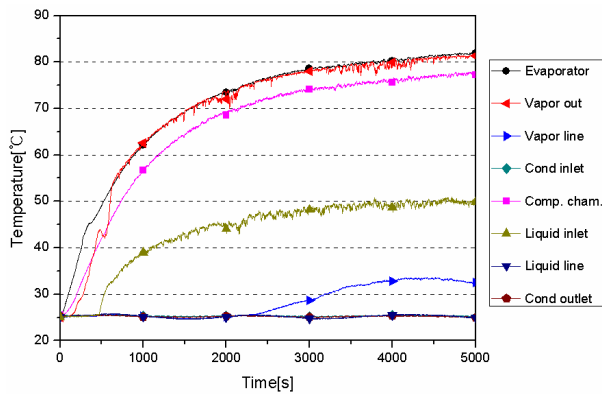
Particularly, in order to see clearly the effect of active cooling of the compensation chamber, the fan was powered on not only at the very beginning of the heat load supply but also at the state of thermal equilibrium when the start-up failed.

In addition to the start-up behavior of the LHPs, the effect of the compensation chamber cooling on the steady state operation was examined. In this case, a normal operation of the LHP from 30 W to 180 W was tested with the compensation chamber cooling.

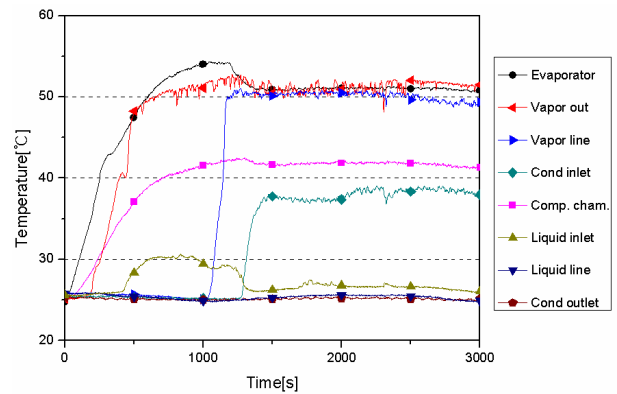
4. Result and discussion

4.1 Effect of the compensation chamber cooling on the start-up heat load

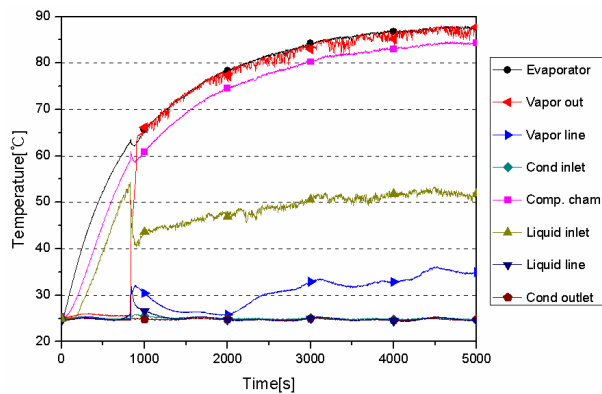
Figures 2 and 3 show the effect of the compensation chamber cooling on the start-up heat load of the LHP. In Figure 2, the temperature variations of components of LHP were shown when the start-up heat load was 25 W and 30 W, respectively. In both cases, the fan was powered off. As shown in these figures, the evaporator, compensation chamber and the liquid inlet temperature continued to rise, and the condenser inlet temperature was not increased. This indicated start-up failure of the LHP, which meant that the working fluid did not circulate throughout the loop. However, as shown in Figure 3, when power was provided to the fan at the beginning of the heat load supply, start-up was



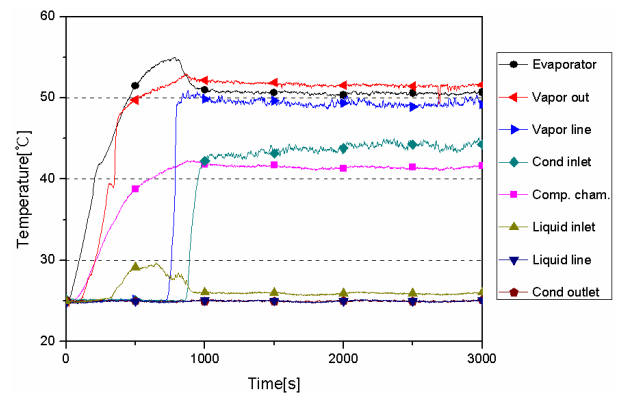
(a) 25 W heat load



(a) 25 W heat load



(b) 30 W heat load



(b) 30 W heat load

Figure 2. Start-up characteristics of Fan off

Figure 3. Start-up characteristics of Fan on

achieved at both heat loads, otherwise failed to operate.

This test showed that the application of the compensation chamber cooling was to lower the minimum start-up heat load. This was clearly due to the increased saturation temperature difference between the evaporator and the compensation chamber as a result of the compensation chamber cooling. The rapid increase of the condenser inlet temperature and the followed decrease in the liquid inlet temperature supported this. Therefore, it was found that the active cooling of the compensation chamber decreased the minimum start-up heat load.

4.2 Effect of the compensation chamber cooling on the failed start-up

In this test, the fan was powered on only after the start-up failure and the LHP achieved thermal equilibrium without working fluid circulation. Figure 4 shows the temperature variation with time at heat loads of 25 W and 30 W, at which the LHP failed to start up. When the fan was powered on at the thermal equilibrium stage of the start-up failure

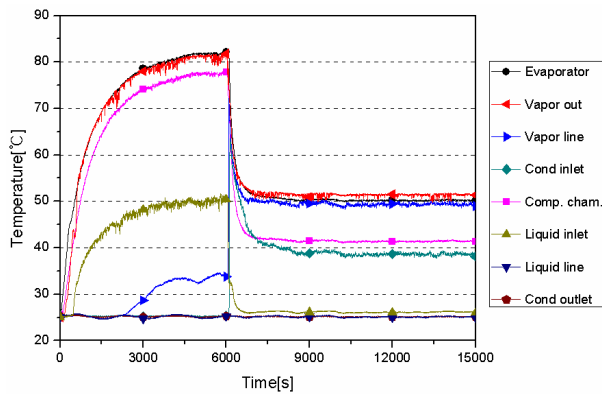
mode, the compensation chamber temperature decreased and the required saturation temperature difference to circulate the working fluid was met. As a result, the vapor phase working fluid rapidly flowed toward the condenser and the cold liquid phase working fluid to the compensation chamber. This was confirmed by the rapid condenser inlet temperature increase and the liquid inlet temperature decrease.

Therefore, it was also demonstrated that the active cooling of the compensation chamber enabled stable operation of the LHP, otherwise operation was failed.

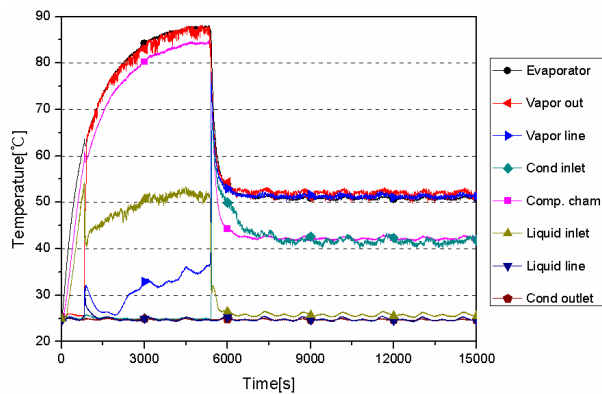
4.3 Effect of the compensation chamber cooling on the steady state operation of the LHP

Figure 5 shows the steady state evaporator temperature variation with heat load when the fan was powered on and off. As shown in this figure, the evaporator temperature was decreased when the fan was powered on.

When it was powered on, the cooled compensation chamber resulted in larger saturation temperature



(a) Transient operation under 25W heat load



(b) Transient operation under 30W heat load

Figure 4. Change of Operation mode with respect to Fan off/on

difference between the evaporator and the compensation chamber. As a result, the mass flow rate of the working fluid increased and the operating temperature decreased. Due to this enhanced heat transfer capability, the operating range was also increased, as shown in Figure 5.

In summary, it was found that cooling the compensation chamber actively decreased the minimum start-up heat load and extended the operating range.

5. CONCLUSIONS

A flat evaporator loop heat pipe with active control of the compensation chamber through heat sink-fan assembly was tested to investigate the effect of the compensation chamber cooling on the start-up and steady state operation of the LHP. The results are summarized as follows:

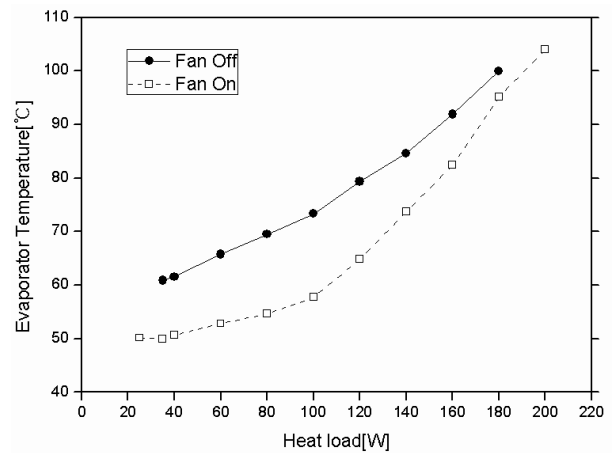


Figure 5. Comparison with temperature depending On Fan off/on

1. At lower heat loads than the minimum start-up heat load, LHP was failed to start up, but when the compensation chamber was actively cooled, successful start-ups were achieved.
2. When the compensation chamber was actively cooled, the LHP showed lower operating temperature than the operation without the compensation chamber cooling. This was due to the increased driving force of the working fluid circulation.
3. The effect of the active compensation chamber cooling was to decrease the minimum start-up heat load and to extend increase the operating range of the LHP.

REFERENCES

- [1] Ku, J. (1999) Operating characteristics of loop heat pipes in: 29th International Conference on Environmental System, Denver, USA, No. 1999-01-2007
- [2] Maydanik, Y. (2005) Loop heat pipes (review), Applied Thermal Engineering, Vol. 25, p. 635-657
- [3] Launay, S. et al. (2007) Parametric analysis of loop heat pipes operation: a literature review, International Journal of Thermal Science, Vol. 46, p. 621-636
- [4] Maydanik, Y., Fershtataer, Y., Solodnik, N. (1994) Design and investigation fo methods of regulation of loop heat pipes for terrestrial and space applications, SAE Paper, No. 941407

- [5] Maydanik, Y., Vershinin, S., Chernysheva, M., Yushakova, S. (2011) Investigation of a compact copper-water loop heat pipe with a flat evaporator, *Applied Thermal Engineering* 31, p. 3533-3541
- [6] Nguyen, X., Sung, B., Choi, J., Ryoo, S., Ko, H., Kim, C. (2011) Study on heat transfer performance for loop heat pipe with circular flat evaporator, *International Journal of Heat and Mass Transfer* 55, p. 1304-1315
- [7] Ku, J., Nagano, H. (2007) Loop heat Pipe Operation with Thermoelectric Converters and Coupling Blocks, *AIAA paper*, No AIAA-2007-4713

DEVELOPMENT OF A FLAT ALUMINIUM PANEL WITH MINICHANNELS AS LHP CONDENSER

Leonid Vassiliev and Maria Liakh

NIS Accosiation "Heat Pipes" 15 P. Brovka Str., 220072, Minsk, Belarus,
Tel: +375-44-5333275, Fax: +375172-842133, E-mail: leonid.l.vasiliev.jr@gmail.com

ABSTRACT

This paper presents a theoretical model to predict the heat transfer with the film condensation in horizontal microchannels of the LHP condenser. The model is encompassed on the basic analysis of the laminar condensate flow in the rectangular mini channel with surface tension and axial vapour shear stress action. Sample numerical results are given for propane and channel size (width \times height) 3.0 mm \times 7.0 mm and 300 mm in length. The general behavior of the condensate flow pattern, streamwise vapour flow variation and local mean heat-transfer coefficient have been analyzed for different initial and boundary conditions. The results of the model were validated by the experimental data.

KEY WORDS condensation, two-phase flow, heat transfer.

1. INTRODUCTION

Film condensation heat transfer in mini-channels has acquired increasing attention in last years with particular emphasis on how to enhance heat transfer to enable even more compact and efficient heat exchangers. Compactness and high efficiency of heat exchangers are very important factors for many applications and especially in aerospace segment, where the low mass of the equipment play a vital role.

Condensers with minichannels have been used successfully in automotive air conditioners for last decades and have proved both as compact and effective. An overview of microchannel condensation has been given by Garimella (2005). In this study aluminum flat panel with minichannels is considered as condenser for innovative LHP for the following reasons:

1. In some cases, the main spacecraft radiator is considered as heat spreader, not only for the heat generated components that have a direct thermal contact with it, but also as the radiator for LHP condenser.

2. It is strongly desirable that LHP condenser will be effective, compact with low inner volume and flat thermal interface due to strong restricted requirements to the radiator space budget.

The paper is devoted to the analysis of the condensation phenomena in aluminum panel with minichannels made from 6063 aluminum alloy (Figure 1 and Figure 2).

The subject of interest was related with the application of such heat pipes encompassed of the heat flow transmission in the interval 50 W-100 W.

In this research propane was used as the working fluid, while recently there has been a great deal of interest in the study of Freon fluid flow and heat transfer, in minichannels (Wang et al., 2004 and Nebuloni et al., 2010).

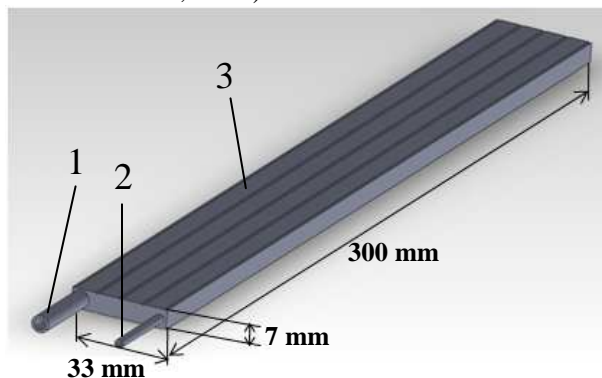


Figure 1. External view of flat condenser:
1 - vapour pipe, 2 - liquid pipe,
3 - panel with rectangular minichannels.

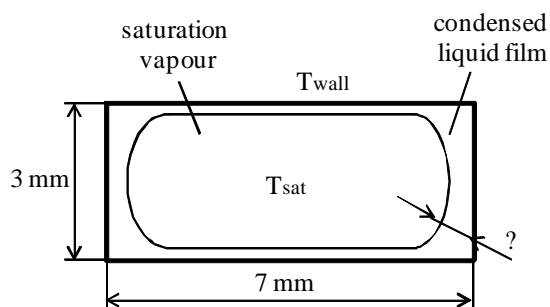


Figure 2. Cross-section of the aluminum condenser channel.

The condenser is made as the aluminum panel with minichannels inside. One minichannel is connected with LHP vapor line, and another one with LHP liquid line. The vapour and liquid flow direction inside minichannel of the LHP condenser are shown on the Figure 3 and Figure 4. At the beginning of the experiment the minichannels inside the condenser were filled with the liquid. The vapor generated in the LHP evaporator pushes the liquid from condenser toward the LHP evaporator, simultaneously condensing on the walls of the minichannel. Condensation in minichannel occurs due to heat sink on one of the surfaces of the condenser. In this study two scenario of external heat transfer have been under consideration: isothermal wall (intense water cooling) and fixed heat transfer coefficient on the cooled condenser side.

2. MATHEMATICAL MODEL

A mathematical model of heat and mass transfer in the condenser consists of Navier-Stokes equation, the heat energy conservation equation and the continuity equation. To determinate the liquid phase in two-phase flow, i.e. amount of liquid fraction, the volume of fluid method is used.

2.1. Navier-Stokes and continuity equations

The velocity field and pressure in each phase are determined by Navier-Stokes and continuity equations. Considering the presence of a phase transition these equations are written as:

$$\rho \frac{\partial \vec{u}}{\partial \tau} + \rho(\vec{u} \cdot \nabla)\vec{u} = \nabla \cdot [-p\vec{I} + \eta(\nabla\vec{u} + \nabla\vec{u}^T)] + \vec{F}_g + \vec{F}_{st} + \vec{F} \quad (1)$$

$$\nabla\vec{u} = \frac{S}{\rho} \quad (2)$$

When condensation takes place, i.e. $T_v < T_{sat}$, parameter S has the form (Yang et al., 2008 and De Schepper et al., 2009):

$$S = -r_v \alpha_v \rho_v \left| \frac{T_v - T_{sat}}{T_{sat}} \right| \quad (3)$$

2.2. Energy conservation equation

The temperature field in the condenser is described by the following conservation equation of heat energy:

$$\rho C_p \left(\frac{\partial T}{\partial \tau} + \vec{u} \cdot \nabla T \right) = \nabla \cdot (k \nabla T) + Q \quad (4)$$

The heat energy released during condensation is determined by the following expression:

$$Q = r_v \alpha_v \rho_v \left| \frac{T_v - T_{sat}}{T_{sat}} \right| \Delta H \quad (5)$$

2.3. Volume of fluid method

The tracking of the interface position between vapour and liquid flow was accomplished by solving continuity equations for the volume fractions of different phases. For the liquid and vapor phases, the equations are (Yang et al., 2008):

$$\frac{\partial \alpha_l}{\partial \tau} + \nabla \cdot (u \alpha_l) = -\frac{S}{\rho_l} \quad (6)$$

$$\frac{\partial \alpha_v}{\partial \tau} + \nabla \cdot (u \alpha_v) = \frac{S}{\rho_v}$$

where the effective parameters are determined as:

$$\begin{aligned} \rho &= \alpha_l \rho_l + \alpha_v \rho_v \\ k &= \alpha_l k_l + \alpha_v k_v \\ \eta &= \alpha_l \eta_l + \alpha_v \eta_v \end{aligned} \quad (7)$$

2.4. Initial and boundary conditions

The initial condition for Navier-Stokes equation:

$$u_l|_{t=0} = 0,$$

for heat energy equation:

$$\begin{aligned} T|_{t=0} &= T_{sink}, \\ T_v|_{t=0} &= T_{sat}, \end{aligned}$$

and for volume fraction equation:

$$\alpha_l|_{t=0} = 1, \quad \alpha_v|_{t=0} = 0.$$

The boundary condition for Navier-Stokes equation is:

$$u_{wall} = 0 \text{ m/s}, \quad p_{in} = p_{sat},$$

and for heat energy equation:

$$T_{wall} = T_{sink} \cdot k$$

3. RESULTS OF MODELING

To solve numerically equations (1)-(7) with above mentioned boundary conditions the finite elements method was used. A grid size of 5000 grid points along minichannel has been applied. The computational code was written using Matlab.

As a result of numerical simulation the main system characteristics are shown. The three-dimensional images of liquid and vapor phase distribution in the condenser channels for both cases are shown on figures 3 and 4. Blue and red colors represent vapor and liquid flows respectively, while the green isosurface illustrates the interface position. As previously mentioned at the very beginning of the experiment condenser channels were completely filled with the liquid. Then the vapor generated in the LHP evaporator enters to the condenser blowing partially away liquid and condenses gradually on the cold wall of the minichannel.

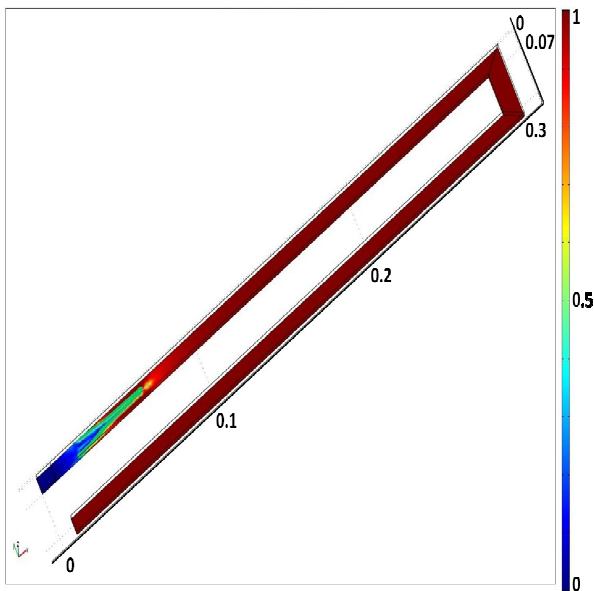


Figure 3. 3D-image of the vapour and liquid distribution inside the condenser channel with isothermal surface.

As it is seen from these figures 3 and 4 vapor condenses considerably faster for case with isothermal surface, than for case when the heat transfer on the outer condenser surface is fixed and equal to $400 \text{ W/m}^2 \text{ K}$.

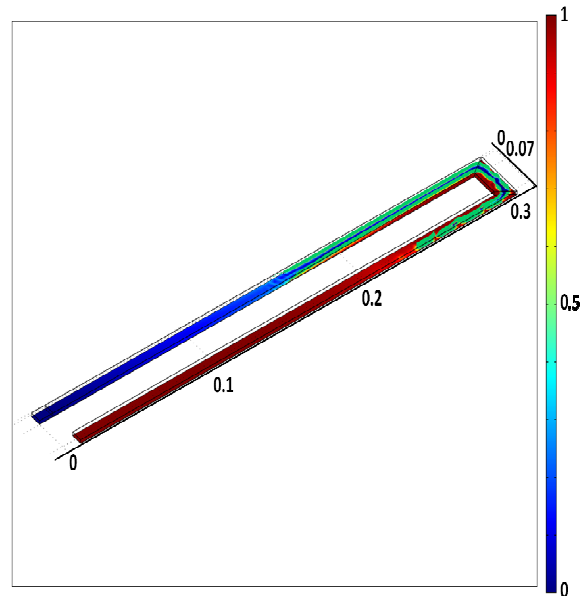


Figure 4. 3D-image of the vapour and liquid distribution inside the condenser channel with the fixed outside heat transfer coefficient equal to $400 \text{ W/(m}^2 \cdot \text{K)}$.

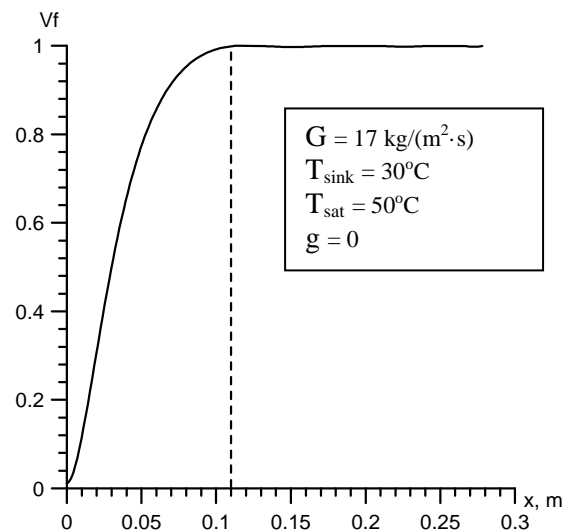


Figure 5. Coordinate dependence of the liquid content (V_l) in two-phase flow for case with isothermal condenser surface, dotted line separates single-phase region from two-phase zone.

Obtaining the liquid content (V_l) dependences along the channel length (fig. 5 and 6) we can determine where the channel liquid flooding happens. For the case with isothermal condenser wall the interface of single and two phase zones takes place in first part of the channel; for case with nonisothermal condenser wall the single-phase region starts at the beginning of second channel. The vapour condensation in the channel significantly depends on the heat sink temperature and boundary conditions on the condenser wall.

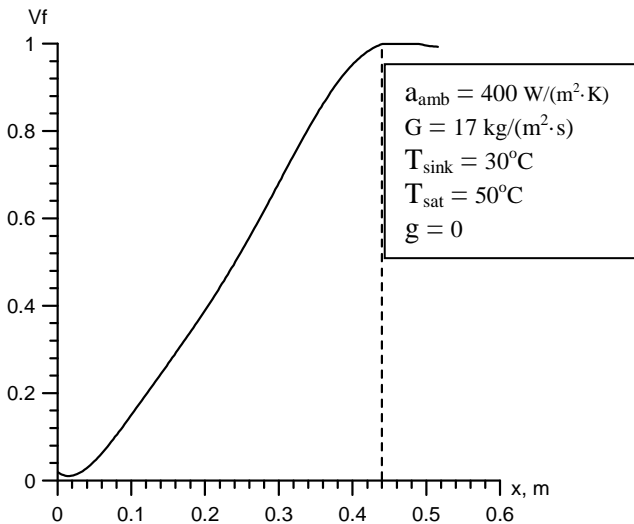


Figure 6. Coordinate dependence of the liquid content (V_f) in two-phase flow for the case with non-isothermal condenser surface; dotted line separates single-phase region from two-phase zone.

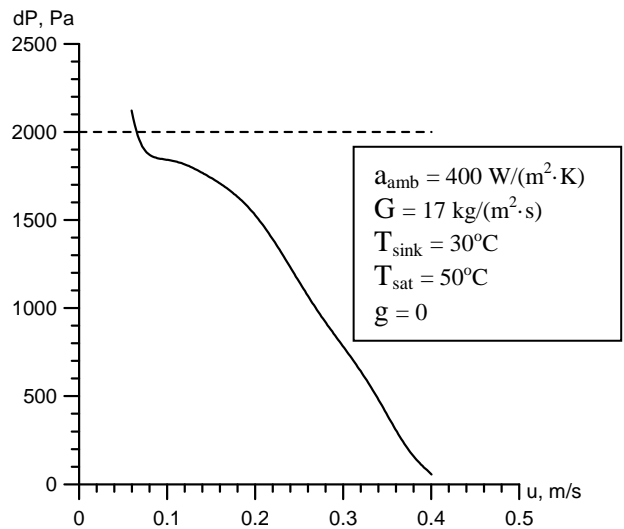


Figure 8. Influence of hydraulic losses on velocity of the fluid flow for case with nonisothermal condenser wall.

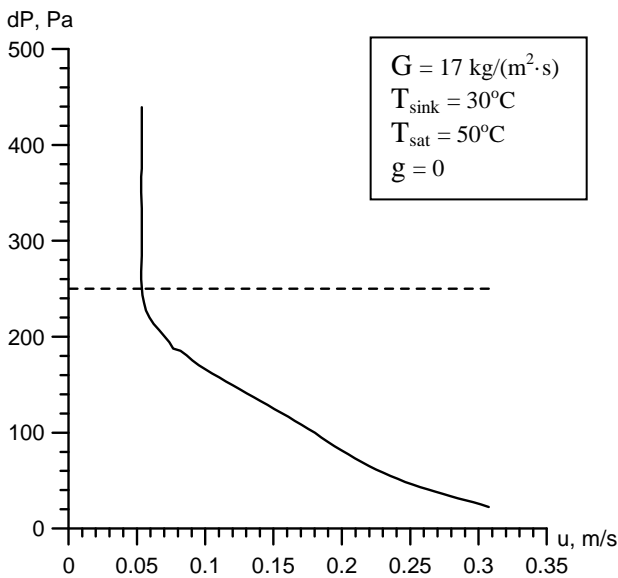


Figure 7. Influence of hydraulic losses on velocity of the fluid flow for case with isothermal condenser wall.

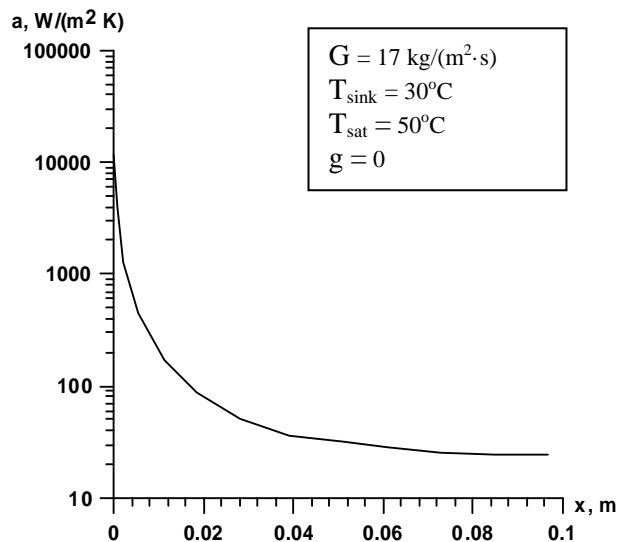


Figure 9. Coordinate dependence of the heat transfer coefficient for case with isothermal condenser wall.

In figures 7 and 8 the influence of hydraulic losses on velocity of the working fluid flow is shown for two cases. Dotted line position in these images illustrates interface of single-phase zone and two-phase zone. These dependences show that heavy hydraulic losses occur in the condenser channel for the case with nonisothermal condenser wall as compared with the isothermal wall. The flow velocity in the two-phase region drops sharply to the defined value, which corresponds to velocity of single-phase flow.

As a result of numerical modeling the coordinate dependences of the heat transfer coefficient of the liquid flow (fig.9 and 10) were obtained. Interface position of single- and two-phase zones can be determined from these dependences. The region, in which heat transfer coefficient is constant, corresponds to the single-phase zone and region, in which heat exchange coefficient is sharply decreasing, corresponds to the two-phase zone. As the heat transfer coefficient is inversely proportional to the thickness of the liquid layer we can assume that the thinner condense liquid layer is

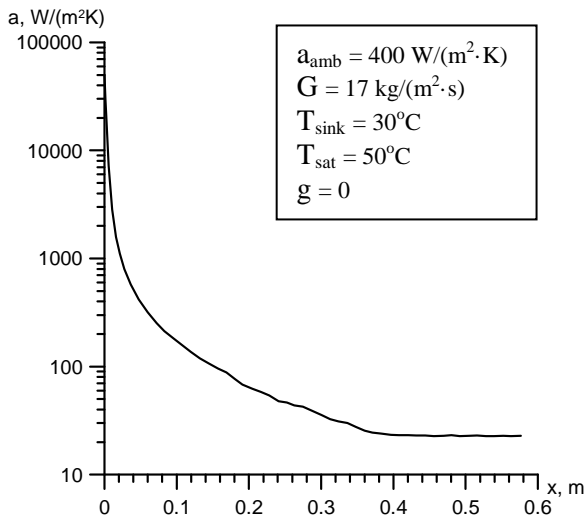


Figure 10. Coordinate dependence of the heat transfer coefficient for case with nonisothermal condenser wall.

the higher heat transfer coefficient could be. The calculated data obtained for the heat load $Q = 50$ W were validated by the experimental data, Fig.11.

As one can see there is a good agreement between calculated and experimental data for $G = 8,5$ $\text{kg/m}^2\text{s}$ mass flow and vapor temperature $T_{\text{sat}} = 30^0$ C. Two degree Celsius difference is occurred due to heat cross flow by the thermal conductance of the condenser aluminum wall which was not taken into account in presented model.

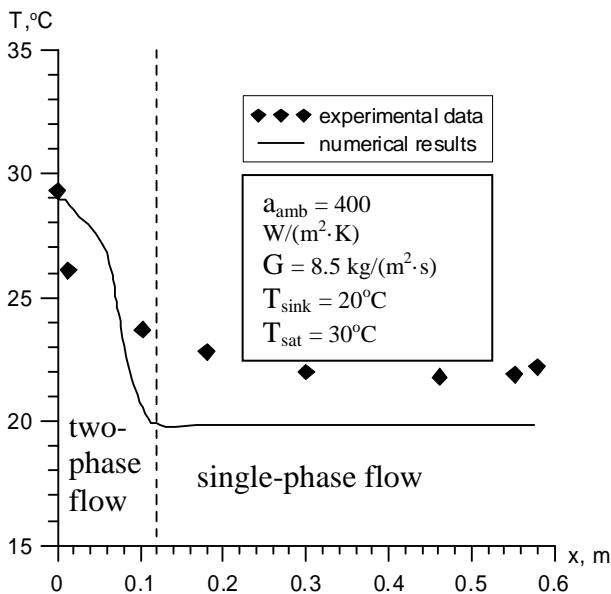


Figure 11. Experimental and numerical data of temperature distribution in the condenser channels.

4. CONCLUSIONS

The numerical modeling and experimental validation of the numerical results of the heat transfer during propane vapor condensation in minichannels of LHP condenser were performed. The model is encompassed on the basic analysis of the laminar condensate flow hydrodynamic and heat transfer in the rectangular mini channel including the surface tension and axial vapour shear stress influence.

In this study, two scenario of external heat transfer were under consideration: isothermal wall (intense water cooling) and fix heat transfer coefficient on the cooled condenser side.

NOMENCLATURE

a	heat transfer coefficient;
C_p	effective specific heat capacity of two-phase flow;
F	external forces;
F_g	gravity force;
F_{st}	surface tension force;
G	mass flow;
g	gravitational acceleration;
ΔH	latent heat of vaporization;
k	effective thermal conductivity;
p	pressure;
Q	heat contribution of additional sources (condensation);
r	time of relaxation of mass transfer;
S	parameter which takes into account condensation;
T	temperature;
t	time;
u	velocity.

Greek symbols

α	phase fraction;
η	dynamic viscosity;
ρ	density.

Subscripts

amb	ambient;
g	gravity;
l	liquid;
sat	saturation;
st	surface tension;
$sink$	heat sink;
v	vapor.

REFERENCES

- Garimella, S. (2005) *Condensation in minichannels and microchannel*, in: Kandlikar, S.G., Garimella, S., Li, D., Colin, S., King, M.R., (Eds.) *Heat Transfer and Fluid Flow in Minichannels and Microchannels*. Elsevier
- De Schepper, Sandra C.K., Heynderickx, Geraldine J., Marin, Guy B. (2009) *Modeling the evaporation of a hydrocarbon feedstock in the convection section of a steam cracker*. *J. Computers and Chemical Engineering*, 33, p. 122–132
- Nebuloni, S., Thome, J. R. (2010) *Numerical modeling of laminar annular film condensation for different channel shapes*. *International Journal of Heat and Mass Transfer*, 53, p. 2615–2627
- Wang, H. S., Rose, J. W., Honda, H. (2004) *A theoretical model of film condensation in square section horizontal microchannels*. *J. Chemical Engineering Research and Design*, 82(A4), p. 430–434
- Yang, Z., Peng, X.F., Ye., P. (2008) *Numerical and experimental investigation of two phase flow during boiling in a coiled tube*. *International Journal of Heat and Mass Transfer*, 51, p. 1003–1016

A CLOSED LOOP THERMOSYPHON WITH CONVENTIONAL OR MINICHANNEL BASED CONDENSER AND EVAPORATOR

Henryk BIELIŃSKI, Jarosław MIKIELEWICZ

Institute of Fluid-Flow Machinery PAS
ul. Fiszera 14, 80-952, Gdansk, Poland
+48 58 341 1271, admin@biel@balta.net.pl, jarekm@imp.gda.pl

Dariusz MIKIELEWICZ

Gdansk University of Technology, Faculty of Mechanical Engineering
ul. Narutowicza 11/12, 80-233 Gdansk, Poland
+48 58 347 2254, +48 58 347 2816, Dariusz.Mikielewicz@pg.gda.pl

ABSTRACT

The purpose of this paper is to present an analysis of heat transfer and fluid flow in a generalized model of the closed loop thermosyphon and its different variants. The analysis of the closed loop thermosyphon is based on the one-dimensional model, which includes mass, momentum and energy balances. In the paper considered are two cases of a general model of a closed loop thermosyphon (CLT), namely the case where there is heating of a vertical part and cooling through the vertical part, and the second one where vertical part of CLT is heated and a horizontal one cooled. Each individual variant was analyzed in terms of two-phase flow in the loop with conventional tubes and minichannels.

KEY WORDS *Closed loop thermosyphon, minichannels, thermal diode*

1. INTRODUCTION

The primary function of a natural circulation loop (i.e. thermosyphon loop) is to transport heat from a source to a sink. Fluid flow in a closed loop thermosyphon (CLT) is created by the buoyancy forces that evolve from the density gradients induced by temperature differences in the heating and cooling sections of the loop. An advanced CLT loop consists of an evaporator, where the liquid boils and a condenser, where the vapour condenses back to liquid. These two devices are connected by a riser and a downcomer. Heat is transferred as the vaporization heat from the evaporator to the condenser. The CLT makes use of gravity for returning the liquid to the evaporator. CLT are less expensive than other heat pipes. The closed-loop thermosyphon is also known as a "liquid fin", Madejski & Mikielewicz, 1971.

There are numerous engineering applications for gravity driven thermosyphons such as, for example, electronic components, thermal diodes, Bieliński & Mikielewicz, 1995, 2001, Chen, 1998, solar water heaters, thermosyphon reboilers and emergency cooling systems in nuclear reactor cores during an accident.

The purpose of this paper is to present the analysis of heat transfer and fluid flow in a generalized model of a closed loop thermosyphon and its different variants. The analysis of the closed loop thermosyphon is based on the one-dimensional model, which includes mass, momentum and energy balances. In the paper considered will be two cases of a general model of CLT, namely the case where there is heating of a vertical part and cooling through a vertical part, and the second one where vertical part of CLT is heated and a horizontal one cooled. Each individual variant was analyzed in terms of two-phase flow in the loop with conventional tubes and minichannels.

2. A GENERALIZED MODEL OF CLT

The CLT loop has a provision for selecting one or two heat sources at vertical or horizontal locations, namely in the bottom horizontal pipe or in the vertical leg. Similarly, the heat sink can be chosen in the top horizontal pipe or on the top part of the vertical leg, see Fig. 1. Therefore, any combination of heaters and coolers can be analysed. In the analysis the constant heat fluxes q_H and q_C are applied in the respective areas of heating and cooling sections L_H (L_{H1} , L_{H2}) and L_C (L_{C1} , L_{C2}).

The heated and cooled parts of the CLT are connected by perfectly insulated channels. The length coordinate s being evaluated along the loop and the characteristic geometrical points on the loop were marked as s_j as shown in Fig. 1. The subscript 0 refers to the start of heating. The total length of the loop is denoted by L , channel diameter by D , the cross-section area of the channel by A and the wetted perimeter by U . Thermal properties of fluid: ρ - density, c_p - heat capacity of constant pressure, λ - thermal conductivity.

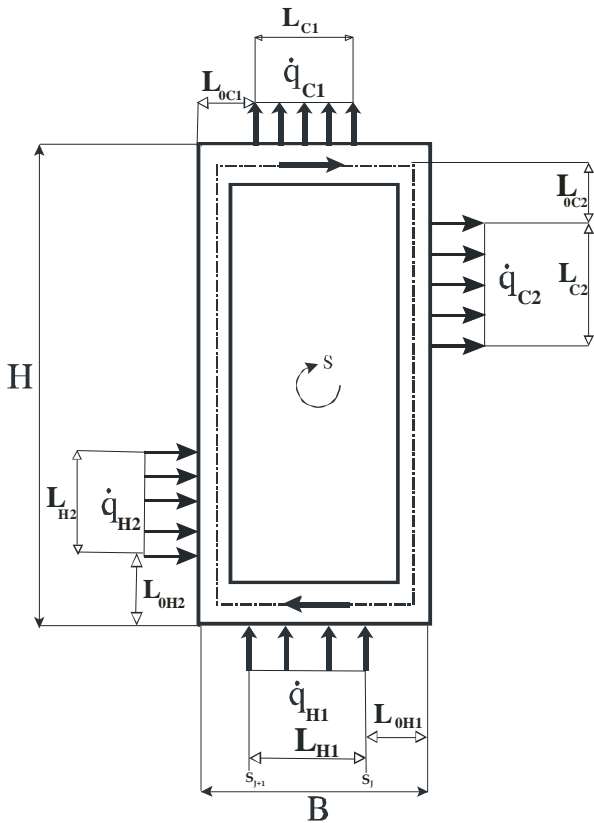


Fig. 1. A schematic diagram of a one-dimensional generalized model of the thermosyphon loop.

The following assumptions are used in the development of the theoretical model of natural circulation in the closed loop thermosyphon:

- 1) thermal equilibrium at any point of the loop,
- 2) problem is considered as incompressible because flow velocity in the natural circulation loop is relatively low compared with the speed of sound under considered model conditions,
- 3) viscous dissipation in fluid is neglected in energy equation,
- 4) heat losses in the CLT are negligible,
- 5) $D/L \ll 1$, one-dimensional models are used and the flow is fully mixed so the velocity and

temperature variation at any cross section is neglected,

- 6) heat exchangers in the CLT can be equipped with conventional size tubes or minichannels,
- 7) fluid properties are constant except for density in the gravity term in momentum equation,
- 8) superheating and subcooling are neglected.

With the above assumptions, the governing equations for natural circulation loop are:

-conservation of mass:

$$\frac{\partial \rho}{\partial \tau} + \frac{\partial}{\partial s}(\rho \cdot w) = 0 \quad (1)$$

where τ - time, w - velocity.

-conservation of momentum:

$$\rho \cdot \left(\frac{\partial w}{\partial \tau} + w \cdot \frac{\partial w}{\partial s} \right) = - \frac{\partial p}{\partial s} + \varepsilon \cdot \rho \cdot \tilde{g} - \tau_w \cdot \frac{U}{A} \quad (2)$$

where

$$\varepsilon = \begin{cases} 0 & \text{for } \vec{e} \perp \vec{g} \\ +1 & \text{for } \vec{e} \uparrow \wedge \vec{g} \downarrow \\ -1 & \text{for } \vec{e} \downarrow \wedge \vec{g} \downarrow \end{cases} \quad (3)$$

$$\tilde{g} = \vec{e} \circ \vec{g} = 1 \cdot g \cdot \cos(\vec{e}, \vec{g}) \quad (4)$$

Additionally, $|\vec{g}| = g$; $|\vec{e}| = 1$; and \vec{e} is versor of the coordinate around the loop, τ_w - wall shear stress. In order to eliminate the pressure gradient and acceleration term, the momentum equation (2) is integrated around the loop. That leads to:

$$\oint \left(\frac{\partial p}{\partial s} \right) ds = 0 \quad (5)$$

-conservation of energy:

$$\frac{\partial T}{\partial \tau} + w \cdot \frac{\partial T}{\partial s} = a_0 \cdot \frac{\partial^2 T}{\partial s^2} + B \quad (6)$$

$$B = \begin{cases} +0 & \text{for } \text{adiabatic section} \\ - \frac{q_c \cdot U}{c_{p0} \cdot \rho_0 \cdot A} & \text{for } \text{cooled section} \\ + \frac{q_H \cdot U}{c_{p0} \cdot \rho_0 \cdot A} & \text{for } \text{heated section} \end{cases} \quad (7)$$

where $a_0 = \frac{\lambda_0}{\rho_0 \cdot c_{p0}}$ - thermal diffusivity. The

subscript 0 refers to the reference state. The flow in natural circulation systems is driven by density distribution variation in heating and cooling sections. In these flows the momentum and the energy equations are coupled and so need to be simultaneously solved. In case of two-phase flow similar conservation equations are used, Bieliński (2004).

3. VERTICAL HEATING/COOLING - VHVC

The CLT heated on the distance L_{H2} on the lower part of vertical leg and cooled on the distance L_{C2} from the upper part of the opposite leg (VHVC) is chosen as a first example to present the analysis of two-phase flow in heat exchangers. First, the case with conventional size channels will be considered. The Stomma, 1979, correlation for void fraction, the Chisholm, Collier and Thome, 1982, correlation for the friction pressure drop of two-phase flow in adiabatic region, the Lottes-Flinn, Collier & Thome, 1982, correlation for the friction pressure drop of two-phase flow in diabatic region and the D. Mikielewicz et al. (2007) correlation for the flow boiling heat transfer coefficient in are used to calculate two phase flow in the thermosyphon loop equipped with conventional tubes. Freon R11 was chosen as a working fluid in the thermosyphon device. According to the notation presented in Fig. 1 in the analysis is assumed that $q_{cl}=q_{hl}=0$.

The gravitational term in the momentum equation (2) for (HVCV) can be expressed as:

$$\oint \{ \varepsilon \cdot g \cdot [(1-\alpha) \cdot \rho_l + \alpha \cdot \rho_v] \} ds = g \cdot (\rho_v - \rho_l) \cdot \{ (s_1 - s_0) \cdot \bar{\alpha}_{(s_0;s_1)} - (s_5 - s_4) \cdot \bar{\alpha}_{(s_4;s_5)} + [(s_2 - s_1) - (s_4 - s_3)] \cdot \bar{\alpha}_{(s_1;s_4)} \} \quad (8)$$

where α is void fraction of the two-phase fluid,

$$\bar{\alpha}_{(s_p;s_k)} = \frac{1}{(s_k - s_p)} \cdot \int_{s_p}^{s_k} \alpha_{(s_p;s_k)}(s) ds \quad .$$

The Stomma empirical correlation for the void fraction at low pressures is applied.

The following additional assumptions are made in the study of VHVC case: 1) flows of liquid and vapour phases in the two-phase regions are both turbulent and flow of liquid in single phase region is also turbulent, 2) friction coefficient is constant in each region of the loop and the frictional

component of the pressure gradient in two-phase regions is calculated according to the two-phase separated model. The pressure drop in two-phase regions due to fluid friction, can be calculated as:

$$\frac{U}{A} \cdot \tau_w = \left(\frac{-dp}{ds} \right)_{TP} = R \cdot \left(\frac{-dp}{ds} \right)_{L0} \quad (9)$$

where R is the local two-phase flow multiplier and $\left(\frac{dp}{ds} \right)_{L0} = \Psi_L^{TUR} \cdot (\dot{m})^{7/4}$ is the liquid only pressure gradient calculated for the total liquid mass flow

$$\text{rate, with } \Psi_L^{TUR} = \frac{0,3164}{\sqrt{128}} \cdot \frac{(v_L)^{1/4}}{(\rho_L)^{3/4}} \cdot \frac{(U)^{5/4}}{A^3} \quad .$$

The local two-phase friction pressure drop in two-phase adiabatic region was calculated using the Chisholm formula. The local two-phase friction coefficient in two-phase diabatic regions was calculated using the Lottes-Flinn formula. After integrating the friction term in (2) around the loop:

$$\frac{U}{A} \cdot \tau_w = \left(\frac{dp}{ds} \right)_{L0} \cdot [(s_1 - s_0) \cdot \bar{R}_{(s_0;s_1)} + (s_4 - s_1) \cdot \bar{R}_{(s_1;s_4)} + (s_5 - s_4) \cdot \bar{R}_{(s_4;s_5)} + (s_8 - s_5)] \quad (10)$$

$$\text{where: } \bar{R}_{(s_p;s_k)} = \frac{1}{(s_k - s_p)} \cdot \int_{s_p}^{s_k} R(s) ds \quad .$$

Hence the momentum equation (2) for the simplified CLT, that is HVCV, can be written as:

$$[(s_1 - s_0) \cdot \bar{R}_{(s_0;s_1)} + (s_4 - s_1) \cdot \bar{R}_{(s_1;s_4)} + (s_5 - s_4) \cdot \bar{R}_{(s_4;s_5)} + (s_8 - s_5)] \cdot \Psi_L^{TUR} \cdot (\dot{m})^{7/4} + g \cdot (\rho_v - \rho_l) \cdot \{ (s_1 - s_0) \cdot \bar{\alpha}_{(s_0;s_1)} - (s_5 - s_4) \cdot \bar{\alpha}_{(s_4;s_5)} + [(s_2 - s_1) - (s_4 - s_3)] \cdot \bar{\alpha}_{(s_1;s_4)} \} = 0 \quad (11)$$

The mass flux rate distributions \dot{G} versus heat flux \dot{q}_H for the steady-state conditions and case of conventional tube, is shown in Fig. 2. Working fluid is R11 ($t=20^\circ\text{C}$, $P=0.895 \times 10^5$ Pa, Gogól, 1976). Calculations were carried out also using the homogeneous model of two-phase flow. In Fig. 2 two flow regimes can be clearly identified, namely GDR - gravity dominant regime and FDR - friction dominant regime. In the gravity dominant regime, for a small change in quality there is a large change in the void fraction and hence the density and buoyancy force. The increased buoyancy force is to be balanced by a corresponding increase in the frictional force

which is possible only at a higher flow rate. As a result, the gravity dominant regime is characterized by an increase in the flow rate with heat flux \dot{q}_H .

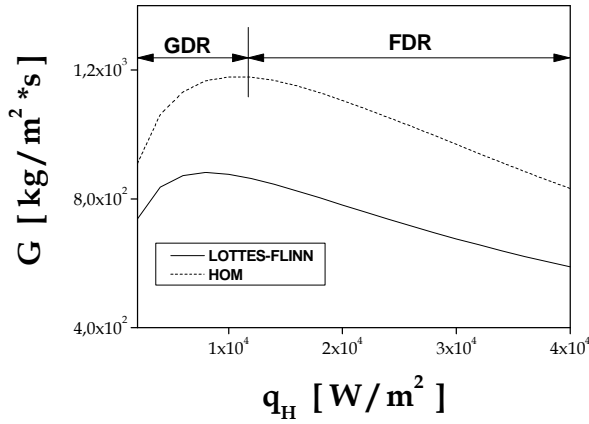


Fig. 2. Mass flux rate \dot{G} as a function of \dot{q}_H for homogeneous model and separate model with Lottes-Flinn correlation. (HVCV).

However, the continued conversion of high density water to low density steam due to increase in heat flux \dot{q}_H requires that the mixture velocity must increase resulting in an increase in the frictional force and hence the decrease in flow rate. Thus the friction dominant regime is characterized by a decrease in flow rate with increase in heat flux \dot{q}_H which is consistent with Vijayan et al., 2005. Comparing the performance of two models of two-phase flow, the homogeneous and the separate model reveal differences of the order of 50%.

The heat transfer coefficient in flow boiling minichannels was calculated using the Mikielewicz (2009) general formula for conventional channels with appropriate modifications. For the purpose of comparison the heat transfer coefficient for flow boiling in minichannels was also calculated using the modified Gungor and Winterton, 1986, formula: The heat transfer coefficient in flow boiling for minichannels α_{TPB} distributions versus heat flux \dot{q}_H for the steady-state conditions are presented in Fig. 3.

4. VERTICAL HEATING/HORIZONTAL COOLING - (VHHC).

The thermosyphon loop heated from the lower part of vertical side and cooled from the upper horizontal side (HVCH) was analyzed for case of two-phase flow in minichannels. In case of a minichannels thermosyphon loop, it is

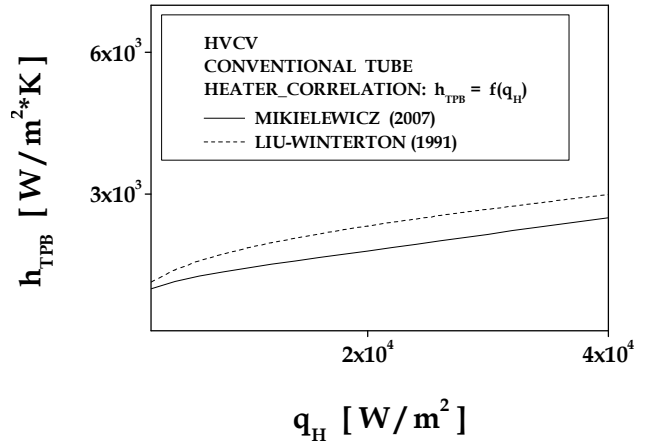


Fig. 3. (HVCV). Heat transfer coefficient α_{TPB} as a function of \dot{q}_H ($L=2$ m ; $B=0.1$ m ; $H=0.9$ m ; $L_H=L_C=0,2$ m ; $L_{OH}=L_{OC}=0,05$ m ; $D=0,008$ m)..

necessary to apply other correlations for void fraction and the local two-phase friction coefficient in two-phase region, and local heat transfer coefficient for flow boiling and condensation. The El-Hajal et al., 2003 correlation for void fraction, the Zhang-Webb, 2001, correlation for the friction pressure drop of two-phase flow in adiabatic region, the Tran et al., 2000 correlation for the friction pressure drop of two-phase flow in diabatic region, the Mikielewicz, 2009, and the Saitoh et al., 2007 correlations for the flow boiling heat transfer coefficient for minichannels, the Mikielewicz, 2009 and the Tang et al., 2000 correlations for condensation heat transfer coefficient for minichannels have been used in the calculations of the thermosyphon loop with minichannels. In the analysis is assumed that $q_{c2}=q_{H2}=0$.

The gravitational term in the momentum equation (2) can be expressed as:

$$\oint \{ \epsilon \cdot \tilde{g} \cdot \rho \} ds = g \cdot (\rho_V - \rho_L) \cdot \left[(s_1 - s_0) \cdot \bar{\alpha}_{(s_0;s_1)} + (s_2 - s_1) \cdot \bar{\alpha}_{(s_1;s_2)} \right] \quad (12)$$

where α is void fraction of the two-phase flow,

$$\bar{\alpha}_{(s_P;s_K)} = \frac{1}{(s_K - s_P)} \cdot \int_{s_P}^{s_K} \alpha_{(s_P;s_K)}(s) ds$$

The frictional component of the pressure gradient in two-phase regions was calculated using the two-phase separate model. Due to friction of fluid, the

frictional pressure gradient in two-phase regions can be written as [7]:

$$\frac{U}{A} \cdot \tau_w = \left(\frac{-dp}{ds} \right)_{2p} = R \cdot \left(\frac{-dp}{ds} \right)_{L0} \quad (13)$$

where R is the local two-phase friction factor,

$$\bar{R}_{(s_p;s_K)} = \frac{1}{(s_K - s_p)} \cdot \int_{s_p}^{s_K} R(s) ds \quad \text{and} \quad \left(\frac{dp}{dz} \right)_{L0} = \frac{f_{L0} \cdot 2 \cdot (\dot{G})^2}{D \cdot \rho_L}$$

is the liquid frictional pressure gradient calculated for the liquid total mass flow rate, f_{L0} is the Churchill's single-phase friction factor.

Hence the momentum equation (2) for the two-phase thermosyphon loop can be written as

$$\begin{aligned} & \left(\frac{dp}{ds} \right)_{L0} \cdot \left\{ (s_1 - s_0) \cdot \bar{R}_{(s_0;s_1)} + (s_3 - s_1) \cdot \bar{R}_{(s_1;s_3)} + (s_4 - s_3) \cdot \bar{R}_{(s_3;s_4)} \right. \\ & \left. + (s_8 - s_4) \right\} + g \cdot (\rho_V - \rho_L) \cdot \left[(s_1 - s_0) \cdot \bar{\alpha}_{(s_0;s_1)} + (s_2 - s_1) \cdot \bar{\alpha}_{(s_1;s_3)} \right] \\ & = 0 \end{aligned} \quad (14)$$

The El-Hajal's empirical correlation for the void fraction at low pressures is used in calculations. The local two-phase friction coefficient in two-phase adiabatic region was calculated using the Zhang-Webb formula whereas the local two-phase friction coefficient in two-phase diabatic regions was calculated using the Tran formula.

The mass flux rate distribution \dot{G} versus heat flux \dot{q}_H distributions was obtained numerically for the steady-state conditions for minichannels, as shown in Fig. 4. Working fluid was R11 ($t=20^\circ\text{C}$, $P=0.895 \times 10^5$ Pa). Again two flow regimes can be clearly identified, GDR - gravity dominant regime and FDR - friction dominant regime.

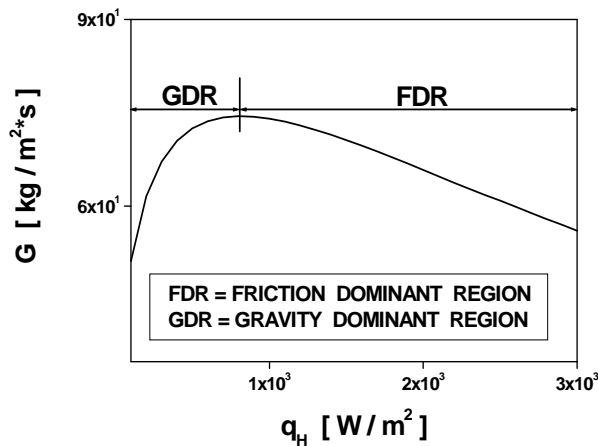


Fig. 11. (HVCH). Mass flux rate \dot{G} as a function of \dot{q}_H ($L=0.2$ m ; $B=0.04$ m ; $H=0.06$ m ; $L_H=L_C=0.03$ m ; $L_{HP}=L_{CP}=0.0001$ m ; $D=0.002$ m).

The heat transfer coefficient in condensation for minichannels was calculated using the general Mikielwicz, 2009, in which the term concerning nucleation process is neglected. The heat transfer coefficient for condensation in minichannels was calculated also using the modified Tang formula. The heat transfer coefficient for condensation in minichannels α_{TPC} versus heat flux \dot{q}_C is presented in Fig. 5.

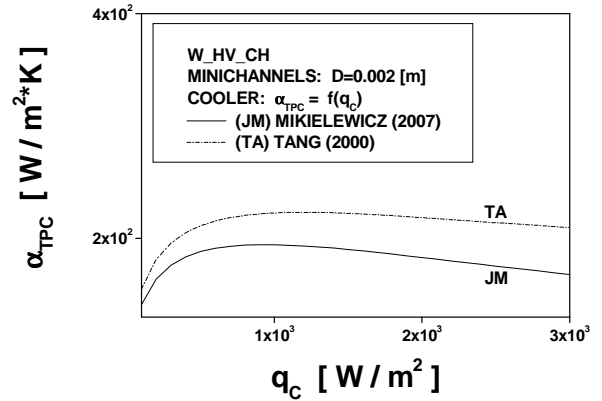


Fig. 5. (HVCH). Heat transfer coefficient α_{TPC} as a function of \dot{q}_H ($L=0.2$ m ; $B=0.04$ m ; $H=0.06$ m ; $L_H=L_C=0.03$ m ; $L_{HP}=L_{CP}=0.0001$ m ; $D=0.002$ m).

5. CONCLUSIONS

The presented variants of gravity driven LHP can be analyzed using conservation equations of mass, momentum and energy based on a generalized model of the closed loop thermosyphon. Our studies demonstrate that the best choice of the presented variants depends on specific technical conditions. The application of the complexity analysis for the various variants of a generalized model of thermosyphon loop can support development of an alternative cooling technology. The results show that the one-dimensional two-phase separated model can be used to describe heat transfer and fluid flow in the gravity driven LHP for conventional tube and minichannels. The Stomma correlation for void fraction, the Chisholm correlation for the friction pressure drop of two-phase flow in adiabatic region, the Lottes-Flinn correlation for the friction pressure drop of two-phase flow in diabatic region and the D. Mikielwicz et al. (2007) correlation for the flow boiling heat transfer coefficient in conventional channels can be used to evaluate the thermosyphon loop.

In order to evaluate the thermosyphon loop with minichannels the El-Hajal correlation for void

fraction, the Zhang-Webb correlation for the friction pressure drop of two-phase flow in adiabatic region, the Tran correlation for the friction pressure drop of two-phase flow in diabatic region and the Mikielewicz correlation for the heat transfer coefficient in evaporator, the Mikielewicz and the Tang et al. correlations for condensation heat transfer coefficient in minichannels can be used in calculations.

The distribution of the mass flux rates against the heat flux approaches a maximum and then slowly decreases for minichannels, and two flow regimes can be clearly identified: GDR- gravity dominant regime and FDR – friction dominant regime.

ACKNOWLEDGEMENT

The work presented in the paper was partly funded from the Polish Ministry for Science and Education research project No. N512 459036 in years 2009-2012, project No. N512 356137 in years 2009-2014 and project N512 479539 in years 2010-2013.

REFERENCES

- Bieliński, H.; Mikielewicz, J. (1995) *Natural Convection of Thermal Diode*. Archives of Thermodynamics, Vol. 16, No. 3-4.
- Bieliński, H.; Mikielewicz, J. (2001) *New solutions of thermal diode with natural laminar circulation*. Archives of Thermodynamics, Vol. 22, pp. 89-106.
- Bieliński, H.; Mikielewicz J. (2004) *The effect of geometrical parameters on the mass flux in a two phase thermosyphon loop heated from one side*. Archives of Thermodynamics, Vol. 29(1), 59-68.
- Chen, K. (1988) *Design of Plane-Type Bi-directional Thermal Diode*. ASME J. of Solar Energy Engineering, Vol. 110, pp. 299-305.
- El-Hajal, J.; Thome, J.R. & Cavallini A. (2003) *Condensation in horizontal tubes, part I; two-phase flow pattern map*. Int. J. Heat Mass Transfer, Vol. 46, No. 18, pp. 3349-3363.
- Gogół, W. (1976) *Heat transfer. Tables and Graphs*, Warszawa 1976 (in Polish).
- Gungor, K.E. & Winterton R.H.S. (1986) *A General Correlation for Flow Boiling in Tubes and Annuli*, Int. J. Heat Mass Transfer, Vol. 29, No. 3, pp. 315-358.
- Kandlikar S.G. (1989) *A General Correlation for Saturated Two-Phase Flow Boiling Heat Transfer Inside Horizontal and Vertical Tubes*. J. Heat Transfer, 112, 219-228.
- Madejski, J.; Mikielewicz, J. (1971) *Liquid Film on a New Device for Heat Transfer Equipment*, Int. J. Heat Mass Transfer, Vol. 14, pp. 357-363.
- Mikielewicz, D.; Mikielewicz, J. & Tesmar J. (2007) *Improved semi-empirical method for determination of heat transfer coefficient in flow boiling in conventional and small diameter tubes*, Int. J. Heat Mass Transfer, Vol. 50, 3949-3956.
- Mikielewicz D. (2010) *A new method for determination of flow boiling heat transfer coefficient in conventional diameter channels and minichannels*, Heat Transfer Engineering, vol. 31, No. 4, pp. 276-287, 2010.
- Saitoh, S.; Daiguji, H. & Hihara, E. (2007) *Correlation for Boiling Heat Transfer of R-134a in Horizontal Tubes Including Effect of Tube Diameter*. Int. J. Heat Mass Transfer, Vol. 50, 5215-5225.
- Tang, L.; Ohadi, M.M. & Johnson, A.T. (2000) *Flow condensation in smooth and microfin tubes with HCFC-22, HFC-134a, and HFC-410 refrigerants, Part II: Design equations*. Journal of Enhanced Heat Transfer, Vol. 7, pp. 311-325.
- Tran, T.N.; Chyu, M.C.; Wambsganss, M.W.; & France D.M. (2000) *Two-phase pressure drop of refrigerants during flow boiling in small channels: an experimental investigations and correlation development*. Int. J. Multiphase Flow, Vol. 26, No. 11, pp. 1739-1754.
- Vijayan, P.K.; Gartia, M.R.; Pilkhwal, D.S.; Rao, G.S.S.P. & Saha D. (2005) *Steady State Behaviour Of Single-Phase And Two-Phase Natural Circulation Loops*. 2nd RCM on the IAEA CRP, Corvallis, Oregon State University, USA.
- Zhang, M. & Webb, R.L. (2001) *Correlation of two-phase friction for refrigerants in small-diameter tubes*. Experimental Thermal and Fluid Science, Vol. 25, pp. 131-139.

A TWO-PHASE LOOP THERMOSYPHON WITH NAPHTHALENE AS WORKING FLUID

Milanez, F. H.

Energy Engineering Dept.,
Federal University of Santa Catarina
Ararangua, Brazil, 88900-000
milanez@labtucal.ufsc.br,
Phone: +55 48 3721 4194

Mantelli, M. B. H.

Mechanical Engineering Dept.,
Federal University of Santa Catarina,
Florianopolis, Brazil, 88040-900
marcia@emc.ufsc.br
Phone: +55 48 3721 9937, Fax: +55 48 3721 7615

ABSTRACT

This work presents an experimental study on a stainless steel loop thermosyphon with naphthalene as the working fluid. A prototype was tested in a hot gas stream with temperatures ranging between 335 and 450°C with the thermal resistance of the thermosyphon ranging from 1.9×10^{-2} to 5.7×10^{-3} m²K/W, respectively. The evaporator and the condenser are connected by vapor and liquid lines which are 5.8m long. In order to operate properly, the thermal losses of the vapor line connecting the evaporator to the condenser must be eliminated, which was accomplished during the tests by using auxiliary heating. Without the auxiliary heating to the vapor lines, pure saturated vapor does not reach the condenser, and the thermosyphon does not operate properly.

KEY WORDS: Loop thermosyphon, Naphthalene.

1. INTRODUCTION

Loop thermosyphon heat exchangers, also known as separated heat pipes, have been applied in industrial waste heat recovery systems. Figure 1 presents a schematic drawing of a typical loop thermosyphon heat exchanger. Dube et al. (2004) also studied this kind of system previously. Both the evaporator and the condenser are geometrically very similar. They consist of two horizontal headers (upper and lower) connected by several vertical tubes in parallel. The two upper headers (condenser and evaporator) are connected by the vapor tube. The two lower headers are connected by the liquid return line. In the evaporator, during operation, the liquid level must be such that the internal walls remain wet.

The concept shown in Fig. 1 normally employs water as the working fluid. However, for applications at higher temperatures, water is not appropriate and other working fluids are needed. The authors are studying the use of this type of loop-thermosyphon with naphthalene as the working fluid.

The main concern about using naphthalene as the working fluid is related to the solidification in cold parts of the loop, such as the liquid return line. This problem is especially important during start-up, when the system is at room temperature. If the working fluid becomes a solid, it obstructs the liquid return line and the system ceases to operate. To prevent that from happening, external heating must be applied on the liquid return line.

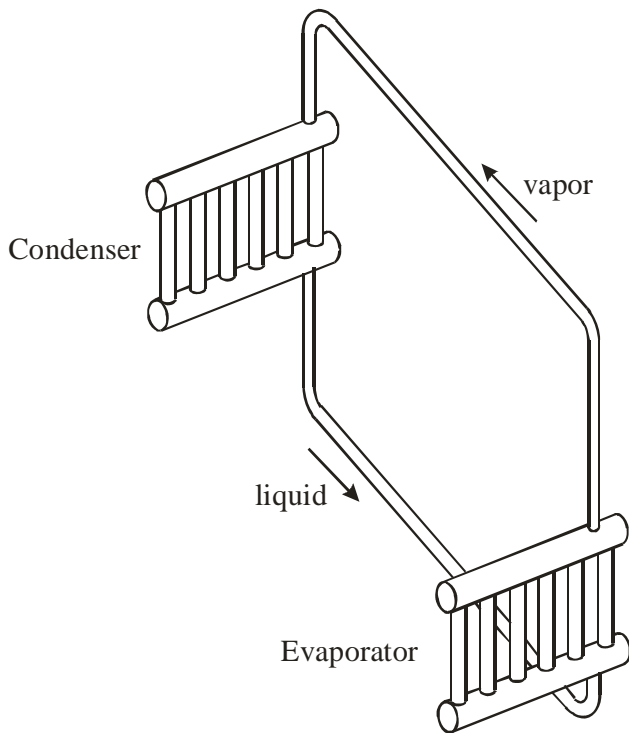


Figure 1. Loop thermosyphon heat exchanger.

External heating is also necessary in case of long vapor lines because of the condensation due to heat losses to the ambient. Even with thermal insulation, the relatively low value of condensation enthalpy of the naphthalene leads to intense condensation inside the vapor tube, which may obstruct the vapor flow. Therefore, an auxiliary heating is necessary to minimize or neutralize the heat loss from the vapor tube.

2. EXPERIMENTAL STUDY

In order to eliminate the problem of working fluid solidification in the liquid return line, a new layout was chosen for this experimental study. The liquid return line is inserted in the vapor tube, i.e., there are two concentric pipes. The liquid returns in the smaller pipe, while vapor flows in the annular duct between the two pipes. Figure 2 presents a drawing of the prototype. The liquid return line is surrounded by the saturated or slightly superheated vapor flowing in the annular channel. As a result, instead of heating both the liquid and the vapor lines, only the vapor line (external tube) is heated externally.

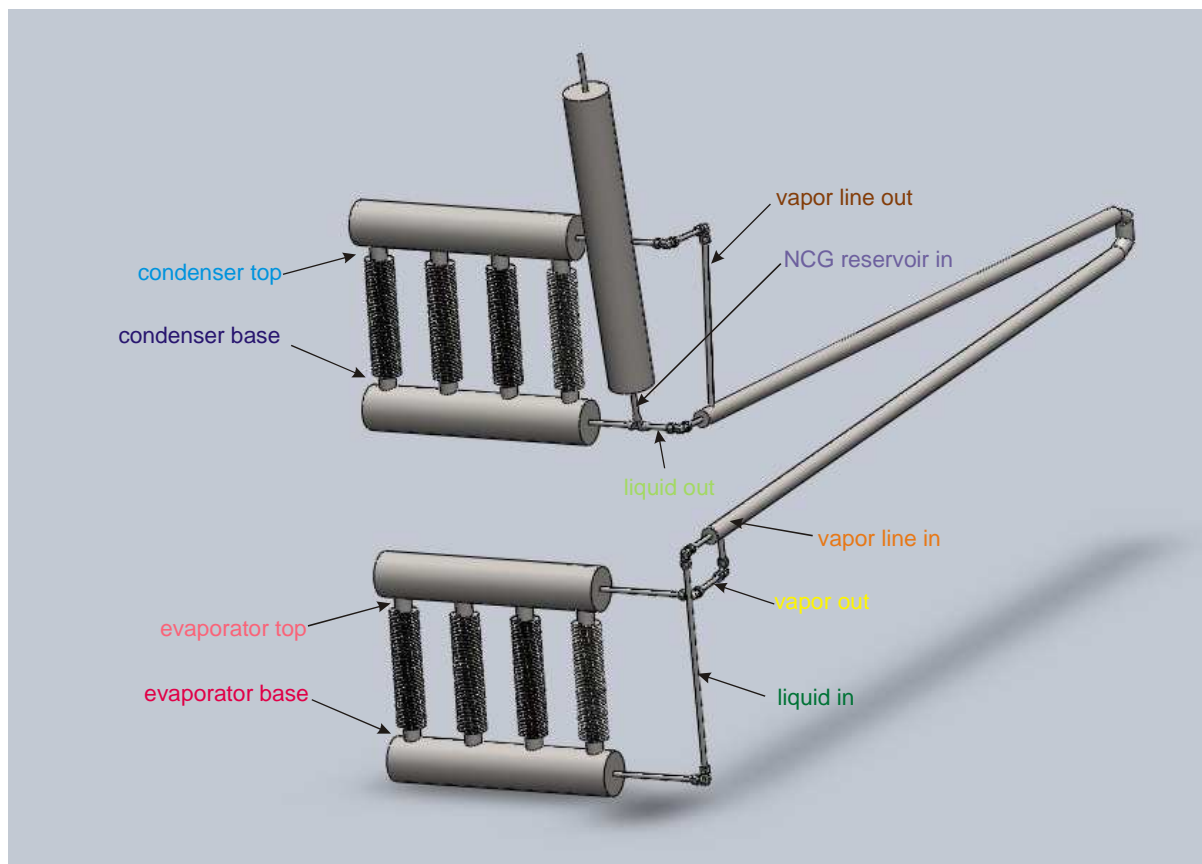


Figure 2. Two-phase loop thermosyphon under study.

2.1 Experimental Set-up

A naphthalene-stainless steel two-phase loop thermosyphon prototype, as shown in the drawing of Fig. 2, was built and tested. Both the condenser and the evaporator consist of four finned 1 ¼" ASTM A106 vertical tubes. The finned tubes are 300 mm long. The four headers are standard 4" ASTM A106 with a length of 700 mm. The liquid return pipe is made of stainless steel with 10 mm i.d. and 12 mm o.d. and the vapor pipe is also made of stainless steel with 38 mm i.d. and 42 mm o.d. The length of both the liquid and the vapor return line is 5.8 m. The device was designed to transfer 4 kW of heat.

The prototype was tested in an air-air heat exchanger test rig. The test rig was built recently at the Heat Pipe Laboratory (LABTUCAL) of Federal University of Santa Catarina-Brazil. It can be used to test two-phase thermosyphon heat exchangers. The rig consists of two gas ducts, one with hot exhaust gases from a 60 kW gas burner and one with ambient air.

In the test section, the flows are countercurrent, with the hot gas stream in the bottom and the ambient air stream at the top. Both the hot gases and the ambient air flow through a rectangular 300 x 700mm cross section duct. The evaporator finned tubes are inserted in the hot exhaust stream, while the condenser tubes are inserted in the air stream.

As the test rig was designed for standard vertical two-phase thermosyphon heat exchangers, the condenser and the evaporator have to be aligned, one on the top of the other. The vertical distance between the top of the evaporator and the bottom of the condenser is only 300 mm. However, in real loop thermosyphon heat exchanger applications, the evaporator and the condenser could be several meters apart from each other. In the present work, the prototype was designed and built so the liquid and vapor lines are 5.8 m long. They have a "U" shape in order to fit between the evaporator and the condenser. That corresponds to a thermosyphon with a horizontal distance of 5.8 m between evaporator and condenser.

The prototype has also a non-condensable gas reservoir coupled to the liquid return line, right after the condenser lower header (see Fig.2). The reservoir is 800 mm long and has an internal diameter of 102.2 mm. As the thermosyphon was

not evacuated prior to charging with the working fluid, the objective of the reservoir is to accommodate the air present in the system during operation. The reservoir was designed based on the procedure also used by Dube et al. (2004). These authors also showed that the exit of the condenser lower header is the best place for the non-condensable gas reservoir in this type of loop thermosyphons. This procedure was also employed successfully by the present authors in other experimental studies, such as Milanez and Mantelli (2010).

As mentioned, heating is provided to the external wall of the vapor pipe. The heating is obtained by wrapping a flexible belt shaped electric heater from Omega® around the tube. The electrical heater is connected to a DC source and the power supply was regulated so it compensates the external thermal losses to the ambient, estimated between 800 and 1000 W, depending on the operation temperature level. The prototype was instrumented with 21 K type thermocouples placed as shown by the arrows of Fig. 2. The temperature of the hot gas and the air streams were measured with RTD probes.

The main objective of this experimental study is to assess whether a naphthalene loop thermosyphon could operate properly. The thermosyphon total thermal resistance was measured, and the importance of the external heating for the vapor line was also analyzed.

3. RESULTS

Figure 3 presents the temperature readings as a function of time during the test. In this test, the system was operating properly with the help of the auxiliary heating to the vapor lines. The black line is the temperature of the hot gas stream reaching the evaporator. The red, yellow, orange and blue lines correspond to the thermocouples attached to the loop thermosyphon, according to Fig. 2.

The red lines correspond to the evaporator, the yellow/orange/brown lines correspond to the vapor tube, the blue lines correspond to the condenser and the green lines correspond to the liquid return tube. Note that there are several red lines. Three of them are close to each other, below the black line. These three light red lines correspond to the thermocouples placed on the condenser top (see Fig. 2). Initially, four thermocouples were attached to the four evaporator tubes, but one of them did

not work after the assembly was completed. There are also four dark red lines, placed below the three light red. These four dark red lines correspond to the condenser base (see Fig. 2). As one can see, there is a considerable difference of temperature between the base and the top of the condenser, (50 to 100°C), which shows that the evaporation resistance is relatively large.

It is important to mention that these thermocouples do not face the hot gas stream. Only the finned portions of the evaporator pipes are subjected to the hot gas stream. The thermocouples are actually attached to a small (20 mm) smooth portion of the pipes below and above the finned length, as pointed by the arrows of Fig. 2. Also, these small portions where the thermocouples are attached are thermally insulated from the environment. The upper and lower headers are also insulated from thermal losses to the ambient. Therefore, the temperature readings of the evaporator thermocouples are more closely related to the working fluid temperature inside the pipes than the hot gas stream. The same is valid for the thermocouples of the condenser.

It can be also observed from Fig. 3 that the orange/brown lines are very close together and also close to the dark red lines of the condenser base. One can conclude that this is the temperature of the saturated vapor inside to thermosyphon. As the naphthalene evaporates at the bottom and flow upwards, it gets superheated (condenser top, light red lines) and flows out of the evaporator still slightly superheated (yellow line). Then it comes back to saturation as it enters in the annular vapor line and flow out of it (orange/brown). The vapor temperature suffers another temperature drop from the vapor line (brown) to the condenser (blue), indicating a relatively large condensation resistance. Note that the condenser is approximately isothermal as the four light blue lines, which correspond to the condenser top and the dark blue lines (condenser base) are close to each other.

The liquid coming out of the condenser (light green) is at the same temperature as the condenser. The liquid then is heated up to the saturation temperature because the liquid return pipe flows inside the annular vapor duct (orange/brown). As one can see, the dark green line (liquid into the evaporator) is at the same temperature of the saturated vapor.

During the test of Fig. 3, the temperature of the hot gas stream (black line) varies with time. Initially, when $5.0 < \text{time} < 5.4$ h, the temperature of the hot gas stream is approximately 370°C. After time=5.4 the temperature was lowered to a set point of approximately 335°C and then, after time=7.4 h, raised to 450°C. During this time interval, the loop thermosyphon was operating properly, with a total thermal resistance ranging from a minimum of 2×10^{-2} to a maximum of 6×10^{-2} K/W. The heat transfer rate ranged from 4 to 1.8 kW, respectively. The total thermal resistance of the thermosyphon is defined here as the difference between the temperatures of the evaporator and the condenser divided by the heat transfer rate through the thermosyphon. The auxiliary heat of the vapor line, ranging between 800 and 1000 W, is not taken into account for calculation of the thermal resistance because the auxiliary power works as a guard heater, i.e., it neutralizes the heat loss to the environment through the vapor tube thermal insulation.

The importance of the auxiliary heating of the vapor lines can be easily visualized in Fig. 4. It presents the test result when the auxiliary heating was turned off (time=3.5h). As one can see the yellow/orange/brown lines start to drop one after the other as time passes. Also, the green lines, i.e., the liquid return line, drop below the evaporator base temperature, which is, as already mentioned, believed to be the saturated vapor temperature. As a consequence, the condenser temperatures (blue lines) start to drop. The auxiliary heating was turned on again at time=4 h. As one can see, after that time, the temperatures of the vapor tube (yellow/orange/brown) start to increase again and, finally, after time=4.5 h, the blue lines of the condenser start to increase too. At this point, the thermosyphon was back to normal operation. That shows that the thermal losses to the ambient need to be eliminated in order for the thermosyphon to operate properly. It is convenient to mention that the time scale of Fig. 4 is the same as of Fig. 3, i.e., the test when the auxiliary heating was turned off (Fig. 4) actually took place before the test when the auxiliary heating was on (Fig. 3).

4. CONCLUSIONS

A stainless steel loop thermosyphon was designed, built and tested with naphthalene as the working fluid. In the lay-out tested here, the liquid return line is placed inside the vapor line so the

condensate does not become solid due to thermal losses to the ambient.

The evaporator and the condenser consist basically of vertical finned pipes that are immersed in gas streams at different temperatures. The temperature of the hot gas stream flowing around the evaporator tubes ranged between 335 and 450°C during the tests, while the thermal resistance of the thermosyphon ranged from 1.9×10^{-2} to 5.7×10^{-2} m²K/W, respectively.

The results of the experiments showed that the naphthalene loop thermosyphon works well if the thermal losses of the vapor line that connects the evaporator to the condenser are eliminated. However, as there is no perfect thermal insulator, the only way to accomplish that is by using auxiliary heating to the vapor lines. Without an auxiliary heating, like a guard heater, pure saturated vapor does not reach the condenser, and the system ceases operation.

ACKNOWLEDGEMENT

The author would like to acknowledge the support of PETROBRAS, the Brazilian Petroleum Company, for their financial support during the development of this work.

REFERENCES

Dube, V., Akbarzadeh, A., and Andrews, J. (2004), *The effects of non-condensable gases on the performance of loop thermosyphon heat exchangers*, Appl. Therm. Eng., vol. **24**, pp. 2439–2451.

Milanez, F.H. and Mantelli, M.B.H. (2010), *Heat Transfer Limit Due to Pressure Drop of a Two-Phase Loop Thermosyphon*, Heat Pipe Science and Technology, An International Journal, Vol. 1 (3), pp. 237-250.

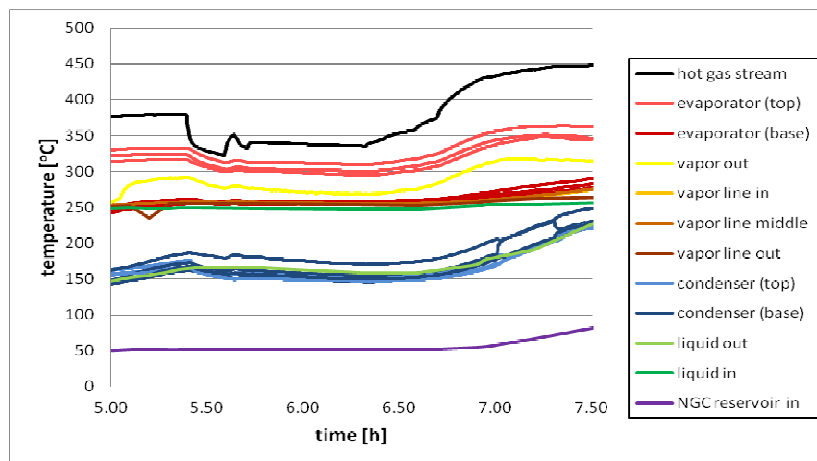


Figure 3. Test results: normal operation, auxiliary heating turned on.

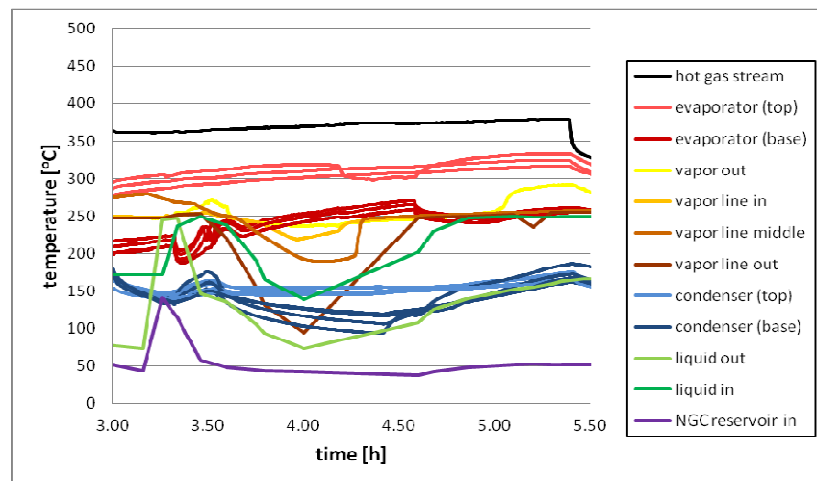


Figure 4. Test results: auxiliary heating tuned off.

COOLING DEVICE USING THE NATURAL CONVECTION, PHASE CHANGE OF SUBSTANCE AND CAPILLARY EFFECT PHENOMENON

Patrik Nemec, Alexander Čaja

University of Žilina, Faculty of Mechanical Engineering, Department of Power Engineering
Univerzitná 1, 01026, Žilina, Slovakia

Phone: +421415132865, Fax: +421415252541, E-mail: patrik.nemec@fstroj.uniza.sk, Phone:
+421415132863, Fax: +421415252541, E-mail: alexander.caja@fstroj.uniza.sk

Milan Malcho

University of Žilina, Faculty of Mechanical Engineering, Department of Power Engineering
Univerzitná 1, 01026, Žilina, Slovakia

Phone: +421415132851, Fax: +421415252541, E-mail: milan.malcho@fstroj.uniza.sk

ABSTRACT

The manuscript deal about testing of device with heat pipes and about research alternative possible applications of heat pipes and potential improvements in purpose effective heat sink from power switches of device. The device constitutes cooler with heat pipes and energy converter, which consisted from power switches IGBT. The main function of the energy converter is change parameters of electric current and voltage and simultaneously during the operation produce extreme heat. Therefore the heat produced by energy converter must be transferred into surroundings, in order to the power switches was not damaged and function of device was continuous. This device is used in various static and moveable applications. Testing device is part of control unit in rail vehicle. The amount of heat produced by power switches depend from working conditions of static converter. Great impact on heat sink has, how as season also this if the vehicle is moving or don't moving. If the vehicle is moving the heat transfer form energy converter to surrounding is caused by forced convection of air flow around device. But the critical conditions occur if the vehicle doesn't move, because the application of this cooling device is based on natural convection. The study deal solution of the problem heat transfer from energy converter to surrounding by natural convection.

KEY WORDS: Heat Pipe, Heat Transfer, Cooling Device

1. INTRODUCTION

Capillary-driven two-phase systems offer significant advantages over traditional single phase systems and heat transfer systems by and thermal conductivity. With the typically increased thermal capacity associated with the phase change of a working fluid, considerably smaller mass flow rates are required to transport equivalent amounts than in other heat transfer systems for a given temperature range. Moreover, heat transfer coefficients of two-phase systems are much greater than others systems and result in enhanced heat transfer. Lower mass flow rates and enhanced thermal characteristics provide the benefits of smaller system size (and weight) while providing increased performance. The thermal capacity of a single-phase system depends on the temperature change of the working fluid; thus, a large temperature gradient or a high mass flow rate is required to transfer a large amount of heat.

However, a two-phase system can provide essentially isothermal operation regardless of variations in the heat load. Additionally, single phase systems require the use of mechanical pumps and fans to circulate the working fluid, while capillary-driven two-phase systems have no external power requirements, which make such systems more reliable and free of vibration. Heat pipes are passive devices that transport heat from a heat source (evaporator) to a heat sink (condenser) over relatively long distances via the latent heat of vaporization of a working fluid (Ochterbeck, 2003). The concept of the heat pipe was first presented by (Gaugler, 1944) and (Trefethen, 1962), but was not widely publicized until an independent development by (Grover, 1964) at the Los Alamos Scientific Laboratories. From the time of heat pipe patent and with this join using the latent heat of substance to heat transfer by phase change in hermetic closed vacuum system, is whereby further more applications in

praxis, which use two phase systems to heat transfer. And whereby further more industrial branch try compose the heat pipe into its heat transfer process or operation of thermal devices in order to cooling or temperature stabilization. The most widespread branch of heat pipe applications is still electrical engineering, where the heat pipes are used to cooling power switches. This situation make researcher in the area of heat pipe research and development do test of various kinds and type configurations heat pipes for these applications. It is expected that heat flux levels in excess of 100 W/cm^2 for commercial electronics will soon become a realistic and immediate challenge to overcome. There is also growing demand for more sophisticated and capable electronics used in harsh environment applications such as those found in defence, automotive and oil exploration systems. Thermal management of harsh environment electronics is vital to the successful design, manufacture, and tactical operation of a variety of electronics systems to meet the high temperature, environmental, reliability, and cost effectiveness requirements (Ohadi, 2005).

2. EXPERIMENT

At first was designed thermostatic chamber to testing of cooling device. The chamber is designed and constructed to simulation surrounding temperature conditions and must have a sufficient capacity for creating conditions for heat transfer by natural convection to simulate the adjustable and continuously stationary temperatures around electronic elements. Construction and measuring in thermostatic chamber describe (Kapjor, 2007).



Figure 1. Thermostatic chamber for testing cooling by natural convection

The cooling device consists from energy converter and cooler. The cooler was constructed from six gravitational heat pipes filled with ethanol. Their evaporation section is embedded into the aluminium block of the energy converter. On the condensation section of the heat pipes are vertically to the axis aluminium ribs. The energy

converter consist from electronic components, which are plug-in the electrical source and heat flux produced by electronic components is transported by heat pipes to the ribbing section. Head point testing of cooling device in thermostatic chamber is monitoring temperature course on the aluminium block of energy converter, heat pipes and multi ribbed cooler at temperature condition $30 \text{ }^\circ\text{C}$ and various positions of device.



Figure 2. Cooler with heat pipes

As an alternative application for heat transfer improvement of cooling device were manufactured and tested on our workplace department various kind of wick heat pipes. There are several types of wick structures: screen, grooves, felt, and sintered powder. Sintered powder metal wicks offer several advantages over other wick structures. An emerging advantage of the sintered powder wick is its ability to handle high heat fluxes with usually low thermal resistance. Since sintered powder wicks are generally more than 50% porous, there is, accordingly, a large surface area for evaporation. Another advantage of a heat pipe with a sintered powder wick is that it can work in any orientation, that including against gravity. For this experiment were made wick heat pipes with sintered, mesh screen and grooved capillary structures (Vasiliev, 2008).



Figure 3. Capillary structures of wick heat pipes

Wick heat pipes with sintered capillary structure were made from copper powders granularity of 100 μ m, 63 μ m and 50 μ m sintering the copper powder in inner wall of the copper pipe. Capillary structure of heat pipes from copper powder was sintered in the high thermal electric oven used in powder metallurgy. By this method was created a 1.5 mm thick coat of sintered capillary structure. Mesh screen capillary structure is one from the most applied structures in heat pipe. For manufacture of heat pipes were used a finely mesh screens from stainless steel with mesh 50, 100 and 200. The rolled piece of screen was inserted in to the pipe, thus rolled screen by acting expansive forces were stable placed in inner surface of pipe. In the grooved heat pipe are along the inner surface of the pipe engraved grooves about depth 0,3 mm, width 0,2 mm and pitch 0,5 mm. The overall length of the heat pipes is 0,5 m. The choices of the capillary system for the wick heat pipes depend from many factors and some of these factors are related to the properties of the working fluid. The working fluid must have good thermal stability in relation to the specific working temperature and pressure. The most important requirements which the working fluid must have are the following: compatibility with the capillary system and with the material of the pipe, high thermal stability, high state of heat, high thermal conductivity, low viscosity of the liquid and vapour phase, high surface tension, acceptable freezing point (Lenhard, 2010). Therefore was as a working fluid in heat pipes chosen water, acetone and ethanol.

3. MEASUREMENT OF THE COOLING DEVICE AND RESULTS

On figures 4, 5 and 6 are graphic results from measurement of cooling device with gravitational heat pipes at various positions. Researching positions of the cooling device were at tilt angle 0°, 10° and 20°. During measuring was recorded temperature course of heat pipes surface, screw connection of the electrical component with aluminium block of the device, surrounding air in thermostatic chamber, circulate fluid on the input and output. The temperature was measured by thermocouples connected to individual parts of the device and fluid mass flow by flowmeter. To determine electrical performance of electrical source and total performance of the cooling device was measured electric current and voltage of the heat source and input and output temperature and mass flow of the circulate fluid in thermostatic

chamber. This all data from measuring enter into measuring centre and next was converted by software AMR to PC. The measurement settings of the cooling device was the same in all the three positions, input heat flux 450 W and surrounding air temperature in thermostatic chamber 30 °C. In all the three position was the highest temperature measured on the aluminium block of the device. At vertical position was the highest temperature measured 141,2 °C, at second position at the inclination 10 ° from vertical position was the highest measured temperature 135,8 °C and at third position at inclination 20 ° from vertical position was the highest measured temperature 133,4 °C. Temperature drop in the same point between vertical position of the cooling device and position at inclination 20 ° from vertical position is approximately 8 °C.

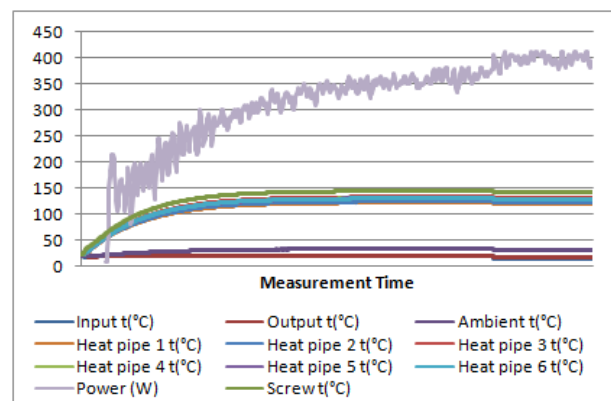


Figure 4. Graphic results from the measurement of the cooling device at outside temperature 30 °C and a tilt angle 0°

Result of the testing is that, the increasing of the tilt angle of the cooler device is possible to increase its ability to heat transfer but only up to a certain point. After exceed the critical point heat transfer ability of the cooler device start decrease.

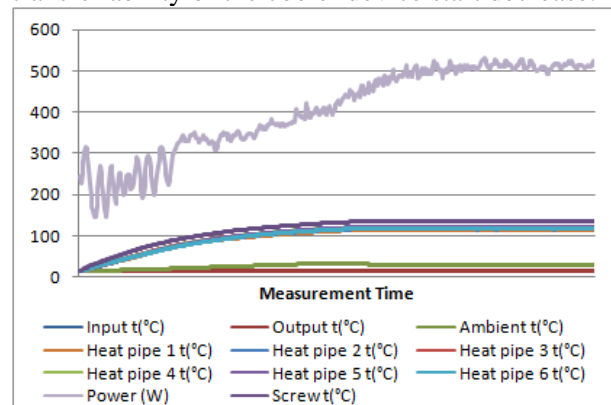


Figure 5. Graphic results from the measurement of the cooling device at outside temperature 30 °C and a tilt angle 10°

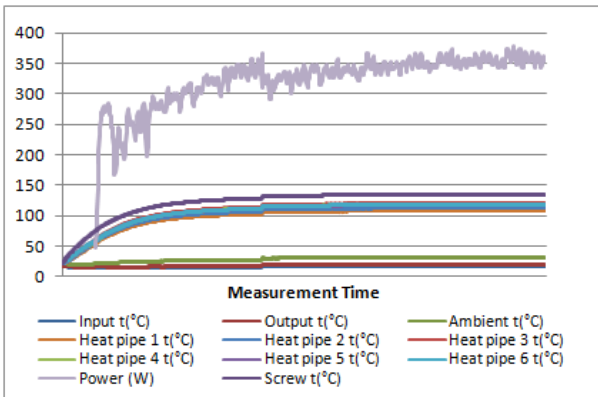


Figure 6. Graphic results from the measurement of the cooling device at outside temperature 30 °C and a tilt angle 20°

Therefore if the cooler is tilted the ribs are tilted in a certain angle from the vertical level too and in that way the heat transfer by natural convection increase too. Increase the tilt angle is possible only up to the point when the condensate in heat pipes is still able return from condensation section to the evaporation section. At a higher tilt angle position of the ribbed cooler is cooled more intensively by natural convection but the return of the condensate to the evaporator section fail and that is reason why its overall ability of the heat transfer decreases. Option how to improve heat transfer by natural convection to the surrounding is application of the wick heat pipe because the wick heat pipe is able operate at tilt angle 45° position without any problems. This claim confirms study about influence working position of wick heat pipe on their performance.

4. WICK HEAT PIPE TESTING

Research of heat pipes ability work at tilt angle position was relate of wick heat pipe mentioned in section 2. One from many methods how to determine performance of heat pipe is calorimetric method emanating from calorimetric equation, where known mass flow, specific heat capacity, input and output temperature of coolant. Total heat power of heat pipe determine from difference between input and output temperature of circumfluent coolant. For the experimental measurement was proposed measuring unit, which consist from measuring apparatus (thermostat, measuring centre, ultrasonic flowmeter, auto-transformer) necessary to measuring thermal performance of heat pipe. The same measurement method use and describe (Nosek, 2009).

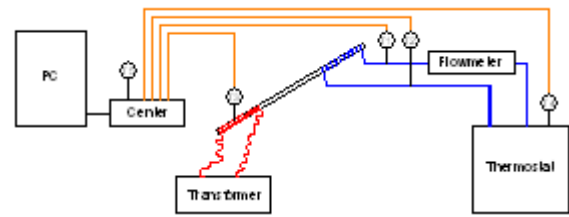


Figure 7. Scheme of measuring unit for measurement of heat pipe performance

Measurement of thermal performance of heat pipe was at vertical position and tilt angel 45° and the temperature of the heat source was 50 °C and 70 °C. On figure 7 are shown dependencies thermal performance of sintered wick heat pipes from position. You can seen, that the performance values of heat pipes at tilt angel are a little bit less than performance value heat pipes at vertical position.

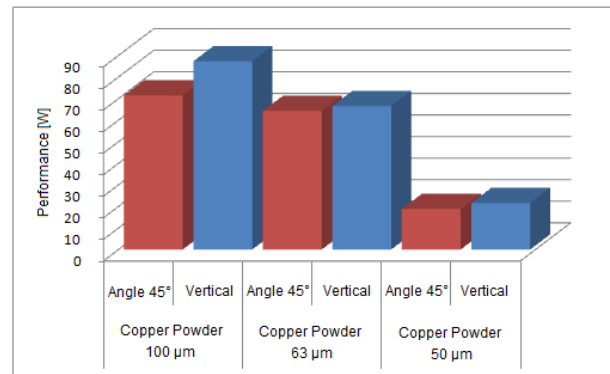


Figure 8. Dependencies of sintered wick heat pipes thermal performance from position

On the figurers 8 and 9 are shown from right to the left test results of all wick heat pipes with sintered, mesh screen and grooved wick structure. In graphs is declared percentage performance of wick heat pipe at tilt angle 45° from vertical position and it is seen, that the operate performance all from 18 various kinds of wick heat pipes were more than 80%. Except for a few kinds tested at heat source temperature 50°. In this case was operate performance only 50 % performance, what could be caused defect in manufacture.

5. CONCLUSIONS

Ideal working position of heat pipe is vertical position and heat pipe operate on maximum performance and is able transfer maximum heat flux in this position. This experiment has testify

that the wick heat pipe is able operate at any other position for example at tilt angle 45° position. Test results clearly declare that the wick heat pipes are able operate at tilt angle 45° position and operate performance is more than 80% in this position. This phenomenon is caused by capillary action in capillary structure of heat pipe. Capillary effect caused return of substance condensate from condensation section to evaporation section of heat pipe. Substitution of wick heat pipes instead of gravitation heat pipes and tilt of cooling device will be occur better heat transfer by natural convection from ribbed cooler to the surrounding and heat transfer from source by wick heat pipes will be approximately the same.

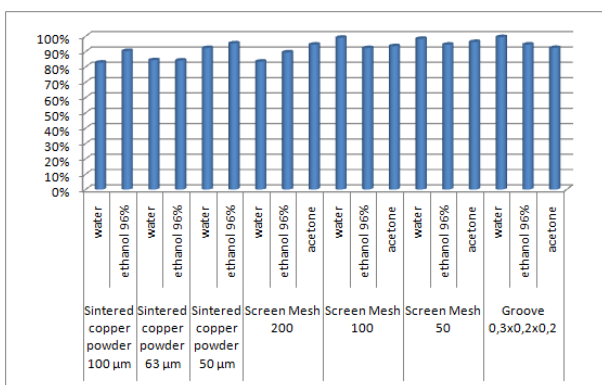


Figure 9. Percentage performance of wick heat pipes measured at tilt angle 45° and heat source 70 °C.

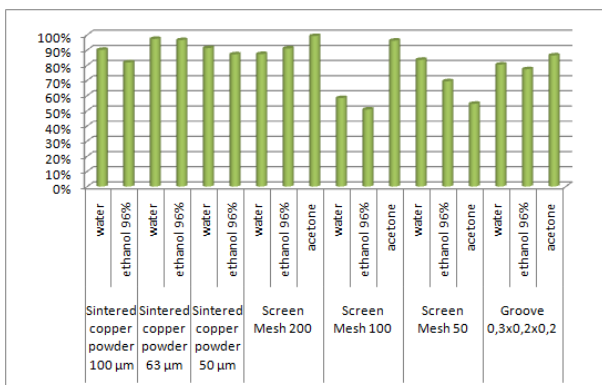


Figure 10. Percentage performance of wick heat pipes measured at tilt angle 45° and heat source 50 °C.

ACKNOWLEDGEMENT

This article was created within the frame of project APVV – 0577 – 10

REFERENCES

- Gaugler, R. S. (1944) *Heat transfer devices, U.S. patent 2,350,348.*
- Grover, G. M., Cotter, T.P. Erikson, G.F. (1964) *Structures of very high thermal conductivity, J. Appl. Phys.*
- Kapjor, A., Lenhard, R., Horváth, Z. (2007) *Power dependence of floor convector on its geometry, Proc. TRANSCOM 2007, 7-th European conference of young research and science workers, Žilina, ISBN 978-80-8070-696-8. - S. 101-104.*
- Lenhard, R. (2010) *Numerical simulation device for the transport of geothermal heat with forced circulation of media, Proc. Power control and optimization, Kuching, Malaysia, ISBN 978-983-44483-32.*
- Nosek, R., Jandačka, J., Szlek, A. (2009) *Experimental measurements in fixed bed reactor, Proc. Experimental fluid mechanics 2009, Liberec, Czech Republic, ISBN 978-80-7372-538-9. - S. 247-256.*
- Ochterbeck, Jay M. (2003) *Heat pipes, In Heat Transfer Handbook, 1. Edition.*
- Ohadi, M., Qi, J. (2005) *Thermal Management of Harsh-Environment Electronics, Microscale Heat transfer, Fundamentals and Applications, NATO Science Series, II Mathematics, Physics and Chemistry, Springer, Vol. 193. Pp. 479-498*
- Trefethen, L. (1962) *On the surface tension pumping of liquids or a possible role of the candlewick in space exploration, GE Tech. Int. Ser. No G15-D114, General Electric Co., NY.*
- Vasiliev, L., Rabetsky, M., Kulakov, A., Vasiliev Jr. L., Li, Z. M. (2008) *An Advanced Miniature Copper Heat Pipes Development for Cooling System of Mobile PC Platform, Proc. of 7th Minsk International Seminar Heat Pipes, Heat Pumps, Refrigerators, Power Sources, Minsk, Belarus, pp. 336-344.*

ACTIVE CONTROL OF THE SET POINT OF A 2-WAY PRESSURE REGULATING VALVE IN A LHP

F. Romera, D. Mishkinis, A. Kulakov, A. Torres

IberEspacio. S. A.

C/Magallanes, 3; 4th floor; 28015 Madrid - Spain

Phone: +34.91.3098000, Fax: +34.91.4451764, frf@iberespacio.es; dmg@iberespacio.es

ABSTRACT

The operation temperature of a LHP with a pressure regulating valve is passively controlled by the argon back pressure of the valve (set point of the valve). Once the valve is charged and sealed with argon, the set point will not change without some kind of active control. This is valid for 3-way (Bypass Line LHP - BLLHP) or 2-way valve configurations (Vapour Modulated LHP - VMLHP).

In this paper it is presented an active control method tested in a LHP provided with a 2-way pressure regulating valve (VMLHP). The control is based on the argon pressure variation caused by an argon temperature variation produced by a dedicated heater or Peltier element attached to the valve body. In this way, the possibility to increase (heating) or decrease (cooling) the set point (argon pressure) can be available.

First, a general explanation of the working principles of a 2-way valve VMLHP is presented and compared to the 3-way BLLHP. Then, some theoretical descriptions are provided for the set point shift versus argon pressure and the required argon temperature and dedicated heater power.

A VMLHP including a heater and a Peltier element is tested in vacuum and in climatic chamber. Nominal valve set point can range from 20 to 30°C. The results show that with very few heater power (less than 1 W), the set point can be modified up to 5°C without exceeding hardware temperature limitations. A ratio of about 1°C set point increase per 10°C argon temperature increase is obtained.

A possible application of this active control is to counterbalance the heat fluxes which can reach the argon from a hot/cold environment or from a superheated vapour of the working fluid. This is very important when high control precision is required to the thermal control system.

KEY WORDS: Pressure regulating valve, Active control, Loop heat pipe

1. INTRODUCTION

A variable conductance LHP with a pressure regulating valve (PRV) is able to passively regulate the working temperature of the evaporator. This regulation is quite accurate: a few degrees for the complete power range and sink thermal conditions. For the majority of the applications this passive regulation is precise enough (Mishkinis, 2011). However, there are some applications which may require a narrower temperature regulation. For that purpose, an active control can be introduced onto the PRV. It consists on the active heating or cooling of the valve argon reservoir. With very few power, the set point can be increased (heating) or decreased (cooling) in

some degrees, providing a more precise temperature control.

2. PRESSURE REGULATING VALVE

2.1. PRV General Working Principles

Principal scheme of the PRV is given in Figure 1. This valve can be used as a 2-way or 3-way valve configuration, depending whether the bypass outlet is closed or connected to the compensation chamber (or liquid line), respectively. The bellows separates the back pressure reservoir from the working fluid. Further in the paper Variable conductance LHP with 3-way PRV is called Bypass Line LHP (BLLHP) and LHP with 2-way PRV is named as Vapour

Modulated LHP (VMLHP) by analogy with Variable conductance Heat Pipes with PRV (Vapour Modulated Heat Pipe - VMHP) proposed in seventies by Marcus et al. (1973).

The valve piston is subjected to the back pressure, the working fluid pressure and the bellows force.

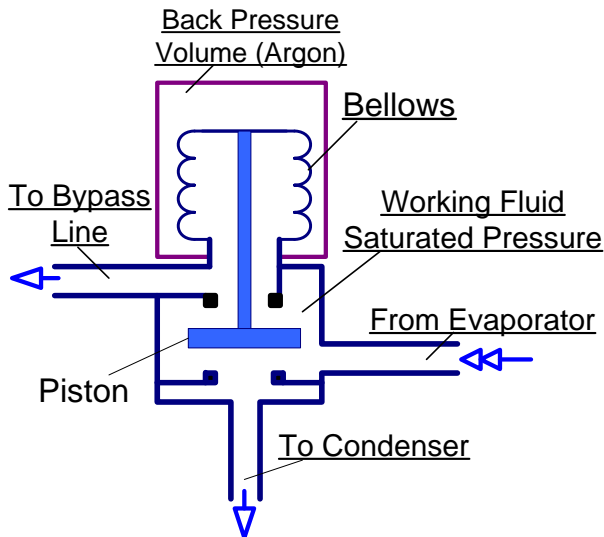


Figure 1. PRV Scheme

Once the valve is charged with the back pressure, if there is a small working fluid pressure coming from the evaporator inlet, the valve piston is pressed in the bottom position (in accordance with Figure 1), closing the condenser path. For increasing working fluid pressure, the piston keeps this position until a first characteristic pressure is reached (called set point pressure) for which the piston starts to take off from the seat (see Figure 2). This set point pressure is a function of the back pressure and the bellows preload.

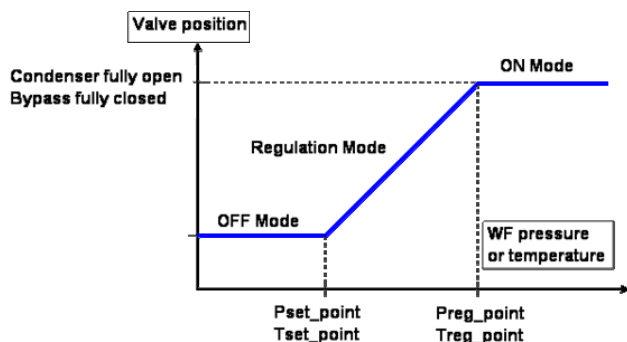


Figure 2. Valve Operation Modes

For further pressure increase, the piston runs the distance between the bottom and the top seat. This situation is kept until the piston reaches the upper seat for another characteristic pressure known as

regulation point pressure. This second pressure is a function of the back pressure, the bellows preload and the valve stroke. For increasing working fluid pressure, the piston keeps in this position.

The pressures mentioned for Figure 2 translate into temperatures in accordance with the saturation line of the working fluid (Figure 2). These temperatures are the LHP evaporator saturation temperatures. The evaporator saturation temperature cannot usually be measured. The nearest saturated temperature that can be referenced is the reservoir one.

The same pressure difference translates in different temperature differences in accordance with the valve set point established and the related dP/dT derivative of the saturation line. For low set points, the derivative is small and the temperature difference is more important than for high set points.

For temperatures between set and regulation points the flow is split between the condenser and the bypass line (BLLHP) or an important pressure drop is introduced in the vapour line (VMLHP). This regime is called regulation mode. For temperatures above the regulation point, the LHP behaves as a regular LHP without valve and this regime is called ON mode.

For a given regular LHP (without valve), the evaporator operating temperature is determined mainly by the input thermal power and the sink temperature. A valve introduced in this LHP has the ability to increase this operating temperature as long as the regulation point is set above it. This effect is obtained because the “conductance degradation” provided by PRV.

2.2. Comparison VMLHP vs BLLHP

In the case of a BLLHP, the conductance degradation is obtained by the bypassed hot vapour injected in the reservoir or liquid line. More subcooling is required to counterbalance this heat injection in the compensation chamber. For power and pressure drop conservation considerations (Romera, 2010), the operating temperature is obtained near the regulation point (Figure 2).

For a VMLHP configuration, the degradation is provided by the additional pressure drop introduced in the vapour line. This pressure drop makes the primary wick to provide more capillary pressure and therefore to work under a higher temperature gradient. Under this circumstance the back

conduction is increased (Mishkinis, 2011). For high power (high working fluid mass flow) and/or low sink conditions, the required pressure drop to reach the necessary back conduction may exceed the pumping capability of the wick. In this condition, the wick provides the maximum pumping capability and the evaporation front in the wick progress toward the evaporator core. This produces a higher heat leakage through the wick even if the gradient between the evaporator and reservoir temperatures is not very important. This is distinguishing difference in operation between VMLHP and VMHP. VMLHP continue to operate when VMHP has dry out in similar conditions due to capillary limit. VMLHP is robust self-regulated system with variable back heat leak into LHP compensation chamber.

On the other hand, the PRV is only able to introduce a high pressure drop when the piston is in the position near the set point (condenser passage section almost choked) and this is therefore the operating temperature (set point, Figures 1&2) for VMLHP configuration.

Apart from this difference, which can be offset with proper argon charging, there are other important differences.

For a BLLHP configuration, a small leakage through the bypass can prevent the start-up event because it makes difficult to obtain a proper temperature gradient between evaporator and reservoir. Besides, this configuration can promote temperature oscillations under gravity due to a coupling phenomenon between the bypass line pressure drop (introduced by the PRV) and sudden liquid column static pressure variations in the condenser (variation of the condensation front position) (Romera, 2010).

In a VMLHP layout, start-up is easier, mainly if it is triggered from an evaporator temperature below the valve set point (condenser closed). What is more, there are not temperature oscillations due to gravity effects.

Detailed analysis and experimental investigation of VMLHP and BLLHP operation were performed by Torres at al. (2012).

2.3. PRV Set point migration

For the PRV operation description it has been assumed that the back pressure is constant. It

means that the argon temperature is constant. But in reality, the argon temperature can vary due to ambient and working fluid temperature changes.

However, the argon is not in saturated state and its pressure evolution with temperature is not as important as for a saturated fluid. The evolution is almost linear (see Figure 3 for two extreme set point values for ammonia LHP).

It can be seen that high temperature variations are needed to get moderate pressure excursions, especially for low valve set points.

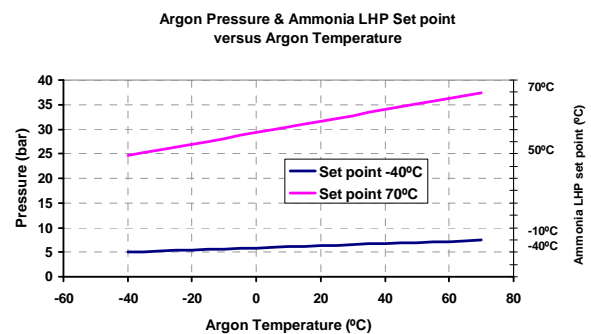


Figure 3. Argon Back Pressure vs Temperature

The argon pressure variations shown in Figure 3 translate directly in set point migration in accordance with the saturation line of the related working fluid, as shown in right vertical axis for ammonia.

3. PRV SET POINT ACTIVE CONTROL

This back pressure evolution with the argon temperature can be of interest in case an active control of the set point is desirable. It is the case of applications requiring a very precise temperature regulation, for which, even the small set point drifts caused by environmental thermal influence is wanted to be counterbalanced.

It is important to remark that the precise temperature control is not usually required for the PRV set point itself but to the saddle temperature. Between these two temperatures there is a gradient which depends on the thermal coupling between the saddle and the evaporator saturation temperature, and the power being transferred by the LHP. The active control discussed here can also be applied to correct this gradient and make the saddle temperature to be really independent of the LHP power level and sink conditions.

The active control presented in this paper doesn't refer to the one used when a two phase fluids is used to provide the PRV back pressure (Goncharov, 2005). This kind of control is intended to provide large variations of the set point, requiring moderate control power and continuous application of power to PRV. In our case, small and precise set point variations can be obtained with relatively small power.

A VMLHP including a heater and a Peltier element is tested in vacuum and in climatic chamber. This VMLHP has been developed for the temperature control of a spacecraft communication system. Hot and cold sink conditions are investigated. Main LHP characteristics are the following:

- Evaporator: 140 mm; ϕ 15 mm
- Compensation chamber: 60 mm, ϕ 30 mm
- Titanium sintered wick: \sim 2.8 μ m pore size, \sim 50% porosity
- Vapour line: 1.3m, ϕ 3 mm
- Liquid line: 1.0m, ϕ 3 mm
- Condenser: 2.5m, ϕ 3 mm
- Ammonia charging: 27 g
- Valve set point: 25 - 27°C

In Figure 4, the increase of the set point obtained by heating the valve body is shown. It refers to a cold sink case (-60°C) test performed in vacuum chamber. Passive set point is 26°C. Three saddle temperatures (EV1, EV2 and EV3) and the top and bottom compensation chamber temperatures (CC1 and CC2) are shown. Green line power is the VMLHP power and red line power is the power applied to the valve case. There is a set point increase of 1°C per every 0.5 W valve heating. Valve body temperature variation is from 26°C to 36°C for 0.5W, and up to 45°C for 1 W (Table 1).

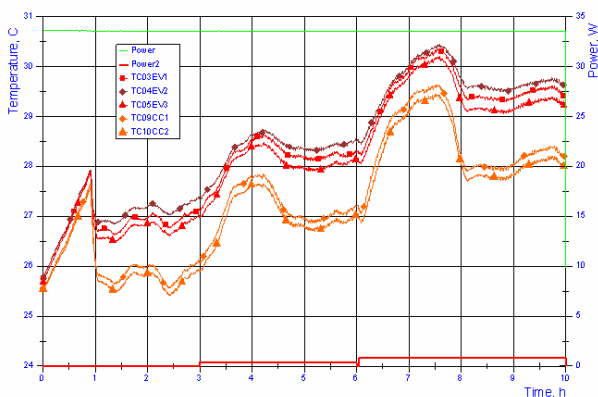


Figure 4. Set point control for cold conditions

Table 1. Active control results (PRV heating).

Control Power(*)	PRV Set Point	PRV Temperature
0 W	26°C	26°C
0.5 W	27°C	36°C
1.0 W	28°C	45°C

(*) 34 W LHP power

In Figure 5, it is presented the same test but performed in a hot sink case (25°C). Similar conclusions can be withdrawn.

It is important to remark that control power is dependant of the power being transported by the VMLHP because the thermal link between the argon reservoir and the circulating working fluid mass flow. Higher the VMLHP power, higher the working fluid mass flow and higher the needed PRV heating power to reach the same argon temperature level.

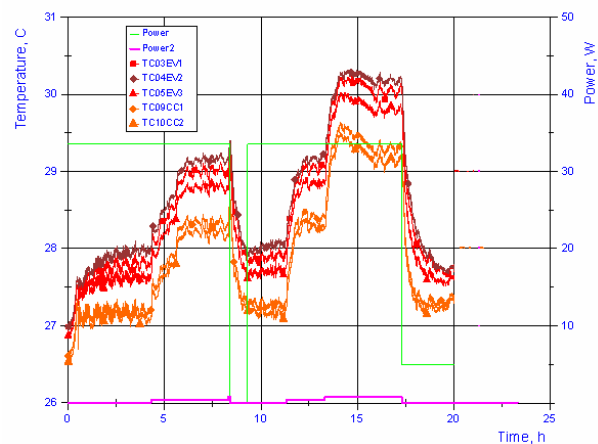


Figure 5. Set point control for hot conditions

Additionally, some tests are performed by using a Peltier element in the valve body. The possibility to decrease the set point by cooling down the valve is verified. This test is performed in climatic chamber. Figure 6 shows the results. In this case, the power removed from the valve can not be easily determined from the power applied to the Peltier element, because it depends of the Peltier efficiency. Besides, the VMLHP power is now higher (100 W). see Table 2.

Table 2. Active control results (PRV cooling).

Power removal(**)	PRV Set Point	PRV Temperature
0 W	26.5°C	26.5°C
\sim 1.5 W	25.5°C	12°C

(**) 100 W LHP power

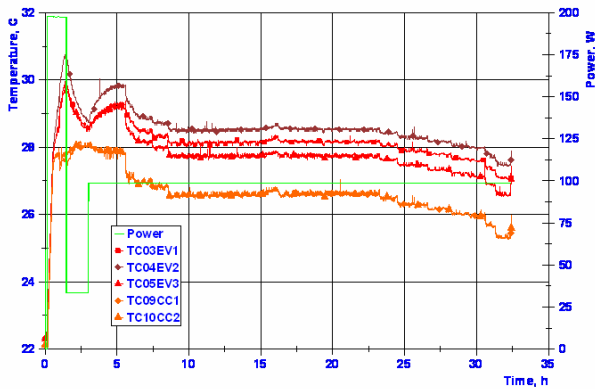


Figure 6. Set point control (decreasing)

4. CONCLUSIONS

Although the passive temperature regulation provided by a Variable Conductance LHP with a pressure regulating valve (PRV) is quite precise, it can be further improved by introducing an active control on the PRV. It consists on the valve body cooling or heating, to modify the temperature of the argon reservoir and hence the back pressure (set point).

A VMLHP provided with a heater and a Peltier element on the PRV has been tested for that purpose. Results show that it is possible to slightly increase or decrease the set point in some degrees using very few control power. For heating, a ratio of 0.5W for every set point degree of variation has been obtained, when the VMLHP power is 34W. It is assumed that this ratio will increase with the VMLHP power but this extent has not been tested. Regarding the valve cooling, such a ratio is more difficult to establish because of the Peltier element efficiency. In all the cases, a ratio of about 10°C valve temperature variation is needed to produce 1°C set point change.

NOMENCLATURE

<i>CC</i>	=	Compensation Chamber
<i>d</i>	=	Derivative
<i>EV</i>	=	Evaporator
<i>LHP</i>	=	Loop Heat Pipe
<i>P</i>	=	Pressure, Pa
<i>PRV</i>	=	Pressure Regulating Valve
<i>T</i>	=	Temperature, °C
<i>TC</i>	=	Thermocouple

REFERENCES

Goncharov, K., Schlitt R., Hildebrand U., *Loop Heat Pipe For High-Precision Satellite Thermal*

Control Int. Two-Phase Thermal Control Technology Workshop, LA, USA March 7th–9th, 2005

Marcus B.D., Edwards D.K., Anderson W.T., *Variable Conductance Heat Pipe Technology*, Research Report No. 4 1973

Mishkinis, D., Kulakov, A., Romera, F., Gregori, C., Torres, A. (2011) *Thermal Control of Loop Heat Pipe with Pressure Regulating Valve*. VIII Minsk International Seminar “Heat Pipes, Heat Pumps, Refrigerators, Power Sources”, Minsk, Belarus, September 12–15, 2011

Mishkinis, D., Gregori, C., Huidobro, D., Torres, A. (2011) *Low Power and Low Temperature LHP for Thermal Control of Rovers*. 41st International Conference on Environmental Systems 17 - 21 July 2011, Portland, Oregon

Romera, F., Mishkinis, D., Kulakov, A., Torres, A. (2010) *Control of LHP operation temperature by a pressure regulating valve*. 15th International Heat Pipe Conference, Clemson, USA, April

Torres, A., Mishkinis, D., Kulakov, A., Romera, F., Gregori, C., Kaya, T. (Published 2012) *Thermal Control of Loop Heat Pipe with Pressure Regulating Valve*. *Heat Pipe Science and Technology*, An International Journal, Volume 1, 2010 / Issue 4, pages 329-357 DOI: 10.1615/HeatPipeScieTech.v1.i4.30.

HYDRODYNAMICS OF A CONFINED MENISCUS IN A CAPILLARY TUBE

Gyana Ranjan Rana, Tushar Sahu, Sameer Khandekar, P. K. Panigrahi

Department of Mechanical Engineering
Indian Institute of Technology Kanpur
Kanpur (UP) 208016 India

Tel: +91-512-259-7038, Fax: +91-512-259-7408, E-mail: samkhan@iitk.ac.in

ABSTRACT

In microchannel fluid flow, liquid-gas interface behavior is vital for developing a wide range of microfluidic devices. In this paper, micro-PIV measurements were used to study the velocity field and its distribution near the moving liquid-air interface in a 1 mm × 1 mm dry square capillary having deionized water as the working fluid. Using high speed camera visualization method, analysis of the high contrast images of the liquid-air meniscus for four different liquids (water, ethanol, glycerin and silicon-oil) has also been discussed at different Capillary numbers. The effect of imposing a velocity on the advancing contact angle has been studied. The respective contour plots and non-dimensional velocity profiles behind the moving water-air interface are shown for two different flow rates of the working fluid. The results demonstrate that very close to the interface the velocity profile is not parabolic in nature but away from the interface it is satisfying the Poiseuille flow condition. The 3-dimensional continuity equation for the micro-PIV data in the plane of observation has been used to analyze the spatial fluid flow distribution inside the fluid flow domain.

KEY WORDS: Square capillary, μ -PIV, Capillary number, Meniscus shape, Interface dynamics

1. INTRODUCTION

Today transport phenomenon inside microscale devices has emerged as an interesting field due to recent progress in micro total analysis system [Juncker et al., 2002], in lab-on-a-chip [Walker and Beebe, 2002], micro fuel cells [Pattekar and Kothare, 2004] and micro-/pulsating heat pipes [Khandekar et al., 2010]. Flow inside microchannel is considered to be the most suitable for heat and mass transfer due to transportation of small volume of fluid having large interfacial area and small diffusion paths. Understanding the hydrodynamics of such flows inside microchannel is helpful for enhancing the performance parameters in applications like high speed coating, dyeing, adhesive printing, flow through porous media (petroleum industry), in cooling of IC chips, in pulsating heat pipes and in chemical and material synthesis. Fundamental understanding of dynamic liquid-air interface behavior is important for developing a wide range of such micro-devices. Though most experimental studies have been carried out using circular capillary tube [Thulasidas et al., 1997], flow inside the square capillary is more complex because of the difficulty in general treatment of motion [Ajaev and Homsy, 2006]. Till now a variety of technique has been

followed to analyze the flow field inside microchannel [Torralba et al., 2005]. One of the most recent is the micro-PIV, which offers a powerful, nearly non-intrusive tool to study the flow field inside microchannel. Most of the experiments have been carried out to study the velocity profiles far from the moving liquid-air interface [Meinhart et al., 1999] or bulk velocity profile inside the liquid slug using micro-PIV [King et al., 2007]. These studies have reported that the liquid velocity profile is parabolic, satisfying the no-slip boundary condition at the wall. However, the flow phenomenon close to the liquid-air interface has not been clear due to its complexity and three-dimensional nature.

Meinhart et al. (1999) have presented the ensemble averaged velocity measurement in a 30 μm x 300 μm rectangular microchannel. Measurements were obtained using low spatial resolution away from the wall and a higher spatial resolution close to the wall. Lima et al. (2007) also obtained nearly parabolic velocity profiles for pure water and in-vitro blood, flowing through a 100 μm square-microchannel at low Re. Gunther et al. (2004) used μPIV to characterize the segmented gas-liquid flow at low Capillary number. They studied the recirculation patterns inside the liquid slug and the symmetric nature of this recirculation. They

pointed that the surface roughness and the compressibility of gas phase, are the main reasons behind the loss of symmetry for the velocity inside liquid slug and concentration fields. This enhances mixing across the centerline of straight micro-channels. Li and Olsen (2006) used micro-PIV to measure instantaneous velocity profiles in a square Poly-di-methyl-siloxane (PDMS) micro-channel with hydraulic diameter ranging from 200 μm to 640 μm and for Reynolds number ranging from 200 to 3971, having water as the working fluid. They calculated mean velocity profiles, velocity fluctuations, Reynolds stresses and spatial correlations of velocity fluctuations. Silva et al. (2008), using micro-PIV technique, observed the effect of the wall surface roughness on velocity profiles inside micro-capillary tubes and compared their results with numerical CFD without taking the surface roughness. They found that without considering the surface roughness leads to underestimation of friction factor by about 11%. Kinoshita et al. (2007) used confocal micro-PIV system to measure and investigate the internal flow of a droplet, transported in a square PDMS microchannel having a size of 100 μm x 58 μm . They showed that the droplets have three-dimensional flow structures. This three-dimensionality originates due to the drag force on the contact surfaces with the surrounding walls of the channel when the droplet moves inside a square microchannel.

In the present work, micro-PIV study has been carried out for the liquid flow (D.I. water) which creates a confined meniscus inside a square glass capillary tube of size dry 1 mm x 1 mm, as it enters in it from one end with a constant velocity. The flow field characteristics just behind the meniscus are of special interest. This is the region where enhanced transport characteristics are manifested due to three-dimensionality of the flow structures.

2. EXPERIMENTAL DESCRIPTION

2.1 Meniscus Visualization

The schematic of experimental setup for video imaging on the confined meniscus moving inside the square minichannel is shown in fig. 1. It consists of a syringe infusion pump (Cole Parmer-#74900-00) for supply of the working fluid, connected to a glass syringe, the output of which is connected to a horizontally placed square capillary tube of cross sectional size 1 mm x 1 mm. Before starting each new run of the experiment, the glass capillary is thoroughly cleaned in an ultrasonic

bath by a standard protocol and completely dried in an oven. The working fluid is supplied at a constant feed rate to the capillary tube; liquid-air meniscus thus formed travels at a fixed Capillary number inside the (already dry) capillary tube.

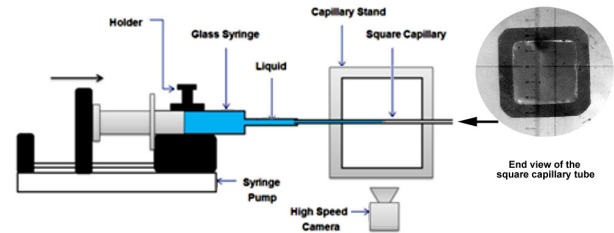


Fig 1. Schematic of the videography setup

The advancing contact angle with respect to the fixed Capillary number is video recorded using a high speed camera, Photron-Fastcam-SA3, after a steady-state is reached. The liquid-air meniscus visualization was performed for four different liquids: de-ionized water, pure ethanol, silicon oil, glycerin. While qualitative visual data is reported here, the detailed numerical data of advancing apparent contact angle with the Capillary number is being reported elsewhere.

2.2 Micro-PIV behind the moving meniscus

Micro-PIV experiments were performed with deionized water, both under bright field mode and fluorescent mode. The experimental setup was essentially the same as used for meniscus videography. The dry glass square capillary was placed horizontally over the stage of the inverted microscope (5x objective) of the micro-PIV unit (Leica Microsystem; DMI 5000). The maximum operating frequency of this micro-PIV experiment was 6 Hz.

The working fluid (de-ionized water), having sufficient seeding particles (glass particles of size 10 μm in concentration 12.5 mg/ml of liquid for bright field imaging and fluorescent carboxylate particles of size 1 μm in concentration 1 $\mu\text{l/ml}$ of liquid for fluorescent mode imaging), was supplied to the square capillary at specified calibrated flow rate. Successive images of the region of interest, just behind the dynamic liquid-air interface, were taken, using a 12 bit, 1344 x 1024 pixels digital CCD Camera, for PIV flow analysis. All the measurements were taken at the mid plane of the meniscus, a plane which was 0.5 mm up from the bottom wall. Proper masking of the acquired PIV image was carried out by carefully tracking the seeding particles movement near the wall and at

the interface to remove the non-flow outside region from the captured image field. The micro-PIV system produced two successive images and an adaptive cross correlation algorithm was applied to estimate the instantaneous flow field. An interrogation area of 64×64 pixels was chosen with a 50% overlap both horizontally and vertically. For removing unreasonable velocity vectors, appropriate filtration was applied after masking the velocity vectors. The acquired PIV images were processed using Dantec[®] Dynamic Analyzer to obtain the velocity at each point in the flow field. The micro-PIV analysis was done for two different water flow rates, 0.6 ml/hr and 1.0 ml/hr, the higher flow rate (corresponding to $U_{avg} = 0.27$ mm/s) being limited by the upper frequency response of the micro-PIV system. Velocity profiles across the channel width, at a fixed z -plane, were plotted for different stream wise locations just near and behind the dynamic liquid-air meniscus. For validation and benchmarking of the data away from the interface, the analytical solution for fully developed Poiseuille velocity profile inside a square channel (Eq. 1), as given by Lima et al. (2007), has been used.

$$u_x(y, z) = \frac{48Q}{\pi^3 h w} \frac{\sum_{n, odd} \frac{1}{n^3} \left[1 - \frac{\cosh(n\pi y/h)}{\cosh(n\pi w/2h)} \right] \sin(n\pi z/h)}{1 - \sum_{n, odd} \frac{192h}{n^5 \pi^5 w} \tanh(n\pi w/2h)} \quad (1)$$

The micro-PIV measurement data provides two components of velocity, i.e. U and V in the directions x and y , respectively, on a definite plane of observation. In all regions where the flow remains essentially two-dimensional in nature, the 2-D continuity equation for the flow field, i.e., $(\partial U / \partial x) + (\partial V / \partial y) = 0$, must be satisfied. If there remains a non-zero residual of the two-dimensional continuity equation, it is a definitive indication that the flow field is no more two-dimensional but is indeed three-dimensional, wherein the residual points towards the gradient of the W velocity in the z -direction. Thus, after obtaining the 2D velocity field (U and V) from the micro-PIV experiments, a four-point central difference method having a fourth order truncation error was applied at each grid point inside the domain to estimate the residual in the 2D continuity equation. The corner points of the domain were handled by either a forward or a backward difference scheme, as applicable. This methodology provides a simple scheme for checking the flow behavior and deviations, if any, from two-dimensional nature.

3. RESULTS AND DISCUSSION

3.1 Effect of Ca on meniscus shape

The images of the liquid-air meniscus for four liquids, at different Capillary numbers in a square glass capillary of size 1 mm x 1 mm are presented in fig. 2. The static wettability of each fluid is different. The meniscus, moving at a constant velocity inside the tube, makes a unique dynamic apparent contact angle, as shown. This angle changes drastically with the applied Capillary number, as seen from the results. At low Capillary number, the water-air meniscus remains nearly flat and close to perpendicular to the channel wall. But increase in Capillary number results in convexity of the meniscus due to variation of dynamic pressure difference between two sides of meniscus. Glycerin-air meniscus behavior is same as of water-air for the chosen range of Capillary number. For ethanol, the liquid-air interface is concave in shape for all the range of applied Capillary number. But in silicon oil, the shape of the interface is changing from concave to convex as the Capillary number is increased. These results clearly indicate the importance of understanding the dynamically changing shape of moving menisci inside small capillaries. The shape has direct consequence on the local transport behavior, just behind the meniscus, as will be seen next.

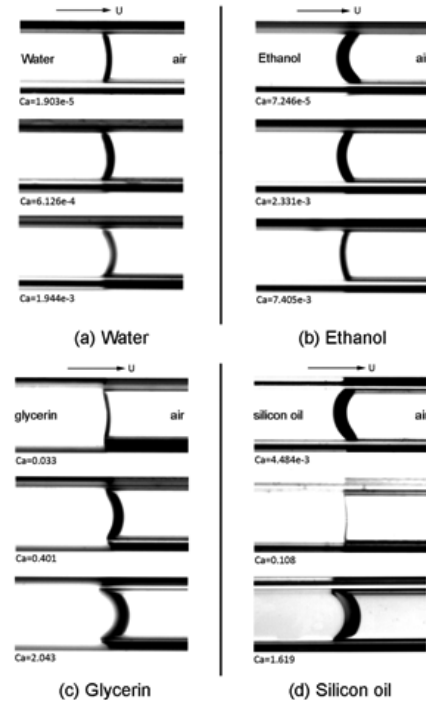


Fig 2. Variation of meniscus shape with increase in Capillary number for four different fluids (a) water (b) ethanol (c) glycerin (d) silicon oil.

3.2 Results from micro-PIV

A typical experimental micro-PIV image, with the applied masking, is as shown in fig. 3. The liquid-air interface is clearly visualized along with the channel wall except some minor shadow effects.

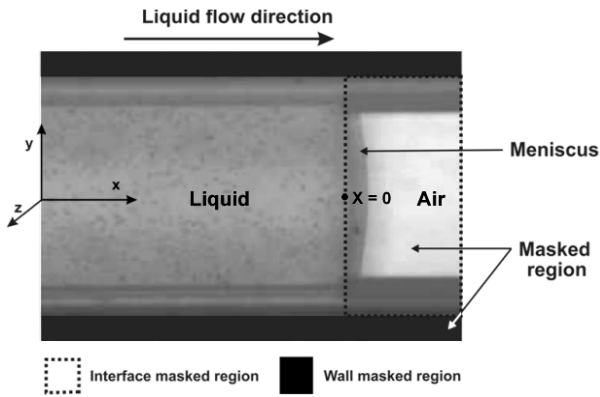


Fig 3. Bottom view of the liquid-air meniscus inside square capillary in the bright field mode. The masked region at the interface and wall is defined to remove bad velocity vectors. This image was taken at the mid-plane of the channel. Gravity vector points towards z direction.

The quantitative analysis of the micro-PIV images has been carried out and the respective U-contour plots (in the x-direction, i.e., the streamwise direction, and V-contour plots (y-axis; transverse direction), for average flow velocity of 0.27 mm/s and 0.166 mm/s respectively, has been plotted in fig. 4 (a) (b) (d) (e). From the U-contours it is clearly observed that the velocity is higher at the centre of the channel away from the interface and it is gradually decreasing as we approach towards the liquid-air interface. The V-contour near to the interface has two dense regions. These regions are having a higher magnitude of V-velocity, albeit in opposite directions, as expected due to fluid circulation near the interface. As explained earlier, applicability of the two-dimensional continuity equation has also been scrutinized, as shown in fig. 4 (c) (f). Away from the interface the continuity is getting satisfying but just behind the meniscus region the residual error in the 2D continuity is more, clearly indicating the existence of gradient of the third component of velocity, W. This three-dimensionality in the flow arises due to the drag force on the contact surface with the sidewalls of the micro-channel and the fact that the meniscus obeys the free surface boundary condition.

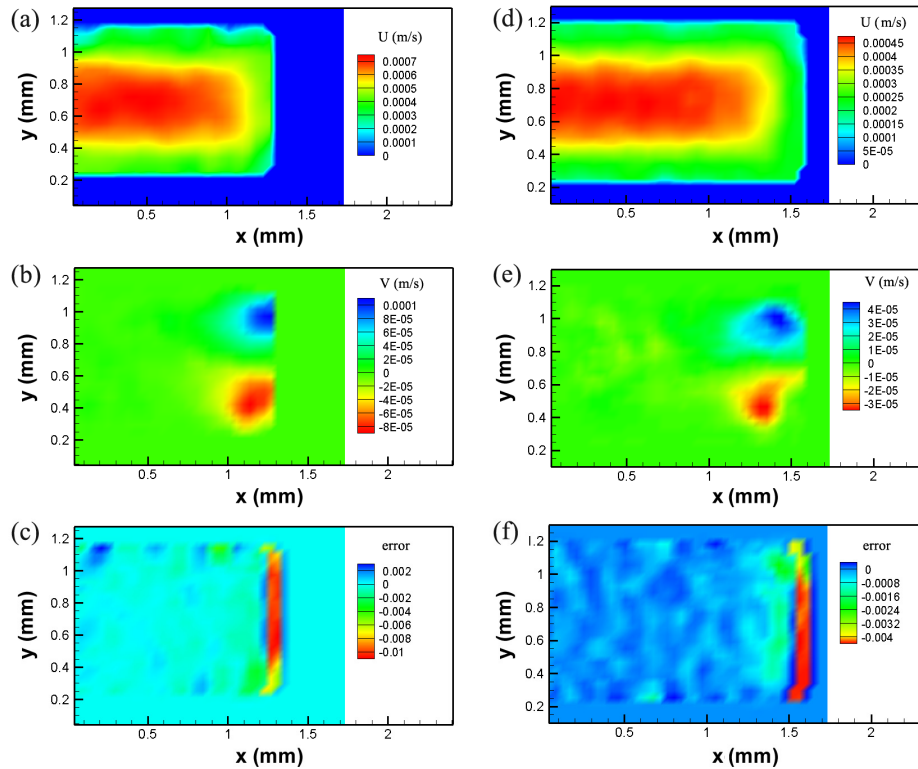


Fig 4. Velocity distribution at the moving liquid-air interface inside the square-microchannel for two different flow rates: (i) $U_{avg} = 0.27$ mm/s (a) U-contour (velocity distribution in x-direction), (b) V-contour (y-component of velocity) and (c) Error in 2-D continuity, and (ii) $U_{avg} = 0.166$ mm/s (d) U-contour, (e) V-contour, (f) Error in 2d-continuity (all results are from the bright-field PIV data).

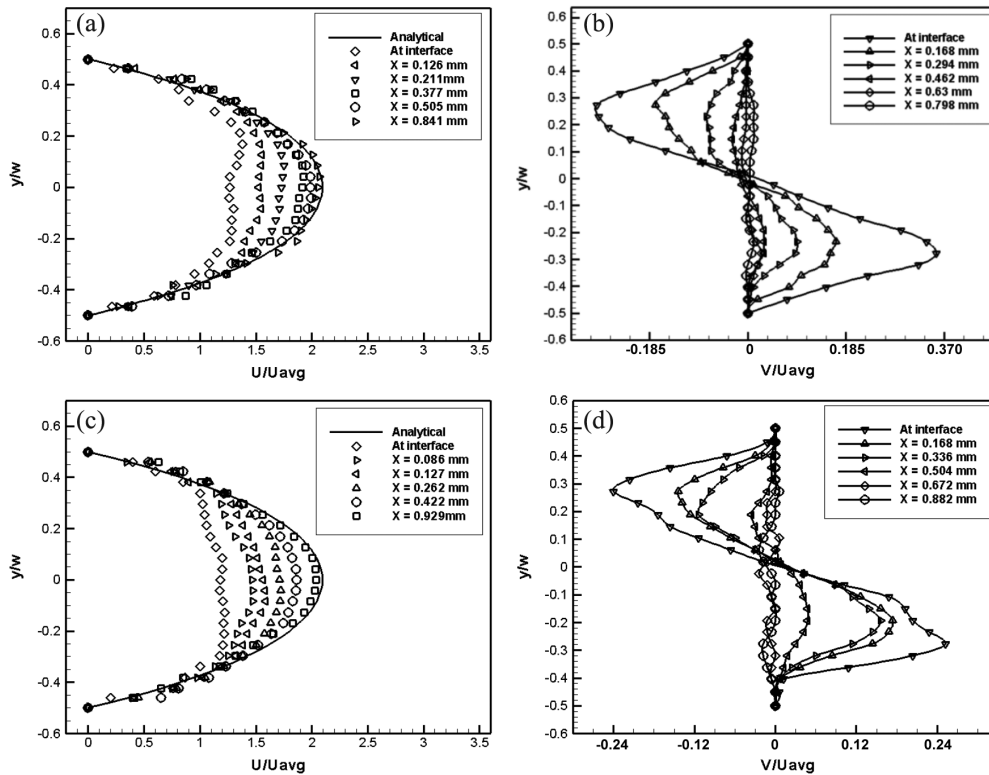


Fig 5. Variation of x and y components of velocities: U and V with respect to channel width when $U_{avg} = 0.00027\text{m/s}$ ($Ca = 3.7\text{e-}6$): (a) non-dimensional U-velocity, (b) non-dimensional V-velocity. Variation when $U_{avg} = 0.000166\text{ m/s}$ ($Ca = 2.27\text{e-}6$): (c) non-dimensional U-velocity and, (d) V-velocity.

Fig. 5 shows the variation of U and V along the channel width at increasing locations from the liquid-air interface. Non-dimensionalization has been done using the respective U_{avg} , which is the average supply velocity based on the cross-section of the channel. All the measurement have been performed at the mid-plane of the tube cross-section. X is the streamwise axial distance from the interface ($X = 0$ corresponds to the interface, as detailed in Figure 3). Close to the interface a significant drop in the magnitude of the U-velocity is seen at the centre region of the channel and this behavior is more prominent at higher flow rates. This behavior is seen due to obstruction of the fluid flow at the liquid-air interface. The meniscus shape, at all times, follows the Young-Laplace condition and only tangential velocities are possible at the interface. Thus, a V and W component of velocity emerges close to the interface to satisfy continuity condition. Moving away from the interface, the U-velocity follows the well defined parabolic profile, essentially satisfying Poiseuille flow. For benchmarking, the analytical profile, given by Eq. 1 has also been plotted. The V-velocity becomes negligible away from the interface. As has been pointed out earlier, close to the interface, the flow becomes three-dimensional in nature.

SUMMARY AND CONCLUSIONS

In this present work isolated dynamic meniscus shape of a moving liquid-air system inside a minichannel has been studied for water, ethanol, glycerin and silicon-oil, with varying Ca. It is shown that a drastic change in the dynamic shape of the meniscus can occur due to the imposed bulk velocity. Subsequently, using micro-PIV, liquid velocity distributions near the moving water-air meniscus were measured at the mid plane of the channel, at low Ca. It was shown that near the liquid-air interface the non-dimensional U-velocity profiles are not parabolic in nature while moving away from the meniscus, these profiles follow the Poiseuille conditions. The V-velocity is moderately dominant only close to the interface, although its absolute value is rather small as compared to the U-velocity. Formation of opposite vortices is clearly indicated by the V-profiles. Checking the continuity close to the interface indicated that the flow is indeed three-dimensional in nature in the proximity of the interface. It is highlighted that near meniscus local transport phenomena is critical in understanding the transport behavior of micro-scale multi-phase systems.

NOMENCLATURE

Ca	Capillary number, $\mu U_{\text{avg}}/\sigma$
h	Height of the channel in mm
Q	Liquid flow rate in ml/hr
Re	Reynolds number
U	x-component of velocity in m/s
U_{avg}	Average velocity in m/s
V	y-component of velocity in m/s
W	z-component of velocity in m/s
σ	Surface tension in N/m

ACKNOWLEDGEMENT

Financial support from the Indo-French Centre for the Promotion of Advanced Research, New Delhi (Project #: 4408-1/2010), under the aegis of Indian Department of Science and Technology and the French Ministry of Foreign Affairs is gratefully acknowledged.

REFERENCES

- Ajaev, V. S. and Homsy, G. M. (2006) *Modelling Shapes and Dynamics of Confined Bubbles*. Annual Review of Fluid Mechanics, 38, p. 277-307
- Chebbi, R. (2003) *Deformation of Gas-Liquid interfaces in capillary tubes*. Journal of Colloid and Interface Science, 265, p. 166-173
- Egorov, A. G., Kornev, K. G. and Neimark, A. V. (2003) *Meniscus motion in a prewetted capillary*. Physics of Fluids, 15, p. 3134-3143
- Gunther, A., Khan, S. A., Thalmann, M., Trachsel, F. and Jensen, K.F. (2004) *Transport and Reaction in Microscale Segmented Gas-Liquid Flow*. Lab on Chip, 4, p. 278-286
- Juncker, D., Schmid, H., Drechsler, U., Wolf, H., Michel, B., Rooij, N. D. and Delamarche, E. (2002) *Autonomous Microfluidic Capillary System*. American Chemical Society, 74, p. 6139-6144
- Khandekar, S., Panigrahi, P. K., Lefevre, F. and Bonjour, J. (2010) *Local Hydrodynamics of Flow in a Pulsating Heat Pipe: A Review*. Frontiers in Heat Pipes, 1, p. 1-20
- King, C., Walsh, E. and Grimes, R. (2007) *PIV Measurement of Flow within Plugs in a Microchannel*. Microfluid Nanofluid, 3, p. 463-472
- Kinoshita, H., Kaneda, S., Fujii, T. and Oshima, M. (2007) *Three-dimensional Measurement and Visualization of Internal flow of a Moving Droplet using Confocal Micro-PIV*. Lab Chip, 7, p. 338-346
- Li, H. and Olsen, M. (2006) *Micro-PIV Measurement of Turbulent Flow in Square Microchannels with Hydraulic Diameters from 200 μm to 640 μm* . International Journal of Heat and Fluid Flow, 27, p. 123-134
- Lima, R., Wada, S., Takeda, M., Tsubota, K. and Yamaguchi, T. (2007) *In Vitro Confocal Micro-PIV Measurements of Blood Flow in a Square Microchannel: The Effect of the Haematocrit on Instantaneous Velocity Profiles*. Journal of Biomechanics, 40, p. 2752-2757
- Malsch, D., Kielpinski, M., Merthan, R., Albert, J., Mayer, G., Kohler, M., Stahl, M. and Henkel, T. (2008) *Micro-PIV Analysis of Taylor Flow in Microchannels*. Chemical Engineering Journal, 135S, p. 166-172
- Meinhart, C. D., Wereley, S. T. and Santiago, J. G. (1999) *PIV Measurement of a Microchannel Flow*. Experiments in Fluids, 27, p. 414-419
- Pattekar, A. V. and Kothare, M. V. (2004) *A Microreactor for Hydrogen Production in Micro Fuel Cell Applications*. Journal of Micro-electromechanical Systems, 13, p. 7-18
- Silva, G., Leal, N. and Semiao, V. (2008) *Micro-PIV and CFD Characterization of Flows in a Microchannel: Velocity Profiles, Surface Roughness and Poiseuille numbers*. International Journal of Heat and Fluid Flow, 29, p. 1211-1220
- Thulasidas, T. C., Abraham, M. A. and Cerro, R. L. (1997) *Flow patterns in Liquid Slugs during Bubble train flow inside Capillaries*. Chemical Engineering Science, 52, p. 2947-2962
- Torralba, M., Pita, J. R., Pita, A. A., Huelsz, G., Rio, A. D. and Ortin, J. (2005) *Measurement of the bulk and interfacial velocity profiles in oscillating Newtonian and Maxwellian fluids*. Physical Review, E72, p. 0163081-0163089
- Walker, G. M. and Beebe, D. J. (2002) *A Passive Pumping Method for Microfluidic Devices*. The Royal Society of Chemistry, 2, p. 131-134

APPLICATION OF MINI HEAT PIPES FOR THERMAL MANAGEMENT OF OPTO-ELECTRONIC INSTRUMENTS

Sandeep Kumar Singh, Sameer Khandekar*
Department of Mechanical Engineering
Indian Institute of Technology Kanpur
Kanpur (UP) 208016, India

Pankaj Srivastava, J. K. Bajpai
Instrumentation Research and Development Establishment
Defense Research and Development Organisation
Dehradun (UK), 248008 India

* Corresponding author: Tel: (+91)-512-259-7038, Fax: (+91)-512-259-7408, E-mail: samkhan@iitk.ac.in

ABSTRACT

Heat dissipation, thermal stresses, size and cost are the key packaging design issues for electronic and opto-electronic instruments. As per defense requirement, instruments are expected to work satisfactorily in the temperature range of -30°C to $+55^{\circ}\text{C}$. In this study, we have explored the thermal management of a sealed enclosure, envisaged as housing for handheld instruments, using different active and passive techniques such as natural convection, conventional heat sinks and copper-water wicked mini-heat pipes. Microelectronic equipment inside the enclosure generated heat and the aim of the study was to apply and compare various thermal management techniques suitable for maintaining a safe operating temperature inside the enclosure. Transient numerical modeling was performed on a commercial platform to compare the various techniques available for thermal management. Effects of both, natural convection inside the enclosure and radiation, were taken into account. The results from the CFD simulations were verified with the real time system level experiments. It was observed that in handheld opto-electronic instruments, heat pipes have potential applications to achieve the required performance in the available enclosure volume.

Keywords: Microelectronic thermal management, numerical modeling, heat pipes and heat sinks, effective thermal conductivity, passive cooling techniques

1. INTRODUCTION

Technological advancement at device, package and system levels led to increased product functionality but squeezed more power into ever-smaller packages. With these technologies, devices are capable of processing more data within a given space and time. This directly leads to enhanced heat generation per unit volume. Each conceived new design coming up in the market results in higher power dissipation levels. In addition, total dissipated power is not the only problem; heat density (power/area) is complementary to it. Major causes of electronic failures are due to temperature, vibration, humidity, dust levels etc. Thus, effective removal of heat and maintenance of safe operating temperature is most vital for reliable instrument operation [Khandekar et al., 2003].

Conventional heat sinks, pin fin arrays, fan-assisted heat sinks, phase-change materials (PCM), thermo electric coolers, etc. are some of the routine

techniques available for thermal management. Present scenario of high thermal loading coupled with high flux levels demands exploration of new heat transfer mechanisms. Efficient heat transfer by passive heat pipe technology is much superior to conventional techniques. Heat pipes, with their unique characteristics of very high thermal conductance, which usually is an order of magnitude larger than conventional metallic conductors, offer great potential for thermal management. Conventional wicked heat pipes allow rapid exchange of heat transfer through evaporation and condensation processes of the working fluid. This continuous cycle can transfer large quantity of heat with very low thermal gradients [Garner, 1996].

The aims of this study (combination of modeling and experiments) are to incorporate and compare different available thermal management strategies for a $\sim 35\text{W}$ power dissipating opto-electronic hand-held instrument for defense needs.

2. HEAT PIPE DESIGN AND TESTING

One of the objectives of this work was to experimentally and theoretically investigate the feasibility of integrating conventional copper-water cylindrical mini heat pipes inside the enclosed opto-electronic instrument. A JAVA[®] based simulation tool was developed to numerically estimate the maximum heat throughput (Q_{max}) possible from a heat pipe at different operating temperatures. The simulation program applies the basic heat pipe theory [Dunn and Reay, 1977; Faghri, 1995] for determining the various operating limits. A mini copper-water heat pipe was also performance tested at different operating adiabatic temperatures and inclination angles. This testing also provided a first-order estimate of the effective thermal conductivity (k_{eff}) of these mini-heat pipes, which was later used for 3D simulation of heat transfer through the enclosure.

The heat pipes were expected to transfer about 35 W thermal power from the control volume of the enclosed instrument to the ambient, while the temperature of the ambience could vary from 25°C-55°C. The maximum length of the heat pipe was constrained to be less than 250 mm and its diameter to be less than 16 mm.

Typical results for the maximum capillary limitation of a copper-water heat pipe with a composite wick, in the temperature range of 25°C - 55°C and having the following specifications is given in Figure 1 and 2:

Table 1: Specifications of the simulated heat pipe

Length of Evaporator Section	0.070 m
Length of Adiabatic Section	0.030 m
Length of Condenser Section	0.050 m
Outer Diameter of Heat Pipe	0.010 m
Number of Layers of Mesh 1	2
Number of Layers of Mesh 2	2
Wall thickness of Heat Pipe	0.000250 m
Wire Diameter of Mesh 1	0.000240 m
Wire Diameter of Mesh 2	0.000060 m
Mesh Number 1	30
Mesh Number 2	160
Fluid Used	Water

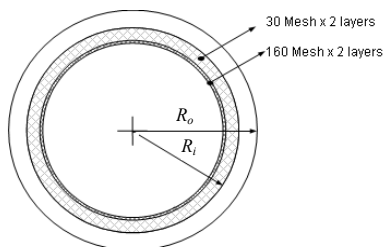


Figure 1. Composite wick structure of the heat pipe.

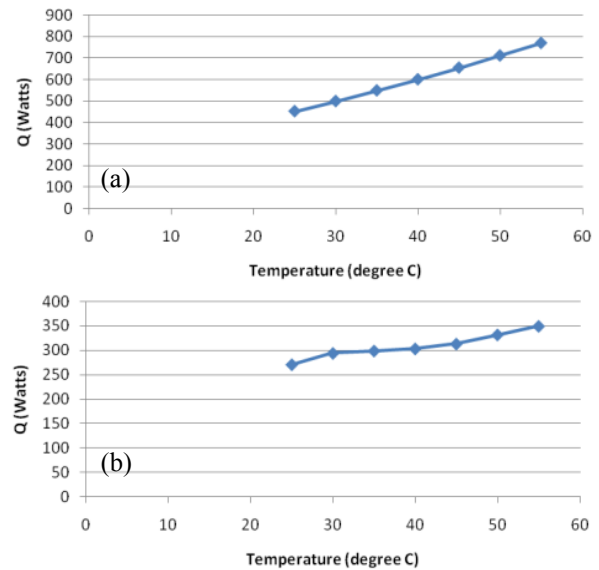


Figure 2. Maximum capillary limit of the simulated heat pipe in (a) horizontal position (b) vertical heater-up position.

It was observed that the capillary pumping power is the most important factor which limits the heat pipe operation under the given boundary conditions. The heat pipe is not limited by other factors such as sonic, entrainment etc.

The experimental setup to check the maximum performance of copper-water mini heat pipes, is as shown in Figure 3 below. Heating was provided to the heat pipe by two electrical film resistance heaters (MINCO[®], 6.6 Ohms each), through a copper block (76 mm x 12 mm x 12 mm) in which the heat pipe was securely inserted. The condenser section was made of Plexiglas enclosure through which coolant water circulated at a very high mass flow rate (by constant temperature circulator (Julabo[®] F34 ME, accuracy $\pm 0.1K$).

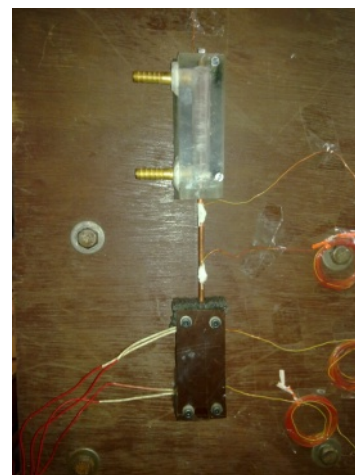


Figure 3. Photograph of the performance testing rig of mini copper-water heat pipes.

The condenser capacity was at least three times larger than the maximum heat throughput expected from this heat pipe, as indicated by the simulations. Several thermocouples (Omega[®], 0.5 mm bead diameter, accuracy ± 0.1 after calibration) were attached throughout the length of the length of the heat pipe to monitor its thermal response. The data was recorded with the help of NI USB-9162 incorporating the LabVIEW[®] Signal Express 2009 platform. It was possible to incline the test bench at any desired inclination from the horizontal. Heat throughput to the evaporator was increased in small steps still a steady state was achieved, at a pre-decided adiabatic (operating) temperature. The operating temperature was maintained constant (from 25°C to 65°C at the interval of 5°C) by varying the condenser coolant inlet temperature. As dry-out approached, a sudden temperature increase in the evaporator section was observed. At any given adiabatic temperature, tests were repeated at least three times to ensure the repeatability of the dry-out phenomena and the corresponding heat throughput.

The maximum heat throughput which was obtained by the performance testing was compared with the theoretical values obtained in the simulation. A typical result of such a comparison is as shown in Figure 4. Here, the length of the copper-water heat pipe was of 280 mm and its outside diameter was 4 mm; the details of the internal wick structure are also depicted.

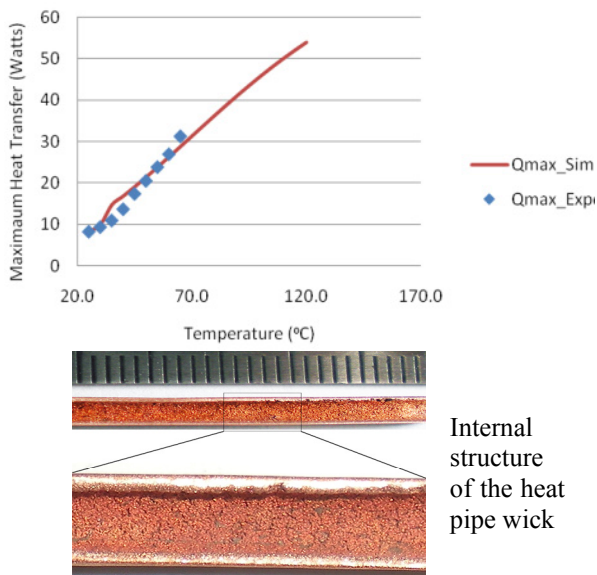


Figure 4. (a) Comparison of the theoretical and experimental values of maximum heat throughput of the copper-water mini heat pipe at different operating temperatures (vertical heater down position). (b) Porous wick inside the heat pipe. The depicted scale divisions are in millimeters.

3. MODELING AND SIMULATION

The opto-electronic device was conceived to be enclosed in an enclosure, as shown in Figure 5 (a). The overall structure is represented by the control volume, containing a heat source of 35 W with size 75 mm x 75 mm x 10 mm with embedded ‘heat pipes’, modeled by a high thermal conductivity rod of size 10 mm x 10 mm x 270 mm, as shown in Figure 5(b). The cross sectional area of the rod roughly represented three equivalent heat pipes, as proposed for use in the final thermal management protocol.

The outer aluminum casing of the device is thin walled. For simulation purpose, apart from heat source, the instrument box is primarily filled up with air. Inside the box, part of the heat transfer also takes place due to the natural convection from the heater surfaces to the air surrounding it. Over and above any forced convective system employed for thermal management, the eventual heat dissipation from the inside of the equipment to the ambient also includes heat transfer through the inside and outside walls of the thin walled casing, by a combination of natural convection and radiation. Several configurations of this basic arrangement were simulated (on Ansys-Fluent[®] platform) as will be discussed later. Refined grids were taken at the boundaries of all the solid-fluid interfaces to resolve the boundary layers. A typical computational domain is as shown in Figure 6.

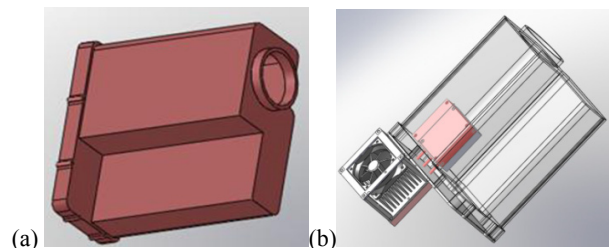


Figure 5. (a) Schematic diagram of the enclosure (b) Volume fitted with heater and fan assembly.

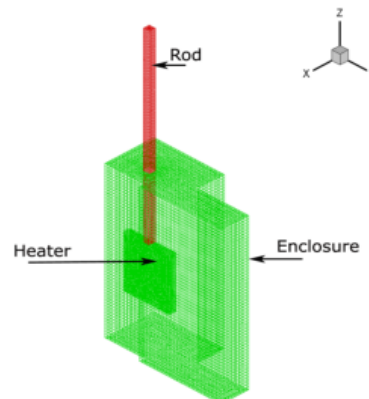


Figure 6. Computational domain representation of the instrument enclosure.

For discretization of momentum and energy equation, ‘second order upwind’ scheme was applied. Absolute convergence criterion set for momentum was 10^{-6} and for energy was 10^{-8} . The properties of air were set to be varying with the temperature.

The CFD simulations were run for the following two cases:

Case #1: The heat pipe attached to the heating surface is not operational and the heating surface loses heat to the air inside the enclosure only by natural convection and radiation. The instrument enclosure eventually loses the heat gained by the inside heater to the ambient by natural convection and radiation taking place through the outside of the enclosure casing. The heat transfer coefficient assumed for natural convection is $6.5 \text{ W/m}^2\text{K}$, while the average hemispherical emissivity of all the surfaces is taken to be 0.8.

Case #2: The heat pipe attached to the power generating source is made active in this simulation. The effective thermal conductivity of the heat pipe is taken to be equal to 3000 W/mK , as suggested by the experiments. The heat pipe is connected to an external heat sink where forced convection is available with an effective heat transfer coefficient of $30 \text{ W/m}^2\text{K}$. This heat pipe-heat sink based thermal energy transfer augmentation is in addition to the natural convection and radiation taking place, as described in Case #1.

Temperature distribution across the cross section of the instrument enclosure, for Case #1 is shown in Figure 7 (a). For this case, with only natural convection and radiation, the maximum temperature inside the enclosure comes out to be more than 400K . Thus, it is clear that such a solution is unfeasible for system deployment.

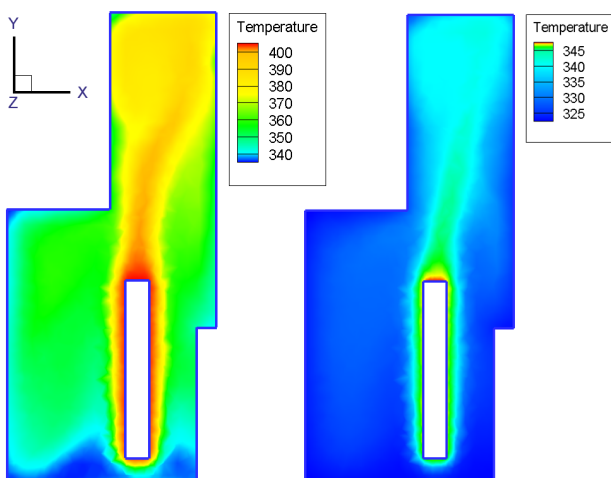


Figure 7. Temperature profile (K) at the cross-section of the enclosure (a) without heat pipe and, (b) with the heat pipe attached to the heat source.

Figure 7(b) shows the temperature distribution across the cross section of the enclosure for Case #2. In this case, the maximum temperature reached inside the enclosure was just above 345K , in the vicinity of the heat source. The bulk temperature inside the enclosure was in the range of 320K to 340K . It is clear that integrating a heat pipe along with active convective cooling to the ambient drastically improves the thermal performance by keeping the internal temperatures at critical junctions below the prescribed values.

4. SYSTEM LEVEL EXPERIMENTS

A series of system level experiments were conducted to establish the effectiveness of different cooling methodologies operating under the actual environmental conditions. Figure 8 shows an enclosure which was made up of the aluminum casting. Heat sources dissipating about 35W of thermal energy were placed inside the enclosure. This enclosure was tested under different ambient temperatures, viz. 22°C , 35°C and 45°C . Three different operating conditions were used for the heat removal at these temperatures (a) Natural convection and radiation without any forced/active heat removal mechanism (b) Forced convection of air on the outside of the casing with the help of a fan and, (c) Use of three copper-water mini heat pipes of outside diameter 4.0 mm embedded inside the heat sources and connected to a finned heat sink outside the enclosure. A dedicated 12V axial flow mini-fan was integrated with the heat sink assembly, as shown in Figure 8. Temperatures were measured with the help of K-type thermocouples suitably located at six positions, two at the heater, two inside the enclosure, one each for ambient temperature and enclosure outer surface. Once a steady-state was reached, the temperatures at all the points were noted.



Figure 8. System level mock-up of the opto-electronic instrument enclosure.

The experiments with embedded heat pipe inside the enclosure were conducted in the real time situation to observe the effect of different operating conditions. The resulting temperature inside the enclosure can be observed in Figure 9 at different ambient temperatures (22°C, 35°C and 45°C) and different thermal management strategies. It was observed that, at all the ambient conditions, the temperature inside the enclosure was highest in the case where no heat pipe or heat sink was used. Even with the usage of heat sink, the temperature inside the enclosure remained high. But, when heat pipes were used along with the heat sink, coupled with active fan cooling from the outside, the maximum temperature inside the enclosure reduced significantly by 25°C at the ambient temperature of 45°C (In this case, the heat pipe was vertical-heater down). When the heat pipe assembly was kept at horizontal position there was some increase in the temperature inside the enclosure; the system worked somewhat more effectively when the heat pipe assembly was kept at the vertical position. Figure 10 compares the transient temperature profile inside the heater body for the three different cases. The advantages of the heat pipe heat sink are obvious.

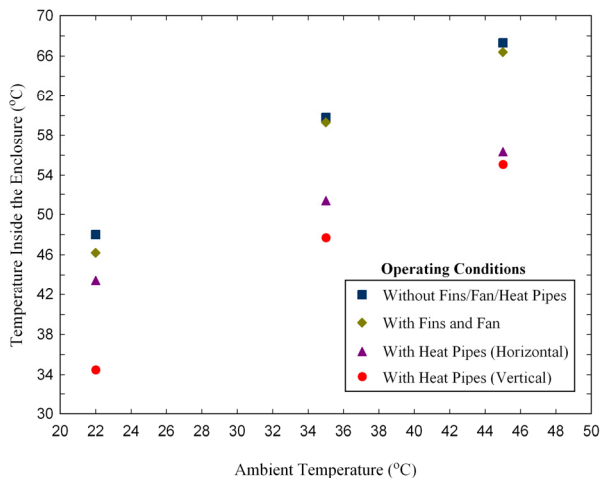


Figure 9. Temperature obtained at a point inside the enclosure at different operating conditions and at different ambient temperatures.

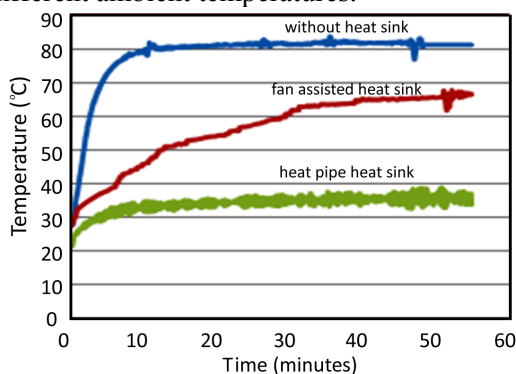


Figure 10. Comparison of the three tested cases.

6. SUMMARY AND CONCLUSIONS

In handheld instrument needs for defense/surveillance, weight, space and the severity of the ambient conditions are the main constraints for design and development. Thermal management of such systems offer quite some challenge due to various design constraints and limitations. In the present study, it has been demonstrated that conventional mini-heat pipes offer very good potential to achieve the required performance in the available instrument volume.

Heat pipes offer an attractive approach to supplement conventional heat sink solutions. They do not replace the conventional heat sink, rather they provide a flexible tool that allows the designer to reconfigure and/or extend the performance of conventional heat sinks. Considerably improved heat sink efficiency and performance was achieved for the opto-electronic instrument enclosure by relatively simple integration techniques. Use of such high conductivity heat pipe interfaces permits higher packaging densities or higher power dissipation in a given volume. On many occasions, heat transfer is limited by the external heat transfer coefficient or the contact resistances in the thermal path from the source to the sink. The thermal resistance of the heat pipe itself is usually the lowest in the composite thermal circuit.

In the present study, mini copper water heat pipes were successfully simulated, performance tested, and implemented in a system level mock-up experiment to dissipate about 35 W of thermal energy from the internal heat dissipating units.

ACKNOWLEDGEMENTS

The work was carried out with financial support from the Instrument Research and Development Establishment (IRDE), Defense Research and Development Organization, Dehradun, India.

REFERENCES

- [1] Dunn, P., Reay, D.A., (1977), *Heat Pipes, Second Edition*, Pergamon Press.
- [2] Faghri, A., (1995), *Heat Pipe Science and Technology*. Taylor & Francis, London.
- [3] Garner, S., (1996), *Heat pipes for Electronics Cooling Applications*, Electronics Cooling, Vol. 2, No. 3.
- [4] Khandekar, S., Groll, M., Luckchoura, V., Findl, W. and Zhuang, J., (2003), *Micro Heat Pipes for Stacked 3D Microelectronic Modules*, Advances in Electronic Packaging, Vol. 2, pp. 245-251.

THERMAL ANALYSIS OF A DIFFUSION MODEL APPLIED FOR A GAS-LOADED VAPOR CHAMBER CONDENSER

Tavares, E. G., Milanez, K. W., Milanese, F.H., Mantelli, M.B.

Federal University of Santa Catarina - Mechanical Engineering Department
Trindade - Florianopolis - SC - Brazil - 88040-900

+55 (48) 37219937, estevan.tavares@labtucal.ufsc.br, kenia@labtucal.ufsc.br, milanez@labtucal.ufsc.br,
marcia@emc.ufsc.br

ABSTRACT

In the present work, heat and mass transfer analyses were made in a vapor chamber with non-condensable gases. The vapor chamber consists of a condenser of a two-phase loop thermosyphon. To induce a variable temperature profile along the condenser length, a non-condensable gas is inserted inside of the vapor chamber. A two-dimensional diffusion model was developed for the geometry of the device under study. With dimensionless governing equations, a radial diffusion parameter was varied to different levels in order to analyze its influence on the system. The radial diffusion parameter is dependent of the condensation heat transfer coefficient and a discussion about the influence of the heat transfer coefficient over the vapor chamber is presented. To determine the solution of the governing equation, an integral method combined with a numerical method was used.

KEY WORDS *Two-Phase Loop Thermosyphon, Vapor Chamber, Non-Condensable Gas*

1. INTRODUCTION

Non-condensable gases (NCG) are in the superheated thermodynamic state inside of the heat pipes and thermosyphons. These gases are undesirable because they reduce the thermal conductance of heat pipes and thermosyphons. When a thermosyphon with NCG is under operation, the working fluid pushes the NCG to the end of the condenser, occupying part of the condenser and reducing the effective heat-transfer area of the condenser. Also, NCG interact with the working fluid vapor by chemical diffusion, leading to a high concentration layer of NCG over the liquid film. As a result, a diffusion barrier is created to the vapor of working fluid, increasing the global thermal resistance of the system.

In some applications, NCG can be useful. The most commonly variable conductance heat pipes (VCHP) is of the Gas-Loaded type. A VCHP is a device designed to hold the temperature of the condenser, or evaporator, constant. The Gas-Loaded VCHP uses a fixed amount of NCG to control its operating temperature. Since the NCG remains in the condenser and forms an inactive

section, this provides a control mechanism for the condensation heat transfer conditions (Faghri, 1995).

This work presents a theoretical study aiming at an application where a variable temperature profile along the condenser length is required. This variable temperature profile is obtained by using a certain amount of NCG. This kind of condition can be useful in applications such as the separation of multi-component mixtures.

2. PROBLEM STATEMENT

The system under study is basically a two-phase loop thermosyphon, where the condenser surrounds a tube, as shown in Fig. 1. This is the same device described by Milanez *et. al.* (2010). The chamber is thermally insulated on the external side, to ensure that almost all of the heat produced by evaporator is delivered to the internal tube. The geometry of the chamber is a cylindrical shell, where L is the height, R_i is the external radius of the internal tube and R_e the internal radius of the cylindrical shell. Fig. 1 shows the cylindrical coordinate system applied for the model.

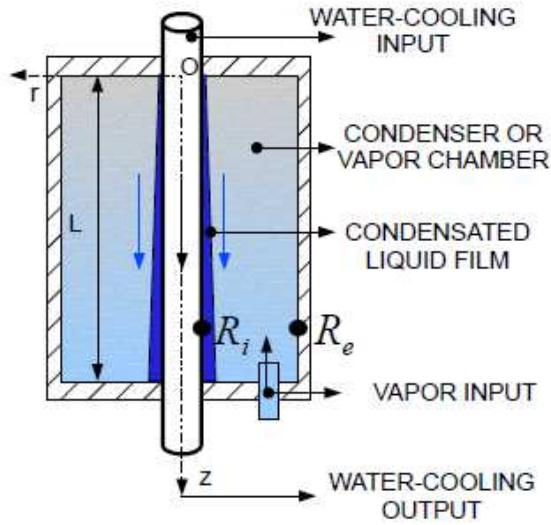


Figure 1. Schematic of the vapor chamber.

The vapor generated in the evaporator reaches the base of the vapor chamber. A certain amount NCG is inserted inside of the chamber. As the vapor flows upwards inside of the chamber, it pushes the NCG to the top of the chamber. The NCG is stagnant and diffuses against the flowing vapor. As a result, there is a variable concentration vapor along the condenser length, which provides the desired temperature profile along the axial length of the condenser. As vapor condenses, it provides heat to the external wall of the internal tube. This surface is also the internal wall of the cylindrical shell. A thin liquid film is formed on this wall and flows downwards by gravity and returns to the evaporator through a liquid return tube.

3. MATHEMATICAL FORMULATION

A simplified model is used to obtain the molar concentration distribution inside of the vapor chamber, which leads to a variable temperature profile along the condensate liquid film.

The adopted model was developed by Hijikata, *et al.* (1984). The model predicts the concentration of NCG in the interior of a gas-loaded thermosyphon using Fick's Law by:

$$\dot{c}_g = \bar{V}c_g - c_s D \nabla x_g \quad (1)$$

The main simplifications of this model are: two-dimensional variation of concentrations, NCG is stagnant, incompressible vapor flow and known

amount of NCG. Based on these hypotheses, Fick's Law in the molar base becomes:

$$\nabla \cdot \left(\frac{1}{x_g} D \nabla x_g \right) = 0 \quad (2)$$

and the derivative properties are:

$$\nabla^2 (\ln x_g) = 0 \quad (3)$$

In cylindrical coordinates, one can write:

$$\frac{1}{r} \frac{\partial}{\partial r} \left(r \frac{\partial \ln x_g}{\partial r} \right) + \frac{\partial^2 \ln x_g}{\partial z^2} = 0 \quad (4)$$

The boundary conditions are:

$$\frac{\partial (\ln x_g)}{\partial z} = 0 \quad \text{at } z = 0 \quad (5)$$

$$\frac{\partial (\ln x_g)}{\partial r} = 0 \quad \text{at } r = R_e \quad (6)$$

$$\ln x_g = \ln \left\{ 1 - \exp \left[T^* \left(1 - \frac{T_i}{T_e} \right) \right] \right\} \quad \text{at } r = R_i \quad (7)$$

$$\ln x_g \rightarrow -\infty \quad \text{at } z = L \quad (8)$$

Equation (5) results from the hypothesis that the top is impermeable. Similarly, Eq. (6) means that the external wall of the chamber is also impermeable. The concentrations of NCG are prescribed by Equation (7) and Eq. (8), at the surface of condensate liquid film and at the base of the vapor chamber, respectively. In Eq. (7), the molar fraction of the NCG is prescribed by the Clausius-Clayperon integral relation. This relation was proposed by Edwards and Marcus (1972) for heat pipes with NCG. The characteristic temperature, appearing in Eq. (7) is given by:

$$T^* = \left(1 - \frac{T_e}{T_c} \right)^{-1} \ln \left(\frac{P_e}{P_c} \right) \quad (9)$$

In this equation, the saturation pressure P must be evaluated at the corresponding temperature T .

The temperature at the interface of the condensate liquid film must be determined. According to Fig. 2, the energy balance at $r=R_i$ is satisfied if:

$$h_{fg} M_v c_e D \frac{\partial(\ln x_g)}{\partial z} = h_c (T_i - T_c) \quad (10)$$

Note that, actually, the boundary condition stated by:

$$N_g = \int_0^L \int_{R_i}^{R_e} c_g 2\pi r dr dz \quad (11)$$

is valid only if the liquid film thickness δ is neglected.

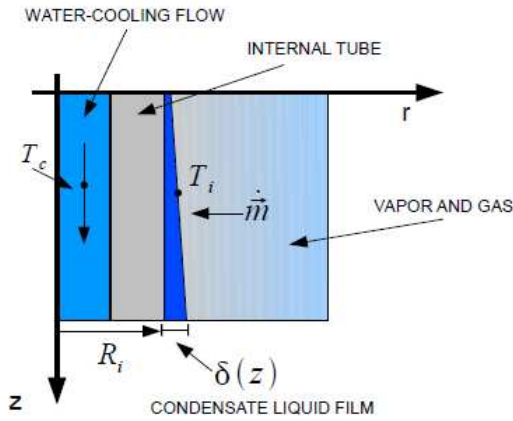


Figure 2. Longitudinal section of the device.

The heat transfer coefficient was estimated by an iterative process, where the convergence condition is the amount of the NCG. An iterative numerical process was employed where h_c is guessed. Edwards and Marcus (1972), Hijikata *et al.* (1984) and Zhou and Collins (1994) used the same iterative process to find the temperature of the liquid film at the top of the thermosyphon.

The problem is closed with Eqs. (4) to (11). In order to make the above equations dimensionless, the following quantities are introduced:

$$r' = \frac{r - R_i}{R_e - R_i} \quad (12a)$$

$$z' = \frac{z}{R_e - R_i} \quad (12b)$$

$$F = E \ln x_g \quad (12c)$$

$$E = \frac{h_{fg} M_v c_e D}{h_c (R_e - R_i)(T_e - T_c)} \quad (12d)$$

$$\theta = \frac{T - T_c}{T_e - T_c} \quad (12e)$$

$$\theta_c = \frac{T_c}{T_e - T_c} \quad (12f)$$

The governing equation (Eq. 4) becomes:

$$\frac{\partial^2 F}{\partial r'^2} + \frac{R_e - R_i}{(R_e - R_i)r' + R_i} \frac{\partial F}{\partial r'} + \frac{\partial^2 F}{\partial z'^2} = 0 \quad (13)$$

and the boundary conditions become:

$$\frac{\partial F}{\partial z'} = 0 \quad \text{at } z' = 0 \quad (14)$$

$$\frac{\partial F}{\partial r'} = 0 \quad \text{at } r' = 1 \quad (15)$$

$$F = E \ln \left\{ 1 - \exp \left[T^* \left(\frac{\theta - 1}{\theta + \theta_c} \right) \right] \right\} \quad \text{at } r' = 0 \quad (16)$$

$$F \rightarrow -\infty \quad \text{at } z' = L \quad (17)$$

$$\frac{\partial F}{\partial r'} = -\theta \quad \text{at } r' = 0 \quad (18)$$

And the closure condition (Eq. 11) becomes:

$$L_g = \frac{N_g}{c_c \pi (R_e^2 - R_i^2)} \quad (19)$$

To find the solution, an Integral Method was employed. This method was already applied by Peterson and Tien (1989) in a study on gas-loaded thermosyphons. In the present work, a parabolic function in the radial direction was chosen. When integrated in this direction, the partial differential equation (Eq. 13) turns into an ordinary differential equation in the axial direction, which is solved numerically.

4. RESULTS AND DISCUSSION

The main parameter of interest is the radial diffusivity parameter E . Three values are considered, with each level associated to a

different value of the heat transfer coefficient between the vapor chamber and internal tube, as it can be seen in Eq. (12d).

Figure 3 shows the temperature profile of the liquid film over the water-cooled tube wall. It can be seen that, with the decrease of the heat transfer coefficient, which corresponds to the increase of E , the capacity of the NCG to diffuse also increases. When the heat input increases, the vapor mass flux inside of the chamber also increases and the vapor flow pushes the NCG to the top of the vapor chamber. As a consequence, the temperature profile of the liquid film tends to be uniform. The results were performed with the dimensionless values presented in the Table 1. The dimensionless values are evaluated with $T_e = 98.4\text{ }^\circ\text{C}$ and $T_c = 65.8\text{ }^\circ\text{C}$, and these temperatures are based on the experimental data,

Table 1. Dimensionless values.

$\theta(z'=0)$	θ_c	T^*
0.085	2.15	2.74

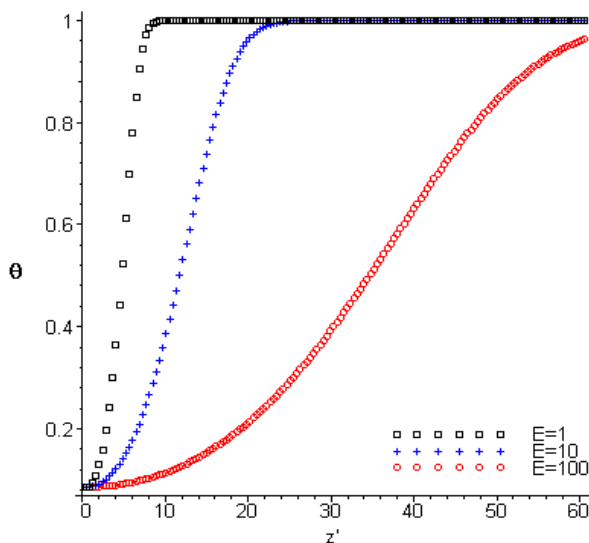


Figure 3. Dimensionless liquid film temperature profile.

The Figure 4 shows the profile of the radial variation of molar fraction of NCG, for $z = 0$. One can observe that the variation of the NCG concentration becomes sharp with the increase of the heat transfer coefficient (or the decrease of the radial diffusivity parameter E). This phenomenon occurs because the increase of heat transfer coefficient results in the increase of the vapor condensation rate. As a consequence, the NCG

tends to accumulate on the condensation surface, forming a NCG boundary layer over the condensate liquid film.

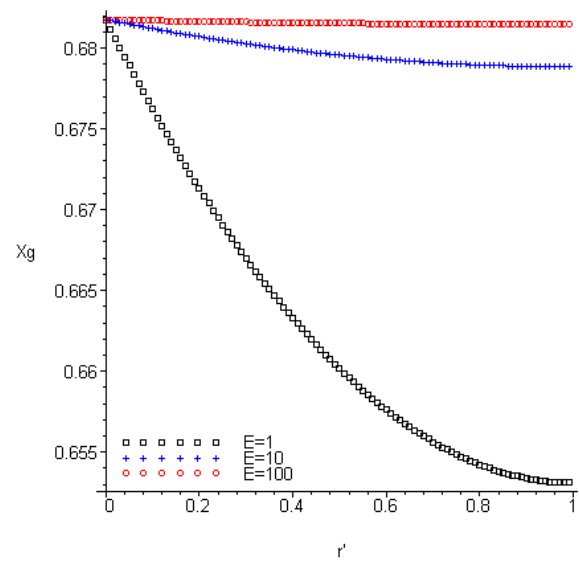


Figure 4. Radial molar fraction profile of the NCG at $z = 0$.

Figure 5 shows the NCG molar fraction profile along the axial direction, at $r' = 0.5$. Note that the NCG is accumulated at the top of vapor chamber ($z' = 0$), as expected. This effect shows clearly that the vapor pushes the NCG, forming a gas-plug at the end of the condenser. This graph also shows that, as expected, the greater the heat transfer between the vapor chamber and the internal tube is, the smaller is the space for the NCG to be confined at the top of the vapor chamber.

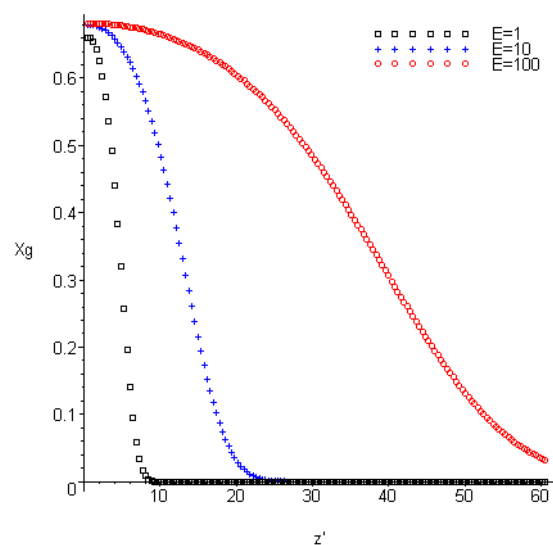


Figure 5. Axial molar fraction of gas at $r' = 0.5$.

5. CONCLUSIONS

Based on similar studies found in literature, a mathematical model was proposed to predict the NCG concentration distribution as well as the liquid film temperature profile in the condenser of a loop thermosyphon.

The model is based on Fick's Diffusion Law and is suitable to a preliminary analysis of the behavior of the vapor chamber. An analysis was performed where a dimensionless radial diffusion parameter, which is related to the condensation heat transfer coefficient, was varied.

The next step of the study is to develop a more sophisticated model taking into account the influence of the natural convection, as proposed by Peterson and Tien, (1990).

NOMENCLATURE

c_s, c_g	molar concentration of saturated steam and NCG
D	diffusion coefficient
E	dimensionless radial diffusion parameter
F	transformed molar fraction
h	heat transfer coefficient
h_{fg}	latent heat of vapor
L	height of chamber
L_g	gas length
\dot{m}	vapor mass flux
M_v	molar mass of vapor
N_g	moles of NCG
P	absolute pressure of saturated steam
R_i, R_e	internal and external radius of vapor chamber
T	absolute temperature
T^\square	characteristic temperature
\vec{V}	molar averaged velocity vector
x_g	molar fraction of NCG
δ	liquid film thickness
θ	dimensionless temperature
r', z'	transformed coordinates

Subscripts

c	flow of water-cooling tube
e	evaporator
i	interface between liquid film and vapour

ACKNOWLEDGEMENT

The authors would like to acknowledge the financial support from CENPES/PETROBRAS and CNPq in the development of this work.

REFERENCES

- Edwards, D.; Marcus, B (1972). *Heat and mass transfer in the vicinity of the vapor-gas front in a gas-loaded heat pipe*. *Journal of Heat Transfer*, Transactions ASME, vol. 94 Ser. C, No. 2, pp. 155-162.
- Faghri, A. (1995) *Heat Pipe Science and Technology*. Taylor & Francis.
- Hijikata, K.; Chen, S.; Tien, C. L. (1984) *Non-condensable gas effect on condensation in a two-phase closed thermosyphon*. *International Journal of Heat and Mass Transfer*, vol. 27, No. 8, pp. 1319-1325.
- Milanez, K. W., Tavares E. G., Milanez, F. H., Mantelli, M. B., Santos, M. C., Gomes, A. Q., Medina, L. C., (2010) *Vapor chamber with non-condensable gas applied to film distillation*, Proc. Of 15 IHPC, Clemson.
- Peterson, P. F.; Tien, C. L. (1989) *Numerical and Analytical Solutions for Two-Dimensional Gas Distribution in Gas-Loaded Heat-Pipes*. *Journal of Heat Transfer*, vol. 111, pp. 598-604.
- Peterson, P. F.; Tien, C. L. (1990) *Mixed Double-Diffusive Convection in Gas-Loaded Heat Pipes*. *Journal of Heat Transfer*, vol. 112, pp. 78-83.
- Zhou, X.; Collins, R. E. (1995) *Condensation in a gas-loaded thermosyphon*. *International Journal of Heat and Mass Transfer*, vol. 38, No. 9, pp. 1605-1617.

VISUALIZATION OF THE CONDENSATION CHARACTERISTICS IN MESH-WICKED HEAT PIPES

Wong S.-C., Tseng, H.-H., Chen, S.-H.

Department of Power Mechanical Engineering
National Tsing Hua University, Hsin-Chu 300, Taiwan, R.O.C.
886 3 5715131ext33749 (phone); 886 3 5722840 (fax)
scwong@pme.nthu.edu.tw

ABSTRACT

The condensation characteristics in sintered multi-layer mesh wicks charged with water are visualized in a flat-plate heat pipe having a glass upper wall. The cooling water temperature is fixed at 30 °C. To reduce the longitudinal conduction through the 3 mm-thick copper base plate, trenches are made across the plate and around the evaporator and the condenser to leave a local plate thickness of 0.6 mm. The effect of non-condensable gas has been carefully controlled to a low level. The condenser resistances R_c and the evaporator resistances R_e are measured at incremented heat loads Q . The water level is highest at the condenser end, attaching to the top mesh layer with the wire tops exposed. Cyclic dropwise condensation is observed on the exposed wick tops due to the finite water/copper contact angle. R_c (in Kcm^2/W) increases slightly with increasing Q and appears several times larger than R_e . The larger R_c result from the thicker liquid layer in the condenser wick and the condensed liquid layer on the wick-top condensation sites.

KEY WORDS: Condensation, heat pipe, condenser resistance, dropwise condensation, non-condensable gases

1. INTRODUCTION

The thermal resistance of a heat pipe or vapor chamber is mainly determined by its evaporator resistance and, to a lesser degree, its condenser resistance (Wang & Vafai, 2000). While intensive research has been devoted to the evaporation process and evaporator resistance associated with heat pipe wicks (Chang et al, 2008; Liou et al., 2010; Wong et al., 2010; Huang et al., 2011; Wong et al., 2011; Wong et al., 2012), the condensation process has drawn less attention. Machiroutu et al. (2006) investigated the effect of non-condensable gas (NCG) on the vapor temperature distribution over the condenser and the resultant enlargement of condenser resistance. Kempers et al. (2008) compared the heat transfer characteristics of the condenser and the evaporator of a copper-water mesh-wicked heat pipe. With an increasing heat load, the condenser resistance varied only slightly, but the evaporator resistance decreased significantly. Their experimental data also reflected significant blockage in the condenser by NCG if the water had not been degassed adequately. The length blocked by NCG decreased with increasing heat load as a result of stronger compression on the NCG toward the heat pipe end by the higher vapor pressure.

In recent years, our lab has developed an experimental technique to simultaneously visualize the evaporation process and measure the evaporator resistances of a flat-plate heat pipe (Liou et al., 2010; Wong et al., 2010; Wong et al., 2011; Wong et al., 2012). Boiling was found absent for water in mesh and powder wicks with a thickness less than 1 mm under heat loads up to at least 100 W/cm^2 . These experiments indicated that the reduction of the evaporator resistance with increasing heat load results from the thinning of liquid layer in the evaporator, rather than boiling as widely believed (e.g., Kempers et al., 2008). Furthermore, the results of Wong et al. (2012) quantitatively confirmed the argument (Chang et al, 2008; Huang et al., 2011) that the evaporator resistance is proportional to the effective liquid-wetted wick thickness, $\delta_{w,\text{eff}}$, as

$$R_e \sim \delta_{w,\text{eff}}/k_{w,\text{eff}}, [\text{Kcm}^2/\text{W}] \quad (1)$$

where $k_{w,\text{eff}}$ is the effective conductivity of the wick. Since visualization of the internal activities helps acquire deeper knowledge into the operational characteristics of heat pipes, this experimental technique is presently applied to the condensation process. The condensation behavior

will be visualized and the condenser and evaporator resistances will be measured. The differences in the condensation and evaporation processes will be explored.

2. EXPERIMENTAL METHODS

Fig. 1 shows the overall test setup. The condensation and evaporation characteristics of a flat-plate heat pipe are visualized through its upper glass window using a CCD camera equipped with a microscopic lens. The detailed structure of the heat pipe and the thermocouple locations are shown in Fig. 2. The wick has been sintered on a 3 mm-thick C1020 oxygenless copper plate under a fixed pressure in a 800 \square hydrogen/nitrogen atmosphere for 2 h. Two different wicks have been used in this study. One is a 6 \times 200 mesh wick, consisting of six layers of 200 mesh screens; the other is a 100+200 mesh wick, consisting of an upper 100 mesh screen over a 200 mesh screen. The inner space of the heat pipe is 128 mm \times 50 mm \times 5 mm. With the contact surfaces between different pieces sealed with o-rings, the whole structure, including the wicked copper base plate, the upper glass window, and stainless-steel frames, is tightened with bolts. The uniform heat load through a copper block, Q_t , is supplied by a Kapton heater attached to the bottom of the copper block. The heating area is 10 mm \times 50 mm; the water-cooled condenser area is 20 mm \times 50 mm. The cooling water temperature is fixed at 30 $^{\circ}$ C. The heating block and the base plate are insulated within a bakelite box stuffed with insulation material. The upper glass window is covered with ceramic wool except when video recording is taken. To reduce the longitudinal conduction through the 3 mm-thick copper base plate, trenches are made across the plate and around the evaporator and the condenser to leave a local plate thickness of 0.6 mm. Twelve K-type thermocouples are used to measure the temperatures at selected positions with a resolution of 0.1 $^{\circ}$ C. Among them, the temperature measured in the middle of the copper plate at the center of the heated area is denoted T1. The temperature measured at about 1 mm above the center of the evaporator is denoted T2, which reflects the vapor temperature leaving the evaporator. They are used to determine evaporation resistances. The two thermocouples T11 and T12 (10 mm apart) embedded in the heating block are used to calculate Q_t . The lateral conduction through the copper plate, Q_{cond} , is estimated using two pairs of

thermocouples embedded in the copper base plate (T6, T8 and T7, T9). The net heat load Q equals $Q_t - Q_{con}$. T3 ~ T5 measure the vapor temperatures near the condenser, with T3 and T4 in the front and T5 at the center of the condenser. T10 measures the plate temperature under T5 and the difference between T5 and T10 is used to calculate the condenser resistances.

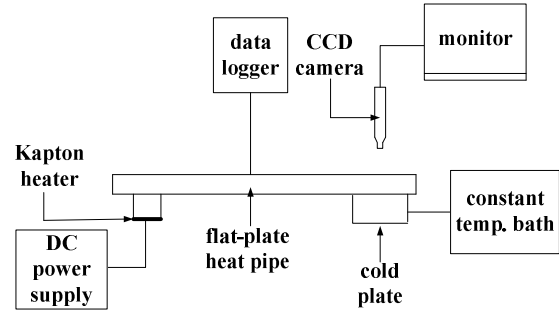


Figure 1. Overall experimental setup.

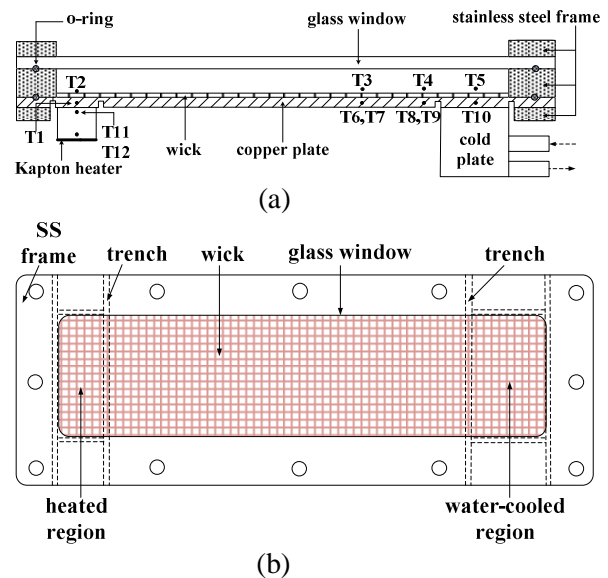


Figure 2. Heat pipe structure and thermocouple locations, (a) side cross-sectional view, (b) top view.

After sintering, the wick thickness of the 6 \times 200 and the 100+200 mesh wick is 0.52 mm and 0.26 mm, respectively. The wire diameter of the 200 mesh screen is 0.055 mm, and that of the 100 mesh screen is 0.11 mm. The porosities of both sintered mesh wicks are approximately 0.6 (Liou et al., 2010). The saturate charge to fill the wick voids are 2.0 cm³ and 1.0 cm³, respectively.

Before each test, the wick-sintered base plate has been carefully cleaned and reduced in a high-temperature hydrogen/nitrogen environment. This procedure ensures a consistent surface wettability.

The static contact angle for a sessile water drop on a reduced smooth copper plate is 10° - 12° .

De-ionized water is selected as the working fluid. To eliminate the non-condensable gas, the de-ionized water is degassed by boiling in a long-neck flask for a sufficient duration before being charged. A selected volume of degassed water is filled into the heat pipe right after the heat pipe has been evacuated down to a pressure of 8×10^{-3} Torr. The heat load is increased stepwise from a low value. Data are taken under a thermally stable condition for each heat load.

The evaporator resistance R_e and the condenser resistance R_c are determined, respectively, as

$$R_e = 1/h_e = (T1-T2)/q_e, [\text{Kcm}^2/\text{W}] \quad (2)$$

$$R_c = 1/h_c = (T5-T10)/q_c, [\text{Kcm}^2/\text{W}] \quad (3)$$

where the net heat fluxes $q_e = Q/A_e$, and $q_c = Q/A_c$, with the heated area $A_e = 5 \text{ cm}^2$ and the cooled area $A_c = 10 \text{ cm}^2$. Eqs. 2 and 3 also define the heat conductances (or convection heat transfer coefficients), h_e and h_c , of the evaporating and the condensing wick, respectively. In this study, the ratios of Q_{cond}/Q_t prior to dryout in the evaporator are less than 7%. The uncertainty in the measurements of Q_t is 5-10%, increasing with increasing heat load. This uncertainty is estimated by comparing the calculated value based on the temperature difference of T12 – T11 and the output of the DC power supply. The uncertainty in R_e is also 5-10%, since it arises primarily from those of Q , according to the definition of R_e in Eq. 2. The uncertainty in R_c is slightly larger due to the extended condensation area A_c , as will be discussed later on.

3. RESULTS AND DISCUSSION

Experiments have been conducted for two conditions: (1) 6×200 mesh wick with $v = 1.8 \text{ cm}^3$, and (2) $100+200$ mesh wick with $v = 1.2 \text{ cm}^3$. The quantitative data of temperature distribution and thermal resistances are presented only for the former case, though. Since the condensation process is very sensitive to the NCG concentration in the condenser section, each test must be very carefully conducted to restrain the NCG amount. In the following, we will first present the longitudinal temperature distributions in the vapor space and the copper base plate. It will be shown that the NCG amount could be controlled at a low level.

Then, the visualization results for the condensation on the $100+200$ mesh condenser wick will be discussed. The different features of the condensation and the evaporation process will be related to the magnitudes of R_c and R_e presented in the third part.

3.1 Temperature Distributions and NCG Effect

Fig. 3 shows the temperatures of vapor and base plate measured at various heat loads for the 6×200 mesh wick at $v = 1.8 \text{ cm}^3$. The slight drops in the vapor temperature outside the condenser result from the temperature drops in the base plate, which reflects the longitudinal conduction therein. According to the temperature readings of T6 ~ T9, $Q_{\text{cond}}/Q_t < 7\%$ in the present test. The last thermocouple, locating above the condenser center, gives slightly lower temperatures than those given by the thermocouple next to it. Besides the influence from the base plate, this may be partially attributed to the presence of NCG, which came into the chamber via different routes. First, a very small amount of NCG remained in the chamber after the evacuation down to 8×10^{-3} Torr. But this is estimated to be negligible. Second, it came with the fill water as a residue after degassing. Thirdly, air leaked in through the interfaces between the o-rings and the structural pieces over the three-hour test duration. The NCG effect may be roughly estimated by assuming that the temperature differences between the last two thermocouples are totally caused by NCG. In fact, they should be partially caused by the cooler base plate. Even so, the NCG effect on R_c should be limited since it contributes at most 10% of the values of (T5 – T10) (cf. Eq. 3).

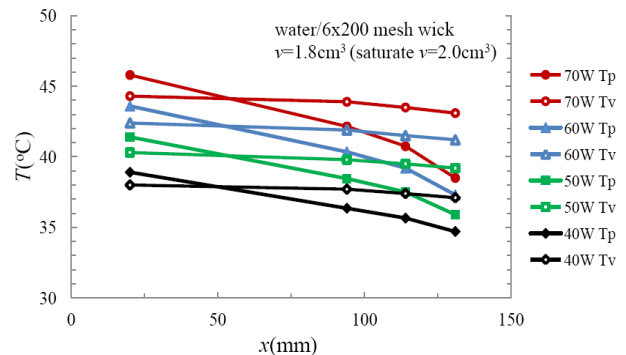


Figure 3. Temperature distributions in the vapor and the base plate at various heat loads.

3.2 Visualized Condensation Characteristics

Fig. 4 shows the typical condensation process on the $100+200$ mesh wick at $v = 1.2 \text{ cm}^3$ and $Q = 18$

W. The water can be seen to flood to the top mesh layer. Cyclic dropwise condensation is observed on most of the exposed wire tops. In Fig. 4a, a large water drop has formed on the wire top. After 2.24 s, two more drops have evolved and the first drop has grown larger (Fig. 4b). These drops keep growing (Fig. 4c) until they coalesce and rupture (Fig. 4d). Shortly afterward, new small drops evolve at the site (Fig. 4e, f). Some large drops sustain a rather long time before rupture. Near the the meniscus edge, there are always quicker cyclic condensation activities of small drops. For the 6×200 mesh wick which provides smaller individual sites, the small-ranged activities are more often observed than distinct drop cycles.

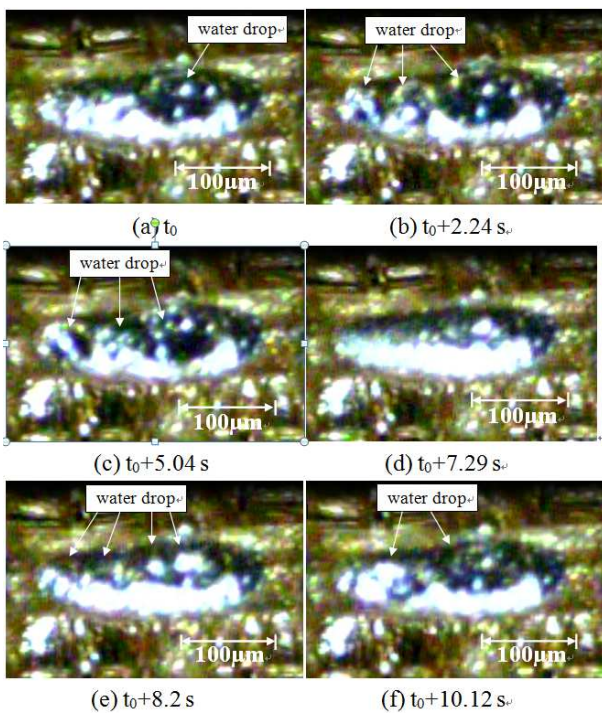


Figure 4. Sequential images of dropwise condensation on an exposed wire top of the 100+200 mesh wick.

The water level is highest at the condenser end, attaching to the top mesh layer with the wire tops exposed. In the direction toward the evaporator, the water layer depth decreases little by little. It is noted that weak condensation could be observed shortly (within 20 mm) in front of the water-cooled region because the 0.6 mm trenched plate thickness could not completely eliminate the longitudinal conduction in the base plate. This phenomenon would slightly affect the quantitative reliability of the measured values of condenser resistance. However, the condensation rates outside the cooled

region are limited, according to the fact that $Q_{\text{cond}}/Q_t < 7\%$ near the condenser region.

3.3 Condenser and Evaporator Resistances

Fig. 5 compares the R_c and R_e versus Q for the case of 6×200 mesh wick. In this case, the liquid charge of $v = 1.8 \text{ cm}^3$ is slightly less than the saturate value of 2.0 cm^3 . It is noted that a small portion of the working fluid is trapped in the chamber crevices or on the chamber walls. Further because water tends to accumulate in the condenser, the water in the evaporator keeps at a low level, leading to low R_{eS} of about $0.1 \text{ Kcm}^2/\text{W}$ (corresponding to $h_e \sim 100,000 \text{ W/cm}^2\text{K}$). At $Q = 58 \text{ W}$, dryout has occurred in the evaporator to lead to a slight increase in R_e . In contrast, R_c grows slightly from 0.63 to $0.74 \text{ Kcm}^2/\text{W}$ ($h_c = 13,500 \sim 15,900 \text{ W/cm}^2\text{K}$) with increasing Q .

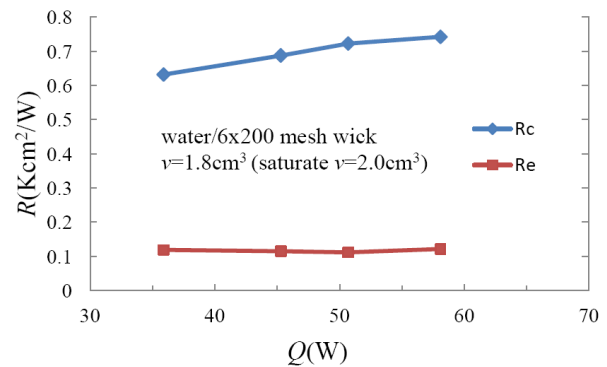


Figure 5. Condenser resistances and evaporator resistances versus heat load for a 6×200 mesh wick with a water charge of 1.8 cm^3 .

Fig. 6 schematically compares the heat transfer mechanisms respectively in the evaporator and the condenser. In the evaporator, thin liquid film are formed on the interlines between the concave menisci and the copper wires. Over these extremely narrow regions, very efficient evaporation prevails. Most of the evaporation goes through the thin films and the remaining through the adjacent non-thin films (Ranjan et al., 2009; Wong et al., 2012). Since the thin-film evaporation presents negligible resistances, $R_e \sim \delta_{w,\text{eff}}/k_{w,\text{eff}}$ (Eq. 1). In the present under-charged condition, R_e maintains near a low value. In the condenser, however, water drops grows and breaks cyclically on the exposed wire tops. The sub-micron thin films prevailing in the evaporator are not likely present in the condenser, except at the instance of drop rupture. In fact, dropwise condensation occurs on the wire surfaces as a result of finite contact

angles, which are larger than the static value of $10\text{--}12^\circ$ with the dynamic nature of condensation. The formation of water drops, especially when they become large, presents additional thermal resistance to that associated with the wick thickness. On the other hand, however, the active condensation area covers all the exposed parts of the wick, much larger than the small active evaporation area associated with the thin-film interlines. With both negative and positive factors, the present data indicate a slight increase of R_c with Q . This trend may be related to the thicker water layers on the wire tops at higher condensation rates. To approximately estimate the δ_w -portion in the total R_c , we take $k_{w,\text{eff}} = 16 \text{ W/mK}$ from our previous measurement for a sintered two-layer 2×100 mesh wick (Liou et al., 2010). With $\delta_w \sim 0.52 \text{ mm}$, a corresponding value of $0.33 \text{ Kcm}^2/\text{W}$ is obtained. The rest part in the measured R_c s is attributed to the condensing drops on the exposed wires as well as the NCG. As discussed earlier, the latter may occupy only about 10% of the total R_c values. In terms of h_c and h_e , h_c is generally several times smaller than h_e . The common knowledge that the condenser resistances are smaller than the evaporator resistances (in units of K/W) is a consequence of the much larger condensation areas in usual applications.

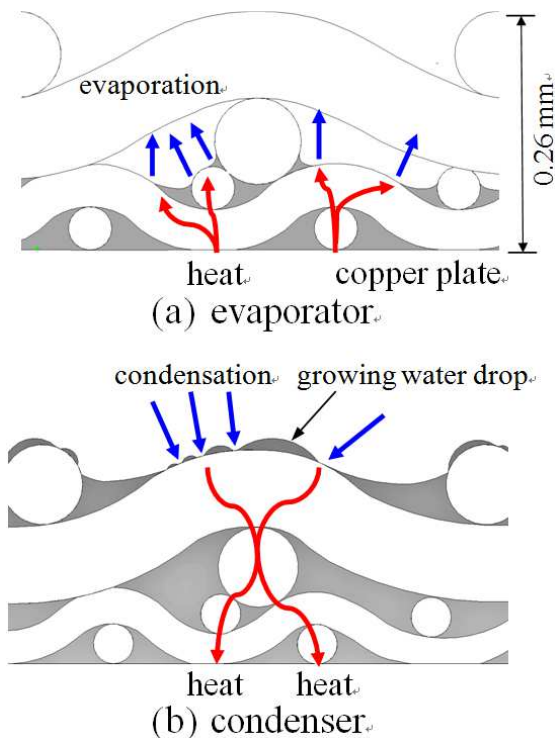


Figure 6. Schematic comparison of the condensation and the evaporation mechanism in the 100+200 mesh wick.

4. CONCLUSIONS

Visualization experiment on the condensation process in a flat-plate heat pipe has been conducted with the condensation heat flux ranging between $3.6 \sim 5.8 \text{ W/cm}^2$. Sintered multi-layer copper mesh wicks were adopted to work with water. The NCG effect was carefully controlled to a low level. The following conclusions are reached:

1. Cyclic dropwise condensation is observed on the exposed wick-top sites, due to the finite water/copper contact angle.
2. The condenser resistance increases slightly with increasing heat load, probably due to the growing average thickness of the condensed liquid layer on the condensation sites.
3. In a mesh-wicked heat pipe, the condenser resistance (in Kcm^2/W) is larger than the evaporator resistance. This is because the liquid layer is thicker in the condenser and an additional condenser resistance is caused by the condensed liquid layer on the condensation sites.
4. In mesh-wicked heat pipes, the heat conductances of the condenser can be several times smaller than those of the evaporator.

Our future work will consider the effects of different wick types and different working fluids, etc.

NOMENCLATURE

A	area
h	heat conductance [$\text{W/m}^2\text{K}$]
k	thermal conductivity
Q	net heat load [W]
Q_{cond}	conduction through base plate [W]
Q_t	total heat load [W]
q	heat flux [W/cm^2]
R	thermal resistance [Kcm^2/W]
T	temperature; thermocouple
v	volumetric fluid charge
x	distance from the evaporator end

Greek symbols

δ	flooded-wick thickness
----------	------------------------

Subscripts

c	condenser
e	evaporator
eff	effective
p	plate
v	vapor
w	wick

ACKNOWLEDGEMENT

This work was financially supported by National Science Council, ROC under Contract NSC99-2221-E-007-029-MY2.

REFERENCES

- Chang, J.-Y., Prasher, R.S., Prstic, S., Cheng, P., Ma, H.B. (2008) *Evaporative thermal performance of vapor chambers under nonuniform heating conditions*. ASME Journal of Heat Transfer 130, 121501
- Chi, S.W. (1976) *Heat Pipe Theory and Practice*, McGraw-Hill, New York
- Hwang, G.S., Fleming, E., Carne, B., Sharratt, S., Nam, Y., Dussinger, P., Ju, Y.S., Kaviany, M. (2011) *Multi-artery heat-pipe spreader: Lateral liquid supply*. Int. J. Heat Mass Transfer 54, p. 2334-2340
- Kempers, R., Robinson, A.J., Ewing, D., Ching, C.Y. (2008) *Characterization of evaporator and condenser thermal resistances of a screen mesh wicked heat pipe*. Int. J. Heat Mass Transfer, 51, p. 6039–6046
- Liou, J.-H., Chang, C.-W., Chao, C., Wong, S.-C. (2010) *Visualization and thermal resistance measurement for the sintered mesh-wick evaporator in operating flat-plate heat pipes*. Int. J. Heat and Mass Transfer, 53, p. 1498-1506
- Machiroutu, S., Kluge, B., Kuroda, M., Pokharna, H. (2006) *Evaluation of heat pipe condenser performance for laptop cooling*, Proc. 8th Int. Heat Pipe Symp., Kumamoto, Japan.
- Ranjan, R., Murthy, J.Y., Garimella, S.V. (2009) *Analysis of the wicking and thin-film evaporation characteristics of microstructures*. ASME J. Heat Transfer, 131, 101001
- Wang, Y., Vafai, K. (2000) *An experimental investigation of thermal performance of an asymmetrical flat plate heat pipe*. Int. J. Heat Mass Transfer, 43, p. 2657-2668
- Wong, S.-C., Liou, J.-H. and Chang, C.-W. (2010) *Evaporation resistance measurement with visualization for sintered copper-powder evaporator in operating flat-plate heat pipes*. Int. J. Heat and Mass Transfer, 53, p. 3792-3798
- Wong, S.-C., Lin, Y.-C., Liou, J.-H. (2012) *Visualization and evaporation resistance measurement in heat pipes charged with water, methanol or acetone*. Int. J. Thermal Sci., 52, p. 154-160

EXPERIMENTAL INVESTIGATION OF TWO-PHASE CLOSED THERMOSYPHON WITH INTERNAL HELICAL MICROFIN

Xinyu Wang^a, Gongming Xin^b, Yifei Wang, Lin Cheng^c

Institute of Thermal Science and Technology, Shandong University

Address: Mailbox 88, No. 17923 Jingshi Road, Jinan, P. R. China, 250061

Phone: +86-531-88399598 Fax: +86-531-88393000

Email: ^a wangxy8831@hotmail.com, ^b xingm@sdu.edu.cn, ^c cheng@sdu.edu.cn

ABSTRACT

The present study investigates experimentally the heat transfer performance of two-phase closed thermosyphons with internal helical microfin. All tested thermosyphons had the length of 1500 mm with the outer diameter of 9.52 mm. The working fluid was distilled water and the filling ratio ranged from 30% to 90%. The condensation heat transfer coefficients of these novel thermosyphons were investigated and compared with conventional thermosyphon under different operating parameters, including heat input, inclination angle, cooling water flow rate and filling ratio. The results show that the internal helical microfins can improve the condensation heat transfer coefficient by 117% for the higher heat input. The maximum condensation heat transfer coefficient occurs at different inclination angles for different thermosyphons with different filling ratios. The cooling water flow rate has a greater influence on the condensation heat transfer coefficient for the filling ratio of 30%, and less for thermosyphons with higher filling ratios. Under the identical condition of heat input, the thermosyphon with lower filling ratio presents the higher condensation heat transfer coefficient.

KEY WORDS: thermosyphon, internal helical microfin, heat transfer enhancement

1. INTRODUCTION

The heat pipe has been regarded as one of the most efficient heat transfer devices. The two-phase closed thermosyphon (TPCT) is a gravity assisted wickless heat pipe, which returns the condensate from the condenser section to the evaporator section under the effect of the gravity (Madam, 1983, Zhang, 2003). A two-phase closed thermosyphon consists of three sections: evaporator section, adiabatic section and condenser section, as shown in Fig. 1.

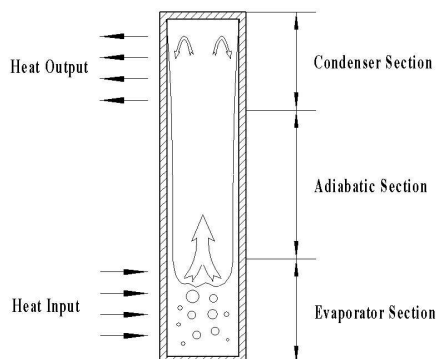


Fig. 1. Schematic of two-phase closed thermosyphon

Heat transfer coefficient and heat transfer limitation are two criteria that evaluate the heat

transfer performance of TPCT. And the structure of TPCT is one of factors determining these criteria. Thus, many scholars ameliorated the heat transfer performance by the method of modifying the structure, such as inserting the inner pipe, inner surface treatment.

Khalid et al. (1999) modified heat pipes with a separator in the adiabatic section and a three layered wick in the evaporator section. He et al. (2009) designed and manufactured an innovative gravity heat pipe with internal circulating pipe which is helpful to improve the heat and mass transfer performance and the working temperature of the heat pipe. Masoud et al. (2010) modified surfaces in the evaporator and condenser internal walls more hydrophilic to enhance the heat transfer rate. Wang et al. (2009) and Tang et al. (2010) developed a novel micro grooves fabrication technique to improve the performance of the heat pipe.

In this study, the authors machine the internal helical microfins in the inner surface of TPCT. The condensation heat transfer performance of a new type of two-phase closed thermosyphon with internal helical microfin (TPCTIHM) is investigated at different filling ratios.

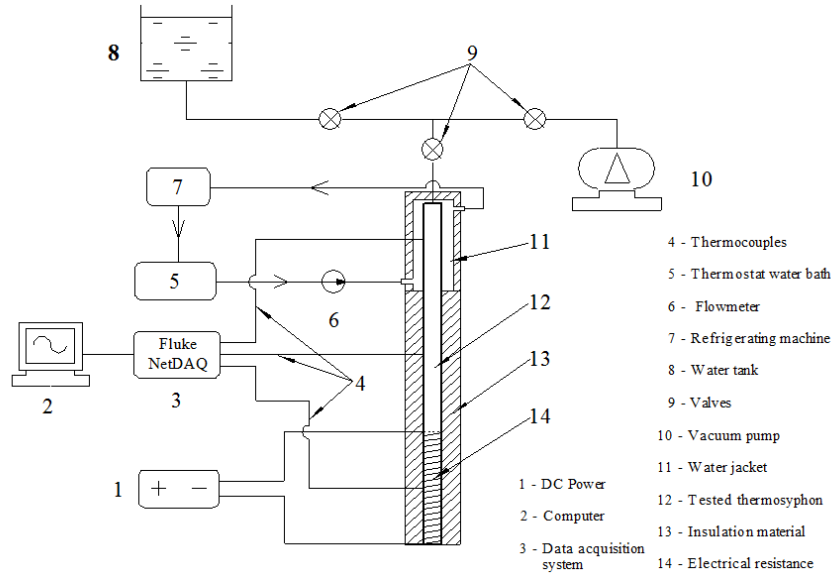


Fig. 2. Schematic diagram of experimental apparatus

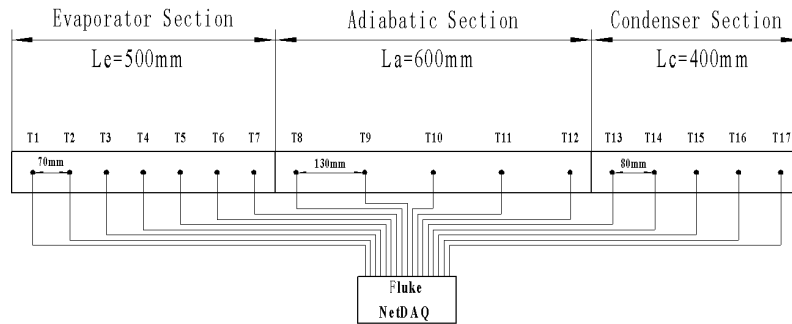


Fig. 3. Location of thermocouples

2. EXPERIMENTAL APPARATUS

Fig. 2 shows the schematic diagram of the experimental apparatus. It includes tested thermosyphon, heat input system, cooling system, charging system, data acquisition system.

The tested thermosyphons are fabricated with copper tubes, having a length of 1500 mm. The length of evaporator, adiabatic and condenser section is maintained constantly at 500 mm, 600 mm and 400 mm, respectively. The working fluid is distilled water. The filling ratio (FR), defined as the ratio of the working fluid volume to the evaporator section volume, varies from 30% to 90%. Insulation materials are used to reduce heat loss to the surroundings. The details of thermosyphons are listed in Table 1.

The heat input is supplied by DC Power. The heat input is calculated from the Eq. (1):

$$Q_{in} = V \cdot I \quad (1)$$

The condenser section is surrounded by a water jacket in which the cooling water powered by a

refrigerating unit takes away the heat output. The inlet temperature of cooling water is kept at $20 \pm 0.5 \text{ }^\circ\text{C}$ by a thermostat water bath during all the experiments. The heat output is determined by the Eq. (2):

$$Q_{out} = \rho_{H_2O} \cdot c_{pl} \cdot \tilde{V} \cdot (T_{out} - T_{in}) \quad (2)$$

As shown in Fig. 3, 17 thermocouples are arranged along the outer surface of the thermosyphon in order to measure the temperature distribution. The other two thermocouples are set in the inlet and outlet of the water jacket to measure the temperature of the cooling water, respectively. The FlukeNet DAQ data acquisition system is applied to collect the experimental data.

The condensation heat transfer coefficient (h_c) is calculated from the Eq. (3):

$$h_c = \frac{Q_{out}}{\pi d_i L_c (T_{sat} - T_c)} \quad (3)$$

The average temperature of the adiabatic section is considered as the saturation temperature (operating temperature) of the thermosyphon. Considering the thermosyphon is surrounded by the insulation materials, the heat loss to the surrounding is ignored. The uncertainty in this study is $\pm 2\%$ for heat input, $\pm 1.5\%$ for flow rate, $\pm 0.5\text{ }^\circ\text{C}$ for temperature.

The investigated parameters in this study include heat input, inclination angle, cooling water flow rate, filling ratio. The range of these parameters is as following:

➤ Heat input (Q_{in}) (W) : 80, 120, 160, 200, 240,

280, 320

- Inclination angle (IA) ($^\circ$) : 15, 30, 45, 60, 75, 90
- Cooling water flow rate (\tilde{V}) (L/h) : 20, 50, 80, 110
- Filling ratio (FR) (%) : 30, 45, 60, 75, 90

At first, the thermosyphon is supplied under the pressure of 2.0×10^{-4} Pa by the vacuum pump. And then the designed amount of distilled water is charged into the thermosyphon. The experimental data used in this study is obtained after the steady condition is established. Each experiment takes more than 60 minutes.

Table 1 Details of tested thermosyphons

Thermosyphon	Inner surface	Filling ratio	Outer diameter (mm)	Thickness (mm)	Helical angle ($^\circ$)	Microfin height (mm)	Microfin number
TPCT1	smooth	60%	9.52	0.6	—	—	—
TPCTIHM1	internal helical microfin	30%		0.4	18	0.2	60
TPCTIHM2		45%					
TPCTIHM3		60%					
TPCTIHM4		75%					
TPCTIHM5		90%					

3. RESULTS AND DISCUSSION

3.1 Influence of heat input

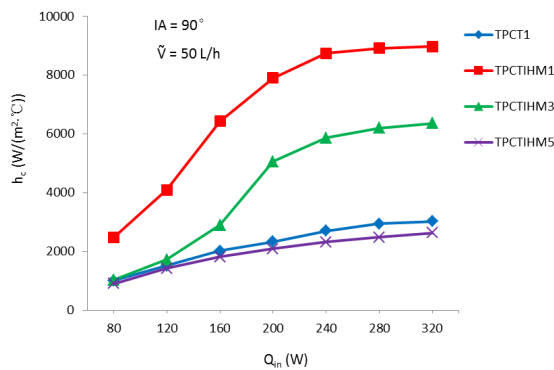


Fig. 4. Influence of heat input on condensation heat transfer coefficient

As shown in Fig. 4, the h_c of TPCT1, TPCTIHM1, TPCTIHM3, and TPCTIHM5 varies with the increasing heat input. Obviously, there is a gradual growth in the h_c when the heat input increases from 80 W to 320 W.

Under the same filling ratio (FR = 60%), the h_c of TPCTIHM3 is higher than that of TPCT1. This increase is very slight at the lower heat input, while at $Q_{in} \geq 240$ W, the h_c of TPCTIHM3 increases 117% in comparison with TPCT1. This enhancement is probably because the internal helical microfins ameliorate the heat transfer

performance of inner surface, such as thinning the fluid film, improving the heat transfer area, yielding the local secondary flow.

According to this figure, the h_c of TPCTIHM1 is obviously higher than that of TPCTIHM3, while the h_c of TPCTIHM5 is lower than that of TPCTIHM3. This result illustrates that the lower the filling ratio of TPCTIHM is, the larger the condensation heat transfer coefficient is.

3.2 Influence of inclination angle

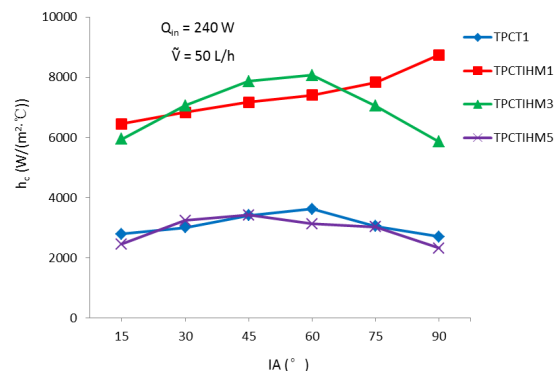


Fig. 5. Influence of inclination angle on condensation heat transfer coefficient

The influence of the inclination angle on h_c is investigated at six inclination angles ranging from

15° to 90° for $Q_{in} = 240$ W and the results are shown in Fig. 5.

When the angle varies from 15° to 90°, the TPCTIHM3 presents a similar trend but a enhanced coefficient, compared to TPCT1. And the maximum heat transfer coefficient of TPCTIHM3 and TPCT1 occurs at 60°, which is regarded as the optimum inclination angle.

For the TPCTIHM1, the h_c keeps on increasing with the inclination increasing. However, the h_c of TPCTIHM5 is similar to that of TPCT1. The optimum inclination angle of TPCTIHM5 is between 30° and 45°.

These phenomena may arise from the comprehensive effect of two factors, namely the gravity and the shear forces of the returning condensate and the rising vapor. These two factors' combination yields an optimum angle. For the TPCTIHM1, the working fluid is relatively little. Thus the thermosyphon needs the returning condensate to supply the working fluid in the evaporator section quickly, in order to maintain the steady operation of the thermosyphon. The effect of gravity for the lower filling ratio at higher inclination angles is predominant. Whereas, the higher filling ratio in the thermosyphon leads to the larger shear forces. The diminish of inclination angle makes for the delamination of the condensate and vapor, which decreases the shear forces and increases the heat transfer coefficient.

3.3 Influence of cooling water flow rate

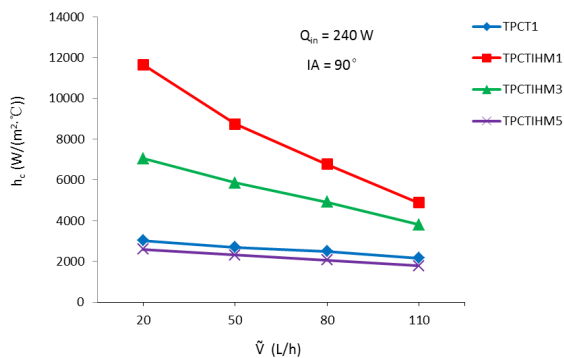


Fig. 6. Influence of cooling water flow rate on condensation heat transfer coefficient

Fig. 6 demonstrates the change of the h_c with respect to cooling water flow rate under $Q_{in} = 240$ W. The h_c decreases with the increasing cooling water flow rate from 20 L/h to 110 L/h. Fig. 6 illustrates that the cooling water flow rate makes a great difference for the h_c . Moreover, the lower the filling ratio is, the more evident the influence is.

This is probably due to the average temperature of the condenser section influenced by the cooling water flow rate. When the filling ratio is very low, the vapor in the condenser section is insufficient. Thus the large cooling water flow rate makes the vapor condense rapidly, resulting in the low average temperature of the condenser section and making the h_c decreases. On the contrary, for the high filling ratio under the same heat input, increasing the cooling water flow rate cannot make the vapor condensate rapidly, which is the result of sufficient vapor in the condenser section.

3.4 Influence of filling ratio

The influence of five different filling ratios on the h_c is investigated for $Q_{in} = 80$ W, 200 W, 320 W. From Fig. 7, it can be seen that this kind of effect on the h_c becomes more and more evident as the heat input increases.

Under the identical heat input, the h_c decreases gradually, with the increasing of filling ratio from 30% to 90%. The influence is more evident for lower heat input. This may be due to the fact that the condensate is difficult to return to evaporator section because of the large shear forces, which enlarges the temperature difference between the adiabatic section and condenser section. For lower filling ratios, the working fluid circulates in the thermosyphon rapidly under the same heat input, and the temperature difference between the adiabatic and condenser section is relatively little, which produces the high condensation heat transfer coefficient.

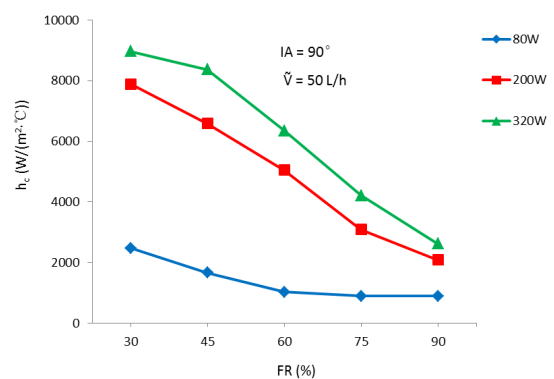


Fig. 7. Influence of filling ratio on condensation heat transfer coefficient

4. CONCLUSIONS

Experimental investigations on a series of two-phase closed thermosyphons with internal helical microfin were performed and compared with conventional thermosyphon. Main conclusions are as following: The internal helical microfins can

ameliorate the condensation heat transfer performance of the thermosyphon. The TPCTIHM with lower filling ratio presents a higher heat transfer coefficient. The thermosyphons at different filling ratios have different optimum inclination angles. But the maximum heat transfer coefficient of both TPCTIHM3 and TPCT1 is achieved at 60°. The effect of cooling water flow rate on the TPCTIHM with lower filling ratio is more distinct. Under the identical heat input, the condensation heat transfer coefficient presents a decreasing trend with the filling ratio increasing from 30% to 90%.

NOMENCLATURE

c_p	specific heat at constant pressure (J/kg·°C)
d	diameter (m)
FR	filling ratio (%)
g	acceleration due to gravity (m/s ²)
h	heat transfer coefficient (W/m ² ·°C)
I	current (A)
IA	Inclination angle (°)
L	length (m)
Q_{in}	heat input (W)
Q_{out}	heat output (W)
T	temperature (°C)
T_c	average temperature of condenser section (°C)
T_{in}	inlet temperature of cooling water (°C)
T_{out}	outlet temperature of cooling water (°C)
T_{sat}	saturation temperature (°C)
V	voltage (V)
\tilde{V}	flow rate of cooling water (L/h)

Greek symbol

ρ	density (kg/m ³)
--------	------------------------------

Subscripts

c	condenser section
i	inner
l	liquid
sat	saturation
v	vapor

ACKNOWLEDGEMENT

The authors are greatly appreciative for supports of National Natural Science Foundation of China (Grant No.51106089) and Shandong Provincial Program of Science and Technology Development (Grant No. 2007GG1HZ06004)

REFERENCES

He Shu, Xia Zaizhong, Wang Ruzhu (2009) *Heat Transfer Characteristics of an innovative gravity*

heat pipe. Journal of Engineering Thermophysics (In Chinese), 30(5), p. 834-836

Hong Zhang, Jun Zhuang (2003) *Research, development and industrial application of heat pipe technology in China*. Applied Thermal Engineering, 23(9), p. 1067-1083

Khalid A. Joudi, A.M. Witwit (1999) *Improvements of gravity assisted wickless heat pipes*. Energy Conversion & Management, 41(18), p. 2041-2061

Madam MY,Hou ZQ, Wu WG (1983) *Heat pipe*. Science Press, Beijing

Masoud Rahimi, Kayvan Asgary, Simin Jesri (2010) *Thermal characteristics of a resurfaced condenser and evaporator closed two-phase thermosyphon*. International Communications in Heat and Mass Transfer, 37(6), p. 703-710

Tang Yong, Chen Ping, Wang Xiaowu (2010) *Experimental investigation into the performance of heat pipe with micro grooves fabricated by Extrusion-ploughing process*. Energy Conversion & Management, 51(10), p. 1849-1854

Wang Xiaowu, Tang Yong, Chen Ping (2009) *Investigation into performance of a heat pipe with micro grooves fabricated by extrusion-ploughing process*. Energy Conversion & Management, 50(5), p. 1384-1388

LOOP THERMOSYPHON FOR THE THERMAL MANAGEMENT OF AN AIRCRAFT ELECTRONIC BOX

C. Sarno, C. Tantolin, R. Hodot

Thales Avionics, 25 rue Jules Védérines, 26027 Valence Cedex France
Tel +33475798657, Fax +33475798606, claude.sarno@fr.thalesgroup.com

Yu. Maydanik, S. Vershinin

Institute of Thermal Physics, Ural Branch of the Russian Academy of Sciences
Amundsen St. 106, Ekaterinburg, 620016, Russia
Phone +7(343) 2678791, Fax +7(343) 2678799, maidanik@etel.ru

ABSTRACT

A new generation of in-flight entertainment systems (IFEs) used on board commercial aircrafts is required to provide more and more services (audio, video, internet, multimedia, phone, etc.). But, unlike other avionics systems most of the IFE equipment and boxes are installed inside the cabin and they are not connected to the aircraft cooling system. The most critical equipment of the IFE system is a seat electronic box (SEB) installed under each passenger seat. Fans are necessary to face the increasing power dissipation. But this traditional approach has some drawbacks: extra cost multiplied by the number of seats, reliability and maintenance. The objective of this work is to develop and evaluate an alternative completely passive cooling system (PCS) based on a two-phase technology including heat pipes and loop thermosyphons (LTSs) adequately integrated inside the seat structure and using the benefit of the seat frame as a heat sink. Previous works have been performed to evaluate these passive cooling systems which were based on Loop Heat Pipe. This paper presents results of thermal tests of a passive cooling system of the SEB consisting of two LTSs and R141b as a working fluid. These tests have been carried out at different tilt angles and heat loads from 10 to 100 W. It has been shown that the cooled object temperature does not exceed the maximum given value in the range of tilt angles $\pm 20^\circ$ which is more wider than the range which is typical for ordinary evolution of passenger aircrafts.

KEY WORDS avionics; in-flight entertainment system; loop thermosyphon; cooling system

1. INTRODUCTION

A new generation of in-flight entertainment systems (IFEs) used on board commercial aircrafts is required to provide more and more services (audio, video, internet, multimedia, phone, etc.). Most of the IFE equipments and boxes are installed inside the cabin and they are not connected to the aircraft cooling system. One of the most critical equipment of the IFE system is a seat electronic box (SEB) installed under each passenger seat. The SEB may be buried in small enclosed zones with limited natural convection cooling capabilities. In order to face the increasing power dissipation of the SEB, one of the solutions is to use fans. But this traditional approach has some drawbacks: extra cost when multiplied by the seat number, reliability and maintenance, risk of blocking by passengers belongings, additional energy consumption, and noise effects disturbance in the overall cabin area. For example, the challenge for the A380 (800 seats) would be to avoid the use of

thousand of fans. Thus it is necessary to find alternative ways for the thermal management of the SEB. The objective of this work is to evaluate solutions based on two-phase technologies including a heat pipe (HP) [1] and a loop thermosyphon (LTS) [2-5]. The HP will be used between the dissipative components and the SEB wall whereas the LTS will be used between the SEB wall and the seat structure. The seat will then act as a natural heat sink which will allow to dissipate the heat to the ambient air.

With the increase of heat densities following Moore's law, we will face tremendous new challenges in which components heat densities are surpassing 10 W/cm^2 and will reach 100 W/cm^2 . It is necessary to use novel technologies which will be able to offer alternate solutions and which will be compatible with high-integrated electronics. European collaboration research programs have been launched on both civil and military sides about the thermal management. One of the most promising and investigated route involves phase

change systems like a heat pipe, a loop heat pipe (LHP) [6] and a loop thermosyphon.

Heat pipes are compatible with the cooling of the component inside the SEB. Indeed they will be used to transfer the heat from the component to the SEB wall. According to the SEB dimensions (about 250x250x40mm), it means that the HP length will be around 100 to 150 mm. According to Peterson [7], these dimensions are compatible with the standard heat pipe length. The HP technology cannot be used to transfer the heat from the SEB wall to the seat. Indeed, depending of the seat structure, the length of the HP would be between 500 and 1000 mm. Furthermore, the condenser portion of the two-phase system needs to be in close contact with the seat structure which has a quite complex shape. As explained by Maydanik [6] LHP and LTS [8] are perfectly adapted to this kind of application: they have the ability to transfer heat efficiently for fairly large distance, they possess high mechanical flexibility owing to the small diameter of liquid and vapor lines, the condenser has dimensions and shapes that adapt easily to the geometrical constraints of the heat sink and specifically, in our application, to the shape of the seat structure. The LTS will be used between the SEB wall and the seat structure, and it will not compromised the seat integrity as it is a small light weight part which will be properly attached.

Previous works [9-10] were performed with the use of LHP in the Project of Cooling of Seat Electronic Box and Cabin Equipment (COSEE) in the frame of the 6th European Framework Programme . The measurements exhibit a strong improvement in the thermal management of the SEB with a temperature reduction of 50% of the temperature rise. In the present work the LHP have been replaced with LTS. Indeed for some seat architecture, the SEB (and then the evaporator part of the LTS) are always placed under the condenser. This configuration is encountered in most of the operating position of the system. In this case, the LHP can be easily replaced by a LTS which is less complex and can be produced at an affordable cost for mass production.

2. DESCRIPTION OF THE EXPERIMENTAL DEVICE

2.1 Loop thermosyphon description

Loop thermosyphons are passive systems which allow to transport large amount of heat over large distance with small temperature difference between the evaporator and the condenser. These

characteristics are explained by the separated flow of liquid and vapor in the liquid line and in the vapor line respectively. The characteristics of the LTSs tested are given in Table 1.

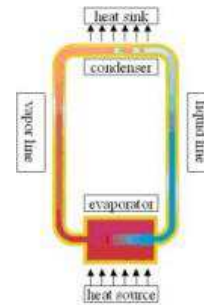


Fig. 1. The LTS scheme

The LTS, which is presented in Figure 2, has a cylindrical evaporator. In order to ensure a good thermal contact with the SEB wall, the evaporator is brazed on a copper interface. In the same way, the LTS condenser is brazed on a semi-cylindrical aluminum sheet having 1.5 mm thickness, 50 mm diameter and 350 mm length which correspond to the diameter of the main cross beam of the seat.

Parameter	LTS1	LTS2
Evaporator diameter (mm)	10	10
Evaporator length (mm)	100	100
Vapor line diameter (mm)	2.6	2.6
Vapor line length (mm)	200	400
Liquid line diameter (mm)	2.6	2.6
Liquid line length (mm)	100	300
Condenser diameter (mm)	2.6	2.6
Condenser length (mm)	600	600
LTS overall length (mm)	700	700
<u>Materials</u>		
Evaporator	SS	SS
Porous	Nickel	Nickel
Condenser	SS	SS
Vapor line / Liquid line	SS	SS
Working fluid	R141b	R141b

Table 1. Main parameters of tested LTSs



Figure 2. View of the LTS

2.2 Seat description

The LTS cooling system is tested on a triple seat, given in Figure 3, provided by RECARO in the frame of the COSEE EFP6 project. This seat has an aluminum structure which is composed of two main crossbeams. The LTS condensers are screwed on these crossbeams with the use of thermal grease as thermal interface material. The measurements performed show that the temperature difference is negligible across the thermal interface. This study has also been done on carbon reinforced material seats, which could be used in the coming years. The system did not behave as well thanks to the low thermal conductivity of the carbon seats, but it still showed promising results.

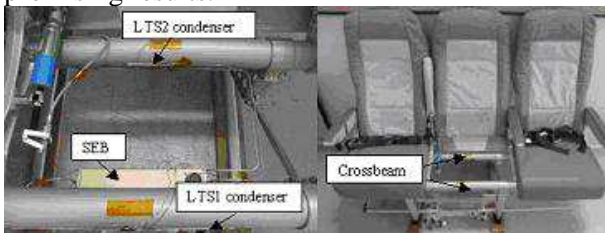


Figure 3. Views of seat

2.3 SEB description

The SEB is made of aluminum sheets having 1.5 mm thickness. It contains two PCB (Printed Circuit Board) which are screwed on the SEB wall. These PCBs are populated with resistive components in order to have a good management of the dissipated power: we use 32 TO220 packages to simulate diffuse heat load and 2 PQFP (Plastic Quad Flat Pack) packages to simulate hot spots. Figure 4 presents the view of the Printed Circuit Board (PCB). Heat pipes are mounted inside the SEB in order to transfer the heat from the component to the SEB wall. These are copper-water heat pipes having 4 mm external diameter. They are bent and brazed on nickel-coated aluminum blocks in order to manage the thermal interface between the heat pipe and the component or between the heat pipe and the SEB wall. Thermal interface materials (0.16 mm thickness, 3.6 W/m.K thermal conductivity) are used on each of the thermal interfaces. Two heat pipes are directly mounted on the PQFP components to manage the hot spots thermal dissipation (view top) and two heat pipes are reported on the PCB via a thermal pad (3 mm thickness, 10 W/m.K thermal conductivity) to manage the diffuse dissipated power (view bottom).

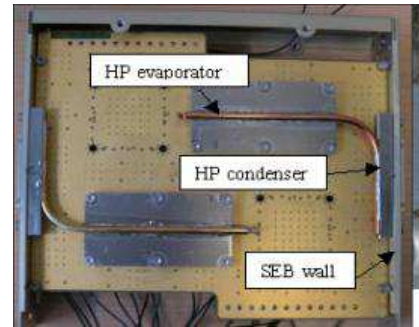


Figure 4. Top view of the PCB

The overall dissipated power reaches 100 W on the SEB (50 W on each PCB).

The SEB external view is demonstrated in Figure 5. The SEB is cooled with two LTSs. The LTS evaporators are mounted outside the SEB in regard to the condenser of the HP. One LTS condenser is linked to the rear crossbeam (LTS2) of the seat whereas the second LTS condenser (LTS1) is linked to the front crossbeam of the seat (see Figure 3).

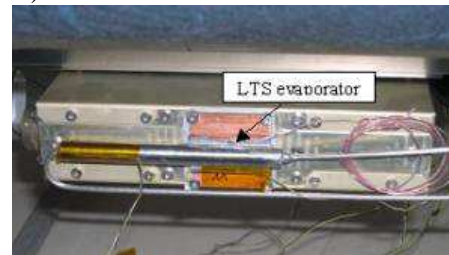


Figure 5. Bottom view of the SEB

3. STATIC TEST RESULTS

3.1 Horizontal measurements

The tests are performed at an ambient temperature of 25°C. Figure 6 shows that the stabilization time is reached after 1 hour. This high time constant is mainly linked to the diffusion process inside the crossbeam and to the thermal inertia of the seat structure. LTS1 and LTS2 exhibit similar thermal behavior. LTS2 and the front crossbeam are hotter than LTS1 and the rear crossbeam. One possible reason is that these two elements are slightly warmed up by the natural convection of the air coming from the SEB.

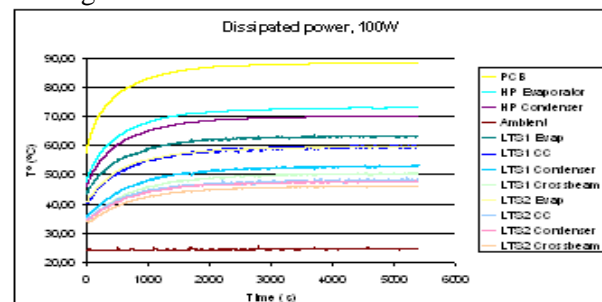


Figure 6. Temperature profiles, power 100 W.

Figure 7 specifically focused on the results obtained on LTS1 for various SEB power dissipation. This figure clearly details the temperature gradient on each part of the thermal path, from the PCB to the ambient air:

- The temperature gradient between the PCB and the heat pipe evaporator is about 16°C at 100W. This gradient is due to the poor thermal conductivity of the PCB and to the thermal resistance of the thermal pad material.
- The temperature between the HP evaporator and condenser is 2.5°C. It is almost constant with the power.
- The temperature gradient inside the SEB wall is 8°C. This gradient includes the resistance of the thermal interface material between the HP condenser and the SEB wall and also between the SEB wall and the LHP evaporator.
- The temperature gradient on the LTS is 10°C for 100W applied on the SEB.
- Finally the temperature gradient between the seat structure and the ambient air is 26°C (more than 40% of the overall gradient). This gradient is linked to the natural convection process.

The same results are obtained on LTS2: the two systems have a similar thermal behavior.

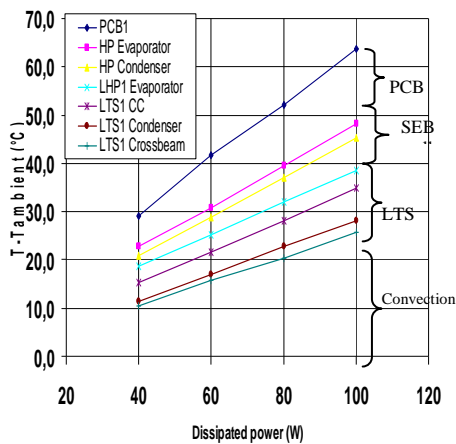


Figure 7. LTS1 temperature profile

Figure 8 gives the PCB temperature according to the number of LTSs which are mounted on the SEB. Without any LTS, the maximum power which can be dissipated by the SEB to obtain a 60°C temperature rise on the PCB is 45 W. With the use of one LTS, this power reaches 80W and 95W with two LTSs. The results obtained with two LHPs are almost similar. In our application, LTS and LHP present similar results.

In the same way, the use of two LTSs for 45W dissipated power on the SEB allows to halve the temperature gradient (32°C instead of 60°C).

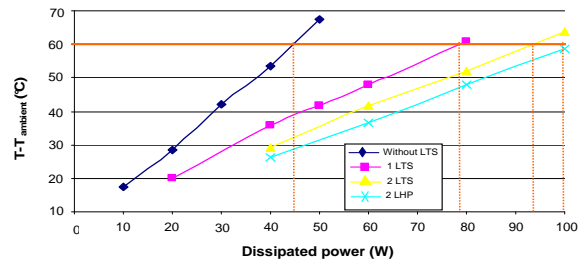


Figure 8. LTS impact on PCB temperature

3.2 Tilt influence

In aircraft, the seat cannot be kept perfectly horizontal. Due to take-off and landing, seat and LTSs are tilted. Their thermal behaviors need to be analyzed since as opposed to the LHP, LTS are gravity sensible.

Take-off

The seat tilt has been increased up to 30°. According to Figure 9, it can be noticed that both LTS performance are stable up to a tilt angle of 23°. Then the thermal performance start to change: with the increase of the inclination, the evaporator of LTS2 is then above the condenser for an angle greater than 25.6°. Thus LTS2 does not operate any more. This induces a drastic increase of the LTS2 evaporator temperature and a reduction of the LTS2 condenser temperature which tends to be at the ambient temperature. In the meantime, since one of the LTSs does not operate, all the SEB temperatures increase. LTS1 is not impacted by the tilt angle during take off: the condenser is always situated over the evaporator for all angles.

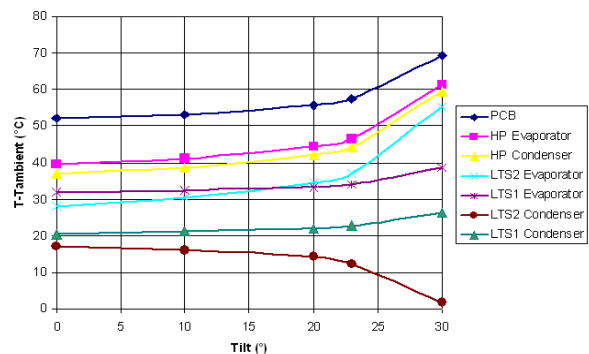


Figure 9. Take-off, tilt impact, power 80W

Landing

In Figure 10 the seat tilt has also been increased up to 30°. But in this configuration there is no impact on the thermal performance of both LTSs. The LTS1 condenser is located just above the SEB. Even with 30° tilt, the condenser remains above the evaporator. It would be necessary to reach 70 to 80° tilt to have a thermal impact. Such tilts are not encountered during landing phase.

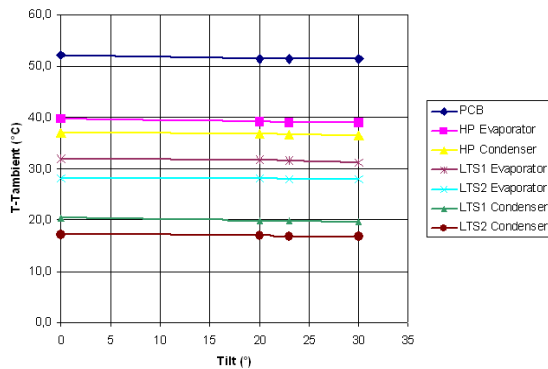


Figure 10. Landing, tilt impact, power 80W

Turning flight

Figure 11 gives the LTS temperatures for a tilt between -40° and +40°. A negative tilt means turning flight on the left, a positive tilt means turning flight on the right. We can notice a low degradation of the PCB cooling efficiency for a positive angle greater than 20°, i.e. an increase of the temperature up to 5°C (Figure 11). It is larger for positive angle. As for the landing and the take-off, with an angle greater than 20°, a part of the condenser is located below the evaporator, this limits the LTS performances.

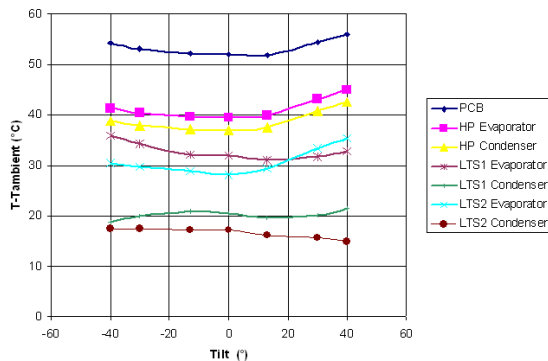


Figure 11. Turning flight, tilt impact, power 80W

This effect is even more visible in Figure 12. With a tilt up to +40°, the temperature difference between the LTS2 evaporator and condenser is doubled. With a negative angle of -40°, the behavior is almost the same on LTS1. But in this

case we can also notice an impact on LTS2: the reason is that a part of the PCB dissipated power is transferred from LTS1 to LTS2, resulting in a greater temperature difference between the evaporator and the condenser. For a positive angle, this effect was not noticed.

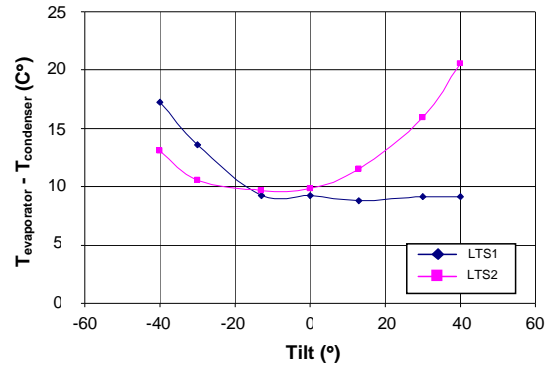


Figure 12. LTS performance during turning flight

All these results highlight how the LTS are sensitive to the tilt, especially when the tilt leads to the situation where the evaporator is at the same level or above the condenser. For the present LTS, the threshold for this angle is about 20° which is far away from the usual value of 10° encountered in a civil aircraft. Furthermore, by using two LTSs which have an opposite behavior according to the gravity effect, even if one LTS fails, the second LTS operates and still continues to correctly manage the SEB temperature.

4. START-UP ANALYSIS

A start-up analysis from ambient temperature has been performed on LTS1. Figure 13 gives the results obtained for 70 W dissipated power on the board. We can notice three steps during the LTS start-up. The first step, at $t=100s$, the vapor line (VL) temperature starts to increase. This means that there is a small flow rate in the loop: there is probably some vaporization at the evaporator. At the second step ($t=180s$), there is a break in the slope of the condensation chamber (CC) and vapor line (VL) profiles and in the meantime an increase of the condenser temperature: there is a strong increase of the mass flow in the loop but during a short time. This may correspond to the formation of the first bubble in the evaporator but since the liquid coming back from the condenser is still cold this nucleation is not stable. In step 3 at $t=320s$, the nucleation appears in the evaporator with a strong reduction of the temperature. From this

point the LTS temperature slightly oscillates ($\pm 1^\circ\text{C}$).

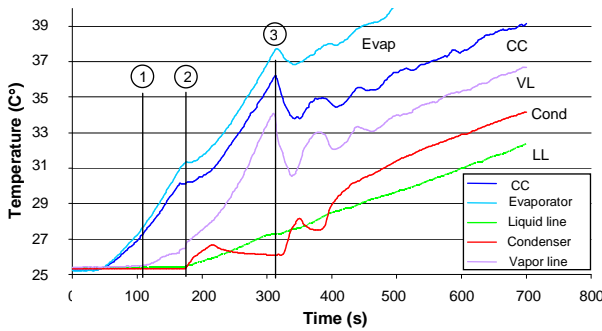


Figure 13. LTS start-up at ambient temperature, power 70 W

Figure 14 demonstrates the period of the oscillations as a function of the SEB dissipated power. The oscillation period decreases when increasing the power. Since the LTS is a closed loop, in order to reach equilibrium, some signal has to propagate over all elements of the loop. This propagation is ensured by the mass flow rate.

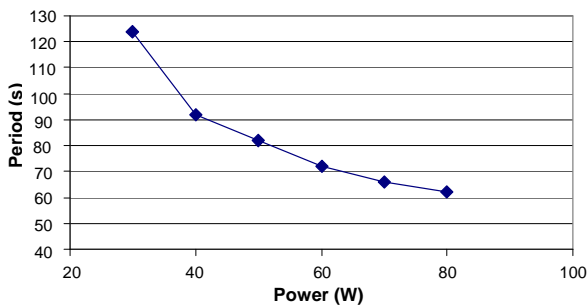


Figure 14. LTS oscillation periods vs SEB power

With the increase of the dissipated power, the flow rate is larger, thus the information can be propagated rapidly through the different parts of the LTS. This induces a reduction of the oscillation period.

5. CONCLUSIONS

The present work describes the integration of a loop thermosyphon for the cooling of a seat electronic box in avionics application. The objective is to use the seat mechanical structure as a natural convection heat sink for the thermal management of the SEB. Various experimental measurements were performed. They show a good efficiency of this cooling solution. The integration of LTSs allows to double the SEB cooling capability for a same PCB temperature.

Since LTSs are gravity-sensitive, the effect of the seat tilt during take-off, landing or turning flight

has been analyzed. The thermal performances are affected for tilts larger than 20° . This value is acceptable and greater than the usual tilt encountered in normal operating conditions (about 10°).

The analyses of the LTS oscillations during start-up from ambient temperature have shown that the oscillation period is directly linked to the power applied to the LTS evaporator.

NOMENCLATURE

CC	Compensation chamber
LL	Liquid line
VL	Vapor line

REFERENCES

- [1] D. Reay, P.Kew, *Heat pipes*, Fifth edition, Linacre House, Jordan Hill, Oxford, 2006.
- [2] I.I. Kapitanchuk, *Development of evaporating cooling systems*, Voprosy Radioelektroniki, Ser. Thermal regimes, thermostating and cooling 2 (1967) 69-74 (in Russian).
- [3] H. Imura, K. Takeshita, K. Doi, K. Noda, *The effect of the flow and heat transfer characteristics in a two-phase loop thermosyphon*, Proceedings of the 4th Int. Heat Pipe Symposium, Tsukuba, Japan, 1994, pp. 95-106.
- [4] L. Rossi, F. Polasek, *Thermal control of electronic equipment by heat pipes and two-phase thermosyphons*, Proceedings of the 11th Int. Heat Pipe Conference, Tokyo, Japan, 1999, pp. 50-74.
- [5] D. Khrustalev, *Loop thermosyphons for cooling electronics*, Proceedings of the 18th IEEE SEMI-THERM Symposium, San Diego, California, 2002, pp. 145-150.
- [6] Y.F. Maydanik, *Loop heat pipes*, Applied Thermal Engineering 25 (2005) 635-657.
- [7] G.P. Peterson, *An introduction to heat pipe: Modeling, Testing, and Applications*, Wiley-Interscience, New York, 1994.
- [8] Yu. Maydanik, V. Dmitrin, V. Pastukhov, *Two-phase loop thermosyphons*, Proceedings of the VIII Int. Seminar "Heat Pipes, Heat Pumps, Refrigerators, Power Sources", Minsk, Belarus, 2011, v.1, pp. 144-154.
- [9] C. Sarno, C. Tantolin, S. Parbaud, *Cooling of seat electronics boxes with loop heat pipe*, Proceedings of IMAPS, La Rochelle, France, 2009.
- [10] Yu. F. Maydanik, S. Vershinin, V. Pastukhov, M. Chernysheva, C. Sarno, C. Tantolin, *Passive cooling system for an aircraft electronic box*, Heat Pipe Science and Technology 1 (3) (2010) 251-260.

POSSIBILITY OF USING BIPHASIC PULSATING PUMP OF HEAT ACTION IN HEATING AND COOLING SYSTEMS

Sasin V.Y., Savchenkova N. M., Parehina I.V., Murotyan D.O.

Department: Heat and Mass Transfer Process and Devices
Moscow Power Engineering Institute (Technical University)
111250, Moscow, Krasnokazarmennaya str., 14
Tel/fax.: (495) 362-71-49
SavchenkovaNM@mpei.ru, SasinVY@mpei.ru

ABSTRACT

The objective of this work is to validate the working capacity non-pumping pulsating vapor ejecting and vapor compression refrigeration machines and evaluating the feasibility of them consuming only heat energy. There are cycles with using only the heat energy from all the possible cooling cycles. Those are the vapor ejecting and absorption cycles. But supply of the working agent in the vapor generator is used by the mechanical pump, which consumes electrical energy and it is the least reliable element at these cycles. Preliminary researches have shown that it is possible to realize a new vapor ejecting refrigeration cycle in which regular mechanical pump can be backed up pump of heat action (PHA). Opportunities of application pulsing systems in refrigerating with use of heat of geothermal sources, secondary resources are considered. Constructive decisions of schemes with ejectors in the additional contours of a vapor line are considered too.

KEY WORDS Pump of heat action, vapor ejecting refrigeration cycle, pulsating

1. INTRODUCTION

This article purposes processes in heat and mass transferred device which was patented in 2010 [Sasin, 2010]. It represents a biphasic pulsating pump of heat action (PHA) which uses the energy of a heat source for pumping fluid by the periodic changing of vapor pressure, and has several advantages over traditional pumps [Sasin, 2009].

There are no leakages of heat carrier through the seals, no needs for electricity and lubrication, no needs of special automatic regulation. It has high reliability, long time resource for work, a possibility of using secondary and renewable sources of heat, great possibilities of use in heating and refrigeration engineering, and other areas.

It does not need the application of a developed production infrastructure for pump of heat action. Technological chain of manufacturing and installing this pump ensures provision of materials and qualified gas-welding work.

The heat can be supplied permanently or intermittently depending on the design of pump. Connection or disconnection of the heater with periodic supply of heat can be implemented by controlled temperatures; pressures; specified time intervals and so on.

Pumping heat carrier occurs, in particular, because the input and output check valves of the pump exist.

The internal volume in the pump is filled with working liquid through the first pipe when the pressure is decreasing and liquid is pushed through another pipe when the pressure is increasing. Increasing and decreasing of the pressure in the pump is achieved, respectively, due to evaporation or condensation pumped liquid by on or off the heat sources that is installed at the pump.

Heating the evaporator in the vapor compression cycle with the transfer pumps can be done through taking away the part of the vapor after the compressor and the received condensate can be directed to the second level of the condenser of the basic counter, unloaded the first level. The part of liquid from the high pressure vessel is supplied through the throttle valve for cooling the shell of the condenser of pump and then goes to the low pressure receiver in the liquid or gaseous form to produce the desired temperature conditions of the condenser-accumulator.

Vapor compression refrigeration systems are widely used in food industry, poultry and fish processing industry, in the technological process and the processing of livestock products and its storage. Transfer electrical pumps are the weakest

part of such devices. They can also be replaced or reserved by developed pumps of a heat action.

The are cycles of all possible cooling cycles in which use only the thermal energy. This is vapor jet and the absorption cycles. But in these cycles to feed the working agent in the vapor generator is used the mechanical pump which consumes electrical energy and it is the least reliable element. However, preliminary studies showed that the possible implementation of a new vapor jet refrigeration cycle which has no mechanical pump.

2. PUMPS IN THE ABSORPTION AND VAPOR COMPRESSION REFRIGERATION AMMONIA MACHINES.

Regular pump can be reserve with pump of heat action in absorption refrigerators. However, additional theoretical and experimental studies are required for inclusion PHA in the refrigerating cycles. For example, the parameters of the cycle can be changed, therefore, pump capacity too. Particular attention should be paid to the method of heating the evaporator PHA to implement the regime of boiling heat carrier and organization of a condenser cooling. Probably, inclusion PHA in the scheme will be the best solution for its use in absorption cycles, but these studies require an interested customer and significant capital investment. The scheme of refrigeration system with PHA is showed at Figure 1.

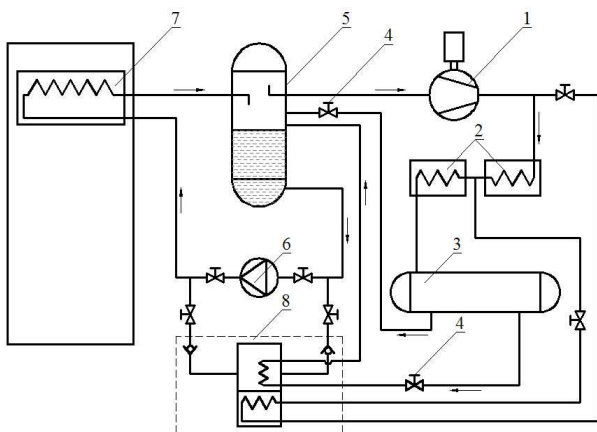


Figure 1. Scheme of vapor compression refrigerating system using the PHA

1 – vapor compressor, 2 – condenser 3 – receiver of high pressure; 4 – regulating valves, 5 – receiver of low pressure; 6 – electrical pump, 7 – evaporator, 8 – pump of heat action.

As shown at Figure 1, the PHA 8 is set parallel to the electrical pump 6. Heating of the evaporator

can be done through the selection of some part of vapor after the compressor and obtained condensate can be directed to the second level of main cycle of the condenser, thus relieving the first level. To produce the necessary temperature of the condenser-accumulator, part of liquid from the high pressure vessel through a throttling valve goes to the cooling the condenser and then goes to the receiver of low pressure in the liquid or gas form.

3. POSSIBILITY OF USING VAPOR EJECTING REFRIGERATING MACHINES WITHOUT MECHANICAL PUMP

Ejecting refrigeration machines are used with mechanical pump for moving the liquid from condensing pressure p_k to evaporating pressure p_0 . In the work of the existing vapor ejecting refrigeration machine, the pressure in the vapor generator is higher than the pressure in the condenser, so the condensate cannot spontaneously flow into the vapor generator. So that condensate can flow into the vapor generator, it was proposed a new pulsating cycle at which the condensate accumulated in the accumulator, which is situated higher than the vapor generator.

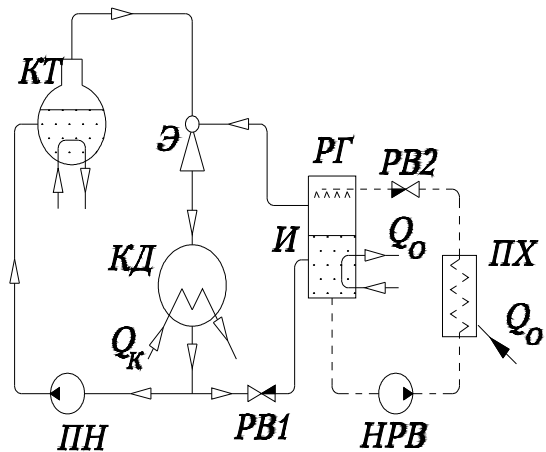


Figure 2. Principal scheme of vapor ejecting refrigeration machine

When the liquid is completely evaporated pressure in the evaporator drops to pressure in the accumulator and the liquid start to flow under gravity from the accumulator to the evaporator (Figure 2).

In the vapor ejecting refrigeration machine by a system of combined processes of direct (force) and reverse (cooling) cycle, in contrast to the

compression chiller in the vapor jet machine processes of compression and condensation of the forward and reverse cycles are inseparable.

The principal scheme of a vapor ejecting refrigeration machine (VERM) is shown at Figure 2. [Sokolov, 1989; Borodkin, 2005].

To facilitate the review of all processes associated with the production of cold and its consumption, the vapor generator, pump and the consumer of cold in addition to elements of the refrigerating machine are also shown in this scheme.

Working vapor forms in the evaporator KT with supplying heat Q_{II} goes to the jet of the ejector Θ . The internal energy of vapor is converted into kinetic energy of flow. Vapor expands and its velocity increases significantly. Working vapor ejects cold vapor coming from the evaporator, and is mixed with them in the ejector mixing volume Θ .

Mixture of working and cold vapor passes through a diffuser of ejector, where the flow velocity is being decreased and pressure is being increased from p_0 in the evaporator to p_k in the condenser, after which the mixture of vapors is being discharged into the condenser $KД$. Heat of condensation Q_K of vapor mixture outlet of cooling water and the formed condensate are separated into two streams: one part in an amount that equal to the quantity of working vapor, supplied with the condensate pump ΠH into evaporator KT , and the other part through the control valve PBI enters into the evaporator Π to compensate for the vaporized agent (working fluid).

Freon ejector cooling machines get new quality, if complicated and expensive freon electrical pump can be excluded from the scheme, and the pressure in the power cycle will be increased by isochoric heat supply to the generator.

Consumption electric capacity of freon ejector refrigeration machines can be decreased significantly (two to three times), and freon ejector cooling machines practically can work only at the heat expense.

These refrigerating machines are called vapor ejecting refrigeration machine without pump (VERMWP).

Regimes operation of generators and ejectors with check valves are shown in the scheme install automatically controlled valves (active control) (Figure 3).

Calculation of the cycle and indicators of VERMWP depends on the scheme, selected cooling carrier, parameters of pressure and temperature and the results of the calculation of the ejector.

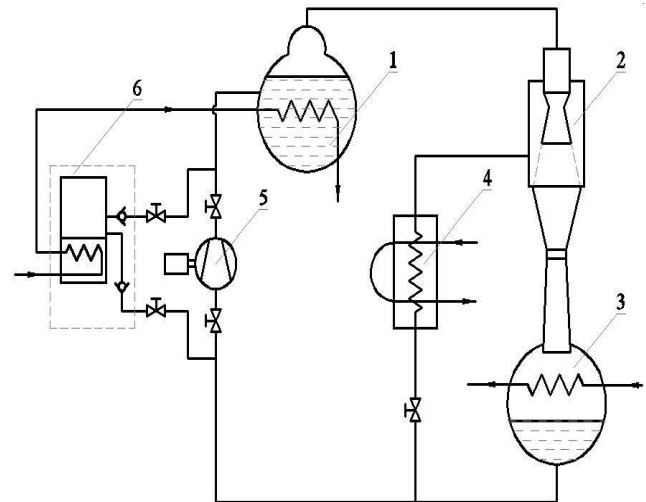


Figure 3. Principal scheme of VERMWP with HA
 1 – vapor generator; 2 – ejector; 3 – condenser;
 4 – evaporator; 5 – electrical pump,
 6 – pump with heat action

For the scheme should also add the need for further design development PHA with separating the cold carrier in the main contour to prevent overheating of the carrier in the PHA (Figure 3).

In the paper, a new pulsating cycle is presented at which the condensate accumulated in the accumulator, which is situated higher than the vapor generator, for flowing of condensate into the vapor generator.

When the liquid is completely evaporated in the vapor generator, pressure in the vapor generator drops to pressure in the accumulator and the fluid under gravity from the battery to start to flow to the vapor generator.

The first stream of liquid in the vapor generator just boils and vapor pressure in the vapor generator rises immediately, stopping the flow of liquid from the accumulator, and the temperature of the walls of the vapor generator quickly rises.

It provides a method of delayed fluid flowing on the surface of the vapor generator by setting the intermediate vessel that supplies the right

amount of liquid for subsequent draining and evaporation in the vapor generator to prevent this process.

It needed G_p kg of working vapor for compression in the ejector G_H kg of cold vapor. The value of $a = G_p / G_H$ is called the specific charge of a working vapor, or a multiplicity of circulation, and it shows that for the 1 kg of cold vapor that circulates in the refrigeration cycle a kg of working vapor is necessary.

Coefficient of specific charge of a working vapor is the reciprocal of the coefficient of ejection $a = 1/u$ and depends on the properties of the working and ejecting vapor, the degree of downward of working vapor pressure in the jet and the degree of increase of cold vapor pressure in the ejector.

When the liquid in the vapor generator ends, pressure p_p rapidly becomes to the values p_k , the check valve OK1 opens and liquid flows from accumulator into the vapor generator. Then the process is repeated.

4. CONCLUSIONS

VERMWP with biphasic pulsating heat transfer contour is a new type of refrigerating machines, which also consumes only heat energy. It can compete in alternative choice of refrigeration.

Vapor ejecting refrigeration machine is more efficient than vapor compression and absorption refrigeration machines if there are cheap sources of low potential heat (heat of exhaust gas turbine electric generators, steel open-hearth furnaces, geothermal and solar energy).

Biphasic pulsating heat transfer contours are one of the solutions for the creation of autonomous systems in which heat is transferred out in the direction of gravity, and it does not require mechanical pumps to return the cooling carrier to the heat source.

Pumps of heat action with various functional principles of the work being developed as an alternative to mechanical electric pumps in monophasic and biphasic cycles.

It is possible to pump aggressive liquids such as ammonia, which will improve the reliability

of ammonia vapor compression refrigerating machines with transfer pump.

NOMENCLATURE

PHA - pump of heat action

VERM - vapor ejecting refrigeration machine

VERMWP - vapor ejecting refrigeration machine without pump

REFERENCES

- Sasin V.Y., Savchenkova N. M., Parehina I.V., Bui Man Ty, Rudenkov A.S. (2010) *Heat and mass transferred device*. Ru Patent № 94320
- Sasin V.Y., Savchenkova N. M., Parehina I.V., Bui Man Ty (2009) *Experimental and theoretical studies of heat and mass transfer in the evaporator biphasic of pulsating pump of heat action*. Newsletter MPEI, 3, Moscow, p. 29–35
- Sokolov E.Y., Zinger N.M. (1989) *Jet apparatuses*. Energoatomizdat, Moscow

DEVELOPMENT OF THE ALPHABUS EXTENDED DEPLOYABLE RADIATOR

C. BEREND, A. LECOSSAIS,

Astrium Satellites FRANCE
31 Av. des Cosmonautes, 31402 Toulouse Cedex - FRANCE
Tel +33 562 197 630, Fax +33 562 195 800, christophe.berend@astrium.eads.net,

E. DEHOMBREUX

Euro Heat Pipe
24 Rue de l'industrie, B 1400, Nivelles - BELGIUM
Tel +32 6788 9475, Fax +32 6788 9499, emmanuel.dedhombreux@ehp.be

T. TJIPTAHARDJA

ESA/ESTEC
European Space Agency
PO Box 299 - 2200 AG Noordwijk ZH - The Netherlands
Tel +31 71 565 8781, Fax +31 71 565 6142, Tisna.Tjptahardja@esa.int

ABSTRACT

The constant trend in telecom satellites over the past decades is a continuous increase of payload power. This trend is limited today by the available volume of the launcher fairing and by mass constraints that both prevent from increasing the radiative surfaces needed to evacuate the payload dissipation heat. Deployable Radiator Panels (DPRs) stowed during launch and deployed on station constitute a solution to remove this bottleneck.

As part of ESA Alphasat Extension program, Astrium Satellites is leading the development of a large size radiator panel (typically 4 m²) made nominally of high-conductivity pitch CFRP skins. This radiator includes embedded high-efficiency Loop Heat Pipes condensers to transfer the heat from the equipments inside the spacecraft to the CFRP panel once deployed. Design and manufacturing of Loop Heat Pipes, routing of the embedded condensers within the radiator panel, deployment mechanism and associated flexibles for two-phase fluid circulation continuity represent challenging issues, but the selected technologies subject of several trade-offs enable to maximize the DPR efficiency. A small breadboard has been already developed and tested in order to validate the critical technologies. A Deployable Radiator PFM is now under development. The current step consists in mechanical and thermal analyses, mechanical testing of material samples and thermal testing of a large size breadboard including CFRP radiator panel and two Loop Heat Pipes.

KEY WORDS: Deployable Radiator, Capillary Pumped Loop Heat Pipe, high efficient radiator panel.

1. INTRODUCTION

In order to cope with the market demand for more powerful and flexible payloads, it was decided in 2005 to develop a new satellite platform called Alphasat, able to host from 12kW up to 18kW payloads. The development of this new platform is performed in partnership between Astrium Satellites and Thales Alenia Space in the frame of Artes 8 ESA program. A picture of the Alphasat platform is shown on figure 1.

In order to increase payload power above 20kW, it is necessary to increase the radiating surfaces of the satellite used to dissipate heat from the electronic equipments. However the North/South walls surfaces cannot be extended because of the limits set by existing launcher fairings.

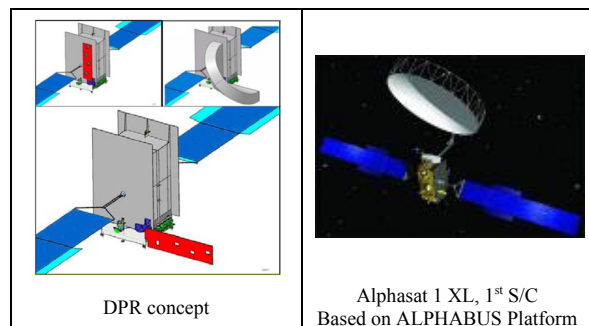


Figure 1. Deployable Panel Radiator concept.

To solve this problem, Astrium Satellites is developing with ESA/CNES funding a Deployable Panel Radiator. During launch the panel is stowed between the solar array panels and the satellite

structure, taking no additional space under the launcher fairing. After orbit insertion the panel is deployed and locked, so as to provide additional radiative surface once the equipments are switched on. Up to 4 DPRs can be implemented on the spacecraft.

The heat from the equipments inside the satellite is transported to the radiator by means of high efficiency loop heat pipes, based on the considerable Astrium Satellites and Euro Heat Pipe heritage. Deployment and locking is performed by means of a specific mechanism.

2. REVIEW OF THE FUNCTIONAL REQUIREMENTS

The DPR must be able to dissipate 1500W under nominal operating conditions, which means that with a maximum of 4 DPR per spacecraft, 6kW of additional dissipated power may be accepted from onboard equipments. The required reliability of the DPR higher than 0.999 impacts directly the design of the heat transport system, the deployment mechanism and radiator panel strength with respect to micrometeorites.

The stowage of each DPR on the satellite North/South walls is done on available wall surfaces on each side of the solar array drive mechanism, which in turn defines the available surface for the DPR: about 4 m². The panel thickness is also constrained by the available space between the stowed solar array panels and the spacecraft wall. Finally, the mass of the DPRs must remain as low as possible.

These main requirements have important consequences on the DPR design. The small thickness available and the stringent mass target lead to select a composite sandwich panel structure for maximum stiffness/mass ratio. Then, the thermal need of maximum radiative dissipation balanced by the minimum mass implies that the heat conducted to the panel by the LHPs must be spread over the panel surface as efficiently as possible: this means the selection of the best compromise between the skin material thermal conductivity and thickness, the pitch of the embedded LHP condensers and the associated length of these last ones, which impacts its reliability with respect to micrometeorites.

Several iterations and trade-offs on the skin material and LHP embedded condenser arrangement have been performed in the frame of the ALPHABUS DPR phase B.

3. TECHNOLOGIES OF THE DPR

The main functional elements of the DPR system are the following:

(1) **A Radiator Panel** that is deployed once in orbit to radiate the heat collected by the DPR system into the Space vacuum,

(2) **One or several Loop Heat Pipes (LHP)** that collect the thermal power through the evaporator and carry the heat to condenser(s) attached to the radiator panel. The LHPs are designed with flexible tubing in the deployment area to ensure the deployment of the radiator panel,

(3) **A Deployment mechanism** that deploys the radiator panel in orbit. The Deployment Mechanism attaches the DPR to the Spacecraft structure, and maintains the radiator in stowed position during launch.

The key technologies that provide the required thermal performance of the DPR are basically the LHP (that shall ensure the maximum heat transfer), the condenser and the radiator panel (that shall be low mass, high stiffness, high thermal efficiency and high reliability vs. micrometeorites). Interfaces between all these elements shall be carefully designed to achieve the best performances.

The innovative DPR design proposed by Astrium and its partners for Alphabus extension is based on a multi-LHP double-face light weight radiator that allows rejecting 30% more power than state-of-the-art solutions for the same mass. The use of a double face radiator with multiple Loop Heat pipes specifically requires to master LHPs cooperative operations both at low and high power, together with a well balanced heat sharing between each radiator faces and the evaporators.

Figure 2 shows the key technologies involved in the DPR.

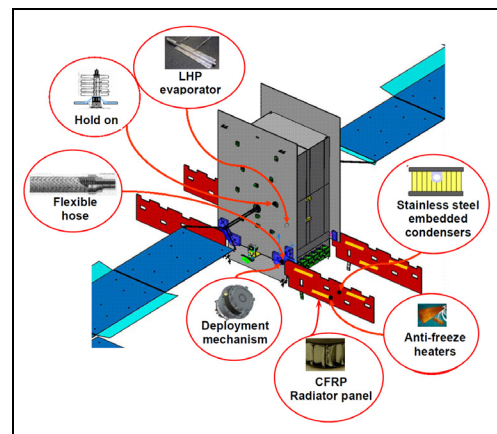


Figure 2. Deployable Radiator technologies.

Several loop heat pipes may be used inside each DPR. Each LHP evaporator is positioned inside the spacecraft, in thermal contact with the equipment or on the wall area from which heat must be extracted. The LHP tubings run from the evaporator to the DPR hinge, next to the deployment mechanism. There, flexible lines connect these tubings with the LHP condenser pipes embedded inside the CFRP radiator panel. Inside the condenser, the LHP fluid is cooled down and runs back to the evaporator.

Anti-freeze heaters must be added on the panel to prevent the fluid from freezing under non-operational low temperature conditions.

For stowage, the solar array hold-down mechanisms are used. For the deployment of the radiator panel, trade-off between passive (spring + viscous dampers) and active (stepper motor) mechanisms is on-going based on overall DPR reliability, development and cost criteria.

The selection of the radiator panel skin has been made after a detailed survey of different solutions using high conductive materials such as Aluminium and high conductive carbon fibers. Pitch carbon fibers has been finally selected for its high thermal conductivity. An optimal skin layout has been designed to achieve the best compromise between high thermal conductivity transverse to the condensers, panel stiffness and strength, CTE mismatch between panel and embedded condensers, total mass and manufacturing constraints.

The thermo-optical characteristics of both DPR faces need to be optimised for its radiator function. As for the satellite North/South walls, the best choice is to cover the radiative surfaces with OSRs as shown on figure 3. OSRs will cover the external DPR side (facing space). For the internal DPR side (facing toward the spacecraft), it was decided to use white paint, which is sufficient to reduce specular reflexion of solar flux on the spacecraft at acceptable level.

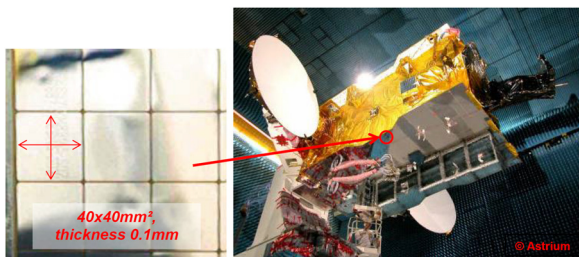


Figure 3. Optical Solar Reflectors (OSRs).

4. DPR TECHNOLOGICAL VALIDATION

Several advanced technological validation have been performed either in the frame of other Research&Technology programs or in the frame of the phase B0 of ALPHABUS extension programs. As shown in the next paragraphs, these validations allowed to the consolidation of technology selection or overall DPR system architecture.

4.1 Small radiator breadboard

In 2005/2006, Astrium Satellites developed and tested a 0.3m² size representative breadboard made of a sandwich panel with high conductive CFRP skins, aluminium honeycomb and embedded condensers as shown on figure 4. Mechanical characterisation, thermal cycling and thermal vacuum tests were performed, in order to assess the criticism of some of the issues mentioned above and obtain preliminary thermal efficiency data.

Thermal vacuum tests were performed by pumping water in the embedded tubings to simulate the heat transport by the LHP fluid in the operational DPR. The goal of these tests was to measure the heat rejection capacity and validate the thermal simulations.

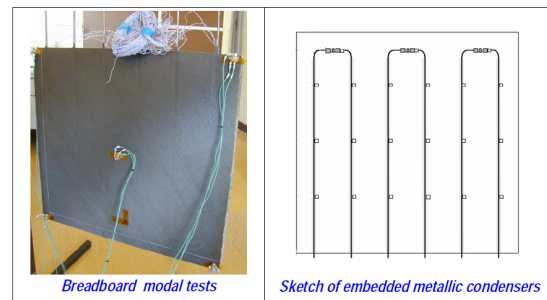


Figure 4. Small radiator CFRP breadboard.

The test results showed that with a flow of fluid representative of a LHP, the radiated power capacity meets the DPR needs. Additionally, the measured performances fitted the predictions within 10% error margins, which validates the soundness of the thermal analyses and gives confidence for the predictions to be performed on the flight DPR.

4.2 Multi-radiator&LHP breadboard

In the frame of an Research&Technology program funded by the CNES, Astrium Satellites has developed a multi-radiator breadboard as shown on figure 5.

This breadboard was constituted by an equipment (i.e a mass dummy with a heater to represent its heat dissipation) connected to 4 mini-LHPs evaporators feeding 4 radiator panels with condensers.

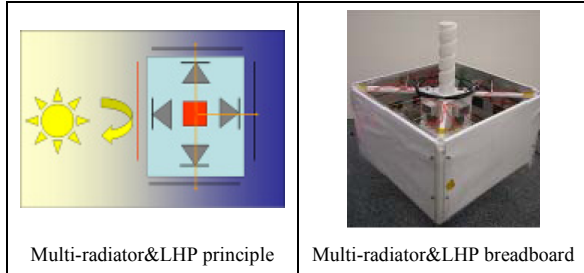


Figure 5. Multi-radiator&LHP breadboard.

This breadboard submitted to thermal vacuum test allowed to validate the heat sharing and the LHPs stability when the several radiators were submitted to different environments such as cold space or sun. The rules for heat sharing and stability derived from the exploitation of this breadboard test results have been used to perform the preliminary thermal analysis of the DPR for what concerns LHP heat sharing and equipment stability.

4.3 CFRP validation program

In the frame of the phase B0 of ALPHABUS DPR, an extensive validation program has been performed in order to consolidate the radiator panel with embedded condenser selected technologies and validate the associated process. CFRP raw material samples and samples representative of the radiator panel with embedded condensers, as shown on figure 6 have been manufactured and tested with and without thermal cycling : the obtained results are currently very promising and leads to the selection of the CFRP materials for the manufacturing of a large size radiator panel (4×0.4m²) with embedded condensers on both radiative faces as described in paragraph 6.

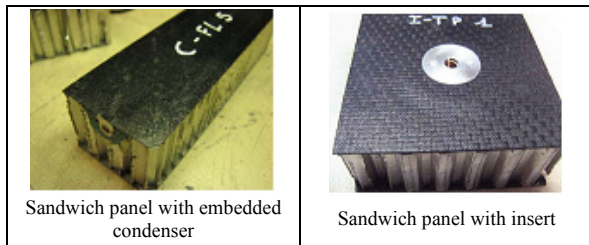


Figure 6. CFRP sandwich panel samples.

5. DPR DESIGN AND PERFORMANCES

5.1 DPR design and justification

The proposed DPR design for the ALPHABUS application shown on figure 7 includes the following elements:

- a radiator panel including an aluminium honeycomb, 0.2mm thick skins made of CFRP high conductive pitch fibers and 4 embedded condenser circuits shared between the two faces and connected to 4 LHPs. The CFRP skin lay-up has been optimized to offer the best compromise between transverse conductivity, mechanical characteristics, condensers CTE mismatch and manufacturing constraints. It is respectively covered by OSR on the face setting-up the cold space and white paint on the face setting up the East/West walls for thermal performance/mass ratio optimization.
- embedded condensers are made of stainless steel tubing soft brazed onto stainless steel saddle for CTE compatibility with the CFRP skin. The detailed routing and associated pitch (2 parallel lines forth and 1 line back = 2A/1R) has been selected to maximize the radiative efficiency of the panel while keeping robustness with respect to micrometeorite and minimizing the overall mass. The implementation of 2 circuits on each face allows maximizing the overall DPR thermal performance while allowing 1 LHP failure with moderate degraded performances.
- metal hoses (stainless steel) provide the flexibility required during radiator deployment of the junction between radiator panel condensers and LHP tubing fixed on the S/C. They have been selected for their high flexibility leading to a residual torque compatible of spring driven deployment mechanism.
- 4 LHP evaporators directly derived from the ALPHABUS LHP² development able to transfer up to 900W with high conductance. They interface directly with a Heat Pipes bus, which collects heats from the high dissipative equipments.
- standard thermal hardware (MLI, heaters, thermostiches, etc...) are used to insure the thermal control of the DPR
- a deployment mechanism, which can be a spring combined with a viscous damper or a stepper motor depending on the S/C and DPR thermal rejection capability. Before deployment, the radiator panel is maintained between the Solar Arrays and the North or South S/C walls by HDRM.

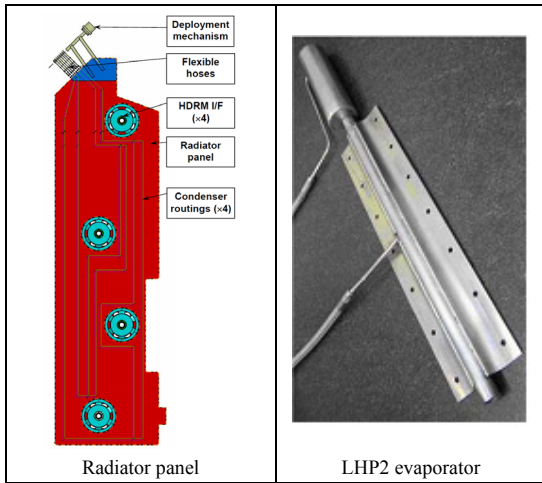


Figure 7. ALPHABUS DPR design.

5.2 DPR performances

In the frame of the DPR phase B development, several trade-offs have been led in order to optimize its thermal performance going further than the strict requirements of the ALPHABUS system level. More particularly, thermal and mechanical analyses have been performed to find the best compromise between mass, mechanical and thermal performances: the overall performance of the DPR is assessed through the so-called DPR overall efficiency expressed by the overall DPR mass / heat rejection capability ration. It shall be noted that the T_{sink} used for the thermal analysis have been derived from S/C system level analysis and therefore correspond to realistic flight environment.

The figures 8 and 9 summarize the results of the main trade-off performed on the radiator panel skin material and condenser routings.

	CFRP skin (0.2mm)	Aluminium skin (0.3mm)
Condenser routing	2 parallel lines forth and 1 line back	
Skin transverse conductivity	$270 \text{ W}\cdot\text{m}^{-1}\cdot\text{K}^{-1}$	$150 \text{ W}\cdot\text{m}^{-1}\cdot\text{K}^{-1}$
Max. rejected power	1810 W	1785 W
DPR overall mass	35 kg	39 kg
DPR efficiency	51.8 W/kg	45.9 W/kg
Pitch transverse temperature profile for both skins / radiative efficiency = $\eta_{\text{rad}} = \frac{T_{\text{panel,max}}^4 - T_{\text{panel,min}}^4}{T_{\text{panel,max}}^4}$		

Table 1. Radiator panel skin material trade-off results.

The figure 9 shows that the use of high conductive CFRP pitch fibre with an optimized lay-up leads to large gains in terms of mass and DPR efficiency while providing a margin of 20% with respect to the heat rejection capability required by the S/C (i.e 1500W).

	CFRP skin (0.2mm)	
Condenser routing	2 parallel lines forth and 1 line back	1 line forth and 1 line back
Skin transverse conductivity	$270 \text{ W}\cdot\text{m}^{-1}\cdot\text{K}^{-1}$	
Max. rejected power	1810 W	1600 W
DPR overall mass	35 kg	33 kg
DPR efficiency	51.8 W/kg	48.5 W/kg
Pitch transverse temperature profile for both skins / radiative efficiency = $\eta_{\text{rad}} = \frac{T_{\text{panel,max}}^4 - T_{\text{panel,min}}^4}{T_{\text{panel,max}}^4}$		

Table 2. Condenser routing trade-off results.

The condenser routing design induces opposite impacts on heat rejection capability and radiator panel mass. Simplification of the design using no parallel routing leads to a degradation of the overall DPR efficiency.

Finally, the overall performances of the DPR design as described in §5.1 are shown in figure 10.

Mass (complete DPR system)	35 kg
1 st eigenfrequency	19.6 Hz
Strength (QS sizing loads)	25g - MoS >0
Strength (thermoelastic)	MoS >0
Strength (acoustic)	Ariane 5, Proton launchers - MoS > 0
Non-operational temperature range	-65°C / +85 °C
LHP operational temperature range	-30°C / +75°C
Heat rejection capacity	Up to 1800 W
DPR efficiency	> 50 W/kg

Table 3. DPR performance synthesis.

On this nominal design, additional preliminary analyses have been performed in order to assess the robustness of the DPR and more particularly of the LHP to adapt their operation when environments are modified at hot source (equipment or HP bus I/F) and at cold sources (T_{sink} variations on each face of the radiator panel).

No significant thermal performance evolution of the LHPs has been observed when heat sharing is modified between the four LHPs or whether unitary LHP performances are balanced or with great differences. For instance, figure 11 shows start-up of all DPR LHPs and stop & restart of one of them.

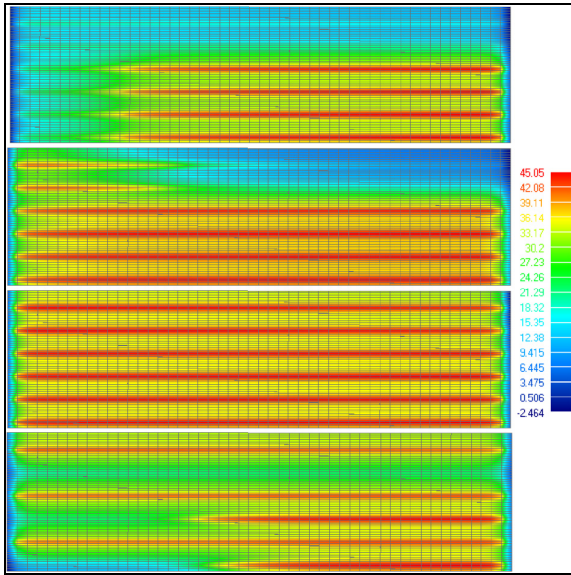


Figure 8. DPR Radiator temperature evolution with transient LHP operation.

Figure 12 shows LHP transported power evolution with respect to T_{sink} and S/C HP network temperature.

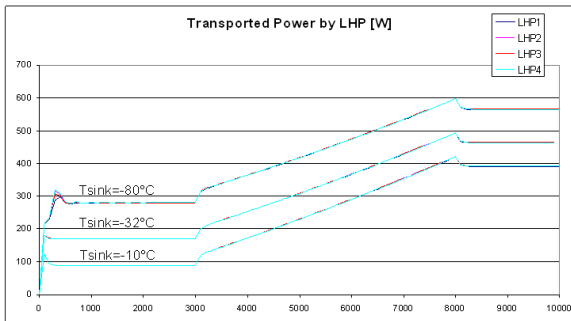


Figure 9. LHP transported heat flux evolution with transient DPR operation.

All these analysis results show the versatility of the DPR system to the boundary conditions to which it is submitted.

6. DPR CHALLENGES AND WAY FORWARD

The next step of the current phase B, which will be concluded soon by the PDR is the manufacturing of a DPR breadboard including a radiator panel using the CFRP technology for the skin and equipped with one embedded condenser routing per face representative of the current DPR nominal design. These condensers will be connected to the LHP via the selected flexible hose. This breadboard will allow consolidating the choice of the CFRP technology for the radiator panel and to assess the thermal performances with respect to the requirements such as: heat rejection capability, start-up, heat sharing, and sensitivity to environmental variations ...

3. CONCLUSIONS

The DPR development is proceeding on schedule. A breadboard TRB is planned in the third quarter of 2012, after the breadboard thermal tests, to validate the DPR concept and technological choices. The development will then continue with a CDR at the end of 2012 and delivery of the DPR proto-flight model at the beginning of 2014 for integration to an Alphabus satellite.

NOMENCLATURE

CFRP	Carbon Fiber Reinforced Polymer
CTE	Coefficient of Thermal Expansion
DPR	Deployable Radiator
ESA	European Space Agency
HDRM	Hold Down and Release Mechanism
I/F	Interface
LHP	Loop Heat Pipe
MLI	Multi-Layer Insulation
OSR	Optical Solar Reflector
PFM	Proto-Flight Model
S/C	Spacecraft
T_{sink}	Equivalent radiative sink temperature seen by the radiator skins

ACKNOWLEDGEMENT

Astrium Satellites would like to thank Euro Heat Pipes as partner on this development and loop heat pipe manufacturer, MS Composites as the panel manufacturer, ESA and CNES for their contribution to the DPR project in the scope of the Alphabus Extension program.

Li-ion Battery thermal management System with Loop Thermosyphon of Electric Vehicle

Ju-Chan Jang and Seok-Ho Rhi[†], Kye-Bock Lee

School of Mechanical Engineering, College of Engineering, Chungbuk National University, 52 Naesoodong-ro, Heungduk-gu, Cheongju, Chungbuk, 361-763, KOREA, 82-43-261-2444, rhi@chungbuk.ac.kr

Ki-Woo Lee, Young-Soo Lee, Wook-Hyun Lee

Korea Institute of Energy Research, 152 Gajeong-ro, Yuseong-gu, Daejeon, 305-343, KOREA, 82-42-860-3166

ABSTRACT

The present experimental study investigated the loop thermosyphon battery thermal management system (TBTMS) for future electric/hybrid vehicle. The experimental system for the thermal management of a Li-ion battery system installed with loop thermosyphon was designed for a future hybrid and electric vehicles. Specially, the present battery thermal management system has adopted a loop thermosyphon cooling/heating method for high efficiency cooling and heating. In the present study, the experimental results show that the present cooling and heating system has ability to transfer the entire dissipated heat and each cell temperature is maintained under 55°C when each cell of battery give off 50 watt of heat. Hence, battery module temperature uniformity is one such parameter and the optimum operating range is different. We then carried out the experimental study with loop type thermosyphon cooling system in battery thermal management system. In the same manner as the cooling, the battery has been heated through the loop thermosyphon.

KEY WORDS: Heat Pipe, Thermosyphon, BMS, Li-ion Battery, Heat Transfer

1. INTRODUCTION

Recently, widely used Li-ion batteries in various areas are the most likely to be commercialized for recent electric vehicles (EVs) applications. Because lithium is the metal with the highest negative potential and lowest atomic weight, in other view, batteries using lithium have the greatest potential for obtaining the high technological and performance level break through that will provide EVs with the high current density and greatest performance characteristics in terms of acceleration and wide range of performance variation. (Dhameja, 2001)

Thermal management of Li-ion battery system with high demand of electric/hybrid vehicles plays a significant role in large power applications such as EVs to guarantee the thermal safety, improving the performance and extending the cell life cycle. The electrochemical performance and characteristics of the Li-ion battery chemistry in the electric vehicles, charge/discharge acceptance, power and energy storage ability, and cycle life are very much dependable on the various operation parameters shown in Fig.1. Specially operating temperature is serious or believable parameter for battery performance and life. Li-ion battery should be operated in the range between -20°C and 60°C. Several factors affect the formation of the batteries, including electrolyte temperature, concentration of

the forming electrolyte, and current density during the formation cycles. These external factors singularly affect the battery efficiency and performance of the EVs. (Dhameja, 2001, Khateeb et al., 2004).

Mainly, a battery cell consists of five major components such as electrodes (anode and cathode), separators, terminals, electrolyte, and a case or enclosure. Li-ion Battery cells installed in EVs are grouped together into a single mechanical and electrical unit called a battery module. Battery modules are electrically connected to form a battery pack, which powers the electronic drive systems. (Dhameja, 2001)

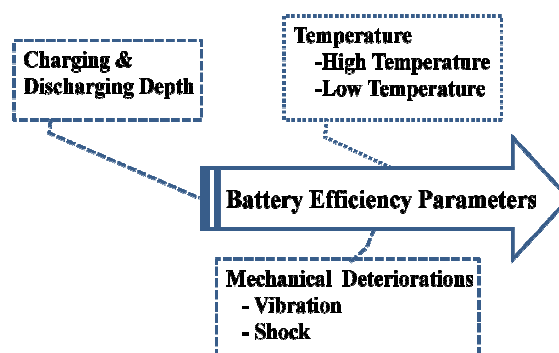


Fig. 1 Lithium-ion polymer battery Heating Module.

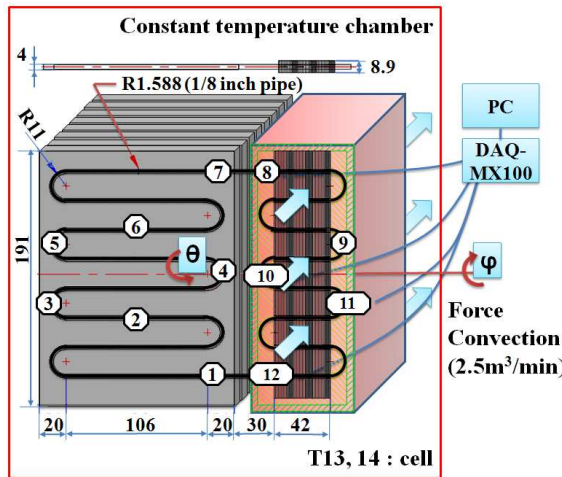


Fig. 2 Battery Thermal Management

Chen et al.(2005) developed a detailed three-dimensional thermal model to examine the thermal behaviour of a lithium-ion battery. Based on their simulation results from the detailed thermal model, it was reported that radiation could contribute 43~63% at most to the overall heat dissipation under natural convection. Forced convection is effective in depressing the maximum temperature, and the temperature uniformity does not necessarily.

Kizilel et al.(2009) reported a compact and properly designed passive thermal management system utilizing phase change material (PCM) for high-power Li-ion packs under stressful or abusive conditions, and compared with a purely air-cooling mode under normal and abuse conditions.

Jeon et al.(2011) reported transient and thermo-electric finite element analysis of cylindrical lithium ion (Li-ion) battery. Their model was the simplified model adopting a cylindrical coordinate. This model provides the thermal behavior of Li-ion battery during discharge cycle.

Wu et al.(2002) investigated two heat pipes with metallic aluminum fin attached to the battery (Li-ion, 12 A h, cylindrical, 40 mm in diameter,

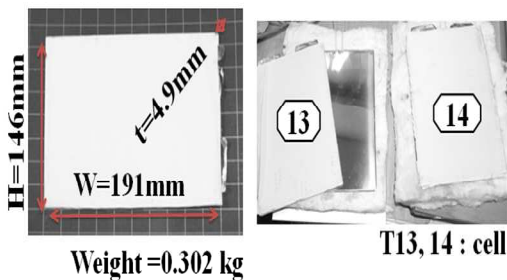


Fig. 3 Lithium-ion polymer battery Heating Module.

Table 1 Specification experimental LHP.

1	Battery cell	Cell size: 191 x 146mm 100% discharged battery cell + electronic heater block
2	Fin, Duct	Fin 0.5t Al 191 x 8.9mm 29ea Fan 120 x 120mm(2.5m ³ /min), duct 191 x 42 mm
3	Thermosyphon Pipe	1/8inch copper pipe

110 mm in length) wall to protect the temperature rise. Their results showed that the heat pipe battery cooling system with the help of metallic aluminum fin reduced the temperature rise.

Swanepoel (2001) designed pulsating heat pipe (PHP) for batteries thermal management(Optima Spirocell (12 V, 65 A h) lead acid) and control of HEV components. His simulation and experiments showed that a PHP system should be constructed with $d < 2.5$ mm for using ammonia as working fluid.

The battery thermal management system may be passive or active, and can be also divided into air heating/cooling/ventilation, liquid cooling/heating, phase change materials and hybrid combinations. And to optimize the performance of a battery and pack/module, the thermal energy management system should have optimum operating temperature, small temperature variations within a cell and module, small temperature variations among various modules, compact and lightweight, easily packaged, reliable, low-cost and easy for service (Pesaran, 2001, Khateeb, 2005).

In the present study, two-phase loop thermosyphon was applied to the battery thermal management system of electric/hybrid vehicle. Various parameters for optimum operation of electric vehicles were investigated.

2. Experimental

As shown in Fig. 2, the present loop thermosyphon battery thermal management system(TBTMS) have an electric heater for heating and a fin for cooling at right one side of loop thermosyphon(Fin section) injecting distilled water or other refrigerant into the inside of sealed loop thermosyphon.

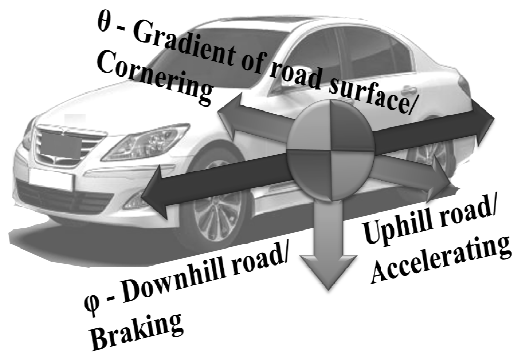


Fig. 4 Experimental Metrological Target

The both sections were made from a copper pipe of 3.2 mm O.D. Fig. 2 shows the dimensions of the current system. A one section inserted and jointed between two rectangular cell plates and the other section was connected with air cooling channel. The loop system was tested under pressure and vacuum for leaks.

The experimental apparatus, schematically illustrated in Fig. 2 and Table 1, consists of three parts; the finned section which extracts heat to the air and supply heat warm the battery cells depending on the environmental temperature conditions, the long smooth transporting section, and the cell modules either cooled or heated.

As shown in Table 1, the fin and tube type condensation or evaporation sections of TBTMS were made from copper tube, duct with the dimensions of 191 mm x 42 mm and the heat transfers from the finned surfaces were by forced convection with fans.

TBTMS and battery cell pack were tightly jointed mechanically with pressure. The whole battery thermal management system assembly was insulated to reduce any heat losses.

Table 2 Experimental Condition.

Division	Working fluid	Power / Temp.	θ	ϕ	T_{air} °C
Cooling mode	Pure water / Acetone	50W	0°	0°	10
		25W	300~60°	0°	
			0°	0~60°	
Heating mode	Acetone	50°C	0°	0°	-10
		55°C			0
		60°C			10
		65°C			20

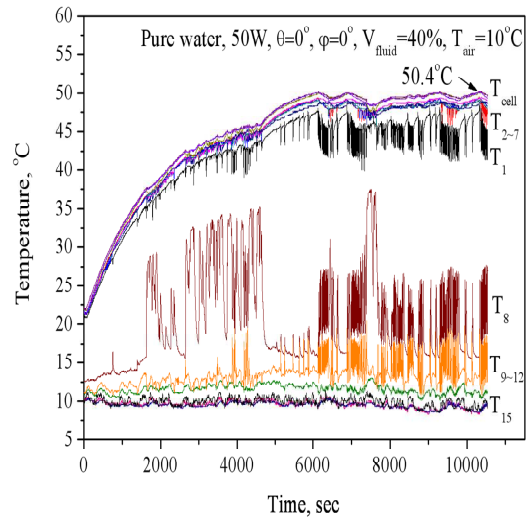


Fig. 5 Transient temperature variation of Cell, 50W, pure water

Battery cell module was manufactured to simulate the real automotive battery module. The battery simulation module has the dimension of 191 mm x 146 mm and was manufactured with two real battery cells without chemical material. Electric heater block was installed inside empty cell pack to simulate heat dissipation. (see Fig. 3)

The evaporator and condenser sections of the TBTMS is connected with two transporting lines as shown in Fig.2; one for the two-phase flow from the evaporator to the condenser, and the other for the condensate return from the condenser to the evaporator. A temporary closure of the loop thermosyphon was made with high grade vacuum valves which were connected to the upper part of the systems through cooper tubes. To measure the temperature distribution over the length of the loop

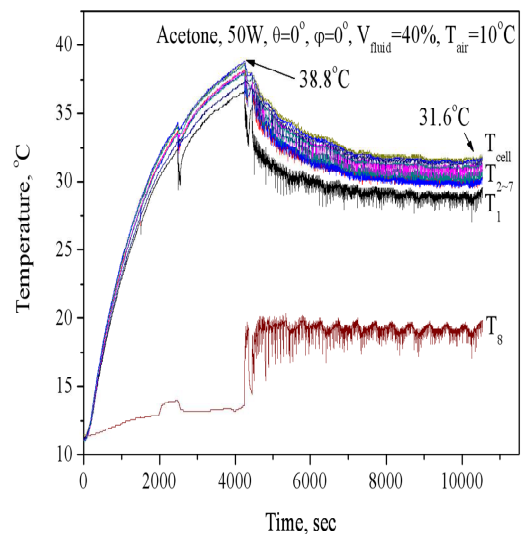


Fig. 6 Temperature variation of cell 50 W, Acetone

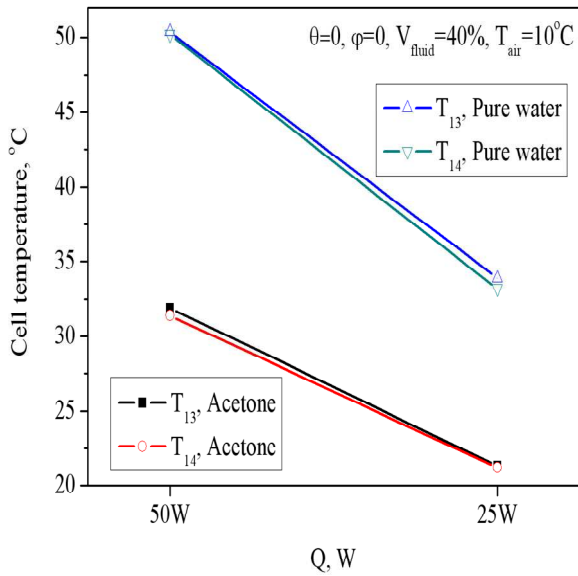


Fig. 7 Cell Temperature on Q, working fluid

thermosyphon, a total of 12 thermocouples (1~7 for cell side and 8~12 for fin side) were installed. All the thermocouples used were calibrated and connected to a computer controlled data acquisition system. The charging system for the working fluids consisted of a vacuum pump, a vacuum gauge, vacuum valves and a connector system which allow charging the desired amount of the working fluid into the test TBTMS.

Water and Acetone were used as the working fluid. In the present study, Acetone was seen to be the most suitable for the systems and used as the working fluid. The TBTMS was thoroughly cleaned by washing with ethanol and then with distilled water. They were then vacuum dried,

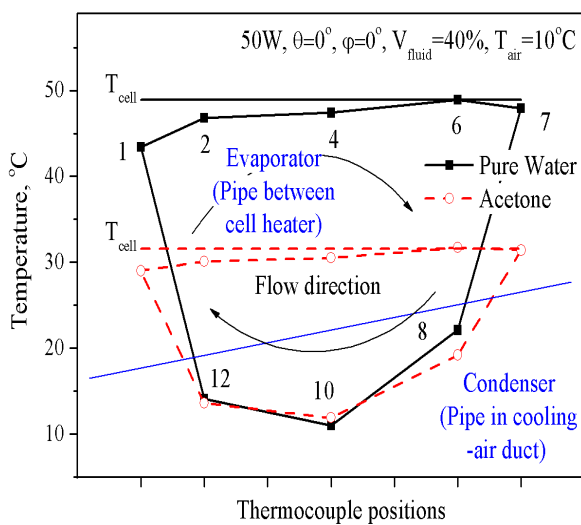


Fig. 8 Transient Temperature Profiles Along Thermocouple Positions

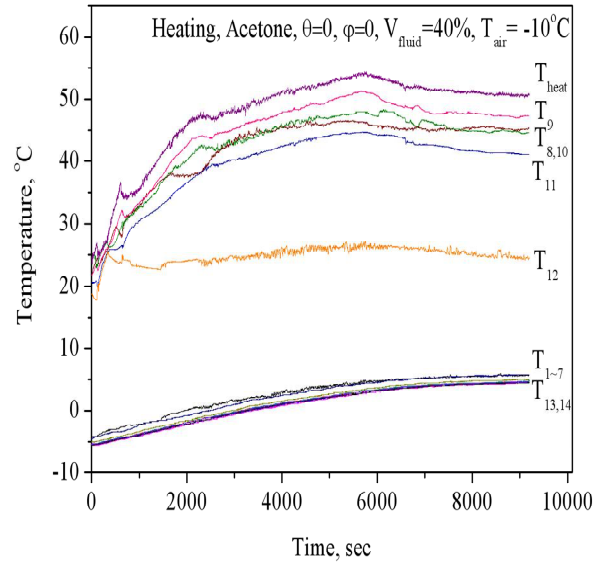


Fig. 9 Temperature variation on heating condition, acetone, $\theta=0, \phi=0$

tested for vacuums and leaks checked. The TBTMS loop thermosyphon was connected to a vacuum pump to remove the inside air and other non-condensable gases. The pump usually reached to the magnitude of 5×10^{-3} torr (Vacuum Pump :DPF-4Z & GHP 240K : ultimate pressure 1×10^{-7} torr) for a dry system.

After the loop thermosyphon was evacuated, a known amount of the working fluid was charged into the tube using the charging system. In the present study, the amounts of the working fluid charged were 2.24 ml as 40 % of total inner volume.

The errors involved in the calculation of the thermosyphon heat transfer coefficient were

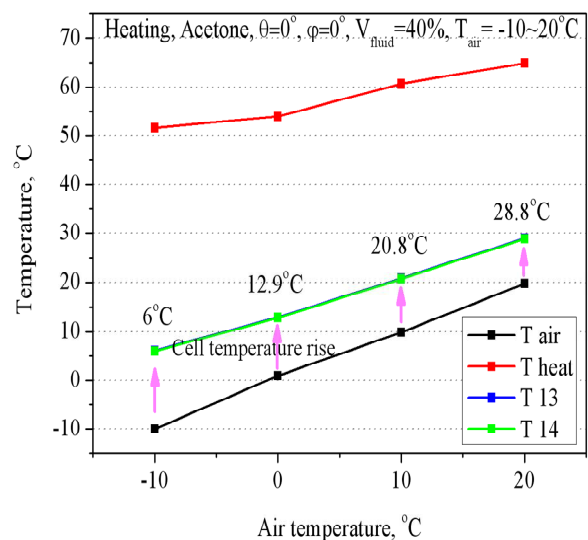


Fig. 10 Battery Heating on Various Outdoor Conditions

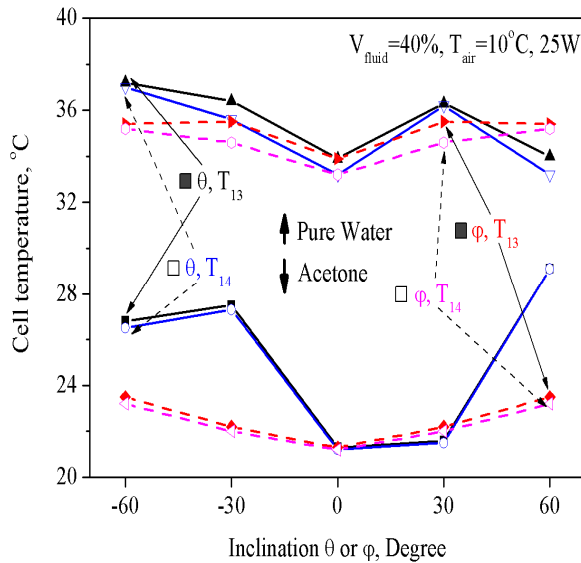


Fig. 11 Cell Temperature on θ or ϕ

generally due to the inaccuracy of the temperature and power measurement. The readings of the temperatures were recorded after the steady state had been reached and fluctuations of about 0.75%+10d for voltage, $\pm 1.3\%$ rdg for current, $\pm 3\text{dgt}$ for the power measurement and about $\pm 0.05\%$ of rdg for temperature (MX100 k-type) were observed.

As shown in Fig. 4, the reason of the orientations in experimental conditions is to suppose to simulate the real road driving conditions with car body's rowing/yawing orientations, shock, cornering, accelerating and braking as gravity force direction on automobile running including battery. 30° and 60° is optional value in experimental conditions shown in Table 2.

3. RESULTS AND DISCUSSIONS

3.1 Battery Cooling Statement

As shown in Fig. 5 and 6, the battery system can be controlled to the optimum operation condition with loop thermosyphon managing unit. Fig. 5 and 6 show that the system is working under critical temperature (55°C with 50 W) to make the optimum working conditions. In these Figures, the battery thermal management system can be applicable for a future battery pack of electric vehicles.

As shown in Fig. 5, battery cell temperatures cooled by loop thermosyphon cooling system with water were converged after 4 hour operations with 50 W heat input. After 2 hours from obtaining the converged temperature, average temperature was observed. Peak temperatures after convergence reached were 50.4°C of T13 and 50.2°C of T14(T_{cell}) respectively.

Figure 6 shows the battery cell cooling operation with 50 W and Acetone was used as the working fluid. As shown in Fig. 6, high and low temperatures were 38.8°C and 31.6°C respectively. The cooling system with Acetone was operated in better condition than the system with water.

As shown in Fig. 5, 6 and 7, operation temperatures were under safe operation temperature. Also temperature difference between high and low temperature were 2.1°C (4.2 %) and 1.9°C (3.8 %) for 50 W input and 1.9°C (5.8%) and 1.3°C (4%) for 25 W. These means that the current battery cooling system can be operated under stable condition.

Figure 8 shows the temperature profiles of the loop thermosyphon battery cooling system. As shown in Fig. 8, the cell temperatures (evaporator section) were sustained in the range less than 10 % uncertainty. And Fig. 8 shows the temperature profiles of finned condenser section from the evaporator inlet (T12) to the evaporator outlet (T8). As shown in Fig. 8, the operation temperatures of battery cells were controlled under the design limit which is ranged between $-20\sim 60^\circ\text{C}$ (Khateeb et al., 2004).

3.2 Battery Heating Statement

As shown in Fig. 9 and 10, the current battery thermal management system in heating condition shows heating performance in various outlet temperatures from -10°C to 20°C .

As shown in Figures, in cold environmental conditions, battery cell were heated by current TBTMS system and temperatures of battery cells with heating were increased to the possible working temperature with rising temperature of $6\sim 12.9^\circ\text{C}$ depending on outside temperatures from -10°C to 20°C by 10°C interval.

Also, as shown in Fig. 11, the effect of various inclinations was investigated. Maximum cell temperatures are in limited range of automotive's normal operation.

As shown in Fig. 11, the operation temperatures of battery cells were sustained under the design temperature.

4. CONCLUSIONS

The present study investigated the automotive battery thermal management system embedded with loop thermosyphon with water and Acetone as working fluid. In the current study, the results of the cooling and heating performance test are as followings with concluding remarks:

In this investigation, the operation temperature of battery cells with the present developed TBTMS

can be sustained under the safe temperature in both working states of heating and cooling.

The present TBTMS can be applicable to the future electric and hybrid vehicles.

ACKNOWLEDGEMENT

This work was supported by the research grant of the KIER(Korea Institute of Energy Research) in 2012.

REFERENCES

Dhameja, S., (2001) *ELECTRIC VEHICLE BATTERY SYSTEMS*, Butterworth-Heinemann, MA.

Khateeb, S.A., Farid, M.M., Selman, J.R., Al-Hallaj, S. (2004) *Design and simulation of a lithium-ion battery with a phase change material thermal management system for an electric scooter*, Journal of Power Sources, 128 (2), pp. 292–307.

Chen, S. C., Wan, C. C., Wang, Y. Y. (2005) *Thermal analysis of lithium-ion batteries*, Journal of Power Sources 140, 111–124.

Kizilel R., Sabbah R., Selman J. R., Al-Hallaj S., (2009) *An alternative cooling system to enhance the safety of Li-ion battery packs*, Journal of Power Sources 194, 1105–1112

Jeon, D.H., Baek, S.M. (2011) *Thermal modeling of cylindrical lithium ion battery during discharge cycle*, Energy Conversion and Management 52, 2973–2981

Wu, M.S., Liu, K.H., Wang, Y.Y., Wan, C.C. (2002) *Heat dissipation design for lithium-ion batteries*, Journal of Power Sources, 109 (1), pp. 160–166

Swanepoel, G. (2001) *Thermal management of hybrid electrical vehicles using heat pipes*, University of Stellenbosch.

Pesaran, A. A. (2001) *Battery thermal management in EVs and HEVs: issues and solutions*, Advanced automotive battery conference, Nevada

Khateeb, S.A., Amiruddin, S., Farid, M., Selman, J.R., Al-Hallaj, S. (2005) *Thermal management of Li-ion battery with phase change material for electric scooters: experimental validation*, Journal of Power Sources, 142 (1–2), pp. 345–353

Index of Authors

AGNEW	B.	323	GOTO	K.	189
AGOSTINI	B.	365	GRAB	T.	213
ALBERTIN	T.	313	GRAKOVICH	L.P.	289
ALIAKHNOVICH	V.A.	319	GROSS	U.	213
AMBROSE	J.	271	GULLY	P.	359
AMELI	M.	323	HABERT	M.	365
ANDERSON	W.G.	69, 277, 329	HARTENSTINE	J.R.	69, 277, 329
ANTONOV	V.A.	105, 283	HIRASAWA	S.	371
AYEL	V.	159, 261, 341	HODOT	R.	455
BAJPAI	A.K.	307	HORIE	R.	225
BAJPAI	J.K.	431	IWATA	N.	267
BARREMAECKER	L.	249	JAN TE RIELE	G.	81
BARTULI	E.	111	JANG	J.C.	471
BASSANI	C.	13	JOUHARA	H.	195
BATURKIN	V.	99	JOUNG	W.	389
BAZZO	E.	153	KABOV	O.	27
BEREND	C.	465	KALED	A.	159
BERTIN	Y.	261, 341	KAMINAGA	F.	225
BERTOLDO Jr.	J.	335	KAMMUANG-LUE	N.	57
BHAUMIK	S.K.	243	KASPER	M.	213
BIELINSKI	H.	401	KAWANAMI	T.	371
BONJOUR	J.	63, 147	KERRIGAN	K.	195
BONNENFANT	J.F.	341	KHANDEKAR	S.	41, 63, 75, 307, 425, 431
BONNET	F.	359	KIM	C.	347
BOUCKAERT	F.	93	KIM	T.H.	389
ČAJA	A.	413	KISEEV	V.M.	219, 335
CÂNDIDO	P.A.	335	KOCHETKOV	A.J.	283
CHAKRABORTY	S.	243	KONEVA	N.	377
CHEN	S.L.	301	KRAVETS	V.Yu.	383
CHEN	S.H.	443	KULAKOV	A.	183, 419
CHENG	L.	449	KUROI	M.	171
CHERKASHIN	V.G.	219	LACHASSAGNE	L.	159, 261
CHERNYSHEVA	M.	177	LARUE DE TOURNEMINE	A.	165
CHOI	J.	347	LECOSSAIS	A.	141, 465
CHOI	C.B.	389	LEE	Y.	347
COQUARD	T.	141	LEE	J.	389
DASGUPTA	S.	243	LEE	K.B.	471
DEHOMBREUX	E.	465	LEE	K.W.	471
DEL COL	D.	201	LEE	Y.S.	471
DEREVYANKO	V.	135	LEE	W.H.	471
DOBSON	R.T.	231	LEFÈVRE	F.	63
DOMOROD	L.	377	LIAKH	M.	395
DOS SANTOS	P.H.D.	153	LYULIN	Y.	27
DUPONT	V.	249	MA	S.P.	389
DUTOUR	S.	159, 165	MAJUMDER	A.	75
ELLIS	D.	69	MALCHO	M.	413
FIGUS	C.	141	MAMELI	M.	41
FILIPPESCHI	S.	201	MANTELLI	M.B.H.	87, 407, 437
FLOREZ	J.P.M.	87	MARCARINO	P.	13
FRANCO	A.	353	MARCHUK	I.	27
GENARO	G.	335	MARENGO,	M.	41
GEORGIN	E.	13	MASHIKO	K.	189, 207
GLUSHCHUK	A.	27	MATSUMURA	K.	225
GOLIKOV	A.N.	105	MAYDANIK	Yu.	111, 177, 255, 455
GONCHAROV	K.A.	105, 283	McGLEN	R.	323

MEHTA	B.	75	SARRAF	D.B.	329
MERINO	A.S.	183	SARTRE	V.	147, 313
MERLONE	A.	13	SASIN	V.Y.	461
MIKIELEWICZ	D.	401	SATO	S.	371
MIKIELEWICZ	J.	401	SAVARD	J.F.	313
MILANESE	F.H.	437	SAVCHENKOVA	N.M.	461
MILANEZ	F.H.	407	SCHILDER	B.	117
MILANEZ	K.W.	437	SHIH	W.P.	301
MISHKINIS	D.	183, 419	SINGH	R.	189, 207
MIYAZAKI	Y.	267	SINGH	J.	323
MOCHIZUKI	M.	189, 207	SINGH	S.K.	431
MUROYTYAN	D.O.	461	SPARASCI	F.	13
MUSACCHIO	C.	13	SRIVASTAVA	P.	431
NAGAN	H.	171	STEPHAN	P.	117, 295
NEKRASHEVYCH	Ia.V.	383	STORCH	T.	213
NEMEC	P.	413	SUNG	B.	347
NESTEROV	D.	135	SUNTSOV	S.	135
NG	B.	323	SUTCLIFFE	C.J.	323
NGUYEN	Thang	189, 207	TAKAHASHI	A.	225
NGUYEN	Tien	189, 207	TAMANNA	S.	69
NUERNBERG	G.G.V.	87	TANTOLIN	C.	123, 455
O'DONNELL	G.E.	195	TARAU	C.	69, 329
OGAWA	H.	267	TARNOVSKY	N.	105
OGER	P.	93	TAVARES	E.G.	437
OLIVEIRA	A.A.M	153	TERDTON	P.	57
PADOVAN	A.	201	TIPTAHARDJA	T.	183, 465
PAIVA	K.V.	87	TORRES	A.	183, 419
PANIGRAHI	P.K.	425	TSENG	H.H.	443
PANIN	Yu.	283	VACCARO	M.	353
PAREHINA	I.V.	461	VAN ES	J.	81
PASTUKHOV	V.G.	255	VAN GEEL	J.	13
PETERS	C.J.	277	VAN OOST	S.	249
PHAN	H.T.	165	VASILIEV	L.L.	129, 289, 319
PLATEL	V.	159, 165	VASILIEV Jr.	L.L.	129, 289
PRADO	P.	183	VASSILIEV	L.	395
RABETSKY	M.I.	289	VELASQUEZ	S.T.R.	87
RADKOV	A.	183	VERSHININ	S.	111, 177, 455
RANA	G.R.	425	VLASSOV	V.	335
RAO	M.	63	WALKER	K.L.	329
RHI	S.H.	471	WANG	X.	449
RIVIÈRE	N.	147	WANG	Y.	449
ROBINSON	A.J.	195	WEICKERT	T.	213
ROMERA	F.	419	WINTER	M.	295
ROMESTANT	C.	261, 341	WITS	W.W.	81
ROSENFELD	J.H.	237	WONG	S.C.	443
RUKOVISHNIKOV	A.	105	WU	G.W.	301
SAHU	T.	425	WUTTIJUMNONG	V.	189, 207
SAITO	Y.	189, 207	XIN	G.	449
SAKULCHANGSATJATAI	P.	57	YAN	X.	13
SANZI	J.L.	237	YUSHAKOVA	S.	177
SARNO	C.	47, 123, 455	ZAGHDOUDI	M..C.	123